AIP Conference Proceedings

AIP Publishing

Volume 3321

Technologies and Materials for Renewable Energy, Environment and Sustainability

TMREES24Fr

Athens, Greece • 8–10 July 2024

Editors • Chafic Salamé, Auday Shaban and Kareem Jaism

Available Online: pubs.aip.org/aip/acp

AIP Conference Proceedings

Volume 3321

ISBN: 978-0-7354-5231-2

ISSN: 0094-243X

pubs.aip.org/aip/acp

AIP Publishing

AIP Conference Proceedings

Technologies and Materials for Renewable Energy, Environment and Sustainability

Volume 3321

Conference collection

Technologies and Materials for Renewable Energy, Environment and Sustainability

TMREES24Fr

Athens, Greece

8–10 July 2024

Editors

Chafic Salamé
European Academy for Sustainable Development, Metz, France

Auday Shaban

Kareem Jaism
University of Baghdad, Baghdad, Iraq

All papers have been peer reviewed.

AIP Publishing

Melville, New York, 2025
AIP Conference Proceedings

Volume 3321

To learn more about AIP Conference Proceedings visit **http://proceedings.aip.org**

Editors

Chafic Salamé
European Academy for Sustainable Development
R & D
11 Rempart Saint Thiebault
Metz, 57000
France

Email: salame@tmrees.org

Auday Shaban
University of Baghdad
Remote Sensing & GIS
Jadryah Campus
Baghdad, 10071
Iraq

Email: auday.h@sc.uobaghdad.edu.iq

Kareem Jaism
University of Baghdad
Physics
Al-Adhamiya District – Antar Square
10011
Iraq

Email: kareem.a.j@ihcoedu.uobaghdad.edu.iq

Authorization to photocopy items for internal or personal use, beyond the free copying permitted under the 1978 U.S. Copyright Law (see statement below), is granted by the AIP Publishing LLC for users registered with the Copyright Clearance Center (CCC) Transactional Reporting Service, provided that the base fee of $30.00 per copy is paid directly to CCC, 222 Rosewood Drive, Danvers, MA 01923, USA: http://www.copyright.com. For those organizations that have been granted a photocopy license by CCC, a separate system of payment has been arranged. The fee code for users of the Transactional Reporting Services is: 978-0-7354-5231-2/25/$30.00

AIP Publishing © 2025 AIP Publishing LLC

No claim is made to original U.S. Government works.

Permission is granted to quote from the AIP Conference Proceedings with the customary acknowledgment of the source. Republication of an article or portions thereof (e.g., extensive excerpts, figures, tables, etc.) in original form or in translation, as well as other types of reuse (e.g., in course packs) require formal permission from AIP Publishing and may be subject to fees. As a courtesy, the author of the original proceedings article should be informed of any request for republication/reuse. Permission may be obtained online using RightsLink. Locate the article online at http://proceedings.aip.org, then simply click on the RightsLink icon/"Permissions/Reprints" link found in the article abstract. You may also address requests to: AIP Publishing Office of Rights and Permissions, 1305 Walt Whitman Road, Suite 300, Melville, NY 11747-4300, USA; Fax: 516-576-2450; Tel.: 516-576-2268; E-mail: rights@aip.org.

ISBN 978-0-7354-5231-2
ISSN 0094-243X
Printed in the United States of America

AIP Conference Proceedings, **Volume 3321**
Technologies and Materials for Renewable Energy, Environment and Sustainability
TMREES24Fr

Table of Contents

Preface: Technologies and Materials for Renewable Energy, Environment and Sustainability 010001

APPLIED PHYSICS

Assessment of heavy metal in abandoned shooting gallery
Milidin Bakalli and Julis Selamaj 020001

Google earth engine app for rapid global assessment of OTEC-suitable zones
Jorge Herrera, Hernando Hernández-Hamon, Juan González, and Andrés Osorio 020002

Role of nanoparticle topography in enhancing random laser performance
Noor Al-Huda A. Abass, Muslim F. Jawad, and Adawiya J. Haider 020003

Comparative analysis of land cover changes in the Amazon region of Colombia
Andrés Felipe Muñoz, Jhonathan F. Maldonado, Julieth Uribe, and Nicole González 020004

Enhancing the performance of a nine-level inverter using an artificial neural network
Sofia Lemssaddak, Abdelhafid Ait Elmahjoub, Mohamed Tabaa, and Mourad Zegrari 020005

Towards maintenance 4.0: Deep learning and LLM-driven bearings fault detection
Adnane Bouchra, Mohamed Tabaa, Mossaab Batal, and Abdelhafid Ait Elmahjoub 020006

Impact of artificial intelligence on mental health and chronic diseases: A literature review
Salma Chebbawi, Mohamed Tabaa, and Hassan Badir 020007

Characterisation of Pt@ ZnO nanoparticles synthesised via laser production in liquid
Sarah M. Talib, Adawiya J. Haider, and Sharafaldin Al-Musawi 020008

Neurotransmitter as a model therapeutic platform: A mini-review
Aliaa A. Razzak, Zahraa S. Al-Garawi, Adawiya J. Haider, and Bahaa Hassan 020009

Study the physical properties of $Se_{65}Sn_{35-x}Te_x$ alloys
Marwa Ayad Abdulmajeed, Jannah Hasan Azzawi, and Kareem Ali Jasim 020010

Morphological and mechanical properties of pure nanocomposite PMMA/ZnO/MgO for teeth-filling applications
Abbas F. Khorsheed, Adnan R. Ahmad, and Alaa J. Ghazai 020011

Analysis of the effect of composition ratio, structure and properties of ZnO/MgO differentiated materials
Abbas F. Khorsheed, Adnan R. Ahmad, and Alaa J. Ghazai 020012

A study of kinetic and thermodynamic on serum Na/K-ATPase in patients with Leukaemia
Tiba A. Khudaer AL-Taiee, Abdulrahman. K. AL-Taiee, Mohammed A. Mohammed, and Kareem A. Jasim 020013

The neutron yield of the (P, N) reactions of ruthenium (Ru44)
Israa Mudher Hassan, Mustafa H. Shareef, and Mohammed H. Shareef 020014

Calculate the cross sections for ^{235} Th (*a, n*) ^{238}U by the revers reaction for the ground state
Saad Jasim Mohammed, Mustafa H. Shareef, and Mohammed H. Shareef 020015

Single and cascade reliability stress-strength models of the truncated Komal-Weibull distribution
Sairan Hamza Raheem and Bayda Atiya Kalaf 020016

Investigation of the form factors and charge density distribution for some upper limit for fp-shell nuclei
Aeshah Ali Hussein, Sarah M. Obaid, Shaimaa A. Abbas, Noor Adil Mohammed, and Fouad A. Majeed 020017

Impact thickness on performance of higher quality ZnTe photodetectors
Hanan K. Hassun, Bushra H. Hussein, Bushra K. H. Al-Maiyaly, Yusra K. H. Moussa, Auday H. Shaban, and Kareem A. Jasim 020018

Digital image enhancement by noise removal post-decryption applied by a combination of wave transformers
May A. Salih, Suad A. Alasadi, and Baydaa Jaffer Al-Khafaji 020019

A comparative study of the effect of thermal neutron and gamma irradiation on the electrical properties of the $Ge_{40}Te_{60}$ semiconductor alloy
Al-Zahraa Y. Abdalsajjad, Rafah Ismael Noori, Kassim Mahdi Wadi, and Kareem A. Jasim 020020

Comparative analysis of Haldar-Wagner and Williamson-Hall methods utilizing x-ray diffraction patterns of magnesium oxide nanoparticles
Marwa Taleb and Khalid Hellal Harbbi 020021

Steganography of image based on random key generation and XOR LSB substitution
Zahraa Modher Nabat, Shaymaa Abdulhussein Shnain, Baydaa Jaffer Al-Khafaji, and May A. Salih 020022

Design and simulation micro strip patch (1×4) array antennas for S-band applications
Hiyam Majeed Ahmed, Abdullah Hamoud Mohammed, and Muatazbullah Ibrahim Abdullah 020023

Meta heuristic algorithms to solve multi objective model based on single machine scheduling
Tahani Jabbar Khraibet and Bayda Atiya Kalaf 020024

Synthesis and characterization of Zn-doped CuO nanoflowers: Enhancing properties through hydrothermal technique
Ali Khudair Abbas, Selma M. H. AL-Jawad, and Natheer Jamal Imran 020025

An examination using semi-empirical methods to study how solvents influence the vibrational properties of the HCOOH molecule
Ibraheem M. Mohammed and Mohammed Rasheed 020026

Temperature-effective substrate on physical properties of copper sulfide thin films prepared by thermal chemical spray
Sabah Salman Hamdi 020027

An approach to sustainability and circularity regarding the influence of the heat treatment duration of sugar syrup and the addition of Aronia Melanocarpa by-products as powder on the physico-chemical characteristics of artisanal chocolate
Tilia Cristina Murariu, Florin Daniel Lipșa, Georgiana Venin, Anca Tulbure, Petru Marian Cârlescu, Bianca Balint, Alessio Vincenzo Tallarita, Gianluca Caruso, Maya Julian, Ramona Giurea, and Elena Cristina Rada 020028

The calculation of ground deformation caused by earthquake through remote sensing and GIS in Diyala-Iraq
Ali A. Hussein, Auday H. Shaban, and Najah A. Abd 020029

Study the effect of each of the dislocation and the burgers vector on the lattice parameters through x-ray peak profile analysis
Maysaa A. Hameed and Khalid H. Harbbi 020030

A comprehensive literature survey on mineral exploration techniques using remote sensing and GIS
Mohammed A. Mohammed, Faisel G. Mohammed, Mustafa E. Hammadi, Maryam H. Ali, and Ali Saeed Jassim 020031

Simulation and analysis the effect of the electron velocity on the electron path and the generation of photons within the undulator of free electron laser
Jaafar Hussein Sabri and Thair Abdulkareem Khalil Al-Aish 020032

Simulation and analysis the effect of the distance between the two rows of magnetic poles on the electron oscillation movement and the characteristics of the output free electron laser
Jaafar Hussein Sabri and Thair Abdulkareem Khalil Al-Aish 020033

Effect of changing the radius curvature of the objective lens on the performance of a binary telescope
Alaa K. Shwayya, Maryam K. Hasan, Noor S. Ahmed, and Alaa B. Hasan 020034

Utilizing applied mathematics, A flat model is used to represent contiguous UTM coordinates over the territory of Iraq
Abeer H. Abdulameer, Baqer H. Sayyid, and Loay E. George 020035

Shape memory polymers and technological development
Rola Abdul Al Khader Abbas, Mohammed Hamza Al-Maamori, and Abdul Hameed Raheem Mahdi Al-Sarraf 020036

Theoretical study of charge transport kinetics of zinc contact with tin oxide using quantum transition theory
Taif Saad Al Maadhede, Raed Mahdi Salih, Hadi J. M Al-Agealy, and Mohsin A. Hassooni 020037

Encryption and security for video conferencing : A review
Baydaa Jaffer Al-Khafaji and Abdul Monem S. Rahma 020038

Virulence of genes *stx2* and *rfbE* detection in enterohemorhagic *E. coli (O157:H7)* isolated from milk and meat products
Harith Basim Ibrahim, Khalid Mahmood Hammadi, and Amal Aziz Kareem 020039

Construction of an industrial fiber optic sensor network for oil field management: A literature survey
Younis M. Hasan, Faisel G. Mohammed, and Mohammed Mejbel Salih 020040

Modern technology for encrypting video conversations
Baydaa Jaffer Al-Khafaji and Abdul Monem S. Rahma 020041

The effect of the percentage of doping with silver and zinc oxide on the properties of the coating layer for nickel and copper
Mina S. Nsaif, Iman Adnan Annon, and Ahmed S. Abbas 020042

A comparison of some robust methods and quantile regression
Rabab Abdulrida Saleh and Iqbal Mahmood Alwan 020043

A study of sustainable polyester composites incorporating recycled materials
Khulood Ibrahim Dawood, Atheed Habeeb Taha Al-Temimi, Nuha Hadi Jasim Al Hasan, Haider Maath Mohammad, and Safaa A. S. Almtori 020044

Bibliometric-statistical study: Biopolymer trend
Segundo Rojas Flores, Santiago M. Benites, Magaly De La Cruz-Noriega, and Renny Nazario-Naveda 020045

Mapping of Rn-222 gas concentrations in Baghdad governorate by using (CR-39) detector and remote sensing
Imad H. Ahmed and Mahmood S. Karim 020046

Simulation investigations of physical docking of drug developed with nanomaterial for cancer tumor treatment
Iman M. Kadhim and Bahjat B. Kadhim 020047

Enhancement and analysis of X-ray images to diagnose pulmonary inflammation
Hawraa Hadi and Dhufr Hadi 020048

Simulation of physical properties for biomaterials docking mechanism with the gouty articular cartilage
Sarah A. K. Athari and Bahjat B. Kadhim 020049

The possibility of electrical transition B ($E2$; $0_1^+ \rightarrow 2_1^+$) and determining the shape of the nuclei of iron
Reem Gani Abdulrazak Mohammed and Sameera Ahmed Ebrahiem 020050

CHEMISTRY, APPLIED BIOLOGY

Investigation of coated nanofibers based on sodium alginate loaded with antimicrobial agents
Hanan M. Khudir, Akram R. Jabur, and Ishraq A. Kadhim 030001

Isolating the prolidase enzyme and studying some pharmaceutical compounds for people with thyroid
Vian Ismael Mohammed and Sayran Sattar Saleh 030002

Detection of polymorphisms and level for the IL-20 cytokine in psoriasis patients
G. R. Schneiter, A. A. N. Dhabaan, and Q. N. Raddam 030003

Histomorphometric and histochemical study of the adrenal gland in adult males of the Iraqi pin-tailed sandgrouse bird (*Pterocles alchata*)
Wafaa Barghash Obaid and Nahla A. Al-Bakri 030004

Study the immunological and hematological parameters of rabbits infected by different *Klebsiella pneumoniae* antigens
Mariam Esam Hamed and Khalid Mahmood Hammadi 030005

A comparative study of some mechanical and thermal properties of single and hybrid composites of polyester and agricultural waste powders
Abdulraheem Dheyaa Ibrahim and Suaad H. Aleabi 030006

Manufacturing of high-quality plastic chairs from (unsaturated polyester/glass fiber) reinforced by nano chicken eggshell particles
Rana Jamal Mizban and Widad Hamdi Jassim 030007

Investigating air pollution and its relationship to geographic and demographic data in Karbala
Khalid H. Abbas Al-Aarajy, Kareem Hassan Alwan, Mohammed A. Mohammed, Zainab H. Mohammed Hassan, and Kareem A. Jasim 030008

The bacterial effectiveness and cytotoxicity of the polymer loaded with the nano silver nitrate
Mohamed Khalil Alioui, Adnan Raad Ahmed, Randa Kamil Hossain, and Ahmed Hussein Ali 030009

Acetylcholine esterase and antioxidative markers: A study of autism spectrum disorder individuals
Ako Saber Kaky and Sayran Sattar Saleh 030010

Blood variations of male albino mice treated with the antibiotic (Cefoperazone)
Hussein Ali Salman AlAmiri and Hanan Y. Muhsin 030011

Blood electrolyte levels and renal functions in the regulation of blood pressure
Safa N. Ali and Mouruj A. Alaubydi 030012

A comparative study of the effectiveness of prolidase, proline dehydrogenase and some hormones in patients with immune and non-immune thyroid disease
Vian Ismael Mohammed and Sayran Sattar Saleh 030013

Effect of fish collagen and natural extracts on burn wound healing
Rusul Alani, Fatimah J. Al-Hasani, and Emad S. Al-Hassani 030014

The role of acetylcholinesterase (AChE) in autism spectrum disorder (ASD): Partial purification and evaluation of inhibitory compounds
Ako Saber Kaky and Sayran Sattar Saleh 030015

Extraction of invertase from Baker's yeast utilizing PEG8000 with potassium phosphate and potassium citrate in aqueous two-phase systems
Meaad H. Kadhim and Khalid W. Hameed 030016

Extraction of invertase enzyme from potato tubers by aqueous two-phase system
Meaad H. Kadhim and Khalid W. Hameed 030017

ENERGY SOURCES IN ADVANCED TECHNOLOGIES

Optimizing biogas production through co-digestion of cow dung and chicken droppings
Basirat Kikelomo Odunola, Wunuken Carlos Solomon, Sani Umar Mohammed, Aisha Sa'ad, Aimé Claude Nyoungue, and Nkague Nkamba Leontine 040001

Simulation of misalignment induced by sun tracking errors in high-concentrator photovoltaic systems across different regions
Ourraoui Imane and Ahaitouf Ali 040002

Bioethanol production from corn straw via steam explosion pretreatment and fed-batch enzymatic hydrolysis
Tatiana Ramírez-Contreras, Laura Camila Porras Borja, and Yineth Piñeros-Castro 040003

Potential use of banana waste as fuel for the generation of electrical current
Segundo Rojas Flores, Santiago M. Benites, Magaly De La Cruz-Noriega, and Renny Nazario-Naveda 040004

Sustainable electrical energy generation using tangerine waste in microbial fuel cells
Segundo Rojas Flores, Santiago M. Benites, Magaly De La Cruz-Noriega, and Renny Nazario-Naveda 040005

Improving energy management and thermal comfort in office buildings: A comparative study of AI models for temperature prediction
Amal Azzi, Mohamed Tabaa, Asmae Chakir, Badr Chegari, and Hanaa Hachimi 040006

Utilization of high alcohol and ferrocene for the production of carbon nanotube from a diesel engine
Mohamed Almanzalawy, Sameh Nada, Ahmed Elwardany, and Marwa Elkady 040007

Optical, thermal and electric properties of PVC-C thick film composites
Laheeb A. Mohammed, Khansaa Nasir Aklo, Shatha H. Mahdi, and Kareem A. Jasim 040008

Exploring key parameters affecting thermal management of lithium-ion batteries: A numerical investigation
Mohamed Kh. Saudi, Mohamed Emam, Hidetoshi Sekiguchi, Ahmed S. G. Khalil, and Hamdy Hassan 040009

Effect of the inlet nozzle on the output power of a small-scale diffuser-augmented wind turbine: Two- and three-dimensional numerical study
Ahmed T. Nile, Mohamed Emam, Shinichi Ookawara, and Sameh Nada 040010

Standalone hydrogen production and storage system powered by photovoltaic under different climate conditions
Mohamed G. Basiony, Sameh Nada, Shinsuke Mori, and Hamdy Hassan 040011

Hybrid solar photovoltaic with vertical axis wind turbine grid-connected system for streetlighting application in Egypt
Masoyi Sanda, Mohamed Emam, Shinichi Ookawara, and Hamdy Hassan 040012

Techno-economic and environmental analysis of a hybrid energy system using a pumped hydro storage system for powering a university building
Simon Juma Bullen, Mohamed Emam, Hidetoshi Sekiguchi, and Hamdy Hassan 040013

Performance analysis of a novel solar chimney design for building ventilation
Prince Adolphus Juah, Mohamed Emam, Sameh Nada, Shinichi Ookawara, and Hamdy Hassan 040014

A developed trombe wall as a passive system for residential buildings: A simulation study
A. Abdelsamea, H. Hassan, H. Shokry, T. Asawa, and H. Mahmoud 040015

Harvesting power from saturated steam: Utilizing TEG systems for waste heat recovery
M. A. Mahmoud, Sameh Nada, Shinsuke Mori, and Hamdy Hassan 040016

Emission characteristics of a gas turbine swirl combustors firing NH_3/H_2 fuel mixture
Ehab Sabry Rashed, Saleh Abo-Elfadl, Mohamed Emam, S. Mori, and Hamdy Hassan 040017

Apply green economy to waste management
Nassif J. Alkhattabi, Hayder Al-Guboori, and Joumana A. Younis 040018

Dye sensitized solar cell based on TiO_2-SnO_2 mesoporous film
Zahraa Faisal Ghazi, Odai N. Salman, and Mohammed O. Dawood 040019

Simulation of interaction energy and thermodynamics properties of developed nano drug docking with glucose for the diabetes treatment
Shaymaa A. Jaber, Bahjat B. Kadhim, and Ali Taher Mohi 040020

ENVIRONMENTAL QUALITY FOR SUSTAINABILITY

The effectuation of changing the weight fraction of some agricultural waste powders on some mechanical and thermal properties of unsaturated polyester composites
Abdulraheem Dheyaa Ibrahim and Suad H. Aleabi 050001

Batch adsorption experiment based mullite/zinc ferrite for heavy metals removal from wastewater
Wasan Ziedan, Mukhlis M. Ismail, and Wafaa A. Hussain 050002

MANAGEMENT, LAWS, AND SUSTAINABLE DEVELOPMENT

The impact of emotional stress on the food behavior of Lebanese population
Reem Elkawam, Rola Elcheikh, Ali Amhaz, Maha Krayem, Samer Sakr, and Imtithal Sheet 060001

Spatial equity in planning youth and sports forums in the city of baghdad
Tahini Salman Fankal and Moheb Kamel AL-Rawe 060002

Knowledge, attitude, practice and prevalence of food allergy among young Lebanese population
Ghinwa Nemer, Samer Sakr, Imtithal Sheet, Lamis Karaki, Nivine Bachir, Suzana Salhab, and Ali Al Khatib 060003

Circular economy and sustainable development goals approaches for environment improvement in Uzbekistan
Ergash Egamberdievich Kobilov, Kh. F. Batirov, F. S. Mardonava, Anzhelika Karaeva, Alberto Pietro Damiano Baltrocchi, Marco Carnevale Miino, Ramona Giurea, Marco Ragazzi, Vincenzo Torretta, and Elena Cristina Rada 060004

Preface: Technologies and Materials for Renewable Energy, Environment and Sustainability

"TMREES Conference Series: Technologies and Materials for Renewable Energy, Environment and Sustainability" aims to promote sustainable, healthy and diverse ecosystems; encourage and support the Sustainability and development of security systems through green-based and clean resources, bringing together participants from international organizations, universities, industry and administrative to exchange innovative ideas, explore enabling technologies, share experiences in sustainability issues, open a new window on the circumstances of the classical energy sources and their harmful impact on the society.
The TMREES program is structured in plenary, oral and poster presentations and covers the entire range of Energy Sources, Environment and Sustainability, focusing on the latest scientific and technological innovations.

The Topics and Special Themes that are treated with Tmrees Conference Series, are:

Applied Physics, Mathematics and Computational for Sustainable Development
Energy Systems, Biophysics, Optical Physics, Condensed Matter and Materials Physics, Nanotec hnology, Mechanics, Computational, Machine Learning, Biomaterials and Tissue Engineering, P olymer Science and Technology

Energy Sources and Advanced Technologies
Photovoltaic Panels and Cells, Concepts, Modeling & simulation, Microelectronics, Characteriza tion, testing, Thin Film, Cells-Modules-Systems-Dye Sensitized, Organic Based-Polymer-Nanotechnologies.
Thermal: Solar applications and Photo chemical Conversion, Integration in buildings and urban p lanning. Recovery from wastes, Wind energy, Bioenergy-biomass-
Biofuels, Hydropower, Marine. Hydrogen Energy and Fuel cells.

Chemistry, Applied Biology
Batteries, Organic chemistry, Analytical chemistry, medicinal and pharmaceutical chemistry, Cat alysts, Polymer, Textiles. Radioactive waste, Biomarkers, biochemistry, biotechnology, marine b iology, plant biology

Environmental Quality for Sustainability
Pollution and waste management, Resources management and policy, Marine ecology, Landscaping, Water resources, Ecological Issues.

Management, Laws, and Sustainable Development
Energy Policy, Building Management Systems, Future Markets, Business Opportunities. Green E conomy, Green growth governance, climate-friendly economy.

Chafic Salame, Elena Cristina Rada, Auday Shaban, Kareem Jasim, Maya Julian
European Academy for Sustainable Development
EURACA, 57-France Decree 818559064

Technologies and Materials for Renewable Energy, Environment and Sustainability
AIP Conf. Proc. 3321, 010001-1–010001-1; https://doi.org/10.1063/12.0036957
Published under an exclusive license by AIP Publishing. 978-0-7354-5231-2/$30.00

Assessment of Heavy Metal in Abandoned Shooting Gallery

Milidin Bakalli[1,a], Julis Selamaj[2,b]

[1]*Faculty of Professional Studies, University of Aleksandër Moisiu – Durrës, Currila venn, 2001 Durrës, Albania*
[2]*Laboratory of Chemistry, Central Laboratory of Armed Forces, Myslym Keta venn, 1002, Tiranë, Albania*

[a)] Corresponding author: *milidinbakallim@uamd.edu.al*

[b)] jselami2@gmail.com

Abstract High concentrations heavy metal poses a major threat in environmental due to toxic effects. They can accumulate in food chain, causing several public health concerns. The objectives of this study are determination of heavy metals (Pb and Cu) contents in abandoned shooting gallery soil and to assess the degree of pollution. Shooting galleries are high loading of bullet which releases lead, antimony, copper, nickel and zinc into the soil. The study is carried out in one of the shooting gallery used until 2005 in the city of Tirana by the Armed Forces. The shooting range has been used by Ministry of Defense as training center for army officers and soldiers around 25 years. The maximum distance from fire position was about 200 meters. 60 soil samples are analyzed for determination of lead and cooper. These metals were determined by flame atomic absorption spectrometry. The concentration of copper in these samples ranges from 153.50 mg/kg to 447.85 mg/kg soil, while the lead concentration ranges from 254.50 mg/kg to 948.44 mg/kg. Based on the data concentration of both heavy metals is high. The high concentration of copper and especially lead can move through the soil and end up in the groundwater and some root plants. This study should consider, due to the amount of released of heavy metals from ammunition and negative effect on soil, water and living organisms. We recommend a continuous assessment to see the effect of pollution and to prepare a management plan in this area, because near the area are many private buildings.

Keywords: shooting range; pollution; human health; soil samples; Tirana

INTRODUCTION

Environmental pollution by heavy metals is one of the most negative impacts on human and ecosystem health. Humans contribute much more to environmental pollution than natural pollution. Shooting galleries are contaminated sites especially by heavy metals. The ammunition can cause significant deposits of heavy metals like lead, antimony, copper and zinc. They accumulate in the soil and still pollute the biota. The objective of our study was to determine the concentration of lead and copper, and to assess the degree of pollution at one abandoned open shooting gallery in Tirana. The assessment of soil contamination was done according to the Finnish legislation for contaminated soil [1].

TABLE 1. Threshold and guideline values for metals in soils (extracted)

Substance	Threshold value mg/kg	Lower guideline value mg/kg	Higher guideline value mg/kg
Copper (Cu)	100	150 (e*)	200 (e)
Lead (Pb)	60	200 (t*)	750 (t)

**The guideline values have been defined on the basis of either ecological risks (e) or health risks (t)*

This shooting gallery was used until 2005 by the Army Forces for military training of lightweight and portable arms. Participating in the shooting gallery is based on the training plan of the Army Forces three times per year. According to the information provided by the Ministry of Defence, after 2005 the shooting range hasn't been used by the Armed Forces. Actually, this site is abandoned, and everywhere has access in this area. Especially used for livestock grazing and near this area are some buildings. During the inspection of this area, we noticed some private wells used by families below the shooting range. This shooting range is near the river of Tirana, where steam and surface water flow into it. So the presence of metals in the soil may pollute the river and equally affect its biota. Metals can deposit on the soil as particles or associated with soil components and can change in pH or redox conditions. They can form some complex with organic compounds and may be transported to the water. Water and heavy metal pollution is evidenced by some studies in several military training areas. We think our investigation is

Technologies and Materials for Renewable Energy, Environment and Sustainability
AIP Conf. Proc. 3321, 020001-1–020001-5; https://doi.org/10.1063/5.0290534
Published under an exclusive license by AIP Publishing. 978-0-7354-5231-2/$30.00

important because we determine the concentration of heavy metals in soil. In this shooting range, weapons are used like calibre 12.7 mm. We know that bullets are composed of some toxic metals like lead, antimony, copper, bismuth, nickel etc. At high doses, these metals and their compounds have negative effects on human health. Properties of heavy metals consist of low degradation for a long period, and may be absorbed by the biota. First, soil microorganisms are exposed to heavy metals. In the ecosystem, heavy metals are entering the food chain, and also affect the biodegradability of organic pollution and cause a double effect of pollution on the environment. Lead can bind strongly to particles, such as soil, sediments and sewage sludge, and forms its salts lead carbonates and sulphates [2, 3, 4]. It can accumulate in biota, feeding primarily on mussels and worms. In humans, lead may accumulate in the bones. In wild mammals, there have not been reported toxic effects of heavy metals. Lead is taken up by terrestrial plants through the roots and, in a lesser way, through the shoots. The toxicity of lead is at a concentration of 100 to 1000 mg/kg in soil. The effects are visible photosynthesis, growth etc. In humans, lead induces carcinogenic processes, DNA damage, repair system and cellular tumour regulatory genes [5]. Lead can affect the transcription process by replacing zinc in certain regulatory proteins [5]. So lead affects the brain and causes neurological toxicity [6]. Cooper is classified as an essential element because it's needed by many enzymes. Due to man's anthropogenic and industrial activities, it can accumulate in the soil and be taken up by plants. Cuproenzymes can change states from Cu^{2+} to Cu+ in redox reactions and may be known as toxic effects, because the radical hydroxyl group from this reaction can react with various biomolecules [7]. So many studies report that cooper induces DNA strands to break and oxidation of bases via oxygen free radicals [8] and in vitro studies confirm that cooper induces low-density lipoprotein oxidation [9]. Based on the physicochemical properties of the soil, heavy metals may have mobility in underground water and plants and consequently can enter into the food chain. This pathway can cause serious health problems [10, 11, 12, 13, 14, 15, 17]. Many studies result in shooting galleries being a major problem with gelation of soil [10, 17, 18, 19]. The concentration of heavy metals in soil is linked by the intensity of shooting activity and total spent ammunition. They can pollute groundwater and wells around the shooting gallery. Prolonged exposure can cause accumulation in the body. In general, the main metal in bullets is lead, but various other metals are also found in bullet composition, like antimony, copper, nickel etc.

MATERIAL AND METHODS

Soil samples were collected at a shooting gallery located in Tirana city (N 41.359331, E 19.856214), 5.8 kilometres from Tirana centre. Its valley is covered by vegetation like grass and surrounded by arbutus unedo. Currently, this area is abandoned, and nearby has new private buildings, but until 2005 it was used as an open shooting gallery for army officers and soldiers. Samples were collected in 2021 according to the recommendation method for metal concentration in soils [20]. We have chosen five plots for sampling (Figure 1). Six samples were collected for a target line. Soil samples were collected from 0, 25, 50, 100, 150 and 200 meters from the fire line. Samples were taken at 0-20 cm depth by a cylinder sampler. During sampling, we found many bullets. Every sample from each plot is mixed and homogenized for a representative sample. All samples are stored in zip-lock polyethylene bags and transported to the Central Laboratory of the Armed Forces for additional treatment. Samples were dried in an oven at 105-0C for 4–5 hours and sieved to 2 mm grain size to remove stone, dry tree leaves and spent bullets. 0.5 gram dried samples were digestion with 100 ml aqua regia (HNO3/H2O) 1: 3 for 12 hours. After that, the digestion procedure continued in a dry heating-block at a temperature of 80-0C for two hours. After digestion, samples are filtrated and analysed by flame atomic absorption spectrometer (Contra AA 300, Analytic Jena). Control and curves were done using reference material (RM) for lead and cooper. The calibration curves for lead and cooper were characterized by a high correlation coefficient respectively (RPb = 0.993) and (RCu = 0.999).

FIGURE 1. Diagram of shooting gallery

RESULTS AND DISCUSSION

The cooper and lead concentration in the shooting gallery varied with sampling. In Figure 2 the minimum and maximum values of Cu concentration at six sampling points. The concentration of Cu on the fire line varies from 40 to 2500 mg/kg; at 25 meters 20-2600; at 50 meters 20- 2520 mg/kg; at 100 meters 300-1540 mg/kg; 150 meters 220-2580 and at 200 meters 80-10400 mg/kg. The lowest concentration of cooper corresponds to 20 mg/kg at 25 and 50 meters from the fire line. The highest concentration of cooper was 10400 mg/kg at 200 meters from the fire line. The concentration of lead (Figure 3) ranges from 700-5800 meters at the meters; 64-6400 meters at 25 meters; 64-8000 mg/kg at 50 meters; 64-5600 mg/kg at 100 meters; 64-5100 mg/kg at 150 meters and 64-2440 mg/kg at 200 meter from the fire line. The highest concentration of Pb corresponds to meters (8000 mg/kg) at 50 meters from the fire line.

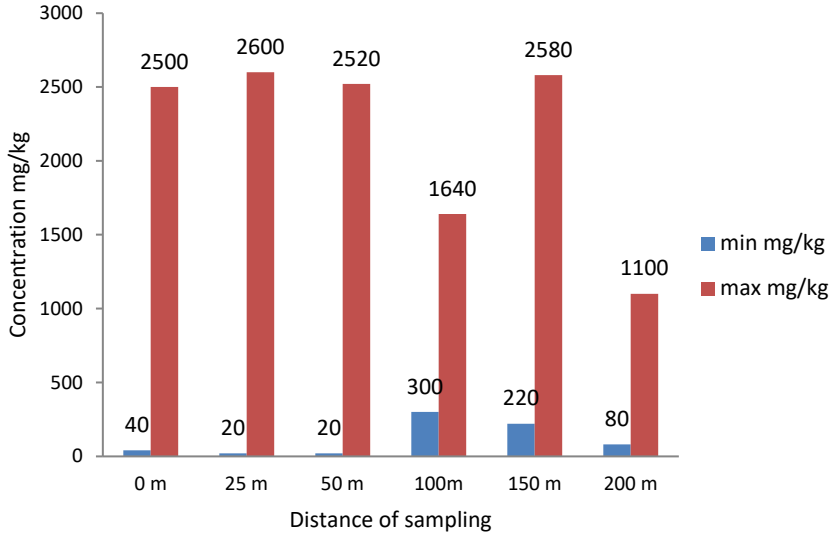

FIGURE 2. Concentration of Cu in shooting range

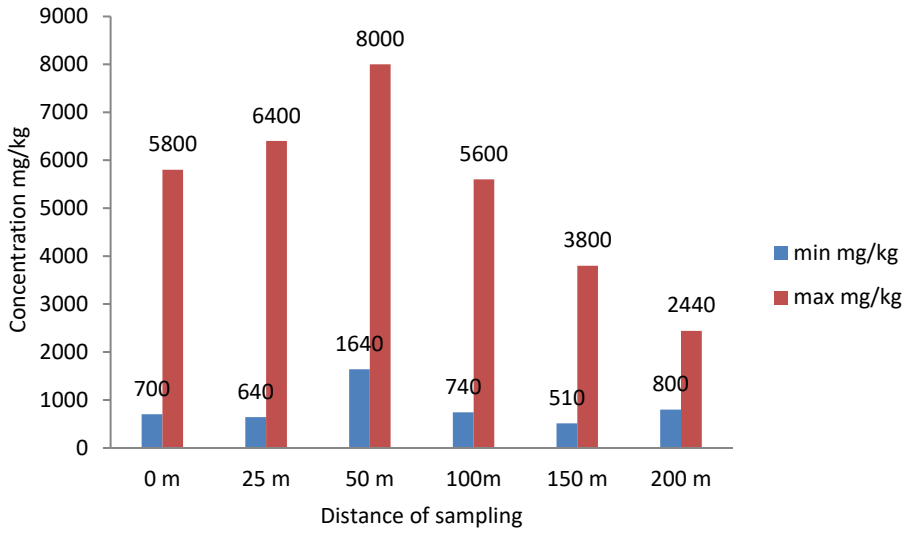

FIGURE 3. Concentration of Pb in shooting range

The average values of lead and cooper are shown in Figure 4. This data showed a different concentration of Cu

and Pb. The average concentration of Cu varies from 614 to 1791 mg/kg, whereas the average concentration of Pb varies from 1018 to 3793 mg/kg. The lowest concentration of lead is registered (1018 mg/kg) at 200 meters from the fire line, whereas the highest concentrations correspond to (3793 mg/kg) at a 50-meter distance from the fire line. The lowest concentration of copper (614 mg/kg) was recorded at the fire line, but the higher concentration was recorded at 200 meters (1791 mg/kg). The different distribution of metals may be due to the shooting dynamics, ammunition sliding and time exposure of bullets [19]. The higher concentration of heavy metal in the fire line lines, 614 mg/kg Cu and 2532 mg/kg Pb, may be due to the cartridge residues at the fire point. The higher concentration of heavy metals correlates to the frequency of shooting ranges used by Army Forces until 2005. Some studies have discovered a higher concentration of lead [21] and copper in shooting ranges [22, 23]. Our data correlate with the above studies.

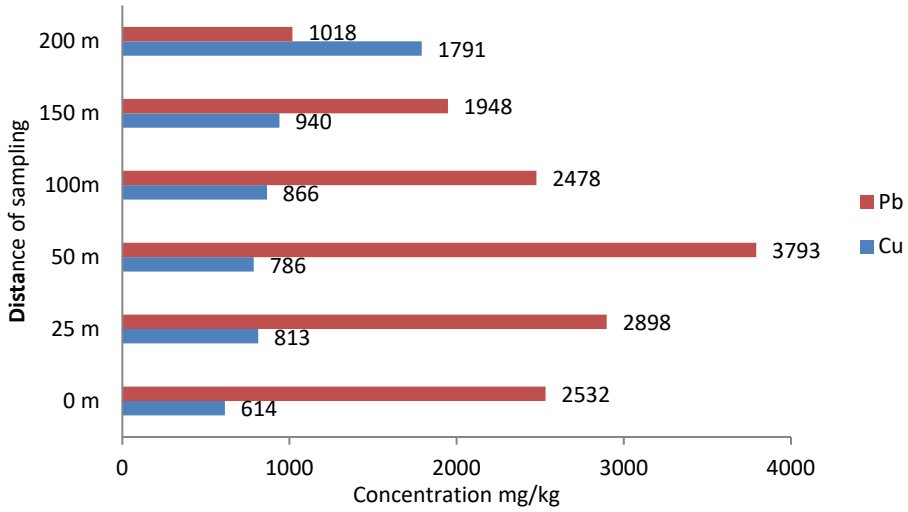

FIGURE 4. Average concentration of heavy metals

The above results of metals in each soil sample were compared with the sample and guideline values of the Finland government Decree. All the samples have high concentrations above the thresholds for copper and lead. Summary statistics (Table 2) also show a higher percentage of samples with a concentration above the lower and higher guideline. 88.3 % of samples have a Cu concentration above the lower value. Regarding lead content, 100% of samples have a concentration above the threshold, a lower and higher value.

Table 2. Soil samples compare with Finnish guideline

Samples for Cu concentration (n= 60)		
Samples with concentration above the threshold value	**Samples with concentration above the lower value**	**Samples with concentration above the higher value**
n 60	53	53
% 100	88.3	88.3
Samples for Cu concentration (n= 60)		
Samples with concentration above the threshold value	**Samples with concentration above the lower value**	**Samples with concentration above the higher value**
n 60	60	60
% 100	100	100

If we compare our data with Directive 86/278/EEC, Annexes IA, IB and IC for limit values for the concentration of heavy metals in soil, 18.3% of samples are within the limit for Cu concentration, and 81.7% are outside the limit. Regarding the Pb content, all samples are outside the limit.

CONCLUSION

The data presented in this paper shows a higher contamination of soil by copper and lead in this abandoned shooting range. The high content of these metals may be a consequence of their long-term use for military training. These data will provide a baseline for subsequent studies. The higher concentration of these heavy metals in the shooting range may be a risk environmental pollution and can affect ecological and human health risks. These metals can penetrate through the soil and at different pH of the soil, can dissolve and contaminate the groundwater. We suggest continued deep monitoring, because this area in recent years has been being urbanized. We suggest some chemical salts that immobilize heavy metals in the soil and remove a layer of soil about 50 cm to 1 meter before building residential buildings in the future.

REFERENCES

1. MEF, Government Decree on the Assessment of Soil Contamination and remediation needs. https://www.finlex.fi/en/laki/kaannokset/2007/en20070214
2. S. Storgard Jorgensen and M. Willems, Ambio, **16**(1), 11-15, (1987)
3. S. Manninen and N. Tanskanen, Archives Environ Contam Toxicol, **2**4(3), 410-414 (1993),
4. K. Murray, A. Bazzi, C. Carter, A. Ehlert, A. Harris, M. Kopec, J. Richardson and H. Sokol, J Soil Contam, **6**(1), 79–93 (1997)
5. J.B Marcus, *Vitamin and mineral basics*: The ABCs of healthy foods and beverages, including phytonutrients and functional foods, Healthy vitamin and mineral choices, roles and application in nutrition, food science and the culinary arts. In: Culinary Nutrition, Elsevier, 279–331 (2013)
6. ATSDR, *Toxicological Profile for Manganese*. Atalanta, Georgia (2012).
7. Y.E. Martin and E.A. Johnson, Progress Physical Geogr, **36**(6), 833–852 (2012),
8. M. Valko, H. Morris and M.T.D. Cronin, Curr Med Chem, 1161–1208 (2005)
9. G. Azeh Engwa, P. Udoka Ferdinand, F. Nweke Nwalo and N.M. Unachukwu, *Mechanism and health effects of heavy metal toxicity in humans*, in: Poisoning in the Modern World. IntechOpen. (2019).
10. P. Sanderson, R. Naidu, N. Bolanand M. Bowman, J Hazard Toxic Radioact Waste, **16**(3), 258-272 (2011)
11. V.V. Masindi and L.K. Muedi, *Environmental contamination by heavy metals*, In: Heavy Metals, InTechOpen, (2018)
12. C.H. Walker, R.M. Sibly and S.P. Hopkin D.B.P, *Principles of Ecotoxicology*. 4th Edition, CRC Press (2012).
13. P. Aronsson and K. Perttu, For Chron, **77**(2) 293–299 (2001)
14. A.P. Jackson and B.J Alloway, Water Air Soil Pollut, **57**, 873–881 (1991)
15. M. Muchuweti, J.W. Birkett, E. Chinyanga, R. Zvauya, M.D. Scrimshaw and J.N. Lester, Agric Ecosyst Environ, **112**(1), 41–48 (2006)
16. N. Gupta, D.K. Kha and S.C Santra, Environ Monit Assess, **184**, 6673–6682 (2012)
17. P. Sanderson, R. Naidu, N. Bolan, M. Bowman and S. Mclure, Sci Total Environ, **438**, 452-462 (2012)
18. A.O. Fayiga and, U.K Saha, Environ Pollut, **216**, 135–145 ,2016)
19. A. Rodríguez-Seijo, M.C. Alfaya, M.L. Andrade and F.A.Vega, Land Degrad Develop, **27**(7), 1721–1730 (2016)
20. USEPA, *Soil Sampling. In industrial waste resource Guidelines*; Washington, DC, USA, (2016).
21. N. Sehube, R. Kelebemang, O. Totolo, M. Laetsang, O. Kamwi and P. Dinake, South African J Chem, **70,** 21–28 (2017)
22. Islam MN, Nguyen XP, Jung H-Y, Park J-H, Bull Environ Contam Toxicol, **96**(2), 179-185 (2016)
23. B.H. Robinson, S. Bischofberger, A. Stoll, D. Schroer, G. Furrer, S. Roulier and R. Schulin, Environ Pollut, **153**(3), 668–676 (2008)

Google Earth Engine App for Rapid Global Assessment of OTEC-Suitable Zones

Jorge Herrera[1,a], Hernando Hernández-Hamon[2,b], Juan González[3,c] and Andrés Osorio[3,4,d]

[1]*Faculty of Natural Sciences and Engineering, Universidad Jorge Tadeo Lozano, 110311 Bogotá, Colombia.*
[2]*Ecomapp Geospatial Solutions, 110231 Bogotá, Colombia.*
[3]*Universidad Nacional de Colombia - Sede Medellín - Facultad de Minas - Departamento de Geociencias y Medio Ambiente - Grupo de investigación OCEANICOS, Cra. 80 No. 65–223 Bloque M2, Medellín, 050041, Colombia*
[4]*Center of Excellence in Marine Science, CEMARIN, 110311 Bogotá, Colombia.*

[a)] Corresponding author: *jorgea.herrerac@utadeo.edu.co*
[b)] hernando.hernandez@ecomapp.co
[c)] jugonzalezgu@unal.edu.co
[d)] afosorioar@unal.edu.co

Abstract. This paper presents the results of developing an application designed on a global scale in Google Earth Engine (GEE) to evaluate suitable areas to implement an ocean thermal energy conversion system in different marine-coastal areas of countries worldwide. The methodology uses freely available cloud-based catalogs of oceanographic data with surface and bottom (1.000 m) water temperatures and velocities. Bathymetric data and proximity to the population determine the selection of these areas. A freely available application is developed that allows users to select the region or country of study and reduce images to composite mosaics by averaging different survey years and selecting weights for each factor. The results show that this type of tool detects specific areas off the continental shelf of the oceans where this type of energy source could be implemented.

INTRODUCTION

The oceans are the largest reservoirs of solar energy on the planet since the earth's surface absorbs 66% of the radiation emitted by the sun to the world, and of said surface, more than two-thirds are covered by water [1,2]. Due to its proximity to the equator, the mixed upper layer of the tropical and subtropical oceans has the most significant amount of stored energy [2]. The energy stored in the upper layer of the oceans can be recovered through ocean thermal energy conversion (OTEC). This technology uses the thermal gradient generated between the upper and deep layers of the ocean, evaporating a working fluid in a Rankine operator cycle [3].

The first functional OTEC prototype was installed in Bahía de Matanzas, Cuba 1929, finishing for ten days with 22 kW of power. The main problem with the plant was its location, which was not ideal for this type of project [4]. In 1979, in Hawaii, the prototype of approximately ~50 kW gross power went into operation, Tokyo in 1.981 (~120 kW gross power), and again in Hawaii in 2015 (~100 kW power capacity) had continued development of OTEC technology [4,5]. Studies on the global OTEC potential estimate a capacity between 5 TW and 1.000 TW [6]. The tropical region has the most significant potential [4]. OTEC's high energy potential makes it one of the promising technologies to meet current and future energy needs [2,7].

An OTEC plant can supply energy constantly, and the OTEC system can be designed to generate some by-products, such as marine aquaculture and desalinated water [8]. This technology is under development; research has recently been conducted to improve efficiency. In this sense, one of the main lines of research lies in the location of OTEC systems. OTEC plants are installed on land near the coast, and floating plants on the high seas are generally built on platforms or ships close to shore [9]. Location is a fundamental factor in designing and implementing an OTEC system. For example, a good decision on time reduces installation costs and increases efficiency; several authors have conducted research concerning the location of an OTEC system, factors considered such as temperature gradient, bathymetric features, and environmental and social factors [10]. For example, [8] presents a bathymetry and thermal gradient study for the location of an OTEC system in the Colombian Caribbean. However, the study did not consider other variables, such as proximity to populations and water speed on the surface or in-depth. In this sense, studies that address these variables comprehensively are needed.

Technologies and Materials for Renewable Energy, Environment and Sustainability
AIP Conf. Proc. 3321, 020002-1–020002-9; https://doi.org/10.1063/5.0289617
Published under an exclusive license by AIP Publishing. 978-0-7354-5231-2/$30.00

Location is a fundamental factor in implementing a sustainable and successful project that aims to exploit oceanic thermal energy, regardless of the objective or benefit sought [7]. Therefore, selecting the right site for the implementation and the viable installation implies the analysis of several variables, qualitative and quantitative. Many criteria can help assess thermal resource potential for a site that can be utilized by OTEC technology addressing sustainability [2]. For example, the efficiency of this technology depends on variables such as depth, deep cold seawater temperature, warm sea surface temperatures, and warm sea surface temperature anomalies. Thus, site selection can quickly become a multi-criteria decision-making (MCD) problem, generating a conflictive scenario that includes technical, social, economic, environmental, and legislative criteria [11,12,13].

The ocean energy potential has been estimated using the hybrid coordinated ocean model with marine coupled ocean data assimilation (HYCOM), for which temperature matrices are analyzed, including water depths up to 1.000 m. In this way, OTEC's electricity production potential is assessed, both in terms of energy production per OTEC plant and in OTEC's overall energy production capacity [6].

Geospatial data with planetary-scale analysis capabilities are now available to scientists, researchers, and developers to detect changes, map trends, and quantify differences in the surface of the oceans. Among these infrastructures, GEE is a platform that allows tracking land changes by analyzing petabyte-scale information collected by remote sensors hosted in data catalogs [14]. Cloud processing of satellite imagery is performed thanks to a robust infrastructure that allows parallel processing on several servers running in an Application Programming Interface (API) in JavaScript or Python. Its image gallery comes from remote sensors such as Landsat, Sentinel, MODIS, and ASTER; additionally, it offers topography, land cover, meteorological (climate, precipitation, and atmospheric data), and population data [14].

This work presents an approach to identifying areas with potential for an OTEC system location. Bathymetric and oceanographic data of water masses from ocean models available in GEE are used. The objective is to conduct an exploratory study based on a multi-criteria analysis of weighted factors and perform raster operations using study layers of temperature, surface, and bottom, the bathymetry of ocean speed, and population proximity. The developed application aims to provide the best location for an OTEC system globally.

The paper is organized as follows. Section Materials and Methods explains the methodology. Then, Section Results exposes the results with different parameters used in the study. Finally, the Section's Conclusions summarize the main findings.

MATERIALS AND METHODS

The study area included all global oceans extending 361.132.000 km (70,9 \%) of the planet's surface area. In addition, it evaluated the deep zones between 500 and 1.200 m close to the coastal regions where OTEC projects could be implemented for this study. Factors associated with the difference between surface and bottom water difference temperature, velocity, bathymetry, and population were evaluated over these zones.

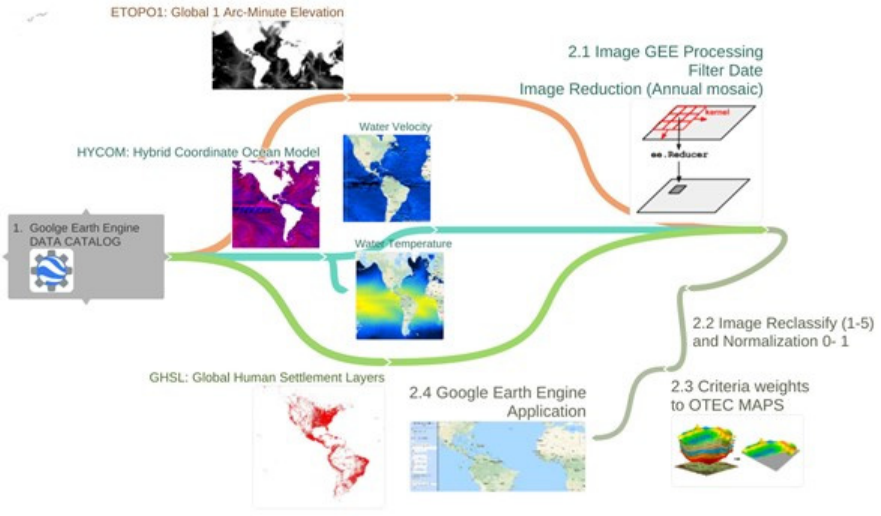

FIGURE 1. Methodology phases to obtain global OTEC maps.

The Global Ocean OTEC assessment zones were performed using GEE. It is a cloud platform for earth observation data analysis that combines a public data catalog with a large-scale computational facility optimized for the parallel processing of geospatial data [15]. The GEE processing allowed the analysis of thousands of scenes from catalogs and ocean models in parallel processing, establishing a multitemporal analysis of the suitable zones to establish possible OTEC projects in various oceans. The methodological phases of the study included:

1. The selection of catalogs and factors associated with OTEC zones.
2. The filtering of scenes by date and reducing images to annual mosaics.
3. The reclassification of the factors to discrete variables.
4. The normalization of the data between 0 and 1

With raster operation, a weighting of each factor was obtained to obtain maps with zones suitable for implementing OTEC projects (Fig. 1). All this was done using the GEE API in JavaScript.

Catalogs with global coverage available in GEE were selected to select factors determining the optimal location conditions for OTEC projects in the world's oceans. These factors were associated with physical characteristics and circulation of water masses, such as bathymetry, surface and bottom temperature differences, surface water velocity, bottom water velocity, and proximity to the population in all oceans between 100 and 1200 m. In addition, open-access catalogs, some with daily images, were used to establish seasonal differences through scene reduction up to monthly mosaics.

GEE Data Catalogues and Factors Selection

HYCOM: Hybrid Coordinate Ocean Model, Water Velocity and Temperature

The Hycom is a Hybrid Ocean general circulation model (OGCM) of isopycnic coordinates that provides a three-dimensional representation of the stratified ocean state with satisfactory real-time resolution [16]. Hycon is a multi-agency effort sponsored by the National Ocean Partnership Program (NOPP) as part of the U.S. Global Ocean Data Assimilation Experiment (GODAE). The advantages of the general circulation model for the present work were:

1. It extended vertical resolution in unstratified or weakly-stratified regions of the ocean.
2. Global coverage.
3. Having a high vertical resolution in coastal regions.
4. Having a high vertical resolution in the surface mixed layer.
5. High spatial resolution (a daily image).

Bathymetry ETOPO1: Global 1 Arcminute: ETOPO1 is a one arcminute global relief model of the earth's surface that integrates land topography and ocean bathymetry. Built from global and regional datasets, it is available in "Ice Surface" (top of the Antarctic and Greenland ice sheets) and "Bedrock (base of the ice sheets) [17].

Global Human Settlement Layers (GHSL): The GHSL represents population distribution and density, expressed as the number of people per cell, based on data mining of global-scale satellite imagery data streams, censuses, and voluntary geographic information sources between 1975 and 2015 [18]. Population estimates are from CIESIN GPW v4.

Catalog preparation: The catalogs were taken by filtering the images and separating the scenes by date. A reduction of the collections into a single scene representing the annual mean value of the proposed factors was also performed. Bathymetry, surface and bottom temperature differences, surface water velocity, bottom water velocity, and proximity to the population in all the oceans between 100 and 1.200 m. For this study, normalization, or standardization of the data between 0 and 1, is proposed using Eq. (1).

$$\text{Factor normalized} = \frac{x - Min}{Max - Min} \tag{1}$$

Where: x is the value of each factor, Min: is the minimum value of the factor within the range contained in the map, and Max is the maximum value of the factor within the range contained in the map.

Image Reclass and Data Normalization: The images of each factor were reclassified to discrete variables in 6 ranges defined as Optimal, Good, Acceptable, bad, limited, and excluding. These were assigned numerical categories from 1 to 6, respectively. The OTEC project implementation technical specifications defined each factor's upper and lower limits, as can be seen in Table 1 and Table 2.

TABLE 1. Example of numerical categories, Part A.

	OPTIMAL		GOOD		ACCEPTABLE	
	Upper	**Lower**	**Upper**	**Lower**	**Upper**	**Lower**
Bathymetry (m)	-500	-700	-699	-1.000	-999	-1.200
Diff temperature 0 to 1.000 (°C)	36	21	20	18	17	16
Water velocity 0 m (m/s)	-1.000	-500	-499	-300	-299	-100
Water velocity 0 to 1.000 m (m/s)	-100	-300	1	-100	100	0
Proximity to population (km)	10	1	11	20	21	30

TABLE 2. Example of numerical categories, Part B.

	BAD		LIMITED		EXCLUDING	
	Upper	**Lower**	**Upper**	**Lower**	**Upper**	**Lower**
Bathymetry (m)	-1.199	-1.500	-1.499	-2.000	-1.999	-1.2000
Diff temperature 0 to 1.000 (°C)	15	14	13	5	4	1
Water velocity 0 m (m/s)	-99	1	0	500	499	1.500
Water velocity 0 to 1.000 m (m/s)	300	100	399	300	999	400
Proximity to population (km)	31	50	51	100	101	5.000

Factors weights: Once the variables were standardized, proposed weights were assigned (through consultation with experts) based on the consideration that only some of the factors of a continuous nature incorporated have the same importance. Therefore, relative weight was assigned so that variables have a greater or lesser impact on the final maps of the OTEC zones. The proposed weighting follows Eq. (2).

$$OTEC_{map} = 0.4B + 0.2\Delta t + 0.1W_{V_o} + 0.1W_{V_{1000}} + 0.2P_p \quad (2)$$

where B is the bathymetry, Δt is the difference temperature, W_{V_o} is the water velocity to 0 m, $W_{V_{1000}}$ is the water velocity to 1.000 m, and P_p is the proximity to population.

Google Earth Engine Application: The coverage selection of the image area derived from the catalogs and the study period and the assigned weights of each factor to obtain the resulting composite maps were obtained from buttons and applications from Java Script in the GEE API. The interface included the main panel with buttons for selecting the study area by country or selecting a location to crop the resulting maps by drawing a polygon from the platform. After choosing the area, the evaluation period is established using an application that averages the images to obtain monthly mosaics. Finally, the weights assigned to each factor can be edited from cells.

RESULTS

The daily global-scale image reduction function of the Hycom model with surface and bottom water temperatures and velocities (1.000) allowed for obtaining global images thanks to the power of the GEE infrastructure. The mosaics corresponded to annual averages for 2.021, corresponding to the processing of 11680 images of the surface and bottom water temperatures and velocities (2.920 images by factor) and two global scale composite images for bathymetry and population proximity. The resulting maps with the exploratory evaluation of areas to implement energy diversion projects based on OTEC technology could be obtained in minutes thanks to the parallel processing of 256x256 tiles, even though the input data averaged results from thousands of images.

The most relevant factor in selecting suitable areas for implementing OTEC projects is the difference in temperature between the surface and the bottom. Using the ocean circulation model available, HYCOM from GEE showed that the annual average of the global temperature difference between 0 and 1.000 m varied between 2 and 25 °C in 2.021. As observed in the annual average, the ideal temperatures for implementing these projects could be in the tropical and subtropical zones as a latitudinal boundary (Fig. 2).

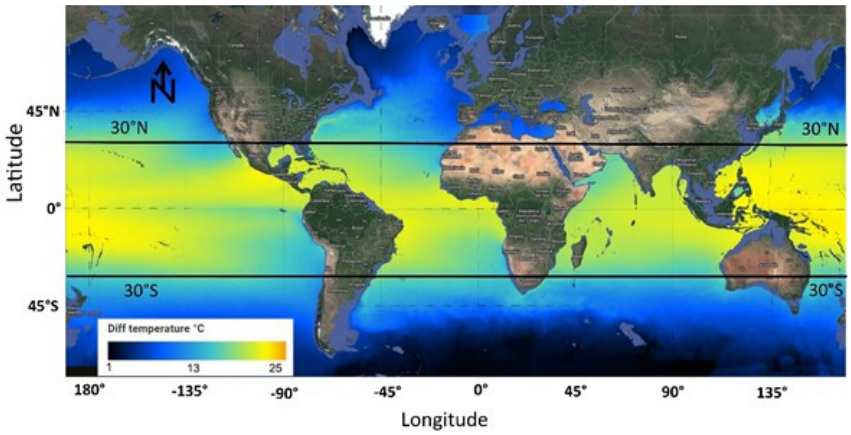

FIGURE 2. Global surface and bottom temperature differential (1.000 m) derived from the HYCOM model.

This annual composite showed differences in temperatures between 19 and 25°C in a band between 30°N and 30°S Parallels in tropical and subtropical latitudes. In the North and South latitudes above or below these parallels, low-temperature differences may limit the project's implementation. These results made it possible to locate a band or effective study area to cut out the maps resulting from the selected factors.

Diff temperature (0 to 1.000m)

The average temperature differential for 2.021 was reclassified for the Atlantic, Pacific, and Indian Oceans areas with optimal, reasonable, and acceptable surface and bottom temperature differentials between the 30°N and 30°S band. Large regions with temperature differentials between 22 and 25°C in the western tropical Atlantic were observed between Brazil and Venezuela and the western Caribbean Sea between Colombia and Mexico.

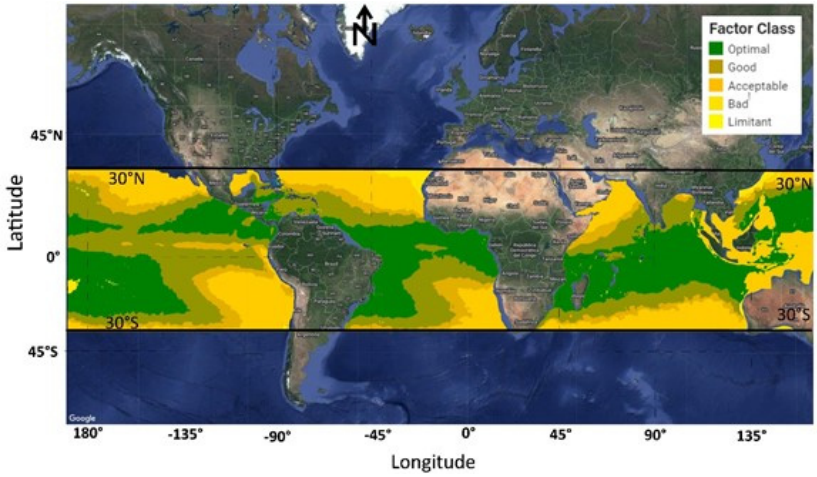

FIGURE 3. Reclassification of the global temperature differential between 30°N and 30°S.

The tropical eastern Pacific showed different temperatures between surface and bottom between the equator and 18°N in latitude and off the Colombian coast up to 135°W. The tropical western Pacific Ocean showed Optimum and suitable zones along most South American coasts from Brazil, at 30°S and 11°N to Trinidad waters. In the eastern African Atlantic, the extent of suitable areas from optimum to good was observed in the annual average between the coasts of the Angola Border at 16°S to the northern coast of Sierra Leone 9°N (Fig. 3).

On the other hand, the optimum to suitable temperature differential range was found in the southwestern Indian Ocean from the southern coast of South Africa to the Kenya-Somalia border at 2°S (Fig. 3). The eastern Indian and the western Pacific had these suitable temperatures along the south coast of India, west of Thailand, Malaysia, the Philippines is Indonesian, and east of the Philippines is Indonesian.

Bathymetry

The bathymetric characterization for the location of an OTEC power generation project is fundamental for the technical implementation of a power generation project in the ocean to obtain the appropriate depth gradient at an adequate distance from the coast. The bathymetric results reclassification from the ETOPO1 model showed wide corridors on the continental shelf edge. In a tropical and subtropical belt. The bathymetry reclassification from optimum to limiting showed how the Caribbean Sea presented extensive optimum zones between 150,000 km2 and 359,000 km2 in the tropical Atlantic Ocean between 30°N and 30°S. The Caribbean has large optimum and suitable zones compared to its limited size (Fig. 4).

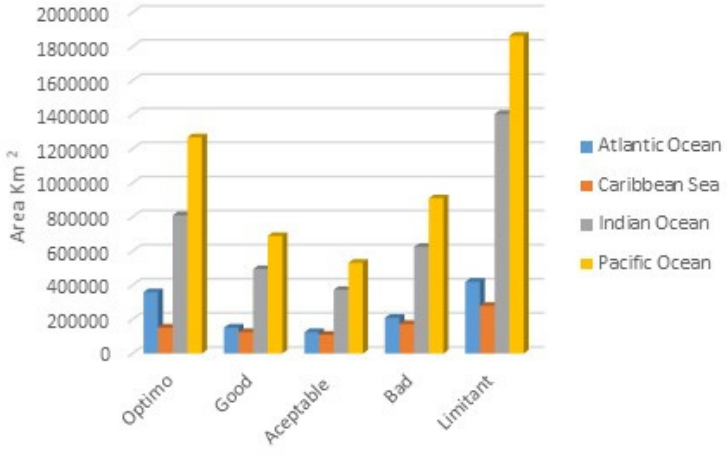

FIGURE 4. Optimal to limited areas by bathymetric reclass factor for world oceans.

Wide corridors between 200 and 1.000 meters at the shelf edge were observed for the Caribbean in Anguilla, St. Kitts, Antigua and Barbuda, and the Southern Caribbean in Venezuela and Colombia. A wider shelf on the Central American coasts could lead to more significant difficulties for the location of projects of this type. This same characteristic was observed in the western Atlantic from Venezuela to Brazil and most East Atlantic coastal areas on the African coasts between Sahara and Namibia. In the Indian Ocean, areas with optimal to good depths were observed reaching 200 to 1.000 m closer to shore if we compare the depths off the coasts of India and Bangladesh with an enormous shelf. To the west and south of the western Pacific islands, such as the Philippines, Indonesia, and Malaysia, large areas of good to optimal depths were observed, as was the north coast of Australia.

Superficial and Bottom Seawater velocity (0 and 1.000 m)

Water velocity due to the circulation of ocean currents could be a factor conditioning the implementation of OTEC projects near coastal areas Fig. 5. A decrease in the seabed water velocity up to 500 m/s compared to surface up to 1300 m/s was observed in global maps. Hycom-derived annual average surface water velocities for 2.021 showed higher surface velocities between 35 and 400 m/s from 3 and 5°N latitude in tropical zones in the Atlantic and Pacific Oceans. Lower surface velocities of -500 to -100 m/s were observed in the tropical East and West Pacific near the equator between 0 and 5°N latitude. The highest surface velocities were observed east of the Sea of Japan (12.047 m/s) and off the coast of New York (950m/s). Surface and bottom velocities generally increase in subtropical and temperate latitudes outside the 30°N and 30°S parallels, where the temperature differential and bottom temperatures are optimal for these projects.

Maps resulting from the raster operation of multiplying the reclassified factors and their weights showed the optimal distribution to limiting zones from annual averages of oceanographic data (surface and bottom temperatures and velocities) and mosaics bathymetry and proximity to the population.

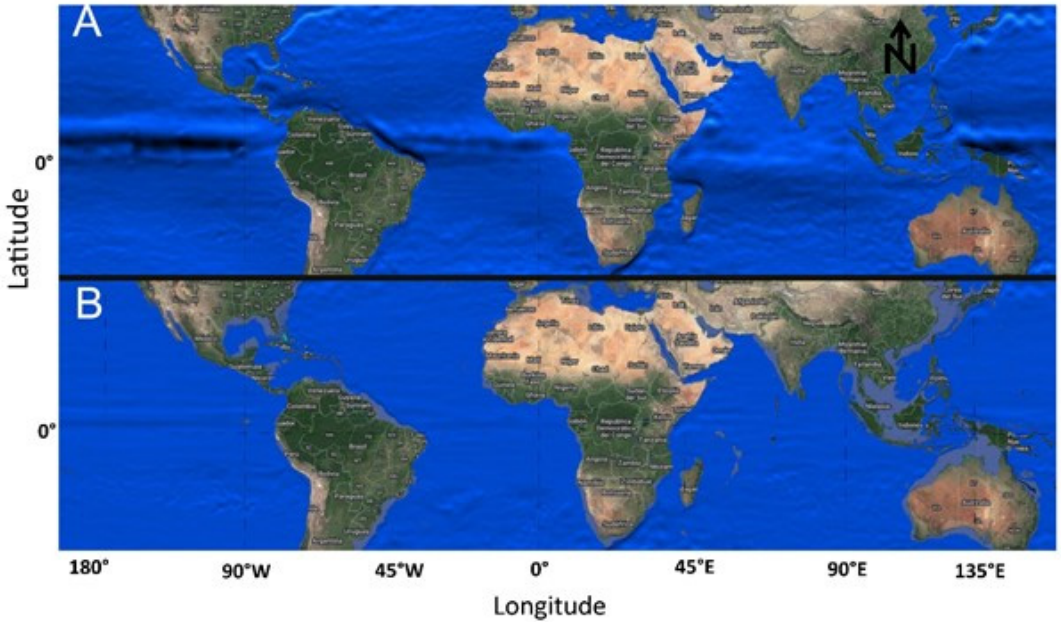

FIGURE 5. Water surface velocities 0 m (A) and bottom 1.000 (B) are derived from the Hycom model.

Global OTEC zones

The insular zones of the Caribbean Sea southeast of Jamaica, northeast of Cuba and Haiti, and on the continental margin of Mexico in Yucatan, the northeast coast of Honduras, the north coast of Colombia, and the central coast of Venezuela presented optimal and good zones where the conjunction of factors and established weights could suggest the implementation of OTEC projects throughout the year.

Similarly, extensive areas with optimal to good results were observed in large zones in the western Pacific Ocean and the Indo-Pacific South of the South China Sea and open waters north of Malaysia and east of Vietnam around island areas such as the Parcel Islands. In the South Pacific, the east coast of West and North Sumatra with optimal and good pixels. Likewise, suitable areas for implementing projects are the shallow shelf of the Amadan and Nicobar Islands in the Indian Ocean east of the Bay of Bengal. On the other hand, the northeast coast of the Australian Coral Sea is the most suitable area over the Queensland offshore area.

In the western Atlantic Ocean from the eastern coast of Venezuela to the southern coast of Brazil, as well as the eastern Atlantic from the Saharan coast to Angola, some of the corridors ranged from acceptable to limiting zones and a minor extension of pixels with optimal and good areas compared to other oceans of the world. Optimal and good areas were observed mainly on the Namibian coast.

DISCUSSION

The implementation of energy projects derived from clean energy taking advantage of the potential offered by the ocean's surface-bottom temperature gradients has been considered a more than viable alternative for many communities, especially in insular or riverine areas with few resources. Therefore, it is essential to establish that it is necessary to carry out a spatial characterization of the regions with potential for implementing OTEC projects, especially in areas with few information or where they are difficult to access. Some developing countries in continental and insular zones could take advantage of these energy sources where other hydrocarbon sources are expensive, especially in riverside and coastal communities.

Satellite technologies associated with big data offer petabytes of data available at spatial scales with unprecedented processing power in recent decades [14]. GEE is to become an effective tool that combines monitoring, modeling, analysis, assessment, and management decisions that can be applied to solve global environmental problems [19].

GEE can analyze big geospatial data, provide a more significant number of geospatial data sets, and support various image-processing raster and vector algorithms [14]. In our results, we observed several advantages in the use of cloud-based applications to obtain suitable areas for the implementation of OTEC projects:

- GEE is a free web platform that provides satellite imagery, vector data, and cloud computing. In addition, it enables access to algorithms for processing these data [15,20]. This is added ocean circulation models derived from global-scale satellite data needed to implement applications like the present one.
- The computational power derived from the parallel processing required to obtain rapid reclassified maps from 11.682 images for the 2.021 average to the native resolution of each catalog has been critical in identifying large areas where the spatial resolution of the products may be a limiting factor in this research.
- It highlights this application's and cloud-based development's ability to establish areas with potential in regions that are difficult to access or where few information is available.
- Ocean models' time-series coverage offers project managers and planners an advantage over annual, monthly, or even weekly periods.
- The advantage of the application is that it offers free access to the catalogs and the graphical interface shared in the following document, which allows selecting the area of each country.
- The application was designed to download the resulting maps in predefined areas in Geotiff format, which allows exporting these areas from optimal to good in different GIS platforms.

CONCLUSION

The results show that the catalogs obtained from cloud computing in GEE allow obtaining a global vision for selecting areas and territorial seas of countries with the potential to implement OTEC projects. These results are possible thanks to the platform's parallel processing capacity in the annual averages, which implies the reduction of thousands of images with global processing of a few minutes.

The factor associated with the difference in surface and bottom temperature allowed limiting these zones in a latitudinal band in the tropical and subtropical oceans, restricting locations in countries in more temperate and colder latitudes. The optimal and suitable areas observed in the raster operations in different oceans show extensive areas highlighted by their extension to implement these projects in the Caribbean Sea, the South China Sea, and the northeast Pacific of Australia. In addition, the western and eastern Atlantic and the western Indian Ocean offered optimal and promising areas in the results of the OTEC maps due to the characteristics of their shelf edge and depth.

This research presented a free application available to the scientific community that allows planning possible OTEC projects in different oceans since island and continental areas can be challenging to access on criteria derived from ocean models and bathymetric models obtained and downloaded from the cloud in GEE.

ACKNOWLEDGMENTS

This work was partially supported by the Sistema General de Regalías from Colombia, under project— BPIN 2020000100671 - “Implementación de una estrategia de uso del agua y energía generada por fuentes de generación de energía renovables En la Isla de San Andrés y Providencia”.

REFERENCES

1. R. Pelc, And R.M.Fujita, Mar Policy, **26**, 471–479 (2002)
2. G. Lopez, M.d.l.A. Ortega Del Rosario, A. James and H. Alvarez, Energies, **15**(9), 3077 (2022)
3. J.R.S. Doorga, O. Gooroochurn, B.A. Motah, V. Ramchandur and S. Sunassee, Int Jof Energ Environ Eng, **9**, 363–382 (2018)
4. J.V. Hernández-Fontes, A. Felix, E. Mendoza, Y.R. Cueto and R. Silva, J Marine Sci Eng, **7,** 191 (2019)
5. K. Rajagopalan and G.C. Nihous, J Energ Resour Technol, **135**(4), 041202 (2013)
6. J.H. VanZwieten, L.T. Rauchenstein and L. Lee, Renew Sust Energ Rev, **75,** 683–691 (2017)
7. E.P. Garduño-Ruiz, R. Silva, Y. Rodríguez-Cueto, A. García-Huante, J. Olmedo-González, M.L. Martínez, A. Wojtarowski, R. Martell-Dubois and S. Cerdeira-Estrada, Energies, **14,** 2121 (2021)
8. J. Herrera, H. Hernández-Hamón, L. Fajardo, N. Ardila, A. Franco and A. Ibeas, J. Marine Sci Eng, **10,** 519 (2022)
9. J. Herrera, S. Sierra, S. and A. Ibeas, J. Marine Sci Eng, **9,** 356 (2021)
10. A. Devis-Morales, R.A. Montoya-Sánchez, A.F. Osorio and L.J. Otero-Díaz, Renew Energ, **66**, 759–769 (2014)

11. Y.Wu, S. Geng, H. Zhang and M. Gao, Appl Energ, **136**, 303–311 (2014)
12. J. Zhang, C. Xu, Z. Song, Y. Huang and Y. Wu, J Cleanr Product, **225**, 771–784 (2019)
13. F. Chen, L. Liu, J. Peng, Y. Ge, H. Wu and W. Liu, Energy **183**, 497–503 (2019)
14. N. Gorelick, M. Hancher, M. Dixon, S. Ilyushchenko, D. Thau and R. Moore, Remote Sens Environ, **202**, 18–27 (2017)
15. M.C. Hansen, P.V. Potapov, R. Moore, M. Hancher, S.A. Turubanova, A. Tyukavina, D. Thau, S.V. Stehman, S.J. Goetz, T.R. Loveland, et al. Science, **342**, 850–853 (2013)
16. J.A. Cummings and O.M. Smedstad, Variational data assimilation for the global ocean. In *Data Assimilation for Atmospheric, Oceanic and Hydrologic Applications* (Vol. II); Springer, 303–343, 2013
17. C. Amante and B.W. Eakins, ETOPO1 arcminute global relief model: procedures, data sources and analysis 2009.
18. M. Pesaresi, and S. Freire, GHS-SMOD R2016A - GHS settlement grid, following the REGIO model 2014 in application to GHSL Landsat and CIESIN GPW v4-multitemporal (1975-1990-2000-2015) - OBSOLETE RELEASE. European Commission, Joint Research Centre (JRC) [Dataset] PID: http://data.europa.eu/89h/jrc-ghsl-ghs_smod_pop_globe_r2016a 2016.
19. Q. Zhao, L. Yu, X. Li, D. Peng, Y. Zhang and P. Gong, Remote Sens, **13**, 3778 (2021)
20. L. Kumar and O. Mutanga, Remote Sens, **10,** 1509 (2018)

Role of Nanoparticle Topography in Enhancing Random Laser Performance

Noor al-huda A. Abass[1], Muslim F. Jawad[1], Adawiya J. Haider[2,a]

[1]*Department of Electrical, Electronic and Systems Engineering, Faculty of Engineering and Built, Baghdad, Iraq*
[2] *Applied Sciences Department/ Laser branch, University of Technology, Baghdad, Iraq*

[a)] Corresponding author: adawiya.j.haider@uotechnology.edu.iq.

Abstract. Random lasers distinguish themselves using a scattering medium for optical feedback, unlike traditional lasers that rely on conventional optical cavities. The generation of random lasers depends on both gain and scattering for optical feedback and amplification. The highest absorption peaks for Ag@Au and Au@Ag dispersions were observed at 500 nm and 400 nm, respectively, while for Ag and Au, the UV absorption peaks were at 490 nm and 400 nm, respectively. A composite PMMA/RhB/NP laser active medium was synthesized. Characterization results indicated that the optimal conditions for achieving the best optical feedback and amplification in the random laser were obtained using a pumping source with a wavelength of 532 nm at various pumping powers (2, 3, 4, 5 mW). The optimal performance was observed at a high-intensity power of 5 mW with a 532 nm Nd: YAG laser. It became evident that modifications in the PMMA/Au@Ag/RhB composite led to a significant increase in the absorption spectrum.

KEYWORDS: random laser, PMMA, RhB, laser performance.

INTRODUCTION

Bimetallic core-shell plasmonic nanoparticles (NPs) with uniformity, presently being prepared with liquid utilizing pulsed laser ablation (PLAL), are in high demand for catalyst and photonics (laser-active medium) applications due to their enhanced surface area and roughness, which significantly influence their catalytic efficiency. PLAL is a two-step process that employs liquid ablation by pulsed laser to process bulk materials like silver (Ag) and gold (Au). Despite its potential, few studies provide detailed information on the formation mechanisms, morphology, and surface characteristics of these core-shell bimetallic nanoparticles. In this investigation, we used these nanoparticles using the pulsed laser ablation technique, which is an uncomplicated, clear-cut, and environmentally friendly method that produces neither surfactants nor byproducts.

Laser action can take place in a powdered active material or an energy medium scattered with scattering particles [1-5]. Numerous organic and inorganic powders, solid-state luminescent or laser crystals [6,7], liquid laser dyes with scatters [8], polymeric films with or without purposefully introduced scatters [9], ZnO scattering films, nanoclusters, dye-infiltrated opals, and porous media infiltrated with liquid crystals and dyes are among the materials in which random laser phenomena are observed. With a variety of scattering techniques, random lasers are an effective light-enhancing medium.

Random laser systems and conventional lasers have a lot in common, both of which rely on media enclosed by a two-mirror cavity designed to give optical feedback. In both cases, the frequency reduction and lasing action threshold are key characteristics. However, random lasers differ significantly from typical lasers in that fluorescence light and the pump propagate diffusively, whereas conventional lasers use cavity systems for feedback. In random lasers, more intense scattering lowers the threshold, as multiple dispersion

Technologies and Materials for Renewable Energy, Environment and Sustainability
AIP Conf. Proc. 3321, 020003-1–020003-8; https://doi.org/10.1063/5.0289987
Published under an exclusive license by AIP Publishing. 978-0-7354-5231-2/$30.00

gives the required feedback. If the photon transport mean free route gets close to the stimulated emission wavelength, the lasing threshold is drastically decreased [10,11].

The three essential factors for random lasers are polymers as host materials, wavelength control with dyes, and nanoparticulate scattering centers. Various polymers perform as host materials, such as Polyimide (PI), Polymethyl Methacrylate (PMMA), and Polyethylene Terephthalate (PET). The emission wavelength can be regulated by using dyes such as Rhodamine 6G (R6G), Rhodamine B (RB), Methyl Orange (MO), and Methylene Blue (MB). Nanoparticles serve as scatter centers and improving the random laser impact. Increasing the nanoparticles' surface area and roughness significantly enhances scattering performance as a consequence, the efficiency of random lasers, which strengthens the optical feedback, and reduces the overall efficiency and lasing threshold of the random laser. [12 -14]. Therefore, nanoparticles' surface area and roughness have a direct contribution in the efficacy of the laser systems.

Random lasers are a very attractive type of laser for various applications, including holography, laser inertial confinement fusion (as driver sources for megajoule lasers), energy transport in fibres for medical applications, etc. Low-coherence random laser is another type of laser with many beneficial properties for different medical applications.

This study investigated the fluorescence spectrum of Rhodamine B (RhB) dye and assessed the effects of nanoparticle colloids (nano colloids) incorporation with Polymethyl Methacrylate (PMMA) to achieve the plasmon phenomenon. The interaction between RhB dye and nanoparticles may improve PMMA matrices, hence, the study aims to explore the optimum nanocomposites to improve optical properties. Additionally, the effect of surface morphology and roughness of the nanocomposite films on laser performance was investigated. For analysing different characterization techniques were used including Atomic Force Microscopy (AFM), UV-Vis spectroscopy, and Photoluminescence (PL) spectroscopy.

EXPERIMENTAL WORK

Synthesis of Ag@ Au and RhB dye

The dimensions of the silver target is 1 cm × 1 cm × 0.3cm with a purity higher than 99.5%, while the gold target dimensions is 1.5 cm × 1 cm× 0.3cm with a purity higher than 99.9%. Both targets are crucial for applications in developed photonic devices and materials. To prepare the Rhodamine B dye laser solution with different dye concentrations ($4x10^{-4}$, $4x10^{-3}$, and $4x10^{-2}$), Rhodamine B dye was dissolved in methanol to produce the desired dye solutions. A balance with a sensitivity of 10-4 grams was used to determine the weight (W) of the dye that was needed (Matter Company). As shown in Figure 1.

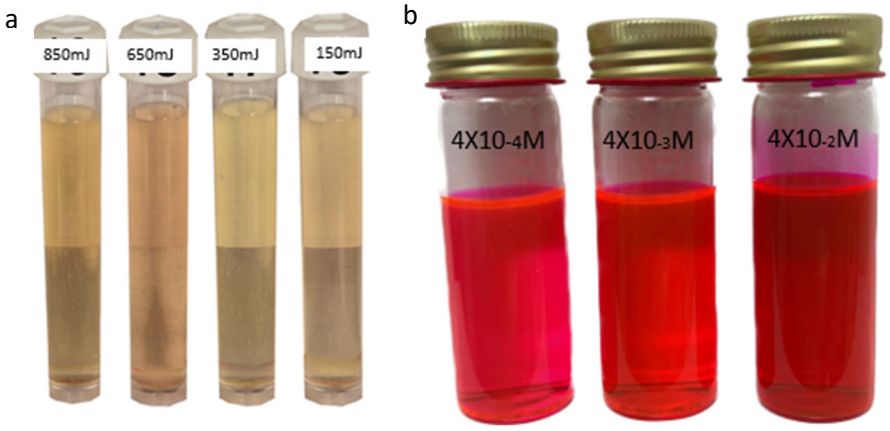

FIGURE 1. (a) different energy for nanoparticles .(b) different dye concentration ($4x10^{-4}$, $4x10^{-3}$,$4x10^{-2}$).

FABRICATED COMPISTE THIN EILM

A flat-sheet nano-polymer membrane was fabricated using the phase inversion approach. Initially, 5 grams of Polymethyl Methacrylate (PMMA) were dissolved in the dichloromethane solution with a

0.25×10^-2 M concentration. This polymer mixture was continuously stirred for 60 minutes at room temperature to ensure a homogeneous solution. Subsequently, different concentrations of dye were added to the polymer solution, and then adding 1 milliliter of colloidal nanoparticles, including gold, silver, $Au_{core}@Ag_{shell}$, and $Ag_{core}@Au_{shell}$. After thorough mixing, the solution was allowed to degas to remove any air bubbles. The degassed solution was then applied to a dry, clean glass substrate in the appropriate amount. The casting process was performed using an automated casting device (AFA-IV MACHINE), ensuring uniform film thickness. The resulting film was immediately placed into a water bath to induce coagulation through the procedure of phase inversion. Finally, the coagulated membrane was withdrawn with caution from the water bath, thoroughly washed with deionized water to eliminate residual solvents, and stored in a sealed container to maintain its wet state until characterization. The casting polymer solutions. (a)The polymer is mixed with concentrations of dye, and nanoparticles collide. (b) The solution was poured on a clean, dry glass substrate with different concentrations. (c) The device, an automated casting.

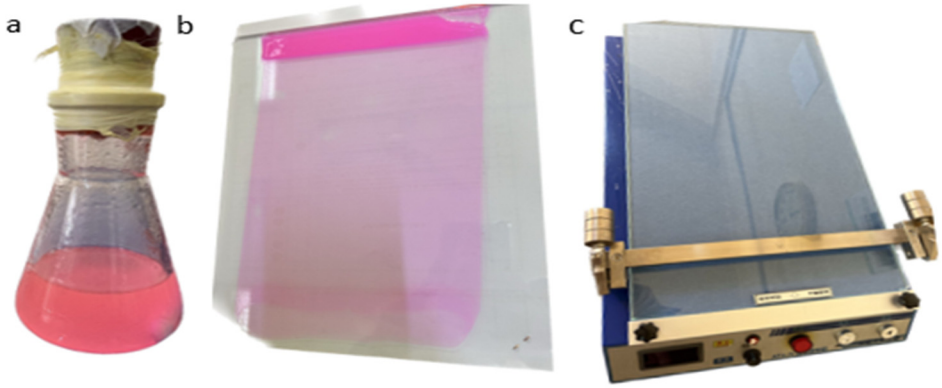

FIGURE 2. (a)The polymer is mixed with concentrations of dye, and nanoparticles collide. (b) The mixture onto a dry, spotless glass substrate. with different concentrations. (c) The device, an automated casting.

RESULTS AND DISCUSSION

Optical properties of Au, Ag, and CORE@SHELL nanoparticles through laser ablation

Figure 3 presents the absorption spectra of (Au), (Ag), (Au@Ag), and silver-core/gold-shell (Ag@Au) nanoparticles synthesized using the (PLAL) technique, measured at a wavelength of 532 nm and an energy density of 850 mJ/cm². The gold nanoparticles displayed a distinguished absorption peak at approximately 500 nm, while silver nanoparticles displayed a sharp absorption peak at approximately 400nm. Both of gold and silver nanoparticles were characterised by localized surface plasmon resonance (LSPR) [15-18]. Additionally, Ag@Au and Au@Ag bimetallic core-shell nanoparticles were generated, which demonstrated distinct optical properties due to their core-shell structures. The spectra of Aucore@Agshell and Agcore@Aushell nanoparticles showed a combination of both metals' characteristics and excellent core-shell structures. The absorption characteristics of Aucore@Agshell nanoparticles showed significant contributions from both the gold core and the silver shell [19,20]. In contrast, there was a gold peak prominent in Ag@Au nanoparticles, accompanied by secondary characteristics attributed to the silver core. The plasmon resonance shifts observation indicated that changing the ablation period and laser influence may adjust the optical properties of these nanoparticles. The shape and features of synthesized nanoparticles can be affected by various factors such as the interaction medium, laser wavelength, and liquid environment. UV-Vis absorption and transmission spectra were used to confirm the formation of core-shell structures, The results demonstrated distinct peaks for both silver and gold at 400 and 500 nm, respectively. This approves the nanoparticles' bimetallic nature and their applicability in advanced photonics [21, 22].

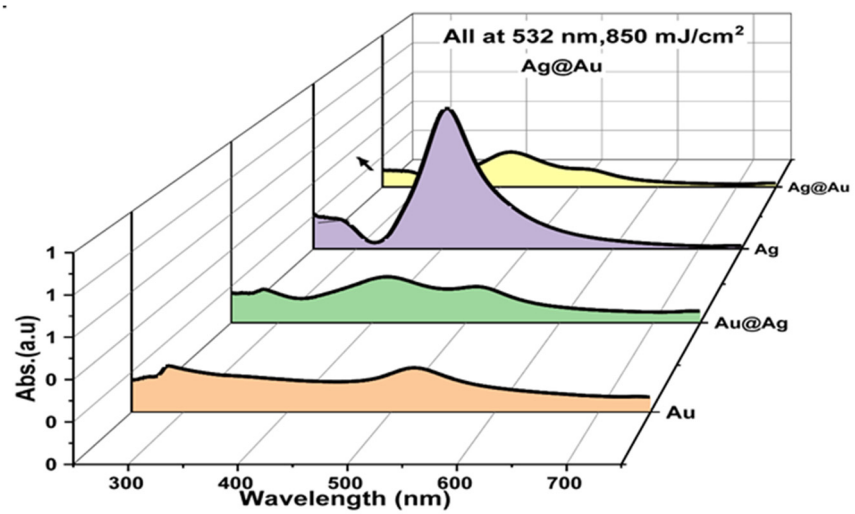

FIGURE 3. PLAL was used to examine the absorption spectra of colloidal nanoparticles of Ag, Au, Ag@A, and Au@Ag.

SURFACE TOPOGRAPHY (AFM)

Previous studies observed that in the synthesis process, the growth kinetics of gold NPs are faster than that of silver NPs, which indicates the gold NPs were synthesized initially. Atomic Force Microscopy (AFM) images confirmed this observation. Figure 4a, b shows the sequential development of the nanoparticles [23,24]. The AFM analysis documented that the nucleation and growth of gold NPs continue at a faster rate than silver NPs, this may be attributed to the differences in respective chemical reduction processes and precursor reactivity.

Further investigation was conducted to determine the size range of the synthetic Au core @ Ag shell and Ag core @ Au shell NPs. The distribution plots recorded an obvious differentiation between the size of synthetic Au core @ Ag shell and Ag core @ Au shell NPs. The size of silver shells was larger than that of the gold cores, this phenomenon might be related to the rapid initial growth of gold NPs followed by the slower deposition of silver.

Atomic Force Microscopy (AFM) imaging confirmed the creation of spherical core-shell structures and provided high-resolution pictures of the nanoparticles' surface shape and topography, consequently confirmed the synthesis of nanostructures (Figure 4c, d).

Furthermore, the AFM results were compatible with UV-Vis spectroscopy data. The UV-Vis spectra revealed distinct absorption peaks corresponding to the plasmonic features of both gold and silver. The large size of silver nanoparticle shells compared to the gold nanoparticle cores was verified by the red shift in the absorption peaks which is associated with larger size and dielectric environment changes surrounding the NPs [25,26].

The comprehensive investigation utilizing AFM and UV-Vis spectroscopy supported the size and shape of the synthesized nanoparticles, as well as providing important insights into the core-shell NPs' growth mechanisms and structural properties.

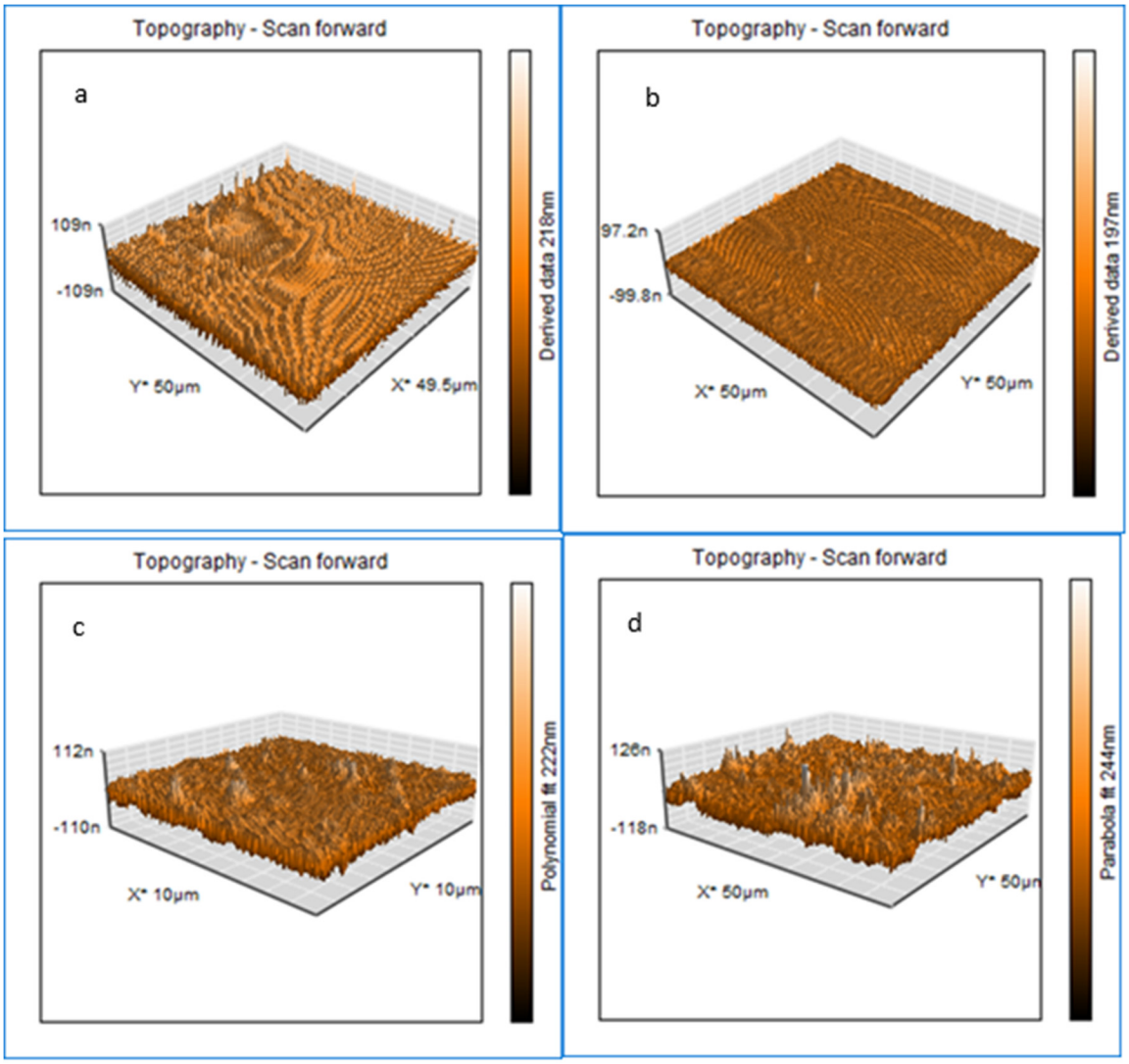

FIGURE 4. AFM images of various nanoparticle types colliding (a)silver NPs, (b)gold NPs, (c)Au @Ag $_{s}$NP (d)Ag @Au Nanoparticles.

CHARACTERISTICS of Au and Ag NANOPARTICLE PHOTOLUMINESCENCE (PL)

At various wavelengths, deionized water (DIW) was used to analyze the PL characteristics of gold (Au) and silver (Ag) nanoparticles. The data showed a consistency in the shape of the PL peak across different wavelengths when using an excitation wavelength of 300 nm at ambient temperature. The gold nanoparticles interacted with the volumetric fractal, thus increasing the silver nanoparticles, leading to more significant PL peaks. Specifically, the gold-silver nanoparticle interface interactions caused a red shift, which in turn impacted the size and photoluminescence spectra of Ag@ Au BNPs and their localized surface plasmon resonance (LSPR).

Furthermore, Ag@ Au BNPs with various crystalline diameters showed wide and sharp PL peaks. Au nanoparticles were more visible in UV spectrum when compared to other samples due to the effect of plasmonic resonance. The laser beam's activation of the LSPR effect had a significant impact on both the plasmon resonance spectra and the luminescence enhancement of gold nanoparticles. When the LSPR was excited, a laser beam focused on the gold surface increased the electromagnetic field surrounding the nanoparticles, consequently enhancing photoluminescence absorption.

PL absorption peaks for Ag@ Au bimetallic nanoparticles in the 350-900 nm range, driven by a 532 nm laser, are illustrated in Figure 5. The observed changes in these peaks were attributed to powerful inter-band transitions and LSPR coupling, which highlighted the nanoparticles' photoluminescence properties. The figure delineates eight distinct peaks within specific wavelength ranges: 360–520 nm for the first peak, 530–550 nm for the second, 555–690 nm for the third, 695–730 nm for the fourth, 752–830 nm for the fifth, and 840–875 nm for the last.

As the crystallite size of Ag@Au BNPs increased, the PL peaks generally became sharper and stronger. Aggregation and adhesion at the interface interactions in these bimetallic systems contributed to enhanced PL absorption, emphasizing the role of nanoparticle size and interface properties in determining photoluminescence behavior. These findings underscore the critical influence of LSPR and nanoparticle size on the optical properties of bimetallic nanoparticle systems.

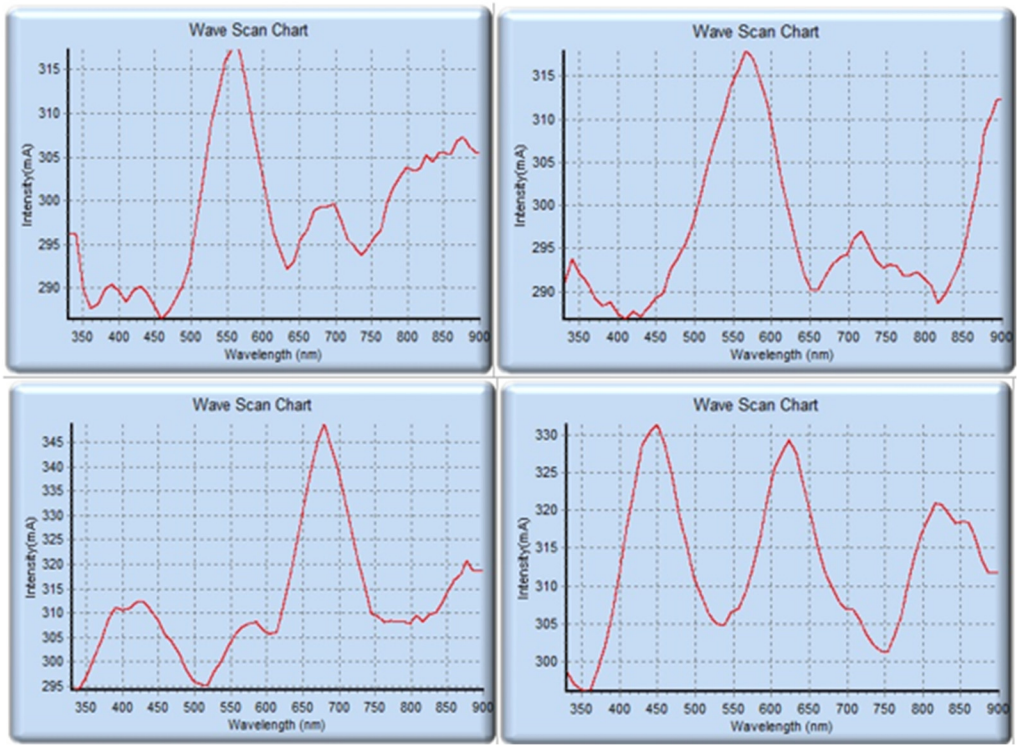

FIGURE 5. Photoluminescence spectra of Au NPs, Ag nanoparticles, and Ag@Au nanoparticles.

FLUORESCENCE CHARACTERIZATION

Figures 6a, b, c, and d illustrate the fluorescence spectra of Rhodamine B (RhB) dye embedded in a Polymethyl Methacrylate (PMMA) matrix with different types of nanoparticles (Ag, Au, Au@Ag, Ag@Au) at varying concentrations. Each figure presents the fluorescence intensity plotted against the wavelength, demonstrating how the presence and concentration of nanoparticles affect the fluorescence properties of RhB dye.

For all nanoparticle types, the fluorescence intensity of RhB dye increases with higher nanoparticle concentrations, reaching a peak at 4×10^{-3} M. However, at the highest concentration (4×10^{-2} M), the fluorescence intensity decreases, likely due to quenching effects where excessive nanoparticles cause non-radiative recombination. Despite the variations in intensity, all figures show a consistent fluorescence peak centered around 580 nm, indicating that nanoparticles do not significantly shift the emission wavelength of RhB dye but rather enhance the intensity.

Core-shell structures (Ag@Au and Au@Ag) exhibit higher fluorescence intensities compared to single-metal nanoparticles (Ag and Au), suggesting enhanced plasmonic interactions in core-shell configurations. This enhancement can be attributed to the more effective coupling between the plasmonic fields of the core

and shell materials, which amplifies the local electromagnetic field and, consequently, the fluorescence intensity of the RhB dye.

Among the core-shell structures, Ag@Au exhibits slightly higher PL intensity than Au@Ag, indicating that the Ag core with Au shell configuration may enhance RhB dye's fluorescence better. Compared to single-metal nanoparticles, Au nanoparticles demonstrated higher PL intensity than Ag nanoparticles. These results proved that Au nanoparticles have a stronger plasmonic enhancement impact on RhB dye fluorescence. Overall, this study suggested that incorporating nanoparticles with PMMA/RhB matrix significantly enhanced the photoluminescence intensity of RhB dye, especially with the core-shell nanoparticles, which provide the most substantial enhancement. The optimal concentration for maximum PL intensity is 4 × 10^-3 M, in addition to that, quenching impacts reduce the fluorescence. The consistent peak position around 580 nm across all samples suggests that the primary effect of nanoparticles is to enhance the emission intensity rather than shift the emission wavelength, highlighting the importance of nanoparticle type and concentration in optimizing the fluorescence properties of dye-doped polymer matrices for applications in photonics and sensing [27].

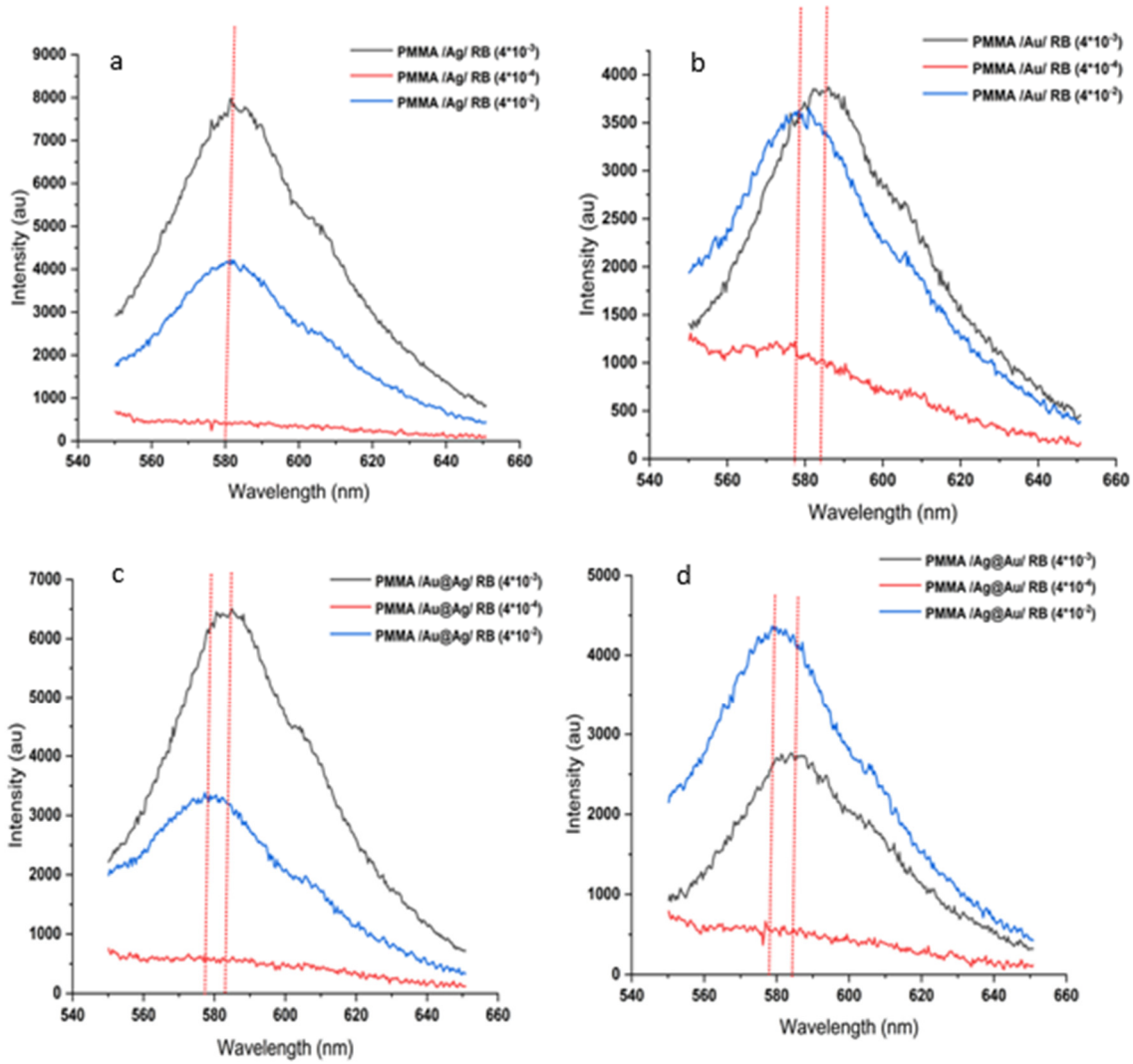

FIGURE 6. Composite Thin Film Types with RhB Dye Absorption at different concentrations and Emission Spectra, (a)PMMA/Ag/Rh.B (b)PMMA/Au/Rh.B (c)PMMA/Ag@Au/Rh.B (d)PMMA/Au@Ag/Rh.B at 3mW power with pumping laser wavelength 532nm.

CONCLUSIONS

This study successfully demonstrated the creation and breakdown of Ag, Au, Ag@Ag, and Ag@Au nanoparticles. Their integration into a PMMA/RhB composite to function as an active medium in random lasers. Characterization methods including photoluminescence (PL), ultraviolet-visible (UV-Vis) and atomic force microscopy (AFM) spectroscopy revealed that: For highest absorption peaks for Au@Ag and Ag@Au were at 500 nm and 400 nm, respectively. Silver and gold NPs exhibited UV absorption peaks at 490 nm and 400 nm, respectively. A composite PMMA/RhB/NP laser active medium was synthesized by mixing a PMMA polymer membrane (at a concentration of 0.25×10^{-2} M) with varying concentrations of rhodamine B dye and 1 ml of nanoparticle colloids. The optimal results indicated that the best optical feedback and amplification were achieved using It was observed that changes in the PMMA/Au@Ag/RhB composite led to a significant increase in the absorption spectrum, indicating enhanced performance of the random laser. A pumping source with a wavelength of 532 nm and pumping powers of 2, 3, 4, and 5 mW.

REFERENCES

1. H. Cao, in *Progress in Optics*, ed. E. Wolf (North-Holland, Amsterdam, 2003) Vol. 45, Chap. 6, p. 317.
2. A.M. Alwan, A.J. Haider and A.A. Jabbar, Surface Coatings Technol, **283** 22-28 (2015)
3. J.A.S. Salman, A.A. Kadhim, and A.J. Haider, J Global Pharma Technol, **10** 348-355 (2018)
4. Z.R. Rhoomi, D.S. Ahmed, M.S. Jabir and A. Kumar, Appl Sci Nanotechnol, **4** (2024)
5. A. J. Haider, F. I. Sultan, & A. Al-Nafiey. Controlled growth of different shapes for ZnO by hydrothermal technique. In AIP Conference Proceedings. 1968 (2018).
6. A. M. Brito-Silva, G. André, S.L. Anderson, J.J. Alcenisio and B.A. Cid, Appl Phys**, 108,** 033508 (2010).
7. F.A. Mutlak and U.M. Nayef. J Appl Sci Nanotechnol, **4** (2024)
8. G. Zacharakis, N.A. Papadogiannis and T.G. Papazoglou, Appl Phys Lett, **81**, 2511-3 (2002).
9. R.C. Polson, A. Chipoline and Z.V. Vardeny, Adv Mater, **13**, 760-4 (2001)
10. Y. Ling, H. Cao, A.L. Burin, M.A. Ratner, X. Liu and R.P.H. Chang, Phys Rev, A64, 063808 (2001)
11. A.H. Attallah, F.S. Abdulwahid, H.J. Abdulrahman, A.J. Haider and Y.A. Ali,. Plasmonics, 1-31 (2024)
12 M.A. Noginov, Other types of solid-state random lasers, pp. 198-221. Springer New York. 2005.
13. D.S. Wiersma, Nature Physics, **4**(5), 359-367 (2008)
14. A.J. Haider, M.J. Haider, M.D. Majed, A.H. Mohammed and H.L. Mansour. Energ Proced, **119,** 256-263 (2017)
15. K.A. Elsayed, H. Imam, M.A. Ahmed and R. Ramadan, Opt Laser Technol, **45.** 495–502 (2013)
16. M. Boutinguiza, R. Comesaña, F. Lusquiños, A. Riveiro, J. Del Val and J. Pou, Appl Surf Sci, **336,** 108–111 (2015)
17. A.A. Yousif, N.F. Habubi and A.A. Haider. J Nano-and Electronic Physics, **4,** 02007-1 (2012)
18. N.A. Aljbar, B.R. Mahdi, A.H. Khalid, A.H. Attallah, F.S. Abdulwahid, and A.J. Haider, Plasmonics. 1-10 (2024)
19. H. Imam, K. Elsayed, M.A. Ahmed and R. Ramdan, Optics Photonics J, **2**(02) (2012)
20. S.A. Mahdi, A.A. Kadhim, S. Albukhaty, S. Nikzad, A.J. Haider, S. Ibraheem and S. Al-Musawi, Electronic J Biotechnol, **52,** 21-29 (2021)
21. A.J. Haider, A.D. Najim and G.A. Ali, Plasmonics **12,** 105-115 (2017)
22. M.A. Al-Kinani, A.J. Haider and S. Al-Musawi. Plasmonics **16,** 1107-1117 (2021)
23. H. Han, Y. Fang, Z. Li, and H. Xu, Appl Phys Lett, **92** (2008).
24. A.M. Mohammed, I.K. Al-Khateeb, A.J. Haider, R.A. Rahim and U. Hashim, Sens Bio-sens Res, **16** 1-5 (2017)
25. E. Kirubha, and p. K. Palanisamy, Adv Natural Sci: Nanosci Nanotechnol, **5**(4), 045006 (2014).
26. A.H. Attallah, F.S. Abdulwahid, Y.A. Ali and A.J. Plasmonics,1-14 (2024)
27. L.A. Muhanmmed, and L.H. Abbod, J Physics: Conf Series, **1999**(1), 012146 (2021)

Comparative Analysis of Land Cover Changes in the Amazon Region of Colombia

Andrés Felipe Muñoz[1,a], Jhonathan F. Maldonado[2,b], Julieth Uribe[1,c] and Nicole González[1,d]

[1]*Faculty of Natural Sciences and Engineering, Universidad Jorge Tadeo Lozano, 110311 Bogotá, Colombia.*
[2]*Independent researcher, 110311 Bogotá, Colombia.*

[a)] Corresponding author: andresf.munozt@utadeo.edu.co [b)] fzambrano573@gmail.com
[c)] julieths.uriber@utadeo.edu.co [d)] nicolej.gonzalezb@utadeo.edu.co

Abstract. This paper analyzes land cover changes occurred between 2002 and 2018 in the Colombian Amazon. In recent years, the exploitation of natural resources has increased significantly and, under climate change effects, has led to an increase in the rates of land cover change, deforestation and landscape connectivity, resulting in habitat fragmentation. To understand the dynamics of this problem, it is necessary to study the causes and interactions of land cover changes. In this context, land cover data (2002-2018) and indigenous territories were used for spatial analysis on ArcGIS software. The cross-tabulation technique was adopted to compare land cover categories to establish gains and losses in the study area. The results reflect an increase in crop and pasture cover, which has led to a reduction in forest cover over the years (> 7000 km^2). Most of the changes are focused on departments of Caquetá, Putumayo and Guaviare, where it is necessary to deepen the causes and effects of land cover changes dynamics at a local scale.

INTRODUCTION

Over the last centuries, the use of natural resources has increased worldwide, due to the global population that has grown rapidly since the Industrial Revolution [1]. In order to achieve the production required for satisfying basic human needs of more than 8 billion people, society has changed the way it used to exploit natural resources [2]. As a result, traditional agricultural systems have turned into large-scale industrial processes, as well as techniques for livestock farming [3]. For instance, over 36.8 percent of the Earth's land surface was used for agriculture and farming in 2021 [4]. Additionally, other processes such as mining, hydrocarbon industry and construction of urban areas, also produce several impacts on natural resources, such as land degradation [5], compaction and loss of nutrients [6].

Although many human activities have been linked as direct causes of deforestation, some underlying causes still have great impacts on deforestation rates in developing countries [7]. It is especially notable in tropical countries with large natural forest cover [8], where deforestation rates continue increasing, because they do not represent just an environmental problem, but also a social, economic and political issue [9]. For example, [10] identified both population density and illicit cropping as drivers for deforestation in Colombia, while [11] found that variables like land appropriation and concentration are critical for Brazil's forest loss.

On the other hand, climate change and its disturbances on variables such as precipitation, temperature and humidity, are direct causes of wildfires [12], and so, are triggers of deforestation [13]. As a result, the growing rates of deforestation have forced governments to develop new policies focused on protected natural areas [14] and to consider in their policies the expansion of land use frontiers as stated by [15]. For instance, countries like Colombia, Peru and Brazil have established regulations for protected areas such as the National System of Protected Areas (SINAP) [16], the National System of Natural Areas Protected by the State (SINANPE) [17] and the Brazilian System of Protected Areas (SNUC) [18]. Nevertheless, deforestation rates have still increased over the last decades in these countries. The global concern about deforestation is so critical, that its reduction has been included as part of the targets defined in the fifteenth Sustainable Development Goal: Life on land [19].

In this context, deforestation in Colombia has reached historical levels over the last years, turning it into one of the main environmental problems in the country [20]. The departments of Putumayo, Guaviare, Caquetá, Meta, Antioquia, Choco, North Santander and Vichada have the highest deforested areas according to [21]. Consequently, Colombia's Amazon region, that includes four of the departments mentioned above, is currently being threatened by the continuous pressure on ecosystems and the loss of natural forest cover [22]. For instance, [23] found an increase of landscape connectivity and habitat loss indexes in the region, apparently linked to the way the government has

Technologies and Materials for Renewable Energy, Environment and Sustainability
AIP Conf. Proc. 3321, 020004-1–020004-11; https://doi.org/10.1063/5.0289822
Published under an exclusive license by AIP Publishing. 978-0-7354-5231-2/$30.00

implemented the peacebuilding process since 2016, which seems to be a decisive variable in future scenarios of deforestation [9].

In order to cope with the loss of natural forests in the country, it is necessary to carry out research projects for studying possible drivers and interactions of land cover processes in Colombia. Thus, GIS technologies including supervised and unsupervised classification [24]; [25]; [26)], remote sensing and proximity analysis [13]; [27], among other tools, have been used for developing inputs to understand land cover dynamics. As a result, decision-makers are able to formulate evidence-based policies [28], for addressing socio-economic and environmental issues linked to land cover change and deforestation. Accordingly, the present study aims to analyze the dynamics of land cover changes in the Amazon region of Colombia.

MATERIALS AND METHODS

STUDY AREA

The Amazon River is the largest and fastest-flowing river in the world, carrying an average discharge of 210.000 m^3/s. The total area of the Amazon basin is up to 7'000.000 km^2 [29], including territories from Brazil, Colombia, Venezuela, Peru, Ecuador, Bolivia, Guyana and Suriname (Figure 1). However, considering that every country has different available information, public policies, and land cover change dynamics, the study area only comprises the Amazon region within the Colombian territory. It represents approximately 341.994,37 km2, only 4.8|% of the total Amazon basin [30]. As shown in Table 1, the Amazon basin inside of Colombia includes ten departments of the country, with higher covered area in the departments of Amazonas, Caquetá, Guaviare, Guainía, Vaupés and Putumayo.

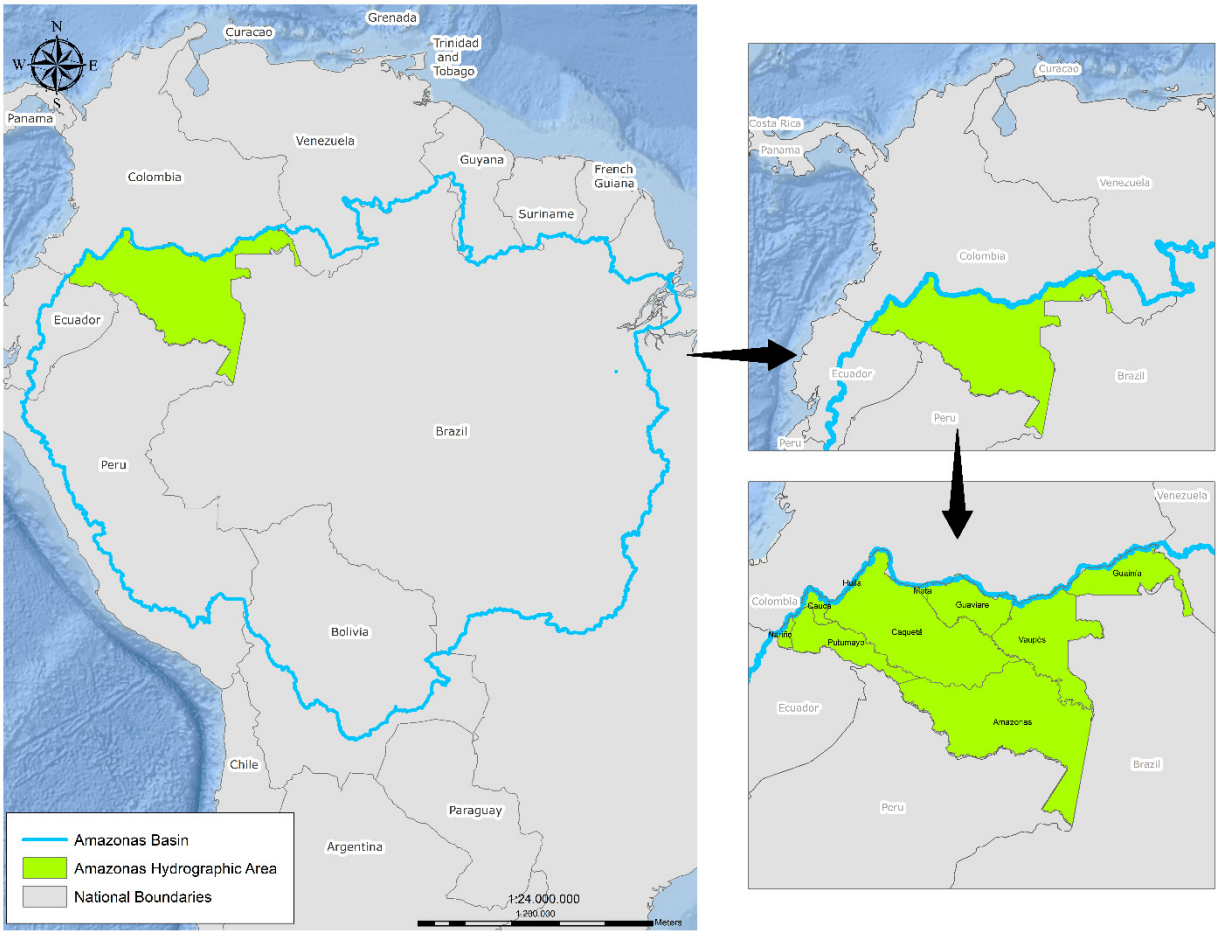

FIGURE 1. Study area: Amazon River basin within Colombia

Table 1. Extension of the Departments of Colombia within the Amazon basin

Department	Area (km^2)	Area within the basin (km^2)	Percentage of the department (%)	Percentage of the basin (%)
Amazonas	108752	108752	100.00	31.89
Caquetá	90150	89911	99.73	26.36
Cauca	31191	4945	15.85	1.45
Guainía	71055	29584	41.64	8.67
Guaviare	55399	24971	45.08	7.32
Huila	18165	20	0.11	0.01
Meta	85276	3542	4.15	1.04
Nariño	31422	2817	8.97	0.83
Putumayo	25960	25901	99.77	7.59
Vaupés	53247	50601	95.03	14.84
Total	570622	341048	-	100

DATA SOURCES

The research project was based on a quantitative and descriptive study, applying a multi-temporal analysis of deforestation within the Colombian Amazon. Among the inputs required for the study, land cover data was collected from the Hydrology, Meteorology and Environmental Studies Institute (IDEAM) of Colombia [30]. This data uses the Corine Land Cover (CLC) methodology and is restricted for years 2000, 2005, 2012 and 2018. Due to the multiple land cover categories defined in the lowest level (57) [30], the third level of CLC hierarchy was selected for the spatial analysis (31 categories), in order to improve the quality of the results obtained. Considering the availability of information for land cover, the study temporality was delimited from 2000 to 2018. On the other hand, the study area was enclosed by the Amazon basin located inside Colombian territory. Technically, it was defined as the hydrographic area 4 according to the Hydrographic Zoning map of IDEAM [31]. It includes hydrographic subzones 41 to 49. Indigenous territories were obtained from the official information reported by the Amazon Institute of Scientific Research (SINCHI). Features of these inputs are shown in Table 2.

Table 2. Sources and features of inputs used for the spatial analysis

Input	Period	Data type	Source
Land Cover 100K	2000-2002	Vector	IDEAM
Land Cover 100K	2018	Vector	IDEAM
Hydrographic Zoning	2013	Vector	IDEAM
Indigenous territories	2019	Vector	SINCHI

SPATIAL ANALYSIS FOR LAND COVER CHANGE

The analysis of land change was performed at a scale of 1:100,000 from the coverages identified at third level under the CLC methodology adapted for Colombia for years 2002 and 2018. To detail the spatial-temporal changes in the Amazon hydrographic area, the spatial analysis was performed in ArcGIS by generating a cut between the Amazon Hydrographic Area and the CLC coverages in shapefile (SHP). All data was processed in vector format to obtain the inputs required to overlap the layers and obtain a final layer identifying the changes in the defined temporality. Data obtained from SINCHI was finally crossed to analyze patterns of land change and the impact of indigenous territories. Additionally, the information obtained from IDEAM and the SINCHI institute is projected under the CTM 12 or Unique National Origin coordinate system, allowing the analysis to be performed under the same geographic system.

CROSS-TABULATION MATRIX

The methodology employed is grounded on the cross-tabulation technique developed by Pontius, which allows analyzing changes in land use by comparing maps from different years, crossing two nominal data matrices representing different land use categories [33]. In the resulting matrix (Table 3), the categories of the first year are organized in rows and those of the second year in columns, making it possible to observe both the persistence of land use in the main diagonal and the transitions between categories in the other cells [34]. This technique makes it easier

to quantify the area of each use class and to determine the changes that have occurred between the different thematic categories represented in the maps at different times, providing a graphical and cartographic representation of the results.

TABLE 3. Cross tabulation matrix for land cover changes.

T_A	T_B				Total Area at T_A	Loss (L_{ij})
	LC_1	LC_2	...	LC_i		
LC_1	P_{11}	P_{12}	...	P_{1i}	P_{1+}	$P_{1+} - P_{11}$
LC_2	P_{21}	P_{22}	...	P_{2i}	P_{2+}	$P_{2+} - P_{22}$
...	...	...	...	...	...	...
LC_j	P_{j1}	P_{j2}	...	P_{ji}	P_{j+}	$P_{j+} - P_{ji}$
Total Area at T_B	P_{+1}	P_{+2}	...	P_{+i}	P	
Gain (G_{ij})	$P_{+1} - P_{11}$	$P_{+2} - P_{22}$	...	$P_{+j} - P_{ji}$		

Source: Pontius et al, 2004 and Pineda et al, 2009.

The main diagonal represents the persistence, an indicator of the stability of the amount of area of a given category that has not changed between two different periods, as seen in cell P_{11}, where the amount of area of LC_1 remains constant between the first two years. A high persistence indicates that most of the territory has remained unchanged, and so that land use has remained stable [35]. On the contrary, transitions are the observed changes that reflect movements in land use between different categories. Cells outside the main diagonal represent transformations, as illustrated in cell P_{12} that indicates a change of LC_1 area in T_A into LC_2 in T_B [36].

The gross loss (L_{ij}) is the amount of area that decreased in a specific category from T_A to T_B (eq. 1). It represents areas that belonged to a LC during T_A but changed to a different one at T_B. On the contrary, the gross gain (G_{ij}) is related to the increase of area by a specific LC category, as a result of transitions from other categories (eq. 2) (Pineda et al., 2009). Finally, the net change of the matrix is the difference between the total gains and losses for a specific LC category. A positive net change indicates the category had a growing pattern over time, while a negative net change means the category had a decreasing pattern.

$$P_{ij} = (P_{i+} - P_{ii})\left(\frac{P_{+j}}{\sum_{j=1,\, j\neq i}^{i} P_{+j}}\right) \tag{1}$$

$$G_{ij} = \left(P_{+j} - P_{jj}\right)\left(\frac{P_{i+}}{\sum_{i=1,\, i\neq j}^{j} P_{i+}}\right) \tag{2}$$

where L_{ij} is the gross loss, G_{ij} is the gross gain, P_{ii} and P_{jj} are the persistence, P_{+j} is the sum of LC_j column and P_{i+} is the sum of LC_i raw.

RESULTS

SPATIAL ANALYSIS FOR LAND COVER CHANGE

In Figure 2 it is shown the main land covers inside the Amazon hydrographic area of Colombia, where it is evident that forest cover was reduced from 2002 to 2018, primarily at the northwest of the basin. On the other hand, it is also possible to identify that crops and pastures are the cover that increases more significantly during the study time. In the southern part of the region, near the border area with Brazil, the presence of industrial or commercial units that were not identified in 2002 has been identified, in addition to the increase in mining sites in this same area; however, they do not represent extensive areas in contrast to agriculture and pasture covers. On the other hand, the northeastern territories do not present significant changes over time in comparison to the departments of the northwest.

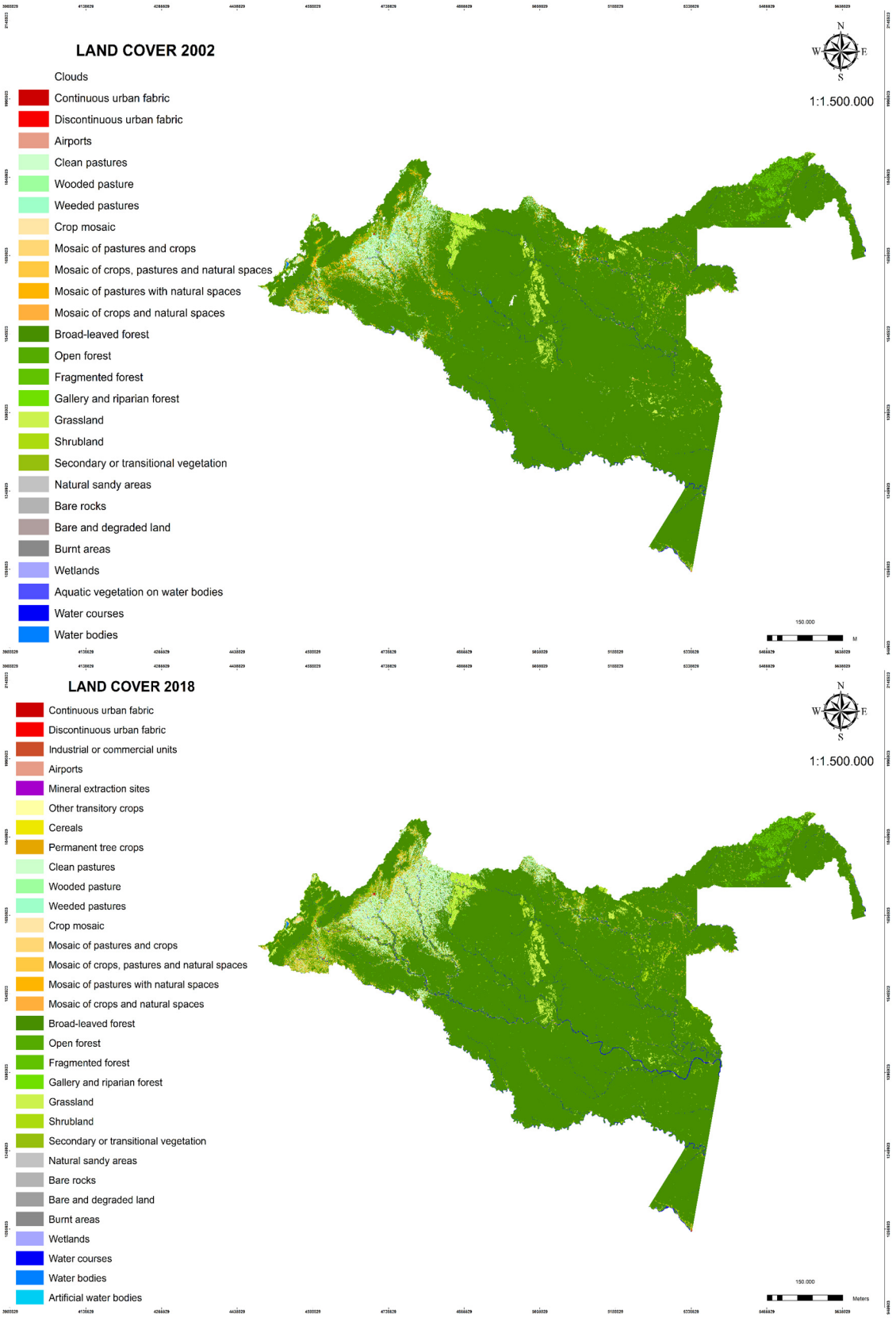

FIGURE 2. Comparison of land cover in the Amazon region between 2002 and 2018

In this context, the higher changes of land cover seem to be related to forest, pastures and agriculture areas. This information is summed up in Table 4, where the area of these three categories of CLC is presented in both years. As we have seen, the departments of Caquetá, Amazonas and Meta have lost more than 7500 km2 of forest cover in less than 20 years, equivalent to 2.20% of the Colombian Amazon basin. Water bodies seem to increase in the ten departments, with an increase of 1632 km2, as well as the areas destined to agriculture, which in some departments increased significantly, as in Caquetá and Meta, where they grew by 52.94% and 143.08%, respectively. In addition, wetlands have also shown a decrease, especially in departments such as Putumayo, Guaviare and Vaupes, with a total decrease of 68.8% in the 10 departments.

TABLE 4. Main changes of Land cover 2002-2018

Department	1. Artificial surfaces (km^2)		2. Agriculture Areas (km^2)		3. Forest and seminatural areas (km^2)		4. Wetlands (km^2)		5. Water bodies (km^2)	
	2002	**2018**	**2002**	**2018**	**2002**	**2018**	**2002**	**2018**	**2002**	**2018**
Amazonas	7	17	259	165	108311	107565	5.1	15	737	1557
Caquetá	22	40	11822	18081	77024	70839	400	86	335	865
Cauca	0	0.7	400	370	4404	4528	1	0	4.1	46
Guainía	1	2.9	91	67	29014	29036	0	0.6	171	170
Guaviare	1	2.5	1155	1700	23636	23130	28	26	111	113
Huila	0	0	0	0.3	17	20	0	0	0	0
Meta	0	0	441	1072	3089	2458	10	0	2.8	12
Nariño	0	0.6	228	233	2268	2533	0	0.6	50	50
Putumayo	20	36	4125	4126	21198	21236	54	22	206	364
Vaupés	16	10	574	509	49464	49481	12	8.4	380	450
Total	**66**	**110**	**19094**	**26323**	**318424**	**310827**	**510**	**159**	**1996**	**3628**

CROSS-TABULATION MATRIX

The cross-tabulation matrix was built up in order to analyze specific interactions between the different LC (see Table 5). As shown in Table 6, the matrix contains a total of 27 categories at the initial time (2002), and 31 categories at the final time (2018). This change in LC number is due to the change of territories to LC that did not exist back in 2002. The persistence (diagonal) is highlighted and represents all the areas that preserved their land cover during the years studied. LC 311 (dense forest) has the highest persistence with over 28 million km^2, while LC 312 and 232 were not identified in 2018, and so have the lowest persistence in the matrix.

TABLE 5. Land Cover (LC) categories used for cross-tabulation matrix

ID	Land Cover category	ID	Land Cover category	ID	Land Cover category
111	Continuous urban fabric	241	Annual crops associated with permanent crops	323	Secondary vegetation
112	Discontinuous urban fabric	242	Mosaic of crops	331	Beaches, dunes, sands
121	Industrial or commercial units	243	Mosaic of crops and natural spaces	332	Bare rock
124	Airports	244	Agro-forestry areas	333	Sparsely vegetated areas
131	Mineral extraction sites	245	Mixed crops	334	Burnt areas
211	Non-irrigated arable land	311	Broad-leaved forest	411	Inland wetlands
212	Permanently irrigated land	312	Open forest	413	Vegetation in water bodies
223	Permanent crops	313	Fragmented forest	511	Water courses
231	Pastures	314	Riparian forest	512	Water bodies
232	Pastures and trees	321	Natural grassland	514	Artificial water bodies
233	Pastures and weeds	322	Shrubland		

TABLE 6. Cross tabulation matrix for land cover changes.

Land Cover Area (km^2) 2002	Land Cover Area (km^2) 2018															
	111	112	121	124	131	211	212	223	231	232	233	241	242	243	244	245
111	31.6	0.4														
112	4	9.2		0.4	0.1				5.6					4.4	2	
124				5.4												
231	11	12.4	2.6	0.8	0.9			1.4	816.5	3.5	62.2	6.4	21.4	35.1	971.2	0.2
232									0.4		0.3					
233	1.4	1.9	0.1				0.4		515		84.1		12.2	22.2	113.5	
241									0.7		0.2			2.9	2.4	
242	1.7	1		0.1	0.1				23		2.1	4	47	67.4	12.8	
243	2.7	5.6	0.1	0.1					56.5		9.9		4.2	153.3	49.5	0.1
244	2.3	3.1			0.3	0.4		173.8	0.7	231.2			46.8	427.7	91.5	0.2
245														2	0.3	0.8
311	0.3	1.5	0.3	1.6	2.5	2.3		1.6	4171.8	0.5	456.9		65.6	82.6	124.5	2.2
312																
313		0.5		0.1				2.9	354.5	0.1	48.9		8.7	153.2	231.7	0.7
314					0.2				1.8		1.3			0.5	8.8	
321					0.1				36.6		2.8		1.8	1.7	17	
322									21		7.1		1	6.8	23.9	
323	0.9	1.8	0.2	0.4	0.2	0.5		0.4	2112.5	0.4	282.3		29.8	346	923.3	1.2
331														0.1	0.5	
332																
333	0.1								0.5				0.4	0.1	0.1	
334									7.7		0.2		0.1	0.1	0.2	
411									179.7		24.5		2.3	3.6	45.9	
413																
511									2.8		1.5		0.2	5.7	8.7	
512									0.5		0.1				1.4	
Total 2002	55.9	37.4	3.2	8.8	4.5	3.2	0.5	1710	15521	235.7	1525.2	10.4	422.2	2328.2	4563.0	5.5
Gain	24.3	28.2	6.5	3.4	9.1	6.3	0.9	3420	7504.5	235.7	1441.1	10.4	375.2	2174.9	3661.5	4.7

TABLE 6. Cross tabulation matrix for land cover changes (cont.)

LC Area (km^2) 2002	Land Cover Area (km^2) 2018															Total 2018	Loss
	311	312	313	314	321	322	323	331	332	333	334	411	511	512	514		
111																32	0
112							1.5						0.1			27	18
124							1									6	1
231	38.1		49.4	6.8	1.6		1289.9	0.9			31.2	6	26.4	0.1	1.2	11587	3571
232			0.5				0.8									2	2
233	3.5		9.9	1.2	1.5		142.6	0.2			1.9	0.7	2.9		0.2	916	832
241	0.5						4.4	0.4					0.1			11	11
242	2.6		0.4				111.7					0.3	0.5			274	227
243	17.8		16.1		0.6	38							6.4			703	549
244	7		94.6	0.9	3.8	0.1	278	0.4			7.2	1.2	11.9			5586	4685
245							11.6									15	14
311	281393	0.3	198.8	37.7	311.3	289.4	344.7	81.4		0.8	146.3	27.3	1614.5	6.4	0.1	296062	14669
312	76.6				5.3	62.1	0.1									144	144
313	34.8		994.7	0.2	2.1	15.8	627.9				3.7	0.5	2.9			2790	1795
314	26.8		1.3	2541.1	18.5		6.6				1.6	0.3	0.1			2618	77
321	281.4		2.2	4.5	5618.2	51.4	51.8	0.6			69.5	1.3	0.7	0.7		6142	524
322	144		1.6	0.9	39.5	1291.7	126	0.6			0.4	0.7	9.5			1675	383
323	475		199.9	8.3	11.7	176	3456.1	2.9			2.8	5.7	58.7	0.2		8115	4659
331	8.2		0.1		27.2	0.7	9.2	1.5				6	29.3	1.5		93	83
332									0.2							0	0
333						1.3	0.4		0.5							3	3
334							0.3									9	9
411	32.5		0.8	1.2	59.3	0.7	5.2				1	11.2	3.9	2	0.6	509	408
413												0.8				1	0
511	17.4		1.6		1.4	0.6	4.7	25.3				2.1	1716.3	3		1827	111
512	22.7				9.3		0.2	1.9				5.4	0.1	139.5		181	41
Total 2002	283657	0.3	3359.6	2602.8	6298.1	2295.3	11431	125.2	0.6	0.8	283.6	159.3	3484.2	153.3	2.1		
Gain	2263.7	0.3	2365.0	61.7	679.8	1003.6	7975	114.7	0.5	0.8	283.6	58.1	1767.8	13.8	2.1		

Furthermore, the overlapping of indigenous territories and land cover was developed by crossing the areas where deforestation was reported between 2002 and 2018, representing the loss of forest cover. As it can be seen in Figure 3, deforestation processes were mainly developed in departments of Caquetá, Putumayo and Guaviare. Indigenous territories are located all around the Amazon Basin, with higher presence in Amazonas, Vaupés and Guanía departments. Finally, the results highlight that the critical areas of deforestation processes in the area are located in the upstream basin, as seen in both 2002 and 2018 maps.

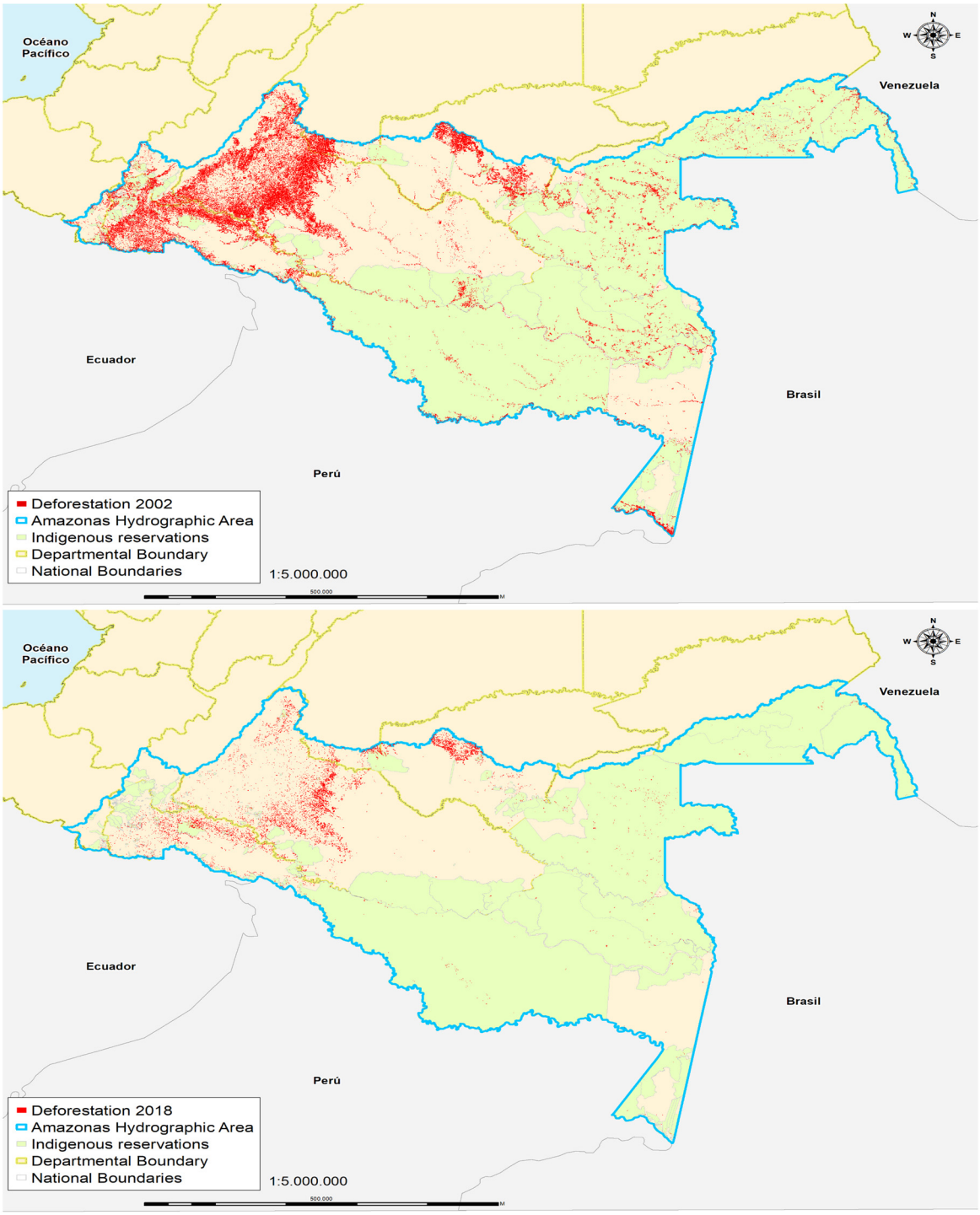

FIGURE 3. Deforestation and Indigenous territories within the Amazon Basin between 2002 and 2018.

DISCUSSION

Land cover changes analysis in the Amazon region of Colombia demonstrate that there are significant differences among the departments of the region, probably related to variables like demographic dynamics and local regulations. Departments of Caquetá, Putumayo and Guaviare have higher values of forest loss, and the change of this LC is mainly associated with increasing areas for agriculture and pastures. Although the Colombian Amazon covers over 40% of the country's territory, approximately 20% of this area has already been affected by anthropogenic actions [37]. The threats related to population growth, urban sprawl, agriculture and livestock expansion have produced an impact on the ecosystem diversity of the Amazon basin and will continue doing so for the next decades [36].

According to the results of the cross-tabulation matrix, the sum of the main diagonal shows the total area of the study site that has remained unchanged. It is equivalent to 306.512 km^2 that indicates some stability of the landscape. However, this value represents only 90% of the total area of the basin, which indicates that 10% of the study area changed its land cover from 2002 to 2018; a similar case to Peru were 3.56% of Amazonian rainforest was lost between 2001 and 2019 [38]. On the other hand, higher net losses are associated with LC 311, 323 and 244, that represent loss of broad-leaved forest, secondary vegetation and agro-forestry areas. Net loss of Forest and semi natural areas as shown in Table 4 are equivalent to 7598 km^2, less in comparison to the losses in Brazil, which in a period of 22 years lost 4.35 million hectares of Amazonian forest [39]. On the other hand, net gains are primarily developed in agricultural areas (up to 7000 km^2). However, even though artificial surfaces have a small percentual coverage (<0.01%), they have doubled the covered area between 2002 to 2018, increasing the impervious area within the basin.

It is important to consider that some ecosystem services provided by the watershed, such as flood regulation and erosion control, can be reduced in those areas more affected by land cover change and deforestation [40], generating higher risks to the population that lives around. For example, mining activities and extensive farming are considered main causes for fauna and flora diversity reduction, which consequently produces less resilient ecosystems [41]. As a result, the land use change in deforested Amazon is contributing to diminish rich nutrients soils, mostly due to the reduction of the amount and diversity of decomposers, that cannot continue producing organic matter and new soil as they did previously [42]. In this context, it is necessary to continue developing quantitative analysis of land cover changes and deforestation, to evaluate the effectiveness of protection policies in the conservation of biodiversity and sustainability of natural resources [43] in the Amazon region of Colombia.

CONCLUSION

The results indicate that land cover changes in the Amazon region of Colombia are higher in the northwest areas of the basin. Even though all LC categories have changed over time, the land cover changes are mainly related to reduction of broad-leaved forest and its transformation to pastures and agriculture areas. This issue has been reported in every country of the Amazon basin, and in Colombia it has been linked to indirect drivers like the lack of authority presence, wildfires, socio-economic dynamics and economic interests. Indeed, according to the cross-tabulation matrix it is possible to state that the forest areas lost are not only being caused for crops and farming, but also for mining and urban territories.

Finally, regarding the development of land cover changes, it is necessary to highlight that although these changes are not concentrated in indigenous territories, some of them are actually developed within areas corresponding to indigenous reserves. Consequently, information about location of indigenous communities, social conflicts and displacement should be studied deeply to understand the local dynamics that can affect not only land cover changes, but stability and life quality of these communities. It is also possible to continue to broaden the scope of these analyses in order to evaluate the relationship between the loss of forest cover and other variables, like road constructions, natural protected areas and illicit crops, among others.

REFERENCES

1. A. Cearreta, El Antropoceno. *Grand Place.* 7, 39-51 (2017)
2. C. Delgado, Del consumismo al consumo sostenible. *Punto de vista.* **4**(6) (2013)
3. V. Toledo, La memoria tradicional: la importancia agroecológica de los saberes locales. (2005)
4. Grupo Banco Mundial. Tierras agrícolas (% del área de la tierra). (2021)
5. S. Tyagi, N. Garg, and R. Paudel, *European Res* **81**(8-2), 1491 (2014)
6. H. Quinto-Mosquera, G. Ayala-Vivas and H. Gutiérrez,. *Rev Academia Colombiana de Ciencias Exactas, Físicas y Naturales*, **46**(179), 514-528 (2022)

7. D. Armenteras, J.M. Espelta, N. Rodríguez, and J. Retana, *Global Environ Change*, **46**, 139-147 (2017)
8. FAO. Global Forest Resources Assessment 2020: Main report. Rome. 2020
9. A. González-González, J.C. Villegas, N. Clerici and J. Salazar, *Ecol Ind,* **126**, 695-698 (2021)
10. D. Armenteras, G. Rudas, N. Rodriguez, S. Sua and M. Romero, *Ecol Ind,* **6**(2), 353-368 (2006)
11. N.C. Ferreira, L.G. Ferreira and F. Miziara, *Earth Interact,* **11**(1), 1-16 (2007)
12. A. Casallas, C. Jiménez-Saenz, V. Torres, M. Quirama-Aguilar, A. Lizcano, E. A. Lopez-Barrera, and R. Arenas, R. *Sensors.* **22**(22), 8790 (2022)
13. C. Ma, R. Pu, J. Downs and H. Jin, *Geosci,* **12**(6), 237 (2022)
14. E. Souza-Rodrigues, Rev Econ Stud, **86**(6), 2713-2744 (2019)
15. I. Tritsch and F. Le Tourneau, Appl Geograph, **76**, 163-172 (2016)
16. Y. Rojas Lenis, Soc Econ, **27**, 155-176 (2014)
17. Ley N° 26834 de 1997.[Congreso de la República Perú]. Ley de Áreas Naturales Protegidas. 4 de julio de 1997. N° 6215
18. N.R.A. Cabral, M.R. Côrtes and M.P. Souza, *Investigaciones Geográficas*, 26, 181-189 (2001)
19. ONU. Transforming our world: the 2030 Agenda for Sustainable Development. 2015
20. OECD. OECD Environmental Performance Reviews: Colombia 2014, OECD Environmental. Paris. 2014
21. IDEAM. Resultados de monitoreo deforestación 2019. 2020
22. A. Etter, C. McAlpine, S. Phinn, D. Pullar and H. Possingham, Global Chang Biol, **12**(8), 1409-1420 (2006)
23. P.J. Murillo-Sandoval, N. Clerici and C. Correa-Ayram, *Global Ecol Conserv,* **38**, 205 (2022)
24. S. Yoshikawa and K. Sanga-Ngoie, Int J Remote Sens, **32**(2), 523-544 (2011)
25. M. Heredia-R, B. Torres, F. Cabrera-Torres, E. Torres, C.G. Díaz-Ambrona and S.E. Pappalardo, *Forests,* **12**(11), 1539 (2021)
26. C.A. Murad and J. Pearse, Remote Sens Applicat: Soc Enviro, **11**, 161-171 (2018)
27. G. Chen, R.P. Powers, L.M. de Carvalho and B. Mora, Appl Geograph. **63**, 1-8 (2015)
28. M. Balcazar, L. Chen, J. Lee and H. Tesfahunegn, Evidence-based Policy Design in Colombia: An Empirical Study of Environmental Interventions and Outcomes in Latin America. 2018
29. Z. Novoa Goicochea, *Espacio y Desarrollo,* **8,** 115-160 (1996)
30. IDEAM. Estudio Nacional del Agua. Bogotá. 2010
31. IDEAM. Zonificación y codificación de unidades hidrográficas e hidrogeológicas de Colombia, Bogotá, D. C. Bogotá. 2013
32. M. Gallardo and V. Martinez,Cambios de usos del suelo en la comunidad de Madrid: analizando el pasado y simulando el futuro. XV Congreso Nacional de Tecnologías de la Información Geográfica, Madrid. 2012
33. R.G. Pontius Jr and X. Li, J Land Use Sci, **5**(1), 31-44, (2004)
34. Pineda, N. B., Bosque, J., Gómez, M., & Plata, W. Análisis de cambio del uso del suelo en el Estado de México mediante sistemas de información geográfica y técnicas de regresión multivariantes: Una aproximación a los procesos de deforestación. Investigaciones geográficas. 2009; 69: 33-52
35. Gómez, L. F. (2021). Análisis de indicadores de cambio de usos del suelo y vulnerabilidad de cambio en la ciudad de Goya, Corrientes, Argentina, entre 1990 y 2016. Huellas. 2021; 25: 8-25
36. IGAC & CORPOICA (2002). Zonificación de los conflictos de uso de las tierras en Colombia.
37. Comisión Económica para América Latina y el Caribe (CEPAL). La pérdida de los bosques de América Latina y el Caribe 1990–2020: evidencia estadística. División de Estadísticas. 2021.
38. S. Barreda, *Revista Electronica Del Medio Ambiente,* **21**(2), 20-39 (2021)
39. L. Ñuflo and A. Marcelino. Captura de Carbono en el Sistema Agroforestal de Theobroma cacao (Cacao), en el distrito de lrazola, región Ucayali. 2013.
40. A. Ochoa Jaramillo and G. Poveda Jaramillo, *Escuela De Geociencias Y Medio Ambiente.* 2008.
41. O. Vargas Rìos, *Acta Biològica Colombiana,* **16**(2), 221-246 (2011)
42. X.A. Sartre, B. Ramìrez, G. Rodriguez, O. Villanueva, O. Johan and P. Lavelle, *Revista Geogrèfica.* **151**, 47-62 (2012)
43. D.H. Wall, R.D. Bardgett, V. Behan-Pelletier, J.E. Herrick, T.H. Jones, J. Six, et al. *Soil Ecology and Ecosystem Services.* 1st ed. Oxford: OUP Oxford; 2012

Enhancing the Performance of a Nine-Level Inverter Using an Artificial Neural Network

Sofia Lemssaddak[1,2], Abdelhafid Ait Elmahjoub[1], Mohamed Tabaa[2a,] Mourad Zegrari[1]

[1]CCPS Laboratory, ENSAM, University of Hassan II, Casablanca, Morocco
[2] Pluridisciplinary Laboratory of Research & Innovation (LPRI), EMSI, Casablanca, Morocco

[a] Corresponding author: *m.tabaa@emsi.ma*

Abstract. The multilevel inverter converts multiple DC voltages into AC voltages, offering significant benefits in high-power applications within the energy sector. However, a notable challenge in power electronics is harmonic distortion. Various control strategies aim to mitigate harmonics, typically assessed using total harmonic distortion (THD). This study compares the effectiveness of a neural network-based approach for commutation angle prediction against a PI controller with both open-loop and closed-loop configurations to minimize THD.A MATLAB R2021b simulation of a nine-level asymmetric multilevel inverter circuit employing sinusoidal PWM modulation was conducted. The results indicate a 1.3% reduction in THD achieved with the neural network compared to the open-loop PI controller. Detailed discussion and analysis of these findings are presented in the conclusions.

Keywords. ANN (Artificial Neural Network), 9MLI (nine multilevel Inverter) (DC (Direct Current), AC (Alternating Current), THD (Total Harmonic Distortion), PI (proportional - integral)

INTRODUCTION

The multi-objective optimization of multilevel converters, which aims to improve modulation strategies to significantly reduce total harmonic distortion (THD) down to the 50th harmonic while maintaining a stable and efficient output voltage, is a significant advancement in the field of power electronics. This process ensures maximum performance, system stability, superior power supply, and compliance with strict criteria [1]. Furthermore, owing to an inventive design that makes use of asymmetrical DC sources, asymmetrical multilevel inverters exhibit considerable promise in solar PV systems, aiding in cost reduction and space optimization [2]. A significant advancement in the assessment of individual cell voltages in multilevel converters is the use of the k-means algorithm for cluster analysis, which provides remarkable accuracy and efficiency without requiring specific controller information. This method increases the flexibility of real-time applications while providing notable savings in terms of cost and complexity [3]. Also, a notable decrease in real-time computational burden is observed when machine learning models are used to simulate MPC (Model Predictive Control) controllers in modular multilevel converters, enhancing both steady-state and dynamic performance. Power electronics systems can be continuously improved with the help of this technique [4]. lower stress on switching devices and better output voltage quality are the two primary benefits of multilayer inverters. The most recent technological developments, including switched-capacitor systems, are designed to minimize converter structural complexity and maximize energy efficiency [5].

These numerous developments show the multilevel converter technologies' continual advancement as well as their increasing significance in the creation of high-performing, sustainable energy solutions for modern applications.

STATE OF THE ART

The use of artificial intelligence (AI) to manipulate multilevel converters represents a significant advancement in power electronics. Multilevel converters are sophisticated devices that change electrical energy in an appropriate way, resulting in higher output quality. Artificial intelligence improves system control precision and responsiveness by utilizing advanced algorithms to predict and alter parameters in real time. This method conserves energy by improving switching transitions and eliminating harmonics in output signals.

Proactive maintenance based on predictive analytics reduces operating costs, increases system reliability, and optimizes power management. By integrating artificial intelligence into multilevel converter management,

Technologies and Materials for Renewable Energy, Environment and Sustainability
AIP Conf. Proc. 3321, 020005-1–020005-9; https://doi.org/10.1063/5.0291041
Published under an exclusive license by AIP Publishing. 978-0-7354-5231-2/$30.00

enterprises can enhance their energy efficiency and encourage more cost-effective and sustainable utilization of electrical resources on a broad scale.

Numerous strategies and tactics can be used to include artificial intelligence (AI) into the multilevel converter control system. A few forms of AI utilized in this field are as follows.

ARTIFICIAL NEURAL NETWORKS (RNA):

RNA is frequently used to model and predict the dynamic behavior of multilevel converters. To optimize the system's performance and adjust the control parameters in real time, they can be trained using historical data.[6] order to reduce harmonic content, it suggests a modified cascaded H-bridge multilevel inverter (M-CHBMI) that makes use of the Selective Harmonic Elimination Pulse Width Modulation (SHE-PWM) technique. Using an ANN controller, the proposed M-CHBMI enhances output voltage and current performance, assisting in reducing total harmonic distortion (THD) in real-time applications.

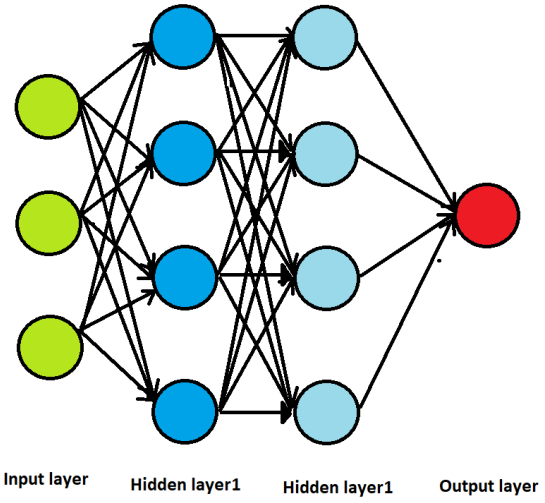

FIGURE 1. Multilevel converter for 9 levels

[7] Using FFT and ANN approaches for precise defect detection based on output tension characteristics, it investigates the effects of defects on an MLI at five levels with a modulation index of 0.85. The main objective of [8] is to simulate and design a three-phase, five-level cascaded inverter to estimate the load current's THD value. An artificial neural network (ANN) system is trained and tested using this dataset to determine the load current's THD value. This enables the selection of the best inverter circuit configuration with the lowest THD prior to experimental implementation.

GENETIC ALGORITHMS

Multilevel converters' control settings can be optimized using genetic algorithms to achieve a variety of goals, including increased output power quality, reduced loss, and energy efficiency. An extensive analysis of metaheuristic methods for multilevel inverters is provided in [9]. The investigation indicates that evolutionary algorithms are widely employed, particularly in setups up to seven layers, RL loads, and cascaded H-bridge multilevel inverter systems. Several case studies have demonstrated their efficacy in enhancing UPS performance and lowering THD. [10] use a genetic algorithm and sinusoidal PWM modulation to decrease line voltage harmonics in three-phase applications. It also contrasts the output of a nine-level model with diodes and a cascaded seven-level multilevel oscillator.[11] studies the reduction of total harmonic distortion (THD) in a multilevel harmonic oscillator with a resistive charge cascading to seven levels using an optimization approach based on teaching and learning.

EXPERT SYSTEMS

Complex control choices for multilevel converters are made by expert systems using logic rules and expert knowledge. Adaptive recovery mechanisms can be programmed to deal with atypical conditions or failures. [12] presents a fault detection method that combines artificial intelligence with decision trees. It shows how to locate faults accurately and efficiently while requiring little computing overhead. We look closely at the artificial

intelligence (AI) methods in [8] that find and identify open circuit (OC) faults in a variety of multilevel inverter layouts. It arranges methods for finding flaws, provides a thorough analysis of AI algorithms, and creates standards for judging the many approaches that are discussed in the literature. [13] examines grid-connected photovoltaic systems with an emphasis on increasing power and enhancing electricity quality. To increase efficiency and lower total harmonic distortion (THD), it offers a cascaded multilayer inverter (MLI) with fewer switches and an MPPT approach based on artificial intelligence [14].

MACHINE LEARNING

This method encompasses several approaches, including reinforcement, unsupervised, and supervised learning. It makes it possible to modify multilayer converter control in response to predetermined goals and real-time data, enhancing system stability and operational effectiveness. To outperform traditional techniques, [15] investigates a solar system that integrates a machine learning-based controller with a reduced-switch multilevel inverter. To ensure accuracy, robustness, and stability in PV system control, machine learning techniques are compared. [16] focuses on applying methods to accurately identify problematic switches based on switch current and capacitor current data to detect open circuit switching faults in multilevel inverters. [17] suggests a way to swiftly identify the best circulating current references using artificial neural networks (ANNs) in place of laborious analytical computations.

MULTILEVEL INVERTER CIRCUITS

Seven switches, three diodes, and two DC power sources make form the construction in [18], which generates nine output voltage levels as opposed to simply one. Unequal DC voltage sources are employed in this topology.

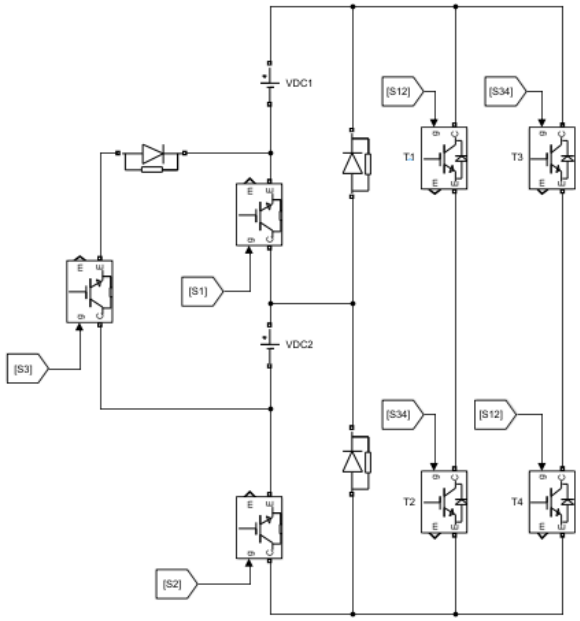

FIGURE 2. Multilevel converter for 9 levels

The output waveform has varied levels when S1, S2, and S3 are switched. This process is referred to as "level generation". S12, S12, S34, and S34 are switched when the output waveform's polarity is reversed. This section is dubbed "polarity generation". Three diodes (D1, D2, and D3) are also included in the circuit to create current channels and prevent short circuits.

Table 1. Switching states of 9 multilevel inverters

Mode	*S1 S2 S3 S12 S34*	Vout
A	ON ON OFF ON OFF	VDC1+VDC2
B	ON OFF OFF ON OFF	VDC1
C	OFF OFF ON ON OFF	VDC1-VDC2
D	OFF ON OFF ON OFF	VDC2
E	OFF OFF OFF OFF OFF	0
F	OFF ON OFF OFF ON	- VDC2
G	OFF OFF ON OFF ON	- (VDC1-VDC2)
H	ON OFF OFF OFF ON	- VDC1
I	OFF OFF ON OFF ON	- (VDC1+VDC2)

Table 1 displays the switching states, where modes A through D correspond to positive half-cycle modes, modes F through I to negative half-cycle modes and mode E for zero. As the table illustrates, the switching sequence for switches S1, S2, and S3 is also the same in both half-cycles. Additionally, it demonstrates that switches in S12 and S34 function at distinct times.

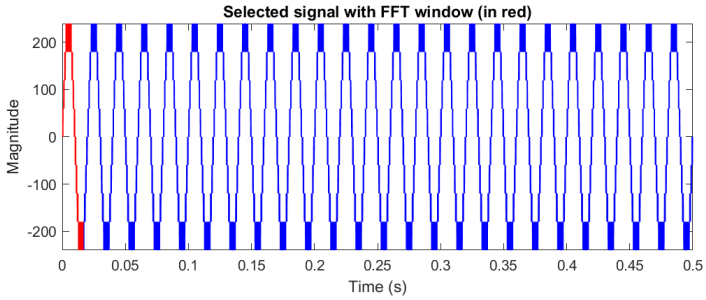

FIGURE 3. The voltage waveform in multilevel inverters- 9 levels

For a generalized half-wave balanced output waveform of a multilevel inverter circuit shown in Figure. y, the output voltage waveform is not sinusoidal, and as stated in eq(1) [19-20], it can be described by a Fourier series expansion.

$$(V)_{(\omega t)} = \sum_{n=1}^{\infty}(A_n sin\ (n\omega t) + (B_n cos(n\omega t)) \tag{1}$$

Since the converter's output form is asymmetric, harmonics are not considered, and only normal sinusoidal terms are considered when extending the formula. As a result, as shown by eq 2, it is possible to reduce the investor's exchange current with charge. Equation 3 is the amplifier of the third harmonic. The expression in Eq. 4 allows one to calculate the THD of a asymmetric half-period vibration while accounting for the tape current of a multilevel inverter.

$$(V)_{(\omega t)} = \sum_{n=1}^{\infty}(A_n sin\ (n\omega t) \tag{2}$$

$$A_n = \left(\frac{4V_{dc}}{n\pi}\right) \sum_{k=1}^{r}(cos\ (n\alpha_k)) \tag{3}$$

$$\text{THD} = \frac{\sqrt{\sum_{n=5,7,11,\ldots}^{r} V_n^2}}{V_1} \tag{4}$$

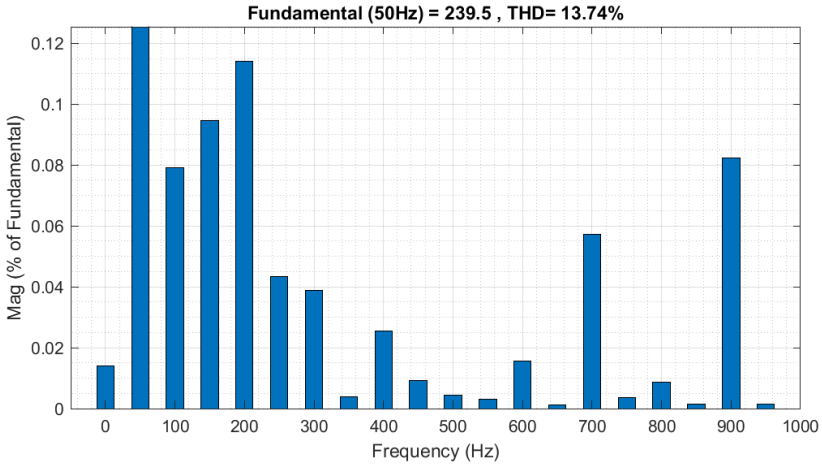

FIGURE 4. Harmonic spectrum of inverter output voltage with an open loop

METHODOLOGY TO IMPLEMENT A CLOSED LOOP

To improve Total Harmonic Distortion (THD), it is essential to include a closed-loop proportional-integral regulator (PI) in multilevel converters, especially those with nine levels. In this method, one begins by precisely modeling the converter to capture its harmonic distortion characteristics. The PI regulator is then developed and adjusted to meet performance requirements to lower THD [21].

It is possible to optimize the PI's parameters, such as the integral Ki and proportional Kp constants, by using advanced manual or automatic adjustment techniques while considering the intricate relationships between the produced harmonics and tension levels. After incorporating the PI controller into the multilevel converter's feedback loop, comprehensive simulations are conducted to verify its efficacy in preserving optimal output quality while minimizing total harmonic distortion. Experimental testing is then conducted to confirm the system's robustness and dependability in actual working environments. This closed-loop PI methodology must be used to get the best possible THD reduction performance, which raises the overall quality of the electrical power that multilevel converter supply.

Table 2. Ziegler-nichols tuning rule

Type of Controller	Kp	Ti	Td
P	0.5Kcr	∞	0
PI	0.45Kcr	Pcr/1.2	0
PID	0.6Kcr	0.5Pcr	0.125Pcr

After comparing the two approaches in [22], it can be shown that the ZN method with the PID control structure performs better than the CC method's PI control in terms of rise and settling times. This work helps address the challenges related to magnetic levitation control and we have :

- Kp, Ki and Kd is set to zero.
- From zero to a critical value, Kp is progressively raised until the oscillation is sustained and stable.

$$Kp=Kp\ ,\quad Ki=Kp/Ti\ ,\quad Kd = KpTd$$

With

- Kp:Proportional gain,
- Ki:Integral gain.
- Kd:Derivative gain
- Kcr:Critical gain
- Pcc:Critical period
- Ti:Integral Time
- Td:Derivative Time

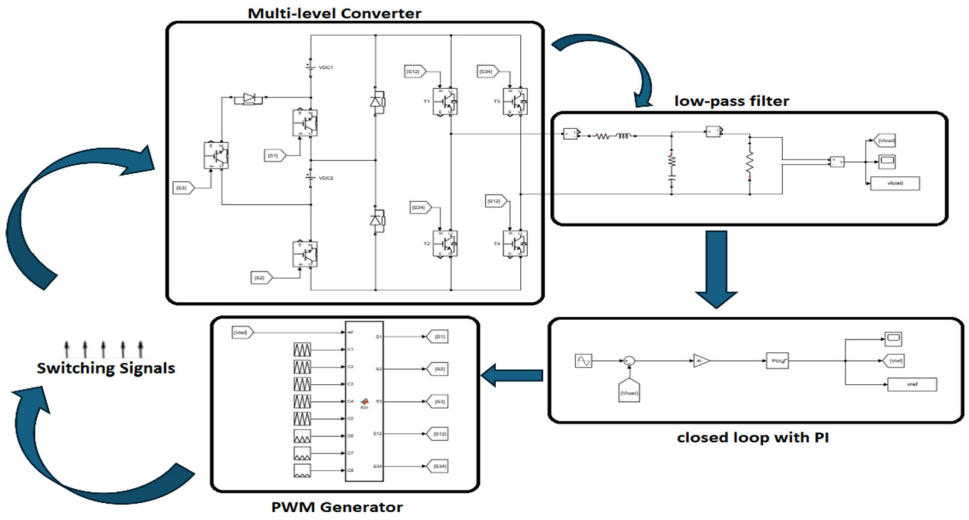

FIGURE 5 Simulation of a nine-level inverter with a closed loop (PI)

Combining a PI with a closed-loop power conversion system optimization tool to manage a multilevel converter's switches and use the generated data to train an artificial neural network is a significant advancement. PI bounce lowers the total harmonic distortion rate (THD), figure 5, which enhances the output quality of the converter and gives useful data for neural network training. The latter can then predict and simulate the behavior of the system, offering more accurate and flexible control. This strategy opens the door for power conversion systems that are more dependable and effective and that are tailored to the ever-increasing needs of modern applications.

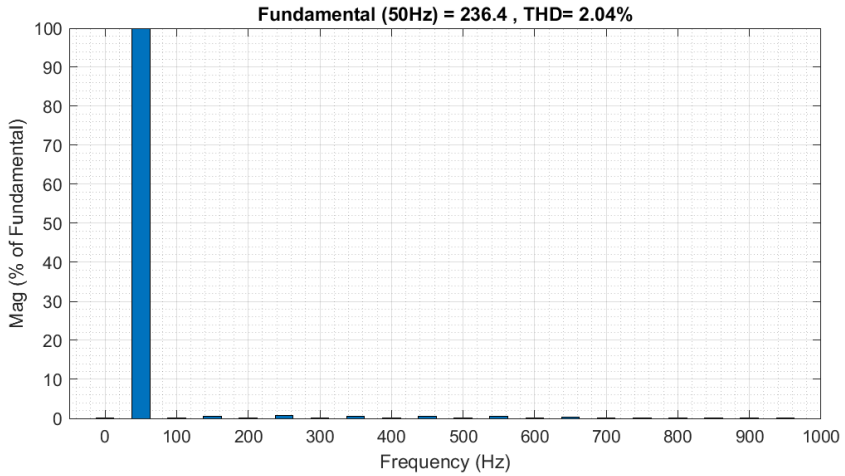

FIGURE 6 Harmonic spectrum from a nine-level inverter with closed-loop control

ARTIFICIAL NEURAL NETWORKS FOR HARMONIC DETECTION

The several neural networks that have been presented have been trained and simulated using a variety of techniques to determine parameter values that ensure optimal performance for each architecture. Two performance indices, the degree of accuracy attained, and the amount of training time needed—were chosen to assess the efficacy of each network examined for the two operational techniques. In terms of accuracy, the ability to quickly train the intended topologies and network parameters was essential for measuring harmonic coefficients. One software tool that was utilized was the Matlab neural network tool [23].

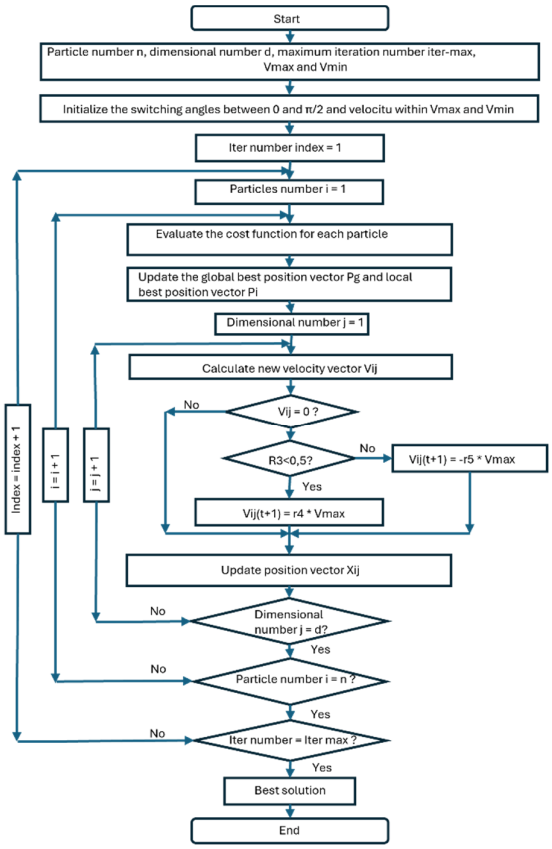

FIGURE 7. The chart of ANN applying harmonic minimization problem

The different steps involved in applying artificial neural networks (ANNs) to the field of harmonic minimization are visually represented in a flow chart figure 7. This diagram can include steps such as gathering input data (harmonics to be reduced), preparing the data, designing a neural network (choosing architecture, activation functions, etc.), training the ANN model using training data, validating and optimizing the model, and finally using the model to predict commands for harmonic correction.

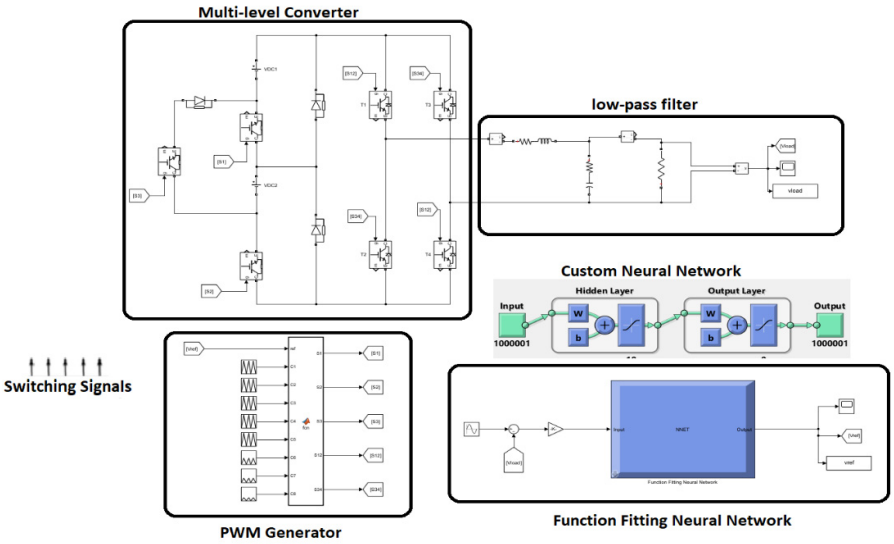

FIGURE 8 simulation of a nine-level inverter with a Neutral Network

According to Figure 8, after using the Artificial Neural Network (ANN), the results revealed a significant improvement in the output signal, as illustrated in detail in Figure 9. The transformation of the initial signal into a smooth, regular form is illustrated in this figure, demonstrating the effectiveness of ANN in correcting and modulating the multilevel converter.

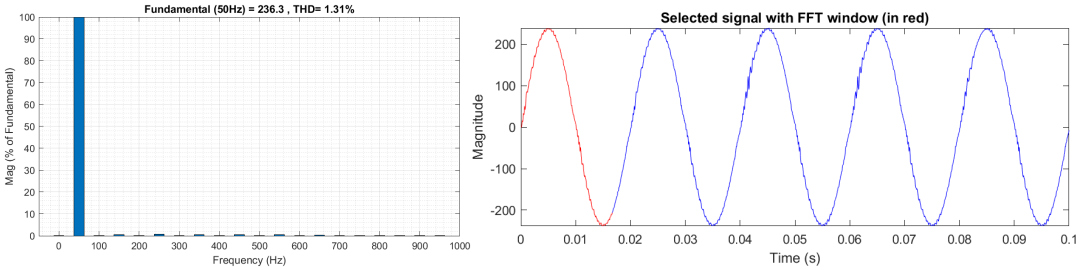

FIGURE 9 Harmonic spectrum of the output signal (Vout) from a nine-level inverter with a Neutral Network

In addition, the implementation of ANN resulted in a significant reduction in the harmonic distortion rate (THD%), as illustrated in Figure 9. This figure's exact data shows how the ANN has been able to successfully lower harmonic distortion, ensuring better output voltage quality that complies with the necessary requirements. Extensive observations demonstrate how ANN can help multilayer converters operate better, leading to higher system efficiency and better power quality.

CONCLUSION

A significant advancement has been made with the integration of artificial neural networks (ANNs) into the PI closed-loop control system. ANNs can be used to more accurately and flexiblely forecast and simulate system behavior by utilizing data from the PI-controlled converter. By employing this dual strategy, THD may be decreased and the converter's output quality can be enhanced. Additionally, the information it yields can be used to continuously optimize the system and modify it to meet the demands of contemporary applications.

With the help of this integrated approach, we can better comply with strict electrical regulations and effectively address the dynamic problems presented by today's power supply applications.

REFERENCES

1. L.D.P. Fernandez, E.A.C. Peñaranda, and J.L.D. Rodriguez, A multiobjective genetic algorithm for the optimization of the THD and the RMS output voltage in a multilevel converter with 17 levels of line voltage. In : *2019 IEEE Colombian Conference on Applications in Computational Intelligence* (ColCACI). 2019. p. 1-5.
2. S.H. Vali, G. Karimulla, and V. Rafi, THD mitigation in grid-tied solar PV system with the multi-level inverter and MMPT by the ANN controller.
3. J.T. Faete Filhozieg, P. Ozpineci, Burak, et al. A Machine Learning Clustering Algorithm for Sensorless Multilevel Converters. In : *2020 IEEE Energy Conversion Congress and Exposition* (ECCE). IEEE, 2020. p. 1973-1976.
4. S. Wang, T. Dragicevic, G.F. Gontijo, et al. *IEEE Transact Indl Electro,* 68(11), 11628-11634 (2020)
5. A. Chaithanakulwat, N. Thungsuk, T. Savangboon, T., et al. *J Southwest Jiaotong Univ,* 57(1), (2022)
6. M. Rasheed, M. Alakkad, R. Omar, et al. *Indonesian J Electri Eng Comput Sci,* 20(3), 1148-1158 (2020)
7. E. Parimalasundar, R.S. Kumar, V.S. Chandrika, et al. *Electric Eng Electromech,* 1, 31-39 (2023)
8. T. Atar, S.Balci, A. Kayabasi, *Measurement,* 210, 112525 (2023)
9. O. Sánchez-Vargas, S. Estefany De León-Aldaco, J. Aguayo-Alquicira, et al. *European J Electr Eng,* **23**(3) (2021)
10. S. Ravikumar, H. Vennila, And B. Ajai, *Int J Adv Intell Paradigms,* **16**(3-4), 306-323 (2020)
11. K.I. Gómez Díaz, S.E.De León Aldaco, J. Aguayo Alquicira, et al. *Eng,* **4**(3) 1761-1786 (2023)
12. M. Fahad, M. Tariq, A. Sarwar, et al. *Energies,* **14**(14), 4302 (2021)
13. B. Masri, H. Al Sheikh, N. Karami, et al. A Review on Artificial Intelligence Based Strategies for Open-Circuit Switch Fault Detection in Multilevel Inverters. In : *IECON 2021–47th Annual Conference of the IEEE Industrial Electronics Society.* IEEE, 2021. p. 1-8.
14. I. Mahendravarman, S.A Elankurisil, M. Venkateshkumar, et al. *Soft Comput* **24**, 18909–18926 (2020)
15. D. Rath, A.K. Patra, S.K. Kar and B. Rout, "Modelling of Machine Learning Controller Based Reduced Switch Multi Level Inverter," 2021 International Conference in Advances in Power, Signal, and Information Technology (APSIT), Bhubaneswar, India, 2021, pp. 1-6

16. P. Achintya and L. Kumar Sahu, "Open Circuit Switch Fault Detection in Multilevel Inverter Topology using Machine Learning Techniques," 2020 IEEE 9th Power India International Conference (PIICON), Sonepat, India, 2020, pp. 1-6.
17. S. Wang, T. Dragicevic, Y. Gao, S.K. Chaudhary and R. Teodorescu, *IEEE Transact Ind Electr,* **6**(5) 4554-4560, (2021)
18. Z.E. Abdulhamed, A.H. Esuri and N.A. Abodhir, "New Topology Of Asymmetrical Nine-Level Cascaded Hybrid Bridge Multilevel Inverter," 2021 IEEE 1st International Maghreb Meeting of the Conference on Sciences and Techniques of Automatic Control and Computer Engineering MI-STA, Tripoli, Libya, 2021, pp. 430-434
19. T. Atar, S. Balci, and A. Kayabasi, *Meas: J Int Meas Confeder,* **210,** 112525(2023).
20. N. Farokhnia, H. Vadizadeh, S. Fathi and F. S. Anvariasl, *IEEE Transact, Ind Electr,* **58**(8), 3359 – 3372 (2011)
21. P.R. Bana, K.P. Panda, S. Padmanaban, et al. *IEEE Access*, **8**, p. 75691-7570 (2020I
22. V.V. Patel, *Resonance,* **25**(10), 1385-1397 (2020)
23. T. Atar, S. Balci, and A. Kayabasi, *Meas: J Int Meas Confeder,* **210,** 112525(2023).

Towards Maintenance 4.0: Deep Learning and LLM-Driven Bearings Fault Detection

Adnane Bouchra[1,2, a)], Mohamed Tabaa[1], Mossaab Batal[1], and Abdelhafid Ait Elmahjoub[2]

[1] Pluridisciplinary Laboratory of Research & Innovation (LPRI), EMSI, Casablanca, Morocco
[2] Laboratory of Complex Cyber Physical System, National School of Arts and Crafts (ENSAM), HIIU, Casablanca, Morocco
[a)] Corresponding author: adnane.bouchra-etu@etu.univh2c.ma

Abstract. The maintenance industrial landscape is changing with the integration of new emerging technologies, such as Deep Learning (DL) and Large Language Models (LLMs), for setting up predictive strategies. This paper discusses the emerging paradigm in the context of predictive maintenance, signifying its importance toward improving equipment reliability, reducing unplanned downtime, and providing ways for cost savings on maintenance through proactive failure prediction. This is a brief review of state-of-the-art predictive maintenance role-plays of DL in analyzing sensor data for early fault detection and, at the same time, leveraging LLMs for the translation of complex diagnostic data into actionable maintenance recommendations. Along with the positive progress in the broad application of these technologies, the implementation has had to face several data integration complexities, model customizations, and a must around human-AI interaction with imperatives. Future important areas for research and development in this regard entail advancements in AI and machine learning algorithms, integration of IoT and sensor technologies with development, and human-AI maintenance, regulations, and ethics of collaborative frameworks. This paper presents an overview of the present achievements and outlines a road map of the efforts that pave a way for overcoming the existing challenges for the realization of Maintenance 4.0. In this paper, it is indicated how the integration of DL and LLMs can become a game-changer in current predictive maintenance practices, deriving from the future trends and the continued evolutions of respective industrial strategies.

INTRODUCTION

Predictive maintenance is a new evolving revolution in the operations of industries, and it targets the prediction of upcoming failure of equipment [1]. This approach uses several tools and techniques to track equipment by predicting the right timing of when maintenance should be done. This reduces the likelihood of unexpected failure, which can sharply reduce both the efficiency and cost effectiveness of the maintenance strategy [2]. This helps in protecting the machinery and lengthening its life but also in making sure that it works with optimum efficiency, hence reducing downtime and costs related to it [3]. Against this backdrop, predictive maintenance becomes quite indispensable in an industry setup. It allows transition from old traditional strategies based on reactive maintenance run-to-failure to a more proactive one [4]. However, the indicated change does not bring benefits to the reliability and availability of machinery alone. It means that the industries can plan the maintenance activity during the scheduled down times with least interruptions to the production processes by predicting the potential failures [5]. Systems of bearing are no doubt critical to the reliability and efficiency of a machine. These are the most important elements designed to reduce friction between moving parts in order to enable smooth functioning of machines [6]. The bearing system's health influences machine performance and life duration [7]. Broadly, the composition elements in a anti-friction bearing are essential: outer race, inner race, rolling elements (balls), and the cage [8]. Together, these articulate the mainstay to mechanisms that can rotate and allow smooth operation of all sorts of applications. Any bearing failure, therefore, presents a massive challenge in maintenance management following the realization of costly downtimes and interruptions to operations [9]. Studies have shown that the cause of most cases of machinery failure and breakdown lies within bearing faults, thus accounting for a large percentage of the total number of failures within industrial environments [10].

Technologies and Materials for Renewable Energy, Environment and Sustainability
AIP Conf. Proc. 3321, 020006-1–020006-9; https://doi.org/10.1063/5.0289744
Published under an exclusive license by AIP Publishing. 978-0-7354-5231-2/$30.00

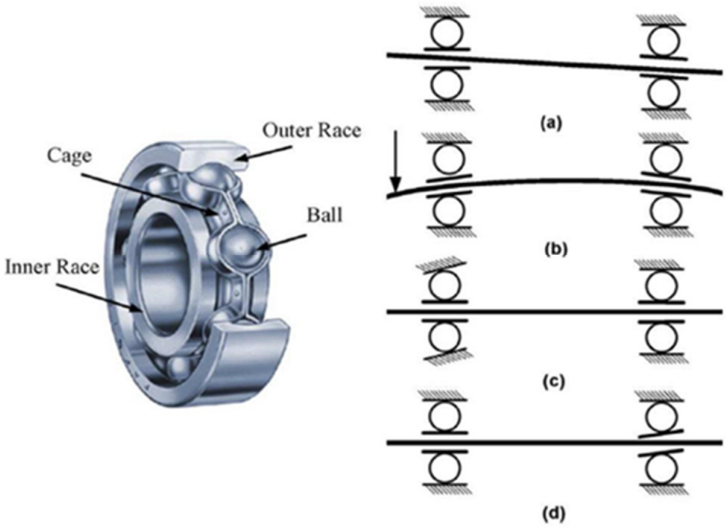

FIGURE 1. Ball Bearing Structure and Misalignment Effects

In respect to the above point, these are predictive maintenance techniques that include vibration analysis, lubricant analysis, and thermal imaging, which usefully monitor the state of bearings [11]. Accordingly, this can be detected with such techniques if the bearings have problems, commonly known as misalignment, imbalance, wear, and lubrication degradation [12]. Predictive maintenance helps to further foresee the early identification of these problems and further prevents the bearing failure, which can result in expensive breakdowns of machinery. It can give further assurance to the reliability of the machinery in the setup [13]. The set of challenges for the early detection of failures to plan maintenance bearing for machinery in an industry could somehow hinder the way predictive maintenance is recommended [14]. These challenges are related to the technical complexities associated with bearing operations and some environmental factors affecting bearing performance [15]. Understanding such barriers is key for devising predictive maintenance strategies that are much more effective. Some of the major challenges have been:

Complexity of the failure modes

The number of failure mode reasons that bearings may fail, such as misalignment, inadequate lubrication, contamination, fatigue, and overloading, all with their different set of symptoms, leads to pinpointing and predicting failures. It is very difficult to draw out a proper interpretation of the data, unless looked upon by the varied techniques and knowledge of the domain, due to the complexity mentioned above [14].

Signal interpretation

The first signs of a bearing fault are, however, usually of low sound pressure and can easily be buried within the noise floor contained in the sensor data. For example, temperature monitoring, vibration analysis, and acoustic emission all have the need to adjust, in sensitivity, each device so it can distinguish operations in its normal variations and the most premature beginning of degradation [16]. This is an advanced challenge, for which it is necessary to have possibilities in data processing and analysis, including learning algorithms based on machines, in order to distinguish most accurately between possible failures:

Sensor placement and quality data

In monitoring the bearing status through data acquired from the bearing, the calling for fitting of the sensors in a position that would hold relevant data is subject to adherence. In regard to this, the design and operational environment of the machinery may block access to the optimal places for placing sensors. In addition, there are environmental restrictions to the data quality that could be collected. All these environmental factors, from temperature variation and electromagnetic interference to physical obstructions, all could appear and hence restrict the quality of data, otherwise high-quality predictions will be made [17].

Lubrication analysis

however, is complex in that it comprises tests not only for wear debris particles but also for a wide range of contaminants and chemical degradation products. This, of course, needs critical equipment and expertise, which shall further be added to the task of detecting incipient failures [18].

Planning and Scheduling Maintenance

Also, bringing in the predictive maintenance findings within the fold of maintenance planning and scheduling would have another set of challenges, i.e., seamless flow of information from the maintenance teams to the decision-makers, and the required flexibility in adjusting the maintenance schedules, guided by predictive insights [19]. It may be difficult, particularly in those organizations that have maintenance work planned rigidly or where there is some kind of resistance to changing the conventional way things are done with respect to maintenance practices [21].

The integration of artificial intelligence (AI) in predictive maintenance strategies has significantly advanced the ability to detect potential failures in machinery and equipment. AI models, particularly those employing machine learning (ML) and deep learning (DL), are capable of analyzing vast amounts of data to identify patterns indicative of future failures [21]. Despite these advancements, a notable gap still exists in the seamless integration of failure detection with actionable solution generation within AI-driven predictive maintenance frameworks [22]. This gap can be attributed to several key areas:

Interpretability and Explainability

AI models, especially those based on deep learning, are often seen as "black boxes" due to their complex nature, which makes it difficult for engineers and maintenance personnel to understand the basis of the predictions. This lack of interpretability can hinder trust in the AI's recommendations and complicate the translation of predictive insights into concrete maintenance actions [23].

Data Integration and Access

Effective AI-driven predictive maintenance requires access to diverse data sources, including historical maintenance records, real-time sensor data, operational parameters, and environmental conditions. However, integrating these disparate data sources remains a challenge, limiting the AI model's ability to provide comprehensive and actionable insights [25].

Customization and Contextual Understanding

AI models require extensive training to accurately predict equipment failures, and these models often lack the ability to understand the specific operational context of the machinery. Without this contextual understanding, AI may recommend solutions that are not viable or optimal for the specific operational constraints or maintenance practices of the facility [26].

Dynamic Adaptation and Learning

Machinery and operational conditions are dynamic, with changes occurring over time due to wear and tear, operational adjustments, and environmental factors. Many AI models struggle to adapt to these changes in real-time, which can lead to outdated or inaccurate predictions and recommendations[27].

Actionable Solution Generation

While AI can excel at detecting anomalies and predicting potential failures, there is often a disconnect in translating these predictions into specific, actionable maintenance tasks. This includes determining the urgency of maintenance actions, the specific steps required to address the predicted issue, and scheduling maintenance activities in a way that minimizes operational disruption [22].

Human-Machine Collaboration

There is a need for enhanced collaboration mechanisms between AI systems and human operators. Effective predictive maintenance requires not just automated predictions but also the expertise of maintenance personnel to interpret and act upon AI recommendations. Bridging the gap between AI predictions and human decision-making is crucial for actionable solution generation [28].

In this paper we try to solve the increasing complexity and demand for reliability in industrial machinery have highlighted the critical role of advanced predictive maintenance strategies. Particularly, bearing systems, as essential components for machinery operation, require sophisticated methods for early failure detection and maintenance planning. This review explores the potential of integrating deep learning and Large Language Models (LLMs) into a hybrid model for predictive maintenance. This approach not only aims to predict failures more accurately but also to generate actionable maintenance solutions, bridging a crucial gap in current practices.

METHODOLOGY ANALYSIS

We adopted the approach proposed by Barbara Kitchenham to adopt relevant works in our study for bearing fault diagnosis using machine learning. With this, a systematic and rigorous approach of literature review is presented here with a huge research value in the area of machine learning and predictive maintenance for bearing fault diagnosis. Relevant articles were identified following the reference lists and by an extended search through several scientific databases, such as Scopus, Springer, Elsevier, and IEEE, to pinpoint articles that addressed predictive maintenance and machine learning applications specifically. It should be noted that the search was between the published works of 2017 and 2024, with specificity in works that are available in the open, where the total of 800 articles was found. In the second phase of the search, results were refined to only journal articles and reduced to about 500 entries. This was then further filtered in the third phase to a selection of articles that specifically mentioned context in relation to bearing fault diagnosis of predictive maintenance. Consequently, a total of 200 articles, following this filtering process, are considered to be relevant. The screening through for in-depth review led to the selection of those that specifically addressed the application of machine learning techniques in the context of bearing fault diagnosis, further reducing to 160 reviewed articles. We thoroughly read the abstract, introduction, and conclusion sections of these articles and compared the contexts with the research goals of our study. This yielded the discarding of 120 articles which were considered either irrelevant for the present study or analyzed only superficially. The remaining 40 articles were reviewed critically for their methodology, success rate, type of bearings, and faults studied. This review is an attempt to pull out the works that demonstrate high diagnostic accuracy or make a novel contribution in using machine learning techniques in the context of predictive maintenance. This rigorous process ended with the selection of 20 articles, which have given outstanding contributions in the field of bearing fault diagnosis using machine learning techniques. All these finally shortlisted the works that were chosen with respect to the techniques of machine learning applied, the type of bearing fault diagnosed, and relevance to the strategy of predictive maintenance. All these classifications make it easier to expose a wide review of real tendencies, challenges, and improvements in the area that influences directly toward developing the methodology for our research and formulating the objectives of work.

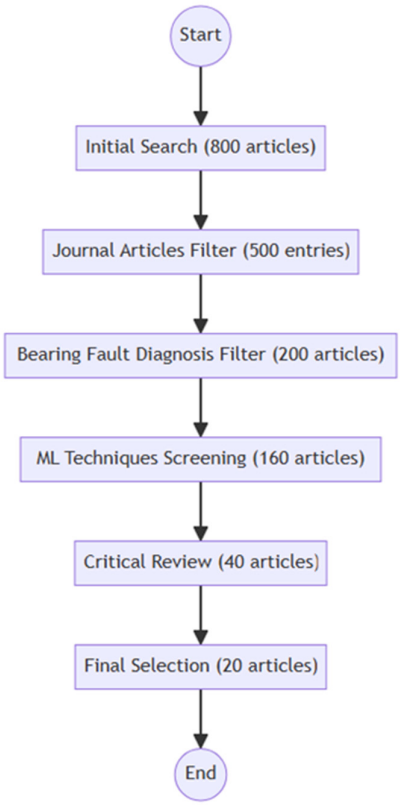

FIGURE 2. Systematic Literature Review Process for Bearing Fault Diagnosis Using Machine Learning Techniques

LITERATURE REVIEW

Deep learning has demonstrated significant success in predictive maintenance, especially in analyzing sensor data to detect anomalies indicative of bearing failures [29]. CNNs (Convolutional Neural Networks) and RNNs (Recurrent Neural Networks) are particularly notable for their ability to process temporal and spatial data, offering nuanced insights into bearing conditions. For instance, the study [30] showcases a data-driven approach, emphasizing the relevance of predictive models in ensuring structural integrity.The evolution of bearing fault diagnosis reflects significant advancements in machine learning (ML) techniques and the utilization of diverse datasets. These developments have been pivotal in enhancing predictive maintenance strategies, offering insights into the reliability and efficiency of industrial machinery. This section provides an expanded overview of notable studies, categorized by the employed ML techniques and datasets. Machine Learning Techniques in Bearing Fault Diagnosis

- **Deep Learning Models:** [31] demonstrated the efficacy of Deep Boltzmann Machines, Deep Belief Networks, and Stacked Autoencoders in diagnosing bearing faults. These models, known for their deep architecture, excel in feature representation and extraction, leading to a high accuracy rate of 99%. Their research underscores the potential of deep learning in capturing the intricate patterns of bearing fault signatures.
- **Hierarchical Diagnosis Network:** [32] introduced a two-layered diagnosis network that significantly outperformed traditional SVM and BPNN models. The first layer identifies the fault type, while the second determines the fault size, showcasing the model's nuanced classification capabilities with a 99% success rate.
- **Classical Machine Learning Algorithms:** [33] employed K-Nearest Neighbors (KNN), Decision Trees, and Random Forest algorithms in conjunction with genetic algorithms to optimize feature selection, achieving a 97% success rate. This combination of traditional ML algorithms with genetic optimization illustrates the ongoing relevance of classical ML techniques in fault diagnosis when enhanced by modern feature selection strategies.

DATASETS IN BEARING FAULT DIAGNOSIS:

CWRU Dataset [34]: This widely recognized dataset from Case Western Reserve University has served as a benchmark for many studies, including those by [35] and [32]. It includes vibration data under various fault conditions, facilitating the development and validation of numerous diagnostic models. The versatility and comprehensiveness of the CWRU dataset have made it a cornerstone in the field of bearing fault diagnosis research.

In-House Datasets

Custom datasets, as utilized in [36] and [37], offer tailored insights into specific machinery and fault conditions. These datasets enable the exploration of unique fault scenarios, such as compound faults, and the development of robust models tailored to specific industrial applications.

University Datasets

The University of New South Wales and Universidad Politécnica Salesiana, Ecuador datasets, explored in [38] and [31], respectively, highlight the global research community's efforts in expanding the diversity of fault diagnosis datasets. These datasets contribute to the field by offering new challenges and opportunities for model testing and validation, reflecting different operational environments and fault conditions.

The exploration of various machine learning techniques and datasets in bearing fault diagnosis has significantly contributed to the advancement of predictive maintenance strategies. Each study, with its unique approach and methodology, adds to the collective understanding and capability in accurately diagnosing bearing faults. From the employment of advanced deep learning models that delve into the complexity of vibration signals to the utilization of classical ML algorithms optimized through genetic algorithms, the research landscape is both diverse and dynamic. Similarly, the datasets—ranging from the widely used CWRU to custom in-house and university datasets—provide a rich foundation for developing and testing diagnostic models.

LARGE LANGUAGE MODELS IN PREDICTIVE MAINTENANCE

The advent of LLMs has opened new avenues in maintenance, particularly in translating diagnostic data into comprehensible maintenance recommendations [39] . Though direct applications in predictive maintenance are nascent, the potential for LLMs to articulate complex diagnostic information into actionable strategies is immense.

The integration of Large Language Models (LLMs) such as ChatGPT, PaLM, and Llama into predictive maintenance strategies for bearing systems represents a [40] groundbreaking shift towards more intelligent and intuitive maintenance solutions. ChatGPT [41] , with its sophisticated text understanding and generation capabilities, excels in analyzing maintenance logs and operational narratives to uncover hidden patterns of wear or failure, facilitating an interactive dialogue-based troubleshooting process. PaLM [42], developed by Google, extends this capability through its scalability and multimodal processing, integrating diverse data types to enhance the prediction of bearing failures and inform maintenance strategies with unparalleled accuracy. Meanwhile, Llama's [43] efficiency and open-source nature allow for its deployment directly into operational monitoring systems, providing real-time data analysis to preemptively identify potential issues. Together, these models offer a comprehensive and dynamic approach to predictive maintenance, leveraging the synergy between advanced textual analysis and real-time data processing to significantly improve the reliability and performance of bearing systems. The collective insights collected from the referenced studies [44][45][46][47] provide compelling evidence of the transformative impact that Natural Language Processing (NLP) and Large Language Models (LLMs) have exerted on the field of predictive maintenance. This advancement is primarily due to the inherent ability of these generative AI technologies to assimilate and analyze real-time equipment data continuously. This dynamic capability allows for an unparalleled level of adaptability, enabling the models to identify and learn from patterns that signify the health and efficiency of operational processes. Such patterns include the normal operating parameters of machinery, deviations that may indicate the onset of failure, and the environmental and operational conditions that could influence performance. By understanding these complex and often subtle indicators, NLP and LLMs can predict potential issues well before they lead to system failures, thereby markedly enhancing the efficiency and accuracy of maintenance interventions. Moreover, the ability of these AI models to process vast datasets—ranging from sensor outputs to maintenance logs and operational reports—further strengthens their predictive capabilities. This comprehensive data analysis not only improves immediate maintenance responses but also contributes to the development of more sophisticated and resilient maintenance strategies over time. The integration of generative AI into predictive maintenance workflows thus not only addresses current maintenance needs but also evolves in tandem with advancements in technology and changes in operational environments. As generative AI technologies like those documented in [48] [49] [50] continue to evolve, their applications within the realm of predictive maintenance are expanding into new and diverse domains. From aerospace to telecommunications, and from manufacturing to supply chain management, the potential for these technologies to revolutionize maintenance practices is immense. The ongoing research and development in this area, suggest a future where predictive maintenance, powered by generative AI, becomes even more accurate, efficient, and adaptable. This future-oriented approach holds the promise of minimizing downtime, reducing maintenance costs, and ensuring the seamless operation of critical systems, thereby heralding a new era in industrial and technological advancement.

DISCUSSION

Predictive maintenance brings together deep learning and LLMs in an entirely new and pioneering approach. The advent of deep learning, especially CNN and RNN models, has shown profound capabilities in accurately predicting bearing failures through sensor data analysis. Such LLM models running with these deep-learning models for actionable maintenance solutions showcase great synergy of AI with physics for comprehensive predictive maintenance strategies. This approach also augers well for the reliability of failure prediction and also suits improving the maintenance process, since the proposed solutions are detailed, understandable, and actionable. The diagram below presents how the Large Language Models (LLMs), in conjunction with deep learning, are set to bring a drastic change in predictive maintenance for bearing systems' care and monitoring. Part and parcel of this spanking new hybrid framework, the coupling of the LLMs with the deep learning techniques will form the basic fabric for this kind of advanced predictive maintenance strategy. The hybrid model is significant in the sense that it can bring remarkable reduction to unplanned downtime and maintenance cost, thereby enhancing operational efficiency and life to machinery. In most traditional methodologies, they either focus on prediction only without coming up with a solution to act upon or make it a manual task to generate a solution, automating the proposed model to the whole process. It captures the spirit of Maintenance 4.0, where intelligent systems self-diagnose and prescribe with no human intervention; therefore, leading to smarter, efficient operations. Though this shows great promise, the integration of deep learning with LLMs in predictive maintenance also has its fair share of challenges. The major ones manifest in data compatibility and model complexity. From moving seamlessly from prediction analytics to solution generation, data compatibility must be maintained, along with very sophisticated algorithms and a lot of computational resources. Further, the challenge of obtaining solutions that remain both interpretable and correct from LLM solutions is a challenge that has to be overcome. It needs an

interdisciplinary approach with expertise in machine learning, natural language processing, and knowledge in the domain of machinery maintenance.

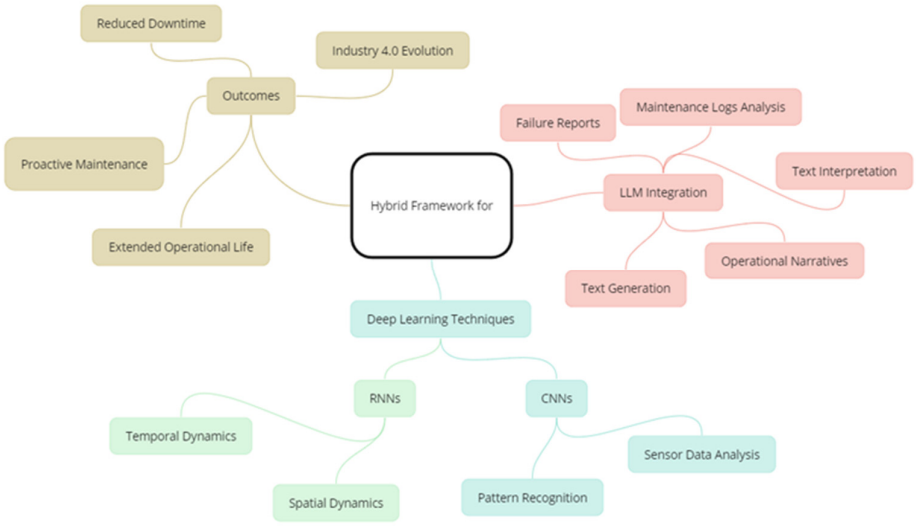

FIGURE 3. Hybrid Framework for Predictive Maintenance

CONCLUSION

This paper, therefore, took the changing landscape of predictive maintenance in industrial setups, focusing majorly on the great and critical role played by such advanced technologies like deep learning (DL) and Large Language Models (LLMs) in increasing machine reliability and efficiency. With this transition from old-time- and usage-based maintenance models to the proactive and predictive maintenance plans, industries stand to reduce unexpected downtime and maintenance costs that remain the biggest contributors to poorer overall operational efficiencies. Integration of AI, especially ML and DL, shows a lot of promise in accurate prediction of equipment failure. The circumstances under which LLMs have arrived also herald an inventive medium through which complex diagnostic data can be transformed into actionable maintenance strategies. This will represent the next big step towards the automation of the maintenance process overall. However, the journey towards fully realizing the potential of these technologies is fraught with challenges. These comprise the complexities of data integration, context-based model customization, dynamic adaptation of algorithms to operational changes, and translation of AI predictions into actionable maintenance items. Still, the most important thing is the establishment of an effective partnership between the AI system and the human operator so that the workflow in predictive maintenance becomes quite smooth.

Overall, the incorporation of deep learning and LLMs into predictive maintenance represents the frontier of a huge opportunity for industry. In addressing the present challenges, it should move toward the areas of future development highlighted above to be more reliable, efficient, and automated in maintenance processes. It would enhance not only the life and performance of industrial machinery but also characterize a new period for Maintenance 4.0, where operational efficiency and resilience will be at a level that has not been seen before.

REFERENCES

1. KIANGALA, Kahiomba Sonia et WANG, Zenghui. An experimental safety response mechanism for an autonomous moving robot in a smart manufacturing environment using q-learning algorithm and speech recognition. Sensors, 2022, vol. 22, no 3, p. 941.
2. SHI, Dachuan, MEYER, Olga, OBERLE, Michael, et al. Dual data mapping with fine-tuned large language models and asset administration shells toward interoperable knowledge representation. Robotics and Computer-Integrated Manufacturing, 2025, vol. 91, p. 102837.

3. S. Sharanya, M. Prakash, and J. Senthilkumar, "Block chain enabled framework for industrial maintenance." In: AIP Conference Proceedings (2024).
4. BHOITE, Sachin, ANSARI, Gufran, PATIL, C. H., et al. Stock market prediction using recurrent neural network and long short-term memory. In : ICT Infrastructure and Computing: Proceedings of ICT4SD 2022. Singapore : Springer Nature Singapore, 2022. p. 635-643.
5. PERERA, Diana, WHIRLOW, Kyle, WHALEN, Tim, et al. Driving Vehicle Maintenance Decisions using Predictive and Prognostic Maintenance Technology.
6. HUSSAIN, Muhammad, ZHANG, Tieling, CHAUDHRY, Muzaffar, et al. Review of prediction of stress corrosion cracking in gas pipelines using machine learning. Machines, 2024, vol. 12, no 1, p. 42.
7. BARKAS, D. A., KATEMLIADIS, S., TAROUSINOF, G., et al. Failure causes and operational life of measuring transformers installed in 150 kV and 400 kV transmission network. Electric Power Systems Research, 2024, vol. 231, p. 110341.
8. SVADKOVSKY, V. A. The Use Of Digital Twins To Improve The Operational Efficiency In The Extractive Industries. Strategic decisions and risk management, 2024, vol. 14, no 3.
9. PASUPULETI, Vikram, THURAKA, Bharadwaj, KODETE, Chandra Shikhi, et al. Enhancing supply chain agility and sustainability through machine learning: Optimization techniques for logistics and inventory management. Logistics, 2024, vol. 8, no 3, p. 73.
10. МОРОЗОВ, К. Д. ПРЕДИКТИВНАЯ ДИАГНОСТИКА МАШИН ПЕРЕМЕННОГО ТОКА.
11. JANSSENS, O., RENNUY, M., DEVOS, S., et al. R. Van de Walle; van Hoecke, S.(2016): Towards intelligent lubrication control: Infrared thermal imaging for oil level prediction in bearings. In : 2016 IEEE Conference on Control Applications (CCA). p. 1330-1335.
12. BEHERA, Pramod K. et SAHOO, Bhabani S. Leverage of multiple predictive maintenance technologies in root cause failure analysis of critical machineries. Procedia Engineering, 2016, vol. 144, p. 351-359.
13. MEHTA, Ankush, GOYAL, Deepam, CHOUDHARY, Anurag, et al. Machine Learning-Based Fault Diagnosis of Self-Aligning Bearings for Rotating Machinery Using Infrared Thermography. Mathematical Problems in Engineering, 2021, vol. 2021, no 1, p. 9947300.
14. SCHWENDEMANN, Sebastian, AMJAD, Zubair, et SIKORA, Axel. Bearing fault diagnosis with intermediate domain based layered maximum mean discrepancy: A new transfer learning approach. Engineering Applications of Artificial Intelligence, 2021, vol. 105, p. 104415.
15. A. Choudhary, S.L. Shimi, and A. Akula, "Bearing fault diagnosis of induction motor using thermal imaging." In: IEEE International Conference on Power Electronics, Drives and Energy Systems (PEDES) (2018).
16. WANG, Jinjiang, LIANG, Yuanyuan, ZHENG, Yinghao, et al. An integrated fault diagnosis and prognosis approach for predictive maintenance of wind turbine bearing with limited samples. Renewable energy, 2020, vol. 145, p. 642-650.
17. ZHANG, Weiting, YANG, Dong, et WANG, Hongchao. Data-driven methods for predictive maintenance of industrial equipment: A survey. IEEE systems journal, 2019, vol. 13, no 3, p. 2213-2227.
18. LEE, Wo Jae, WU, Haiyue, YUN, Huitaek, et al. Predictive maintenance of machine tool systems using artificial intelligence techniques applied to machine condition data. Procedia Cirp, 2019, vol. 80, p. 506-511.
19. SERRADILLA, Oscar, ZUGASTI, Ekhi, RODRIGUEZ, Jon, et al. Deep learning models for predictive maintenance: a survey, comparison, challenges and prospects. Applied Intelligence, 2022, vol. 52, no 10, p. 10934-10964.
20. ROSATI, Riccardo, ROMEO, Luca, CECCHINI, Gianalberto, et al. From knowledge-based to big data analytic model: a novel IoT and machine learning based decision support system for predictive maintenance in Industry 4.0. Journal of Intelligent Manufacturing, 2023, vol. 34, no 1, p. 107-121.
21. STEURTEWAGEN, Bram et VAN DEN POEL, Dirk. Adding interpretability to predictive maintenance by machine learning on sensor data. Computers & Chemical Engineering, 2021, vol. 152, p. 107381.
22. FERRARO, Antonino, GALLI, Antonio, MOSCATO, Vincenzo, et al. Evaluating eXplainable artificial intelligence tools for hard disk drive predictive maintenance. Artificial Intelligence Review, 2023, vol. 56, no 7, p. 7279-7314.
23. LINARDATOS, Pantelis, PAPASTEFANOPOULOS, Vasilis, et KOTSIANTIS, Sotiris. Explainable ai: A review of machine learning interpretability methods. Entropy, 2020, vol. 23, no 1, p. 18.
24. MATZKA, Stephan. Explainable artificial intelligence for predictive maintenance applications. In : 2020 third international conference on artificial intelligence for industries (ai4i). IEEE, 2020. p. 69-74.
25. HRNJICA, Bahrudin et SOFTIC, Selver. Explainable AI in manufacturing: a predictive maintenance case study. In : IFIP International Conference on Advances in Production Management Systems. Cham : Springer International Publishing, 2020. p. 66-73.

26. SHARMA, Jeetesh, LAL MITTAL, Murari, SONI, Gunjan, et al. Explainable Artificial Intelligence (XAI) Approaches in Predictive Maintenance: A Review. Recent Patents on Engineering, 2024, vol. 18, no 5, p. 18-26.
27. SHUKLA, Bibhudhendu, FAN, Ip-Shing, et JENNIONS, Ian. Opportunities for explainable artificial intelligence in aerospace predictive maintenance. In : PHM Society European Conference. 2020. p. 11-11.
28. KRISHNAMURTHY, Vikram, NEZAFATI, Kusha, STAYTON, Erik, et al. Explainable AI framework for imaging-based predictive maintenance for automotive applications and beyond. Data-Enabled Discovery and Applications, 2020, vol. 4, no 1, p. 7.
29. Y. Chen, and Z. Zhao, J Mech Eng, 68(5), 337-356 (2022).
30. F. Li, J. Wang, and L. Zhang, Adv Eng Inform, 45, 101022 (2024).
31. Z. Chen, C. Deng, X. Chen, C. Li, R.V. Sanchez, and H. Qin, Microelectronics Reliability, 75, 327–333 (2017).
32. M. Gan, C. Wang, and C. Zhu, Mech Syst Signal Process, 72–73, 92–104 (2016).
33. R.N. Toma, A.E. Prosvirin, and J.M. Kim, Sensors 20(7). (2020).
34. SINKITTIYANONT, Supasin et RATANASUMAWONG, Chanat. Fault Diagnosis of Rolling Element Bearing from Vibration Signal Using One Dimensional Convolutional Neural Networks. In : 2024 21st International Joint Conference on Computer Science and Software Engineering (JCSSE). IEEE, 2024. p. 390-397.
35. M. Delgado, G. Cirrincione, A.G. Espinosa, J.A. Ortega, and H. Henao, "Dedicated Hierarchy of Neural Networks Applied to Bearings Degradation Assessment," in Proceedings of the 2013 9th IEEE International Symposium on Diagnostics for Electric Machines, Power Electronics and Drives (SDEMPED), Valencia, Spain. (2013).
36. Y. Lei, Z. He, and Y. Zi, Expert Syst Appl, 38(6), 7334–7341 (2011).
37. M. Cococcioni, B. Lazzerini, and S.L. Volpi, IEEE Transact Ind Inf, 9(4), 2256–2263. (2013
38. B. Muruganatham, M.A. Sanjith, B. Krishnakumar, and S. Satya Murty, Mech SystSignal Process, 35(1–2), 150–166. (2013).
39. RANE, Nitin. Role of ChatGPT and similar generative artificial intelligence (AI) in construction industry. Available at SSRN 4598258, 2023.
40. L. Ouyang, J. Wu, X. Jiang, D. Almeida, C. Wainwright, P. Mishkin, C. Zhang, S. Agarwal, K. Slama, and A. Ray, Adv Neural Inf Process Syst, 35, 27730–27744 (2022).
41. BUBECK, Sébastien, CHANDRASEKARAN, Varun, ELDAN, Ronen, et al. Sparks of artificial general intelligence: Early experiments with gpt-4. arXiv preprint arXiv:2303.12712, 2023.
42. CHOWDHERY, Aakanksha, NARANG, Sharan, DEVLIN, Jacob, et al. Palm: Scaling language modeling with pathways. Journal of Machine Learning Research, 2023, vol. 24, no 240, p. 1-113.
43. TOUVRON, Hugo, LAVRIL, Thibaut, IZACARD, Gautier, et al. Llama: Open and efficient foundation language models. arXiv preprint arXiv:2302.13971, 2023.
44. J. Singh, L. Samborowski, and K, Mentzer, K. "A Human Collaboration with ChatGPT: Developing Case Studies with Generative AI," in Proceedings of the ISCAP Conference on Information Systems and Computing Education, Albuquerque, NM, USA. (2023).
45. SONG, Lei, ZHANG, Chuheng, ZHAO, Li, et al. Pre-trained large language models for industrial control. arXiv preprint arXiv:2308.03028, 2023.
46. FREDERICO, Guilherme Francisco. ChatGPT in supply chains: initial evidence of applications and potential research agenda. Logistics, 2023, vol. 7, no 2, p. 26.
47. WANG, Jingyu, ZHANG, Lei, YANG, Yiran, et al. Network meets chatgpt: Intent autonomous management, control and operation. Journal of Communications and Information Networks, 2023, vol. 8, no 3, p. 239-255.
48. RANE, Nitin Liladhar. Multidisciplinary collaboration: key players in successful implementation of ChatGPT and similar generative artificial intelligence in manufacturing, finance, retail, transportation, and construction industry. 2023.
49. VOß, S. Bus Bunching and bus bridging: What can we learn from generative AI tools like Chat-GPT? Sustainability 15 (12): 9625. 2023.
50. AKHBARDEH, Farhad, DESELL, Travis, et ZAMPIERI, Marcos. NLP tools for predictive maintenance records in MaintNet. In : Proceedings of the 1st conference of the asia-pacific chapter of the association for computational linguistics and the 10th international joint conference on natural language processing: System demonstrations. 2020. p. 26-32.

Impact of artificial intelligence on mental health and chronic diseases: A literature review

Salma Chebbawi[1,2,a], Mohamed Tabaa[1,b] and Hassan Badir[2,c]

[1]*Pluridisciplinary Laboratory of Research and Innovation (LPRI), Moroccan School of Engineering Sciences (EMSI), Casablanca 20250, Morocco*
[2]*IDS Team ENSA Tangier, University Abdelmalek Essaadi, Tangier, Morocco*

[a] *chebbawi.salma@etu.uae.ac.ma*
[b] *Corresponding Author: m.tabaa@emsi.ma*
[c] *badir.hassan@uae.ac.ma*

Abstract. The adoption of AI in healthcare has brought significant improvements in diagnostic capabilities, therapeutic outcomes, and health facility management. AI has the capability to analyze the big data sets of patients quickly and accurately thereby changing the medical scene. In this article, the author discussed the role of AI in general healthcare, particularly its use in diagnosing and treating chronic diseases, cancer, vitamin deficiency, and mental disorders. Applying AI in healthcare entails early diagnosis and management of chronic illnesses and enhancing patients' recovery. In oncology, AI algorithms improve the evaluation of medical images and genetic data to identify cancer cells earlier and offer appropriate treatment. Lack of essential nutrients, AI systems analyze the consumption habits to offer recommendations on proper nutrition and deficiency warning. In mental health, AI assists in diagnosing conditions through analyzing the speech patterns, behavior, and physiological characteristics; providing support via virtual therapists and identifying individualized intervention techniques. The article also includes ethical issues and data privacy. Preserving the privacy and confidentiality of people's delicate health records while making AI decisions more understandable is the key. AI's ability to compound existing disparities in healthcare if not addressed properly is also discussed and this led to the need for proper deployment of AI in healthcare.

INTRODUCTION

In the last several years, physicians practicing medicine and giving care to patients with the help of AI systems, have the same meaning of revolution in the medical sphere. This revolutionary integration and breakthrough have not only improved mapping of diagnostic accuracy and treatment efficiency but also reshaped the sphere of preventive healthcare and chronic diseases management. AI's potential in the processing of data and in advanced analytics renders a signal of hope for addressing some of the disease chronicity-related issues in medicine. From the applications of prediction modeling that detect possible health risks to intelligent systems that allow for tailored treatment drugs, AI's lead is unmatched and ever-increasing. Today as medicine seems to be on the brink of the dawn of a new era, the article presents different views on how artificial intelligence becomes a crucial partner in the aim to achieve better health outcomes and healthcare delivery. In the process of dissecting the implementations of today and speculating on the possible future ones, we seek to outline the Transformative nature of AI in medicine, describing how it's improving patient care, streamlining operations, and stimulating innovation.As we delve deeper into the specific realms where artificial intelligence is making significant strides, two areas stand out due to their profound impact on public health: mental health and vitamin-related diseases. Applying AI in diagnosis and treatment of vitamins-related diseases marks a key stage in the future development of nutritional doctors. Through analyzing global data located in vast data sets, the AI algorithms can diagnose nutritional disorders and give clear predictions about the likelihood of dis- eases development with impressive precision. This leads to detecting the problems early enough for early intervention.

Technologies and Materials for Renewable Energy, Environment and Sustainability
AIP Conf. Proc. 3321, 020007-1–020007-11; https://doi.org/10.1063/5.0290416
Published under an exclusive license by AIP Publishing. 978-0-7354-5231-2/$30.00

Moreover, it brings about personal dietary recommendation as well as supplementation that is genetically unique and lifestyle matching to the individual specifics. In the end, there is a crucial and improved tactic to fight the disorders stemming from vitamin inadequacy by means of the greater capability to detect the early signs and cure in time. Hence, it is possible to observe the positive impact of such approach on general health and quality of life.AI's contribution to mental health is no less revolutionary. There is a consensus across the globe about the growing burden of mental health disorders, and more pro- found solutions that are scalable and efficient are needed. AI-driven tools and apps are cutting edge to adjust disease diagnosis, while revitalizing personalized treatment regimens. Through the examination of speech patterns, the expression of the face, and even social media activity, the AI algorithms can detect the early signs of mental health problems, for instance, depression and anxiety, which usually come to the notice of individuals or their relatives/doctors only after situation gets worse. Furthermore, AI-aided bots and virtual therapists can reach mental health patients easily and reduce the gap created by access to mental health services. Such AI interventions not only are breaking taboos that surround seeking mental health assistance and thus are making care more available but also are offering support in the most effective way for every person.

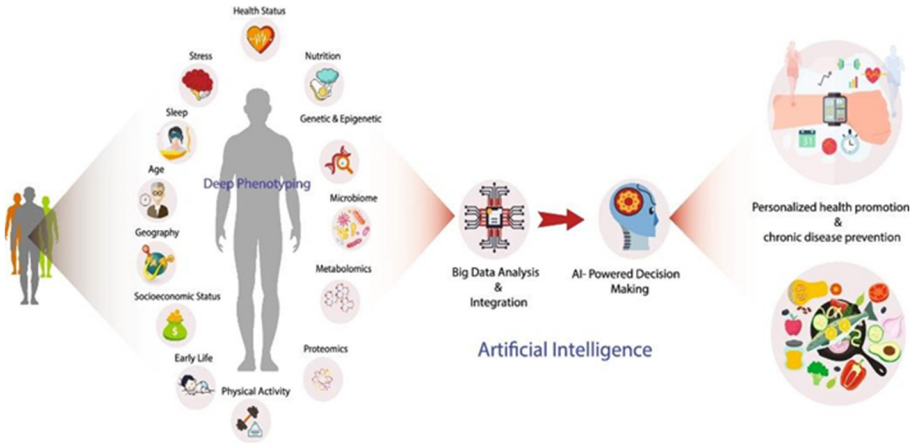

FIGURE 1. SUBRAMANIAN, Murugan, WOJTUSCISZYN, Anne, FAVRE, Lucie, et al. Precision medicine in the era of artificial intelligence: implications in chronic disease management. Journal of translational medicine, 2020, vol. 18, p. 1-12

This article attempts to highlight in deep how vitamins play a key part in general health, with special emphasis on them as prevention and treatment of chronic diseases, cancer, and mental health disorders. By using a thorough analysis of the recent data, enabled by the recent technological advancements in the artificial intelligence area of the analysis of large volumes of biomedical information, we hope to be able to under- stand the processes through the which vitamins are able to affect this pathologies By doing an elaborate review of the main scientific literature, this paper aims to provide a detailed synopsis of the current understanding, as well as to reveal the variety of re- search in which authors agree and in which they disagree, and the direction which it could take in the future. In the long run, we seek to illuminate the way how the x-Iran addressation of artificial intelligence in medical research can transform disease exploration and management and finally pave the path towards creative and preventative dis- ease control measures.

Revolutionizing Healthcare: The Impact of Artificial Intelligence on Medical Practices and Patient Care

Artificial intelligence and machine learning (AI and ML) integration into health care are presented in different studies in the field, as, in many ways, this process shaped the diagnostics, patient care and predictive analytics and caused multidimensional trans- formation. [1] sets the scene by figuring the advancement of AI representative in medication issues, points to its parameter in conclusion and patient consideration, it demonstrates the key to transform medicine utilizing the human psychological capacities imitating, general medical profile, and the fast advancements in computerized illustrations. It [1] is settled as a review of AI applications, focusing on various data types like structured and unstructured, and highlighting various fields of study such as cancer, neurology and cardiology to illuminate both major and minor disease subtypes. It has focused on the determinants and lays false emphasis and emphasis on the role artificial intelligence plays stroke care early diagnosis, treatment, outcome prediction, and prognosis estimates. [2][3] are some of studies that signify how AI is used to improve hospital operations which in turn focus on quality care and patient dismissal predictions; The research [3] aims at applying machine learning models to forecasts patient dis- charged from ICUs of those who suffer from cardiovascular complications. It uses the MIMIC-III database to work with different regression models to evaluate the effects of the characteristics of admission, clinical advice, biophysical parameters, and discharge characteristics on predicting discharge preparedness demand. The same study [3] concludes that targeted time predicting of discharges is a key condition to achieve timely resource allocation, shorten long term hospital periods for patients and lead patient flow. Its concludes that machine learning techniques can assist the personnel of the hospital in significantly improving the efficacy of their daily operations through the provision of reliable discharge predictions and hence help in the decision-making process for the healthcare providers. The cost of medical care in the US has become a very important issue which is the author's discussion in his article. Other severe challenges for health care system are infections and failures in delivery of care. By focusing on the capabilities of AI and machine learning to enhance patient care quality and reduce costs, it helps take ad- vantage of accurate patient information enabled with electronic health records data and health insurance claims. Previous attempts and advancements in AI for patient care have been discussed previously, implemented as clinical decision support systems, ma- chine learning models for risk stratification, and predictive models for patient outcomes. It also personalized the addresses future challenges and perspective of AI in health care, stating the need for scalable algorithms and approaches for managing health data's complexity and size to improve patient care and safety. The combination of artificial intelligence (AI) and digital technologies in healthcare is transforming the delivery of medical services, offering huge benefits in terms of diagnosis and patient outcomes. As shown in paper [4], the involvement of AI into the medical sphere is deep into almost all fields; it is penetrating various branches of medicine such as radiology, pathology, dermatology, ophthalmology, cardiology among others and even psychology. This technology not only increases the overall scope of healthcare procedures but also reveals issues like data bias, confidentiality, and accurate validation. His significance in dealing with these challenges for future development cannot be overemphasized. In prospect, the paper depicts a harmonious cooperation of humans and ma- chines, stressing ethical sensibilities and the robotic tech to improve healthcare service standards. Developing the digitalization of healthcare further, the paper in [5] elaborates on the implementation of DT tech combined with IoT devices, data analytics, and machine learning. Such a novel framework facilitates virtual cloning of patients whose operations include continuous monitoring and early detection of disease deviations. The paper describes a successful application using ECG classifier model that combines DT and IoT for the diagnosis of heart disease which is capable of high accuracy that exemplifies the capacity of these technologies to transforms modern healthcare system.Taken in its entirety, these developments represent a milestone along the path to a smarter, data-driven, and patient-oriented healthcare system, where the synthesis of AI, modelling and digital twin technologies tackles present problems and paves the way for the future. Another study [6] where researchers developed a regional atherosclerotic cardiovascular disease (ASCVD) risk calculator using machine learning (ML) techniques and 101,110 unique electronic medical record (EHR) spanning the time from January 1, 2009, to April 30, 2020 was called "Automating and improving cardiovascular disease prediction using Machine learning and The main purpose of the study was to develop a more accurate and efficient calculator than PCE (Pooled Cohort Equations) risk calculator, which is widely used among doctors nowadays. The proposed calculator should be based on patients' data, which will be analyzed in cross-sectional and longitudinal ways. Research results demonstrated unrivaled predictive power of all ML models compared to PCE calculator. The random forest technique using the blend of cross-sectional and longitudinal attributes produced, at the end, an AUC score of 0.902, the highest score among these methods. Surprisingly, less than half, 43% of the patients needed to be sampled to detect 90% of the cases, which is as compared to 69% needed to be screened by the PCE estimator. That ML technologies,

especially when integrated longitudinal along the with the cross-sectional practices, can have a significant impact on the process prediction of ASCVD, which ultimately can reduce the need for an Aller- inclusive mass screening, hence may offer a more efficient and arguably quite cost- effective solution to the prevention of heart and circulatory disease. In addition to this, Artificial Intelligence (AI) infusion into healthcare, particularly doing the diagnosis of Impending death occurrences among the hospitalized patients suffering from diabetes in the Intensive Care Units (ICUs) is a chronological step in patient care and resource utilization. The Authors' approach by Julian Theis etal [7], AI is employed, which com- bines a process mining and leads deep learning techniques to discover complex patterns contained in a big set of data like electronic health records. It also goes beyond the simple precision of the older severity scoring methods, which only provides a specific snapshot of a patient's health at the point in time, by offering a more detailed and descriptive story of a patient's healthcare journey. Relying on AI means having access to historic medical data involving patients while using algorithms that with higher precision estimate the results. To get an idea, we look at how AI can transform the healthcare area by presenting doctors with the most effective tools that enable them to select be- tween several options so that ultimately the health outcome gets improved, and the medical resources get optimized.

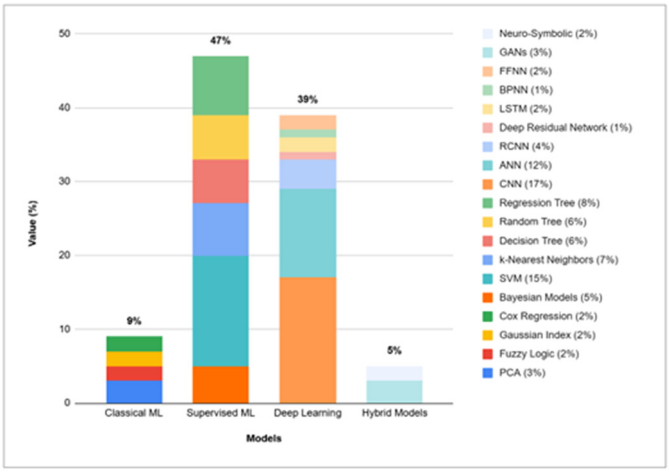

FIGURE 2. Artificial intelligence-based prediction models (Adapted from KUMAR, Yogesh, KOUL, Apeksha, SINGLA, Ruchi, et al. Artificial intelligence in disease diagnosis: a systematic literature review, synthesizing framework and future research agenda. Journal of ambient intelligence and humanized computing, 2023, vol. 14, no 7, p. 8459-8486)

Despite the difficulty of hospital overcrowding. With the dynamic nature of healthcare, the combination of AI and IoT devices is the key enabler of hospital operations and delivery of care. As healthcare facilities are increasingly facing the concomitant challenge of validating both ambulatory and inpatient services, as well as managing patient overcrowding, the use of these technologies comes with the promise of a solution document [8] introduces extensive research on a model which was created to maximize patient flow and resource utilization. The model employs heterogeneous non- homogeneous discrete-time Markov chains to simulate patient trajectories in a hospital setting considering factors such as pathology, bed availability, and survival probabilities. A real-time bed occupancy prediction model validated with data from a UK NHS organization has been proved efficient in predicting bed occupancy and improving re- source allocation, thus exemplifying a practical approach to the overcrowding problem in hospitals.

AI in the service of mental health

The AI and mental health crossroads are a promising area, where the future of mental health care can reach more people, taking individual characteristics and requirements into account and producing desired results is being created. Moving on, as we do our best to understand this advanced field, its pros and cons should be scrutinized for it has its advantages and disadvantages when it comes to AI technology and mental health service delivery. Machine learning abilities from unlocking messages hidden in speech or behavioral manner to online therapy and crisis interventions, as discussed ahead, open a new era of care. Nevertheless, such an inventive development will undoubtedly give way to ethical questions, privacy considerations, and accuracy issues. This segment will explain how AI is changing the face of mental health, this change with routine, new research, and the contention between the merits and liabilities of AI in the particular area of the healthcare system, which is in reality a very human field, is being upheld.
In article [9] the author aims at giving a detailed look at the employment of AI in mental health care and contributes to the assertion that it can disrupt by a novel level the existing reality of diagnosis, treatment and patient monitoring. AI chip in when it comes to digital phenotyping, also NLP (natural language processing) and chatbots, all of which are revolutionary for mental health treatment. Digital phenotyping uses the unobtrusive data collected by digital devices such as smartphones and digital devices to predict some mental health conditions, and with the advancement of NLP that can analyze voice and language behavior, one may identify emotional/behavioral states that one is in and flags out disorders. From simple chatbots to NLP-based intelligent systems, these technologies meet the standard of treatment for mental illness, such as de- pression and anxiety, through group conversations. AI can improve the situation for people suffering from mental illnesses; It is what's has been analyzed in the paper [10]: It emphasizes AI's two-fold character of transforming service delivery in mental health sector on one hand and consequentially offers a space for discussions on pros, cons, and ethical concerns. The narrative mentions AI applications for detecting, classifying, and segmenting mental health conditions based on different data resources such as electronic health files, mood rating measurements, brain scanning details, innovative ex- amination assessments and social media sites. These AI tools demonstrate a high degree of precision and serve as an initial indication of the predictive power of Machine Learning algorithms by giving an accurate answer to complex mental health related questions. It is the global priority whose aims are to gain ground in the field of mental health and well-being as the Lancet Digital Health [11] postulates. Among them is the fact that depressed state did not change since 1990 and the anxiety and depressive disorders increased by more than 25% during pandemic's recent year. Additionally, it evaluates the flood of digital and virtual mental health interventions from social distancing as an alternative tool for coping with mental health problems, constraints of its effectiveness in giving full solution. The story highlights some benefits of several digital tools like mobile and internet apps, as well as video games with all support and self-support roles and even, they disclose the possibility to predict mental health status using social network data. Above depicts an AI approach framework in general to detect Alzheimer's disease by using brain images as a substrate. The plan delineates a sequential procedure: starting with the imaging equipment using imaging apparatus. Whole images proceed the feature extraction, where only the features that are relevant to Alzheimer's disease detection among original data set are singled out.

The two studies [13][14] are a major leap in the utilization of AI in health with respect to the non-surgical diagnosis of the aging disease of the brain. Illustrating the potential of using retinal photos, the clinicians raised new wakes in the condition detection, which can be applied for screening and management of the condition with the hope of improving the condition outcomes for millions around the world. The fact that this research involves interdisciplinary technologies, as the data science, ophthalmology, and neurology are among them, means that experts of several fields take part in the process of dealing with complex health problems via new high technologies. It uses an original basis for screening definite alterations in Alzheimer's disease using retinal pictures. This method that is non-invasive, harnesses the benefit of the retina, utilizing it as a gateway to the brain's health condition. Cheung and colleagues employed a sophisticated deep learning algorithm, incorporating the EfficientNet-b2 as the low-level engine responsible for generating features for retinal images. The algorithm was educated, validated and tested on a representative sample of 648 Alzheimer's patients rep- resenting multiple countries and 3240 controls suffering from other diseases. The variety seen in this dataset illustrates the mode's strength and scope past the mere specific population. Discussing another complex chronic mental health disorder, the writer in his study [15] highlighted the potential AI techniques have shown in diagnosing disorders such as schizophrenia and ADHD more accurately. in his article, he also refers to AI as a fresh tool that can deliver an analysis of the data from electronic medical records and health records in order to improve the diagnosis, prediction, and treatment of mental illnesses; And as a diagnosis tool, AI techniques such as LSA (Latent Semantic Analysis) and machine learning that analyze speech and other data may be used to identify patients with psychiatric disorders and to differentiate it from people who don't have psychiatric

disorders, This diagnosis procedure underlines AI's application of foreseeing mental states, including the onset of psychosis and the likelihood of com- mitting suicide, with higher precision than the old approaches. It emphasizes the work which shows machines' learning techniques on digital medical data, and sound processing gave better forecasts for such illnesses. The author in his article [16] gives a detailed discussion on AI and ML, the most significant implementation in the psychiatry revolution. It highlights the possibilities of these techs to advance our acquaintance about mental disorders, improve the accuracy of diagnosis and develop innovative therapeutic techniques, more specifically machine learning and AI as instruments which will completely change the way disease modelling in psychiatry is done, therapeutic invention as well as preventive strategies. Machine Learning Processes consists of a series of learning objectives and clearly states the phases of the application of machine learning which range from defining research questions and datasets to the algorithm building, training, testing and validation. Specific techniques such as linear regression, decision trees and neural networks are being discussed as they relate to what they bring forth while focusing on psychiatric research. Furthermore, there is a study [17] that casts light on the fact that mental illnesses are abundant and digital technologies can be of high effectiveness in improving the state of mental health. It highlights that AI is endowed with an enormous capacity for helping us in making sense of the data created by mobile applications, wearables, and electronic health records (EHR) among other sources to boost the detection, diagnosis, and treatment of mental disorders. Data sources serve as a diverse range for ML applications in mental health settings. Where sensors, text, structured data and multimodal interactions are utilized. These apps are concerned mainly with pointing out the tendencies, symptoms, and complexities of signs and reminders to change the pattern. There is a growing interest in their predictive modeling and improving treatment methodologies.

AI and chronic diseases

The field of AI and chronic disease treatment consists of a new paradigm in the patient treatment approach based on AI applications. Intrinsically, chronic diseases are a set of conditions that are characterized by their long-term character and progressive development, and they spread widely through all the health spectrums including heart disease, diabetes and chronic respiratory disorders among several others. Being widely spread, these diseases affect the health of everyone around the globe with high death rate as their main consequence, along with the problems of poor overall well-being. The current generalized and reactive methods of managing such problems have often been targeted toward symptom management rather than developing individualized care programs and disease prevention.

The arrival of AI technologies features a transformative opportunity for chronic dis- eases to be innovative living instruments. Combined with machine learning algorithms, big data analysis, and predictive modelling, AI will give healthcare professionals, more efficient diagnostics tools, patient treatment that is personal, as well as the ability to foresee the development of conditions before they reach harder level. This segment wants to reveal the multifaceted way AI is revolutionizing in the management of chronic illnesses. This following section will open up the door for an exhaustive discussion on how AI solutions address the less than desirable outcomes of chronic diseases and pinpoint the advantages and disadvantages that will be brought up. The evolving era in which we live makes it all-too-apparent that AI not only can be a game-changer in the delivery of healthcare but also a big deal that revolutionizes the way we comprehend, treat, and eventually live with chronic illnesses

How AI can help with vitamin deficiency

In [18] research work serves as a charge schedule that provides the necessary review of the emerging function of AI across different domains of nutrient science research. The review categorizes the studies into three primary areas: biomedical nutrients re- search by nutritionists, clinical nutrients research by nutritionists, and nutritional epidemiology. It points out the way in which the research has been done, referring to the most popular methodologies and algorithms like artificial neural networks, machine learning, and deep learning, bringing their use in food composition analysis, nutrient production optimization, the investigation of the physiological consequences of nutrients' absorption and gut microbiota studies. The integration of artificial intelligence has shaped a new era of transformation in the fertile field of nutrients science research, thereby presenting new approaches to disclose the intricate interplay between diet, health and disease. Use of these AI technologies in vitamin science and complex data analysis help pave the way for the evolution in nutrigenomics and holistic health strategies.

The interaction of AI and nutritional science is a highly optimistic one - it has a strong potential for greatly improving our knowledge of how vitamins relate to health and disease and for ushering in the era of the precision nutrition that is aligned to each individual's health needs and food preferences. Employing the latest machine learning (ML) techniques such as support vector machine (SVM), least squares support vector machine (LS-SVM), support vector regression (SVR), and broad range of neural net- work models, it is now possible with improved precision to study proteins, minerals, trace elements, and their physiological consequences; Besides, it mentions the role of AI in clinical areas that concerns nutritional assessments, risk evaluations of the dis- eases connected with vitamins, and personalized nutritional systems creation.

There is a report [19] that deals with an artificially intelligent diagnostic system meant for early diagnostic of vitamin and mineral deficiencies; It applies the reinforcement method of chaining and the Mycin which is an early expert system utilizing artificial intelligence for diagnosing severe bacterial infections like bacteremia- certainty factor method to tackle the diagnostics process; The system is designed in such a way that it is also accessible and easy to use considering it is strategically designed for mobile technology. It efficiently deals with the intricacies and ambiguities while diagnosing nutritional deficiencies, with integration of AI; This is an impressive way of AI application in healthcare as a technological innovation which makes it possible to identify vitamins related health issues early before it gets worse, and the system is almost perfect in diagnosis (100% accuracy rate during testing).

Furthermore, [20] is a paper offering a comprehensive review of how artificial intelligence, for example, ChatGPT and other generative AI models, could be exploited in detecting the teratogenic risks that are associated with vitamin A supplementation during pregnancy. It stresses the capacity of AI in this regard to explore the features of dietary supplements assessment, primarily vitamin A due to fetal health importance. Through AI utilization, AI study demonstrates a way of doing precise calculations of vitamin A content and its safety thresholds, despite the complicated nature of the different labeling practices and regulations.

This demonstrates the breakthrough changes that are brought about by AI in terms of public health intervention and nutritional advice and provides a smart and powerful tool for risk assessment in the prenatal setting. Moreover, the paper [21] describes in detail the developed AI system set up to screen vitamin deficiencies with the help of image processing. This innovative mechanism extricates insights from the visual cues by combining the CNNs-based method with fuzzy logic to interpret the signs of nutrient deficiencies presented in the photographs of body parts like eyes, lips, tongue, and nails in a more precise manner. It adds precision to the diagnosis and presents it as a respective non-invasive method of health monitoring. Through dietary advice based on recognized nutritional deficiencies, the application italicizes the transformative character of preventive health care in terms of a proactive strategy for nutritional health.

Moreover, [22] supports this and elaborately examines the AI-enabled models, which include the Adaptive Neuro-Fuzzy Inference System (ANFIS) and Artificial Neural Networks (ANN) along with Multilinear Regression (MLR) for predicting TSH levels using macro-elements and vitamins as inputs. It draws conclusions on the superiority of AI-based models with respect to the linear models in the TSH prediction task. It is established that the ANFIS model outperforms the ANN and MLR models in accuracy and efficiency in its prediction of TSH levels. This creates room for AI in which the accuracy of diagnostic and individualized healthcare could be improved. On the same view, research [23], the NHANES (National Health and Nutrition Examination Survey) dataset incorporating a wide range of dietary and life- style information, is used as a basis to predict plasma vitamin C levels by employing ML methods. It assesses the suitability of regression models, which are XGBoost and Random Forest, on the diet and lifestyle factors relating to dietary intake and nutritional status. It is research which verifies the interrelation of AI and nutrition science, clearly showing the potential and bottlenecks of using ML for precision nutrition and individualized dietary advice.

Table 1. Comparison Table.

Document Title	Approach	Dataset Type	Outcomes	Accuracies
[20] Using Artificial Intelligence to Assess the Teratogenic Risk of Vitamin A Supplements	Utilized ChatGPT to calculate vitamin A content in supplements and assess teratogenic risks.	Information on vitamin A supplement content, including mcg RAE and IU con- versions.	Provided a way to understand potential risks associated with vitamin A supplements, high- lighting the need	Qualitative assessment; no numerical accuracies pro- vided.

			for better regulation.	
[22] Applications of Artificial Intelligence- Based Models and Multi-Linear Regression for the Prediction of Thyroid Stimulating Hormone Level in the Human Body	Compared AI models (ANFIS, ANN) with multilinear regression for predicting TSH levels from microelements and vitamins.	Blood sample data for macro-elements, vita- mins, and TSH levels.	Demonstrated superior performance of AI models, especially ANFIS, in predicting TSH levels over traditional methods.	ANFIS achieved highest R^2 values, indicating better performance, but specific numerical values not pro-vided.
[21] Vitamin Deficiency Detection Using Image Processing and Neural Network	Developed a smartphone application for detecting vitamin deficiencies through images of body parts.	Images of eyes, lips, tongue, nails showing deficiency symptoms.	Successfully diagnoses vitamin deficiencies and suggests dietary corrections, improving access to nutritional information.	High level of precision noted, but specific accuracy rates were not provided.
[18] Artificial Intelligence in Nutrients Science Research: A Re-view	Reviewed AI applications in biomedical, clinical, and nutritional epidemiology research related to nutrients.	Varied, including biochemical, dietary intake, health records, and nutritional surveys.	Highlighted AI's role in predicting disease risks based on dietary pat-terns, optimizing nutrient production, and personalizing nutrition ad- vice.	Mentioned superior performance of AI methods in nutrient science tasks, but no detailed accuracy rates.
[23] Predicting Plasma Vitamin C Using Ma- chine Learning	Aimed to predict plasma Vitamin C levels using machine learning models from dietary and lifestyle data.	NHANES dataset on 2952 American adults including dietary intake and health indicators.	Found XGBoost regressor had the best performance among tested algorithms for predicting Vitamin C levels, though with modest success.	XGBoost achieved a cross-validated R-squared score of approximately 0.303, indicating room for improvement.
[19] An Expert System for Early Diagnose of Vitamins and Minerals Deficiency on the Body	Developed an expert system with forward chaining and certainty factor method for diagnosing vitamin and mineral deficiencies.	Expert knowledge on symptoms associated with specific vitamin and mineral deficiencies.	Provided diagnoses of deficiencies with recommendations, facilitating early identification and intervention.	Claimed 100% ac- curacy in diagnosing deficiencies, aligning with ex- pert diagnoses.

AI Innovations in Oncology: Transforming Cancer Diagnosis, Treatment, and Research

The power of AI is key to better outcomes in the healthcare field; that's what many research highlight in for instance "cancer": This is indicated by [24] in mentioning the power of AI to enhance breast cancer diagnostic accuracy, furthermore, [25] is a deep study of an AI system that works with mammography images to improve breast cancer screening. It compares the performance of AI system as compared to human radiologists from different datasets in UK and USA regarding number of False Positives and false Negatives where it has minimized. The present study details the promising nature of system's capacity to increase accuracy in diagnosing breast cancer through screening and demonstrates its generalizability across populations, as well assimilated into work- flows. This study highlights AI's revolutionary performance in the world of healthcare not only through but also within which require meticulous image analysis. Analyzing the same cancer type: The article "Artificial Intelligence System for Breast Cancer Screening in International Testing"[26], authors presented an exemplary AI system which was intended to outsmart human radiologists in diagnosing breast cancer via mammograms. This research has been done across several sites in the United States and the United Kingdom, and it utilized a very another large and diverse dataset to demonstrate that the AI system can accurately and precisely detect, reduce both false negatives, and false positives, and. As revealed by the AI system which showed superior results in the reader study, to MDs the technology can improve diagnostic accuracy and efficiency. In addition, the study has found the way to put the AI system into the actual screening workflows, and it appeared that this task would have reduced radiologists' workloads but not quality of diagnostics. This is a major AI-medical innovation which allows clinical trials in future with a perspective to bring ultimate refinement of the screening process of breast cancer.

Moreover, the document [27] addresses deep learning, particularly the convolutional neural networks (CNNs), for skin cancer classification purposes with diagnostic results equal to professional dermatologists. The authors of the study use a large database with clinical images as monitors, who have trained CNNs and tested their performance on key binary classifications made in relation to skin lesions. The outcomes reflected the power of AI in precise skin cancer diagnosis, particular melanomas and keratinocyte carcinoma through employing images as sole input. This study emphasizes the opportunity offered by AI to enhance diagnostic mechanisms in dermatology, increasing accessibility and efficacy of skin cancer identification.

The article [28] delivers a wide-ranging look at the use of AI in the field of cancer research, with the emphasis on diagnosis and prognosis. It begins with the fascinating story about the sophisticated artificial intelligence technologies that has particularly deep learning applied, and association of them with clinical cancer research, their new levels of accuracy in cancer prediction reaching the unmatched level; His study examines work that shows that the use of AI can help improve precision in early diagnosis and prognosis thus people might have high survival rates. Thus, through the development and adoption of AI for cancer imaging, this exploration will bring a new perspective to improve cancer diagnosis and prognosis, with the intent to eventually help with early cancer detection and subsequently treat cancer.

About AI in gastric cancer, the review of Peng Jin et al... [29] Journal of Cancer Research and Clinical Oncology is a topic discussing the Artificial Intelligence (AI) application in gastric cancer management which covers various aspects of the topic. By following the PRISMA guidelines, the systematic review in the study aims to explore different AI techniques used in non-lanthanide compounds including early detection tools, molecular bio-information analysis, endoscopic detection, predictive modeling for lymph node metastasis, response to drugs, prognosis, surgical training, skill assessment, and surgery guidance. It demonstrates that gastric cancer diagnostic tool becoming found in AI that enables potential therapeutic interventions clinically in precision medicine.

Furthermore, the power of AI in the medical imaging cancer is explored in "Clinical Challenges and Applications,"[30] which identifies cancer as the focus of the article and details the extent of AI's impact on diagnosis, treatment, and monitoring of the disease. It explains not only how AI and especially deep learning techniques can improve the understanding of cancer imagery across various cancer types such as lungs, brain, breast or prostate, but it can support the medical specialists in the process as well. As AI facilitates the radiologic picture analysis, doctors expect greater accuracy and efficiency in detection that does not end with better treatment strategies but also with the discovery of tumor features which were not visible before. Besides, Wenya Linda Bi examines the problems associated with the clinical practice implementation of AI, for example, the number of big datasets required for training AI models and the significance of the validation of these models on the broad clinical background. In the said article [31], all the vast applications of artificial intelligence (AI) which perform significant tasks in oncology including diagnosis, therapeutic target discovery, and precision medicine are well explored. It stresses the role of AI and Deep Learning

which uses bulk data and computational power for spotting and classifying cancer cells precisely, helping doctors in forecasting the treatment outcomes. CNN is resourceful, in that it can efficiently detect cancerous tissue in radiological slides and imagery. The same paper continues to demonstrate how AI plays a role in genomics for pinning therapeutic directives, predicting drug responses, and detecting drug repositioning chances. Additionally, it establishes the predictive model for diagnosing diseases and treatment response thus indicating AI capacity in personalizing each patients' treatment plan to his profile.

CONCLUSION

In this comprehensive review, we have explored the ascending role of artificial intelligence (AI) with varied contributions to healthcare, from diagnosis to rehabilitation. AI technologies span across a wide field, ranging from the treatment of patients for chronic diseases to cancer research which aims at advancing understanding of the nature of the disease and treatment, and eventually personalized cure. In addition, this intelligent application of AI in monitoring vitamin levels illustrates that AI can be used in solving the issue of nutrition which is a basic component of health.

Utilization of AI in the context of mental health services has created a new path for identifying and dealing with mental disorders, which is more available and even effective. Thanks to analytics and machine learning, AI can locate the association between mental health issues and trend observations, so with their assistance, early interventions and personalized treatment rules will be provided. This feature of AI applications turns out to be pivotal, especially given the fact that the mental health burden is growing in the world and yet so do the biases and the stigma associated with seeking the treatment of mental health disorders.

Finally, AI in healthcare is the result of the change in the worldwide situation, and in the meantime, its solutions to the most serious health problems of our era were found. AI presence in the field including chronic diseases, vitamin levels, cancer and mental health is undoubtedly the most remarkable; it is ushering in precise medicine, a new era in which treatments are as distinctive as each patient. With the future ahead, we ought to read more and more the full scope of AI in healthcare where these technologies are developed and applied with an ethical, fair and humanized point of view that ensures people everywhere are in a better health and well-being situation. Concerns about the development and AI in healthcare are just starting, and their real influence still has to be determined. Though some issues are still faded, one thing is definite, that the future in healthcare depends largely on the progress of AI innovations, to the great health profit of people every city and country.

REFERENCES

[1] Jiang, F., Jiang, Y., Zhi, H., Dong, Y., Li, H., Ma, S., ... & Wang, Y. (2017). Artificial intelligence in healthcare: past, present and future. Stroke and vascular neurology, 2(4).

[2] Neill, D. B. (2013). Using artificial intelligence to improve hospital inpatient care. IEEE Intelligent Systems, 28(2), 92-95.

[3] Karboub, K., & Tabaa, M. (2022, May). A machine learning based discharge prediction of cardiovascular diseases patients in intensive care units. In Healthcare (Vol. 10, No. 6, p. 966). MDPI.

[4] Topol, E. J. (2019). High-performance medicine: the convergence of human and artificial intelligence. Nature medicine, 25(1), 44-56..

[5] Elayan, H., Aloqaily, M., & Guizani, M. (2021). Digital twin for intelligent context-aware IoT healthcare systems. IEEE Internet of Things Journal, 8(23), 16749-16757.

[6] Li, Q., Campan, A., Ren, A., & Eid, W. E. (2022). Automating and improving cardiovascular disease prediction using Machine learning and EMR data features from a regional healthcare system. International Journal of Medical Informatics, 163, 104786.

[7] Theis, J., Galanter, W. L., Boyd, A. D., & Darabi, H. (2021). Improving the in-hospital mortality prediction of diabetes ICU patients using a process mining/deep learning architec- ture. IEEE Journal of Biomedical and Health Informatics, 26(1), 388-399.

[8] Karboub, K., Tabaa, M., Dellagi, S., Monteiro, F., Dandache, A., & Moutaouakkil, F. (2021). Modeling and validation of the hospital's ambulatory and inpatients operations using a non-homogenous discrete time Markovian chains. IEEE Access, 9, 103044-103055.

[9] D'ALFONSO, Simon. AI in mental health. Current opinion in psychology, 2020, vol. 36, p. 112-117.
[10] GRAHAM, Sarah, DEPP, Colin, LEE, Ellen E., et al. Artificial intelligence for mental health and mental illnesses: an overview. Current psychiatry reports, 2019, vol. 21, p. 1-18.
[11] HEALTH, The Lancet Digital. Mental health in the digital age. The Lancet. Digital health, 2022, vol. 4, no 11, p. e765.
[12] SUBASI, Abdulhamit. Use of artificial intelligence in Alzheimer's disease detection. Arti- ficial intelligence in precision health, 2020, p. 257-278.
[13] CHEUNG, Carol Y., RAN, An Ran, WANG, Shujun, et al. A deep learning model for de- tection of Alzheimer's disease based on retinal photographs: a retrospective, multicentre case-control study. The Lancet Digital Health, 2022, vol. 4, no 11, p. e806-e815.
[14] MARSHALL, Charles R. et UCHEGBU, Ijeoma. Artificial intelligence for detection of Alz- heimer's disease: demonstration of real-world value is required to bridge the translational gap. The Lancet Digital Health, 2022, vol. 4, no 11, p. e768-e769.
[15] FAKHOURY, Marc. Artificial intelligence in psychiatry. Frontiers in Psychiatry: Artificial Intelligence, Precision Medicine, and Other Paradigm Shifts, 2019, p. 119-125.
[16] TAI, Andy MY, ALBUQUERQUE, Alcides, CARMONA, Nicole E., et al. Machine learn- ing and big data: Implications for disease modeling and therapeutic discovery in psychiatry. Artificial intelligence in medicine, 2019, vol. 99, p. 101704.
[17] THIEME, Anja, BELGRAVE, Danielle, et DOHERTY, Gavin. Machine learning in mental health: A systematic review of the HCI literature to support the development of effective and implementable ML systems. ACM Transactions on Computer-Human Interaction (TOCHI), 2020, vol. 27, no 5, p. 1-53.

[18] Sak, J., & Suchodolska, M. (2021). Artificial intelligence in nutrients science research: a review. Nutrients, 13(2), 322.
[19] Ula, M., Hendriana, Y., & Hardi, R. (2016, October). An expert system for early diagnose of vitamins and minerals deficiency on the body. In 2016 international conference on infor- mation technology systems and innovation (ICITSI) (pp. 1-6). IEEE.
[20] Holla, S., Zamil, D. H., Paidisetty, P. S., Wang, L. K., & Katta, R. (2023). Using Artificial Intelligence to Assess the Teratogenic Risk of Vitamin A Supplements. Cureus, 15(9).
[21] ELDEEN, Ahmed Saif, AITGACEM, Mohamed, ALGHLAYINI, Saifeddin, et al. Vitamin deficiency detection using image processing and neural network. In : 2020 Advances in Sci- ence and Engineering Technology International Conferences (ASET). IEEE, 2020. p. 1-5.
[22] Ghali, U. M., Usman, A., Degm, M. A. A., Alsharksi, A. N., Naibi, A. M., & Abba, S. I. (2020). Applications of artificial intelligence-based models and multi-linear regression for the prediction of thyroid stimulating hormone level in the human body. Int. J. Adv. Sci. Technol, 29(4), 3690-3699.
[23] KIRK, Daniel, CATAL, Cagatay, et TEKINERDOGAN, Bedir. Predicting plasma vitamin C using machine learning. Applied artificial intelligence, 2022, vol. 36, no 1, p. 2042924.
[24] McKinney, S. M., Sieniek, M., Godbole, V., Godwin, J., Antropova, N., Ashrafian, H., ... & Shetty, S. (2020). International evaluation of an AI system for breast cancer screening. Na- ture, 577(7788), 89-94.
[25] McKinney, S. M., Sieniek, M., Godbole, V., Godwin, J., Antropova, N., Ashrafian, H., ... & Shetty, S. (2020). International evaluation of an AI system for breast cancer screening. Na- ture, 577(7788), 89-94.
[26] MCKINNEY, Scott Mayer, SIENIEK, Marcin, GODBOLE, Varun, et al. International eval- uation of an AI system for breast cancer screening. Nature, 2020, vol. 577, no 7788, p. 89- 94.
[27] Esteva, A., Kuprel, B., Novoa, R. A., Ko, J., Swetter, S. M., Blau, H. M., & Thrun, S. (2017). Dermatologist-level classification of skin cancer with deep neural networks. nature, 542(7639), 115-118.
[28] HUANG, Shigao, YANG, Jie, FONG, Simon, et al. Artificial intelligence in cancer diagno- sis and prognosis: Opportunities and challenges. Cancer letters, 2020, vol. 471, p. 61-71.
[29] JIN, Peng, JI, Xiaoyan, KANG, Wenzhe, et al. Artificial intelligence in gastric cancer: a systematic review. Journal of cancer research and clinical oncology, 2020, vol. 146, p. 2339- 2350.
[30] BI, Wenya Linda, HOSNY, Ahmed, SCHABATH, Matthew B., et al. Artificial intelligence in cancer imaging: clinical challenges and applications. CA: a cancer journal for clinicians, 2019, vol. 69, no 2, p. 127-157.
[31] BHINDER, Bhavneet, GILVARY, Coryandar, MADHUKAR, Neel S., et al. Artificial in- telligence in cancer research and precision medicine. Cancer discovery, 2021, vol. 11, no 4, p. 900-915

Characterisation of Pt@ ZnO Nanoparticles Synthesised Via Laser Production in Liquid

Sarah M. Talib [1, a)], Adawiya J. Haider [1, b)] and Sharafaldin Al-Musawi [2, c)]

[1] *Applied Sciences Department, Laser Science and Technology Branch, University of Technology, Baghdad, Iraq.*
[2] *Biotechnology Department, College of Food Sciences, Al-Qasim Green University, Babylon, Iraq.*

[a)] *Corresponding Author:* sarahmtalib@gmail.com.
[b)] adawiya.j.haider@uotechnology.edu.iq.
[c)] dr.sharaf@biotech.uoqasim.edu.iq.

Abstract. Nanotechnology's interdisciplinary reach has propelled advancements across various fields, including biomedicine and material science. The synthesis and manipulation of nanoparticles (NPs) have enabled significant innovations, particularly in drug delivery and diagnostic tools. This research has studied synthesizing zinc oxide nanoparticles (ZnO NPs) and platinum nanoparticles (Pt NPs) employing Laser Ablation in Liquid (PLAL), and the subsequent formation of Pt@ZnO core-shell structures. ZnO nanoparticles were synthesized using 250 mJ and 500 mJ, but Pt NPs were produced at 1900 mJ, resulting in bandgap energies of 3.38 eV and 3.74 eV, respectively. The integration between Pt and ZnO (250 mJ) caused a band gap increase to 3.97 eV, indicating a significant correlation may be due to voltage and electronic impacts. The bandgap slightly increased to 3.78 eV for ZnO synthesized at 500 mJ, suggesting less interaction. The formation of a core-shell structure with distinguishing absorption peaks for the Pt and ZnO components has been proven by UV-Vis spectroscopy. The band gap energy was determined via the Tauc equation, confirming its effect on particle size, optical properties, and quantum size effects. AFM found stable particle sizes and consistent surface features, signaling less agglomeration—vital to supporting unique properties. In distilled water, the synthesis process creates well-dispersed nanoscale at 250 mJ and 500 mJ. Further, the presence of Pt@ZnO core-shell nanoparticles is proved; these particles reveal a homogeneous formation of tiny platinum particles on the substrate, uniform dispersion, and similar advantages. These results illustrate the capacity of core-shell nanoparticles to adjust how they conduct electricity for numerous uses and highlight that the Pt@ZnO structure exhibits an enhanced band gap energy, which can be useful for optoelectronic and biomedical uses. Additional research exists to comprehend the complexity of the interaction and customize the synthesis to specific objectives.

INTRODUCTION

As an interdisciplinary field, Nanotechnology spans a wide range of scientific and technological domains, including biomedical, pharmaceutical, agricultural, environmental, advanced materials, chemical science, physics, electronics, and information technology [1-5]. The synthesis, properties, and applications of materials and devices at the nanoscale (under 100 nanometers) have driven significant advancements in various fields, particularly in biomedicine. These advancements provided a vital opportunity to develop imaging agents, drug delivery systems, and diagnostic tools, making a major contribution to life-saving innovations [6-9].

The past decade has seen the rapid development of nanotechnology, and Much literature has been published from the early 1990s to recent years. These significant developments have expanded our understanding of biochemical processes necessary for diagnosing diseases and the required therapy by surface modifying that plays a critical role in applications linking to cellular repair, drug delivery, and medical therapeutic interventions [6,10].

Nanoparticles, a key invention in nanotechnology, outperform bigger particles due to their high surface-to-volume ratio and unique optical, electrical, and magnetic characteristics [11-14]. These distinctive features enable nanoparticles to succeed in several applications, making them essential to the continuous advancement in nanotechnology.

Metal and metal oxide nanoparticles have remarkable prospects across many applications. ZnO are metal oxide nanoparticles evaluated for their nontoxicity, biocompatibility, and unique features dependent on size, shape, and morphology. They have been used in sunscreens, ointments, food packaging, and everyday-care products [15-19] and their potential for antibacterial and anticancer, which might be owing to their capability of generating reactive oxygen

Technologies and Materials for Renewable Energy, Environment and Sustainability
AIP Conf. Proc. 3321, 020008-1–020008-8; https://doi.org/10.1063/5.0289589
Published under an exclusive license by AIP Publishing. 978-0-7354-5231-2/$30.00

species (ROS). In addition, ZnO exhibited antitumor activity, which was proved by the FDA [20]. However, the awareness of the toxicity limited their therapeutic applications. Therefore, further studies with more attention is suggested to reduce the risk of the nanoparticles' toxic effects. [21,22].

Platinum nanoparticles (Pt NPs) are metal nanoparticles distinguished in manufacturing fuel cells and catalytic converters due to their outstanding catalytic characteristics [23]. Pt NPs have been widely used in biomedical applications due to their stability, biocompatibility, and cellular penetration. Additionally, they showed anticancer and antioxidant activities, with the potential of surface modification to improve drug delivery systems and therapeutic efficiency.

Platinum nanoparticles (Pt NPs) were introduced as a promising, effective cancer therapy due to their ability to generate reactive oxygen species (ROS), which induce apoptosis in cancer cells. Nonetheless, a comprehensive toxicological examination is required to ensure the safe clinical usage of ZnO and Pt NPs [24,25]. Core-shell nanoparticles comprise a core material covered with an outer shell of different materials that offer several advantages, such as cytotoxicity reduction, increase in dispersibility, improvement of bio- and cytocompatibility, stronger combination with bioactive molecules, and thermal and chemical stability enhancement. These advantages make core-shell nanoparticles especially desirable for biological applications, reducing toxicity and simplifying production [26].

MATERIAL AND METHOD

The synthesis of core-shell nanoparticles involved using a target of high-purity platinum and zinc materials. 99.9% A 99.9% pure platinum was utilized to synthesize platinum nanoparticles (Pt NPs) in a 1 cm by 1 cm and 1 mm thick plate. A Q-switched Nd: YAG laser system was employed at wavelengths of 532 nm and energy of 1900 mJ, at a repetition frequency of 32 Hz, delivering 3000 pulses per wavelength for ablating the platinum plate. This process forms the core nanoparticles. For zinc oxide nanoparticles (ZnO NPs), 99.9% pure zinc sheets measuring 1 cm by 1 cm and 0.5 mm thick were utilized. The plate was immersed in 10 mL of deionized water (DI water) and placed in a beaker. A Q-switched Nd: YAG laser system operating at 532 nm, with energies of 250 mJ and 500 mJ, and a repetition rate of 10 Hz, delivered 800 pulses per wavelength to ablate the zinc sheet. The resulting zinc nanoparticles oxidized upon exposure to air, forming ZnO NPs. To create the core-shell structure, precursor compounds of the shell material were introduced into the liquid medium containing the core nanoparticles. Laser ablation continued, facilitating the reduction or deposition of the shell material onto the core nanoparticles. For optical characterization, spectra were recorded using a quartz cuvette with an optical path length of 10 millimeters. Measurements encompassed a wavelength range from 200 to 1100 nanometers.

RESULTS AND DISCUSSION

UV-VISB AND BANDGAP ENERGY

The results of the samples' absorption spectra were documented by a UV–vis spectrophotometer, with wavelengths ranging from 200 to 1100 nm, to assess the energy of the optical band gap. As shown in Figure 1, the absorption spectrum of the synthesized nanoparticles (NPs) displayed a peak within a range of 200–260 nm, indicating a blue shift towards shorter wavelengths, confirming the decrease in particle size [27]. In Figure 2, the spectra of ZnO NPs (250 mJ) display a distinct high ZnO peak in the UV region (300–400 nm). Specifically, surface plasmon bands were observed at 350 nm for ZnO synthesized at energy settings of 250 mJ, indicating a blue shift and a trend toward shorter wavelengths. This phenomenon is attributed to the impact of quantum confinement [28]. By introducing Pt NPs to form a core-shell structure, two peaks appear within the absorption spectrum. The first peak, at 210 nm, is consistent with the absorption spectrum of platinum nanoparticles, and the second peak, at 350 nm, corresponds to the absorption peak of zinc oxide. The clarity of the peaks is enhanced compared to those of individual zinc oxide and platinum nanoparticles due to the increased concentration of the solution after adding Pt NPs, which led to an increase in absorbance according to the Beer-Lambert law. Fig. 3 shows the absorption spectra of zinc oxide synthesized at 500 mJ, where an absorption peak was observed at a wavelength of 350 nm [28]. The core-shell nanoparticles exhibit two distinct absorption peaks: the first peak at 210 nm corresponds to Pt nanoparticles, and the second peak at 350 nm indicates ZnO nanoparticles. These peaks confirm the successful formation of both the core and shell components.

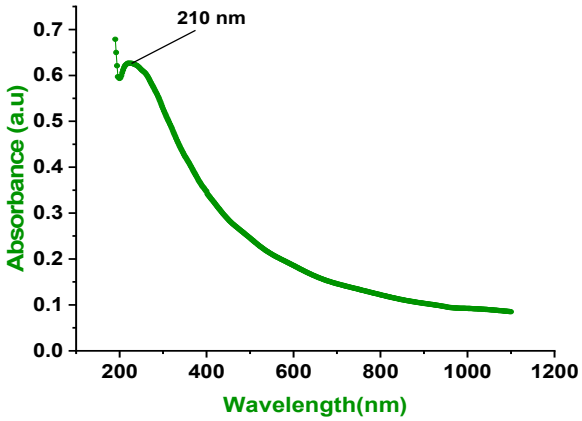

FIGURE 1. Absorbance peak of Platinum Nanoparticles ablated with wavelength 532 nm, frequency 32 Hz, energy 1900 mJ, and 3000 pulses

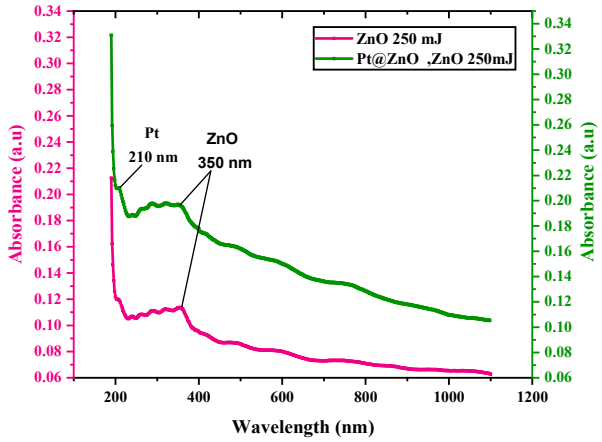

FIGURE 2. Absorption spectrum for both individual ZnO at an energy of 250 mJ and the core-shell nucleus Pt@ZnO at an energy of ZnO of 250 mJ.

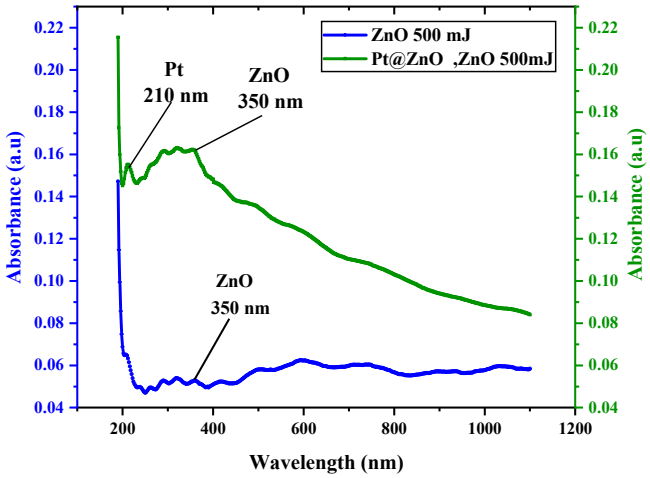

FIGURE 3. Absorption spectrum for both individual ZnO at an energy of 500 mJ and the core-shell nucleus Pt@ZnO at an energy of ZnO of 500 mJ.

For determination of the band gap of all ZnO NP samples, we employed the Tauc equation [29-31], utilizing absorbance data from UV-Vis spectroscopy (Fig. 3). The equation used for a direct band gap is Eg = (αhν)2, where α is the optical absorption coefficient, hν is the photon energy, Eg is the direct band gap, and ED is a constant. The direct band gap values were determined by plotting (αhν)2 against photon energy and extrapolating the linear portion of the curve to the point of zero absorption (Table 1).

The band gap energy increased as the particle size decreased, which was attributed to the effects of quantum size. ZnO NPs with an energy level of 500 mJ exhibit the highest band gap, indicating the presence of small nanoparticles with strong quantum confinement effects [29,32]. In contrast, ZnO NPs with 250 mJ energy suggest larger nanoparticle sizes than those at 500 mJ. By introducing Pt NPs to ZnO NPs of 250mJ and 500mJ the bandgap energy elevates Fig. 5.

TABLE 1. Band gap values

Form of NPs	Energy (mJ)	Wavelength (nm)	Bandgap (ev)
Individual Zno Nps	250	350	3.38
	500	350	3.74
Pt@ZnO Core-Shell	250	350	3.97
	500	350	3.78

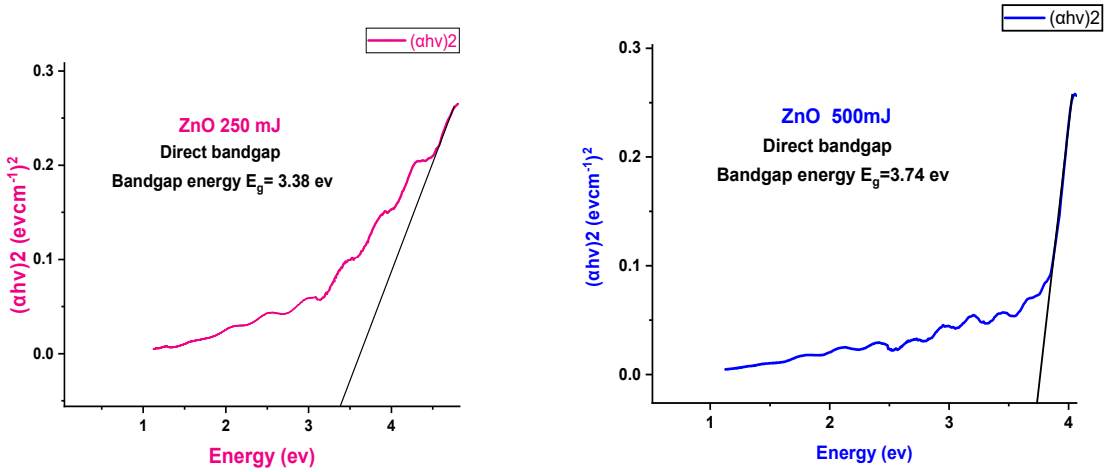

FIGURE 4. Bandgap energy for Zinc oxide NPs at 250mJ and 500mJ.

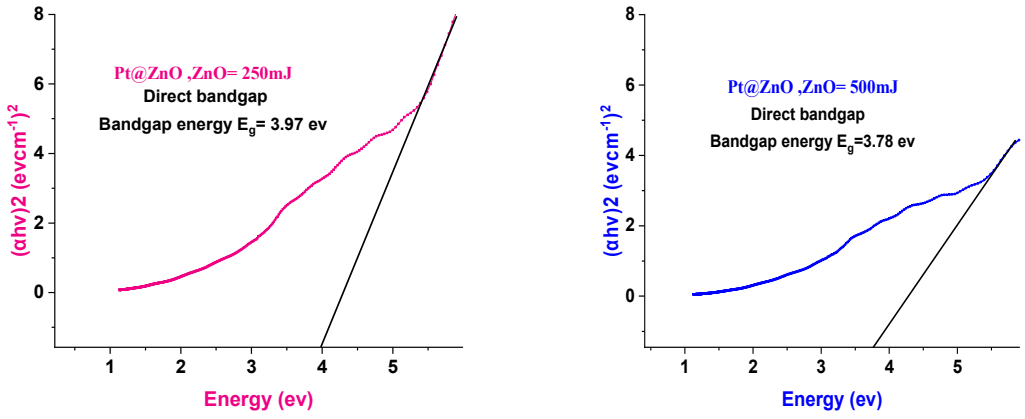

FIGURE 5. Bandgap energy for Pt@ZnO core shell when Zinc oxide NPs at 250mJ and 500mJ.

For ZnO NPs prepared with 250 mJ, there was an increase in the bandgap from 3.38 eV to 3.97 eV upon forming the Pt@ZnO structure [33]. This significant increase suggests a strong interaction between Pt and ZnO, possibly due to strain or electronic effects that enhance quantum confinement or introduce new electronic states [34]. The bandgap of the prepared ZnO NPs with 500 mJ, increased from 3.74 eV to 3.78 eV upon forming the Pt@ZnO structure. This minor increase indicates a less pronounced interaction than the 250 mJ case, possibly due to differences in particle size, strain, or the nature of the Pt-ZnO interface [35].

TOPOGRAPHY ANALYSIS

The surface topology of synthesised nanoparticles was examined using Atomic Force Microscopy (AFM). There are several methods to quantify the surface roughness of nanoparticles. The most commonly used approach is the root mean square (RMS) amplitude derived from the height assessment related to the mean level along a specific profile across the particle surface.

This technique, often called root mean squared profile roughness (RMS-RQ), measures the acceptable deviation from the particle's ideal shape within a specific domain. This is in contrast to coarse deviations, which pertain to the general shape deviations of the particle. Another parameter used for roughness quantification is the peak-to-valley height, which indicates the maximum height difference and is particularly useful when the density of acceptable deviations is very low [36]. Surface roughness significantly affects the accessibility of grafted functional bio-molecules, which act as binding units.

Consequently, this influences the sensitivity in bio-analytical applications [36]. In biomedical applications, the surface roughness of core-shell particles is crucial because it affects cell adhesion and growth, influencing how cells adhere to and proliferate on the particles, which impacts tissue engineering and implant success. Additionally, surface roughness plays a significant role in drug delivery efficiency, as rough surfaces can enhance drug loading and control the release of therapeutic agents, thereby improving targeted delivery and treatment efficacy. The immune response is also affected by surface roughness, as it influences how the immune system recognises and responds to the particles, affecting their circulation time and biocompatibility. Moreover, controlling surface roughness can prevent bacteria biofilm formation, ensuring medical device safety and functionality.

Furthermore, the mechanical properties of core-shell particles, such as their structural integrity and durability in physiological conditions, are influenced by their surface roughness, which is crucial for their performance in biomedical applications [37,38]. Platinum nanoparticles, as depicted in Fig. 6, show a homogeneous deposition across the substrates. The surfaces exhibit numerous peaks, indicating the presence of nanoparticles with consistent heights, implying a uniform size distribution. These nanoparticles are well-dispersed across the substrates with minimal agglomeration, which is essential for maintaining their unique properties. In Figure 7, we observe the surface morphology of zinc oxide nanoparticles subjected to two different energy levels.

The first image (a) captures the surface at an energy level of 250 mJ. Here, the surface appears relatively smooth, with height variations ranging from -232 nm to 271 nm. There is moderate roughness and some peak formations, indicating a stable structure under this energy input. The second image (b) in Figure 7 illustrates the effect of a higher energy level of 500 mJ. The height variations are more pronounced, ranging from -491 nm to 558 nm.

This significant increase in surface roughness suggests that the higher energy level induces more substantial surface deformation or restructuring of the nanoparticles. The surface now exhibits more pronounced peaks and valleys, showing a more complex topography compared to the 250 mJ condition.

Moving on to Figure 8, we explore the surface morphology of platinum-coated zinc oxide core-shell nanoparticles. The first image (a) represents these nanoparticles at 250 mJ. Here, the surface roughness is more significant, with height variations from -910 nm to 926 nm.

The topography reveals a highly textured surface with numerous peaks, suggesting intricate surface features likely due to the core-shell structure. The second image (b) in Figure 8 shows the same Pt@ZnO core-shell nanoparticles at an energy level of 500 mJ. The height variations become even more extreme, ranging from -1.54 μm to 1.51 μm. This indicates an even greater surface roughness, with a more pronounced texture characterized by higher peaks and deeper valleys. The increased energy level causes more significant morphological changes, emphasizing the material's sensitivity to energy input. [39,40].

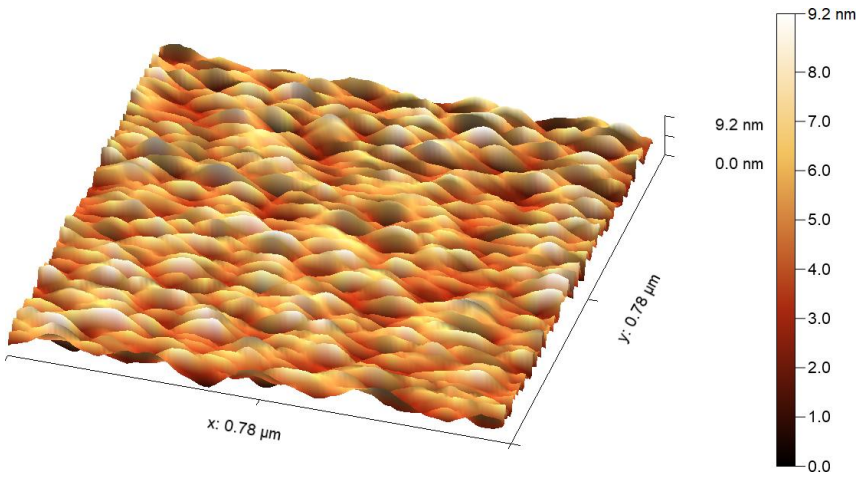

FIGURE 6. AFM image for platinum NPs with wavelength 532 nm, frequency 32 Hz, energy 1900 mJ, and 3000 pulses.

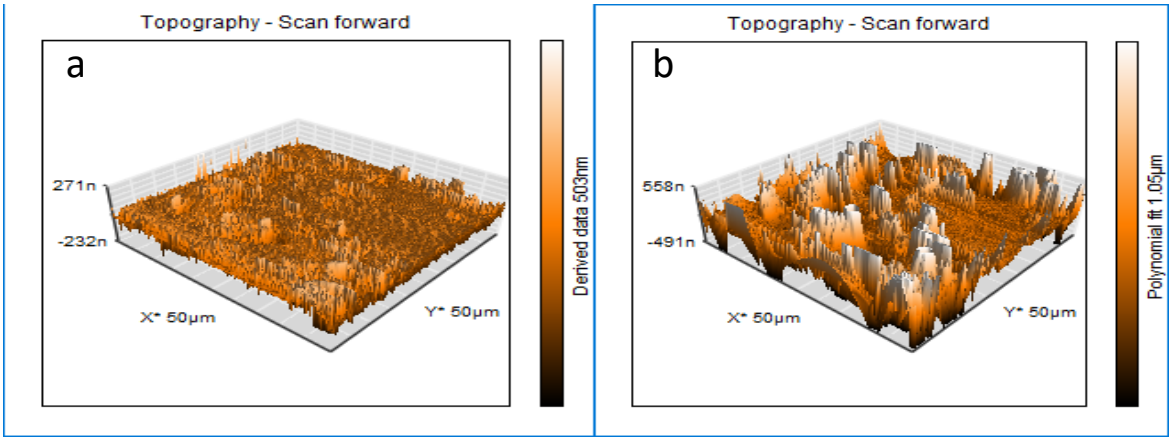

FIGURE 7. AFM image for Zinc oxide NPs at a) 250mJ b) 500mJ.

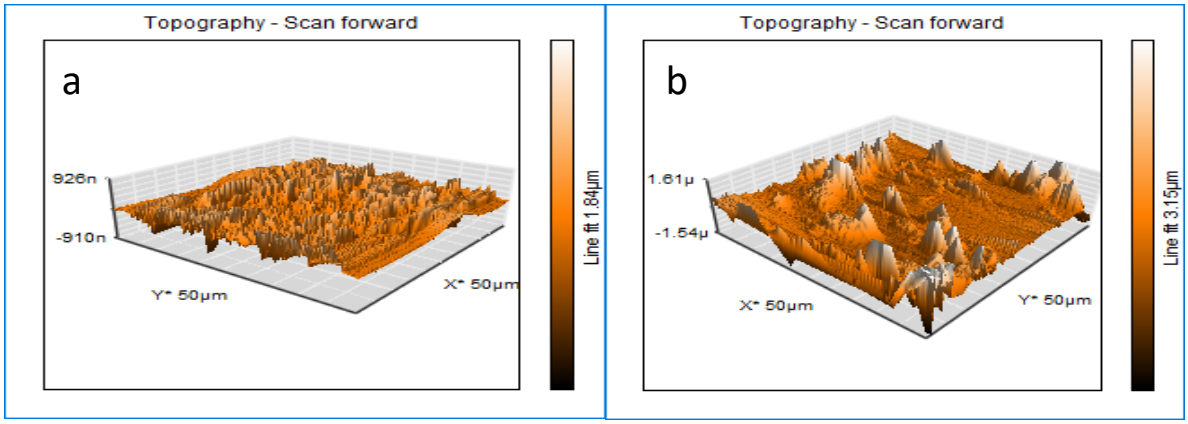

FIGURE 8. AFM image for Pt@ZnO core-shell when Zinc oxide NPs at 250mJ and 500mJ.

CONCLUSION

This study succeeded in synthesizing zinc oxide nanoparticles (ZnO NPs) and platinum nanoparticles (Pt NPs) using Pulsed Laser Ablation in Liquid (PLAL) and subsequently formed Pt@ ZnO core-shell structures. The bandgap energies of ZnO NPs, initially 3.38 eV for 250 mJ and 3.74 eV for 500 mJ, were significantly altered upon forming core-shell structures. The Pt@ ZnO structure with ZnO nanoparticles (NPs) synthesised at 250 mJ exhibited a bandgap energy increase to 3.97 eV, indicating strong Pt-ZnO interactions, likely due to quantum confinement. In contrast, ZnO NPs synthesized at 500 mJ showed a minor bandgap increase to 3.78 eV, suggesting weaker interactions. UV-

Vis spectroscopy confirmed the formation of Pt@ ZnO core-shell structures, and the Tauc equation highlighted quantum size effects on the band gap. AFM images revealed that higher energy synthesis (500 mJ) resulted in greater surface roughness and more pronounced topographical features for both ZnO and Pt@ZnO NPs. ZnO NPs exhibited less roughness than Pt@ ZnO core-shell NPs. This research highlights the importance of optimising synthesis parameters to tailor nanoparticle properties for specific applications, with future studies needed to explore interaction mechanisms and further optimization.

ACKNOWLEDGMENTS

The authors gratefully acknowledge the financial and technical support from the Applied Sciences Department, University of Technology, Baghdad-Iraq.

REFERENCES

1. S. Malik, K. Muhammad, and Y. Waheed, Molecules, **28**(2), 661 (2023)
2. M. A.Al-Kinani, A.J. Haider, and S. Al-Musawi, Plasmonics, 16(4), 1107-1117 (2021)
3. A.J. Haider, A.D. Thamir, D.S. Ahmed, and M.R. Mohammad, AIP Conf Proceed, 1758(1) (2016)
4. H. Nahedh, O.N. Salman, and M.M. Ismail, J Appl Sci Nanotechnol, **4**(2), (2024)
5. A.J. Haider, A.A. Najim, and M.A. Muhi, Optics Commun, **370**, 263-266 (2016)
6. S. Sim and N. Wong, Biomed Rep, **14**(5),(2021)
7. A.J. Haider, S S. Shaker, and A.H. Mohammed, Energ Proced, **36**, 776-787 (2013)
8. A.M. Alwan, A.J. Haider, A.A. Jabber, Surface Coatings Technol, **283**, 22-28 (2015)
9. J.A.S. Salman, A.A. Kadhim, and A.J. Haider, J Global Pharma Technol, 1(03), 348-355 (2018)
10. A.J. Haider, A.D. Thamir, A.A. Najim, and G.A. Ali, Plasmonics, **12**,105-115, (2017)
11. S. Kumari, S. Raturi, S. Kulshrestha, K. Chauhan, S. Dhingra, A. Kovács, K. Thu, R. Khargotra, and T. Singh, J Mater ResTechnol, (2023)
12. Ali H. Attallah, F. S. Abdulwahid, H. J. Abdulrahman, A. J. Haider, and Y. A. Ali, Plasmonics, 1-31 (2024)
13. F. A. Mutlak, and U. M. Nayef", J Appl Sci Nanotechnol, 4(1), (2024)
14. M.S. Edan, F.I. Sultan, A.H. Attallah, A.J. Haider, M.J. Haider, A.T. Tawfeeq, and O.H. Khalif, Iraqi J Sci, **64**(12), (2023)
15. N. Hossain, M.H. Mobarak, M.A. Mimona, M.A. Islam, A. Hossain, F.T. Zohur, and M.A. Chowdhury, Result Eng, **19**, 101347 (2023)
16. A.H. Attallah, F.S. Abdulwahid, Y.A. Ali, and A.J. Haider, Plasmonics, **18**(4), 1307-1323 (2023)
17. N.A. Aljbar, B.R. Mahdi, A.H. Khalid, A.H. Attallah, F.S. Abdulwahid, and A.J. Haider" Plasmonics, 1-10, (2024)
18. A.M. Negrescu, M.S. Killian, S. Naidu, P. Schmuki, A. Mazare, and A. Cimpean, J Funct Biomat, **13**(4) (2022)
19. S.H. Ahmed, A.M. Hameed, and K.F. Al-Azawi, J Appl Sci Nanotechnol, **4**(1), (2024)
20. A. Sirelkhatim, S. Mahmud, A. Seeni, N.H.M. Kaus, L.C. Ann, S.K.M. Bakhori, H. Hasan, and D. Mohamad, Nano-Micro Lett, 7(3), 219–242 (2015)
21. G. Bisht and S. Rayamajhi, Nanobiomed, **3**, 9 (2016)
22. A.H. Attallah, F.S. Abdulwahid, Y.A. Ali, and A.J. Haider, Plasmonics, 1-14.
23. O.T. Holton and J.W. Stevenson, Platinum Metals Rev, **57**(4), 259–271 (2013)
24. A. Abed, M. Derakhshan, M. Karimi, M. Shirazinia, M. Mahjoubin-Tehran, M. Homayonfal, M.R. Hamblin, S.A. Mirzaei, H. Soleimanpour, S. Dehghani, F.F. Dehkordi, and H. Mirzaei, Frontier Pharmacol, **13**, (2022)
25. S. Gurunathan, M. Jeyaraj, M.H. Kang, and J.H. Kim, Nanomater, **9**(8), 1089 (2019)
26. K. Chatterjee, S. Sarkar, K.J. Rao, and S. Paria, Adv Colloid Interface Sci, **209**, 8–39 (2014)
27. M. Abdollahi, B. Jaleh, R.M.,W. Arnaouty, and R.S. Varma, Pramāna, **96**(4), (2022)
28. N. Mintcheva, A. Aljulaih, W. Wunderlich, S. Kulinich, and S. Iwamori, Materials, **11**(7), 1127 (2018)
29. Rogach, A. (Ed.). (2008). Semiconductor Nanocrystal Quantum Dots. Springer.
30. P. Makuła, M. Pacia, and W. Macyk, J Physic Chem Lett, **9**(23), 6814–6817 (2018)
31. P.R. Jubu, E. Danladi, U.I. Ndeze, O. Adedokun, S. Landi, A.J. Haider, A.T. Adepoju, Y. Yusof, O.S. Obaseki, & F.K. Yam, Result Optics, **14**, 100606 (2024). 06.
32. A.M. Smith and S. Nie, Account Chem Res, **43**(2), 190–200 (2010)
33. A. J. Haider, F. I. Sultan, M. J. Haider, and N. M. Hadi, Appl. Phys. A, 125(4) (2019)
34. A. Piyadasa, S. Wang, and P.X. Gao, Semicond Sci Technol, **32**(7), 073001 (2017)
35. A.J. Haider, A.A. Jabbar, and G.A. Ali, J. Phys. Conf. Ser., **1795,** 012015 (2021).

36. D. Hülagü, C. Tobias, E. Climent, A. Gojani, K. Rurack, and V.D. Hodoroaba, Adv. Eng. Mater. **24**, 2101344 (2022)
37. K. Chatterjee, S. Sarkar, K. Jagajjanani Rao, and S. Paria, Adv Colloid Interface Sci, **209,** 8–39 (2014):
38. M. Lotfi, M. Nejib, and M. Naceur, Adv Biomater Sci Biomed Appl, (2013)
39. A.A. Salih, A. Nazar, and A.J. Haider, Antibacterial Activity of ZnO Nanoparticle Prepared by Pulsed Laser Ablation in Liquid for Biological Sensor, (2019)
40. M. Cueto, M. Sanz, M. Oujja, F. Gámez, B. Martínez−Haya, and M. Castillejo, J Phys Chem C, **115**(45), 22217–22224 (2011)

Neurotransmitter as a Model Therapeutic Platform: A Mini-Review

Aliaa A.Razzak [1,2, a)], Zahraa S.Al-Garawi[2], Adawiya J.Haider[3] and Bahaa Hassan[4]

[1] *Chemistry Department, College of Science, Mustansiriyah University, Baghdad, Iraq.*
[2] *Applied Sciences Department, Chemistry Branch, University of Technology, Baghdad, Iraq.*
[3] *Applied Sciences Department, Laser Science and Technology Branch, University of Technology, Baghdad, Iraq.*
[4] *Department of Neurology, Saad Al-Witry Neuroscience Hospital, Baghdad, Iraq.*

[a)] Corresponding Author: 100038@uotechnology.edu.iq

Abstract. In this Review, we specified the basic properties of polydopamine (PDA) and dopamine (DA) as catecholamine neurotransmitters. PDA neurotransmitter has been widely used in recent applications of nanobiotechnology and medicine for its excellent biocompatibility, biodegradability, photothermal transfer ability, and good stability. Herein, we explored polydopamine nanoparticles (PDA NPs) for the development of a safe and efficient antioxidant protection platform as a neuroprotective platform drug in scavenging ROS overtake in neuroretinal diseases, periodontal disease, and for the treatment of other degenerative diseases. PDA NPs have also been successfully developed in bone-tissue repair engineering, gene detection, and antibiotic loading, in addition to developing a novel approach for cancer therapy in living cells with the presence of phototherapy and chemotherapy techniques. Finally, the relationship between PDA NPs with SARS-CoV-19 is summarized. Our strategy in this review will be considered as a definitive revelation for the next human treatment development.

1. INTRODUCTION

Poly Dopa Amine (PDA) is considered a melanin-semi polymer that, by nature and structure, is a neurotransmitter (DA) [1]. DA is naturally produced from amino acids (tyrosine) or 3,4-dihydroxyphenylalanine(L-DOPA), and that means PDA is similar in structure to L-DA [2]. PDA is a major pigment of naturally forming melanin and has excellent biocompatibility. Nanosystems are gaining increased importance in a wide variety of applications as including general applications and in the specific field of tumor and disease therapy, or even biomarker diagnosis [3,4]. Various studies have specified the therapeutic potential of PDA nanomaterials for various diseases, including diabetes, cancer, inflammation, decreasing periodontal inflammation, and many other diseases [5,6]. The development of catecholamine-based coatings was a great advance in recent science [5,7]. These coatings depend on the oxidation reaction of catecholamines, such as dopamine, norepinephrine, and L-DOPA [7]. Fig. (1). The subsequent polymerization and self-assembly of a eumelanin-like material called "polydopamine" (PDA).

In addition, catecholamine-based coatings are prepared from DA in alkaline solutions with buffer (pH = 8.5), and using O_2 dissolved in water as an oxidant factor. In addition, many available oxidants such as sodium periodate and ammonium peroxodisulfate [7,8].The use of UV- UV-irradiation to form and generate free radical species is also studied as an oxidant factor[9].

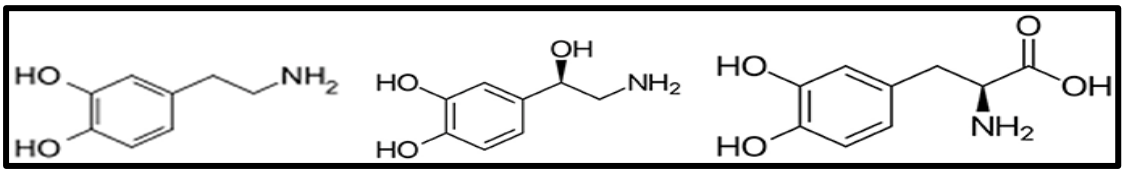

Figure 1. Structure of catecholamine: dopamine, norepinephrine, and L-DOPA Dop.

DA is a hormone and catecholamine neurotransmitter that is produced in the substantia nigra, the ventral tegmental area, and the hypothalamus in the brain [10]. DA occurs naturally in the human body and plays an important role

Technologies and Materials for Renewable Energy, Environment and Sustainability
AIP Conf. Proc. 3321, 020009-1–020009-11; https://doi.org/10.1063/5.0289997
Published under an exclusive license by AIP Publishing. 978-0-7354-5231-2/$30.00

model for various brain functions [2,11]. It's expressed mainly in the central nervous system, also found in blood vessels, kidneys, heart, retina, and adrenals that control catecholamine release and the renin-angiotensin system [11,12]. These monoamine neurotransmitters play important roles in the regulation of motor neurons, arousal, spatial memory function, pleasure, and motivation, as well as lactation, sexual, and maternal behavior, and Parkinson's disease [2,13,14]. DA plays an essential role in the modulation of behavior and cognition; motivation, voluntary movement; punishment and reward; inhibition of prolactin production; sleep with mood; attention; working memory; and learning [15,16].

Furthermore, the other most important function of DA in metabolism and the pathway in the human body is the pathogenesis of hypertension by regulating the transport of sodium from the epithelium and reactive oxygen, and by interacting with vasopressin, renin-angiotensin, and the sympathetic nervous system [17]. See Fig. (2,3),

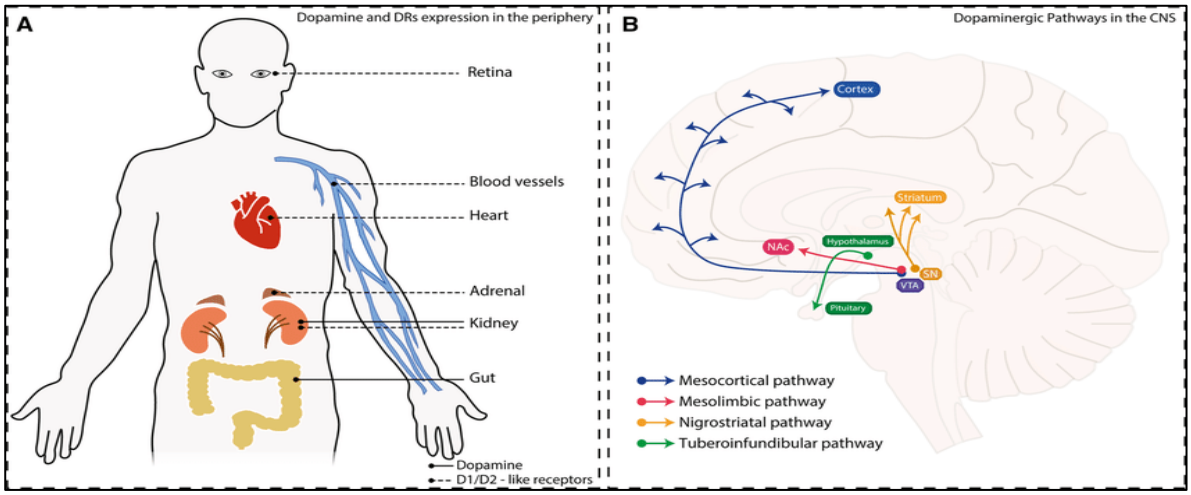

Figure 2. Distribution of dopamine, dopamine receptors, and pathways in the human body.

This introduced recent potential targets for the development of therapeutic interventions that depended on antioxidants. Decreased renal DA production and/or impaired DA receptor function have been described in hypertension [18].

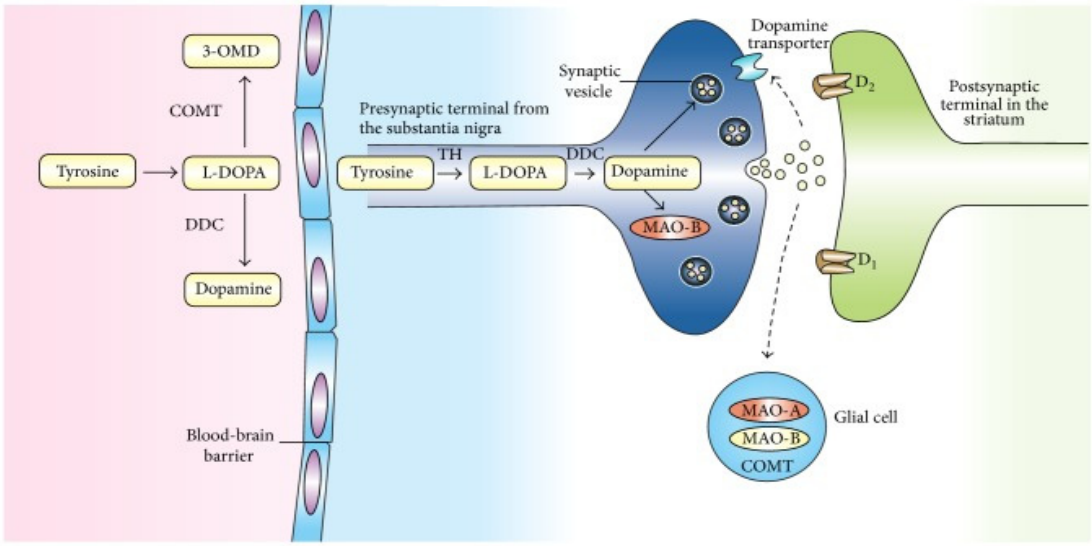

Figure 3. Mechanism of PDA in the brain.

In every decade of aging, a loss of 5–10% of dopaminergic neurons has occurred, and an increase in oxidative damage in the brain is associated with age. Alejandro Olvares-H. et al.,2021 have shown different DA receptors (D1–D5) and defense effects against hypertension and kidney disorders [19].Dopamine can increase the rate of glomerular filtration by postglomerular arteriolar constriction. DA modulates renin expression and angiotensin II, and controls

the concentration of sodium excretion and blood pressure (BP) [20]. In some studies, an increase in insulin resistance or a decrease in insulin secretion is observed. The role of insulin secretion as a response to dopamine is incompletely understood [21]; see also Fig. 3.

The in vitro experiment showed that DA inhibits glucose-stimulated insulin secretion at concentrations in the pancreas [21]. It has been posited that this can be due to the down-regulation of D2 receptors, causing increased catecholamine production, decreased cell membrane depolarization, and cytosolic calcium influx, causing a decrease in insulin secretion [22]. Summarize some of the most important features of PDA nanostructure properties and applications in Table 1.

Table 1. Summarizes Some of The Most Important Features Of PDA.

Factors	Influence	Ref
Monomer Concentration	NP size increases dopamine concentration	[23,24]
Buffer system	The particle size varies in different buffers	[25-27]
Reaction time	Increasing the reaction time would improve the deposition of dopamine	[28]
Oxidant	An oxidant such as sodium periodate or potassium chlorate would speed up the polymerization in an alkaline aqueous solution.	[29]
pH	Higher pH conditions result in a higher yield of particles with smaller diameters.	[25]
Mental ion	Metal ions facilitate dopamine polymerization	[30]
Free radical	Free radical scavengers inhibit NP formation, while stable free radicals facilitate seed formation. Both decreased NP size	[31]

2. PDA AS A BIOMIMETIC ADHESIVE

The proteins in the extremity of the mussel byssus are rich in L-DOPA (more than 30 mol%) and L-lysine residues [32]. The specific amino acid residues allow for the best adhesion of the mussel to all kinds of substrates in a wet and slightly basic medium of seawater. Vincent Ball et al. (2018) showed that the rationale behind the use of catecholamine to deposit adhesive coatings on all types of substances was the simultaneous presence of a catechol and an amine functional group, as Fig (1)[4] . Maier Gp et al. (2015) describe the important role of catechols in participating in the adhesion strength through the cooperation of three groups: the first group with both catechol and amine, another one without catechol but presented amine, and the third group was without amine but presented catechol. The weak adhesion resulted when both compounds were not present simultaneously, suggesting that catechol and amine are essential to initiate good adhesion [33].

Polydopamine (PDA), inspired by the adhesive substance of sea mussels, is precisely an adhesive substance that allows it to coat almost any surface while having many advantages: easy to synthesize, biocompatible, and antioxidant properties [4]. V.Ball et al [2018] suggested that PDA moved into the spotlight as a novel coating material in (2007) [34,35]

2.1 PDA catecholamine-based coating modification

The proteins in the extremity of the mussel byssus are rich in L-DOPA (more than 30 mol%) and L-lysine residues [32]. The specific amino acid residues allow for the best adhesion of the mussel to all kinds of substrates in a wet and slightly basic medium of seawater. Vincent Ball et al. (2018) showed that the rationale behind the use of catecholamine to deposit adhesive coatings on all types of substances was the simultaneous presence of a catechol and an amine functional group, as Fig. 1.[4] . Maier et al. (2015) describe the important role of catechols in participating in the adhesion strength through the cooperation of three groups: the first group with both catechol and amine, another one without catechol but presenting amine, and the third group without amine but presenting catechol. The weak adhesion resulted when both compounds were not present simultaneously, suggesting that catechol and amine are essential to initiate good adhesion [33].

Polydopamine (PDA), inspired by the adhesive substance of sea mussels, is a precise adhesive substance that allows it to coat almost any surface while having many advantages: easy to synthesize, biocompatible, and with

antioxidant properties [4]. V.Ball et al [2018] suggested that PDA moved into the spotlight as a novel coating material in 2007. [34,35]

2.2 Application of PDA NPs in nanobiotechnology and the medical field:

A- PDA NPs in the drug delivery system (cancer therapy*):*

Nanobiotechnology has shown promising prospects to change the landscape of pharmaceutical and biomedical industries principality. The last years of biomedical research have shown that nanoparticles have the potential [30,60]. to be a beneficial tool for a variety of applications in vitro and in vivo [38].

In these types of applications, many strategies for diagnosis and treatment were explained and provided a wide range of prospective uses. Methods of special clinical importance include cell separation, magnetic resonance imaging (MRI), and magnetically targeted administration of medicines [39].

It is of utmost importance that these particles do not have any toxic effects or are incompatible with biological organisms to be used in the health or medicine field, particularly those that take place in living organisms. Investigations on relevant particles led to the development of different types of nanostructures with distinct variations in their surface chemistry, sizes, and materials. Meanwhile, nanoparticles are used in the commercial field as contrast agents for MRI scans and as separation tools for the monitoring of metastatic cancer cells in blood after the administration of systemic chemotherapy [40].

An investigation is still being done for the use of nanoparticles as a biomedical delivery method and for inducing hyperthermia. Compared with traditional drug delivery systems, the use of nanoparticles as drug carriers offers the significant usefulness of a more targeted delivery of the system to the tissue of interest by the application of an external magnetic field. Endovascular delivery of nanomagnetic material is possible, which makes it possible to access even physiologically delicate and difficult-to-reach tissue. In addition to this, the drug carrier can penetrate tissue through the capillary system [41].

DA nanoparticles have been widely used clinically, and experimentally in several biomedical applications such as hyperthermia, targeting agents, and in the field of cancer therapy, Fig. 4. The specific physic-chemical properties that DA possess good stability in biological media and due to the extended surface area, in addition, some applications use DA as a hydrophilic agent to coat other nanoparticles such as Fe_3O_4 to make the water dispersible and biocompatible [42].

The surface coating of PDA NPs is not only applicable for nontoxic and biocompatible nanomaterials, but can also be exploited to bind with drugs, enzymes, proteins, and antibodies that can be targeted to the target point by applying the external magnetic field or by bioengineering application. The propriety of drug loading capacity by $\pi - \pi$ stacking interaction and hydrogen bond [43]

A new natural polymer that has good physicochemical advantages: modest preparation, good biocompatibility, and unparalleled drug-loading methods, PDA has attracted tremendous attention in applications of drug delivery and the combination of chemotherapy and other therapies or diagnostic methods, such as photo thermotherapy (PTT), photoacoustic imaging (PAI), magnetic resonance imaging (MRI) [44].

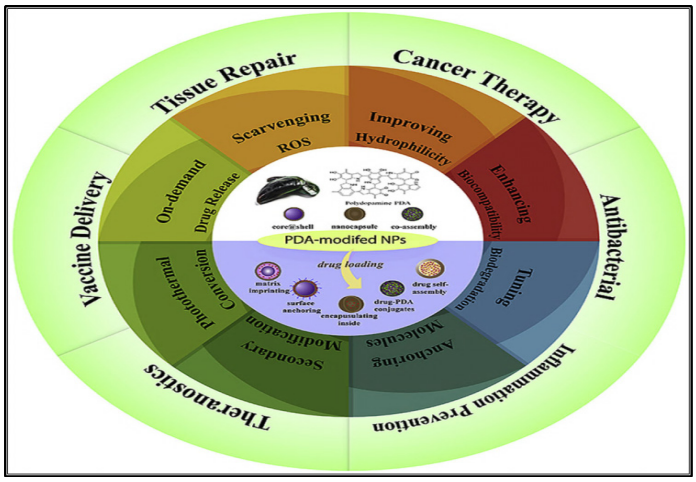

Figure 4. PDA- modified NPs.

Table 2. Summarizes Some of The Clinical Biomedical Applications Of Pda

Some Clinical Biomedical Applications	Ref.
PDA binds with enzymes	43
PDA binds with proteins	43
PDA binds with antibodies	43
PDA binds with drugs	43
PDA combined with photothermal therapy PTT	44
PDA combined with photoacoustic imaging PDI	44
DA hydrophilic factor coating nanoparticles Fe3O4	42
PDA combined with magnetic resonance imaging MRI	44
PDA binds with DNA	46

Also, nano PDA has been used as a promising therapeutic in the treatment of neurodegenerative disorders by showing lower toxicity in an example of Parkinson's disease (PD) [43]

The PDA nanoparticles and their modified structure were used as an active agent/drug delivery tool as a model drug that can be readily loaded into particles and released at higher times at higher amounts for the modified p(DA) particles under several conditions. The size (100 nm), and degradation of p(DA) are slight at pH 1 and pH 7.4 with weight losses of $13.01 \pm 0.08\%$ and $7.26 \pm 0.23\%$ in 11 days, respectively. At pH 11, a sustained degradation that is almost linear with time was described for up to 30 days. [45]. It confirms that drug-loaded capsules performed better than free drug demonstrations, demonstrating the great potential of the PDA nanosystem in biomedical applications. A combination of both phototherapy and chemotherapy can be investigated for the treatment of life-threatening disorders.

Therefore, a synergistic nano platform was developed for lauded. Sweet PDA NPs that were synthesized by oxidative polymerization of lactosylated DA. This case was achieved with high photothermal conversion efficiency and good stability by NPs that exhibited strong NIR laser absorption, as shown in Fig. 5 [46]. PDA NP could be loaded with doxorubicin. Doxorubicin was adsorbed on the surface of PDA NP by hydrophobic interaction and other interactions [47].This proposed model combines radiotherapy and chemotherapy by Zhonng et al. 2015. In glaucoma disease, microRNA is delivered by cationic nanoparticles (PDA-polyethyleneimine) to improve permeability in the pathway and inhibit intraocular pressure by PDOPA serving as a therapeutic nanoplatform to prevent the secretion and degeneration of retina ganglion cells secretion and degeneration [48] .

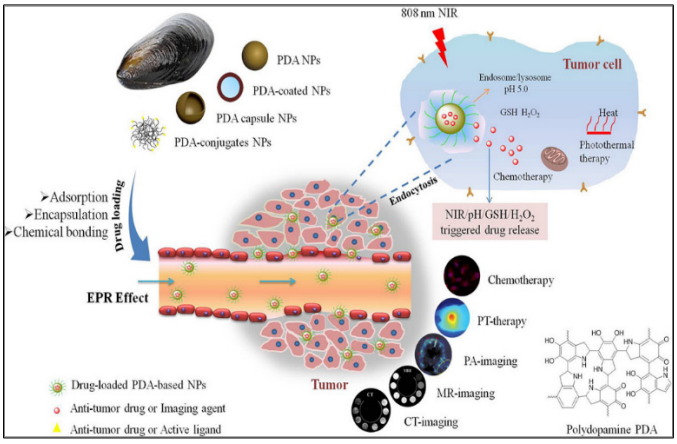

Figure 5. Mechanism of DAP Nps in Therapy of Tumor [46].

B- PDA NPs in DNA and Gene Detection

In vivo data showed that tumor development was inhibited in mice treated with this nanocarrier compared to those treated with the noncarrier nanodrug [49]. PDA was processed with arginine–glycine–aspartic–cysteine acid to produce the target action in the tumor position, as shown by Li et al. (2017) [50].

Table 3. Models of PDA and DA in Some Vitro Disorders

PDA or DA combination	Function.	Type of disorder	Ref.
PDA NPs loaded in Doxorubicin Liposomes	radiotherapy and chemotherapy therapeutic	Tumor Targeted Therapy	47
PDA loaded with microRNA	improve permeability in the pathway and inhibit intraocular pressure	glaucoma disease	51
PDA therapeutic	lower toxicity	Parkinson's disease (PD)	43
PDA collagen sponge scaffold with platelet-plasma (PDA-CSS@PRP)	increase osteoblast cell proliferation and calcium deposition, and improve the living pathway	skin wound and any defect healing, such as bone, heart, cartilage, and nerve	55
Brimonidine treatment loaded in PDA NPs	Increase RGCs protection		59
PDAs as smart scavengers of ROS	decreased periodontal inflammation	glaucoma models	48
dopamine production pathways from DA drugs	leading to an improvement in the life cycle of SARS-CoV-2	periodontal disease	62,62,64

c- PDA in Bone and Tissue Engineering Repair

The 3D-bio printed PLA-PDA scaffolds have good potential as an alternative material for repairing bone disorders. this study takes advantage of PDA coating on Poly Lactic Acid (PLA) to fabricate nanoparticles with various sizes and different properties, and the chemical reactivity of PDA PLA particles enhances platelet adhesion, while PDA particles reduce platelet adhesion on the patterned surface; Particles interact with platelets by activating bone [51]. The development of PDA nanoparticles in tissue engineering applications is shown by Yanmei Tany et al. 2021 involving the repair of bone, cartilage, skin, heart, and nerve, to provide strategies for the design of new biomaterials on the living pathway[52]. PDA has been reported to enhance and increase osteoblast cell proliferation and calcium deposition, and the effect could be further strengthened in the combination of growth factors [Shishu H. et al., 2016)[53]. PDA can enhance the attachment of fibroblast cells. PDA-assisted surface modification uses PDA as a biocompatible surface modifier to interact with various chemical components at the interface of bone bio-substitutes [54]. Such a targeted modification makes the biphasic interface of the substance more stable for the requirements of bone tissue repair. Ziju Zheng et al., 2021, reported that the new PDA-based modified collagen sponge scaffold was clinically suggested to repair and heal with less scar for all skin defects [55]as shown in Fig. 6).

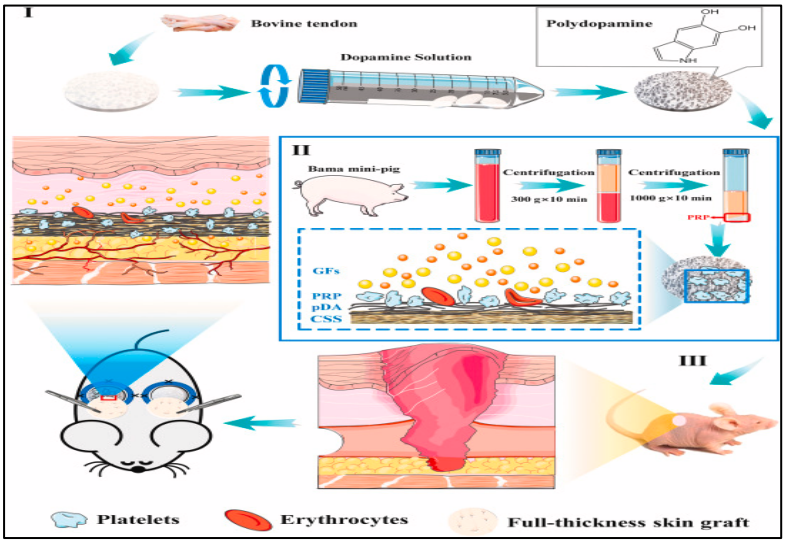

Figure 6. Preparation of PDA Collagen Sponge Scaffold Added to Platelet-Rich Plasma (PDA-CSS@PRP) To Accelerate All-Thickness Skin Wound and Any Defect Healing.

D- PDA in ROS scavenging

The nanocarriers are capable of having an enhanced effect on cell death and apoptosis induction compared to the unloaded nanocarriers [56,57]. In an antioxidant therapy that is considered an efficient method for the treatment of a series of excessive reactive oxygen species (ROS) triggered disorders or diseases, polydopamine showed ROS [57,27] scavenging prosperities in ROS-mediated inflammation, as well as body injury, as shown in Figs.. 7 and 8). Different ocular diseases and periodontal diseases [58], such as ocular vein occlusion and glaucoma, and trauma to the ocular is identified by damage to retinal ganglion cells (RGC), leading to irreversible vision loss and ROS production due to the imbalance between ROS and antioxidant defenses [59]. ROS induces oxidative damage to mitochondrial DNA [61].

Developing a high-performance platform by using the biodegradable PDA nanoparticles as smart scavengers of ROS in oxidative stress-induced. periodontal disease and decreased periodontal inflammation without any side effects have been previously reported[48]. Furthermore, the surface of PDA NPs can be modified by terminating with –SH- or -NH_2.

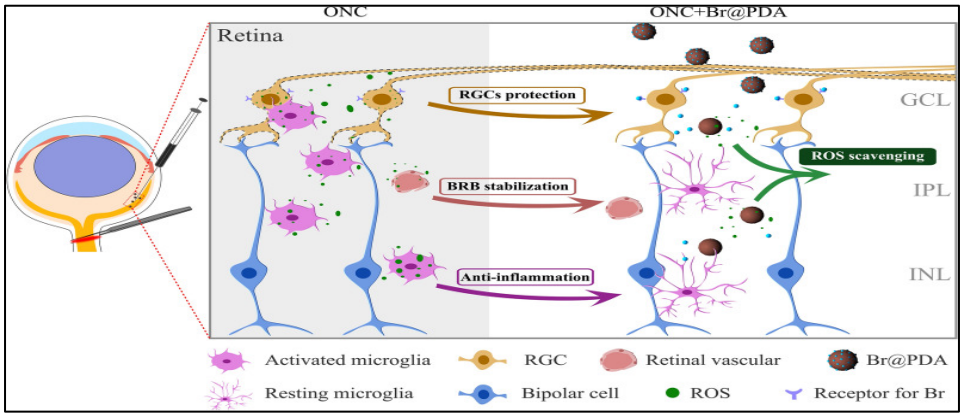

Figure 7. Illustration of Br@PDA Nps In Retina Protection

ligands. In glaucoma models, the brimonidine treatment loaded in PDA NPs serves as a neuroprotection and nanotherapeutic system to increase RGC protection [59].

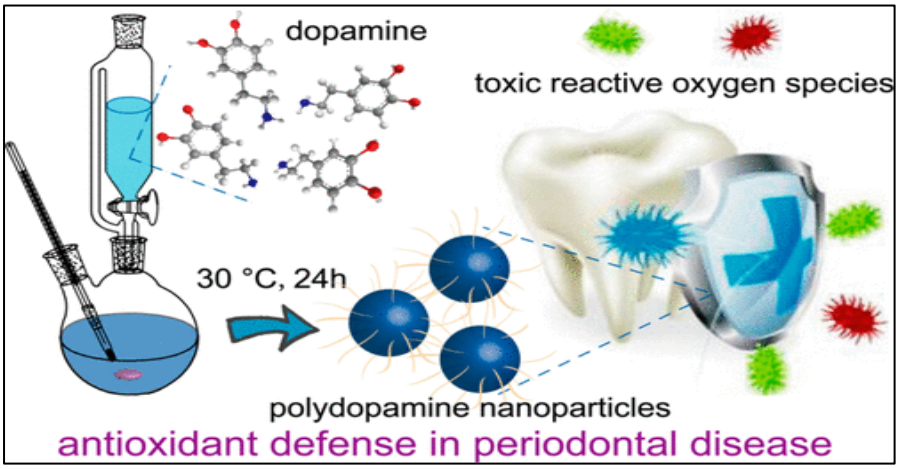

Figure 8. PDA NPs in periodontal diseases

E- DA and COVID-19

Muad M. Khalefah et al. (2020 investigated dopamine production pathways in the central nervous system. These efforts can find a new cure for pandemic coronavirus disease (COVID-19) [62]. DA could negatively regulate the immune response during infection, leading to an improvement in the life cycle of SARS-CoV-2, which could be particularly relevant in patients receiving medications that include DA agonists. ARS-CoV-2 could exploit dopamine

as an entry pathway into the body, with dopamine receptors supporting virus pathogenicity. SARS-CoV-2 hinders innate and adaptive immune responses through DA-mediated disruption of intracellular biosynthesis, and the viral life cycle of SARS-CoV-2 could be increased in the presence of high levels of catecholamine. SARS-CoV-2 and dopamine could participate in the responsible for impaired ventilation. Third, dopamine is a good bioregulator of immune function [62,63]. The virus can manipulate the immune system by enhancing dopamine levels to increase the possibility of viral entry and lead to the progression of COVID-19. Here is a strong relationship between the concentration of dopamine controlled by these drugs and the severity of COVID-19 complications [64].

CONCLUSION

PDA has attracted a great deal of interest due to several advantages such as a simple preparation process, good biocompatibility, strong adhesive properties, easy functionalization, and excellent degradation. In addition, PDA can be exploited to bind to drugs, proteins, DNA, RNA, enzymes, and antibodies as a catecholamine-based platform. The stability in the biological media and the extent of the surface area of PDA nanomaterial, hydrophilic prosperity, and water dispersability, lead to many applications in the biofield by green chemistry, which effort solves the biggest challenge in nanobiotechnology. In this review article, we studied the general features of PDA and DA with their synthesis and metabolism. They serve as much faster oxidizing agents and allow for the formation of thicker films in other methods. Our review focused on showing many of the most important biomedical applications of PDA, such as in drug-delivery-based platforms, cancer treatment, gene expression, DNA repair and adsorption, and bone engineering. The good elimination of ROS is hypothesized and scavenging of toxic ROS in retinal microglia and vascular endothelial cells, in addition to inducing RGCs apoptosis, therefore, it is suggested that improving the treatment of neurodegeneration still needs to be understood and studied until now. The relationship between DA and COVID-19 is of special interest and needs to be improved. It is helping facilitate future uses of PDA NPs as a way to treat, reduce, and detect their influences. Finally, this paper suggests that more exciting studies concerning PDA nanoparticles are the first important step toward greater potential in various types of treatment and therapy.

.

REFERENCES

1. D'Ischia, M., Napolitano, A., Ball, V., Chen, C.-T., and Buehler, M. J. "Polydopamine and Eumelanin: From Structure-Property Relationships to a Unified Tailoring Strategy." Accounts of chemical research, Vol. 47, No. 12, 2014, pp. 3541–3550.
2. AL-OGAIDI, A. J. M., Hamid, D. M., and Mohammed, A. A. R. "Ultra-Higher Assessment of CEA by Using Sensing Technology." Biochemical and Cellular Archives, Vol. 20, No. 2, 2020, pp. 5307–5309.
3. Al-Kinani, Maha A., Adawiya J. Haider, and Sharafaldin Al-Musawi. "Design and synthesis of nanoencapsulation with a new formulation of Fe@ Au-CS-CU-FA NPs by pulsed laser ablation in liquid (PLAL) method in breast cancer therapy: in vitro and in vivo." Plasmonics 16.4 (2021): 1107-1117.
4. Abdulwahid, F.S., Haider, A.J., Al-Musawi, S.(2023), Folate decorated dextran-coated magnetic nanoparticles for targeted delivery of ellipticine in cervical cancer cells, Advances in Natural Sciences: Nanoscience and Nanotechnology, 2023, 14(1), 015001
5. Hong, S., Wang, Y., Park, S. Y., and Lee, H. "Progressive Fuzzy Cation-π Assembly of Biological Catecholamines." Science advances, Vol. 4, No. 9, 2018, p. eaat7457.
6. Mohammed, A.M., Al-Khateeb, I.K., Haider, A.J., Rahim, R.A. and Hashim, U "Preparation of DNA biosensor application from fuel oil waste by functionalization and characterization of MWCNT." Sensing and bio-sensing research, Vol 16, 2017, pp.1-5.
7. Wei, Q., Zhang, F., Li, J., Li, B., and Zhao, C. "Oxidant-Induced Dopamine Polymerization for Multifunctional Coatings." Polymer Chemistry, Vol. 1, No. 9, 2010, pp. 1430–1433.
8. Attallah, Ali H., Abdulwahid, F. S., Ali, Y. A., & Haider, A. J. (2024). Enhanced characteristics of iron oxide nanoparticles for efficient pollutant degradation via pulsed laser ablation in liquid. Plasmonics, 1-14.
9. Pezzella, A., Barra, M., Musto, A., Navarra, A., Alfe, M., Manini, P., Parisi, S., Cassinese, A., Criscuolo, V., and d'Ischia, M. "Stem Cell-Compatible Eumelanin Biointerface Fabricated by Chemically Controlled Solid State Polymerization." Materials Horizons, Vol. 2, No. 2, 2015, pp. 212–220.

10. Tokura, Y., Harvey, S., Chen, C., Wu, Y., Ng, D. Y. W., and Weil, T. “Fabrication of Defined Polydopamine Nanostructures by DNA Origami-templated Polymerization.” Angewandte Chemie International Edition, Vol. 57, No. 6, 2018, pp. 1587–1591.
11. Hong, S., Kim, J., Na, Y. S., Park, J., Kim, S., Singha, K., Im, G., Han, D., Kim, W. J., and Lee, H. “Poly (Norepinephrine): Ultrasmooth Material-independent Surface Chemistry and Nanodepot for Nitric Oxide.” Angewandte Chemie International Edition, Vol. 52, No. 35, 2013, pp. 9187–9191.
12. Sabah, T., Jawad, K.H. and Essam, N. “Assessing the Toxicity of Aluminum Oxide Nanoparticles (Al2O3 NPS) Prepared by Laser Ablation Technique on Blood Components.” Journal of Applied Sciences and Nanotechnology, Vol. 3, 2023, No.1.
13. Razzak, A.A., Al-Garawi, Z.S., Haider, A.J., Hassan, F.A.A.N.B. (2025). New nanomanufacturing strategy through bioinspired design, for promising treatment of Parkinson’s disease, Scientific Report 2025, 15(1), 6904.
14. Aljbar, Nahla A., et al. "Enhanced surface plasmon resonance (SPR) fiber optic sensor for environmental monitoring: a coreless fiber–based design." Plasmonics (2024): 1-10.
15. Burhan, R., and Moradzadeh, J. “Neurotransmitter Dopamine (DA) and Its Role in the Development of Social Media Addiction.” Journal of Neurology & Neurophysiology, Vol. 11, No. 7, 2020, pp. 1–2.
16. Abbas, S.F., Haider, A.J. and Al-Musawi, S “Antimicrobial and Wound Healing Effects of Metal Oxide Nanoparticles Enriched Wound Dressing.” NANO, Vol. 18, 2023, No. 08, p.2330005.
17. Medic-Stojanoska, M., Icin, T., Pletikosic, I., Bajkin, I., Novakovic-Paro, J., Stokic, E., Spasic, D. T., Kovacev-Zavisic, B., and Abenavoli, L. “Risk Factors for Accelerated Atherosclerosis in Young Women with Hyperprolactinemia.” Medical Hypotheses, Vol. 84, No. 4, 2015, pp. 321–326.
18. Shankar, E., Santhosh, K. T., and Paulose, C. S. “Dopaminergic Regulation of Glucose-induced Insulin Secretion through Dopamine D2 Receptors in the Pancreatic Islets in Vitro.” IUBMB life, Vol. 58, No. 3, 2006, pp. 157–163.
19. Olivares-Hernández, A., Figuero-Pérez, L., Cruz-Hernandez, J. J., González Sarmiento, R., Usategui-Martin, R., and Miramontes-González, J. P. “Dopamine Receptors and the Kidney: An Overview of Health-and Pharmacological-Targeted Implications.” Biomolecules, Vol. 11, No. 2, 2021, p. 254.
20. Armando, I., Van Anthony, M. V., and Jose, P. A. “Dopamine and Renal Function and Blood Pressure Regulation.” Comprehensive Physiology, Vol. 1, No. 3, 2011, p. 1075.
21. Tavares, G., Martins, F. O., Melo, B. F., Matafome, P., and Conde, S. V. “Peripheral Dopamine Directly Acts on Insulin-Sensitive Tissues to Regulate Insulin Signaling and Metabolic Function.” Frontiers in pharmacology, Vol. 12, 2021, p. 713418.
22. Shankar, E., Santhosh, K. T., and Paulose, C. S. “Dopaminergic Regulation of Glucose-induced Insulin Secretion through Dopamine D2 Receptors in the Pancreatic Islets in Vitro.” IUBMB life, Vol. 58, No. 3, 2006, pp. 157–163.
23. Ball, V., Del Frari, D., Toniazzo, V., and Ruch, D. “Kinetics of Polydopamine Film Deposition as a Function of PH and Dopamine Concentration: Insights in the Polydopamine Deposition Mechanism.” Journal of colloid and interface science, Vol. 386, No. 1, 2012, pp. 366–372.
24. Guo, Y., Baschieri, A., Mollica, F., Valgimigli, L., Cedrowski, J., Litwinienko, G., and Amorati, R. “Hydrogen Atom Transfer from HOO. to Ortho-Quinones Explains the Antioxidant Activity of Polydopamine.” Angewandte Chemie International Edition, Vol. 60, No. 28, 2021, pp. 15220–15224.
25. Ho, C.-C., and Ding, S.-J. “The PH-Controlled Nanoparticles Size of Polydopamine for Anti-Cancer Drug Delivery.” Journal of Materials Science: Materials in Medicine, Vol. 24, 2013, pp. 2381–2390.
26. Liu, Y., Ai, K., Liu, J., Deng, M., He, Y., and Lu, L. “Dopamine-melanin Colloidal Nanospheres: An Efficient Near-infrared Photothermal Therapeutic Agent for in Vivo Cancer Therapy.” Advanced materials, Vol. 25, No. 9, 2013, pp. 1353–1359.
27. Attallah, Ali H., Abdulwahid, F. S., Ali, Y. A., & Haider, A. J. (2024). Enhanced characteristics of iron oxide nanoparticles for efficient pollutant degradation via pulsed laser ablation in liquid. Plasmonics, 1-14..
28. Wei, Q., Zhang, F., Li, J., Li, B., and Zhao, C. “Oxidant-Induced Dopamine Polymerization for Multifunctional Coatings.” Polymer Chemistry, Vol. 1, No. 9, 2010, pp. 1430–1433.
29. Ponzio, F., Barthès, J., Bour, J., Michel, M., Bertani, P., Hemmerlé, J., d’Ischia, M., and Ball, V. “Oxidant Control of Polydopamine Surface Chemistry in Acids: A Mechanism-Based Entry to Superhydrophilic-Superoleophobic Coatings.” Chemistry of Materials, Vol. 28, No. 13, 2016, pp. 4697–4705.
30. Yeroslavsky, G., Richman, M., Dawidowicz, L., and Rahimipour, S. “Sonochemically Produced Polydopamine Nanocapsules with Selective Antimicrobial Activity.” Chemical Communications, Vol. 49, No. 51, 2013, pp. 5721–5723.

31. Ferreira, A. C., Sousa, N., Bessa, J. M., Sousa, J. C., and Marques, F. “Metabolism and Adult Neurogenesis: Towards an Understanding of the Role of Lipocalin-2 and Iron-Related Oxidative Stress.” Neuroscience & Biobehavioral Reviews, Vol. 95, 2018, pp. 73–84.
32. Lee, H., Dellatore, S. M., Miller, W. M., and Messersmith, P. B. “Mussel-Inspired Surface Chemistry for Multifunctional Coatings.” science, Vol. 318, No. 5849, 2007, pp. 426–430.
33. Maier, G. P., Rapp, M. V, Waite, J. H., Israelachvili, J. N., and Butler, A. “Adaptive Synergy between Catechol and Lysine Promotes Wet Adhesion by Surface Salt Displacement.” Science, Vol. 349, No. 6248, 2015, pp. 628–632.
34. Ball, V. “Impedance Spectroscopy and Zeta Potential Titration of Dopa-Melanin Films Produced by Oxidation of Dopamine.” Colloids and Surfaces A: Physicochemical and Engineering Aspects, Vol. 363, Nos. 1–3, 2010, pp. 92–97.
35. Ball, V. “Polydopamine Nanomaterials: Recent Advances in Synthesis Methods and Applications.” Frontiers in bioengineering and biotechnology, Vol. 6, 2018, p. 109.
36. Bain, C. D., Troughton, E. B., Tao, Y. T., Evall, J., Whitesides, G. M., and Nuzzo, R. G. “Formation of Monolayer Films by the Spontaneous Assembly of Organic Thiols from Solution onto Gold.” Journal of the American Chemical Society, Vol. 111, No. 1, 1989, pp. 321–335.
37. Yu, X., Fan, H., Wang, L., and Jin, Z. “Formation of Polydopamine Nanofibers with the Aid of Folic Acid.” Angewandte Chemie International Edition, Vol. 53, No. 46, 2014, pp. 12600–12604.
38. Haider, Adawiya J., Suaad S. Shaker, and Asma H. Mohammed. "A study of morphological, optical and gas sensing properties for pure and Ag doped SnO2 prepared by pulsed laser deposition (PLD)." Energy Procedia 36 (2013): 776-787.
39. Alexiou, C., Jurgons, R., Seliger, C., and Iro, H. “Medical Applications of Magnetic Nanoparticles.” Journal of nanoscience and nanotechnology, Vol. 6, Nos. 9–10, 2006, pp. 2762–2768.
40. Harish, V., Tewari, D., Gaur, M., Yadav, A. B., Swaroop, S., Bechelany, M., and Barhoum, A. “Review on Nanoparticles and Nanostructured Materials: Bioimaging, Biosensing, Drug Delivery, Tissue Engineering, Antimicrobial, and Agro-Food Applications.” Nanomaterials, Vol. 12, No. 3, 2022, p. 457.
41. Flores-Rojas, G. G., López-Saucedo, F., Vera-Graziano, R., Mendizabal, E., and Bucio, E. “Magnetic Nanoparticles for Medical Applications: Updated Review.” Macromol, Vol. 2, No. 3, 2022, pp. 374–390.
42. Haider, A. J., Thamir, A. D., Ahmed, D. S., and Mohammad, M. R. Deposition of Silver Nanoparticles on Multiwalled Carbon Nanotubes by Chemical Reduction Process and Their Antimicrobial Effects. No. 1758, 2016.
43. Taha, B. A., Mashhadany, Y. Al, Al-Jumaily, A. H. J., Zan, M. S. D. Bin, and Arsad, N. “SARS-CoV-2 Morphometry Analysis and Prediction of Real Virus Levels Based on Full Recurrent Neural Network Using Tem Images.” Viruses, Vol. 14, No. 11, 2022, p. 2386.
44. Yousif, A. A., Habubi, N. F., and Haider, A. A. “Nanostructure Zinc Oxide with Cobalt Dopant by PLD for Gas Sensor Applications.” 2012.
45. Sahiner, N., Sagbas, S., Sahiner, M., Blake, D. A., and Reed, W. F. “Polydopamine Particles as Nontoxic, Blood Compatible, Antioxidant and Drug Delivery Materials.” Colloids and Surfaces B: Biointerfaces, Vol. 172, 2018, pp. 618–626.
46. Zhao, J., Gao, J., Xue, W., Di, Z., Xing, H., Lu, Y., and Li, L. “Upconversion Luminescence-Activated DNA Nanodevice for ATP Sensing in Living Cells.” Journal of the American Chemical Society, Vol. 140, No. 2, 2018, pp. 578–581.
47. Bi, D., Zhao, L., Li, H., Guo, Y., Wang, X., and Han, M. “A Comparative Study of Polydopamine Modified and Conventional Chemical Synthesis Method in Doxorubicin Liposomes Form the Aspect of Tumor Targeted Therapy.” International Journal of Pharmaceutics, Vol. 559, 2019, pp. 76–85.
48. Lou, X., Hu, Y., Zhang, H., Liu, J., and Zhao, Y. “Polydopamine Nanoparticles Attenuate Retina Ganglion Cell Degeneration and Restore Visual Function after Optic Nerve Injury.” Journal of Nanobiotechnology, Vol. 19, 2021, pp. 1–15.
49. Abdulwahid, F. S., Haider, A. J., and Al-Musawi, S. “Iron Oxide Nanoparticles (IONPs): Synthesis, Surface Functionalization, and Targeting Drug Delivery Strategies: Mini-Review.” Nano, Vol. 17, No. 11, 2022, p. 2230007.
50. Li, W.-Q., Wang, Z., Hao, S., He, H., Wan, Y., Zhu, C., Sun, L.-P., Cheng, G., and Zheng, S.-Y. “Mitochondria-Targeting Polydopamine Nanoparticles to Deliver Doxorubicin for Overcoming Drug Resistance.” ACS applied materials & interfaces, Vol. 9, No. 20, 2017, pp. 16793–16802.

51. Huang, Z., Li, J., Chen, X., Yang, Q., Zeng, X., Bai, R., and Wang, L. “Photothermal Sensitive 3D Printed Biodegradable Polyester Scaffolds with Polydopamine Coating for Bone Tissue Engineering.” Polymers, Vol. 15, No. 2, 2023, p. 381.
52. Tang, Y., Tan, Y., Lin, K., and Zhu, M. “Research Progress on Polydopamine Nanoparticles for Tissue Engineering.” Frontiers in Chemistry, Vol. 9, 2021, p. 727123.
53. Huang, S., Liang, N., Hu, Y., Zhou, X., and Abidi, N. “Polydopamine-Assisted Surface Modification for Bone Biosubstitutes.” BioMed research international, Vol. 2016, 2016.
54. Wilson, C. J., Clegg, R. E., Leavesley, D. I., and Pearcy, M. J. “Mediation of Biomaterial–Cell Interactions by Adsorbed Proteins: A Review.” Tissue engineering, Vol. 11, Nos. 1–2, 2005, pp. 1–18.
55. Zheng, Z., Li, M., Shi, P., Gao, Y., Ma, J., Li, Y., Huang, L., Yang, Z., and Yang, L. “Polydopamine-Modified Collagen Sponge Scaffold as a Novel Dermal Regeneration Template with Sustained Release of Platelet-Rich Plasma to Accelerate Skin Repair: A One-Step Strategy.” Bioactive Materials, Vol. 6, No. 8, 2021, pp. 2613–2628.
56. Al-Obaidy, R., Hadier, A. J., Al-Musawi, S., and Arsad, N. “Study of the Effects of Solution Types on Concentration of Iron Oxide by Pulsed Laser Ablation in Liquid.” Journal of Applied Sciences and Nanotechnology, Vol. 3, No. 1, 2023, pp. 137–150.
57. Alwan, A. M., Hadier, A. J., & Jabbir, A. A. (2015). Study on morphological and structural properties of silver plating on laser etched silicon. Surface and Coatings Technology, 283, 22-28.
58. Bao, X., Zhao, J., Sun, J., Hu, M., and Yang, X. “Polydopamine Nanoparticles as Efficient Scavengers for Reactive Oxygen Species in Periodontal Disease.” ACS nano, Vol. 12, No. 9, 2018, pp. 8882–8892.
59. Lee, D., Kim, K.-Y., Shim, M. S., Kim, S. Y., Ellisman, M. H., Weinreb, R. N., and Ju, W.-K. “Coenzyme Q10 Ameliorates Oxidative Stress and Prevents Mitochondrial Alteration in Ischemic Retinal Injury.” Apoptosis, Vol. 19, 2014, pp. 603–614.
60. Haider, A. J., Najim, A. A., & Muhi, M. A. (2016). TiO2/Ni composite as antireflection coating for solar cell application. Optics Communications, 370, 263-266.
61. Attallah, Ali H., et al. "Investigate Toxicity and Control Size and Morphological of Iron Oxide Nanoparticles Synthesis by PLAIL Method for Industrial, Environmental, and Medical Applications: A Review." Plasmonics (2024): 1-31.
62. Khalefah, M. M., and Khalifah, A. M. “Determining the Relationship between SARS-CoV-2 Infection, Dopamine, and COVID-19 Complications.” Journal of Taibah University Medical Sciences, Vol. 15, No. 6, 2020, pp. 550–553.
63. Yuki, K., Fujiogi, M., and Koutsogiannaki, S. “COVID-19 Pathophysiology: A Review.” Clinical immunology, Vol. 215, 2020, p. 108427.
64. Wang, L., Wang, Q., Davis, P. B., Volkow, N. D., and Xu, R. “Increased Risk for COVID-19 Breakthrough Infection in Fully Vaccinated Patients with Substance Use Disorders in the United States between December

Study the physical properties of $Se_{65}Sn_{35-x}Te_x$ alloys

Marwa Ayad Abdulmajeed [1, a] Jannah Hasan Azzawi [2, b], Kareem Ali Jasim [1, c]

[1] *Department of Physics, College of Education for Pure Sciences ibn Al-Haitham, University of Baghdad, Baghdad, Iraq*
[2] *Directorate of Education, Diyala, Iraq*

[a)] mohammedcute2018@gmail.com
[b)] Jannah.hasan3@ec.edu.iq
[c)] Corresponding author: kareem.a.j@ihcoedu.uobaghdad.edu.iq

Abstract: In this research, the physical properties of the glass alloy ($Se_{65}Sn_{35-x}Te_x$ alloys) were studied. The alloy samples were prepared by partially replacing Sn with T_e at different concentrations (x=0,5,10,15) with a thickness of 0.25-0.3 mm and a diameter 1.5 cm of using the solid-state reaction method. The samples were measured with a sensitive balance, then they were compressed and melted in ampoules at a temperature of 800 c°. then they were cooled at room temperature and placed in ampoules. The insulating properties represented by imaginary dielectric constant, Tangent loss, real dielectric constant and electrical conductivity were studied as a function of frequency range from 50 Hz to 1 MHz at room temperature and the thermal properties were studied as a function of temperature. the results showed that the partial replacement of Sn with Te plays an important role in changing the insulating and thermal properties of this alloy.

Keywords: concentrations, Insulating, dielectric constant, electrical conductivity, imaginary dielectric constant, thermal properties, important role.

INTRODUCTION

As a result of the development that has occurred in the field of electronic and optics industries in recent years and as a result of studies and research in this field, the development of semiconductor materials has tended to include them in electronic circuits due to their unique properties, the low cost of manufacturing, and the ease of obtaining customized specifications, in addition to the fact that the physical, structural, electrical, and electronic properties can be controlled By changing their chemical composition, conductive materials with high efficiency in electrical conductivity are obtained by adding some impurities and controlling these additions [1].

Many semiconductor materials have different properties that suit specific applications.[2] They can be manufactured in different shapes and sizes and are used in several fields, including solar cells, amplifiers, transistors, electronic circuits and other applications [3].

The dielectric permittivity of semiconductors is low, so they are grafted with impurities to increase the charge carriers and raise the Fermi level, thus increasing their electrical conductivity.[4] Grafting has another effect on its thermal conductivity, as this conductivity can be controlled by controlling these additions.[5] Therefore, the sensitivity of the semiconductors to these factors makes it a materials extremely important in electronic applications.[6] AC electrical conductivity is a measure of the rate of heat that is expected to be generated due to the rotation of the dipoles in their positions or due to the vibration of electrical charges when the electric field changes with time [7].

Therefore, the insulation constant depends on temperature and frequency, so the electric field changes as a result of changing the frequency of the voltage applied to the insulating material [8].

The researchers were interested in studying the thermal conductivity (k) because it is important in identifying the behavior and nature of the thermal behavior of these materials, through which their uses in several fields can be determined.[9] Researchers Fouad Wahid and Kareem Ali studied the thermal and insulating properties of the (HgBa2Ca2Cu3O8+δ) compound, where they found that the thermal conductivity is straight proportional to rise in the compound. The findings demonstrated that as the sample is heated, its conductivity drops, as the conductivity curve decreases to 0.09888 at 553k, the real and imaginary dielectric constant decreases.

The frequency value is applied to the sample [10].

Technologies and Materials for Renewable Energy, Environment and Sustainability
AIP Conf. Proc. 3321, 020010-1–020010-7; https://doi.org/10.1063/5.0289588
Published under an exclusive license by AIP Publishing. 978-0-7354-5231-2/$30.00

The dielectric properties were studied by researchers (N. Shukla, and at all) where it was concluded that the dielectric constant ε', imaginary the dielectric constant ε" decrease with increasing frequency and increasing temperature, as the results showed that ε', ε" has low values at high frequencies.[11]. The thermal properties of epoxy resin were studied by adding aluminum by researchers' thermal conductivity where it was found that compound thermal conductivity increased by increasing the additions, reaching a value of (1.549549 w/ m. k) [12]. The researchers Mohamed Muthana Ghazi, Kareem Ali Jasim, prepared samples of the compound S_{60}-Se_{40-x}-Pb_x and it was concluded that the molecular replacement of selenium with lead has an effect on the insulating properties of the compound. [13]

THE EXPERIMENTAL

Samples of the glassy alloys of ($Se_{65}Sn_{35-x}Te_x$) selenium (Se), tin (Sn) and tellurium (Te) were prepared by quenching technology with high purity (99.999%). weighed according to the ratio of their atomic percentages and proportions of additions (x = 0, 5, 10, 15) using a sensitive electronic balance. Each sample was ground manually for 30 minutes using an agate mortar and with the addition a little of alcohol solution to homogenize the components of the compound. The manually mixed samples are then placed in an electric mixer for 60 minutes to obtain a homogeneous and very fine mixture.
These samples are then placed in an electric furnace at a temperature of 120 c° for drying. Each sample is pressed with a hydraulic press under load of 6 Ton/cm^2 for two minutes. The diameter of each sample ranges from 1.5 cm and its thickness is o.25-30 mm. The samples are placed in completely vacuumed glass ampoules under 10^{-4}Torr to avoid any reaction with oxygen at higher temperature, they are placed in an electric oven at 800 c°. The ampoules are frequently rocked for 20 hours at the highest temperature at rate of 10k/min for melting them homogeneously. They are gradually cooled at the same heating rate to reach room temperature. The glass ampoules are crushed to take out the samples are re-grinded and turned into a fine powder with an agate hand grinder and pressed again with a hydraulic press under the same pressure for two minutes. After that, these samples are placed in ampoules for the purpose of studying the electrical, insulating and thermal properties.

THE THEORY PART

study of insulation properties

Solid materials are classified in terms of their electrical conductivity into three categories:
Insulating materials, semi-conducting materials, and electrically conducting materials. Insulating materials are characterized by the conduction band being devoid of free electrons, therefore an electric current cannot flow through it when the electrical field was applied, because the movement of the electrons cannot exceed a few particles of matter. Although the movement of electrons is limited and there is no flow from the matter, this restricted movement is of great importance in determining the insulating properties of the material [14].
Conductors are considered materials that are good electrical conductors because there is an abundance of free electrons that contribute mainly to the process of electrical conduction. As for semiconductors, they are materials that contain a small percentage of charge carriers and their conductivity can increase with high temperatures.
In this research, the dielectric properties of each sample are measured as a function of frequency by using a device (LCR) by placing it between two wide plates connected to an electrical measuring circuit consisting of a set of coils, an electrical resistance, an ammeter and an alternating power supply, where the dielectric constant and loss factor are measured according to equations 1,2 The applied frequency ranges from 50-50*10^{5}Hz at a temperature of 300-330 K.

$$\varepsilon' = Cd/A\ \varepsilon_o \quad (1)$$

ε_o: free space permittivity (8.85*10-12F/m), d is the thickness of the pellet, C is the capacitance of the sample (Farad), A is the area of the pellet. ε': the real dielectric constant.

$$\varepsilon'' = \varepsilon' \tan \delta \quad (2)$$

where, δ=90º-θ and θ is the phase angle, ε"= constant of imaginary dielectric , tan δ: loss tangent. conductivity is given as

$$\sigma_{ac}(\omega) = \omega\ \varepsilon_o\ \varepsilon'' \quad (3)$$

σ_{ac}: electrical conductivity (a.c), ω is the frequency of an applied signal

$$(\omega)=2\pi f \varepsilon_o \varepsilon' \tan\delta \quad (4)$$

Thermal conductivity

Thermal conductivity describes the materials ability to transformation heat from areas with a high temperature to areas with a low temperature is the property of thermal conductivity and is given by the relationship:

$$q= -k\, T/dx \quad (5)$$

where q=heat flow or heat flux, which is measured in W/m2 per unit time per unit area, k= is thermal-conductivity and measured in W/m. k and dT/dx: change in temperature in thermal conductivity.

Heat is transferred through the molecules of the medium without the molecules of the medium itself being transferred. The process of thermal conduction occurs in all solid materials, but to varying degrees, as heat transfer depends on the nature of the material, as each material has a thermal conductivity that differs from the thermal conductivity of the rest of the materials. Materials are generally classified into three categories in terms of their conduction of heat:

Metals, as they are all good thermal conductors due to the presence of free electrons in very large numbers that contribute to the process of thermal conductivity.

This is because their electrons do not scatter easily and because they have a high speed, so these materials are good thermal conductors. Metals in particular are characterized by their high efficiency in thermal conductivity as well. [15]

As for insulators, they are non-metallic materials that are considered thermal insulators because they lack the presence of large numbers of free electrons. Therefore, phonons are the primary responsible for thermal conductivity in them.

As for semiconductors, they are an intermediate state in thermal conductivity between metals and insulating materials, and their conductivity increases with increasing temperature, such as germanium, silicon and carbon.

To measure thermal conductivity in this research, the sample (S) is placed between 2 copper disk B and disk C, while heater is placed between disks A and B as the figure (1). where heat is prepared from a thermometer device that is equipped with a variable voltage, where the amount is changed and thus the temperature increases gradually.

After calculating the sample's thickness (dA) and radius (r), the values of its thermal conductivity coefficient (K) are computed using the equation [15].

$$KT\left[\frac{(TB-TA)}{dS}\right] = e\left[\left(TA+\frac{2}{r}\right)\left(dA+\frac{1}{4}\right)+ds\left(\left(TA+\frac{2}{r}\right)dsTB\right. \quad (6)$$

dA: are thickness of the sample, TB, TA: are disks temperature A, B , and e: heat loss in (sec/cm2). r: radius of disc and d: thickness of disc.

RESULT AND DISCUSSION

Dielectric properties

In this research, investigate the dielectric properties for samples were prepared for the ($Se_{65}Sn_{35-x}Te_x$) glass alloy with different additions(x=0,5,10,15) in the frequency range 5 to 1 M Hz. the dielectric properties were obtained using an LCR meter testing, where the real dielectric constant (ε') the imaginary dielectric constant(ε"), loss tangent (Tan δ), and electrical conductivity(σ_{ac}) were calculated as a function of frequency at room temperature, as shown in figures 1,2,3,4.

Figure (2) illustrates the relationship between ε' and frequency, were equation (1) has been applied to calculated real dielectric constant ε' and it can be observed that the values of ε' decrease as the frequency increases, the reason is due to mechanisms of polarization and due to changing the concentration of the additives can contribute to reducing the values of ε' [13, 16].

It is clear from figure (2) that the relationship between frequency and ε". Equation (2) was applied to calculate ε", where it was observed that the value of ε" decreased with increasing frequency. decrease of ε" with frequency can be attributed to the fact that the migration of ions in the material and ionic vibration in addition to the movement of charge carriers through the crystal lattice and the absorption of electromagnetic energy within the materials leads to a decrease in the values of ε" [9, 17].

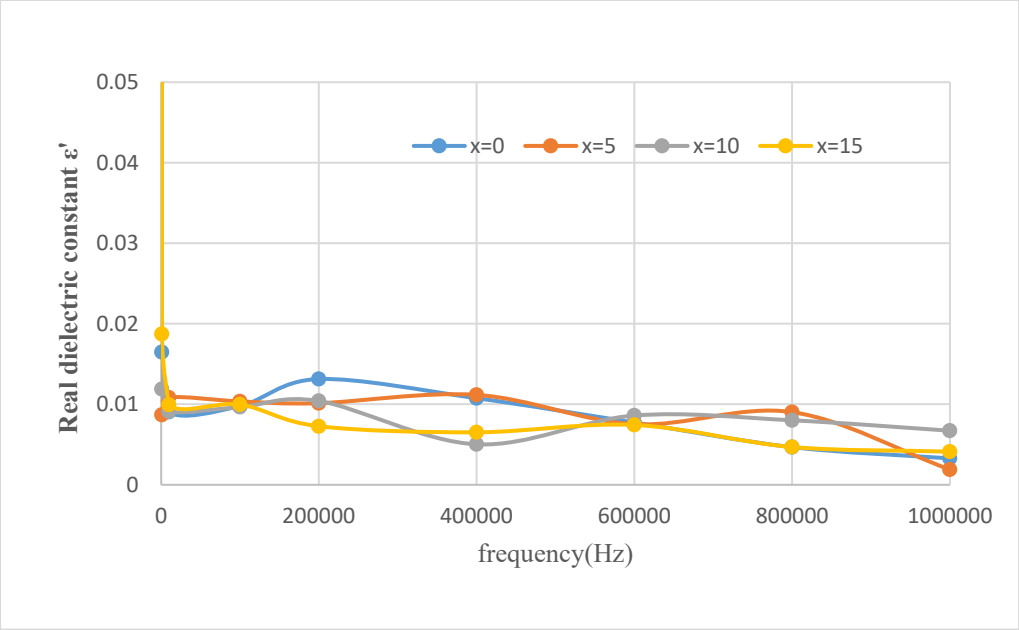

Figure 1: Real dielectric constant (ε') with frequencies changed from 50-1 M Hz

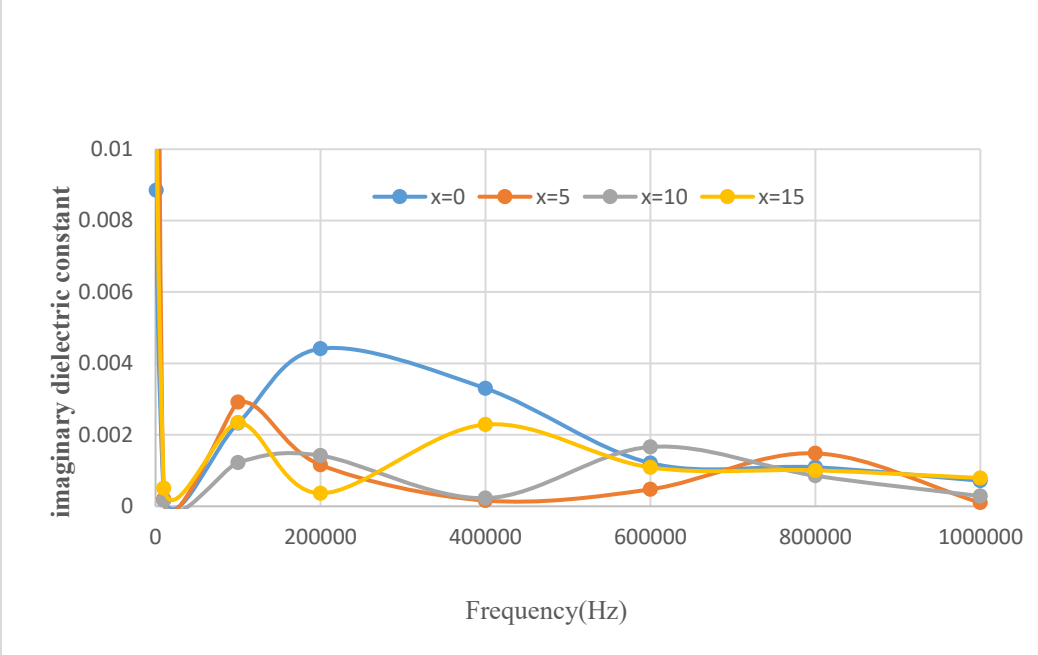

Figure 2: Imaginary dielectric constant ε" with frequencies changed from 50-1M Hz

Figure 3 shows the change and variation in tangent loss values, as a loss was observed in these values with increasing frequency. This is due to the fluctuation of the electric field of the dipoles, which works to increase friction, thermal agitation, and loss of energy. and due to the sample's heterogeneity of the distribution of phases, which is caused by a difference in the distribution of heat oven the sample is inside the furnace during the preparation process [18].

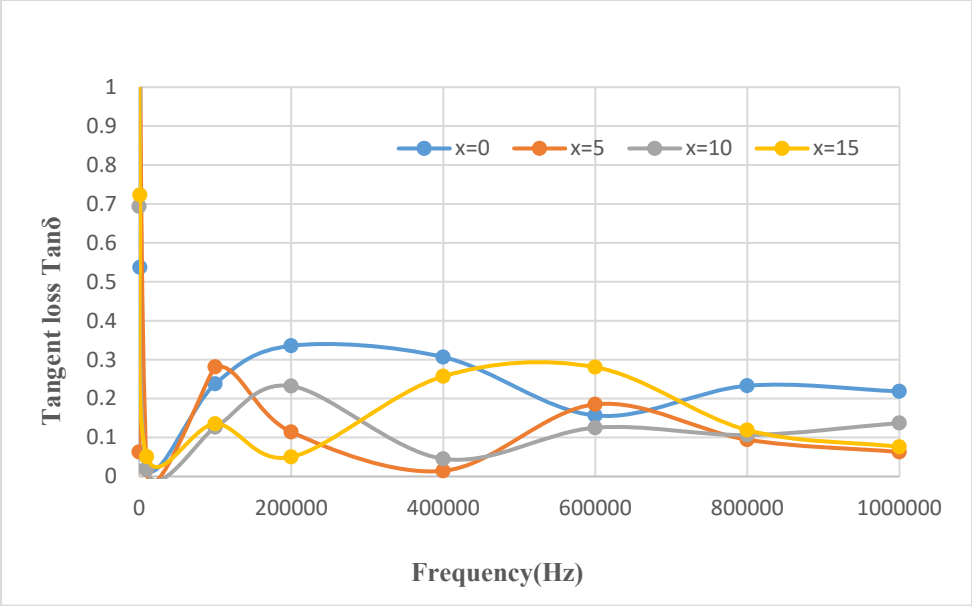

Figure 3: Tangent loss (Tan δ) with frequencies changed from 50-1M Hz

Figure 4 shows the relationship between alternating electrical conductivity and frequency. with applying the equation 4, Where we note the increasing in the alternating electrical conductivity values of the samples with increasing frequency and This increase can also be attributed to the defects present in the samples, as well as due to the nature of the impurities added to the alloy, in addition to the effect of temperature and sintering time of the sample, which leads to a reduction in dissipation energy [19].

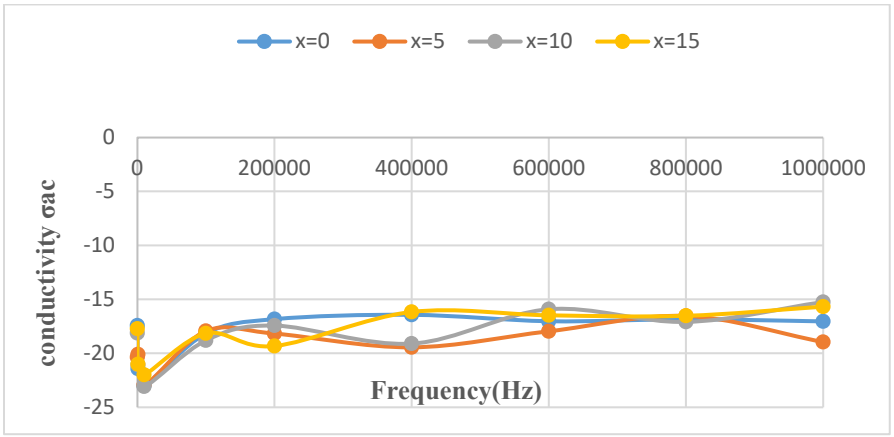

Figure 4: σ_{ac} with frequencies changed from 50-1 M Hz

Thermal conductivity

The result was obtained after measuring the sample thickness (0.3-0.5) mm and radius is 1.5 cm and apply equation (6) through which a thermal conductivity coefficient of the samples which was measured according to concentrations(x=0,5,10,15) at different temperatures, where figure 5 shows association between conduction coefficient thermal conductivity as function of temperature. It was observed that the thermal conductivity coefficient reductions with rising temperature and this behavior can be explained according to the quantity and type of elements contained in the sample, as decreases with increasing Te concentration [20].

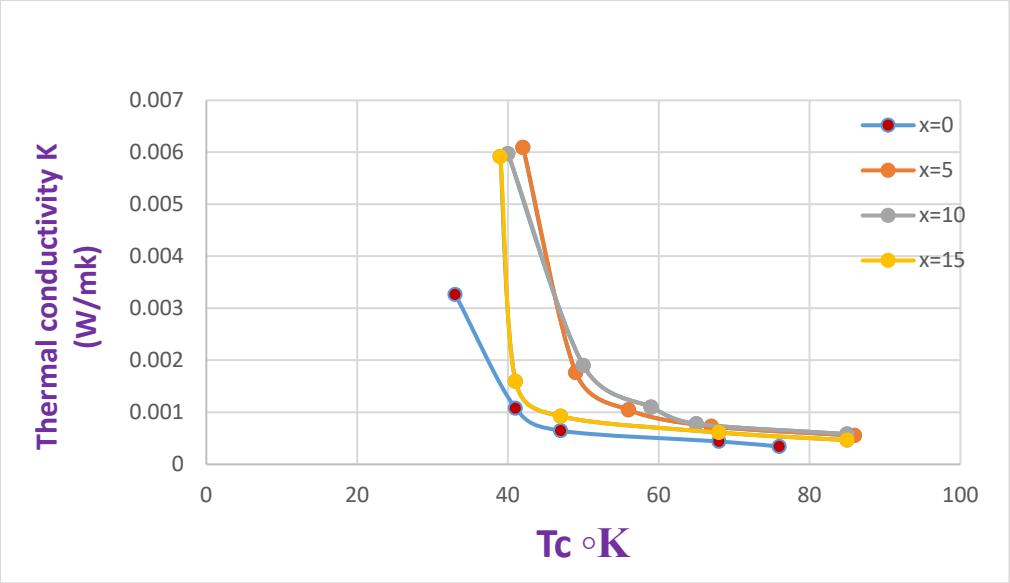

Figure 5: Thermal conductivity VS. temperature for **(**$Se_{65}Sn_{35-x}Te_x$) alloys sample

CONCLUSIONS

In this research, the components of alloy $Se_{65}Sn_{35-x}Te_x$ were prepared with different concentrations of x(x=0,5,10,15) the dielectric properties were measured as function of frequency including the real and imaginary dielectric constant, the loss tangent and AC electrical conductivity. It was found that the partial replacement of Te with tin varies these properties. Thermal conductivity measurements show that k increases with increasing temperatures.

REFERENCES

1. Abdulateef, Aqeel N., Kassem w., Kareem A. Jasim, Calculating the Mechanisms of Electrical Conductivity and Energy Density of States for Se85Te10Sn5-xInx Glasses Materials. *Journal of Green Engineering (JGE)*, 2020, 10.9: 5487-5503.
2. Arkhipov, V. I., et al. Effect of doping on the density-of-states distribution and carrier hopping in disordered organic semiconductors. Physical Review B—Condensed Matter and Materials Physics, 2005, 71.4: 045214.
3. RAM, Indra Sen, et al. Effect of Pb addition on dielectric relaxation in Se80In20 glassy system. Journal of alloys and compounds, 2013, 552: 480-485.
4. Azzawi, J. H., Ahmed, B. A., Jasim, K. A., & Salman, E. M., Calculation of the localized and extended energy states density for Ge60Se40-xTex alloy prepared by melting point method. Chalcogenide Letters, 2023, 20.9: 649-656.https://doi.org/10.15251/cl.2023.209.649.
5. Petkov, P., Ilcheva, V., Petkova, T., Ilchev, P., Angelopoulos, A., & Fildisis, T., Thermal Studies of Ge-Te-Ga Glasses. In: AIP Conference Proceedings. American Institute of Physics, 2010. p. 932-937.
6. Mehra, R., Arora, M., Mathur, P., & Kumar, H.. Electrical transport properties of as evaporated and annealed amorphous GexSe1− x thin films. Materials chemistry and physics, 1987, 17.4: 343-356.
7. Salmon, Philip S. Structure of liquids and gasses in the Ge–Se binary system. Journal of Non-Crystalline Solids, 2007, 353.32-40: 2959-2974.
8. Tanaka, Keiji. Structural phase transitions in chalcogenide glasses. Physical Review B, 1989, 39.2: 1270.
9. Omar, B.A., Fathi, S.J., Jassim, K.A., Effect of Zn on the structural and electrical properties of high temperature HgBa2Ca2Cu3O8+δ superconductor, AIP Conference Proceedings, 2018, 1968, 030047.
10. Bekheet, A. E., Afifi, M. A., Hegab, N. A., Wahab, L. A., & Shehata, H. A. (2007). The effect of cd addition on the optical properties of Se70Te30 films. Journal of Physics: Condensed Matter, 19(49), 496218. https://doi.org/10.1088/0953-8984/19/49/496218.
11. Ali, Fouad Waheed; JASIM, Kareem Ali. Study of the structural, electrical, thermal and dielectric properties of HgBa2Ca2Cu3O8+ δ superconducting. In: AIP Conference Proceedings. AIP Publishing, 2023.
12. Shukla, N.; Kumar, V.; Dwivedi, D. K. Dependence of dielectric parameters and AC conductivity on frequency and temperature in bulk Se90Cd8In2 glassy alloy. J. Non-Oxide Glasses, 2016, 8.2: 47-57.

13. Jasim, Kareem A.; FADHIL, Rihab N. The Effects of micro-aluminum fillers In Epoxy resin on the thermal conductivity. In: Journal of Physics: Conference Series. IOP Publishing, 2018. p. 012082.
14. Chillab, R.K., Jahil, S.S., Wadi, K.M., Jasim, K.A., Shaban, A. H., Fabrication of Ge30Te 70-xSbx glasses alloys and studying the effect of partial substitution on d.C electrical energy parameters, Key Engineering Materials, 2021, 900, pp. 163–171. https://doi.org/10.4028/www.scientific.net/kem.900.163.
15. Mahdi, S.H., Jassim, W.H., Hamad, I.A., Jasima, K. A., Epoxy/Silicone Rubber Blends for Voltage Insulators and Capacitors Applications, Energy Procedia, 2017, 119, pp. 501–506.
16. Ghazi, Mohamed Muthana, Jasim Kareem Ali. A study of the Electrical and Dialectical proprieties of S60-Se40-X-PbX Chalcogenide Compound. In: Journal of Physics: Conference Series. IOP Publishing, 2024. p. 012027.
17. Haider Haider MJ; Jasim Kareem A. Effect of Composition and Dielectric Properties for (YBCO) superconductor compound in different preparation methods. Ibn AL-Haitham Journal For Pure and Applied Sciences, 2020, 33.1: 17-30.
18. Amin, M., Afriyanti, F., & Putra, N. (2018). Thermal properties of paraffin-based nano-phase change material as thermal energy storage. IOP Conference Series: Earth and Environmental Science, 105, 012028. https://doi.org/10.1088/1755-1315/105/1/012028.
19. Wadi, K.M., Jasim, K.A., Shaban, A.H., Kamil, M.K., Nsaif, F.K., The effects of sustainable manufacturing pressure on the structural properties of the pb2ba2ca2cu3o9+σ compound, Journal of Green Engineering, 2020, 10(9), pp. 6052–6062.
20. Jasim, K.A., The effect of cadmium substitution on the superconducting properties of Tl1-x Cd x Ba2Ca2Cu 3O9-δ compound, Journal of Superconductivity and Novel Magnetism, 2013, 26(3), pp. 549–552.

Morphological and Mechanical Properties of Pure Nanocomposite PMMA/ZnO/MgO for Teeth-Filling Applications

Abbas F. Khorsheed[1,a], Adnan R. Ahmad[1], Alaa J. Ghazai[2]

[1] *Department of Physics, College of Education for pure science, Tikrit University, Tikrit, Iraq*
[2] *Department of Physics, College of Science, Al-Nahrain University, Baghdad, Iraq*

[a)] Corresponding author: eabaas.f.khurshid@st.tu.edu.iq

Abstract. This work effectively synthesized pure nanocomposite (70% ZnO/30% MgO) and mixed it with PMMA at weight concentrations of 2%, 4%, 6% and 8%. The as-prepared 70% ZnO/30% MgO nanocomposite's morphologies, composition, and purity were assessed using atomic force microscopy (AFM), field emission scanning electron microscopy (FESEM), energy dispersive X-ray (EDX), and X-ray diffraction (XRD) studies. Furthermore, the mechanical properties of pure PMMA and Zno/Mgo, with PMMA at weight concentrations of 2%, 4%, 6% and 8%, have been characterized by X-ray diffraction (XRD) examinations of the PMMA/ZnO/MgO nanocomposite. The MgO powder may have been efficiently integrated at the centre of the ZnO particles because the single-phase XRD pattern of the MgO/ZnO NC sample resembled all planes of the ZnO sample with the same hexagonal wurtzite structure. Moreover, flat and dumbbell-shaped morphologies were seen in many spherical morphologies with an average particle size of 88 nm. Moreover, the surface morphology is covered by randomly distributed islands with the addition of MgO content. The surface roughness increases from 66.3 nm to 77 nm, improving the microstructure and crystalline quality of the 70%ZnO/30%MgO composite. Additionally, it demonstrates how adding ZnO/MgO nanoparticle powders as reinforcement particles to PMMA affects the tensile strength under study, which is reduced with continued ZnO/MgO addition. It may be argued that adding ZnO/MgO nanopowders was essential for giving the nanocomposite high adhesion. ZnO/MgO can also be used to enhance significantly mechanical qualities

INTRODUCTION

PMMA is a popular biomaterial for dental applications because of its unique traits. It includes low density, appealing appearance, affordability, ease of manipulation, and customizable mechanical and physical attributes. However, because of water sorption, insufficient impact, and flexural strength, it also causes severe denture breakage. Numerous researchers have developed various measures to address these issues and improve the mechanical and physical qualities of PMMA materials. Several types of fibers are used to reinforce them [1,2]: nanoparticles [3,4] and nanotubes [5], among which are metals and ceramics [6]. These investigations revealed that the addition of particles enhanced the denture base's mechanical characteristics [7] and thermal conductivity, enabling a more accurate assessment of food temperature [8,9], dimensional stability [10], and antibacterial activity [11]. They decreased PMMA solubility and water sorption [12]. When employed in such materials, nanoparticles have several benefits because of their unique characteristics, which include their high surface area and excellent distribution. Additionally, the characteristics of nanoparticles (morphology, loading, and kind) impact the ultimate characteristics of reinforced PMMA [13]. Adding nanoparticles enhances the thermal conductivity. The results of different hybrid reinforcement combinations were encouraging, but more research is needed to further investigate different materials and combinations to enhance PMMA materials' capabilities. PMMA has certain benefits over other materials, including less toxicity of ZnO NPs, a white look, and the capacity to reinforce composite resin [14]. The MgO NPs enhance mechanical characteristics and promote bone regeneration in vitro and in vivo. Dental cements made of MgO-based nanocomposites have been employed in the past. It is well known that they possess antibacterial, antibiofilm, and

Technologies and Materials for Renewable Energy, Environment and Sustainability
AIP Conf. Proc. 3321, 020011-1–020011-12; https://doi.org/10.1063/5.0291598
Published under an exclusive license by AIP Publishing. 978-0-7354-5231-2/$30.00

antimicrobial properties against microorganisms responsible for endodontic and cariogenic diseases [15]. The current investigation aims to learn more about the mechanical characteristics of ZnO/MgO nanocomposite NPs in PMMA.

MATERIAL AND METHODS

We acquired 99.99 % pure zinc oxide (ZnO) and magnesium oxide (MgO) from Sigma-Aldrich. A hydraulic press with a 4-tone pressure compressed 70 weights percenr ZnO and 30 weight% MgO. It was then sintered to create a pellet with a diameter of 1 cm and a height of 2 mm in an oven at 900° C for two hours. The characterization has been examined, including XRD, SEM, EDS, and AFM of pure ZnO and MgO composes. Then, the sample was ground to obtain a homogeneous powder to make the requirement tester by mixing ZnO/MgO nanocomposite with PMMA. Nanofillers powder of ZnO/MgO of weight concentration 2wt%, 4%, 6% and 8% have been added to the monomer. Each parentage is mixed with monomer by magnetic stirring for one hour, followed by ultra-sonication in a cold-water bath for 30 minutes to prevent excessive liquid heating. The monomer with nanofillers was suspended with acrylic powder for fifteen minutes to achieve a manageable dough-like consistency and lessen the likelihood of particle aggregation and phase separation. Then, cast in the centre of a mould according to standard conditions, and place the mould in a hot water bath for an hour to make the surface hard, as shown in Figure 1. The weight concentration of mixed materials used in this work has been listed in Table 1

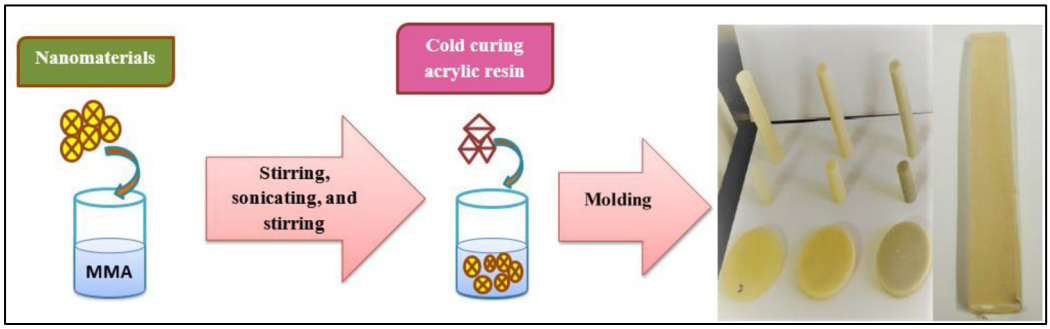

FIGURE 1. Fabrication process of nanomaterial-enhanced acrylic composites, illustrating the stages from nanomaterial dispersion in MMA, through stirring and sonication, to molding and curing of the final shapes

Table 1. Nanocomposites prepared with different contents of ZnO: MgO

Samples	PMMA (wt.%)	ZnO: MgO (wt.%)
PMMA	1	0
PMMA/ZnO: MgO 2%	0.98	0.02
PMMA/ZnO: MgO 4%	0.96	0.04
PMMA/ZnO: MgO 6%	0.94	0.06
PMMA/ZnO: MgO 8%	0.92	0.08

Plastic Patterns Preparation

As seen in Figure 2, three distinct plastic patterns were created by employing a laser cutting machine to cut plastic plates into the required test's shape and dimensions:

A. A test of transverse flexural strength using a rectangular specimen with dimensions of 65 mm by 10 mm by 2.5± 0.1 mm, following ADA specification No.12, 1999, for denture base polymers. The identical form and dimensions were used to generate the samples of surface hardness and roughness.

B. Compressive strength test: An ASTM-D-695-compliant block with dimensions of 5 mm in length, 5 mm in width, and 10 mm in height serves as the sample for the compressive strength test.
C. Thermal conductivity test: Per the instrument's specifications, the sample for the thermal conductivity test is a disc that is 40 mm in diameter and 2.5 mm in thickness.

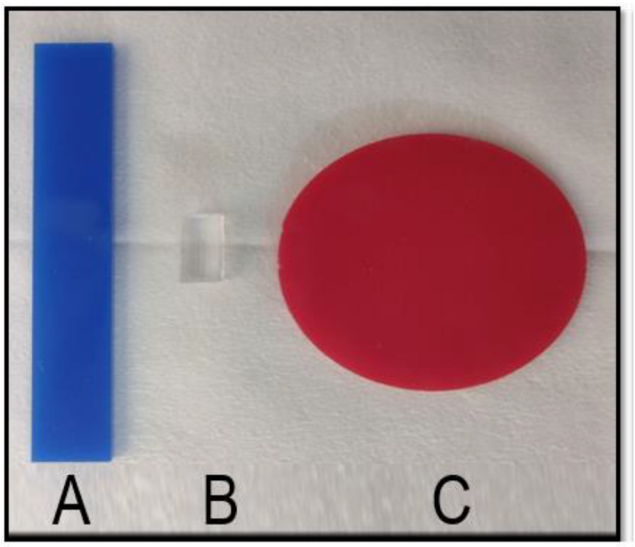

Figure 2. A plastic pattern used for A-Transverse Strength, Surface Roughness, Surface Hardness; B-Compressive Strength; C-Thermal Conductivity

Characterization of ZnO/MgO nanocomposite

First, field emission scanning electron microscopy (FESEM) and X-ray diffraction (XRD) measurements were used to characterize the morphologies of the as-prepared nanocomposite 70% ZnO/30% MgO. The composition and purity of the as-prepared nanocomposite materials are examined using an atomic force microscope (AFM) and energy-dispersive X-ray (EDX). The second is the X-ray diffraction (XRD) measurement and the mechanical and thermal conductivity properties of ZnO/MgO at 70/30 weight percent mixing with PMMA at weight concentrations of 2%, 4%, 6% and 8%.

RESULTS AND DISCUSSION

X-Ray Diffraction Analysis Pure ZnO and ZnO/MgO Nanocomposite

A successful synthesis depends on a good match between the produced and standard peaks. X-ray diffractograms help study the structural analyses of NPs and NCs. Figure 3 shows XRD potter of pure ZnO-NPs and 70/30 wt.% of ZnO/MgO respectively revealed several peaks at 2θ= 31.8°, 34.44°, 36°, 47.56°, 56.6°, 62.9°, 66°, 68.34° and 69.68° for pure ZnO-NPs which corresponds to orientation (100), (002), (101), (102), (110), (103), (200), (112) and (201). It has been determined that the hexagonal segment of ZnO-NPs, which matched to (JCPDS file No. 89-1397), causes the observable peaks [16, 17]. Some weak peaks may be caused by residuals from the synthesis process. The XRD pattern showed no signs of additional solid peaks. Figure 3 shows the XRD pattern of for nanocomposite of concentration of 70%ZnO/ 30%MgO; new peaks were detected at 2Θ= 43° diffraction pattern, which revealed some peaks; however, they belong to MgO (JCPDS: 89-7746) [18, 19]. All planes of the ZnO sample with the same hexagonal wurtzite structure are identical to the single-phase XRD pattern of the MgO/ZnO NC sample, indicating that MgO powder was successfully integrated at the core of ZnO particles. The other metals in the composite sample attenuate the MgO and ZnO phases' peak intensity. The confirmation of the loss of crystalline nature or the absence

of crystalline character due to lattice faults is once again provided by the shift in the theta angle to the lower value. Zn ions within MgO or an improved ZnO periodic crystal lattice create negligible strain. Therefore, the change in the lattice causes a change in the crystal's regularity [20]. The literature has already shown how adding dopant elements modify the lattice characteristics of the host materials. This is brought on by their differences in atomic radii [21, 22]. The preferred diffraction peaks of pure ZnO and ZnO/MgO Nanocomposite of 70/30 wt % were at 2Θ = 36.32 and 36,4, respectively.

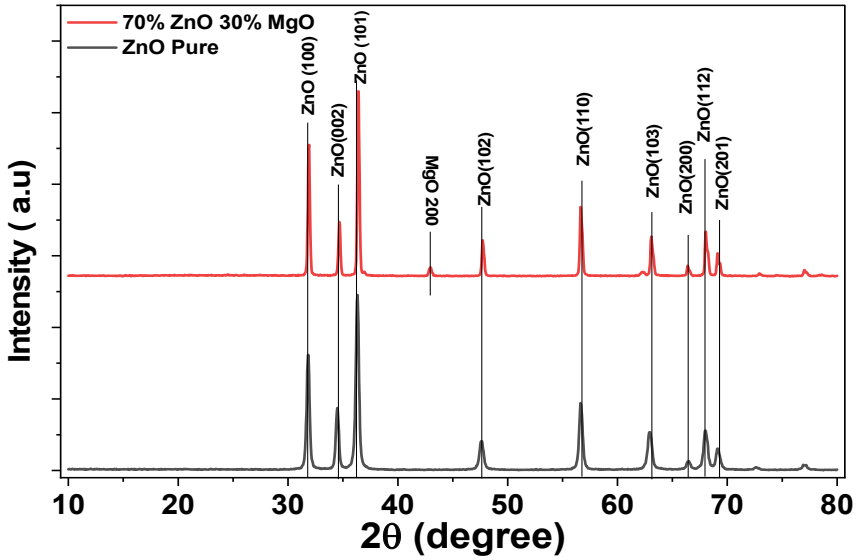

Figure 3. XRD analysis for pure ZnO and 70%ZnO/30%MgO

Composites with various types and fraction fillers were created using the blending technique outlined in the experimental section. Figure 4 shows the XRD patterns of PMMA-ZnO@MgO composited with various ZnO@MgO weight fractions. Given that PMMA is an amorphous polymer, no distinct diffraction peaks can be seen. Diffraction peaks from ZnO/MgO and the curve bread from PMMA can be seen in the XRD patterns of the composites. The steady decrease in the X-ray diffraction peak curve width with increasing ZnO/MgO content indicates that ZnO/MgO exerts a dominant influence on the nanocomposites' crystallization behaviour.

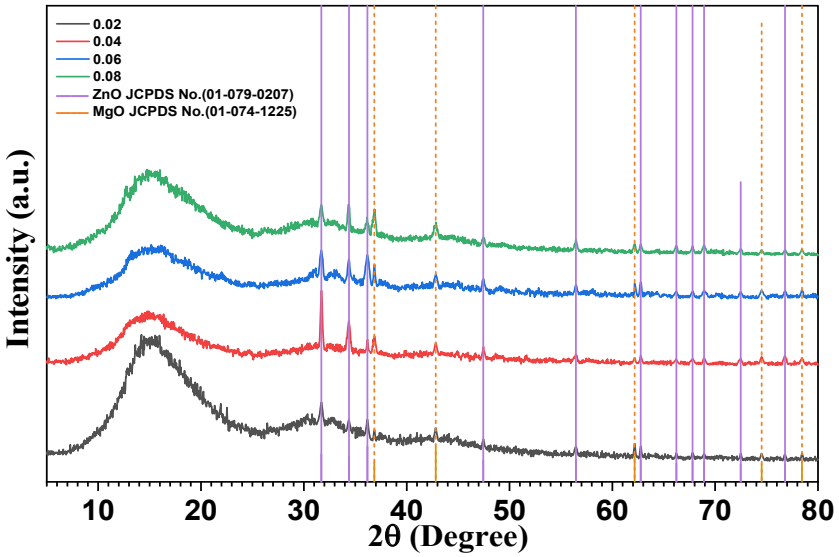

Figure 4. XRD analysis for PMMA/ZnO: MgO

Field Emission Scanning Electron Microscopy (FE-SEM) and (EDS)

Figures 5 and 6 show an FE-SEM image of pure ZnO and ZnO/MgO with 70/30 wt % nanocomposite, which the Fig revealed that ZnO nanoparticles (NPs) had an average particle size of 88 nm and a morphology that is primarily flat and dumbbell-shaped-Figure 5. The cause of some larger particles may be related to the temperature and incubation period. The ZnO NPs are clumped and agglomerated.

Various-sized dumbbell-shaped morphological particles are also observed. The smaller-sized average particle size is 200 nm Figure 6. Combining the two oxide morphologies with a few Mg-Zn alloys produced the observed morphology.

It is well known that at annealing temperatures of more than 800 °C, ZnO and MgO may combine to create MgZnO compounds [23]. The observed form is associated with ZnO's hexagonal crystal habit and the triangular plane's crystal habit of MgO. Atomic unit deposition explains the development of a dense structure.

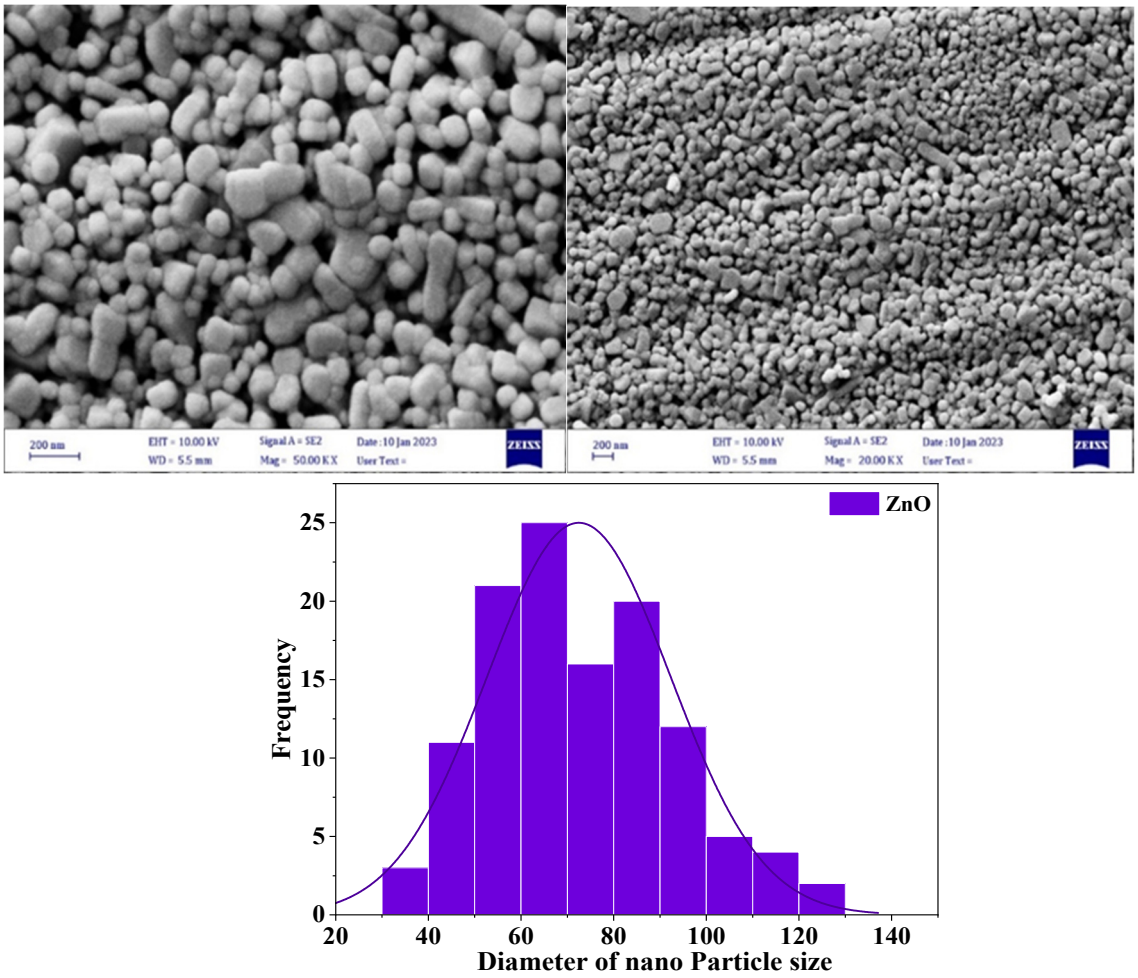

Figure 5. FE-SEM analysis for pure ZnO**.**

Figure 7 shows the 70% ZnO/30% MgO EDS spectra and Tables. Their weight percentages for the Zn, O, and Mg peaks are 73.7, 13.5 and 12.8, correspondingly. The presence of a Mg signal in the EDS spectra of ZnO/MgO NCs suggests that MgO has been well integrated into the core of ZnO NPs, which supports the formation of a core-shell structure.

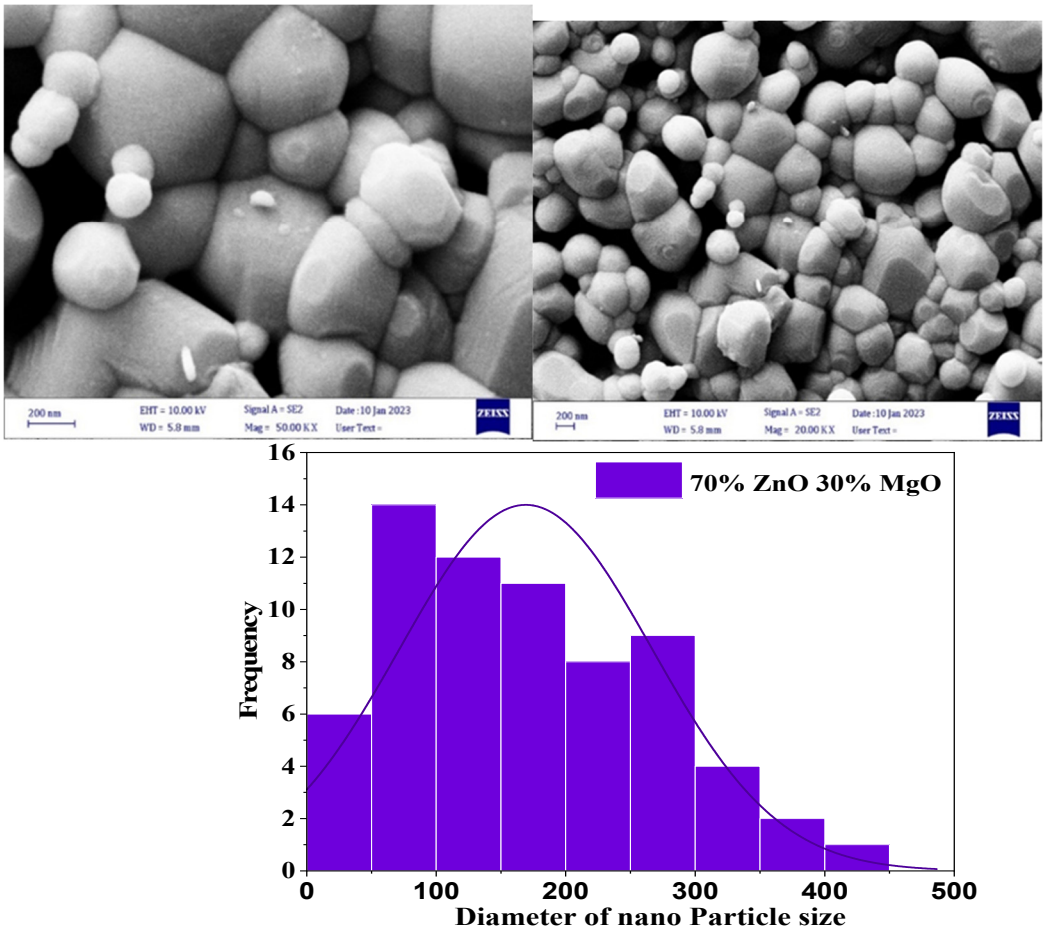

Figure 6. FE-SEM analysis for 70%ZnO/30%MgO

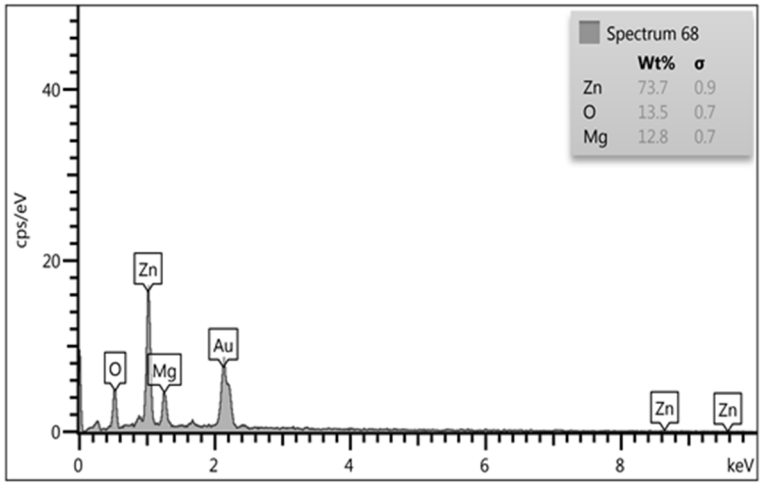

Figure 7. EDS analysis for 70%ZnO/30%MgO

Topography Analyses

Figures 8 and 9 Show AFM images of pure ZnO and ZnO/MgO pellets, respectively. Randomly distributed islands cover the surface morphology by adding MgO content, increasing the surface RMS and roughness from 66.3 nm to

77nm. The above results show an improvement in the microstructure and the crystalline quality of the 70%ZnO/30%MgO composite. The observed fluctuations in the size of crystal grains indicate that the development mechanism is influenced by the MgO component of the ZnO-MgO mixed materials [24]. The most notable feature was that the ZnO MgO morphologies were not hexagonal but had flat, triangular ends. This suggests that the introduction of magnesium into the ZnO lattice could be the origin of this phenomenon, which is consistent with [25].

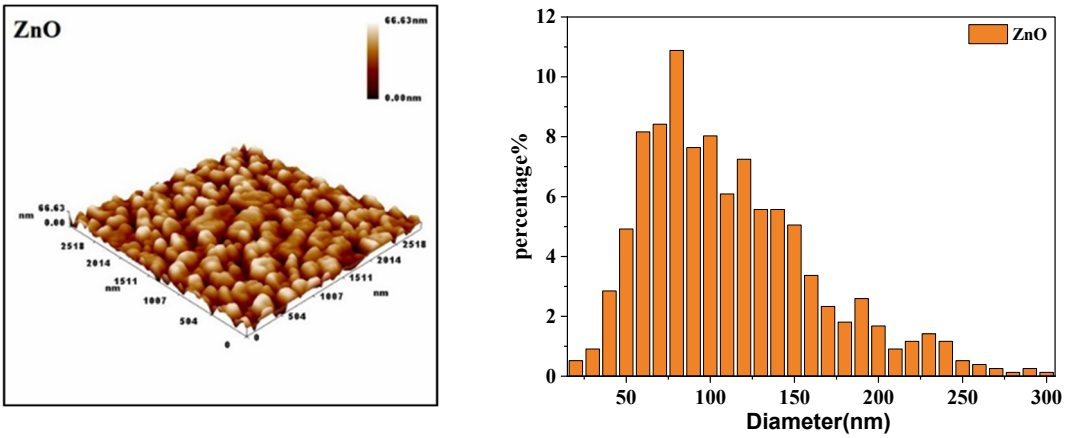

Fig.8. Atomic force microscopy (AFM) analysis for pure ZnO.

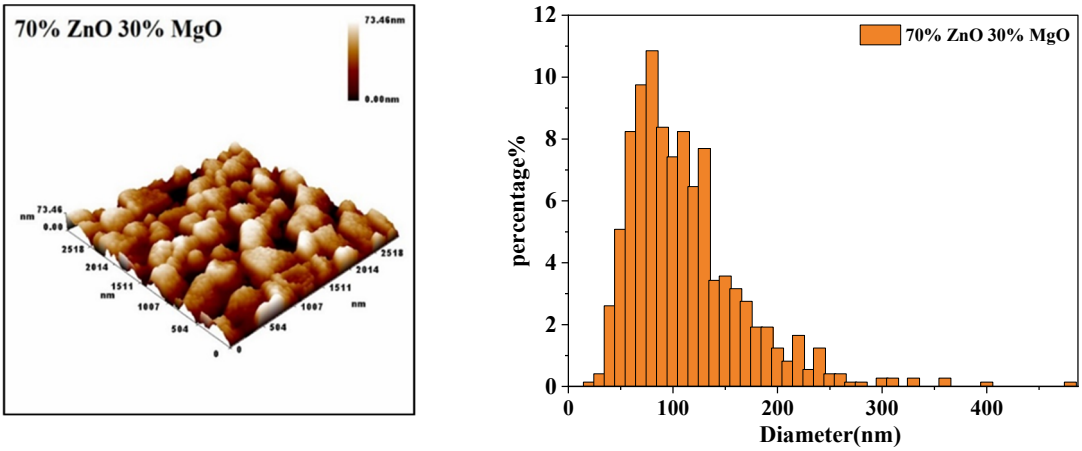

Figure 9. Atomic force microscopy (AFM) analysis for 70%ZnO/30%MgO.

Figure 10 shows the influence of concentrations inserted of ZnO/MgO (2,4,6, and 8) wt% into PMMA nanocomposite on the roughness. It was revealed that the roughness increased with the increase in ZnO/MgO. Maintaining the filling's strength, durability, and stability increases roughness because more molecules are in the same space.

This causes the molecules to lose energy in sufficient amounts to form molecular agglomerations, which rise to the surface as small granules and begin to grow as scars or meanders. It may be considered that these surfaces do not provide any risk of plaque formation since the beginning point of bacterial plaque accumulation and the threat of caries and periodontal infections should be less than (200) nm [26].

The presence of impurities enhances dental adhesion and the durability of packing; this occurs when nano-oxides are introduced, leading to the formation of agglomerates. However, an increase in impurities is associated with a rise in roughness and average grain size. A uniform distribution of molecules within the material is crucial for improved properties that enhance the polymer's strength and toughness and to aid in better stacking. Adding more nano-oxides facilitates this by improving the crystal structure [27].

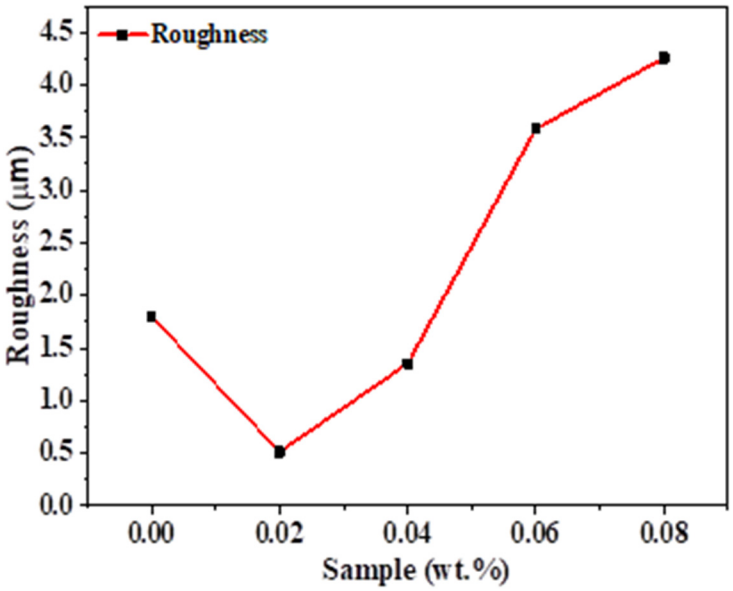

Figure 10. Roughness for pure PMMA and PMMA with (2, 4, 6, and 8) wt.% of ZnO: MgO

Figure 11 Shows the influence of concentrations inserted of ZnO/MgO (2%,4%,6%, and 8% wt%) into PMMA nanocomposite on the compression test. High-yield brittle composites have different behaviour than low-yield ductile polymers. Including additives increases the elastic modulus and ultimate stress because the nanoparticles shut the interfaces between the composite and fill the pores.

Thus, they change the material's behaviour from polymer-like to more substantial due to density. This explains why the polymer PMMA behaves differently depending on the weight ratio after loading with ZnO/MgO nanoparticles. Consequently, Young's modulus increases noticeably.

Polymers have a low youthful elasticity due to their limited number of interatomic bonds.Nanoparticles considerably changed the elasticity of juveniles because the type and quantity of NPs utilized directly affect their mechanical properties, including interfacial adhesion and elastic modulus. An increase in the number of nanoparticles caused the composite to lose its elasticity and become brittle.

At lower concentrations of the filler ZnO/MgO particles, the PMMA matrix's increased compression strength may result from a combination of factors. They included uniform dispersion of the nanoparticles in the polymer matrix (caused by intense microturbulence created by ultrasound), interfacial solid interaction, adhesion between phases (perhaps via H bonds), and an increase in the material's crystallinity.

The limit of moving scale of the PMMA matrix chain segments with the addition of ZnO/MgO may also cause the nanocomposite's increased compression strength, as noted by [28]. They have also observed that the confinement of polymer chains and specific polymer–surface interactions affect the dynamics of polymer chains.

The local and global conformations of the polymers within host galleries of nanoparticles differ significantly from those in bulk or neat polymers. A decrease in compression strength for increased ZnO/MgO loading may be due to non-uniform ZnO/MgO particle distribution and agglomeration/segregation in the polymer matrix, Resulting in the matrix and a decrease in compression strength. As mentioned by [29], a higher ZnO/MgO nanoparticle concentration in a polymer matrix might cause flaws in the nanocomposites that lower the compression strength by reducing the interfacial contact area [28].

It is observed that in a matrix containing a concentration of nanofiller particles, the stress field is focused on the aggregate, leading to the easy and quick propagation of cracks and consequent early failure. Elastic modulus: An explanation along the same lines as the previously mentioned trends in compression strength might be provided for these trends in elastic modulus.

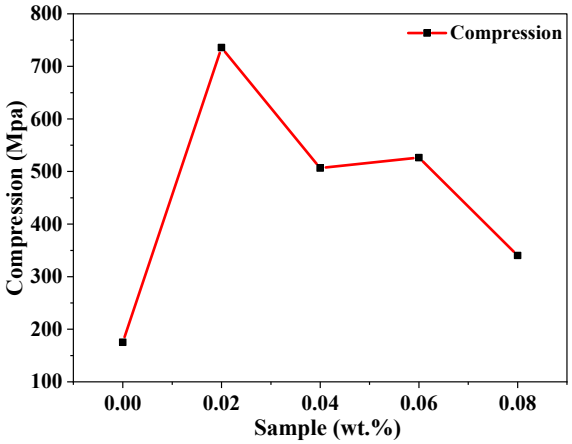

Figure 11. Compression test for PMMA with (2, 4, 6, and 8) wt.% of ZnO: MgO

Figure 12 ’illustrates how adding ZnO/MgO nanoparticle powder as reinforcement particles to PMMA affects the tensile strength. With the continual addition of ZnO/MgO, tensile strength was reduced. You might contend that adding ZnO/MgO nanopowders was crucial to give the nanocomposite strong adhesion, which can improve the material's mechanical properties.

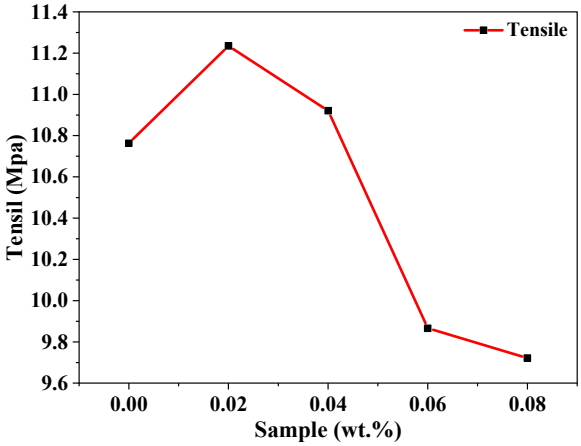

Figure 12. Tensile test for PMMA with (2, 4, 6, and 8) wt.% of ZnO: MgO

Figure 13 shows shore D hardness was performed hardness values of the samples PMMA/ZnO/MgO samples composites, and the value decreases when adding Nano Zno Nano MgO increases. The human body's hardest dental crown above the gum tissue is enamel tissue, which is almost entirely waterless. Enamel covers the entire anatomy, comes into contact with food while being chewed and protects the dentin by comparing hardness values [30]. Enamel has a hardness range of 72 to 82, whereas dentin ranges from 50 to 60. As a result, it is possible to obtain high-quality samples of a nanocomposite material that will be utilized to create or fill the enamel layer of artificial teeth. A minor increase in particle filler content led to a rise in hardness; an increase in particle filler content led to a loss in hardness, as seen in ‘Figure 13 ’.This is because a higher concentration of complex and brittle ZnO/MgO nanoparticles stiffened the matrix material's elasticity and enhanced the material's resistance to surface indentations. A composite including nanoparticles with a higher hardness is associated with better binding. It is important to remember that a smaller filler size will enhance the filler's dispersion inside the polymer, strengthening the bond between the filler and polymer at the interfacial area. These findings demonstrated how significantly nanoparticle additions impact the mechanical characteristics of polymer composites.

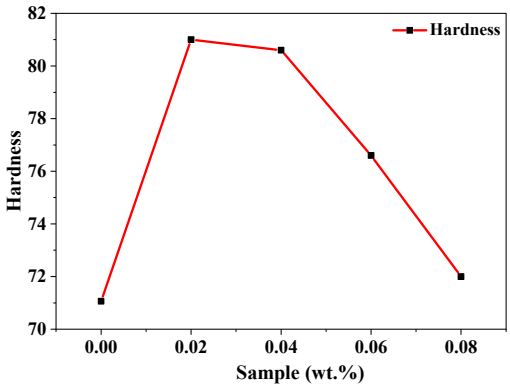

Figure 13. Hardness test for pure PMMA and PMMA with (2, 4, 6, and 8) wt.% of ZnO: MgO.

The impact strength was noted for each of the specimens in 'Figure 14'. Because the Van der Waals bonds in the polymer are weak, the impact strength test's effect of stress results in cracking in the polymer surface. The polymer was strengthened for stress resistance by the addition of nanoparticles. The impact strength rose due to the nanoparticle enforcement's enhanced absorbed energy [31]. The impact strength of the PMMA/ZnO/MgO specimens on fracture energy increased with the addition of Nano ZnO/MgO. So, the optimum fracture energy value is obtained at 6% of ZnO/MgO, which leads to a reduction in fracture energy. This behaviour demonstrated that the material brittleness occurs at 8% ZnO/MgO, a high filler concentration.

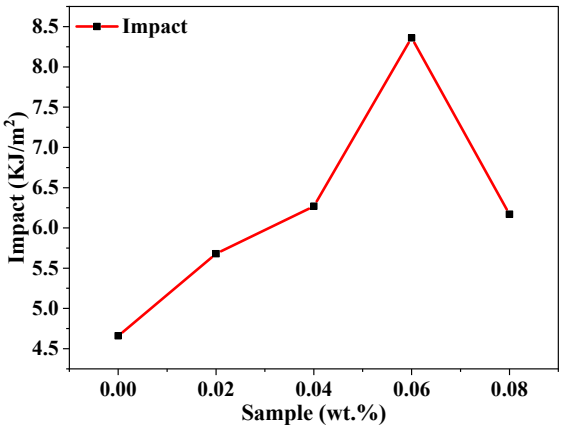

Figure 14. Impact strength for pure PMMA and PMMA with (2, 4, 6, and 8) wt.% of ZnO: MgO.

CONCLUSION

The results of this study include (70% Zinc oxide and 30% magnesium oxide) mixed by weight ratios (2, 4, 6, and 8) wt.% as reinforcement Nanopowders to poly methyl methacrylate polymer. The higher dispersion and homogeneity of microparticles may improve the mechanical properties of modified acrylic resin (PMMA-NP nanocomposite). The mechanical properties of the material were found with promising results. It can also be used to manufacture dental prosthetics or fillers for the enamel layer. It is advised that more research be done to examine the effectiveness of these NPs in mixing with PMMA.

REFERENCES

1. Chang, Min-Chieh, et al. "Effects of pontic span and fibre reinforcement on fracture strength of multi-unit provisional fixed partial dentures." Journal of Dental Sciences 14.3 (2019): 309-317.
2. Al-Thobity, Ahmad M. "The impact of polymerization technique and glass-fibre reinforcement on the flexural properties of denture base resin material." European Journal of Dentistry 14.01 (2020): 092-099.
3. Aldabib, Jamal Moammar, and Zainal Arifin Mohd Ishak. "Effect of hydroxyapatite filler concentration on mechanical properties of poly (methyl methacrylate) denture base." SN Applied Sciences 2.4 (2020): 732.
4. Alamgir, Md, et al. "Development of PMMA/TiO 2 nanocomposites as excellent dental materials." Journal of Mechanical Science and Technology 33 (2019): 4755-4760.
5. Wang, Russell, Ramazan Kayacan, and Cenker Küçükeşmen. "Nanotubes/polymethyl methacrylate composite resins as denture base materials." Carbon nanomaterials for biomedical applications (2016): 227-240.
6. Raszewski, Zbigniew, et al. "Influence of silanized silica and silanized feldspar addition on the mechanical behavior of polymethyl methacrylate resin denture teeth." The Journal of Prosthetic Dentistry 123.4 (2020): 647-e1.
7. Balos, Sebastian, et al. "Modulus, strength and cytotoxicity of PMMA-silica nanocomposites." Coatings 10.6 (2020): 583.
8. Kul, Esra, Lütfü İhsan Aladağ, and Ruhi Yesildal. "Evaluation of thermal conductivity and flexural strength properties of poly (methyl methacrylate) denture base material reinforced with different fillers." The Journal of Prosthetic Dentistry 116.5 (2016): 803-810.
9. Yadav, Pratibha, et al. "Effect of incorporation of silane-treated silver and aluminum microparticles on strength and thermal conductivity of PMMA." Journal of Prosthodontics: Implant, Esthetic and Reconstructive Dentistry 21.7 (2012): 546-551.
10. Mansour, Mohamed M., Warren C. Wagner, and Tien-Min G. Chu. "Effect of mica reinforcement on the flexural strength and microhardness of polymethyl methacrylate denture resin." Journal of Prosthodontics: Implant, Esthetic and Reconstructive Dentistry 22.3 (2013): 179-183.
11. Kurt, Ayşegül, et al. "The antifungal activity and cytotoxicity of silver containing denture base material." Nigerian Journal of Clinical Practice 20.3 (2017): 290-295.
12. Bacali, Cecilia, et al. "The influence of graphene in improvement of physico-mechanical properties in PMMA denture base resins." Materials 12.14 (2019): 2335.
13. Safi, Ihab N. "Evaluation the effect of nano-fillers (TiO2, AL2O3, SiO2) addition on glass transition temperature, E-Moudulus and coefficient of thermal expansion of acrylic denture base material." Journal of Baghdad College of Dentistry 26.1 (2014): 37-41.
14. Salahuddin, Nehal, Maged El-Kemary, and Ebtisam Ibrahim. "Reinforcement of polymethyl methacrylate denture base resin with ZnO nanostructures." International Journal of Applied Ceramic Technology 15.2 (2018): 448-459.
15. Ghose, Debarati, and Dhiraj Kumar. "Emerging Nanostructures in Dental Applications." Emerging Materials: Design, Characterization and Applications. Singapore: Springer Nature Singapore, 2022. 265-313.
16. Wani, A. H., and M. A. Shah. "A unique and profound effect of MgO and ZnO nanoparticles on some plant pathogenic fungi." Journal of Applied Pharmaceutical Science Issue (2012): 40-44.
17. Saravanan, R., et al. "Preparation and characterization of V2O5/ZnO nanocomposite system for photocatalytic application." Journal of Molecular Liquids 198 (2014): 409-412.
18. Goryczka, Tomasz, et al. "Crystallite size determination of MgO nanopowder from X-ray diffraction patterns registered in GIXD technique." Solid State Phenomena 163 (2010): 177-182.
19. Saravanan, R., et al. "Comparative study on photocatalytic activity of ZnO prepared by different methods." Journal of Molecular Liquids 181 (2013): 133-141.
20. Saleh, Tawfik A., and Vinod K. Gupta. "Photo-catalyzed degradation of hazardous dye methyl orange by use of a composite catalyst consisting of multi-walled carbon nanotubes and titanium dioxide." Journal of colloid and interface science 371.1 (2012): 101-106.
21. Stan, Manuela, et al. "Enhanced photocatalytic degradation properties of zinc oxide nanoparticles synthesized by using plant extracts." Materials Science in Semiconductor Processing 39 (2015): 23-29.
22. Saravanan, R., et al. "Visible light-induced degradation of methylene blue using CeO2/V2O5 and CeO2/CuO catalysts." Materials Science and Engineering: C 33.8 (2013): 4725-4731.
23. Qin, Lirong, et al. "Controlled growth and morphology evolution of urchin-like ZnO/MgO hierarchical structures." Journal of crystal growth 308.2 (2007): 417-423.

24. Nishimoto, Naoki, et al. "Evaluation of ZnO-MgO mixed thin films grown by metal-organic decomposition." e-Journal of Surface Science and Nanotechnology 13 (2015): 185-189.
25. Torres-Huerta, Aide Minerva, et al. "Effect of the substrate on the properties of ZnO–MgO thin films grown by atmospheric pressure metal-organic chemical vapor deposition." Thin Solid Films 519.18 (2011): 6044-6052.
26. Marghalani, Hanadi Yousif. "Effect of filler particles on surface roughness of experimental composite series." Journal of Applied Oral Science 18 (2010): 59-67.
27. Marghalani, Hanadi Y. "Effect of finishing/polishing systems on the surface roughness of novel posterior composites." Journal of Esthetic and Restorative Dentistry 22.2 (2010): 127-138.
28. Poddar, Maneesh Kumar, Sachin Sharma, and Vijayanand S. Moholkar. "Investigations in two-step ultrasonic synthesis of PMMA/ZnO nanocomposites by in–situ emulsion polymerization." Polymer 99 (2016): 453-469.
29. S.K. Esthappan, Polypropylene/metal oxide nanocomposites: Fiber spinning and evaluation, Ph.D. Dissertation, Department of Polymer Science and Rubber Technology, Cochin University of Science and Technology, Kochi (Kerala), India, May 2012.
30. K. Chun, H. Choi, and J. Lee, "Comparison of mechanical property and role between enamel and dentin in the human teeth," Journal of Dental Biomechanics, vol. 5, 2014.
31. Salih, Sihama Issa, Jawad Kadhim Oleiwi, and Arkan Saad Mohamed. "Investigation of mechanical properties of PMMA composite reinforced with different types of natural powders." ARPN Journal of Engineering and Applied Sciences 13.22 (2018): 8889-8900.

Analysis of the effect of composition ratio, structure and properties of ZnO/MgO differentiated materials

Abbas F. Khorsheed [1,a)], Adnan R. Ahmad[1], Alaa J. Ghazai[2]

[1] *Department of Physics, College of Education for pure science, Tikrit University, Tikrit, Iraq*
[2] *Department of Physics, College of Science, Al-Nahrain University, Baghdad, Iraq*

[a)] Corresponding author: eabaas.f.khurshid@st.tu.edu.iq

Abstract. This study involved the production of a nanocomposite consisting solely of zinc oxide and magnesium oxide. The mixing ratios of the two components were varied (90/10, 60/40, and 50/50) by weight. The nanocomposite was characterized using atomic force microscopy (AFM), field emission scanning electron microscopy (FESEM), and scattering X-rays. Energy-dispersive X-ray (EDX) and X-ray diffraction (XRD) investigations. The ZnO/MgO nanocomposites were characterized by X-ray diffraction (XRD) investigations. The MgO powder likely achieved effective integration inside the core of the ZnO particles due to the similarity between the single-phase XRD pattern of the MgO/ZnO NC sample and all planes of the ZnO sample, both possessing the hexagonal wurtzite structure. Furthermore, several spherical structures exhibited flat and dumbbell forms, with an average particle size of 88 nm. Additionally, a noticeable enhancement in the crystal structure was found. Furthermore, the surface morphology is characterized by the presence of randomly dispersed islands with additional MgO content. The compound's microstructure and crystalline quality are enhanced when the surface roughness increases from 66.3 nm to 77 nm. Furthermore, it demonstrates the impact of including ZnO/MgO nanoparticle powders on the behavior of MgO nanoparticle powders. The inclusion of ZnO/MgO nanoparticles was essential in order to provide the nanocomposite with strong adhesion. The utilization of ZnO/MgO can effectively enhance mechanical characteristics.

INTRODUCTION

Nanomaterials and nanotechnology, as a burgeoning discipline in contemporary society, are widely employed in the life sciences and different biomedical applications [1]. Semiconductor nanoparticles, due to their unique physical and chemical properties, have signifi cant advantages in biomedical applications, such as bioimaging and drug delivery. Among them, metal oxide nanoparticles, particularly zinc oxide (ZnO) and magnesium oxide (MgO) nanoparticles, have attracted significant attention due to their unique capabilities, such as electrical, magnetic, optical, and antibacterial characteristics [2-9]. ZnO nanoparticles, as a new type of low-cost and low-toxicity material, are expected to perform better in biomedical applications [10-14]. In addition, ZnO possesses remarkable surface and elemental characteristics, making it a versatile and biocompatible material [15-18]. Zinc oxide (ZnO) has been demonstrated to be a superior antibacterial agent, and it is extensively utilized in the manufacturing of medications for wound healing, inflammation, and itching [19-20]. Additionally, it is utilized in nutritional goods, antidandruff shampoos, antiacne lotions and ointments, and several other uses [20]. MgO nanoparticles provide a comparable array of desirable characteristics to those of ZnO. This material is characterized by its chemical and thermal stability, as well as its highly reactive surface. MgO nanoparticles has the unique characteristic of being non-toxic, setting them apart from other metal oxide nanoparticles in the field of medicinal applications. In the realm of biomedicine, nanoparticles have become increasingly utilized in magnetic resonance imaging (MRI), in addition to ZnO and Fe3O4 nanoparticles [21-23]. Zinc oxide (ZnO) and magnesium oxide (MgO) nanoparticles may be produced using several methods such as controlled precipitation, sol-gel synthesis, solvothermal synthesis, and green synthesis. Both of these materials may also be manufactured using deposition processes such as physical vapor deposition, chemical vapor deposition, sputtering, and electrochemical deposition techniques [24-31]. Nevertheless, the antibacterial properties of ZnO/MgO nanocomposites remain uncertain and require further examination on various bacterial strains. As far as we know, ZnO-MgO nanocomposites have not been investigated for their effectiveness against positive cocci and

Technologies and Materials for Renewable Energy, Environment and Sustainability
AIP Conf. Proc. 3321, 020012-1–020012-8; https://doi.org/10.1063/5.0291604
Published under an exclusive license by AIP Publishing. 978-0-7354-5231-2/$30.00

negative rod pathogens/bacteria across different compositions [32]. The primary objective of this research is to produce nanocomposites with varying ratios of ZnO/MgO utilizing the powder technology approach. In addition, the manufactured composite particles undergo characterisation, namely X-ray diffraction (XRD), to verify the intended material composition, crystal sizes, and other relevant parameters.

MATERIAL AND METHODS

We source 99.99% pure zinc oxide (ZnO) and magnesium oxide (MgO) from Sigma-Aldrich. A hydraulic press with a capacity of four tons is placed inside a 10 mm stainless steel mold according to the Figure *1*. Pure materials are applied to it in mixing ratios (90/10, 60/40, 50/50) according to Table 1, then sintered to form a disc with a diameter of 1 cm and a height of 2 mm. In an oven at 900°C for two hours. Characterization, including XRD, SEM, EDS, and AFM, was studied for both pure and mixed ZnO and MgO composites.

FIGURE 1. 10 mm stainless steel mold

TABLE 1. Nanocomposites prepared with different contents of ZnO: MgO

Samples	ZnO(wt.%)	MgO (wt.%)
ZnO	0.2002	0
MgO	0	2010
Mix_1 ZnO (90) /MgO (10)	18	0.02
Mix_2 ZnO (60) /MgO (40)	0.12	0.08
Mix_3 ZnO (50) /MgO (50)	0.10	0.10

RESULTS AND DISCUSSION

X-Ray Diffraction Analysis Pure ZnO and ZnO/MgO Nanocomposite

In Figure 2 the X-ray diffraction patterns of pure ZnO, pure MgO, and ZnO/MgO mixtures with various amounts are shown next to each other. A successful synthesis depends on a good match between the produced and standard peaks. X-ray diffractograms help study the structural analysis of NPs and NCs. You can see that the patterns have diffraction peaks that match JCPDS (card number 01-079-0207) and JCPDS (card number 01-074-1225), which shows that zinc oxide has a hexagonal crystal system and magnesium oxide has a cubic crystal system Figure 3 shows the XRD potter of pure (ZnO, MgO) NPs and (90/10, 60/40, and 50/50) wt.% of ZnO/MgO, respectively, which revealed several peaks at $2\theta = 31.8°$, 34.44°, 36°, 47.56°, 56.6°, 62.9°, 66°, 68.34°, 69.68° and 78.56° for pure ZnO-NPs, which corresponds to orientations (100), (002), (101), (102), (110), (103), (200), (112), (201) and (202). It has been determined that the hexagonal segment of ZnO-NPs, which matches JCPDS file No. 89-1397, causes the observable peaks [33, 34]. Residue from the synthesis process may be the cause of some weak peaks. The XRD pattern showed no signs of additional solid peaks Figure 3 shows the XRD pattern of the nanocomposite at all ZnO/MgO concentrations. New peaks were detected at diffraction pattern 2Θ=43°, which revealed some peaks; However, it belongs to MgO (JCPDS: 89-7746) [35, 36]. The ZnO sample has the same hexagonal wurtzite structure as the

MgO/ZnO NC sample's single-phase XRD pattern. This means that the MgO powder was successfully mixed with the ZnO particles at their core. The other metals in the composite sample attenuate the MgO and ZnO phases' peak intensity. The confirmation of the loss of crystalline nature or the absence of crystalline character due to lattice faults is once again provided by the shift in the theta angle to the lower value. Zn ions within MgO or an improved ZnO periodic crystal lattice create negligible strain. Therefore, the change in the lattice causes a change in the crystal's regularity [37]. The literature has already shown how adding dopant elements modify the lattice characteristics of the host materials. This is brought on by their differences in atomic radii [38, 39].

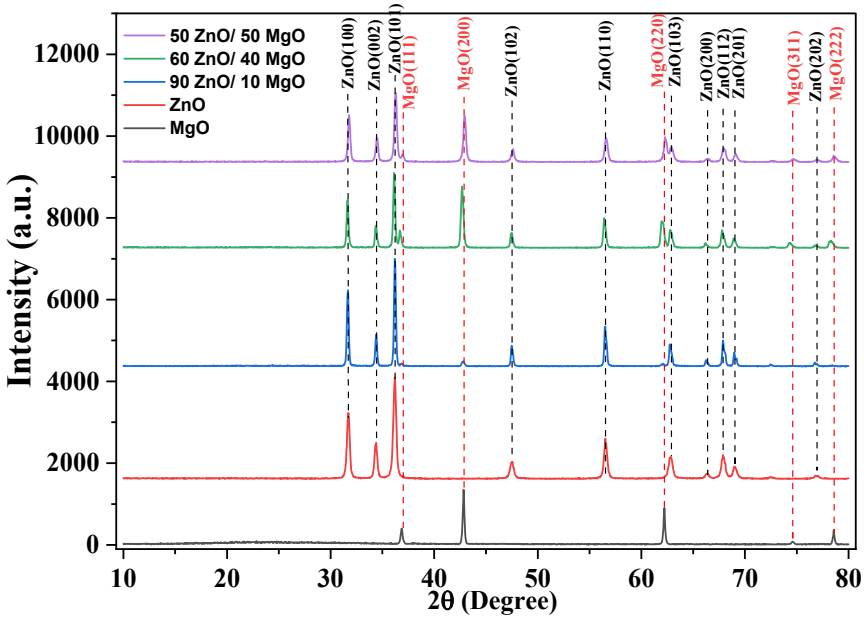

Figure 2. XRD analysis of pure ZnO and MgO with different contents of ZnO/ MgO Nanocomposites.

Field Emission Scanning Electron Microscopy (FE-SEM)

Figure 3 shows the FE-SEM image of pure zinc oxide, pure magnesium oxide, and zinc/magnesium oxide at different weight ratios, which revealed that the zinc oxide nanoparticles (NPs) have an average particle size of 72 nm and their morphology is mainly flat and dumbbell-shaped. The observed crystal habit of ZnO (hexagonal) correlates with that observed for MgO (trigonal planes). The evolution of the dense structure can be explained by atomic unit deposition. The figure also shows pure magnesium oxide, which revealed particles having an average particle size of 200 nanometers, when zinc oxide was mixed with magnesium oxide in different proportions. The reason for some of the larger particles may be related to temperature and incubation time. The observed morphology was the result of a mixture of oxide forms and some magnesium-zinc alloy. It is known that ZnO and MgO can react and form MgZnO compounds at annealing temperatures above 800 °C [40].The observed crystal habit of ZnO (hexagonal) correlates with that observed for MgO (trigonal planes). The evolution of the dense structure can be explained by atomic unit deposition. It shows an FE-SEM image of pure zinc oxide and zinc/magnesium oxide with (90/10) % nanocomposite, which revealed that the zinc oxide nanoparticles (NPs) have an average particle size of 600 nm. This indicates that the solution increased the particle size and basically formed a flat and dumbbell shape. ‘Figure 3’ . Some of the larger particles may be related to temperature and incubation time. ZnO NPs are synthesized and synthesized. Dumbbell-shaped morphological particles of different sizes were also observed. The average size of the smallest particles is 200 nanometers. Figure 3 shows that a compound with a mixing ratio of (80/20) % showed that the material had a decrease in the rate of granular size to 150nm. This indicates that magnesium oxide had a significant impact on the granular size when its percentage was increased, and this is also what we obtained in the mixing ratio of (50/50) %. The average particle size decreased to 90nm. It is known that at annealing temperatures above 800 °C, ZnO and MgO may combine to form MgZnO composites [41]. The observed shape is related to the hexagonal crystal habit of ZnO and the triangular crystal habit of MgO.

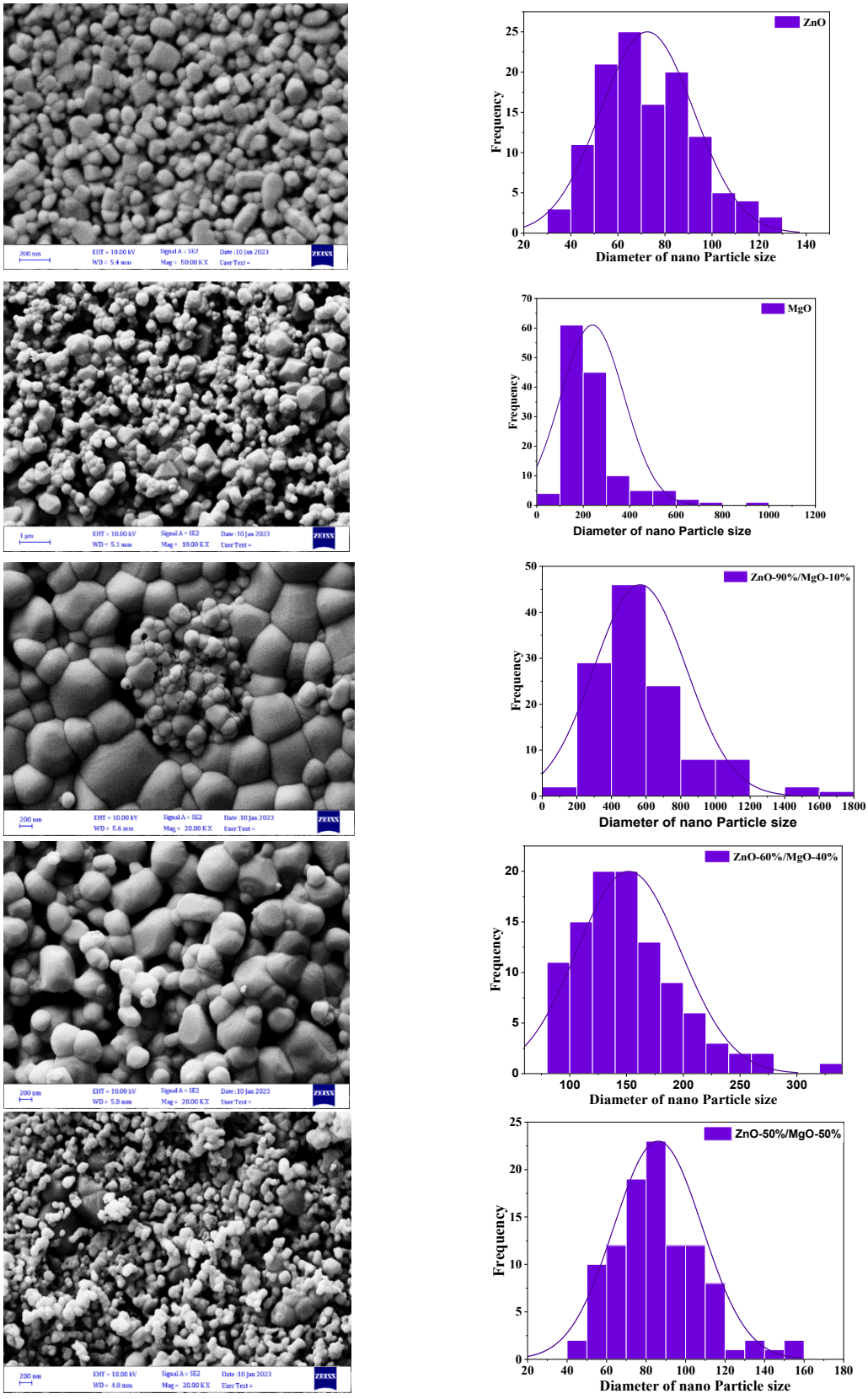

Figure 3. FE-SEM analysis for pure ZnO and MgO with different contents of ZnO/ MgO Nanocomposites

EDS Analysis

Figure 4 a and b analyses the outcomes obtained from the energy dispersive spectra of zinc and magnesium oxide, each examined individually. The findings revealed that the proportion of zinc oxide to oxygen was 48.7%, but the proportion of zinc was 51.3%. The magnesium content accounted for 55.1% of the total, while the oxygen content accounted for 44.9%. Figure 4 ' c illustrates the composition of ZnO and MgO as 90% and 10%, respectively, in terms of their mixing ratio. The research revealed that the zinc content accounted for 65.6%, magnesium 14.1%, and oxygen 20.2%. Figure 7d reveals a mixing ratio of 60% oxygen and 40% other materials. The examination showed a 15.9% decrease in the percentage of oxygen, a 27.6% increase in the percentage of magnesium, and an increase of 56.5% in the percentage of zinc. With the final mixing ratio of 50/50% shown in Figure ' e, the results were also similar between zinc, magnesium, and oxygen, where zinc was 35.6%, magnesium 26.4%, and oxygen 38%.

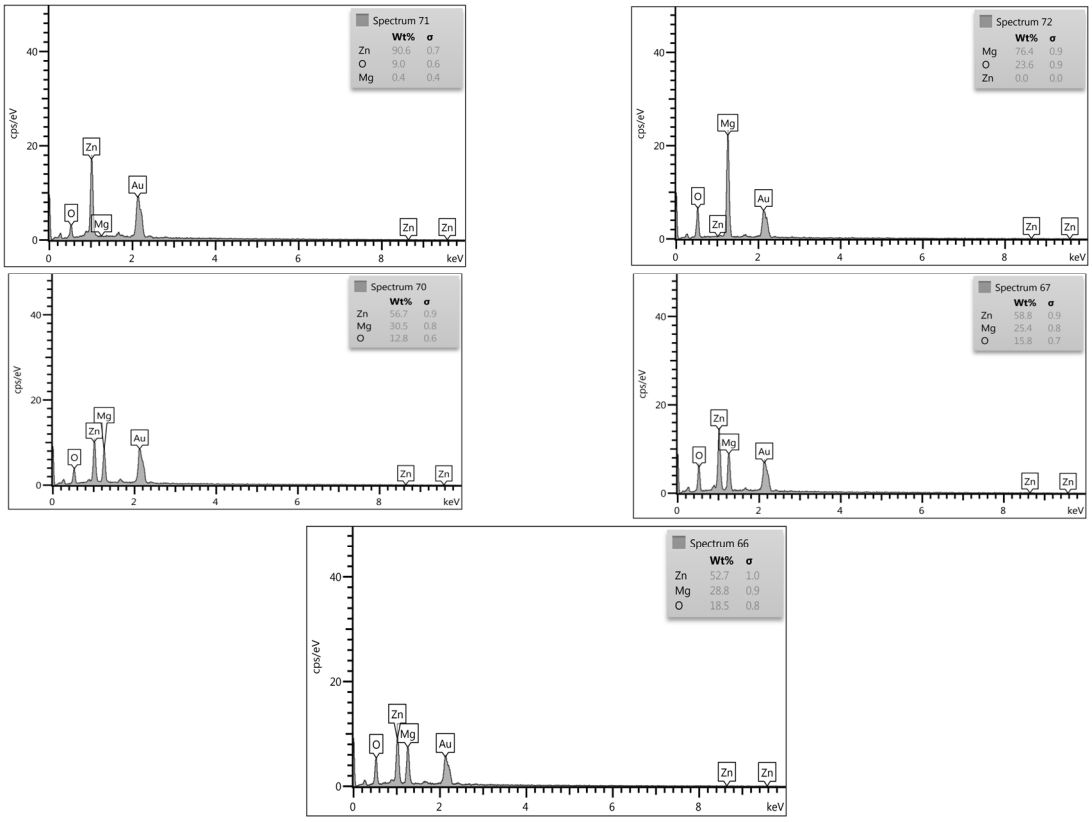

Figure 4. EDS analysis for pure ZnO and MgO with different contents of ZnO/ MgO Nanocomposites

Topography Analyses

Figures (a) ' Shows AFM images of pure ZnO, pure MgO, and ZnO/MgO pellets with different weight ratios, respectively. The surface morphology of the ZnO films as observed from the AFM micrographs confirms that the grains are uniformly distributed within the scanning area (5 µm X 5 µm) and fit closely together and that the average surface roughness is 12 nm, with individual columnar grains extending upward at an elevation rate of 61.6. nm. The Figures(b) ' of MgO shows that the average surface roughness is 17.3 nm and the grain growth rate is 53.8 nm. The surface appearance is that the grains are not compact and of different sizes and are not well distributed [42]. The observed fluctuations in crystal grain size indicate that the evolution mechanism is influenced by the element MgO present in the ZnO-MgO alloy materials. Therefore, when the two materials are mixed at a ratio of 90/10%, as in Figure C, the average surface roughness of the material is 16.5 nm, the particle height reaches 82.1 nm, and the surface particles are well arranged. Figure D ' shows the mixing ratio of 60/40%. The average roughness decreases to 14.8 nanometers when the percentage of zinc oxide decreases and the percentage of magnesium in the mixture increases, and the particle height decreases to 63.5 nanometers. This is demonstrated by the final mixing ratio of 50/50%, as shown in Figure f the average roughness increases slightly with equal proportions between the two materials, and in

all mixing ratios there is an effect. The change in surface roughness and particle size of the two materials is obvious [43]. The most notable feature was that the ZnO / MgO morphologies were not hexagonal but had flat, triangular ends. This suggests that the introduction of magnesium into the ZnO lattice could be the origin of this phenomenon, which is consistent with [44].

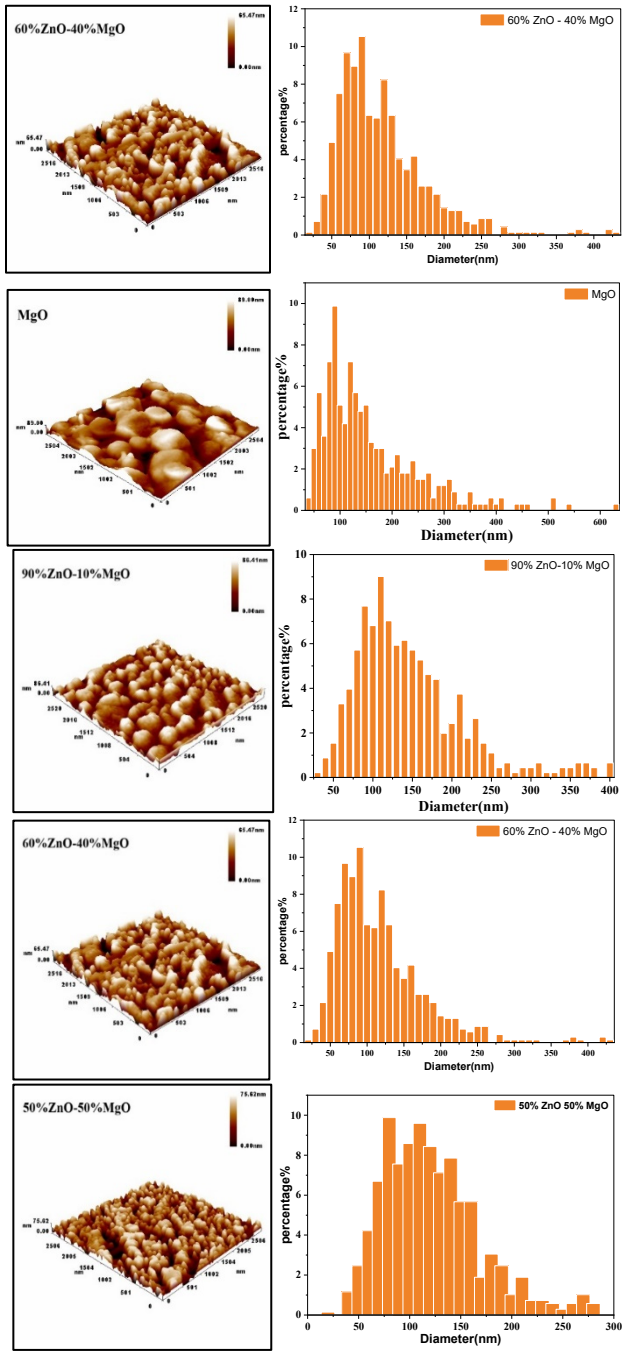

Figure 5. Atomic force microscopy (AFM) analysis pure ZnO and MgO with different contents of ZnO/ MgO Nanocomposites

CONCLUSION

The results of this study included mixing nanopowders of zinc oxide and magnesium oxide at different mixing ratios. There was a significant effect of adding MgO on the nano-zinc oxide material, an effect and change in the crystal sizes by X-ray diffraction, and an effect on the surface properties of the material in terms of roughness. These changes were demonstrated in FESEM images. Variable with increasing levels of magnesium oxide to improve the overall properties of the ZnO/MgO composite.

REFERENCES

[1]Ramos, A. P., Cruz, M. A., Tovani, C. B., & Ciancaglini, P. (2017). Biomedical applications of nanotechnology. *Biophysical reviews*, *9*(2), 79-89.

[2] Martirosyan, A., & Schneider, Y. J. (2014). Engineered nanomaterials in food: implications for food safety and consumer health. *International journal of environmental research and public health*, *11*(6), 5720-5750.

[3] Patil, S. K., Shinde, S. S., & Rajpure, K. Y. (2013). Physical properties of spray deposited Ni-doped zinc oxide thin films. *Ceramics International*, *39*(4), 3901-3907.

[4] Suwanboon, S., Amornpitoksuk, P., Sukolrat, A., & Muensit, N. (2013). Optical and photocatalytic properties of La-doped ZnO nanoparticles prepared via precipitation and mechanical milling method. *Ceramics International*, *39*(3), 2811-2819.

[5] Yılmaz, S., Nisar, J., Atasoy, Y. A. V. U. Z., McGlynn, E., Ahuja, R., Parlak, M., & Bacaksız, E. (2013). Defect-induced room temperature ferromagnetism in B-doped ZnO. *Ceramics International*, *39*(4), 4609-4617.

[6] Jin, T., & He, Y. (2011). Antibacterial activities of magnesium oxide (MgO) nanoparticles against foodborne pathogens. *Journal of Nanoparticle Research*, *13*, 6877-6885.

[7] Mageshwari, K., Mali, S. S., Sathyamoorthy, R., & Patil, P. S. (2013). Template-free synthesis of MgO nanoparticles for effective photocatalytic applications. *Powder technology*, *249*, 456-462.

[8] Mastuli, M. S., Roshidah, R., Mahat, A. M., Saat, N., & Kamarulzaman, N. (2012). Sol-gel synthesis of highly stable nano sized MgO from magnesium oxalate dihydrate. *Advanced Materials Research*, *545*, 137-142.

[9] Kaviyarasu, K., Mola, G. T., Oseni, S. O., Kanimozhi, K., Magdalane, C. M., Kennedy, J., & Maaza, M. (2019). ZnO doped single wall carbon nanotube as an active medium for gas sensor and solar absorber. *Journal of Materials Science: Materials in Electronics*, *30*, 147-158.

[10] Alivisatos, A. P. (1996). Semiconductor clusters, nanocrystals, and quantum dots. *science*, *271*(5251), 933-937.

[11] Gao, X., Cui, Y., Levenson, R. M., Chung, L. W., & Nie, S. (2004). In vivo cancer targeting and imaging with semiconductor quantum dots. *Nature biotechnology*, *22*(8), 969-976.

[12] Medintz, I. L., Uyeda, H. T., Goldman, E. R., & Mattoussi, H. (2005). Quantum dot bioconjugates for imaging, labelling and sensing. *Nature materials*, *4*(6), 435-446.

[13] Petros, R. A., & DeSimone, J. M. (2010). Strategies in the design of nanoparticles for therapeutic applications. *Nature reviews Drug discovery*, *9*(8), 615-627.

[14] Doane, T. L., & Burda, C. (2012). The unique role of nanoparticles in nanomedicine: imaging, drug delivery and therapy. *Chemical Society Reviews*, *41*(7), 2885-2911.

[15] Kaviyarasu, K., Magdalane, C. M., Kanimozhi, K., Kennedy, J., Siddhardha, B., Reddy, E. S., ... & Maaza, M. (2017). Elucidation of photocatalysis, photoluminescence and antibacterial studies of ZnO thin films by spin coating method. *Journal of Photochemistry and Photobiology B: Biology*, *173*, 466-475.

[16] Özgür, Ü., Alivov, Y. I., Liu, C., Teke, A., Reshchikov, M. A., Doğan, S., ... & Morkoç, A. H. (2005). A comprehensive review of ZnO materials and devices. *Journal of applied physics*, *98*(4).

[17] Bhattacharyya, S., & Gedanken, A. (2008). A template-free, sonochemical route to porous ZnO nano-disks. *Microporous and Mesoporous Materials*, *110*(2-3), 553-559.

[18] Ludi, B., & Niederberger, M. (2013). Zinc oxide nanoparticles: chemical mechanisms and classical and non-classical crystallization. *Dalton Transactions*, *42*(35), 12554-12568.

[19] Liu, H., Yang, D., Yang, H., Zhang, H., Zhang, W., Fang, Y., ... & Xi, Z. (2013). Comparative study of respiratory tract immune toxicity induced by three sterilisation nanoparticles: silver, zinc oxide and titanium dioxide. *Journal of hazardous materials*, *248*, 478-486.

[20] Mirhosseini, M., & Firouzabadi, F. B. (2013). Antibacterial activity of zinc oxide nanoparticle suspensions on food-borne pathogens. *International Journal of Dairy Technology*, *66*(2), 291-295.

[21] Richards, R., Li, W., Decker, S., Davidson, C., Koper, O., Zaikovski, V., ... & Klabunde, K. J. (2000). Consolidation of metal oxide nanocrystals. Reactive pellets with controllable pore structure that represent a new family of porous, inorganic materials. *Journal of the American Chemical Society*, *122*(20), 4921-4925.
[22] Vidic, J., Stankic, S., Haque, F., Ciric, D., Le Goffic, R., Vidy, A., ... & Delmas, B. (2013). Selective antibacterial effects of mixed ZnMgO nanoparticles. *Journal of nanoparticle research*, *15*, 1-10.
[23] Srivastava, S., Awasthi, R., Gajbhiye, N. S., Agarwal, V., Singh, A., Yadav, A., & Gupta, R. K. (2011). Innovative synthesis of citrate-coated superparamagnetic Fe3O4 nanoparticles and its preliminary applications. *Journal of colloid and interface science*, *359*(1), 104-111.
[24] Krishnamoorthy, K., Moon, J. Y., Hyun, H. B., Cho, S. K., & Kim, S. J. (2012). Mechanistic investigation on the toxicity of MgO nanoparticles toward cancer cells. *Journal of materials chemistry*, *22*(47), 24610-24617.
[25] Rao, K. G., Ashok, C. H., Rao, K. V., & Chakra, C. S. (2014). Structural properties of MgO nanoparticles: synthesized by co-precipitation technique. *International Journal of Science and Research*, *3*(12), 43-46.
[26] Vatsha, B., Tetyana, P., Shumbula, P. M., Ngila, J. C., Sikhwivhilu, L. M., & Moutloali, R. M. (2013). Effects of precipitation temperature on nanoparticle surface area and antibacterial behaviour of Mg (OH) 2 and MgO nanoparticles. *Journal of Biomaterials and Nanobiotechnology*, *4*(04), 365.
[27] Benhebal, H., Chaib, M., Salmon, T., Geens, J., Leonard, A., Lambert, S. D., ... & Heinrichs, B. (2013). Photocatalytic degradation of phenol and benzoic acid using zinc oxide powders prepared by the sol–gel process. *Alexandria Engineering Journal*, *52*(3), 517-523.
[28] Tamilselvi, P., Yelilarasi, A., Hema, M., & Anbarasan, R. (2013). Synthesis of hierarchical structured MgO by sol-gel method. *Nano Bulletin*, *2*(1), 130106.
[29] B Djurisic, A., Y Chen, X., & H Leung, Y. (2012). Recent progress in hydrothermal synthesis of zinc oxide nanomaterials. *Recent patents on nanotechnology*, *6*(2), 124-134.
[30] Patil, A. B., & Bhanage, B. M. (2013). Novel and green approach for the nanocrystalline magnesium oxide synthesis and its catalytic performance in Claisen–Schmidt condensation. *Catalysis Communications*, *36*, 79-83.
[31] Di Ventra, M., Evoy, S., & Heflin Jr, J. R. (Eds.). (2004). *Introduction to nanoscale science and technology*. Boston, MA: Springer US.
[32] Kumar, N. B., Crasta, V., & Praveen, B. M. (2014). Advancement in microstructural, optical, and mechanical properties of PVA (Mowiol 10-98) doped by ZnO nanoparticles. *Physics Research International*, *2014*.
[33] Wani, A. H., and M. A. Shah. "A unique and profound effect of MgO and ZnO nanoparticles on some plant pathogenic fungi." Journal of Applied Pharmaceutical Science Issue (2012): 40-44.
[34] Saravanan, R., et al. "Preparation and characterization of V2O5/ZnO nanocomposite system for photocatalytic application." Journal of Molecular Liquids 198 (2014): 409-412.
[35] Goryczka, Tomasz, et al. "Crystallite size determination of MgO nanopowder from X-ray diffraction patterns registered in GIXD technique." Solid State Phenomena 163 (2010): 177-182.
[36] Saravanan, R., et al. "Comparative study on photocatalytic activity of ZnO prepared by different methods." Journal of Molecular Liquids 181 (2013): 133-141.
[37] Saleh, Tawfik A., and Vinod K. Gupta. "Photo-catalyzed degradation of hazardous dye methyl orange by use of a composite catalyst consisting of multi-walled carbon nanotubes and titanium dioxide." Journal of colloid and interface science 371.1 (2012): 101-106.
[38] Stan, Manuela, et al. "Enhanced photocatalytic degradation properties of zinc oxide nanoparticles synthesized by using plant extracts." Materials Science in Semiconductor Processing 39 (2015): 23-29.
[39] Saravanan, R., et al. "Visible light-induced degradation of methylene blue using CeO2/V2O5 and CeO2/CuO catalysts." Materials Science and Engineering: C 33.8 (2013): 4725-4731.
[40] L. Qin, J. Zhao, L. Zhang, and X. Zou, "Controlled growth and morphology evolution of urchin-like ZnO/MgO hierarchical structures," *J. Cryst. Growth*, vol. 308, no. 2, pp. 417–423, 2007.
[41] Qin, Lirong, et al. "Controlled growth and morphology evolution of urchin-like ZnO/MgO hierarchical structures." Journal of crystal growth 308.2 (2007): 417-423.
[42] N. Al-Hardan, M. J. Abdullah, A. Abdul Aziz, The gas response enhance-ment from ZnO film for H2 gas detection. Appl. Surf. Sci. 255:7794 – 7, (2009).
[43] Nishimoto, Naoki, et al. "Evaluation of ZnO-MgO mixed thin films grown by metal-organic decomposition." e-Journal of Surface Science and Nanotechnology 13 (2015): 185-189.
[44] Torres-Huerta, Aide Minerva, et al. "Effect of the substrate on the properties of ZnO–MgO thin films grown by atmospheric pressure metal-organic chemical vapor deposition." Thin Solid Films 519.18 (2011): 6044-6052.

A Study of Kinetic and Thermodynamic on Serum Na/K-ATPase in Patients With Leukaemia

Tiba A. Khudaer AL-Taiee [1,a], Abdulrahman. K. AL-Taiee [2,b], Mohammed A. Mohammed [3,c] and Kareem A. Jasim [4,d]

[1] *Department of Chemistry, College of Science, Al-Nahrain University, Baghdad, Iraq*
[2] *Department of Medical Laboratory Technologies, University College, Baghdad, Iraq*
[3] *Department of Remote Sensing and GIS, College of Science, University of Baghdad, Baghdad, Iraq*
[4] *Department of Physics, College of Education for pure sciences Ibn Al-Haitham, University of Baghdad, Baghdad, Iraq*

[a] Corresponding author: tiba.abdulrahman@nahrainuniv.edu.iq
[b] abdrahman.K.Abdalhussen@alsalam.edu.iq
[c] mohammed.a.m@sc.uobaghdad.edu.iq
[d] kareem.a.j@ihcoedu.uobaghdad.edu.iq

Abstract. This study includes the determination of serum Na^+/K^+-ATPase levels in patients with leukemia and healthy subjects was determined. The statistical analysis showed a significant increase ($P<0.05$) inactivity of serum Na^+/K^+-ATPase in patients compared with healthy subjects. The isolation and partial purification of the enzyme have been done by using Ionic-exchange chromatography, The results showed after Dialysis two bands, and the first band showed the highest activity of the enzyme. This isoenzyme was used to study the kinetic and thermodynamic properties. The optimum conditions of the enzyme showed the highest activity was at 1.25 mmol/L of the substrate (ATP), pH 7.4, and at 37°C. Michaels-Menten Km value was 0.72mmol/L while the maximum velocity value was 21.7U/L. Thermodynamic properties for the transition state showed that the activated energy was 6.22 $Cal.mol^{-1}$ and Q10 equals to 1.0002, and ΔH^* for ES* complex was 5.63 $Cal.mol^{-1}$ and ΔS^* was -34.83 Cal.mol-1. K^{-1}, while ΔG^* value was 10.79 $Kcal.mol^{-1}$ (need for energy).

INTRODUCTION

Serum enzymes, are of clinical importance, and they are cellular in origin, and they rise in diseases, tumors, or injury to the tissues of the heart, liver, pancreas, bones and muscles [1]. Sodium Potassium Adenosine Tri Phosphatase is also known as the sodium pump or sodium-potassium pump Na+/K+-ATPase (one of these enzymes) is the major cation pump that represents a process in which sodium inside the cell is exchanged for potassium on the outside, and energy is supplied by ATP [2,3]. It has a binding site for Na^+ and K^+ ions and spans the plasma membrane similarly to a gating pore. Three sodium ions are released and two potassium ions are introduced for every molecule of ATP that is transformed to adenosine diphosphate. [3,4]. Many $Na^+/K+$ pumps are found in most cells, and they are usually active. The sodium pump is a protein that contains two large units of α and β types. For instance, there are approximately 200 Na^+ and K^+ pumps per red blood cell, about 35,000 per white blood cell, and several million per cell in a part of the tubules within the kidney. This represents an enormous energy expenditure used to maintain a steep gradient of Na+ and K+ across the plasma membrane [5,6]. The 110 kDa α subunits of the enzyme include binding sites for both Na+ and K+, as well as an ATP binding site; on the other hand, the β subunit is a glycoprotein complex that is required for the enzyme to function [7]. Leukemias are classed as myeloid or lymphoid based on the differentiation status of the cells, and they are further split into chronic and acute leukemias [9]. Leukemias are defined as malignant clone dermatosis devoid of a hemopoietic stem cell [8]. Leukemia comes in four main forms as well as a few less common ones. Acute myeloid leukemia (AML), chronic myeloid leukemia (CML), acute lymphoblastic leukemia (ALL), and chronic lymphocytic leukemia (CLL) are the four main forms [10].

MATERIALS AND METHODS

Samples of serum leukemia patients were obtained from Medical City Hospital for blood diseases in Baghdad and the samples were stored at -20 °c until used.

Technologies and Materials for Renewable Energy, Environment and Sustainability
AIP Conf. Proc. 3321, 020013-1–020013-8; https://doi.org/10.1063/5.0290000
Published under an exclusive license by AIP Publishing. 978-0-7354-5231-2/$30.00

Determination of Na^+/ K^+-ATPase activity

Kirchgessner M. method was used to determine Na+/ K+-ATPase activity from serum leukemia patients [11].

Determination of protein amount

The prepared kit by AGGAPY company was used to estimate the amount of protein.

Partial purification of Na^+/ K^+-ATPase from serum

Precipitation: Proteins precipitating by 70%W/V ammonium sulphate (NH4)2SO4 were used to extract Na+/K+-ATPase from leukemia patients' serum. The precipitate was then dissolved by a small volume of Tris-HCL-0.125M solution at pH 7.4 [12]. Through dialysis in Tris-HCl 0.125M at pH 7.4, ammonium sulfate has been extracted from a solution. Multiple different batches were run for an overnight period at 4°C. Protein was then concentrated by soaking it in 4°C sucrose for a considerable amount of time.

Partial purification of Na^+/K^+-ATPase from the serum by Ion Exchange Chromatography

The DEAE-Cellulose column was used in this technique, and it had a flow rate of 1 ml per minute. Tris-HCL (0.125M) (pH 7.4), the eluting buffer, included increasing concentrations of NaCl (0, 25, 50, and 75 mM). The column's extracting portions were collected at a size of 3 ml. The colorimetric approach was used to evaluate the enzyme activity, and protein absorbance was measured at 280 nm (10) Until used, samples were stored at -20°C.

Kinetic studies of the Na^+/K^+-ATPase isoenzyme I

Substrate concentration: Different concentrations of ATP were used to estimate the optimum concentration of the substrate (0.25, 0.5, 1, 1.25, 1.5, 1.75, 2 mM) [13].

Michaels -Menten constant

Many concentrations of ATP were used to calculate Km by using the Lineweaver-Burk plot.

$$\frac{1}{v_o} = \frac{Km}{Vmax} \times \frac{1}{[S]} + \frac{1}{Vmax} \quad (1)$$

Optimum pH

Different pH solutions were used with 1.25mM substrate (6 ، 6.5 ، 7 ، 7.4 ، 8 ، 9) to determine pH optimum at 30°C.

Optimum Temperature

Several temperatures (20, 25, 30, 37, and 40°C), substrate concentrations of 1.25 mM, and pH 7.4 were used to conduct the thermodynamic Studies of the Na^+/K^+-ATPase isoenzyme I:

Activated Energy

Arrhenius equation has been used to calculate activated energy

$$rate = Ae^{(-Ea/RT)} \quad (2)$$

And to calculate Q10 equation (3) has been used [15, 16].

$$E_a = (2.3RT_1 * T_2 \log Q10)/10 \quad (3)$$

Enthalpy, Entropy, and free energy for transition state

Trying the Polanyi equation (15) was used to calculate the Enthalpy and Entropy for the transition state [17]

$$ln\frac{K}{T} = \frac{-\Delta H^*}{R} \times \frac{1}{T} + ln\frac{KB}{h} + \frac{\Delta S^*}{R} \quad (4)$$

while free energy is calculated by

$$\Delta G^* = \Delta H^* - T\Delta S^* \quad (5)$$

RESULTS

Enzyme activity in patients with Leukemia

The activity of Na^+/K^+-ATPase expressed as (mean+SD) was estimated in the serum of patients with leukemia and healthy subjects as clear in Table (1):

TABLE 1. Na/K-ATPase levels in Leukemia

State	Na/K-ATPase activity U/ml Mean ± SD	P-value
Control	2.4± 0.29	$P \leq 0.05$
Leukemia	10.73± 0.35	

Partial purification of Na+/K+-ATPase from leukaemia patients' serum

Table (2) shows the steps of purification for Na^+/K^+-ATPase from serum. The first step was protein precipitation by using Ammonium Sulphate (70%), Specific activity was 5.86 U/mg, and purification folds were 3.6. then ion-exchange chromatography was used to separate isoenzymes depending on the difference of net charges, two Isoezymes were obtained as shown in Fig (1) with a specific activity of 27.76 U/mg and purification folds was 17.3for isozyme-I.

TABLE 2. Purification of Na+/K+ -ATPase steps

Steps	Total activity U	Specific activity U/mg	Fold	Yield(%)
Crude	52.65	1.6	1	100
Precipitation	35.07	5.86	3.6	66.6
Isomer I	43.32	27.76	17.3	82.2
Isomer II	27.69	98.89	61.7	52.6

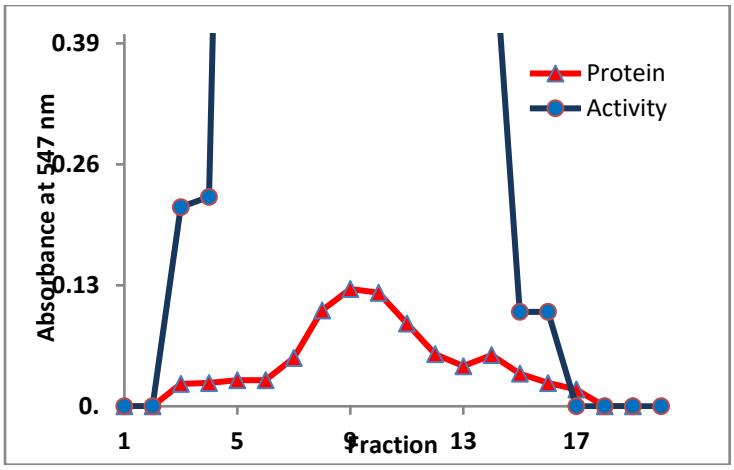

Figure 1. Separation of the enzyme with ionic-exchange chromatography by DEAE-Celluloseand

The kinetic parameters of Na^+/ K^+-ATPase

Optimum substrate and Km Condition

The impact of various substrate concentrations on the activity of partly purified isoenzyme I. As the substrate concentration was increased, the activity grew until it reached its maximum activity at 1.25 mM, at which point it started to drop, as seen in figure 3. Vmax was 21.7 mM, and the Michaels-Menten constant was 0.72 mM.L-1.min-1, as depicted in figure 3.

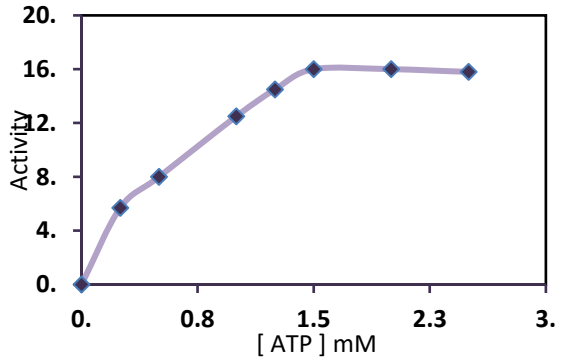

Figure 2. Effect of ATP concentration on the activity of Na/K-ATPase in patients with Leukemia

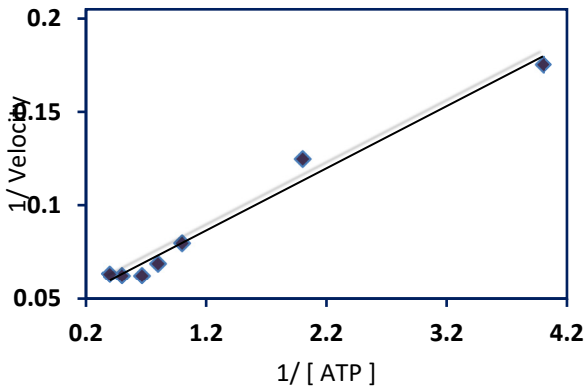

Figure 3. Lineweaver-Burk Plot to calculate Km

pH effect

As the pH rose, the results demonstrated a rise in velocity that peaked at pH 7.4. At pH values greater than 7.4, the activity declined, as seen in fig. 4

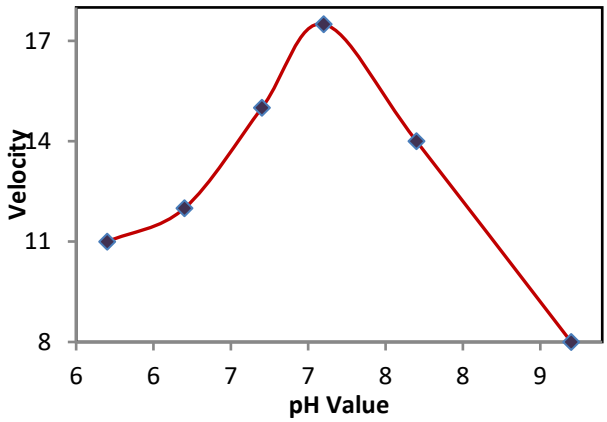

Figure 4. Effect of pH on enzyme velocity.

Temperature effect

The findings showed that the maximum activity of the enzyme was observed at 37 °C as shown in Fig (5).

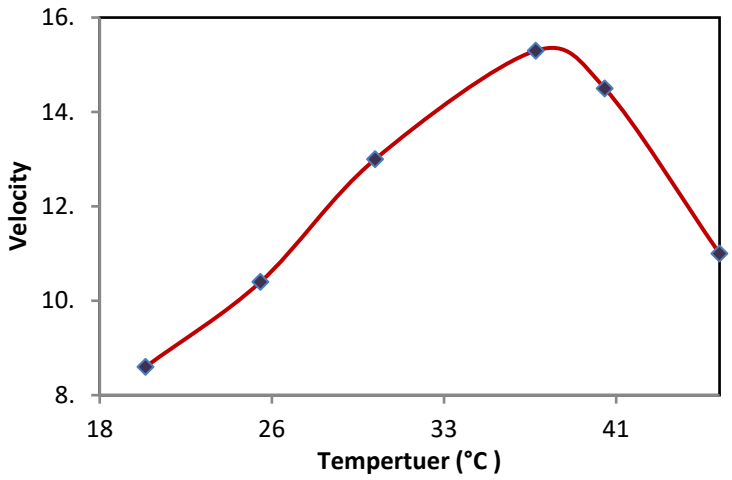

Figure 5. effect of temperatures on isoenzyme activity.

Thermodynamic parameters of Na^+/ K^+-ATPase (isoenzyme I)

Activated energy was calculated by the Arrhenius equation as shown in Fig 6 and Table 3 shows the activated energy Ea value to form ES complex and Q10.

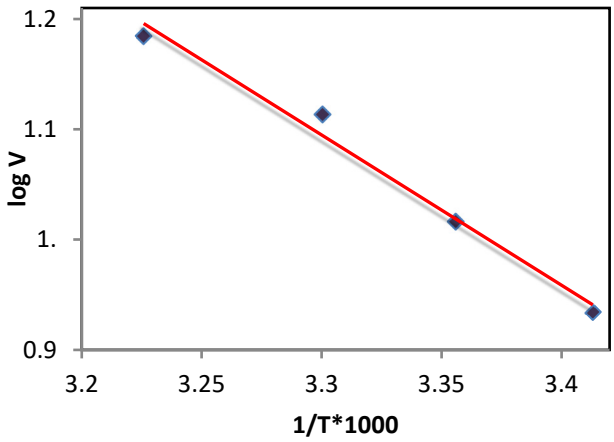

Figure 6. Arrhenius equation.

TABLE 3. Activated energy and Q10 values

Ea	Q10
6.22 Cal.mol^{-1}	1.0002

Eyring-Polanyi equation has been used to calculate enthalpy, entropy, and free energy for transition state as shown in fig 7.

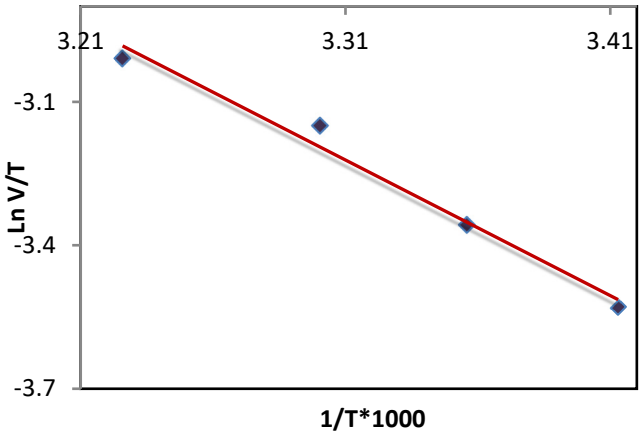

Figure 7. Erring-Polanyi equation

TABLE 4. Thermodynamic parameters for a transition state to form an ES complex

ΔH*	ΔS*	ΔG*
5.63 Cal.mol^{-1}	-34.83Cal.mol^{-1}K^{-1}	10.79Kcal. mol^{-1}

DISCUSSION

Results appear that there's a significant increase in Na/K-ATPase levels in leukemia patient serum, this increase belongs to quick analytics for RBCs and WBCs in Peripheral blood [16]. The first step in partial purification was precipitation by ammonium sulfate (70%) to remove amino acids and other extra peptides other than Na/K-ATPase, this step leads to reduced protein solubility because of the salting-out phenomenon [18]. Kinetic studies for isoenzyme I indicated that the optimum concentration of ATP was 1.25 mM. It is subject to the Michaels-Menten equation as is shown in Fig (3), these findings are in agreement with other studies [19], the Km value was 0.72mM, while the maximum velocity was 21.7U.min-1. While Km for the purified enzyme from sheep kidney was 0.19 mM this variance in Km values can be attributed to the difference of tissue sources [20,21]. The effect of pH made clear that enzyme activity increases with pH increase till it shows the highest activity at pH 7.4 then enzyme activity was reduced with increasing pH as shown in fig (4) because of the ionic groups of amino acids which compose the enzyme [18], since increase activity, more than 7.4 activated sites of the enzyme become very sensitive for H+ concentration and unable to form ES complex that might lead to loss of the activity [22]. These results agree with other studies [13, 23]. The optimum temperature for isoenzyme I was 37°C and this result agreed with other studies that made clear that the optimum temperature was 37°C [13,24] since enzymes have an optimum temperature similar to the temperature of tissues which is coming from them. In thermodynamic studies, the effect of temperature results undergoes to Arrhenius equation until 37°C since the rate of reaction changes with temperature change, activated energy was calculated from the Arrhenius equation slope as shown in fig (6). Q10 has been calculated by using equation (3), **the** Q10 value **agrees** with the fact that enzymatic reaction has **a** Q10 value between (1-2) [15**, 25**]. Table (4) made clear that the enthalpy value for the transition state was 5.63 cal.mol-1 this positive value refers to the endothermic reaction to form ES complex, and the entropy value was -34.83Cal.mol-1K-1 this negative value refers to ES complex much order than enzyme and substrate (less randomly), ΔG* value was 10.79Kcal.mol-1 this means that ES complex formation was not spontaneous (need for energy).

CONCLUSIONS

ATPase pump has distinct properties and varies with different sources. The Vmax of the conversion of ATP to ADP and Pi by Na/K-ATPase was 21.7 mM/min and Km was 0.72 mM. The optimum substrate concentration, optimum temperature, and pH were found to be 1.25mM, 37°C and 7.4 respectively.

REFERENCES

1. Greer JP, Foerster J,Rodgers GM, Glader B, Daniel A. Arber et al. Wintrobe's Clinical Hematology.14thed.Philadelphia, PA: WoltersKluwerHealth/Lippincott Williams & Wilkins;2019.
2. Nguyen, P.T., Deisl, C., Fine, M., Tippetts, T.S., Uchikawa, E., Bai, X.C.,& Levine, B.(2022). Structural basis for the gating mechanism of the human sodium-potassium pump. National library medicine 13(1),5293.
3. Pirahanchi,Y.,Jessu,R.,&Aeddula,N.R,(2023). Physiology, sodium-potassium pump.In StatePearls [Internet]. StatePearls Publishing.
4. Smith RS, et al ."Early role forNa+/K+-ATPase(ATP1A3) in brain development". Proceedings of the National Academy of Sciences of USA. 2021.118(25): e2023333118.
5. Clausen MV, Hilbers F, Poulsen H . The Structure and Function of the Na/K-ATPase Isoforms in Health and Disease, Front. Physio. 2017;8: 371.
6. Prabhakar S, Rajesh K, Krishna M, Syed I. "The modulation of erythrocythemia+/K+-ATPase activity by curcumin ". J Adv. Res. 2015; 6(6): 1023-1030.
7. Thomas L, Nicolas F, Markus K, Linda W, Kristoffer B, Alexander B, et al . Regulation of Neuronal Na/K-ATPase by Extracellular Scaffolding Proteins, Int. J Mole. Sci. 2018; 19(8): 2214.
8. Zhang Xi, Liang Zhong, Bei-Zhong Liu, Yan-Jun Gao, Yuan-Mei Gao and Xiu-Xiu Hu. (2013). Effect of GINS2 on proliferation and apoptosis in leukemic cell Line. International Journal of Medical Sciences. 10.1795-1804.
9. Jemal, A,. Siegel, R,. Xu, J et al. Cancer statistics. CA Cancer J Clin(2011).61:133.
10. Hulegårdh, E. GUPEA_ Epidemiological studies in de novo and secondary acute leukemia, (2018).90(3), 90–91.
11. Kirchgesser M, Dahlmann N. A Colorimetric Assay for the Determination of Acid Nucleoside Triphosphatase Activity. J Clin Chem Clin. Biochem . 1990; 28(6):407-411.

12. Duongly K C, Gabelli S B, Chapter 7-salting out of protein using ammonium sulfate precipitation.Meth Enzymol(2014):541:85.
13. Al Samurai, S. J. A., & Al Shaya, R. R. Z. M. (2019). Kinetic studies of Na+/K+-ATPase in tissue aerobic thyroid patients. Baghdad Science Journal, 16(3), 740–746.
14. Paul M, "Physical Chemistry Understanding our Chemical World ".John Wiley & Sons Ltd. UK..(2004).
15. Atkins. P.W ., "Physical Chemistry .,8th.Oxford.Univ, press Oxford 2006.
16. Jassim, K.A., Jassim, W.H., Mahdi, S.H., The effect of sunlight on medium density polyethylene Water pipes, Energy Procedia, 2017, 119, pp. 650–655.
17. Chaillou M, Rigoard P, Fares M, François C, Sottejeau Y, Maixent JM. Relation between -isoform and phosphatase activity of Na+,/K+-ATPase in rat skeletal muscle fiber types. Cell Mol Biol (Noisy-le-grand). 2011;25:57. Suppl: OL1520-7.
18. Mahdi, H.A., Jasim, K.A., Shaban, A.H., Manufacturing and improving the characteristics of the isolation of concrete composites by additive Styrofoam particulate, Energy Procedia, 2019, 157, pp. 158–163.
19. Holm TH, Lykke-Hartmann K . Insights into the Pathology of the α3 Na(+)/K(+)-ATPase Ion Pump in Neurological Disorders; Lessons from Animal Models, Front Physio. 2016; 7:209.
20. George J, Losos J. The living world .6th ed. New York: NY MC, Graw-Hill, 2010.
21. Helms JB, Saunders LP, Meyer J, Costa CJ, Plowman E, Williford N, Kinetic Characterization of Na, K-ATPase Inhibition by the Acetaminophen Metabolite N-Acetylbenzoquinoneimine. O J Mol Integ Physio.2015; 5: 1-17.
22. Jasim, K.A., Fadhil, R.N., The Effects of micro Aluminum fillers in Epoxy resin on the thermal conductivity, Journal of Physics: Conference Series, 2018, 1003(1), 012082.
23. Qader UI, Iqbal SA, Niazi. Z. Partial purification and characterization of intracellular alkaline phosphatase from the newly isolated strain of Bacillus subtillis KIBGE-HAS. Inter J of Microbiol. 2009;7(1).
24. Al ZahraaYaseen Alsajjad Mohammed A MohammedShow, Yaseen Alsajjad, Preparation of Ge -Se -Sb ternary alloys and study of the effect of antimony on electrical properties, extended and localized energy states, AIP Conf. Proc. 3018, 020037 (2023.
25. Méndez E, Caruso- Neves C, López Mananes AA. Two sodium pumps in the hepatopancreas of the intertidal euryhaline crab Neohelice granulate: biochemical characteristics and differential modulation after feeding. Canad J Zool. 2018; 96(6): 576-584.

The Neutron Yield of the (P, N) Reactions of Ruthenium (Ru44)

Israa Mudher Hassan [1,a], Mustafa H. Shareef [2,b], Mohammed H. Shareef [2,c]

[1] *Mustansiriyah University, College of basic education, Baghdad, Iraq*
[2] *College of Science, University of Karabuk ,Karnabuk, Turkey*

[a] Corresponding author: israamudher1@gmail.com
[b] samaeb85@gmail.com
[c] Ammar.m.1999.aa@gmail.com

Abstract. Calculated the cross sections of the 101Ru (p, n) 101Rh reaction in the current work. A computer software (MATALAB-17.0) in the ground level interaction in increments of energies (0.1 MeV). The stopping power was also computed and tabulated, and the Zeigler formula was utilized using the program-SRIM to account for the neutron yield in the creation of the quasi-experimental equation. The results were tabulated and linked a particular cross-section with energies. The average value of the integrand across this energy interval can be found by measuring the yield at two closely spaced energies, E1 and E2. It turns discovered that the values are directly proportional up to a value of more than 9 MeV for proton energy. When the proton energy approaches 9 mev, the neutron yield figures begin to rise and become almost constant. We observe that there has been very little change in the values.

INTRODUCTION

In general, the products m3 and m4 that result from particles colliding between two nuclei [1]. Note that any nuclear event that does not lead to the formation of a complex nucleus, erosion, and capture reactions, is considered a direct nuclear reaction. This means that the interaction between the falling particle and the target nucleus occurs in a much shorter period of time than the lifetime of the equivalent complex nucleus, but the products resulting from the formation of a complex nucleus appear fundamentally different [2]. Because of this, the time scales for the two reaction processes are completely different.

Nuclear Reaction Cross Sections

The cross-section, which measures the likelihood of a certain nuclear reaction [3] [*4*]:

$$\sigma = R / I \tag{1}$$

Where σ is the cross sections, R is the number of reactions per unit time per nucleus, and I is the number of incident particles per unit time per unit area [5] [6]. The cross-section, which lies inside the nuclear radius square, is a measurement of area. The barn is a frequently utilized unit [7][8].

The Stopping Power

It is a measure of how matter affects the kinetic energy of a charged particle as it passes through it. [9]. The ionization of all electrons of the target substance, and the excitation of the lower levels, are the main reasons for the stopping power of alpha particles and protons, i.e. charged particles. [10] [11], that is:

$$S_{tot.} = S_{neutron} + S_{electron} \tag{2}$$

Neutron YielD

Detection of the neutron yield for each incident particle and a unified target for single-energy particles, incident energy Eb, [12].

Technologies and Materials for Renewable Energy, Environment and Sustainability
AIP Conf. Proc. 3321, 020014-1–020014-4; https://doi.org/10.1063/5.0291606
Published under an exclusive license by AIP Publishing. 978-0-7354-5231-2/$30.00

$$Y = nt\,\sigma(E_b)\,\epsilon(E_b) \quad (3)$$

n = no. of atoms / volume, t= thickness, σ=cross sections, ϵ = efficiency of neutron[13].

$$Y(E_b) = \int_{E_{thr}}^{E_b} \frac{n\sigma(E)dE}{-(dE/dx)} \quad (4)$$

RESULTS AND DISCUSSIONS

Cross sections (E.A. Skakun, A.I. Stojanov, V.G. Batij) [14] for the energy range of 5 to 9 mev were used by the researcher in this investigation. Cross sections were derived using energy increments of 0.1 mev using simulation tools, as indicated in Table No.1. cross sections and their correlation with the proton energy are displayed in Figure 1. Also, figure (2) yielded the semi-empirical equation that is displayed below:

$$y = -0.00024x^3 + 0.015x^2 - 0.041x - 0.1 \quad (5)$$

y = cross-sections & x=protons energy

For values between 5 and 9 MeV, the connection is straightforward. Up until it hits 0.5598 barn times 9 mev, the reaction is more likely to occur at higher proton energies. Total stopping power were determined using Table No. 1 and the Zeckler equations in conjunction with the SRIM program [15, 16]. Equation No. 2 was then used to depict the findings, which are shown in Figure 2. A steady drop in the proton incident on the Ruthenium was observed in the link between the stopping powers.

$$ys = 0.00034x^2 - 0.0078x + 0.068 \quad (6)$$

Applying equation (4), the average cross-section, and st.p. =, the neutron yield for the 101Ru (p, n) 101Rh reaction was calculated and is shown in Table No. (1). Therefore, the values are directly proportional to the energy values of the incident proton, which reach 9 mev. As Figure (3) illustrates, we see that the numbers have just slightly changed. Figure 3 illustrates that the reaction's maximum neutron yield can be achieved at values between 9 and 4 mev.

Table 1. Proton energy as a function of the cross-section for the ^{101}Ru (p, n) ^{101}Rh reaction, Stopping power (MeV/(mg/cm^2)) and neutron yieldx10^4 (n/10^{6}proton).

proton Energy (MeV)	Cross Sections (barn)	Stopping power (MeV/(mg/cm^2))	neutron yieldx10^4 (n/10^{6}proton)	proton Energy (MeV)	Cross Sections (barn)	Stopping power (MeV/(mg/cm^2))	neutron yieldx10^4 (n/10^{6}proton)
5	0.0374	0.0377	0.1987	7.1	0.2883	0.0299	20.1758
5.1	0.0453	0.0372	0.4422	7.2	0.299	0.0296	22.1936
5.2	0.0532	0.0368	0.7315	7.3	0.3097	0.0294	24.3021
5.3	0.0611	0.0363	1.068	7.4	0.3204	0.0291	26.5031
5.4	0.069	0.0359	1.4527	7.5	0.3311	0.0289	28.7982
5.5	0.0769	0.0354	1.8869	7.6	0.3418	0.0286	31.1892
5.6	0.0848	0.035	2.371	7.7	0.3525	0.0283	33.6777
5.7	0.0926	0.0346	2.9062	7.8	0.3632	0.0281	36.2657
5.8	0.1005	0.0342	3.4937	7.9	0.3739	0.0278	38.9549
5.9	0.1084	0.0338	4.1346	8	0.3846	0.0275	41.7474
6	0.1227	0.0334	4.8686	8.1	0.3982	0.0273	44.6612
6.1	0.1386	0.0331	5.7064	8.2	0.4161	0.0271	47.7306
6.2	0.1545	0.0327	6.6503	8.3	0.4341	0.0269	50.9579
6.3	0.1704	0.0324	7.7025	8.4	0.4521	0.0267	54.3457
6.4	0.1863	0.032	8.8654	8.5	0.47	0.0265	57.8966
6.5	0.2022	0.0317	10.1413	8.6	0.488	0.0263	61.6132
6.6	0.2181	0.0314	11.5311	8.7	0.5059	0.026	65.4983
6.7	0.234	0.0311	13.037	8.8	0.5239	0.0258	69.5546
6.8	0.2499	0.0308	14.6613	8.9	0.5419	0.0256	73.7851
6.9	0.2658	0.0305	16.4064	9	0.5598	0.0254	78.1926
7	0.2776	0.0302	18.2473	-------	--------	--------	--------

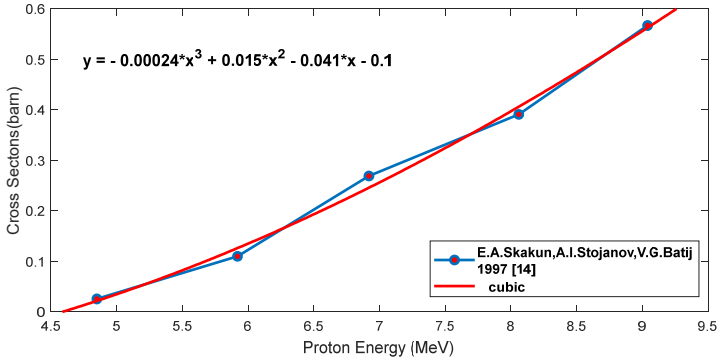

Figure 1. The cross sections as a function of 101Ru (p, n) ^{101}Rh reaction

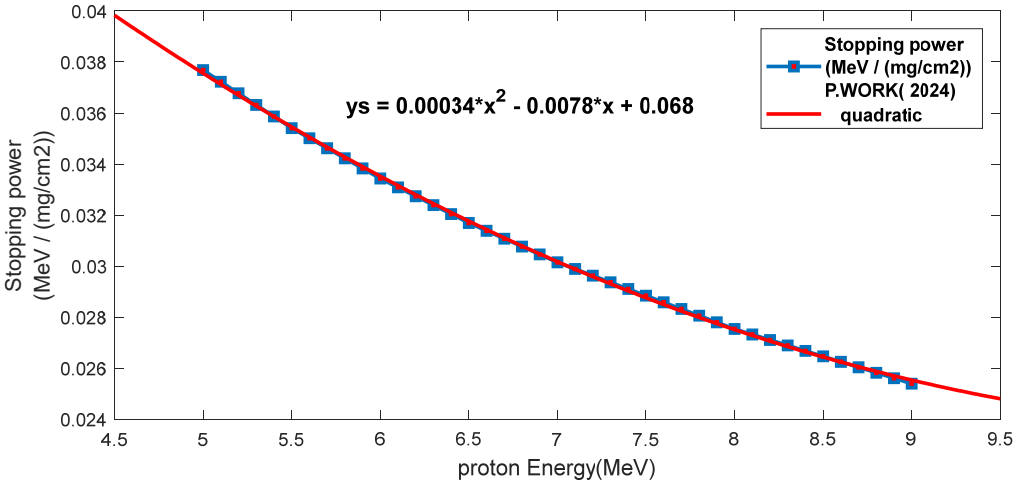

Figure 2. The total Stopping power as a function of proton energy for ^{101}Ru (p,n) ^{101}Rh reaction.

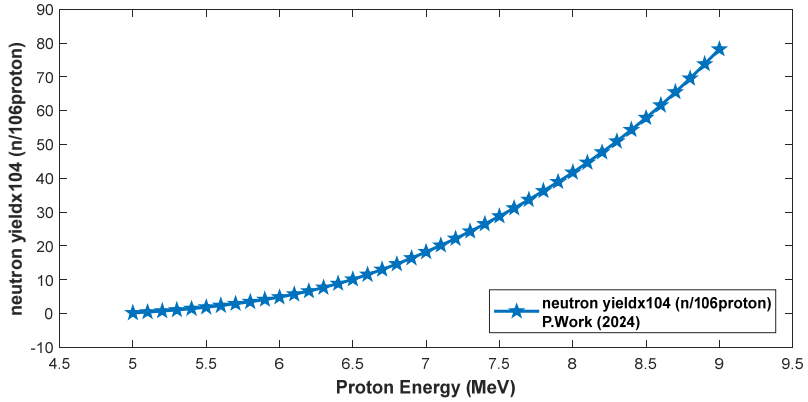

Figure. The yield of neutron as a function of proton energy for ^{101}Ru (p, n) ^{101}Rh reaction.

CONCLUSIONS

The cross sections shown in the table are linearly proportional to the proton energy for values between 5 and 9 MeV; And then it starts to decrease dramatically. The stopping power values have an inverse relationship with the proton power, exhibiting a gradual drop with increasing proton power. After the proton energy hits 9 mev, the neutron yield numbers start to rise and eventually approach a constant value.

REFERENCES

1. Podgoršak E. B.; "Radiation Physics for Medical Physicists" McGill University, Montreal, Book ,(2005).
2. Meyerhof W. E.; "Elements of Nucl. Phys." Mc Graw- Hill Book Inc. (1967).
3. Sameera A Ebrahiem, Maher N Sarsam, Hermez M Youhana, Nebras T Abd-Al-Hameed , " Determining of Cross Sections for 16O (n, α) 13C reaction from Cross Sections of 13C (α, n) 16O for the ground state" , Ibn AL-Haitham Journal For Pure and Applied Science, 26,1 , 109-115 , (2013).
4. Sameera Ahmed Ebrahiem and Sameer . H. AL- khalidi," Interaction Samarium and Holmium with Charged Particles (Alpha particles) " , JOURNAL OF COLLEGE OF EDUCATION , 17, 5 , p399-414 , (2016) .
5. H . M. Youhana, M. N. Sarsam, S. A. Ebrahiem , " Study of Cross Sections for 10 Li 10 Reaction From Cross Sections of Li a, n) Reaction Using the Reciprocity Theory for the Ground State" , Ibn AL-Haitham Journal For Pure and Applied Science , 22,1,2017 .
6. H..M. T. Hamadani, T. A. Younis, SA Ebrahiem, " Evaluation Of The Nuclear Data On(α,n)Reaction For Natural Molybdenum" , Ibn Al – Haitham Journal for pure and Applied Sciences , 23,3,2010 .
7. HM Youhana and SA Ebrahiem , " Determining of Cross Sections for 22Na (n, Î±) 19F reaction from Cross Sections of 19F (Î±, n) 22Na reaction using the reciprocity theory for the ground state" , Ibn AL-Haitham Journal For Pure and Applied Sciences , 22 , 2 , (2009).
8. Sameera Ahmed Ebrahiem Thurya Ali Ahmed Ali , "Study of the cross-sections of neutron interaction with lithium isotopes according to the reaction of the reverse reaction" AIP Conference Proceedings, 3018, https://doi.org/10.1063/5.0172831 , 020039-1- 020039-6 .
9. Jasim, K.A., Alwan, T.J., Mahdi, K.H., Mansour, H., The effect of neutron irradiation on the properties of Tl 0.6Pb0.3Cd0.1Ba2Ca 2Cu3O9-δ superconductors, Turkish Journal of Physics, 2013, 37(2), pp. 237–241. https://doi.org/10.3906/fiz-1203-16.
10. Saad Jasim Mohammed , Ali kalaf Aobaid , Sameera Ahmed Ebrahiem , " Calculation of total stopping power of the radioactive isotopes of Carbon-14 and Florine-18 used to treat cancer patients " AIP Conference Proceedings 3018 (https://doi.org/10.1063/5.0172339), 020032, (2023).
11. Z. J. Raheem, "Stopping Power and range of heavy ions in human body tissues." Ph.D. Thesis, University of Baghdad, Iraq, 2019.
12. Saad Jasim Mohammed , Ali kalaf Aobaid , Sameera Ahmed Ebrahiem " Calculation of protons stopping power in Yttrium-90 and Iodine -131 radioactive isotopes" , AIP Conference Proceedings 3018 (https://doi.org/10.1063/5.0172340), 020036 , (2023).
13. Bariq H. Walya , Sameera A. Ebrahiemb , " Study of the nuclear properties of an aluminum isotope in the production of third cycle elements" AIP Conference Proceedings 2437, 020087 (2022).
14. Ibrahim, Z.H., Ibrahim, S.A., Shaban, A.H., Jasim, K.A., Mohammed, M.K., Radiological Dose Assessments for Workers at the Italian Fuel Fabrication Facility at Al-Twaitha Site, Baghdad - Iraq with Aid of GIS Techniques, Energy Procedia, 2017, 119, pp. 709–717.
15. Noor Adil Mohammed* and Sameera Ahmed Ebrahiem , " Radioactivity levels of 238U, 234Th, 40K and 137C in the soil surface of selected regions from Baghdad governorate" , Int. J. Nuclear Energy Science and Technology, Vol. 14, No. 1 , (2020).
16. E.A.Skakun,A.I.Stojanov,V.G.Batij, "Excitation functions of (p,n) reactions on 99-Ru,100-Ru, 101-Ru and 102-Ru. 101-m-Rh production.", C,97TRIEST,2,1649,1997.

Calculate the cross sections for ^{235}Th (α, n) ^{238}U by the revers reaction for the ground state

Saad Jasim Mohammed [1,a)], Mustafa H. Shareef [2, b)] Mohammed H. Shareef [1]

[1] *Department of Basic Education College, Al-Anbar University, Anbar, Iraq*
[2] *College of Science, University of Karabuk, Karabuk, Turkey*

[a)] Corresponding author: saad.jassim@uoanbar.edu.iq
[b)] samaeb85@gmail.com

Abstract. Uranium-238 represents the largest percentage of natural uranium found in nature. Uranium represents an unstable element, as it releases radiation when it decays, as it releases alpha particles and a little of gamma rays, as alpha particles can travel short distances and cannot penetrate the human body, unlike... Gamma rays that penetrate the human body.In this research, The values of the cross sections were reached within the energy range (10-20 MeV) for neutron incident and increasing (0.2 MeV) each time, and it was found that the values of the cross sections change slightly with the energy of the incident neutron within the energy range (10-16 MeV), and after that they begin Increasing until the energy reaches (20 MeV), as shown in Figure 1, where we obtained the highest value for the cross sections, which is (15.4818 mbarn). The cross sections of the alpha particle for the reaction were obtained, and the reaction energy and threshold energy values were calculated using reverse reaction theory and relying on the spin and valence values of the reactants, products, and complex nuclei. It was also found that the values of the cross sections increase with the increase in the energy of the incident particle (alpha particle), because the target nucleus is heavy and has a large mass number, in addition to the fact that the alpha particle is also heavy.

INTRODUCTION

Thorium is a naturally radioactive element without human intervention. It is important for the production of nuclear energy [1], as thorium-based nuclear reactors have great safety features that reduce the risk of the spread of nuclear accidents. It is also of great importance in the economic, technical, and environmental aspects due to its natural abundance, as it exists naturally and is abundant. It is large compared to uranium and has a long half-life[2][3]. Uranium-238 represents the largest percentage of natural uranium found in nature [4] . Uranium represents an unstable element, as it releases radiation when it decays, as it releases alpha particles and a little of gamma rays, as alpha particles can travel short distances and cannot penetrate the human body, unlike... Gamma rays that penetrate the human body [5].

NUCLEAR REACTION CROSS SECTIONS

The cross-section is the specific nuclear reaction that is likely to occur and by determining the actual size of the nucleus [6], the study of cross-sections of reactions is fundamental and important in the study of Nuclear Systems [7]:

$$\sigma = R / I \tag{1}$$

Where σ is the cross-section of the nuclear reaction, R is the Number of interactions per unit of time, I is The number of incident particles per unit of time per unit area.The reaction cross section refers to a physical term that is calculated through a specific area. The larger the area, the more likely the reaction is to occur [8,9]. The cross-section is meant as a unit of area since its incidence is within the square of the nuclear radius The barn unit is always used to calculate the cross-section of a nuclear reaction, since barn = 10^{-24} cm^2 .Mostly, when particles are bombarded, the

Technologies and Materials for Renewable Energy, Environment and Sustainability
AIP Conf. Proc. 3321, 020015-1–020015-5; https://doi.org/10.1063/5.0289690
Published under an exclusive license by AIP Publishing. 978-0-7354-5231-2/$30.00

target reacts many times and produces a variety of elements, and the cross-section of the reaction products is calculated each time, as well and the cross-section of the reaction is calculated completely through the relationship: [10, 11]

$$\sigma_{tot} = \Sigma_i \sigma_i \quad (2)$$

Where σ_i is the cross-section of each reaction within the main reaction

Any specific reaction can be studied by calculating the kinetic energies of the reaction products, as devices for sensing radiation and particles are designed to classify the energy of each of them. Therefore, the basic and important information depends on cross-section calculations [12]. The cross-section of any reaction can be calculated through the use of quantum mechanics using mathematical models of nuclei. It is also possible to calculate the expected and observed values of the different cross-sections and compare them. The hypotheses of the nuclear models can be verified [13]. From the above, the cross-section gives a description of the interaction of particles with the substance that was defined above

RECIPROCITY THEOREM

If cross sections *A* (α, n) B are measured as functions of kinetic energy Kα (Kα = Kinetic energy of α-particle) [14, 15]. Using the reciprocity theorem, the cross sections B (n, α) A for the reverse reaction are calculated as a function of the kinetic energy of the neutrons Kn (Kn = Kinetic energy of neutrons)[16,17]. The reciprocity theorem is given according to the following relationship*:*

$$\sigma(\alpha,n) / \sigma(\alpha,n) D^2{}_\alpha = \sigma(n,\alpha) / g(n,\alpha) D^2{}_\alpha \quad (3)$$

Where σ (α, n), σ(n,α) represent cross-sections of (α,n) and (n, α) reactions respectively g is a statistical factor, D is the De–Broglie Wave Length divided by 2π and is given by:

$$D = \hbar / MV \quad (4)$$

Where ħ is the Dirac constant (h /2π), h is the plank constant, and *M* and *V* are the mass and velocity of α or n particle

RESULTS AND DISCUSSIONS

The values of the cross sections were obtained in energy steps of 0.2 MeV as shown in Table (1) and for an energy range of (10-20). MeV. Figure (1) shows the values of the cross sections and their relationship to the energy of the incident neutron, as the values of the cross sections change slightly with the power of the incident neutron for energy values that range between (10-16) MeV. Also, a semi-empirical equation was obtained from Figure (1), as shown below [18]:

$$y = - 0.0001x^5 + 0.011x^4 - 0.38x^3 + 6.1x^2 - 46x + 1.3e^{+02} \quad (5)$$

y= cross sections x= neutron energy

It was also shown that the cross sections begin to increase at the incident neutron energy of 16 MeV until it reaches 20 MeV, which is clear in Figure 1. where the highest value of the cross sections is 15.4818 mbarn.

Table 1. Cross section as a function of energies neutron $^{238}U\ (n,\alpha)\ ^{235}Th$ reactions

En (MeV)	Xn (mbarn)	En (MeV)	Xn (mbarn)	En (MeV)	Xn (mbarn)	En (MeV)	Xn (mbarn)
10	0.0274	12.6	0.1694	15.4	1.0962	18.0	5.55790
10.2	0.0326	12.8	0.1946	15.6	1.2507	18.2	6.28780
10.4	0.0378	13	0.2197	15.8	1.4294	18.4	7.01760
10.6	0.0437	13.2	0.2548	16.0	1.6081	18.6	7.83570
10.8	0.0503	13.4	0.2900	16.2	1.8516	18.8	8.74200
11	0.0568	13.6	0.3320	16.4	2.0951	19.0	9.64830
11.2	0.0660	14	0.4299	16.6	2.3811	19.2	10.7341

11.4	0.0752	14.2	0.4979	16.8	2.7095	19.4	11.8199
11.6	0.0862	14.4	0.5660	17.0	3.0378	19.6	12.9866
11.8	0.0990	14.6	0.6472	17.2	3.4748	19.8	14.2342
12	0.1119	14.8	0.7415	17.4	3.9117	20.0	15.4818
12.2	0.1299	15	0.8358	17.6	4.4157	----	-------
12.4	0.1479	15.2	0.966	17.8	4.9868	----	-------

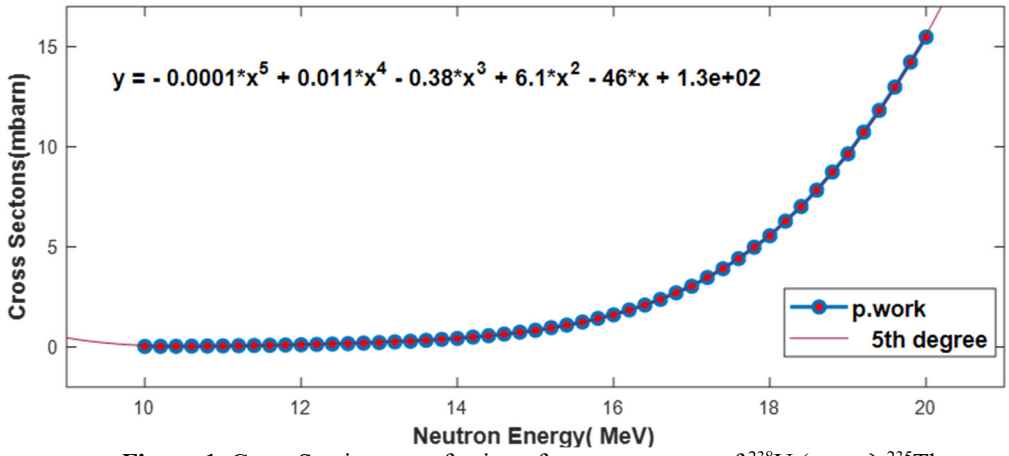

Figure 1. Cross Sections as a faction of neutron energy of ^{238}U (n, α) ^{235}Th

Using the theory of the reverse reaction, relying on the spin and parity values of the reactants, products, and complex nuclei, calculating the reaction energy and threshold energy values, the cross sections of the alpha particle for the reaction were obtained ^{235}Th (α, n) ^{238}U reaction as shown in Table No. 2. From Figure 2, it appears that the relationship between the cross sections of the reaction ^{235}Th (α, n) ^{238}U reaction with the energy of the incident alpha particle is relatively constant for the energy range (19.2080-24.4732) MeV, and after that, it begins to increase smoothly until it reaches the peak, which is the values confined between energies (24.6757-26.2958) MeV, so the relationship is with growing energy.Semi-empirical equations for the cross sections and their relationship with the falling particle were obtained from Figure 2 through a mathematical method (interpolation) and are shown below [19].

$$y = 9.7e\text{-}05x^4 - 0.0082x^3 + 0.26x^2 - 3.7x + 20 \quad (6)$$

Where y= cross sections x= alpha energy

The reason is that the target's nucleus is heavy and has a large mass number, in addition to the fact that the alpha particle is also heavy.

Table 2. cross section as a function of energies alpha particl^{235}Th (α, n) ^{238}U reaction.

ea (M)	xa(m bar)	ea (MeV)	xa (m bar)	ea (M)	xa (mbar)	ea (MeV)	xa (mbarn)
19.2080	0.0009	21.8406	0.0053	24.6757	0.0344	27.3084	0.1747
19.4105	0.0010	22.0431	0.0061	24.8782	0.0393	27.5109	0.1976
19.6130	0.0012	22.2456	0.0069	25.0808	0.0449	27.7134	0.2205
19.8155	0.0014	22.4481	0.0080	25.2833	0.0505	27.9159	0.2462
20.0180	0.0016	22.6506	0.0091	25.4858	0.0582	28.1184	0.2747
20.2205	0.0018	22.8531	0.0104	25.6883	0.0658	28.3209	0.3032
20.4230	0.0021	23.2582	0.0135	25.8908	0.0748	28.5234	0.3373
20.6255	0.0024	23.4607	0.0156	26.0933	0.0851	28.7259	0.3714
20.8280	0.0027	23.6632	0.0178	26.2958	0.0955	28.9284	0.4081
21.0306	0.0031	23.8657	0.0203	26.4983	0.1092	29.1309	0.4473
21.2331	0.0035	24.0682	0.0233	26.7008	0.1229	29.3335	0.4865
21.4356	0.0041	24.2707	0.0263	26.9033	0.1388	-------	-------
21.6381	0.0046	24.4732	0.0304	27.1059	0.1567	-------	-------

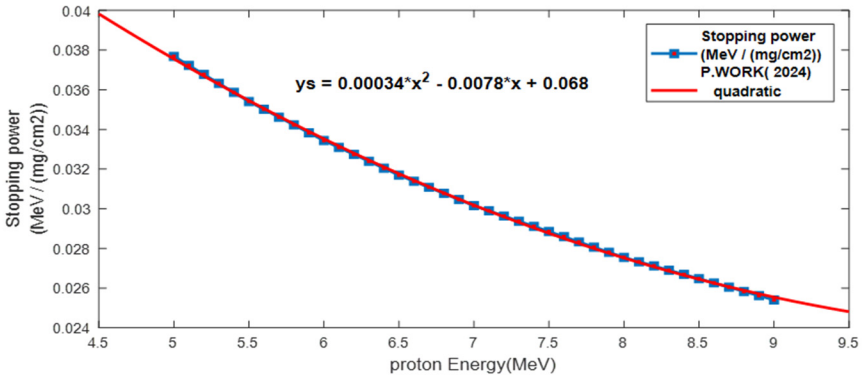

Figure 2. Cross Sections as a faction of alpha energy ^{235}Th (α, n) ^{238}U reaction

CONCLUSIONS

From comparing the results with studies available in the international literature, the values of the cross sections increase with the increase in the energy of the incident particle (the alpha particle). This concerns the target's heavy nucleus.

REFERENCES

1. Noor Adil Mohammed* and Sameera Ahmed Ebrahim, "Radioactivity levels of 238U, 234Th, 40K and 137C in the soil surface of selected regions from Baghdad governorate", Int. J. Nuclear Energy Science and Technology, Vol. 14, No. 1, (2020).
2. Rajesh Kumar Jyothi, Leonardo Gadelha Tumajan Costa De Melo, Rafael M. Santosand Ho-Sung Yoon," An overview of thorium as a prospective natural resource for future energy", Frontiers in Energy Research, 2023, DOI 10.3389/fenrg.2023.1132611.
3. Ebrahiem, Sameera A; Falih, Esraa H; Mahdi, Hind Abdul Majeed; Shaban, Auday H, "Indoor 222Rn measurement and hazards indices in houses of Al-Najaf province—Iraq", AIP Conference Proceedings, 2018.
4. Mohammed, N.A., Ebrahiem, S.A.; " Assessment of radiation risk parameters for natural radon in three Iraqi institutions for February", AIP Conference Proceedings 2307, 020003 (2020).
5. Iqra Zubair Awan and Abdul Qadeer Khan ," Uranium – The Element: Its Occurrence and Uses" , J.Chem.Soc.Pak., Vol. 37, No. 06, 2015.
6. Podgoršak E. B.; "Radiation Physics for Medical Physicists" McGill University, Montreal, Book, (2005).
7. W Packer, J Kopecky, R A Forrest A J Koning, and D A Rochman, The European Activation, File: EAF-2010 neutron-induced cross section Library - CCFE-R (10) 05
8. J-Ch Sublet, L, Howard Matis," Nuclear Science—A Guide to the Nuclear Science", Contemporary Physics Education Project (CPEP), Fifth Edition – October 2019.
9. S. Mubarakmand, M. Ahmad, et al,"Cross-section measurements with a neutron generator", Nuclear Instruments and Methods, vol. 115, pp. 345-347, 1974.
10. Thurya Ali Ahmed Ali, Sameera Ahmed Ebrahiem, " Study of the cross-sections of neutron interaction with lithium isotopes according to the reaction of the reverse reaction" , AIP Conference Proceedings 3018, 020039-1–020039-6, 2023.
11. Lilley J. " Nuclear physics " John Wiley & Sons, Ltd . (2001).
12. Bariq H. Walya, Sameera A. Ebrahiemb, " Study of the nuclear properties of an aluminum isotope in the production of third cycle elements" AIP Conference Proceedings 2437, 020087 (2022).
13. Jasim, K.A., Alwan, T.J., Mahdi, K.H., Mansour, H., The effect of neutron irradiation on the properties of Tl 0.6Pb0.3Cd0.1Ba2Ca 2Cu3O9-δ superconductors, Turkish Journal of Physics, 2013, 37(2), pp. 237–241. https://doi.org/10.3906/fiz-1203-16.
14. Ulrik S. Kesmodel, "Cross-sectional studies–what are they good for? ", Nordic Federation of Societies of Obstetrics and Gynecology, Acta Obstetricia et Gynecologica Scandinavica 97(2018) 388–393389.

15. Sameera Ahmed Ebrahiem Thurya Ali Ahmed Ali, “Study of the cross-sections of neutron interaction with lithium isotopes according to the reaction of the reverse reaction” AIP Conference Proceedings, 3018, 020039-1 - 020039-6.
16. Ibrahim, Z.H., Ibrahim, S.A., Shaban, A.H., Jasim, K.A., Mohammed, M.K., Radiological Dose Assessments for Workers at the Italian Fuel Fabrication Facility at Al-Twaitha Site, Baghdad - Iraq with Aid of GIS Techniques, Energy Procedia, 2017, 119, pp. 709–717.
17. Sameera Ahmed Ebrahiem and Sameer. H. AL- Khalidi, Interaction Samarium and Holmium with Charged Particles (Alpha particles), JOURNAL OF COLLEGE OF EDUCATION, 17, 5 , p399-414 , (2016).
18. Wagemans C., Weigmann H., Barthelemy, " Measurement and resonance analysis of the 33S(N,A)30Si cross sections", (W, WAGEMANS,860218) ,"SUBMITTED TO NUCL. PHYS. A", (1986).
19. Abbood, Noor Mohammed; Ebrahiem, Sameera Ahmed, Study of Nuclear Properties of High Purity Germanium”, Ibn AL-Haitham Journal for Pure and Applied Sciences, Vol. 33 No. 1 (2020).

Single and Cascade Reliability Stress-Strength Models of the Truncated Komal-Weibull Distribution

Sairan Hamza Raheem[1,2,a)] and Bayda Atiya Kalaf [1,b)]

[1] *Department of Mathematics, College of education for Pure Sciences- ibn Al-Haitham, University of Baghdad, Baghdad, Iraq*
[2] *IT Department, College of Computing and Information Technology, University of Garmian, Karkuk, Iraq*

[a)] sairan.hamza@garmian.edu.krd
[b)] Corresponding author: baydaa.a.k@ihcoedu.uobaghdad.edu.iq

Abstract. The stress-strength reliability models play a crucial role across various disciplines in advancing mathematical statistics, engineering, and medicine, but in many cases of lifetime data, the standard distribution can't fit all problems. Therefore, this paper considers two models of stress-strength models of the reliability system based on the [0,1] truncated mixture Komal-Weibull distribution. The first model is the single stress-strength model, while the second model is the cascade (1+1) model when the independent random variables belong to the interval [0,1].

Keywords: Stress-strength, reliability, truncated distribution, Weibull distribution, cascade model, mixture distribution

INTRODUCTION

In statistical engineering, the ability of an object to perform as required in a given operating context and over a given period of time is called reliability[1,2]. Rao defined reliability as "the probability that a system will perform its task over a specified time and under specified operating conditions" [3]. Since any device can fail and cause losses, whether in the form of human, moral, and material losses or in the form of time and labor losses [4], recent studies have focused on the stress strength (S-S) model of reliability as an important branch of reliability analysis, as it plays a role in various fields of science, including medicine, communication, military operations, and technology. The formula R=P(Y<X) for stress-strength single system shows that a system undergoing a stress-resistance build-up can fail in its function if the applied stress, normally represented by the random variable X, exceeds a random variable representing the strength Y of the system. This model is often considered in various research papers and has been studied extensively based on standard distributions [5-10]. An n-cascade system is a type of standby system with n components, functioning as a stress-strength model. Its reliability is defined by a function that includes parameters from identical and independent distributions for strength (X) and stress (Y), along with an attenuation factor (K) that reduces the stresses on subsequent components. This factor can be a constant, vary for different components, or be a random variable. The concept of this system was initially introduced by Pandit and Sriwastav [11]. Subsequently, Rekha and Chechu Raju [12] provided a closed-form solution for the stress-attenuated reliability function of an n-cascade system. In statistics, modeling lifetime data using standard probability distributions like Weibull, Lomax, Exponential, and Lindley is crucial for assessing reliability [13]. However, failures in a component population can arise from various sources [14], leading to heterogeneity that deviates from standard distributions. In such cases, mixture distributions are essential for accurately fitting the data and addressing complexities in reliability analyses [15]. Additionally, incomplete or absent sample values can lead to truncation, where certain values of a random variable are unmeasured due to being below or above a threshold [16]. This issue is common across various fields, including industry, biology, hydrology, reliability theory, and medicine. Recent studies give great attention to both S-S single and cascade reliability based on mixture and truncated distributions. Kanaparthi et al [17] dissected the

Technologies and Materials for Renewable Energy, Environment and Sustainability
AIP Conf. Proc. 3321, 020016-1–020016-10; https://doi.org/10.1063/5.0290563
Published under an exclusive license by AIP Publishing. 978-0-7354-5231-2/$30.00

statistical model of the New Rayleigh-Pareto cascade model. Haddad [18] discussed the mathematical formulas of a single system reliability stress-strength model, based on the Rayleigh Pareto distribution. Alamri et al [19] used Rayleigh and half-normal distribution in studying the S-S reliability. Mohamed [20] considered the reliability based on the gamma Lindley distribution. Raikar et al [21] utilized S-S for a two-parameter Weibull distribution. Ali [22] Reliability analysis of the Stress-Strength model from truncated Pareto distribution. EL-Sagheer et al [23] presented S-S model using uniform truncated negative Binomial distribution.

Thus, this paper aims to drive two models of S-S (single, cascade) of reliability function based on the right truncated Komal-Weibull distribution.

MATHEMATICAL FORMULATION

The Komal-Weibull distribution was introduced by [24] as a new mixture of Komal [25] and Weibull [26] distributions with the following probability density function and cumulative distribution function respectively

$$f_{kwd}(x,\Theta,\gamma,\rho)=\frac{\left(\Theta+\frac{\gamma}{\rho}\left(\frac{x}{\rho}\right)^{\gamma-1}\right)(\Theta^2+\Theta+\Theta x+1)-\Theta}{(\Theta^2+\Theta+1)}e^{-\left(\Theta x+\left(\frac{x}{\rho}\right)^{\gamma}\right)} \tag{1}$$

$$F_{kwd}(x,\Theta,\gamma,\rho)=1-\left(\frac{(\Theta^2+\Theta+\Theta x+1)}{(\Theta^2+\Theta+1)}e^{-\left(\Theta x+\left(\frac{x}{\rho}\right)^{\gamma}\right)}\right) \tag{2}$$

Such that $x\geq 0,\Theta,\gamma\ and\rho>0$, where γ represents the shape parameter while $\Theta and\rho$ represent the scale parameters. then based on [27] the pdf and cdf of the [0,1] truncated Komal-Weibull distribution (TKWD) can be obtained and defined as

$$g_{TIGRD}(x,\Theta,\gamma,\rho)=\frac{f(x)}{F(1)} \tag{3}$$

Thus, the probability density function is:

$$g_{TKWD}(x,\Theta,\gamma,\rho)=\frac{\left[\frac{\left(\Theta+\frac{\gamma}{\rho}\left(\frac{x}{\rho}\right)^{\gamma-1}\right)(\Theta^2+\Theta+\Theta x+1)-\Theta}{(\Theta^2+\Theta+1)}\right]e^{-\left(\Theta x+\left(\frac{x}{\rho}\right)^{\gamma}\right)}}{1-\left[\frac{(\Theta^2+2\Theta+1)}{(\Theta^2+\Theta+1)}\right]e^{-\left(\Theta+\frac{1}{\rho^{\gamma}}\right)}}$$

$$=\frac{\left[\left(\Theta+\frac{\gamma}{\rho}\left(\frac{x}{\rho}\right)^{\gamma-1}\right)(\Theta^2+\Theta+\Theta x+1)-\Theta\right]e^{-\left(\Theta x+\left(\frac{x}{\rho}\right)^{\gamma}\right)}}{(\Theta^2+\Theta+1)-(\Theta^2+2\Theta+1)e^{-\left(\Theta+\frac{1}{\rho^{\gamma}}\right)}} \tag{4}$$

And the cumulative distribution function is derived as follows:

$$G_{TKWD}(x,\Theta,\gamma,\rho)=\frac{F(x)}{F(1)} \tag{5}$$

then

$$G_{TKWD}(x,\Theta,\gamma,\rho)=\frac{1-\left(\frac{(\Theta^2+\Theta+\Theta x+1)}{(\Theta^2+\Theta+1)}e^{-\left(\Theta x+\left(\frac{x}{\rho}\right)^{\gamma}\right)}\right)}{1-\left[\frac{(\Theta^2+2\Theta+1)}{(\Theta^2+\Theta+1)}\right]e^{-\left(\Theta+\frac{1}{\rho^{\gamma}}\right)}} \tag{6}$$

or

$$G_{TKWD}(x,\Theta,\gamma,\rho)=\frac{(\Theta^2+\Theta+1)-(\Theta^2+\Theta+\Theta x+1)e^{-\left(\Theta x+\left(\frac{x}{\rho}\right)^{\gamma}\right)}}{(\Theta^2+\Theta+1)-(\Theta^2+2\Theta+1)e^{-\left(\Theta+\frac{1}{\rho^{\gamma}}\right)}} \tag{7}$$

RELIABILITY AND HAZARD FUNCTIONS

Let X be continuous r.v with probability density function and the cumulative distribution function as in (6) and (4) respectively then the survival function of [0,1] truncated Komal-Weibull distribution is:

$$R_{TKWD}=1-G_{TKWD}(x,\Theta,\gamma,\rho)=\frac{(\Theta^2+\Theta+\Theta x+1)e^{-\left(\Theta x+\left(\frac{x}{\rho}\right)^{\gamma}\right)}-(\Theta^2+2\Theta+1)e^{-\left(\Theta+\frac{1}{\rho^{\gamma}}\right)}}{(\Theta^2+\Theta+1)-(\Theta^2+2\Theta+1)e^{-\left(\Theta+\frac{1}{\rho^{\gamma}}\right)}} \tag{8}$$

And the hazard function is:

$$H_{TKWD}(x)=\frac{g_{TKWD}(x,\Theta,\gamma,\rho)}{R_{TKWD}(x,\Theta,\gamma,\rho)}=\frac{\left[\left(\Theta+\frac{\gamma}{\rho}\left(\frac{x}{\rho}\right)^{\gamma-1}\right)(\theta^2+\Theta+\Theta x+1)-\Theta\right]e^{-\left(\Theta x+\left(\frac{x}{\rho}\right)^{\gamma}\right)}}{(\Theta^2+\Theta+\Theta x+1)e^{-\left(\Theta x+\left(\frac{x}{\rho}\right)^{\gamma}\right)}-(\Theta^2+2\Theta+1)e^{-\left(\Theta+\frac{1}{\rho^{\gamma}}\right)}} \tag{9}$$

THE SYSTEM RELIABILITY IN STRESS-STRENGTH SINGLE COMPONENT MODEL R_{SI} =P(Y<X)

Suppose x and y are two random variables that follow the RTKWD with parameters $(\boldsymbol{x},\boldsymbol{\theta_1},\boldsymbol{\gamma},\boldsymbol{\rho})$ and $(\boldsymbol{x},\boldsymbol{\theta_2},\boldsymbol{\gamma},\boldsymbol{\rho})$ as strength and stress, respectively. From equation (4) the probability density function of random variables x and y which are distributed as RTKWD have the following forms;

$$g(x,\theta_1,\gamma,\rho)=\begin{cases}\dfrac{\left[\dfrac{\left(\theta_1+\frac{\gamma}{\rho}\left(\frac{x}{\rho}\right)^{\gamma-1}\right)\left(\theta_1^2+\theta_1+\theta_1x+1\right)-\theta_1}{(\theta^2+\theta+1)}\right]e^{-\left(\theta_1x+\left(\frac{x}{\rho}\right)^{\gamma}\right)}}{1-\left[\dfrac{(\theta_1^2+2\theta_1+1)}{(\theta_1^2+\theta_1+1)}\right]e^{-\left(\theta_1+\frac{1}{\rho^{\gamma}}\right)}} & for\ 0\le x\le 1,\ \theta_1,\gamma\ and\rho\ >0\\ 0 & \text{other wise}\end{cases} \tag{10}$$

$$z(y,\theta_2,\gamma,\rho)=\begin{cases}\dfrac{\left[\dfrac{\left(\theta_2+\frac{\gamma}{\rho}\left(\frac{x}{\rho}\right)^{\gamma-1}\right)\left(\theta_2^2+\theta_2+\theta_2x+1\right)-\theta_2}{(\theta^2+\theta+1)}\right]e^{-\left(\theta_2x+\left(\frac{x}{\rho}\right)^{\gamma}\right)}}{1-\left[\dfrac{(\theta_2^2+2\theta_2+1)}{(\theta_2^2+\theta_2+1)}\right]e^{-\left(\theta_2+\frac{1}{\rho^{\gamma}}\right)}} & for\ 1\le y\ \le 1,\ \theta_2,\gamma\ and\rho\ >0\\ 0 & \text{other wise}\end{cases} \tag{11}$$

And from equation (6), the cumulative distribution function (c.d.f) of X and Y have the form below:

$$G(x,\theta_1,\gamma,\rho)=\frac{1-\frac{\left(\theta_1^2+\theta_1+\theta_1x+1\right)}{(\theta_1^2+\theta_1+1)}e^{-\left(\theta_1x+\left(\frac{x}{\rho}\right)^{\gamma}\right)}}{1-\left[\frac{(\theta_1^2+2\theta_1+1)}{(\theta_1^2+\theta_1+1)}\right]e^{-\left(\theta_1+\frac{1}{\rho^{\gamma}}\right)}} \tag{12}$$

$$Z(y,\theta_2,\gamma,\rho)=\frac{1-\frac{\left(\theta_2^2+\theta_2+\theta_2y+1\right)}{(\theta_2^2+\theta_2+1)}e^{-\left(\theta_2y+\left(\frac{y}{\rho}\right)^{\gamma}\right)}}{1-\left[\frac{(\theta_2^2+2\theta_2+1)}{(\theta_2^2+\theta_2+1)}\right]e^{-\left(\theta_2+\frac{1}{\rho^{\gamma}}\right)}} \tag{13}$$

The system reliability in the S-S model is defined as below:

$$R_{si}=\ P(Y<X\ )=\int_0^1\int_0^x g(x,\theta_1,\gamma,\rho)z(x,\theta_2,\gamma,\rho)dxdy$$

$$R_{si}=\int_0^1 G_y(x,\Theta,\gamma,\rho)g(x,\Theta,\gamma,\rho)dx$$

$$R_{si}=\int_0^1\frac{1-\frac{\left(\theta_2^2+\theta_2+\theta_2x+1\right)}{(\theta_2^2+\theta_2+1)}e^{-\left(\theta_2x+\left(\frac{x}{\rho}\right)^{\gamma}\right)}}{1-\left[\frac{(\theta_2^2+2\theta_2+1)}{(\theta_2^2+\theta_2+1)}\right]e^{-\left(\theta_2+\frac{1}{\rho^{\gamma}}\right)}}\cdot\frac{\left[\dfrac{\left(\theta_1+\frac{\gamma}{\rho}\left(\frac{x}{\rho}\right)^{\gamma-1}\right)\left(\theta_1^2+\theta_1+\theta_1x+1\right)-\theta_1}{(\theta_1^2+\theta_1+1)}\right]e^{-\left(\theta_1x+\left(\frac{x}{\rho}\right)^{\gamma}\right)}}{1-\left[\dfrac{(\theta_1^2+2\theta_1+1)}{(\theta_1^2+\theta_1+1)}\right]e^{-\left(\theta_1+\frac{1}{\rho^{\gamma}}\right)}}dx \tag{14}$$

$$= \frac{1}{\left(1-\left[\frac{(\theta_2^2+2\theta_2+1)}{(\theta_2^2+\theta_2+1)}\right]e^{-\left(\theta_2+\frac{1}{\rho^\gamma}\right)}\right)}\int_0^1\left[1\right.$$

$$\left.-\frac{(\theta_2^2+\theta_2+\theta_2x+1)}{(\theta_2^2+\theta_2+1)}e^{-\left(\theta_2x+\left(\frac{x}{\rho}\right)^\gamma\right)}\right].\frac{\left[\frac{\left(\theta_1+\frac{\gamma}{\rho}\left(\frac{x}{\rho}\right)^{\gamma-1}\right)(\theta_1^2+\theta_1+\theta_1x+1)-\theta_1}{(\theta_1^2+\theta_1+1)}\right]e^{-\left(\theta_1x+\left(\frac{x}{\rho}\right)^\gamma\right)}}{1-\left[\frac{(\theta_1^2+2\theta_1+1)}{(\theta_1^2+\theta_1+1)}\right]e^{-\left(\theta_1+\frac{1}{\rho^\gamma}\right)}}e^{-\left(\theta_1x+\left(\frac{x}{\rho}\right)^\gamma\right)}dx$$

Since $g(x,\theta_1,\gamma,\rho)$ is pdf then

$$R_{si} = \frac{1}{\left(1-\left[\frac{(\theta_2^2+2\theta_2+1)}{(\theta_2^2+\theta_2+1)}\right]e^{-\left(\theta_2+\frac{1}{\rho^\gamma}\right)}\right)}$$

$$-\frac{1}{\left(1-\left[\frac{(\theta_2^2+2\theta_2+1)}{(\theta_2^2+\theta_2+1)}\right]e^{-\left(\theta_2+\frac{1}{\rho^\gamma}\right)}\right)}\int_0^1\left[\frac{(\theta_2^2+\theta_2+\theta_2x+1)}{(\theta_2^2+\theta_2+1)}e^{-(\theta_2x+(x)^\gamma)}\right]$$

$$\times\frac{\left[\frac{\left(\theta_1+\frac{\gamma}{\rho}\left(\frac{x}{\rho}\right)^{\gamma-1}\right)(\theta_1^2+\theta_1+\theta_1x+1)-\theta_1}{(\theta_1^2+\theta_1+1)}\right]e^{-\left(\theta_1x+\left(\frac{x}{\rho}\right)^\gamma\right)}}{1-\left[\frac{(\theta_1^2+2\theta_1+1)}{(\theta_1^2+\theta_1+1)}\right]e^{-\left(\theta_1+\frac{1}{\rho^\gamma}\right)}}e^{-\left(\theta_1x+\left(\frac{x}{\rho}\right)^\gamma\right)}dx$$

Let $w_1 = \frac{1}{\left(1-\left[\frac{(\theta_1^2+2\theta_1+1)}{(\theta_1^2+\theta_1+1)}\right]e^{-\left(\theta_1+\frac{1}{\rho^\gamma}\right)}\right)}$ and $w_2 = \frac{1}{\left(1-\left[\frac{(\theta_2^2+2\theta_2+1)}{(\theta_2^2+\theta_2+1)}\right]e^{-\left(\theta_2+\frac{1}{\rho^\gamma}\right)}\right)}$

then

$$R_{si} = w_2 - w_1w_2\int_0^1\left[\frac{(\theta_2^2+\theta_2+\theta_2x+1)}{(\theta_2^2+\theta_2+1)}e^{-\left(\theta_2x+\left(\frac{x}{\rho}\right)^\gamma\right)}\right]\times\frac{\left[\left(\theta_1+\frac{\gamma}{\rho}\left(\frac{x}{\rho}\right)^{\gamma-1}\right)(\theta_1^2+\theta_1+\theta_1x+1)-\theta_1\right]e^{-\left(\theta_1x+\left(\frac{x}{\rho}\right)^\gamma\right)}}{(\theta_1^2+\theta_1+1)}dx$$

$$= w_2 - \frac{w_1w_2}{(\theta_2^2+\theta_2+1)(\theta_1^2+\theta_1+1)}\int_0^1\left[(\theta_2^2+\theta_2+\theta_2x+1)e^{-\left(\theta_2x+\left(\frac{x}{\rho}\right)^\gamma\right)}\right]\times\left[\left(\theta_1+\frac{\gamma}{\rho}\left(\frac{x}{\rho}\right)^{\gamma-1}\right)(\theta_1^2+\theta_1+\theta_1x+1)-\theta_1\right]e^{-\left(\theta_1x+\left(\frac{x}{\rho}\right)^\gamma\right)}dx$$

$$= w_2 - \frac{w_1w_2}{(\theta_2^2+\theta_2+1)(\theta_1^2+\theta_1+1)}\int_0^1\left[(\theta_2^2+\theta_2+\theta_2x+1)e^{-\left(\theta_2x+\left(\frac{x}{\rho}\right)^\gamma\right)}\right]$$

$$\times\left[\theta_1^3+\theta_1^2+x\theta_1^2+\frac{\gamma}{\rho}\left(\frac{x}{\rho}\right)^{\gamma-1}\theta_1^2+\frac{\gamma}{\rho}\left(\frac{x}{\rho}\right)^{\gamma-1}\theta_1+\frac{\gamma}{\rho^\gamma}x^\gamma\theta_1+\frac{\gamma}{\rho}\left(\frac{x}{\rho}\right)^{\gamma-1}\right]e^{-\left(\theta_1x+\left(\frac{x}{\rho}\right)^\gamma\right)}dx$$

$$= w_2 - \frac{w_1w_2}{(\theta_2^2+\theta_2+1)(\theta_1^2+\theta_1+1)}\int_0^1\left[(\theta_2^2+\theta_2+1)+(\theta_2x)\right]e^{-\left(\theta_2x+\left(\frac{x}{\rho}\right)^\gamma\right)}$$

$$\times\left[\theta_1^3+\theta_1^2+x\theta_1^2+\frac{\gamma}{\rho}\left(\frac{x}{\rho}\right)^{\gamma-1}\theta_1^2+\frac{\gamma}{\rho}\left(\frac{x}{\rho}\right)^{\gamma-1}\theta_1+\frac{\gamma}{\rho^\gamma}x^\gamma\theta_1+\frac{\gamma}{\rho}\left(\frac{x}{\rho}\right)^{\gamma-1}\right]e^{-\left(\theta_1x+\left(\frac{x}{\rho}\right)^\gamma\right)}dx$$

$$= w_2 - \frac{w_1 w_2}{(\theta_2^2+\theta_2+1)(\theta_1^2+\theta_1+1)}[(\theta_2^2+\theta_2+1)]\int_0^1 \left[\theta_1^3+\theta_1^2+x\theta_1^2+\frac{\gamma}{\rho}\left(\frac{x}{\rho}\right)^{\gamma-1}\theta_1^2+\frac{\gamma}{\rho}\left(\frac{x}{\rho}\right)^{\gamma-1}\theta_1+\frac{\gamma}{\rho^\gamma}x^\gamma\theta_1 + \frac{\gamma}{\rho}\left(\frac{x}{\rho}\right)^{\gamma-1}\right].e^{-\left\{(\theta_1+\theta_2)x+2\left(\frac{x}{\rho}\right)^\gamma\right\}}dx$$

$$-\frac{w_1}{w_2}\int_0^1 [(\theta_2 x)]\left[\theta_1^3+\theta_1^2+x\theta_1^2+\frac{\gamma}{\rho}\left(\frac{x}{\rho}\right)^{\gamma-1}\theta_1^2+\frac{\gamma}{\rho}\left(\frac{x}{\rho}\right)^{\gamma-1}\theta_1+\frac{\gamma}{\rho^\gamma}\theta_1+\frac{\gamma}{\rho}\left(\frac{x}{\rho}\right)^{\gamma-1}\right].e^{-\left\{(\theta_1+\theta_2)x+2\left(\frac{x}{\rho}\right)^\gamma\right\}}dx$$

Let

$$R_{si} = w_2 - \frac{w_1 w_2}{(\theta_2^2+\theta_2+1)(\theta_1^2+\theta_1+1)}(A+B) \quad (15)$$

Where

$$A = [(\theta_2^2+\theta_2+1)]\int_0^1\left[\theta_1^3+\theta_1^2+x\theta_1^2+\frac{\gamma}{\rho}\left(\frac{x}{\rho}\right)^{\gamma-1}\theta_1^2+\frac{\gamma}{\rho}\left(\frac{x}{\rho}\right)^{\gamma-1}\theta_1+\frac{\gamma}{\rho^\gamma}x^\gamma\theta_1+\frac{\gamma}{\rho}\left(\frac{x}{\rho}\right)^{\gamma-1}\right].e^{-\left\{(\theta_1+\theta_2)x+2\left(\frac{x}{\rho}\right)^\gamma\right\}}dx \quad (16)$$

$$B = \int_0^1[(\theta_2 x)]\left[\theta_1^3+\theta_1^2+x\theta_1^2+\frac{\gamma}{\rho}\left(\frac{x}{\rho}\right)^{\gamma-1}\theta_1^2+\frac{\gamma}{\rho}\left(\frac{x}{\rho}\right)^{\gamma-1}\theta_1+\frac{\gamma}{\rho^\gamma}\theta_1+\frac{\gamma}{\rho}\left(\frac{x}{\rho}\right)^{\gamma-1}\right].e^{-\left\{(\theta_1+\theta_2)x+2\left(\frac{x}{\rho}\right)^\gamma\right\}}dx \quad (17)$$

We'll evaluate q (15) as bellow:

$$A = (\theta_2^2+\theta_2+1)\int_0^1\left[\theta_1^3+\theta_1^2+x\theta_1^2+\frac{\gamma}{\rho}\left(\frac{x}{\rho}\right)^{\gamma-1}\theta_1^2+\frac{\gamma}{\rho}\left(\frac{x}{\rho}\right)^{\gamma-1}\theta_1+\frac{\gamma}{\rho^\gamma}x^\gamma\theta_1+\frac{\gamma}{\rho}\left(\frac{x}{\rho}\right)^{\gamma-1}\right].e^{-\left\{(\theta_1+\theta_2)x+2\left(\frac{x}{\rho}\right)^\gamma\right\}}dx$$

A Taylor expansion is used to reduce

$$e^{-\left\{(\theta_1+\theta_2)x+2\left(\frac{x}{\rho}\right)^\gamma\right\}} = \sum_{r=0}^{\infty}\frac{(-\theta_1-\theta_2)^r}{r!}\sum_{s=0}^{\infty}\frac{(-2)^i}{s!\,\rho^{\gamma s}}\,x^{\gamma s+r}$$

$$A = (\theta_2^2+\theta_2+1)\sum_{r=0}^{\infty}\frac{(-\theta_1-\theta_2)^r}{r!}\sum_{s=0}^{\infty}\frac{(-2)^s}{s!\,\rho^{\gamma s}}\int_0^1 x^{\gamma s+r}\left[\theta_1^3+\theta_1^2+x\theta_1^2+\frac{\gamma}{\rho}\left(\frac{x}{\rho}\right)^{\gamma-1}\theta_1^2+\frac{\gamma}{\rho}\left(\frac{x}{\rho}\right)^{\gamma-1}\theta_1 + \frac{\gamma}{\rho^\gamma}x^\gamma\theta_1+\frac{\gamma}{\rho}\left(\frac{x}{\rho}\right)^{\gamma-1}\right]dx$$

$$= (\theta_2^2+\theta_2+1)\sum_{r=0}^{\infty}\frac{(-\theta_1-\theta_2)^r}{r!}\sum_{s=0}^{\infty}\frac{(-2)^s}{s!\rho^{\gamma s}}\left(\frac{\theta_1^3+\theta_1^2}{\gamma s+r+1}+\frac{\theta_1^2}{\gamma s+r+2}+\frac{\gamma(\theta_1^2+\theta_1+1)}{\rho^\gamma[\gamma(s+1)+r]}+\frac{\gamma\theta_1}{\rho^\gamma[\gamma(s+1)+r+1]}\right) \quad (18)$$

recall equation (16)

$$B = \theta_2\sum_{r=0}^{\infty}\frac{(-\theta_1-\theta_2)^r}{r!}\sum_{s=0}^{\infty}\frac{(-2)^s}{s!\rho^{\gamma s}}\left(\frac{\theta_1^3+\theta_1^2}{\gamma s+r+2}+\frac{\theta_1^2}{\gamma s+r+3}+\frac{\gamma(\theta_1^2+\theta_1+1)}{\rho^\gamma[\gamma(s+1)+r+1]}+\frac{\gamma\theta_1}{\rho^\gamma[\gamma(s+1)+r+2]}\right) \quad (19)$$

Substitute (17) and (18) in (14) we get with simplifying to get:

$$R_{si} = w_2 - \frac{w_1 w_2}{(\theta_2^2+\theta_2+1)(\theta_1^2+\theta_1+1)}\sum_{r=0}^{\infty}\frac{(-\theta_1-\theta_2)^r}{r!}\sum_{s=0}^{\infty}\frac{(-2)^s}{s!\rho^{\gamma s}}\left\{(\theta_2^2+\theta_2+1)\left(\frac{\theta_1^3+\theta_1^2}{\gamma s+r+1}+\frac{\theta_1^2}{\gamma s+r+2}+\frac{\gamma(\theta_1^2+\theta_1+1)}{\rho^\gamma[\gamma(s+1)+r]}+\frac{\gamma\theta_1}{\rho^\gamma[\gamma(s+1)+r+1]}\right)+\theta_2\left(\frac{\theta_1^3+\theta_1^2}{\gamma s+r+2}+\frac{\theta_1^2}{\gamma s+r+3}+\frac{\gamma(\theta_1^2+\theta_1+1)}{\rho^\gamma[\gamma(s+1)+r+1]}+\frac{\gamma\theta_1}{\rho^\gamma[\gamma(s+1)+r+2]}\right)\right\} \quad (20)$$

CASCADE RELIABILITY MODEL (1+1)

Let $X_1 and\ X_2$ are the strengths with one fundamental component and one standby component and i.i.d with pdf follows [0,1] truncated Komal-Weibull distribution with unknown parameter θ_1 when activated faces the stresses random variables $Y_1 and\ Y_2$ followed[0,1] truncated Komal-Weibull distribution with unknown

parameter θ_2 In a cascade system, after every failure, the stress gets modified by attenuation factor (k) such that: $Y_2 = kY_1, Y_3 = kbY_2 = k^2Y_1, \dots, Y_i = k^{i-1}Y_i; k > 1$.[28] the expression for the reliability cascade model (1+1) function is given by

$$R_c = R_1 + R_2$$

Where

$$R_1 = R_{si} = P(Y < X)$$

And

$$R_2 = p[X_1 < Y_1, X_2 \geq Y_2 = p[X_1 < Y_1, mX_1 \geq bY_1]$$

$$R_2 = \int_0^1 [G_{x_1}(y_1)][\bar{G}_{x_1}(\frac{b}{m} y_1)]z(y_1)dy_1 \tag{21}$$

Thus, based on equation (11) and (12)

$$R_2 = \int_0^1 \frac{1-\frac{(\theta_1^2+\theta_1+\theta_1 y_1+1)}{(\theta_1^2+\theta_1+1)}e^{-\left(\theta_1 y_1+\left(\frac{y_1}{\rho}\right)^\gamma\right)}}{1-\left[\frac{(\theta_1^2+2\theta_1+1)}{(\theta_1^2+\theta_1+1)}\right]e^{-\left(\theta_1+\frac{1}{\rho^\gamma}\right)}} \times \left[1 - \frac{1-\frac{(\theta_1^2+\theta_1+\theta_1\frac{k}{m}y_1+1)}{(\theta_1^2+\theta_1+1)}e^{-\left(\theta_1\frac{ky_1}{m}+\left(\frac{ky_1}{m\rho}\right)^\gamma\right)}}{1-\left[\frac{(\theta_1^2+2\theta_1+1)}{(\theta_1^2+\theta_1+1)}\right]e^{-\left(\theta_1+\frac{1}{\rho^\gamma}\right)}}\right] \times \frac{\left[\frac{\left(\theta_2+\frac{\gamma}{\rho}\left(\frac{y_1}{\rho}\right)^{\gamma-1}\right)(\theta_2^2+\theta_2+\theta_2 y_1+1)-\theta_2}{(\theta_2^2+\theta_2+1)}\right]e^{-\left(\theta_2 y_1+\left(\frac{y_1}{\rho}\right)^\gamma\right)}}{1-\left[\frac{(\theta_2^2+2\theta_2+1)}{(\theta_2^2+\theta_2+1)}\right]e^{-\left(\theta_2+\frac{1}{\rho^\gamma}\right)}} dy$$

$$= \int_0^1 \frac{1-\frac{(\theta_1^2+\theta_1+\theta_1 y_1+1)}{(\theta_1^2+\theta_1+1)}e^{-\left(\theta_1 y_1+\left(\frac{y_1}{\rho}\right)^\gamma\right)}}{1-\left[\frac{(\theta_1^2+2\theta_1+1)}{(\theta_1^2+\theta_1+1)}\right]e^{-\left(\theta_1+\frac{1}{\rho^\gamma}\right)}} \times \frac{\left[\frac{\left(\theta_2+\frac{\gamma}{\rho}\left(\frac{y_1}{\rho}\right)^{\gamma-1}\right)(\theta_2^2+\theta_2+\theta_2 y_1+1)-\theta_2}{(\theta_2^2+\theta_2+1)}\right]e^{-\left(\theta_2 y_1+\left(\frac{y_1}{\rho}\right)^\gamma\right)}}{1-\left[\frac{(\theta_2^2+2\theta_2+1)}{(\theta_2^2+\theta_2+1)}\right]e^{-\left(\theta_2+\frac{1}{\rho^\gamma}\right)}} dy -$$

$$\int_0^1 \frac{1-\frac{(\theta_1^2+\theta_1+\theta_1 y_1+1)}{(\theta_1^2+\theta_1+1)}e^{-\left(\theta_1 y_1+\left(\frac{y_1}{\rho}\right)^\gamma\right)}}{1-\left[\frac{(\theta_1^2+2\theta_1+1)}{(\theta_1^2+\theta_1+1)}\right]e^{-\left(\theta_1+\frac{1}{\rho^\gamma}\right)}} \times \frac{1-\frac{(\theta_1^2+\theta_1+\theta_1\frac{k}{m}y_1+1)}{(\theta_1^2+\theta_1+1)}e^{-\left(\theta_1\frac{ky_1}{m}+\left(\frac{ky_1}{m\rho}\right)^\gamma\right)}}{1-\left[\frac{(\theta_1^2+2\theta_1+1)}{(\theta_1^2+\theta_1+1)}\right]e^{-\left(\theta_1+\frac{1}{\rho^\gamma}\right)}} \times \frac{\left[\frac{\left(\theta_2+\frac{\gamma}{\rho}\left(\frac{y_1}{\rho}\right)^{\gamma-1}\right)(\theta_2^2+\theta_2+\theta_2 y_1+1)-\theta_2}{(\theta_2^2+\theta_2+1)}\right]e^{-\left(\theta_2 y_1+\left(\frac{y_1}{\rho}\right)^\gamma\right)}}{1-\left[\frac{(\theta_2^2+2\theta_2+1)}{(\theta_2^2+\theta_2+1)}\right]e^{-\left(\theta_2+\frac{1}{\rho^\gamma}\right)}} dy \tag{22}$$

but

$$\int_0^1 \frac{1-\frac{(\theta_1^2+\theta_1+\theta_1 y_1+1)}{(\theta_1^2+\theta_1+1)}e^{-\left(\theta_1 y_1+\left(\frac{y_1}{\rho}\right)^\gamma\right)}}{1-\left[\frac{(\theta_1^2+2\theta_1+1)}{(\theta_1^2+\theta_1+1)}\right]e^{-\left(\theta_1+\frac{1}{\rho^\gamma}\right)}} \times \frac{\left[\frac{\left(\theta_2+\frac{\gamma}{\rho}\left(\frac{y_1}{\rho}\right)^{\gamma-1}\right)(\theta_2^2+\theta_2+\theta_2 y_1+1)-\theta_2}{(\theta_2^2+\theta_2+1)}\right]e^{-\left(\theta_2 y_1+\left(\frac{y_1}{\rho}\right)^\gamma\right)}}{1-\left[\frac{(\theta_2^2+2\theta_2+1)}{(\theta_2^2+\theta_2+1)}\right]e^{-\left(\theta_2+\frac{1}{\rho^\gamma}\right)}} dy = w_1 -$$

$$\frac{w_1 w_2}{(\theta_2^2+\theta_2+1)(\theta_1^2+\theta_1+1)} \sum_{j=0}^{\infty} \frac{(-\theta_1-\theta_2)^j}{j!} \sum_{i=0}^{\infty} \frac{(-2)^i}{i!\rho^{\gamma i}} \left\{(\theta_1^2+\theta_1+1)\left(\frac{\theta_2^3+\theta_2^2}{\gamma i+j+1} + \frac{\theta_2^2}{\gamma i+j+2} + \frac{\gamma(\theta_2^2+\theta_2+1)}{\rho^\gamma[\gamma(i+1)+j]} + \frac{\gamma\theta_2}{\rho^\gamma[\gamma(i+1)+j+1]}\right) + \theta_1\left(\frac{\theta_2^3+\theta_2^2}{\gamma i+j+2} + \frac{\theta_2^2}{\gamma i+j+3} + \frac{\gamma(\theta_2^2+\theta_2+1)}{\rho^\gamma[\gamma(i+1)+j+1]} + \frac{\gamma\theta_2}{\rho^\gamma[\gamma(i+1)+j+2]}\right)\right\} \tag{23}$$

It remains to find the other part which is:

$$\int_0^1 \frac{1-\frac{\left(\theta_1^2+\theta_1+\theta_1 y_1+1\right)}{\left(\theta_1^2+\theta_1+1\right)} e^{-\left(\theta_1 y_1+\left(\frac{y_1}{\rho}\right)^\gamma\right)}}{1-\left[\frac{\left(\theta_1^2+2\theta_1+1\right)}{\left(\theta_1^2+\theta_1+1\right)}\right] e^{-\left(\theta_1+\frac{1}{\rho^\gamma}\right)}} \times \frac{1-\frac{\left(\theta_1^2+\theta_1+\theta_1\frac{k}{m} y_1+1\right)}{\left(\theta_1^2+\theta_1+1\right)} e^{-\left(\theta_1\frac{k y_1}{m}+\left(\frac{k y_1}{m\rho}\right)^\gamma\right)}}{1-\left[\frac{\left(\theta_1^2+2\theta_1+1\right)}{\left(\theta_1^2+\theta_1+1\right)}\right] e^{-\left(\theta_1+\frac{1}{\rho^\gamma}\right)}} \times \frac{\left[\frac{\left(\theta_2+\frac{\gamma}{\rho}\left(\frac{y_1}{\rho}\right)^{\gamma-1}\right)\left(\theta_2^2+\theta_2+\theta_2 y_1+1\right)-\theta_2}{\left(\theta_2^2+\theta_2+1\right)}\right] e^{-\left(\theta_2 y_1+\left(\frac{y_1}{\rho}\right)^\gamma\right)}}{1-\left[\frac{\left(\theta_2^2+2\theta_2+1\right)}{\left(\theta_2^2+\theta_2+1\right)}\right] e^{-\left(\theta_2+\frac{1}{\rho^\gamma}\right)}} dy$$

$$= w_1^2 \int_0^1 \left[\left(1-\frac{\left(\theta_1^2+\theta_1+\theta_1 y_1+1\right)}{\left(\theta_1^2+\theta_1+1\right)} e^{-\left(\theta_1 y_1+\left(\frac{y_1}{\rho}\right)^\gamma\right)} - \frac{\left(\theta_1^2+\theta_1+\theta_1\frac{k y_1}{m}+1\right)}{\left(\theta_1^2+\theta_1+1\right)} e^{-\left(\theta_1\frac{k y_1}{m}+\left(\frac{k y_1}{m\rho}\right)^\gamma\right)} + \frac{\left(\theta_1^2+\theta_1+\theta_1 y_1+1\right)}{\left(\theta_1^2+\theta_1+1\right)} e^{-\left(\theta_1 y_1+\left(\frac{y_1}{\rho}\right)^\gamma\right)} \times \frac{\left(\theta_1^2+\theta_1+\theta_1\frac{k y_1}{m}+1\right)}{\left(\theta_1^2+\theta_1+1\right)} e^{-\left(\theta_1\frac{k y_1}{m}+\left(\frac{k y_1}{m\rho}\right)^\gamma\right)}\right)\right] \left[\frac{\left[\frac{\left(\theta_2+\frac{\gamma}{\rho}\left(\frac{y_1}{\rho}\right)^{\gamma-1}\right)\left(\theta_2^2+\theta_2+\theta_2 y_1+1\right)-\theta_2}{\left(\theta_2^2+\theta_2+1\right)}\right] e^{-\left(\theta_2 y_1+\left(\frac{y_1}{\rho}\right)^\gamma\right)}}{1-\left[\frac{\left(\theta_2^2+2\theta_2+1\right)}{\left(\theta_2^2+\theta_2+1\right)}\right] e^{-\left(\theta_2+\frac{1}{\rho^\gamma}\right)}}\right] dy$$

$$= w_1^2 \int_0^1 \left[1-\frac{\left(\theta_1^2+\theta_1+\theta_1 y_1+1\right)}{\left(\theta_1^2+\theta_1+1\right)} e^{-\left(\theta_1 y_1+\left(\frac{y_1}{\rho}\right)^\gamma\right)} - \frac{\left(\theta_1^2+\theta_1+\theta_1\frac{k y_1}{m}+1\right)}{\left(\theta_1^2+\theta_1+1\right)} e^{-\left(\theta_1\frac{k y_1}{m}+\left(\frac{k y_1}{m\rho}\right)^\gamma\right)} + \frac{\left(\theta_1^2+\theta_1+1\right)^2+\left(\theta_1^2+\theta_1+1\right)\theta_1\frac{k y_1}{m}+\theta_1 y_1\left(\theta_1^2+\theta_1+1\right)+\theta_1^2\frac{k}{m} y_1^2}{\left(\theta_1^2+\theta_1+1\right)^2} e^{-\left(\frac{\theta_1(m+k)}{m} y_1+\left(\frac{y_1}{\rho}\right)^\gamma\left(1+\left(\frac{k}{m}\right)^\gamma\right)\right)}\right] \times \left[\frac{\left[\frac{\left(\theta_2+\frac{\gamma}{\rho}\left(\frac{y_1}{\rho}\right)^{\gamma-1}\right)\left(\theta_2^2+\theta_2+\theta_2 y_1+1\right)-\theta_2}{\left(\theta_2^2+\theta_2+1\right)}\right] e^{-\left(\theta_2 y_1+\left(\frac{y_1}{\rho}\right)^\gamma\right)}}{1-\left[\frac{\left(\theta_2^2+2\theta_2+1\right)}{\left(\theta_2^2+\theta_2+1\right)}\right] e^{-\left(\theta_2+\frac{1}{\rho^\gamma}\right)}}\right] dy$$

$$= w_1^2 + w_1^2 \left\{ \int_0^1 -\frac{\left(\theta_1^2+\theta_1+\theta_1 y_1+1\right)}{\left(\theta_1^2+\theta_1+1\right)} e^{-\left(\theta_1 y_1+\left(\frac{y_1}{\rho}\right)^\gamma\right)} \times \frac{\left[\frac{\left(\theta_2+\frac{\gamma}{\rho}\left(\frac{y_1}{\rho}\right)^{\gamma-1}\right)\left(\theta_2^2+\theta_2+\theta_2 y_1+1\right)-\theta_2}{\left(\theta_2^2+\theta_2+1\right)}\right] e^{-\left(\theta_2 y_1+\left(\frac{y_1}{\rho}\right)^\gamma\right)}}{1-\left[\frac{\left(\theta_2^2+2\theta_2+1\right)}{\left(\theta_2^2+\theta_2+1\right)}\right] e^{-\left(\theta_2+\frac{1}{\rho^\gamma}\right)}} dy - \int_0^1 \frac{\left(\theta_1^2+\theta_1+\theta_1\frac{b}{m} y_1+1\right)}{\left(\theta_1^2+\theta_1+1\right)} e^{-\left(\theta_1\frac{b y_1}{m}+\left(\frac{b y_1}{m\rho}\right)^\gamma\right)} \times \frac{\left[\frac{\left(\theta_2+\frac{\gamma}{\rho}\left(\frac{y_1}{\rho}\right)^{\gamma-1}\right)\left(\theta_2^2+\theta_2+\theta_2 y_1+1\right)-\theta_2}{\left(\theta_2^2+\theta_2+1\right)}\right] e^{-\left(\theta_2 y_1+\left(\frac{y_1}{\rho}\right)^\gamma\right)}}{1-\left[\frac{\left(\theta_2^2+2\theta_2+1\right)}{\left(\theta_2^2+\theta_2+1\right)}\right] e^{-\left(\theta_2+\frac{1}{\rho^\gamma}\right)}} dy + \int_0^1 \frac{\left(\theta_1^2+\theta_1+1\right)^2+\left(\theta_1^2+\theta_1+1\right)\theta_1\frac{k}{m} y_1+\left(\theta_1^2+\theta_1+1\right)\theta_1 y_1+\theta_1^2\frac{k}{m} y_1^2}{\left(\theta_1^2+\theta_1+1\right)^2} e^{-\left(\frac{\theta_1(m+k)}{m} y_1+\left(\frac{y_1}{\rho}\right)^\gamma\left(1+\left(\frac{k}{m}\right)^\gamma\right)\right)} \times \frac{\left[\frac{\left(\theta_2+\frac{\gamma}{\rho}\left(\frac{y_1}{\rho}\right)^{\gamma-1}\right)\left(\theta_2^2+\theta_2+\theta_2 y_1+1\right)-\theta_2}{\left(\theta_2^2+\theta_2+1\right)}\right] e^{-\left(\theta_2 y_1+\left(\frac{y_1}{\rho}\right)^\gamma\right)}}{1-\left[\frac{\left(\theta_2^2+2\theta_2+1\right)}{\left(\theta_2^2+\theta_2+1\right)}\right] e^{-\left(\theta_2+\frac{1}{\rho^\gamma}\right)}} dy \right\} \quad (24)$$

Using the Taylor expansion

$$e^{-\left\{(\theta_1+\theta_2)y_1+2\left(\frac{y_1}{\rho}\right)^\gamma\right\}}=\sum_{j=0}^{\infty}\frac{(-\theta_1-\theta_2)^j}{j!}\sum_{i=0}^{\infty}\frac{(-2)^i}{i!\rho^{\gamma i}}\,y_1^{\gamma i+j}$$

and

$$e^{-\left(\theta_1\frac{ky_1}{m}+\left(\frac{ky_1}{m\rho}\right)^\gamma\right)}e^{-\left(\theta_2y_1+\left(\frac{y_1}{\rho}\right)^\gamma\right)}=e^{-\left(\left(\theta_1\frac{k}{m}+\theta_2\right)y_1+(k^\gamma+m^\gamma)\left(\frac{y_1}{m\rho}\right)^\gamma\right)}$$

Then

$$e^{-\left(\left(\theta_1\frac{k}{m}+\theta_2\right)y_1+(k^\gamma+m^\gamma)\left(\frac{y_1}{m\rho}\right)^\gamma\right)}=\sum_{j=0}^{\infty}\frac{(-\theta_1\frac{k}{m}-\theta_2)^j}{j!}\sum_{i=0}^{\infty}\frac{(-k^\gamma-m^\gamma)^i}{i!(m\rho)^{\gamma i}}y_1^{\gamma i+j}$$

$$e^{-\left(\frac{\theta_1(m+k)}{m}y_1+\left(\frac{y_1}{\rho}\right)^\gamma\left(1+\left(\frac{k}{m}\right)^\gamma\right)\right)}e^{-\left(\theta_2y_1+\left(\frac{y_1}{\rho}\right)^\gamma\right)}=e^{-\left(\left[\frac{\theta_1(m+k)}{m}+\theta_2\right]y_1+\left(\frac{y_1}{\rho}\right)^\gamma\left[2+\left(\frac{k}{m}\right)^\gamma\right]\right)}$$

$$e^{-\left(\left[\frac{\theta_1(m+k)}{m}+\theta_2\right]y_1+\left(\frac{y_1}{\rho}\right)^\gamma\left[2+\left(\frac{k}{m}\right)^\gamma\right]\right)}=\sum_{j=0}^{\infty}\frac{\left[-\frac{\theta_1(m+k)}{m}-\theta_2\right]^j}{j!}\sum_{i=0}^{\infty}\frac{(2+\left(\frac{k}{m}\right)^\gamma)^i}{i!(\rho)^{\gamma i}}y_1^{\gamma i+j}$$

And substitute in equation (23) we get

$$\begin{aligned}
&=w_1^2+w_1^2\Bigg[-\frac{w_1w_2}{(\theta_2^2+\theta_2+1)(\theta_1^2+\theta_1+1)}\sum_{j=0}^{\infty}\frac{(\theta_1-\theta_2)^j}{j!}\sum_{i=0}^{\infty}\frac{(-2)^i}{i!\rho^{\gamma i}}\Big\{(\theta_1^2+\theta_1+1)\Big(\frac{\theta_2^3+\theta_2^2}{\gamma i+j+1}+\frac{\theta_2^2}{\gamma i+j+2}+\frac{\gamma(\theta_2^2+\theta_2+1)}{\rho^\gamma[\gamma(i+1)+j]}+\\
&\quad\frac{\gamma\theta_2}{\rho^\gamma[\gamma(i+1)+j+1]}\Big)+\theta_1\Big(\frac{\theta_2^3+\theta_2^2}{\gamma i+j+2}+\frac{\theta_2^2}{\gamma i+j+3}+\frac{\gamma(\theta_2^2+\theta_2+1)}{\rho^\gamma[\gamma(i+1)+j+1]}+\frac{\gamma\theta_2}{\rho^\gamma[\gamma(i+1)+j+2]}\Big)\Big\}-\\
&\quad\frac{w_1w_2}{(\theta_2^2+\theta_2+1)(\theta_1^2+\theta_1+1)}\sum_{j=0}^{\infty}\frac{\left(-\theta_1\frac{k}{m}-\theta_2\right)^j}{j!}\sum_{i=0}^{\infty}\frac{(-k^\gamma-m^\gamma)^i}{i!(m\rho)^{\gamma i}}\Big\{(\theta_1^2+\theta_1+1)\Big(\frac{\theta_2^3+\theta_2^2}{\gamma i+j+1}+\frac{\theta_2^2}{\gamma i+j+2}+\frac{\gamma(\theta_2^2+\theta_2+1)}{\rho^\gamma[\gamma(i+1)+j]}+\\
&\quad\frac{\gamma\theta_2}{\rho^\gamma[\gamma(i+1)+j+1]}\Big)+\theta_1\frac{k}{m}\Big(\frac{\theta_2^3+\theta_2^2}{\gamma i+j+2}+\frac{\theta_2^2}{\gamma i+j+3}+\frac{\gamma(\theta_2^2+\theta_2+1)}{\rho^\gamma[\gamma(i+1)+j+1]}+\frac{\gamma\theta_2}{\rho^\gamma[\gamma(i+1)+j+2]}\Big)\Big\}+\\
&\frac{w_2}{(\theta_1^2+\theta_1+1)^2}\sum_{j=0}^{\infty}\frac{\left[-\frac{\theta_1(m+k)}{m}-\theta_2\right]^j}{j!}\sum_{i=0}^{\infty}\frac{(2+\left(\frac{k}{m}\right)^\gamma)^i}{i!(\rho)^{\gamma i}}\Big\{(\theta_1^2+\theta_1+1)^2\Big(\frac{\theta_2^3+\theta_2^2}{\gamma i+j+1}+\frac{\theta_2^2}{\gamma i+j+2}+\frac{\gamma(\theta_2^2+\theta_2+1)}{\rho^\gamma[\gamma(i+1)+j]}+\frac{\gamma\theta_2}{\rho^\gamma[\gamma(i+1)+j+1]}\Big)+\\
&(\theta_1^2+\theta_1+1)\theta_1\frac{k}{m}\Big(\frac{\theta_2^3+\theta_2^2}{\gamma i+j+2}+\frac{\theta_2^2}{\gamma i+j+3}+\frac{\gamma(\theta_2^2+\theta_2+1)}{\rho^\gamma[\gamma(i+1)+j+1]}+\frac{\gamma\theta_2}{\rho^\gamma[\gamma(i+1)+j+2]}\Big)+(\theta_1^2+\theta_1+1)\theta_1\Big(\frac{\theta_2^3+\theta_2^2}{\gamma i+j+2}+\frac{\theta_2^2}{\gamma i+j+3}+\\
&\frac{\gamma(\theta_2^2+\theta_2+1)}{\rho^\gamma[\gamma(i+1)+j+1]}+\frac{\gamma\theta_2}{\rho^\gamma[\gamma(i+1)+j+2]}\Big)+\theta_1^2\frac{k}{m}\Big(\frac{\theta_2^3+\theta_2^2}{\gamma i+j+3}+\frac{\theta_2^2}{\gamma i+j+4}+\frac{\gamma(\theta_2^2+\theta_2+1)}{\rho^\gamma[\gamma(i+1)+j+2]}+\frac{\gamma\theta_2}{\rho^\gamma[\gamma(i+1)+j+3]}\Big)\Big\}\Bigg] \qquad (25)
\end{aligned}$$

So, from equations (22) and (24)

$$\begin{aligned}
R_c&=R_{si}+\frac{w_1w_2}{(\theta_2^2+\theta_2+1)(\theta_1^2+\theta_1+1)}\sum_{j=0}^{\infty}\frac{(-\theta_1-\theta_2)^j}{j!}\sum_{i=0}^{\infty}\frac{(-2)^i}{i!\rho^{\gamma i}}\Big\{(\theta_1^2+\theta_1+1)\Big(\frac{\theta_2^3+\theta_2^2}{\gamma i+j+1}+\frac{\theta_2^2}{\gamma i+j+2}+\frac{\gamma(\theta_2^2+\theta_2+1)}{\rho^\gamma[\gamma(i+1)+j]}+\\
&\quad\frac{\gamma\theta_2}{\rho^\gamma[\gamma(i+1)+j+1]}\Big)+\theta_1\Big(\frac{\theta_2^3+\theta_2^2}{\gamma i+j+2}+\frac{\theta_2^2}{\gamma i+j+3}+\frac{\gamma(\theta_2^2+\theta_2+1)}{\rho^\gamma[\gamma(i+1)+j+1]}+\frac{\gamma\theta_2}{\rho^\gamma[\gamma(i+1)+j+2]}\Big)\Big\}+w_1^2+\\
&\quad w_1^2\Bigg[-\frac{w_1w_2}{(\theta_2^2+\theta_2+1)(\theta_1^2+\theta_1+1)}\sum_{j=0}^{\infty}\frac{(\theta_1-\theta_2)^j}{j!}\sum_{i=0}^{\infty}\frac{(-2)^i}{i!\rho^{\gamma i}}\Big\{(\theta_1^2+\theta_1+1)\Big(\frac{\theta_2^3+\theta_2^2}{\gamma i+j+1}+\frac{\theta_2^2}{\gamma i+j+2}+\frac{\gamma(\theta_2^2+\theta_2+1)}{\rho^\gamma[\gamma(i+1)+j]}+\\
&\quad\frac{\gamma\theta_2}{\rho^\gamma[\gamma(i+1)+j+1]}\Big)+\theta_1\Big(\frac{\theta_2^3+\theta_2^2}{\gamma i+j+2}+\frac{\theta_2^2}{\gamma i+j+3}+\frac{\gamma(\theta_2^2+\theta_2+1)}{\rho^\gamma[\gamma(i+1)+j+1]}+\frac{\gamma\theta_2}{\rho^\gamma[\gamma(i+1)+j+2]}\Big)\Big\}-\\
&\quad\frac{w_1w_2}{(\theta_2^2+\theta_2+1)(\theta_1^2+\theta_1+1)}\sum_{j=0}^{\infty}\frac{\left(-\theta_1\frac{k}{m}-\theta_2\right)^j}{j!}\sum_{i=0}^{\infty}\frac{(-k^\gamma-m^\gamma)^i}{i!(m\rho)^{\gamma i}}\Big\{(\theta_1^2+\theta_1+1)\Big(\frac{\theta_2^3+\theta_2^2}{\gamma i+j+1}+\frac{\theta_2^2}{\gamma i+j+2}+\frac{\gamma(\theta_2^2+\theta_2+1)}{\rho^\gamma[\gamma(i+1)+j]}+\\
&\quad\frac{\gamma\theta_2}{\rho^\gamma[\gamma(i+1)+j+1]}\Big)+\theta_1\frac{k}{m}\Big(\frac{\theta_2^3+\theta_2^2}{\gamma i+j+2}+\frac{\theta_2^2}{\gamma i+j+3}+\frac{\gamma(\theta_2^2+\theta_2+1)}{\rho^\gamma[\gamma(i+1)+j+1]}+\frac{\gamma\theta_2}{\rho^\gamma[\gamma(i+1)+j+2]}\Big)\Big\}+\\
&\frac{w_2}{(\theta_1^2+\theta_1+1)^2}\sum_{j=0}^{\infty}\frac{\left[-\frac{\theta_1(m+k)}{m}-\theta_2\right]^j}{j!}\sum_{i=0}^{\infty}\frac{(2+\left(\frac{k}{m}\right)^\gamma)^i}{i!(\rho)^{\gamma i}}\Big\{(\theta_1^2+\theta_1+1)^2\Big(\frac{\theta_2^3+\theta_2^2}{\gamma i+j+1}+\frac{\theta_2^2}{\gamma i+j+2}+\frac{\gamma(\theta_2^2+\theta_2+1)}{\rho^\gamma[\gamma(i+1)+j]}+\frac{\gamma\theta_2}{\rho^\gamma[\gamma(i+1)+j+1]}\Big)+\\
&(\theta_1^2+\theta_1+1)\theta_1\frac{k}{m}\Big(\frac{\theta_2^3+\theta_2^2}{\gamma i+j+2}+\frac{\theta_2^2}{\gamma i+j+3}+\frac{\gamma(\theta_2^2+\theta_2+1)}{\rho^\gamma[\gamma(i+1)+j+1]}+\frac{\gamma\theta_2}{\rho^\gamma[\gamma(i+1)+j+2]}\Big)+(\theta_1^2+\theta_1+1)\theta_1\Big(\frac{\theta_2^3+\theta_2^2}{\gamma i+j+2}+\frac{\theta_2^2}{\gamma i+j+3}+\\
&\frac{\gamma(\theta_2^2+\theta_2+1)}{\rho^\gamma[\gamma(i+1)+j+1]}+\frac{\gamma\theta_2}{\rho^\gamma[\gamma(i+1)+j+2]}\Big)+\theta_1^2\frac{k}{m}\Big(\frac{\theta_2^3+\theta_2^2}{\gamma i+j+3}+\frac{\theta_2^2}{\gamma i+j+4}+\frac{\gamma(\theta_2^2+\theta_2+1)}{\rho^\gamma[\gamma(i+1)+j+2]}+\frac{\gamma\theta_2}{\rho^\gamma[\gamma(i+1)+j+3]}\Big)\Big\}\Bigg]
\end{aligned}$$

CONCLUSION

To cover a complicated and complex part of reliability study that may appear because of heterogeneity populations that deviate from standard distributions. This paper presented the stress-strength model reliability as an important branch of reliability study. The [0.1] truncated Komal-Weibull distribution was defined and the Hazard rate function and reliability function were given. The single stress-strength model reliability based on [0,1] truncated Komal-Weibull distribution has been driven. Also, the cascade model reliability for the same distribution has been utilized.

ACKNOWLEDGMENTS

The authors would like to thank the referees for providing very helpful comments and suggestions that helped in improving the quality of the paper.

REFERENCES

1. W. B. Nelson, "Statistical Methods for Reliability Data," Second Edition, edited by William Q. Meeker, Luís A. Escobar, and Francis G. Pascual, New York, Wiley, 2021
2. M. Rausand, and A. Hoyland, "System Reliability Theory: Models, Statistical Methods, and Applications," 2nd Ed, John Wiley & Sons, Hoboken. (2004)
3. S. S. Rao, "Reliability engineering," Pearson Higher Ed. (2014).
4. K. C. Kapur, and, L. R. Lamberson, Reliability in engineering design. Wiley; 1st edition (January 16, 1991.
5. M.M. Yousef, E.M. Almetwally, "Multi Stress-Strength Reliability Based on Progressive First Failure for Kumaraswamy Model: Bayesian and Non-Bayesian Estimation," *Symmetry*, 13(11).(2021) https://doi.org/10.3390/sym13112120
6. S. Dey, J. Mazucheli, and M. Z. Anis, "Estimation of reliability of multicomponent stress–strength for a Kumaraswamy distribution," *Communications in Statistics - Theory and Methods,*46(4), 1560–1572 (2017). https://doi.org/10.1080/03610926.2015.1022457
7. B.A. Hameed, A.N. Salman, and B.A Kalaf, "On Estimation of P(Y< X) in Case Inverse Kumaraswamy Distribution,"*Ibn AL-Haitham Journal for Pure and Applied Science*, 2020. Doi: 10.30526/33.1.2375
8. B.A. Kalaf, S.H. Raheem, A.N. Salman, "Estimation of the reliability system in a model of stress- strength according to distribution of inverse Rayleigh," *Periodicals of Engineering and Natural Sciences,*9(2), 524-533(2021). http://dx.doi.org/10.21533/pen.v9i2.1811
9. S.H Raheem, B.A Kalaf and A.N Salman, "Comparison of Some of Estimation methods of Stress-Strength Model: R=P(Y<X<Z) ," *Baghdad Science Journal,* 1103-1112 (2021). https://doi.org/10.21123/bsj.2021.18.2(Suppl.).1103
10. I. Kamel, T. Anwar, A.N. Salman, "Different estimation methods of reliability in stress-strength model under Chen distribution," *AIP Conf. Proc.* 2591, 050023 (2023) https://doi.org/10.1063/5.0120602
11. S. N. N. Pandit, G.L. Sriwastav, "Studies in Cascade Reliability I," *IEEE Trans. On Reliability*,24(1) 53-56(1975,)
12. A. Rekha, V.C. C. Raju, "Cascade System Reliability with Rayleigh Distribution," *Botswana Journal of Technology*, 8, 14-19(1999**)**
13. R. Shanker, F. Hagos, and S. Sujatha, "On modeling of Lifetimes data using exponential and Lindley distributions," *Biometrics & Biostatistics International Journal*, 2 (5), 1-9 (2015)
14. A.M. Razali, A. A. Al-Wakeel, "Mixture Weibull distributions for fitting failure times data," *Applied Mathematics and Computation*, 219 (24), 11358-11364 (2013)
15. J.A. Carta, P. Ramírez, "Analysis of two-component mixture Weibull statistics for estimation of wind speed distributions," *Renewable Energy*, 32(3), (2007)
16. F. Jamal, H.S. Bakouch and M.A. Nasir. "A Truncated General-G Class Of Distributions With Application To Truncated Burr-G Family," *REVSTAT - Statistical Journal,* 19(4), 513–530 (2021) https://doi.org/10.57805/revstat.v19i4.352
17. R. Kanaparthi, J. Palakurthi, L. N. Sanka. "Cascade reliability of stress-strength system for the new Rayleigh-Pareto distribution," *Int J Stat Appl Math*,5(2), 131-139 (2020).

18. E. Sh. Haddad, and F. Sh. Batah, "On Estimating Reliability of a Stress – Strength Model in Case of Rayleigh Pareto Distribution," *Iraqi Journal of Science*, 62(12), 4847-4858 (2021). https://doi.org/10.24996/ijs.2021.62.12.23
19. O. A. Alamri, M. M Abd El-Raouf, E.A. Ismail, "Estimate stress-strength reliability model using Rayleigh and half-normal distribution,". *Comput Intell Neurosci*.:7653581 (2021). https://doi.org/10.1155/2021/7653581
20. M. O. Mohamed, "Estimation of reliability function based on the upper record values for generalized gamma Lindley stress–strength model: Case study COVID-19," *International Journal Of Advanced And Applied Sciences* , 9(8): 92-99 (2022) https://doi.org/10.21833/ijaas.2022.08.012
21. S.L. Raikar, S. Rajesh, P. Gaonkar, "Jaya algorithm in estimation of P[X > Y] for two parameter Weibull distribution[J] ," *AIMS Mathematics*, , 7(2): 2820-2839 (2022). doi: 10.3934/math.2022156
22. H. M Ali, Reliability analysis of the Stress-Strength model from truncated Pareto distribution based on progressive Type-II censored samples, A Project Submitted to the College of Arts and Sciences in Partial Fulfillment of the Requirements for the Degree of Masters of Science in Master of Science in Applied Statistics January 2023
23. R.M. EL-Sagheer, M.S. Eliwa, M. El-Morshedy, L. A . Al-Essa, A. Al-Bossly, A. Abd-El-Monem Analysis of the Stress–Strength Model Using Uniform Truncated Negative Binomial Distribution under Progressive Type-II Censoring. Axioms. 2023; 12(10):9 https://doi.org/10.3390/axioms12100949
24. S.H. Raheem, B.A. Kalaf, "A New Mixture of Komal and Weibull Distribution," AIP Conference Proce 0094-243X, 1551-7616
25. R. Shanker, "Komal distribution with properties and application in survival analysis," *Biometrics & Biostatistics International Journal,*12(2),40–44(2023). https://doi.org/10.15406/bbij.2023.12.00381
26. W . Weibull, " Wide applicability," *Journal of Applied Mechanics*,1951.
27. Aryuyuen, S., & Bodhisuwan, W. (n.d.). The Truncated Power Lomax Distribution: Properties and Applications. http://wjst.wu.ac.th
28. S.H Raheem,Comparison Among Three Estimation Methods to Estimate Cascade Reliability Model (2+1) Based On Inverted Exponential Distribution," *Ibn Al-Haitham Journal. for Pure and Applied Science*, 33(4), 82-91(2020) Doi: 10.30526/33.4.2512

Investigation of the form factors and charge density distribution for some upper limit for fp-shell nuclei

Aeshah Ali Hussein[1], Sarah M. Obaid[2,a], Shaimaa A. Abbas[1], Noor Adil Mohammed[3], Fouad A. Majeed[4]

[1]*Department of Physics, College of Education for Pure Science (Ibn-Alhaitham), University of Baghdad, Baghdad, Iraq.*
[2]*Technical College of Al-Mussaib, Al-Furat Al-Awsat Technical University, Babylon, Iraq.*
[3]*Ministry of Education, Directorate General of Education Rusafa3, Baghdad, Iraq.*
[4]*Department of Physics, College of Education for Pure Sciences, University of Babylon, Babylon, Iraq.*

[a]Corresponding author: sarah.mahdi@atu.edu.iq

Abstract: The charge form factors C0 and the distribution of charge density (CDD) of $^{70, 72, 74,76}$Ge nuclei were examined by inelastic electron scattering using the Sk35-Skzs* parametrization of the Skyrme-Hartree-Fock method. Using Tassie and Bohr-Mottelson models, the elastic C0 form factor for the transitions was calculated, taking into account core-polarization effects and associated with the effective charges for the proton and neutron. A comparison of the theoretical predictions and empirical data for C0 and CDD form factors demonstrated a significant agreement.

Keywords: Elastic charge form factors; Charge density distribution; Skyrme-Hartree-Fock; fp-shell nuclei; Core-polarization effects.

INTRODUCTION

One of the models used to examine the static and dynamic properties of nuclei and to investigate nuclear structure is the shell model, which takes configuration mixing into account. This model centers on a small set of active nucleons surrounding a passive core, capturing the nuclear state by constraining configurations within its wave function while incorporating important components determined with precision through adjustable parameters in shell-model computations. Oxbash [1], Nushell [2], and Nushellx [3] are examples of nuclear shell-model configuration mixing software that is used to theoretically examine nuclear structure. Certain software tools are necessary to integrate acceptable and effective interactions using sets of energies of the single-particle (SPE) and the matrix element of two bodies (TBME). Electron scattering serves as a valuable tool for investigating the properties and structure of target nuclei, offering precise assessments of the validity of various microscopic models used in nuclear structure studies. Many nuclear properties have been satisfactorily explained by the nuclear shell model, particularly when calculations are improved by means of a microscopic theory called core polarization (CP) effects, which integrates wave functions from higher configurations outside of the designated model space with shell-model wave functions [4,5]. Hamoudi and Abbas examined the effects of correlations between short range two bodies on a number of elastic electron scattering parameters, including form factors of charge, densities of charge, and root mean square charge radii. They examined a number of N50-shell nuclei ^{90}Zr and ^{88}Sr ^{50}Cr, ^{48}Ca, ^{54}Fe, ^{70}Ge, ^{58}Ni, and ^{74}Se, fp-shell nuclei. They improved their analysis by adding one- and two-body terms to the single-particle harmonic oscillator wave functions and the cluster expansion [6]. Srivastava et al. [7] examined B(E2) values as well as the low-energy levels of Cu and Ni isotopes within the 40–50 neutron range. ^{56}Ni was used as an inactive closed core in the $f_{5/2}$ $p_{3/2}$ $p_{1/2}$ $g_{9/2}$ model space, and their research used shell model predictions with three contemporary interactions. Salman et al. [8] investigated the longitudinal form factors in the F5P model space related to the 2^+ state in the isotopes $^{64, 66,68}$Zn. They used the F5PVH interaction, and discovered that the observed data and their results on the lowered transition

Technologies and Materials for Renewable Energy, Environment and Sustainability
AIP Conf. Proc. 3321, 020017-1–020017-9; https://doi.org/10.1063/5.0289695
Published under an exclusive license by AIP Publishing. 978-0-7354-5231-2/$30.00

probabilities and form factors were reasonably aligned. Numerous studies [9-13] have explored the effects of Coulomb polarization (CP) on form factors, quadrupole moments, and transitions in p, sd, and fp nuclei. These investigations have shown significant success in accurately modeling form factors in alignment with experimental data.

The aim of this work is to investigate charge form factors (C0) and the charge distribution of the density (CDD) of the ^{70,72,74,76}Ge nuclei in the fp-shell nuclei. The work will entail shell model calculations for the FP model space without model space limits using the jj44b interaction and the NushellX@ MSU code. Moreover, the inelastic form factors will be analyzed using the Bohr-Mottelson and Tassie models with effective charges of protons and neutrons. To validate the theoretical results, they will be compared with available observed data.

THEORETICAL BACKGROUND

The Effective Interaction of Skyrme

Fitting experimental data relevant to nuclear properties such as binding energies and charge radii is made easier by effective interactions [17]. For Hartree-Fock (HF) calculations on nuclei, Skyrme proposed an effective interaction [15, 16]. There are roughly ten movable parameters in this interaction. The Skyrme forces are made up of three body zero range term and a momentum-dependent of the term between two bodies, both with a zero-range character. As a result, in computations of the Hartree-Fock, the term between three bodies can be compensated with a the term of the density dependent of the two bodies, allowing the Skyrme forces to be combined into an extended Skyrme force [18]. The formulation for the interaction of two bodies [15], using the Skyrme formalism, is as follows:

$$\nu_{12} = \Big[t_0\big(1 + x_0\hat{P}_\sigma\big)\delta(\vec{r}_1 - \vec{r}_2) + \frac{t_1}{2}\big(1 + x_1\hat{P}_\sigma\big)\Big(\hat{k}^2\delta(\vec{r}_1 - \vec{r}_2) + \delta(\vec{r}_1 - \vec{r}_2)\hat{\acute{k}}^2\Big) + t_2\big(1 + x_2\hat{P}_\sigma\big)\hat{\acute{k}}.\,\delta(\vec{r}_1 - \vec{r}_2)\hat{k} + \frac{t_3}{6}\big(1 + x_3\hat{P}_\sigma\big)\rho^\alpha\big(\vec{R}\big)\delta(\vec{r}_1 - \vec{r}_2) + iW_0\hat{\acute{k}}(\hat{\sigma}_1 + \hat{\sigma}_2) \times \hat{k}\delta(\vec{r}_1 - \vec{r}_2)\Big] \quad (1)$$

where $\left\{\vec{\boldsymbol{R}} = \frac{\vec{\boldsymbol{r}}_1 + \vec{\boldsymbol{r}}_2}{2}\right\}$ and Skyrme force parameters is $\boldsymbol{\alpha}$. $\left[\hat{\boldsymbol{k}} = \left[\frac{(\vec{\nabla}_1 - \vec{\nabla}_2)}{2i}\right], \left[\hat{\acute{\boldsymbol{k}}} = -\frac{(\vec{\acute{\nabla}}_1 - \vec{\acute{\nabla}}_2)}{2i}\right]\right]$ are the operators denoting the wave vector momenta of two nucleons relative to each other, operating on Wavefunctions of complex conjugates with $\boldsymbol{r}$ coordinates, corresponding to the right and left sides, respectively. The Pauli matrices is $(\hat{\boldsymbol{\sigma}})$, $\hat{\boldsymbol{P}}_{\boldsymbol{\sigma}} = \left[\frac{\mathbf{1}}{\mathbf{2}}\ (\mathbf{1} + \hat{\boldsymbol{\sigma}}_{\mathbf{1}} \cdot \hat{\boldsymbol{\sigma}}_{\mathbf{2}})\right]$ is spin-exchange operator, and $\boldsymbol{\delta}(\vec{\boldsymbol{r}}_{\mathbf{1}} - \vec{\boldsymbol{r}}_{\mathbf{2}})$ is the Dirac delta function. The conventional Skyrme-Hartree-Fock (SHF) model expresses a nucleus's total energy density as [15].

$$\boldsymbol{E} = \left(\boldsymbol{E_{kin}} + \boldsymbol{E_{Sky}} + \boldsymbol{E_{Coul}} + \boldsymbol{E_{pair}} - \boldsymbol{E_{cm}}\right) \quad (2)$$

The formula below can be used to calculate $\boldsymbol{E_{kin}}$ The nucleon's kinetic energy, which are protons and neutrons [16]:

$$E_{kin} = \left(\sum_{i=1}^{A} \frac{\hbar^2}{2m_i} \int \tau_i d^3r\ \right) \quad (3)$$

The Skyrme force's energy functional $\boldsymbol{E_{sky}}$ can be expressed as

$$E_{sky} = \left(\int d^3r \left[\frac{b_0}{2}\rho^2 - \frac{\acute{b}_0}{2}\sum_q \rho_q^2 + \frac{b_3}{3}\rho^{\alpha+2} - \frac{\acute{b}_3}{3}\rho^\alpha \sum_q \rho_q^2 + b_1\tau_q - \acute{b}_1 \sum_q \rho_q\tau_q - \frac{b_2}{2}\rho\Delta\rho + \frac{\acute{b}_2}{2}\sum_q \rho_q\Delta\rho_q - b_4\rho\nabla.J - \acute{b}_4 \sum_q \rho_q\nabla.J_q\right]\right) \quad (4)$$

ρ_q These represent the protons' and neutrons' local densities, that take into account the total density and are dependent on the value of q. τ_q They are referring to the kinetic energy densities of the proton and the neutron, where the current density of the spin-orbit is represented by ρ. The following expressions describe these relationships [16].

$$\rho_q(r) = [\sum_{i\sigma}|\phi_i(r,\sigma,q)|^2],\ \tau_q(r) = \left[\sum_{i\sigma}\left|\vec{\nabla}\phi_i(r,\sigma,q)\right|^2\right], J_q(r) = [-i\sum_{i\sigma\acute{\sigma}}\phi_i^*(r,\sigma,q)[\nabla\phi_i \times \langle\sigma|\hat{\sigma}|\acute{\sigma}\rangle]\ ] \quad (5)$$

The densities of nucleon $\rho_n(r)$ and $\rho_\rho(r)$ and is derivable from the wave function of a single particle. established by the Hartree-Fock computations. The most comprehensive product wave functions ϕ_β in the (SHF) theory with Skyrme forces cover separately moving single particles, therefore yielding the neutron and proton densities as shown below.

$$\boldsymbol{\rho_q}(\vec{\boldsymbol{r}}) = \left(\sum_i|\boldsymbol{\varphi_i}(\boldsymbol{r})|^2 = \sum_{\boldsymbol{\beta}} \boldsymbol{\omega_\beta} \frac{\mathbf{2}\boldsymbol{j_\beta}+\mathbf{1}}{\mathbf{4}\boldsymbol{\pi}}\left(\frac{\boldsymbol{R_\beta}}{\boldsymbol{r}}\right)^{\mathbf{2}}\right) \quad (6)$$

where the state is denoted by β, its probability is represented by ω_β, and its angular momentum is indicated by j_β. The energy of Coulomb is designated as the third component in the equation for total energy. Because of the unlimited

range of the Coulomb interaction, the energy of Coulomb is mostly determined by the exchange component's energy contribution. The following procedure is used to compute the energy of Coulomb [16, 18]. in where R_β The radial component of the wavefunction of the harmonic oscillator is defined as

$$R_\beta = \left[\sqrt{\frac{2n!}{b^3\,\Gamma\left(n+l+\frac{3}{2}\right)}}\left(\frac{r}{b}\right)^l e^{-r^2/2b^2}\; L_n^{\left(l+\frac{1}{2}\right)}\left(\frac{r^2}{b^2}\right)\right] \tag{7}$$

The associated Laquerre polynomials are expressed as $\left(L_n^{\left(l+\frac{1}{2}\right)}\right)$, where b is the size parameter of the harmonic oscillator.

$$E_{Coul} = \left(\frac{e^2}{2}\iint \frac{\rho_q(\vec{r})\rho_q\left(\vec{\acute{r}}\right)}{|\vec{r}-\vec{\acute{r}}|} d^3r d^3\acute{r} + E_{Coul,exch}\right) \tag{8}$$

$$E_{Coul,exch} = \left(-\frac{3}{4}e^2\left(\frac{3}{\pi}\right)^{1/3}\int \rho^{4/3}{}_q(\vec{r})\, d\vec{r}\right) \tag{9}$$

$$E_{coul,exch} = \left(-\frac{\langle P_{cm}^2\rangle}{2\,A\,m}\right) \tag{10}$$

($P_{cm} = \sum_i \hat{p}_i$) is the operator of the total momentum, represented by the letter A, where m is the mass of the nucleons and A is their average number.

The models of Bohr-Mottelson and Tassie

The flexible and adaptive model of Tassie (TM) offers a non-uniform distribution of charge and mass densities for core polarization in NushellX@MSU [3]. The nuclear ground-state density of charge sis said to be a determining factor for the core polarization charge density in the thermodynamic model. The ground state charge density of each occupied shell, including the core, was found using the two-body charge density. A detailed explanation of the Tassie-shaped core polarization transition density is provided in [19].

$$\rho_{Jt_z}^{core} = \left[\frac{1}{2}C(1+\tau_z)\, r^{J-1}\frac{d\rho_0(i,f,r)}{dr}\right] \tag{11}$$

a proportionality constant, C, and the(CCD) is the distribution of charge density for the ground state two-body system, denoted as ρ_0, is shown [20].

$$\rho_0 = \left\langle\psi\middle|\hat{\rho}_{eff}^{(2)}(\vec{r})\middle|\psi\right\rangle = \left(\sum_{i<j}\left\langle ij\middle|\hat{\rho}_{eff}^{(2)}(\vec{r})\middle|ij\right\rangle - \left\langle ij\middle|\hat{\rho}_{eff}^{(2)}(\vec{r})\middle|ji\right\rangle\right) \tag{12}$$

where,

$$\hat{\rho}_{eff}^{(2)}(\vec{r}) = \left[\frac{1}{2(A-1)}f\left(r_{ij}\right)\sum_{i\neq j}\left\{\delta(\vec{r}-\vec{r_i}) + \delta\left(\vec{r}-\vec{r_j}\right)\right\}f\left(r_{ij}\right)\right] \tag{13}$$

In whatever case j and i the fundamental quantum numbers representing the two-body short-range correlation are represented by $f\left(r_{ij}\right)$. The present study [21] has utilized a simple short-range correlation model, specifically

$$f\left(r_{ij}\right) = \left(1 - e^{-\beta\left(r_{ij}-r_c\right)^2}\right) \tag{14}$$

where r_c is the variable denoting a correlation-related parameter and the appropriate hard-core radius. The Coulomb form factor is altered as follows in this model [21]:

$$F_J^L(q) = \sqrt{\frac{4\pi}{2J_i+1}}\frac{1}{Z}\left\{\int_0^\infty r^2 j_J(qr)\rho_{Jt_z}^{ms}(i,f,r)\, dr + C\int_0^\infty\left(j_J(qr)\, r^{J+1}\frac{d\rho_0(i,f,r)}{dr}\right)dr\right\}\, F_{cm}(q)\, F_{fc}(q) \tag{15}$$

Consequently, the form factor of equation (14) is represented by [20]:

$$F_J^L(q) = \sqrt{\frac{4\pi}{2J_i+1}}\frac{1}{Z}\left\{\int_0^\infty r^2 j_J(qr)\rho_{Jt_z}^{ms}(i,f,r)\, dr - qC\int_0^\infty r^{J+1}\rho_0(i,f,r)\, j_{J-1}(qr)\, dr\right\}F_{cm}(q)\, F_{fc}(q) \tag{16}$$

By substituting q=k into the preceding equation [20], we were able to obtain the proportionality constant C, which was derived from the form factor evaluated at q=k.

$$C = \frac{\int_0^\infty r^2 j_J(kr)\rho_{Jt_z}^{ms}(i,f,r)\, dr - ZF_J^L(k)\sqrt{\frac{2J_i+1}{4\pi}}}{\int_0^\infty r^{J+1}\rho_0(i,f,r)\, j_{J-1}(kr)\, dr} \tag{17}$$

RESULTS AND DISCUSSION

This section will mostly focus on computations, defining expected outcomes, and comparing them to experimental data. Given the different theoretical techniques targeted at clarifying the properties of fp-shell nuclei, focus will be made to the model space, parameters, and the methodology for fitting two-body matrix components to observed data, as outlined in Reference [21]. In this context, the fp-shell nuclei are envisaged as a core made of ^{56}Ni nucleons

scattered over the $f_{5/2}$, $p_{3/2}$, $p_{1/2}$, and $g_{9/2}$ shells, which together constitute the mandated model space for the theoretical computations. The utilization of this particular model space is crucial for capturing the delicate interactions and structural characteristics of the fp-shell nuclei under investigation.

The wavefunctions employed in shell model computations are essential for determining the quantum states and properties of the nucleus inside the chosen model space. These wavefunctions, important for accurate quantum mechanical description, will be acquired from the jun45 effective interaction, which is widely recognized and validated for addressing nuclear structural problems.

Notably, the jj44b interaction is intended to define the complicated dynamics and correlations inside the nuclei, so giving a strong foundation for theoretical calculations. The (Sk35−Skzs*) residual interaction in the jj44 shell model space is crucial for understanding how matrix elements interact in the system's initial and final states. The (Sk35−Skzs*) residual interaction is a crucial tool for comprehending the intricate interplay of forces and correlations in fp-shell nuclei. This ensures a thorough evaluation of the nuclear structural phenomena under study. The theoretical paradigm includes the (Sk35−Skzs*) residual interaction, which accounts for additional pressures beyond the fundamental jj44b interaction. This comprehensive approach is critical for capturing the nuanced characteristics of charge density and form factors within fp-shell nuclei, as well as supplementing the theoretical framework with a full investigation of the complicated matrix element interactions.

^{70}Ge Nucleus

The jj44 model space was utilized for the shell model computations, with a core centered at ^{56}Ni, resulting in 4 valence protons and 10 valence neutrons for the ^{70}Ge nucleus. Figure 1 illustrates the C0 charge form factor for the state within the fp-shell. The calculations used the effective interaction jj44b and the residual interaction (Sk35-Skzs*) to generate the matrix elements for the interactions from the start to the final states.

Both the Tassie Model and Bohr-Mottelson calculations notably replicate the first and second maxima, as evidenced in the experimental data [22]. Additionally, Figure 2 illustrates the discrepancy in charge distribution (CDD) using the Skyrme interaction in comparison with observed charge distributions for the ^{70}Ge nucleus. The computed CDD closely matches the theoretical estimates using the Skyrme parameterization, highlighting a strong theoretical understanding of the charge distribution within ^{70}Ge [22].

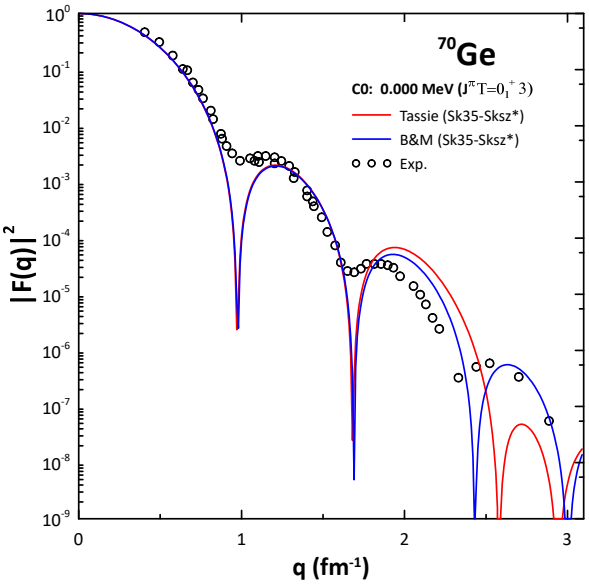

Figure 1. The C0 form factor represents the 0_1^+3 state in ^{70}Ge. Data that was observed from [22].

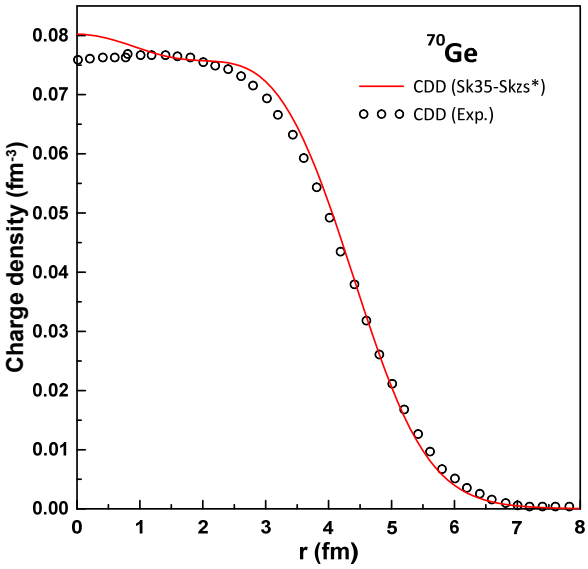

Figure 2. displays the distribution of charge density (CCD) for ^{70}Ge with the "Sk35-Skzs*" Skyrme parameterization. Data that was observed from [23].

^{72}Ge Nucleus

The form factor C0 multipolarity for the ground state 0^+ is shown in Figure 3. Core polarization effects were taken into account by including effective charges into the Tassie and Bohr-Mottelson models, which both employed the (Sk35−Skzs∗) Skyrme interaction. The experimental data comes from [22]. Theoretical computations effectively replicate the experimental findings for all momentum transfer values. Both the Bohr-Mottelson and the Tassie models closely match the experimental data in terms of core polarization integration, especially up to a momentum transfer close to the observed value. Additionally, Figure 4 compares the observed charge distributions for the ^{72}Ge nucleus with the distribution of charge density (CCD) (CDD) derived in this work using the Skyrme interaction. A detailed comparison was made between the current measured data for CDD and the expected theoretical results.

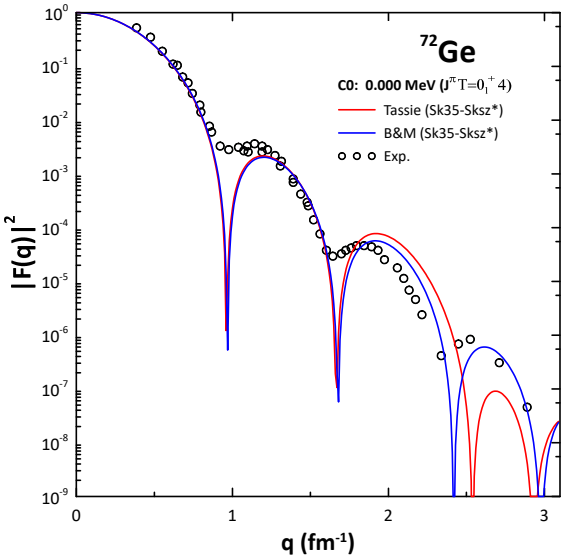

Figure 3. The C0 form factor represents the 0_1^+4 state in ^{72}Ge. Data that was observed from [22].

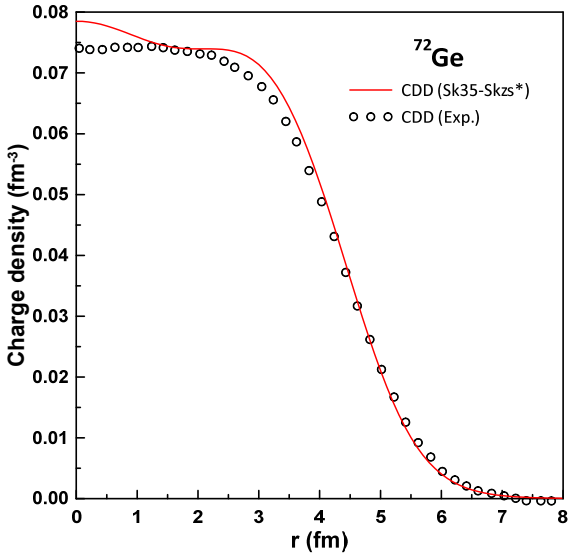

Figure 4. displays the distribution of charge density (CCD) for ^{72}Ge with the "Sk35-Skzs*" Skyrme parameterization. Data that was observed from [23].

^{74}Ge Nucleus

The ground state of the stable 74Ge nucleus, an even-even nucleus with 42 neutrons and protons, is 0+. Using the Bohr-Mottelson and Tassie models, a computational investigation of the charge form factor for the ground states of 74Ge is shown in Figure 5. The shell model calculations utilize the jj44b residual interaction as the effective interaction. As stated in Ref. [22], the Bohr-Mottelson and Tassie models both satisfactorily describe the first and second maxima observed in the experimental data for this state. Comparing the observed charge distributions for the ^{74}Ge nucleus with the distribution of charge density (CCD) (CDD) produced using the Skyrme parameterization Sk35-Skzs* is shown in Figure 6. There is a significant amount of agreement when comparing the experimental data for CDD with the theoretical expectations.

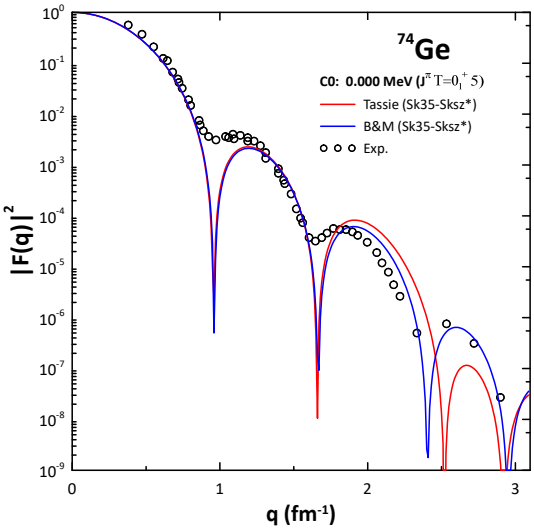

Figure 5. The C0 form factor represents the 0_1^+5 state in ^{74}Ge. Data that was observed from [22].

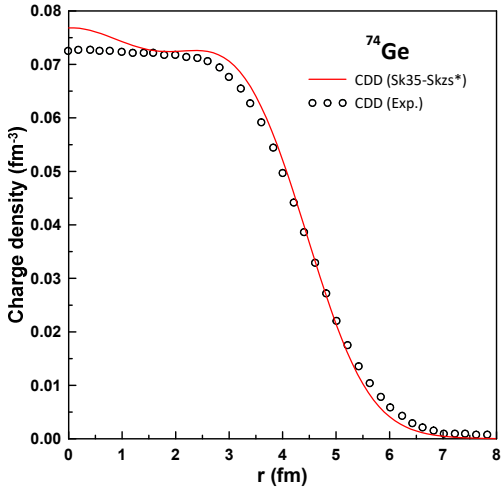

Figure 6. displays the distribution of charge density (CCD) for ^{74}Ge with the "Sk35-Skzs*" Skyrme parameterization. Data that was observed from [23].

^{76}Ge Nucleus

Within the jj44 model space, shell model calculations were performed for the ^{76}Ge nucleus, which consists of a ^{56}Ni core surrounded by 16 neutrons and 4 protons. The C0 charge form factor for the ^{76}Ge nucleus is computed using the Tassie and Bohr-Mottelson models, as shown in Figure 7. The shell model calculations used the interaction jj44b, and the element matrix for the interactions from the start to the final states were determined using the (Sk35-Skzs*) residual interaction. The Bohr-Mottelson and Tassie predictions accurately recreated the experimental results for the ^{76}Ge nucleus, according to Ref. [22]. Furthermore, Figures 8 show the experimental charge distributions for the ^{76}Ge nucleus, as well as the distribution of the charge density (CCD) derived using the Skyrme interaction used in this study. When the available observed data for CDD and C0 form factors were compared to the expected and theoretical values, there was a substantial degree of agreement.

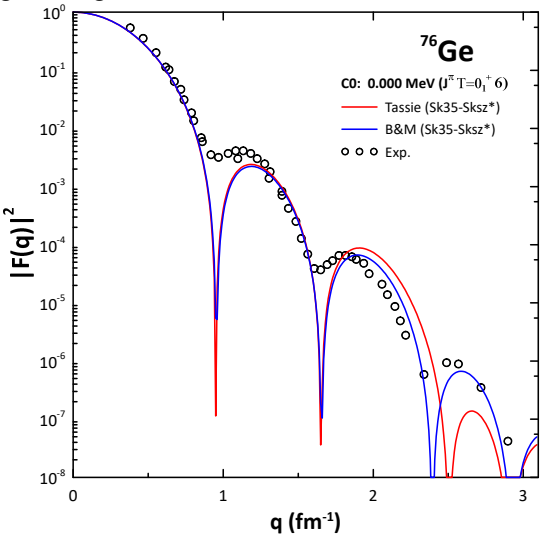

Figure 7. The C0 form factor represents the 0_1^+6 state in ^{76}Ge. Data that was observed from [22].

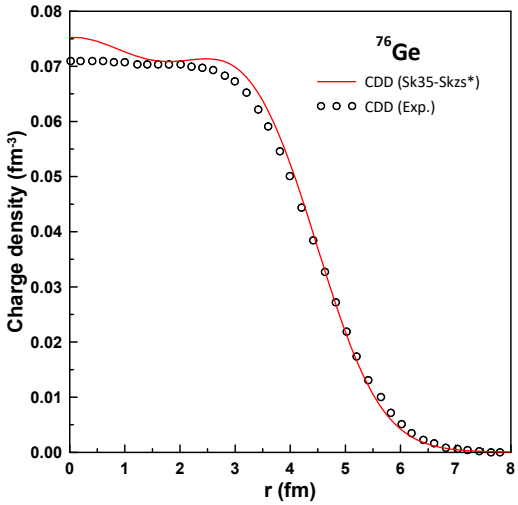

Figure 8. displays the distribution of charge density (CCD) for ^{76}Ge with the "Sk35-Skzs*" Skyrme parameterization. Data that was observed from [23].

CONCLUSION

The present work presents a thorough theoretical examination of the density distribution of the charge and the form factors associated with electron scattering in a specific *fp* shell nuclei subset. The Skyrme-Hartree-Fock technique, parametrized by (Sk35-Skzs*), was used to do theoretical computations. By carefully comparing the expected theoretical findings with the quantifiable data that has been established about CDD and C0 form factors, The work demonstrates a strong match between theoretical understanding and experimental results. This study provides important insights into the structural characteristics and electron scattering properties of fp-shell nuclei by demonstrating a strong agreement between empirical data for C0 form factors and density distribution of the charge and theoretical predictions obtained from the Skyrme-HF method with Skyrme potential.

REFERENCES

1. B. A. Brown, A. Etchegoyen, N. S. Godwin, W. D. M. Rae, W. A. Richter, W. E. Ormand, E. K. Warburton, J. S. Winfield, L. Zhao, and C. H. Zimmerman, *Oxbash for Windows*, MSU-NSCL Report Number 1289 (2004).
2. B. A. Brown and W. D. M. Rae, *NuShell@MSU*, MSU-NSCL Report (2007).
3. B. A. Brown and W. D. M. Rae, *Nucl. Data Sheets* 120, 115 (2014).
4. P. J. Brussaard and P. W. M. Glademans, *Shell-Model Applications in Nuclear Spectroscopy* (North-Holland Publishing Company, Amsterdam, 1977).
5. F. Petrovich, H. McManus, J. Borysowicz, and G. R. Hammerstein, *Phys. Rev. C* 16, 839 (1977).
6. Adel K. Hamoudi and Mahmoud A. Abbas, "Electron scattering from some even fp- and N50-shell nuclei with implanting the influence of short-range correlation functions," *Chinese Journal of Physics* 60, 623 (2019).
7. Praveen Chandra Srivastava and I. Mehrotra, "Nuclear structure study around Z = 28," *Int. J. Mod. Phys. E* 21 (2012): 1250007.
8. A. D. Salman, S. A. Al-Ramahi, and M. H. Oleiwi, "Inelastic electron-nucleus scattering form factors for 64, 66, 68Zn isotopes," *AIP Conf. Proc.* 2144(1), 030029 (2019).
9. F. A. Majeed, "The effect of core polarization on longitudinal form factors in 10B," *Phys. Scr.* 85(6), 065201 (2012).
10. F. A. Majeed, "The role of core polarization on C2 and C4 form factors of fp-shell nuclei," *Phys. Scr.* 59(1-2), 95-105 (2014).
11. F. A. Majeed and L. A. Najim, "Contribution of high energy configurations to longitudinal and transverse form factors in p- and sd-shell nuclei," *Indian J. Phys.* 89(6), 611-618 (2015).

12. F. A. Majeed and S. M. Obaid, "Nuclear structure study of ^{22,} ^{24}Ne and ^{24}Mg nuclei," *Indian J. Phys.* 65(2), 159-167 (2019).
13. Sarah M. Obaid and Fouad A. Majeed, "Longitudinal and transverse form factors from ^{65}Cu and ^{71}Ga nuclei," *J. Korean Phys. Soc.* 82(4), 329-339 (2023).
14. M. Honma, T. Otsuka, T. Mizusaki, and M. Hjorth-Jensen, "New effective interaction for—shell nuclei," Phys. Rev. C 80, 064323 (2009).
15. T. H. R. Skyrme, "The effective nuclear potential," Nucl. Phys. 9, 615-620 (1959).
16. M. Ghafouri, H. Sadeghi, and M. Torkiha, "Self-consistent description of the SHFB equations for ^{112}Sn," Results Phys. 8, 734-710 (2018).
17. R. Baldik and A. Dombayci, "Investigation of the production of 68Ga using pre-equilibrium models," Appl. Radiat. Isot. 113, 10-17 (2016).
18. P. Sarriguren, O. Moreno, E. M. de Guerra, D. N. Kadrev, A. N. Antonov, and M. K. Gaidarov, "Elastic Magnetic Electron Scattering from odd-A Nuclei," J. Phys.: Conf. Ser. 1555, 012001-012008 (2020).
19. L. J. Tassie, "A Model of Nuclear Shape Oscillations for g-Transitions and Electron Excitation," Aust. J. Phys. 9(4), 407-412 (1965).
20. J. Heisenberg, J. S. McCarthy, and I. Sick, "Inelastic electron scattering from several Ca, Ti, and Fe isotopes," Nucl. Phys. A 164(2), 353-366 (1971).
21. J. Friedrich and P.-G. Reinhard, "Skyrme-force parametrization: Least-squares fit to nuclear ground-state properties," Phys. Rev. C 33, 335 (1986).
22. G. K. Mallot, "Electron Scattering of Germanium and Muonic Atoms of Krypton as a Contribution to the Systematics of the Nuclear Charge Densities," Ph.D. thesis, University of Mainz (1984).
23. H. De Vries, C. W. De Jager, and C. De Vries, "At. Data Nucl. Data Tables" 36, 495 (1987).

Impact thickness on performance of higher quality ZnTe photodetectors

Hanan K. Hassun [1,a)], Bushra H. Hussein [1], Bushra K.H. Al-Maiyaly [1], Yusra K. H. Moussa [2] , Auday H. Shaban [2], Kareem A. Jasim [1]

[1] *Department of physics, College of Education for Pure Science (Ibn Al-Haitham), University of Baghdad, Baghdad, Iraq*

[2] *Department of Remote Sensing & GIS, College of Science, University of Baghdad, Baghdad, Iraq.*

[a)] Corresponding author: hanan.k.h@ihcoedu.uobaghdad.edu.iq

Abstract. The applications of the photodetectors are developed in many fields. The influence thickness of ZnTe thin films will improve the performance and the efficiencies responsivity for suitable application of detectors. The fabrication of (ZnTe) alloy equipped with evacuate quartz tubes then heated in a furnace to be homogeneous alloy. A thin films were prepared with diverse thickness (400, 450, and 500) nm through evaporation procedure. Electrical properties of the manufactured films were investigate to achieve activations energy. Hall Effect expression for entire samples had (p-type), in addition the carriers mobility increased by rise thickness. Furthermore, current vs voltage for ZnTe:SI heterojunctions display the forward current for dark currents upsurges. The saturated currents and ideality factors reduce per cumulative thickness. The photoelectric properties designated growth illuminated currents for junctions through growing occurrence illuminate intensity. The highest rate for spectra response stretched 650 nm at a thickness of 500nm and the spectrally responsive show photodetectors were sensitively in visible sections.

Keywords: Zinc telluride, photoelectric, electrical conductivity, and specific detectivity.

INTRODUCTION

Semiconductors encourage the researchers for fabricated semiconductor lasers and light- emitting diodes in the blue and green regions of wavelengths then other optoelectronic devices, manufacture of such devices involves good characteristics[1-3] , II-VI semiconductors nanostructure had be examined generally besides established potential submission in lasers system [4] optically wave guide [5] photo detector[6] then field effects transistor[7] . Zinc telluride was best candidate, with gap for 2.25 eV besides p types conductive character, the bandgaps for binary otherwise typical inadvertently doping semiconductors nanostructure could barely been tuned with certain component, where limits the additional request on diverse fields [8]. ZnTe had be manufactured via several systems, for instance hydrothermally method [9,10], metal-organic chemicals deposit [11,], also vapor deposit technique [12]. While numerous varieties of intrinsic ZnTe nanowires have synthesize for fabricated FETs plus photodetectors, the fusion of higher quality ZnTe nano structure for suitable highest recital procedures through faster responsed time, decent reproducibly besides higher quantum efficiency was motionless great task [13,14]. Zinc telluride have cubic sphalerites or zinc blende crystallize structures, nevertheless that one could similarly prepare in hexagonally crystal [15]. Similarly, that quality made Zinc telluride excellently materials in flexible radiate detector. Also, utilized intended for radiate monitor, medically then technically tomography's [16]. Zinc telluride was most sensitives for UV lights, although had be about investigation for synthase in ZnTe structures, moreover about mechanism obtainable in research besides optoelectronics property for ZnTe nanostructure ,the low then room temperature PL ranges for single crystalline ZnTe nanowire, synthesize thru vapor phase transport technique, presented close band edges emission. Conferring for energy bands theory emission wavelength plus the emitting color was grounded in higher purities superiority then band edges emission. [17–21], renowned that insufficient works had approved out to study their

Technologies and Materials for Renewable Energy, Environment and Sustainability
AIP Conf. Proc. 3321, 020018-1–020018-7; https://doi.org/10.1063/5.0289998
Published under an exclusive license by AIP Publishing. 978-0-7354-5231-2/$30.00

photoelectric properties [22]. The II–VI thin films could be fictional thru several practices, which contain thermal evaporation [23], electrodeposition [24] sputtering [25], and wet chemical and spin coating processes [26]. In this work, we had fabricate ZnTe thin films utilized evaporation techniques in diverse thickness and demonstrate their applications as high performance photodetector.

EXPERIMENTAL PART

Zinc telluride (ZnTe99.999%) powder had deposited utilized thermal vacuum evaporation on glass substrates with thicknesses films (400, 450, 500) nm used Ed-ward Unit structure. That electrically conductive and resistivity of Zinc telluride film had be restrained by way of meaning temperatures done variety 293˚K to 423˚K thru utilizing electrically circuits. Measurement had be complete uses sensitives numerical electrometers kind. Hall effect measure was determines through utilized HMS 3000 setting, then determining majority carrier concentrations and type of carrier. Since conspiracy for forward currents against apply voltage, the ideal factors besides the saturate currents were gotten rendering the relative [27].

$$I_f = I_s \exp\left(\frac{q\,V}{\beta k_B T}\right) \quad \text{..... (1)}$$

Wherever I_s was saturation current, besides β was ideality factor had charge between 1.0 then 2.0. Current voltage characters aimed at wholly equipped ZnTe:Si junctions are complete reverse bias voltages, after were unprotected for Halogen lamps Philips 1100W, the spectrally responsive, quantum efficiency besides specifically detectives for completely sample can be expressed from equations [28],

$$\mathcal{R} = \frac{I_{ph}}{P_s} \quad \text{..... (2)}$$

Wherever (I_{ph}) was photo current graceful among the electrodes, P_s incident radiate powers appropriate organization utilize for contained mono chromates assortment [100-1000] nm.

RESULTS AND DISCUSSION

Fig.(1) demonstrations disparity for d.c conductive thin films meaning for reciprocally temperatures with dissimilar thickness, twice mechanism for activated energy E_{a1} besides E_{a2} during that temperatures variety (239- 423) K, Table.1 realized. highest temperature choice 353 to 423K the conduction mechanisms was as a result of carriers animated to extend state beyond mobility edges via thermally excitations in addition lowers temperature series 293 to 353K, the conduct mechanism attributable to carrier transported near localize state close the valence and conduction band besides hopping amongst constrained level inside energy gap [29]. After D.C measurements could realize conductive upsurges then resistivity reductions through cumulative temperatures, that attributable to properties of semiconductor where resistance of negative thermally coefficient. Moreover, the conductivities rises thru films thickness growths although activation energy diminutions, this intensifications could accredited to upsurge on mobility and the carrier concentration [30, 31].

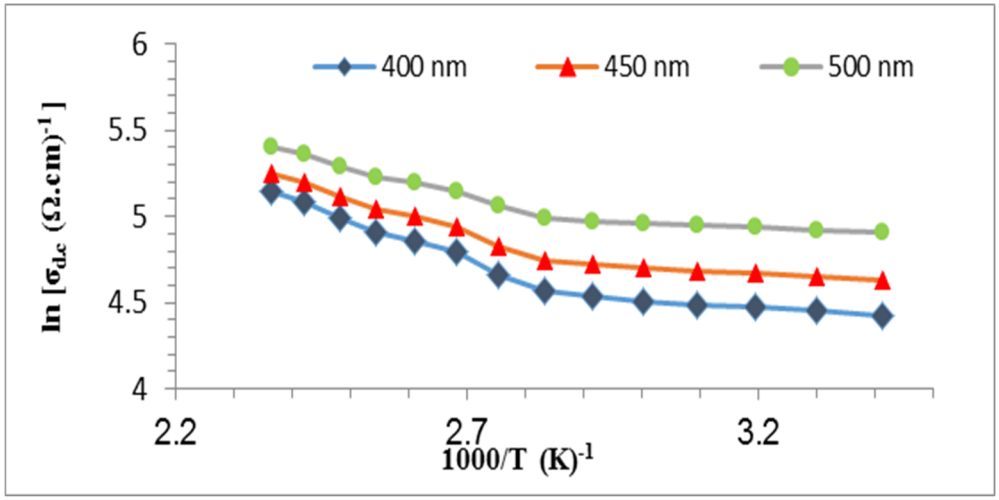

Figure 1. Ln $\sigma_{d.c}$ as opposed to $\frac{1000}{T}$ aimed at Zinc telluride film on diverse thickness.

Table 1. Activate energy intended for Zinc telluride film by dissimilar thickness.

thickness	E_{a1}(e V)	T. series(K)	E_{a2}(e V)	T. series(K)
400nm	0.0362	(293 – 353)	0.1455	(353 -423)
450nm	0.0311	(293 – 353)	0.1166	(353 -423)
500nm	0.0271	(293 – 353)	0.1078	(353 -423)

Positively sign Hall coefficients designates the conductive natures at films was p type. Figure (2) expressions that disparities of carrier concentrate besides Hall mobility thru thickness, the carrier attentiveness amplified per growing thickness, the intensification thickness for films reasons reduction on resistivity, the eventual modification on resistivity was down to the consistent grain size according to differ thickness .

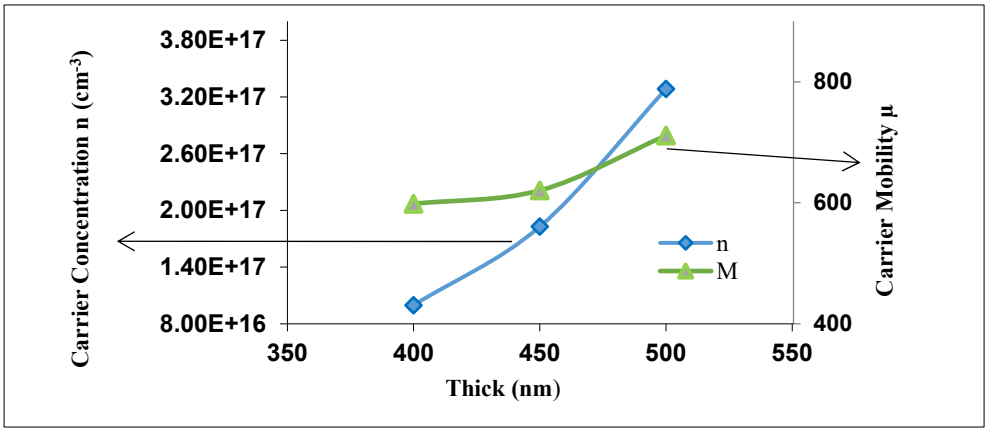

Figure 2. Disparity for carriers concentrate with mobility Zinc telluride film.

Fig.(3) demonstrations current against voltage characteristic for ZnTe:Si hetero junction depositing through dissimilar thickness, forward current had exponentially growth by lower voltages that forward dark currents were produced as a result of movement majorities carrier besides the apply voltages injected majorities carrier which centrals toward reduction the built in potential. By means of majorities and minorities carriers concentrate were highest than intrinsic carriers concentrate, that generated recombination currents with low voltages county [32]. That was result of the excited electron since valence band towards conduction band resolve recombined them per hole [33].

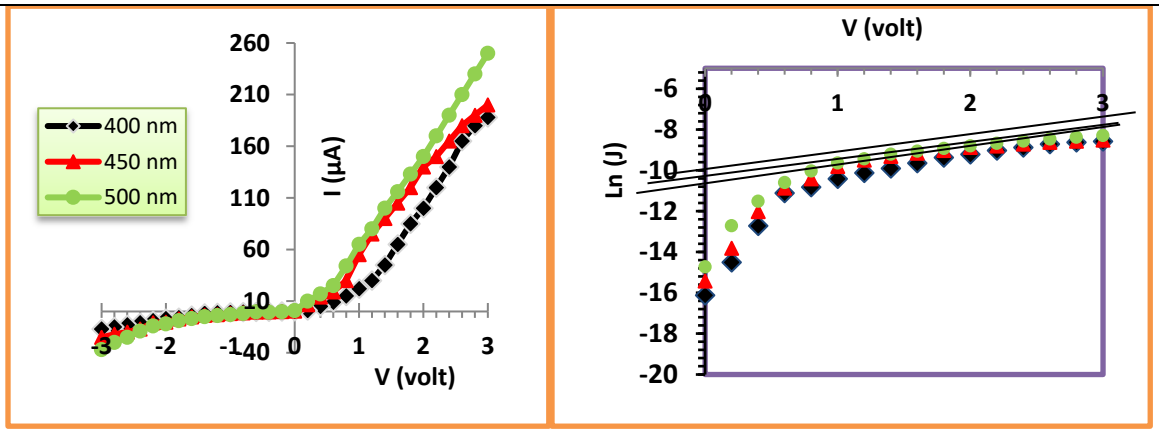

the saturation current and ideality factor			
Thick	400nm	450nm	500nm
Ideality factor	**2.13**	**1.87**	**1.62**
Saturate currents	**2.03**	**3.74**	**5.33**

Figure 3. I-V Characteristic plus Ln J against V intended forward bias in dark for ZnTe heterojunctions under dark with different thickness

Also, values of currents upsurges through cumulative thickness for ZnTe film that was recognized towards effect of mobility charges carriers by interfaces. The quantities are accepted below diverse incident powers density equivalent near [200, 157, 100, 69, and 30] mW/cm3 .Figure 4. expressions photocurrent plus the reverse bias voltage for ZnTe:Si heterojunction by changed thickness, the photocurrents rises thru growing reverse bias voltages, by reason of separated the electrons holes pairs at that time rises the photocurrents [34], the resistivity was comparatively higher, then mobility carrier was ample low since carrier were simply seize formerly photocurrents are comparative weak. The photocurrents similarly growths speedily thru thickness cumulative. Correspondingly, completely fabricated detector had higher responses through amplified incident power density besides concluded improved illuminated currents value per augmented powers. That attributable for growing intensity for incident lights resources growth incident photon that cause intensification on generate charges carrier then increased generate illumination currents thru collective powers density [35].

Fig.(5) expression dissimilarity for spectrally responsivity thru wavelength , investigate with wavelength resonated 400nm to 1000nm through 3 V basis, where low wavelength area signifies wavelength under 500nm, twice district characterizes wavelength above 500nm under 680nm, then latter wavelength extended 680nm. The responsivity of the ZnTe/Si device was slightly lower after wavelength is dumpier than 500 nm, the responsivity influences extreme with 500 nm. also for the wavelength extensive than 680 nm, where determined the development for spectral responsivity was attributable to e electrons holes pair motivated thru the incident light. Table. (2) Demonstration some of the optical spectrum parameters obtained using equations [36, 37].

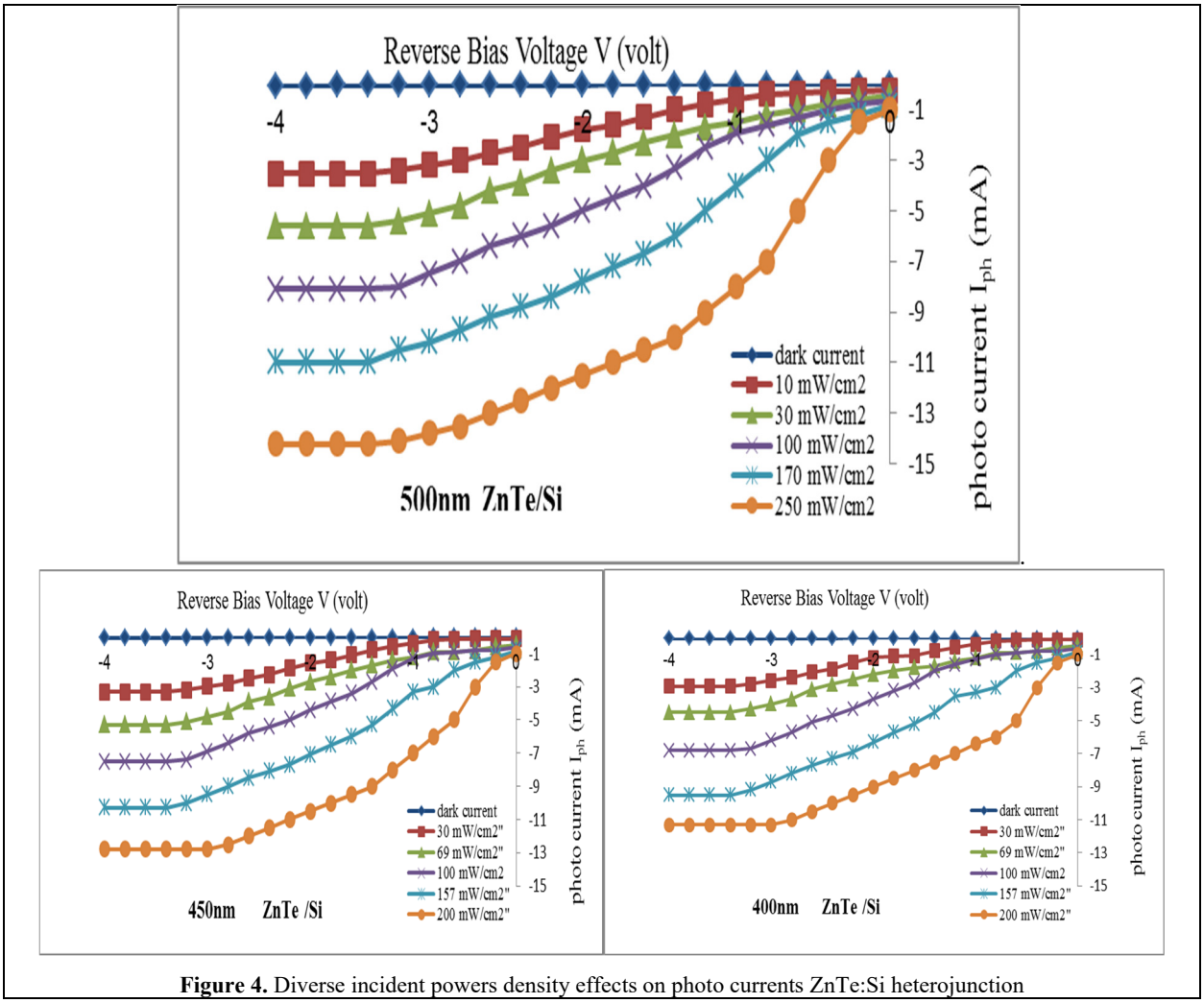

Figure 4. Diverse incident powers density effects on photo currents ZnTe:Si heterojunction

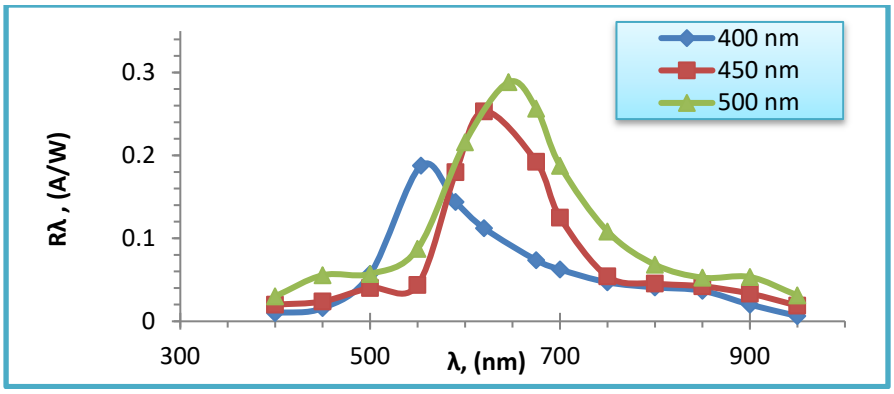

Figure 5. The spectral responsivity for ZnTe/Si detectore with different thickness

Table 2. Optical Spectrum Parameters aimed at ZnTe:Si detectors in dissimilar thickness

Thickness	wavelength λ	Optical Spectrum Parameters				
		refractive index	Band gap Eg (eV)	Transmittance%	Reflection%	extinction coefficient
400	553	2.645	2.25	49.459	19.965	0.777
450	620	2.615	2.16	35.768	19.604	0.913
500	650	2.589	1.98	31.875	18.431	1.066

Slight increase of responsivity in the long wavelength side is possibly is accredited for improved absorptive of higher energy photon in nearest surface regions of semiconductors. Likewise that augmented of responsivity could qualified towards lessening on resistances on larger rate for ZnTe 500nm thickness besides tended to improved photocurrents, then since reducing the density of state which acts in recombinant center concentrate on twice side of interface, totally sample had good response in the visible region.

Fig.(6) demonstration that distinction of quantum efficiency η besides specific detectivity D* through wavelength of ZnTe:Si hetero junction by altered thickness influenced on 3V, Figure illustrations the extreme rate of quantum efficiency 58.476% on around 650nm aimed at thickness 500nm, Table.(3) shows the maximum value the spectral responsivity, quantum efficiency and specific detectivity according to the corresponding wavelengths.

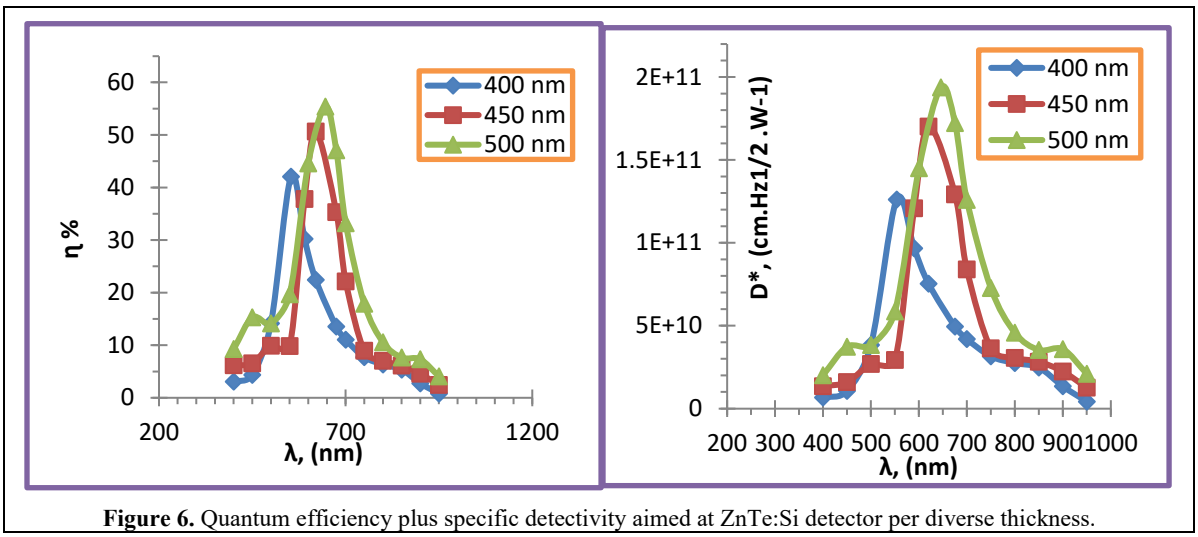

Figure 6. Quantum efficiency plus specific detectivity aimed at ZnTe:Si detector per diverse thickness.

Table 3. Responsivity, quantum efficiency and specific detectivity for ZnTe:Si detectors

Thickness	wavelength	responsivity	quantum efficiency	specific detectivity
400	553	0.187	42.061	1.26156×10^{11}
450	620	0.253	50.641	1.70117×10^{11}
500	650	0.288	55.387	1.93804×10^{11}

Specific detectivity growths through cumulative thickness, the higher rate by round 650nm aimed at thickness 500nm like mention in table 3, dissimilarity for quantum efficiency was unpaid reduction the recombination center where consequence values of specific detectivity, besides reduction the noise currents rendering towards decline dark currents. Moreover Fig.(7) expression [NEP] Noise Equivalent Powers were view frequently utilize on count sensitivity for detectors, the inequality of NEP for thin films below deduction of thickness , that lower NEP occurs as soon as R_λ had exciting. NEP reductions thru influence thickness characteristic by reduced the recombination procedure.

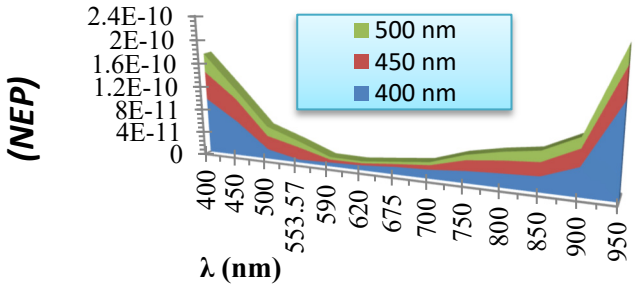

Thickness	NEP	R_λ
400	5.04884E-12	0.187772926
450	3.74414E-12	0.253205128
500	3.28653E-12	0.288461538

Figure 7. Variation of Noise Equivalent Power (NEP) with disparity thickness for ZnTe/Si photodetectors

CONCLUSIONS

ZnTe thin films have been manufactured thru thermal evaporation procedure per consequence of thickness ,twice mechanism for activate energy reductions through growing thickness then the conductivity upsurges with thick films, the highest value for D.C conductivity for 500nm thickness, Hall measure demonstration completely films were p types besides the mobility intensifications. Also, current voltage measures aimed at ZnTe:Si hetero junction displayed reduction dark currents thru result of thickness in addition wholly photodetector had high responses on visible regions intended for diverse thickness besides higher rate for spectrally responses, quantum efficiency plus specific detectivity with 500 nm.

REFERENCES

1. Nakashima, S., Nakakura, Y. and Fujiyasu, H., “Raman scattering from ZnTe-ZnSe strained-layer superlattices”, Appl. Phys. Lett., Vol.48, No.3, 1986, pp.236-238.
2. Basol, B.M. and Kapur, V.K., “Preparation of ZnTe thin films using a simple two-stage process”, Thin Solid Film, Vol.165, 1988, pp.237-241.
3. Kuskovsky, I.L., Tian, C. and Neumark, G.F., “Optical properties of ZnSe:Te grown by MBE”, Phys. Rev. B, Vol.63, 2001, pp.1-8.
4. Pan, A. L; Liu, R. B; Zhang, Q. L; Wan, Q; He, P.B; Zacharias, M; Zou, B. S J. Phys. Chem. C 2007, 111, 14253.
5. Pan, A. L.; Liu, D.; Liu, R. B.; Wang, F. F.; Zhu, X.; Zou, B. S.Small 2005, 1, 980.
6. Singh, A.; Li, X. Y.; Protasenko, V.; Galantai, G.; Kuno, M.; Xing, H. L.; Jena, D. Nano Lett. 2007, 7, 2999.
7. Wang, Y. G.; Zou, B. S.; Wang, T. H.; Wang, N.; Cai, Y.; Chan, Y. F.; Zhou, S. X. Nanotechnology 2006, 17, 2420.
8. Samir A Maki, Hanan K Hassun, Effect of Aluminum on Characterization of ZnTe/n-Si Heterojunction Photo detector, IOP Conf. Series: Journal of Physics: Conf. Series 1003 (2018) 012085 doi :10.1088/1742-6596/1003/1/012085.
9. J. Zhang, P. C. Chen, G. Z. Shen, J. B. He, A. Kumbhar, C. W. Zhou, and J. Y. Fang, “P-type field-effect transistors of single-crystal zinc telluride nanobelts,” Angew. Chem. Int. Ed. Engl. 47(49), 9469–9471 (2008).
10. Bushra H. Hussein, Iman Hameed Khudayer, Mohammed Hamid Mustafa, Auday H. Shaban, Effect of V, In and Cu doping on properties of p-type ZnSe/Si heterojunction solar cell, Progress in Industrial Ecology – An International Journal, Vol. 13(2): 173-186 (2019).

11. Z. Li, J. Salfi, C. D. Souza, P. Sun, S. V. Nair, and H. E. Ruda, "Room temperature single nanowire ZnTe photoconductors grown by metal-organic chemical vapor deposition," Appl. Phys. Lett. 97, 063510 (2010).
12. S. Y. Li, Y. Jiang, D. Wu, B. B. Wang, Y. G. Zhang, J. W. Li, X. M. Liu, H. H. Zhong, L. Chen, and J. S. Jie,"Structure and electrical properties of p-type twin ZnTe nanowires," Appl. Phys., A Mater. Sci. Process. 102(2), 469–475 (2011).
13. Bushra K H AlMaiyaly, Bushra H Hussein, Auday H Shaban, Fabrication and characterization study of ZnTe/n-Si heterojunction solar cell application, IOP Journal of Physics: Conference Series, Vol. 1003, conf. 1, pp: 012084(1-10), 2018.
14. Zhe Liu, Gui Chen, Bo Liang, Gang Yu, Hongtao Huang, Di Chen, and Guozhen Shen, Fabrication of high-quality ZnTe nanowires toward high-performance rigid/flexible visiblelight photodetectors, 22 Mar 2013 (C) 2013 OSA 25 March 2013 / Vol. 21, No. 6 / OPTICS EXPRESS 7799.
15. D. O'Dell, MBE Growth and Characterization of ZnTe and Nitrogen-doped ZnTe on GaAs(100) Substrates, Department of Physics, University of Notre Dame, (2011).
16. A. F. Wells. Structural Inorganic Chemistry, Oxford Clarendon Press, 5th ed, (1984).
17. Bushra K. H. Al-Maiyaly, Bushra H. Hussein, Ayad A. Salih, Auday H. Shaban, Shatha H. Mahdi, Iman H. Khudayer, Synthesis and characterization study of n-Bi2O3/p-Si heterojunction dependence on thickness, AIP Conf. Proc., Vol.1968, pp:030046-1–030046-11, 2018.
18. L. Li, Y. W. Yang, X. H. Huang, G. H. Li, and L. D. Zhang, "Fabrication and characterization of single-crystalline ZnTe nanowire arrays," J. Phys. Chem. B 109(25), 12394–12398 (2005).
19. H. B. Huo, L. Dai, D. Y. Xia, G. Z. Ran, L. P. You, B. R. Zhang, and G. G. Qin, "Synthesis and optical properties of ZnTe single-crystalline nanowires," J. Nanosci. Nanotechnol. 6(4), 1182–1184 (2006)
20. Y. L. Cao, Y. B. Tang, Y. Liu, Z. T. Liu, L. B. Luo, Z. B. He, J. S. Jie, R. Vellaisamy, W. J. Zhang, C. S. Lee, and S. T. Lee, "Coaxial nanocables of p-type zinc telluride nanowires sheathed with silicon oxide: synthesis, characterization and properties," Nanotechnology 20(45), 455702 (2009).
21. Samir A. Maki Hanan K. Hassun, The Structural and Optical Properties of Zinc Telluride Thin Films by Vacuum Thermal Evaporation Technique, Ibn Al-Haitham J. for Pure & Appl. Sci. Vol.29 (2) 2016.
22. Q. F. Meng, C. B. Jiang, and S. X. Mao, "Ohmic contacts and photoconductivity of individual ZnTe nanowires," Appl. Phys. Lett. 94(4), 043111 (2009).
23. A. K. S. Aqili, A. Maqsood and Z. Ali: Appl. Surf. Sci., 2001, 180, 73–80.
24. N. B. Chaure, J. P. Nair, R. Jayakrishan, V. Ganesan and R. K Pandey: Thin Solid Films, 1998,324, 78.
25. T. A. Gassert, A. R. Mason, R. C. Reedy, R. Maton, T. J. Cutts and P. Sheldon: J. Electron. Mater, 1995, 24, 1443.
26. J. Chen, D. Chen, J. He, S. Zhang and Z. Chen: Appl. Surf. Sci., 2009, 255, 9413–9419.
27. Hanan K. Hassun, AIP Conf Proc 2018; 1968. 020017; https://doi.org/10.1063/1.5039176
28. Hanan K. Hassun, Bushra H. Hussein, Ebtisam M.T. Salman, Auday H. Shaban, Energy Report, 2020, Vol.6, pp:46-54; https://doi.org/10.1016/j.egyr.2019.10.017
29. S. M. Sze, Physics of Semiconductor Devices, 3rd Edition. John Wiley and Sons, Inc Publication, Canada, (2007).
30. K.Z. Yahiya, E. T. Salem, M.S. Muhammad. Optical Constants of Zinc Telluride Thin Films in the Visible and Near-Infrared Regions, Laser Research Unit, School of Applied Sciences, Univ. of Tech. Eng.&Tech.,Vol.26,No.5,(2008).
31. Sa. M. Alia, H. K. Hassuna, A. A. Saliha, R. H. Athabb, B. K. H. Al-Maiyalya, B. H. Husseina, Study the properties of Cu2Se thin films for optoelectronic applications, Chalcogenide Letters Vol. 19, No. 10, October 2022, p. 663 – 671, https://doi.org/10.15251/CL.2022.1910.663.
32. B. H. Hussein, H. K. Hassun, B. K.H. Al-Maiyaly, S. H. Aleabi, Effect of copper on physical properties of CdO thin films and n-CdO: Cu / p-Si heterojunction , Journal of Ovonic Research Vol. 18, No. 1, January - February 2022, p. 37- 42.
33. Y.Segui, F.Carrere and A.Bui, Thin Solid Films, Vol.92, p. (303-310), (1982).
34. M.Burgelman, P.Nollet and S.Degrave, Applied Physics A,69,149, p. (423 -434), (1999).
35. B. L. Sharma and R. K. Purohit, Semiconductor Heterojunctions, 1st Edition. Pergamon Press Ltd, NewYork, (1974).
36. H. K. Hassun, B. K.H. Al-Maiyaly. A. H. Shaban, Fabrication and evaluation of CuAlSe2/Si photodetector, Chalcogenide Letters Vol. 20, No. 2, February 2023, p. 145 - 152 https://doi.org/10.15251/CL.2023.202.145
37. Rana Hameed Athab, Bushra H. Hussein, Growth and Characterization of Vacuum Annealing AgCuInSe2 Thin Film, Ibn Al-Haitham Journal for Pure and Applied Sciences, IHJPAS. 35(4)2022.

Digital image enhancement by noise removal post-decryption applied by a combination of wave transformers

May A. Salih[1,a)], Suad A. Alasadi[2,b)], Baydaa Jaffer Al-Khafaji[3,c)]

[1] *Department of Information security, College of Information Technology, University of Babylon, Babil, Iraq*
[2] *Department of Information Networks, College of Information Technology, University of Babylon, Babil, Iraq*
[3] *Computer Science Department College of Education for Pure Science/ Ibn Al-Haitham University of Baghdad, Baghdad, Iraq*

[a)] *Corresponding author: may.abd@uobabylon.edu*
[b)] *suad.alasady@uobabylon.edu.iq*
[c)] *Baydaa.j.s@ihcoedu.uobaghdad.edu.iq*

Abstract. In numerous digital image processing applications, the observed image is typically represented as being contaminated by various forms of noise, leading to the creation of a noisy version. Therefore, picture DE noising is a significant problem that seeks to identify an estimated version of the noisy image that closely resembles the original image. A proposed approach involving hybrid transformations and the associated methods of processing. Multiple local transforms are combined to create a novel hybrid transform that possesses outstanding attributes and delivers remarkably high visual performance. We have introduced a novel approach for improving image quality by utilizing both linear and nonlinear enhancement functions. The results obtained from these methods have been quite satisfactory. The average Peak Signal-to-Noise Ratio (PSNR) of the noisy image improves to 35.3799 in the Multiwavelet reconstructed image and 42.7543 in the suggested transform reconstructed image, based on a database of cooled images. The efficacy of these strategies has been assessed computationally using MATLAB, version 7 software tools.

Keywords: DMWT, DE noising , STFT, image processing , PSNR, (2-D IFFT), FFT

INTRODUCTION

Given that our eyes perceive an increased quantity of information compared to our other sensory organs, and considering the dominance of the visual cortex in the brain, it may be concluded that images hold a pivotal position in our existence [1]. The rise of computers and their expanding significance in all aspects of daily life have made the representation and manipulation of digital images more significant. Images are of great importance in computer graphics, particularly in tasks such as picture synthesis, processing, and evaluation [2].The rapid advancement of digital scientific instruments has brought up a plethora of intriguing challenges in the realm of data analysis & signal processing. In various fields such as extra galactic astronomy, molecular spectroscopy, medical imaging, synthetic aperture radar imaging, and computer vision, it is necessary to extract a signal, curve, image, spectrum, or density from data that is incomplete, indirect, and noisy [3].

Transformation is a procedure that moves an object from one domain to another in order to extract significant implicit information that can be leveraged for its identification [4].

Image de noising is a crucial effort in the realm of image processing and analysis, and it holds great importance in contemporary applications across various domains, such as medical imaging and preprocessing for computer vision. The objective of DE noising is to eliminate the noise while incurring minimal degradation to the image. Typically, when the end user is a human, the measure of how well the noise is removed is based on how humans perceive the visual quality of the outcome, rather than using any established mathematical criteria [5].image enhancement techniques are employed to improve the visual perception of a picture by reducing noise and enhancing and sharpening

Technologies and Materials for Renewable Energy, Environment and Sustainability
AIP Conf. Proc. 3321, 020019-1–020019-7; https://doi.org/10.1063/5.0289593
Published under an exclusive license by AIP Publishing. 978-0-7354-5231-2/$30.00

image elements for the purpose of display and analysis. Image enhancement is the utilization of certain strategies to aid in the resolution of a computer imaging problem. [6,7].

Figure(1) demonstrates the significance of the application through the feedback loop that connects the output image to the beginning of the enhancement process. This feedback loop represents the experimental aspect of the development. The enhanced picture is defined as E(r, c) in this figure. Image enhancement techniques can be applied as prior to treatment phases to facilitate subsequent processing or as post-processing processes to enhance the visual experience of a processed image. Alternatively, image enhancement can also be the primary objective. In general, image enhancement techniques are employed to improve the visual quality of photographs [8,9].

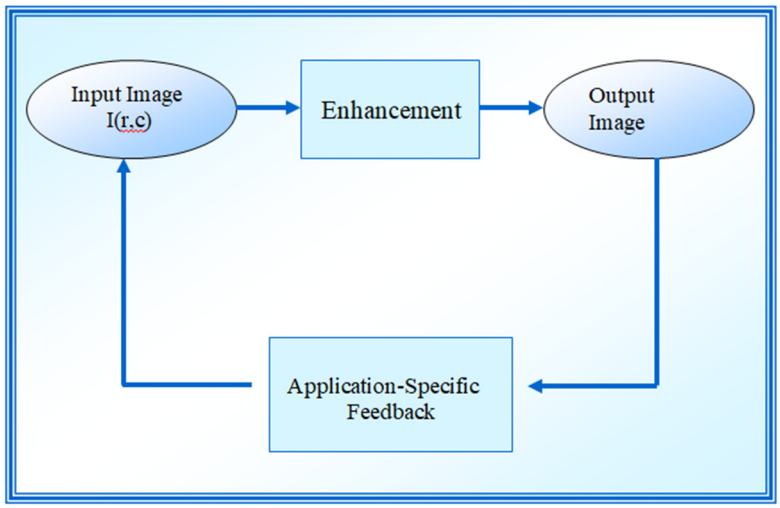

Figure 1: The Image Enhancement Process

The process of transformation is achieved by convolving functions that are often orthogonal, resulting in an invertible transform. This implies that the initial function in the initial domain can be retrieved without any loss of data [10].

In the nineteenth century, the French scientist J. Fourier demonstrated that any periodic functional may be represented as an endless series of periodic complex functions that are exponential. After the discovery of this notable characteristic of periodic functions, the concepts were extended to non-periodic functions and subsequently to regular or non-periodic time discrete signals. Subsequently, the Fourier transform (FT) gained widespread recognition as a highly renowned computational tool for computers. The given function f(t) can be transformed into its Fourier transform F(□).. [11,12].

$$F(\omega) = \int_{-\infty}^{\infty} f(t)\, e^{-j\omega t}\, dt \quad \ldots\ldots\ldots \quad \ldots(1)$$

The inverse Fourier Transform, then is:

$$f(t) = \frac{1}{2\pi} \int_{-\infty}^{\infty} F(\omega)\, e^{j\omega t}\, d\omega \quad \ldots\ldots\ldots \quad \ldots(2)$$

It is important to observe that in the equation for the Fourier Transform, the integration is performed over the entire time domain, ranging from negative infinity to positive infinity. Regardless of the timing of the part with frequency ω, it will have an equal impact on the integration result. A significant drawback of the Fourier Transform is its failure to provide temporal information in the spectrum. The algorithm for the Fast Fourier Transform (FFT) has been discovered to have a broad range of applications.

This transformation can be applied to the two-dimensional domain using its efficient algorithm. Therefore, it is employed for the purpose of picture processing. In order to enhance the efficiency of the Fourier transform, it was adapted into a short-time Fourier transform (STFT) [13,14]. which proves to be effective for signals that are not steady. The fundamental concept is to partition the signal into sufficiently short segments, where those sections can be presumed to be in a state of rest. The breadth of the window in question must match the portion of the signal when this assumption is true. The Short-Time Fourier Transform (STFT) is associated with many limitations. [15, 16].

When an infinitely long window is used, the Fourier Transform produces accurate frequency resolution but does not provide any time information. Conversely, to achieve a stationary sample, it is necessary to use a window size that is sufficiently tiny for the signal to remain stationary.

The Wavelet Transform (WT) is an advanced variation of the Fourier transform that has been created to be more efficient [17]. The wavelet is considered the most efficient transform for handling images, sounds, or any other patterns due to its powerful representation of time and frequency [18].The core concept underlying wavelets is to examine the signal at many scales or resolutions, a process known as multiresolution analysis. The impact of the wavelet transform on an image can be described as the process of extracting the image's information and representing it in a universal space that is approximately orthogonal and statistically independent. This universal space comprises projections of the subject matter.

The original subject before the abstraction process can be obtained by taking the algebraic sum of each of these projections and adjusting the scale in each projection [19, 20]. Wavelet transforms in certain applications necessitate filters that possess several desirable qualities, including orthogonality and symmetry, in order to achieve optimal performance. Nevertheless, the design options for wavelets are restricted as they are unable to contain all of these desirable qualities concurrently [21].

Wavelets are a valuable tool in signal processing applications, particularly in tasks like picture compression and noise reduction. Until recently, the only type of wavelets that were known were scalar wavelets, which are formed by a single scale function. However, it is possible to envision a scenario where there are multiple scaling functions. [22,23].

The emerging field of multiwavelets demonstrates potential in overcoming some constraints associated with wavelets. Features such as brief support, orthogonality, symmetry, and vanishing moments are seen as crucial in signal processing. It is not possible for a scalar wavelet to have all of these qualities simultaneously. In contrast, a multiwavelet system has the ability to achieve The reconstruction process is done perfectly while additionally preserving the length of the original data (symmetry). In addition, the performance at the borders is remaining due to linear-phase symmetry, and an excellent degree of accuracy is achieved by vanishing moments. Multiwavelets possess the power to surpass scalar wavelets that are in image processing tasks. [24,25].

The aim of this a novel approach to image improvement that employs a recently developed set of hybrid transformations. These have been suggested as substitutes for the Wavelet and Multiwavelet methods of representing image data.

METHODOLOGY

Wavelet bases have challenges when detecting highly anisotropic elements, such as alignment in an image. This is These hybrid transformations are composed of fundamental components that possess extraordinary directional sensitivities and are extremely anisotropic. The suggested transform consists of three core transformations that compose its main structure. The Fast Fourier Transform (FFT), Radon Transform, and Multiwavelet Transform, Figure (2).

In order to enhance the accuracy of the individual transformations and address their inherent constraints, another transformation is suggested. The main idea underlying the transform is to initially employ the two-dimensional fast Fourier transformation (2-D FFT) on the two-dimensional signal (image). Next, we will convert a line sampling method into a point sampling technique using the Radon transformation. Therefore, it is necessary to perform a one-dimensional inverse Fast Fourier Transform (1-D IFFT) on each column of the resulting two-dimensional signal. Ultimately, it is necessary to apply the Multiwavelet transformation to every row of the resulting two-dimensional signal. The architecture of this transform has four key components, namely:

a) Two-dimensional Fast Fourier Transformation (2-D FFT).

c) The Radon transform.

b) The one-dimensional inverse fast Fourier transformation (1-D IFFT).

d) The one-dimensional discrete multiwavelet transformation (1-D DMWT)

e) The novel hybrid transform is expected to demonstrate exceptional performance and robust features. This is because it incorporates the positive attributes of the local transformations. The Multiwavelet transform has superior features and performance compared to the Wavelet transform. The quality of the signal's one level Multiwavelet transform is equivalent to the output result signal of the Wavelet transformation at two levels. The Multiwavelet transformation has the ability of handling signals with two dimensions that have increased complex than to the Wavelet transform.

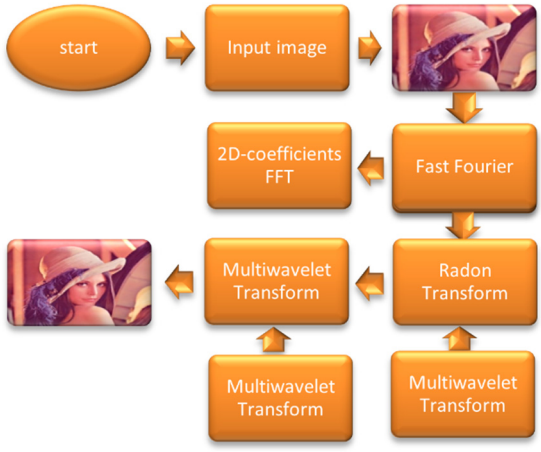

Figure 2. The flowchart of proposed system

THE RESULTS & DISCUSSION

As a result, the approaches used to improve anything are tailored to the application in question and are typically created via direct experience This study examines the outcomes of image de noising applying both DMWT & DMWLT transformations on a database of color images, specifically focusing on a building image. Various levels of noise were added to the image to assess the efficacy of the de noising techniques. The average Peak Signal-to-Noise Ratio (PSNR) of the noisy image improves to 35.3799 in the Multiwavelet reconstructed image and 42.7543.

Below is a table that compares the outcomes of applying the proposed method to both the same noisy images and different noisy images with the same Signal-to-Noise Ratio (SNR). Then, by comparing the SNR value before and after the procedure has been performed. It has significance to observe that a higher value of SNR corresponds to an improved image quality. It must be noted that the Signal to Noise Ratio (SNR) is calculated using this equation:

$$SNR = 10 \log_{10}\left[\frac{\sum_{r=0}^{M-1}\sum_{c=0}^{N-1}\left(\hat{I}(r,c)\right)^2}{\sum_{r=0}^{M-1}\sum_{c=0}^{N-1}\left(X(r,c)-(r,c)\right)^2}\right] \quad \text{.....(3)}$$

The symbol (r, c) indicates the data stream, which is the de noised image. The signal has r rows, each with a size of M, and c columns, each with a value of N. Let X(r, c) indicate the mistakes in the noisy image, where r is the number of rows and c is the number of columns. The size of each row is M and the size of each column is N.

The objective measures of this algorithm with both hard and soft-thresholding schemes are compared in table (1) that describes the PSNR and SNR of a database of images. However, the estimated images obtained from hard-thresholding typically exhibit spurious oscillations and do not have the desired smoothness properties.

Table 1: PSNR, SNR results of the filtered image with multiwavelet transform in Hard Thresholding (HT) and Soft Thresholding (ST).

Noisy image		De noising by multiwavelet thresholding			
		HT	ST	HT	ST
PSNR	SNR DB	PSNR	PSNR	SNR dB	SNR Db
26.5217	12.2979	36.5271	37.7004	22.3866	23.7658
24.1953	10.0038	34.3593	35.8722	20.5484	21.6517
20.7081	7.9383	31.8699	32.9439	18.8841	19.7680
16.7599	5.1354	28.9270	29.7543	16.6750	17.6279

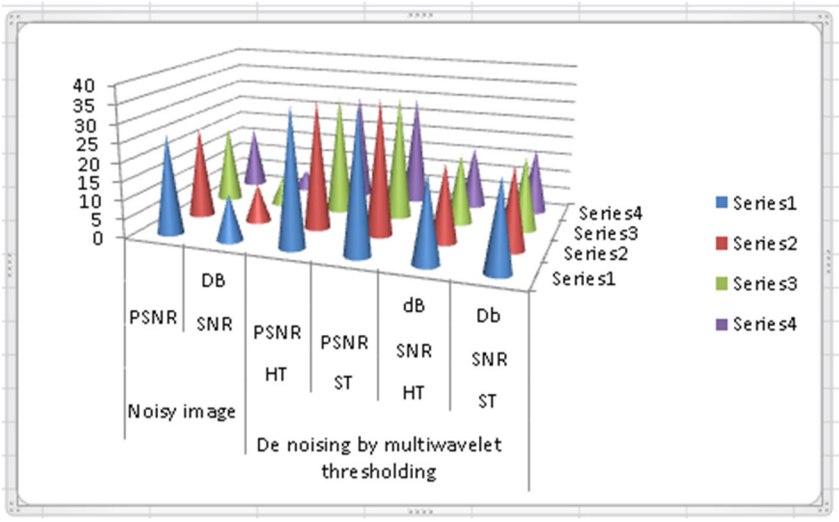

Figure (2): chart DE noisy by MWT Thresholding

in table (2). The table provides information on the SNR and PSNR of an array of images. Soft thresholding yields superior outcomes compared to harsh thresholding in numerous images. The PSNR and SNR values of the filtered picture using Hard Thresholding (HT) and Soft Thresholding (ST) for image de noising are provided

Table 2: The Results of the SNR and PSNR of an array of images

Noisy Image		*De noising by Thresholding*			
		HT	ST	HT	ST
PSNR Db	SNR Db	*PSNR* Db	PSNR D b	SNR D b	SNR Db
26.44217	12.2979	42.5279	48.7004	27.3866	29.1658
25.1553	10.0038	40.0393	45.9222	25.9484	27.0911
22.7001	7.9383	37.8499	41.8393	22.8841	23.9873
20.7599	5.1354	35.3300	36.9303	19.9001	21.6222

The algorithm's objective measures, using both hard and soft thresholding approaches, are contrasted. Ratios of PNCR,SNR for noisy image &De noisy shown in Figure (4).

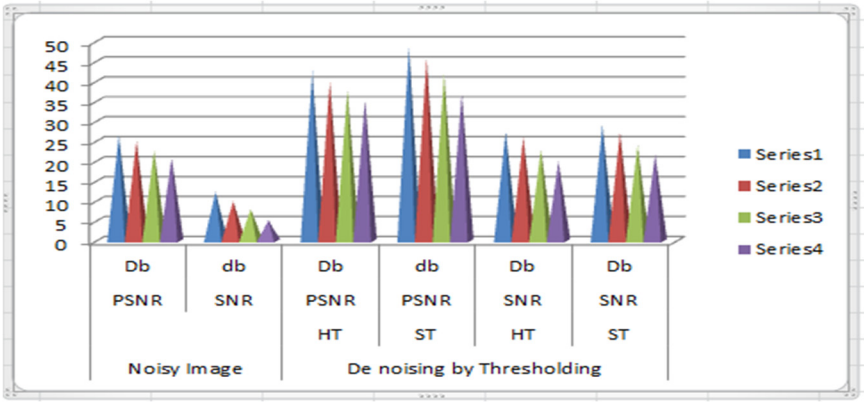

Figure (4): chart Ratios of PNCR,SNR for noisy image &De noisy

table (3), DMWLT provides SNR and PSNR values that are higher when DMWT is applied to all levels of noise established to the image. For instance, the Peak Signal-to-Noise Ratio (PSNR) is 35.3799 in the Discrete Multi-Wavelet Transform (DMWT) and 42.7543 in the Discrete Multi-Wavelet Laplace Transform (DMWLT). The table (2) shows many photos and presents a comparison of the outcomes obtained from the DMWT & DMWLT transformations.

Table 3: De noising by DMWT(proposed) Thresholding

Noisy Image		De noising by DMWT Thresholding		De noising by DMWT(proposed) Thresholding	
SNR	PSNR	SNR	PSNR	SNR	PSNR
14.4667	27.5217	28.0858	51.6679	31.8965	62.7004
7.5567	25.1953	24.6896	47.4354	27.8659	56.8722
5.6787	18.7081	21.9754	41.8693	24.4536	50.9439
3.8354	14.7599	18.5437	35.3799	20.6569	42.7543

The Signal-to-Noise Ratio (SNR) and Peak Signal-to-Noise Ratio (PSNR) outcomes of the de noised filtered image are evaluated using various noise ratios of Multiwavelet transforms. Figure (5).

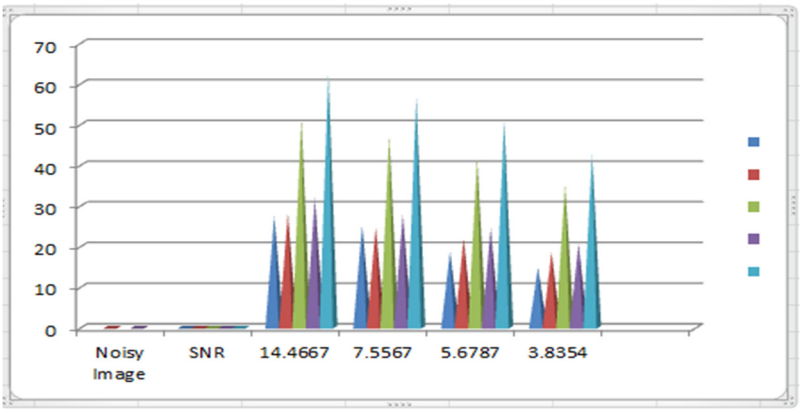

Figure (5): chart noisy image &SNR De noising by DMWT Thresholding

CONCLUSION

The suggested transform shown excellent efficacy in image de noising and enhancement applications by successfully removing noise while simultaneously sharpening and smoothing the image. An effective transform is achieved by combining the benefits of several transforms and hybrid techniques. The novel transforms for data filtering involve the introduction of separate incremental white noise corrupt images. By evaluating the Multiwavelet and suggested transforms, it becomes evident that the latter is more effective in removing noise from images than the former. For instance, when using a database of cooled photos, the average Peak Signal-to-Noise Ratio (PSNR) of the noisy image is 14.7599. However, when applying the Multiwavelet transform, the PSNR increases to 35.3799. Furthermore, when using the suggested transform for image reconstruction, the PSNR further improves to 42.7543. After testing one hundred various collar photos, it is evident that the suggested method outperforms Multiwavelet in noise reduction. Consequently, the enhanced photographs produced by the proposed method are visually more appealing than those produced by Multiwavelet. A non-linear enhancement function was applied to the discrete coefficients, resulting in superior performance compared to a linear enhancement function in multiple images for the purpose of sharpening and smoothing. The success of the thresholding-de noising method is crucial for the thresholding algorithm. The suggested transform offers a more straightforward and easily implementable approach, as the geometric structure of the optimal sequence of directions (Radon transform) remains consistent in both the forward and inverse sequences.

REFERENCES

[1] B.J AlKhafaji, “Image Improvement Using The Combination of Wavelet and Multiwavelet Transform “2010 - Ibn AL-Haitham Journal For Pure and Applied Science VO L.23 (3).

[2] Portilla, J., Strela, V., Wainwright, M., Simoncelli, E.P., “Image Denoising using Gaussian Scale Mixtures in a Wavelet Domain”, TR2002-831, Computer Science Dept, New York University. 2002.

[3] Iptehaj Alhakam, Nassir H Salman(*2022*), An Improved Probability Density Function (PDF) for Face Skin Detection, *Iraqi Journal of Science, Vol. 63, No. 10, pp: 4460-4473,* DOI: 10.24996/ijs.2022.63.10.31

[4] B.J AlKhafaji, M Salih, S Shnain, Z Nabat ,segmenting video frame images using genetic algorithms,2020 Periodicals of Engineering and Natural Sciences 8 (2), 1106-1114
[5] W. H. Abdulsalam, R. S. Alhamdani, and M. N. Abdullah, "Emotion recognition system based on hybrid techniques," International Journal of Machine Learning and Computing, vol. 9, 2019.
[6] B.J AlKhafaji, MA Salih, SAH Shnain, OA Rashid, AA Rashid, MT Hussein,2021, Applying the Artificial Neural Networks with Multiwavelet Transform on Phoneme recognition ,Journal of Physics: Conference Series 1804 (1), 012040.
[7] RAHMA, A.M.S., RAHMA, M.A.S., and RAHMA, M.A.S. (2015) Automated analysis for basketball free throw. In: Proceedings of the 7th International Conference on Intelligent Computing and Information Systems, Cairo, December 2015. Piscataway, New Jersey: Institute of Electrical and Electronics Engineers, pp. 447-453.
[8] B.J AlKhafaji Steganography techniques using tunes and Discrete Cosine Transform (DCT) Journal of Xi'an University of Architecture & Technology, S. (2020). Volume XII, Issue IV, - 5234- 5244
[9] Abdulsalam WH, Alhamdani RS, Abdullah MN. Facial emotion recognition: A survey. International Journal of Advanced Research in Computer Engineering & Technology (IJARCET). 2018 Nov;7(11)
[10] B.J AlKhafaji, M Salih, S Shnain, Z Nabat ," Improved technique for hiding data in a colored and a monochrome images",2020, Periodicals of Engineering and Natural Sciences 8 (2), 1000-1010
[11] Ali RH, Abdulsalam WH." The prediction of COVID 19 disease using feature selection techniques". InJournal of Physics: Conference Series 2021 May 1 (Vol. 1879, No. 2, p. 022083). IOP Publishing.
[12] Baydaa Jaffer Al-Khafaji, Abdul Monem S Rahma, (2023). "Proposed new modification of AES algorithm for data security", Global Journal of Engineering and Technology Advances, *Vol. 3, No. 12, pp* 117–122
[13] AlSaidi, Bushra Kh, Baydaa Jaffer Al-Khafaji, and Suad Abed Al Wahab. "Content Based Image Clustering Technique Using Statistical Features and Genetic Algorithm." *Engineering, Technology & Applied Science Research* 9.2 (2019).
[14] Al-Khafaji, Baydaa Jaffer. "Proposed speech analyses method using the multiwavelet transform." *Ibn AL-Haitham Journal For Pure and Applied Science* 27.1 (2017): 394-401.
[15] Baydaa J Al-Khafaji, Detect The Infected Medical Image Using Logic Gates." Ibn AL-Haitham Journal For Pure and Applied Science Vol. 27.2 (2014): p.260-267.
[16] Baydaa Jaffer Al-Khafaji Color image analyses using four deferent transformations (FFT-DCT-DWT-DMWT).(2014) Computer Engineering and Intelligent Systems www.iiste.org ISSN 2222-1719 Vol.5, No.10, *pp* 16–24
[17] Baydaa-Jaffer Al-Khafaj Abdul Monem S. Rahma, Optimizing Symmetric vs. Asymmetric Image encryption mathematically, International Journal of Advances in Engineering and Management (IJAEM) Volume 4, Issue 9 Sep. 2022
[18] BJ Al-Khafaji, AMS Rahma A Modern Encryption Approach to Improve Video Security as an Advanced Standard Adopted(2024)Ibn AL-Haitham Journal For Pure and Applied Sciences 37 (2), 475-485
[19] Baydaa-Jaffer Al-Khafaj Abdul Monem S. Rahma , Wisam Abed Shukur New technology for advanced results for security wireless sensor networks (2024) Wasit Journal for Pure sciences, Vol. 3 No. 1 p. 83-89.
[20] Abdulsalam WH, Alhamdani RS, Abdullah MN. Speech emotion recognition using minimum extracted features. In2018 1st Annual International Conference on Information and Sciences (AiCIS) 2018 Nov 20 (pp. 58-61). IEEE
[21] Al-Khafaji, Baydaa Jaffer. "Steganography techniques using tunes and Discrete Cosine Transform (DCT)." JOURNAL OF XI'AN UNIVERSITY OF ARCHITECTURE & TECHNOLOGY 12 (2020)
[22] Al-Khafaji, Baydaa Jaffer. "Proposed speech analyses method using the multiwavelet transform." Ibn AL-Haitham Journal For Pure and Applied Science 27.1 (2017): 394-401.
[23] Al-Khafaji, Baydaa Jaffer. "Proposed speech analyses method using the multiwavelet transform." Ibn AL-Haitham Journal For Pure and Applied Science 27.1 (2017): 394-401.
[24] Majeed Ban Hassan, Wisal Hashim Abdulsalam, Zainab Hazim Ibrahim, Rasha H Ali, Shahlaa Mashhadan, Digital Intelligence for University Students Using Artificial Intelligence Techniques ,international Journal of Computing and Digital Systems, University of Bahrain, Volume 6, Issue 1
[25] Robert D. Nowak, "Wavelet Based Rician Noise Removal", IEEE Transactions on Image Processing, vol. 8, no. 10, pp.1408, October 1999.
[26] S. G. Mallat and W. L. Hwang, "Singularity detection and processing with wavelets," IEEE Trans. Inform. Aory, vol. 38, pp. 617–643, Mar. 1992.
[27] Imola K. Fodor, Chandrika Kamath, "Denoising through wavlet shrinkage: Anempirical study", Center for applied science computing Lawrence Livermore National Laboratory, July 27, 2001.
[28] R. Coifman and D. Donoho, "Translation invariant denoising," in Lecture Notes in Statistics: Wavelets and Statistics, vol. New York: Springer-Verlag, pp. 125-- 150, 1995.

A comparative study of the effect of thermal neutron and gamma irradiation on the electrical properties of the $Ge_{40}Te_{60}$ semiconductor alloy

Al-Zahraa Y. Abdalsajjad [1], Rafah Ismael Noori [2], Kassim Mahdi Wadi [3], Kareem A. Jasim [2,a)]

[1] *Ministry of Education, Karkh Education Directorate, Baghdad, Iraq*
[2] *Department of Physics, College of Education for Pure Sciences Ibn Al-Haitham, University of Baghdad, Baghdad, Iraq*
[3] *Al-Ma'amoun University College, Electrical Engineering Techniques Department, Baghdad, Iraq*

[a)] Corresponding author: kareem.a.j@ihcoedu.uobaghdad.edu.iq

Abstract. The current article discusses the effect of thermal neutrons and gamma rays on the electrical properties of $Ge_{40}Te_{60}$ alloy. These alloys are made by sudden cooling of the melt. Sample A was exposed to thermal neutron radiation using a radioactive neutron source for seven days with an energy of about 6.04 x 10^{10}. Sample B was bombarded with gamma rays with ^{137}Cs source with the dose 0.168 sv. Sample A was characterized by having a lower electrical resistivity than sample B. At the same time, the electrical conductivity was higher than in sample B. This change in electrical properties can be attributed to the decrease in grain boundary dispersion of charge carriers when sample A is exposed more than B. The electrical properties of $Ge_{40}Te_{60}$ alloy glass alloys were studied. Two active processes are observed to express the DC conductivity of the alloys under study. The first process prevailed at higher temperatures, while the other process prevailed at lower temperatures. The low-temperature activation energy results from some fundamental mechanism that is independent of composition, while the high-temperature activation energy depends on the amount of germanium present.

Keyword: Thermal neutrons, gamma rays, electrical properties, electrical conductivity and grain boundary.

INTRODUCTION

The physical characteristics of semiconductors are studied because they provide valuable information for numerous real-world applications, including solar cells, photodetectors, and electronic circuits used in science and technology for both military and civil applications. Semiconductors are also used in integrated circuits, magnetic memory devices, electronic opening and closing circuits, and resistor manufacturing [1]. 1962 saw the start of research into how radiation affects semiconductor devices after earlier findings revealed that radiation's action on the semiconductor structure causes the lattice atoms to move and that these motions last for roughly 103 seconds at a temperature of one degree [2]. Studies have revealed that atomic defects and interstitial voids are the most important defects caused by radiation in the structure of semiconductors and that there is a high probability of annihilation between the two [3]. Radiation has a transient effect on semiconductor structures, while it has a permanent or semi-permanent effect on surfaces .[4] Studies have emphasized the importance of surface effects in the atoms of the retinal system. Research indicates that when exposed to ionizing radiation, the capacitance, voltage and conductivity characteristics of these devices change [5]. The thermal neutron is a free neutron that is not bound by the atomic nucleus, and its average kinetic energy is equal to the average energy of the molecules in the surrounding matter. In some chain reaction applications, thermal neutrons are preferred because of their large fission cross-sections and relatively slow, low-energy behavior. Furthermore, thermal neutrons are useful in many neutron optics applications due to their long wavelengths. The process of producing thermal neutrons involves slowing down the most energetic neutrons that are released from atomic nuclei during nuclear events such as fission, in a substance known as a moderator. The thermal energy of each particle is about 0.025 electron volts, which is equivalent to the wavelength of a neutron of 2 angstroms, and its speed is about 2000 meters per second. Thermal neutron beams are ideal for studying the structure of crystals, especially for determining the location of atoms of some chemical elements, because their wavelength corresponds to the natural spacing between atoms in crystalline materials [6]. Also, the duration of exposure of chemicals to thermal

Technologies and Materials for Renewable Energy, Environment and Sustainability
AIP Conf. Proc. 3321, 020020-1–020020-6; https://doi.org/10.1063/5.0290001
Published under an exclusive license by AIP Publishing. 978-0-7354-5231-2/$30.00

neutrons leads to the reshaping of the crystal structure of the atoms within the Material Therefore, many researchers have studied the effects of radiation with thermal neutrons on some alloys and chemical compounds to know the extent of the effect of radiation on their physical properties [7-11]. In their investigations of how neutron irradiation affects the physical properties of superconductors, Karim Jassim and his colleagues discovered that the transition temperatures of samples are sensitive to radiation; After a release of 18.12×10^{10} n cm−2 s^{-1}, the temperature of the samples decreased from 116 K to 111 K. The movement of defects, gaps and their interaction with radiation may be responsible for the fluctuation in Tc [6]. Frasca, A., and Schwarze, G. talk about how semiconductor materials are affected by gamma and neutron radiation, and how this affects the electrical and switching properties of solid-state power switches. They discovered experimental evidence showing how gamma and neutron radiation affected the performance characteristics of bipolar junction transistors. Gamma radiation was found to cause a rapid drop in gate threshold voltage, while neutron radiation caused a rapid drop in gain, tripping voltage, and storage time [7]. In investigating the effects of increased gamma and neutron radiation on PIN photodiodes and phototransistors and their output characteristics, Dejan Nikolic and Aleksandra Vasic-Milovanovic found that when photoelectric detectors are exposed to neutron radiation after gamma irradiation, the distorted semiconductor structure partially repairs itself and the faulty output characteristics increase (Photosynthesis current, spectral response) [8]. They also studied the identification of radiation-induced changes in the parameters of silicon solar cells that affect their operation, and they presented a comparative study of the effects of gamma and neutron irradiation on the parameters of solar cells. They found that both gamma and neutron radiation have a clear effect on the parameters of silicon solar cells [9]. The effects of gamma radiation on the superconducting properties of superconductors have been studied by many researchers. They concluded that transition temperatures increase directly with radiation exposure [10-12]. Jahil, S.S., et al. studied the effect of laser irradiation on the electrical and structural properties of superconducting materials, and they found that although there were changes in peak intensity, lattice parameters, mass density, oxygen content, and volume fraction, the XRD data showed that there were no phase transitions before or after laser irradiation and that the irradiated samples also had a certain bone crystal structure [11]. The main objectives of the manuscript are to prepare and study the effect of a beam of thermal neutrons and gamma rays on the electrical properties of $Ge_{40}Te_{60}$ alloy.

EXPERIMENTAL DETAILS

Two samples (A, B) of $Ge_{40}Te_{60}$ alloy were prepared using the molten cooling technique. The high purity of the basic powder of germanium (Ge)and trillium (Te) was chosen, with a purity of up to (99.99%). Using weight ratios of the elements according to their atomic weights, they were mixed and stored in an ampoule. The ampoule was emptied of air to 103 torr to withstand the pressure resulting from the interaction of the components of the alloy after it was tightly closed. After that, it was placed in the electric furnace. The ampoule was gradually heated and kept at 400°C for approximately 3 hours followed by 700°C during the process at a rate of 10°C/min. The ampoule was quickly cooled in ice water to obtain the glassy state. Next, the alloy components were extracted and crushed using a pestle and mortar to produce the sample powder. The powder was pressed into a mold using an automatic press with a pressure of 5 tons per square centimeter, tablets with a width of 1.5 cm and a thickness of 4 mm were obtained. Sample A was exposed to thermal neutron radiation for a week with a dose of 6x1010 (n.cm-2), while sample B was exposed to gamma rays for a week also with the dose 0.168 sv. The electrical conductivity of irradiated samples was measured using IV techniques at ambient temperatures up to 225°C. Electrical conductivity properties and activation energies were calculated using computer programs.

RESULT AND DISCUSSION

Resistivity and electrical conductivity values were calculated as a function of temperature for irradiated samples A and B. Figure 1 shows the relationship between resistivity, electrical conductivity, and temperature in the range (300-450 K). Two mechanisms of electrical resistivity have been revealed, indicating a behavior that fits Equation 1 [13, 14]. The results confirm that the eyes have a semiconductor behavior, as the electrical resistance decreases with increasing temperature [15, 16]. It is also noted from the figure that the electrical conductivity of sample A is lower than that of sample B, and this indicates that the effect of thermal neutrons is greater than that of gamma rays on the pore composition of the samples. d **r**

$$\boldsymbol{\rho = \rho_{01} e^{\left(\frac{\Delta E_1}{KT}\right)} + \rho_{02} e^{\left(\frac{\Delta E_2}{KT}\right)}} \quad (1)$$

Where (ρ_{01} and ρ_{02}) are past pre-dramatic variable boundaries, T = the outright temperature, K = Boltzmann's consistent, and (ΔE_1 and ΔE_2) are the enactment energy of each term.

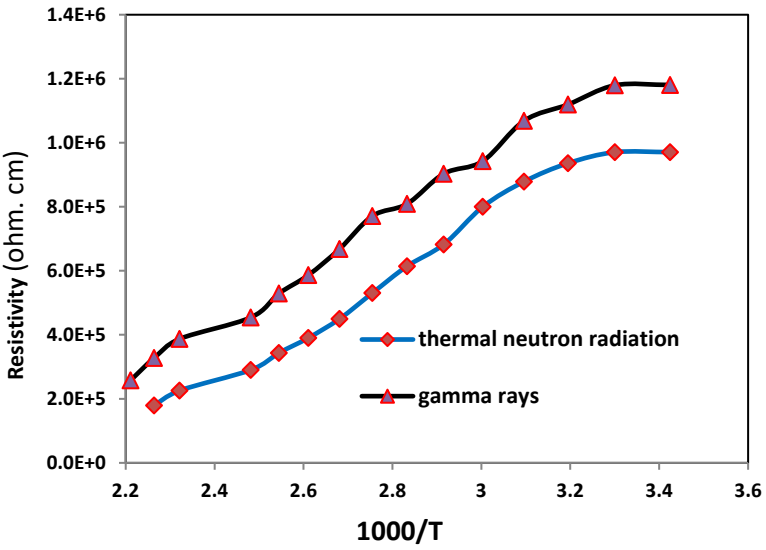

Figure 1. Resistivity conductivity Ln σ for $Ge_{40}Te_{60}$ samples as a function of temperature

The electrical conductivity values for samples B and A were calculated as a function of temperature. Figure 2 shows the relationship between temperature and the logarithm of electrical conductivity Ln (□) in the range (300-500 K). Two electrical conduction mechanisms have been revealed, indicating behavior that fits Equation 2 [17, 14]. All $Ge_{40}Te_{60}$ samples are semiconductors with electrical conductivity that increases with temperature in an exceptional relationship according to Mott and Davis [17].

$$\sigma = \sigma_{01} e^{(-\frac{E_1}{KT})} + \sigma_{02} e^{(-\frac{E_2}{KT})} + \sigma_{03} e^{(-\frac{E_3}{KT})} \quad (2)$$

Where (σ_{01}, σ_{02}, σ_{03}) are past pre-dramatic variable boundaries, T = the outright temperature, K = Boltzmann's consistent and (ΔE_1 and ΔE_2) are the enaction energy of each term.

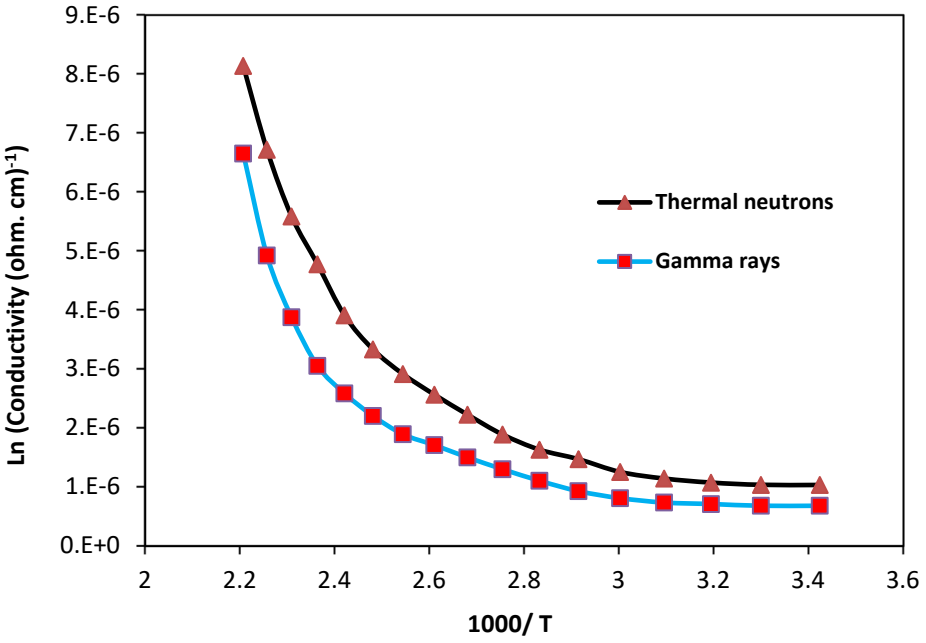

Figure 2. Electrical conductivity Ln σ for $Ge_{12}Te_{80}Sn_8$ samples as a function of temperature

The electrical conductivity of each conductive area (at low and high temperatures) was measured. According to Figure 1, it appears that the conduction curves in the two thermal regions are affected by irradiation. It was noted that the gamma effect is moderate, which has the lowest electrical conductivity compared to the sample irradiated with thermal neutrons, and it can explain the slope of the curve, Equation 2. These results are consistent with the authors' findings in references [18, 19].

Samples exposed to thermal neutron beams or gamma rays show semiconductor electrical conductivity with different curve heights. The increased mobility of atoms as a result of radiation made them tend to become more electrically conductive, which explains the change in the crystal structure of the alloy [20, 21]. The curves that reflect the conduction process have been segmented. The glassy amorphous chalcogenide materials included two conductors, the first in the tails of the bands at high temperatures and the second at high temperatures in the extended levels of the energy bands [22-27].

In the second region, electrons move through the region extending over the conduction and valence bands, which leads to electrical conduction at high temperatures (400 to 500 K). In the first, at high temperatures (300 to 400 K), electrons move through the tails of the conduction and valence bands [20, 28]. Compared with sample B, the electrical conductivity of sample A increased much more rapidly. This indicates that numerous grain boundaries and defects resulting from insufficient atomic bonding were the cause of the high conductivity [24, 29]. The curves in Figures 1 and 2 also show two separate paths leading to two distinct slopes produced by two activation energies in thermal conductivity. According to Equation 2, the slope of the plot of ln versus 1000/T can be used to determine the activation energy (E1, E2), and Table 1 includes these values .Equation 2 can calculate the prior exponential factors σ_{01} and σ_{02} for all samples in the regions based on the extent of the curves and their intersection with the y-axis when the x-axis equals zero. Table 1 shows the pre-exponential factor values and activation energies, which were calculated [26, 27].

Table 1. values of activation energies (ΔE_1 and ΔE_2) and pre-exponential factor (σ_{01} and σ_{02}) are dependence neutron Irradiation and gamma reys of $Ge_{40}Te_{60}$ alloy

Radiation Dose x10^{10} (n.cm^{-2})	**E_1 (ev)**	**$\sigma_{o\ extended}$ (Ohm^{-1}.cm^{-3})**	**E_2 (ev)**	**$\sigma_{o\ Loc}$ (Ohm^{-1}.cm^{-3})**
A	**0.183**	**39.21**	**0.15**	**2.7 E^{-4}**
B	**0.179**	**40.25**	**0.14**	**5.4 E^{-5}**

CONCLUSIONS

This research deals with studying the effect of a dose of thermal neutrons and gamma rays on the electrical properties at the temperature range of 300-500 K in the Ge40 Te60 alloy produced by the melt-quenching process. When calculating the electrical conductivity as a function of temperature, the electrical conductivity was found to be high, indicating the presence of extended and localized states within the energy gap. It was discovered that differences in the type of radiation doses and activation energy.

REFERENCES

1. Ben Nasrallah, T., Amlouk, M., Bernde, J. C., & Belgacem, S. (2004). Structure and morphology of sprayed ZnS thin films. physica status solidi (a), 201(14), 3070-3076. https://doi.org/10.1002/pssa.200406872.
2. Gromov, D. V. (2007). Radiation effects in microwave semiconductor devices. 2007 17th International Crimean Conference - Microwave & Telecommunication Technology. https://doi.org/10.1109/crmico.2007.4368889Mitchell.
3. J. P. and Wilson, D. K., 1967. Surface Effect of Radiation on Semiconductor Devices, The Bell Sustem Technical J, No. 1, P.1.
4. Vavilov, V. S., & Ukhin, N. A. (1995). Radiation effects in semiconductors and semiconductor devices. https://doi.org/10.1007/978-1-4684-9069-5Nicollian, E.H. and Brews, T.R., 1982. MOS Physics and Technology, Murrey Hill, New Jersey, 200 p.
5. Lee, J.., Park, S. D., Kim, B. S., Oh, M. W., Cho, S. H., Min, B. K., Lee, H. W., & Kim, M. H. (2010). Control of thermoelectric properties through the addition of Ag in the Bi0.5Sb1.5Te3Alloy. Electronic Materials Letters, 6(4), 201-207. https://doi.org/10.3365/eml.2010.12.201.

6. Jasim, K. A. (2013). The effect of neutron irradiation on the properties of tl0.6pb0.3cd0.1ba2ca2cu3o9-? superconductors. Turkish Journal of Physics, Vol. 37 ,(2013), No. 2, p. 237-24. https://doi.org/10.3906/fiz-1203-16.
7. Schwarze, G., & Frasca, A. (n.d.). Neutron and gamma irradiation effects on power semiconductor switches. *Proceedings of the 25th Intersociety Energy Conversion Engineering Conference*. https://doi.org/10.1109/iecec.1990.748024.
8. Nikolić, D., & Vasić-Milovanović, A. (2016). The impact of successive gamma and neutron irradiation on characteristics of PIN photodiodes and Phototransistors. *Radiation Effects in Materials*. https://doi.org/10.5772/62756.
9. Nikolić, D., & Vasić-Milovanović, A. (2016). Comparative study of gamma and neutron irradiation effects on the silicon solar cells parameters. FME Transaction, 44(1), 99-105. https://doi.org/10.5937/fmet1601099n.
10. Kadhim, B. B., Khaleel, I. H., Hussein, B. H., Jasim, K. A., Shaban, A. H., AL-Maiyaly, B. K., & Mahdi, S. H. (2018). Effect of gamma irradiation on the tlba2ca2cu3o9-δ superconducting properties. AIP Conf. Proc. 1968, 030054. https://doi.org/10.1063/1.5039241.
11. Hammed Aleabi, S., W. Watan, A., A. Mahdi, H., Nassr Fadhil, R., K. A. Jasim, Study the effect of gamma irradiation on the superconducting properties of $HgBaSrCa_2Cu_3O_{8+\delta}$. *Journal of Physics: Conference Series*, *1178*, 012019. https://doi.org/10.1088/1742-6596/1178/1/012019.
12. Jahil, S. S., Khazaal, A. R., Mahdi, S. H., Jasim, K. A. (2019). Superconductor enhancements by laser irradiations. *AIP Conf. Proc. 2190, 020048 (2019)*. https://doi.org/10.1063/1.5138534.
13. Mehra, R., Kumar, H., Koul, S., & Sikka, P. (1984). Electrical transport properties of bulk amorphous Gex Se1−x. Materials Chemistry and Physics, 11(5), 481-494. https://doi.org/10.1016/0254-0584(84)90070-1.
14. Aqeel N. Abdulateef, Ahlam Alsudani, Riyadh Kamil Chillab, Kareem A. Jasim, Auday H. Shaban , (2020) "Calculating the Mechanisms of Electrical Conductivity and Energy Density of States for Se85Te10Sn5-xInx Glasses Materials". Journal of Green Engineering (JGE), Volume-10, Issue-9, September 2020, P.5487-5503.
15. Shore, K. A. (2014). Electronic processes in non-crystalline materials (Second edition), by N.F. Mott and E.A. Davis. Contemporary Physics, 55(4), 337-337. https://doi.org/10.1080/00107514.2014.933254.
16. Chillab, R. K., Jahil, S. S., Wadi, K. M., Jasim, K. A., & Shaban, A. H. (2021). Fabrication of $Ge_{30}Te_{70-x}Sb_x$ Glasses alloys and studying the effect of partial substitution on D.C electrical energy parameters. Key Engineering Materials, 900, 163-171.
17. Zainab j. Neamah, Balqees A. Ahmed, Mohammed A. Thejeel, Kareem A. Jasim, Auday H. Shaban, The Effect of Gamma Radiation on the Manufactured HgBa2Ca2Cu2.4Ag0.6O8+δ Compound, Materials Science Forum, Vol. 1050, pp 41-47, (2022); https://www.scientific.net/MSF.1050.41.
18. Mott, N. F.; Davis, E. A. Electronic Processes in Non-Crystalline Materials. Clarednon Press. Oxford 1979, 591. https://doi.org/10.1016/0040-6090(72)90068-5.
19. Khudhair, N. H., & Jasim, K. A. (2023). A study of the effectiveness of tin on the thermal conductivity coefficient and electrical resistance of $se_{60}te_{40-x}sn_x$ Chalcogenide glass. Ibn AL-Haitham Journal For Pure and Applied Sciences, 36(1), 149-157. https://doi.org/10.30526/36.1.2892.
20. Nawal Hassan khudhair, Kareem Ali Jasim, Study the Effect of Tin on the Energy Density of States ofSe60Te40-Xsnx Chalcogenide Glass, AIP Conf. Proc. 2769, 020062-1–020062-7; https://doi.org/10.1063/5.0129373.
21. Nawal Hassan khudhair, Kareem Ali Jasim, Preparation and Study the effective of Sb on the energy density of states of Se60 Te40, AIP Conf. Proc. 2769, 020056-1–020056-7; https://doi.org/10.1063/5.0129550.
22. Mobarak, M., Shaban, H., & Elhady, A. (2008). Electrical and thermoelectric properties of CuInS2 single crystals. Materials Chemistry and Physics, 109(2-3), 287-290. https://doi.org/10.1016/j.matchemphys.2007.11.025.
23. Mohammed, J. S., Nsaif, F. K., Jawad, Y. M., Jasim, K. A., & Al Dulaimi, A. H. (2023). Investigating the optical and electrical characteristics of as60cu40-xsex thin films. Chalcogenide Letters, 20(7), 449-458. https://doi.org/10.15251/cl.2023.207.449.
24. Sikka, P., Ferdinand, K. V., Jagadish, C., & Mathur, P. C. (1985). Effect of vacuum and H2S annealing on the electrical properties of CdS thin films. Journal of Materials Science, 20(1), 246-254. https://doi.org/10.1007/bf00555918.
25. Ram, I. S., Kumar, S., Singh, R. K., Singh, P., & Singh, K. (2015). Electrical conduction mechanism in $se_{90-x}Te_5Sn_5In_x$ (X = 0, 3, 6 and 9) multi-component glassy alloys. AIP Advances, 5(8), 087164. https://doi.org/10.1063/1.4929577.
26. Ahmed, B. A., Mohammed, J. S., Fadhil, R. N., Jasim, K. A., Shaban, A. H., & Al Dulaimi, A. H. (2022). The dependence of the energy density states on the substitution of chemical elements in the $Se_6Te_{4-x}Sb_x$ thin film. Chalcogenide Letters, 19(4), 301-308. https://doi.org/10.15251/cl.2022.194.301.

27. Shpotyuk, O. (1995). Amorphous chalcogenide semiconductors for dosimetry of high-energy ionizing radiation. Radiation Physics and Chemistry, 46(4-6), 1279-1282. https://doi.org/10.1016/0969-806x(95)00369-9.
28. Wadi, K.M., Jasim, K.A., Shaban, A.H., Kamil, M.K., Nsaif, F.K., The effects of sustainable manufacturing pressure on the structural properties of the pb2ba2ca2cu3o9+σ compound, Journal of Green Engineering, 2020, 10(9), pp. 6052–6062.
29. Mahdi, S.H., Jassim, W.H., Hamad, I.A., Jasima, K. A., Epoxy/Silicone Rubber Blends for Voltage Insulators and Capacitors Applications, Energy Procedia, 2017, 119, pp. 501–506.

Comparative Analysis of Haldar-Wagner and Williamson-Hall Methods Utilizing X-ray Diffraction Patterns of Magnesium Oxide Nanoparticles

Marwa Taleb [a] and Khalid Hellal Harbbi [b]

Department of Physics, College of Education (Ibn Al-Haitham), University of Baghdad, Baghdad, Iraq

[a] Corresponding author: marwa.Taleb1204a@ihcoedu.uobaghdad.edu.iq
[b] khalid.h.h@ihcoedu.uobaghdad.edu.iq

Abstract. This study investigates the elastic properties of MgO nanocrystals synthesized via wet chemical methods by analyzing their X-ray diffraction (XRD) data using the Williamson-Hall (W–H) and Halder-Wagner (H–W) techniques. The research evaluates and compares the efficacy, accuracy, and applicability of these methods in characterizing the structural properties of nanoparticles. Through rigorous analysis and comparison, this work aims to advance nanomaterial characterization techniques and deepen our understanding of the physiochemical properties of MgO nanocrystals. The comparison highlights distinct approaches between the Williamson-Hall and Haldar-Wagner methods in deriving structural parameters from XRD data. The Williamson-Hall analysis utilizes peak broadening analysis to estimate crystallite size, employing linear regression on reciprocal lattice spacing against peak broadening parameters. Experimental diffraction angles and corresponding parameters yielded crystallite sizes ranging from 1 to 28.78 through the Williamson-Hall analysis. The implications of this study extend to the optimization of nanoparticle synthesis methods and the refinement of characterization techniques, facilitating advancements in nanotechnology applications such as catalysis, sensing, and optoelectronics.

Keywords: nanocrystals, X-ray diffraction, Williamson-Hall analysis sensing, and optoelectronics

INTRODUCTION

Semiconductor nanoparticles, with 1-100 nm dimensions, show distinct physical properties that are size-dependent and differ from those of their bulk counterparts [1]. It has been documented that the manipulation of elastic properties, which in turn can impact various physical attributes like optical and surface properties, holds significant importance [2]. Consequently, numerous semiconductor nanoparticles have found extensive implementation in various scientific fields, including optoelectronic devices such as light-emitting diodes and solar cells [3,4]. MgO is an II-VI semiconductor nanoparticle with a band gap energy of 1.74 eV and an exaction Bohr radius of 6 nm [1]. These nanocrystals have cubic and hexagonal lattice structures; various techniques can achieve their synthesis [5,6]. The nanocrystals undergo intrinsic strain owing to size confinement, a consequential elastic characteristic that can be modulated by manipulating synthesis parameters like pH and concentration. Consequently, this alteration of parameters has a direct impact on the optical and other characteristics. X-ray Diffraction (XRD) investigation of a nanocrystal has the capability to validate the crystallinity of the specimen, as evidenced by distinct peaks corresponding to distinct reflection planes [7-10]. It is a widely acknowledged fact that the XRD peaks are broadened due to the confinement of size within nanocrystals and the presence of inherent strain resulting from such confinement [11,12]. Thus, the broadening of the physical peaks can be attributed primarily to two factors: size-dependent broadening and strain-induced broadening. The lattice strain is typically caused by various sources, including dislocation density, grain boundary junctions, or sinter stress, as well as stacking faults [13-18]. Therefore, through the application of XRD peak broadening analysis, it becomes feasible to indirectly ascertain the intrinsic strain magnitude, as well as the dimensions of the nanocrystals. In addition to this, various elastic properties such as stress

Technologies and Materials for Renewable Energy, Environment and Sustainability
AIP Conf. Proc. 3321, 020021-1–020021-8; https://doi.org/10.1063/5.0291545
Published under an exclusive license by AIP Publishing. 978-0-7354-5231-2/$30.00

and energy density, which are inherently linked to strain, can also be deduced. There exist several methodologies that can be employed for this purpose, including the Williamson-Hall Method [19-22], Warren-Averbach Method [23-25], and Balzar Method [20]. The Warren-Averbach and Balzar methods incorporate the Stokes-Fourier de-convolution technique, while the Williamson-Hall method relies on the Full Width at Half Maximum (FWHM) of the diffraction peak [26-31]. Consequently, the Williamson-Hall method emerges as a straightforward and suitable approach for determining diverse elastic properties, inclusive of strain, as well as facilitating the calculation of average size [32]. Here, this investigation aims to ascertain the various elastic properties of the MgO nanocrystals produced through wet chemical synthesis. To accomplish this, we will analyze their XRD data using three distinct techniques: The Williamson-Hall (W–H) method and the Halder-Wagner (H–W) method. The article aims to evaluate and compare two prominent methods, namely the Haldar-Wagner and Williamson-Hall techniques, in analyzing the X-ray diffraction patterns of magnesium oxide nanoparticles. By conducting this comparative study, the article seeks to provide insights into the effectiveness, accuracy, and applicability of these methods in characterizing the structural properties of nanoparticles. Through rigorous analysis and comparison, the article seeks to contribute to the advancement of techniques utilized in nanomaterial characterization, thereby enhancing our understanding of the physical and chemical properties of magnesium oxide nanoparticles.

PREPARATION METHODS

The synthesis of MgO nanoparticles (NPs) was achieved through the sol-gel technique using disintegrated Mg (NO3)2.6H2O (Alfa Aesar) in distilled water, stirred at a constant temperature of 80 degrees Celsius to form a gel. The gel got dried at about 150°C forming solid materials which were then ground and annealed at 500°C for two hours to get the final powder form of the MgO NPs. RIGAKU X-ray diffractometer with a $Cu_{K\alpha}$ (λ=1.54 Å) source and scanning range from 20° to 80° at a scan rate of 2° per min, an operating current of 30 mA and voltage of 40 kV was employed for XRD analysis of the synthesized nanoparticles. The comprehensive exploration of both morphology and structure relied on the sophisticated capabilities of a field emission scanning electron microscope, specifically the FEI-NanoSEM-450 model. This cutting-edge instrument provided the necessary resolution and analytical power to delve deeply into the intricate details of the sample's physical characteristics and arrangement at the microscale level.

RESULTS AND DISCUSSION

The XRD examination of chemically synthesized MgO nanoparticles (2θ) spans from 20° to 60° with a step size of 0.02°. This analysis was carried out using the advanced Bruker D8 diffractometer, employing CuKα1 radiation with a wavelength of 1.5406 Å and an accelerating voltage of 40 kV. Notably, the diffraction pattern exhibits clear peaks at 25°, 30°, 42°, and 50°, which correspond to the crystallographic planes (111, 200, 220, 222, and 311), respectively. Significantly, these detected peaks align with the distinctive stick pattern provided by the Joint Committee on Powder Diffraction Standards (JCPDS) for cubic MgO nanocrystals, thereby confirming the identified crystalline structure. After this, a comprehensive analysis utilizing the diffraction data has been undertaken to ascertain both particle size and inherent strain, with detailed findings expounded upon in the subsequent section.

Halder-Wagner analysis

The implementation of the H-W method for analysing XRD data, particularly concerning magnesium oxide (MgO) nanoparticles, unfolds through a systematic series of steps. Initially, experimental XRD data is meticulously collected, encompassing diffraction peaks indicative of various crystallographic planes within the material. These peaks are then indexed with their corresponding Miller indices, providing crucial insights into the material's crystal structure. Subsequently, essential parameters including the strain (B) and crystallite size (D) are computed for each diffraction peak, utilizing mathematical formulations predicated upon the observed diffraction angles and peak intensities. Following parameter computation, regression analysis is employed to delineate empirical relationships between D, B, and other experimental variables, ultimately yielding regression equations elucidating these intricate connections. These equations serve as potent tools for deciphering the structural characteristics of the nanoparticles, such as average crystallite size and lattice strain, thereby offering invaluable insights into their properties. Furthermore, the method's robustness is fortified through validation against complementary characterization techniques and refinement to accommodate specific material attributes or experimental conditions.

Crystallite Size (D): A usual technique to compute crystallite size D is the Scherrer equation which connects the broadening of XRD peaks with crystallite size. The general form of the Scherrer equation is:

$$D = \frac{k\lambda}{\beta \cos(\theta)} \quad (1)$$

Where: D is the crystallite size, k is the shape factor (typically taken as 0.9 for isotropic particles), λ is the wavelength of the X-ray radiation, β is the FWHM of the diffraction peak and θ is the Bragg angle.
in the Haldar-Wagner method is often related to the broadening of diffraction peaks and can be calculated using a variety of empirical formulas. One possible formulation is:

$$D = K\ tan(\Theta) + \frac{16\varepsilon^2}{Bsin\Theta} \ldots\ldots\ldots\ldots \quad \ldots..(2)$$

Where: K is a constant determined through regression analysis, D is the crystallite size and θ is the Bragg angle.
The provided Tables (1 and 2) illustrate the application of the Haldar-Wagner method to scrutinize XRD patterns emanating from magnesium oxide nanoparticles, elucidating crucial structural parameters including strain (B) and crystallite size (D). In the initial table, a comprehensive array of experimental data is meticulously tabulated, encompassing diffraction peaks' characteristics such as Miller indices (HKL), observed diffraction angles (2Θ and Θ), and the corresponding intensity of diffraction peaks (B). These data serve as the foundation for subsequent analyses, whereby the crystallite size (D) is deduced utilizing a prescribed equation incorporating trigonometric functions and empirical constants derived from regression analysis. However, the regression analysis for this dataset yields a linear equation with a meager coefficient of determination ($R^2 = 0.0032$), suggesting a limited linear correlation between D and the observed diffraction angles within this specific dataset.

Table 1: Experimental Data and Regression Results for Crystallite Size (D) Calculation

hkl	**2Θ**	**Θ**	**B**	$\boldsymbol{D = K\ tan(\Theta) + \frac{16\varepsilon^2}{Bsin\Theta}}$
111	22.51548	11.25774	0.08652	0.491249961
200	30.56452	15.28226	0.013242	47.47139722
220	56.4712	28.2356	0.08768	1.13948306
311	73.10793	36.553965	0.008921	16.19417604
222	78.23996	39.11998	0.005223	31.07002348
		y = 0.0909x + 16.902 = 0.0032		

On the other hand, Table 2 presents meticulously calculated values based on the experimental data, incorporating trigonometric functions such as sine and tangent of the observed diffraction angles. These values facilitate the determination of strain (B) utilizing an equation intertwining empirical constants, diffraction angles, and the previously derived crystallite size (D). Notably, the regression analysis for this dataset engenders a robust linear equation with a coefficient of determination ($R^2 = 1$), indicative of a perfect fit of the data to the regression line. This underscores a strong correlation between strain (B) and the observed diffraction angles within this dataset.

Table 2. Calculated Values and Regression Results for Strain (B) Determination.

hkl	**Θ**	**sinΘ**	**tanΘ**	$\boldsymbol{D = K\ tan(\Theta) + \frac{16\varepsilon^2}{Dsin\Theta}}$
111	11.25774	0.195222813	0.199052953	0.930785072
200	15.28226	0.263574389	0.273236277	1.256674716
220	28.2356	0.47309826	0.536995537	2.255642112
311	36.553965	0.595579649	0.741419671	2.839609973
222	39.11998	0.630946389	0.813255067	3.008231832
		y = 4.7678x + 2E-06		

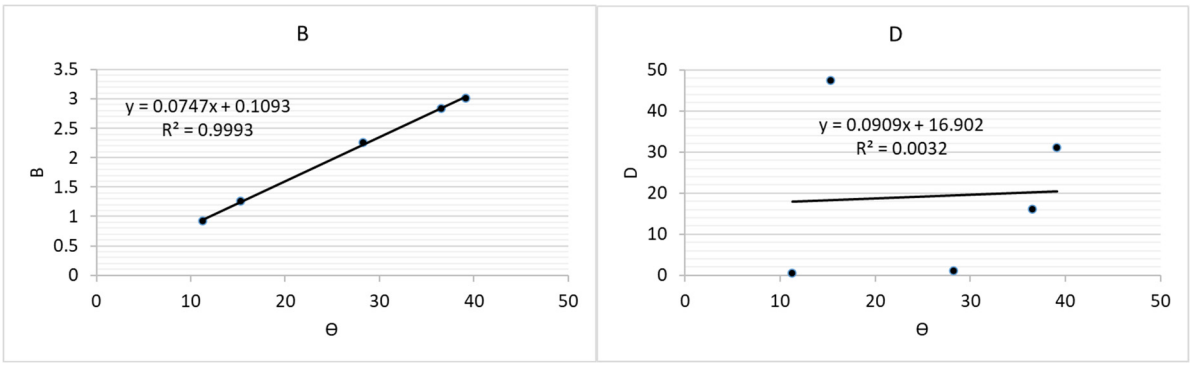

Figure 1. Calculated Values of B and D according to Θ using H-W method

W-H analysis

The implementation of W-H analysis entails a systematic process for extracting crucial information regarding crystallite size and lattice strain from X-ray diffraction (XRD) data, particularly in polycrystalline materials. Initially, experimental data is meticulously collected through XRD experiments, capturing diffraction peaks corresponding to various crystallographic planes within the material. Subsequently, these peaks are subjected to rigorous peak profile analysis to discern characteristics such as broadening, which serves as a key indicator of lattice strain and crystallite size. The W-H plot is then constructed, where parameters reflecting peak broadening, such as the FWHM, are plotted against reciprocal lattice spacings or sin(θ)/λ. Through linear regression analysis applied to the Williamson-Hall plot, crucial parameters including the slope and intercept of the linear fit are extracted. The slope provides insights into the crystallite size, whereas the intercept offers information on lattice strain. Utilizing appropriate equations, such as the Scherrer equation for crystallite size and the Williamson-Hall equation for strain, these parameters are quantified. The obtained results are interpreted within the context of the material's microstructure and properties, providing valuable insights into its mechanical and thermal behaviour, as well as processing conditions. Validation of the results against complementary techniques and refinement of the methodology further enhance the reliability and accuracy of the analysis.

The provided tables offer a comprehensive glimpse into the outcomes of the Williamson-Hall analysis applied to the XRD patterns of the material of interest. Table 3 meticulously delineates the experimental data obtained from the analysis, featuring crucial parameters such as HKL, observed diffraction angles (2Θ and Θ), and the computed parameter B, which characterizes the broadening of diffraction peaks. This broadening is influenced by factors including crystallite size (D) and lattice strain within the material, as encapsulated by the formula (3):

$$D = \frac{K}{B} + 4sin(\Theta) \tag{3}$$

The calculated values of B serve as vital indicators of the material's structural properties. Additionally, the regression analysis conducted on this dataset yields a highly significant linear equation (y=0.0564x+0.2234), referring a robust linear correlation between the variables.

Table 3. Experimental Data and Regression Results for Parameter B in Williamson-Hall Analysis.

hkl	2Θ	Θ	B
111	22.51548	11.25774	0.809649409
200	30.56452	15.28226	1.083055713
220	56.4712	28.2356	1.918062157
311	73.10793	36.553965	2.411076753
222	78.23996	39.11998	2.255663376
		y = 0.0564x + 0.2234 = 0.971	

Table 4 provides supplementary experimental data derived from the Williamson-Hall analysis, showcasing diffraction angles (2Θ and Θ), the sine of Θ, and the resultant crystallite size computed via the equation (3):

Table 4. Experimental Data and Regression Results for Crystallite Size (D) in Williamson-Hall Analysis

hkl	2Θ	Θ	sin Θ	D
111	22.51548	11.25774	0.195222813	2.365650845
200	30.56452	15.28226	0.263574389	1.054418356
220	56.4712	28.2356	0.47309826	3.457097339
311	73.10793	36.553965	0.595579649	18.5192029
222	78.23996	39.11998	0.630946389	28.77563516
			y = 53.626x - 12.315 = 0.7274	

These values offer valuable insights into the average size of crystalline domains within the material, indicative of its structural characteristics. Furthermore, the regression analysis for this dataset furnishes a linear equation (y=53.626x−12.315) with a moderately high coefficient of estimation (R^2 = 0.7274), indicating a robust linear correlation between the variables albeit with a slightly lower level of significance compared to Table 3.

Overall, these findings underscore the efficacy of Williamson-Hall analysis in elucidating the structural properties of materials through XRD data interpretation. The regression-derived equations not only provide predictive capabilities but also offer a deeper understanding of the intricate relationship between diffraction characteristics and material microstructure. Such insights are invaluable in various scientific and engineering endeavours, ranging from materials characterization to the optimization of manufacturing processes.

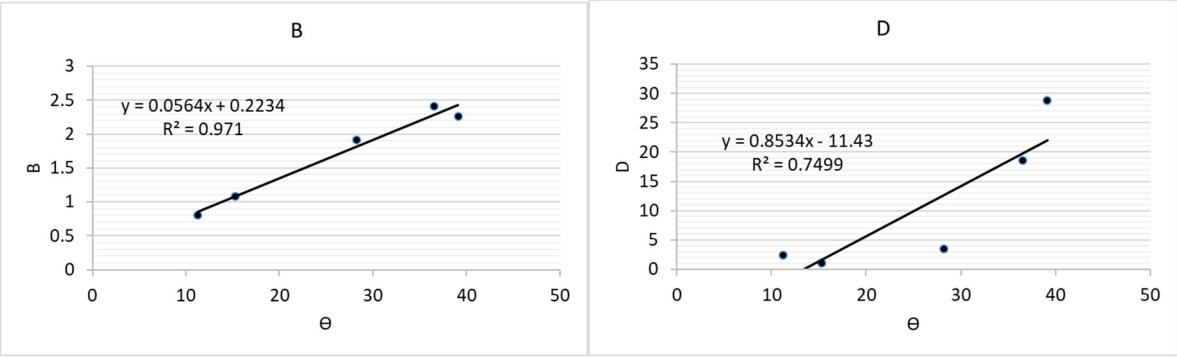

Figure 2. Calculated Values of B and D according to Θ using the Williamson-Hall –method

The comparison between the Williamson-Hall and Haldar-Wagner methods shows distinct approaches to deriving structural parameters from X-ray diffraction (XRD) data, illustrated through the provided results. In the Williamson-Hall analysis, crystallite size estimation is predicated upon peak broadening analysis, typically achieved by plotting reciprocal lattice spacings against peak broadening parameters, such as the FWHM. Linear regression applied to such plots provides a means to determine crystallite size. For instance, in the provided data, the Williamson-Hall analysis yielded crystallite sizes ranging from 1 to 28.78, inferred from experimental diffraction angles and corresponding parameters.

Conversely, the Haldar-Wagner method adopts equations directly linking diffraction angles to parameters like B and D for crystallite size and lattice strain calculations. This method is exemplified by the provided results, showcasing crystallite sizes spanning from 0.49 to 47.47, alongside parameters reflecting lattice strain. For instance, parameter B, derived explicitly from diffraction angles and experimental factors, serves as a direct indicator of lattice strain, with values ranging from 0.809 to 2.412.

The differences in obtained results come from variations in mathematical formulations and underlying assumptions between the two methods. While the Williamson-Hall analysis emphasizes peak broadening analysis for crystallite size determination, the Haldar-Wagner method focuses on explicit equations relating diffraction data to structural parameters. Accordingly, discrepancies in the range and interpretation of crystallite sizes and lattice strain arise. These

differences illustrate the necessity of comprehending the theoretical foundations and limitations of each method for robust interpretation of XRD data and comprehensive characterization of material properties.

Our findings contribute to the literature by shedding light on the suitability and limitations of the Williamson-Hall method in determining elastic properties, with a specific emphasis on strain [32]. This method, known for its reliance on the FWHM of diffraction peaks [26-31, emerges as a straightforward approach for assessing various elastic properties and facilitating the calculation of average size. By juxtaposing the Williamson-Hall method with the Haldar-Wagner approach, our study enriches the discussion surrounding methodology selection for nanomaterial characterization.

The discrepancy between the results obtained through the Williamson-Hall and Halder-Wagner methods, as evidenced by the provided values for strain (B) and crystallite size (D), underscores the distinct approaches and underlying assumptions of these techniques in analysing X-ray diffraction data as shown in Figure 3. In the Williamson-Hall analysis, the calculated strain value (B) of 1.755135553 indicates a significant degree of lattice strain within the crystallites, while the corresponding crystallite size (D) of 10.23440092 suggests relatively moderate-sized crystalline domains contributing to the diffraction pattern. This method is renowned for its ability to simultaneously evaluate strain and crystallite size by plotting peak broadening against the reciprocal of the square root of the crystallite size. On the other hand, the Halder-Wagner method yielded notably different results, with a much lower strain value (B) of 0.041796235 and a substantially larger crystallite size (D) of 19.27326595. The Halder-Wagner approach, also known as the modified Warren-Averbach method, utilizes Gaussian function fitting of diffraction peaks to extract strain and crystallite size information independently [33]. The disparity in the derived parameters between the two methods can be attributed to their unique computational methodologies and assumptions. While both techniques offer valuable insights into the crystalline structure of materials, the choice between them should be carefully considered based on the specific research objectives and characteristics of the sample under investigation.

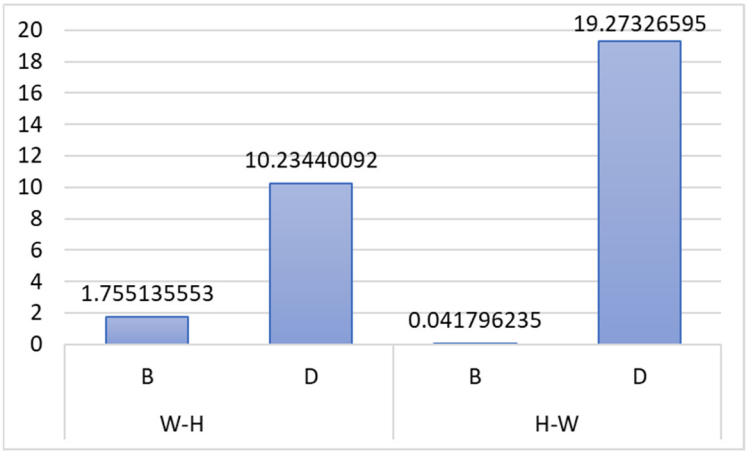

Figure 3. Comparison of Strain and Crystallite Size Parameters Obtained Using Williamson-Hall and Halder-Wagner Methods.

CONCLUSIONS

In conclusion, our comparative study of the Haldar-Wagner and Williamson-Hall methods based on the XRD pattern of magnesium oxide nanoparticles has provided valuable insights into their respective strengths and limitations in characterizing nanomaterials. Through meticulous analysis of experimental data and regression results, we have observed notable differences in the approaches and outcomes of these two methods. The Haldar-Wagner method demonstrated a broader range of D and explicit calculation of lattice strain parameters, while the W-H analysis focused on peak broadening analysis for crystallite size determination. These distinctions underscore the importance of understanding the underlying principles and mathematical formulations of each method for accurate interpretation of XRD data. Moving forward, leveraging the complementary strengths of both methods could yield more comprehensive insights into the structural properties of nanomaterials, facilitating advancements in materials science and nanotechnology. Further research may delve into refining the methodologies, exploring additional factors influencing crystallite size and lattice strain, and validating the findings through complementary techniques to enhance the precision and reliability of structural characterization techniques for nanomaterials.

REFERENCES

1. Baig, N., Kammakakam, I., & Falath, W. (2021). Nanomaterials: A review of synthesis methods, properties, recent progress, and challenges. Materials Advances, 2(6), 1821-1871.
2. Huma, T., Hakimi, N., Younis, M., Huma, T., Ge, Z., & Feng, J. (2022). MgO heterostructures: from synthesis to applications. Nanomaterials, 12(15), 2668.
3. Hossain, N., Mobarak, M. H., Mimona, M. A., Islam, M. A., Hossain, A., Zohur, F. T., & Chowdhury, M. A. (2023). Advances and significances of nanoparticles in semiconductor applications–A review. Results in Engineering, 101347.
4. Terna, A. D., Elemike, E. E., Mbonu, J. I., Osafile, O. E., & Ezeani, R. O. (2021). The future of semiconductors nanoparticles: Synthesis, properties and applications. Materials Science and Engineering: B, 272, 115363.
5. Singh, V., More, P. V., Hemmer, E., Mishra, Y. K., & Khanna, P. K. (2021). Magic-sized mgo nanoclusters: a review on synthesis, properties and white light potential. Materials Advances, 2(4), 1204-1228.
6. Pareek, A., & Borse, P. H. (2022). Hurdles and recent developments for CdS and chalcogenide-based electrode in "Solar electro catalytic" hydrogen generation: A review. Electrochemical Science Advances, 2(6), e2100114.
7. Döring, A., Ushakova, E., & Rogach, A. L. (2022). Chiral carbon dots: synthesis, optical properties, and emerging applications. Light: Science & Applications, 11(1), 75.
8. Jasim, K. A., & Mohammed, L. A, The partial substitution of copper with nickel oxide on the structural and electrical properties of HgBa2Ca2Cu3-xNi xO8+δ superconducting compound. Journal of Physics: Conference Series, 2018, 1003(1), 012071. https://doi.org/10.1088/1742-6596/1003/1/012071
9. Rani, N., Chahal, S., Chauhan, A. S., Kumar, P., Shukla, R., & Singh, S. K. (2019). X-ray analysis of MgO nanoparticles by modified Scherer's Williamson-Hall and size-strain method. Materials Today: Proceedings, 12, 543-548.
10. Craddock, P. R., Herron, M. M., & Herron, S. L. (2017). Comparison of quantitative mineral analysis by X-ray diffraction and Fourier transform infrared spectroscopy. Journal of Sedimentary Research, 87(6), 630-652.
11. Mourdikoudis, S., Pallares, R. M., & Thanh, N. T. (2018). Characterization techniques for nanoparticles: comparison and complementarity upon studying nanoparticle properties. Nanoscale, 10(27), 12871-12934.
12. Omar, B.A., Fathi, S.J., Jassim, K.A., Effect of Zn on the structural and electrical properties of high-temperature HgBa2Ca2Cu3O8+δ superconductor, AIP Conference Proceedings, 2018, 1968, 030047.
13. Bindu, P., & Thomas, S. (2014). Estimation of lattice strain in ZnO nanoparticles: X-ray peak profile analysis. Journal of Theoretical and Applied Physics, 8, 123-134.
14. Rabiei, M., Palevicius, A., Monshi, A., Nasiri, S., Vilkauskas, A., & Janusas, G. (2020). Comparing methods for calculating nanocrystal size of natural hydroxyapatite using X-ray diffraction. Nanomaterials, 10(9), 1627.
15. Wadi, K.M., Jasim, K.A., Shaban, A.H., Kamil, M.K., Nsaif, F.K., The effects of sustainable manufacturing pressure on the structural properties of the pb2ba2ca2cu3o9+σ compound, Journal of Green Engineering, 2020, 10(9), pp. 6052–6062.
16. Thool, G. S., Singh, A. K., Singh, R. S., Gupta, A., & Susan, M. A. B. H. (2014). Facile synthesis of flat crystal ZnO thin films by solution growth method: a micro-structural investigation. Journal of Saudi Chemical Society, 18(5), 712-721.
17. Cullity, B. D. (1956). Elements of X-ray Diffraction. Addison-Wesley Publishing.
18. Al-Shakarchi, E. K., & Mahmood, N. B. (2011). Three techniques are used to produce BaTiO 3 fine powder. Journal of Modern Physics, 2011.
19. Nath, D., Singh, F., & Das, R. (2020). X-ray diffraction analysis by Williamson-Hall, Halder-Wagner and size-strain plot methods of CdSe nanoparticles-a comparative study. Materials Chemistry and Physics, 239, 122021.
20. Vinjamuri, K. B., Viswanadha, S., Basireddy, H., & Borra, R. K. (2021). X-Ray Diffraction Analysis by Williamson-Hall, Size-Strain, Halder-Wagner Plot Methods for Ni Doped CdS Nanoparticles. Applied Mechanics and Materials, 903, 27-32.
21. Mohammed, E. A. (2021). A comparative study of the method of Williamson Hall and the pattern of cadmium oxide nanoparticles for X-rays. Turkish Journal of Computer and Mathematics Education (TURCOMAT), 12(4), 881-889.
22. Dey, P. C., & Das, R. (2021). Impact of silver doping on the crystalline size and intrinsic strain of MPA-capped CdTe nanocrystals: A study by Williamson–Hall method and size–strain plot method. Journal of Materials Engineering and Performance, 30, 652-660.
23. Jasim, K.A., Alwan, T.J., Mahdi, K.H., Mansour, H.L., The effect of neutron irradiation on the properties of Tl 0.6Pb0.3Cd0.1Ba2Ca 2Cu3O9-δ superconductors, Turkish Journal of Physics, 2013, 37(2), pp. 237–241. https://doi.org/10.3906/fiz-1203-16.

24. Nath, D., & Das, R. (2022). Assessing the dislocation density in CdSe nanocrystals from XRD peak profile analysis (XDPPA) assisted by first principles method. Physica E: Low-dimensional Systems and Nanostructures, 144, 115376.
25. Dutková, E., Baláž, P., & Pourghahramani, P. (2009). CdS nanoparticles mechanochemically synthesized in a high-energy mill. Journal of optoelectronics and advanced materials, 11(December 2009), 2102-2107.
26. Kumari, S., Padalia, D., Kumar, U., & Kumari, R. (2022). Investigation of structural properties of pure and Ce-doped barium titanate. Ionics, 28(9), 4401-4411.
27. Jassim K.A., Jassim, W.H., Mahdi, S.H., The effect of sunlight on medium density polyethylene Water pipes, Energy Procedia, 2017, 119, pp. 650–655. https://doi.org/10.1016/j.egypro.2017.07.091.
28. Alani, A. T., & Al-Saadi, T. M. (2021). X-ray analysis by williamson-hall methods of pure and doped ZnO nanoparticles. Annals of the Romanian Society for Cell Biology, 6836-6845.
29. Soleimanian, V., & Mojtahedi, M. (2015). A comparison between different X-ray diffraction line broadening analysis methods for nanocrystalline ball-milled FCC powders. Applied Physics A, 119, 977-987.
30. Desai, K. R., Alone, S. T., Wadgane, S. R., Shirsath, S. E., Batoo, K. M., Imran, A., ... & Kadam, R. H. (2021). X-ray diffraction based Williamson–Hall analysis and Rietveld refinement for strain mechanism in Mg–Mn co-substituted CdFe2O4 nanoparticles. Physica B: Condensed Matter, 614, 413054.
31. Kamil, M.K., Jasim, K.A., Calculating of crystalline size, strain and Degree of crystallinity of the compound (HgBa2Ca2Cu3O8+σ) by a different method, IOP Conference Series: Materials Science and Engineering, 2020, 928(7), 072109.
32. Singla, G., Singh, K., & Pandey, O. P. (2013). Williamson–Hall study on synthesized nanocrystalline tungsten carbide (WC). Applied Physics A, 113, 237-242.
33. Whitfield, P., & Mitchell, L. (2004). X-ray diffraction analysis of nanoparticles: Recent developments, potential problems and some solutions. International Journal of Nanoscience, 3(06), 757-763.

Steganography of Image Based on Random Key Generation and XOR LSB Substitution

Zahraa Modher Nabat[1, a)], Shaymaa Abdulhussein Shnain [2,b)], Baydaa Jaffer Al-Khafaji[3, c)], May A. Salih [4, d)]

[1]*University of Babylon, Department of Registration and Student Affairs, Hilla, Iraq*
[2] *University of Babylon, Math Department, Basic Education College, Hilla, Iraq*
[3] *Computer Science Department, College of Education for Pure Science/ Ibn Al-Haitham University of Baghdad, Baghdad, Iraq*
[4] *Information Technology College, University of Babylon, Hilla, Iraq*

[a)] *Corresponding author: zahraa.modher@uobabylon.edu.iq*
[b)] *shaima.almorshedy3@uobabylon.edu.iq*
[c)] *Baydaa.j.s@ihcoedu.uobaghdad.edu.iq*
[d)] *may.abd@uobabylon.edu*

Abstract . Steganography is the act of concealing a confidential communication within another type of information, such as a picture, audio file, or text. Secret information is becoming more vital nowadays because security and numerous applications range from secure trade and payment to private, which is why we need private communication, and the demand has become crucial. In electronic key systems, encryption is a key tool for keeping data secret and signing papers digitally. Cryptography aims to encrypt communications by transforming data into a form that an eavesdropper cannot interpret. This study focuses on the use as an image file carrier, so a Taxonomy has been developed for existing image files through stenographic approaches. The main objective of this paper is the random selection of pixels by three levels of protection (security), Second by testing the current image bit and stego. by applying XOR operation. Text. And finally, the initiated seed of the random generator thus reduces the possibility of finding the secret message, depending on the current time for the device to generate the Instead of a simple LSB.

Keywords: RSA, Masking, Filtering,XOR, LSB.

INTRODUCTION

The objective of steganography is to obfuscate the presence of the message itself, rendering it arduous for unauthorised entities to discern. In steganography, the structure of the data is typically left unchanged Common forms of steganography encompass various mediums such as text, audio, video, images, as well as network or protocol-based techniques Conversely, cryptography is concerned with rendering a message incomprehensible to unauthorised individuals by means of encryption. In the field of cryptography, the initial message, commonly referred to as plaintext, is transformed into cypher text through the utilisation of encryption techniques. Only authorised persons with the decryption key can reverse the cypher text into plaintext. Cryptography guarantees the secrecy and accuracy of the information being sent Cryptography utilises mathematical transformations, number theory, and algorithms to alter data [1].

Goal Steganography is the practice of concealing the presence of a message within other data, with the intention of making it challenging to detect.Cryptography aims to ensure the confidentiality of a message by preventing unauthorised access to its contents. Data Modification:Insteganography, Principles of Security: Steganography mainly upholds the concepts of confidentiality and authenticity in terms of security Cryptography is a field that upholds the principles of confidentiality and authenticity, ensuring the security of data integrity and preventing the denial of involvement. Concealment: In the field of steganography, the act of hiding the existence of a covert communication is referred to as visibility. [2]. Cryptography In the field of cryptography, the only thing that is concealed is the actual content of the secret message.Mathematical Involvement: Steganography has limited mathematical transformations.Cryptography is the application of number theory, mathematics, and other

Technologies and Materials for Renewable Energy, Environment and Sustainability
AIP Conf. Proc. 3321, 020022-1–020022-6; https://doi.org/10.1063/5.0289728
Published under an exclusive license by AIP Publishing. 978-0-7354-5231-2/$30.00

mathematical principles to alter data. Steganography primarily ensures confidentiality as its major security service.[3]
measures.Steganography serves several functions, such as watermarking, establishing ownership, safeguarding copyright, and ensuring data authenticity. Secret communication with others has long been one of the famous bogus things of the Age. The secure communication of cryptography and steganography is now employed. However, in nature, they are distinct. It cannot be understood when communication is reformed by cryptography, while steganography disguises the message to prevent it from being seen.Steganography aims to integrate the communication content into public media coverage and the following. Since a secret message may be present, it may be concealed. The practice of sending encrypted digital signals is known as steganography.Therefore, steganography is a form of security technology in which the sender and the recipient of a message are concealed. There are 3 types of steganographyusing LSB (Least Significant Bit algorithm), Filtering and masking, Transformations and Algorithms. [4,5]The sender and receiver in this design share the same encryption and decryption method. The cover text reads first. Then the message is buried [6,7]The stego key is where the message in the sender/receiver section has now been saved. The image of color has turned into a gray image since it has less color. It has 266 bits along with the pixel, as well as the color image. It gradually minimizes shadows between bytes and bytes. The tint of a gray image has a pixel of 8 bits.The grayscale is primarily used to extract stego. The image in a carrier image should be limited to 300K bits of data. . [8,9] Turn the text into a binary format with the procedure termed uniform and strange technique or secret message parking. Thus, the alphabet is split into standard and unusual positions, 0 and 1 bits. The stego. key is divided into dual-layer utilizing the odd and even partitioning to make the system robust. . [10,11] The next step consists in calculating the LSB of each pixel of the transport image and, in each bit, replacing the LSB of the carrier image. Write a few step picture instructions, combining the image cover and the stego key. The above method is also followed to extract the message.[12,13]

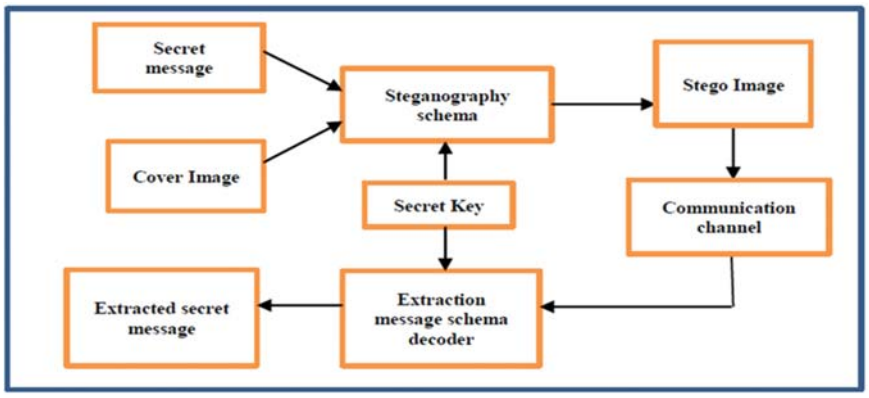

Figure 1. The architecture of image steganography

Image Steganography requires the following items to carry out the work of Image teganography:
The medium of the cover: it's a secret message graphic. [14,15] The message of secrecy is to convey that the text, photos, or any other data may be simple or encrypted.Steg-Key: the key to conceal the message (May or may not be used).Steganography picture Continued In Steganography, the techniques of picture compression are often used. compression is two kinds of techniques. Compression with loss, Compression without loss is normally employed in image steganography, loss compression may not preserve the integrity of the original image, whereas lossless compression keeps the data precise. The lossless picture compression does not affect the original image.

RELATED WORK

Because of its plainness and non-detectability, the LSB steganography was utilized to hide information in the picture. Data concealment was accomplished using multiple writers to swap visible pixels for hidden data bits using low-level synchronous bit-exchange (LSB) methods [20]. Combining the work of cryptologists like Rivest-Shamir Adleman and LSB stenographers like Zhou, Gong, Fu, and Jin resulted in the creation of a new method (RSA) [16]. This strategy achieved a 5.8 percent boost in the PSNR value compared to the usual LSB replacement methodology [17]. An approach based on bit inversion has been suggested for Akhtar, Khan, and Johri using two separate LSB methods [18]. We utilized multiple pictures in this article to mask three separate messages [19] . The PSNR has been enhanced by 5.92 percent and 15.8 percent, respectively, in the first and second recommended methods [20], after conducting the tests were done. An LSB steganography method developed by A. Singh and H. Singh uses 2-2-4 message bits embedded in the R-G-B. Significant increases of 36.44 and 64.54 percentage points in PSNR were achieved. [21] when the approach was used on two separate photos. To conceal their message

in black and white and color images, Goyal, Ramaiya, and Dubey presented 1-2-4 LSB encrypted with the RSA algorithm. The strategy was tested using four distinct photos, and PSNR improved up to 41.48 percent [22]. Sugathan suggested a new stenographic LSB technique using various message embedding directions. Applying the method to 10 different images, we found that the PSNR value increased by 1.32 percent compared to the traditional LSB method. [23]. On the other hand, Kaur and Kochhar introduced two separate steganography LSB and DCT approaches. The method exhibited a satisfactory outcome and increased safety with the use of DCT compared to the PSNR values with earlier efforts [24]

PROPOSED METHOD

Any software product's user interface design is essential for its success. No matter what a fantastic idea the product owner has made and what the software development team's extensive technologies are, if people are confused, terrified, or need help figuring out how to use it. The product will not succeed if we use the Matlab version (R2018b). Figure.2 illustrates the GUI of the project.

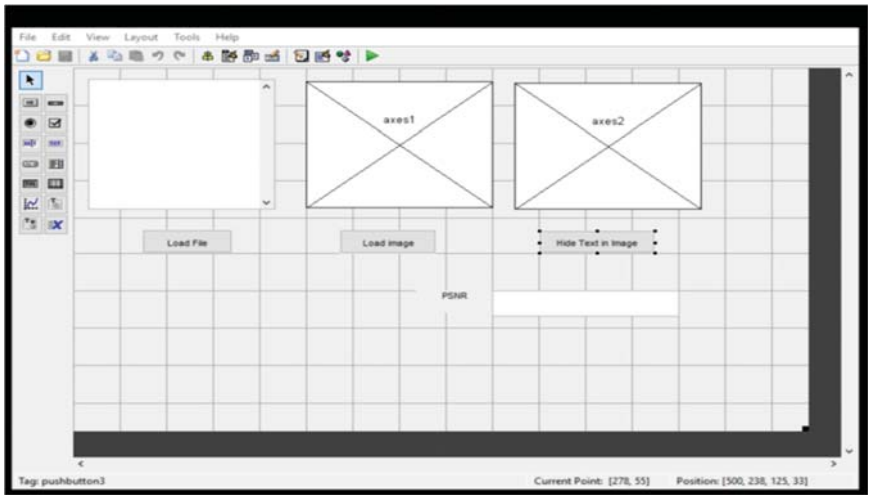

Figure 2. Graphical user interface

The algorithm of proposel system is:

Step 1: secret text: A pixel consists of 8 bits, and text consists of a series of bits, each letter with the message translated into 7 bits.

step 2: choose a random pixel: Select a random pixel to hide a little of your message The whole message, for example, is translated into:0111010,1011000

step 3: steps to hide:

a: The first bit of text is hidden in a random pixel in LSB.

b: Comparing the first bit with the next bit is worth it?

If the equal bits are less critical in pixel 1.

if different bits are less influential in pixel 0.

The hexadecimal pixel is as follow:00110100.

And then, choose another random pixel and let 00001110 because the current bit with the same bit length is the least important bit in the pixel =1 pixel will be 11110001. Figure 3

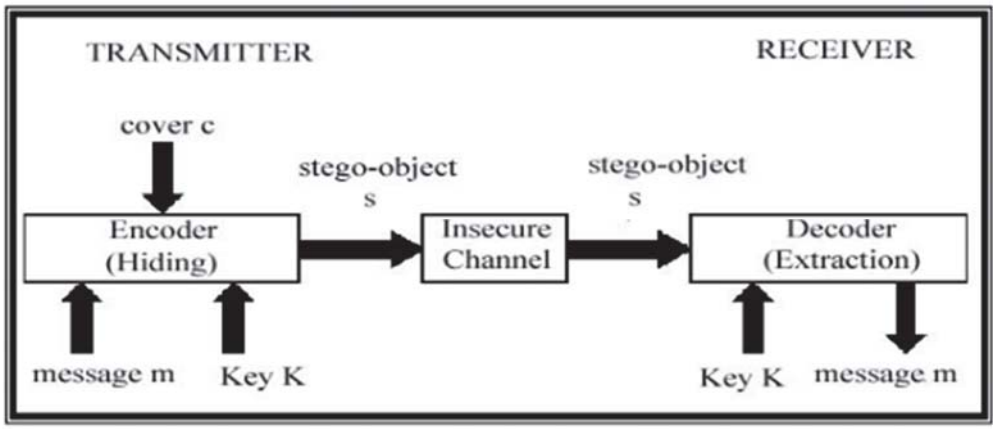

Figure. 3 the blok diagram of proposel

RESULT AND DISCUSSION

The procedure of extracting the massage byte 01000101 is demonstrated in Table 1. The bit locations randomly selected by the second PRNG for the identical seed value are as follows: 2, 1, 7 for the R; 4, 5, 3 for G; and 5, 1,7 for the B.

Table 1. Retrieval of a single byte of data on an image pixel

(R/G/B)	randomly pixel	Implement XOR of bit message	Bit of Message
R	11100101	$1 \oplus 1 = 0$	0
R	10000101	$1 \oplus 0 = 1$	1
R	11111111	$1 \oplus 1 = 0$	0
G	10010001	$1 \oplus 0 = 1$	1
G	10101010	$1 \oplus 0 = 1$	1
G	00110011	$0 \oplus 1 = 1$	1
B	11001100	$1 \oplus 1 = 0$	0
B	10101010	$1 \oplus 0 = 1$	1
B	10010010	$0 \oplus 1 = 1$	1

The previous explanation demonstrates that the suggested approach is an easy approach that utilises LSB replacement. This method incorporates two pseudorandom strategies to conceal a single byte worth of data within a single pixel of the cover image. The utilisation of two pseudorandom layers is anticipated to enhance both the concealment and confidentiality of the system. Additionally, the inclusion of a single byte of information in a single pixel enables a substantial quantity of hidden data to be embedded into the image used as the cover.

In MATLAB (R2018b), the suggested steganography approach was used to measure three 24-bit pictures (Alice, house, and boat), with the dimensions 512 Till 512 as illustrated in . and with MSE, SNR, and PSNR.
The findings presented in Table 2 demonstrate that the suggested method yields a satisfactory Peak Signal-to-Noise Ratio (PSNR), indicating that the stego pictures closely resemble the cover image, as indicated by the Mean Squared Error (MSE). Figure 4,5 depicts a bar chart illustrating the Mean Squared Error (MSE) and Peak Signal-to-Noise Ratio (PSNR) for the Alice.bmp image at various message capacities. According to the chart, it is evident that as the communication capacity grows, the PSNR lowers and the MSE improves. The MSE and PSNR are deemed appropriate given the message's maximum file size, while also taking into account message protection.

Table 2. calculate MSE, SNR, and PSNR for 3 Images

Image name	SNR	MSE	PSNR
Alice	63.7638	1.5275	48.1602
house	63.7690	1.4834	48.2873
boat	63.6736	1.4974	48.2466

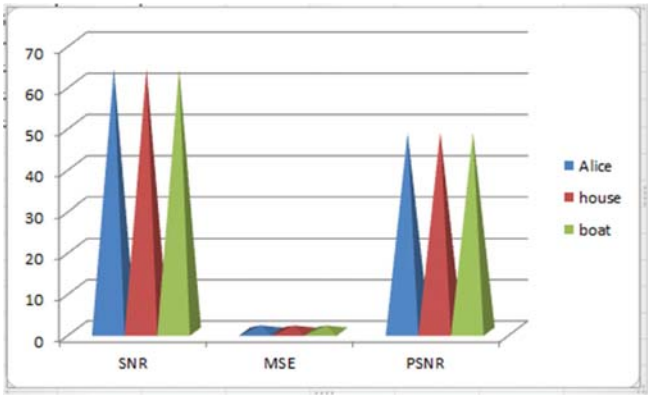

Figure 4 chart illustrating of SNR,MSE,PSNR

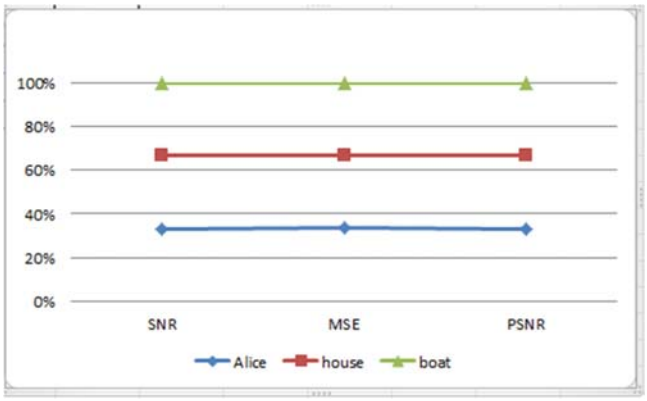

Figure 5 the Ratios of SNR,MSE,PSNR

CONCLUSION

Hiding a message utilizing the steganography method minimizes the likelihood of a message being found. Steganography alone is not a good secrecy option, but neither is a simple replacement or short block permutation for encryption. But you get far stronger encryption processes if these strategies are coupled. As with every technology, steganography is intrinsically neither good nor evil; the way it is utilized determines whether or not it is to our society's benefit.Image Stenography It's easy to spread a hidden message via the Internet and message boards using an image. Modifying the text's layout or altering the properties of individual textual parts constitutes text steganography, "e.g., characters." Audio Steganography: Secret message is integrated into a digitalized audio signal in audio steganography, slightly altering the related audio file's binary sequence.

REFERENCES

1. B.J. AlKhafaji, MA Salih, SAH Shnain, OA Rashid, AA Rashid, MT Hussein,2021,Applying the Artificial Neural Networks with Multiwavelet Transform on Phoneme recognition ,Journal of Physics: Conference Series 1804 (1), 012040.
2. W. H. Abdulsalam, R. S. Alhamdani, and M. N. Abdullah, "Emotion recognition system based on hybrid techniques," International Journal of Machine Learning and Computing, vol. 9, 2019.
3. Zahraa Modher Nabat, Mushtaq Talib Mahdi, Shaymaa Abdul Hussein Shnain Face Recognition Method based on Support Vector Machine and Rain Optimization Algorithm (ROA) Webology. Vol. 19, No. 1, 2022.
4. B.J AlKhafaji, M Salih, S Shnain, Z Nabat ,segmenting video frame images using genetic algorithms,2020 Periodicals of Engineering and Natural Sciences 8 (2), 1106-1114
5. B.J AlKhafaji, M Salih, S Shnain, Z Nabat ,improved technique for hiding data in a colored and a monochrome images,2020, Periodicals of Engineering and Natural Sciences 8 (2), 1000-1010
6. B.J AlKhafaji, MA Salih, SAH Shnain, OA Rashid, AA Rashid, MT Hussein,2021,Applying the Artificial Neural Networks with Multiwavelet Transform on Phoneme recognition ,Journal of Physics: Conference Series 1804 (1), 012040.

7. RAHMA, A.M.S., RAHMA, M.A.S., and RAHMA, M.A.S. (2015) Automated analysis for basketball free throw. In: Proceedings of the 7th International Conference on Intelligent Computing and Information Systems, Cairo, December 2015. Piscataway, New Jersey: Institute of Electrical and Electronics Engineers, pp. 447-453.
8. B.J AlKhafaji, M Salih, S Shnain, Z Nabat ,segmenting video frame images using genetic algorithms,2020 Periodicals of Engineering and Natural Sciences 8 (2), 1106-1114
9. Zahraa Modher Nabat, Mushtaq Talib Mahdi, Shaymaa Abdul Hussein Shnain Face Recognition Method based on Support Vector Machine and Rain Optimization Algorithm (ROA) Webology. Vol. 19, No. 1, 2022.
10. B.J AlKhafaji Steganography techniques using tunes and Discrete Cosine Transform (DCT) Journal of Xi'an University of Architecture & Technology, S. (2020). Volume XII, Issue IV, - 5234- 5244
11. B.J AlKhafaji, Image Improvement Using The Combination of Wavelet and Multiwavelet Transform 2010 - Ibn AL-Haitham Journal For Pure and Applied Science VO L.23 (3).
12. Baydaa Jaffer Al-Khafaji, Abdul Monem S Rahma, (2023). Proposed new modification of AES algorithm for data security, Global Journal of Engineering and Technology Advances, *Vol. 3, No. 12, pp* 117–122
13. Al-Khafaji, Baydaa Jaffer. "Proposed speech analyses method using the multiwavelet transform." Ibn AL-Haitham Journal For Pure and Applied Science 27.1 (2017): 394-401.
14. Al-Khafaji, Baydaa Jaffer. "Proposed speech analyses method using the multiwavelet transform." Ibn AL-Haitham Journal For Pure and Applied Science 27.1 (2017): 394-401.
15. Baydaa Jaffer Al-Khafaji Color image analyses using four deferent transformations (FFT-DCT-DWT-DMWT).(2014) Computer Engineering and Intelligent Systems www.iiste.org ISSN 2222-1719 Vol.5, No.10, *pp* 16–24
16. Halim, S., & Sani, M. F. A. (2010, November). Embedding using spread spectrum image steganography with GF (2m). In Proc. of the 6th IMT-GT Conference on Mathematics, Statistics and its Applications (pp. 659-666).
17. Cox, I. J., Kilian, J., Leighton, T., & Shamoon, T. (1996, September). Secure spread spectrum watermarking for images, audio and video. In Proceedings of 3rd IEEE international conference on image processing (Vol. 3, pp. 243-246).
18. Al-Hazaimeh, O. M. A. (2012). Hiding data in images using new random technique. International Journal of Computer Science Issues (IJCSI), 9(4), 49.
19. El-Emam, N. N. (2007). Hiding a large amount of data with high security using steganography algorithm. Journal of Computer Science, 3(4), 223-232.
20. Zhou, X., Gong, W., Fu, W., & Jin, L. (2016, June). An improved method for LSB based color image steganography combined with cryptography. In 2016 IEEE/ACIS 15th international conference on computer and information science (ICIS) (pp. 1-4). IEEE.
21. Akhtar, N., Khan, S., & Johri, P. (2014, February). An improved inverted LSB image steganography. In 2014 International Conference on Issues and Challenges in Intelligent Computing Techniques (ICICT) (pp. 749-755). IEEE.
22. Singh, A., & Singh, H. (2015, March). An improved LSB based image steganography technique for RGB images. In 2015 IEEE International Conference on electrical, computer and communication technologies (ICECCT) (pp. 1-4). IEEE.
23. Goyal, S., Ramaiya, M., & Dubey, D. (2015, December). Improved detection of 1-2-4 lsb steganography and rsa cryptography in color and grayscale images. In 2015 International Conference on Computational Intelligence and Communication Networks (CICN) (pp. 1120-1124). IEEE.
24. Sugathan, S. (2016, July). An improved LSB embedding technique for image steganography. In 2016 2nd International Conference on Applied and Theoretical Computing and Communication Technology (iCATccT) (pp. 609-612). IEEE.
25. Kaur, G., & Kochhar, A. (2012). A steganography implementation based on LSB & DCT. International Journal for Science and Emerging Technologies with Latest Trends, 4(1), 35-41.

Design and Simulation Micro Strip Patch (1×4) Array Antennas for S-Band Applications

Hiyam Majeed Ahmed [1,a], Abdullah Hamoud Mohammed [2,b], Muatazbullah Ibrahim Abdullah [3,c]

[1]*Department of Physics, College of Education for Women, Kirkuk University, Kirkuk, Iraq.*
[2]*Department of Physics, College of Education for Pure Sciences- Kirkuk University, Kirkuk, Iraq.*
[3]*Ministry of Education Directorate General of Education in Kirkuk, Al-Jawhara Intermediate School for Girls, Kirkuk, Iraq.*

[a] hiyam.majeed28@gmail.com
[b] dr.abdulla@uokirkuk.edu.iq
[c] Corresponding author: mutazalalmi1990@gmail.com

Abstract: At first, we defined the antenna as a simple antenna with a rectangular element, but after evaluating the results of the antenna characteristics such as gain, direction and radiation patterns, we converted it to a MPA (1x4) rectangular matrix antenna using a fixed distance. we did between the elements of the matrix and in the range (λ1). To achieve high profitability and direct return loss (parameter S11) and improve low radiation patterns. MPA antenna was designed using FR-4 as a dielectric material with loss tangent tanδ = 9.10-4, dielectric constant 4.3 and thickness 1.6. The feed was from a microstrip line, and the input impedance of the feed line was equal to 50 ohms. The final antenna has a directivity of 11 dB. MPA antenna (1x4) suitable for S-band applications is designed and simulated using CST2019 simulation software.

Keyword: Antenna, MPA, FR-4, S-band applications, WiMAX

INTRODUCTION

Antennas are a key technology in the any other wireless system. In a wireless system, an antenna converts guided radio wave energy to energy that is emitted or "radiated" out into free space. An antenna also does the reverse - it receives radio waves from the air and feeds them into the devices that detect, decode, and amplify them [1]. In the last years, the developing of wireless and telephone communications has necessitated the active developing of these that's where they are able to keep high performance over a wide range of the frequency. Antenna can be considered almost the main factor for wireless communication systems. The wireless field requires a high performance antenna with low return loss, wide bandwidth and small size [2] [3]. This technological trend has focused a lot of effort on the design of the Micro strip patch antenna. This type of antenna is very popular for its ease of manufacture, light weight, low cost, low appearance and easy integration with FR devices. MPA antennas can be designed in different geometric shapes such as rectangular, circular, triangular, annular patch etc. The rectangular patch is more popular than the rest of the shapes and can be easily adjusted to produce a range of impedance values, radiation patterns and working frequencies. Best Feeding Technique Micro strip line is one of the most common feeding techniques, because it is easily designed and easily matched to the antenna through internal position control [4]. The gain and direction of the antenna increases slightly with the dimensions of the patch and the number of layers of the manufactured antenna [5]. In order to design a compact MPA antenna, substrates with high isolation constants should be used which result in lower efficiency and narrow bandwidth. Therefore, optimization should be chosen between the antenna dimension and the antenna performance [6] [7] Profit can be increased by increasing the number of Micro strip patch antenna. The larger the number of patch, the better the antenna matrix gain but the final size goes to the giant.

Technologies and Materials for Renewable Energy, Environment and Sustainability
AIP Conf. Proc. 3321, 020023-1–020023-7; https://doi.org/10.1063/5.0290313
Published under an exclusive license by AIP Publishing. 978-0-7354-5231-2/$30.00

An array can be defined as continuous antennas arranged in a regular structure to form a single antenna. The developed matrix antenna is a multiple antenna, through which an antenna pattern can be enhanced in a given direction and suppressed from unwanted directions. The direction of the matrix radiation can be directed electronically to avoid the need for any mechanical rotation. The load resistance must be the same as the feed source resistance [8]. The technology uses a quarter of the wavelength to divide power equally to all radioactive patches [9] To design a matrix we need a feed grid that connects all elements together. Matrix antennas are extremely versatile, used among other types of antennas to assemble a desired pattern that cannot be achieved with a single element. In addition they are used to scan beam antenna system, increase directivity, gain, and perform various functions that are difficult to perform with a single component [10]. One of the downsides of the thin chip antenna is that it has a limited bandwidth; nevertheless, a lot of research has been done recently to increase and improve the bandwidth including using thick substrates with low dielectric constants and metal patch cracks [11].

The proposed antenna design

This section provides information on the design of the MPA antenna. Figure 1 shows the basic structure of the thin chip antenna. The MPA antenna is installed from the patch, dielectric substrate, ground plane and feed line [12].

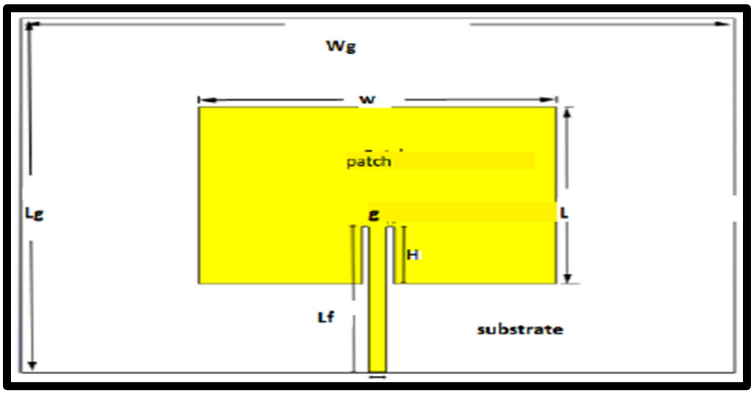

FIGURE 1. shows the basic structure of the thin chip antenna.

The MPA antenna is designed on the FR-4 substrate with a relative tolerance of =εr = 4.3mm with a thickness of h = 1.6mm. The designed antenna operates at 2.4GHz with an impedance of 50 ohm.

A) Calculation of the dimensions of the chip:

The dimensions of the micro strip patch antenna are calculated from the design equations of the standard antennas [13] at the reference resonant frequency.

1- Width of the patch:

$$W = \frac{V_\circ}{2F_r}\sqrt{\frac{2}{\varepsilon_r+1}} \tag{1}$$

2- Calculate the effective length of the thin chip (l_{eff})

$$l_{eff} = \frac{v_\circ}{2f\sqrt{\varepsilon_{reef}}} \tag{2}$$

Where: ε_{reef} is the effective relative permittivity and equal:

$$\varepsilon_{reef} = \frac{\varepsilon_r+1}{2} + \frac{\varepsilon_r-1}{2}[1+12\frac{h}{w}]^{-\frac{1}{2}} \tag{3}$$

The actual length of the patch is equal to:

$$L = L_{eff} - 2\Delta L \tag{4}$$

$$\Delta L = 0.412h\,\frac{(\varepsilon_{ree}+0.3)(\frac{W}{h}-0.264)}{(\varepsilon_{reef}-0.258)(\frac{W}{h}+0.8)} \tag{5}$$

B- Calculate the dimensions of the ground level:

The dimensions of the ground level are about twice the dimensions of the patch around the outer surface. The dimensions of the ground level are calculated from the following relationship:

1- Ground plane width:

$$W_g = 2 \times W \tag{6}$$

2- Ground plane length:

$$L_g = 2 \times L \tag{7}$$

C - Calculate the thickness of the substrate (dielectric substrate)

It is necessary that the height of the substrate and the relative permittivity meet the equation shown below as a minimum height

$$h \geq 0.06 \frac{\lambda}{\sqrt{\varepsilon_r}} \tag{8}$$

D-Calculation of feeding line dimensions:

The relationship between the width of the feed line (w_f)and the thickness of the insulating material (h) is given by:

$$\frac{W_f}{h} = 7.4/e^{\sqrt{0.33(\varepsilon_r+1.41}} \tag{9}$$

1. The length of the feed line is calculated from the following relationship:

$$L_f = \lambda/4\sqrt{\varepsilon_r} \tag{10}$$

2. Inset Feed Depth

$$H \; or \; F_i = \frac{0.822 \times L}{2} \tag{11}$$

3. The gap (GPF) between the patch and the length of the feed line inside the patch (Notch Gap):

$$GPF = \frac{C}{\sqrt{2\varepsilon_{reef}}} . \frac{4.65 \times 10^{-12}}{f(in\ GH_Z)} \tag{12}$$

Based on the above equations, the dimensions of the MPA thin strip antenna with micro type line feeding are shown as shown in FIGURE 2. Table 1 shows the dimensions of the proposed antenna measured in millimeters.

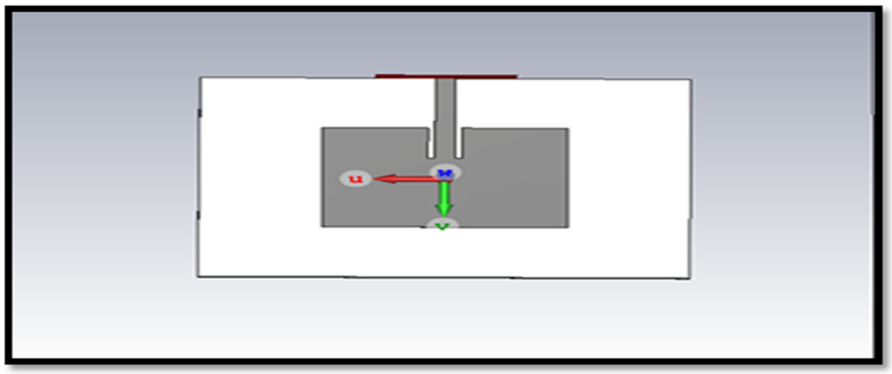

FIGURE. 2 Microstrip patch antenna in cst studio.

TABLE 1. Dimensions of the proposed antenna

Parameters	Dimensions
Center frequency, (F_o)	2.4GH_Z
Substrate	FR-4
Substrate height (h)	1.6mm
dielectric constant (ε_r)	4.3
Length of the patch (L)	29mm
Width of the patch (W)	38mm
Length of the substrate (L_g)	58mm
Width of the substrate (W_g)	76mm
Length of micro-strip feed (L_f)	13.5mm
Width of micro-strip feed(W_f)	3.137mm
Distance of inset feed(H)	8.85mm
Gap between micro-strip feed patch(GPF)	1mm
Thickness of the patch	0.035

Array Design (1 × 4)

In order to obtain a high performance antenna (gain, directivity) to meet long distance communication requirements the easy way to do this is to increase the patch. A conventional MPA antenna array is composed of more than one identical element that is fed using a corporate feeding technique deployed on the dielectric substrate. The distance between the elements is within the limits (λ, λ / 2, λ / 4, λ/8) and is determined empirically.

To design an MPA matrix (1 × 4) use the same insulating material (FR-4) with the same dimensions as the single element MPA antenna. The distance between the radioactive elements of the array is λ, and the four elements are connected to a uniform transmit ion line. [14] In order to obtain a good fit we will need to tie the elements from the point where the input impedance of the thin strip is identical to the line impedance [15]. Figure 3 shows the basic structure of the array antenna (1 × 4).

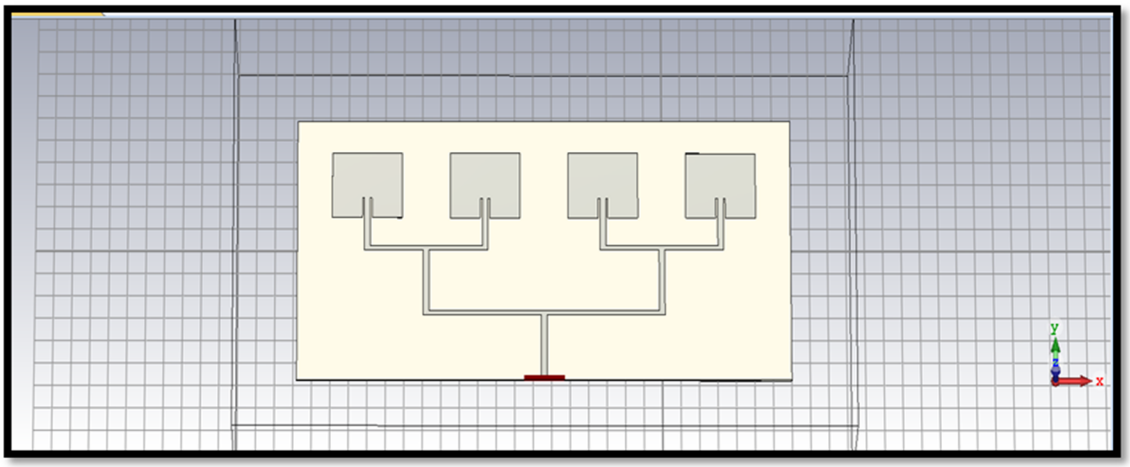

FIGURE 3. the basic structure of the array antenna (1 × 4).

TABLE 2. the dimensions of the matrix (1 × 4)

Variables	Values (mm)
L($1 \times 4\ array\ antenna$)	116mm
W($1 \times 4\ array\ antenna$)	152mm
W_f	3.137mm
W_2	2mm

Simulation and Discussion Results

In this part we present a comparative study between the simple MPA antenna and the matrix MPA antenna (1 × 4) using the CST2019 simulation software based on the selected integration method. The use of the matrix antenna has been greatly increased in communications by transmitting its signal over long distances directly without the need for relay stations [16]. Here the rectangular MPA (1 × 4) antenna array is designed to resonate at S-band frequencies. So the antenna matrix has been used in many applications such as Wi-MAX and WLAN.

The simulation was accomplished to reach the desired results in terms of (Zin, VSWR, S11, Gain, Directivity, Bandwidth).

A- Return loss (S11-parameter):

Figure 4 shows a comparison between the return loss of the two designs (simple single-element antenna and (1x4) matrix antenna.

The return loss value is equal to the simple MPA antenna equals -22.22 dB and equals -17.84 dB for the array antenna (4 × 1).

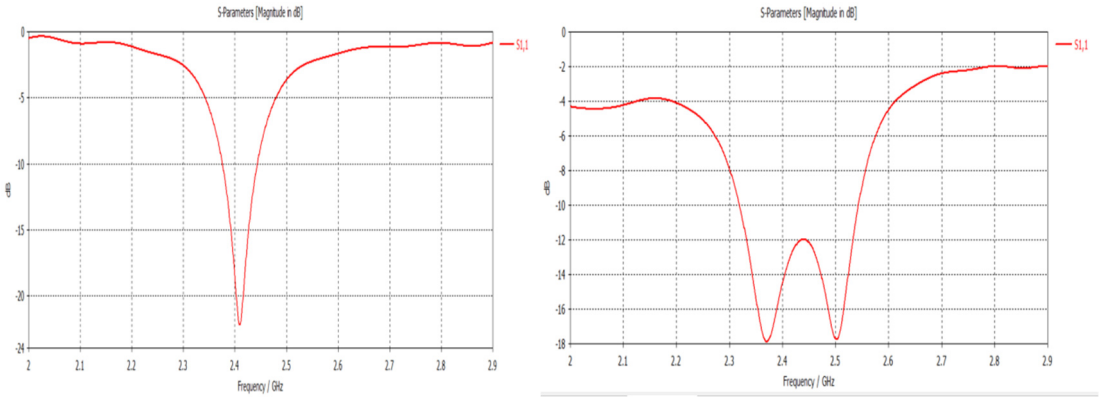

(a) Return loss for single element (b) Return loss for(1×4) array

FIGURE 4. Return loss for MPA.

B- Voltage standing wave (VSWR):

The quality of the antenna performance is also defined by either its input resistance or its VSWR, which must be less than 2 at the resonant frequency, in order for the antenna to be well adapted. The interrupted wave voltage varies for the two designs as the simple MPA antenna VSWR is 1.6 and the matrix antenna (1 × 4) is 1.29 as shown in figure 5.

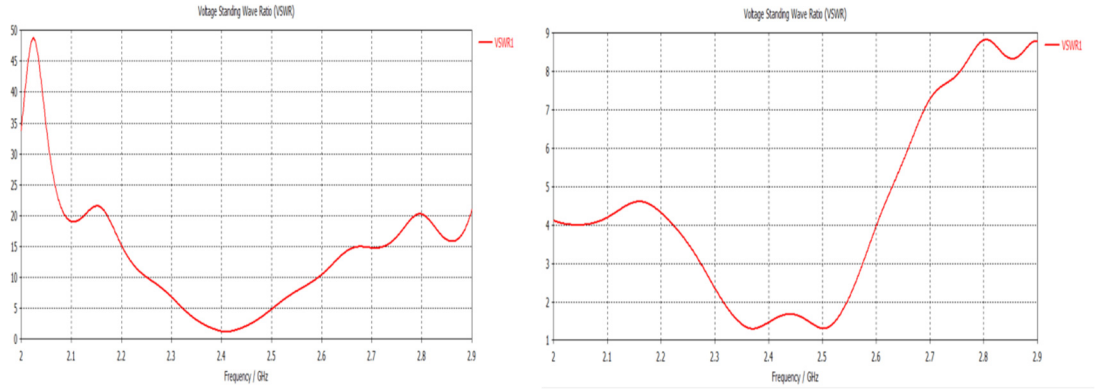

(a) VSWR for single element (b) VSWR for (1×4)array

FIGURE 5. voltage standing wave ration.

C- The Input impedance:

It is seemed that the input impedance is also considered as a factor for studying antenna performance as well as VSWR. Figure (6) clarifies the real and imaginary part of the input impedance of the two designs.

(a) Smith chart for single MPA (b) smith chart for (1×4) array

FIGURE 6. smith chart.

It is evident, From figure 6, that the input impedance (for the simple antenna) is 49.01Ω . Additionally, the matrix antenna (1 × 4) is 48.78.

D- Gain and Directivity:

Directivity and gain are key factors for determining the radiation intensity of the antenna. Figure 7 shows the directivity and gain value of the simple antenna and matrix antenna (1 × 4).

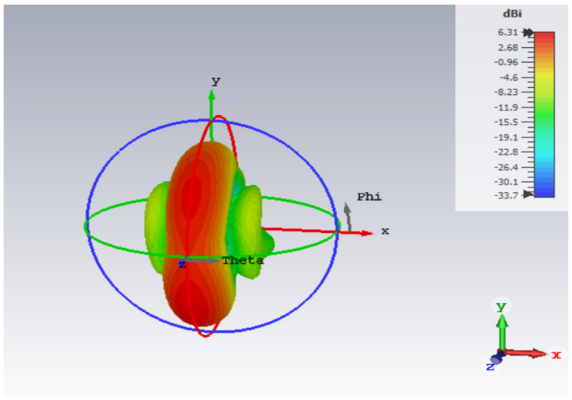

(a) Gain for single element MPA array MPA

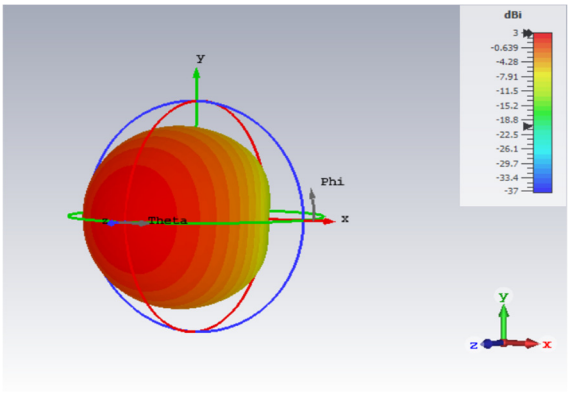

(b) Gain for (1×4)

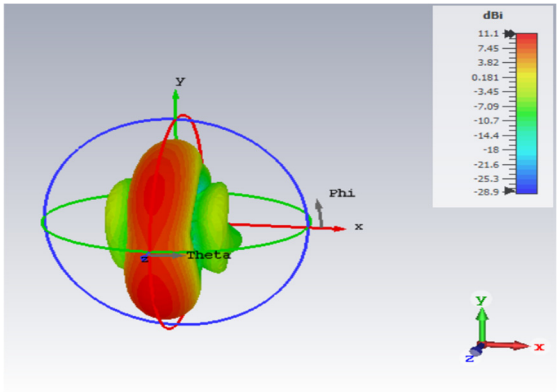

(C) Directivity for single element MPA array MPA

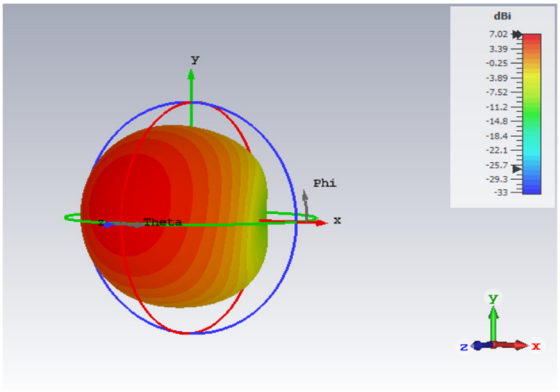

(d) Directivity for (1×4)

FIGURE 7. Gain &Directivity.

E- Band width:

The bandwidth is calculated from the return loss scheme as a function of frequency. The bandwidth can be determined by taking the return loss value -10 dB as a reference. Figure shows (8) bandwidth for design.

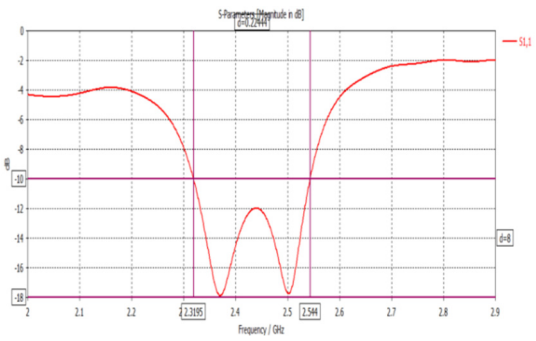

(a) Band width for single element MPAarray MPA

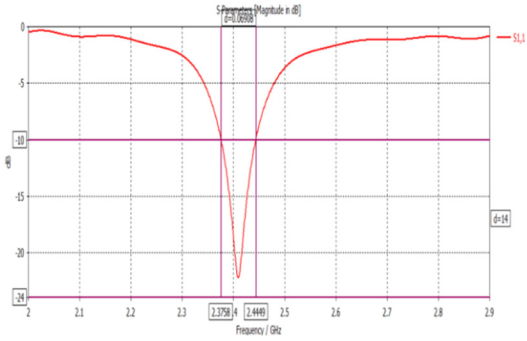

(b) band width for (1 × 4)

FIGURE 8. bandwidth.

CONCLUSION

Basically, this research focuses on design and analysis of a single-element, four-element rectangular thin-film antenna. The characteristics of the presupposed antennas are analyzed during employing the CST2019 Microwave Studio simulation software. It was discovered that the antennas resonate at the desired frequency of (2-2.5GHz) with an improved return loss, gain, directivity, VSWR and BW. Well gain, routing and the improvements of BW is achieved by using the matrix antenna technology (4 × 1). The gain of the antenna could be increased through increasing the number patch in matrix structure. Applications (WiMAX, WLAN) particularly.

REFERENCES

1. Saeid, Sabah Hawar, and Saba Fadhel Ahmed. "Study and assessment of performance of mobile phones base stations antennas using MATLAB and TEAMS." European Journal of Scientific Research 53.2 (2011): 249-257.
2. David M. Pozar, “Microwave Engineering”, 4th ed., Jhon Wiley & sons inc.2012.
3. Roy, Atser A., Joseph M. Môm, and Gabriel A. Igwue. "Enhancing the bandwidth of a microstrip patch antenna using slots shaped patch." American Journal of Engineering Research (AJER) 2.9 (2013): 23-30.
4. Shimu, Nusrat Jahan, and Anis Ahmed. "Design and performance analysis of rectangular microstrip patch antenna at 2.45 GHz." 2016 5th International Conference on Informatics, Electronics and Vision (ICIEV). IEEE, 2016.
5. Kaymaram, F., and Lotfollah Shafai. "Enhancement of microstrip antenna directivity using double-superstrate configurations." Canadian Journal of Electrical and Computer Engineering 32.2 (2007): 77-82.
6. Pozar, D. A. V. I. D. M. "A reciprocity method of analysis for printed slot and slot-coupled microstrip antennas." IEEE Transactions on Antennas and Propagation 34.12 (1986): 1439-1446.
7. Balanis, Constantine A. Antenna theory: analysis and design. John wiley & sons, 2016.
8. Datto, Sham, Md Rafiqul Islam Sheikh, and Nur Mohammad Sohayeb. "Optimized microstrip patch antenna (MPA) array design to enhance gain for s-band application." IOSR Journal of Electrical and Electronics Engineering 12 (2017): 74-78.
9. Constantine A.Balanis, Antenna Theory- Analysis and Design (Second Edition: Reprint 2007, John Wiley Publications).
10. Constantine A. Balanis, “Antenna Theory: Analysis and Design”, 3rd ed., NJ: Wiley, 2005.
11. Ali, Saad N., Faris S. Atallah, and Abdullah H. Muhammad. "Design and Simulation of Rectangular Microstrip Patch Antenna Using a Computer Simulation Technology Operating at 4.5 GHz." Iraqi Journal of Applied Physics 19.2 (2023).
12. James, James R., and Peter S. Hall, eds. Handbook of microstrip antennas. Vol. 1. IET, 1989.
13. C.A. Balanis, Antenna theory analysis Design, 2nd Edition, John Wiley & sons.), Microstrip Antenna Design Handbook, pp.1-68,253-316 Artec House Inc. Norwood,MA.
14. Bahadir S. Yildirim, Bedri A. Cetiner, et al, “Integrated and uwb antenna”,IEEE antenna & wireless propag. Letters, vol. 8,2009.
15. Khatun, Mst Hasneara, Reefat Inum, and Nazia Tasnim. "Design of rectangular patch antenna array using different feeding technique." 2017 2nd International Conference on Electrical & Electronic Engineering (ICEEE). IEEE, 2017.
16. Minervino, Diego R., et al. "Arrays of rectangular patch microstrip antennas for aerospace applications." 2013 SBMO/IEEE MTT-S International Microwave & Optoelectronics Conference (IMOC). IEEE, 2013.

Meta Heuristic Algorithms to Solve Multi Objective Model Based on Single Machine Scheduling

Tahani Jabbar Khraibet [1,2,a)] and Bayda Atiya Kalaf [1,b)]

[1]*Department of Mathematics, Thi-Qar Directorates of Education, Ministry of Education, Thi-Qar, Iraq*
[2]*Department of Mathematics, College of education for Pure Sciences- ibn Al-Haitham, University of Baghdad, Baghdad, Iraq*

[a)] Corresponding author: Tahany.Jabbar2103p@ihcoedu.uobaghdad.edu.iq
[b)] baydaa.a.k@ihcoedu.uobaghdad.edu.iq

Abstract. This paper proposes a multi-objective model for single Machine scheduling problems by minimizing the total weighted discounted completion time $\sum_{h=1}^{m} w_h(1-e^{-\alpha C_h})$, the number of tardy jobs $\sum_{h=1}^{m} U_h$, the maximizing earliness E_{max} and the maximizing weighted tardiness $T_{max}^{w}$with release dates. The objective function is denoted $((\mathbf{1}/r_h/\sum_{\mathbf{h=1}}^{\mathbf{m}}(\mathbf{w_h}(\mathbf{1}-\mathbf{e}^{-\alpha C_h})+U_h+E_{max})+\mathbf{T_{max}^{w}})$. Then, we solve the mathematical model by using two a meta-heuristic algorithm (Meerkat Clan Algorithm and Bald Eagle Search) to find the near optimal solution for a single machine scheduling problem. To evaluate the performance of the algorithm in terms of accuracy and running time, computational experiments are conducted. The results show that the Meerkat Clan Algorithm is the most effective in practical experiments and can solve up to 2500 jobs and Bald Eagle Search solve up to n = 1000 jobs. Arithmetic results are calculated by coding (programming) algorithms using (MATLAB 2023a).

Keywords: Machine Scheduling problem, Meerkat Clan Algorithm, Bald Eagle Search, discounted completion time, maximum earliness, maximum weighted tardiness.

INTRODUCTION

The Machine Scheduling Problem (MSP), a crucial area of Operation Research (OR), can be defined as the problem of scheduling is the process of allocating resources over a period of time to perform a collection of tasks Baker [1]. Machines and jobs refer to resources and tasks, which can take several forms. Scheduling theory refers to the process of assigning a given set of tasks to available resources over a given period of time with the goal of minimizing certain criteria kind and Croce [2].

For the manufacturing and service sectors, it used to reduce or enhance the costs and benefits of industrial production so that companies are competitive William [3]. Furthermore, scheduling entails assigning machines to jobs in order to complete all tasks within the specified limits. Single machine scheduling is a well-researched variant of scheduling because it can divide complex machine environments into smaller subproblems Pinedo [4]. The job scheduling problem employed by a company is solved by employing mathematical methods and heuristic techniques to allocate limited resources in order to find near-optimal solutions.

Several researchers have extensively studied and documented this (Atiya et al [5] , Khraibet and Ghafil, [6], Yousif & Ali [7] ,Abbas and Ghayyib [8], Neamah and Atiya [9] and Neamah and Atiya [10]). Most studies on scheduling theory assume that the processing of orders takes the same amount of time over the entire planning horizon. In addition, most previous studies on scheduling have focused on a single method of measuring performance. A company evaluates a production plan based on a variety of factors, including work-in-process inventory and meeting deadlines. Regardless of which criterion is evaluated, an unbalanced result is likely if only one criterion is considered. Maintaining a low

Technologies and Materials for Renewable Energy, Environment and Sustainability
AIP Conf. Proc. 3321, 020024-1–020024-8; https://doi.org/10.1063/5.0290562
Published under an exclusive license by AIP Publishing. 978-0-7354-5231-2/$30.00

work in progress inventory as a primary objective may result in certain goods being completed far beyond their due date. We categorize this problem as a multi-criteria planning problem.

Abdul-Razaq and Motair [11] used three local search algorithms descent method, simulated annealing, and tabu search to solve the problem $1// \sum C_j + \sum T_j + T_{max} + E_{max}$ up to 2000. In 2022, Ibraheem et al [12] used simulated annealing, Genetic Algorithm, and Firefly algorithm to solve the problem of $\mathbf{1}//\sum_{\mathbf{j=1}}^{\mathbf{n}}(\mathbf{C_j} + \mathbf{T_j} + \mathbf{E_j} + \boldsymbol{V_j} + \boldsymbol{U_j})$. Abbas [13] applied two metaheuristic algorithm; Descent method (DM), Simulated Annealing and Genetic Algorithm to solve the problem $1 // F(\sum U_i, \sum T_i, T_{max})$. Karrar and Aws [14] presented the problem of $1// V_{max} + T_{max} + E_{max}$ using three metaheuristic algorithm (Descent Method, Simulated Annealing and Genetic algorithm) to find near optimal solution.

Although metaheuristic algorithms have been successful in solving challenging real-world MSP problems, there isn't a universally applicable algorithm that can solve every problem involving the no-free-lunch theorem, according to Wolpert and Macready [15].

This paper proposed multiple-objective model for minimizing the total weighted discounted completion time $\sum_{h=1}^{m} w_h(1 - e^{-\alpha C_h})$, the number of tardy jobs $\sum_{h=1}^{m} U_h$, maximum earliness E_{max} and the maximum weighted tardiness T_{max}^{w}. with release dates for a single machine scheduling problem. Then, we introduced the Meerkat Clan Algorithm and Bald Eagle Search to solve the mathematical model for SMSP.

The remainder of this paper is organized as follows: Presents the methodology of the mathematical formulation of the problem. Present metaheuristic algorithms (Meerkat Clan Algorithm and , Bald Eagle Search) for solving the multiple-objective model. Results and discussion are presented. Finally, conclusions and suggestions for future work are given.

METHODOLOGY

The mathematical model

In this section, we examined the concept of MSP with m jobs on a single machine that is consistently accessible and capable of performing them. Assumed a schedule $(1,2,\dots,m), \forall h$ has needs a processing time p_h and a positive weighted w_h on the machine and ideally would be completed at its due date d_h and release date r_h .The machine can only run one job at a time, and each job has its own deadline. Thus, no two jobs can run concurrently to minimize the total weighted discounted completion time, the number of tardy jobs, maximum earliness and the maximum weighted tardine (i.e., to minimize the multi-objective) defined as:$\sum_{h=1}^{m} w_h(1 - e^{-\alpha C_h})$ where $\mathrm{C_h}$ be a completion time for job h, given by the relationship: $\mathrm{C_1} = \mathrm{r_1} + \mathrm{p_1}$, $\mathrm{C_h} = \max\{\mathrm{r_h}, \mathrm{C_{h-1}}\} + \mathrm{p_h}$ for h=2,3,…,n, and if a job h is completed after it's due date $(C_h > d_h \; then \; U_h = 1)$, $(C_h \leq d_h \; then \; U_h = 0)$, $\mathrm{E_{max}} = \max\{d_h - \mathrm{C_h}, 0\}$ and $\mathrm{T_{max}^{w}} = \max\{\mathrm{w_h} T_h\} = \max\{\mathrm{w_h}(\mathrm{c_h} - \mathrm{d_h}), 0\}$.

Notations

Some primary symbols of the multi objective model were presented as follows:

- $\mathrm{N} = \{1,2,3,\dots,m\}$.
- σ = is the set of all schedules.
- p_h = processing time for job h.
- w_h = weight of job h.
- d_h = due date of job h.
- r_h = release date of job h.
- C_h = completion time of job h.
- α = discount rate.
- $\sum_{h=1}^{m} w_h(1 - e^{-\alpha C_h})$ = minimize the total weighted discounted completion time.
- $\sum_{h=1}^{m} U_h$ = the number of tardy jobs.
- E_{max} = the maximum earliness
- $T_h = max\{C_h - d_h, 0\}$ = The tardiness of job h.
- T_{max} = the maximum tardiness.

- T_{max}^{w} = the maximum weighted tardine.
- MSP = machine scheduling problem.
- MOF = multiple objective's function.
- MCA = meerkat clan algorithm.
- BES= Bald Eagle Search

Objective Function and Constraint

In present study, four objective functions were solved at the same time, that is, to minimize the total weighted discounted completion time $\sum_{h=1}^{m} w_h(1-e^{-\alpha C_h})$, the number of tardy jobs $\sum_{h=1}^{m} U_h$, the maximum earliness E_{max} and the maximum weighted tardiness T_{max}^{w} with release date $(1/r_h/\sum_{h=1}^{m}(w_h(1-e^{-\alpha C_h})+U_h)+T_{max}^{w})$. By using the conventional nomenclature for classifying scheduling problems, the main problem is shown by (TA), and it can be in this way.

$$TA = min_{\sigma\in S}\{M_{(\sigma)}\} = min_{\sigma\in S}\left\{\sum_{h=1}^{m}(w_h(1-e^{-\alpha c_h})+U_h)+E_{max}+T_{max}^{w}\right\}\ldots \quad (1)$$

$$\left.\begin{array}{c} C_{(h)} \geq r_{(h)} + p_{(h)} \\ C_{(h)} = C_{h-1} + p_{(h)} \\ O < \alpha < 1 \\ U_{(h)} = \begin{cases} 1 & if\ C_{(h)} > d_{(h)} \\ 0 & otherwise \end{cases} \\ E_{(h)} \geq d_{(h)} - C_{(h)} \\ L_{(h)} = C_{(h)} - d_{(h)} \\ T_{(h)} \geq max\{C_{(h)} - d_{(h)}, 0\} \\ r_h \geq 0, w_{(h)} \geq 1, d_{(h)} > 0,\ E_{(h)} \geq 0,\ T_{(h)} \geq 0\ \ p_{(h)} > 0 \end{array}\right\} h\ from\ 1\ to\ m \Bigg\}\ldots \quad (2)$$

We can divide the problem (TA), which is strongly NP-hard, into four subproblems. It explains it as follows:

$$\left.\begin{array}{l} min_{\sigma(h)} = \left\{\sum_{h=1}^{m} w_h(1-e^{-\alpha c_{\sigma(h)}})\right\} \\ s.t \\ C_{\sigma(h)} \geq r_{\sigma(j)} + p_{\sigma(h)} \\ C_{\sigma(h)} = C_{\sigma(h-1)} + p_{\sigma(h)} \\ 0 < \alpha < 1 \\ r_{\sigma(j)} \geq 0, w_{\sigma(h)} \geq 1, p_{\sigma(h)} > 0, d_{\sigma(h)} > 0 \end{array}\right\} \begin{array}{c} h\ from\ 1\ to\ m\ and \\ h = 2,3,\ldots,m \end{array} \quad (3)$$

$$
\left.
\begin{aligned}
& min_{\sigma(h)} = \left\{ \sum_{h=1}^{m} U_{\sigma(h)} \right\} \\
& s.t \\
& \quad C_{\sigma(j)} \geq r_{\sigma(j)} + p_{\sigma(j)} \\
& \quad C_{\sigma(h)} = C_{\sigma(h-1)} + p_{\sigma(h)} \\
& \quad U_{(h)} = \begin{cases} 1 & if\ C_{(h)} > d_{\sigma(h)} \\ 0 & otherwise \end{cases} \\
& r_{\sigma(h)} \geq 0, p_{\sigma(h)} > 0, d_{\sigma(h)} > 0
\end{aligned}
\right\}
\begin{matrix} h\ from\ 1\ to\ m\ and \\ h = 2,3, \dots, m \end{matrix}
\tag{4}
$$

$$
\left.
\begin{aligned}
& min_{\sigma(h)} = \{E_{max}\} \\
& s.t \\
& \quad C_{\sigma(j)} \geq r_{\sigma(j)} + p_{\sigma(j)} \\
& \quad C_{\sigma(h)} = C_{\sigma(h-1)} + p_{\sigma(h)} \\
& \quad L_{(h)} = C_{\sigma(h)} - d_{\sigma(h)} \\
& \quad E_{max} = max\{-L_j, 0\} \\
& \quad E_{(h)} \geq\ max\left\{d_{(\sigma h)} - C_{\sigma(h)}, 0\right\} \\
& r_{\sigma(h)} \geq 0, p_{\sigma(h)} > 0, d_{\sigma(h)} > 0\ , E_{\sigma(h)} \geq 0
\end{aligned}
\right\}
\begin{matrix} h\ from\ 1\ to\ m\ and \\ h = 2,3, \dots, m \end{matrix}
\tag{5}
$$

$$
\left.
\begin{aligned}
& min_{\sigma(h)} = \{T_{max}^{w}\} \\
& s.t \\
& \quad C_{\sigma(j)} \geq r_{\sigma(j)} + p_{\sigma(j)} \\
& \quad C_{\sigma(h)} = C_{\sigma(h-1)} + p_{\sigma(h)} \\
& \quad L_{\sigma(h)} = C_{\sigma(h)} - d_{\sigma(h)} \\
& \quad T_{\sigma(h)} \geq\ max\left\{C_{\sigma(h)} - d_{\sigma(h)}, 0\right\} \\
& r_{\sigma(h)} \geq 0, w_{\sigma(h)} \geq 1, p_{\sigma(h)} > 0, d_{\sigma(h)} > 0\ , T_{\sigma(h)} \geq 0
\end{aligned}
\right\}
\begin{matrix} h\ from\ 1\ to\ m\ and \\ h = 2,3, \dots, m \end{matrix}
\tag{6}
$$

MEERKAT CLAN ALGORITHM

The metaheuristic Meerkat Clan Algorithm (MCA) is a global optimization metaheuristic created by picking the best structure for randomness and presented by Sadiq et al. [16]. MCA was inspired by swarm behavior. Meerkats are social animals that live in groups of several; each group has its area that inhabits states with five to thirty individuals. As amicable creatures, they collaborate on lavatory duties and parental supervision. Every group has a dominant alpha female and a commanding alpha male who exerts a strong influence. Every crowd has a territory they occasionally relocate to when food is scarce or when a more dominant group displaces them. The leader splits the clan into two groups. One group is in charge of finding food called (foraging), and the other group is in charge of taking care of the young people (care). Also, the algorithm must find a better balance between care and hunting. Finally. The best solution the clan came up with was picked and given the name Sentry. Researchers have studied and written about Meerkat Clan Algorithm (MCA) including (Hussein and Yousif [17] and Saleh and Sadiq [18]). The following stages of the recommended algorithm to solve multi objective model for SMSP as bellow:

1. Initialize the population of meerkats, each representing a possible solution (i.e., a sequence of jobs), define parameters such n: Clan count falls between thirty to fifty ; m : Size for foraging when $m < n$, c: Care size is equal to n-m-1, Fr: The worst foraging rate, Cr: The lowest possible care rate, k: Finding a neighbor solution.
2. Calculate the fitness function ($\boldsymbol{min_{\sigma \in S}\{\sum_{h=1}^{m}(w_h(1 - e^{-\alpha c_h}) + U_h) + E_{max} + T_{max}^{w}\}}$)
3. Repeat until a stopping criterion

- **Exploration**: Explore new solutions. This involve generating new sequences of jobs
- **Exploitation**: Exploit the best-known solutions by making small adjustments to improve the current best solutions.
- **Information Sharing**: This can involve updating a shared memory or a set of best-known solutions.
- **Selection**: Select the next generation based on fitness, favoring solutions with better fitness values.
- **Update**: Update the population for the next iteration, including any new solutions generated during exploration and exploitation.

4. When the stopping condition is met, output the best solution found, which represents the optimal or near-optimal schedule for the single machine.

BALD EAGLE SEARCH OPTIMIZATION ALGORITHM

In 2020, the Bald Eagle Search Optimization Algorithm (BESOA) was introduced as a novel metaheuristic optimization method Alsattar et .al [19]. It draws inspiration from the hunting behaviour exhibited by the bald eagle. Many Researchers studied and written about BESOA algorithm including (Huang et al. [20]. Alsaidan et al. [21]. Kankılıç and Karpat [22], Huang (2023) ; Zaky et al. [23] and Youssef, H. et.al [24]).

The bald eagle inhabits expansive, open spaces with abundant prey and ancient trees for nesting. Their keen vision allows them to locate prey from considerable distances, and they are capable of seeing in both directions at once. This condor's prey-prey behaviour is simulated by the BESOA algorithm, which divides the process into three stages: selection, search, and soaring. During the selecting phase, the eagle selects the area containing the most significant number of praise. During the searching phase, it searches for prey within the designated area.

The following Bald eagle search algorithm to solve mathematical model for a single machine scheduling problem as below:

Step 1: Randomly generate the first population.

Step 2: Determine every node's fitness function ($\boldsymbol{min}_{\sigma \in S}\{\sum_{h=1}^{m}(\boldsymbol{w_h}(\mathbf{1}-\boldsymbol{e}^{-\alpha c_h})+\boldsymbol{U_h})+\boldsymbol{E_{max}}+\boldsymbol{T}^{\boldsymbol{w}}_{\boldsymbol{max}}\}$) for all the initialized populations and select the best cluster head.

Step 3: Set the iteration number t=0.

Step 4: Set t_{Max} is the maximum iteration

Step 5: Check the termination criteriat < t_{max}, if it is greater, then replace the initial position with the updated position else generate the random numbers for determining the best values.

Step 6: Gather every nodes from the initial population and follows three steps to find out the best cluster head node.

Step 7: At first, as per equation ($E_{t new,i} = E_{t best} + \alpha * r(E_{t mean} - E_{ti})$), in which α is a position control parameter with a value between 5 and 10 and r is a random number between 0.5 and 2, bald eagle selects the region to hunt for the best solution.

Further, evaluate the fitness function for both the new position and the best position for acquiring the best search space.

Steps 8: The bald eagle can choose the hunting area depending on the search space using an equation:

$E_{ti,new} = E_{ti} + y(i) * (E_{ti} - E_{ti+1}) + x(i) * (E_{ti} - E_{tmean})$

Where $x(i) = \frac{xr(i)}{max|xr|}$ and $\gamma(i) = \frac{\gamma r(i)}{max|\gamma r|}$

$xr(i) = r(i) * \sin(\theta(i))$, $yr(i) = r(i) * \cos(\theta(i))$

$\theta(i) = \alpha * \pi * rand$ $and\, r(i) = \theta(i) + R * rand$, where $C1, C2 \in \{0.1\}$.

Like search space, it also finds the fitness and acquires the best position for select space.

Step 9: In this swooping stage bald eagle deploying search space's new position for swooping the prey towards.

Step 10: Repeat above step can be repeated until it attains the termination criteria.

RESULTS AND DISCUSSION

To verify and evaluate the performance of the Meerkat Clan Algorithm for solving the single machine scheduling problem, we examined various problem sizes from 3 to 2500 jobs. We considered the Bald Eagle Search Algorithm (BSA) .These experiments were implemented on a PC with an Intel (R) Core (TM) i7-4500U CPU @ 1.80 GHZ, with RAM 8.00 GB. For the MCA, we used different numbers of n, with several generations to analyze the accuracy and CPU Time. The parameters set for the MCA population m=$n = 6, m = 3(m < n), c = 2(c = n - m - 1), F_r = 0.3, C_r = 0.25\ and\ k = 2$ respectively. For BSOA experimentation, $\alpha \in [5,10]\ and\ r \in [0.5,2]$.

We used a variety of problems with medium and big size limits and significantly equal constraints. The Matlab programming language encoded and resolved these examples in a comparable manner, according to an analysis of the algorithms' performances. Each algorithm, including MCA, and ESA was executed for 1,000 iterations as the stopping criterion. Comparable performance values of each method, including best solutions and running times, are summarized in Table 1.

While, using the Meerkat Clan Algorithm and Bald Eagle Search over the long term, the computational results appeared highly effective in terms of the quality of objective function values and computational time, with up to 2500 and up to 1000 jobs to find a near-optimal solution. Overall, the results illustrated that the MCA and BSA algorithms are highly effective in terms of quality solution and computational time for large-scale problems. In particular, the MCA provided robust performance and is well-suited for solving complex scheduling problems.

TABLE 1. comparison results between MCA and BES with ($\mathbf{n = 3\ to\ 2500}$)

N	MCA		BES		best value
	Av. of MCA	Av. of time	Av. of BES	Av. of time	
3	26.47522058	0.0868756	26.47522058	0.017374	26.47522058
4	33.26664467	0.0895359	33.26664467	0.0011148	33.26664467
5	43.5302227	0.0929754	43.5302227	0.0011907	43.5302227
6	65.74338951	0.0998785	65.74338951	0.1166167	65.74338951
7	72.96141739	0.1019178	72.96141739	0.1212509	72.96141739
8	84.02862244	0.1060379	84.02862244	0.1292639	84.02862244
9	84.57283554	0.1119938	84.57283554	0.1394093	84.57283554
10	98.95079422	0.1143529	98.95216408	0.145494	98.95079422
15	132.8858467	0.135921	133.3699562	0.1827836	132.8858467
20	167.2395264	0.15586	169.3547623	0.2144844	167.2395264
25	214.8035522	0.1775284	215.6303558	0.2488022	214.6757965
30	246.0692749	0.1976324	248.0312943	0.2865933	245.5426331
35	311.1116226	0.2193918	318.885556	0.3226866	311.1116226
40	337.3576691	0.233601	339.8407135	0.3552381	335.2764526
45	383.093045	0.2452809	388.1354828	0.3874522	382.1591614
50	409.7425232	0.2703094	412.5900909	0.410501	408.5584595
100	881.3315918	0.4676712	886.6137939	0.794018	878.8554871
150	1356.344812	0.7372828	1347.24834	1.229569	1347.209827
200	1781.637903	1.0426751	1786.442029	2.291122	1777.941711
250	2255.243066	1.1944861	2248.079419	3.1091054	2245.942297
500	4610.176685	1.8896038	4588.388477	5.561972	4585.503271
750	6935.02876	2.6990514	6911.458936	8.1035469	6911.457959
1000	9389.300293	3.5259007	9360.508154	10.000	9359.608154
1500	13992.77891	5.2375055	---------	---------	---------
2000	18673.21934	7.2102999	---------	---------	---------

2500	23381.71914	9.2497647	---------	---------	---------

CONCLUSION AND FUTURE

In this study, we introduced the Meerkat Clan Algorithm as a novel metaheuristic approach for solving the multi-objective single machine scheduling problem ($1/r_h/\sum_{h=1}^{m}(w_h(1-e^{-\alpha C_h})+U_h)+E_{max}+T_{max}^{w}$). Based on the results, the performance of the Meerkat Clan Algorithm was appropriate and appeared highly effective in terms of the quality of objective function and computational time with up to 2500 jobs. While, the second rank was Bald Eagle Search algorithm delivered and solved up to 1000 jobs. Some suggestions for further studies were presented as follows:

$1//\sum_{h=1}^{m} w_h(1-e^{-\alpha C_h}), T_{max}, \sum_{h=1}^{m} V_h$, and $F_m//\sum_{h=1}^{m}(w_h C_h+E_j)+E_{max}^{w}$.

ACKNOWLEDGMENTS

The authors would like to thank the referees for their extremely useful remarks and recommendations that helped to improve the caliber of the paper.

REFERENCES

1. K.R. Baker, Introduction to Sequencing and Scheduling (Wile New YORK,1973).
2. V.T. Kindt and F.D Croce, A Single machine adversarial bilevel scheduling problems (European Journal of Operational Research, 2024),pp. 63–72.
3. J.S. William, Operations Management, Fourteenth., (New York-United States of America 2021), McGraw-Hill Education.
4. M.L. Pinedo, Scheduling: Theory, algorithms, and systems, (Nova Iorque: Springer -Verla, 2016).
5. B. k. Atiya, A.J. Bakheet, I.T. Abbas, L.L. Soon and M.B. Monsi, Application of simulated annealing to solve multi-objectives for aggregate production planning, (In AIP Conference Proceedings, 2016),pp. 020086-1–020086-6
6. T.J. Khraibet, and W.K. Ghafil, Using hybrid GA-PSO algorithm to Solve $F_2//(\sum_{k=1}^{n} E_K+U_K)$ Problem in Machine Scheduling (Journal of Discrete Mathematical Sciences and Cryptography, 2021) ,pp. 2027–2035.
7. S.F. Yousif, and F.H, Solving Maximum Early Jobs Time and Range of Lateness Jobs Times Problem Using Exact and Heuristic Methods, (Iraqi Journal of Science, 2024), pp. 923- 937.
8. I.T. Abbas, and M.N. Ghayyib, Using Sensitivity Analysis in Linear Programming with Practical Physical Applications, (Iraqi Journal of Science, 2024). pp. 907- 922.
9. N.M. Neamah and B.K. Atiya, solving tri-criteria: total completion time, total late work, and maximum earliness by using exact, and heuristic methods on single machine scheduling problem, (Iraqi Journal for Computer Science and Mathematics, 2024 a).
10. N.M. Neamah and B.K. Atiya, Solving the Multi-Criteria Problem: Total Completion Time, Total Late Work, Total Earliness Time, Maximum Earliness, and Maximum Tardiness, (Iraqi Journal of Science 2024 b), pp. 2724-2735.
11. T.S. Abdul Razaq and H. M. Motair, Solving Composite Multi objective Single Machine Scheduling Problem Using Branch and Bound and Local Search Algorithms, (Al-Mustansiriyah Journal of Science, 2017),pp. 200-208.
12. M.H Ibrahim, and F.H. Ali and H.A Chachan, Solving multi-objective's function problem using branch and bound and local search methods,(The International Journal of Nonlinear Analysis and Applications (IJNAA), 2022), pp. 1649-1658.
13. D.A. Abbas, Search method for solving multicriteria scheduling problem, (International Journal of Nonlinear Analysis and Applications (IJNAA). 2022), pp. 1709-1720.
14. A.Karrar and A. Awas, Algorithms for Multicriteria Scheduling Problems to Minimize Maximum Late Work, Tardy, and Early, (Journal of Applied Mathematics and Physic*s*, 2024)**, pp.** 661-682.

15. D.H Wolpert and W.G, No free lunch theorems for optimization, (IEEE Trans Evol Comput, 1997), pp. 67–82.
16. , A.T. Sadiq, H.S. Abdullah, and Z.O. Ahmed, Solving Flexible Job Shop Scheduling Problem Using Meerkat Clan Algorithm, (Iraqi Journal of Science, 2018), pp. 753-761.
17. S.A Hussein, and A.Y. Yousif, An Improved Meerkat Clan Algorithm for Solving 0-1 Knapsack Problem (Iraqi Journal of Science, 2022 pp. 773-784,
18. M.A. Saleh. and A.T. Sadiq, Modified Meerkat Clan Algorithm for Association Rules Mining, (Baghdad Science Journal, 2023).
19. H.A. Alsattar, A.A. Zaidan and B.B. Zaidan, Novel Meta-heuristic Bald Eagle Search Optimization Algorithm, (Artificial Intelligence Review, 2020), pp. 2237–2264.
20. Y. Huang, H. Jiang, W. Wang, and D. Sun, Prediction Model of Soil Electrical Conductivity Based on ELM Optimized by Bald Eagle Search Algorithm,(Electronics Journal, 2021), pp. 50-56.
21. I. Alsaidan , A.M. Shaheen, H.M. Hasanien and A.S Alnafisah,, (A PEMFC model optimization using the enhanced bald eagle algorithm, (Ain Shams Engineering Journal,2022).
22. S. Kankılıç and E. Karpat, Optimization of Multilayer Absorbers Using the Bald Eagle Optimization Algorithm, (Applied sciences, 2023).pp.2-17.
23. A.A, Zaky, R.M. Ghoniem and F. Selim, Precise Modeling of Proton Exchange Membrane Fuel Cell Using the Modified Bald Eagle Optimization Algorithm, (Sustainability, 2023)., pp. 2-16.
24. H. Youssef, S. Kamel, M.H. Hassan, L. Nasrat, and F. Jurado, An improved bald eagle search optimization algorithm for optimal home energy management systems, (Soft Computing, 2024).pp. 1367–1390.

Synthesis and characterization of Zn-doped CuO nanoflowers: Enhancing properties through hydrothermal technique

Ali Khudair Abbas [1, a], Selma M. H. AL-Jawad [2, b] and Natheer Jamal Imran [2, c]

[1] *Applied Sciences Department, University of Technology- Iraq, Baghdad, Iraq*
[2] *Environment and Water Directorate, Ministry of Science and Technology, Baghdad, Iraq*

[a)] Corresponding author: alikhudayr7@gmail.com
[b)]selma.m.aljawad@uotechnology.edu.iq
[c)]Natheer Jamal Imran2020@yahoo.com

Abstract. The hydrothermal approach was used to manufacture CuO nanoparticles that were either undoped or doped with zinc. Electron microscopy, X-ray diffraction, field-emission scanning electron microscopy, energy dispersive X-ray spectroscopy, zeta potential analysis, ultraviolet-visible spectrophotometry, and Fourier-transform infrared spectroscopy were some of the characterization techniques used to examine these nanoparticles. Zinc significantly altered CuO nanoparticles' band gap energies, crystallite size, and lattice properties after addition. Both nanoparticle kinds were found to have a covellite monoclinic polycrystalline structure, according to the XRD data. By measuring the sizes of the crystallites, the effects of adding zinc were shown. According to FESEM images, the nanoparticles have a big, cauliflower-like form that shows they have a lot of surface area that can be used for many things. Optical property tests showed that adding Zn changed the electrical properties of the CuO nanoparticles. The band gap values were found to be between 2.58 and 2.48 eV. This in-depth study shows that both undoped and Zn-doped CuO nanoflowers have better potential. Within the TEM study, Transmission Electron Microscopy was used to learn more about the exact shape and structure of CuO nanoparticles that were either Zn-doped or not doped with Zn. The TEM pictures' great clarity allowed us to see the complex nanoscale structure details. This method was very important for checking the hierarchical nanoparticles and figuring out how useful they might be for certain tasks, especially in areas that needed exact material properties.

INTRODUCTION

A lot of attention has been paid to making and studying nanostructured materials, especially metal oxides [1], because scientists are looking for new materials with better qualities for use in technology. One of these is copper oxide (CuO), a p-type semiconductor with high electron correlation and low photon energy. It has gotten a lot of attention because it can be used in so many different areas, including biology, electronics, and catalysis [2]. It has been found that adding other elements to CuO can change and improve its electrical, visual, and physical properties, which makes it more useful [3]. Zinc (Zn), a two-valent metal, is often mixed with CuO to change the band gap and help the CuO nanoparticles kill germs and use light better [4]. When Zn is added to CuO structures, it changes some important things, such as the size of the crystallites, the lattice parameters, and the electronic band structures. Many times, this makes CuO work better [5]. The main goal of this study is to use the hydrothermal method to make Zn-doped CuO nanoflowers. This method is known for being simple, inexpensive, and good for the environment [12]. Chemical reactions happen at high temperatures and pressures inside a closed autoclave during the hydrothermal synthesis [6]. It is easier to make well-defined nanostructures with this method, and you have full control over the form and crystallinity of the nanoparticles you make [7]. You can get CuO bits that are all the same size and shape with the geothermal method better. This is important for commercial uses. Scientists believe that adding Zn to CuO will give the nanoflowers new forms that are connected to changes in their chemical and physical properties [8]. You should look into these Zn-doped CuO nanoflowers to see how the zinc changes their shape and how well they work. Two methods, X-ray diffraction (XRD) and field-emission scanning electron microscopy (FESEM), can be used to clearly see the crystal structure and shape of the nanoparticles [9]. XRD helps figure out how clear the phase is and what the crystal structure is. Zn-related peaks or changes in the places of the CuO peaks show that the doping of CuO worked. The nanoflower structure is correct because you can see it in the shape of the surface with FESEM. This is important for uses that need a lot of surface area. You can also use energy dispersive X-ray spectroscopy (EDS) to check the Zn level and make sure it is spread out properly in the CuO matrix [10]. Zeta potential research will be used

Technologies and Materials for Renewable Energy, Environment and Sustainability
AIP Conf. Proc. 3321, 020025-1–020025-8; https://doi.org/10.1063/5.0289724
Published under an exclusive license by AIP Publishing. 978-0-7354-5231-2/$30.00

to find out how charged the nanoparticles' surfaces are. This charge changes how stable the nanoparticles are in liquids, which is important for uses in medicine and industry [11]. UV-visible spectrophotometry is used to talk about the band gap and other visual properties. This shows how the structure of the electrons changes when Zn is added [3]. Finally, Fourier-transform infrared spectroscopy (FTIR) will be used to find functional groups and prove that the nanoparticles are chemically linked [12]. The goal of this all-around method to making and studying Zn-doped CuO nanoflowers is to find out how doping concentration affects the shape and function of these nanoparticles. The expected results will not only help us learn more about doped metal oxide nanostructures, but they will also show how these materials might be able to improve the performance of CuO for certain technological uses, like killing bacteria and turning sunlight into energy. Through this study, we want to show how Zn doping can help change the features of CuO nanoparticles to meet the strict needs of current technology. This study goes into depth about how Zn-doped CuO nanoflowers were made and analyzed using hydrothermal methods. We used X-ray powder diffraction to look at the crystal structure of these Zn-doped CuO nanocrystals. TEM was used to learn more about them and Field-emission scanning electron microscopy was used to see how they looked. The optical bandgap was used to check the electrical properties, and the zeta potential was used to understand how the surface charge works. An FTIR was used to find out more about the nanoparticles' chemical make-up. The special features of Zn-doped CuO nanoflowers are shown to be useful in many tech areas in these in-depth studies.

MATERIALS AND METHODS

Chemical materials

The lab-grade chemicals urea and sodium dodecyl sulfate from Alpha Chemika Co., Ltd. were used without being cleaned any further. Using hydrothermal methods, nanoparticles of doped CuO and copper oxide were created. This step started with mixing 2 mmol of copper acetate, 30 ml of water, and 10 ml of ethanol to make a solution. Later, 4.5 g of SDS was added, and the mixture was left at room temperature for 10 minutes to stir. After being mixed all the time at room temperature for 20 minutes, 8 mmol of urea was added.

Preparation of CuO and doped CuO

Copper oxide and Zn doped CuO were synthesized using a hydrothermal process. The solution began by dissolving 2 mmol of copper acetate in 30 ml of water and 10 ml of ethanol. The aforementioned solution was then supplemented with 4.5 g SDS and left to agitate at room temperature for a duration of 10 minutes. The aforementioned solution was then supplemented with 8 mmol of urea and left to stir at room temperature for 20 minutes. For Zn doping at 3%, the copper acetate $Cu(CH_3COO)_2$ precursor was supplemented with Zn $(CH_3COO)_2.2H_2O$; for Zn doping at 3 weight percent, the same solution was used. The combined mixture was thereafter placed in a stainless steel autoclave that was lined with 100 mL of Teflon and kept at a temperature of 170 ^oC for 10 hours. The nanoparticles were centrifuged to separate them after cooling to room temperature. They were then washed many times with distilled water and 100% ethanol before being dried at 60 ^oC for 30 minutes.

Characterizations

Copper oxide nanoparticles were synthesized at a temperature of 170 °C using a hydrothermal method. The CuO nanocrystals that were formed were studied using an X-ray powder diffractometer (XRD-6000, Shimadzu, Japan) that was fitted with monochromate Cu-Kα radiation (λ= 0.15406 nm). The ZCO nanostructure's morphology was examined using a Hitachi Type S-4160 field-emission scanning electron microscope (FE-SEM) operating at 20-30 kV with magnifications ranging from 8000 to 60,000. A Zeta plus (Brookhaven, USA) was used for zeta potential measurements. An ultraviolet-visible spectrophotometer (UV-1800, Shimadzu) was used to examine the optical bandgap of the undoped and Zn doped CuO nanostructure. The composition and chemical bonding were determined by observing the absorption or emission of the infrared spectrum using Fourier-transform infrared spectroscopy (FTIR) (SHIMADZU IRAFFINITY).

RESULTS AND DISCUSSION

X-ray diffraction

The CuO samples' crystal structure and phase purity were determined using XRD analysis. Figure 2 shows the diffraction patterns of the CuO nanostructures that were doped with Zn and undoped. The lattice constants of a = 4.684 Å, b = 3.425 Å, and c = 5.129 Å, which are in close agreement with the values recorded in the JCPDs database card No. 48-1548, are compatible with the normal monoclinic covellite phase of CuO, as shown by the observed diffraction pattern [13]. It is consistent with the samples' great purity that the produced nanoparticles do not include any secondary phases, as there are no extra peaks in the XRD patterns. With the addition of Zn doping, the peak intensity was somewhat reduced, but with the addition of Zn 3 wt.% doping, it was increased [14]. The introduction of dopants that cause structural disorder in the sample may be necessary for this behavior to occur [15].

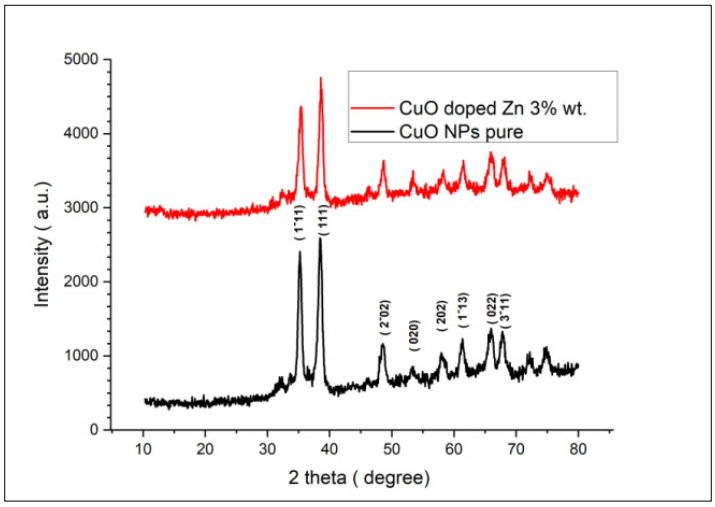

Figure 1. X-ray diffraction spectra of the nanostructures resulting from CuO NPs doped with Zn and those without doping

In addition, it was shown that a wider range of peaks was associated with higher levels of Zn doping. A possible explanation for this phenomenon is shrinkage of the crystals. Figure 2 also shows that there is a little change in the peak location relative to pure CuO, indicating that Cu^{+2} and Zn^{+} have been substituted inside the CuO lattice. Applying Scherer's calculation, which takes into account the whole width at half diffraction maximum, allowed us to determine the average crystalline size of CuO.

$$D = \frac{K\lambda}{\beta\cos\theta} \tag{1}$$

Important factors are the average crystal size (D), form factor (K), wavelength (λ), full width at half maximum (FWHM) in radians (β), and Bragg angle of the peaks (θ). Table 1 displays the results of determining the crystalline size using Eq. 1 and the XRD data. The results suggest that smaller crystalline structures were the result of increased Ni doping concentration and the addition of Zn doping. The following equation was used to get the 'a', 'b', and 'c' lattice parameters for monoclinic CuO.

$$\frac{1}{d_{hkl}^2} = \frac{h^2}{a^2\sin^2 y} + \frac{k^2}{b^2\sin^2 y} - \frac{2hk\cos y}{ab\sin^2 y} + \frac{l^2}{c^2} \tag{2}$$

(h, k, l) stands for the planes' Miller indices, a, b, and c for the lattice parameters, and the interplanar spacing Miller indices. Also, as seen in Table 1, the addition of doped Zn to copper oxide causes a reduction in the a, b, and c lattice parameters (Figure 2).

TABLE .1 Sizes of crystallites and lattice constants of CuO nanostructures that are undoped and doped

Samples	Crystal structure	Dave (nm)	a	b	c
CuO undoped	monoclinic	15.48	4.6896	3.4343	5.1378
3%Zn/97%CuO	monoclinic	16.82	4.6865	3.4333	5.1341
Standard	JCPDS card no. 48–1548		4.6840	3.4250	5.1290

Utilizing the W-H formula, one may get the sample grainsize with the help of the following equations

$$\beta = \left(\frac{k\lambda}{Dcos\theta}\right) + 4\varepsilon tan\theta \tag{3}$$

where ε represents lattice strain and Dave represents crystallite size. The form factor is denoted by K:, while the wavelength of Cu-Kα radiation is represented by λ: (λ = 0.154 nm). All samples likely included strain, as shown by the positive slope of the W-H plot. After looking at the data, it's clear that adding more doping levels causes the goods' crystallite size to shrink. This decrease is mostly caused by the doped material changing the crystal growth kinetics and being integrated into the CuO basic structure. In addition, it has been shown that the microstrains decrease after Zn doping, as shown in Table 2. Compared to the simplified assumptions of the Debye-Scherrer formula, the W-H method provides a more accurate assessment of the real crystallite dimensions by accounting for these additional factors, and it may even provide smaller readings [16].

Table 2. shows the concentration of polyvinyl chloride and polyvinyl chloride-carbon composite

CuO Samples	Dave (nm) Scherrer method	Dave (nm) W–H method	Microstrain (ε)×10-4
CuO pure	15.48	45.01	0.6
3%Zn/97%CuO	16.82	12.01	0.1

X-ray diffraction

The scanning electron microscopy (SEM) pictures of undoped and Zn-doped CuO are shown in Figure 2 (A) and (B), respectively. Figure 2 (A) shows that the microspheres of the pure CuO product have a diameter between 36.46 and 109.5 nm. Not only that, but the sample also shows a cauliflower-like nano-structure and a hollow spherical nano-structure. Figure 2 (B) shows that when 3% Zn is doped, homogeneous morphologies are formed, including nanorods with a diameter ranging from 27.72 to 154.9 nm, which form a cross-structure, and strip nanoplates. The thickness of CuO nanoplates is increased by Zn doping.

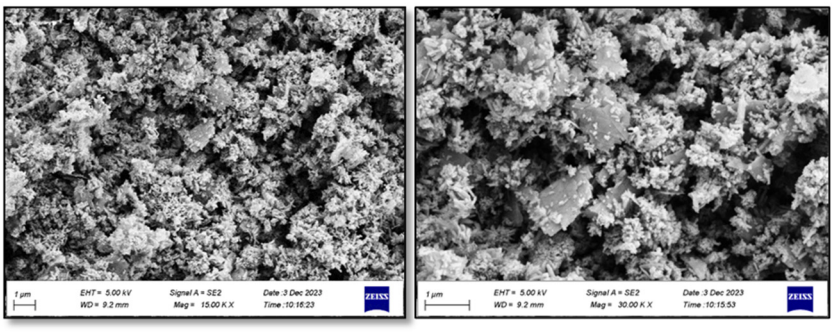

Figure 2. FE-SEM images of undoped and Zn doped CuO NPs

The TEM images provided high-resolution insights, revealing the fine structural details at the nanoscale. This allowed for a clear visualization of the particle sizes and shapes, confirming the cauliflower-like structures previously observed in FESEM images. Moreover, TEM analysis helped in identifying the uniformity and distribution of zinc within the doped nanoparticles, offering a deeper understanding of how Zn incorporation affects the overall crystal structure and morphology. This technique was essential for validating the hierarchical nanostructures and assessing their potential for targeted applications, especially in fields requiring precise material properties as shown in Figure 3.

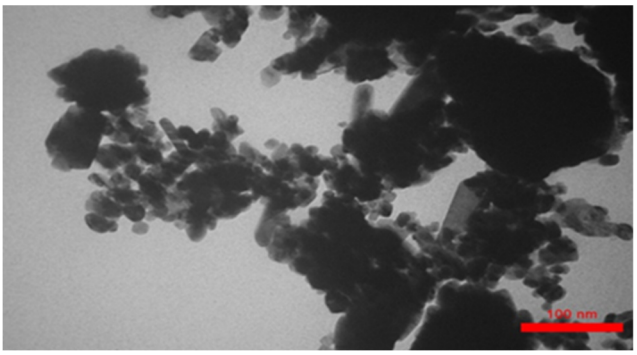

Figure 3. TEM image of Zn doped CuO NPs

The hierarchical structures of the cauliflower leaves make up the 3 wt.%Zn-doped CuO sample. The TEM scans showed that this structure was built from bundles of nanorods. Additionally, it was found that the cauliflower-like structure was formed by the interweaving of nanorods. According to the EDS scans, the undoped sample only showed Cu and O elements. On the other hand, as can be seen in Figure 4 (A) and (B) from the doped CuO samples, the presence of (Cu, O, and Zn) components confirmed both the samples' purity and the effective integration of Zn into the CuO host structure.

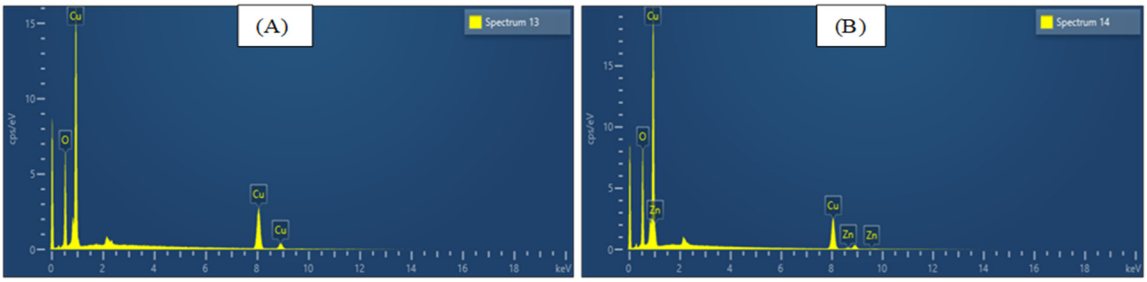

Fig.4. EDX of pure with Zn doping of CuO NPs

Element	**Weight %**	**Atomic %**
O	26.98	59.47
Cu	73.02	40.53
Total	100.00	100.00
Element	Weight %	Atomic %
O	26.32	58.72
Cu	66.97	37.62
Zn	6.71	3.66
Total	100.00	100.00

X-ray diffraction

The electrostatic potential in the solvent suspension was measured using zeta potential analysis. A zeta potential that is more than 20 mV is ideal, and one that is mostly negative or positive indicates that the colloidal solution is reasonably stable, with little aggregation. The sample's mobility was -2.07 mV, while the zeta potential values with a 3 wt.% addition of Zn doped CuO NPs were around 26.48 mV. Figure 5 (A) and (B) show the results; the positive charge is a benefit for cell internalization because it binds electrostatically to the negatively charged cell membranes, which improves the process.

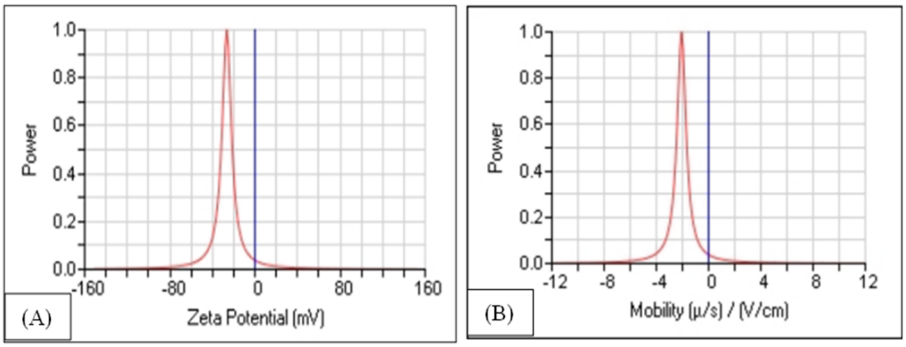

Figure 5. A) Zeta potential and (B) mobility graphs for CuONPs doped with 3 weight percent zinc

X-ray diffraction

The following equation was used to estimate the absorption coefficient (α)

$$\alpha = \frac{2.303 \times A}{d} \tag{5}$$

The absorption coefficient, the absorbance, and the thickness are all represented by α, A, and d, respectively. The following equation is used to estimate the optical energy gap (Eg).

$$\alpha h\nu = A\left(h\nu - E_g\right)^r \tag{6}$$

Where the variables α (absorption coefficient), hν (photon energy), A (constant), Eg (optical energy band gap of the material), and r (factor governing the direct and indirect transfer of the electrons from the valence band to the conduction band) are all mentioned. Figure 6 (A) and (B) show the graphs of $(\alpha h\nu)^2$ vs hν for undoped and Zn-doped CuO nanostructures, respectively. The values of the direct optical bandgap for CuO and CuO-3 wt.% Zn, respectively, were 2.58 and 2.48 eV, as derived from the analysis of the intercepts of the straight line on the photon energy axis. As the Zn concentration increases by 3 weight percent, the Eg of CuO NPs decreases from 2.58 to 2.48 eV, as shown in Figure 6 (A) and (B).

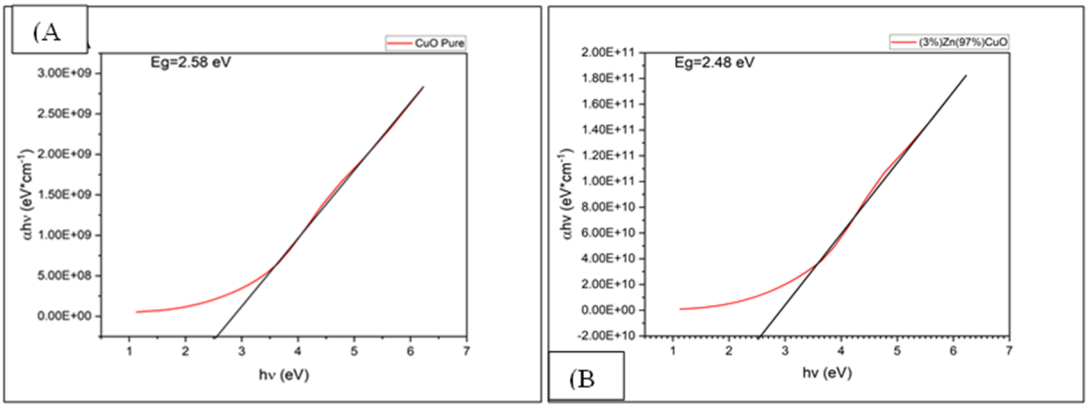

Figure 6. (A) Plot of $(\alpha h\nu)^2$ versus hν of (A) pure CuO, and (B) Zn-doped CuO nanostructures

X-ray diffraction

When copper oxide (CuO) and zinc (Zn) are co-doped in a material, the FTIR spectra will show distinct peaks that correspond to the vibrational modes of the two components. Various experimental parameters, including Zn concentrations and the final compound's crystal structure, may affect the precise locations of these peaks. In particular, peaks corresponding to Zn-O stretching may be seen in the 400-600 cm^{-1} region for Zn. Furthermore, it is anticipated that CuO will exhibit vibrational modes in the 550-650 cm^{-1} range, which are linked to Cu-O stretching vibrations. There will also be additional features in the 460-550 cm^{-1} range, which are associated with metal-oxygen bonds. On the surface of CuO, there should be a peak near 3400 cm^{-1}, which is indicative of O-H stretching vibrations caused by absorbed water or hydroxyl groups. The exact locations and strengths of these peaks are dependent on the co-doped material's unique chemical make-up and crystal structure. As seen in Figure 7, the FTIR results for CuO doped with Zn.

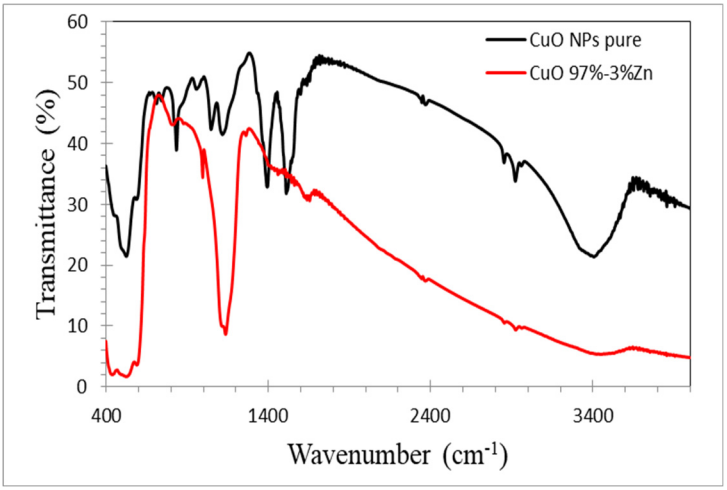

Figure 7. (A) Plot of $(\alpha h\nu)^2$ versus hν of (A) pure CuO, and (B) Zn-doped CuO nanostructures

CONCLUSIONS

The detailed research in this paper shows how adding Zn changes the structure, shape, and electronic properties of CuONPs made using the hydrothermal method. The XRD study proved that the nanoparticles had a covellite monoclinic structure. It also showed small changes in peak strengths and lattice parameters, which showed that the

Zn had been successfully added to the CuO matrix. The FESEM and TEM studies confirmed these changes. They showed clear structural changes, like the creation of nanorods, strip nanoplates, and traditional cauliflower-like structures in the Zn-doped samples compared to the ones that weren't doped with Zn. The study also showed that the optical band gap dropped from 2.58 eV in pure CuO to 2.48 eV in samples with Zn added. This shows that adding Zn changes the electronic features of CuO. This lower band gap makes the material better for uses that need specific band gap conditions, like photocatalytic activities and electronic devices. The EDS results showed that the elements were pure and that the Zn doping worked, which added to the structural information from the XRD. Zeta potential tests showed that the nanoparticles were more stable in colloidal solutions, which is important for biological uses, especially in drug delivery systems where particle accumulation can hurt performance. The study shows that adding Zn can change the features of CuONPs to make them work better in a number of different situations. This study not only gives us a better idea of the physical features of Zn-doped CuONPs, but it also shows that they could be used to make CuO-based materials work better in a wide range of environmental and industrial settings.

REFERENCES

1. Selma M.H. AL-Jawad, Natheer Jamal Imran, and Mohammad R. Mohammad "Effect of electrolyte solution and deposition methods on TiO2/CdS core–shell nanotube arrays for photoelectrocatalytic application" Eur. Phys. J. Appl. Phys. (2020), 92, 20102.
2. M. Rasheed, Suha Shihab, O. Alabdali, and H. H. Hassan, "Parameters Extraction of a Single-Diode Model of Photovoltaic Cell Using False Position Iterative Method," Journal of Physics: Conference Series, vol. 1879, no. 3, p. 032113, May 2021, doi: https://doi.org/10.1088/1742-6596/1879/3/032113.
3. Al-Jawad, S.M.H., Ismail, M.M., Ghazi, S.F. Characteristics of diluted magnetic semiconductor based on Mn-doped TiO2 nanorod array films, Journal of Solid State Electrochemistry, 2021, 25(2), pp. 435–443
4. Assoudi, N., Chaabani, A., Dhahri, E., Alawsi, T., Bouras, D., & Barille., "Comparative examination of the physical parameters of the sol gel produced compounds La0.5Ag0.1Ca0.4MnO3 and La0.6Ca0.3Ag0.1MnO3," Optical and Quantum Electronics, vol. 54, no. 9, Jul. 2022, doi: https://doi.org/10.1007/s11082-022-03927-x
5. AL-Jawad, S.M.H., Taha, A.A., AL-Barram, L.F.A., Effective cancer treatment by targeted pH sensitive–gold nanoparticles without using laser irradiation, Journal of Sol-Gel Science and Technology, 2019, 89(2), pp. 473–485
6. Allawi, N.H., Al-Jawad, S.M.H., Facile growth of kesterite CZTS film by one-pot hydrothermal route using EDTA as complex agent for heterojunction solar cell applications: influence of zinc concentration, Optical and Quantum Electronics, 2023, 55(12), 1089
7. M. Rasheed, S. Shihab, O. Y. Mohammed, and A. Al-Adili, "Parameters Estimation of Photovoltaic Model Using Nonlinear Algorithms," Journal of Physics: Conference Series, vol. 1795, no. 1, p. 012058, Mar. 2021, doi: https://doi.org/10.1088/1742-6596/1795/1/012058.
8. Rodriguez, J. A., Kim, J. Y., Hanson, J. C., Pérez, M., & Frenkel, A. I. (2003). Reduction of CuO in H_2: in situ time-resolved XRD studies. Catalysis letters, 85, 247-254.
9. Hsieh, C. T., Chen, J. M., Lin, H. H., & Shih, H. C. (2003). Field emission from various CuO nanostructures. Applied Physics Letters, 83(16), 3383-3385.
10. Asbrink, S., & Waskowska, A. (1991). CuO: X-ray single-crystal structure determination at 196 K and room temperature. Journal of Physics: Condensed Matter, 3(42), 8173.
11. Grigore, M. E., Biscu, E. R., Holban, A. M., Gestal, M. C., & Grumezescu, A. M. (2016). Methods of synthesis, properties and biomedical applications of CuO nanoparticles. Pharmaceuticals, 9(4), 75.
12. Zheng, S. F., Hu, J. S., Zhong, L. S., Song, W. G., Wan, L. J., & Guo, Y. G. (2008). Introducing dual functional CNT networks into CuO nanomicrospheres toward superior electrode materials for lithium-ion batteries. Chemistry of Materials, 20(11), 3617-3622.
13. Wang, Z., Li, N., Zhao, J., White, J. C., Qu, P., & Xing, B. (2012). CuO nanoparticle interaction with human epithelial cells: cellular uptake, location, export, and genotoxicity. Chemical research in toxicology, 25(7), 1512-1521.
14. Zou, G., Li, H., Zhang, D., Xiong, K., Dong, C., & Qian, Y. (2006). Well-aligned arrays of CuO nanoplatelets. The Journal of Physical Chemistry B, 110(4), 1632-1637.
15. Zou, G., Li, H., Zhang, D., Xiong, K., Dong, C., & Qian, Y. (2006). Well-aligned arrays of CuO nanoplatelets. The Journal of Physical Chemistry B, 110(4), 1632-1637.

16. T. Rashid and M. M. Mokji, "Low-Resolution Image Classification of Cracked Concrete Surface Using Decision Tree Technique," Lecture Notes in Electrical Engineering, pp. 641–649, 2022, doi: https://doi.org/10.1007/978-981-19-3923-5_55.

An examination using semi-empirical methods to study how solvents influence the vibrational properties of the HCOOH molecule

Ibraheem M. Mohammed [1, a] and Mohammed Rasheed [2, b]

[1] *Department of Physics, College of Education, Mustansiriyah University, Baghdad, Iraq*
[2] *Applied Sciences Department, University of Technology- Iraq, Baghdad, Iraq*

[a)] ibraheemmm2017@uomustansiriyah.edu.iq
[b)] corresponding author: rasheed.mohammed40@yahoo.com

Abstract. The Gaussian 09w program has been utilized and the Hartree-Fock (HF) method to study the HCOOH molecule in this study. We chose 6-31G as the basis set to look at its vibrational modes. Utilizing the rule for the number of degrees of freedom for molecules that don't move in a straight line, we were able to find nine vibrating modes. Additionally, we examined their infrared (IR) levels and utilized the polarizable continuum model (PCM) to determine how the liquids changed these vibrating modes. Because the fluid was neutral and had hydrogen bonds, the red and blue colors changed in a clear way. Infrared intensity behavior showed that values were going up for all absorption bands except the v2 (Torsion) band. Although ethyl ethanoate is a non-polar solvent, this band's strength dropped a lot from 243.9847 km.mol-1 to 95.0318 km.mol-1 in acetone, which is a polar solvent. This behavior shows how the polarity of the solvent affects the HCOOH molecule's vibrational features. The HCOOH molecule doesn't have a center of symmetry, so the vibrational modes were IR active. This puts it in the Cs point group. These results show how important solvent effects are in vibrational spectroscopy studies. They show how solvent interactions can change molecular vibrational properties in a big way. It's now clearer to us how liquids and chemicals affect vibrational spectroscopy. This is very important for working with real data and creating theory models. Movements and changes in strength seen in various solvents demonstrate the complex interaction between molecular structure and liquid surroundings. Additionally, this information can help with future studies in computer chemistry and molecular spectroscopy.

Keywords: IR, HCOOH, Gaussian 09w, 6-31G, intensity

INTRODUCTION

Recently, vibrational spectra [1-6] have become very popular among scientists who want to learn more about how molecules behave and how they are linked. Many people are interested in formic acid (HCOOH) since it is utilized in various settings [7-8]. Medical professionals have used formic acid to treat common warts successfully, and it works very well and is safe [9–10]. For a low price, 85% formic acid has been shown to be a successful way to get rid of warts, and the treatment only takes a short time [11, 13]. Formic acid is useful for more than just medicine. Its special qualities make it a good way to store hydrogen and a valuable source of carbon monoxide in the new hydrogen economy [14-16]. New catalysts, especially those made from zeolites, have been found that make it easier for formic acid to break down. This has led to these possible uses [17–20]. Gaussian 09w has been used in many works to look at the vibrational modes of different molecules, such as proteins [21, 22], small molecules [23–25], and polymers [26–28]. These studies have taught us a lot about how molecules vibrate and proven that Gaussian 09w is a reliable tool for studying vibrations [29]. In particular, a number of studies have looked at how carboxylic acids behave when they are dissolved in different solvents, including water, ethanol, and acetonitrile [30–33]. Different approaches were used in these studies, but the results always showed that the type of liquid has a big effect on the vibrational spectra of carboxylic acids [34-36]. There were noticeable red and blue changes in the vibrational modes. These were caused by

Technologies and Materials for Renewable Energy, Environment and Sustainability
AIP Conf. Proc. 3321, 020026-1–020026-10; https://doi.org/10.1063/5.0289719
Published under an exclusive license by AIP Publishing. 978-0-7354-5231-2/$30.00

the liquids' polarity and hydrogen bonding properties [37]. It was mostly an increase in values for all absorption bands except the v2 (Torsion) band in the IR intensity behavior [38-40]. The strength of this band dropped significantly from 243.9847 km.mol-1 in ethyl ethanoate, which is a non-polar solvent, to 95.0318 km.mol-1 in acetone, which is a polar solvent [41]. This shows how strongly the polarity of the liquid affects the vibrational features of the HCOOH molecule [42-44]. It was discovered that the vibrational modes were IR active [45]. This is because the HCOOH molecule doesn't have a center of symmetry, which puts it in the Cs point group [46-48]. It's clear from these data that liquid effects are very important in vibrational spectroscopy research [49–51]. They also show that interactions with solvents can change the way molecules move in big ways [52]. This study helped us learn more about how chemicals and fluids work together and how that changes vibrational spectroscopy [53]. This is important for both building models of theories and getting a handle on real facts [54]. The shifting and changing of strength in different solvents shows how the shape of molecules and the fluid environment interact in a complex way [55]. It can help people who study computer science and molecular spectroscopy [56–58] do more work. In the end, they help us understand how formic acid works in different situations [59, 60]. Because this paper is so in-depth, we hope it will help people find better ways to use formic acid in business, medicine, and the environment [57].

The goal of the study was to look into the vibrational modes of the HCOOH molecule using the Gaussian 09w program and the Hartree-Fock (HF) method with the 6-31G basis set. Our goal was to learn more about the HCOOH vibrational modes and find out how strong they were in the infrared range. The polarizable continuum model (PCM) was another tool we planned to use to study what the fluids did. Chemists have found nine vibrational states, which is the right number for molecules that don't move in a straight line. Different liquids with different polarization strengths were used to look at the vibration patterns and IR levels that went with them.

MATERIALS AND METHODS

Polarizable continuum model (PCM)

A useful tool for figuring out molecule free energy in solution is the Polarizable Continuum Model (PCM), which was created by Tomasi and his friends [40, 41]. The PCM model can compute the total solvation-free energy, Gsol, by looking at three key factors:

For example,

$$Gsol = Ges + Gdr + Gcav \quad (1)$$

Specifically, Gsol is the total solvation-free energy, Ges is the electrostatic contribution, Gdr is the dispersion-repulsion contribution, and Gcav is the cavitation energy [42].

When using the PCM model to get correct estimates of the solvation energy, the electric input (Ges) is very important. This test checks how the solute molecule and the solution around it change things. According to the PCM, this word is incomplete. Assuming that all of the salt and liquid's interactions are thought through, it draws the line between them. There are forces in the PCM model that pull and push molecules of solids and liquids apart. One of them is the input from dispersion and repulsion (Gdr). This part requires you to look at how the liquid reacts with the close solvent molecules and the area of the surface that the solvent can reach [59]. Fully comprehending these connections is necessary because they affect the solute's stability in the liquid and its functionality in it. Cavitation energy, or Gcav, is another important part of the PCM model. How much energy does the salt molecule need to get into the solvent? Look at the shape of the solute-solvent system and the surface made up of the solute atoms' van der Waals radii to find this term. To make room for the solute, the molecules of the solvent have to be moved. This number tells you how much work it takes. That energy is there as a part of the total solvation-free energy [60].

Figure 1 show how the van der Waals spheres are used by the PCM model to determine the boundary between the solution and the solvent. Through this method, we can be sure that the PCM model gives us correct and dependable solvation energies. We need these to understand how molecules act in solutions and to guess how they will interact and stay stable in various solvent environments. Cavitation energy (Gcav) in the PCM model is the energy needed to make a hole in the solvent when the salt molecule is added. Finding this energy term requires looking at the shape of the solute-solvent system and the surface made up of van der Waals spheres, which you can see in Figure 1

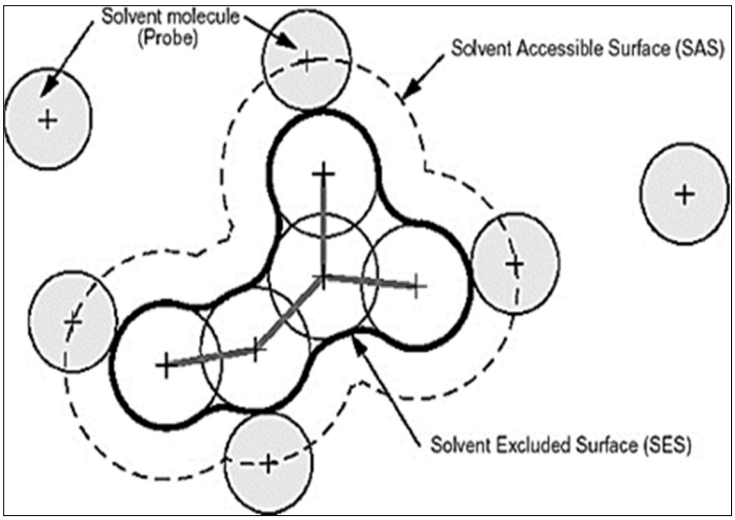

Figure 1. A solvent-accessible surface (SAS) in the middle of the probe, which stands for a liquid molecule

The SCRF term and PCM-specific tweaks have been used to make Gaussian 09w work with the PCM model. It is possible to pick the fluid and use it to work with different parts of the solvation formula. There are a lot of different solvents, such as water, DMSO, nitro methane, methanol, and more. By adding the Read tag to the SCRF term at the end of the input file, you can give the engine more choices. We can get the right solvation energies and gradients at both the Hartree-Fock (HF) and Density Functional Theory (DFT) levels when we use the PCM model with Gaussian 09w. Making these calculations can teach us a lot about the system we are looking at. We can find the single-point energy, the Raman bands, and the infrared bands, among other things. Our guess about what solvation is and what it does is right, and we learn important things about how solutes and liquids work together with this method. This model also helps us understand how different fluids can change the shape of the salt molecules and how they work. This will help us understand the solvation process better and make better liquid systems for chemistry and materials science. Please let us know more about the test results.

RESULTS AND DISCUSSION

A Pentium(R) Dual-Core CPU T4500 running at 2.30 GHz, 4.00 GB of RAM, and a 64-bit operating system were used on a home computer for these measurements. We used both the 6-31G and 6-31G(D) basis sets along with the Gaussian 09w program and the Hartree-Fock method to study the formic acid molecule. It was possible to do the calculations in both harmonic and anharmonic states. We used the FREQ term to describe the harmonic waves. To find anharmonic waves, we used the keywords Opt FREQ=(ANHARM, RAMAN). In Table 1, you can see the results of these estimates, which include single-point energies and specific vibrational rates. In addition, the IR bands of both harmonic and anharmonic motions were recorded and can be seen in Figure 2 (a) and (b). This in-depth study helps us learn more about the vibrational features of formic acid. It shows the differences between harmonic and anharmonic states and gives us useful information about how molecules behave in different situations.

Table 1. Basic vibrational frequencies of the HCOOH molecule.

Vibrational Modes	Harmonic Frequencies (cm^{-1})	Anharmonic frequencies (cm^{-1})	Symmetry	Description	Frequencies (cm^{-1}) in the gas phase [25]
ν_1	676.962	704.6973	A'	OCO deform	625"M
$\nu 2$	863.9679	878.9620	A"	Torsion	638"S
ν_3	1229.676	1227.6547	A"	CH bend	1033"W
ν_4	1230.946	1227.8367	A'	C-O str	1105.3 S
ν_5	1516.111	1474.5294	A'	OH bend	1229"W
ν_6	1572.977	1549.2714	A'	CH bend	1387"VW
ν_7	905.994	1893.9565	A'	C=O str	1770" VS
ν_8	3122.776	3170.8311	A'	CH str	2942.8"M
ν_9	3730.051	3767.9571	A'	OH str	3570"M

The following signs and phrases are used to talk about the different types of vibrational patterns shown in Table 1. "str" stands for modes of stretching, "deform" for modes of deformation, "bend" for modes of bending, and "torsion" for modes of torsion. Mulliken's symbols stand for other modes. For example, (A') represents a one-dimensional shape that is equal when rotated around the main rotating axis and when viewed from a plane parallel to that axis. On the other hand, (A") stands for a one-dimensional image that is equal when rotated around the main rotating axis but not when rotated around a mirror plane that is parallel to the axis. This explanation helps group and understand the vibrational modes seen in the HCOOH molecule by giving a thorough account of their symmetries and how they behave within the structure of the molecule. Putting things into groups like this makes it easier to look at vibrating bands and figure out what they mean for molecular motion and relationships

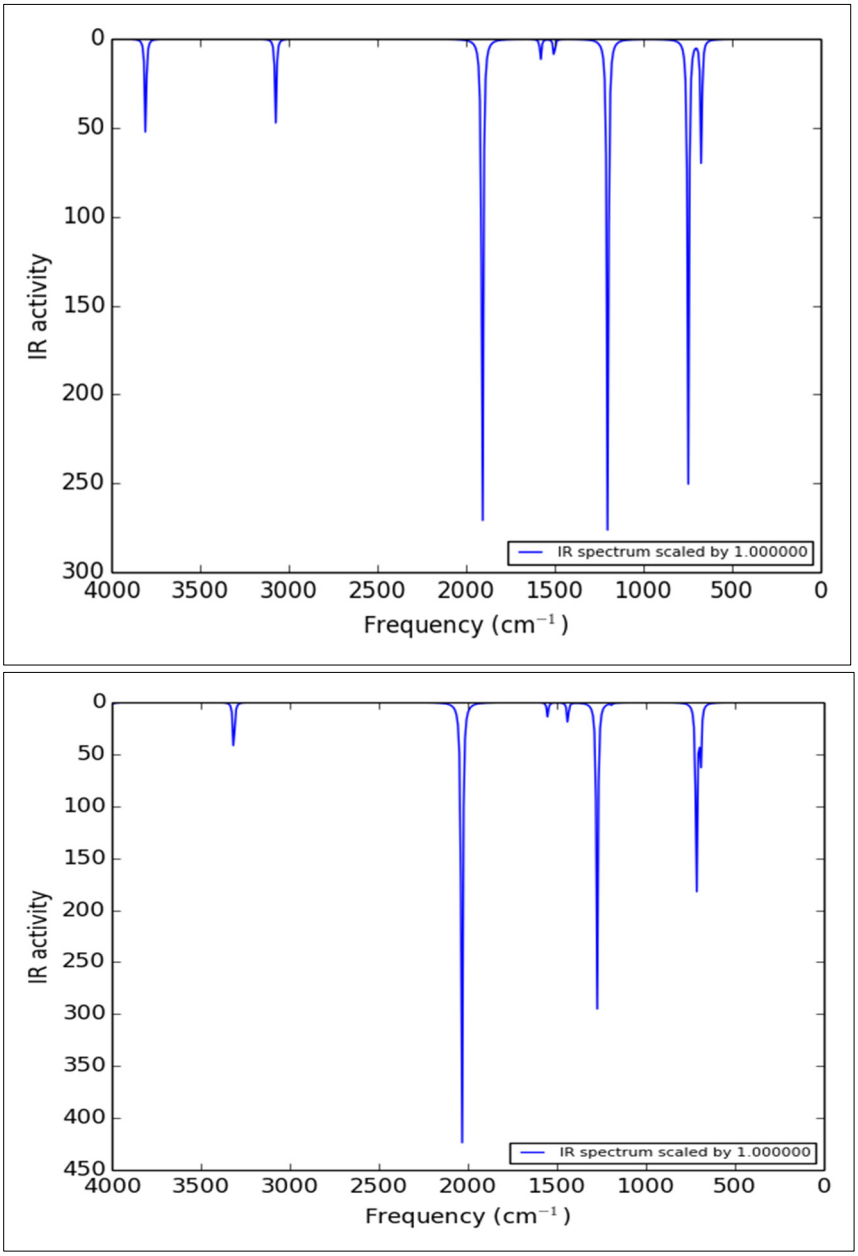

Figure 2. Infrared spectra of the HCOOH molecule ((a) scenario 1 and (b) scenario 2).

The Hartree-Fock method with the SCRF = (Solvent = Solvent) term and the 6-31G(d) basis set were used. For example, the job line was set to #P FREQ/6-31G(d) Opt SCRF = (Solvent = Carbon tetrachloride) when carbon tetrachloride was used as the solvent. The results of these calculations are shown in Table 2

TABLE 2. The fluid changes the basic vibrating frequencies of the formic acid molecule

Vibrational Modes	Symmetry	Harmonic Frequencies (cm^{-1})						Description
		Carbon tetrachloride	Toluene	Ethyl Ethanoate	Acetone	Methanol	Dimethyl sulfoxide	
ν1	A'	688.2424	688.0659	686.6040	684.6825	683.4977	682.8711	O, C, C, To C, O, C- H rsi O, H, H, O, be be str nd nd defo rm
ν2	A'	702.4372	701.5447	691.3681	685.9771	685.8826	685.8343	
ν3	A'	1199.0271	1199.3626	1202.5581	1204.0489	1204.2710	1204.3839	
ν4	A'	1269.5677	1269.3354	1267.2573	1266.2587	1266.1040	1266.0246	
ν5	A'	1436.9251	1436.8050	1435.8074	1435.2924	1435.2078	1435.1638	
ν6	A'	1554.8669	1554.9858	1556.0462	1556.5084	1556.5779	1556.6134	
ν7	A'	2009.7508	2008.1711	1991.4289	1981.9599	1980.3911	1979.5729	
ν8	A'	3326.6732	3327.2378	3333.089	3336.2938	3336.8180	3337.0906	
ν9	A'	4028.0043	4027.2741	4019.9002	4015.9822	4015.3489	4015.0204	

TABLE 3. Impact of solvent on the IR intensities (km/mol) of the formic acid molecule.

Vibrational mode	IR intensities (km/mole)								Symmetry
	Ccl_4	Benzene	Toluene	ethyl ethanoate	Acetone	Ethanol	Methanol	DMSO	
ν1	80.1142	80.3727	80.9693	89.9596	253.8421	254.6272	255.5184	256.3977	A'
ν2	226.0691	226.5179	227.5581	243.9847	95.0318	95.4264	95.8726	96.3112	A'
ν3	1.7228	1.7226	1.7220	1.7276	1.7421	1.7436	1.7453	1.7471	A'
ν4	344.4026	345.2872	347.3309	378.4903	396.0497	397.4119	398.9519	400.4649	A'
ν5	24.8083	24.8800	25.0461	27.6313	253.8421	29.3935	29.5438	29.6926	A'
ν6	15.3652	15.3946	15.4635	16.6808	95.0318	17.6008	17.6826	17.7639	A'
ν7	546.4661	548.1070	551.9039	610.6845	1.7421	647.4482	650.4766	653.4571	A'
ν8	54.9307	54.9401	54.9628	55.4455	396.0497	55.8776	55.9178	55.9580	A'
ν9	132.5863	133.1131	134.3309	152.9464	163.5708	164.4000	165.3381	166.2606	A'

The Figures 3 and 4 show the infrared spectrum of formic acid in the fluid system. They were made with software called Gauss Sum.

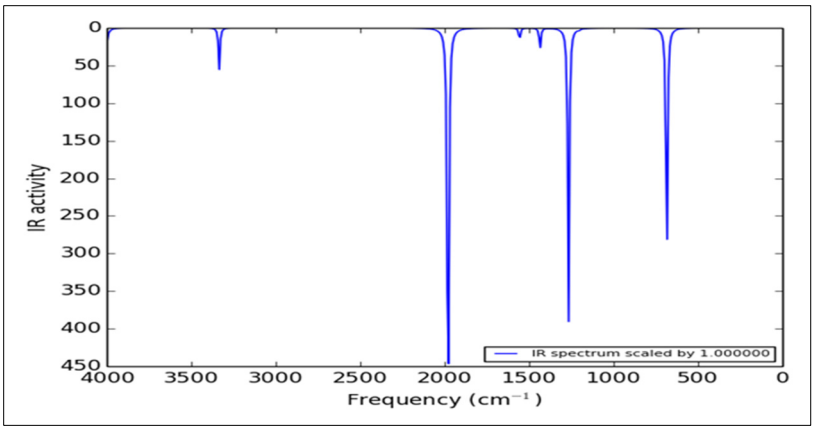

Figure 3. The infrared spectrum of the molecule of formic acid when it is mixed with DMSO.

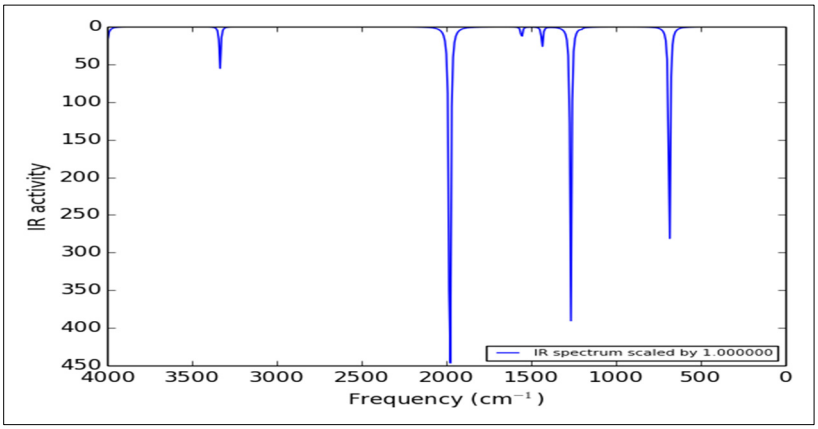

Figure 4. Infrared spectrum of the molecule of formic acid when it is mixed with methanol.

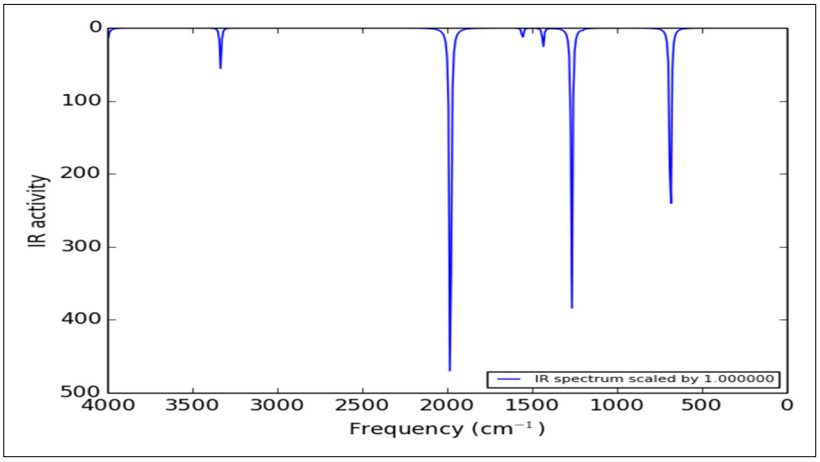

Figure 5. The infrared spectrum of the molecule of formic acid when it is mixed with acetone.

Figures 6, 7, and 8 show different ways that the formic acid molecule (HCOOH) can vibrate.

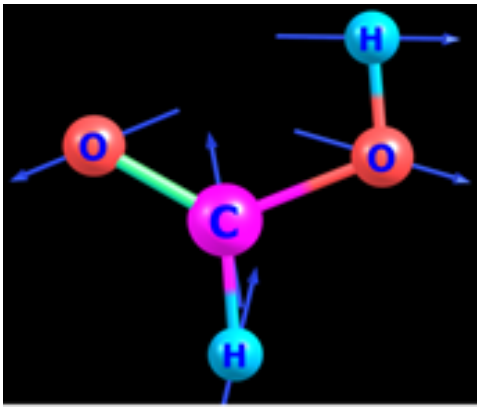

Figure 6. CO deformation-vibration mode v1

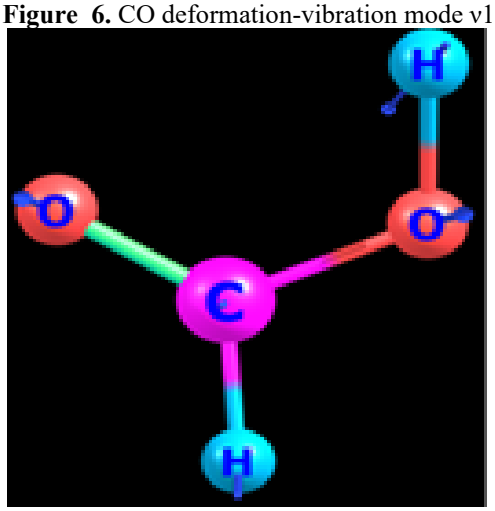

Figure 7. Torsion-vibration mode v2

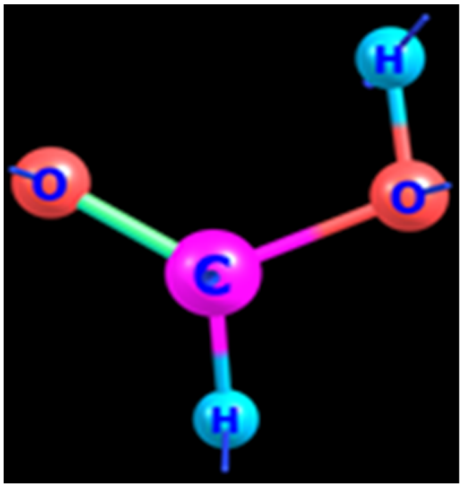

Figure 8. C-O str-vibration mode v3

The molecular structure of formic acid (HCOOH) was improved using repeated self-consistent-field calculations (SCF). This made sure that the energy level would converge at a single point after several rounds of relaxation. The optimization showed nine basic vibrating modes, which is in line with the 3N-6 rule for molecules that don't behave in a straight line. Because it is in the Cs point group, formic acid doesn't have a center of symmetry, which changes how it vibrates. Anharmonic effects were seen in the frequencies of vibrations, showing that they are different from harmonic vibrations. In Table 2, you can see how the liquid changes these frequencies, which shows big changes. It's

important to note that polar liquids caused ν1 (CO deformation), κ2 (Torsion), κ4 (C-O stretch), κ5 (OH bend), κ7 (C=O stretch), and κ9 (OH stretch) frequencies to drop, which is a sign of red shifts. ν3 (CH bend), ν6 (CH bend), and ν8 (CH stretch) frequencies, on the other hand, showed blue changes in the same conditions. These changes happen because of dipole-dipole interactions between formic acid and liquids. These happen when differences in electronegativity make partial charges that change the vibrational energy levels. When you look at Table 3, which shows how the fluid changes IR levels (km/mol), you can see that all of the absorption bands are higher except for ν2 (Torsion). The strength of this band dropped noticeably from 243.9847 km/mol in ethyl ethanoate (a non-polar solvent) to 95.0318 km/mol in acetone (a polar solvent). These changes show how the polarity of the solvent affects the IR levels. They are caused by changes in the molecular motions caused by hydrogen bonds and other interactions between molecules. Anharmonic interaction between vibrational modes like (O-H) stretching and (OH) bending was also seen, which changed how strong the ν2 (Torsion) mode was. Because of intramolecular hydrogen bonds, energy can move between these modes, which can make some bands less intense while making others more intense. In the future, researchers will look more closely at how liquids change bond lengths and angles. This will give us a full picture of how molecules behave in different weather situations.

CONCLUSIONS

Our research shows that the fluid has a big effect on how the molecules of HCOOH move and vibrate. In the infrared range, all nine of the basic frequencies we found were active. Several things, like the orientation of the fluid, hydrogen bonds, and dipole-dipole interactions, had a big effect on the levels of these IR-active modes. A lot about how different liquids change the vibrational features of HCOOH by using Gaussian 09w and the Hartree-Fock method can be examined in our study. We were able to improve the molecular structure and get correct numbers for the vibrational frequencies when the fluid conditions changed using the computational method. This showed big changes in vibrational frequencies, called red and blue shifts, which are linked to changes in the polarity of the fluid. When it came to stretching and bending modes, polar solvents tended to cause red shifts in the frequencies, while non-polar solvents tended to cause blue shifts in those modes. The IR absorption bands' strengths changed a lot depending on the watery surroundings as well. A lot of the time, polar liquids raised the IR levels because they interacted better with the solute molecules. Non-polar liquids, on the other hand, made the IR strength weaker. It was also very important that the fluid and solution system had hydrogen bonds. These bonds changed how the energy was spread among the different spectral modes, which in turn changed the levels that could be seen. The answers we got show how hard it is for a solvent to change how molecules move. It also shows how important it is to think about the properties of the fluid in spectroscopic studies and models. This full understanding helps us read lab data properly and gives us information that is useful in many areas, from making drugs to studying the environment. Some interactions between solvents and solutes need more research into what they mean for molecules and how they act in different chemistry settings.

REFERENCES

1. S. Noothongkaew, O. Thumthan, and K.-S. An, “UV-Photodetectors based on CuO/ZnO nanocomposites,” Materials Letters, vol. 233, pp. 318–323, Dec. 2018, doi: https://doi.org/10.1016/j.matlet.2018.09.024.
2. M. Cossi, V. Barone, R. Cammi, and J. Tomasi, "Ab initio study of solvated molecules: a new implementation of the polarizable continuum model," Chemical Physics Letters, vol. 255, no. 4-6, pp. 327-335, 1996.
3. V. Sathyanarayanamoorthi, S. Mahalakshmi, and V. Kannappan, "Polarizable continuum studies on auxin derivatives," Journal of Molecular Liquids, vol. 154, no. 2-3, pp. 88-93, 2010.
4. T. M. Raschke, J. Tsai, and M. Levitt, "Quantification of the hydrophobic interaction by simulations of the aggregation of small hydrophobic solutes in water," Proceedings of the National Academy of Sciences, vol. 98, no. 11, pp. 5965-5969, 2001.
5. N. Assoudi et al., “Comparative examination of the physical parameters of the sol gel produced compounds La0.5Ag0.1Ca0.4MnO3 and La0.6Ca0.3Ag0.1MnO3,” Optical and Quantum Electronics, vol. 54, no. 9, Jul. 2022.
6. N. Elangovan, S. Sowrirajan, A. Y. A. Alzahrani, D. S. Rajendran Nair, and R. Thomas, "Fluorescent Azomethine by the Condensation of Sulfadiazine and 4-Chlorobenzaldehyde in Solution: Synthesis, Characterization, Solvent Interactions, Electronic Structure, and Biological Activity Prediction," Polycyclic Aromatic Compounds, pp. 1-22, 2023.

7. K. Jayasheela et al., "Probing vibrational activities, electronic properties, molecular docking and Hirshfeld surfaces analysis of 4-chlorophenyl ({[(1E)-3-(1H-imidazol-1-yl)-1-phenylpropylidene] amino} oxy) methanone: A promising anti-Candida agent," Journal of Molecular Structure, vol. 1159, pp. 83-95, 2018.
8. G. Khanum et al., "Vibrational Spectroscopy, Quantum Computational and Molecular Docking Studies on 2-[(1H-benzimidazol-1-yl)-methyl] benzoic acid," Crystals, vol. 12, no. 3, p. 337, 2022.
9. M. Karabacak and M. Cinar, "FT-IR, FT-Raman, UV spectra and DFT calculations on monomeric and dimeric structure of 2-amino-5-bromobenzoic acid," Spectrochimica Acta Part A: Molecular and Biomolecular Spectroscopy, vol. 86, pp. 590-599, 2012.
10. E. Tyrode and R. Corkery, "Charging of carboxylic acid monolayers with monovalent ions at low ionic strengths: Molecular insight revealed by vibrational sum frequency spectroscopy," The Journal of Physical Chemistry C, vol. 122, no. 50, pp. 28775-28786, 2018.
11. S. W. Han, S. W. Joo, T. H. Ha, Y. Kim, and K. Kim, "Adsorption characteristics of anthraquinone-2-carboxylic acid on gold," The Journal of Physical Chemistry B, vol. 104, no. 50, pp. 11987-11995, 2000.
12. T. Vreven, B. Mennucci, C. O. da Silva, K. Morokuma, and J. Tomasi, "The ONIOM-PCM method: Combining the hybrid molecular orbital method and the polarizable continuum model for solvation. Application to the geometry and properties of a merocyanine in solution," The Journal of chemical physics, vol. 115, no. 1, pp. 62-72, 2001.
13. M. Rasheed, S. Shihab, O. Y. Mohammed, and A. Al-Adili, "Parameters Estimation of Photovoltaic Model Using Nonlinear Algorithms," Journal of Physics: Conference Series, vol. 1795, no. 1, p. 012058, Mar. 2021, doi: https://doi.org/10.1088/1742-6596/1795/1/012058.
14. M. Zunita, M. David, and W. Natola, "Prediction of CO2 with amine functionalized ionic liquids interaction using density functional theory," Case Studies in Chemical and Environmental Engineering, vol. 8, p. 100355, 2023.
15. R. Sakthivel, P. Sankudevan, P. Vennila, G. Venkatesh, S. Kaya, and G. Serdaroğlu, "Experimental and theoretical analysis of molecular structure, vibrational spectra and biological properties of the new Co (II), Ni (II) and Cu (II) Schiff base metal complexes," Journal of Molecular Structure, vol. 1233, p. 130097, 2021.
16. J. Charles and S. Gunasekaran, "Experimental and theoretical investigations of natural rubber (cis-1, 4-polyisoprene) using Coloumb attenuating and Hartree–Fock theoretical methods," Optik, vol. 127, no. 1, pp. 279-287, 2016.
17. J. Geethapriya et al., "Solid state synthesis of a fluorescent Schiff base (E)-1-(perfluorophenyl)-N-(o-toly) methanimine followed by computational, quantum mechanical and molecular docking studies," Results in Chemistry, vol. 5, p. 100819, 2023.
18. Y. Liu, J. Jasensky, and Z. Chen, "Molecular interactions of proteins and peptides at interfaces studied by sum frequency generation vibrational spectroscopy," Langmuir, vol. 28, no. 4, pp. 2113-2121, 2012.
19. O. Sjökvist, C. Smolle, D. Jensson, and F. Huss, "A full-thickness chemical burn to the hand using formic acid-based anti-wart treatment: a case report and literature review," Scars, burns & healing, vol. 6, p. 2059513119897888, 2020.
20. X. Liu, S. Li, Y. Liu, and Y. Cao, "Formic acid: A versatile renewable reagent for green and sustainable chemical synthesis," Chinese Journal of Catalysis, vol. 36, no. 9, pp. 1461-1475, 2015.
21. M. Rasheed, SuhaShihab, O. Alabdali, and H. H. Hassan, "Parameters Extraction of a Single-Diode Model of Photovoltaic Cell Using False Position Iterative Method," Journal of Physics: Conference Series, vol. 1879, no. 3, p. 032113, May 2021, doi: https://doi.org/10.1088/1742-6596/1879/3/032113.
22. Z.-L. Wang, J.-M. Yan, H.-L. Wang, Y. Ping, and Q. Jiang, "Pd/C synthesized with citric acid: an efficient catalyst for hydrogen generation from formic acid/sodium formate," Scientific reports, vol. 2, no. 1, p. 598, 2012.
23. J. Yang, C. Tian, L. Wang, and H. Fu, "An effective strategy for small-sized and highly-dispersed palladium nanoparticles supported on graphene with excellent performance for formic acid oxidation," Journal of Materials Chemistry, vol. 21, no. 10, pp. 3384-3390, 2011.
24. T. Rashid and M. M. Mokji, "Low-Resolution Image Classification of Cracked Concrete Surface Using Decision Tree Technique," Lecture Notes in Electrical Engineering, pp. 641–649, 2022.
25. J. M. Hankett, Y. Liu, X. Zhang, C. Zhang, and Z. Chen, "Molecular level studies of polymer behaviors at the water interface using sum frequency generation vibrational spectroscopy," Journal of Polymer Science Part B: Polymer Physics, vol. 51, no. 5, pp. 311-328, 2013.
26. Z. D. Schultz and I. W. Levin, "Vibrational spectroscopy of biomembranes," Annual review of analytical chemistry, vol. 4, pp. 343-366, 2011.
27. Z. Chen, "Investigating buried polymer interfaces using sum frequency generation vibrational spectroscopy," Progress in polymer science, vol. 35, no. 11, pp. 1376-1402, 2010.

28. G. Trudeau, J.-M. Dumas, P. Dupuis, M. Guérin, and C. Sandorfy, "Intermolecular interactions and anesthesia: Infrared spectroscopic studies," Van der Waals systems, pp. 91-125, 1980.
29. Yu, C., Liang, D., Yang, C., Zhao, B., Dong, Q., Wu, A., Li, L., & Zang, H., "Research progress and the application of near-infrared spectroscopy in protein structure and molecular interaction analysis," Vibrational Spectroscopy, vol. 121, p. 103390, 2022.

Temperature-Effective Substrate on Physical Properties of Copper Sulfide Thin Films Prepared by Thermal Chemical Spray

Sabah Salman Hamdi

University of Tikrit, College of Computer Science and Mathematics, Tikrit, Iraq

Corresponding author: Sabah.S.Hamdi@tu.edu.iq

Abstract: This work reports on fabricating thin copper Sulphur (CuS) films at glass substrate temperature (100–150 °C). (X-ray) diffraction results showed that the CuS thin films have a polycrystalline nature of the hexagonal type and the preferred direction of growth (103). Optical properties proved the direct optical energy gap for CuS-100C0 thin film, which equals 2.12eV. At the same time, at (150 C^0), it was 1.98eV. The thickness of the CuS-100 film was equal to (120 nm). In comparison, at 150 C^0, 128 nm was measured by a simulation program (Hebal Optic), which was used on the computer to determine approximate values. The continuous conductivity measurements showed that the electrical resistance of all thin films changes inversely with increasing temperature and that the prepared thin films have two activation energies.

Keywords: Chemical Spray Pyrolysis, Thiourea, Structural and optical properties.

INTRODUCTION

Sulphur (S) and copper (Cu) combine to generate Copper Sulphide (CuS), a complicated chemical combination that is found in nature as lumps or dark powders [1]. Copper sulfide is a member of the significant family of semiconductor compounds known as chalcogenides, which are created when one of the transition elements—such as sulfur, tellurium, or selenium—reacts with an element from the Periodic Table's sixth column [2-5]. These compounds have gained great attention because of their great diversity in their different properties and the high possibility of controlling these properties, and as the case with most of the compounds of chalcogenides, the compound (Cu_xS) has many stages depending on the compound's ratio of copper to sulfur [6]. There is the compound (Cu_xS) at 25C^0 with five known stable phases starting from the phase of chalcocite Cu_2S The copper-rich phase has an Orthorhombic system, the Digenite phase has a cubic system, and also the Anillite phase has a cubic system and ends with the sulfur-rich Covellite phase (CuS) and has a hexagonal system [7,8] .Caprylate (CuS) is characterized by the fact that it crystallizes in a hexagonal form and is found in the form of mass, thin layers or granules spread in other copper metals, with a density of ((4.6-4.76) gm/cm^3). The (CuS) thin films are of great importance in the field of industrial applications where photovoltaic applications are used in the manufacture of solar cells, which is an important source of new energy sources, and these thin films were discovered in (1954) by the scientist (Reynolds)The most famous solar cells are the(CdS /Cu_xS) the preferred phase in these cells is chalcocite Cu_2S as well as cells($Cu_xS/(Cd,Zn)S$) [9, 10], and it is also used in thermal photovoltaic conversion (Photothermal) for solar energy and thin film (CuS) also work as absorbing coatings for sunlight, where they have a high absorption coefficient of visible wavelengths and are used as selective radiation filters on architectural windows (Architectural) for the control of solar radiation in warm climates, and good reflectivity of infrared wavelengths, it has been used in thermal mirror coatings, as well as these thin films can be used as electrically conductive coatings coated with organic polymers [11, 12], as well as used in the manufacture of compounds involved in multi-device and multilayer structures (Multijunction Type Multilayer Heterojunction) [13] CuS thin films are used in the manufacture of gas sensors especially ammonia [14]. In this research, thin Copper Sulfide (CuS) films were prepared at glass substrate temperature (100-150 °C). (X-ray)

Technologies and Materials for Renewable Energy, Environment and Sustainability
AIP Conf. Proc. 3321, 020027-1–020027-7; https://doi.org/10.1063/5.0289791
Published under an exclusive license by AIP Publishing. 978-0-7354-5231-2/$30.00

EXPERIMENTAL WORK

CuS thin films were prepared using the chemical pyrolysis spray method on a glass substrate from 0.005 M copper chloride ($CuCl_2.2H_2O$) and 0.01 M of thiourea ($CS(NH_2)_2$) as starting materials for Cu and S ion sources, respectively. Also, after that, an equal volumetric ratio (1:1) of both solutions is taken and mixed. The solutions are placed on the magnetic stirrer for a period of (10 min) to obtain a homogeneous solution. The thermochemical spraying method has been used because it is suitable for the preparation of oxides and sulfate materials, economical due to the low cost of the manufactured devices used in the preparation of these thin films and can be prepared from the mixing of two or more materials with different melting points, the thin films are prepared under normal conditions. CuS solution is deposited on glass substrates at a temperature of $(100-150)C^{\circ}$, the distance between the substrates and nozzle is (28 cm) because more than that causes the material to evaporate before it reaches the substrates. Thin films were deposited on a glass substrate with a thickness of (0.1 cm), and the glass substrate was cleaned well before spraying to get rid of impurities as the presence of impurities affects the properties of the thin films that are prepared and the substrate was cleaned after cutting them into small squares of size (2.5 x 2.5 cm^2) where the bases were washed first with water to get rid of plankton, and then the substrate was placed in a glass flask containing acetone with a purity of (99.99%) for a period of (10 min) then the substrate was placed in another peach containing ethanol with 99% purity for a period of (10 min) and finally, the substrate was placed with a flask containing distilled water only and left for (15 min) to get rid of acetone and ethanol residues. Finally, the glass substrate was dried with cloth for cleaning glass lenses, and then CuS thin film was deposited at a substrate temperature of 100-150 C^0 on the glass substrate.

RESULTS AND DISCUSSION

Structural properties

The results of XRD for the copper sulfide thin film CuS Figure (1) prepared at different substrate temperatures T1, T2, and annealing at a temperature of 300 $^{\circ}$ and for a period of Half an hour, the thin film of T1 and T2 was polycrystalline of the hexagonal type, and the preferred direction of growth (103) and the locations of the entices the T1 were at the angle$2\theta\sim(10.18,32.09)$ and opposite the plane (002) and(103), while the locations of the eaks of the T2 we at the angles 2θ~(28.07,32.16,33.28,48.42) and opposite the planes (101), (10), (006), and (110). Respectively the prevailing trend at (006) and this is almost consistent with the results of the study [8,9], and when comparing the locations of the peaks with the standard card (ICDD) for copper sulfide numbered (00-006-0464), we find that they are close as shown in Table (1). We also note that the intensity of the tops of the thin films (CuS) increases as well as the decrease in the curve width of the mid-great peak (FWHM) with increasing the temperature of the substrate, and this confirms that the crystallization rate has improved because the increasing in peaks highest is evidence of increased crystallization and reduction of crystalline defects[10]. The average granular size was calculated using the sparks equation (1)[11], and it was found that the measured granular size values fall within the range (12.35-113.95nm).

$$D_{ave} = 0.9\lambda/\beta cos\theta \quad (1)$$

Where λ =1.54 Å is X-ray wavelength (Kα -line), β (also called FWHM) is the full-width of half-maximum (in radians), θ is the Bragg's diffraction angle.

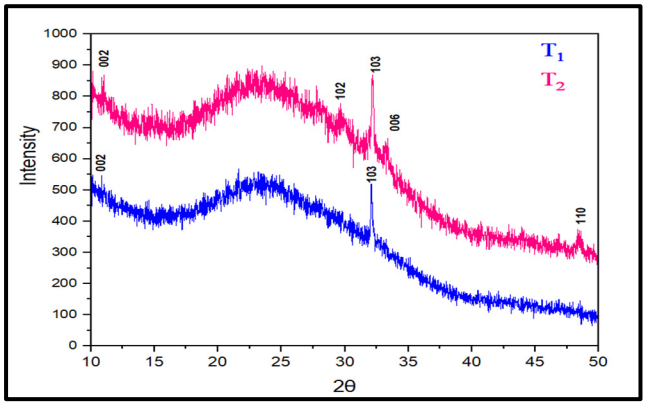

Fig. 1. Shows XRD for T_1 and $T_2$and annealed at a temperature of (300) for half an hour.

Table (1) Structural parameters of T_1 and T_2

Sample	2Θ	2Θ Stander	Hkl	$d_{hkl}\,(A^{\circ})$	FWHM	D(nm)
T_1	10.18	10.807	(002)	8.686	0.4330	19.25
	32.09	31.785	(103)	2.7891	0.0758	113.95
T_2	28.07	27.681	(101)	3.178	0.6927	12.35
	32.16	31.785	(103)	2.78	0.0866	99.75
	33.278	32.853	(006)	2.69	0.2598	33.35
	48.42	47.942	(1100	1.878	0.4224	21.55

Results of scanning electron microscopy

By studying the surface morphology (scanning electron microscope (FESEM)) of the prepared thin films, it was shown in Figure (2) that the structure of T1 is in the form of composite nanosheets. As the temperature increases, the size of T2 decreases. The reason for the crystals is the increase in the kinetic energy of the precipitated atoms, making it easier to occupy their correct positions in the crystal lattice. Then the size of the grains decreases [10], and thus these shapes are formed, and they become more aligned and arranged on top of each other and more cohesive among themselves, and this is harmony [9-11], as shown in Figures (2) and (3). A simulation program (Hebal Optic) was used on the computer to determine the thickness of the tin layer, which determines the approximate thickness values based on the transmittance values. The T1 thickness was equal to 120 nm, and the T2 thickness was equal to 128 nm.

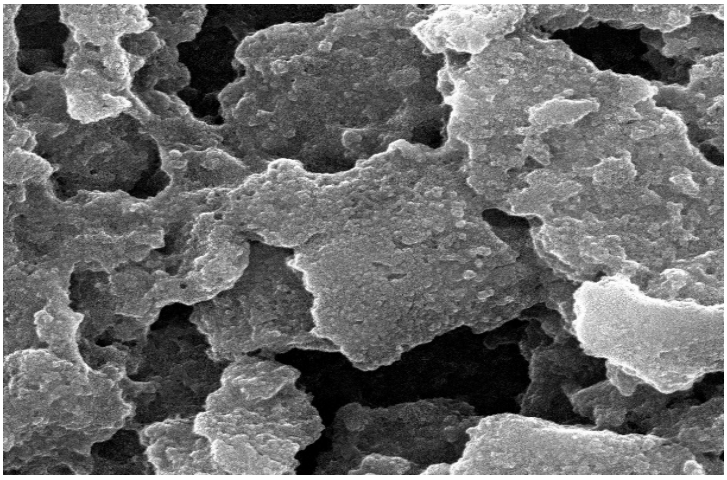

Fig. 2 FESEM for T_1

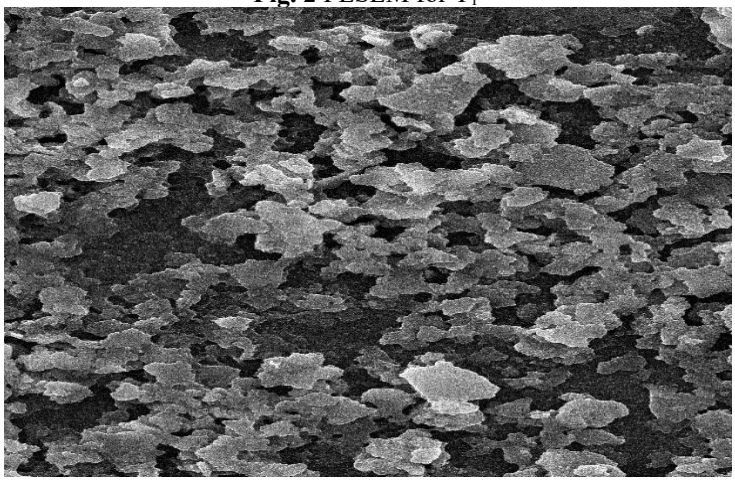

Fig. 3 FESEM for T_2

Optical properties

The absorption coefficient of the prepared thin films was calculated by equation (2), and Figure (4) shows the absorbency spectrum as a function of the wavelength; the results showed that the absorbency of the prepared thin films increases with increasing substrate temperature, which is evidence of better crystallization (increase in crystal size). Fig. (5) shows the absorption coefficient change as a function of the energy of the photon incident; the results showed that the absorption coefficient increases with the increase in photon energy of the prepared thin films, as the greatest values of the absorption coefficient are at high photon energies (4-4.3) eV, and this indicates the occurrence of the absorption process in this range (which includes the optical absorption edge) and the possibility of the process of electronic transitions between the valence and conduction bands, this is consistent with the results of studies [12-14] The energy gap value was calculated to estimate the difference between the valence band and conduction bands, which can help determine the electrical, thermal and electronic properties of materials. The Tauc formula in equation (3) determined the direct energy gap.[15] Since the transitions are of the permissible direct type, i.e., the value of the constant (r = 1/2) and drawing the relationship between $(\alpha h\vartheta)^2$ and the energy of the incident photon (hν); and the value of the optical energy gap can be found by extending the straight part of the curve to find the point where it intersects the photon energy axis (X) at ($(\alpha h\vartheta)^2 = 0$), as seen in Figure (6), where it was found that the value of the optical energy gap of T_1 is equal to 2.6 eV while for T_2 is equal to 2.4 eV, and this is approximately consistent with the results of [16,17]

$$h\vartheta = A(hv - E_g)^r \quad (2)$$

Where is A a constant, α is a absorption coefficient, hν is a incident photon's energy, r=1/2 is the allowed direct transition, and Eg is the optical bandgap.

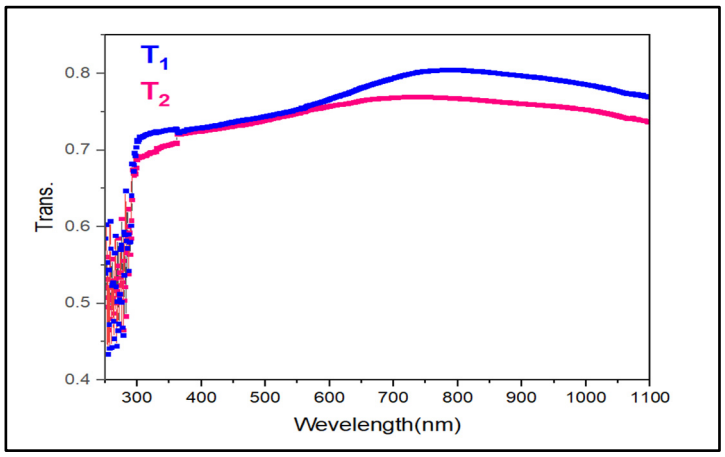

Fig. 4 Trans. spectrum of the thin films prepared as a function of the λ(nm)

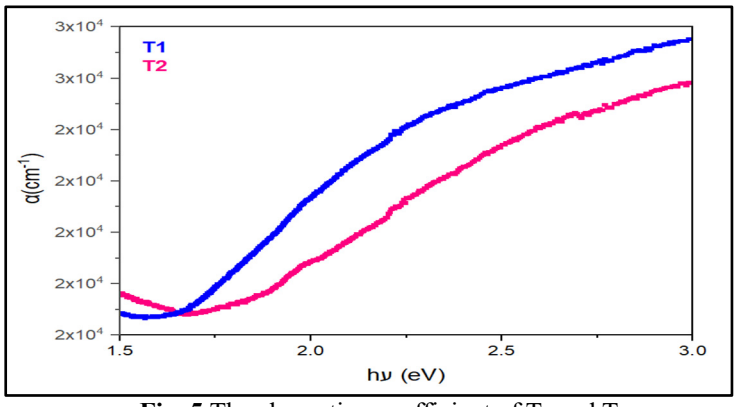

Fig. 5 The absorption coefficient of T_1 and T_2

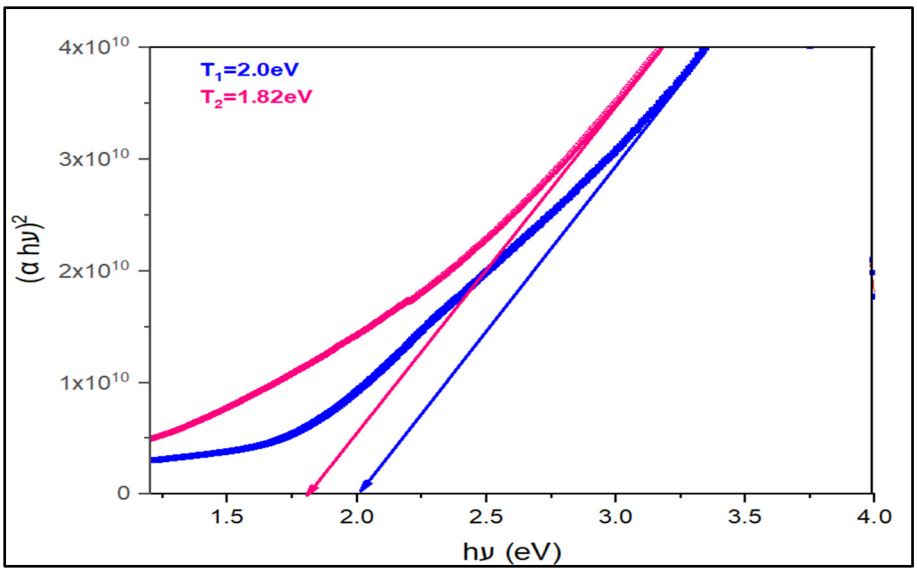

Fig 6. plot of T_1 and T_2

Electrical characteristics

The thin film's continuous electrical conductivity (σ_{dc}) was calculated using equation (4). [18-20] By studying the change in electrical resistivity (ρ) as a function of temperature (T) within the thermal range (313–453)K. Adopting equation (5) and as shown in Fig. (7), we notice from the Figure that the electrical resistivity of all prepared thin films changes inversely with increasing temperature per sample, and this is one of the characteristics of semiconductors [21-23], as they are characterized by having a resistivity with a negative thermal coefficient unlike the characteristics of conductors, that is, the continuous electrical conductivity increases with increasing temperature and for all thin films. Figure 6 shows the linear relationship between σ ln and 1000/T, which is used to calculate the activation energy (E_a) The change in the conduction mechanism is caused by the presence of two connected regions ،For CuS-100 and CuS -150, the first zone is at a low temperature (313-343K). The second zone is at a higher temperature (343-453K), showing the two-activation energy increases with increased substrate temperature and activation energy [24-26].

$$\sigma = J/E = e\,(n\,\mu_e + p\,\mu_h) \ldots\ldots\ldots\ldots \quad \ldots\ldots (3)$$

Whereas J: electric current density, E Applied electric field strength, e: electron charge, μ_e: electron kinetics: μ_h gap kinetic and p: electron concentration and gap concentration, respectively,

$$\rho = R\,\frac{A}{L} \quad where\ \{\ A = b\,.\,t\ \} \ldots\ldots\ldots \quad \ldots\ldots (4)$$

ρ: Resistivity). R: electrical resistance of the thin film measured in practical units (Ω), L: distance between the two poles of aluminum (cm). A: cross-sectional area of the movement of electrons through the thin film, b: Electrode width (cm), (t): film thickness (nm) and converts in units (cm)

Table (2) Difference in connectivity band and optical energy gap for T_1 and T_2

Sample	E_{a1} (303-343)	E_{a2} (343-383)	E_g
T_1	0.5786	0.7410	2.12eV
T_2	0.3329	2.3688	1.82eV

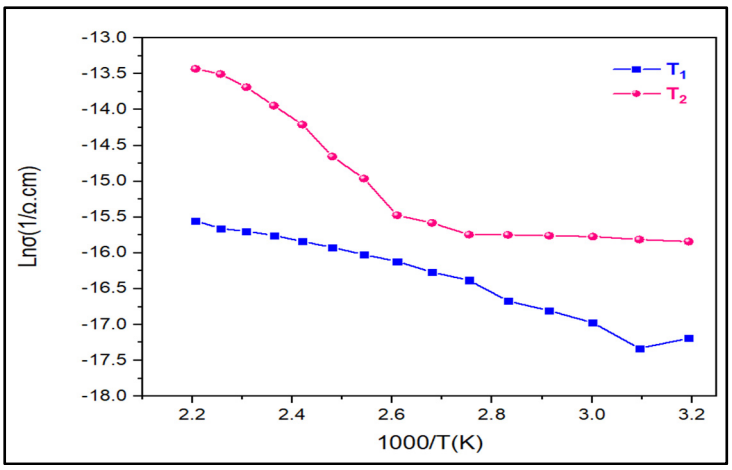

Fig.7 Activation energy of T_1 and T_2

CONCLUSION

In this paper, CuS thin films were prepared by Thermal Chemical Spray on a glass substrate, and the effect of different substrate temperatures on the properties of CuS thin films was studied. The analysis of XRD showed that all the CuS films were hexagonal structures with preferred (103) orientation. As the substrate temperature increased, the crystalline quality of the movie became better, and particle sizes became smaller, ranging from 12.35 to 113.95nm, A simulation program. (Hebal Optic), the thickness of the thin films increased with the increasing temperature. The optical band gap Eg value decreased from 2.12eV to 1.82eV with the increasing substrate temperature, making this material suitable for solar cell devices. The electrical resistivity of all prepared thin films changes inversely with increasing temperature, and the continuous electrical conductivity increases due to the increase in crystallinity quality, resulting from reduced defects during the thermal process. The two activation energies increase with increased substrate temperature, which increases activation energy.

ACKNOWLEDGMENT

The author would like to express their sincere gratitude to Dr. Huda Saadi Ali and Dr. Iftikhar Mahmood Ali, who helped us to some extent in working on this article.

REFERENCES

1. Wells A.F, "Structural Inorganic Chemistry " 3d edition, Oxford University Press, (1962).
2. Ahmed, B.A., Mohammed, J.S., Fadhil, R.N., ...Shaban, A.H., Al Dulaimi, A.H., The dependence of the energy density states on the substitution of chemical elements in the Se_6 $Te_{4-x}Sb_x$ thin film, Chalcogenide Letters, 2022, 19(4), pp. 301–308.
3. Khudhair, N.H., Jasim, K.A., Preparation and study the effective of Sb on the energy density of states of $Se_{60}Te_{40}$, AIP Conference Proceedings, 2023, 2769, 020056.
4. Khudhair, N.H., Jasim, K.A., Preparation and study the effective of Sb on the energy density of states of $Se_{60}Te_{40}$, AIP Conference Proceedings, 2023, 2769, 020056.
5. Chillab, R.K., Jahil, S.S., Wadi, K.M., Jasim, K.A., Shaban, A. H., Fabrication of Ge30Te 70-xSbx glasses alloys and studying the effect of partial substitution on d.C electrical energy parameters, Key Engineering Materials, 2021, 900, pp. 163–171. https://doi.org/10.4028/www.scientific.net/kem.900.163.
6. A.A. Hassan "study some of the structural and optical and electrical properties of the thin films of copper sulfide by chemical spraying pyrolysis "MSc thesis, University of Technology, (2001).
7. J. Santamaria, E. Iobrra, "Thin Cu_xS Sputtered films in Ar/H_2 atmosphere" vacuum, Vol.37.No,516, (1987) pp.437-439.
8. Santamaria, E. Iobrra, "Sputtering process of Cu_2S in an AR atmosphere" vacuum, Vol.37.No,510, (1987) pp.433-436.

9. A.Setkus, A . Galdikas " Properties of Cu_xS thin film-based structures influence the sensitivity to ammonia at room temperatures "thin solid films, Vol.391, (2001) pp.275-281.
10. Fayroz A.Sabah , Naser M. Ahmed ,Z.Hassan, Hiba S. Rasheed," Effect of Annealing on the electrical properties of CuS Thin films," Procedia Chemistry 19(2016) PP.15-20.
11. Cristina Nascu , IIeana Pop,Violeta Ionescu,E.Indrea, I. Bratu, "pyrolysis deposition of CuS thin films" Materials Letters, No.32,(X=1,2),(1997)PP.73-77.
12. Sheng. Y. Wang, Wei, W, Zu .H.lu," Asynchronous – pulse ultrasonic spray," pyrolysis deposition of Cu_xS (X=1,2) Thin films " Materials Science and Engineering B103, (2003) pp.184-188.
13. Mustafa. A.h, "The effect of doping in some physics properties of Cu_2S thin film prepared by spraying pyrolysis", MSc. In Applied Physics, University of Technology,(2006).
14. L.An Isac, a. Duta, I.An Enesca, M Nanu, "The growth of CuS thin films by spray pyrolysis "Journal of Physics: Conference Series 61,(2007)pp. 477-481.
15. M. Xin, K. Li, and H. wang, "Synthesis of CuS Thin Films by Microwave Assisted Chemical Bath Deposition, "Appl.Surf.Sci, Vol.256,pp.(1436-1442),(2009).
16. W. Daranfed, M. S. Aido, A. Hafdallah, and H. Lekiket, "Substrate Temperature Influence on ZnS Thin Films Prepared by Ultrasonic Spray," Thin Solid Films, Vol.518, pp.(1082-1084),(2009).
17. L. Q. Li, H. Shi, Z. A. Wang, Z. Sun and S. M. Huang, "Effect of [Zn]/[S] ratios on The Properties of Chemical Bath Deposited Zinc Sulfide Thin Films," Appl. Surf. Sci, Vol.257, PP. (122-126), (2010.
18. - Abdulateef, A.N., Alsudani, A., Chillab, R.K., Jasim, K.A., Shaban, A.H., Calculating the mechanisms of electrical conductivity and energy density of states for Se85Te10sn5-xinx glasses materials, Journal of Green Engineering, 2020, 10(9), pp. 5487–5503.
19. Jin. H.Y. Jia and Yufang Li "Excellent near-infrared response performance in p-CuS/n-Si heterojunction using a low-temperature solution method.
20. Kadhim Mustafa Kadhim "Structural and Optical Characteristics of thin film (Zno: V)', 'MSc Thesis, Science College of Science University Diyala, (2001).
21. K. Yang, J. Wang, Z. Zhao, Z. Zhou, M. Liu, J. Zhang, Z. He, F. Zhang, Smart Strategy, Transparent hole-transporting polymer as a regulator to optimize Photomultiplication-type polymer photodetectors, ACS Appl. Mater.
22. N. Mukherjee, A. Sinha, G. G. Khan, D. Chandra, A. Bhaumike, and A. Mondal, "A study on the Structural and Mechanical Properties of Nanocrystalline CuS Thin Films Grown by Chemical Bath Deposition Technique," Mater. Res. Bull, Vol. 46, pp. (6-11), (2011).
23. Wadi, K.M., Jasim, K.Ali., Shaban, A.H., Kamil, M.K., Nsaif, F.K., The effects of sustainable manufacturing pressure on the structural properties of the pb2ba2ca2cu3o9+σ compound, Journal of Green Engineering, 2020, 10(9), pp. 6052–6062.
24. Mahdi, S.H., Jassim, W.H., Hamad, I.A., Jasima, K. A., Epoxy/Silicone Rubber Blends for Voltage Insulators and Capacitors Applications, Energy Procedia, 2017, 119, pp. 501–506.
25. Niedik، C. F.، Freye، C.، Jenau، F.، Häring، D.، Schröder، G.، & Bittmann، J. (2016، July). Investigation on the electrical characterization of silicone rubber using DC conductivity measurement. In 2016 IEEE International Conference on Dielectrics (ICD) (Vol. 2، pp. 1114-1118). IEEE.
26. McLachlan، D. S.، & Sauti، G. (2007). The AC and DC conductivity of nanocomposites. Journal of Nanomaterials،، 2007.

An approach to sustainability and circularity regarding the influence of the heat treatment duration of sugar syrup and the addition of Aronia melanocarpa by-products as powder on the physico-chemical characteristics of artisanal chocolate

Tilia Cristina Murariu[1], Florin Daniel Lipșa[1], Georgiana Venin[1], Anca Tulbure[2], Petru Marian Cârlescu[1], Bianca Balint[1], Alessio Vincenzo Tallarita[3], Gianluca Caruso[3], Maya Julian[4], Ramona Giurea[5], Elena Cristina Rada [6,a)]

[1]*Department of Food Technology, Ion Ionescu de la Brad Iasi University of Life Sciences, Aleea Mihail Sadoveanu 3, 700490, Iași Romania*
[2]*Department of Food Industry and Environmental Protection, Lucian Blaga University of Sibiu, 7-9 Dr. Ion Ratiu Street, 550012 Sibiu, Romania*
[3]*Department of Agricultural Sciences, University of Naples Federico II, Via Università 100, 80055, Naples, Italy*
[4]*European Academy for Sustainable Development, 11 rue du Rempart Saint Thiebault, 57000, Metz, France*
[5]*Department of Industrial Engineering and Management, Lucian Blaga University of Sibiu, 4 Emil Cioran Street, 550025 Sibiu, Romania*
[6]*Department of Theoretical and Applied Science, Insubria University, Via G.B. Vico, 46, 21100 Varese, Italia*

corresponding author: [a)]elena.rada@uninsubria.it

Abstract. The main aim of the current research was to assess the possibilities of integrating *Aronia Melanocarpa* coarse powder, a by-product resulting from the processing of aronia juice, to obtain innovative chocolate with an appropriate commercial formula, in the context of the circular economy and sustainability approach, thus valorising the mentioned waste. *Aronia* powder is a versatile product that can be easily integrated into semi-viscous or thick food products. The experimental protocol was based on the factorial combination between 3 different concentrations of coarse *Aronia* powder addition (1%, 2%, 3%) plus an untreated control, and two durations of heat treatment of the sugar syrup at 103.5°C (7 and 10 minutes). The research results showed that both the concentration of chokeberry powder addition and the heat treatment duration had a significant impact on the textural parameters maximum strength and mechanical work, as well as on the colour components L*, a* and b*, whereas pH was only affected by *Aronia* powder addition. This research highlights the need to identify the most effective *Aronia* powder addition percentage and the technological process to obtain a qualitative or healthy chocolate.

INTRODUCTION

Sustainability and circular economy are critical concepts in the food industry, addressing pressing challenges such as resource depletion, waste management, and environmental degradation [1-7]. By prioritizing sustainable practices, the industry can reduce its ecological footprint, promote responsible sourcing, and enhance food security [7-9]. The circular economy model emphasizes minimizing waste through strategies like recycling, upcycling, and regenerative practices, fostering a system where resources are kept in use as long as possible [10-11]. Implementing these principles not only benefits the planet but also drives innovation, meets consumer demand for ethical products, and creates economic opportunities, ultimately leading to a more resilient and responsible food system.

In the current era of technology, which allows to spread information in a fast and efficient way, consumers have become more and more learned so that to desire consuming healthy and nutritionally beneficial foods which could play an important role in improving the quality of living [13-17]. In the last decade, the consumption rate of functional food has increased due to consumer concerns about a healthier lifestyle [18-22]**.** Among confectionery products, chocolate

Technologies and Materials for Renewable Energy, Environment and Sustainability
AIP Conf. Proc. 3321, 020028-1–020028-7; https://doi.org/10.1063/5.0290580
Published under an exclusive license by AIP Publishing. 978-0-7354-5231-2/$30.00

is one of the most popular foods in terms of consumption rate with an environmental impact, classified as dark, white and milk chocolate according to the ingredients it contains [23,24]. Due to its high consumption, chocolate represents a suitable matrix to be transformed into functional food by adding appropriate by-products [25-28]**.** Trends in chocolate fortification began in the last years, especially for children and elderly, benefitting from the high health and antioxidant properties of various fruits which are increasingly being analysed [29-32].In this respect, the addition of *Aronia melanocarpa* by-product powder to confectionery-type foods led to a significant increase in antioxidant activity (61%) and nutritional value [33]. *Aronia melanocarpa* powder obtained from the gooseberries resulting from the processing of *Aronia* juice is frequently introduced into food products, leading to functional products under a circular economy frame [34]. *Aronia melanocarpa* belongs to Rosaceae family, originated from North America and has been cultivated in Europe for a century [35-38]. Depending on the colour of the fruits, the species *Aronia melanocarpa* includes two subspecies, i.e., *Aronia melanocarpa* Elliot with black fruits and *Aronia melanocarpa* subsp. arbutifolia with red fruits; Aronia prunifolia is a hybrid obtained crossing the two mentioned subspecies, which has purple fruits [39,40]. *Aronia* has been appreciated mainly for its high intake of bioactive components, such as vitamins, minerals and polyphenols [41-44]. Anthocyanins are the main group of polyphenols found in this plant, which give the deep purple colour to the fruit and have a beneficial role on health, especially for the circulatory system and heart functioning [45]. In addition to the mentioned components, these fruits have a high antioxidant capacity, as well as anti-inflammatory, anti-cancer, antimicrobial, antiviral, anti-diabetic, anti-inflammatory properties [46-48].

The main objective of this study was to investigate the effect of incorporating chokeberry powder, a by-product resulting from chokeberry juice extraction, at three concentrations, 1%, 2% and 3%, respectively, in factorial combination with two heat durations (7 and 10 minutes) on rheological, physical-chemical and colour characteristics of chocolate.

MATERIALS AND METHODS

Material and experimental protocol

White chocolate, serving as the control (PMC), was correctly produced in accordance with a technological flux adapted to the industrial level. It is important to carry out innovative chocolate adding the appropriate amount of *Aronia* by-product powder to fresh chocolate made of raw milk, sugar, and cocoa butter. The experimental protocol of this research was based on the factorial combination between three concentrations of *Aronia melanocarpa* by-product powder (1% - CAU; 2% - CAD, 3% - CAT) plus an untreated white control - PMC, and two durations of sugar syrup heating process (7 mins – F7; 10 mins – F10). The experimental treatments, shown in Figure 1, are associated to the mentioned codes whose letters have the following meanings: C, chocolate; A, *Aronia*; U, 1% concentration; D, 2% concentration; T, 3% concentration. F7 and F10 represent the time of flowering to the syrup, 7 mins and 10 mins, respectively.

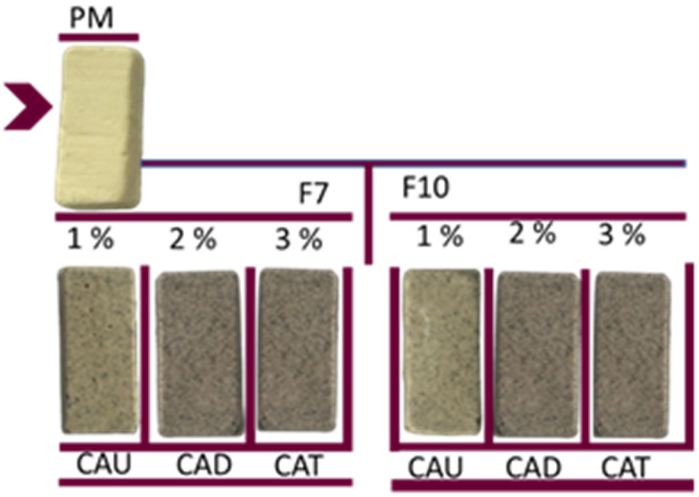

Figure 1. The chocolate samples: PM is the control sample; CAU, CAD, CAT are the samples with the addition of chokeberry powder at 1%, 2% and 3% concentrations; F7 and F10, are the samples with syrup boiling time of 7 and 10 minutes.

Technological process

The production process followed a technological flux adapted to the industrial level, as shown in Figure 2.

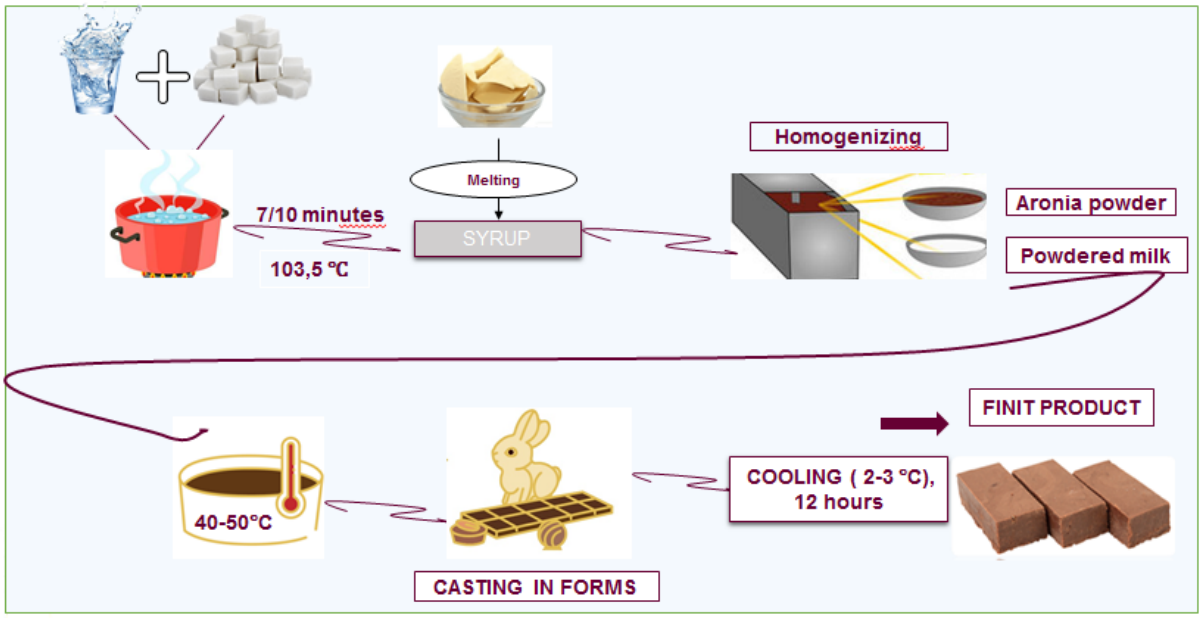

Figure 2. Technological flux to produce the experimental treatments

The technological process begins with the operation of boiling water, to which sugar is added to form a thick and sticky syrup, obtained by dissolving sugar in water at a temperature of 110-115°C for 7 or 10 minutes. It is essential to avoid mixing the two ingredients until boiling beginning, to prevent the sugar from crystallizing. Later, the butter is melted into the resulting syrup. Powdered milk and *Aronia* powder for the added samples were inserted into the resulting syrup and homogenized for 10 minutes at a temperature of 45°C. The resulting composition was poured into molds with well-established dimensions of 9 cm long, 3 cm wide and 2 cm height, cooled to 2-3°C to form a specific structure [49].

Analytical methods

The ***pH*** was determined by the Hanna Instruments potentiometer by inserting the 2 electrodes into the extract to be analysed consisting of the sample and H_2O brought to a temperature of 20°C. The apparatus was pre-prepared by calibrating it with pH solutions of 4.01 and 7.01 according to the Association of Official Analytical Chemistry method 981.12 [50].

The determination of ***textural parameters*** was carried out by a Mark 10 Plus texturometer (USA) using a Warner Bratzel V-type knife. The measurement range was between 0 and 100, with a resolution of 0.2 N in diameter. The results obtained after cutting bar-type samples of approximately equal weight (70-80 g), length (8-9 cm), width (3-3.5 cm) and height (2 cm) were interpreted with the Measure Plus program. Following the interpretation of the data obtained in 3 repetitions, the maximum force [N] and mechanical work required for cutting [N] were determined [51].

The determination of the ***colorimetric parameters*** L (black-white), a (red-green), b (blue-yellow) of the 8 samples was carried out with the Chroma Meter CR-410 instrument (Konica Minolta, INC, Japan). The chocolate samples were brought to the same size (length, width, height), levelled evenly, transferred to a colourless glass container and subjected to analysis. The results were expressed in the CIEL*a*b* system [52].

RESULTS AND DISCUSSION

As can be observed in Figure 3, the Maximum strength and Mechanical work showed similar trends. Indeed, the highest values corresponded to the 2% Aronia powder addition when chocolate was carried out at 103.5°C for 7 minutes and upon 1% Aronia addition under 10 minutes heating treatment; the lowest levels of the two mentioned variables were generally recorded in the untreated control and highest Aronia melanocarpa powder addition. Moreover, the values of Maximum strength and Mechanical work were higher with the longer heating treatment corresponding to 1% and 2% additions figure 3.Increasing trends of pH were recorded from the untreated control to the highest Aronia powder addition both under the 7 and 10 minutes heating treatments, whereas no significant differences arose in the comparisons between the two latter treatments at each Aronia percentage figure 4.Chocolate brightness (L* colour component) showed the highest values in the untreated control and decreased with increasing Aronia powder addition (Figure 5). Similar trend was recorded for the b* colour component, i.e., with a rising tendency to yellow colour with Aronia addition increase, whereas the a* colour component diplayed the opposite trend turning more and more to red colour with Aronia percentage augmentation figure 5.

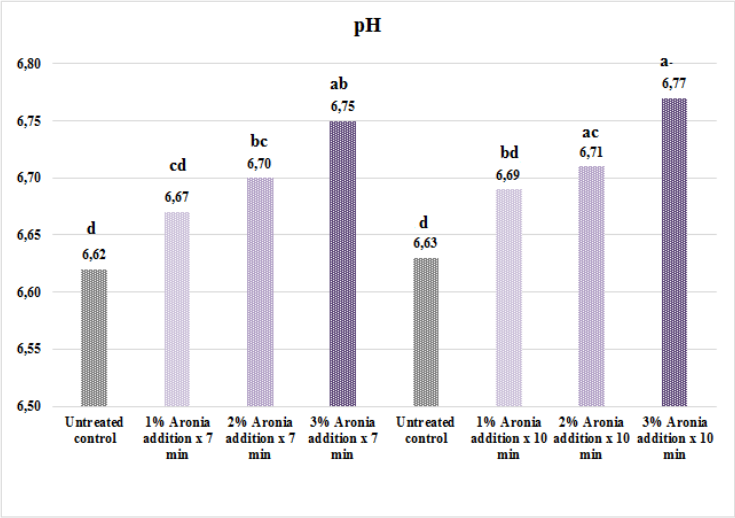

Figure 3. Effects of *Aronia melanocarpa* powder addition and heating duration on Maximum strength and Mechanical work of chocolate.

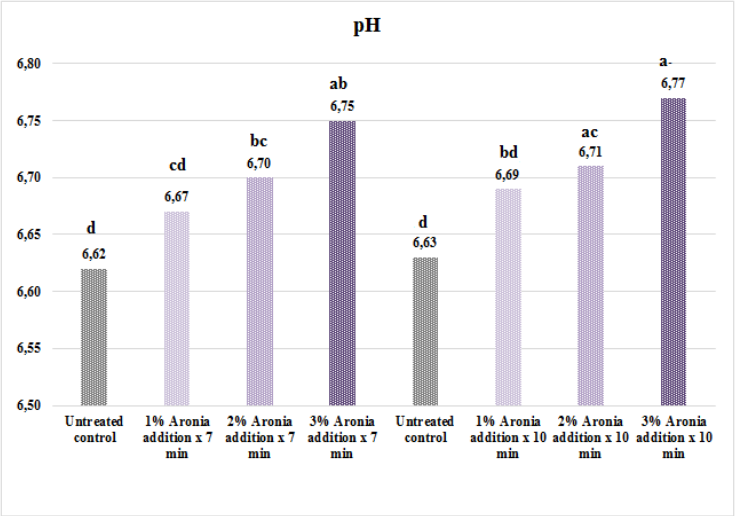

Figure 4. Effects of *Aronia melanocarpa* powder addition and heating duration on pH of chocolate.

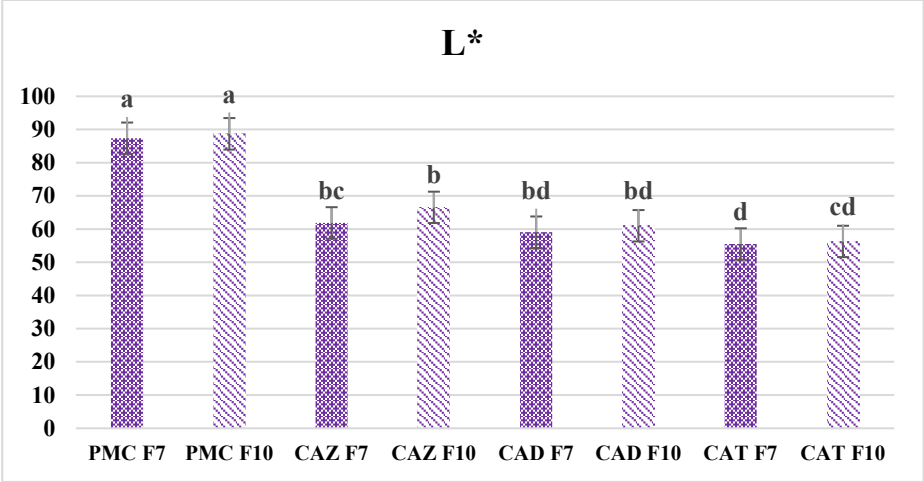

(a)

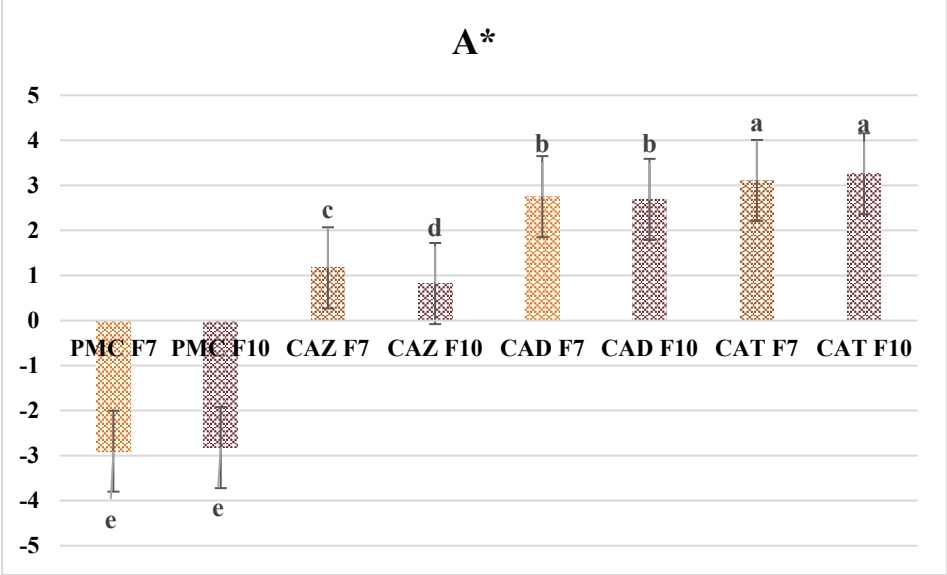

(b)

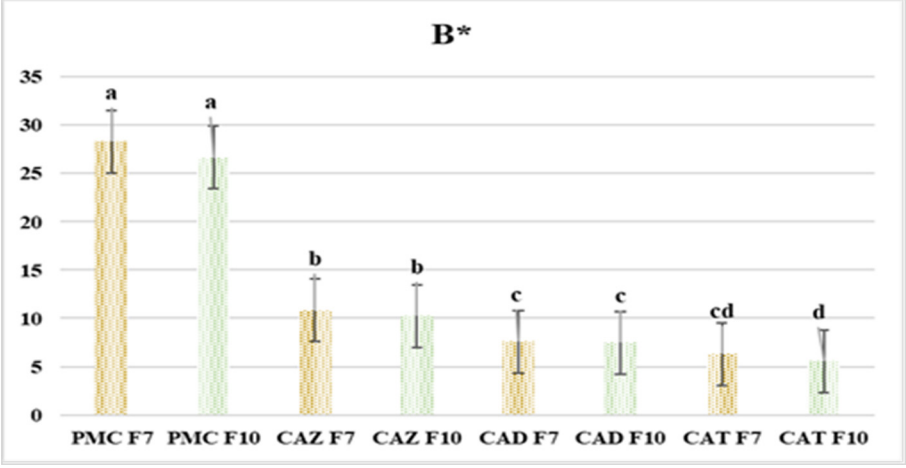

(c)

Figure 5. Effects of *Aronia melanocarpa* powder addition and heating duration on colour components L*, A* and B* of chocolate

The rheological properties of the chocolates are important for the efficiency of the processes applied during production, such as mixing, pumping, transferring/transportation, moulding, coating, sensory properties and filling of rough surfaces [53]. Previous research [54] the effects of the addition to chocolate of omega 3 fatty acids (EPA/DHA) with different forms (encapsulated form, microalgae containing form) of Eicosa-Pentaenoic-Acid (EPA) and Docosa-Hexaenoic-Acid (DHA) were assessed. After conching process, the chocolate samples showed shear thinning behaviour, in agreement with previous studies, which can be explained by the structural breakdown caused by the applied shear force [55] and alignment of the constituent molecules [56] present in the chocolates. Compared to the control samples, the addition of EPA/DHA source component in different forms (microalgae/oil and powder) generally had slight impact on rheological parameters of the chocolates [54].

CONCLUSIONS

From the present research aimed to valorise Aronia melanocarpa by-products through their addition to chocolate, it arose that the effects of the mentioned addition on the examined rheological parameters, pH and colour components varied as a function of the Aronia powder concentration and the heating duration. Indeed, the Maximum strength and Mechanical work showed the highest values between the lowest (1%) and medium (2%) concentration, whereas pH increased with rising the Aronia addition percentage. Augmenting the Aronia powder addition led to decreasing chocolate brightness, as well as increasing tendency to the yellow and red colour. The described results allow to infer the interesting chance to valorise Aronia melanocarpa by-products with the target to produce an innovative chocolate-based food.

REFERENCES

1 Rajković, M.B., Popović, M.D., Milinčić, D. and Zdravković, M., 2020. *Zastita materijala*, 61(3), pp. 229-250.
2 Bigdeloo, M., Teymourian, T., Kowsari, E., Ramakrishna, S. and Ehsani, A., 2021. *Mater Circular Econ*, 3, 3.
3 Despoudi, S., Bucatariu, C., Otles, S. and Kartal, C., 2021. *Food Easte Recover,* 3-19.
4 Danciu C.A., Tulbure A., Stanciu M.A., Antonie I., Capatana C., Zerbeș M.V., Giurea R. and Rada E.C., 2023. *Foods*, 12(20), 3770.
5 Danya, U., Kamaraj, M., Babu, P.S. and Aravind, J., 2024. *Global J Environ Sci Manage*, 10(4), 2127–2144.
6 Rabbi, M.F. and Amin, M.B., 2024. *Clean Responsib Consum*, 14, 100206.
7 Giurea, R., Carnevale Miino, M., Torretta, V. and Rada, E.C., 2024. *Frontiers Environ Sci,* 12,1363024.
8 Osei-Owusu, A.K., Read, Q.D. and Thomsen, M., 2023. *Environ Sci Technol,* 57(43), pp. 16296–16308.
9 Husain, D., Garg, P. and Prakash, R., 2021. *Intel J Sustain Eng*, 14(1), pp. 26–38.
10 Schöggl, J.P., Stumpf, L. and Baumgartner, R.J., 2020. *Resour Conserv Recycl*, 163,105073.
11 Rada, E.C., 2023. *Environ Climate Technol*, 27(1), 989-998.
12 Davies, K.P., Gibney, E.R. and O'Sullivan, A.M. 2023. *J Human Nutr Dietetics,* 36(6), 2256–2267.
13 Malleshi, N.G., Agarwal, A., Tiwari, A. and Sood, S., 2020. *Millets and Pseudo Cereals: Genetic Resour Breeding Advanc*, 159–16.
14 Bahn, R., EL Labban, S. and Hwalla, N., 2019. *Sustain Sci,* 14(4), 1131–1146
15 Julio, L. M., Copado, C. N., Crespo, R., Diehl, B. W. K., Ixtaina, V. Y., Tomas, M. C., 2019. *Powder Technol*, 345, 750–757.
16 Schiavon, M., Ragazzi and M., Rada, E.C., 2013. *Chemosphere,* 93(8), 1639-1645.
17 Smith, J., 2010 Functional Food Product Development; Blackwell Publishing Ltd.: Chichester, West Sussex, UK, 2010; ISBN 9781405178761.
18 Briazu, R.A., Masood, F., Hunt, L., Pettinger, C., Wagstaff, C., McCloy, R. 2024. *BMC Public Health*, 24(1), 1770.
19 Vignesh, A., Amal, T.C. and Vasanth, K., 2024. *Food Resear Int*191, 114739.
20 Bojang, K.P. and Manchana, V. 2023. *Current Nutr Reports,* 12(3), 369–375.
21 Arrieta, E.M. and Aguiar, S. 2023. *Progress Cardiovascular Diseases*, 77, 107–118.
22 Essa, M.M., Bishir, M., Bhat, A., Chidambaram, S.B., Al.Balushi, B., Hamdan, H., Govindarajan, N., Freidland, R.P.and Qoronfleh, M.W., 2023. *J Food Sci Technol,* 60(3), 820–834.
23 Hosseinzadeh-Bandbafha, H. and Kiehbadroudinezhad, M., 2022. *Trends Sustain Choc Prod*, 229–258.
24 Afoakwa, E.O., Paterson, A., Fowler, M., Vieira, J., 2009. *Int J Food Sci Technol,* 44(1), 162–167.
25 Gültekin O.M., Karadag, A., Duman, S¸ Ozkal, B., Ozçelik, B. 2016. *Food Che,* 201, 205–212.
26 Taşoyan, İ.C., Yolaçaner, E.T., Öztop, M.H., 2023. *J Texture Stud,* 54(2), 334–346.

27 Muhammad, D.R.A., Fibri, D.L.N. and Prakash, S., 2022. *Trends Sustain Choc Prod,* 113–152.
28 Konar, N., Palabiyik, I., Toker, Ö.S., Saputro, A.D. and Pirouzian, H.R., 2022. *Trends Sustain Choc Prod*, 75–112.
29 Konar, N., Poyrazoglu, E.S. and Artik, N., 2015. *J Food Sci Technol,* 52(4), 2033–2042.
30 Muhammad, D.R.A., Saputro, A.D., Rottiers, H., Van de Walle, D. and Dewettinck, K., 2018. *Eur Food Res Technol*, 244(7), 1185–1202.
31 Angor, M., Al Khalaileh, N., Al-Marazeeq, K., Al-Rousan, W. and Ajo, R., 2023. *Frontiers Sustain Food Syst,* 7, 1204403.
32 Huaman-Rojas, D., Maicelo-Quintana, J.L., Mori-Mestanza, D., Auquinivin-Silva, E.A., medina-Mendoza, M., Cayo-Colca, I.S., Maldonado-Ramirez, I., Castro-Alayo and E.M., Balcázar-Zumaeta, C.R., 2024. *Appl Food Res,* 4(1), 100433
33 Bratosin, B.C., Martău, G.A., Ciont, C., Ranga, F., Simon, E., Szabo, K., Darjan, S., Teleky, B.E. and Vodnar, D.C., 2024. *Appl Sci*, 14(6), 2338.
34 Lazăr M.A., Catană M., Catană L., Burnete A.-G., Teodorescu R.I., Asănică A.C., Belc N., 2020. *Sci Papers. Series B*, *Horticulture*, LXIV(2).
35 Kulling S.E. and Rawel, H.M., 2028. *Planta Medica,* 74(13), 1625–1634
36 Özdemir, K. and Özkan, E.E., 2020. *Ankara Universitesi Eczacilik Fakultesi Dergisi*, 44(3), 534–547
37 Jurendić, T. ad Ščetar, M., 2021. *Antioxidants,* 10(7), 1052.
38 Ren, Y., Frank, T., Meyer, G., .Lei, J., Grebenc, J.R., Slaughter, R., Gao, Y.G. and Kinghorn, A.D., 2022. *Molecules,* 27(22), 7823
39 Jurendić, T. and Ščetar, M. 2021. *Antioxidants,* 10(7), 1052.
40 Kwak, M.C., Choi, C.H., Choi, Y.E. and Moon, H.K., 2015. *J Plant Biotechnol*,42(4), 380–387.
41 Chrubasik C., Li G. and Chrubasik S., 2010. *Phytotherapy Res,* 24, 1107–1114.
42 Jurikova, T., Mlcek, J., Skrovankova, S., Sumczynski, D., Sochor, J., Hlavacova, I., Snopek, L. and Orsavová, J., 2017. *Molecules* 22, 944.
43 Szopa, A., Kokotkiewicz, A., Kubica, P., Banaszczak, P., Wojtanowska-Krośniak, A., Krosniak, M., Marzec-Wróblewska, U., Badura, A., Zagrodzki, P., Bucinski, A., Luczkiewicz, M. and Ekiert H., 2021. *Eur Food Res Technol*, 243(9), 1645–1657.
44 Tasic, N., Jakovljevic, V.L.J., Mitrovic, M., Djindjic, B., Tasic, D., Dragisic, D., Citakovic, Z., Radoman, K., Zivkovich, S., Bolevich, S. and Turnic, T.N., 2021. *Molecular Cellular Biochem,* 476(7), 2663–2673.
45 Caruso M.C., Galgano F., Tolve R., Pecora M., Tedesco I., Favati F., Condelli N., 2016. *J Berry Res,* 6, 321–332.
46 Li, D., Wang, P., Luo, Y., Zhao, M. and Chen, F., 2017. *Critical Rev Food Sci Nutr,* 57(8), 1729–1741.
47 Borowska, S. and Brzóska, M.M., 2016. *Compr Rev Food Scie Food Safet,* 15(6), 982–1017.
48 Kulling, S.E. and Rawel, H.M., 2008. *Planta medica,* 74(13), 1625-1634.
49 Banu C., 2009, Tratat de industrie alimentară, Ed. ASAB, vol 2,ISBN 978-973-7725-62-2.
50 Brezeanu C., Brezeanu P.M., Stoleru V., Irimia L.M., Lipsa F.D., Teliban G.-C., Ciobanu M.M., Murariu F., Puiu I., Branca F. and Murariu O.C., 2022. *Agriculture* 12, 1863.
51 Lutfiye Y.E., Tulay O., Arzu A.B., Cheima M., Esra T., Saliha K. and Tugce O., 2019. *J Animal Husbandry Dairy Sci*, 3(1), 9-13.
52 Goyal, A., Sharma, V., Sihag, M. K., Tomar, S. K., Arora, S., Sabikhi, L., Singh, A.K., 2015. *Powder Technol,* 286, 527–537.
53 Servais, C., Jones, R. and Roberts, I., 2002. *J Food Eng,* 51(3), 201-208.
54 Toker, O.S., Konar, N., Pirouzian, H.R., Oba, S, Polat, D.G., Palabiyik, I., Poyrazoglu, E.S. and Sagdic O., 2018. *LWT,* 87, 177-185.
55 Fernandes, V.A., Müller, A.J. and Sandoval, A.J., 2013. *J Food Eng,* 116(1), 1226-1231.
56 Izidoro, D.R., Scheer, A.P., Sierakowski, M.R. and Haminiuk, C.W.I., 2008. *LWT,* 41(6), 1018-1028.

The Calculation of Ground Deformation Caused by Earthquake Through Remote Sensing and GIS in Diyala-Iraq

Ali A. Hussein [1,a], Auday H. Shaban [1,b], Najah A. Abd [2,c]

[1] *Department of Remote Sensing & GIS, College of Science, University of Baghdad, Baghdad, Iraq*
[2] *Department of Geology, College of Science, University of Baghdad, Baghdad, Iraq*

[a] Ali.Ayad2209m@sc.uobaghdad.edu.iq
[b] auday.h@sc.uobaghdad.edu.iq
[c] Corresponding author: najah.abd@sc.uobaghdad.edu.iq

Abstract: This study depends on the remote sensing and geographic information system techniques to calculate the ground deformation made by natural hazards (earthquake swarm) in, Iraq (Diyala), although sometimes minor, can have significant impacts on the earth's surface. The study area, located on the border between Iraq and Iran, is subject to frequent seismic activity due to plate collisions. This study leveraged Sentinel-1 SAR data to detect ground displacements with millimetre level accuracy using Differential Interferometry (DInSAR). Data from two sources, including earthquake and geographic data, these data processed using SNAP and ArcGIS Pro software to create deformation map and interferograms that show displacement amount before and after the seismic event. The analysis depends on differences in elevation, with some areas being higher and others being lower, distinguish the ability of remote sensing to accurately detect even the smallest deformations. The results show the earthquake swarm (2.5to 5.0 mw) made maximum subsidence in baladruz (-161mm) while in khanaqin the highest uplift appear (35mm) so the importance of these techniques in monitoring geological changes and planning disaster response measures, showing that even earthquakes of low magnitude can cause detectable ground deformation. This research contributes to the understanding of earthquake effects and the effectiveness of modern tools in geological studies.

Keywords: Remote Sensing, Deformation, GIS, SAR, Earthquake, InSAR.

INTRODUCTION

The Earth surface is changeable for many reasons. The nature and shape of the Earth's surface changes called deformation phenomenon [1]. Where the deformation is in the form of collapses or elevations from several causes that may be man-made, such as drilling, construction, and demolition operations, or mine explosions in cases of war, and it can be a result of the action of nature represented by seismic activities resulting from the movement of tectonic plates and volcanoes, in addition to floods and landslides.[2-4] Earthquakes are one of the most important causes of natural deformation, which come in different types and strengths.[5,6] There is the destructive one that leads to the death of thousands of people, and there are those that are barely felt, despite the small effect of weak earthquakes, but if they are in the form of a series containing many of them in a short period of time, they can affect and cause minor deformations in the Earth's surface [7-9] After technological progress and modern science, researchers were able to study the deformations that occur due to earthquakes by using remote sensing techniques [10], accurate positioning systems, and drones[11], which made remote sensing A very effective and useful tool in these studies. One of the most important of these techniques is radio imaging, as this type of imaging is not affected by weather conditions or darkness and is able to collect data at all times[10]. The most common type of radar images used is sar images, as two images can be taken before and after the earthquake to study the amount of deformation resulting from this earthquake through InSAR [11], through which the phase difference in the radio wave is calculated and then converted into

Technologies and Materials for Renewable Energy, Environment and Sustainability
AIP Conf. Proc. 3321, 020029-1–020029-8; https://doi.org/10.1063/5.0289999
Published under an exclusive license by AIP Publishing. 978-0-7354-5231-2/$30.00

displacement, which represents the deformation through the distance difference. This rapid development has enabled dinsar to calculate the deformation with very high accuracy, reaching the millimeter as a subsidence or rise in the Earth's surface.[14] This study is depends on several research deal with the same topic. Bellow the illustration for the most important three that used the DInSAR as method:

Jin and Fialko in (2021) studied the earthquakes that occurred in China in 2021. They were used InSAR data and a fault model to study the surface changes resulting from the earthquake. The result of this study was showing extensive surface deformations and a surface fault with a strike-slip mechanism, in addition to early deformations that persisted for several days after the earthquake. The study illuminate the importance of monitoring these deformations to understand the dynamics of damage caused by earthquakes and its effects.[15]

Baqer H. Sayyid et al in (2023): Focused on InSAR as an effective tool for identifying ground surface movements and monitoring deformations resulting from natural disasters in their study. InSAR depend on comparing radar signals reflected from at least two images of the same scene of the same location, allowing for the detection of any changes either small or large damage in earth surface (deformations). The data of Sentinel-1 was used in InSAR applications, where the process includes data collection, pre-processing, generating interferometric images, and analysing time series of deformations[16, 19].

Md. Abdul Kader in (2019): relies on remote sensing techniques in studying earthquakes, from estimation them to assessing damage and recovery processes. technologies such as satellite imagery in addition to (LiDAR) and InSAR were used to collect data. The importance of spatial data accuracy in measuring damage was also emphasized, with high-resolution satellite images like (QuickBird) and medium resolution (Landsat) being used to identify affected locations.[18]

Overall, these studies highlight the importance of remote sensing techniques and its effects in understanding earthquakes and their impacts, contributing to the improvement of disaster management strategies.

The study aims to find out the effect of large number of earthquake (swarm) with low magnitude in period of time and calculate the deformation

STUDY AREA

The eastern Iraq region on the Iranian-Iraqi border, specifically between two longitudes (46°54'15"E and 44°29'55"E) and two latitudes (35°5'15"N and 32°37'4"N) as shown in figure 1 was studied in this research. This region is divided into two parts represented by part of (Diyala) Governorate (Khanaqin and Baladruz), part of (Wasit) Governorate (north of Badra) on the Iraqi side, and parts of (Kamanshah and Ilam governorates) in Iran. This border area represents a collision zone between the Arabian and Iranian tectonic plates.[16] This region is exposed to a large number of earthquakes during the recent years, which causes morphological changes and deformations, and sometimes causes damage to buildings and leads to the death of some people

Figure1 shows the study area map the discrete red line refers to the boundary between Iraq and Iran on the right is Iranian lands while in the left is the Iraqi lands.

MATERIALS AND METHODS

dataset

In this study, a diverse dataset consisting of three types was used. First, geographical data that includes information about the administrative borders of Iraq and Iran at three levels: national borders, provinces, and sub-regions, which was obtained from diva GIS [20]. Second, earthquake data was used, obtained from the Earthquake Laboratory and Spatial Data Analysis at the University of Baghdad, which includes a complete record of earthquakes with their dates, times, locations, as well as their magnitudes and depths. The third type is specific radar images (SAR) from satellites, where data from the European Satellite Sentinel 1A was used, with three scenes of SLC IW Band C covering the earthquake locations in the study area.

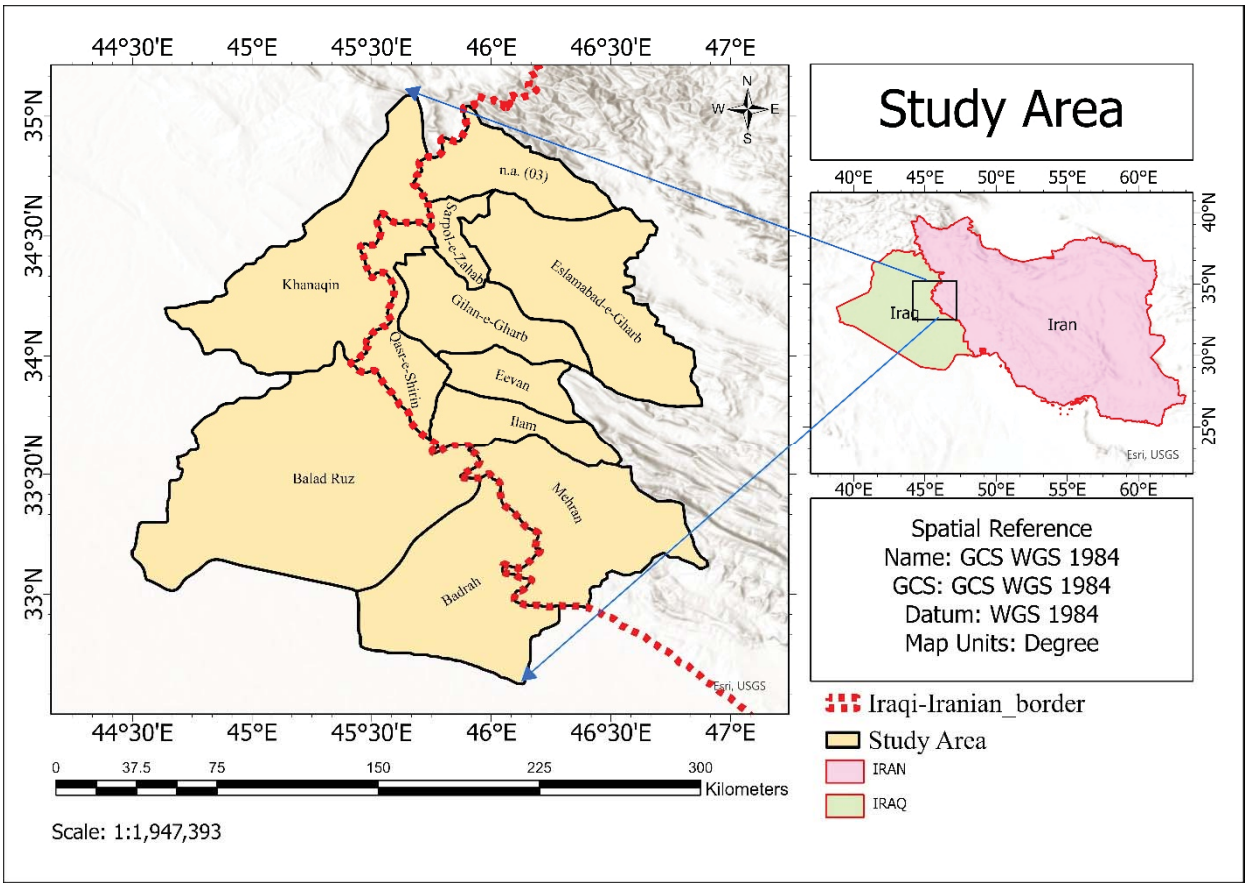

Figure 1. Study area map

Methodology

ArcGIS Pro software from Esri and Snap software established by the European Space Agency (ESA) were used to process the Sentinel satellite data and create the maps. This study focused on the analysis of synthetic aperture radar (SAR) imagery data to monitor ground deformation due to a seismic event earthquake swarms, using the Sentinel-1 SAR dataset because it is very accurate in detecting large-scale surface deformation. The analysis was performed using the SNAP program provided by the European Space Agency, in which interferogram were created using two SAR images taken before and after the earthquake. The study used a differential interferometric synthetic aperture radar (DInSAR) technique to calculate earth surface displacements with high precision, using three SLC IW images selected at the same time of the seismic event (earthquake swarm) to ensure the accuracy of the analysis. The image processing must be included to do important correctives to improve the quality of the results, the corrections including spectral correction to improve spectral noise, spatial correction to remove geometric effects caused by the curvature of the earth and sensor motion, and the orbital correction to ensure accurate image alignment. After data pre-processing, DInSAR is used to calculate deformation values with millimetre level accuracy, allowing for accurate assessment of the impact of earthquakes and other geological events or manmade. The analysis results were exported to GIS Pro, in the GIS the data were classified and exported as a map were generated showing the extent and severity of ground displacement. These maps are essential tools for understanding the distribution of deformation and planning mitigation strategies in affected areas. This study reflects a comprehensive understanding of advanced SAR image analysis and deformation calculation techniques, contributing to improved geological monitoring and disaster mitigation capabilities the methodology work flow shown in figure 2

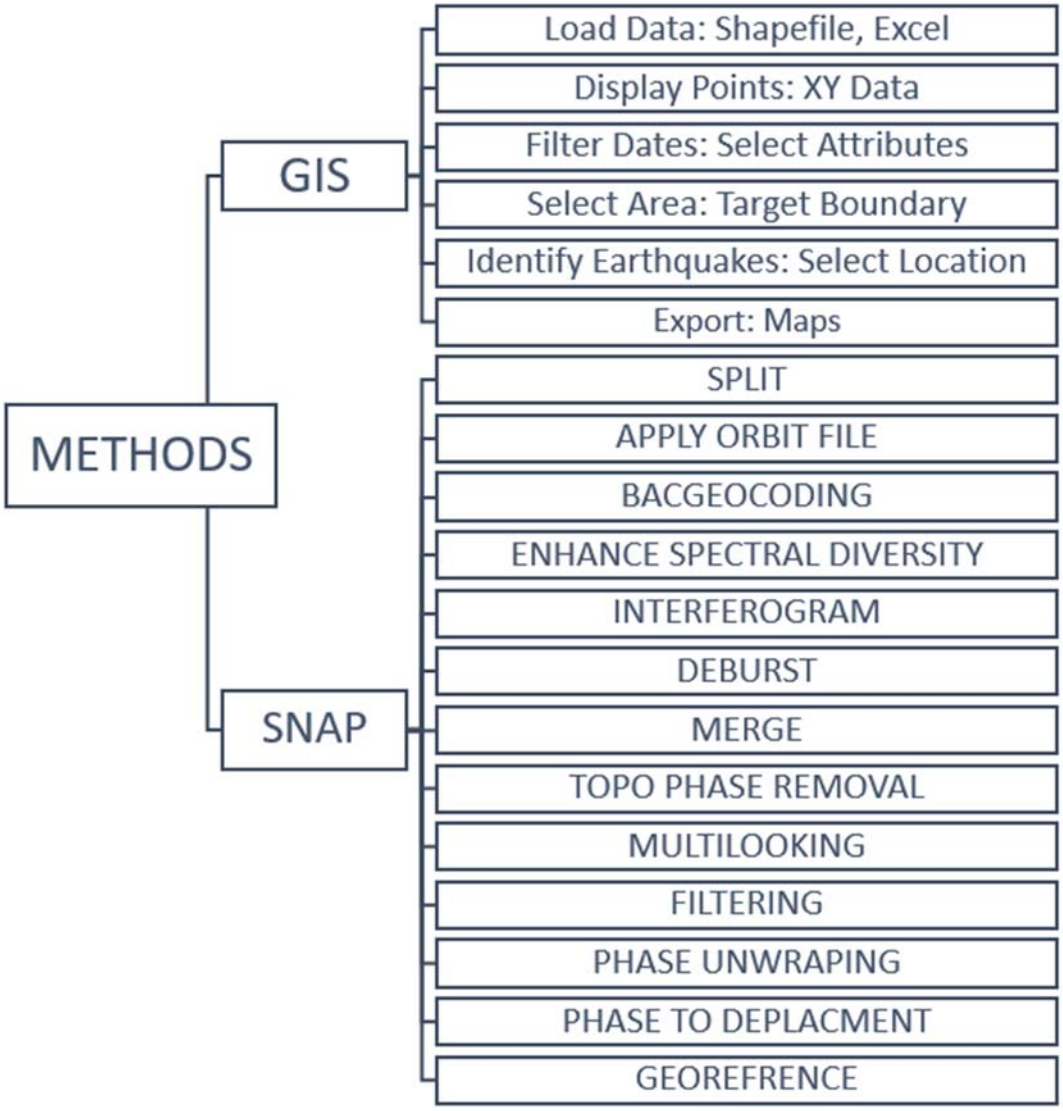

Figure 2. The methodology work flow

RESULTS AND DISSCUSIONS

The results of deformations in Khanaqin district the epicentre of earthquakes indicate that there is a process of uplift in the centre, while a subsidence occurs in the surface as we move away from it. The height is 39mm, while the drop is -47mm. The highest elevation value, which ranges between 1 and 39 mm, as shown in the figure3.

Figure 3 shows the deformation map of the swarms in the study area During the period from January to March 2019, the map created using two SAR images the first was in 30\12\2018 and the second was in 12\3\2019 the deformation calculated by snap then exported to GISpro to classified as this discredit colours. The red colour refers to the uplift area reached 39 mm while the blue refers to subsidence

(-47) mm. This deformation mad by swarm of 129 earthquakes with deferent magnitude and depth as shown in figure 4 and 5 these earthquakes classified with deferent size yellow circles.

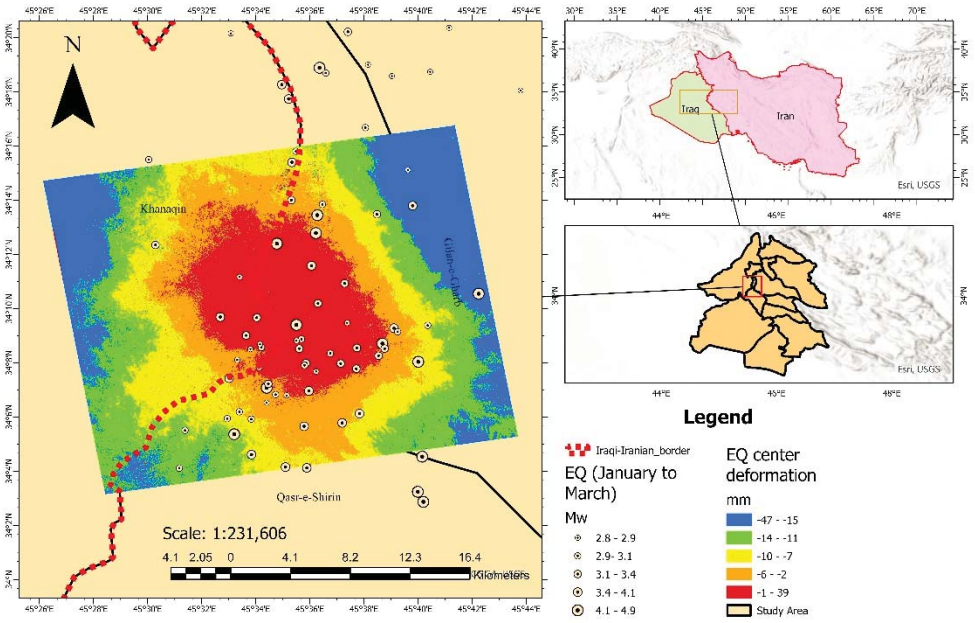

Figure 3. The displacement map of khanaqin swarms

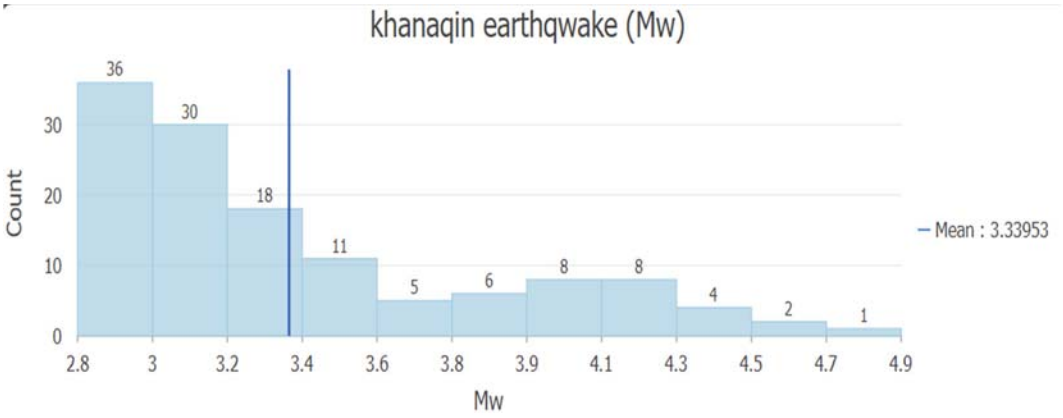

Figure 4. Magnitude (Mw) Frequency in Khanaqin Earthquake swam

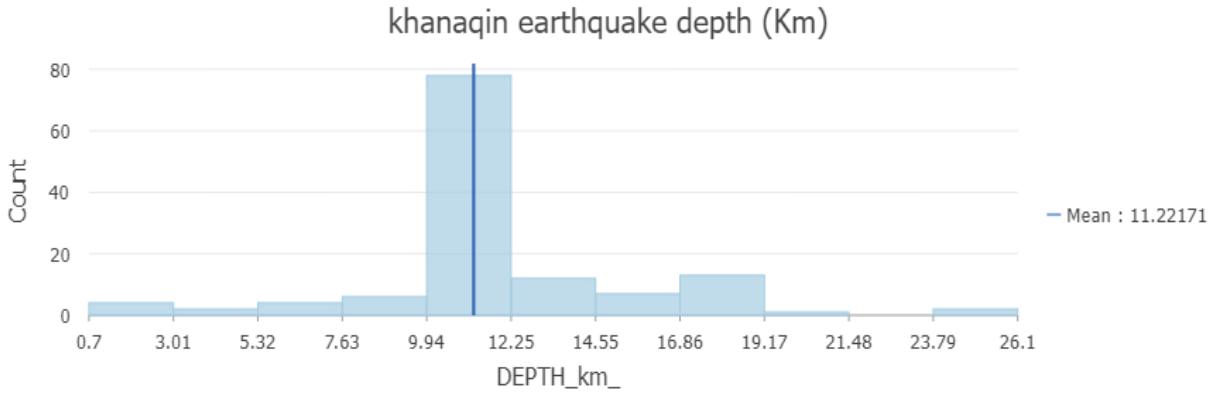

Figure 5. Depth (Km) Frequency in Khanaqin Earthquake Data

Figure 4 and 5 shows the swarms in Khanaqin during the period from January to March 2019, the Khanaqin region witnessed the occurrence of 129 earthquakes, whose magnitude ranged between 2.8 and 4.9 Mw, with an average of 3.34 Mw. These tremors occurred at depths ranging between 0.7 and 26.1 km, with an average depth of 11.4 km, The deformation distribution in Baladruz District is quit deferent. The entire area was exposed to varying subsidence ranging between -1 mm and -161 mm. The lowest percentages of decreases were in the Iraqi side, while Ilam Province in Iran recorded the highest percentage of decreases as shown in figure 6.

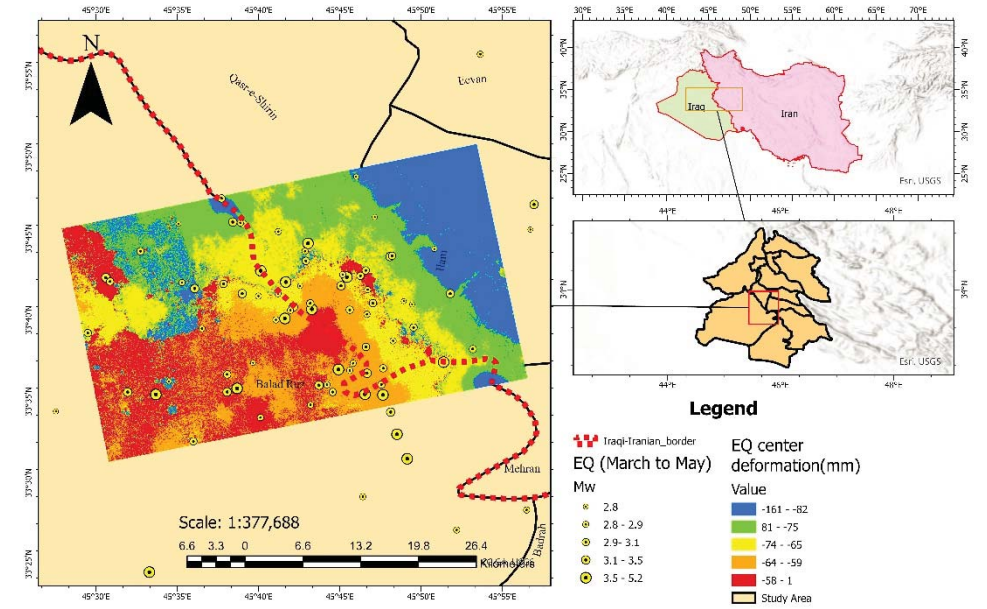

Figure 6. The displacement map of baladruz Earthquake swam

Figure 6 shows the deformation map of the swarms in Baladruz District during the period from March to May 2019, the map created using two SAR images the first was in 12\3\2019 and the second was in 11\5\2019 the deformation calculated by snap then exported to GISpro classified as this discredit colors. The red color refers to the less subsidence area below -58mm while the blue refers to high subsidence reached -161mm. This deformation mad by swarm of 135 earthquakes with deferent magnitude and depth as shown in figure 7 and 8 these earthquakes classified with deferent size yellow circles

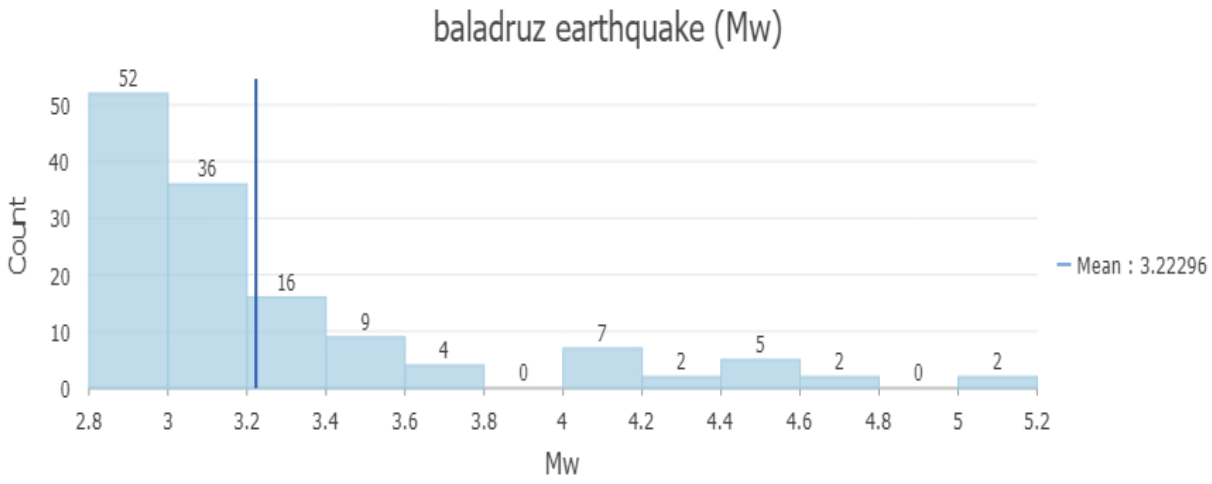

Figure 7. Mw Frequency in Baladruz Earthquake Data

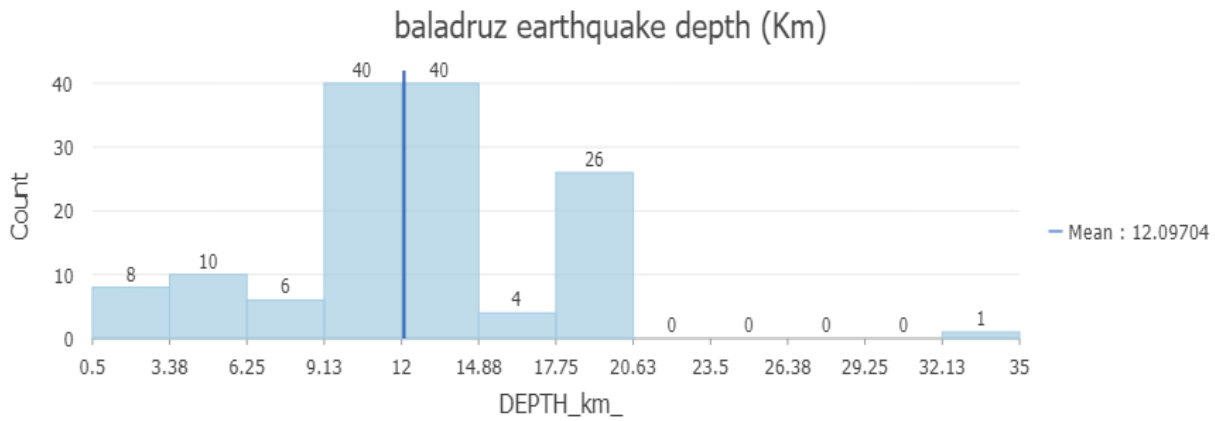

Figure 8. Depth Frequency in Baladruz Earthquake Data

Figure 7 and 8 shows the swarms in Baladruz District During the period from March to May 2019 region witnessed the occurrence of 135 earthquakes, their intensity ranged between 2.8 and 5.2 Mw, with an average of 3.2 Mw. These tremors occurred at depths ranging from 0.5 to 35 km, with an average depth of 12 km,
Due to Baladruz's proximity to the floodplain, earthquakes there caused the land to subside due to the soft soil and its relative distance from the fault. While in Khanaqin, the effects of earthquakes caused some areas to subside and others to rise, due to their relative proximity to faults.

CONCLUSION

The results show that low-magnitude earthquakes from 2.5 to 5.0 Mw cause minor, almost unnoticeable deformations. However, thanks to remote sensing techniques and SAR satellite images, these deformations can be identified with very high accuracy down to millimetres. In addition, Snap is considered one of the most powerful tools for processing and analysing these images, and we should not forget the role of Geographic Information Systems (GIS) programs in classifying, producing maps, and adding final touches. In addition, the earthquakes that occurred in the two regions are not only related to the number, depth, or intensity of the earthquakes, but are also more influenced by the nature of the earth. In general, the lower the intensity and depth of the earthquakes, the smaller their effects, and vice versa. The low intensity earthquake can have made deformations but no damage or causing people death.

REFERENCES

1. Aydan Ö, Nasiry N Z, Ohta Y and Ulusay R 2018 Effects of earthquake faulting on civil engineering structures Journal of Earthquake and Tsunami 12 1841007
2. Sarah T. Yaseen, Auday H. Shaban, Kareem A. Jasim, Flood Behavior of Al-Hammar Marshes, IOP: Journal of Physics: Conference Series, 032062, Volume 1879, 2021.
3. Eyidoğan H 1988 Rates of crustal deformation in western Turkey as deduced from major earthquakes Tectonophysics 148 83-92
4. Auday H. Shaban, Flood Scenario of Tigris River in Baghdad City, Iraqi Journal of Science, Vol 64 No 7, pp: 3717-3724 ,2023
5. Ali Adnan N. Al-Jasim, Taghreed Abdulhameed Naji, Auday H. Shaban, The Effect of Using the Different Satellite Spatial Resolution on the Fusion Technique, Iraqi Journal of Science, Vol. 63, No. 9, pp: 4131-4141, 2022.
6. Siebert L, Cottrell E, Venzke E and Andrews B 2015 Earth's volcanoes and their eruptions: An overview The encyclopedia of volcanoes 239-55
7. Glago F J 2021 Flood disaster hazards; causes, impacts and management: a state-of-the-art review Natural hazards-impacts, adjustments and resilience 29-37
8. Oro A, Blanc P A, Colavitto B, Rivas C, Rothis L M, Vargas H N and Perucca L P 2023 Surface deformation and secondary effects of the January 18, 2021 (Mw 6.5) San Juan (Argentina) earthquake from remote sensing techniques International Journal of Earth Sciences 112 2267-91
9. Yin Y, Wang F and Sun P 2009 Landslide hazards triggered by the 2008 Wenchuan earthquake, Sichuan, China Landslides 6 139-52

10. Scaioni M, Marsella M, Crosetto M, Tornatore V and Wang J 2018 Geodetic and remote-sensing sensors for dam deformation monitoring Sensors 18 3682
11. Dering G M, Micklethwaite S, Thiele S T, Vollgger S A and Cruden A R 2019 Review of drones, photogrammetry and emerging sensor technology for the study of dykes: Best practises and future potential Journal of Volcanology and Geothermal Research 373 148-66
12. Dierking W and Dall J 2007 Sea-ice deformation state from synthetic aperture radar imagery—Part I: Comparison of C-and L-band and different polarization IEEE transactions on Geoscience and Remote Sensing 45 3610-22
13. Osmanoğlu B, Sunar F, Wdowinski S and Cabral-Cano E 2016 Time series analysis of InSAR data: Methods and trends ISPRS Journal of Photogrammetry and Remote Sensing 115 90-102
14. Stramondo S, Chini M, Bignami C, Salvi S and Atzori S 2010 X-, C-, and L-band DInSAR investigation of the April 6, 2009, Abruzzi earthquake IEEE Geoscience and Remote Sensing Letters 8 49-53
15. Jin Z and Fialko Y 2021 Coseismic and early postseismic deformation due to the 2021 M7. 4 Maduo (China) earthquake Geophysical Research Letters 48 e2021GL095213
16. Sayyid B H, Shaban A H and Abd N A 2023 The 25 november 2018 Mw 6.3 Iraq-Iran border earthquake by using InSAR technique. In: AIP Conference Proceedings: AIP Publishing)
17. Baqer H. Sayyid, Auday H. Shaban, Najah A. Abd, Estimated deformation for two events 6 Mw and 7.3 Mw Iraq-Iran border earthquake by using Sentinel-1 satellite imagery, AIP Conf. Proc., Vol. 3018, pp: 020057(1-9), 2023
18. Kader M A and Jahan I 2019 A review of the application of remote sensing technologies in earthquake disaster management: Potentialities and challenges. In: Proceedings of the International Conference on Disaster Risk Management, Dhaka, Bangladesh, pp 12-4
19. Al-Banna A S and Ali K K 2018 The transition tectonic zone between the two parts of the platform in Iraq: A review study Iraqi Journal of Science 59 1086-92
20. diva gis https://diva-gis.org/.

Study the effect of each of the dislocation and the burgers vector on the lattice parameters through x-ray peak profile analysis

Maysaa A. Hameed [a] , Khalid H. Harbbi [b]

Department of Physics, College of Education for Pure Sciences, University of Baghdad, Baghdad, Iraq

[a] Corresponding author: Missaa.Akram2204m@ihcoedu.uobaghdad.edu.iq
[b] Khalid.h.h@ihcoedu.uobaghdad.edu.iq

Abstract. This research uses the X-ray diffraction technique to obtain the lines of the X-ray diffraction pattern of ZnO nanoparticles, which are (100), (002),(101),(102),(110),(103),(112). An analysis of these peaks uses two analysis methods, the Scherrer and the Halder-Wagner methods. The results of these methods for the crystalline size are (21.74) nm of the Scherrer method and (39.65) nm of the Halder-Wigner method. And the lattice strain was (0.00412) through the Scherrer method and (0.0033) for the Halder-Wigner method. Other results of dislocation density and burger vector for the Scherrer method are (0.0021) nm and (0.340) and for the Halder-Wigner method are (0.000636) and (0.5017), respectively.

Keywords: X-ray diffraction, Scherrer method, The crystalline size, Dislocation density.

INTRODUCTION

The first scientist "Paul Scherrer" showed his findings in a 1918 paper that included the equation that would later be known as the Scherrer equation [1]. An increasingly common method for testing materials is X-ray diffraction (XRD). The material's composition, including its crystalline size, strain, stress, density, and energy, was determined by diffraction data, for determining crystallite size, X-ray peak, profile analysis is the most commonly used technique [2,3]. uses various techniques, X-ray diffraction (XRD) including methods to analyze such as Halder -Wagner and Scherrer, which depend on analyzing the full width at half maximum (FWHM) and the angle 2θ of X-ray diffraction. By analyzing the X-ray profile, one can learn more about nanoparticle composition, size, and shape [4,5]. In the method of Halder-Wagne where Gauss and Lorentzian describe the strain and crystallite size profiles [4.6]. Scanning electron microscopy and X-ray diffraction examined the sample ZnO shape and structure. ZnO wurtzite structure was discovered using X-ray diffraction. Lattice contraction rate and average, the sample's particle size were also determined using the XRD. ZnO nanoparticles' spherical form was visible in SEM micrographs [6,7]. At room temperature, ZnO exhibits a very valuable excitation binding energy of 60 meV and a band gap energy of 3.37 eV [8]. Zinc oxide (ZnO) has a fully ionic molecular bonding (Zn+2-O-2), with corresponding radii of about 0.074 nm for Zn+2 and 0.140 nm for O-2[9]. It has a hexagonal lattice structure with properties determined in the laboratory such as a=b=0.325nm, and c=0.5207nm. and its angles alpha=beta=90 and gamma=120. Its calculated density is 5.67 g/cm^3 and the volume of the cell is 47.63 x 106 pm^3.

PREPARATION METHODS

Scherrer Method

the Scherrer formula is most likely the most widely used formulation in X-ray science. The full width (FWHM) and the breadth are connected by the Scherrer method expansion brought on by the crystal's size and the mineral's lattice

Technologies and Materials for Renewable Energy, Environment and Sustainability
AIP Conf. Proc. 3321, 020030-1–020030-6; https://doi.org/10.1063/5.0291626
Published under an exclusive license by AIP Publishing. 978-0-7354-5231-2/$30.00

strain. Each of these processes has a complex contribution that leads to an overall expansion of the diffraction peaks [10,11]. Scherrer's equation for the ideal state of a series, monochromatic (X-ray) beams incident on the monodisperse powder of crystals shaped like a cube is derived. The approach is a simple, useful, and widely used way to calculate crystallite size using XRD analysis peak broadening, the crystallite size can be calculated from the equation:

$$D= K \lambda/\beta \cos \theta \text{ [10] } \ldots\ldots \quad \ldots. (1)$$

Where K is the form factor (0.89), D denotes crystallite size, θ is Bragg's angle in degree, and λ is the x-ray beam wavelength 0.15406 nm. The lattice strain ξ can be determined using the equation derived from line broadening. Where ξ is the lattice strain and (β) is the integral breadth [1-14]:

$$\xi= (\beta \cos \theta/ 4) \ldots\ldots \quad \ldots\ldots(2)$$

The Halder-Wagner method

Halder and Wagner suggested a different equation that included the lattice plane spacing d, and the integral breadth β, to determine D and ε.

$$(\beta/d) ^2= (k /D). ((\beta/d) ^2) +(2\xi) ^2\ldots\ldots\ldots \quad . (3)$$

$$B=\beta\cos/\lambda\ldots\ldots\ldots \quad . (4)$$

$$d=2\sin\theta/\lambda\ldots\ldots \quad \ldots. (5)$$

based on an assumption that the size and strain effects alone account for the Lorentzian and Gaussian components of β, respectively:

$$(\beta \ /\tan)^2=(k \lambda/D). (\beta/ \tan \theta \sin \theta)+ (16 \xi) ^2\ldots\ldots\ldots\ldots\ldots \quad \ldots(6)$$

The Halder-Wagner (HW) plot involves plotting $y = (\beta /\tan \theta)^2$ against $x = \beta/ (\tan \theta \sin \theta)$, resulting in a straight line from which K λ/D and $16\varepsilon^2$ can be determined from the slope and y-intercept can be determined by the equation:

$$D= k \lambda/\text{slope}\ldots\ldots \quad \ldots. (7)$$

To calculate the lattice strain, use the following equation [11-16]:

$$\xi= (\text{intercept}/16)^(1/2) \ldots \quad \ldots\ldots(8)$$

Dislocation density (ρ) and Burger vector (b)

dislocation density (ρ) can be determined by using the following equation in manometer: The symbol ρ represents the dislocation density, while D represents the crystallite size, Determine the Burgers vector(b) using the equation:

$$b = ((14.4\xi^{2}) /\rho)^{1/2} \ldots\ldots\ldots\ldots \quad \ldots\ldots\ldots(9)$$

Where (b) represents the Burgers vector in manometer [17].

RESULTS AND DISCUSSION

Various peaks corresponding to different planes of ZnO were observed in the XRD patterns. Using the Japanese SHIMADZU model (6000) Cu-k diffractometer, ZnO nanoparticle intensity data was collected for all seven peaks. This data is utilized to create the outline of the peaks with the help of an analytical program called Origin Pro Lab. The program calculates the area under the curve and the FWHM and is then used to calculate the integral breadth [18, 19]. This process was demonstrated for only one surface (100) and the same steps were performed for the rest of the other surfaces.

The Scherrer method

Estimated the crystallite size D of the ZnO nanoparticle in the manometer using equation (1) , the lattice strain ξ by using equation(2), and dislocation density (ρ) using equation(9)and to determine the Burgers factor(b) using the equation(10), The results shown in Table(1)and (2), Which was created using Excel.

Table 1. calculation used for the Scherrer method.

(hkl)	2θ(dgree)	Θ (rad.)	Cos θ	Tan θ	β (rad.)
(100)	31.84184	0.277731604	0.961679849	0.285099959	0.005443344
(002)	34.48514	0.300787054	0.955103603	0.310198827	0.005735701
(101)	36.32342	0.316820941	0.950230645	0.327864927	0.006134363
(102)	47.61562	0.415314019	0.914989666	0.44096375	0.0081126
(110)	56.68438	0.494413759	0.880247042	0.539071049	0.007029933
(103)	62.94059	0.548981813	0.853056274	0.611705165	0.009168982
(112)	68.03268	0.593396153	0.829046403	0.67448554	0.00856896

Table 2. Estimating crystallite size, lattice strain, dislocation density, and burgers vector for the Scherrer method.

Dav.(nm)	ξav.	ρ (1/nm^2)	b
21.74	0.00412	0.0021	0.340

Halder -Wagner method

An analytical tool called Origin Pro Lap was used to analyze the shape of the peaks in ZnO. The peaks were zoomed in on using the magnification tool before the analysis process began. To start the analysis, click on the "Gadget Tool" tab at the top of the Origin window. This will open another window where you can go to the "Find Peak" tab. Then Set the height to the maximum and the baseline to a straight line [20, 21]. After completing the fitting, select "Fit Peak" and click on the Gaussian to apply the fitting. The program calculates the area under the curve and the full width at half maximum (FWHM). we get the results shown in Table (3) Which was created using Excel. from fig. (1), (2), and (3).

Table 3. Calculation used for (H.W) plot.

(hkl)	2θ(dgree)	θ(rad.)	tanθ	sinθ	β(rad)	β/(tanθsinθ)	(β/tanθ)²
(100)	31.84	0.277	0.285	0.274	0.0054	0.0696	0.000364

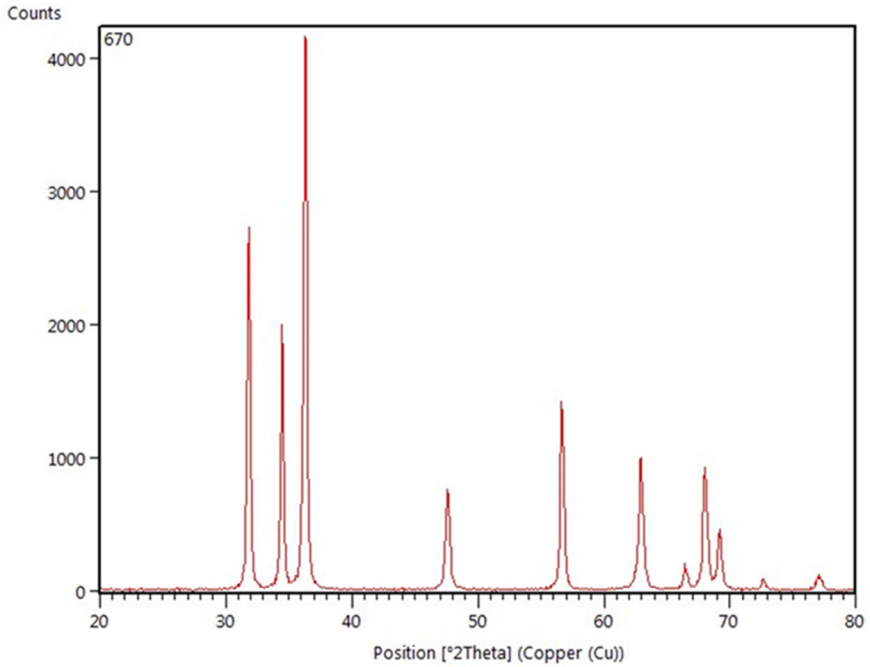

Figure 1. X-ray pattern of ZnO nanoparticle.

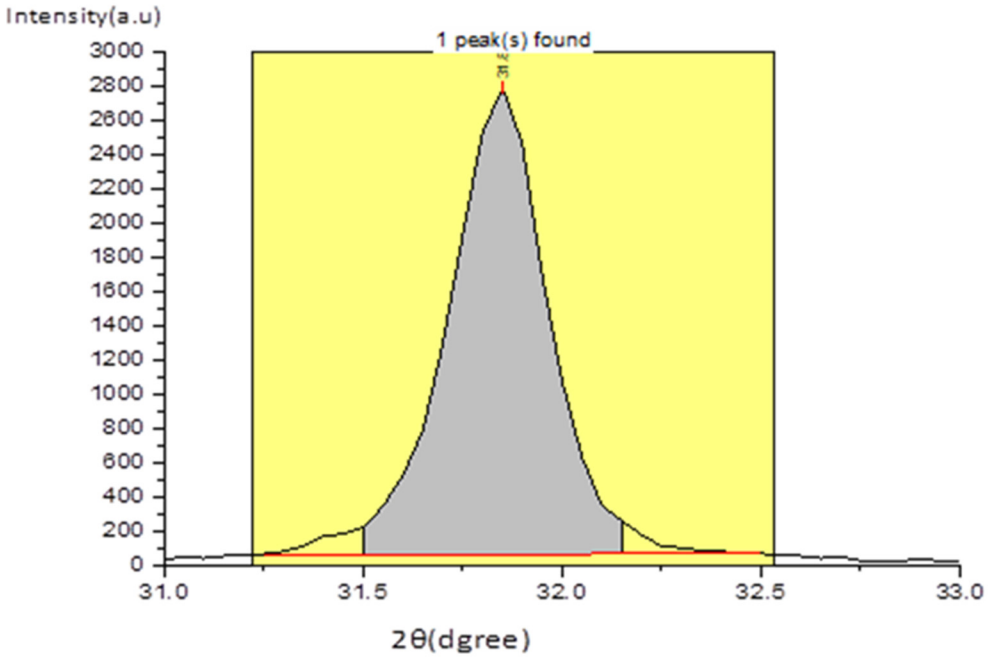

Figure 2. peak (100) of ZnO nanoparticle.

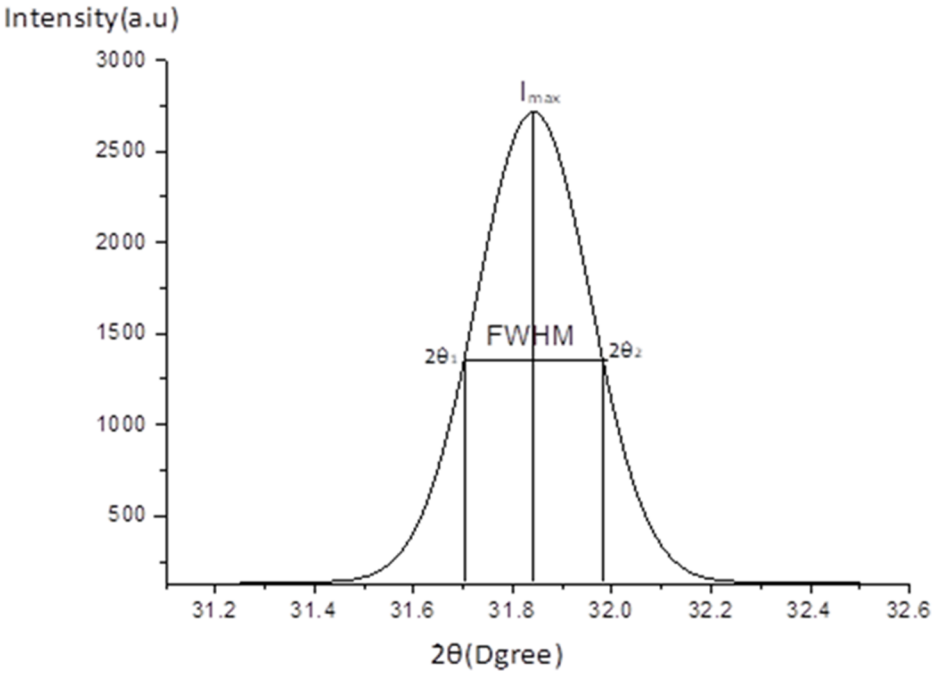

Figure (3): After fitting and determined (FWHM) peak (100).

To determine the crystallite size, lattice strain, dislocation density, and Burger vector. we plot a graph with the x-axis representing (β /tan θ sin θ) and the y-axis representing (β/ tan θ)^2 shown in Fig (4).

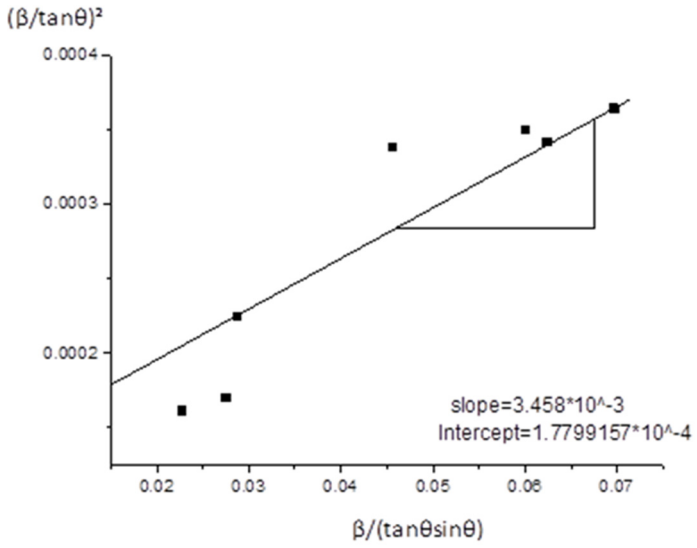

Figure (4): plot relation between (β /tan θ) and (β/ tan θ sin θ).

This helps us to obtain the intercept and the slope, which we can then use to calculate the required parameters using equations (7), (8), (9) and (10). The results are shown in Tables (4) and (5).

Table (4). results of the slope and intercept for the (H.w) method.

(hkl)	X1	X2	Y1	Y2	slope	intercept
(100)	0.0461	0.0674	0.000284	0.000358	0.00345	0.000177

Table (5). Estimating crystallite size and lattice strain for (H.W) method.

hkl	D (nm)	ξ	ρ(1/nm^2)	b
(100)	39.65	0.0033	0.000636	0.5017

CONCLUSIONS

The Halder-Wegner and Debye-Scherrer methods were used to calculate the crystal size D, lattice strain ξ, dislocation density ρ, and burger vector b. The Debye-Scherrer approach was found to be one of the quick ways to calculate the aforementioned coefficients, When the results from the two methods were compared, it was discovered that the Halder-Wigner method produced more accurate results because it uses a rate that is obtained from the shape chart and seven diffraction lines to calculate the dislocation density ρ and the burger vector b, as well as the crystal size D and lattice strain ξ.

REFERENCES

1. Sami, A. M., & Harbbi, K. H. (2022). Analysis the average lattice strain in the crystal direction (hkl) in MgO nanoparticles by using modified Williamson-hall method. *International Conference for and applied (SICPS2021): SICPS2021*. https://doi.org/10.1063/5.0122941
2. Jahil, S. S., Mohammed, I. A., Khazaal, A. R., Jasim, K. A., & Harbbi, K. H. (2022). Application the Halder – Wagner to calculation crystal size and micro strain by X-ray diffraction peaks analysis. NeuroQuantology, 20(1), 199-204. https://doi.org/10.14704/nq.2022.20.1.nq22074
3. Kamil, M.K., Jasim, K.A., Calculating of crystalline size, strain and Degree of crystallinity of the compound (HgBa2Ca2Cu3O8+σ) by different method, IOP Conference Series: Materials Science and Engineering, 2020, 928(7), 072109.
4. M. T. Jaleel and K. H. Harbbi, "Study of the x-ray diffraction lines of calcium titanate nanoparticle using SSP method and Scherrer method," in AIP Conference Proceedings, AIP Publishing, 2023. Jaleel, M. T., &

Harbbi, K. H. (2023). TECHNOLOGIES AND MATERIALS FOR RENEWABLE ENERGY, ENVIRONMENT AND SUSTAINABILITY: TMREES22Fr. https://doi.org/10.1063/5.0129557
5. P. M. Kibasomba et al., "Strain and grain size of TiO2 nanoparticles from TEM, Raman spectroscopy and XRD: The revisiting of the Williamson-Hall plot method," Results Phys., vol. 9, pp. 628–635, 2018.
6. Jasim, K.A., Makki, S.A., Almohsin, A.A. Comparison study of transition temperature between the superconducting compounds Tl0.9 Pb 0.1Ba2Ca2Cu3O9, Tl0.9Sb0.1Ba2Ca2Cu3O9-δ and Tl0.9Cr0.1Ba2Ca2Cu3O9-δ, Physics Procedia, 2014, 55, pp. 336–341.
7. K. H. Harbbi and K. A. Alsoltani, "The Effect of Annealing Temperatures on Cu2O Nanoparticle Structural Properties," Ibn Al-Haitham J. Pure Appl. Sci., vol. 36, no. 3, 2023.
8. Jasim, K.A., Mohammed, L.A., The partial substitution of copper with nickel oxide on the Structural and electrical properties of HgBa2 Ca2 Cu3xNix O8+δ superconducting compound, Journal of Physics: Conference Series, 2018, 1003(1), 012071.
9. M. Soosen Samuel, L. Bose, and K. C. George, "Optical properties of ZnO nanoparticles," Acad. Rev., vol. 16, pp. 57–65, 2009.
10. K. Alsoltani and K. H. Harbbi, "Effect of the Synthesis Time on Structural Properties of Copper Oxide," Ibn AL-Haitham J. Pure Appl. Sci.,vol. 36, no. 2, pp. 181–190, 2023, doi: 10.30526/36.2.3024.
11. Omar, B.A., Fathi, S.J., Jassim, K.A., Effect of Zn on the structural and electrical properties of high temperature HgBa2Ca2Cu3O8+δ superconductor, AIP Conference Proceedings, 2018, 1968, 030047.
12. A. K. Arora, S. Devi, V. S. Jaswal, J. Singh, M. Kinger, and V. D. Gupta, "Synthesis and characterization of ZnO nanoparticles," Orient. J. Chem., vol. 30, no. 4, pp. 1671–1679, 2014.
13. Mohammed, J.S., Hasan, M.A., Alatta, H.J., ...Shaban, A.H., Fadil, R.A.A.-Z Investigate the structural properties of Tl1-xHgxSr2Ca2Cu3O8+δcompound by using Scherrer modified equation, AIP Conference Proceedings, 2023, 2769, 020064.
14. Hasan, M.A.A., Jasim, K.A., Miran, H.A.J., Synthesis and Comparative Analysis of Crystallite Size and Lattice Strain of Pb2Ba1.7Sr0.3Ca2Cu3O10+δ Superconductor, Korean Journal of Materials Research, 2022, 32(2), pp. 66–71.
15. P. Uikey and K. Vishwakarma, "Review of zinc oxide (ZnO) nanoparticles applications and properties," Int. J. Emerg. Technol. Comput. Sci. Electron., vol. 21, no. 2, pp. 239–242, 2016.
16. S. B. A. Abbas and K. H. Harbbi, "Elimination of the broadening in X-ray diffraction lines profile for nanoparticles by using the analysis of diffraction lines method," in AIP Conference Proceedings, AIP Publishing, 2022.
17. D.-M. Smilgies, "Scherrer grain-size analysis adapted to grazing-incidence scattering with area detectors," J. Appl. Crystallogr., vol. 42, no. 6, pp. 1030–1034, 2009.
18. S. A. A. Jabir and K. H. Harbbi, "A comparative study of Williamson-Hall method and size-strain method through Xray diffraction pattern of cadmium oxide nanoparticle," AIP Conf. Proc., vol. 2307, 2020, doi: 10.1063/5.0033762.
19. F. Izumi and T. Ikeda, "Implementation of the Williamson-Hall and Halder-Wagner methods into RIETAN-FP," 2015.
20. M. T. Jalil and K. H. Harbbi, "Using the Size Strain Plot Method to Specity Lattice Parameters," Ibn AL-Haitham J. Pure Appl. Sci., vol. 36, no. 1, pp. 123–129,
21. M. A. Obaid , K. H. Harbi , A. N. Abd, "Preparation and characterization of copper oxide by addingturmeric powder,"Ibn Al-Haitham Journal for Pure and Applied Sciences, vol.36, no.1, pp.1879,2021.

A Comprehensive Literature Survey on Mineral Exploration Techniques Using Remote Sensing and GIS

Mohammed A. Mohammed [a], Faisel G. Mohammed [b], Mustafa. E. Hammadi [c], Maryam H. Ali [d], and Ali Saeed Jassim [e]

Department of Remote Sensing and GIS, College of Science, University of Baghdad, Baghdad, Iraq

Corresponding author: [a]mohammed.a.m@sc.uobaghdad.edu.iq
[b]faisel.mohammed@sc.uobaghdad.edu.iq
[c]Mustafa.e@sc.uobaghdad.edu.iq
[d]maryammarooshaa97@gmail.com
[e]alis.alrammhi@uokufa.edu.iq

Abstract. The use of remote sensing and GIS in mineral exploration is becoming increasingly important, providing valuable tools to identify potential mineral deposits and improve exploration efforts. The objectives of this literature survey are to collect relevant studies on the application of remote sensing and GIS in mineral exploration, and to assess effectiveness and progress in this field. A systematic literature search of reputable academic databases was performed to identify peer-reviewed articles related to mineral exploration using remote sensing and GIS. Articles were screened for relevance, and a comprehensive review was performed to assess suitability for inclusion. Data from selected studies were analysed to identify trends and developments in remote sensing and GIS applications for mineral exploration. The table summarizes the basic information from the relevant works, including the dataset, study area, mineral types, exploration technique and the results obtained from each study. The results generally showed the effectiveness of using remote sensing and machine learning techniques in mineral exploration. These methods produced accurate prospectively maps, identified potential mineralized areas, and reduced exploration costs. Machine learning algorithms and advanced techniques have shown high predictive accuracy in mapping the presence of minerals. Future directions promise to revolutionize mineral exploration, promoting efficiency, accuracy and sustainability in resource development.

INTRODUCTION

Mineral exploration is crucial for finding and evaluating valuable mineral deposits. The rising demand for minerals necessitates efficient exploration methods. Traditional approaches can be limited, but technological advancements have transformed the field [1]. Modern exploration relies on remote sensing and GIS. Remote sensing uses aerial data to map geological features, while GIS organizes and analyzes spatial data, aiding geoscientists in extracting insights [2]. Benefits of remote sensing include large-scale assessments, detecting subtle geological features, and identifying mineral signatures. Various devices provide valuable information on mineral groups and alteration zones [3]. GIS complements remote sensing by integrating data and enabling spatial analysis. It helps identify geological structures and potential mineralization indicators. Moreover, it aids in creating predictive models and exploration maps for decision-making [4].

The objective of the current of research works is to provide a comprehensive overview of recent developments and applications of remote sensing and GIS in mineral exploration. It aims to review and analyze the methodologies, techniques and case studies presented in relevant works to understand the state of the art in this field. By examining a range of research papers from the past five years, this survey seeks to identify trends, challenges, and opportunities in the use of remote sensing and GIS for mineral exploration. The objective of this survey is to gain insight into the effectiveness of various remote sensing techniques, such as multispectral, hyperspectral, thermal and radar systems, in mapping mineral potential. In addition, this research will explore the integration of diverse datasets, including geological and geochemical data and remote sensing, using GIS for spatial analysis and modeling. The survey will

Technologies and Materials for Renewable Energy, Environment and Sustainability
AIP Conf. Proc. 3321, 020031-1–020031-7; https://doi.org/10.1063/5.0290583
Published under an exclusive license by AIP Publishing. 978-0-7354-5231-2/$30.00

also highlight the application of machine learning algorithms, data mining techniques, and predictive modeling approaches to predictive mineral mapping.

Remote Sensing and GIS Techniques in Mineral Exploration

Remote sensing and GIS play a pivotal role in modern mineral exploration, providing valuable tools for data collection, analysis and visualization. Through the use of airborne and satellite sensors, remote sensing enables the acquisition of multispectral and hyperspectral data, providing insights into the spectral fingerprints of minerals and rock units. On the other hand, GIS allows the integration of different geospatial datasets, allowing researchers to overlay geological, topographical and remote sensing information [5].

Machine Learning (ML) and Deep Learning in Mineral Exploration

Machine learning (ML) and deep learning have emerged as transformative technologies in various fields, including mineral exploration. These technologies use algorithms to analyze massive amounts of data and identify patterns and relationships, making them well-suited for processing complex geological and remote sensing datasets. Machine learning and deep learning algorithms can be combined with remote sensing and GIS data to enhance the efficiency and accuracy of mineral exploration. By training models on historical exploration data and remote sensing imagery, ML algorithms can predict potential mineral deposits and geological mapping with greater accuracy [6, 7].

PROBLEM STATEMENT

In this section, the difficulties and obstacles faced by researchers during their mineral exploration endeavors will be explored.

However, the application of ML and deep learning in mineral exploration is not without challenges. A major challenge is the need for high-quality, labeled training data, which may be scarce in some areas. In addition, the complexity of deep learning models and their computational requirements can pose difficulties for small-scale exploration projects.

As technology advances and more labeled data sets are available, the use of ML and deep learning in mineral exploration is expected to grow. Ongoing research and development in these areas holds promise to revolutionize the industry by opening up new opportunities and improving the accuracy and efficiency of mineral exploration. By integrating ML, deep learning, remote sensing, and GIS technologies, geologists can gain deeper insights into the Earth's interior, leading to more successful discoveries of valuable mineral resources [8].

The researcher faced challenges in finding a reliable tool for mineral exploration, which led them to explore machine learning methods such as support vector machines, artificial neural networks, and random forests [9, 10]. There was difficulty in testing the effectiveness of the silicate metal mapping waveform algorithm in supra spectral thermal infrared data, especially in dealing with reststrahlen features [11]. Challenges have been faced in detecting geological features using machine learning methods in remote sensing data, underscoring the need for interdisciplinary research in this area [12, 13]. Challenges were faced in accurate mapping of mineral deposits in the Bokor region, such as dealing with data bias and geological complexity and preventing over processing of the model while using GIS data and machine learning algorithms [14].

RESEARCH OBJECTIVE

The primary objective of this literature survey is to collect relevant studies and research articles that explore the application of remote sensing and GIS in mineral exploration. The survey seeks to identify the various remote sensing and GIS technologies used, their effectiveness, and any progress made in this field. In addition, the survey aims to assess the impact of these technologies on mineral exploration, identify successful case studies, and highlight areas for further improvement and future research.

RELATED WORKS

the related works to the current study on mineral exploration includes a range of research endeavors focused on the use of advanced technologies, such as remote sensing, geographic information system, and machine learning, to

enhance the efficiency and accuracy of mineral exploration and mapping. Some important related works could be summaries in the following points:

- In 2019, Tao Sun et al., [9]. Utilized machine learning methods, including support vector machine (SVM), artificial neural networks (ANN), and random forests (RF), have been used to map GIS-based mineral exploration in the Tongling ore region in eastern China. The study used a mineral systems approach to create 12 predictive maps representing critical ore formation processes. Predictive models (SVM, ANN, and RF) were trained and validated using cross-validation, demonstrating high predictive accuracy and consistent ranking of significant features. The RF model outperformed the SVM and ANN models, providing the most accurate and effective copper potential maps, capturing 80.95% of the known deposits in 13.97% of the study area. The probability map generated by the RF model successfully identified the newly discovered sediment, confirming its effectiveness in establishing the exploration target.
- In 2019, Christoph Hecker and et al. [10], Developed a 'wavelength plot' algorithm for hyperspectral thermal infrared data. The algorithm extracts the wavelength position of the deepest absorption feature in each pixel, serving as a proxy for mineralogy, and the feature depth as a proxy for relative abundance. The algorithm was tested on a multispectral airborne TIR dataset over Yerington Batholith, Nevada, and resulted in coherent spatial patterns across the airliners. They successfully represented different types of igneous, sedimentary, and hydrothermal rocks based on the relative abundances of minerals such as quartz, feldspar, garnet, mica, and emote. The waveform plot provides a simple and reproducible per-pixel overview map to capture rock-forming mineral events.
- In 2020, Michał Lupa, et al. [11], The researchers used satellite remote sensing methods in prospecting for minerals in the Selak region of Kosovo. They collected rock samples at the site and measured their spectral properties in the laboratory. By analyzing Landsat 8 satellite images and using a curve-index fitting technique, they created mineral cluster maps. The results show that the free multispectral data from Landsat 8 effectively narrowed the exploration areas, lowering costs while identifying potential mineral areas in the region. This approach has been validated by field reconnaissance and comparison with geological and mineralogical maps.
- In 2021, Hojat Shirmard et al., [12] Reviewed the role of machine learning in processing remote sensing data for mineral exploration. They stressed the importance of geological mapping using remote sensing datasets, including rock units, modification types, structures, and indicator minerals. Machine learning methods have been found to be effective in processing spectral and ground truth measurements and creating potential maps for mineral exploration. The study highlighted the potential of advanced methods such as deep learning to handle new generation remote sensing data with high spatial and spectral resolution, leading to improved mineral exploration maps.
- In 2021, Sima Peyghambari and et al., [13] performed an updated review of hyperspectral remote sensing in geological applications. They focused on techniques for extracting geological information from high-spectral-resolution remote-sensing images, including rock and mineral mapping, mineral exploration, and environmental geology. The review covered various steps, such as atmospheric correction, dimensional processing, end-organ extraction, and image classification. The study determined that per-pixel and subpixel image classifiers can generate accurate mineral maps of change, making hyperspectral images a valuable tool in the mining industry and environmental geology. The paper included case studies to illustrate the potential of these technologies in various geological applications.
- In 2022, Nouriddine Houran and et al.,[14] This study conducted in Morocco's eastern High Atlas region, exploration geologists used geographic information systems (GIS) and machine learning methods (random forests and artificial neural network) to map mineral deposits. The methodology achieved a classification accuracy of 98%, producing predictive maps of potentially mineralized areas. By integrating different geospatial datasets such as geology, topography, and GIS, the researchers determined the spatial correlation between different features and training sites. Machine learning algorithms such as Random Forest and artificial neural networks have gained popularity in mineral mapping due to their ability to handle nonlinear correlations between known mineral deposits and spatial features. The study showed the effectiveness of machine learning in identifying different areas with mineralization potential.
- In 2023, Mahnaz Abedini and et al., [15] The researchers used mining geochemistry models to draw machine learning-based copper probability maps. By studying the distribution of indicator elements from 50 copper deposits in the CIS countries, mineralogy and geochemical (MGT) types of anomalies associated with copper mineralization were identified. Geochemical zonal models were generated using porphyry copper deposit data from Iran and Kazakhstan. The results were used to produce geochemical evidence variables and to improve remote sensing-based variables. The Random Forest algorithm combined the variables to generate a county-level probability map of porphyry copper deposits. The study highlights the effectiveness of machine learning and data integration for mineral exploration mapping.

DATASET

Data used in mineral exploration is increasingly accessible due to advances in technology and data sharing initiatives. Satellite images, one of the primary sources, can be obtained free of charge from various satellite missions. For example, the United States Geological Survey (USGS) (USGS Earth Explorer) offers Landsat, which provides decades of multispectral images available for free download [16]. The European Space Agency's (ESA) [17] Copernicus Program (ESA Copernicus Open Access Hub) offers Sentinel satellites with open access data, including Sentinel-2, which provides high-resolution multispectral images. Furthermore, radar data, which is valuable for penetrating cloud cover and detecting subterranean features, can also be obtained for free. The European Space Agency's Sentinel-1 mission provides free radar data for observations of the Earth's surface, including areas of mineral exploration. In terms of geological samples, some government geological surveys and academic institutions maintain databases and repositories where researchers can access geological samples for study and analysis [18]. For example, the United States Geological Survey (USGS) operates the National Geochemical Database (NGDB) and the National Repository for Rock and Mineral Analysis (NORMAN) (USGS National Geochemical Database (NGDB) and National Rock and Mineral Analysis (NORMAN) repositories.), providing access to geochemical data and rock samples. Apart from geological and satellite data, various online databases and repositories offer maps, reports, and valuable geological datasets for free. Organizations such as the World Bank (World Bank Open Data. [19]) and Open Topography (Open Topography [20]) provide open access geospatial data and tools for mineral exploration studies.

MATERIALS AND METHODS

The methodology used in these related works ensures a rigorous and systematic approach to collecting, reviewing and analyzing relevant studies, providing valuable insights into the current state and prospects of the use of remote sensing and GIS in mineral exploration. Regular literature search was performed in reputable academic databases, such as Web of Science, Scopus, and IEEE Xplore, to identify peer-reviewed articles related to mineral exploration using remote sensing and GIS. The search was performed using relevant keywords and topic terms, including “mineral exploration,” “remote sensing, “GIS,” spectral analysis, “machine learning,” “mapping,” and others. The inclusion criterion for the selected studies was that they should focus on the use of remote sensing and GIS techniques for mineral exploration [21].

RESULTS AND DISCUSSION

Articles were selected based on their relevance to the research topic and inclusion criteria. Initially, all selected articles were screened based on their titles and abstracts to remove studies that were not directly related to mineral exploration or did not involve remote sensing and GIS [22]. The remaining articles then underwent a comprehensive full-text review to assess their suitability for inclusion in the survey [23].

Table 1 summarizes key information from work related to remote sensing and GIS mineral exploration technologies. It includes details such as the data used, the types of minerals extracted, the methodology used, the study areas, and the results obtained from each study.

Table 1: Mineral explorations related works

Paper ID no	Dataset	Study Area and Mineral Types	Exploration technique	Outcome
[5]	GIS-based predictor maps, mineral systems approach	-Tongling ore district, China - Copper (Cu)	Support Vector Machine (SVM), Artificial Neural Networks (ANN), Random Forest (RF)	High predictive accuracy, RF model outperformed SVM and ANN, successfully identified known deposits and newly discovered deposits to generate exploration target.
[6]	Hyperspectral thermal infrared data	- Yerington Batholith, Nevada - Non-hydroxylated silicate minerals (e.g., quartz,	Wavelength Mapper algorithm	Coherent spatial patterns of different types of igneous and sedimentary rocks and hydrothermal changes based on relative abundance of minerals, per-pixel overview map of dominant rock-forming mineral events.

		feldspars, garnets, mica, epidote)		
[7]	Landsat 8 satellite images, in-situ rock samples	- Selac region, Kosovo - Not specified mineral types	Curve-index fitting technique, Landsat 8 multispectral data	Landsat 8's multispectral data effectively narrowed down exploration areas, lowered costs, identified potential mineral areas in the region, and suggested through field reconnaissance and comparison with geological and mineralogical maps.
[8]	Remote sensing data, including lithological units, alteration types, structures, indicator minerals	- Not specified area study - Various minerals relevant to mineral exploration	Machine learning methods (not specified in the summary)	Machine learning has effectively processed spectral and ground truth measurements, and advanced methods such as deep learning have been highlighted as a potential for improving mineral exploration maps.
[9]	Hyperspectral remote sensing images	- Not specified area study - Not specified mineral types	Atmospheric correction, dimensionality processing, endmember extraction, image classification	Hyperspectral images have effectively produced accurate mineral change maps, and are a valuable tool in the mining industry and environmental geology.
[10]	GIS data, machine learning (Random Forest, Artificial Neural Network)	- Eastern Anti-Atlas, Morocco - Not specified mineral types	Machine learning methods (Random Forest, Artificial Neural Network)	It achieved approximately 98% classification accuracy, produced predictive maps of potentially mineralized areas, and demonstrated the effectiveness of machine learning in determining mineralization potential.
[11]	Remote sensing data, mining geochemistry models	-Iran, Kazakhstan -Copper (Cu)	Random Forest algorithm	A provincial-level probability map of porphyry copper deposits was generated, highlighting the effectiveness of machine learning and data integration for mineral prospecting mapping.

The collected data was analyzed to identify common trends, recurring themes, and developments in the application of remote sensing and GIS in mineral exploration. The analysis focused on comparing different techniques used by different researchers, assessing their effectiveness, and identifying any emerging technologies or approaches in the field.

CONCLUSIONS

Based on findings from related works, the use of remote sensing and GIS in mineral exploration has emerged as a powerful and versatile toolkit. The studies reviewed demonstrate the effectiveness of these techniques in various aspects of mineral exploration, and offer significant advantages for identifying potential mineral deposits and improving exploration efforts.

The related works provides valuable insights into the use of advanced techniques and methodologies for mineral prospectively mapping and exploration. Researchers have explored various data sources, including remote sensing data, GIS datasets, and mining geochemistry models, to effectively identify and map different types of minerals for exploration purposes. The application of machine learning algorithms, such as Random Forest, Support Vector Machine, and Artificial Neural Networks, has been demonstrated to achieve high predictive accuracy in mapping mineral occurrences.

The studies highlight the importance of hyperspectral remote sensing images in geological applications, including rock and mineral mapping, mineral exploration, and environmental geology. These high-resolution spectral images, combined with specialized algorithms, can generate accurate mineralogy maps of change, making them valuable tools in the mining industry and environmental geology.

The use of a 'wavelength plot' algorithm for hyperspectral thermal infrared data showed promising results, producing per-pixel overview maps of the dominant rock-forming mineral events. This algorithm allows identification of different types of igneous, sedimentary, and hydrothermal rocks based on the relative abundance of minerals.

Data integration and GIS-based approaches have been effective in identifying potential mineral areas, significantly reducing exploration costs and narrowing down exploration areas efficiently. Validation of these methods through field survey and comparison with geological and mineralogical maps enhances their practicality and reliability.

Studies emphasize the critical role of machine learning, GIS techniques, and advanced algorithms in processing and analyzing diverse geospatial datasets for mineral exploration. The ability to handle large amounts of data and identify patterns and correlations between mineral events and spatial features make machine learning methods a valuable tool for creating mineral exploration maps.

The combination of cutting-edge technologies, such as machine learning and remote sensing, with traditional fieldwork methods enhances the accuracy and efficiency of mineral exploration. These innovative approaches allow geologists and exploration experts to make informed decisions, target potential mineral deposits more effectively, and improve exploration efforts. The continuous development and application of advanced methodologies will improve mineral exploration mapping, support sustainable resource exploration and contribute to the growth of the mining industry.

In conclusion, the methodology used in these related works provided a solid foundation for understanding the current landscape of mineral exploration using remote sensing and GIS. The insights gained from this survey can serve as a valuable resource to guide future research directions and facilitate progress in the field of mineral exploration. Overall, the integration of remote sensing and GIS into mineral exploration is a critical area of ongoing research and has huge potential to shape the future of the mining industry.

Future trends and emerging trends in mineral exploration include developments in sensing technologies (hyperspectral, lidar, drones), artificial intelligence and machine learning algorithms for data processing and predictive modeling, integration of diverse data sources, and use of unmanned aircraft and mobile systems for real-time analysis. , Cloud Computing for Data Storage and Collaboration , Integration of Satellite and Ground Data , Remote Sensing for Environmental Monitoring , Developments in Autonomous Exploration Technologies , Establishing Spatial Data Infrastructure (SDI) for Data Interoperability. These trends promise to revolutionize mineral exploration by promoting efficiency, accuracy, and sustainability, leading to informed decision-making and responsible resource development.

Acknowledgments

In this section, you can acknowledge any support given which is not covered by the author contribution or funding sections. This may include administrative and technical support or donations in kind (e.g., materials used for experiments).

REFERENCES

[1] Kumar, S. S., Arivazhagan, S., & Rangarajan, N. (2013). Remote sensing and GIS applications in Environmental Sciences – A review. Journal of Environmental Nanotechnology, 2(2), 92-101.

[2] Mansouri, E., Feizi, F., Jafari Rad, A., & Arian, M. (2018). Remote-sensing data processing with the multivariate regression analysis method for iron mineral resource potential mapping: A case study in the Sarvian area, Central Iran. Solid Earth, 9, 373–384. doi:10.5194/se-9-373-2018.

[3] Yousefi, M., et al. (2019). Exploration information systems – A proposal for the future use of GIS in mineral exploration targeting. Ore Geology Reviews, 111, 103005.

[4] Soe, M., Takashima, I., Zaw, K., & Swe, Y. M. (2017). Remote sensing and GIS studies of alteration and predictive mineral exploration in the Central Volcanic Arc, Myanmar. Geological Society, London, Memoirs, 48(1), 473-96.

[5] Chattoraj, S. L., Prasad, G., Sharma, R. U., van der Meer, F. D., Guha, A., & Pour, A. B. (2020). Integration of remote sensing, gravity and geochemical data for exploration of Cu-mineralization in Alwar basin, Rajasthan, India. International Journal of Applied Earth Observation and Geoinformation, 91, 102162.
[6] Zuo, R. (2017). Machine Learning of mineralization-related geochemical anomalies: a review of potential methods. Natural Resources Research, 26, 457–464.
[7] Sun, T., Li, H., Wu, K. X., Chen, F., Zhu, Z., & Hu, Z. J. (2020). Data-driven predictive modeling of mineral prospectivity using machine learning and deep learning methods: A case study from Southern Jiangxi Province, China. Minerals, 10, 102. https://doi.org/10.3390/min10020102
[8] Xiong, Y. H., Zuo, R. G., & Carranza, E. J. M. (2018). Mapping mineral prospectivity through big data analytics and a deep learning algorithm. Ore Geology Reviews, 102, 811–817. https://doi.org/10.1016/j.oregeorev.2018.10.006.
[9] Sun, T., Chen, F., Zhong, L., Liu, W., Wang, Y. (2019). Machine learning-based GIS mineral prospectivity mapping in the Tongling ore district, China. Ore Geology Reviews, 105, 95-107. DOI: 10.1016/j.oregeorev.2018.11.010.
[10] Hecker, C., van Ruitenbeek, F. J. A., Bakker, W. H., Fagbohun, B. J., Riley, D., van der Werff, H. M. A., ... van der Meer, F. D. (2019). Wavelength Mapper: An algorithm for hyperspectral thermal infrared data to identify dominating rock-forming minerals. Remote Sensing of Environment, 233, 111368. DOI: 10.1016/j.rse.2019.111368.
[11] Lupa, M., Adamek, K., Leśniak, A., & Pršek, J. (2020). Satellite remote sensing methods in mineral prospecting in Kosovo's Selac region. Journal of Applied Remote Sensing, 14(3), 034528. DOI: 10.1117/1.JRS.14.034528.
[12] Shirmard, H., Farahbakhsh, E., Muller, R. D., & Chandra, R. (2021). Machine learning's role in processing remote sensing data for mineral exploration. International Journal of Applied Earth Observation and Geoinformation, 104, 102594. DOI: 10.1016/j.jag.2021.102594.
[13] Peyghambari, S., & Zhang, Y. (2021). Hyperspectral remote sensing in geological applications: A review. Remote Sensing of Environment, 255, 112342. DOI: 10.1016/j.rse.2021.112342.
[14] Houran, N., Ait Raoui, H., Manaan, M., Aabi, A., Simou, M. R., & Rhinane, H. (2022). Using GIS data and machine learning for mineral mapping: Case study, Bou Skour Eastern Anti-Atlas, Morocco. Arabian Journal of Geosciences, 15(5), 248. DOI: 10.1007/s12517-022-09101-6.
[15] Abedini, M., Ziaii, M., Timkin, T., & Beiranvand Pour, A. (2023). Mining Geochemistry Method and Remote Sensing Satellite Data for Machine Learning-Based Copper Mineralization Prospectivity Mapping. International Journal of Applied Earth Observation and Geoinformation, 106, 102791. DOI: 10.1016/j.jag.2022.102791.
[16] USGS Earth Explorer. URL: https://earthexplorer.usgs.gov/.
[17] ESA Copernicus Open Access Hub. URL: https://scihub.copernicus.eu/dhus.
[18] USGS National Geochemical Database (NGDB) and National Rock and Mineral Analysis (NORMAN) repositories. URL: https://mrdata.usgs.gov/ngdb/rock/.
[19] World Bank Open Data. URL: https://data.worldbank.org/.
[20] Open Topography. URL: https://www.opentopography.org/.
[21] Al ZahraaYaseen Alsajjad Mohammed A Mohammed Show, Yaseen Alsajjad, Preparation of Ge -Se -Sb ternary alloys and study of the effect of antimony on electrical properties, extended and localized energy states, AIP Conf. Proc. 3018, 020037 (2023. DOI: 10.1063/5.0171583.
[22] Mohammed A. Mohammed, Khansaa N. Aklo, Anaam W. Watan, Kareem A. Jasim, Ebtisam M-T. Salman, Iraqi Journal of Applied Physics, Vol. 20, No. 2B, May 2024, pp. 393-398
[23] Al Zahraa Yaseen Alsajjad; Mohammed A. Mohammed; Kareem A. Jasim, AIP Conf. Proc. 3018, 020037 (2023)

Simulation and analysis the effect of the electron velocity on the electron path and the generation of photons within the undulator of free electron laser

Jaafar Hussein Sabri [a], Thair Abdulkareem Khalil Al-Aish [b]

Department of Physics, College of Education for Pure Sciences Ibn Al-Haitham, University of Baghdad, Baghdad, Iraq.

[a] Corresponding author: Jaafar.Sabri2204p@ihcoedu.uobaghdad.edu.iq
[b] thair.ak.i@ihcoedu.uobaghdad.edu.iq

Abstract. in this paper, it has been an investigates the dynamic interplay between the speed of the electron beam and various key parameters in a Free Electron Laser (FEL) system. Through extensive simulations and empirical data, a clear correlation is established between the energy supplied to the electron beam and its velocity. This relation is pivotal in understanding the behavior of the (FEL), as it directly influences the Lorentz force, a critical component in laser production. The study elucidates how the Lorentz force, manipulated by factors like magnetic flux strength, electron speed, and the beam's entry angle, governs the oscillatory movement of electrons in the undulator. This movement results in variable speeds, aligning with the magnetic field's direction and facilitating the emission of coherent photons. Additionally, the research highlights the direct proportionality between electron beam energy and initial power (P_0) and an inverse relationship with photon energy (E_{ph}) and the number of photons (N_{ph}). Furthermore, a direct relationship is observed between the energy of the electrons (E_e) and the laser power (P_z). These findings significantly contribute to the understanding of (FEL) systems and pave the way for optimizing laser output through precise control of electron beam parameters.

Keywords. Free Electron Laser, Electron Beam Speed, Lorentz Force, Magnetic Flux, Photon Emission, Laser Power, Undulator, Coherent Photons, Beam Dynamic.

INTRODUCTION

In the seventies of the last century, the physicist John Madey invented and designed a laser system that works in an innovative and new way, This system is better than traditional lasers in several aspects, including that it can generate and produce a wide spectrum of laser wavelengths without the need to change the type of active medium material or geometry of resonator, The general definition of the laser system is called the free electron laser (FEL) [1], and the effective medium of this (FEL) laser is a beam or stream of electrons passing through a system of magnets consisting of two rows and arranged periodically, alternating and opposite, generating a periodic and opposite magnetic field, and this periodic magnetic field works to impede the movement of these The beam or stream of electrons moves in an oscillatory manner, where a force called the Lorentz force will arise [2], which affects the electron particles, which are considered negatively charged particles. As a result of this obstruction and this oscillation, the high energy that was supplied to the electron beam is transformed and translated into the form of high speeds with which the electron travels within the magnetic field. A laser beam consisting of coherent photons will be generated [3] [4]
By reviewing previous research and the literature that devoted its calculations to the subject of the free electron laser, it was found that the effect of the electron velocity on the electron path and the generation of photons has not been studied extensively, despite its extreme importance in influencing the generation of coherent photons and the oscillatory movement of the electron, Therefore, the focus of this work was to analyze the effect of the electron velocity on the electron path and the generation of photons within the undulator of free electron laser

Technologies and Materials for Renewable Energy, Environment and Sustainability
AIP Conf. Proc. 3321, 020032-1–020032-9; https://doi.org/10.1063/5.0290410
Published under an exclusive license by AIP Publishing. 978-0-7354-5231-2/$30.00

In this paper, the (FEL) executive program was created and designed using (MATLAB R2023a (9.14.0.2206163)), as shown in Figure (1). The interface shown for the executive program contains several parameters to simulate the requirements of the calculations that were completed for this research in terms of the change in the energy of the electrons and the change in their speed or the change in their movement pattern from accelerated linear movement to sinusoidal movement to form the synchrotron beam. During the study of this research, some factors affecting the formation of the Lorentz force were also investigated, such as the effect of the angle of entry of the electron beam into the magnetic flux or the speed of the beam. The research was conducted by dividing the movement of the electron wave into regions that differ according to the direction of the magnetic field, The effect of increasing or decreasing the speed was also calculated, and the wavelength of the photons generated in the free electron laser system depends on the electron beam. Several other important parameters were also calculated, which are (Lorentz-factor (γ), photons wavelength (λ), initial power (P_0), photon energy (E_{Ph}), number of photons (N_{ph}), gain-length (L_G), the laser power (P_Z)).

Figure 1. Shows the simulation program to analysis the effect of the electron velocity on the electron path

THEORY OF THE FREE ELECTRON LASER (FEL)

The electron beam is considered the active medium of the free electron laser, which is the most important characteristic that distinguishes the free electron laser (FEL) from traditional and conventional lasers [5], which gives it specifications that other types lack. Among these advantages is the ability to produce a wide range of wavelengths in the electromagnetic spectrum, which extends from low to very high output energies [3] [5].

There are four main components that make up the (FEL) as shown in Figure (2) [3].

1. Electron gun (source).
2. Linear accelerator of electrons (to rise speed).
3. Undulator: is defined as set of magnets arranged in reverse and periodically.
4. Resonator: is two mirrors, one of which is partially reflective and the other is fully reflective. [6] [7]

The method of its work or the mechanism of action of (FEL) is in sequential steps that begin by releasing the beam of electrons from the gun to be accelerated through the linear accelerator which works to increase its speed of electrons [8]. When the beam of electrons enters the undulator, the magnetic field generated by the undulator will strongly affect the passing beam of electrons. by Lorentz force, which hinders the movement of the electron beam and forces the electrons to oscillate in a sine wave motion, emitting two coherent photons, one at the top of the sine wave and the other at the bottom of the wave, forming a laser. [3] [9]

After using the equations found in the literature and scientific references and performing some calculations, the following were calculated: speed of electrons beam (v), magnetic field (B), Lorentz force (F), wavelength of wiggler

(λ_u), Lorentz-factor (γ), wiggler parameter (k), photons wavelength (λ), initial power (P_0), photon energy (E_{ph}), number of photons (N_{ph}), gain-length (L_G), The laser power (P_z))

$$v = c\sqrt{1 - \frac{m_e{}^2 c^4}{E_e{}^2}} \quad (1)$$

Where: v represents the velocity of the electron and depends on the energy of the particle, (m) represents the standard mass of the electron, © speed of light, (Ee) energy of electrons particles [1] [10] [11]

$$B = 4.22\, exp(-\frac{gu}{\lambda u}(5.08 + 1.54\frac{gu}{\lambda u})) \quad (2)$$

Where (B) is the magnetic field, (g_u) is undulator gap, (λ_u) wavelength of wiggler [5] [9]

$$F = qvB\, sin\, \emptyset \quad (3)$$

Where: (F) Lorentz force, (q) Standard electron charge [12] [13]

$$\gamma = \frac{Ee}{m_e c^2} \quad (4)$$

$$K = 93.3\lambda_u \beta_u \quad (5)$$

$$\lambda = \lambda_u(\frac{1}{2\gamma^2} + \frac{k^2}{4\gamma^2}) \quad (6)$$

Where: (γ) Lorentz-factor, (k) wiggler parameter, (λ) wave length of laser [14] [15]

$$P_0 = \frac{1}{9}\frac{\chi^2 c E_e}{\lambda} \quad (7)$$

Where: (P_0) initial power, (χ) scaling parameter its take value (10-2 or 10-3) [15]

$$E_{ph} = h\frac{c}{\lambda} \quad (8)$$

Where: (E_{ph}) photon energy [1] [15]

$$N_{ph} = \frac{\chi E_e}{E_{ph}} \quad (9)$$

Where: (N_{PH}) number of photons [5]

$$L_G = \frac{\lambda_u}{4\pi\sqrt{3}\chi} \quad (10)$$

Where: (L_G) gain-length [2]

$$P_z = N_{PH} P_0\, exp(z/L_G) \quad (11)$$

Where: (z) length of undulator

RESULTS AND DISCUSSION OF SIMULATION:

The main and most important benefit of the linear accelerator is that the negatively charged electrons gain very high speeds, reaching speeds close to the speed of light after these electrons have reached the accelerator from the gun [16]. Referring to Figure (2), the electrons are supplied with very high energy through a high voltage source with a range ranging from one megaelectron volt to five hundred mega electron volts. In this research, we will study the range from (1-300Mev), as calculations and simulations have shown that the speed of the electron beam is directly proportional to the energy supplied, and to calculate the effect of energy on the speed of the electron beam, this is done through equation (1) and the result recorded in Table (1) The relationship between electron energy supplied and the speed of the electron beam was also drawn through Figure (2)

Table 1. The speed of the electron beam resulting from the energy supplied to the beam

	E_e *in (MeV)*	E_e *in (J)*	v *in* ($\frac{m}{sec}$)
1	1	1.6e-13	257572004.6
2	30	4.8e-12	299748846.5
3	60	9.6e-12	299781555.7
4	90	1.44e-11	299787612.6
5	120	1.92e-11	299789732.5
6	150	2.4e-11	299790713.7
7	180	2.88e-11	299791246.7
8	210	3.36e-11	299791568
9	240	3.84e-11	299791776.6
10	270	4.32e-11	299791919.6

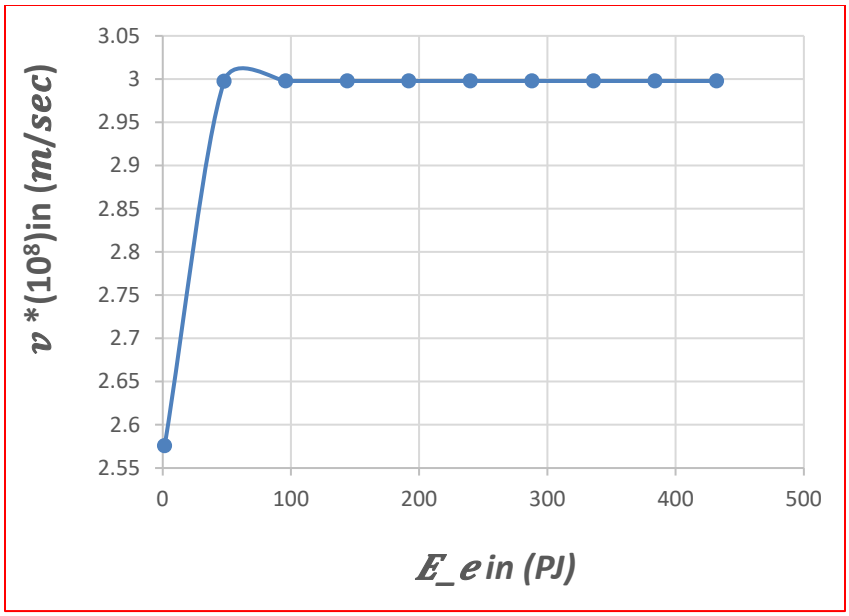

Figure 2. Graph of speed of the electron beam resulting from the energy supplied to the beam

In order to calculate the effect of the speed of the electron beam on the Lorentz force in the normal case, that is, when the entry of the electron beam is perpendicular to the magnetic field lines of the undulator, meaning that the angle between them is 90 degrees, this is done by applying equations (2,4,5,6), Simulation calculations have found that the magnitude of the magnetic flux if $\lambda_u = 0.02$ & $g_u = 0.01$, based on equation (2), is B = 0.226465 (T), In the same way, the value was calculated K = 0.422584 if $\lambda_u = 0.02$ & B = 0.226465 (T) based on equation (5), In the same way, the value of the wavelength of the laser was calculated by applying equation (6) if we consider that the mass of the electron $m_e = 9.10938356 * 10^{-31}$ *& C= 299,792,458*, the values resulting from the calculations were recorded in table (2). The relationship between the speed of the electron beam with the wavelength of the laser output was drawn through Figure (4.a) while the relationship between the speed of the electron beam with the Lorentz force was drawn through Figure (3.b)

Table 2. The value of the wavelength and the Lorentz force for the speeds studied

	v *in* $(\frac{m}{sec})$	γ	λ *in* (m)	*Lorentz force (N)*
1	257572004.6	1.95429	0.0028521	9.345663577e-12
2	299748846.5	58.6288	3168.99e-9	1.087599517e-11
3	299781555.7	117.258	792.242e-9	1.087718198e-11
4	299787612.6	175.886	352.112e-9	1.087740174e-11
5	299789732.5	234.515	198.062e-9	1.087747866e-11
6	299790713.7	293.144	126.76e-9	1.087751426e-11
7	299791246.7	351.773	88.0274e-9	1.087753360e-11
8	299791568	410.401	64.6735e-9	1.087754526e-11
9	299791776.6	469.03	49.5156e-9	1.087755283e-11
10	299791919.6	527.659	39.1234e-9	1.087755802e-11

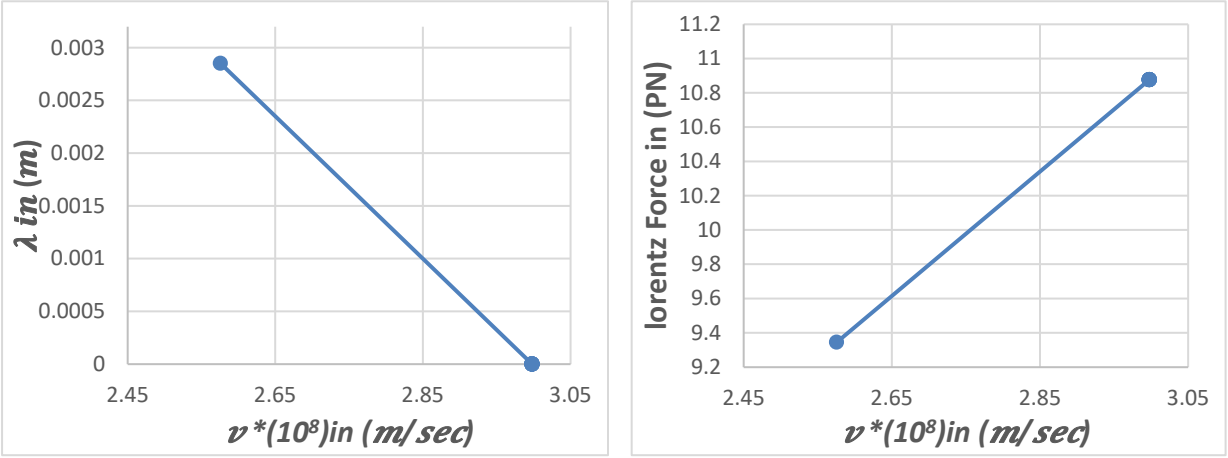

(a) (b)

Figure 3. graph that shows the relationship between the speed of the electron beam and (a) the wavelength of the laser output (b) the Lorentz force

It is noted that there is an inverse behavior between the speed of the electron beam and the wavelength of the resulting laser output

To detail and explain the magnitude of the Lorentz force affecting the electrons for each of the studied speeds and for different angles, where (θ) represents the angle between the speed of the electron beam and the magnetic flux lines of the undulator [17], this is done by applying equation (6) The results are recorded in Table (3) and the effect of different angles on the Lorentz force for the velocities studied was drawn in figure (**5**), and To find the direction of the Lorentz force, this is done using the left-hand rule, where the index finger of the left palm represents the direction of movement of electrons, while the other fingers of the same palm represent the direction of movement of electrons. The magnetic flux lines of the undulator, while the thumb will represent the direction of the Lorentz force resulting from the interaction of the magnetic field with the particle field [2].

Table 3. showing the effect of different angles on the Lorentz force for the velocities studied

θ	F at v $=257572004.6$	F at v $= 299748846.5$	F at v $=299781555.7$	F at v $=299787612.$	F at v $= 299789732.5$
90	9.345663174	1.587599470	2.087718151	2.587740160	3.087747819
110	8.782050721	1.522009196	2.022120720	2.522141402	3.022148599
130	7.159193342	1.333149530	1.833240445	2.333257305	2.833263173
150	4.672831587	1.043799735	1.543859075	2.043870080	2.543873910
170	1.622857379	6.888596660	1.188880275	1.688884097	2.188885427
190	-1.622857379	3.111403340	8.111197253	1.311115903	1.811114573
210	-4.672831587	-4.379973490	4.561409246	9.561299199	1.456126090
230	-7.159193342	-3.331495302	1.667595549	6.667426948	1.166736828
250	-8.782050721E	-5.220091960	-2.212072000	4.778585980	9.778514010
270	-9.345663174	-5.875994700	-8.771815100	4.122598400	9.122521810
290	-8.782050721	-5.220091960	-2.212072000	4.778585980	9.778514010
310	-7.159193342	-3.331495302	1.667595549	6.667426948	1.166736828
330	-4.672831587	-4.379973490	4.561409246	9.561299199	1.456126090
350	-1.622857379	3.111403340	8.111197253	1.311115903	1.811114573
370	1.622857379	6.888596660	1.188880275	1.688884097	2.188885427
390	4.672831587	1.043799735	1.543859075	2.043870080	2.543873910
410	7.159193342	1.333149530	1.833240445	2.333257305	2.833263173
430	8.782050721	1.522009196	2.022120720	2.522141402	3.022148599
450	9.345663174	1.587599470	2.087718151	2.587740160	3.08774781
470	8.782050721	1.522009196	2.022120720	2.522141402	3.022148599

490	7.159193342	1.333149530	1.833240445	2.333257305	2.833263173
510	4.672831587	1.043799735	1.543859075	2.043870080	2.543873910
530	1.622857379	6.888596660	1.188880275	1.688884097	2.188885427
550	-1.622857379	3.111403340	8.111197253	1.311115903	1.811114573

θ	***F at v =299790713***	***F at v = 299791246***	***F at v = 299791568***	***F at v = 299791776***	***F at v = 299791919***
90	3.587751379	4.087753313	4.587754479	5.087755236	5.587755755
110	3.522151944	4.022153762	4.522154857	5.022155569	5.522156056
130	3.333265900	3.833267381	4.333268274	4.833268854	5.333269252
150	3.043875690	3.543876657	4.043877240	4.543877618	5.043877877
170	2.688886045	3.188886381	3.688886583	4.188886715	4.688886805
190	2.311113955	2.811113619	3.311113417E	3.811113286	4.311113195
210	1.956124310	2.456123343	2.956122760	3.456122382	3.956122123
230	1.666734100	2.166732619	2.666731726	3.166731146	3.666730749
250	1.477848056	1.977846238	2.477845143	2.977844431	3.477843944
270	1.412248621	1.912246687	2.412245521	2.912244764	3.412244245
290	1.477848056	1.977846238	2.477845143	2.977844431	3.477843944
310	1.666734100	2.166732619	2.666731726	3.166731146	3.666730749
330	1.956124310	2.456123343	2.956122760	3.456122382	3.956122123
350	2.311113955	2.811113619	3.311113417	3.811113286	4.311113195
370	2.688886045	3.188886381	3.688886583	4.188886715	4.688886805
390	3.043875690	3.543876657	4.043877240	4.543877618	5.043877877
410	3.333265900	3.833267381	4.33326827	4.833268854	5.333269252
430	3.522151944	4.022153762	4.522154857	5.022155569	5.522156056
450	3.587751379	4.087753313	4.587754479	5.087755236	5.587755755
470	3.522151944	4.022153762	4.522154857	5.022155569	5.522156056
490	3.333265900	3.833267381	4.333268274	4.833268854	5.333269252
510	3.043875690	3.543876657	4.043877240	4.543877618	5.043877877
530	2.688886045	3.188886381	3.688886583	4.188886715	4.688886805
550	2.311113955	2.811113619	3.311113417	3.811113286	4.311113195

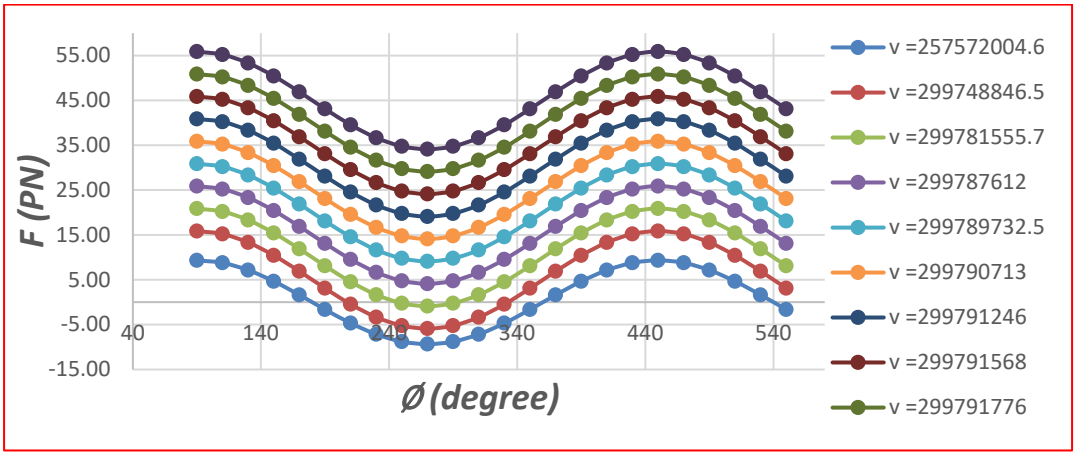

Figure 4. Graph showing the effect of different angles on the Lorentz force for the velocities studied

The theoretical calculations in the simulation program by using equation (7) showed that there is a direct proportionality to the increase in the energy of the electron beam and thus the speed of the beam at the initial power (P_0) when LG.= 0.0919348, The calculations and results of this theoretical paper, using Equation (8), also showed that there is an inverse proportionality between the speed of electrons beam (v) and photon energy (E_{ph}) and by employing both Planck's constant and the speed of light in the aforementioned equation, The number of photons (N_{ph})

was also calculated through equation (9), and the behavior between it and the speed of the electron beam was drawn. The laser power (P_z) was also calculated through equation (9) and the behavior between (P_z) and (E_e) energy of electrons particles was drawn. All calculated values are recorded in the table (4) The relationships between the energy of the electron beam and initial power were drawn in Figure (5) While the relationship between the speed of the electron beam and photon energy was drawn in Figure (6) Also, the relationship between the speed of the electron beam and number of photons was drawn in Figure (7) and, the relationship between the energy of the electron beam and the laser power was drawn in Figure (8)

Table 4. showing the effect of speed of the electron beam on initial power (P0) & photon energy (Eph) & number of photons (N_{ph}) & The laser power (P_z)

	E_e in (J)	v in ($\frac{m}{sec}$)	P_0 in (w)	E_{ph}	N_{ph}	P_z
1	1.6e-13	257572004.6	1.86867e-07	0.0028521	2.29724e7	1.20398e10
2	4.8e-12	299748846.5	0.00504543	6.26839e-20	765749	1.08359e13
3	9.6e-12	299781555.7	0.0403638	2.50737e-19	382871	4.33436e13
4	1.44e-11	299787612.6	0.136226	5.64152e-19	255250	9.75227e13
5	1.92e-11	299789732.5	0.322908	1.00294e-18	191436	1.73373e14
6	2.4e-11	299790713.7	0.630677	1.56709e-18	153150	2.70897e14
7	2.88e-11	299791246.7	1.08982	2.25662e-18	127624	3.90092e14
8	3.36e-11	299791568	1.73058	3.0715e-18	109393	5.30959e14
9	3.84e-11	299791776.6	2.58326	4.01176e-18	95718.7	6.93498e14
10	4.32e-11	299791919.6	3.67812	5.07739e-18	85083.1	8.77706e14

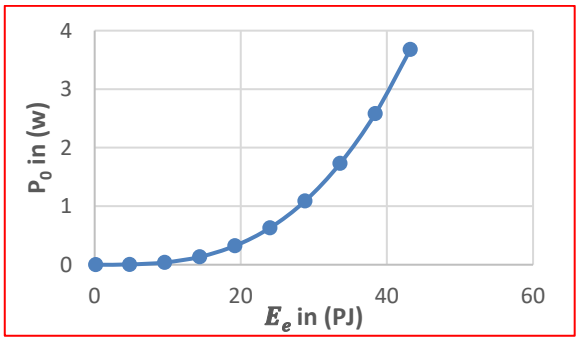

Figure 5. Graph showing the relationship between the energy of the electron beam and initial power (P_0)

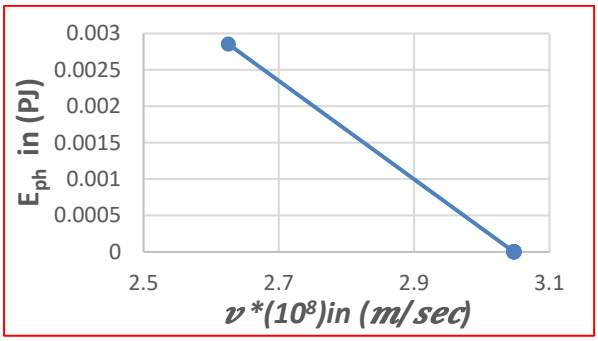

Figure 6. Graph showing the relationship between the speed of the electron beam and photon energy (E_{ph})

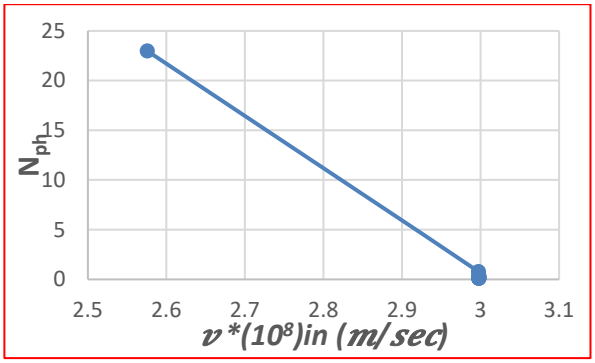

Figure 7. Graph showing the relationship between the speed of the electron beam and number of photons (N_{ph})

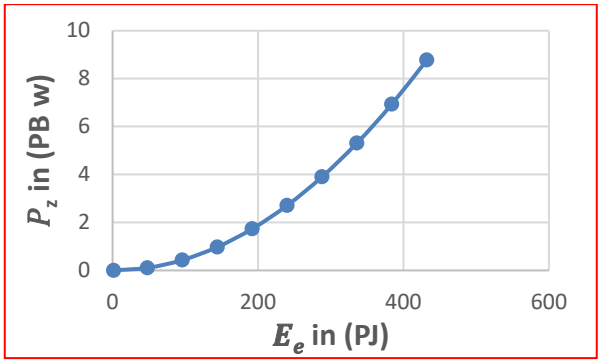

Figure 8. Graph showing the relationship between the energy of the electron beam and the laser power (P_z)

CONCLUSIONS

Through the simulation program that was designed and also through the calculations and results that were calculated and obtained, it can be concluded that there is a direct effect of the speed of the electron beam in the free electron laser (FEL) on several very important parameters and in the behavior of the laser system as a whole, as well as the direct effect on the wavelengths at the output. laser,

This paper showed that there is a direct proportionality between the energy supplied in the laser system to the electron beam and the speed of this beam. The calculations and results also showed that there is a direct proportionality between the speed of the electron beam and the Lorentz force, and that the Lorentz force is an important factor and is responsible for producing the output. The laser in the free electron laser system, as the electrons in the undulator will suffer an oscillatory movement that slows down the electrons and then accelerates them. Thus, the speed changes according to the direction of the magnetic field, and then coherent photons are emitted.

The Lorentz force can be controlled through several factors, which are the strength of the magnetic flux of the undulator, as well as the speed of the electrons emitted from the electron gun, the angle between the direction of entry of the beam and the magnetic flux, and the resulting change in the wavelength of the output laser. The calculations also showed that there is a direct relationship between the energy of the electron beam and initial power (P_0), while there is an inverse proportion between the speed of the electron beam and photon energy (E_{ph}). There is also an inverse relationship between the speed of the electron beam and the number of photons (N_{ph}), as well as There is a relationship and there is a direct relationship between the energy of the electrons (E_e) and the laser power (P_z).

Acknowledgments

I extend my sincere thanks and appreciation to the College of Education for Pure Sciences ibn Al-Haytham/University of Baghdad for providing support and assistance in completing this research paper by providing scientific facilities in all areas of work In the Physics Department To help overcome the obstacles faced by the research project.

REFERENCES

1. Al-Aish, T. A. K., and Kamil, H. A., 2022, Simulation and analysis the effect of the Lorentz force in a free electron laser, Ibn Al Haitham Journal for Pure and Applied Sciences, Doi: 10.30526/35.2.2775 Vol. 35 No. 2 (2022)
2. Mohammad, A. A. S., Harby., K. H., and Al-Aish, T. A. K., 2011, A New design of fractal optical modulation, Ibn AL-Haitham Journal for Pure and Applied Science, March 23; Vol: 24(3)
3. Yahaghi, A., Fallahi, A., and Kartner, F., 2016, Free electron laser simulation tool based on fdtd/pic in the lorentz boosted frame, in International Particle Accelerator Conference (IPAC'16), Busan, Korea, pp. 3061–3063 Vol:24(3)
4. Jawad, R. L., Al-Aish, T. A. K., and Kamil, H. A., 2019, Design and simulation a high-energy free electron laser HEFEL, in AIP Conference Proceedings (Vol. 2123, No. 1, p. 020068).
5. Saleh, M. K. and, Al-Aish, T. A. K., 2023, Design and establishment of an implementation program to simulate the far field propagation for a gaussian beam of x-ray laser, in AIP Conf. Proc. Vol:3018, 020059 (2023, NOVEMBER 08)
6. Dhedan, Z. A. J., 2021, Design study of a free electron laser production system with and without a resonator, Submitted to the Council of College of Education ibn Al-Haitham University of Baghdad in Partial Fulfillment of the Requirements for The Degree of Master in Science physics
7. Wu, S., Su, C., Wu, X., Luo, T. and Li, X., 2020, A Simple method to estimate the refractive index structure parameter (cn2) in the atmosphere" Publ. Astron. Soc. Pacific Vol:132, 1–11
8. Liu, T., Zhang, T., Wang, D., and Huang Z., 2017, Compact beam transport system for free electron lasers driven by a laser plasma accelerator, Phys. Rev. Accel. Beams, vol. 20, no. 2, pp. 1–10,
9. Dhedan, Z. A. J., and Al-Aish, T. A. K., 2022, Design and simulation of a new system for producing laser beams without resonator "NSPLBR"," in AIP Conference Proceedings 2437, Vol:020012, 17 August.
10. Scarel, G., 2019, Quantum and non-quantum formulation of eye's adaptation to light's intensity increments, World Journal of Condensed Matter Physics, vol. 9.3, pp. 62-74
11. Al-Aish, T. A. K., 2017, Analysis and study of the effect of atmospheric turbulence on laser weapon in iraq, Baghdad Science Journal, Vol. 14 No. 2 (2017)

12. Saleh. M. K., and Al-Aish, T. A. K., 2022, Simulation and analysis the attenuation effect of atmospheric layers on a laser beam within the visible range, Ibn Al-Haitham Journal for Pure and Applied Sciences, Vol. 36 No. 3 (2023)
13. Kulikov, V. M. A., 2017, Analysis of the joint impact of atmospheric turbulence and refractivity on laser beam propagation, Opt. Express Vol:25, 28524
14. Mahmood, H. K., and Al-Aish, T. A. K., 2019, Rain formation by free electron laser pulse system FELPS, in AIP Publishing LLC, Volume: 2190
15. Ghalib, M. A. A., 2021, Study and Design of Free Electron Laser System to Break Up Blood Clots in The Human Body, Submitted to the College of Education for Pure Science / Ibn Al Haitham - University of Baghdad in a Partial Fulfillment of The Requirements for the Degree of Doctor of Philosophy in Physics
16. Jawad, R. L., 2017, Calculating and analysing of some atmospheric effects on the beam of free electron laser, Baghdad, The council of College of Education for pure science/Ibn Al-Haitham,
17. University of Baghdad in Partial Fulfillment of the Requirements for the Degree of Master of Science in Physics
18. Mahmood, H. K., 2020, Design and study of msm detector for free electron laser, Baghdad: To the College of Education Pure Sciences / Ibn Al-Haytham University of Baghdad as Partial Fulfillment of the Requirements for the Degree Masters of Science in Physics

Simulation and analysis the effect of the distance between the two rows of magnetic poles on the electron oscillation movement and the characteristics of the output free electron laser

Jaafar Hussein Sabri [a], Thair Abdulkareem Khalil Al-Aish [b]

Department of Physics, College of Education for Pure Sciences Ibn Al-Haitham, University of Baghdad, Baghdad, Iraq.

[a] Corresponding author: Jaafar.Sabri2204p@ihcoedu.uobaghdad.edu.iq
[b] thair.ak.i@ihcoedu.uobaghdad.edu.iq

Abstract. This study investigates the dynamics of electron beams in the presence of magnetic fields generated by undulator magnets within the context of free electron laser systems (FELs). Focusing on the undulator gap (g_u) ranging from 0.001 to 0.05 meters, this research paper focuses on the influence of undulator gap (g_u) on the magnetic field strength (B), photon wavelengths (λ), initial laser power (P_0), photon energy (E_{ph}), number of photons (N_{ph}), gain-length (L_G), laser power (P_z), and output power from the mirror (P_m) across electron energies of 300 MeV and 500 MeV. This research paper also showed that the magnetic field will disappear at g_u = 0.03 m which is called (cut-off) point. This research paper also showed that there is no direct effect of changing the undulator gap (g_u) on the oscillation of the electron beam and that (λ_u) wavelength of Wiggler will remain a constant value. research paper simulations demonstrate that the magnetic field is inversely proportional to the undulator gap, significantly affecting the trajectory and speed of electrons, which in turn influences the characteristics of the emitted radiation. By employing a series of equations, this paper calculated the wiggler parameter (k), Lorentz factor (γ), and other relevant parameters, revealing direct and inverse relationships between the undulator gap and various performance metrics of the FEL. Notably, the research findings suggest a direct relation between the undulator gap and the initial power for both studied energies, whereas an inverse relation is observed with the number of photons generated. Additionally, a constant relationship between the undulator gap and the output power from the mirror was established for the studied range. These insights into the modulation of FEL characteristics through the undulator gap manipulation offer valuable implications for optimizing the performance and efficiency of synchrotron radiation sources.

Keywords. Undulator Gap, Magnetic Field, Photon Wavelength, Lorentz Factor, Wiggler Parameter, Photon Energy, Number of Photons, Output Power

INTRODUCTION

The invention of the free electron laser system in the 1970s sparked a revolution [1]. He invented an innovative laser technology that is superior in many aspects to traditional laser systems with multiple advantages. This technology, known as free electron laser (FEL) [2], is characterized by its ability to produce a wide spectrum of laser wavelengths without the need to modify or change the active medium or the resonator design of the laser system as a whole [3]. In a free electron laser, the active medium will not be an active solid, liquid metal, or semiconductor Rather, it is particles of negatively charged electrons traveling at very high speeds approaching the speed of light After supplying it with energy from a voltage source [4], which is lined up with each other during transmission as a current in the form of a beam This beam or stream of electrons passes through a magnet system consisting of two rows of magnets with certain geometric dimensions and arranged periodically [3], i.e. once a north pole, followed by a south pole, and so on it continues. That is, in an alternating and opposite manner, generating a regular and opposite periodic magnetic field [5]. This alternating magnetic field works to curb and impede the movement of the beam of these electrons, forcing

Technologies and Materials for Renewable Energy, Environment and Sustainability
AIP Conf. Proc. 3321, 020033-1–020033-10; https://doi.org/10.1063/5.0290411
Published under an exclusive license by AIP Publishing. 978-0-7354-5231-2/$30.00

them to move in an oscillatory manner, where a force called the Lorentz force will arise [2]
The undulator gap (g_u) is one of the most important factors that directly affects the magnetic field, which in turn affects the electron beam in particular. And the wavelength of the laser output and the power of the laser as a whole in general [4]
By reviewing in a survey of the literature previous research that devoted its attention and calculations to developing the free electron laser system and working to improve its performance.
A review of the research revealed that the effect of the undulator gap (g_u) on the free-electron laser system has not been studied extensively from various aspects, whether its effect on the magnetic field, on the wavelength of the laser output, or on the total power of the free-electron laser system. Despite its great importance in influencing the generation of coherent photons and the oscillatory movement of the electron, Therefore, the focus of this work was to analyze the effect of the undulator gap (g_u) on the electron path and the generation of photons inside the laser free electron wave.
In this research, the executive program (FEL) was created and designed using (MATLAB R2023a (9.14.0.2206163)) as shown in Figure (1).
The executive program interface shown in the figure (1) consists of several parameters to simulate the requirements of the calculations that were completed for this research in terms of the change in undulator gap (g_u). During the study of this research, some factors affecting the wavelength formation of the photons generated in the free electron laser system were studied, such as the magnetic field (B), as well as Several other important parameters were also calculated, which are (Lorentz factor (γ), photons wavelength (λ), initial power (P_0), photon energy (E_{ph}), number of photons (N_{ph}), gain-length (L_G), The laser power (P_z), out power from mirror(P_m))

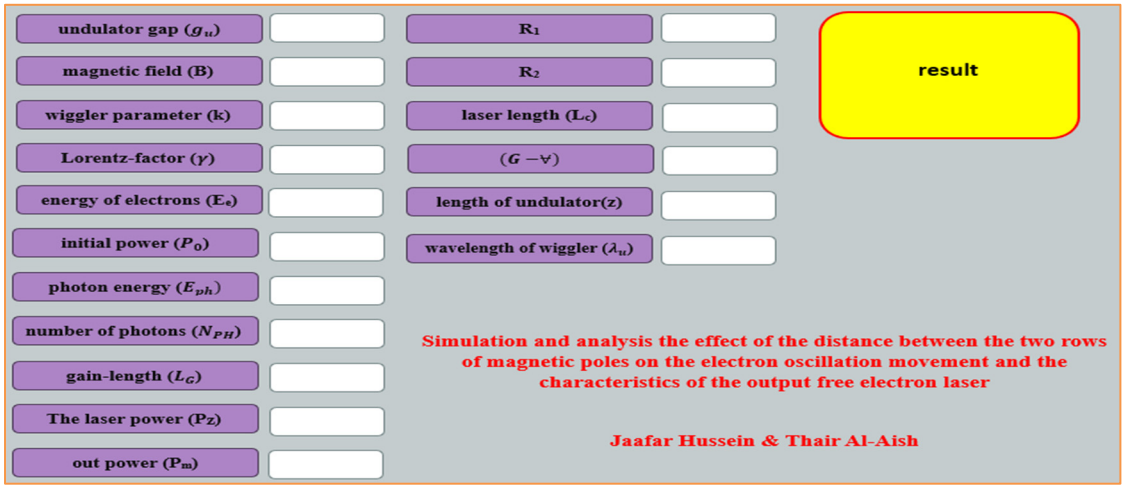

Figure 1. Shows the simulation program to analysis the effect of undulator gap (g_u) on the output laser

THEORY

There are several parameters that can be used in the free electron laser system in order to obtain a wide and variable range of wavelengths in the electromagnetic spectrum [6]. This wide spectrum can be used in many scientific, medical and military applications [7]. The free electron laser is characterized by the ability to generate a wide range of wavelengths, extending from radio wavelengths to X-rays. Without the need to replace the system as a whole or change the active medium, but only by making some modifications in the geometrical design of the free electron laser system [8], whether these modifications include the entire device or only in certain parts of it. One of the most important of these parts, which if the geometry of its formation is modified, leads to a change in the laser output in terms of wavelength and output power is the undulator geometry [3]. This feature of the free electron laser is one of the important advantages that adds important properties to the system, including (high brightness, pulsed laser, wide tenability, short pulses, high power, short wavelengths). The working principle of the free electron laser is based on the idea of a stream of electron beams at high speeds approaching the speed of light passing through a magnetic field generated through an undulator. These electrons are accelerated through an electron accelerator and these electrons pass through the magnetic field generated by the undulator [6]. The main components of the free electron laser system are the following: (the electron generator gun, which is the source of generating electron particles, equipped with high

voltage, it is a system that works to provide the electrons with the necessary kinetic energy. Electron accelerator is a system that works to increase the speed of electrons to very high speeds. The undulator is a system of magnets arranged in a specific way that works to generate a regular magnetic field through which the electron beam [5]. The principle of its work is to convert part of the kinetic energy of the electrons traveling at high speeds into coherent electromagnetic radiation. The resonator is a system of mirrors that amplifies the laser beam) [1].

After using the equations found in the literature and scientific references and performing some calculations, the following was calculated: the effect of the undulator gap (g_u) on the magnetic field (B), and the relationship between them was found and drawn in a graphical form. It was also calculated wiggler parameter (k), and Lorentz-factor (γ) for two different energies, (300 MeV) and also for (500 MeV), photon wavelength (λ) for the two different energies mentioned, and the relationship between (g_u) and (λ) was drawn in a graphical form for both energies, and the initial power (P_0), photon energy (E_{Ph}), number of photons (N_{ph}), and gain-length (L_G), the laser power (P_z), and out power. from mirror. (P_m) for both of the mentioned energies is (300 MeV), as well as for the energy of (500 MeV)

$$B = 4.22\, exp(-\frac{gu}{\lambda u}(5.08 + 1.54\frac{gu}{\lambda u})) \quad (1)$$

Where:(B) is the magnetic field, (g_u) is undulator gap, (λ_u) wavelength of wiggler [3] [9]

$$K = 93.3\lambda_u\beta_u \quad (2)$$

$$\gamma = \frac{E_e}{m_e c^2} \quad (3)$$

$$\lambda = \lambda_u(\frac{1}{2\gamma^2} + \frac{k^2}{4\gamma^2}) \quad (4)$$

Where: (k) wiggler parameter, (γ) Lorentz-factor, (Ee) energy of electrons particles, (λ) wavelength of laser [2] [10]

$$P_0 = \frac{1}{9}\frac{\chi^2 c E_e}{\lambda} \quad (5)$$

Where: (P_0) initial power, (χ) scaling parameter its take value (10^{-2} or 10^{-3}) [6] [11]

$$E_p = h\frac{c}{\lambda} \quad (6)$$

Where: (E_{ph}) photon energy [8] [12]

$$N_{PH} = \frac{\chi E_e}{E_{ph}} \quad (7)$$

Where: (N_{PH}) number of photons [11] [13]

$$L_G = \frac{\lambda_u}{4\pi\sqrt{3}\chi} \quad (8)$$

Where: (L_G) gain-length [1] [11]

$$P_z = N_{PH} P_0\, exp(z/L_G) \quad (9)$$

Where: (PZ) The laser power, (z) length of undulator [9] [11]

$$P_m = P_z R_1 R_2\, exp\, 2L_c(G - \forall) \quad (10)$$

Where: (Pm) out power from mirror, (R1, R2) Reflection coefficients, (Lc) laser length =3m, $(G - \forall) = 1$, [10] [12].

RESULTS AND DISCUSSION OF SIMULATION

The main and most important benefit of the undulator magnet system is the generation of a magnetic field measured by the Tesla unit that works to suppress the very high speeds of the electron beam coming from the accelerator after it has gained very high energy through a high-voltage source with a range from one mega-electron volt to five hundred mega-electron volts [14]. As they reach speeds close to the speed of light, after these electrons reach the undulator, they will be exposed to a regular magnetic field, and this field will hinder the high speed of the electrons, which will deviate the path of these particles into a curved path [11]. Two photons will then be generated, one at the crest of the wave and the other at the bottom [15], as shown in Figure (2). In this research paper, we will study the effect of the undulator gap (g_u), which is the distance between two rows of magnets for the Wiggler system, with a range from (0.001 to 0.05 m). Where calculations and simulations have proven that the magnetic field is inversely proportional to the undulator gap (g_u), and the effect of the undulator gap (g_u) on the magnetic field is calculated through equation (1) when $\lambda_u = 0.02$. The results of calculations and simulations are recorded in Table (1)

In order to calculate the effect of changing the undulator gap (g_u) on magnetic field (B) and wavelengths produced in the free electron laser (λ), this is done using equations (1, 2, 3, 4). Where the effect of changing the undulator gap (g_u) was studied on two different energies of electron particles, which are (8e-10) and (4.8e-11) joule which is equivalent to the unit of electron-volts (500 and 300 MeV) respectively. This research paper showed that the magnetic field will disappear at g_u = 0.03 m which is called (cut-off) point. while The value of (k) Wiggler parameter was calculated through equation (2) Based on equation (2), the value of (λ_u) wavelength of Wiggler = 0.02 (m), In the same way, the

amount (γ) Lorentz-factor = 9771.46, which was calculated through equation (3) If we consider that the mass of the electron m_e=9.10938356*10^{-31} (kg) and the typical speed of light is C=299,792,458 (m/s) The values resulting from the calculations and simulations were recorded in Table (1). The relationship of magnetic field resulting from changing undulator gap was drawn in figure (2) while the relationship of wavelength values resulting from changing the undulator gap (g_u) of energy 500 MeV and energy 300 MeV was drawn in figure (3. **a**) and (3. **b**).

Table 1. Magnetic field and wiggler parameter(k) and Wavelength values (λ) resulting from changing the undulator gap (g_u) of energy (300 and 500) MeV

$\lambda_u = 0.02$						
			$E_{BM} = 8e-10$ & γ = 9771.46		$E_{BM} = 4.8e-11$ & γ = 586.288	
	undulator gap (g_u) in (m)	**magnetic field (B) in (T)**	**wiggler parameter (k)**	**Laser wavelength (λ)**	**wiggler parameter (k)**	**Laser wavelength (λ)**
1	0.001	3.26084	6.08473	2.04354e-9	6.08473	5.67648e-7
2	0.002	2.50036	4.66567	1.24466e-9	4.66567	3.4574e-7
3	0.003	1.90253	3.55012	7.64722e-10	3.55012	2.12423e-7
4	0.004	1.43654	2.68058	4.8101e-10	2.68058	1.33614e-7
5	0.005	1.07636	2.00849	3.15979e-10	2.00849	8.77719e-8
6	0.006	0.800303	1.49337	2.21517e-10	1.49337	6.15324e-8
7	0.007	0.590483	1.10184	1.68308e-10	1.10184	4.67521e-8
8	0.008	0.432331	0.80673	1.38813e-10	0.80673	3.85591e-8
9	0.009	0.314109	0.586127	1.22723e-10	0.586127	3.40895e-8
10	0.01	0.226465	0.422584	1.14084e-10	0.422584	3.16899e-8
11	0.012	0.11503	0.214646	1.07145e-10	0.214646	2.97625e-8
12	0.014	0.0566556	0.105719	1.05318e-10	0.105719	2.92549e-8
13	0.016	0.0270582	0.0504906	1.04866e-10	0.0504906	2.91294e-8
14	0.018	0.0125308	0.0233825	1.04761e-10	0.0233825	2.91002e-8
15	0.02	0.00562708	0.0105001	1.04738e-10	0.0105001	2.90939e-8
16	0.022	0.00245025	0.00457217	1.04734e-10	0.00457217	2.90926e-8
17	0.024	0.00103457	0.00193051	1.04733e-10	0.00193051	2.90923e-8
18	0.026	0.000423581	0.000790402	1.04732e-10	0.000790402	2.90923e-8
19	0.028	0.000168165	0.000313796	1.04732e-10	0.000313796	2.90923e-8
20	0.03	6.47378e-5	0.000120801	1.04732e-10	0.000120801	2.90923e-8
21	0.032	2.4166e-5	4.50938e-05	1.04732e-10	4.50938e-5	2.90923e-8

22	0.034	8.74731e-6	1.63225e-05	1.04732e-10	1.63225e-5	2.90923e-8
23	0.036	3.07021e-6	5.72901e-06	1.04732e-10	5.72901e-6	2.90923e-8
24	0.038	1.04493e-6	1.94984e-06	1.04732e-10	1.94984e-6	2.90923e-8
25	0.04	3.44847e-7	6.43485e-07	1.04732e-10	6.43485e-7	2.90923e-8
26	0.042	1.10355e-7	2.05922e-07	1.04732e-10	2.05922e-7	2.90923e-8
27	0.044	3.42436e-8	6.38986e-08	1.04732e-10	6.38986e-8	2.90923e-8
28	0.046	1.03037e-8	1.92267e-08	1.04732e-10	1.92267e-8	2.90923e-8
29	0.048	3.00627e-9	5.6097e-09	1.04732e-10	5.6097e-9	2.90923e-8
30	0.05	8.50527e-10	1.58708e-09	1.04732e-10	1.58708e-9	2.90923e-8

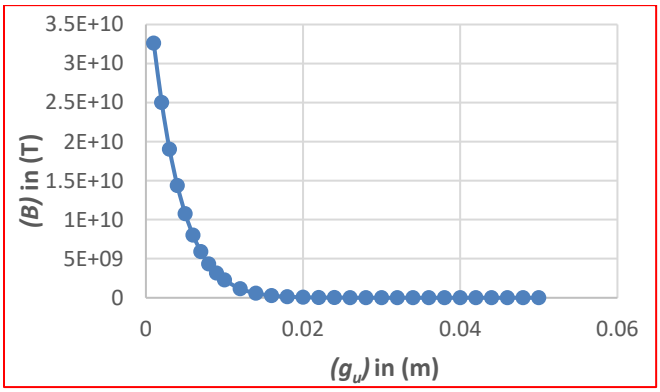

Figure 2. Change in magnetic field resulting from changing undulator gap (g_u)

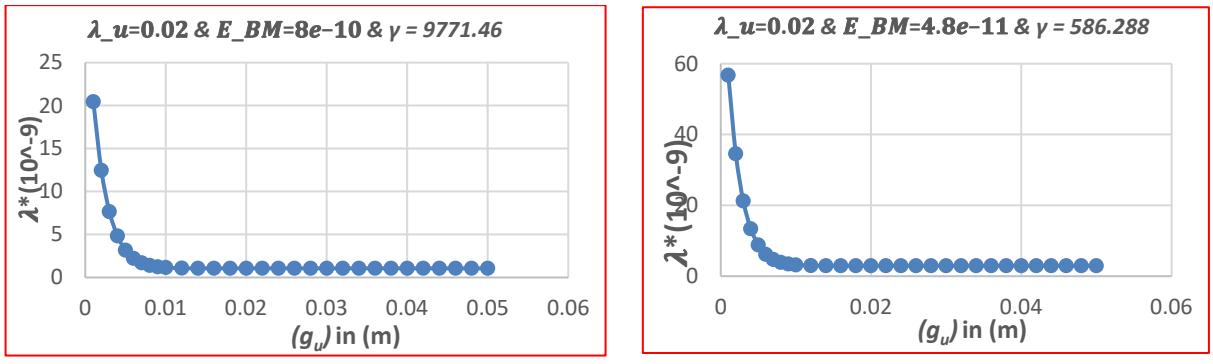

(a) (b)

Figure 3. Plot of wavelength values resulting from changing the undulator gap (g_u) of (a) energy 500 MeV (b) energy 300 MeV

In order to calculate the effect of changing the undulator gap (g_u) over the studied range from (0.001 to 0.05 m) on the initial power (P_0) in the free electron laser, this is done using equation (5) and for both energies studied (500 and 300 MeV), where the values and constants have been substituted. (χ) scaling parameter its take value (0.01). In order to calculate (P_z) the laser power, this is done through equation (9) for both energies studied (500 and 300 MeV), where (E_{ph}) photon energy was calculated through equation (6), and (N_{ph}) number of photons was also calculated for both two energies mentioned through equation (7) Likewise, (L_G) gain-length = 0.0919348 was calculated through equation (8). Simulation calculations have found that there is a direct relationship between the undulator gap (g_u) and the initial

power (P_0) for both energies studied, while there is an inverse relationship between the undulator gap (g_u) and the (N_{ph}) number of photons. The values resulting from calculations and simulations were recorded in Table (2) for energy 500 MeV and Table (3) for energy 300 MeV. The relationship between the undulator gap with initial power was drawn in the figure (4), while the relationship between the undulator gap with the number of photons in the figure (5), While the relationship between the undulator gap with the laser power is in the figure (7) For each of the two mentioned energies studied 300 and 500 MeV

Table 2. Values of initial power (P_0) and photon energy (E_{Ph}) values of number of photons (N_{ph}) resulting from changing the undulator gap (g_u) of energy 500 MeV

$\boldsymbol{\chi = 0.01\ \&\ \lambda_u = 0.02\ L_G = 0.0919348}$
$\boldsymbol{E_{BM}} = 500$ MeV

	Initial power (P_0) in (w)	**Photon energy (Ep) $*10^{-15}$**	**NO. photon (N_{ph})**	**The Laser Power (Pz) $*10^{17}$**	**Laser powers average $(Pz)_{aver}$**
1	1304.02	0.0972061	82299.4	3.00996	
2	2141	0.159597	50126.3	3.00996	
3	3484.69	0.259761	30797.5	3.00996	
4	5540.05	0.412974	19371.7	3.00996	
5	8433.54	0.628664	12725.4	3.00996	
6	12029.9	0.896746	8921.14	3.00996	
7	15833	1.18024	6778.28	3.00996	
8	19197.2	1.43102	5590.42	3.00996	
9	21714.1	1.61864	4942.42	3.00996	
10	23358.4	1.74121	4594.51	3.00996	
11	24871.2	1.85398	4315.04	3.00997	
12	25302.6	1.88614	4241.47	3.00997	
13	25411.7	1.89427	4223.26	3.00997	
14	25437.2	1.89617	4219.03	3.00997	
15	25442.7	1.89659	4218.1	3.00996	3.00996e17
16	25443.7	1.89666	4217.94	3.00996	
17	25444	1.89668	4217.9	3.00997	
18	25444.2	1.89669	4217.87	3.00997	
19	25444.2	1.89669	4217.87	3.00997	
20	25444.2	1.89669	4217.87	3.00997	
21	25444.2	1.89669	4217.87	3.00997	
22	25444.2	1.89669	4217.87	3.00997	
23	25444.2	1.89669	4217.87	3.00997	
24	25444.2	1.89669	4217.87	3.00997	
25	25444.2	1.89669	4217.87	3.00997	
26	25444.2	1.89669	4217.87	3.00997	
27	25444.2	1.89669	4217.87	3.00997	
28	25444.2	1.89669	4217.87	3.00997	
29	25444.2	1.89669	4217.87	3.00997	
30	25444.2	1.89669	4217.87	3.00997	

Table 3. Values of initial power (P_0) and photon energy (E_{Ph}) values of number of photons (N_{ph}) resulting from changing the undulator gap (g_u) of energy 300

$\boldsymbol{\chi = 0.01\ \&\ \lambda_u = 0.02\ L_G = 0.0919348}$
$\boldsymbol{E_{BM}} = 300$ MeV

	Initial power (P_0) in (w)	**Photon energy (Ep) $*10^{-18}$**	**NO. photon (N_{ph})**	**The laser Power (Pz) $*10^{15}$**	**Laser powers average $(Pz)_{aver}$**

1	0.28167	0.349943	1.37165e6	1.08359	
2	0.462455	0.574549	835438	1.08359	
3	0.752693	0.935137	513294	1.08359	
4	1.19665	1.4867	322863	1.08359	
5	1.82165	2.26319	212090	1.08359	
6	2.59846	3.22829	148686	1.08359	
7	3.41994	4.24889	112971	1.08359	
8	4.1466	5.15169	93173.3	1.08359	
9	4.69028	5.82715	82373	1.08359	
10	5.04543	6.26839	76574.7	1.08359	
11	5.37217	6.67432	71917.4	1.08359	
12	5.46539	6.79013	70690.8	1.08359	
13	5.48893	6.81938	70387.6	1.08359	
14	5.49444	6.82623	70317	1.08359	
15	5.49563	6.82771	70301.8	1.08359	1.08359e15
16	5.49588	6.82801	70298.7	1.08359	
17	5.49593	6.82808	70297.9	1.08359	
18	5.49593	6.82808	70297.9	1.08359	
19	5.49593	6.82808	70297.9	1.08359	
20	5.49593	6.82808	70297.9	1.08359	
21	5.49593	6.82808	70297.9	1.08359	
22	5.49593	6.82808	70297.9	1.08359	
23	5.49593	6.82808	70297.9	1.08359	
24	5.49593	6.82808	70297.9	1.08359	
25	5.49593	6.82808	70297.9	1.08359	
26	5.49593	6.82808	70297.9	1.08359	
27	5.49593	6.82808	70297.9	1.08359	
28	5.49593	6.82808	70297.9	1.08359	
29	5.49593	6.82808	70297.9	1.08359	
30	5.49593	6.82808	70297.9	1.08359	

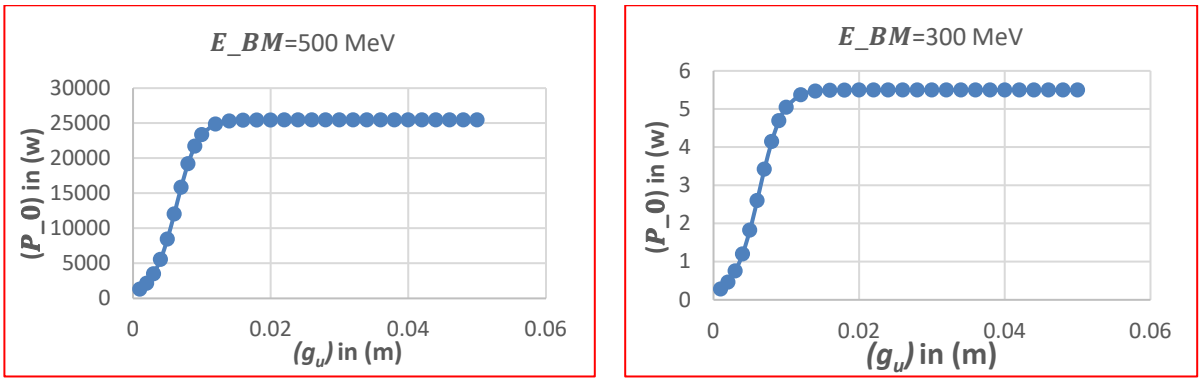

(a) (b)

Figure 4. plot of initial power (P_0) resulting from changing the undulator gap (g_u) (a) at the energy of 500 MeV, (b) at the energy of 300 MeV

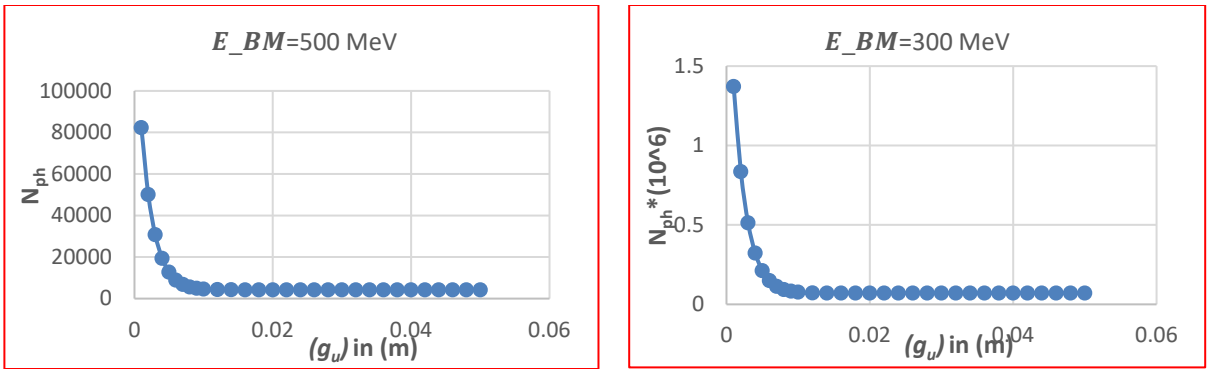

(a) (b)

Figure 5. plot of number of photons (N_{ph}) resulting from changing the undulator gap (g_u)
(a) at the energy of 500 MeV, (b) at the energy of 300 MeV

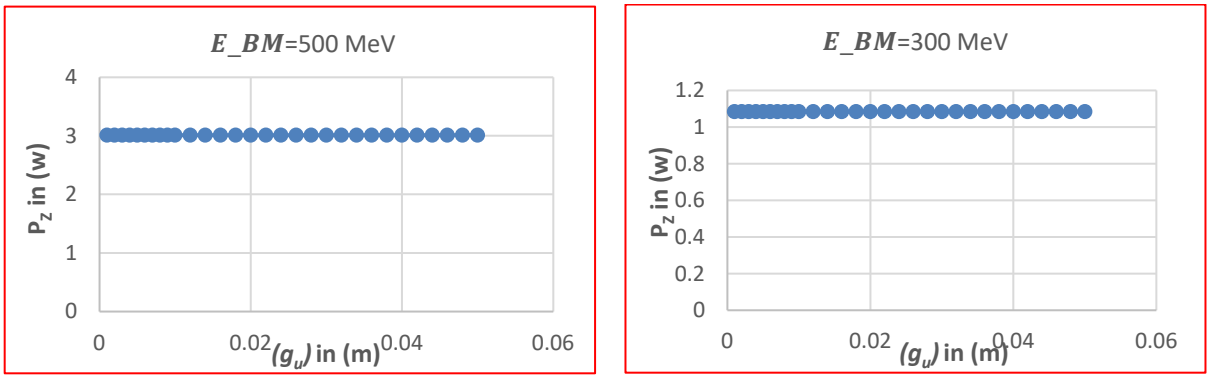

(a) (b)

Figure 6. plot of the laser power (P_z) resulting from changing the undulator gap (g_u)
(a) to the energy of 500 MeV, (b) to the energy of 300 MeV

In order to calculate the effect of changing the undulator gap (g_u) over the studied range from (0.001 to 0.05 m) on (Pm) out power from the mirror In the free electron laser, this is done using equation (10) and for both energies studied (500 and 300 MeV), where the values and constants (Lc) were replaced, laser length = 3m, and also (G-∀) = 1, while (R1, R2) were considered Reflection coefficients 100% and 0.95%, respectively Simulation calculations have found that there is a constant relationship between the undulator gap (g_u) for the studied range from (0.001 to 0.05 m). With (P_m) out power from the mirror for both energies studied. the values resulting from calculations and simulations were recorded in Table (4).

Table 4. Values (P_m) out power from the mirror resulting from changing the undulator gap (g_u) of energy by 300 and 500 MeV

	confocal resonator type $L_R = 3m$ & R1= 100% & R2=0.95 & $G - \alpha = 1m^{-1}$	
	***E_BM*=500 MeV & (PZ)aver=1.02339e19**	***E_BM*=300 MeV & (PZ)aver=1.08359e15**
	out pow. from mirror (P_m)	
1 . . . 30	**3.92222e21**	**4.15294e17**

As for the effect of the undulator gap (g_u) on the oscillation of the electron beam, the results of calculations and simulations resulting from the equations have proven that there is no direct effect on the oscillation of the electron beam and (λ_u) wavelength of Wiggler with reference to equations (1,2,3,4). the undulator gap (g_u) will have a direct

effect on (λ) wavelength of the laser, as it will change the values of each of the parameters: (B) the magnetic field, as well as (k) the Wiggler parameter as shown in

CONCLUSIONS

Through calculations that were conducted using scientific equations related to the subject of the free electron laser mentioned in references and sources, and through the simulation program that was designed, the calculations that were performed showed that there is a large and direct effect of the undulator gap (g_u) parameter on the electron beam in the electron laser. The free flow (FEL) affects several very important parameters and the behavior of the laser system as a whole, as well as the direct effect on the wavelengths at the laser output.

This research paper showed that the magnetic field will disappear at g_u = 0.03 m which is called (cut-off) point and showed that there is an inverse proportionality between the undulator gap (g_u) and the magnetic field, as it is observed that there is a decrease in the magnetic field (B) whenever it is matched by an increase in the undulator gap (g_u).

The calculations and results taken from the simulation also showed that there is an inverse proportionality between the undulator gap (g_u) with the wavelengths produced in the free electron laser (λ), and for both energies studied in this research paper, 300 and 500 MeV

The calculations and results taken from the simulation also showed that there is a direct proportionality between the undulator gap (g_u) with the initial power (P_0), while there is an inverse proportionality between the undulator gap (g_u) with the number of photons (N_{ph}), and for both energies studied in this research paper 300 MeV and 500 MeV

The calculations and results taken from the simulation also showed that there is a stability in the rate between the undulator gap (g_u) and (P_z) the laser power of 3.00996e17 for the energy of 500 MeV, whereas the amount of (P_z) of the laser power for the energy of 300 MeV is 1.08359e15.

Calculations and simulation results also showed that out pow. from the mirror (P_m) at energy 300 MeV is 4.15294e17 while out pow. from the mirror (P_m) at the energy of 500 MeV is 3.92222e21, meaning that (P_m) is larger at the energy of 500 MeV than it is at the energy of 300 MeV.

This research paper also showed that there is no direct effect of changing the undulator gap (g_u) on the oscillation of the electron beam and that (λ_u) wavelength of Wiggler will remain a constant value.

REFERENCES

1. Al-Aish, T. A. K., and Kamil, H. A., 2022, Simulation and analysis the effect of the Lorentz force in a free electron laser, *Ibn Al Haitham Journal for Pure and Applied Sciences*, Doi: 10.30526/35.2.2775 Vol. 35 No. 2 (2022)
2. Saleh, M. K. and, Al-Aish, T. A. K., 2023, Design and establishment of an implementation program to simulate the far field propagation for a gaussian beam of x-ray laser, *in AIP Conf. Proc*. Vol: 3018, 020059 (2023, NOVEMBER 08)
3. Saleh. M. K., and Al-Aish, T. A. K., 2022, Simulation and analysis the attenuation effect of atmospheric layers on a laser beam within the visible range, *Ibn Al-Haitham Journal for Pure and Applied Sciences,* Vol. 36 No. 3 (2023)
4. Jawad, R. L., Al-Aish, T. A. K., and Kamil, H. A., 2019, Design and simulation a high-energy free electron laser HEFEL, *in AIP Conference Proceedings* (Vol. 2123, No. 1, p. 020068).
5. Ali, M. A., Al-Aish, T. A. K., and Kamil, H. A., 2022, Analyzing and simulating the mechanism of laser medical therapy, *AIP Conference Proceedings* Vol: 2437, 020020
6. Ali, M. A., Al-Aish, T. A. K., and Kamil, H. A, 2022, Simulation breakdown the blood clot using a free electron laser system, in *AIP Conference Proceedings*, Vol:2437, 1, 20021.
7. Yahaghi, A., Fallahi, A., and Kartner, F., 2016, Free electron laser simulation tool based on fdtd/pic in the lorentz boosted frame, in *International Particle Accelerator Conference (IPAC'16), Busan, Korea*, pp. 3061–3063, Vol:4233
8. Kamel, M. H., and Al-Aish, T.A.K., 2020, Design and stimulated the detectors of high-power lasers DHPL, In *AIP Conference Proceedings* December 2020, AIP Publishing LLC. Vol: 2307, 1, 020025.
9. Al-Aish, T. A. K., 2017, Analysis and study of the effect of atmospheric turbulence on laser weapon in iraq, *Baghdad Science Journal*, Vol. 14 No. 2 (2017)

10. Al-Aish, T. A. A., 2015, Design and analysis the fiber laser weapon system FLWS, *Advances in Physics Theories and Applications,* vol. 47
11. Dhedan, Z. A. J., 2021, Design study of a free electron laser production system With and without a resonator, A Thesis Submitted to the Council of College of Education ibn Al Haitham University of Baghdad in Partial Fulfillment of the Requirements for The Degree of Master inScience physics
12. Ghalib, M. A. A., 2021, Study and design of free electron laser system to break up blood clots in the human body, *thesis Submitted to the College of Education for Pure Science / Ibn Al Haitham - University of Baghdad in a Partial Fulfillment of The Requirements for the Degree of Doctor of Philosophy in Physics*
13. Mahmood, H. K., 2020, Design and study of msm detector for free electron laser, *To the College of Education Pure Sciences / Ibn Al-Haytham University of Baghdad as Partial Fulfillment of the Requirements for the Degree Masters of Science in Physics*
14. Jawad, R. L., 2017, Calculating and analysing of some atmospheric effects on the beam of free electron laser, *A thesis Submitted to the council of College of Education for pure science/Ibn Al-Haitham, University of Baghdad in Partial Fulfillment of the Requirements for the Degree of Master of Science in Physics*
15. Jawad, R. L. and Al-Aish, T. A. K., 2017, Design and simulate a new defense system of free electron laser DSFEL, *Engineering & Technology Journal*, Vol. 35, Part B. No. 2, 2017

Effect of Changing the Radius Curvature of the Objective Lens on the Performance of a Binary Telescope

Alaa K Shwayya [1], Maryam K Hasan [1] , Noor S Ahmed [2], and Alaa B Hasan [3,a]

[1]*Al-Maamoun University College, Department of Laser Engineering and Optoelectronics, Baghdad, Iraq*
[2]*Ministry of Education, Directorate of Al-Karkh Education, Baghdad, Iraq*
[3]*University of Baghdad, College of Education for Pure Science Ibn Al-Haitham, Department of Physics, Baghdad, Iraq*

[a] Corresponding Author: alaa.b.h@ihcoedu.uobaghdad.edu.iq

Abstract. The research includes the design of a binocular ground refractor telescope by simulation in the Zemax program for optical designs. The design consists of a group of primary and secondary optical elements, the basic elements include an achromatic objective lens (consisting of two contact lenses that are biconvex and positive crescent) that control the amount of light entering the optical system, and a double perpendicular Porro prism with a vertical angle of (45°), to obtain Perpendicular to the reflected rays and to change the path of light rays to reach the eyepiece lens. The telescope includes an achromatic eyepiece (consisting of two contact lenses, a biconvex, and a positive crescent) that transmits light to the observer's eye or the camera. The secondary component of the telescope includes a plano-convex lens to regulate rays to the eyepiece and to reduce the stray rays from the optical system. The value of the effective focal length in the telescope has been changed by varying the radius of curvature of the objective lens to study the effect of this factor on the image quality and thus on the performance of the optical system.

INTRODUCTION

Each binocular has an objective lens that collects light from the observed object. This lens is an image of the object, but this image is inverted, and the right and left sides are inverted. In most types of binoculars known as prisms, there is a set of prisms in each tube that adjusts the image. Then the light travels through several lenses to the lens near the eye. These lenses magnify the image, and the viewer sees a moderate and magnified image through the eyepiece. Changing the distance between the eyepiece and the objective lens enables the observer to focus objects at different distances. Binoculars differ in their means of focusing the light, where the focus of the telescopes can be focused by rotating a small wheel between the two tubes [1,2].
A prismatic binocular can give greater magnification and a wider field of view than other types of binoculars such as opera theater binoculars and field binoculars. High-quality binoculars have achromatic refractive lenses that prevent the formation of colored halos around the image due to the presence of chromatic aberration. The surfaces of all lenses in binoculars are specially coated to increase image clarity and reduce glare [3].

ZOOM POWER

The power of magnification is one of the most important factors that depend on when using any binoculars. Small magnification binoculars are good when observing the galaxy, nebula or star clusters and they have a wide angle, while binoculars with high magnification are narrow, but they are good when observing the sun, moon, and planets, but the binoculars must be held by hand [4].

Technologies and Materials for Renewable Energy, Environment and Sustainability
AIP Conf. Proc. 3321, 020034-1–020034-9; https://doi.org/10.1063/5.0291625
Published under an exclusive license by AIP Publishing. 978-0-7354-5231-2/$30.00

THE DIAMETER OF THE EYEPIECE

The diameter of the lens in the binoculars plays an important role in image quality, and the widespread concept is that the larger the lens, the better. This concept is true for telescopes and not always in binoculars. The appropriate lens must be chosen for the eye and the location from which it is being monitored [5].
The human eye is an accurate and wonderful machine, as it automatically adapts to the surrounding light, and controls the amount of light entering the eye through the pupil. For most people, the pupil becomes smaller to (2.5 mm) in the day and expands to (7 mm) in total opacity to match the endoscope with the monitoring process. The optical cone outside the ocular lens must be appropriate and the same diameter as the pupil. If the diameter of the light emerging from the ocular lens is small, part of the eye's ability to collect light is lost. But if the diameter of the light coming out of the lens is large, we do not use the telescope with its full efficiency. The diameter of the light outside the lens or the so-called pupil of the lens is measured for any telescope by dividing the magnification power of the lens by its diameter [6].
Binoculars are two telescopes that are mounted side by side, aligned to a point in the same direction, allowing the viewer to use both eyes (ocular vision) when viewing distant objects. Typical borough prism binoculars design unlike a telescope (monocular), binoculars give users a three-dimensional (3D) image; for closer objects, the two views, are presented to each of the viewer's eyes from slightly different perspectives, resulting in a combined view with an impression of depth [7].

GLASS PORRO PRISM

Optical prisms added to the design allowed the image to be displayed correctly without the need for many lenses, and to reduce the overall length of the instrument, by using a Porro prism which consists of two identical orthogonal prisms to change the direction of rays coming from the objective lens at an angle of (90o) at each prism. This procedure reduces the length of the telescope without reducing the length of the optical path, as well as changes the direction of the ray projections to suit the vision with the observer's eye [8].

FIELD OF VIEW

The field of view is the angle of incidence of the rays on the objective lens to obtain a clear image of the observed object. The angle of the field of view varies according to the diameter of the objective lens and the type of telescope. If the telescope is two-lens, the angle of the field of view is relatively large due to the binocular vision technology [9]. The larger the diameter of the objective lens, the greater the angle of the field of view, because the amount of light entering the optical system is greater when the diameter of the objective lens increases. The concept of numerical aperture is the ratio between the diameter of the lens aperture to its focal length, and it is a very important concept in photo-optical systems to determine the angle of the field of view.

EXIT PUPIL

A larger pupil facilitates exit from the position of the eye where it can receive light; anywhere in the large cone of pupil light will do. This ease of placement helps avoid vignetting, especially in large field-of-view binoculars, which brings the viewer an image with dark borders because the light emitted from it is partially obscured, meaning that the image can be found quickly. Narrow iris scopes can also be cumbersome because the instrument must be held in place exactly in front of the eyes to provide a useful image [10]. Finally, many people use their binoculars at dusk, in cloudy conditions, and at night when their pupils are larger. Thus, pupil exiting during the day is not a universally desirable standard. For convenience, ease of use, and flexibility in applications, larger binoculars with larger pupils are satisfying choices even if their capabilities are not fully utilized during the day [11].

ALIGNMENT

The two telescopes in the binoculars are aligned in parallel (parallel) to produce a single circular image that appears to be three-dimensional. Misalignment will result in binoculars producing a double image. Even slight misalignment will cause visual fatigue as the brain tries to combine skewed images. The alignment of the two main parts of the binocular telescope includes the two telescopes rowing with each other parallel to the two optical axes, considering

the distance between them to match the diameter of the ray entry aperture and the diameter of the eyepiece. The Zemax software program used in the design provides a multi-configuration editor to align the telescope to the appropriate dimensions [12] .

The alignment of optical elements within the image optical system is important in forming images of high specification, free of aberration and diffraction. This requires precision in the design in addition to choosing the appropriate optical parameters, which include the radii of curvature of the lenses and mirrors, the distances between them, and the size and length of the optical system. In addition to the technique of assembling the parts to suit the required design.

OPTICAL DESIGN

Telescope lenses usually consist of three or more lens elements in two or more groups. The lens furthest from the viewer's eye is called the objective lens, and the closest to the eye is the ocular lens. The lens of the eye is a biconvex achromatic lens and a positive meniscus, and the objective lens is a double achromatic lens consisting of a biconvex lens and a positive meniscus. In the design, a glass type (BK7, SF2) was used for both lenses to obtain an achromatic lens with a low dispersion to reduce chromatic aberration to the maximum extent. These two types of glass were chosen, but they are commonly used because of their important optical advantages such as the refractive index, durability, and appropriate thermal expansion coefficient [13].

The binocular telescope contains an objective lens, a Porro prism, a plano-convex lens, and an eyepiece lens. The achromatic objective lens collects the light emitted by the objects to enter the telescope by controlling the amount of light through the pupil aperture and changing the direction of the rays through refraction in the lens [14]. The light travels to the prism to reflect it at an angle of (90º) each time, thus we get a shortening of the length of the telescope without changing the length of the optical path, as well as changing the direction of the rays to match the observer's vision. The plano-convex lens collects the stray light coming from the prism to direct it to the achromatic eyepiece lens so that the light collects with a beam diameter that matches the diameter of the observer's pupil (figure 1).

The process of passing the light rays through this series of lenses achieves an adjustment in the image position and ensures that it is almost free of aberration while obtaining a good close-up image. The use of suitable types of optical parameters for the components of the telescope gives high-performance efficiency and thus a good image. Choosing the type of transparent materials for lenses and prisms and choosing suitable radii for the lenses, as well as choosing the wave number that represents the focal length of the lens divided by the diameter of the pupil aperture [15, 16].

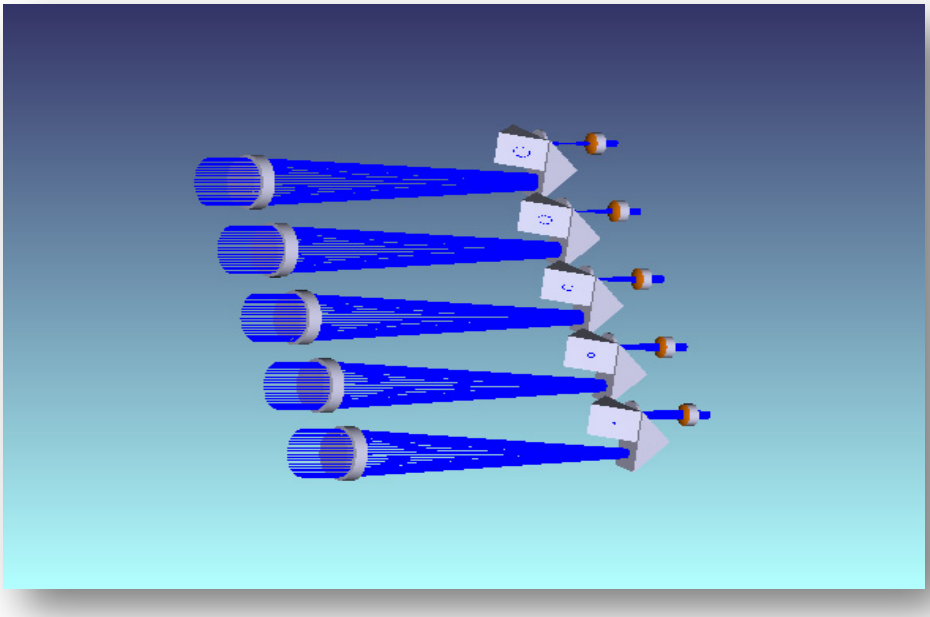

Figure 1. 3-D layout of internal components of the binocular telescope in zemax program.

The designed optical system has a pupil aperture of (10 cm) at the objective lens. The objective lens is an achromatic lens consisting of two contact lenses made of different glass (N-BK7, SF2). The total length of the telescope is (35 cm), with the length of the optical auscultator shortened by a Porro prism made of glass (N-BK7). The rays coming from the prism are collected by the plano-convex lens made of glass (N-BK7), to reach the rays in the end to the achromatic eye lens, which consists of two contact lenses made of glass type (N-BK7, SF5) [17]. The purpose of using an achromatic lens is to reduce chromatic aberration and to produce erect and clear image .

RESULTS

Many image analysis tools can be used to evaluate the performance of the designed optical system. To obtain a comprehensive study of the quality of the image formed in the optical system, a set of these tools were used that differ in terms of work technique and the type of the resulting function. All these tools contribute to giving a clear idea of the quality of the performance of the optical system.

Figure (2) shows the spot diagram in the image plane of the binocular telescope for different values of the radius of curvature when the field of view angle changes. The legends of configurations (1, 2, 3, 4, 5) in the figure refer to values of radius of curvature (r=175mm, 165mm, 155mm, 145mm, 135mm) respectively. The figure shows the change in the distribution of light ray propagation when the radius of curvature changes due to the change in the direction of light entering the optical system, which causes a change in the amount of aberration present in the system when the angle of view of the telescope changes; the distribution of rays in the image plane will also change because the state of asymmetry is in the distribution of rays, which leads to the occurrence of asymmetric aberration such as coma aberration.

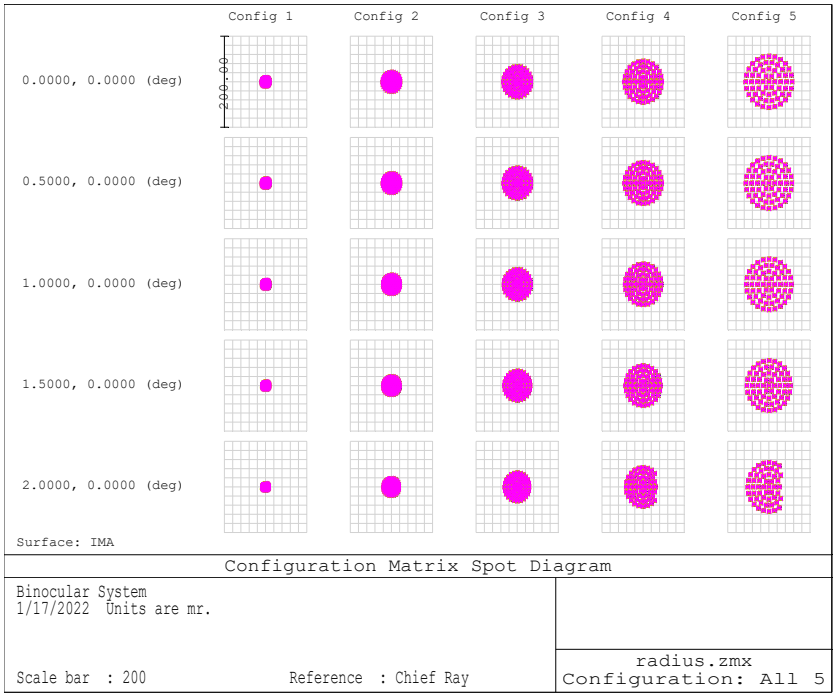

Figure 2. Spot diagram in a binocular telescope when changing the radius of curvature of the objective lens for different values of the field of view angle.

Figure (3) shows the ray fan aberration curve at the image plane when the curvature radius of the objective lens of the optical system changes. The figure consists of four sub-shapes related to the optical system when the field of view angle changes.

The figures show the variation of the ray projections of the aberration curves when the curvature radius of the objective lens changes because of changing the path of the rays after refraction, which leads to the appearance of aberration. An increase in the deviation of the curve from the sagittal or tangential axis of the image plane shows an increase in the amount of aberration in the optical system, because of increasing the deviation of the rays from their original position

in the image plane, with a slight difference between the two axes of the image plane as a result of changing the angle of the field of view in the x-axis only (tangential).

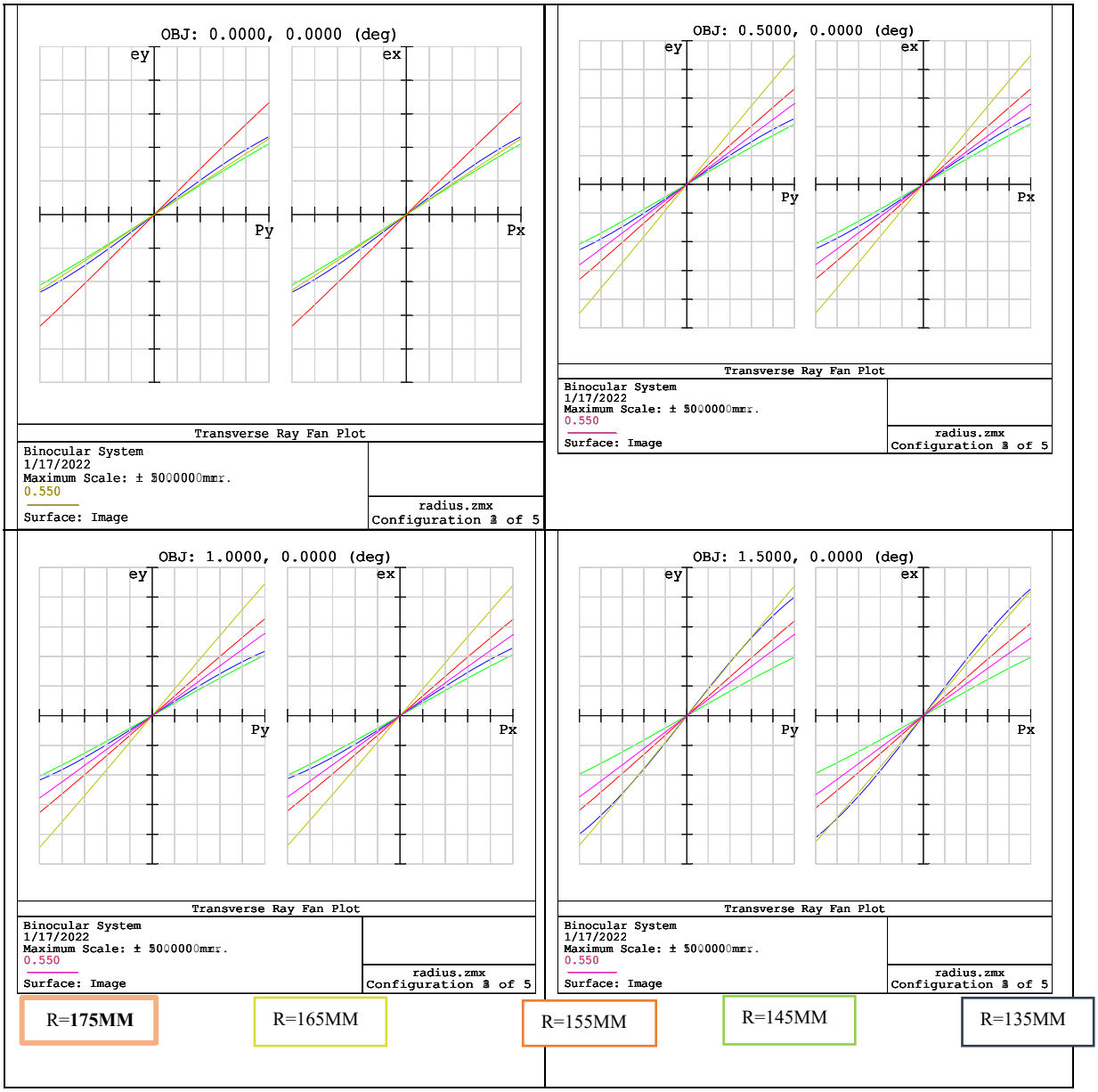

Figure 3. Ray fan aberration in a binocular telescope when changing the radius of curvature of the objective lens for different values of the field of view angle.

The perfect optical system is perfect produces a spherical wavefront that is refracted by the lens will be another spherical wavefront centered by the focal point. But if the system is limited by diffraction or contains aberration, the formed wavefront changes its path to be a second spherical center other than the focal point.
Figure (4) shows the optical path difference (OPD) of the wavefront generated inside the telescope and falling into the image plane. Different curves of the optical system at which the curvature radius of the objective lens changes, with a change in the angle of the field of view for each case. The figure shows the effect of changing the apparent curvature radius on the change of the optical path of the wavefront due to the increase in the amount of aberration formed in the optical system.

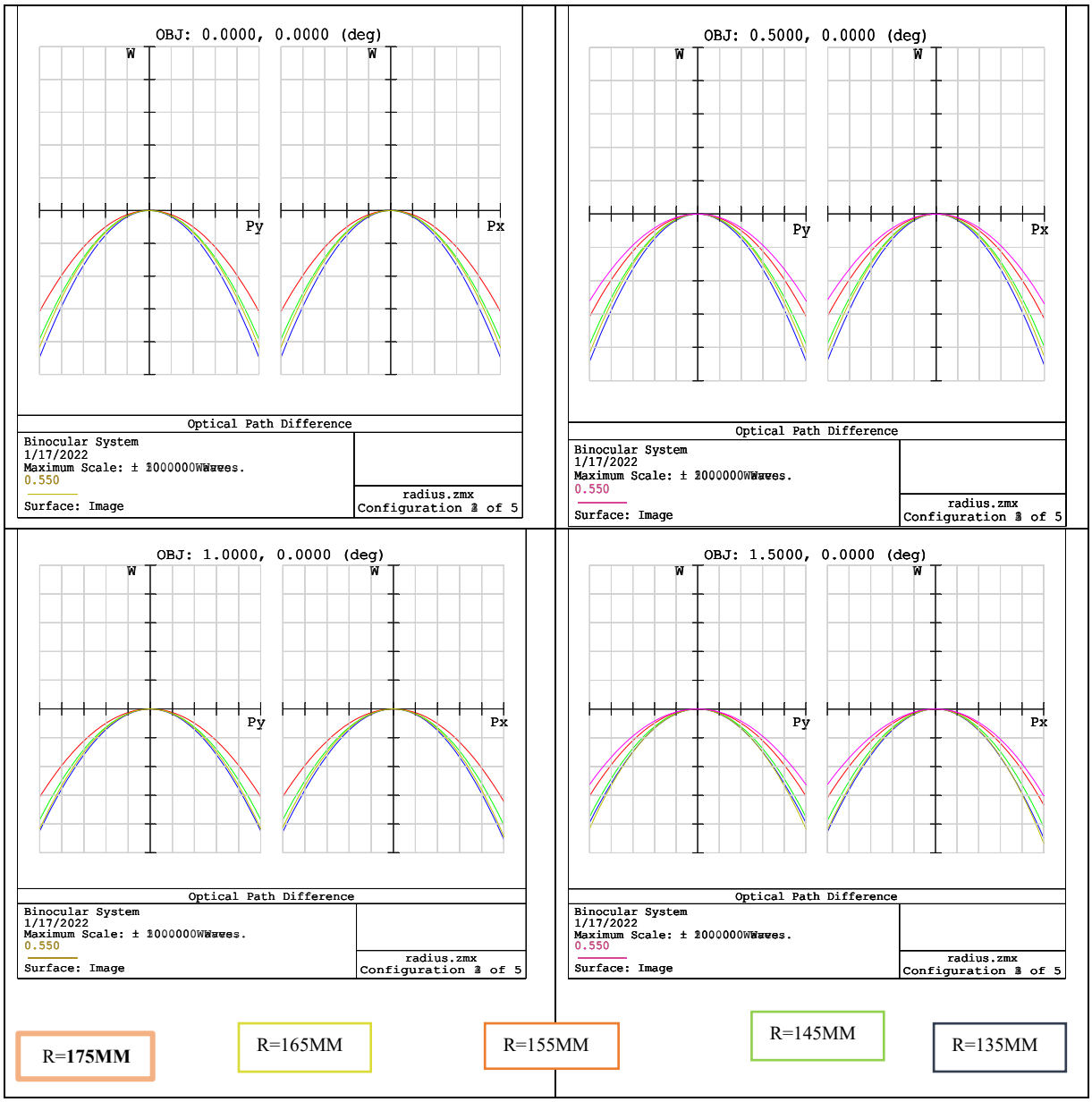

Figure 4. OPD in a binocular telescope when changing the radius of curvature of the objective lens for different values of the field of view angle.

The optical transfer function (OTF) is considered an appropriate criterion for evaluating the performance of the optical system by calculating the contrast in the image concerning the spatial frequency. If the transmission and refracting media between the optical system are homogeneous, then the modified optical transfer function (MTF) can be used to a maximum value of one.

Figure (5) shows the MTF of the optical system in the image plane, for different values of the curvature radii of the objective lens when changing the field of view angle. The figure shows the change in the value of the function when the value of the curvature radius changes and the angle of the field of view changes for the reasons mentioned above.

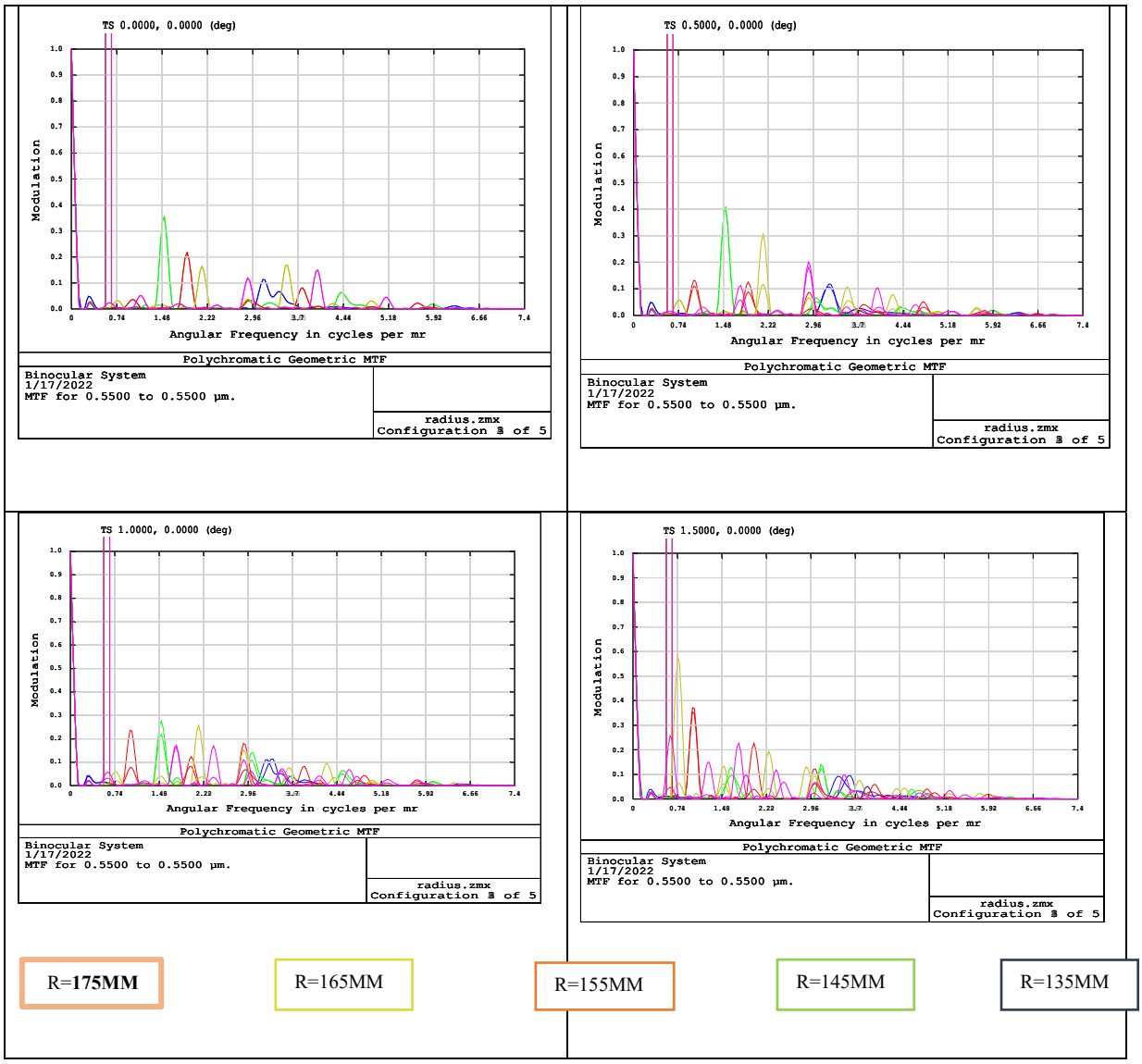

Figure 5. MTF in a binocular telescope when changing the radius of curvature of the objective lens for different values of the field of view angle.

The scheme of the encircled energy represents the amount of radiant energy distribution of light in the receiver surface (the image surface).

The image surface is represented in the form of concentric circular segments, or square segments, which are often useful for evaluating digital images in which the pixel system operates.

The energy collected from the center of the image surface to its edge is calculated in an energy aggregative format. The aggregate power diagram is often useful for evaluating point source images to know the distribution of the image distribution in the image plane.

Figure (6) shows the scheme of the encircled energy collected in the image plane of the optical system when changing different values of the field of view angle.

The figure shows convergence in the curves for all angles except for the angle (2°), which gives a greater power distribution due to the lack of image contrast due to the increase in the amount of aberration.

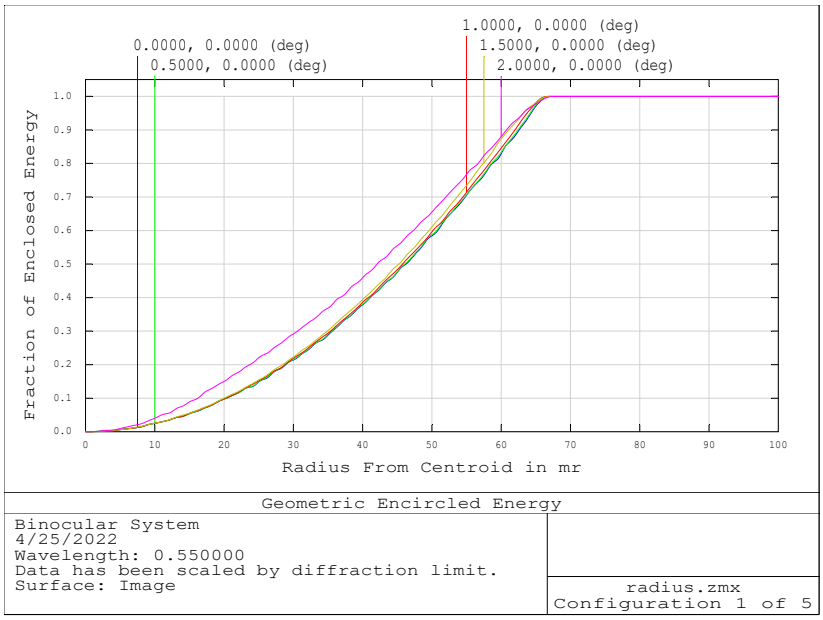

Figure 6. Encircled energy in binocular telescope for different values of the field of view angle.

CONCLUSION

Many optical parameters affect the quality of optical system performance. These parameters vary depending on the type of system and the purpose for which it is designed. The curvature radius of the objective lens affects the effective focal length of the optical system, and as a result, affects the location of the focus and the number of light rays arriving at the observer to produce the image. The research showed the clear effect of this parameter on the image quality by changing the amount of aberration formed in the image, which directly affects the image quality.

Acknowledgment

I extend my thanks to the College of Education for pure science Ibn Al-Haitham, University of Baghdad for assisting in completing this work by opening private laboratories and providing scientific facilities by the staff of the Physics Department to help support the research project.

REFERENCES

1. Betul S, Barbara L, Xavier L, Adaptive optics with pupil tracking for high resolution retinal imaging. 2012 *Biomed Opt Express.* **3** 225–239.
2. Navarro R, Santamar J, Bescos J, Accommodation dependent model of the human eye with aspherics. 1985 J. Opt Soc. Am. 2 1273–1281.
3. Lu N, Gao Z, Design of the new 0.88 zoom stereo microscope objective. 2011 Optical Instruments. 33 36–42.
4. Al-Hamdani A H, Rashid H G, Hasan A B, Irradiance distribution of image surface in microlens array solar concentrator. 2014 ARPN Journal of Engineering and Applied Sciences 33 125-134.
5. Al-Saadi T M, Hussein B H, Hasan A B, Shehab A A, Study the structural and optical properties of Cr doped SnO2 nanoparticles synthesized by sol-gel method. 2019 Energy Procedia 157 457–465.
6. Hasan A B, Husain S A, Design of Light Trapping Solar Cell System by Using Zemax Program. 2018 Journal of Physics: Conference Series 1003 (1) 123-135.
7. Ferster D A, comparison of binocular depth mechanisms areas 17 and 18 of the cat visual cortex. 1981 J. Physiol 311 623–655.
8. Fleet D J, Wagner H, Heeger D J, Encoding of binocular disparity: energy models, position shifts and phase shifts. 1996 Vision Res. 36 1839–1858.
9. Santamaría J, Artal P, Bescós L, Determination of the point spread function of human eyes using a hybrid optical-digital method. 1987 J. Opt. Soc. Am. 4 1109–1114.

10. Liang J, Grimm B, Goelz S, Bille J F, Objective measurement of wave aberrations of the human eye with the use of a Hartmann-Shack wave-front sensor. 1994 J Opt. Soc. Am. 11 1949–1957.
11. Rodríguez P, Navarro R, Double-Pass versus aberrometric modulation transfer function in green light. 2007 Journal of Biomedical Optics 12 044018.
12. Chirre E, Prieto P M, Artal P, Binocular open-view instrument to measure aberrations and pupillary dynamics. 2014 Optics Letters 39 4773–4775.
13. Fernández E J, Prieto P M, Artal P, Binocular adaptive optics simulator. 2009 Optics Letters 34 2628–2630.
14. Sabesan R, Zheleznyak L, Yoon G, Binocular visual performance and summation after correcting higher order aberrations. 2012 Biomedical Optics Express 3 3176–3189.
15. Hasan A B, Studying Optical Properties of Quantum Dot Cylindrical Fresnel Lens. 2022 NeuroQuantology 20 (2) 97–104.
16. Hasan A B, Efficiency Evaluation of Optical System Includes Different Stop Apertures When Using Relative Moving Factor. 2022 NeuroQuantology 20(3), 211–215.
17. Hassanein N H, Hasan A B, Design of Truncated Hyperboloid Solar Concentrator by Using Zemax Program. 2022 Ibn Al-Haitham Jour. for Pure & Appl. Sci. 35(1) 1-7.
18. Abdulrahman M W, Hasan A B, Computer simulation of the optical system performance of Maksutov–Cassegrain Telescope. 2023 4th International Scientific Conference of Alkafeel University (ISCKU 2022). 2977(1) https://doi.org/10.1063/5.0182000
19. Shwayyea A K, Hasan A B, Studying the optical properties of a binocular telescope with a different pupil aperture using Zemax image simulation program. 2023 Technologies and Materials for Renewable Energy, Environment and Sustainability: Tmrees22Fr. 2769 020043 1–10. https://doi.org/ 10.1063/5.0129390
20. Khudair Y Y, Hasan A B, Mahdi H S, Performance efficiency effectiveness of incidence angle of concave trough solar concentrator. 2023 Materials Today: Proceedings. 3467 https://doi.org /10.1016 /j.matpr.2023.03.066
21. Hamzah H N, Hasan A B, Simulation and evaluation of elliptical hyperboloid solar concentrator by using Zemax program. 2022 Technologies And Materials for Renewable Energy, Environment and Sustainability: Tmrees21gr. 2437 https://doi.org/10.1063/5.0092683

Utilizing applied mathematics, a flat model is used to represent contiguous UTM coordinates over the territory of Iraq

Abeer H. Abdulameer [1,a], Baqer H. Sayyid [2], Loay E. George [3]

[1]*Department of Mathematics, College of Science, University of Baghdad, Baghdad, Iraq*
[2]*Department of Remote Sensing and GIS, College of Science, University of Baghdad, Baghdad, Iraq*
[3]*University of Information Technology and Communication, Baghdad, Iraq*

[a] Corresponding author: abeer.h@sc.uobaghdad.edu.iq

Abstract The process of converting coordinates from a spherical geographic system to a flat projected system continues to be substantial and challenging. Despite the widespread utilization of the contiguous Universal Transverse Mercator (UTM) system, users often encounter challenges with continuity, particularly in expansive areas spanning multiple zones. Using a mathematical model based on Taylor series, this work aims to address the nuances of multi-zone coverage across Iraqi land. The most precise translation equation for this inquiry is determined by using a two-factor sixth-order polynomial. The coefficients for these equations were calculated using the least squares technique, using various point values such as latitude, longitude, East, and North. There are two primary transformations that occur throughout the conversion process: forward and reverse. At first, we transfer the values from Longitude/Latitude to East/North, and then we do the converse, from East/North to Longitude/Latitude. A comprehensive examination of the location accuracy is done at each level. The data indicate that the mathematical model that was employed to carry out the adjustment was effective. An average error of around 1 cm in the East direction and less than 0.1 cm in the North direction was attained employing the sixth-order polynomial formulae, indicating the precision of the technique.

Keywords: GIS, UTM, Polynomial, Transformation, WGS84, Zone

INTRODUCTION

The Universal Transverse Mercator (UTM) system operates as a projection coordinate system, generating a subset of the Cartesian coordinate scheme applied for identifying points on a two-dimensional plane [1]. Within this system, a point's position is determined by its distance from the x and y axes, denoted as X and Y coordinates, respectively, and typically measured in meters or kilometers. Each point's location on Earth is characterized by its UTM zone number, in conjunction with the easting and northing values inside that particular zone [2].

The starting point of each UTM zone is set at the junction of the equator and the zone's central meridian, carefully positioned at 500,000 meters East to avoid negative values [3]. Consequently, a point with an easting of 400,000 meters within any zone is approximately 100 kilometers west of its respective central meridian, albeit slightly farther due to projection distortion. At the equator, UTM eastings range from approximately 167,000 to 833,000 meters [4, 5].

The Universal Transverse Mercator (UTM) system provides extensive coverage of the Earth's surface, with the exception of polar regions beyond latitudes of 84° North and 80° South. The Earth is divided into 60 zones, each comprising 6 degrees of longitude [6, 7]. These UTM zones are sequentially numbered from 1 to 60, with the numbering starting at 180° West longitude [8].

This system facilitates the representation of Earth's points using flat coordinates (X, Y or Easting, Northing), offering advantages such as simplified planar mapping, straightforward derivation of spatial metrics (e.g., distances, angles,

Technologies and Materials for Renewable Energy, Environment and Sustainability
AIP Conf. Proc. 3321, 020035-1–020035-12; https://doi.org/10.1063/5.0290304
Published under an exclusive license by AIP Publishing. 978-0-7354-5231-2/$30.00

areas), and ease of coordinate-based calculations [9]. With all measurements standardized in meters, UTM enables convenient computation of distances, directions, and areas compared to the geographic coordinate system [10].

The challenge associated with the continuity of UTM

The UTM system, while exhibiting some challenges in coordinate conversion like any other system, demonstrates fewer issues compared to alternative conversion methodologies [11]. Its underlying principle involves dividing the globe into zones, each with unique characteristics not necessarily shared with neighboring zones [12, 13]. The complexity arises particularly in regions encompassing multiple zones, leading to potential discrepancies when transitioning between zones during conversion processes [14].

For instance, the United States spans across ten UTM zones, with densely populated areas often encountering difficulties due to zone boundaries [15]. Take, for instance, the comparison between Philadelphia and Pittsburgh in Pennsylvania. Despite being within the same state, their locations in different UTM zones result in disparities in centroid Eastings, with Philadelphia (approximately 486 km) appearing to be farther east than Pittsburgh (almost 586 km) due to their respective zone placements (Philadelphia closer to Zone 18, Pittsburgh situated in Zone 17) [16].

Comparable problems exist throughout the breadth of Iraqi country, this incorporates three unique UTM zones (37, 38, and 39).

Zone 37 comprises areas of western Iraq, and Zone 38 encompasses the preponderance of the country's region. Zone 39 comprises a tiny part of Basra in the east-south area of Iraq [17, 18]. This scenario of multiple zones adds intricacy to coordinate conversions within Iraq, demanding careful consideration of zone boundaries to ensure precise spatial depiction [19]. Figure 1 visually delineates the demarcation of zones 37, 38, and 39 across Iraqi territory [20].

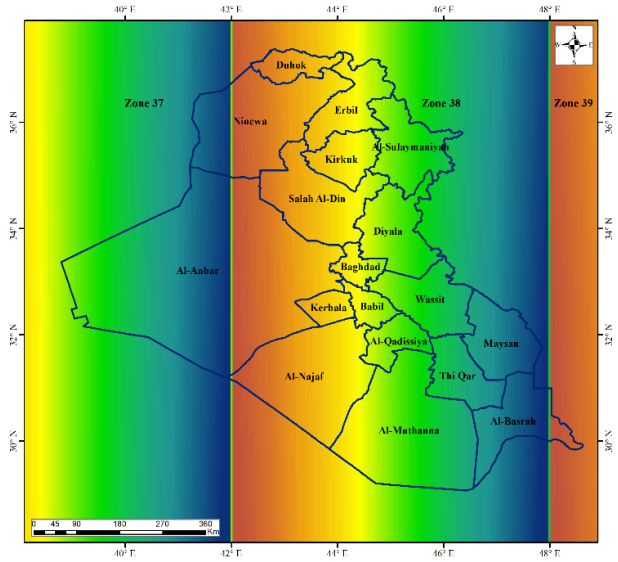

Figure 1. Depicts the intersection of zones 37, 38, and 39.

THEORETICAL FRAME WORK

This component elucidates the mathematical framework utilized for the change method [21]. Four polynomial equation models were utilized to conduct the correction, as indicated below**.**

Absolute Polynomial Representation:

$$Forward: \qquad X_k = \sum_{i=0}^{Ord} \sum_{j=0}^{i} a_L \lambda_k^j \varphi_k^{i-j} \tag{1a}$$

$$Y_k = \sum_{i=0}^{Ord} \sum_{j=0}^{i} b_L \, \lambda_k^j \, \varphi_k^{i-j} \tag{1b}$$

$$Inverse: \quad \lambda_k = \sum_{i=0}^{Ord} \sum_{j=0}^{i} c_L \, X_k^j \, Y_k^{i-j} \tag{2a}$$

$$\varphi = \sum_{i=0}^{Ord} \sum_{j=0}^{i} d_L \, X_k^j \, Y_k^{i-j} \tag{2b}$$

Relative Polynomial Representation:

$$Forward: \quad X_k = \sum_{i=0}^{Ord} \sum_{j=0}^{i} a_L \left(\lambda_k - \bar{\lambda}\right)^j (\varphi_k - \bar{\varphi})^{i-j} \tag{3a}$$

$$Y_k = \sum_{i=0}^{Ord} \sum_{j=0}^{i} b_L \left(\lambda_k - \bar{\lambda}\right)^j (\varphi_k - \bar{\varphi})^{i-j} \tag{3b}$$

$$Inverse: \quad \lambda_k = \sum_{i=0}^{Ord} \sum_{j=0}^{i} c_L \, (X_k - \bar{X})^j (Y_k - \bar{Y})^{i-j} \tag{4a}$$

$$\varphi_k = \sum_{i=0}^{Ord} \sum_{j=0}^{i} d_L \, (X_k - \bar{X})^j (Y_k - \bar{Y})^{i-j} \tag{4b}$$

Normalized Polynomial Representation

$$Forward: \quad X_i = \sum_{i=0}^{Ord} \sum_{j=0}^{i} a_L \left(\frac{\lambda_i}{\bar{\lambda}}\right)^j \left(\frac{\varphi_i}{\bar{\varphi}}\right)^{i-j} \tag{5a}$$

$$Y_i = \sum_{i=0}^{Ord} \sum_{j=0}^{i} b_L \left(\frac{\lambda_i}{\bar{\lambda}}\right)^j \left(\frac{\varphi_i}{\bar{\varphi}}\right)^{i-j} \tag{5b}$$

$$Inverse: \quad \lambda_k = \sum_{i=0}^{Ord} \sum_{j=0}^{i} c_L \left(\frac{X_k}{\bar{X}}\right)^j \left(\frac{Y_k}{\bar{Y}}\right)^{i-j} \tag{6a}$$

$$\varphi_k = \sum_{i=0}^{Ord} \sum_{j=0}^{i} d_L \left(\frac{X_k}{\bar{X}}\right)^j \left(\frac{Y_k}{\bar{Y}}\right)^{i-j} \tag{6b}$$

Relative Normalized Polynomial Representation

$$Forward: \quad X_k = \sum_{i=0}^{Ord} \sum_{j=0}^{i} a_L \left(\frac{\lambda_k - \bar{\lambda}}{\bar{\lambda}}\right)^j \left(\frac{\varphi_k - \bar{\varphi}}{\bar{\varphi}}\right)^{i-j} \tag{7a}$$

$$Y_k = \sum_{i=0}^{Ord} \sum_{j=0}^{i} b_L \left(\frac{\lambda_k - \bar{\lambda}}{\bar{\lambda}}\right)^j \left(\frac{\varphi_k - \bar{\varphi}}{\bar{\varphi}}\right)^{i-j} \tag{7b}$$

$$Inverse: \quad \lambda_k = \sum_{i=0}^{Ord} \sum_{j=0}^{i} c_L \left(\frac{X_k - \bar{X}}{\bar{X}}\right)^j \left(\frac{Y_k - \bar{Y}}{\bar{Y}}\right)^{i-j} \tag{8a}$$

$$\varphi_k = \sum_{i=0}^{Ord} \sum_{j=0}^{i} d_L \left(\frac{X_k - \bar{X}}{\bar{X}}\right)^j \left(\frac{Y_k - \bar{Y}}{\bar{Y}}\right)^{i-j} \quad (8b)$$

In which, (λ_k, φ_k, X_k, Y_k) indicate the latitude, longitude (East, North) coordinates of the k[th] point, whereas the associated mean values are as follows [2, 22]:

$$\bar{\lambda} = \frac{1}{N}\sum_{k=1}^{N} \lambda_k \quad , \qquad \bar{\varphi} = \frac{1}{N}\sum_{k=1}^{N} \varphi_k \quad (9a)$$

$$\bar{X} = \frac{1}{N}\sum_{k=1}^{N} X_k \quad , \qquad \bar{Y} = \frac{1}{N}\sum_{k=1}^{N} Y_k \quad (9b)$$

The sequences of polynomial coefficients denoted by $\{a_L\}$, $\{b_L\}$, $\{c_L\}$, $\{d_L\}$ were employed. Upon study of the four techniques, the data disclose that the Relative Normalized Polynomial comes out as the most alluring solution for implementation [2, 23].

Forward Representation

From a mathematical viewpoint, the coordinates corresponding to the East and North directions (X and Y) may be appropriately stated as:

$$X = F(\varphi, \lambda) \ , \ Y = G(\varphi, \lambda) \quad (1)$$

These functions exhibit continuity across the majority of the Earth's surface, with the exception of the polar regions [2, 24]. Consequently, the Taylor series development of both functions round the point (φ_o, λ_o) are as follows:

$$X = F(\varphi_o, \lambda_o) + \sum_{m=0}^{\infty}\sum_{n=0}^{\infty} \left.\frac{\partial F^{m+n}(\varphi,\lambda)}{\partial^m \varphi \, \partial^n \lambda}\right|_{\varphi_o,\lambda_o} \frac{(\varphi-\varphi_o)^m}{m!}\frac{(\lambda-\lambda_o)^n}{n!} \ , \qquad \text{where } n+m>0 \quad (2)$$

$$Y = G(\varphi_o, \lambda_o) + \sum_{m=0}^{\infty}\sum_{n=0}^{\infty} \left.\frac{\partial G^{m+n}(\varphi,\lambda)}{\partial^m \varphi \, \partial^n \lambda}\right|_{\varphi_o,\lambda_o} \frac{(\varphi-\varphi_o)^m}{m!}\frac{(\lambda-\lambda_o)^n}{n!} \ , \qquad \text{where } n+m>0 \quad (3)$$

If the vicinity around (φ,λ) is confined to an area extending only a few degrees away from (φ_0, λ_0) under these conditions, the parameters m and n can be limited to modest values, generally falling below 5 or 6 [25]. In such scenarios, the aforementioned equations can be approximated as follows [26, 20]:

$$X = \sum_{i=0}^{Order} \sum_{j=0}^{i} a_{n(i)+j} (\Delta\varphi)^{i-j} (\Delta\lambda)^j \quad (4c)$$

$$Y = \sum_{i=0}^{Order} \sum_{j=0}^{i} b_{n(i)+j} (\Delta\varphi)^{i-j} (\Delta\lambda)^j \quad (4d)$$

where, $n(i) = \frac{1}{2} i(i+1)$, $\Delta\varphi = \varphi - \varphi_o$, $\Delta\lambda = \lambda - \lambda_o$

For the 6[th] Order Polynomials

$$X = a_0 + a_1\Delta\varphi + \cdots + a_{27}(\Delta\lambda)^6 \quad (6c)$$

$$Y = b_0 + b_1\Delta\varphi + \cdots + b_{27}(\Delta\lambda)^6 \quad (6d)$$

Backward Representation

Moreover, the inverse mapping equations may be represented roughly as:

$$\varphi = H(X, Y) \ , \ \lambda = Q(X, Y) \quad (7)$$

Additionally, within the region of interest (namely, the territory of Iraq), the equation maintains continuity [27]. Therefore, the Taylor series expansions for both equations 2 and 3 can be represented as depicted in equations 8 and 9 below [1, 28]:

$$\varphi = H(X_o, Y_o) + \sum_{m=0}^{\infty}\sum_{n=0}^{\infty} \left.\frac{\partial H(X,Y)}{\partial^m X \, \partial^n Y}\right|_{X_o,Y_o} \frac{(X-X_o)^m}{m!}\frac{(Y-Y_o)^n}{n!} \ , \text{where } n+m>0 \quad (8)$$

$$\lambda = Q(X_o, Y_o) + \sum_{m=0}^{\infty}\sum_{n=0}^{\infty} \left.\frac{\partial Q^{m+n}(X,Y)}{\partial^m X\, \partial^n Y}\right|_{X_o,\lambda_o} \frac{(X-X_o)^m}{m!}\frac{(Y-Y_o)^n}{n!} \quad \text{where } n+m>0 \qquad (9)$$

Equivalent mathematical techniques can be employed to reformulate the aforementioned equations within the framework of 2D polynomials [1, 29]:

$$\varphi = \sum_{i=0}^{Order}\sum_{j=0}^{i} c_{n(i)+j}(\Delta X)^{i-j}(\Delta Y)^j \qquad (10c)$$

$$\lambda = \sum_{i=0}^{Order}\sum_{j=0}^{i} d_{n(i)+j}(\Delta X)^{i-j}(\Delta Y)^j \qquad (10d)$$

$$\text{where, } \; n(i) = \frac{1}{2}i(i+1)\,, \quad \Delta x = x - x_o \qquad \Delta y = y - y_o$$

For the 6th Order Polynomial

$$\varphi = c_0 + c_1\Delta x + \cdots + c_{27}(\Delta y)^6 \qquad (12a)$$

$$\lambda = d_0 + d_1\Delta x + \cdots + d_{27}(\Delta y)^6 \qquad (12b)$$

RESULTS AND DISCUSSIONS

A dataset encompassing the coordinates of grid points (Longitude, Latitude) spanning the territory of Iraq and its adjacent areas was assembled. The spacing between grid elements was maintained at 0.25 degrees. Subsequently, these coordinates underwent changing to (X, Y) coordinates utilizing UTM system conversion instruments, with a concentrate notably on Zones 38. The resultant (X, Y) coordinate values were determined. The error figures shown below underscore the reasons for choosing the relative normalized polynomial over other models, including the absolute polynomial, relative polynomial, and normalized polynomial.

Table 1. Presents the error rates derived from the utilization of sixth-order polynomial equations for absolute polynomial representation.

	Error rate of X_easting (m)	Error rate of Y_northing (m)
Maximum	0.0694013914	0.0079115005
Minimum	0.0000052704	0.0000031944
Average	0.0136680932	0.0012384682

Table 2. Displays the error rates obtained through the application of sixth-order polynomial equations for relative polynomial representation.

	Error rate of X_easting (m)	Error rate of Y_northing (m)
Maximum	40.5496530521	11.0027611395
Minimum	0.0004472306	0.0003896439
Average	5.6521726798	1.5270945414

Table 3. Illustrates the error rates resulting from the use of sixth-order polynomial equations for normalized polynomial representation.

	Error rate of X_easting (m)	Error rate of Y_northing (m)
Maximum	0.0694013621	0.0079116337
Minimum	0.0000052890	0.0000032531
Average	0.0136680929	0.0012384687

The decision to opt for relative normalized polynomial equations is supported by the insights gleaned from the error tables.

Forward

In this phase, the error rates are computed for the second test, both in the eastward (X) and northward (Y) directions, employing polynomial equations of varying orders (up to the 6th order), determined based on the least squares error

criterion. The following list presents the error rates for several polynomial orders, based on the relative standardized polynomial equation.

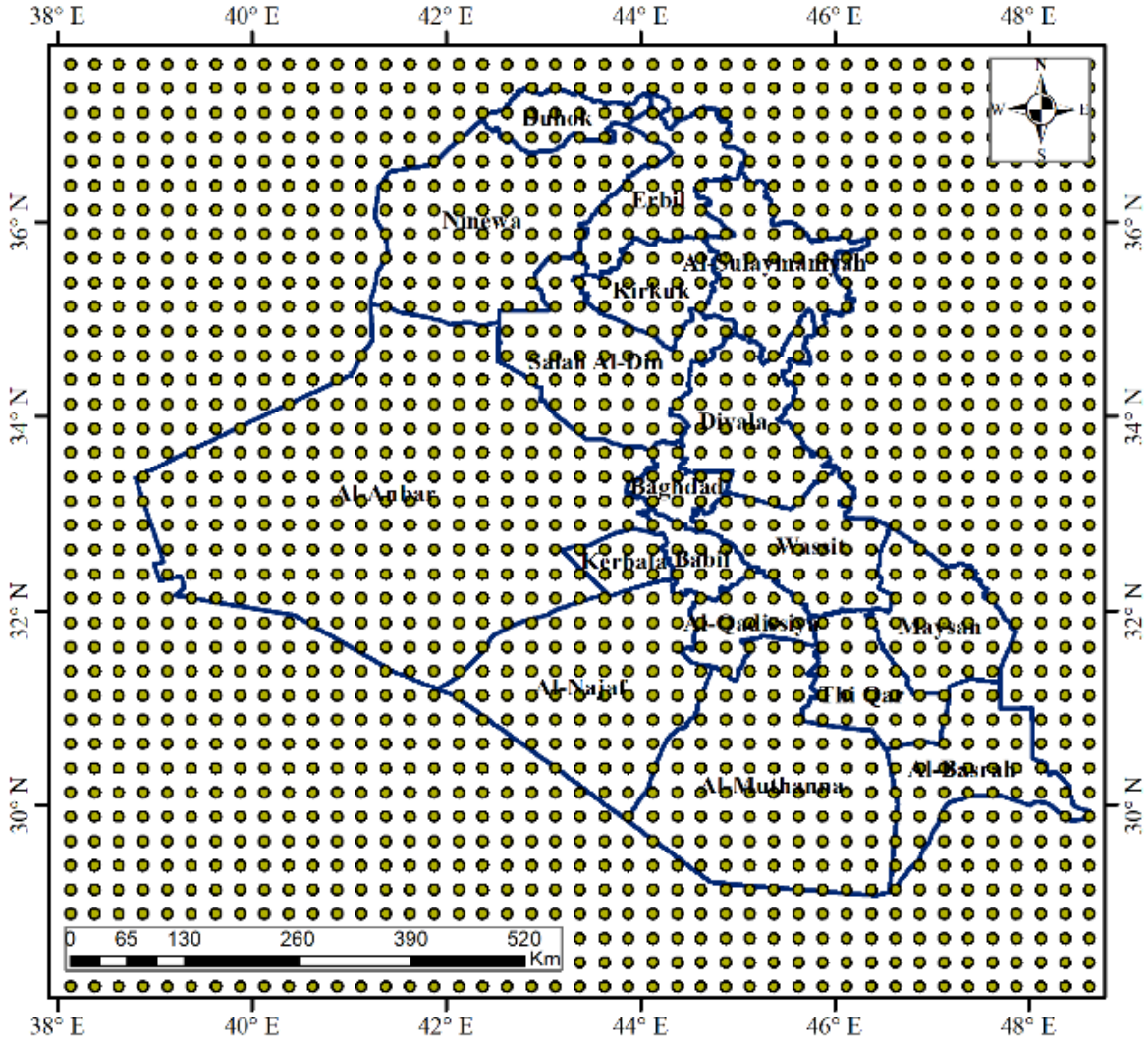

Figure 2. Illustrates the dataset comprising grid points.

Table 4. The error rate values obtained through the utilization of first-order polynomial equations (4c and 4d).

	Error rate of X easting (m)	Error rate of Y northing (m)
Maximum	41863.9430468056	8661.1365766544
Minimum	1.2162380774	3.7031756891
Average	9784.8705609217	3252.9318121544

Table 5. The error rate values obtained through the utilization of second-order polynomial equations (4c and 4d).

	Error rate of X easting (m)	Error rate of Y northing (m)
Maximum	1617.2721945947	727.1169847893
Minimum	0.0215703859	0.0468150200
Average	246.3190924989	140.2877139533

Table 6. The error rate values obtained through the utilization of third-order polynomial equations (4c and 4d).

	Error rate of X easting (m)	Error rate of Y northing (m)
Maximum	102.5081482735	100.7658141581

Minimum	0.0024759048	0.0037078243
Average	19.9858206927	15.8291561954

Table 7. The error rate values obtained through the utilization of fourth-order polynomial equations (4c and 4d).

	Error rate of X easting (m)	Error rate of Y northing (m)
Maximum	16.1870591318	1.3521496123
Minimum	0.0009327258	0.0000944715
Average	2.4375069151	0.2343347337

Table 8. The error rate values obtained through the utilization of fifth-order polynomial equations (4c and 4d).

	Error rate of X easting (m)	Error rate of Y northing (m)
Maximum	1.4778963692	0.1819764599
Minimum	0.0001740494	0.0000123847
Average	0.2258239929	0.0233749648

Based on the error rates observed across different polynomial orders, it was deduced that the sixth order yields the lowest error value.

Tables (9) and (10) exhibit the polynomial coefficient values with the concomitant error rates in the eastward (X) and northward (Y) directions employing sixth-order polynomials (equations 6a and 6b), as specified in the relevant tables. Moreover, the error ranges are indicated in figures 3 and 4.

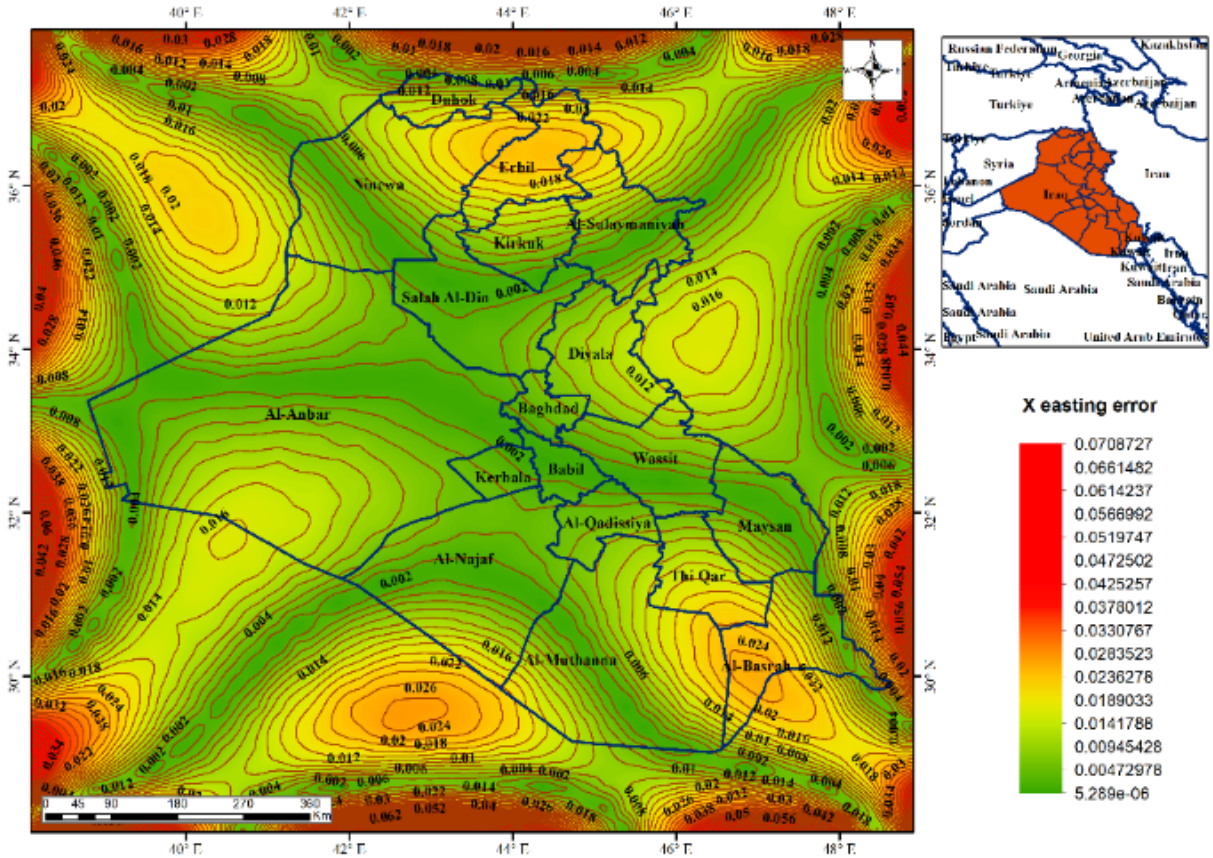

Figure 3. Illustrates the distribution of error values concerning the easting (X) direction employing a sixth-order polynomial.

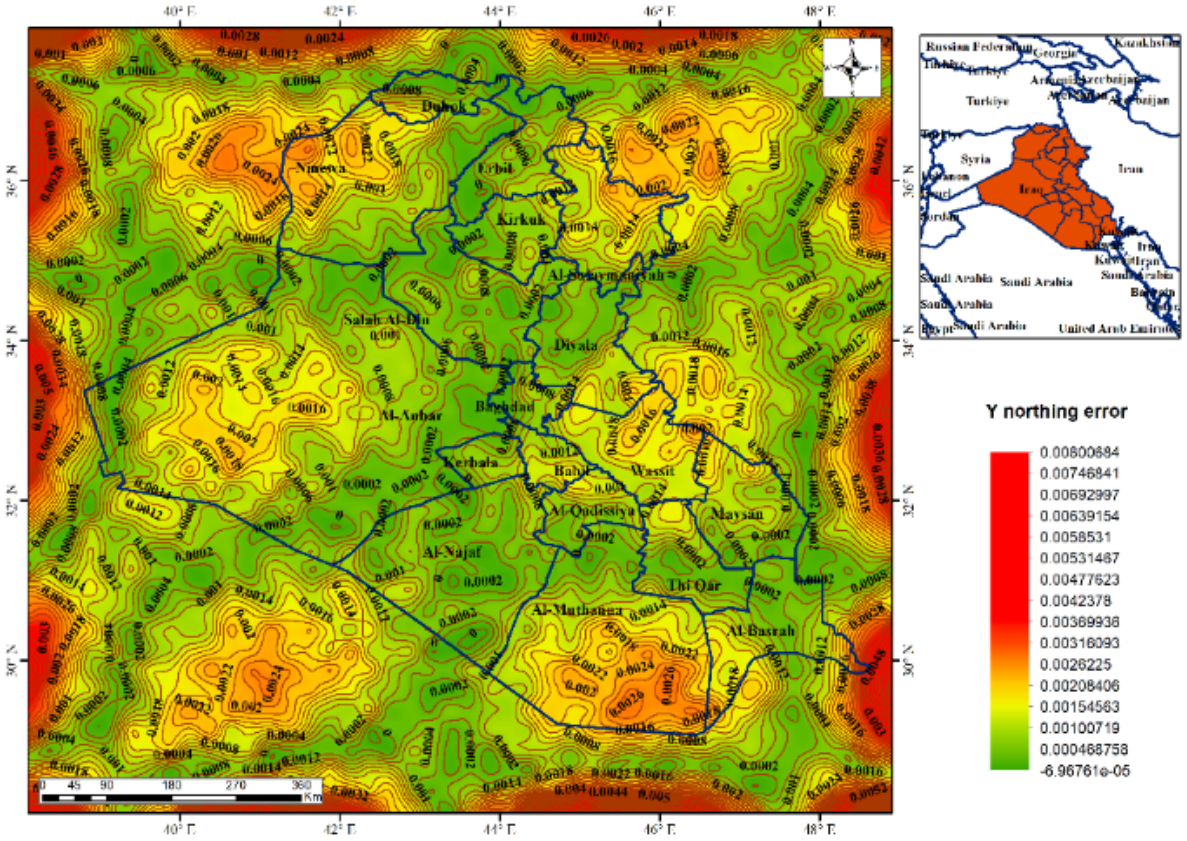

Figure 4. Displays the distribution of error values associated to northing (Y) employing a sixth-order polynomial.

Table 9. The forward *c*oefficients values derived from the application of sixth-order polynomial equations (6c and 6d).

Symbol	Coefficients	Symbol	Coefficients	Symbol	Coefficients	Symbol	Coefficients
a_0	0.001185	a_{14}	-0.460322	b_0	0.001417	b_{14}	-0.001590
a_1	-5.677741	a_{15}	0.296079	b_1	-0.079900	b_{15}	-0.000205
a_2	-1.521101	a_{16}	-0.000069	b_2	0.990888	b_{16}	-0.000178
a_3	-0.129586	a_{17}	-0.356180	b_3	0.113301	b_{17}	-0.016399
a_4	-0.576173	a_{18}	-2.772906	b_4	-0.012919	b_{18}	0.010912
a_5	4.326414	a_{19}	0.009646	b_5	-0.003437	b_{19}	0.014302
a_6	0.388496	a_{20}	0.166172	b_6	-0.009486	b_{20}	-0.017900
a_7	0.152990	a_{21}	-0.000227	b_7	0.000017	b_{21}	0.000098
a_8	-0.627672	a_{22}	0.007707	b_8	-0.002654	b_{22}	-0.000180
a_9	1.369311	a_{23}	0.203850	b_9	0.092711	b_{23}	0.003627
a_{10}	-0.555833	a_{24}	3.312290	b_{10}	0.006632	b_{24}	-0.005006
a_{11}	0.011913	a_{25}	0.573520	b_{11}	0.002500	b_{25}	-0.033229
a_{12}	0.742303	a_{26}	-1.082128	b_{12}	0.020926	b_{26}	0.025184
a_{13}	1.241424	a_{27}	-0.038013	b_{13}	-0.131774	b_{27}	0.001748

Table 10. The forward error rate values obtained through the utilization of sixth-order polynomial equations (6c and 6d).

	Error rate of X_easting (m)	Error rate of Y_northing (m)
Maximum	0.0694013621	0.0079116337
Minimum	0.0000052890	0.0000032531
Average	0.0136680929	0.0012384687

Backward

Tables (11) and (12) present the coefficient values and error rates pertinent to longitude and latitude, employing sixth-order polynomial equations (9a and 9b) to measure the correctness of the conversion operation, as indicated in the corresponding tables. Furthermore, error distributions are provided in figures (5) and (6).

Table 11. The backward coefficients values derived from the application of sixth-order polynomial equations (12a and 12b).

Symbol	Coefficients	Symbol	Coefficients	Symbol	Coefficients	Symbol	Coefficients
$\mathbf{c_0}$	0.00058	$\mathbf{c_{14}}$	-0.10301	$\mathbf{d_0}$	-0.00138	$\mathbf{d_{14}}$	-0.01495
$\mathbf{c_1}$	-0.17224	$\mathbf{c_{15}}$	0.00000	$\mathbf{d_1}$	-0.01386	$\mathbf{d_{15}}$	0.00000
$\mathbf{c_2}$	-0.26368	$\mathbf{c_{16}}$	-0.21159	$\mathbf{d_2}$	0.98794	$\mathbf{d_{16}}$	-0.01426
$\mathbf{c_3}$	0.00199	$\mathbf{c_{17}}$	-0.00036	$\mathbf{d_3}$	-0.00322	$\mathbf{d_{17}}$	-0.00008
$\mathbf{c_4}$	-0.29325	$\mathbf{c_{18}}$	-0.00142	$\mathbf{d_4}$	-0.01985	$\mathbf{d_{18}}$	-0.00036
$\mathbf{c_5}$	-0.12026	$\mathbf{c_{19}}$	0.00960	$\mathbf{d_5}$	-0.02104	$\mathbf{d_{19}}$	-0.00398
$\mathbf{c_6}$	0.00009	$\mathbf{c_{20}}$	-0.08645	$\mathbf{d_6}$	0.00004	$\mathbf{d_{20}}$	-0.01371
$\mathbf{c_7}$	-0.25670	$\mathbf{c_{21}}$	0.00000	$\mathbf{d_7}$	-0.01587	$\mathbf{d_{21}}$	0.00000
$\mathbf{c_8}$	0.00361	$\mathbf{c_{22}}$	-0.19104	$\mathbf{d_8}$	-0.00497	$\mathbf{d_{22}}$	-0.01250
$\mathbf{c_9}$	-0.12815	$\mathbf{c_{23}}$	-0.00001	$\mathbf{d_9}$	-0.01515	$\mathbf{d_{23}}$	-0.00001
$\mathbf{c_{10}}$	-0.00007	$\mathbf{c_{24}}$	-0.00076	$\mathbf{d_{10}}$	-0.00001	$\mathbf{d_{24}}$	-0.00020
$\mathbf{c_{11}}$	-0.23802	$\mathbf{c_{25}}$	-0.00232	$\mathbf{d_{11}}$	-0.01367	$\mathbf{d_{25}}$	-0.00055
$\mathbf{c_{12}}$	-0.00059	$\mathbf{c_{26}}$	0.01448	$\mathbf{d_{12}}$	-0.00007	$\mathbf{d_{26}}$	-0.00336
$\mathbf{c_{13}}$	0.00656	$\mathbf{c_{27}}$	-0.06227	$\mathbf{d_{13}}$	-0.00374	$\mathbf{d_{27}}$	-0.01197

Table 12. The backward error rate values obtained through the utilization of sixth-order polynomial equations (12a and 12b).

	Error rate of Longitude (SEC)	Error rate of Latitude (SEC)
Maximum	0.0000019712	0.0000010443
Minimum	0.0000000003	0.0000000000
Average	0.0000003726	0.0000001317

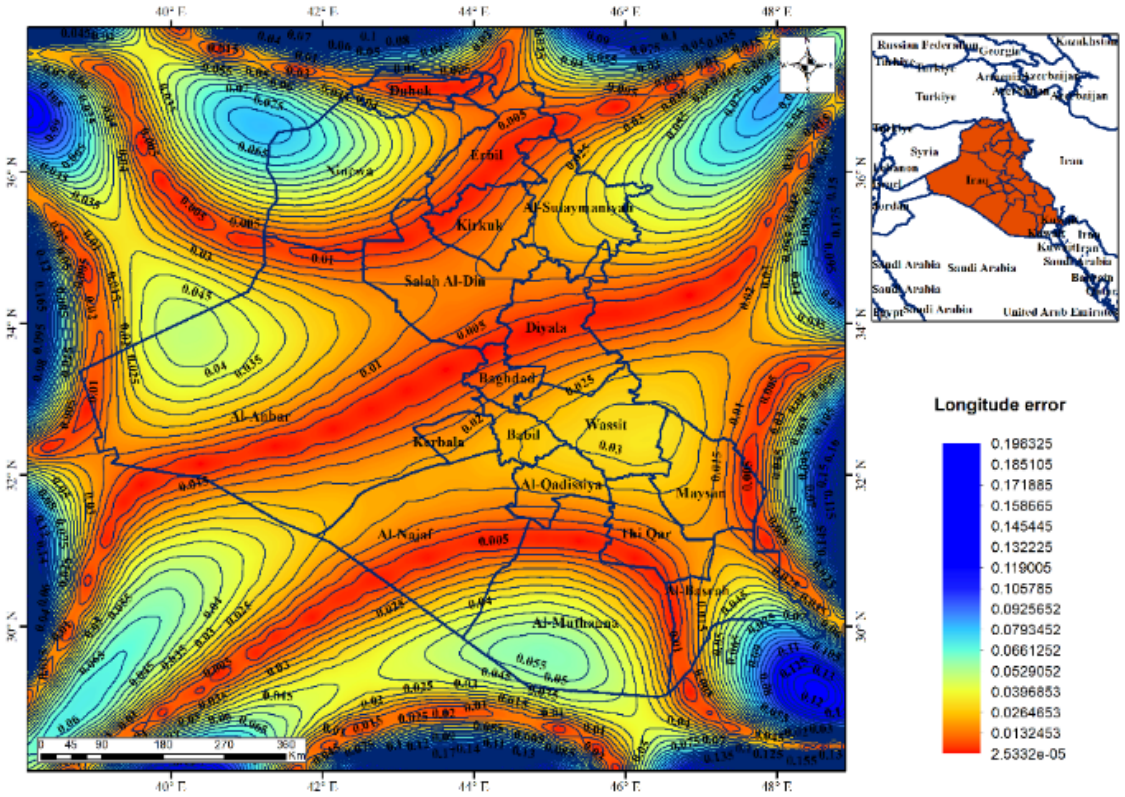

Figure 5. Displays the distribution of error values associated with longitudes applying a sixth-order polynomial.

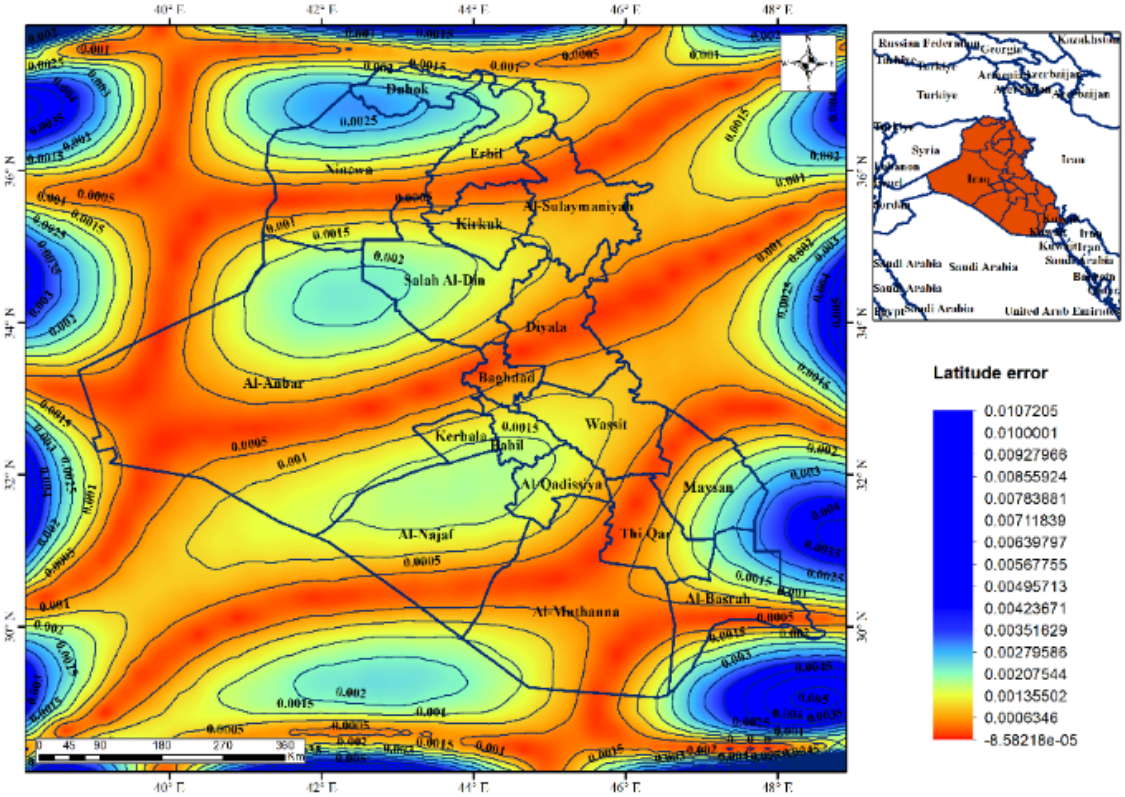

Figure 6. Displays the distribution of error values relative to latitude using a sixth-order polynomial.

CONCLUSIONS

During the initial test, significantly elevated error rates were noted, leading to the unsuccessful completion of the conversion process. However, upon implementing the normalization method in the subsequent test, the error rates progressively decreased, reaching their minimum value when utilizing a sixth-degree polynomial equation. This significant reduction in errors facilitated the success of the conversion process, yielding outcomes closely aligned with ideal expectations.

Utilizing the sixth-order polynomial equation, the average inaccuracy measured around 0.013 meters in the eastward (X) direction and around 0.001 meters in the northward (Y) direction. These results demonstrate exceptional precision, affirming the suitability of this model for converting coordinates from longitude and latitude to easting and northing, particularly within the Iraqi region.

REFERENCES

1. B. H. Sayed and L. E. George, "Flat Model for Representing Contiguous UTM Coordinates over Iraq Territory," Iraqi J. Sci., pp. 908–919, Apr. 2020, doi: 10.24996/ijs.2020.61.4.24.
2. A. A. Saud, L. E. George, and B. H. Sayyid, "Simplified Flat Coordinate Model for Northern Parts of Arabian Gulf," Iraqi J. Sci., pp. 3282–3290, Sep. 2021, doi: 10.24996/ijs.2021.62.9.39.
3. H. Tian et al., "Extraction of Citrus Trees from UAV Remote Sensing Imagery Using YOLOv5s and Coordinate Transformation," Remote Sens., vol. 14, no. 17, p. 4208, Aug. 2022, doi: 10.3390/rs14174208.
4. K. Wang, S. Ye, P. Gao, X. Yao, and Z. Zhao, "Optimization of Numerical Methods for Transforming UTM Plane Coordinates to Lambert Plane Coordinates," Remote Sens., vol. 14, no. 9, p. 2056, Apr. 2022, doi: 10.3390/rs14092056.
5. S. A. Salman and A. H. Abd-Almeer, "Clotting detection in the vascular network," Indones. J. Electr. Eng. Comput. Sci., vol. 20, no. 2, p. 1103, Nov. 2020, doi: 10.11591/ijeecs.v20.i2.pp1103-1108.
6. M. Jannati, N. R. N. Idris, M. J. A. Aziz, S. H. Asgari, A. Monadi, and A. A. M. Faudzi, "A new method for RFOC of single-phase induction motor based on rotational transformations," in 2013 IEEE Student Conference on Research and Developement, IEEE, Dec. 2013, pp. 215–220. doi: 10.1109/SCOReD.2013.7002574.
7. M. Z. Syahmi, W. A. W. Aziz, M. A. Zulkarnaini, A. Anuar, and Z. Othman, "The movement detection on the landslide surface by using Terrestrial Laser Scanning," in 2011 IEEE Control and System Graduate Research Colloquium, IEEE, Jun. 2011, pp. 175–180. doi: 10.1109/ICSGRC.2011.5991851.
8. Z. Rajion et al., "Coordinate Systems Integration for Development of Malaysian Craniofacial Database," in 2005 IEEE Engineering in Medicine and Biology 27th Annual Conference, IEEE, 2005, pp. 5112–5115. doi: 10.1109/IEMBS.2005.1615627.
9. Changxiong Wang, Shanjun Mao, Mei Li, Huiyi Bao, and Ying Zhang, "Integration of vector and raster-based coal mines surface and underground contrast map," in 2012 Second International Workshop on Earth Observation and Remote Sensing Applications, IEEE, Jun. 2012, pp. 309–312. doi: 10.1109/EORSA.2012.6261189.
10. S. F. Behadili and B. H. Sayed, "Oli and gas explorations via satellite remote sensing techniques for Al_Nasiriya," Iraqi J. Sci., vol. 60, no. 10, pp. 2308–2314, 2019, doi: 10.24996/ijs.2019.60.10.25.
11. R. S. Hameed, L. E. Georg, and B. H. Sayyid, "Modified Vegetation Detection Index Using Different-Spectral Signature," Iraqi J. Sci., pp. 4208–4217, Nov. 2021, doi: 10.24996/ijs.2021.62.11.38.
12. H. J. Alatta, S. F. Behadili, and B. H. Sayyid, "Analyze Water Scarcity in Basrah City Via Geoinformatics," AIP Conf. Proc., vol. 2398, no. October, 2022, doi: 10.1063/5.0093409.
13. A. A. Saud, L. E. George, and B. H. Sayyid, "Effect of the polynomial parameters on the conversion process using a simplified flat model for northern parts of the Arabian Gulf," 2022, p. 020034. doi: 10.1063/5.0093845.
14. A. Al-Barrak, H. J. Alatta, S. F. Behadili, B. H. Sayyid, A. Adham, and M. A. Mahmood, "Modeling and analysis of thermal contrast based on LST algorithm for Baghdad city," 2024, p. 040010. doi: 10.1063/5.0202094.
15. H. J. Alatta, L. E. George, S. F. Behadili, B. H. Sayyid, and M. H. Ali, "Geospatial Data Analysis of School Distribution in Baghdad City," Iraqi J. Sci., pp. 6675–6685, Dec. 2023, doi: 10.24996/ijs.2023.64.12.45.
16. B. H. Sayyid, A. H. Shaban, and N. A. Abd, "Estimated deformation for two events 6 Mw and 7.3 Mw Iraq-Iran border earthquake by using Sentinel-1 satellite imagery," 2023, p. 020057. doi: 10.1063/5.0171979.
17. F. K. M. Al-Ramahi, F. H. Mahmood, and A. K. M. Ali, "Finding the Best Analysis for the Sleeper Cells of Terrorist Acts in the Crowded Areas of Human Activities in the City of Baghdad," Iraqi J. Sci., pp. 6662–6674, Dec. 2023, doi: 10.24996/ijs.2023.64.12.44.

18. F. H. Mahmood and S. A.-J. Aziz, “An Improved Segmentation Technique for Early Detection of Exudates of Diabetic Retinopathy Disease,” Iraqi J. Sci., pp. 2520–2530, Nov. 2019, doi: 10.24996/ijs.2019.60.11.25.
19. N. S. Abd-Alwahab and N. K. Ghazal, “Change Detection between Landsat 8 images and Sentinel-2 images,” Iraqi J. Sci., pp. 1868–1876, Aug. 2019, doi: 10.24996/ijs.2019.60.8.24.
20. B. H. Sayyid, A. H. Shaban, and N. A. Abd, “The 25 november 2018 Mw 6.3 Iraq-Iran border earthquake by using InSAR technique,” 2023, p. 020031. doi: 10.1063/5.0171975.
21. A. N. Abdul-Hammed and A. S. Mahdi, “Monitoring Vegetation Area in Baghdad Using Normalized Difference Vegetation Index,” Iraqi J. Sci., pp. 1394–1401, Mar. 2022, doi: 10.24996/ijs.2022.63.3.40.
22. A. S. Mahdi, “The Digital Change Detection for Low Resolution Satellite Images in Weathering Estimation,” Iraqi J. Sci., pp. 1007–1017, Feb. 2023, doi: 10.24996/ijs.2023.64.2.42.
23. A. N. Abdul-Hammed and A. S. Mahdi, “The Satellite Images Matching and Mosaic Techniques,” Iraqi J. Sci., pp. 1545–1554, Mar. 2023, doi: 10.24996/ijs.2023.64.3.42.
24. A. A. N. Al-Jasim, T. A. Naji, and A. H. Shaban, “The Effect of Using the Different Satellite Spatial Resolution on the Fusion Technique,” Iraqi J. Sci., vol. 63, no. 9, pp. 4131–4141, 2022, doi: 10.24996/ijs.2022.63.9.40.
25. L. A. Jawad, A. A. Zaeen, and T. Z. Hamood, “Horan Valley Basin Geomorphological Aspects Assessment by Integrating Hypsometric Analysis with Remotely Sensed Morphometric Characteristics,” Iraqi J. Sci., pp. 583–592, Jan. 2024, doi: 10.24996/ijs.2024.65.1.45.
26. M. E. Homadi and L. A. Jawad, “Integration of Remotely Sensed Digital Elevation Model Data and Geographic Information System Facilities to Estimate Net Solar Radiation Variances in Iraq (1987-2017),” Iraqi J. Sci., pp. 689–698, Feb. 2021, doi: 10.24996/ijs.2021.62.2.32.
27. L. A. Jawad, A. S. Mahdi, and F. H. Mahmood, “The Simulation of Old Human Remains Detecting Utilizing Ground Penetrating Radar Image Processing,” Iraqi J. Sci., pp. 4892–4901, Sep. 2023, doi: 10.24996/ijs.2023.64.9.46.
28. N. Ghazal, A. Shaban, F. Mashi, and A. Raihan, “Change Detection Study Of Al Razaza Lake Region Utilizing RemoteSensing And GIS Technique,” Iraqi J. Sci., vol. 53, no. 4Appendix, pp. 950–957, Apr. 2024, doi: 10.24996/iraqijournalofscience.v53i4Appendix.12949.
29. M. S. Shimal and A. H. Shaban, “Evaluation of the Pollution Elements at Samara Water Table â€“ Iraq,” Iraqi J. Sci., pp. 898–907, Apr. 2020, doi: 10.24996/ijs.2020.61.4.23.

Shape memory polymers and technological development

Rola Abdul Al Khader Abbas[1,a], Mohammed Hamza Al-Maamori[2,b], Abdul Hameed Raheem Mahdi Al-Sarraf[3,c]

[1] *University of Technology /Applied Sciences/ Medical and Industrial Materials Sciences Branch, Baghdad, Iraq*
[2] *University of Babylon/ College of Materials Engineering- Polymer and The Petrochemical Industries, Babylon, Iraq*
[3] *Department of Physics, College of Education for Pure Science Ibn-Al-Haitham, University of Baghdad, Baghdad, Iraq*

[a] Corresponding author: 100153@uotechnology.edu.iq
[b]prof.almemori@gmail.com
[c] hameed.r.m@ihcoedu.uobaghdad.edu.iq

Abstract. Smart materials are those materials that sense environmental events and perform operations on the information they have obtained. It then affects the surrounding environment. Smart materials are used in products or systems whose design requires the ability to take acceptable reactions to meet their functional performance needs, knowing that the stimuli for these reactions can arise internally or externally. This article reviews the vast world of shape-memory polymer smart materials, by identifying the main features, properties, and response mechanisms of shape-memory polymers, as well as providing a comprehensive overview of the applications of this type of smart materials.

Keywords: Smart materials, Shape memory effect, Shape memory polymers environmental stimuli, Responsive polymers.

INTRODUCTION

Speaking of the scientific progress and development witnessed by the countries of the world must lead the memory of scientists and engineers to the strenuous efforts that enabled them to overcome the restrictions that were imposed on the concepts and transforming the design into an applied construction that actually exists, especially in the framework of the process and production by focusing on the relation between science and technology. So that, scientists and engineers are not only obliged with implementing the correct solutions to problems, but also with creating radical transformations in the tools and engineering materials resulting from the outputs of human thought represented in innovation and technological creativity that touches all the aspects of the engineering materials science. So, the civilized creativity in materials science throughout history, has led to name the ages by the materials names, such as the stone age, bronze age, and iron age, etc. Where the relationship of materials science and ages was built with the availability of materials in that age [1,2]. Whereas in the stone age, the materials science associated with the materials available in the nature, such as stone, wood, bones, and other materials used by the ancient man in his daily life. Although, with the approach of the stone age to the end, the materials science history began to develop and modernize successively by using gold, silver, copper, and bronze in daily life mainly. Thus, entering materials science in the bronze age, and then the iron age by moving to new, advanced and renewable events that occurred with the development of furnaces whose temperature reaches more than 1200°C, which helped a lot in the work of many of metal alloys [2]. In general, all this development led to a real scientific rise in materials science by moving from conventional materials to advanced materials. Examples of that, what have been seen of electronic materials, metallic superconducting materials, modern materials (as ceramics, advanced ceramics, and superconducting ceramics), semiconductors, polymers, and biodegradable polymeric materials [2]. Due to the entry of oil into industry, the speed of polymeric activity has increased after the setting up of many petrochemical plants in the world. In addition, materials science entered the nanotechnology age, theoretically and practically.

Technologies and Materials for Renewable Energy, Environment and Sustainability
AIP Conf. Proc. 3321, 020036-1–020036-14; https://doi.org/10.1063/5.0289811
Published under an exclusive license by AIP Publishing. 978-0-7354-5231-2/$30.00

With the activity of studies in the field of internal composition that are related to the properties required in the applications of engineering, industry, agriculture, sport, and in other life fields [3-4]. Reaching the shape memory smart materials, where the smart planes, smart textiles, smart homes, and other smart industries refer to the change of the vocabulary of the material world with the emergence of smart materials science, especially based on shape memory polymers. Whereas the past decades have witnessed a tremendous growth in interest in this type of smart materials since the publication of the first scientific articles in the early nineties on these smart polymers [5-9]. It is worth noting in this field that the scientific references agree that the science of polymeric smart materials is divided into four main categories: hydrogels, shape memory, self-healing, and smart- packaging [5]. Where these four classes of smart polymeric materials have led humanity to countless pioneering inventions and rapid technological development in the twenty-first century. It is expected globally that this technological growth within the next fifty years will be 4 million times greater than the emergence of this thought [5,6].

Materials of Future

Nano-engineered Materials

This approach is referred to as the bottom-up method, and the scientific study of the properties and applications of such materials falls under the field of nanotechnology. The prefix "nano" signifies that the structural components involved are on the nanometer scale—typically less than 100 nanometers (i.e., less than 10^{-9} meters). To put this into perspective, a nanometer is approximately one seventy-thousandth the width of a human hair and is comparable to the size of around 500 atoms lined up in a row. One notable example of materials developed using this approach is the carbon nanotube, which exhibits exceptional electrical, thermal, and mechanical properties [3,4,10]..

Smart Materials

The “smart” term means that these materials can sense the environment changes surrounding them, and subsequently react to these changes in pre-determined behaviors-traits which can be seen in living organisms. [3,4,10].

Types of Smart Materials

Smart materials can be generally classified into two types relying on their functional properties as follows [4,5,6]:

Energy-Exchanging Smart Materials

These materials are also called actively smart materials, as these materials have the ability to modify their engineering properties when applying electrical, thermal or magnetic fields; so these materials acquire the ability to convert energy from one form to another.
According to that, these smart materials work to convert the energy from one form to another, there are two types of it:
- Irreversible Energy-exchange smart materials.
- Reversible Energy-exchange smart materials [4,5,6].

Property-Changing Smart Materials

This category of smart materials is known as passively smart materials. Although they are classified as smart materials, they do not possess the inherent capability to actively transfer or convert energy. Instead, their intelligence lies in their ability to respond automatically to external stimuli. These materials undergo changes in their chemical, mechanical, optical, electrical, magnetic, thermal, or other physical properties in response to environmental variations—such as changes in temperature, pressure, light, or moisture—without the need for any active control or external intervention [4,5]. Figure 1 illustrates the various types of smart materials, categorized according to the nature and mechanism of their response to external stimuli.

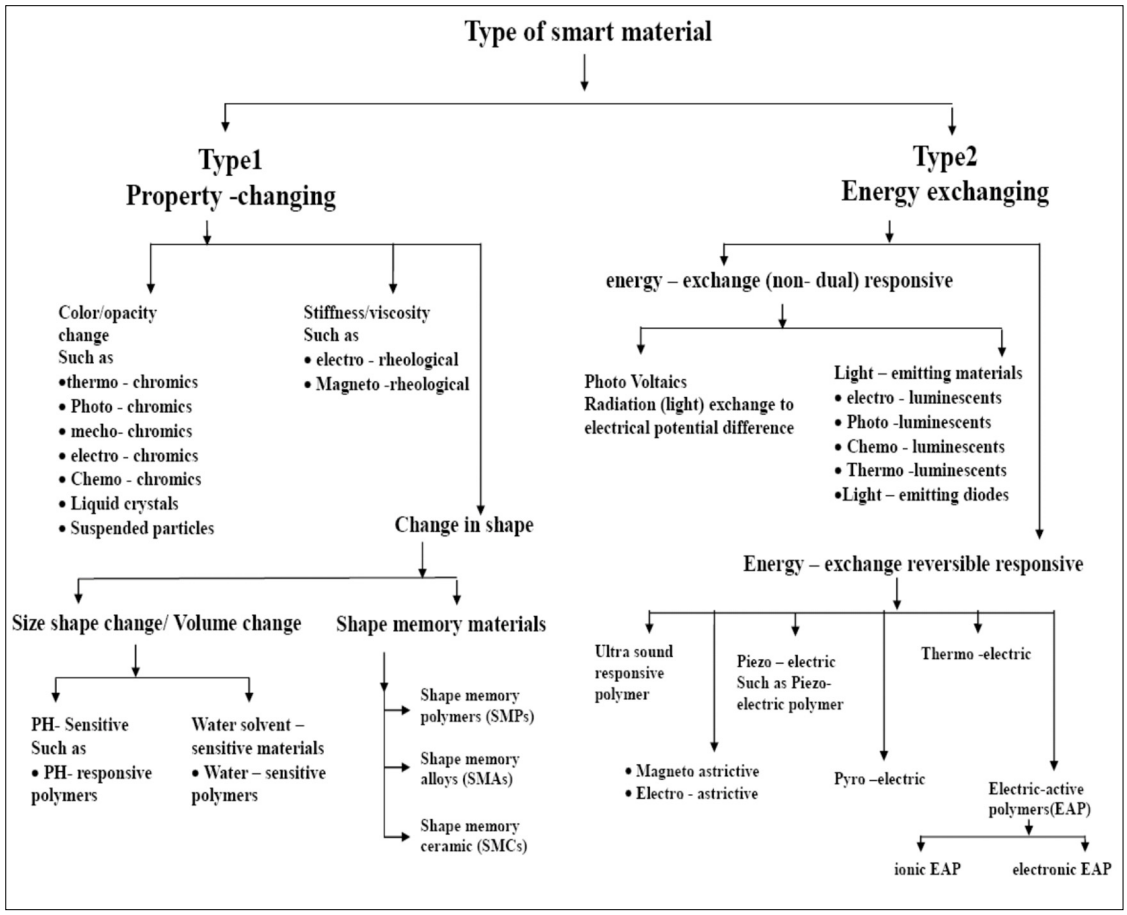

Figure 1. Type of smart materials according the nature of response.

Properties of Smart Materials

- Bionicity
- Sensor Ability
- Adaptability

Shape Memory Materials (SMMs)

Shape memory materials are those types of materials which are able to memorize or retain an obvious lasting shape, which can be controlled, stabilized or fixed to a brief and torpid shape under stress and temperature specific states. Then they can return to the initial state, stress free condition under electrical, thermal, or environmental order. This recovery is correlated with the elastic deformation prior to manipulation.

SMMs have stirred unusual attention from scientists and researchers due to their ability to be in two shapes at several circumstances.

This property gives SMMs great potential for plenty of applications such as media recorders, sensors, smart devices, and actuators [11].

There are different types of advanced and untraditional SMMs such as the following as illustrated in Figure (2) [11,12].

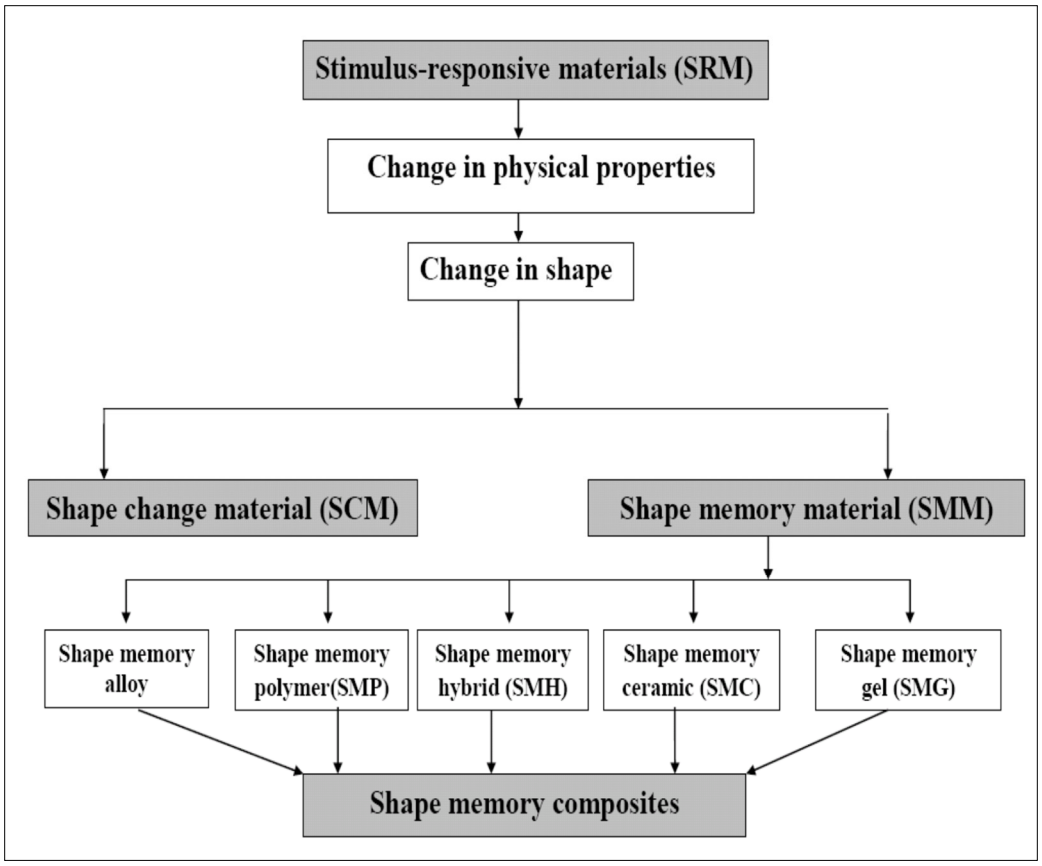

Figure 2. A schematic of tree of shape memory materials (SMMs).

Shape-Memory Alloys (SMAs)

SMAs are a group of metal compounds that experience a shape change in accordance to mechanical or thermal stimuli which are able to be pre-programmed in the material. This is attributed to the two crystallographic phases that this material can be transformed through the transformation (martensitic thermo-elastic), these phases are "martensite" and "austenite". That transformation is affected by three parameters; temperature, strain, and stress. The phase "martensite" is easily deformed, and when the stress is absent, martensite is stable at low temperatures. It experiences a change in shape with increasing stress or temperature. Multi variant crystal structure is induced with higher temperatures named "twinned martensite", while single variant crystal structure is induced at higher stress named"detwinned martensite" [13].

Shape-Memory Polymers (SMPs)

SMPs are materials collection that can change their shape in response to multiple external stimuli e.g., light, solvent vapors, laser heating, heat, leg pressure, moisture, solvents, pH, microwaves, and electricity [13].

Shape-memory ceramics (SMCs)

Ceramic ZrO_2 can undergo a transformation from tetragonal to monoclinic structure, such as the thermal transfer of martensite through the application of stresses, this is called "martensitic ceramics" [3].

Shape Memory Polymers and Shape Memory Alloys Advantages and Disadvantages Comparison

The comparison of SMPs and SMAs properties shown in Table (1) refers to the great number of advantages / disadvantages of these shape memory materials classes [12].

Table 1. Properties of Shape Memory Polymers and Shape Memory Alloys.

Material Property	Shape Memory Polymers	Shape-Memory Alloys
Density/g cm^{-3}	1	6-7
Extent of deformation (%)	50-600	6
Stress required for deformation (MPa)	1–3	50–200
Stress generated during recovery (MPa)	1–3	150–300
Corrosion performance	Excellent	Excellent
shaping	easy	difficult
At low temperature	rigid	soft
At high temperature	soft	hard
Heat conductivity	Low	High
Biocompatibility and biodegradability	Can be biocompatible and/or biodegradable	Some are biocompatible (i.e. Nitinol), not biodegradable
Processing conditions	<200 °C, low pressure	High temperature (>1000 °C) and high pressure required
cost	Low	high

Shape-Memory Effect (SME) Property

The shape memory effect (SME) property refers to the ability of some materials to remember a specific shape on demand, even after very severe deformations [14]; or it is a property that refers to the ability of the material to change its shape under a variety of external stimuli [15]. Also, this property refers to the ability of the material to memories its shape [16], it also means the ability of the material to trap the deformation mechanical energy or back stress in the fixed temporary shape and then release it through morphology changes or changes in the molecular relaxation rate. This property is sometimes known as a phenomenon that expresses a reversible process that allows to store and recover the deformation mechanical energy during the shape change cycle which is called “shape memory cycle”, SMC.
On the other hand, (SME) property refers to the material ability to change its properties by changing its shape as a behavior response for undergoing heat effects or stimuli; usually these shape changes are reversible [1].
Moreover, SME property indicates the capability of some materials to store a prescribed shape indefinitely and recover it by the specific external triggers such as heat [17].
The SME property expresses the possession of some materials a memory that memorize their permanent original shape [1], it is established that this term refers to the recovery of the original shape or size of the material as a result of heating above a distinct and specific temperature [18].
From what was mentioned, It can be said that the definitions may differ, but the effect has the same result, as shown in Figure (3) [19]. This property arises due to morphology and processing conditions, so it is considered an intrinsic property in shape memory materials with all their types [13,18].

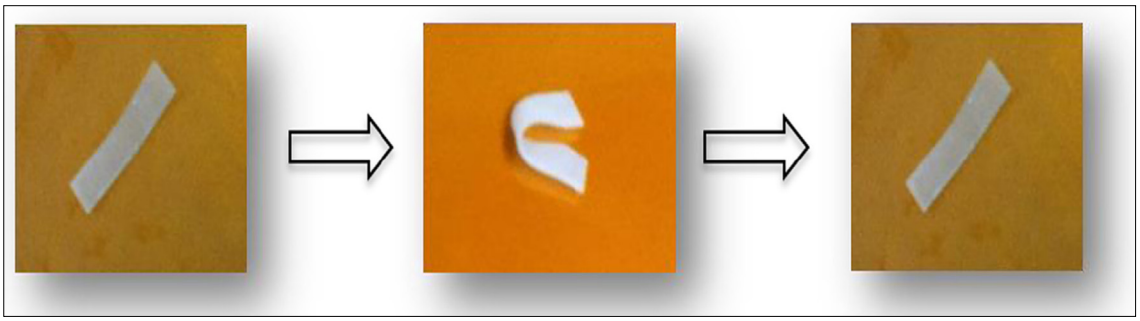

Figure 3. Photographs of The polymeric material showing shape memory effect.

For example, the shape memory behavior of SMPs derives from an association of their deformation history and molecular architecture. Where molecular architecture relies on the polymerization process and composition, that is hard to change at the moment of polymerization process completion, while the deformation history can be practically changed by external forces, which is termed as "training" or "programming". According that fact, shape memory is an engineered system characteristic and it is not an intrinsic property in the material.
Shape memory polymers should be trained, educated, or programmed for the SME property demonstration. This is unique for shape memory polymers since traditional polymers as indicated by their name cannot experience physical or mechanical changing without polymer damaging. Therefore, programming provides a solution for engineers, rather than chemists, to change the behavior of polymers at will [1]. Meaning that polymers do not display this effect by themselves [20]. The shape memory effect (SME) is a special mechanical phenomenon usually described by the shape memory cycle (SMC) [21].

Mechanism of the Shape-Memory Effect (SME) in SMPs and SMAs

In SMAs, shape memory effect depends on the phase transition between the crystalline phases marten site and austenite. While with SMPs, the polymeric chains rearrangement is the responsible for SME property [18].

Types of Shape Memory Effect (SME) in SMPs

- One-way Shape Memory Effect (1W-SME)
- Two-Way Shape Memory Effect (2W-SME)
- Multiple-Way Shape Memory Effect (Multiple-SME)

The SMPs various shape memory effects, are presented in Figure (4) [22].

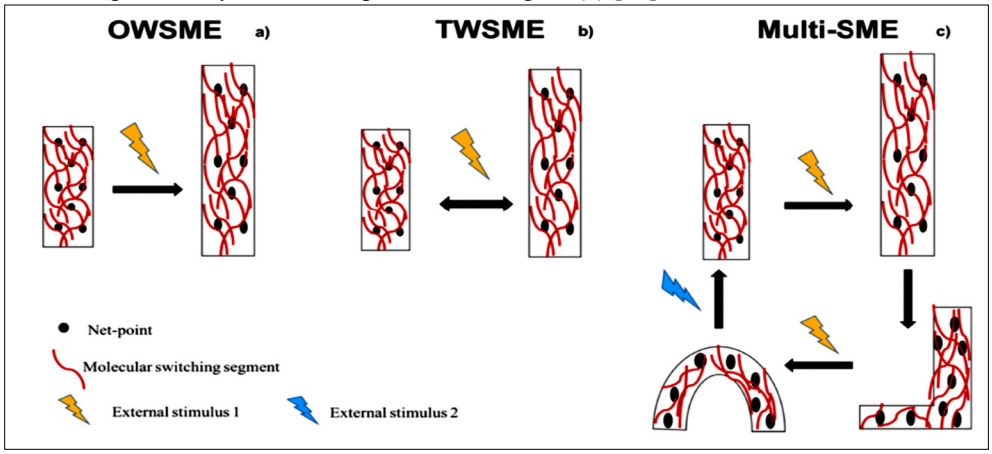

Figure 4. Various Shape-Memory Effect (SME) of SMPs, (a) (1W-SME), (b) (2W-SME) and (c) Multiple-SME.

Activation and Deactivation of SME Property During the Shape Memory Cycle (SMC)

The complete process is known to demonstrate the shape memory effect (SME) property by the shape memory cycle, SMC [12, 23], where this type of cycles includes two stages, as shown in Figure (5):

1- Programming stage: It is a process in which the SME property activation is done under different external conditions by allowing the material to be mechanically deformed and fixing that deformation temporarily, where after the end of the programming stage this temporary fixed mechanical deformation is called the programmed shape [1, 12, 20, 23, 24].

2- Recovery stage: A process in which SME property is deactivated when restoring the original external conditions by allowing the temporary fixed shape material to return to its permanent original shape [1, 12, 20, 23, 24].

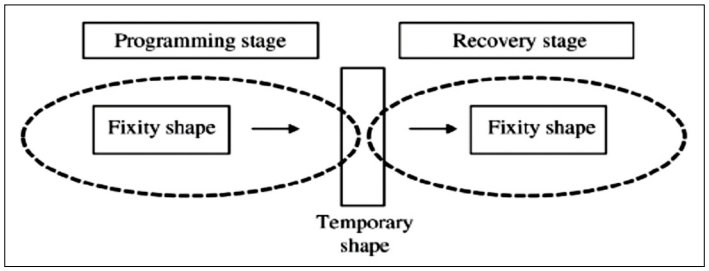

Figure 5. Shape memory technique includes two stages understood as programming and recovery stages.

In general, there are classifications of the shape memory cycle according to the SME property activation method, which are [1, 14, 20, 23]:-
First: Shape memory cycle with cold-programming (SMC-cold programming). In this cycle, the SME property is activated based on stress relaxation.
Second: The classical shape memory cycle with hot-programming, also called “thermo-mechanical cycle”. In this cycle, the SME property is activated based on thermal induction, which is one of the most popular types of cycles used in shape memory elastomer materials [1].
The recover stage may occur in any of these cycles by four methods in order for SMP to recover its original shape, these methods are [23]: -
1- Direct or indirect thermal activation.
2- Solvents.
3- Light (Frequency).
4- Mechanically driven.
Thermal activation, whether direct or indirect, is considered as one of the most widely used methods for deactivating SME property during the shape memory cycle.

THERMO-MECHANICAL CYCLE

The SMP usual thermo-mechanical cycle is conducted through the procedure shown below [12] :-
1- Fabrication of SMP into an original shape.
2- Thermal transition temperature (T_{trans}) is determined, the sample is heated above the transition temperature, with no applied stress.
3- Next to the programming time, the sample is stressed until it deformed, at this moment the shape memory effect must be studied (ε_m).
4- Applying stress is continued till cooling down the sample temperature below the transition temperature, fixing the temporary shape, then removing the applied stress. The material ability for fixing the temporary shape can be determined in this step.
5- lastly, reheating the polymer above T_{trans} for the initial shape recovery, then determining the material ability for the original shape recovery. This procedure should be cyclically repeated

Net-Points and Switching Phase in SMP

The difference between shape memory polymers, SMPs classified in Figure (6) and shape changing polymers is termed as "programmability". Shape changing polymers, SCPs are a class of smart polymers whose their shape change is limited to their size change as shown in Figure (7) by instant and spontaneous way in response to the external stimuli. While shape memory polymers (SMPs) are characterized by a procedure by which external stress or force is applied during the programming stage of the shape memory cycle, in which the shape shifting pathway is defined. That procedure, which is called programmability, primarily is not related to how the shape memory polymer fabricated or prepared. Shape memory polymers fall within this distinct class of SCPs, where after the fabrication step, they can be programmed to set the temporary fixation step for the subsequent recovery of the original shape using stimulation (typically heating). As it is clear, all of the fixation and recovery processes include two main shapes, which are temporary and permanent shapes, all of this is indicated by the phenomenon termed as dual shape memory effect symbolizing for the most usual -known shape memory polymers [25].

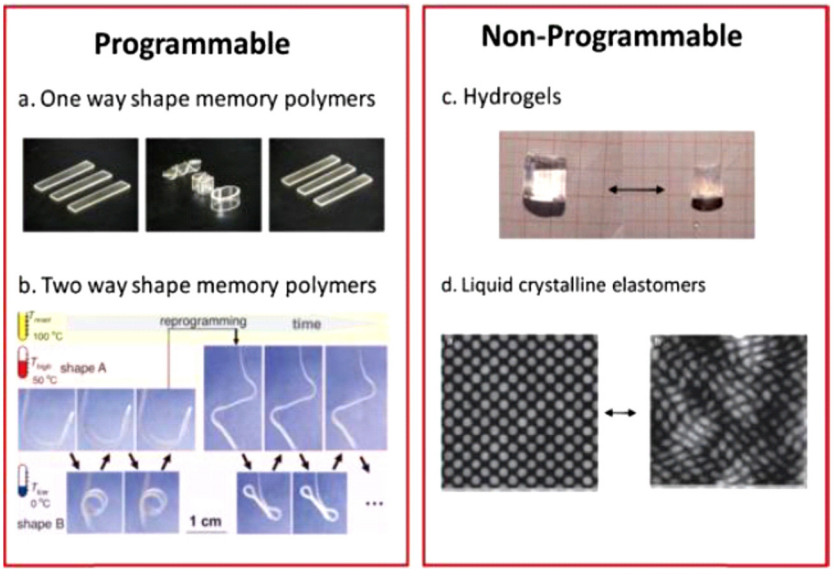

Figure 6. Classification of Shape Changing Polymers.

For obtaining shape memory effect, the polymer material must have at least two various phases, which are [16]:-

Net-Points

Hard phase (segment), otherwise known as "net points", it retains the shape memory article permanent shape. At the soft segment transition temperature, this hard phase (segment) does not soften or melt. These net points might be entanglements or local structures characterized by cross-linking and rigidity, they do not disentangle at the temperature of recovery [26].

Switching Phase

Soft phase (segment), also known as "switch units". During heating, they softened and have the role of a switch for remembering the article original permanent shape [27, 28]

SMP Characteristic Parameters During SM-Cycle

The shape memory polymer ability is quantified by using two basic parameters which are the "shape fixity ratio" otherwise known as strain fixity ratio, (R_f) and shape recovery ratio, also known as "Strain recovery ratio, (R_r)", [19,21,28-31].

Shape Fixity Ratio

Shape fixity ratio refers to SMP ability for fixing the strain transmitted into the sample through the step of deformation after succeeding cooling and unloading. Shape fixity ratio, R_f expression is given by [19,21,28-31] ;

$$Shape\ fixity\ rate, R_f = \frac{Fixed\ deformation, d_F}{Maximum deformation, d_{\max}} \quad (1)$$

Shape recovery ratio

Shape recovery ratio refers to SMP ability for recovering the accumulated strain through the step of deformation after succeeding cooling and unloading when reheating thermal transition temperature (T_{trans}). It can be defined by two:-
1- First way is expressed as [12, 18, 29 , 31];

$$Shape\ recovery\ rate, R_r = \frac{Deformation\ recovered\ in a certain\ cycle, d_R}{Maximum\ deformation, d_{\max}} \times 100\% \quad (2)$$

2- The second way is expressed as [12, 28 , 29];

$$Shape\ recovery\ rate, R_r = \frac{Deformation\ recovered\ in a certain\ cycle, d_R}{Fixed\ deformation, d_F} \quad (3)$$

R_f and R_r ratios are generally linked with the mechanical deformation and recovery ability of the original shape, they can also be calculated utilizing the following equation [32,33];

$$R_f(\%) = \frac{\varepsilon_u}{\varepsilon_m} \times 100,\ \ R_r(\%) = \frac{(\varepsilon_m - \varepsilon_p)}{\varepsilon_m} \times 100\ \ Or\ R_r(\%) = \frac{\varepsilon_u - \varepsilon_p}{\varepsilon_u} \times 100 \quad (4)$$

Where ε_m is Maximum strain during loading, ε_u represents Fixed strain after cooling and removal of load ε_p corresponds to Recovered strain after sample reheating.
The parameters R_f and R_r will be mentioned as shape memory cycle steps in chapter (3).
Also, there are main parameters must be counted in the characterization of SMPs, which are [19, 28].

Recovery Time

The shape-recovery speed was expressed by the time when SMP reached the maximum recovery ratio [19,28].

Shape Memory Cycle Time (TSM)

TSM refers to the whole necessary time for SMPs temporary shape programming to its permanent shape. It is significant for choosing shape memory polymers for certain applications needs. Shape memory cycle time, TSM, relies on the material geometry, characteristics, and experimental circumstances; so that, it must always be reported in the presence of these parameters for suitable selection [19,28].

Shape Memory Index

Shape memory effect (SME) can be assessed by the shape memory index (SMI or SM-index), which is a combination of two parameters calculated above and attained by the following equation [30];
SM-index =($R_f \times R_r$) ×100% ….(5)

STRUCTURAL CATEGORIZATION OF SMPS

Thermoplastic Shape Memory Polymers

Thermoplastic shape memory polymers comprise of two separated domains. The first domains are termed as “hard domains” which are linked with the highest temperature of thermal transition. They work as physical net points. In

addition, the second domains are termed as “switching segments” which are linked to relatively lower temperatures of thermal transition. They function as molecular switches. Thermoplastics could by more categorized as branched, linear, or complex polymers [12].

Thermosetting Shape Memory Polymers

They are networks that are cross-linked covalently which have structures that are chemically interconnected. These structures determine the shape memory polymers original macroscopic shape.
The chemically cross-linked shape memory polymers switching segments are mainly network chains between the net-points. The shape memory switch here is represented by the polymer segment thermal transition.

SHAPE MEMORY MATERIALS OF RUBBERS

Lightly Cross-Linked Shape Memory Natural Rubber (SMNR)

Lightly cross-linked SMNR networks possess a cross-linking density less than 0.4%. After releasing the force of stretching, the crystals still present, where they stabilize the network in the very stretched state, reaching 1000% at room temperature. This network recovery could be triggered by heating the network beyond its melting temperature, which is termed as the “trigger temperature”. SMNR trigger temperature can be adjusted in between (20-50)°C. This material is quickly elongated and stays on this shape, without recovering its original shape. A small heat is enough for it to recover its original shape, as the heat of the body. So that, lightly cross-linked NR are programmable under its trigger temperature, also, semi-crystalline polymer stretching gives incomplete recoverability.NR cross-liking in-between heat and thermoplastics permits crystal formation under strain that can tolerate the network at high elongation temperature [18,34]. SMNR tepical formulation is listed in Table (2) [18].

Table 2. Constituents to be Counted When Producing SME Natural Rubber

Components	Phr
Natural rubber	100
Sulphur	0.2
ZnO	0.15
Zinc diethyldithiocarbamate	0.15

ELASTOMER/SMALL MOLECULE BLEND SMPS

Conventionally, shape memory polymers are synthesized by chemical or physical cross-linking. These processes incorporate the permanent and reversible networks directly into a single polymer with a wide range of choices of different network formers.
However, there is also an alternative method to synthesize shape memory polymers by blending elastomer and small molecule additive together, a shape memory blend can be acquired. The elastomer will serve as permanent network and small molecule additive will serve as temporary network.
The elastomer-small -molecule blend synthesis is superior in many aspects. Firstly, its process is much easier than that of conventional chemical or physical cross-linking.
By simply blending specific elastomer with choice of small molecules, certain shape memory blend can be fabricated. Secondly, in some cases, researchers would use commercial rubbers as elastomers. They are not only cheaper but also offer more varieties. Many commercial rubbers are available that have consistent chemical and physical properties. Some of them have excellent performance when used as elastomer in shape memory blends.
These cross-linked polymers would form permanent network in the blend which gives the material rubbery properties including elasticity. On the other hand, choice of small molecules form the temporary networks. Their switching behavior according to temperature is the key to the shape memory effect.
With different choice of combination of elastomer and small molecule, shape memory of different mechanical properties and switching temperature can be easily fabricated. Since the separation of the synthesis of cross-linked

polymer network and reversible network formation makes these two components contribute to the properties of shape memory blend respectively in specific aspects [35-44].
Table (3) clarifies in general some of SMP applications, while Table (4) clarifies specifically shape memory rubber applications.

Table 3. Examples of SMPs Application.

Potential application		SMPs in application		Features achieved	Ref.
Deployable architecture (small scale buildings)	•Retractable house. • Small display areas. •Temporary shelters. •Temporary parking areas.	Shape –memory tent		•Temporary structure. • Reduce the time required for construction. • Reduce reuse and recycle. • Can be reused for anther structures.	[36]
Building energy savings	Movable window blinds	Window blinds		Can be used in hinges of the blind structures.	[37]
Textile design	Pillow	Shape –memory pillow		Can be adjust its shape to the contour of the neck and shoulder according to body temperature .	[38]
	Sock- shoes	Demonstration of the fitting process of shape memory sock-shoe. a- Original shape. b- During programming process. c- Temporary shape.		Programmable by process:- Heating by hair dryer + wearing.	[39]
	Cloth	a- Original shape b1,2 -After stretching to different length c-After heating again for shape recovery Shape – memory cloth		Cloth can be programmed at room temperature or body temperature.	
Slipper shoes manufacturing	Shoe	a- Shape memory shoe.	b- Shape memory shoe for 3D printing	Avoid localized over – stretching during wearing many through holes are made to make it more stretchable.	[39]
	Slipper	Shape memory slipper		Perfectly fit the profile of a particular foot for casual wear	
	3D printed insole	Shape memory insole during SMC		The SME in 3D printed insole using flexible.	
Aerospace		Gliders with solar powered engines for meteorology			[36]
Medical equipment engineering	Cardiovascular devices	Delivery and implantation of the IMPEDE Embolization Plug.		IMPEDE and IMPEDE-FX Embolization Plugs in their crimped shape and expanded shapes.	[40]
	Degradable sutures	The temperature – induced shrinkage of fibber suture		Devalue smart degradable for biomedical application	[41]
	Orthopedic	Shape memory splint			[36]

Table 4. Examples of ahape memory rubber application.

Potential application		Shape memory rubber in application			Features achieved	Ref.
Medical equipment engineering	Surgical tube	Shape- memory Surgical tube.			SM- behavior of natural rubber surgical tube swollen with stearic acid,	[36]
	Medical glove	Shape- memory medical glove			Medical glove from SMPs in shapes optimized for working and wearing	[42]
		Shape memory fingerless glove			It is able to fit the particular shape of a hand in the meantime , provides flexibility and protection by the hand.	[39]
	Elbow hand	Original	After wearing (during programming process).	After taking off (temporary shape).	Comfort fitting elbow hand.	
	Orthopedic	a- The shape of piece before (top) and after (bottom) fitting (after programming process)	b- After fitting into the position (during programming process).		Halluy valgus correction device to provide comfort fitting and just right for correction.	
	Splint tape	1- Original shape of splint. 2- Splint in warm water (15sec). 3,4- Splint was wrapped around fractured finger and locked. 5,6- Temporary shape,			Shape memory splint programming by warm water.	[43]
Forensic application		Comparison of imprint prepared from different techniques.			Thermo plastic natural rubber (TPNR) shows fine imprint with improved performance and it is easy to handle on compared to the other silicone – based material.	[44]

CONCLUSIONS

The “smart” adjective means that these materials can sense the environment changes surrounding them then react to these changes in pre-determined behaviors-traits that can be seen in living organisms.
Smart materials can be generally classified into two types relying on their functional properties as follows: (Energy-Exchanging Smart Materials, Property-Changing Smart Materials).
SMPs are materials collection that can change their shape in response to multiple external stimuli e.g., light, solvent vapors, laser heating, heat, leg pressure, moisture, solvents, pH, microwaves, and electricity.
The shape memory effect (SME) property refers to the ability of some materials to remember a specific shape on demand, even after very severe deformations.
In SMAs, shape memory effect depends on the phase transition between the crystalline phase’s marten site and austenite. While with SMPs, the polymeric chains rearrangement is the responsible for SME property.
Various Shape-Memory Effect (SME) of SMPs, (a) (1W-SME), (b) (2W-SME) and (c) Multiple-SME.
Shape Memory Technique Includes Two Stages Understood as Programming and Recovery Stages.
Shape changing polymers is what it called “programmability”. Shape changing polymers, SCPs are a class of smart polymers whose shape changes are limited to their size change by instant and spontaneous way in response to the external stimuli.
For obtaining shape memory effect, the polymer material must have at least two various phases, which are: (Net-Points, Switching Phase).
There are main parameters must be counted in the characterization of SMPs, which are: (Shape fixity, ratio, Shape recovery ratio, Recovery Time, Shape Memory Cycle Time, Shape Memory Index, Structural Categorization of SMPs).

More than twenty type of SMPs have been fabricated and researched widely in the last years. SMPs will be classified according to structure as there is also an alternative method to synthesize shape memory polymers by blending an elastomer and small molecule additive together, a shape memory blend can be acquired. The elastomer will serve as permanent network and small molecule additive will serve as temporary network.

REFERENCES

1. G. Li, "Self –Healing composites: shape memory polymer – Based structures", published by John wiley and Sons, 2015.
2. W. D. Callister, Jr. and David G. Rethwisch, "Materials Science and Engineering an introduction 9th Edition ", published by John wiley and Sons, 2014.
3. V. K. Wadhawan," Smart structure Blurring the Distinction Between the living and Nonliving", published in the united states by Oxford University press Inc, New York, 2007.
4. D. Michelle Addington, Daniel Schodek,"Smart Materials and Technologies For the Architecture and Design Professions", Published by Routledge and Taylor and Francis group, 2004.
5. L. Peponi, M.P. Arrieta, A. Mujica-Garcia and D. Lopez ,"6 - Smart Polymers", Modification of Polymer Properties, Published by Elsevier Inc, 2017.
6. M. Addingron and D.L.Schedek, "Smart materials and new technologies for the architecture and design professions", Published by Elsevier, 2005.
7. S. K. Melly, L. Liu, Y. Liu & J. Leng,"Active composites based on shape memory polymers: overview, fabrication methods, applications, and future prospects", Journal of Materials Science, Vol .55, pp .10975–11051, 2020, https://doi.org/10.1007/s10853-020-04761-w.
8. F. Quadrini ,Leandro Iorio,Denise Bellisario and Loredana Santo ,"Durability of Shape Memory Polymer Composite Laminates under Thermo-Mechanical Cycling ", Journal of Composites Science, Vol. 6,No. 91, pp.2-12, 2022; https://doi.org/10.3390/jcs6030091.
9. A. Kausar, " Shape memory polymer/graphene nanocomposites: State-of-the-art", journal e-Polymers, Vol.22, No.1, 2022, https://doi.org/10.1515/epoly-2022-0024.
10. S. Zhu," Study on Smart Materials Using in Civil Engineering", Advances in Social Science, Education and Humanities Research, Vol.631,pp.1462-1466, 2022, https://doi.org/10.2991/assehr.k.220105.269.
11. M. Bashir, Chih Fang Lee and Parvathy Rajendran, "Shape memory materials and their applications in aircraft morphing: an introspective study", ARPN Journal of Engineering and Applied Sciences, Vol.12, No. 19, pp. 5434 – 5446, 2017.
12. A. Basit, "Development and characterization of shape memory polymer composite actuator for morphing structures", thesis submitled to fulfil the requirement for the degree of Doctor of philosophy (PhD) in mechanics, University de Haute Alsace (UHA) Laboratoire de physique et Mecanique Textiles (LPMT), 2016.
13. H. Holman, Minoo Naozer Kavarana, Taufiek Konrad Rajab, "Smart materials in cardiovascular implants: Shape memory alloys and shape memory polymers, "Artificial Organs, Vol.45, No.5, pp.454-463, 2021.
14. F. Li, Richard C. Larock, "New soybean oil–styrene–divinylbenzene thermosetting copolymers. v. shape memory effect", Journal of Applied Polymer science , Vol.84, No. 8, pp. 1533-1543, 2002.
15. A. Lendlein , Steffen Kelch,"Shape-Memory Polymers",Angewandte intornotional Edition Chemie, Vol.41, No.12, pp. 2034-2057, 2002.
16. M. J. Haskew and John G. Hardy, "A Mini-Review of Shape-Memory Polymer-Based Materials : Stimuli-responsive shape-memory polymers",Johnson Matthey Technology Rev., Vol. 64, No.4, pp.425-442, 2020.
17. A. Shojaei and Guoqiang Li, "Thermomechanical constitutive modelling of shape memory polymer including continuum functional and mechanical damage effects", Proceedings of the Royal Society, 2014, http://rspa.royalsociety publishing.org/ subscriptions.
18. A. Reghunadhan, Keloth Paduvilan Jibin , Abitha Vayyaprontavida Kaliyathan , Prajitha Velayudhan , Michał Strankowski , and Sabu Thomas,"Shape Memory Materials from Rubbers", Journals Materials Vol. 14 No.23, pp .1-19, 2021, https://doi.org/10.3390/ma14237216.
19. C. F. Jasso-Gastinel, Jose M. Kenny, "Modification of polymer properties", Published by Elsevier, 2017.
20. T..Mu, Liwu.Liu, Xin.Lan, Yanju.Liu, Jinsong.Leng,"Shape memory polymers for composites",Composites Science and Technology,Vol. 160, , pp.169-198, 2018, https://doi.org/10.1016/j.compscitech.2018.03.018.
21. M. Behl, Andreas Lendlein,"Shape-Memory Polymers", Journal materials today,Vol. 10, No. 4, pp. 20-28, 2007, https://doi.org/10.1016/S1369-7021(07)70047-0.
22. S. Pisani , Ida Genta , Tiziana Modena , Rossella Dorati , Marco Benazzo and Bice Conti, "Shape-Memory Polymers Hallmarks and Their Biomedical Applications in the Form of Nanofibers", International Journal of Molecular Sciences, Vol. 23, No. 3,pp.2-20, 2022, https://doi.org/10.3390/ijms23031290.

23. D.L. Safranski, Jack C Griffis, "Shape-memory polymer device design", Published by Elsevier Inc, 2017.
24. W.M. Huang, Bin Yang, Yong Qing Fu, "Polyurethane Shape Memory Polymers". Published by CRC press Taylor and Francis Group, LLC.2012.
25. T. Ramani, "Thermo-mechanical characterization of carbon-reinforced shape memory polymer", Thesis Submitted in partial fulfill of the requirements for the degree of Master of Science in Civil Engineering in the Graduate College of the University of Illinois at Urbana-Champaign, 2017.
26. S. Rezanejad, Mehrdad Kokabi,"Shape memory and mechanical properties of cross-linked polyethylene/clay nanocomposites", European Polymer Journal, Vol. 43, No. 7, pp.2856-2865, 2007.
27. S. Kirwa Melly, Liwu Liu, Yanju Liu, Jinsong Leng, "Active composites based on shape memory polymers: overview, fabrication methods, applications, and future prospects", Journal of Materials Science Vol.55, pp. 10975-11051, 2020.
28. I. A. Rousseau and Tao Xiea,"Shape memory epoxy: Composition, structure, properties and shape memory performances",Journal of Materials Chemistry,Vol.20, No. 17, pp. 3431-3441, 2010.
29. S.Cai- Li, Li-Nong Lu, Wei Zeng, "Thermostimulative shape-memory effect of reactive compatibilized high-density polyethylene/poly(ethylene terephthalate) blends by an ethylene–butyl acrylate–glycidyl methacrylate terpolymer", Journal of Applied Polymer Science ,Vol.112 , No.6, ,pp. 3341 - 3346,2009.
30. P. A. Quiñonez, Leticia Ugarte, Diego Bermudez, Paulina Chinolla,"Design of Shape Memory Thermoplastic Material Systems for FDM-Type Additive Manufacturing", Materials, Vol.14, No.15, pp.6-19,2021.
31. S.N.Saud AL-Humair, H.Sh.Majdi, A.N.Saud Al-Humair and M.H.Al-Maamori," Future Prospects: Shape Memory Features in Shape Memory Polymers and Their Corresponding Composites", chapter in Book ,"Smart and Functional Soft Materials ", Edited Xufeng Dong, publish with Intechopen. 2019, doi: http://dx.doi.org/10.5772/intechopen.84924.
32. N. Lehman, Ladawan Songtipya, Jobish Johns and Korakot Maliwankul,"Shape memory thermoplastic natural rubber for novel splint applications", eXPRESS Polymer Letters, Vol.15,No.1,pp.28-38,2021, https://doi.org/10.3144/expresspolymlett.2021.4.
33. J. Sze- Huawee, Ai Bao Chai , Jee -Hou Ho, " Fabrication of shape memory natural rubber using palmitic acid," Journal of King Saud University – Science,Vol.29, No.4, pp, 494-501, 2017.
34. B. Heuwers, D. Quitmann, F. Katzenberg, J. C. Tiller, "Stress-Induced Melting of Crystals in Natural Rubber: a New Way to Tailor the Transition Temperature of Shape Memory Polymers", Macromolecular Rapid Communications, Vol. 33, No. 18, pp. 1517-1522, 2012.
35. L. Zhou, "Investigation of the Shape Memory Behaviour of Stearic Acid Swollen, Crosslinked EPDM Elastomers ", Thesis submitted Fulfillment Of the Requirement for the Degree Master of Science, University of Akron, 2019.
36. S. Pimple, Shilpa Nagapurkar, "Shape Memory Polymers in Deployable Architecture", International Journal of Engineering Research, Vol.7, No. 3, pp. 321-324, 2018, doi : 10.5958/2319-6890.2018.00085.5.
37. J. Li, Qiuhua Duan, Enhe Zhang, Julian Wang."Applications of Shape Memory Polymers in Kinetic Buildings" Hindawi,Advances in Materials Science and Engineering, Vol. 2018, pp.1-13, Article ID 7453698,2018 ,https://doi.org/10.1155/2018/7453698.
38. M. O. Goka , Mehmet Z. Bilira, Banu H. Gurcumb," Shape-Memory Applications in Textile Design", Procedia - Social and Behavioral Sciences, Vol.195, pp. 2160 – 2169 , 2015, https://doi.org/10.1016/j.sbspro.2015.06.283.
39. L. Sun, W.M. Huang, T.X. Wang, H.M. Chen, C. Renata, L. W. He, P. Lv, C.C. Wang," Elastic polymeric shape memory materials for comfort fitting: a brief reviewof recent progress", Materials & Design, Volume Vol. 136, pp. 238-248, 2017,https://doi.org/10.1016/j.matdes.2017.10.005.
40. D. J. Maitland, Landon Nash,"Shape Memory Polymer Technology", Nsert to Endovascular Today , Vol. 20, No. 4, pp. 74-78, 20 https://evtoday.com/articles/2021-apr/shape-memory-polymer-technology.
41. M. C. Serrano, Guillermo A. Ameer, "Recent Insights into the Biomedical Applications of Shape-memory Polymers", Macromolecular bioscience, Vol.12, No.9, pp. 1156-1171, 2012, https://doi.org/10.1002/mabi.201200097.
42. M. Bothe."Shape Memory and Actuation Behavior of Semicrystalline Polymer Networks", presented by Dipl.-Phys. Martin Bothe from Tuebingen from Faculty II – Mathematics and Natural Sciences of the Technical University of Berlin for obtaining the academic degree Doctor of Science, Berlin 2014.
43. N. Lehman, Ladawan Songtipya, Jobish Johns and Korakot Maliwankul,"Shape memory thermoplastic natural rubber for novel splint applications", eXPRESS Polymer Letters, Vol.15,No.1,pp.28-38,2021, https://doi.org/10.3144/expresspolymlett.2021.4.
44. A. C Rustan, Christian A Drevon, "Fatty Acids: Structures and Properties", Encyclopedia of life Sciences, 2005, https://doi.org/10.1038/npg.els.0003894.

Theoretical Study of Charge Transport Kinetics of Zinc Contact with Tin Oxide Using Quantum Transition Theory

Taif Saad Al Maadhede[1,a], Raed Mahdi Salih[2], Hadi J.M Al-Agealy [3] and Mohsin A. Hassooni [3]

[1]*Department of Renewable Energy and Environmental-College of Energy and Environmental Sciences, Al-Karkh University of Science, Baghdad, Iraq*

[2]*Automated Manufacturing Engineering Department, Al-Khwarizmi College of Engineering, University of Baghdad, Baghdad, Iraq*

[3]*Department of Physics, College of Education for Pure Science Ibn-ALHaitham, University of Baghdad, Baghdad-Iraq.*

[a] Corresponding author: t.saad@Kus.edu.iq

Abstract. In this research, the charge transport process in zinc-tin oxide heterogeneous interface passivation was particularly studied using quantum charge transition theory. The highest charge transfer based on Zn- SnO_2 achieves an efficiency of 11. 786× 10-5 at driving energy 0.41 eV, which is significantly higher than 9.423 × 10-5 that of the driving force 0.37 with coupling 610-2 eV. The increased charge transfer rate of the Zn- SnO_2 with increased driving energy could be attributed to the largest electronic extraction, best alignment energy levels with material, and more charge carrier transfer in the device. The strength coupling at the interface affected the charge transfer process, it limited the electric properties of Zn- SnO_2 devices, and the charge transfer increases with strength increases and vice versa. Most importantly, the increased transition energy on the interface of Zn - SnO_2 can effectively transfer the charge from Zn metal to SnO_2 semiconductor and reduce charge recombination at the interface .Charge transfer results in zinc tin oxide offering desirable electronic characteristics for manufacturing electronic devices with different synthesis processes. The results indicate that the Zn-SnO_2 composite can be promising for improving electronic devices.

Keywords: Charge Transport, Zinc Metal, Tin Oxide SnO_2.

INTRODUCTION

The charge transport process is the main reaction in a variety of science, it's basic much more different systems in biophysics, physical chemistry and physics. A classical theory of charge transport was a basic theory introduced by Marcus awarded the Nobel Prize in 1992 [1]. The metal contact to semiconductor interface in hetero-structures devices is investigated in many applied physics optically devices; photo catalysis photonic devices and solar cells [2]. The metal-semiconductor interfaces play an important role in charge transport properties because these interface play in optoelectronic devices creation potential at contacts [3].

Metal oxide semiconductors such as SnO_2were used in optoelectronics devices mostly for photovoltaic devices, flat panel displays, heat-reflecting mirrors and gas sensors due to their suitable band gaps (2.8–4.2 eV), n-type conductivity and other useful characteristics [4]. The metal oxide SnO_2 is an n-type has a widest band gap in about 3.6 eV [1]. It has various applications in gas sensors, catalysis, transparent conductor electrode preparation, solar cells and antistatic coated process. The multifunctionality of SnO_2 nanostructures arose due to the larger band gap, highest surface-to-volume ratio, highest exaction binding energy of 130 meV at (300 K), diverse remarkable resistance in gaseous environment, and thermal, mechanical, and chemical stability. The opto-electronic characteristics of SnO_2 depended on the presence of different impurities as well as stoichiometry related to oxygen. In recent, several SnO_2-based nanomaterial devices were fabricated from different dimensions in different ranges (0D to 3D) to build SnO_2 blocks,

Technologies and Materials for Renewable Energy, Environment and Sustainability
AIP Conf. Proc. 3321, 020037-1–020037-6; https://doi.org/10.1063/5.0290401
Published under an exclusive license by AIP Publishing. 978-0-7354-5231-2/$30.00

nanowires, Nano whiskers, nanoribbons, Nano sheets, nanoparticles, Nano belts, nanotubes and others, using variety synthesis techniques such as spray pyrolysis [5].
The charge transport occurs across the metal-semiconductor interface when a semiconductor is coupled with a metal. It occurs when the work function for metal is higher than that of semiconductors. The electrons would flow from semiconductor to metal until the Fermi levels were aligned with each other [6-7], the states of semiconductor –metal interface.
In this work, the charge transport process through interface of Zn metal contact with SnO_2 semiconductor was studied and investigated theoretically using quantum transition theory. It will be evaluated using a simple theoretical model for transfer from Zn- donor to SnO_2- acceptor through the potential of Zn- SnO_2 devices at the interface.

THEORY

The charge transport produces through zinc contact to SnO_2 devices under a continuum levels for both solids. The charge transport rate is [8].

$$\mathrm{R}^{ZTI} = \frac{2\pi}{\hbar}\int |C_{ZTI}(E)|^2 \mathrm{F(E)}\delta(E - E_{ZTI})dE \quad \text{.....(1)}$$

Where $\hbar$ is the Dirac constant, $C_{ZTI}(E)$ iss overlapping coupling parameters, $\delta(E - E_{ZTI})$ is the Dirac distribution for energy at Zn- SnO_2 system, E is energy of system and E_{ZTI} is the energy at interface .
For the Zn- SnO_2 system ,we introduce the density of states $\rho_{Zn}^{\mathrm{SnO2}}(\mathrm{E})$,then Eq.(1) become .

$$\mathrm{R}^{ZTI} = \frac{2\pi}{\hbar}\int |C_{ZTI}(E)|^2 \mathrm{F(E)}\rho_{Zn}^{\mathrm{SnO2}}\delta(E - E_{ZTI})dE \quad \text{.....(2)}$$

The second term in Eq.(2) reduces with $\int_{-\infty}^{+\infty} F(m)\delta(m-n)\mathrm{dE} = F(m)$ [9] in form .

$$\int_{-\infty}^{+\infty} \mathrm{F(E)}\ \delta(E - E_{ZTI})dE = F_{ZTI}(\mathrm{E}) \quad \text{.....(3)}$$

Then Eq. (2) with Eq. (3) reduce to.

$$\mathrm{R}^{ZTI} = \frac{2\pi}{\hbar}\int |C_{ZTI}(E)|^2 \rho_{Zn}^{\mathrm{SnO2}} F_{ZTI}(\mathrm{E})dE \quad \text{.....(4)}$$

The density of state of Zn-SnO_2 system was given with density in ref. [10].

$$\rho_{Zn}^{\mathrm{SnO2}} = \ (4\pi\ \mathrm{ET}_{Zn}^{SnO2}\mathrm{k_B T})^{\frac{-1}{2}} exp\frac{-(\mathrm{ET}_{Zn}^{SnO2}+\Delta\mathrm{U})^2}{4\mathrm{ET}_{Zn}^{SnO2}\mathrm{k_B T}} \quad \text{.....(5)}$$

Where ET_{Zn}^{SnO2} , $\mathrm{k_B}$ and T are transition energy ,Boltzmann constant and temperature and ΔU is driving energy is function of work function $\Phi_{Zn}$of Zn and affinity $\chi_{SnO2}$of SnO2 relative to $\Delta U^{\circ} = \Phi_{Zn} - \chi_{SnO2}$ .Inserting Eq.(5) in Eq.(4) becomes.

$$\mathrm{R}^{ZTI} = \frac{2\pi}{\hbar}\int |C_{ZTI}(E)|^2 (4\pi\ \mathrm{ET}_{Zn}^{SnO2}\mathrm{k_B T})^{\frac{-1}{2}} exp\frac{-(\mathrm{ET}_{Zn}^{SnO2}+\Delta\mathrm{U})^2}{4\mathrm{ET}_{Zn}^{SnO2}\mathrm{k_B T}} F_{ZTI}(\mathrm{E})dE \quad \text{.....(6)}$$

Where ΔU is a function of effective driving force energies and energy of system E by [11];

$$\Delta U = \Delta U^{\circ} - E \quad \text{.....(7)}$$

Inserting Eq.(7) in Eq.(6) to give.

$$\mathrm{R}^{ZTI} = \frac{2\pi}{\hbar}\int |C_{ZTI}(E)|^2 (4\pi\ \mathrm{ET}_{Zn}^{SnO2}\mathrm{k_B T})^{\frac{-1}{2}} e\frac{-(\mathrm{ET}_{Zn}^{SnO2}+\Delta U^{\circ}-E)^2}{4\mathrm{ET}_{Zn}^{SnO2}\mathrm{k_B T}} dE \quad \text{..... (8)}$$

The distribution function $F_{ZTI}(\mathrm{E})$ is given by [12]

$$F_{ZTI}(\mathrm{E}) = (exp^{\frac{E}{\mathrm{k_B T}}} + 1)^{-1} \quad \text{.....(9)}$$

The charge transport parameters in Eq.(8) with Eq.(9) becomes .

$$\mathrm{R}^{ZTI} = \frac{2\pi}{\hbar}\int \frac{|C_{ZTI}(E)|^2}{exp^{\frac{E}{\mathrm{k_B T}}}+1} (4\pi\ \mathrm{ET}_{Zn}^{SnO2}\mathrm{k_B T})^{\frac{-1}{2}} e\frac{-(\mathrm{ET}_{Zn}^{SnO2}+\Delta U^{\circ}-E)^2}{4\mathrm{ET}_{Zn}^{SnO2}\mathrm{k_B T}} dE \quad \text{..... (10)}$$

The exponential in Eq. (10) is.

$$e\frac{-(\mathrm{ET}_{Zn}^{SnO2}+\Delta U^{\circ}-E)^2}{4\mathrm{ET}_{Zn}^{SnO2}\mathrm{k_B T}} = e\frac{-(\mathrm{ET}_{Zn}^{SnO2}+\Delta U^{\circ})^2}{4\mathrm{ET}_{Zn}^{SnO2}\mathrm{k_B T}} e\frac{2\mathrm{E}(\mathrm{ET}_{Zn}^{SnO2}+\Delta U^{\circ})}{4\mathrm{ET}_{Zn}^{SnO2}\mathrm{k_B T}}\ e\frac{-(E)^2}{4\mathrm{ET}_{Zn}^{SnO2}\mathrm{k_B T}} \quad \text{.....(11)}$$

The term $e\frac{2\mathrm{E}(\mathrm{ET}_{Zn}^{SnO2}+\Delta U^{\circ})}{4\mathrm{ET}_{Zn}^{SnO2}\mathrm{k_B T}}$ vanishes [13] and for $E \gg T$, $e\frac{-(E)^2}{4\mathrm{ET}_{Zn}^{SnO2}\mathrm{k_B T}} \approx 1$,the Eq.(10) reduces to .

$$\mathrm{R}^{ZTI} = \frac{2\pi}{\hbar}\int \frac{|C_{ZTI}(E)|^2}{exp^{\frac{E}{\mathrm{k_B T}}}+1} (4\pi\ \mathrm{ET}_{Zn}^{SnO2}\mathrm{k_B T})^{\frac{-1}{2}} e\frac{-(\mathrm{ET}_{Zn}^{SnO2}+\Delta U^{\circ})^2}{4\mathrm{ET}_{Zn}^{SnO2}\mathrm{k_B T}} dE \quad \text{..... (12)}$$

However ,the $F_{ZTI}(\mathrm{E})$) is reduce to.

$$F_{ZTI}(\mathrm{E}) = (exp^{\frac{E}{\mathrm{k_B T}}} + 1)^{-1} \approx e^{\frac{-E}{\mathrm{k_B T}}} \quad \text{.....(13)}$$

Inserting Eq.(13) in Eq.(12)

$$R^{ZTI} = \frac{2\pi}{\hbar}\frac{|C_{ZTI}(E)|^2}{(4\pi\, ET_{Zn}^{SnO2} k_B T)^{\frac{1}{2}}} e^{\frac{-(ET_{Zn}^{SnO2}+\Delta U^{\circ})^2}{4ET_{Zn}^{SnO2} k_B T}} \int e^{\frac{-E}{k_B T}} dE \quad \ldots\ldots (14)$$

The solution of integral gives

$$\int_0^{\infty} e^{\frac{-E}{k_B T}}\, dE = k_B T \quad \ldots\ldots (15)$$

The barrier height [13],

$$\Delta = \frac{(ET_{Zn}^{SnO2} + (\Phi_{Zn} - \chi_{SnO2}))^2}{4ET_{Zn}^{SnO2}} \quad \ldots\ldots (16)$$

Together Eq.(15) and Eq.(16) can insert in Eq.(14) to

$$R^{ZTI} = \frac{2\pi}{\hbar}\frac{|C_{ZTI}(E)|^2}{(4\pi\, ET_{Zn}^{SnO2} k_B T)^{\frac{1}{2}}} e^{\frac{-(ET_{Zn}^{SnO2}+(\Phi_{Zn}-\chi_{SnO2}))^2}{4ET_{Zn}^{SnO2} k_B T}} k_B T \quad \ldots\ldots (17)$$

Transition energy $ET_{Zn}^{SnO2} eV$ for charge transport is [14].

$$ET_{Zn}^{SnO2} = \frac{(\Delta q)^2}{4\pi\varepsilon_0}\left[\frac{F_{n_s^2,\varepsilon_s}}{2a_s} + \frac{F_{n_m^2\varepsilon_m}}{2a_m} - \frac{F_{n_m^2\varepsilon_m, n_s^2,\varepsilon_s}}{4d_s} - \frac{F_{n_s^2,\varepsilon_s, n_m^2\varepsilon_m}}{4d_m} - \frac{2F}{Rm-s}\right] \quad \ldots\ldots (18)$$

Here $F_{n_s^2,\varepsilon_s}$ is polar coefficient to equal to $(\frac{1}{n^2} - \frac{1}{\varepsilon})$, Δq is differences in charge , *a*s, and *a*m refer to semiconductor and metal radii, *ds* and *dm* are the distance between SnO_2, Zn and interface alternatively , $Rm\text{-}s$ is the distance between SnO_2 and Zn, ε and *n* were the statistical and optical dielectric constant . Radii of the Zn and SnO_2 materials could be estimated using an expression approach [15].

$$a_i = (\frac{3M}{4\pi ND})^{\frac{1}{3}} \quad \ldots\ldots (19)$$

where M is the molecular weight, D is the mass density and N is Avogadro's number**.**

RESULTS AND DISCUSSION

The charge transport rate for Zn/ SnO_2 *system* has calculated by using Eq.(17) taken into account reorganization energy ET_{Zn}^{SnO2} , the driving force energy ΔU, strength coupling $|C_{ZTI}(E)|$,work function Φ_{Zn} of Zn metal and electron affinity χ_{SnO2} of SnO_2 .The physical properties of SnO_2 semiconductor has listed in table(1)[16].

Table 1. Physical properties of SnO_2[16].

Properties	Values
Atomic molar mass	150.70 g/mole
Form	SnO_2
Crystal structure	Wurtzite
Density	6.95 (g/cm3)
Lattice constants	a = 4.74 Å c=3.20 Å
Refractive index	1.94
Dielectric constant	4.175
Density of states	2.537×10^{-22} (cm^{-3})
Energy gap	3.6 (eV)
Electron affinity	3.96 eV
Melting point (ºC)	1630 ºC
Radius Calculated	2.048 Å

However, the reorganization energy factor for electronic transfer reaction in Zn/ SnO_2 may be calculated with calculated the rate of Zn metal and SnO_2 semiconductor have been estimated using Eq.(19) by inserting the molecule

weight for Zn is 65.38 g/mol [17] and 150.69 g/mol [16] for SnO_2 and mass density for Zn is 7.14 g/cm³[18] and 6.95 g/cm³ for SnO_2 [16], results are $a_{Zn} = 1.537A^o$ and $a_{SnO2} = 2.048A^o$ respectively. Next, the reorganization energy has been calculated according to Eq.(18) with radii of Zn metal and SnO_2 semiconductor and dielectric constant of metal and semiconductor from table(2). The dielectric constant and refractive index of SnO_2 are taken be $\varepsilon = 4.175$ and n=1.94 for SnO2 [19], while the dielectric constant ε and refractive index of Zn are estimated using $|\varepsilon| = {\varepsilon_1}^2 - {\varepsilon_2}^2$ and $n = n + k$ where $\varepsilon_1 = n^2 - k^2$ and $\varepsilon_2 = 2nk$ [20]. The results are shown in table (2).

Table 2. The results of reorganization energy $ET_{Zn}^{SnO2}eV$ for Zn/ SnO_2 system

E(eV)	n[20]	k[20]	The reorganization energy $ET_{Zn}^{SnO2}eV$
1.150	25.489	5.869	0.0625
1.180	23.262	5.779	0.0629
1.210	22.293	5.568	0.0635
2.240	29.874	6.667	0.0624
2.270	30.285	6.387	0.0719
2.310	21.556	5.864	0.0387

First, the reorganization energy is principle calculations to study the charge transport and investigate the dynamic of charge transport cross interface of Zn-SnO_2 using quantum postulates. It was revealed that the reorganization energy of the Zn-SnO_2 interaction depends on the size of the radii of Zn and SnO_2 and the distance between which affects the driving energy for the charge transport process. In the results, the numerical data for the calculation of radii ($a_{Zn} = 1.537A^o$ and $a_{\mathbf{SnO2}} = 2.048A^o$) were presented to calculate reorganization energy and also the total charge transport rate from the Zn metal to the conduction band of SnO_2 in heterojunction system through the different strength coupling and driving energy (0.37eV, 0.39eV and 0.41eV)at room temperature with the introduction of work function and electron negatively of metal and semiconductor parameterization respectively. The charge carrier moves from Zn to SnO2 depending on the reorganization energy, and the morphology of the configuration of the energy levels interfaces in the heterojunction. It was effected by modifying the charge transfer through the interface to facilitate electron movement, thereby increasing the charge transport probability. With an increasing energy (1.150 ,1.180,1.210,2.240 and 2.270) eV, the refractive index and dielectric constant were decreased and increased alternatively, the reorganization energy can have affected by hindering the energy of charge transport ability of charges having to move a distance to reach the SnO_2 electrode from Zn metal by decreasing the charge transport rate. The reorganization energy is calculated for different values of the metal's optical and dielectric constant due to different supplied energy. In Table 2, the reorganization energy evaluation at the different statically dielectric and refractive index for the charge transport process shows that both parameters limited the polarity behaviour.

Table 2 shows that the refractive index and dielectric constant decrease with increasing energies (1.150,1.180 and 1.210) eV for the system, while the refractive index (29.874 and 30.285) increases and the dielectric constant decreases from 6.667 to 6.387at energy from 2.240 eV to 2.270 eV. However, the dielectricity of 5.864 and the birefringence of 21.556 add up to 2.310 eV.

The charge transfer rate can be calculated using the expression in Eq.(17) with a work function of Zn metal $\Phi_{Zn} = 4.33\ eV$[21] and electron affinity for SnO_2 semiconductor $\chi_{SnO2} = 3.960eV$ [22]and reorganization energy taken from table (2) ,results are listed in table (3).

Table3. Results of rate of charge transport at Zn/SnO_2 system at driving energy 0.37eV.

Reorganization energy	The electron transfer rate constant × 10^{-5} The coupling of electron transfer $\mu^{CT}(E)$ × 10^{-2} eV/state					
	3.5	4.0	4.5	5.0	5.5	6
0.0625	2.977	3.389	3.884	4.364	4.847	5.484
0.0629	2.651	2.975	3.382	3.793	4.166	4.673
0.0635	3.176	3.682	4.172	4.66	5.274	5.897
0.0624	3.481	3.971	4.467	4.087	4.592	6.022
0.0719	4.481	5.163	5.982	6.747	7.790	8.629
0.0747	5.582	6.484	7.169	7.587	8.398	9.423

Table 4. Results of rate of charge transport at Zn/SnO_2 system at driving energy 0.39eV.

Reorganization energy	The electron transfer rate constant × 10^{-5} The coupling of electron transfer $\mu^{CT}(E)$ x 10^{-2} eV/state					
	3.5	4.0	4.5	5.0	5.5	6
0.0625	3.098	3.983	4.489	4.836	5.274	5.694
0.0629	2.941	3.279	3.678	4.102	4.489	4.802
0.0635	3.779	4.289	4.785	5.245	5.785	6.247
0.0624	3.986	4.432	4.987	5.567	6.098	6.472
0.0719	5.121	5.769	6.239	6.984	7.890	8.887
0.0747	6.431	7.345	8.239	9.123	10.423	11. 203

Table 5. Results of rate of charge transport at Zn/SnO_2 system at driving energy 0.41eV.

Reorganization energy	The electron transfer rate constant × 10^{-5} The coupling of electron transfer $\mu^{CT}(E)$ x 10^{-2} eV/state					
	3.5	4.0	4.5	5.0	5.5	6
0.0625	3.513	4.454	4.984	5.863	5.348	5.897
0.0629	3. 491	3.978	4.548	5.112	5.659	6.232
0.0635	4.234	4.786	5.215	5.785	6.385	6.896
0.0624	4.453	4.987	5.498	5.967	6.560	7.179
0.0719	5.678	6.189	6.698	7.204	7.976	8.980
0.0747	6.987	7.456	8.438	9.729	10.989	11. 786

However, the charge transport rate in Tables (3,4 and 5) indicates that the rate increases with the reorganization energy, which means that increases in reorganization energy lead to an increase in the total driving energy of charge to transport from Zn metal to SnO_2. On the other hand, the calculation of the charge transport rate for Zn/ SnO_2 system were showing the rate increased with increased of strength coupling between the energy levels of Zn and SnO_2 materials in the range of free energy 0.37eV ,0.39eV and 0.41 eV. Suppose the strength coupling increases from 3.5 to 6 eV. In that case, the charge transfer rate will be increased with an increased reorganization, because alignment energy levels become closer and changes can transfer. Furthermore, as described in the three tables (3,4 and 5), the charge transfer rate increased with driving force energy and increased reorganization energy. The charges will be transferred and cross-interced by more electrons having energy larger than the potential barrier at the interface with room temperature. Due to increasing the driving energy leads to increased charge transfer by pushing more charges into the carriers across the Zn- SnO_2 interface, which indicates that SnO_2 semiconductor is used based on the features of excellent mobility, conduction and valence bands, wide band gap, and high transparency, optical properties,, and chemical stability. The high charge transport in Zn contact with SnO_2 shows good alignment and good optical and electrical properties making Zn-SnO2 the best for solar cell l applications and photovoltaic cells.

CONCLUSION

we conclude that the estimation of the reorganization energy through the polarity factor (refractive index and dielectric constant) enhanced the charge transport process that occurred at low reorganization and charge rate of the system. Low reorganization energy (0.0625 eV to 0.0747 eV) at room temperature was necessary to become Zn-SnO2 more potential candidate for solar cell application devices. The overall calculation of charge transfers rate production as a function of reorganization energy, driving energy, work function, electronic negatively and coupling strength incorporating the factor gives increased improved results in the charge rate of charge transfer products with driving force energy and increased reorganization energy from the Zn metal to SnO_2 semiconductor. The charges were transferred cross-interface with more electrons having energy larger than the potential barrier at the interface with increasing strength coupling at room temperature .

Thus, the consideration of driving energy, reorganization energy as well as coupling for the system have an important role in the evolution as well as in the charge transfer of the high energy coupling strength by pushing more electrons to cross the Zn-SnO_2 interface .

So, this charge transfer model gives improved results over the other theoretical models to investigate the transfer mechanism in the Zn/SnO_2 system.

REFERENCES

1. Hadi.J.Mujbel. AL-agealy , Khaled.H.Harbbi,Mohsin.A.Hassooni and Rafah.I.Noori" Theoretical Study of Charge Transfer in Styryl Thiazilo Quinoxaline Dyes STQ-1, STQ-2,and STQ-3 in Organic Media System " Baghdad Science Journal, Vol.10,No.4,2013.
2. Kenji Iida and Masashi Noda" Electron transfer governed by light–matter interaction at metal–semiconductor interface " npj Computational Materials (2020) 5 .
3. Zhu Mao, Wei Song, Lei Chen, Wei Ji, Xiangxin Xue, Weidong Ruan, Zhishi Li, Huijuan Mao, Stephen Ma, John R. Lombardi, and Bing Zhao" MetalSemiconductor Contacts Induce the Charge-Transfer Mechanism of Surface-Enhanced Raman Scattering"J. Phys. Chem. C 2011, 115, 18378–18383.
4. H. Bendjedidi ; A. Attaf , H. Saidi , M. S. Aida , S. Semmari , A. Bouhdjar , and Y. Benkhetta" Properties of n-type SnO2 semiconductor prepared by spray ultrasonic technique for photovoltaic applications" Journal of Semiconductors , Vol. 36, No. 12 , 2015.
5. smritimah S. and Kumar "Optical properties of SnO2 Nanoparticles"Indian J.Phys.,Vol.84,No.9,PP1211-1221,2010.
6. Yong-sheng Fu , Jun Li * and Jianguo Li "Metal/Semiconductor Nanocomposites Photocatalysis: Fundamentals Applications and Properties" Nanomaterials 2019, 9, 359; doi:10.3390/nano9030359.
7. Razeghi, M. (2019). Semiconductor p-n and Metal-Semiconductor Junctions. In: Fundamentals of Solid State Engineering. Springer, Cham. https://doi.org/10.1007/978-3-319-75708-7-9.
8. Al-Agealy Hadi J.,M., and Al-Saadi Adil.A.,M."Barrier for Charge Transfer at Liquid/Liquid Interface"V Journal of Madent Alelem College,Vol.4,No2,2012.
9. John W. Norbury" Quantum Mechanics"Book, Physics Department University Of Wisconsin-Milwaukeep.O. Box 413milwaukee, Wi 53201november 20, 2000.
10. Hadi J. M. Al-Agealy, Waleed Bdaiwi salih, Taif S. Murdhi" Probability of Electron Transfer Rate Constant at Nanoscale Metal/Molecule Interface System" International Journal of Application or Innovation in Engineering & Management (IJAIEM) Volume 2, Issue 11, November 2013.
11. Hussein K.M,2011"study of the electric transfer at metal/semiconductor interface"MSc,Baghdad University,college of education ibn al hatham .
12. Hadi. J. M. Al-agealy Mohsin A. Hassooni Abbas K. Sadoon Ahmed M. Ashwiekh "Study and Invistagation of Electric Properties of Dye Sensitized Solar Cell" Mesop. environ. j. 2016, Spicial Issue A.;93-105.
13. Gao.Y. Q., Georgievskii. Y and Marcus. R. A.," on the theory of electron transfers reaction at semiconductor electrode/ liquid interface" J. chem. Phys. 2000, Vol (112), No 7.
14. Hadi J. M. Al-Agealy "Theoretical Analysis of the Kinetics Electron Transport at Solid/Solid Processes" Journal of Physical Science and Application 1 (6) (2016) 1-11.doi: 10.17265/2159-5348/2016.01.001.
15. Hadi Jabbar Al-Agealy and Adil Ali Al-Saadi" Theory and Calculation of the Reorganization Energy of Electron Transfer at Liquid/Liquid Interface " Ibn Al-Haitham Jour. for Pure & Appl. Sci. Vol. 26 (2) 2013
16. Sarmad S. Al-Obaidi , Hadi J. M. Al-Agealy and Saadi R. Abbas" Investigation And Study Of Electronic Transition Current For Au Metal Contact With Pentacene Molecule " Solid State Technology , Vol.63 ,Issue: 6 ,2020.
17. Sarfraz Hussain, Maryam Khan, Taha Majid Mahmood Sheikh, ,Muhammad Zahid Mumtaz, Talha Ali Chohan, Saba Shamim, and Yuhong Liu ,Zinc Essentiality, Toxicity, and Its Bacterial Bioremediation: A Comprehensive Insight, Front Microbial. 2022; 13: 900740.Published online 2022 May 31. doi: 10.3389/fmicb.2022.900740.
18. Xianfu Zhang , Long Zhang , Xinyuan Jia , Wen Song and Yongchang Liu , Design Strategies for Aqueous Zinc Metal Batteries with High Zinc Utilization: From Metal Anodes to Anode‐Free Structures, Nano-Micro Lett.(2024) 16:75
19. Taif S. Murdhi" Theory of Charge Transfer Rate at Coumarin–TiO2and Coumarin–SnO2 systems" IOSR Journal of Agriculture and Veterinary Science (IOSR JAVS), vol. 10, no. 11, 2017, pp. 26-31.
20. Marvin J. Weber "OPTICAL MATERIALS "Book, CRC Press LLC, 2003 .
21. Hadi J. M. Al-Agealy1 and Raghad L. Mohammed, Theoretical Study and Evaluation of Charge Transfer Rate At Zn Metal Contact with SnO2 Semiconductor Devices,IOP Conf. Ser.: Earth Environ. Sci. 790 012019, DOI 10.1088/1755-1315/790/1/012019.
22. Vo Pham Hoang Huy,Thi My Huyen Nguyen and Chung Wung Bark ,Recent Advances of Doped SnO2 as Electron Transport Layer for High-Performance Perovskite Solar Cells, Materials 2023, 16(18), 6170; https://doi.org/10.3390/ma16186170

Encryption and Security for Video Conferencing : A Review

Baydaa Jaffer Al-Khafaji [1, a)], Abdul Monem S. Rahma [2]

[1] *Iraqi Commission for Computers and Informatics, Informatics institute for postgraduate studies, Baghdad, Iraq*

[2] *Computer Science Department, Al-Maarif University College, Baghdad, Iraq*

Corresponding author: [a)] Baydaa.j.s@ihcoedu.uobaghdad.edu.iq

Abstract. This review article examines the evolving landscape of encryption and security for video conferencing and data transmission.It contains an in-depth analysis of cryptographic algorithms and inverted matrices in cryptography, and different types of threat models and attack vectors. This is why you will hear about authentication mechanisms and end-to-end encryption when someone talks about securing virtual communications. It also discusses the challenges and solutions offered by cloud-based video streaming services and explores video streaming delivery networks in the form of Content Delivery Networks (CDNs) and Peer-to-Peer (P2P) live streaming. With this review, the article aims to provide a comprehensive overview of the state-of-the-art and the future trends that are shaping the security of digital communications.

Keywords: Video Conferencing Security, Cryptographic Algorithms, End-to-End Encryption, Cloud-Based Video Streaming, Content Delivery Networks, Peer-to-Peer Streaming.

INTRODUCTION

Over the past years, the communication landscape has changed rapidly, especially in professional and educational contexts. Video conferencing technology has allowed for the simple and quick movement to virtual meetings, a move that has greatly expedited thanks to the effects and realities of COVID-19 [1]. Reliance on virtual meeting platforms increased drastically as organizations and institutions hadto make arrangements for working remotely. This move highlighted the huge necessity for high-security barriers to ensure the data remained honored, intact, and not leaking out. As virtual meetings involve sensitive discussions, sharing of confidential data, and the right process of decision-making, this becomes a lucrative opportunity for cyber threats and attacks [2].

While virtual meetings can be efficient and convenient, existing encryption techniques that secure these communecations are not sufficient to protect these messages from advanced attacks. With traditional encryption algorithms, it can be difficult to enable both security and performance, which is even more difficult when these are to be used for encryption of video and audio streams in real time.The challenge is now to provide secure end-to-end real- time communication without latency and quality of media degrading, needing an encryption system that is secure and lightweight on resources [3]. Given that sensitive data may be passing over insecure networks, it is essential that the integrity confidentiality, and authenticity of the sensitive information is maintained. Virtual meeting security breaches can result in the lossof IP, disclosure of confidential information, organizationalfinancial losses, and reputational damage to a great extent. Therefore, developing an effective encryption approach to address these security concerns is crucial [4]. This review article delves into the related works onencryption and security for video conferencing and data transmission. It explores various cryptographic algorithms and the role of inverted matrices in cryptography. Additionally, it examines threat models and attack vectors,authentication mechanisms, and the implementation of end-to-end encryption. The article also discusses cloud-based video streaming services, highlighting the challenges and solutions associated with these technologies, and provides insights into video streaming delivery networks, focusing onContent Delivery Networks (CDNs) and Peer-to-Peer (P2P)live streaming.

Technologies and Materials for Renewable Energy, Environment and Sustainability
AIP Conf. Proc. 3321, 020038-1–020038-11; https://doi.org/10.1063/5.0289624
Published under an exclusive license by AIP Publishing. 978-0-7354-5231-2/$30.00

Literature Review

The literature review spans several papers discussing advancements in encryption and security for video conferencing and data transmission, reflecting significant techno- logical responses to challenges heightened by the COVID- 19 pandemic. Zhu et al.[4] proposed a hybrid encryption scheme for quantum-secure video conferencing, integrating quantum key distribution with blockchain to enhance security against sophisticated attacks. Arnold Mashud Abu kariet al. [5] addressed vulnerabilities in Zoom's encryption amidst increased scrutiny during the pandemic, proposing enhanced security controls. Similarly, Kumar et al. [6] evaluated AES and RSA encryption methods for cloud data protection, advocating a hybrid approach for improvedperformance. Isobe and Ito [7].provided a critical analysis of Zoom's end-to-end encryption, revealing potential vulnerabilities and suggesting countermeasures.

Gauthier et .[8] reviewed the security of some popularplatforms such as Zoom, Google Meet, Microsoft Teams and even detected serious flaws in their end-to-end encryption standards and in what refers to transparency. Liuet al. [9]introduced m Tunnel, which is a software layerthat makes sure conference apps are secure while usingonly strong encryption, but without reducing robustness. A Tawney et al. [10].presented an end-to-end security frame- work for online meeting platforms, suggested that govern nance and technical controls be employed to protect user data. Lastly, Zhao etal.[11]. The hybrid encryption algorithm that they have designed has been proposed effectivelya hybrid algorithm to provide DES with RSA algorithm to secure the traditional encryption algorithm setup quickly and securely to develop a mechanism for communication. A series of new studies just reported major privacy and security risks of using the Zoom system, a platform thathas exploded in popularity worldwide for hosting online interactions and meetings [12].The most striking find of thereport was the poor authentication method of Zoom which allows unauthorized access and further leads to compare missing the user privacy and data theft[13]. Deploying for maximum security Goodyear 2019 [14] advances the idea that most of the security locks are behavioral and policy related lock than technical ones. He suggests that even a large part of the problem for companies is simply a lackof understanding about data usage because of insufficient compliance with security assurance standards (such as the US and European Exchange Commission's Safe Harborprinciples). Online meeting security concerns have already been outlined, warning that first-time users are particularly likely to be naive about securing video [15].

CRYPTOGRAPHY ALGORITHM

The combination of the Rivest–Shamir–Adleman (RSA)algorithm and the Advanced Encryption Standard (AES) is a key component of the current cryptographic environment for protecting virtual communications [3]. Symmetric encryption algorithms like AES are recognized for their efficiency and security, which makes them perfect for encrypting media material that is updated in real time. On the other hand, the asymmetric encryption method known as RSAis renowned for its strong key management features that enable safe key transfers between parties involved in the communication process.

AES and other symmetric encryptions use a single key for both encryption and decryption, providing speed and efficiency that are essential for managing massive amounts of data. However, this approach has difficulties with key distribution and administration, which means that the system's security depends on the [16]. In order to ensure a high level of security and operational efficiency both necessaryfor the real-time processing demands of video and audio streaming AES is structured around a series of complex operations called Sub Bytes, Shift Rows, Mix Columns, and Add Round Key [17] . However, asymmetric encryption, such as that used by RSA, employs two keys instead of one, increasing security by removing the requirement for sharing a single secretkey. Because of its computational intensity, this techniqueis less efficient than symmetric methods, but it is especially useful for secure key exchanges and digital signatures [18]. RSA maintains security even in situations where the public key is widely dispersed by employing two big prime numbers to produce a private key for decryption and apublic key for encryption [20]. In practice, RSA and AES are often used in conjunctions,combining RSA's secure key distribution capabilities with AES's efficiency in data encryption. This dual approach notonly enhances the security of data transmissions by pro- tecting the exchange of encryption keys but also maintains the performance necessary for seamless communication in virtual meetings. [19] Thus, by leveraging both RSA andAES, the proposed encryption system provides a robust framework for securing sensitive media content against a variety of cyber threats while supporting the dynamic requirements of modern virtual communication platforms [21].

Cryptographic key management is crucial in encryption systems, encompassing the generation, distribution, storage, usage, and replacement of keys to safeguard information. The primary challenge in key management is maintaining the confidentiality of keys, as their exposure can lead to unauthorized data access [22]. Secure key distribution is also

critical; for instance, even with the use of asymmetric encryption, the security of the system can be compromised if public keys are not exchanged securely [23]. Ensuring ongoing security throughout the key lifecycle and during secure communications is essential [24]. Moreover, keyrotation is necessary to mitigate risks associated with key interception and to minimize potential damage from com- promised keys.

To protect keys from unauthorized access, hardwaresecurity modules or secure key vaults are recommended, with access limited to systems that require the keys for operation. Regular audits of key usage can help detect and prevent unauthorized activities, maintaining trust in thesecurity system's integrity [25]. Key distribution methods must handle the secure generation, sharing, and storage of cryptographic keys. While manual key exchange is straightforward, it is impracticalfor large-scale or automated systems due to the risk ofinterception and human error [26].Symmetric key distribution might involve secure physical couriers or encrypted transmission channels, but maintaining these channels can be costly and complex [28]. Asymmetric key distribution, using public key infrastructure, offers a more scalable solution where public keys are openly distributed without compromising security, while private keys remain confidential [26]. Key management also requires secure storage solutions. Hardware security modules provide a tamper-proof environment for key storage, whereas software-based key management systems offer centralized control and automated key rotation, enhancing security and compliance with regulatorystandards [29]. Key escrow and recovery procedures are included to maintain continuity in the event of key loss, andautomatic key rotation is incorporated to minimize exposurerisk [30]. Lifecycle management practices provide appropriate control over keys from their creation to destruction. Table 1.

TABLE 1. Related Work encryption and security for video conferencing

Related Work	Aim	Method	Highest Results
Zhu et al., 2022 [4]	Address vulnerabilities of traditional video conference systems by proposing a hybrid encryption scheme for quantum-secure video conferencing combined with blockchain	Integrate quantum key distribution with classical network; "classical + quantum" hybrid encryption; real-time monitoring; blockchain with B+ trees	Enhances resistance to security threats; 3.15 times higher query efficiency
Arnold Mashud Abu kari et al., 2020 [5]	Propose a new system architecture to secure Zoom meetings in response to increased use and security concerns during the COVID-19 pandemic	Novel system architecture for user-controlled security of video and audio files	Enhanced overall security of Zoom conferencing solution
Kumar et al., 2020 [6]	Address the vulnerabilities in cloud environments by analyzing AES and RSA and proposing a hybrid encryption process	Hybrid encryption process combining AES and RSA	AES preferred for data encryption in cloud applications
Isobe and Ito, 2021 [7]	Evaluate the end-to-end encryption (E2EE) introduced by Zoom Video Communications	Security analysis of Zoom's E2EE cryptographic protocols; propose countermeasures	Insights for improving Zoom's encryption protocols
Abir et al., 2022 [8]	Address security and privacy issues in videoconferencing due to the COVID-19 pandemic	Lightweight, scalable blockchain-based authentication mechanism; time-based consensus algorithm	Enhanced security with low latency for video systems
Gauthier et al., 2021 [9]	Investigate the security of popular videoconferencing platforms like Zoom, Google Meet, and Microsoft Teams	Simulating calls, analyzing network traffic	Revealed lack of true end-to-end encryption, security concerns
Liu et al., 2024 [10]	Provide a secure solution for remote conference applications addressing privacy concerns	M Tunnel: transparent software layer; I/O virtualization; supports E2EE group conversations	Feasibility and low overhead demonstrated
Antwane et al., 2024 [11]	Address security and privacy concerns in virtual meetings due to the COVID-19 pandemic	Security framework with governance and technical controls	Improved security and privacy of Zoom meetings

Zhao et al., 2023 [12]	Address the need for secure information transmission over internet networks	Hybrid encryption algorithm combining DES and RSA	Fast encryption speeds, robust security

INVERTED MATRICES IN CRYPTOGRAPHY

Due to the requirement for high-quality transmissionwith low latency, encrypting real-time video and audio streams for applications like virtual meetings and webinars presents considerable hurdles. A significant obstacleis the computational intricacy of conventional encryption techniques like RSA and AES. Although these protocols have strong security features, they can cause large latency problems and deteriorate high-throughput video and audio stream quality, which can have a poor impact on user experience [31] . Sustaining synchronization between encrypted video and audio streams is another crucial concern. Precise timingis necessary for real-time communication in order to maintain synchronization between audio and video and improve user experience. In order to avoid desynchronization, whichcan be very disruptive, encryption and decryption processesneed to be efficiently managed [32]. Furthermore, to properly address these changes, flexible encryption solutionsare required due to fluctuations in network conditions and device capabilities [33].Another important issue that comes up is scalability, particularly in situations when there are plenty of people.As the number of users increases, each stream must beindependently encrypted and decrypted without compromising the system's overall performance. Scalable encryption techniques that can handle several streams at once are needed for this [34].Another level of complication is added when end-to-end encryption (E2EE) is ensured in real-time communications. Security and privacy cannot be preserved without E2EE, which makes the safe sharing and handling of encryption keys imperative. To prevent complicating the user experience, this procedure needs to be integrated smoothly and transparently [35].Real-time stream encryption is further complicated by interoperability problems. It can be difficult to guarantee that encrypted streams are available and function as wellas possible on all platforms given the variety of devicesand systems in use. Performance variations and possible security threats might result from differences in hardware and software [35]. Furthermore, following legal and regulatory requirements, like the GDPR in Europe or the CCPA in California, necessitates strict control over encryption protocols and user data. The implementation of efficient encryption techniques for real-time communication is mademore difficult by this regulatory factor [35].Addressing these challenges involves optimizing several key aspects of virtual meeting platforms. Latency is crucial, with the goal being to keep it under 150 milliseconds to support fluid, natural conversations. For this it needs highly efficient protocols of compression, encryption and trans- mission [36]. Video and audio quality are also important, requiring codecs that are not only able to compress data well, but that can also do so without significantly affecting quality, such as Opus for audio and H.264 or H.265 (aka HEVC) for video [37]. Lower-latency performance relies onupgrading the network infrastructure to implement peer-to- peer interactions via WebRTC and increasing data pathway efficiencies through content delivery networks (CDNs) to [38]. Additionally, the device's performance has to satisfy the real-time processing requirements, with software optimizations using multi-threading and hardware acceleration [39].Finally, echo cancellation, noise reduction and otheraudio and video enhancements together with a good user interface for simple configuration and troubleshooting all lead to good quality [40]. This whole solution makes sure the encryption is powerful enough to provide the required high performance and quality optimized for virtual
communication and at the same time.

THREAT MODELS AND ATTACK VECTOR

In this new landscape of cybersecurity, digital safety often depends on identifying and addressing these vulnerabilities in virtual meeting encryption, and adapting virtual security accordingly [37]. As virtual meetings often involve sharing information of sensitive nature – they should bemet with an equal measure of vigilance and offensive / defensive strategy to the same level than what is being donein real world face to face meetings, being that they have notonly become a part of today's communication landscape, but an integral one at that. Threats are categorized based upon attack vector in that each attack vector has different challenges and also different effects and these encompasses a spectrum of malign intents and tactics [38].
One of the biggest concerns people have with virtual classrooms is eavesdropping — where malicious individualslisten

in on virtual meetings to steal confidentialinformation. Identified vulnerabilities in the encryption algorithms designed to keep communication channels secure mean that criminals can easily eavesdrop on and endanger the privacy of private conversations. Man-in-the-middle attacks are also a major issue, because they can intercept communication between two parts and can modify/send butit is crucial to maintain the reliability and protect that data from interception and modification [41].

Data interception is a type of attack where the hackers will intercept the data packets sent over virtual meeting tools. Such severe breaches of confidentiality and privacy that are committed when recording not only the privacyof participants, but the ability of attackers to recover full conversations or lectures [37] All of these dangers requirea wide variety of defensive tactics. The reason strong encryption systems matter is because they keep data informats that can only be converted to readable form by people who have the specific process required for making that translation. This way, no one can read your secretsin transit and the chances for man-in-the-middle attacks are minimal. It is important that the encryption methods you use are secure and have had sound testing to ensure messagescan't be hijacked or altered surreptitiously [37].

More measures of security mean better protected virtualmeeting places. Firewalls enforce secure access and Intrusion Detection Systems probe and if required neutralizethe Intercepted danger. Secured transmission of the datahas been ensured by secure communication protocols like HTTPS that ensure that the secrecy and integrity of the data cannot be compromised. In the same way, one of the articles provides that also the public should be trained on better security best practice to add a robust people factor to the defines of security and reducing the chances of security breaches [42].

Authentication Mechanisms

Approaches for keeping the information shared confidential and intact, such as authentication mechanisms actingas guards in virtual meetings which are intended to keepthe unwanted persons away so that a discussion can only be engaged by the right entity [43]. The authentication of these users is of paramount importance since virtual meeting infrastructures are extended, in a sense, in the digital domainand this extension makes them appealing to thereat agents [44]. Various types of authenticating techniques with varying degrees of exactness are used to ensure the identities of participants in these online meeting circumstances. Single- factor authentication, the least complex authentication type, typically asks for a password or personal identification number (PIN). Its apparent simplicity, but the vulnerability to dictionary or brute force attacks of this method, couldput in risk the security of the meeting environment [43].

Multi-factor authentication (MFA), which greatly improves security measures, has been used by numerous platforms to address these weaknesses. In order to authenticate themselves, users of MFA must present several types of proof. Knowledge-based elements like passwords, possession-based elements like security tokens or mobile devices, and inheritance-based elements like biometric in- formation are some examples of this evidence. This setof elements significantly lowers the likelihood of security breaches by offering a far stronger protection against un- wanted access [45]. By employing distinctive biological characteristics like fingerprints, facial features, or speech patterns to confirm user identity, biometric authentication stands at the forefrontof authentication technology. To accurately verify the legitimacy of participants in virtual meetings, technologies such as facial recognition scanning camera feeds or voice recognition analyzing vocal signatures may be used. Although biometric authentication increases security, it also brings up serious privacy issues and needs sophisticated technology infrastructure to be implemented successfully and adhere to legal requirements [46].

End-To-End EncRYpTIon (E2EE)

End-to-End Encryption (E2EE) represents the pinnacle of security in digital communications, ensuring that only the intended communicating parties, who hold the necessary cryptographic keys, can decrypt messages. This level of security prevents anyone from telecom providers to thecommunication service providers themselves from accessing sensitive information. E2EE is the ultimate form of dataconfidentiality, making data transmitted across networks unreadable by anyone except the intended recipients, thus protecting digital exchanges from unauthorized surveillance and intrusions. In contrast to traditional encryption methods such as Transport Layer Security (TLS), where encryption and decryption occur at various points, including intermediate servers, E2EE maintains its robust architecture by limiting encryption and decryption strictly to the communicationendpoints. While TLS exposes data to potential vulnerabilities during transit, E2EE eliminates these risks by encrypting data at its source and decrypting it only at its final destination, thereby securing the data throughout its entire journey [47].

However, integrating E2EE into virtual meeting plat- forms introduces several challenges, particularly in the complex area of key management. Effective key management requires secure generation, distribution, and storage of cryptographic keys, essential for both encryption and decryption processes. This necessitates a strict adherence to cryptographic protocols and best practices to prevent unauthorized access to or compromise of these keys. Additionally, maintaining user privacy while enabling content moderation and abuse prevention presents a significant challenge, requiring a careful balance between privacy needs and regulatory requirements [48].Despite these hurdles, a range of best practices supports the effective implementation of E2EE in virtual meeting environments. Adhering to proven cryptographic protocols and continuously auditing security measures are essential to protect against breaches and build trust in the security of communications. Furthermore, empowering users to verify the identities of other participants enhances transparency and accountability, thereby reinforcing a secure and user- focused meeting experience [49].

Cloud-based video streaming services

Cloud-based video streaming services have significantly transformed the way media content is delivered and consumed worldwide. These services leverage cloud computing to provide scalable and cost-effective solutions for streaming video content to a global audience. They offer the advantages of high scalability, flexibility, and efficiency in managing and delivering video content, making it accessible from anywhere and on any device, all supported by the cloud infrastructure.

Cloud-based streaming utilizes various technologies to optimize performance and user experience. Adaptive bitrate streaming, for instance, adjusts the video quality in real-time based on the user's bandwidth, ensuring smooth playback without buffering [50]. Content Delivery Networks (CDNs) are used extensively to reduce latency and improve load times by caching content at various geographical locations closer to the users. This approach not only enhances the viewing experience but also handles large volumes of traffic effectively, preventing server overloads during peak times [51].Moreover, cloud services integrate advanced features like artificial intelligence and machine learning to im- prove content recommendation systems, video analytics, and enhance security measures. According to [52], these technologies support content security against illegal access and piracy, personalize the viewing experience, and offer content suggestions based on user preferences and viewing history. Notwithstanding these benefits, network neutrality, data privacy, and the requirement for strong DRM systems to safeguard intellectual property are some of the problems that cloud-based video streaming services must overcome. To ensure user data safety and compliance with international regulatory requirements, these problems need to be carefully considered and strict security mechanisms put in place [53].

CHALLENGES AND SOLUTIONS OF CLOUD-BASED VIDEO STREAMING SERVICES

Numerous issues with cloud-based video streaming services need to be addressed in order to guarantee smooth, excellent content delivery. The main issue is latency, which has a big influence on user experience, especially when it comes to live streaming situations like gaming and real- time events [54]. The interactive aspect of these services can be interfered with by high latency, which can lead to delays between capture and playback [54]. Utilizing content delivery networks (CDNs) is one way to reduce latency and buffering concerns by distributing material closer to the end users [51,55].Another major issue is bandwidth limitations. High- definition video streaming needs a lot of bandwidth, which can be troublesome in areas with inadequate internet infrastructure or when networks are busy during peak usage hours [53]. Adaptive bit-rate streaming techniques are utilized to mitigate this issue. They dynamically modify the video stream quality according to the user's current internet speed, guaranteeing uninterrupted playback [56]. Furthermore, to save bandwidth, video compression methods like H.264 [57] and H.265 are used to decrease the size of video files without sacrificing quality [58].Large audiences require scalability, particularly for live events when viewing might fluctuate dramatically [59]. Such demands may be too much for traditional infrastructure to handle, which could result in service interruptions or poor performance. Scalability is a feature of cloud-based architecture that enables services to dynamically allocate resources in response to demand. Regardless of the number of concurrent viewers, load balancing and other techniques disperse traffic among several servers, avoiding any one server from becoming a bottleneck and guaranteeing a constant user experience [60, 61].Since cloud-based video streaming services manage enormous volumes of sensitive customer data, security and privacy must be guaranteed. Hacking, piracy, and unauthorized access are examples of security hazards [62,63]. Strong encryption techniques and safe key management procedures are used to lessen these risks [64]. Furthermore, the application of

digital rights management (DRM) tech- neologies aids in the prevention of illicit content distribution and copying, safeguarding intellectual property [65,66].High-quality video content delivery can be prohibitively expensive, particularly for smaller suppliers. Spending maybe controlled with the use of cost-efficient cloud services and effective resource management [67]. In accordance withdemand, server less designs, for example, enable providers to only pay for the computing resources they really utilize [68]. Additionally, reducing computational overheadthrough workflow optimization for encoding and transcoding can further minimize operating expenses [69].

VIDEO STREAMING DELIVERY NETWORKS

Video streaming delivery networks are essential for making sure that video material is delivered to users all overthe world in an effective and high-quality manner. Peer-to- peer (P2P) live streaming and content delivery networks (CDNs) are the two main categories of delivery networks [70].Global networks of computers arranged in a deliberate manner to cache and distribute web information, including movies, to consumers more effectively depending on their location are called content delivery networks, or CDNs.CDNs reduce latency, boost website performance, and ensure that media-rich content is efficiently delivered to the right user. Showing content closer to the end users in a non-capital region has a performance benefit to load time and directly reduces load on origin servers, since the content is cached on edge servers. For example, some of the more popular CDN companies (i.e., Google Cloud CDN, Amazon Cloud Front, and Azure CDN) offer solutionsthat are both flexible and scalable, significantly improving the streaming experience for Netflix and YouTube and thousands of other sites. In addition, CDNs serve as a security buffer against Distributed Denial of Service (DDoS)attacks, allowing traffic to be routed across a range of servers that reduces server strain, and, moreover, ensuresthe content is always available [71]. Conversely, live streaming through peer-to-peer (P2P) combines the available upload bandwidth from multipleusers to distribute video feeds. P2P live streaming is where every single viewer is a broadcaster and may share the feed they receive with other users. This distribution provides better scalability and cost, as well as offloading the central servers. Peer-to-peer live streaming technologies areprotocols such as Bit Torrent Live, Web RTC or Sop Cast. Web RTC, for instance, is important for low-latency ap-applications, it facilitates real-time communication thanks to the peer-to-peer direct data transfer. Nonetheless, shifts in upload capabilities and network conditions — which can vary greatly between users — can also impact the QoS of the overall stream, particularly in the case of P2P streaming [72].Though they use distinct approaches, P2P networks and CDNs both meet the need for dependable, scalable,and effective video transmission. CDNs are well knownfor providing stable performance, and excellent consist- teensy, especially when it comes to massively popular videostreaming services using a network of servers distributed allover the planet. On the other hand, a P2P type of network solves the problem of load division between users and give an affordable and scalable solution overall, but in additionto the previous restrictions, they can encounter problems of the upload bandwidth and network speed instability. CDNs and P2P live streaming are different types of streamingsystems, and the choice between these systems is oftendetermined by the specific requirement of the streaming service including audience size, audience distribution and type of content available [73].

CONCLUSION

This review has underscored the critical importance of robust encryption and security protocols in the context of video conferencing and data transfer. By analyzing cryptographic algorithms, the use of inverted matrices, threat and attack vector scenarios, and other key factors, it becomes clear that a comprehensive strategy is essential to ensure both performance and security. To maintain safe and secure virtual communications, strong and uncompromising authentication protocols are necessary, alongside rigorous end-to-end cryptography.

The course begins by addressing the challenges associated with cloud-based video streaming services and how to leverage their capabilities. It then introduces the fundamental principles of content delivery networks (CDNs), peer-to-peer (P2P) streaming, and examines how these technologies influence media consumption patterns.

Looking ahead, future research will focus on developing more efficient encryption algorithms, exploring advanced cryptographic techniques, and investigating next-generation authentication methods. In addition, it will delve into integrating emerging technologies such as quantum cryptography and blockchain to enhance the security and trustworthiness of digital communication networks. Through continuous innovation and research, the field will evolve further ensuring the integrity, confidentiality, and reliability of information exchange.

REFERENCES

1. D. P. Hove and B. Watson, "The shortcomings of video conferencingtechnology, methods for revealing them, and emerging or solutions," PRESENCE: Virtual and Augmented Reality, vol. 31, pp. 283–305,2022.
2. R. Hasan and R. Hasan, "Towards a threat model and securityanalysis of video conferencing systems," in 2021 IEEE 18th AnnualConsumer Communications & Networking Conference (CCNC). IEEE, 2021, pp. 1–4.
3. S. Fatima, T. Rehman, M. Fatima, S. Khan, and M. A. Ali, "Comparative analysis of AES and RSA algorithms for data security in cloud computing," Engineering Proceedings, vol. 20, no. 1, p. 14, 2022.
4. D. Zhu, J. Zheng, H. Zhou, J. Wu, N. Li, and L. Song, "A hybrid encryption scheme for quantum secure video conferencing combined with blockchain," Mathematics, vol. 10, no. 17, p. 3037, 2022.
5. A. M. Abu kari, E. K. Bankas, and M. M. Iddrisu, "A securedvideo conferencing system architecture using a hybrid of two homomorphic encryption schemes: A case of zoom," International Journal of Engineering Research & Technology (IJERT), vol. 9,no. 8, pp. 237–240, 2020.
6. A. Kumar, V. Jain, and A. Yadav, "A new approach for security in cloud data storage for IOT applications using hybrid cryptography technique," in 2020 international conference on power electronics& IoT applications in renewable energy and its control (PARC). IEEE, 2020, pp. 514–517.
7. T. Isobe and R. Ito, "Security analysis of end-to-end encryption for zoom meetings," IEEE access, vol. 9, pp. 90 677–90 689, 2021.
8. N. H. Gauthier and M. I. Husain, "Dynamic security analysis of zoom, google meet and Microsoft teams," in Silicon Valley Cyber- Security Conference: First Conference, SVCC 2020, San Jose, CA, USA, December 17–19, 2020, Revised Selected Papers 1. Springer, 2021, pp. 3–24.
9. Y. Liu, H. Chen, and Z. Yang, "Enforcing end-to-end security for remote conferencing," in 2024 IEEE Symposium on Security and Privacy (SP). IEEE Computer Society, 2024, pp. 202–202.
10. S. Antwane, Z. Alshammari, A. Mousa, and B. A. Shawar, "Asecurity framework for addressing privacy issues in the zoom conference system."
11. J. Zhao, "Des-co-RSA: a hybrid encryption algorithm based on des and RSA," in 2023 IEEE 3rd International Conference on Power, Electronics and Computer Applications (ICPECA). IEEE, 2023, pp. 846–850.
12. V. Susu Kailo, I. Olitsky, and S. Vasylyshyn, "Analysis of theattack vectors used by threat actors during the pandemic," in 2020 IEEE 15th International Conference on Computer Sciences andInformation Technologies (CSIT), vol. 2. IEEE, 2020, pp. 261– 264.
13. M. Mohanty and W. Yaqub, "Seamless authentication for online teaching and meeting," in 2020 IEEE Sixth International Conferenceon Multimedia Big Data (Big MM). IEEE, 2020, pp. 120–124.
14. M. Goodyear, "The dark side of videoconferencing: The privacy tribulations of zoom and the fragmented state of us data privacy law," Holer: Off Rec., vol. 10, p. 76, 2019.
15. P. P. Santoso, E. Silvani, A. B. Trishaan, K. Adiy Arta, D. Na- pitifully, T. Sabari, and R. Rahim, "Systematic literature review: Comparison study of symmetric key and asymmetric key algorithm,"in IOP Conference Series: *Materials Science and Engineering*, vol. 420. IOP Publishing, 2018, p. 012111.
16. J. Kaur, S. Lamba, and P. Saini, "Advanced encryption standard: at-tacks and current research trends," in *2021 international conferenceon advance computing and innovative technologies in engineering (ICACITE)*. IEEE, 2021, pp. 112–116.
17. M. J. Dworkin, E. B. Barker, J. R. Nechvatal, J. Foti, L. E. Bassham. Roback, and J. F. Dray Jr, "Advanced encryption standard (AES),"2001.
18. R. Banoth and R. Regar, "Asymmetric key cryptography," in *Clas- sisal and Modern Cryptography for Beginners*. Springer, 2023, pp. 109–165.
19. R. L. Rivest, A. Shamir, and L. Adleman, "A method for obtaining digital signatures and public-key cryptosystems," *Communications of the ACM*, vol. 21, no. 2, pp. 120–126, 1978.
20. H. T. Sihota, S. Efendi, E. M. Zamzami, and H. Maegan, "Design and implementation of Rivest shammer Addleman's (RSA) cryptography algorithm in text file data security," in *Journal of Physics: Conference Series*, vol. 1641, no. 1. IOP Publishing, 2020, p. 012042.
21. F. Lalem, A. Loudi, M. Kara, M. Al-Khalidi, and A. Eleyana, "A novel digital signature scheme for advanced asymmetric encryption techniques," *Applied Sciences*, vol. 13, no. 8, p. 5172, 2023.
22. A. Ever Spaugh, K. Paterson, T. Risten part, and S. Scott, "Key rotation for authenticated encryption," in *Advances in Cryptology– CRYPTO 2017: 37th Annual International Cryptology Conference, Santa Barbara, CA, USA, August 20–24, 2017, Proceedings, PartIII 37*. Springer, 2017, pp. 98–129.
23. E. Diamanti and A. Leverrier, "Distributing secret keys with quean- tum continuous variables: principle, security and implementations," *Entropy*, vol. 17, no. 9, pp. 6072–6092, 2015.

24. M. Somerhalders, "Hardware security module," *Trends in Data Protection and Encryption Technologies*, pp. 83–87, 2023.
25. A. Atakora, O. A. Fragola, B. S. Ayinla, O. O. Amoo, T. O. Abra- hams, and F. Osasuna, "A comparative review of data encryption methods in the USA and Europe," *Computer Science & IT Research Journal*, vol. 5, no. 2, pp. 447–460, 2024.
26. J. Gonza´ lez Nieto, K. Viswanathan, C. Boyd, and E. Dawson, "Key recovery system for the commercial environment," in *Information Security and Privacy: 5th Australasian Conference, ACISP 2000, Brisbane, Australia, July 10-12, 2000. Proceedings 5*. Springer, 2000, pp. 149–162.
27. M. Rahman, L. Zhou, and S. Chakraborty, "Spoked: a protocol for symmetric key distribution over public channels using self-powered timekeeping devices," *IEEE Transactions on Information Forensics and Security*, vol. 17, pp. 1159–1171, 2022.
28. H.-K. Lo, M. Montagna, and M. von Willich, "Distributed Sim- metric key exchange: A scalable, quantum-proof key distribution system," *arid preprint arXiv:2205.00615*, 2022.
29. S. Myers and A. Shull, "Practical revocation and key rotation," in *Topics in Cryptology–CT-RSA 2018: The Cryptographers' Track at the RSA Conference 2018, San Francisco, CA, USA, April 16-20, 2018, Proceedings*. Springer, 2018, pp. 157–178.
30. I. Santos-Gonzalezm. Rivero-Garci's, J. Molina-Gil, and. Caballero-Gil, "Implementation and analysis of real-time streaming protocols," *Sensors*, vol. 17, no. 4, p. 846, 2017.
31. M. I. Bhat and K. J. Giri, "Impact of computational power on cryptography," *Multimedia Security: Algorithm Development, Analysis and Applications*, pp. 45–88, 2021.
32. M. Yamni, A. Daoui, H. Karmon, M. Sayuri, H. Qaida's. Matahir, O. Jamil, W. El-Shafai, A. D. Alarni, N. F. Soliman *et al.*, "An efficient watermarking algorithm for digital audio data in security applications," *Scientific Reports*, vol. 13, no. 1, p. 18432, 2023.
33. Y. DoDI's, D. Jost, B. Kesavan, and A. Marceron, "End-to- end encrypted zoom meetings: Proving security and strengthening liveness," in *Annual International Conference on the Theory and Applications of Cryptographic Techniques*. Springer, 2023, pp. 157–189.
34. M. A. Talib, S. Abbas, Q. Nasir, F. Dealba, T. Mohhamed. Hassan, and K. Sanjib, "Interoperability among heterogeneous blockchains: A systematic literature review," *Trust Models for Next- Generation Blockchain Ecosystems*, pp. 135–166, 2021.
35. I. Khan, T. X. Tran, M. Hiltunen, T. Karaliuses, and D. Kout- Sanicolas, "An experimental study of low-latency video streaming over 5g," *arid preprint arXiv:2403.00752*, 2024.
36. L. Rubinger, A. Gawenda, S. Akthari, N. Nucci, A. Paynight. Johal, V. Khanduja, and M. Bhandari, "Maximizing virtual meetings and conferences: a review of best practices," *International orthopedics'*, vol. 44, pp. 1461–1466, 2020.
37. S. Morrison-Smith and J. Ruiz, "Challenges and barriers in virtual teams: a literature review," *SN Applied Sciences*, vol. 2, no. 6, pp. 1–33, 2020.
38. K. A. Karl, J. V. Polichetti, and N. Aghakhani, "Virtual work meetings during the covid-19 pandemic: The good, bad, and ugly," *Small group research*, vol. 53, no. 3, pp. 343–365, 2022.
39. N. Nurmi and S. Pakarinen, "Virtual meeting fatigue: Exploring the impact of virtual meetings on cognitive performance and active versus passive fatigue." *Journal of* occupational health psychology, 2023.
40. M. A. Al-Shareeda and S. Manickam, "Man-in-the-middle attacks in mobile ad hoc networks (manets): Analysis and evaluation," *Symmetry*, vol. 14, no. 8, p. 1543, 2022.
41. L. R. Bays, R. R. Oliveira, M. P. Barcellos, L. P. Gaspary, and E. R. Mauro Madeira, "Virtual network security: threats, countermeasures, and challenges," *Journal of Internet Services and Applications*, vol. 6, pp. 1–19, 2015.
42. I. Anastasi, G. Rosato's, G. Pavlidis, and K. Ranos, "User authentication mechanisms based on immersive technologies: A systematic review," *Information*, vol. 14, no. 10, p. 538, 2023.
43. G. Crohan, L. Dumitriu, and M. V. Craciuns, "Preliminary expel Imants of a real-world authentication mechanism based on facial recognition and fully homomorphic encryption," *Applied Sciences*, vol. 14, no. 2, p. 718, 2024.
44. K. Abhishek, S. Roshan, P. Kumar, and R. Ranjan, "A compere- tensive study on multifactor authentication schemes," in Advances in Computing and Information Technology: Proceedings of the Second International Conference on Advances in Computing and Information Technology (ACITY) July 13-15, 2012, Chennai, India-Volume 2. Springer, 2013, pp. 561–568.
45. F. Mathis, H. I. Fawaz, and M. Khamis, "Knowledge-driven biometric authentication in virtual reality," in Extended Abstracts of the 2020 CHI Conference on Human Factors in Computing Systems, 2020, pp. 1–10.

46. O. J. Bamini, S. Misra, F. Ida Chaba, and J. Oluranti, “End-to-end security in communication networks: a review,” in Innovations in Bio-Inspired Computing and Applications: Proceedings of the 11th International Conference on Innovations in Bio-Inspired Computingand Applications (IBICA 2020) held during December 16-18, 2020 11. Springer, 2021, pp. 492–505.
47. A. Salomaa and A. Salomaa, “Cryptographic protocols: Surprising vistas for communication,” in *Public-Key Cryptography*. Springer,1990, pp. 181–218.
48. S. E. Hampton, B. S. Halpern, M. Winter, J. K. Balch, J. N. Parker, J. S. Baron, M. Palmer, M. P. Schildhauer, P. Bishop, T. R. Meagher *et al.*, “Best practices for virtual participation in meetings: Experiences from synthesis centers,” *Bulletin of the Ecological Society of America*, vol. 98, no. 1, pp. 57–63, 2017.
49. Z. Dunnum, W. Liu, Z. Li, D. Chen, Z. Wang, Y. Wang, and W. Gao, “Assessing the quality-of-experience of adaptive bitrate video streaming,” *arid preprint arXiv:2008.08804*, 2020.
50. V. Stocker, G. Saridakis, W. Lehr, and S. Bauer, “The growing complexity of content delivery networks: Challenges and imply-cations for the internet ecosystem,” *Telecommunications Policy*,vol. 41, no. 10, pp. 1003–1016, 2017.
51. A. Qayyum, A. Ijaz, M. Usama, W. Iqbal, J. Qadir, Y. Elkhatib,and A. Al-Fuqaha, “Securing machine learning in the cloud: Asystematic review of cloud machine learning security,” *Frontiers in big Data*, vol. 3, p. 587139, 2020.
52. W. Moina-Rivera, M. Garcia-Pineda, J. Gutierrez-Aguado, and J. M. Alcaraz-Calero, “Cloud media video encoding: review and challenges,” *Multimedia Tools and Applications*, pp. 1–48, 2024.
53. B. Taraghi, H. Hell Wagner, and C. Timeer, “Ill-advised: live low-latency cloud-based adaptive video streaming evaluation frame-work,” *IEEE Access*, vol. 11, pp. 25 723–25 734, 2023.
54. M. Wang, P. P. Jayaraman, R. Ranjan, K. Mitra, M. Zhang, E. Lis. Khan, M. Pathan, and D. Georgeakopoulos, “An overview of cloud-based content delivery networks: Research dimensions and state-of-the-art,” *Transactions on Large-Scale Data-and Knowledge-Centered Systems XX: Special Issue on Advanced Techniques for BigData Management*, pp. 131–158, 2015.
55. Y. Qin, “Adaptive bitrate streaming over cellular networks:Rate adaptation and data savings strategies,” *Ariv preprintarXiv:2104.01104*, 2021.
56. G. J. Sullivan, J.-R. Ohm, W.-J. Han, and T. Wiegand, “Overviewof the high efficiency video coding (have) standard,” *IEEE Transarc- tins on circuits and systems for video technology*, vol. 22, no. 12,pp. 1649–1668, 2012.
57. L. Mechura'd, “A comparison of machine learning-based and conventional technologies for video compression,” *Technologies*, vol. 12, no. 4, p. 52, 2024.
58. W. Moina-Rivera, M. Garcia-Pineda, J. M. Claver, and J. Gutierrez- Aguado, “Event-driven serverless pipelines for video coding and quality metrics,” *Journal of Grid Computing*, vol. 21, no. 2, p. 20, 2023.
59. S. Sandhya and N. Cauvery, “Dynamic load balancing for video processing system in cloud,” in *Computational Vision and Robotics:Proceedings of ICCVR 2014*. Springer, 2015, pp. 189–197.
60. A. R. Khan, “Dynamic load balancing in cloud computing: Op- itemized rl-based clustering with multi-objective optimized task scheduling,” *Processes*, vol. 12, no. 3, p. 519, 2024.
61. M. A. Almira, I. Obaidat, Y. Jaareh, and M. Al-Saleh, “Asecurity framework for cloud-based video surveillance system,” *Multimedia Tools and Applications*, vol. 76, pp. 22 787–22 802, 2017.
62. S. K. Kotha, M. S. Rani, B. Subedi, A. Chunduru, A. Karroubi. Neupane, and V. Sathishkumar, “A comprehensive review on secure data sharing in cloud environment,” *Wireless Personal Com-medications*, vol. 127, no. 3, pp. 2161–2188, 2022.
63. M.-Y. Kang, “Parallel security video streaming in cloud server environment,” in *Intelligent Computing Theories and Application: 17th International Conference, ICIC 2021, Shenzhen, China, August12–15, 2021, Proceedings, Part I 17*. Springer, 2021, pp. 346–357.
64. T. Pellegrini, “Digital rights management–technologies, application areas, and governance,” in *Handbook of Media and CommunicationEconomics: A European Perspective*. Springer, 2023, pp. 1–17.
65. A. Rafi, C. Shepherd, and K. Marcantonio's, “A first look at digital rights management systems for secure mobile content delivery,” *arid preprint arXiv:2308.00437*, 2023.
66. M. Darwich, T. Alghamdi, K. Khalil, Y. Ismail, and M. Bayoumi, “Cost-optimized cloud resource management for video streaming: Arima predictive approach,” *Cluster Computing*, pp. 1–15, 2023.
67. K. Konstantoudakis, D. Breitigan'd, A. Domangue, N. Zeulis. Weit, K. Christakos, P. Dra Koulis, E. Christakis, D. Zapalas', and P. Daras, “Serverless streaming for emerging media: towards 5g network-driven cost optimization: A real-time adaptive streaming Faas service for small-session-oriented immersive media,” *Multimax- die Tools and Applications*, pp. 1–40, 2022.

68. D. K. Krishnappa, M. Zink, and R. K. Sitaraman, “Optimizingthe video transcoding workflow in content delivery networks,” in *Proceedings of the 6th ACM Multimedia Systems Conference*, 2015,pp. 37–48.
69. M. Gurmeher and M. Analia, “Envy-free resource allocation and request routing in hybrid can–p2p networks,” *Journal of Network and Systems Management*, vol. 24, pp. 884–915, 2016.
70. D. DESIGN, “Peer-to-peer live streaming and video on.”
71. D. Halder, P. Kumar, S. Bhushan, and A. M. Basware, “Fireteam:A wart based efficient and scalable p2p live streaming platform, "in *2021 International Conference on Computer Communicationsand Networks (ICCCN)*. IEEE, 2021, pp. 1–9.
72. S. Budhaka and V. Tamara Alli, “An overlay management strategy to improve qi's in cdn-p2p live streaming systems,” Peer-to-peer networking and applications, vol. 13, no. 1, pp. 190–206, 2020 in 2021 International Conference on Computer Communicationsand Networks (ICCCN). IEEE, 2021, pp. 1–9.
73. S. Budha and V. Tamarah alli, “An overlay management strategy to improve qi's in cdn-p2p live streaming systems,” *Peer-to-peer networking and applications*, vol. 13, no. 1, pp. 190–206, 2020.

Virulence of genes *stx2* and *rfbE* detection in Enterohemorhagic *E. coli (O157:H7)* isolated from milk and meat products

Harith Basim Ibrahim[1,a], Khalid Mahmood Hammadi [1], Amal Aziz Kareem [2]

[1] *Iraqia University, College of Education, Dept. of Biology, Baghdad, Iraq*
[2] *Middle Technical University, College of Health and Medical Technologies, Baghdad, Iraq*

[a] Corresponding author: ha94basim@gmail.com

Abstract. This study aimed to investigate the presence of Escherichia coli O157:H7 in dairy and meat products in Baghdad Governorate, Iraq, and to identify the virulence genes stx2 and rfbE. A total of 300 samples were collected from various local markets in Baghdad from February 21, 2023, to April 25, 2023. Thirty isolates (10%) of E. coli O157:H7 were identified, with a higher prevalence in meat products (73.33%) compared to dairy products (26.67%). The highest contamination rate for meat samples was observed in the Adl district (25%), while the lowest was in the Al-Bayaa district (0%). For dairy products, the highest contamination rate was in the Al-Sha'alah district (14.3%), and the lowest was in Abu Ghraib (2.8%). The antimicrobial susceptibility testing using the VITEK 2 Compact system revealed resistance to cefotaxime, ceftazidime/avibactam, ceftolozane/tazobactam, aztreonam, ampicillin/sulbactam, and meropenem/vaborbactam (40%), intermediate susceptibility to colistin, cefazolin, and chloramphenicol (15%), and susceptibility to doripenem, cefoxitin, piperacillin/sulbactam, tobramycin, levofloxacin, doxycycline, minocycline, tetracycline, and tigecycline (45%).PCR analysis for the stx2 and rfbE genes revealed the presence of the rfbE gene in five isolates (16.67%) with a molecular weight of 239 bp. The stx2 gene was not detected in any of the isolates. The five rfbE-positive isolates were registered in the National Center for Biotechnology Information (NCBI) as new E. coli strains. Sequence analysis of the rfbE gene showed 73% similarity to the reference sequence (ID: CP124740.1) for four isolates and 75% similarity for one isolate. Phylogenetic analysis revealed 99% genetic similarity to isolates from the UK and Canada, 82% similarity to another Iraqi isolate, and 84% similarity to E. coli isolates from the USA and China.

Keywords: *E.coli o157:H7*, *Stx2, rfbE* , Milk products , Meat products

INTRODUCTION

The Enterobacteriaceae family contains a large and diverse group of bacteria, with the majority of its members naturally occurring in the intestines of humans and animals [1] The genera of this family are described as rod-shaped, growing on conventional culture media. Most genera of the Enterobacteriaceae family are intestinal pathogens (Intestinalpathoge) or are commensals in the intestines (Commensals), and a few of its genera are saprophytic, containing antigens in their composition [2] Since *Escherichia coli* can act as a large reservoir for resistance genes that directly impact therapy in human and veterinary medicine, the debate about the transmission of multidrug-resistant *E.coli* strains between animals and humans through multiple pathways has become increasingly important. However, the interaction between food-producing animals, humans, and the environment in relation to the transmission of resistant pathogens has not been fully understood [3] .*E.coli O157:H7* is one of the most frequently reported causes of foodborne diseases. It works by disrupting the host's intestinal mucosa and producing Shiga like toxins (*Stx*) that cause hemorrhagic colitis and hemolytic uremic syndrome. The AE (Attaching and Effacing) phenotype is controlled by the bacterial pathogenicity islands (PAIs), and this bacterium is considered to be the locus of enterocyte effacement (LEE). Induction of both AE and Stx is subject to very complex regulatory mechanisms. The major proteins expressed, and the environmental signals involved in regulating the expression of virulence genes are vital to finding a way to

Technologies and Materials for Renewable Energy, Environment and Sustainability
AIP Conf. Proc. 3321, 020039-1–020039-9; https://doi.org/10.1063/5.0291619
Published under an exclusive license by AIP Publishing. 978-0-7354-5231-2/$30.00

control host colonization, especially in livestock [4] O-antigen is a chain of lipopolysaccharide (LPS) that is formed from a variable number of repeating units, with a minimum of eight units [5] *E coli O157* contains LPS. The O-antigen side chain/, or O-antigen, also contains multiple repeats. It is a part of the LPS lipopolysaccharide (LPS) found in the outer membrane of Gram-negative bacteria such as *E. coli* [6]. The *rfbE* gene encodes for the chemical composition of LPS, which means that LPS is a major component of bacterial cell walls. Therefore, the *rfbE* gene is essential for the biosynthesis of O-antigen in bacteria. In the case of *E. coli O157:H7*, inactivation of the rfbE gene results in the loss of O-antigen, making the bacteria more susceptible to killing by the immune system [7].The purpose of this study is to detect the presence of the stx2 and rfbE genes in E. coli (O157:H7) bacteria isolated from milk and meat products. Stx2 and rfbE genes are pathogenic genes that produce toxins that can lead to serious diseases, such as hemorrhagic colitis. Detection of the presence of these genes in E. coli (O157:H7) bacteria isolated from milk and meat products can help to identify sources of infection and take preventive measures to reduce its spread

MATERIALS AND METHODS

Collection of samples

A total of 300 samples of dairy and meat products were collected from different areas of Baghdad, Iraq, from 21 February to 25 April 2023. Of these, 57 samples were collected from Abu Ghraib, 48 from Bab Al-Muazzam, 36 from Hay Al-Adl, 72 from Al-Shulla, 45 from Al-Hurriyah, and 42 from Al-Baya'. Samples were collected in sterile plastic containers and transported immediately to the laboratories of the College of Health and Medical Technologies in Baghdad for culture, isolation, and diagnosis using conventional methods. After collecting the samples, a swab was taken from each sample in the sterile plastic container and culture in 5 mL of Brain Heart infusion Broth. The mixture was then mixed and incubated at 37 °C for 24 hours to activate the samples.

Bacterial Isolation

A suitable number of samples were taken using a bacterial inoculation loop from the dilutions prepared from the liquid culture medium of Brain Heart infusion Broth to be inoculated onto the Sorbitol MacConkey Agar medium prepared in advance according to the instructions of manufacturer instructions. The plates were incubated at 37 °C for 24 hours to detect the presence of *E. coli* O157:H7 by the SMAC culture medium. The colonies were collarless or slightly brown and transparent, characterized by their inability to ferment sorbitol [8]. Then, it was inoculated onto the CHROMagar *E. coli* O157:H7 medium by streaking and incubated for 24 hours at 37 °C. Then, the growth was observed and the bacteria that fermented lactose and investigated for *E. coli O157:H7* were distinguished. It is a dark pink to reddish colour [9] diagnosis was performed using the VITEK 2 diagnostic system [10-13]. Antibiotic susceptibility testing of bacteria was performed using the Vitek2 system. The *stx2* and *rfbE* genes were also detected.

Polymerase chain reaction

E. coli O157:H7 genomic DNA was extracted according to the manufacturer's instructions of the HiGenoMB kit. After DNA extraction. The purity and concentration of the DNA were measured by Nano Drop. Primers used in the study were listed in table 1.

Table 1, primers

Gene	**bP**		**Sequence of primers (3-5)**	**Company**	
RfbE	239	F	5'- GTGCTTTTGATATTTTTCCGAGTAC- 3'	Alpha DNA USA	(16)
		R	5'-TTTATATCACGAAAACGTGAAATTG-3'		
stx2	255	F	5'-GGCACTGTCTGAAACTGCTCC - 3'		
		R	5'-TCGCCAGTTATCTGACATTCTG - 3'		

The PCR reaction can be performed by adding DNA,2µl of DNA was used as a template, 1 µl of Forward primer, 1 µl of Reversed primer, 16 µl of Deionized nuclease free water and 5 µl of Taq PCR PreMix were added. The total volume of the added components was 25 µl. The conditions for the rfbE and stx2 genes in the PCR reaction were adjusted according to [14-16]. The initial DNA denaturation temperature was 94°C for 5 minutes and the number of cycles was 1. In the DNA denaturation step, the temperature was the same for 30 seconds. In the annealing step, the

temperature was 58°C for 30 seconds. In the extension step, the temperature was 72°C for 1 minute. The number of cycles for the last three steps was all 45 cycles. The final extension step was 72°C for 7 minutes and 1 cycle.

RESULTS AND DISCUSSION

Three hundred samples of meat and milk products were collected from several areas of Baghdad governorate. The number of milk and meat products collected from the Abu Ghraib area was (57), from the Bab al-Muadham area (48), from the Al-Adl neighborhood area (36), from the Al-Shuala area (72), from the Al-Hurriya area (45), and from the Al-Bayaa area (42). Colonies of *E.coli* bacteria which grows on the selective and differential medium, MacConkey agar, Sorbitol MacConkey Agar (SMAC) medium, the colonies of *E. coli O157:H7* appeared small and pale yellow due to their inability to ferment and consume sorbitol. They were also grown on Cefixime Tolerate, Sorbitol MacConkey Agar (CT-SMAC) medium. The diagnostic result showed the growth of 30 *E. coli O157:H7* isolates due to their resistance to this antibiotic, while the remaining isolates gave a negative result. The researchers used these special media, which were designed to diagnose *E.coli H7:O157*, which does not ferment sorbitol, for the bacteria isolated from beef [7-19].

E.coli grew on Chromagar as intense blue colonies, unlike the O157 strain, which grew as purple colonies, as shown in Figure 1 (a,b) below. The results indicated by [20] showed that only 10% of *E. coli* isolates were pathogenic for urinary tract infections, and the bacteria were heterogeneous in the production of hemolysin, thus they were of low virulence. The medium contains peptone, pyruvate, and sorbitol, which allows *E. coli* and its strains to grow rapidly. The medium is highly selective for *E. coli* because it contains tergitol, which inhibits the growth of Gram-positive and some Gram-negative bacteria without affecting the growth of *E. coli* and its strains. Selectivity is further enhanced by the addition of two antibiotics, cefsulodin and vancomycin, which work against *Pseudomonas spp*. and Gram-positive bacteria such as Enterococci. The differentiation between the growing bacterial colonies is due to the chromogenic mixture, which consists of the basic substance 6-chloro-3-indoxyl-β-D-galacto-pyranoside and 5-bromo-4-chloro-3-indoxyl-β-D-glucuronide. The first compound is cleaved by an enzyme produced by intestinal bacteria called β-D-galactosidase, giving the *O157* strain a purple color. The second compound is cleaved by the enzyme β-D-glucuronidase produced by *E. coli*, causing its colonies to appear light blue. Many of the *E. coli* strains possess both enzymes, resulting in their colonies appearing dark blue. The study by [21] also agreed that *E. coli O157* showed purple colonies on Chromagar agar, white colonies with sharp edges on blood agar, and 78% of them showed pink colonies on MacConkey agar.

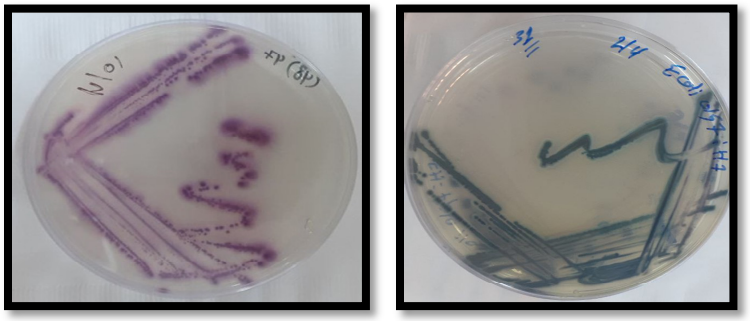

A **B**

Figure 1. A) Growth of *E.coli* O157 strain isolates B) Growth of *E.coli* bacterial isolates

Other bacterial species isolated

Some bacterial species were identified visually based on their cultural characteristics. Some isolates appeared on Sorbitol MacConkey Agar (SMAC) medium (Figure 2), with no colonies of *E. coliO157:H7* on the culture media containing the isolates identified using cultural characteristics. The characteristics of *E.coli O157:H7* were small and pale yellow in color due to their inability to ferment and consume sorbitol, and their number was 30 isolates. For other *E.coli* isolates, the colonies were pink, and the results showed that the number of *E. coli* isolates diagnosed in this medium was 5 isolates. The results also showed the presence of *Klebsiella* bacteria (4 isolates), which were diagnosed in this medium. This is similar to the results of the researcher [22], who showed that the colonies appear pink when cultured. These bacterial isolates were also cultured on Cefixime Tolerate Sorbitol MacConkey Agar (CT-SMAC)

medium, and the diagnostic result was the growth of isolates of the *E. coli O157:H7* strain due to its resistance to this antibiotic, while the rest of the isolates gave a negative result. Many studies have reported similar results to what we found when tested with a medium containing the antibiotic Cefixime, as mentioned by [23], as shown in Table (2) below

Table 2. the number of isolates resulting from meat and milk products

Simple Type	No.isolates	(%)
E.coli O157:H7	30	37.50
E.coli	45	56.25
Klebsiella	5	6.25
Total	80	100

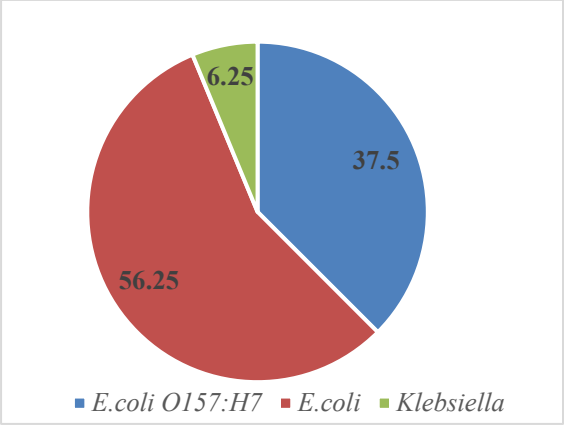

Figure 2. The percentages of bacteria isolated from milk and meat products

the results showed that 30 isolates of *E. coli* O157:H7 were obtained, representing 10% of the total samples, these results suggest that *E. coli O157:H7* is a significant foodborne pathogen in Baghdad governorate. as shown in table 3 below:

Table 3. Number and (%) of Isolation of E. coli O157:H7 from meat and milk products in Baghdad governorate

NO. and (%)of positive isolates		NO. and (%)of negative		The Total	
Number	**(%)**	**Number**	**(%)**	**Number**	**(%)**
30	**10**	**270**	**90**	**300**	**(100)**

The incidence of *E. coli O157:H7* was higher in meat products than in milk products collected, as follows: 22 (73.33%) and 8 (26.67%) respectively, as shown in table 4

Table 4. *E.coli O157:H7* isolation ratio

Sample type	Number	(%)
Milk products	**8**	**26.67**
Meat products	**22**	**73.33**
The total	**30**	**100**

According to sources, the most common bacteria that contaminates milk and meat products is *E. coli*. This is a type of intestinal bacteria that naturally grows in the intestines of humans and other mammals, including cattle [24]. Beef products such as ground beef are a major source of *E. coli* infections [25]. The table below shows the contamination percentage of meat and milk samples collected from different areas of Baghdad. As shown in Table 5.

Table 5. Numbers and Percentage of contamination in collection areas in Baghdad

Collection area	Products type	No.of samples	No.of isolates	(%)
Abi Gharib	Milk products	**36**	**1**	**2.8**
	Meat products	**21**	**3**	**14.3**
Bab Al-Moatham	Milk products	**30**	**1**	**3.3**
	Meat products	**18**	**4**	**22.2**
Al-Adel	Milk products	**16**	**1**	**6.3**
	Meat products	**20**	**5**	**25.0**
Al-Shu'ala	Milk products	**14**	**2**	**14.3**
	Meat products	**58**	**9**	**15.2**
Al-Hurriya,	Milk products	**30**	**2**	**6.7**
	Meat products	**15**	**1**	**6.7**
Baiyaa	Milk products	**24**	**1**	**4.2**
	Meat products	**18**	**0**	**0**
Total o specimens		**300**	**30**	**10.0**

The highest percentages of bacterial contamination with *E. coli* were found in samples collected from Al-Adel district, with 25% for meat and 0% for milk. The highest percentage of contamination was in Al-Shu'ala district, with 14.3% for milk and 2.8% for milk in Abu Ghraib district. It is worth noting that the samples were collected randomly from markets in different areas of Baghdad. The reason for this may be due to the lack of hygiene in the slaughterhouses in these different areas during the slaughter process and the contamination of the carcass with waste and contaminated entrails, as bacteria from contaminated meat can be transferred to meat cutting equipment, thereby contaminating the meat, as mentioned by [26]. As for milk, the poor storage conditions, with varying storage conditions of heat, humidity, and other conditions, can lead to contamination of milk with *E. coli*. Research has concurred with these findings, indicating that contamination is the cause of meat being present in stores for variable lengths of time and in an unfavorable manner, which is consistent with [27].

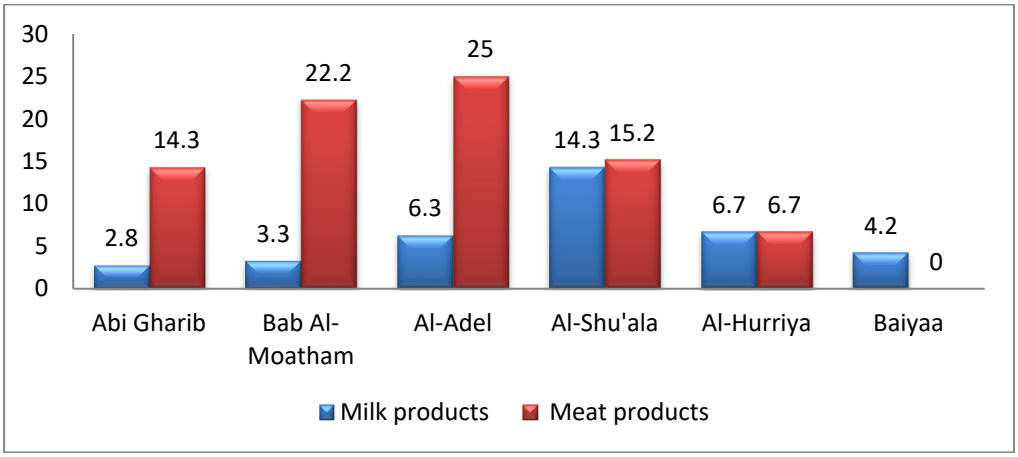

Figure 3 . The percentage of product contamination in the collection areas of Baghdad city.

The Vitek2 system confirmed the results of previous tests and was consistent with them, as 30 of the samples were positive for *E. coli O157:H7* bacteria (98%),as shown in the table (5). The Vitek 2 diagnostic system is one of the accurate methods that rely on the automatic system for the diagnosis of bacterial strains. Two samples of meat and milk products, (one sample of each type), were diagnosed and gave the same results as those obtained in the culture media. The accuracy of the results of this test depends on the age of the bacterial culture, the type of culture medium, the density of the bacterial suspension, and the concentration of the dilution solution. Other researchers have used this accurate system to diagnose *E. coli O157:H7*. This detection was considered a rapid and relatively inexpensive detection, with a high accuracy rate. It has been used by many researchers to detect colon bacteria, where it gave

results similar to those reported in many studies, as mentioned in the study by (28), which stated that 99% of the results were negative for the Sac analysis, as well as for PYrA, while they were 99% positive for GlyA.

The Vitek2 Compact system used also to determine the minimum inhibitory concentration (MIC) for 18 antibiotics. A sample from each product was diagnosed according to the resistance results of *E.coli* 0157 and the use of many antibiotics [18]. The bacteria were resistant to 6 antibiotics (30%), sensitive to 9 antibiotics (45%), and 3 antibiotics (15%) had intermediate sensitivity and required a higher dose to become sensitive to them. The results of the local researcher [28, 29] and the local results of the researcher [30] showed that the percentage of multidrug-resistant bacterial isolates was 100%. The results of the researcher [31] also showed similar results due to the fact that they were diseased isolates. The current research results were close to the results of the researcher [20], which were 21% resistant to antibiotics and 63% sensitive to antibiotics. The main cause of this serious problem is due to the large increase in bacterial resistance to broad-spectrum antibiotics due to the excessive use of these antibiotics. Also, if the isolates are diseased or food, the diseased ones are more resistant than the food ones due to the reasons mentioned earlier [32]**, as shown in table 6.**

Table 6. Minimum inhibitory concentration (MIC) values and percentages of resistance and sensitivity to some antibiotics used against two isolates from milk and meat products using the VITEK-2 device

MIC (µg/ml) P. Meat	MIC (µg/ml) P. Milk	*E. coliO157:H7*						Antibiotic Name
		(%)	R	I	S	Products type	Products type	
>=32	>=16	100	+	--	--	Milk products	Meat products	Ampicillin/Sulbactam
<= 4	<= 2	100	--	--	+	Milk products	Meat products	Piperacillin/Sulbactam
<= 2	<= 4	100	--	--	+	Milk products	Meat products	Cefoxitin
>= 64	>= 64	100	+	--	--	Milk products	Meat products	Cefotaxime
>= 18	>= 16	100	+	--	--	Milk products	Meat products	Ceftazidime/Avibactam
>= 34	>= 32	100	+	--	--	Milk products	Meat products	Ceftolozane/Tazobactam
>= 64	>= 64	100	+	--	--	Milk products	Meat products	Aztreonam
<= 0.5	<=0.25	100	--	--	+	Milk products	Meat products	Doripenem
<=32	<=32	100	+	--	--	Milk products	Meat products	Meropenem/Vaborbactam
<= 1	<= 1	100	--	--	+	Milk products	Meat products	Tobramycin
<=0.12	<= 0.25	100	--	--	+	Milk products	Meat products	Levofloxacin
1	1	100	--	--	+	Milk products	Meat products	Doxycycline
<= 0.5	<= 0.12	100	--	--	+	Milk products	Meat products	Minocycline
<= 1	<= 1	100	--	--	+	Milk products	Meat products	Tetracycline
<= 0.5	<= 0.5	100	--	--	+	Milk products	Meat products	Tigecycline
<=16	<=16	100	--	+	--	Milk products	Meat products	Chloramphenicol
<=16	<=16	100	--	+	--	Milk products	Meat products	Colistin
<=16	<=16	100	--	+	--	Milk products	Meat products	Cefazolin

R: Resistance, S: Sensitive I: Intermediate MIC: Minimum Inhibitor Concentration. Detection of Stx2 and rfbE genes *Stx2* and rfbE genes in 30 bacterial isolates represented the *E.coli* O157:H7. PCR technology is a rapid and easy protocol that is highly sensitive and specific for detecting nucleic acid sequences in the genomes of pathogens, the genes were detected in 5 isolates (two isolates from dairy products and three isolates from meat products) [33-35], as shown in Figures (7) (A) and (B) below, which show the results of the *stx2* and *rfbE* genes. The results of the study for the gene polymerase test showed a discrepancy with the results of other studies, such as the study [36], which mentioned that the size of the *stx2* gene of *E.coli* O157 is 255 bp, and all isolated bacteria were not producing this

gene. As for the rfbE gene, which is produced by bacteria that cause meat poisoning as well as cheeses and produces one of the most dangerous toxins, Shiga-like toxin, its results were comparable to the results obtained from another similar study, where they were similar to the expected size for the same primers that were adopted in the study, and which showed that toxin-producing genes are more common in meat than in dairy products [37]

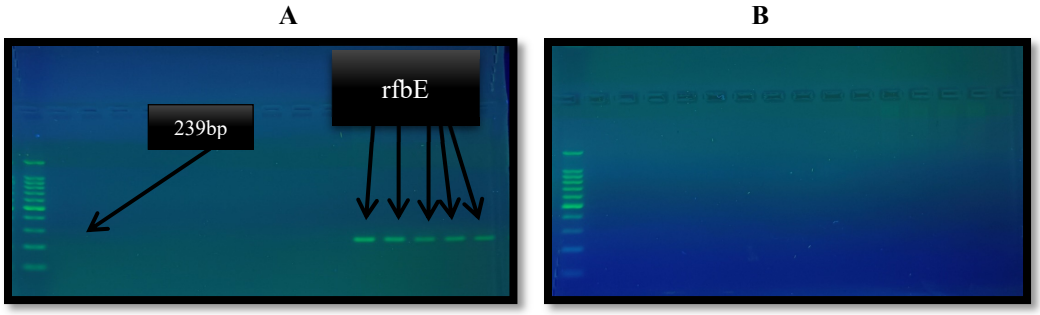

Figure 4. A-Electrophoresis of the product of the polymerase chain reaction (PCR) for the rfbE gene B- rfbE gene , as it appears that the molecular weight Mwt of the bands is (239) base pairs. Agarose was used at a concentration of (1.5%) in the electrophoresis with a potential difference of (70) volts/cm2 for (60) days.

Table 7. The results of PCR products for the Stx2 and rfbE genes

NO.	DNA extracted	stx2 255 bp	rfbE 239 bp
No.of isolates	30	0	5

CONCLUSIONS

The study found that the prevalence of Escherichia coli O157:H7 contamination in meat products was higher than in dairy products. The contamination rate in meat products was 73.33%, while in dairy products it was 26.67%. Escherichia coli O157:H7 bacteria were resistant to a number of antibiotics. The bacteria showed a high ability to form biofilms, with 76.92% of isolates in meat products and 17.65% in dairy products having a high biofilm-forming ability. Five new strains of Escherichia coli O157:H7 were isolated containing the rfbE gene, which encodes Shiga toxin. The phylogenetic tree showed that the five new strains were highly similar (99%) to strains from the UK and Canada, while they were 82% divergent from another Iraqi strain and 84% from strains from the USA and China.

REFERENCES

1. Rusdianto, R., Nuha, U., Wahyuni, D., Supeno, S., & Amaliyah, T. Identification of bacterial diversity in the feces of children with diarrhea. Edubiotik: Jurnal Pendidikan, Biologi dan Terapan, 2022. 7(01), 43-50. DOI: https://doi.org/10.33503/ebio.v7i01.1532
2. Brooks , G. F.; Butel , J. S.;Carroll, K. C. and Morse, S. A. . Jawetz , Melinick , J.L. and Adlebergs Medical Microbiology, 24th ed. A lange medical book. 2007. P.23.
3. Clifford, K., Desai, D., Prazeres Da Costa, C., Meyer, H., Klohe, K., Winkler, A. S., Rahman, T., Islam, T. & Zaman, M. H.. Antimicrobial resistance in livestock and poor quality veterinary medicines. Bull World Health Organ, 2018. 96, 662-64. DOI: 10.2471/BLT.18.209585
4. Gelalcha, Benti D., et al. "Regulation mechanisms of virulence genes in enterohemorrhagic Escherichia coli." Foodborne Pathogens and Disease. 2022. 19.9 .: 598-612. DOI: https://doi.org/10.1089/fpd.2021.0103
5. Sarmikasoglou, E., & Faciola, A. P.. Ruminal bacteria lipopolysaccharides: an immunological and microbial outlook. Journal of Animal Science and Biotechnology, 2022. 13(1), 1-7. DOI: https://doi.org/10.3390/ani11010195.
6. West N.P. Sansonetti P. Mounier J. Optimization of virulence functions through glucosylation of Shigella LPS Science . 2005. 307:1313–1317 DOI: 10.1126/science.1108472

7. Desmarchelier, Patricia M.,. "A PCR specific for Escherichia coli O157 based on the rfb locus encoding O157 lipopolysaccharide." Journal of Clinical Microbiology. 1998. 36.6: 1801-1804. DOI: https://doi.org/10.1128/jcm.36.6.1801-1804.1998
8. Azar Dokht Khosravi, Soheila Khaghani, Ahmad Farajzadeh Sheikh, Ali Ahmadzadeh,and Ahmad Shamsi zadeh. Prevalence of Escherichia coli O157:H7 in Children with Bloody Diarrhea Referring to Abuzar Teaching Hospital, Ahvaz, Iran. Journal of Clinical and Diagnostic Research, 2016. Vol-10(1): DC13-DC15. doi: 10.7860/JCDR/2016/16689.7134
9. Sultana, T., Rabbi, M. F., Sarker, B. R., Islam, M. S., Begum, M. I. A., & Hossain, K. M. M.. Prevalence and Antibiotic Resistance Patters of Escherichia Coli Isolated From Milk and Milk Product. Journal of Bio-Science, 2021. 29(2), 81- 91. DOI:10.3329/jbs.v29i2.54957
10. Weagent, S.D.; Bryant, J.L.; and Jinneman, K.G.. An improved rapidtechnique for isolation Escherichia coli O157:H7 from foods. J. Food prot. 1995. 58:7-12. https://doi.org/10.4315/0362-028X-58.1.7
11. Gouali, M.; Ruckly,C.; Carle,I.; Collin, M.L. and Xavier-weill. Evaluation of CHROMagar STEC and STEC O104 Chromogenic Agar Mediafor Detection of Shiga Toxin-Producing Escherichia coli inStool Specimens. J. Clin. Microbiol, 2013. 51(3): 894-900 DOI: https://doi.org/10.1128/jcm.03121-12
12. Forbes, B. A., Sahm, D. F., & Weissfeld, A. S. Diagnostic microbiology. 2007. (pp. 288-302). St Louis: Mosby
13. Al-Ayash M. A.. Detection of E .coli O157:H7 Bacteria from Raw Cow's Milk and Soft Arab Chesses by Using Molecular and Conventional Methods. Msc thesis, Genetic Engineering andBiotechnology:UniversityofBaghdad.Iraq.2016.DOI: http://dx.doi.org/10.21474/IJAR01/1302
14. Mishra, V., V. L. Nag, R. Tandon, and S. Awsthi. Response surface methodology-based optimisation of agarose gel electrophoresis for screening and electropherotyping of rotavirus. Appl. Biochem. Biotechnol. 2010. 160 (8):2322-2331 https://doi.org/10.1007/s12010-009-8693-x
15. Sambrook, Joseph, Edward F. Fritsch, and Tom Maniatis. Molecular cloning: a laboratory manual. No. Ed. 2. Cold spring harbor laboratory press, 1989. (pp. 28-30). .
16. Fathi, J., Ebrahimi, F., Nazarian, S., & Tarverdizade, Y.. Purification of Shiga-like Toxin from Escherichia coli O157: H7 by a Simple Method. Journal of Applied Biotechnology Reports,2017. 4(4),707-711.
17. https://www.biotechrep.ir/article_67498_44584304332be848d80554e7e8a5e603.pdf
18. Levinson, W.. Review of Medical Microbiology and Immunology. 14thed McGraw-Hill education, Inc. 2016. PP 821.
19. Ahmed, S. T., Jasim, A. N., & Ali, A. M.. Isolation and characterization E. coli O157: H7 from meat &cheese and detection of Stx1, Stx2, hlyA, eaeA by using multiplex PCR. Journal of Biotechnology Research Center, 2011. 5(2), 15-24 DOI: https://doi.org/10.24126/jobrc.2011.5.2.155
20. Ali, R. M., Mohammed, D. H. A., Dhaher, F. H., & Jamil, M. M. Prevalence of E. coli O157: H7 in beef meat products and dairy products sold in Baghdad local markets. iraq journal of market research and consumer protection, 2010. 2(4). https://www.iasj.net/iasj/article/1750
21. Bhattacharyya, S.; Sarfraz, A.; Ansari, M. A. A. and Jaiswal, N.. Characterization and antibiogram of Uropathogenic Escherichia coli from a tertiary care hospital in Eastern India. Int J Curr Microbiol App Sci. 2015. 4(2): 701-705. https://www.ijcmas.com/vol-4-2/Sayan%20Bhattacharyya,%20et%20al.pdf
22. Sharmin, S.; Alamgir, F. Begum, F. and Jaigirdar, K. H.. Use of Chromogenic Agar Media for Identification of Uropathogen. Bangladesh J Med. Microbiol. 2010. 4 (1): 18-23. https://doi.org/10.3329/bjmm.v4i1.8464
23. Brown, A. E. and Smith, H. R. Benson's microbiology Applications, Laboratory Manual in General Microbiology. 14th ed. McGraw-Hill Higher Education. New York. 2017. PP:438.
24. Kafilzadeh, F. and Farsimadan, F. Investigating Multidrug Efflux Pumps in Relation to the Antibiotic Resistance Pattern in Escherichia coli Strains from Patients in Iran. Biomed Res. 2016. 27(4): 1130-1135. https://www.alliedacademies.org/articles/investigating-multidrug-efflux-pumps-in-relation-to-the-antibiotic-resistance-pattern-in-escherichia-coli-strains-from-patients-in.pdf
25. Wilshaw, G.A., Cheasty, T., Smith, H.R. Escherichia coli. In: Lund, B.M., Baird-Parker, T.C., Gould, G.W. (Eds.), The Microbiological Safety and Quality of Food II. Aspen Publishers Inc., Gaithersburg, Maryland, .2000 . pp. 1136-1177.
26. Doyle, M.P., Zhao, T., Meng, J., and Zhao, S. Escherichia coli O157:H7. In : Food Microbiology: Fundamentals and Frontiers, ed. M.P. Doyle, L.R. Beuchat, and T.J. Montville, 1997. pp. 171–191. ASM Press,
27. Shaw, W. G. A.; Smith, H. R.; Roberts, O. Well, J. T.; Cheasty, T. and Rowe, B. Examnation of beef for the presence of vero cytoxin producing Escherichia coli particularly of thoseserotype O157. J. App. Bacteriol. 1993. 75: 420-426 https://doi.org/10.1111/j.1365-2672.1993.tb02797.x

28. Mohammed, Z. A. Isolation and Identification of Escherichia coli O157: H7 from locally minced meat and imported minced and chicken meat: Zuhair. A. Mohammed, Fadia Abd AL-MuhsinAL-Khyat. The Iraqi Journal of Veterinary Medicine, 2008. 32(1), 100-113 DOI: https://doi.org/10.30539/iraqijvm.v32i1.771
29. Dragy, W. A., & Baqer, A. A. Detection of Escherichia coli O157: H7 in Human patients Stool and Food by Using Multiplex PCR Assays Targeting the rfbE and the eaeAGenes compared with Detection by Biochemical Test and Serological Assay. Al-Nahrain Journal of Science,2014. 17(3),124-131DOI:10.22401/JNUS.17.3.17 https://anjs.edu.iq/index.php/anjs/article/view/415/358
30. Ibrahim, I. A.; Al-Shwaikh, R. M. and Ismaeil, M. I. Virulence and Antimicrobial Resistance of Escherichia coli Isolated from Tigris River and Children Diarrhea. Infect Drug Resist. 2014. 7: 317- 322. DOI: 10.2147/IDR.S70684
31. Wadi, K.M., Jasim, K.A., Shaban, A.H., Kamil, M.K., Nsaif, F.K., Journal of Green Engineering, 2020, 10(9), pp. 6052–6062.
32. Mahdi, S.H., Jassim, W.H., Hamad, I.A., Jasima, K. A., Energy Procedia, 2017, 119, pp. 501–506.
33. Al-Obeidi, N. A. H., & al-Kanani, Z. A. H. Isolate and diagnose some types of bacteria from patients with urinary tract and determine their ability to resist antibiotics Life. Journal of Education for Pure Science, 2017. 7(1). https://www.iasj.net/iasj/article/133342.
34. Ali, I. ; Kumar, N. ; Ahmed, S. and Dasti, J. I. Antibiotic Resistance in Uropathogenic E. coli Strains Isolated from Non-Hospitalized Patients in Pakistan. J of Clin and Dia Res. 2014. 8(9): 1-4. doi: 10.7860/JCDR/2014/7881.4813.
35. Gawad W E, Helmy O M , Tawakkol W M and Hashem A M . Antimicrobial Resistance, Biofilm Formation and Phylogenetic Grouping of Uropathogenic Escherichia Coli Isolates In Egypt: The Role Of Efflux Pump-Mediated Resistance. Jundis hapur J Microbiol. 2018. 11(2), 1-7. DOI: https://doi.org/10.5812/jjm.14444.
36. Blanco, P.; Hernando-Amado, S.; Reales-Calderon, J. A.; Corona, F.; Lira, F.; Alcalde-Rico, M.; Bernardini, M.; Sanchez, M. B. and Martinez, J. L. Bacterial Multidrug Efflux Pumps: Much More than Antibiotic Resistance Determinants . Microorganisms. 2016. 4(14):2-19. DOI: 10.3390/microorganisms4010014.
37. Paton, A. W. and Paton, J. C. “Detection and characterization of Shiga toxigenic Escherichia coli by using multiplex PCR assays for stx1, stx2, eaeA, Entero hemorrhagic E. coli hlyA, rfbO111, and rfbO157”. J. Clin. Microbial.; 1998. 36: 598– 602. DOI: 10.1128/JCM.36.2.598-602.1998,

Construction of an Industrial Fiber Optic Sensor Network for Oil Field Management: A Literature Survey

Younis M Hasan [1a], Faisel G. Mohammed [1b], Mohammed Mejbel Salih [2c]

[1] *Department of Remote Sensing and GIS, College of Science, University of Baghdad, Baghdad, Iraq*
[2]*Collage of Civil Engineering, University of Technology, Baghdad, Iraq*

[a] Corresponding author: *Younis.Hasan2209m@sc.uobaghdad.edu.iq*
[b] faisel.mohammed@sc.uobaghdad.edu.iq
[c] 40339@uotechnology.edu.iq

Abstract. This writing audit explores the application and advancement of mechanical fiber optic sensor systems within the administration of oil areas. Much accentuation is put on the improvement of sensor innovation, fundamentally developments that advance checking and operational viability in exceptionally hostile situations. The papers checked on are chosen from among peer-reviewed diaries, licenses, and industry reports crossing the past twenty a long time. Major discoveries demonstrate that fiber optic sensors altogether offer assistance in making real-time information collection more exact and dependable, which is crucial in optimizing generation and keeping operations secure. The paper moreover covers the challenges that exist within the integration of such frameworks and what conceivably lies ahead in terms of future improvement, citing that end of the of fiber optic innovation might hold more versatile and cost-effective choices for the oil and gas industry. This survey will act as a base for engineers, analysts, and policymakers managing with making advance in oil field operations through mechanical progression.

Keywords: Oil, Gas, Fiber optic sensors, Remote Sensing, Data analysis.

INTRODUCTION

This paper presents a basic survey of the inquire about that has been carried out to cultivate the improvement of a mechanical optical fiber sensor organize for the control of oil areas. In so doing, it'll highlight issues that analysts have been confronting and how those issues have been overcome, how the strategies work, how to classify and improve information, conjointly distinguish the most results of these ponders. Observing frameworks inside oil areas nowadays depend on point sensors and either wired or remote advances with impediments in run, information rates, and unwavering quality. A fiber optic sensor arrange may offer real-time observing over the oil field foundation for early blame location and optimization of operations. Differentiated with conventional electrical sensors, which battle with high-pressure, tall temperature, and chemical exposures, fiber optic sensors are impenetrable to EMI and work in such unforgiving situations with a tall degree of exactness [1, 2]. This report too studies progressive progresses in fiber optic sensor innovation that have developed from improvements in fiber optic broadcast communications and optoelectronic gadgets. Among the modern advancements to be made conceivable are the substitution of numerous existing natural sensors and the opening of unused markets where no comparable sensors right now exist. Integration of these advances with propels in optical transducers has moreover permitted inaccessible vibration observing in profoundly localized ranges of electrical apparatus utilizing compact, convenient instrument bundles. This has inalienable electrical separation, prevalent dielectric properties, and insusceptibility to electromagnetic obstructions. More so, fiber optic sensors give a noncontact, disturbance-free strategy of checking, advertising a totally modern strategy for vibration monitoring in electromechanical equipment. Fiber optic sensors are fundamentally partitioned into two categories:
outward sensors detecting happens exterior the fiber; and natural sensors detecting happens inside the fiber itself. They can moreover be classified with their operation standards such as intensity-based sensors (IBSs), Fabry-Perot

Technologies and Materials for Renewable Energy, Environment and Sustainability
AIP Conf. Proc. 3321, 020040-1–020040-8; https://doi.org/10.1063/5.0290587
Published under an exclusive license by AIP Publishing. 978-0-7354-5231-2/$30.00

interferometric (FPIs), and Fiber Bragg gratings (FBGs), each having distinctive implies of detecting from the light property changes [3, 4, 6].

Previous Papers Summary

The point of this survey paper is to look at in detail engineered fiber optic sensors and their application within the handle of oil field administration. It'll offer assistance to get it each piece of investigate work, the values it presents, and the importance of setting up an mechanical optical fiber sensor arrange for oil field administration. The article centers on the most recent logical writing managing with mechanical fiber optic sensors, their part in oil areas, and ways in which information determined from these sensors can be utilized to oversee the oil field successfully. The survey will see at these components in detail to bring out the significance of fiber optic sensors within the oil industry. Such a survey might be profoundly instrumental for researchers and analysts within the field of allergens and petroleum studies. This survey of the writing endeavors too to distinguish the foremost later logical ponders within the field of fiber optic sensors and their administration in oil areas. Particularly, the audit ought to approve the plausibility of the utilization of a fiber optic sensor arrange within the observing of natural impacts on oil pipelines, comprehensive of temperature, weight, and/or development changes [15, 22, 44].
(Jincy; Solomon and Radhakrishna, 2021) As oil and gas (O&G) investigations expand to more profound regions to upgrade oil and gas recuperation, major safety concerns are rising around the world. It is particularly important to screen basic parameters like HPHT and chemicals accessible in genuine time at expanded separations. The utilize of customary electrical sensors is getting to be less and less compelling beneath serious conditions conjointly defenceless to electromagnetic impedances. Progressed sensors, supplanting these ordinary ones, must not as it were offer way better estimation capabilities but too give dependable information to improve oil and gas generation. In expansion, these sensors must be able to distinguish wellbore judgment and security. The deeper-zone particular detecting needs of the O&G industry require longer transmission lengths, moved forward spatial scope, and numerous sensors with multimodal detecting capabilities. Associated with these prerequisites are a few challenges, which incorporate flag weakening, crosstalk, and cross sensitivities. Optical fiber- based sensors are anticipated to give superior detecting capabilities than standard electrical sensors. The display survey work has given wide examination to different sorts of fiber-optic detecting advances and points at finding a potential sensing arrangement for the O&G industry [17, 21, 30].

Alin, Marcelo, Marius et al., 2021 Stream rate observing is an critical estimation in numerous diverse areas, counting biomedical building, chemical building, the nourishment industry, and the oil and gas businesses. We propose a stream meter that's one of a kind in a number of ways since it does not interfere into the liquid stream, has no moving parts, has small plausibility of getting to be clogged, and can work in unforgiving situations. This specific meter depends on optical fiber detecting of temperature conveyances along a liquid conduit. By injecting optical warming within the frame of beats to locally raise the temperature of the liquid, we degree the liquid speed from the rate at which the warm is moved downstream. This strategy has been tentatively illustrated in both water and ethanol, utilizing optical recurrence space reflectometry (OFDR) for millimetric spatial determination along a 1.2-metre-long conduit. It appears that the strategy yields exact, direct reaction information. The strategy can be expanded to degree over lengths expanding a few tens of kilometers by basically moving the mode of cross examination of the optical fiber to time space disseminated detecting. Then again, the procedure can be miniaturized, for case, through the utilize of coordinates optical waveguides, and connected to microfluidic frameworks or, conceivably, open up modern "lab-in-a-fibre" innovations with conceivable biomedical applications[1, 2].
Marianne, Henrique, Jehan and Joaquim, 2018 Usually a logical diary article, distributed in December 2018, by Marianne S. P. e Silva, Henrique P. Alves, Jehan F. do Nascimento, and Joaquim F. Martins-Filho within the "Diary of Microwaves, Optoelectronics and Electromagnetic Applications". The title of the paper is "Effect of Beat Width on the Affectability and Extend of a Raman-based Dispersed Fiber-optic Temperature Sensor", which bargains with the utilitarian flow of a disseminated fiber-optic temperature sensor based on unconstrained Raman scrambling. The investigate utilizes a commercial Optical Time-Domain Reflectometer and a standard Erbium-Doped Fiber Speaker. The affectability and common execution of the sensor beneath diverse setups are examined by utilizing OTDR beats extending from 100 ns to 4000 ns. This paper reports on the trade-off between affectability, determination, and extend accomplished along a 27 km standard single-mode fiber sensor interface. The comes about deliver a full characterization of how the sensor affectability depends on the diverse OTDR beat widths, in this way optimizing the discovery capabilities for both brief and long separations. this paper outlines the rule of the Raman scattering-based sensor utilizing straightforward and reasonable methods, showing hypothetical and test comes about. Affectability and execution measurements of the sensor are sketched out for seven distinctive arrangements related to two specific

detection regions that's at the starting and at the conclusion of the 27 km-long fiber connect the comes about show the sensitivity-resolution-range trade-offs which come to pass in choosing the diverse OTDR beat widths [31, 28, 13].
Maximilian Fisser, 2018 Maximilian Fisser's Ph.D. proposal, submitted to Victoria College of Wellington in 2018, presents the improvement of a exceedingly touchy hydrogen sensor for online wellbeing observing of transformers. The sensor is based on palladium and fiber Bragg gratings and measures hydrogen levels as an sign of the state of wellbeing of a transformer. A few of the notable focuses of the proposition are Setting and Inspiration:
It clarifies how the electrical framework is progressively requested by the rise of electric vehicles and photovoltaic control era which an successful observing framework is required. Additionally, it says that the hydrogen collection within the transformer oil may be a basic pointer of the wellbeing of transformers. Sensor Plan and Advancement:
It portrays in detail the plan and exploratory testing of a unused hydrogen sensor. Its employments palladium, which extends on hydrogen retention, and the development is measured by the FBG. The affectability of the sensor can be balanced by changing the geometry of palladium and strategies of connection, among which are vapor statement and adhesive holding. Tests and comes about:
The sensors were tried beneath distinctive conditions to assess their execution in gas and oil media. Affectability of the sensor, the reaction time of the sensor to diverse hydrogen concentrations, and the impact of temperature were surveyed. Impedances from other gasses like carbon monoxide was too considered. Usage:
It clarifies the viable usage of the sensor. As of now, it is in utilize in a Modern Zealand organize transformer. The proposition advance clarified the troubles within the plan of sensors, the significance of precise location of hydrogen for the appraisal of transformer wellbeing, and how this method might offer assistance to make strides grid stability and upkeep methods [25, 34, 42].
Mohamed J. Ali, Alaa H. Ali, Aseel I. Mahmood, Mohammed A hussien2020 the paper talks around the plan and recreation of a Fiber Bragg Grating-based sensor for noninvasive therapeutic applications. They are designed to distinguish the foremost imperative biomedical parameters, like blood weight and body temperature, utilizing the preferences of the FBG sensor innovation such as tall affectability, compactness, and non-susceptibility to electromagnetic impedances. Key focuses from the archive incorporate:
FBG sensors were planned in arrange to identify a body temperature run from 35°C (hypothermia) to 40°C (hyperthermia) and the blood weight from 40 mmHg (hypotension) to 190 mmHg (hypertension) the usefulness of these sensors was evaluated by making reenactments utilizing program devices such as Opti Grinding and Opti Framework. Comes about have appeared that these sensors have a really tall affectability, with temperature affectability of 13.632 pm/°C and affectability to weight of 15.75 pm/mmHg. Rundown:
This paper clearly shows that the FBG sensors have the potential for non-invasive and persistent checking of the imperative signs utilized for therapeutic diagnostics and persistent care [14, 19, 45].

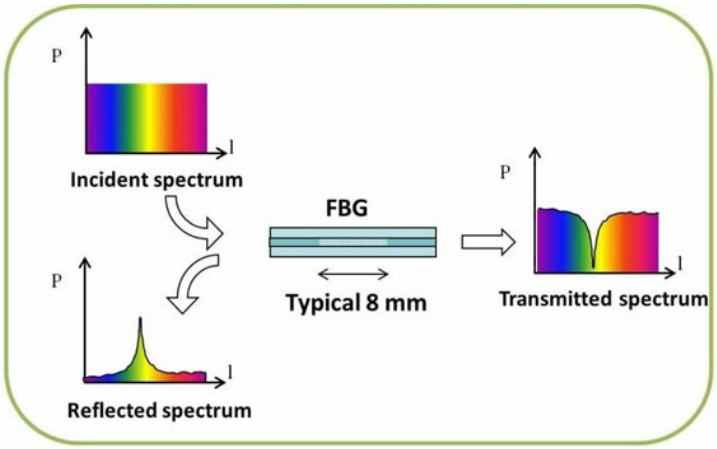

Figure 1. Working principle of FBG

Islam Ashry, Biwei Wang, Frode Hveding, Ahmed Y. Bukhamsin, Tien KheeNg, 2021 Fiber-optic sensors have found applications in a wide run of areas. Their utilization has developed consistently since the 1980s. Conveyed fiber-optic sensors, which degree parameters persistently and in genuine time along the length of an optical Fiber cable, have made critical progresses within the important businesses. The oil and gas industry utilizes the capacity of dispersed fiber-optic sensors to deliver critical estimations all through the whole lifecycle of a well and for the checking of long-distance hydrocarbon pipelines. Here, we survey the application of Rayleigh-based fiber-optic DAS (Conveyed

Acoustic Detecting), Raman-based DTS, and Brillouin-based DTSS (Disseminated Temperature and Strain Detecting) within the oil and gas segment. We clarify the working standards and basic exploratory set-ups of DAS, DTS, and DTSS and highlight their applications within the upstream, midstream, and downstream segments of the industry. We have too created and tried a model crossover DAS-DTS framework in an operational oil well, which measures both vibration and temperature along a MMF. The paper too talks about conceivable challenges that may diminish the development of the disseminated fiber-optic detecting showcase within the petroleum industry and proposes future headings in investigate [3].

Wen-Bo CHEN, Jian-Hua YIN, Jie-Qiong QIN, 2020 An acknowledged original copy for a diary article examines a novel Fiber Bragg Grating-based instrument outlined to degree minor and major outspread strains in a triaxial device. This paper presents comprehensive data on the advancement and approval of this modern gadget, counting its plan, calibration, execution approval, and testing on soil examples. Particular highlights incorporate the taking after:

The gadget highlights two burdens and compass-type components, whereby the discovery of little misshapen Ings made on the soil example is improved for exactness. It utilizes metal strips prepared with FBG sensors as the detecting components, which are more often than not characterized by tall affectability and tall signal-to-noise ratio. The FBG sensors can reflect particular wavelengths of light and let others go through, and the changes in wavelength are a coordinate degree of changes in strain and temperature at the area of the sensor This gadget has been tried beneath inactive and cyclic stacking conditions and has appeared solid execution with precise estimations The calibration and execution approval included tests conducted submerged for exactness beneath assorted natural conditions. The estimation of outspread strain is of paramount significance in triaxial tests, in spite of the fact that gadgets to degree it are rarer compared to those that degree vertical strain. The recently created gadget utilizes two burdens and compass-type components situated on inverse sides of the example to intensify the minor distortions of the example. The metal strips fortified with the FBG sensors are introduced on both closes of the legs of the compass-type component, and the small deformations are intensified to distinguishable levels with an progressed signal-to-noise proportion. Given the temperature affectability of the FBG sensors and the real working conditions, the gadget experienced fastidious submerged calibration. Approval tests conducted on an intaglio triaxial example affirmed that the gadget works dependably and precisely beneath both inactive and cyclic stacking conditions [22] [29].

Yue Qin, Qiankun Wang, Dongsheng Xu*, Jiaming Yan, Shanshan Zhang2022 A unused fiber Bragg grinding (FBG) sensor, employing a three-dimensional (3D) intertwined testimony modelling (FDM) method, is displayed for effective push estimation in soil masses. This sensor incorporates a three-diaphragm structure and is formulated for measuring both soil and water weights at the same time. The striking highlights of this transducer are its little measure, tall affectability, low-cost, electromagnetic immunity, and quick prototyping. The fundamental standards of operation and plan points of interest of such a transducer are portrayed. In expansion, the forms for manufacturing the transducer are clarified. [34] [36].

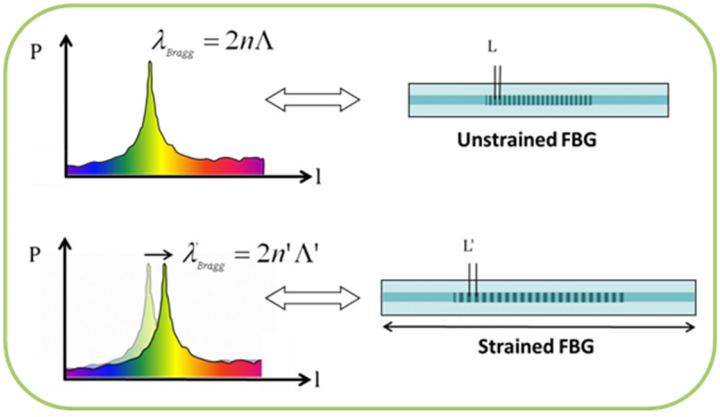

Figure 2. FBG response as function of strain.

Paul Gerard Edmond Lumens, 2014 This extends, at Technische Universiteit Eindhoven, centered on the improvement and arrangement of fiber-optic detecting innovations in oil and gas wells. A rundown of the benefits of utilizing fiber-optic sensors in checking wells and supplies incorporates the truth that they work inactively, are fetched viable, and offer the potential to convey thick, disseminated estimations along the length of the fiber. The thesis, composed by Paul Gerard Edmond Lumens, is committed to utilizing equipment based on both fiber Bragg gratings and Rayleigh

scrambling methods for information change from sensors into significant experiences implied to optimize oil and gas generation proficiency, security, and by and large recuperation. These innovations are examined in terms of their capacity to outlive beneath extraordinary conditions that win in oil and gas wells, such as temperature, weight, and destructive environment. The paper incorporates points of interest on the advancement of modern cross examination gadgets for these sensors and their field approval. The expounded proposition is based on two essential fiber-optic detecting strategies:
fiber Bragg gratings and Rayleigh diffusing. FBGs are point sensors along the length of a fiber-optic cable, measuring distinctive physical marvels such as temperature and weight. They are known for their precision and unwavering quality beneath unforgiving conditions. Rayleigh scrambling is connected in Dispersed Acoustic Detecting, analyzing backscattered signals from fiber-optic cables to screen acoustic exercises such as the development of liquids or the spread of breaks inside a well. The real-time checking capability that's advertised will, in this manner, give the vital security and upgrade operational effectiveness. His investigate at Lumens incorporates the advancement, calibration, and testing of these detecting innovations. The case ponders he presents, and the field trials, outline how fiber-optic sensors can offer nitty gritty, ceaseless, and real-time data along the whole span of oil and gas wells. This information is basic to optimize generation strategies, boost recuperation rates, and guarantee oil and gas extraction. This proposition underlines the need to make these innovations a portion of customary operational strategies and clarifies the troubles and procedures for their field arrangement. The ponder will offer assistance grow the frontiers of geotechnical observing, having far-reaching repercussions for end of the of the extractive asset businesses, because it advances more compelling and more secure implies of extraction [4].

Figure 3. fiber optic sensor system applied to oil and gas wells.

The fiber optic cables mounted on a complicated setup of an oil well, applying fiber Bragg gratings and Rayleigh scattering technologies. The visual exhibits the rugged and industrial environment that is characteristic of oil and gas extraction operations.

LITERATURE SURVEY RESULTS AND DISCUSSION

The paper titled "Development of a Mechanical Fiber Optic Sensor Arrange for Oil Field Administration: A Writing Overview" gives a comprehensive investigation of the advance, deterrents, and future bearings of fiber optic sensor systems within the setting of oil field management. Here could be a brief outline of its discoveries and Observing and Effectiveness: Fiber optic sensors give much more prominent precision and unwavering quality of real-time data gathering in cruel oil field situations. Fiber optic sensors play a really vital part in optimizing generation, moving forward security, and lessening operation dangers. Progressions in Innovation: Advancement of fiber optic sensors in terms of affectability, strength, and integration capability got to be competent of working in extraordinary conditions such as tall weight, temperature, and chemical presentation. Methods created incorporate Dispersed Acoustic Detecting, Dispersed Temperature Detecting, and Disseminated Temperature and Strain Detecting, which are giving vital subsurface data. Integration Issues: A few issues of joining fiber optic sensors into existing frameworks incorporate flag misfortune, crosstalk, and advanced information investigation instruments to handle the gigantic sum of information created. Fetched Effectiveness: In spite of the fact that generally costly at first, fiber optic sensor systems offer long-term budgetary benefits due to decreased support needs and made strides operational effectiveness. These viewpoints position them as cost-efficient for oil field administration. Future Work: Progressing investigate and

advancement in fiber optic innovation might result in cost-effective and more adaptable arrangements. The potential headings for improvement are joining different detecting innovations with distinctive data analysis techniques and sensor solidness. Discourse Innovation Integration: The marriage of fiber optic sensors with other innovations, such as inaccessible detecting and GIS, can offer all-encompassing observing arrangements competent of giving real-time, high-resolution data for oil field operations decision-making. Information Administration: So much information is created by fiber optic systems, which must have solid information administration and investigation frameworks for preparing. Headway of calculations and execution of machine learning will empower the capacity to realize from such information noteworthy experiences to progress operation efficiencies and security. Natural Thought: Fiber optic sensors permit for natural preservation through the early discovery of spills and dangers that cause natural hurt and empower adherence to legitimate prerequisites. Mechanical Collaboration: Industry players, colleges, and innovation engineers must work together to discover arrangements to existing issues and realize the complete potential of fiber optic sensor innovation through joint inquire about and information sharing. Arrangement and Administrative Alterations: Fiber optic sensor systems for the purposes of oil field administration may require changes to industry benchmarks and directions to guarantee that they are secure and can be utilized viably. This abstract summarizes the focuses within the paper with respect to the advancement and current improvements related to the utilize of fiber optic sensors in compelling oil field administration.

CONCLUSION

The audit concludes that fiber optic sensors have imperative preferences compared to customary sensors within the cruel conditions of oil areas. These sensors are competent of conveying real-time, exact information that can be utilized within the optimization of operations in an oil field and indeed improving security. Other than, assist investigate and advancement are required in arrange to overcome existing issues and upgrade the usefulness of fiber optic sensor networks. Moreover, the investigation of past works displayed within the surveyed paper talks for the pertinence and viability of fiber optic sensors in oil field administration and in numerous other businesses. Intensely contributed to compiling and surveying existent investigate, which might donate a great stage for the proposed inquire about.

REFERENCES

1. Mohammed, M.A., T.A. Naji, and H.M. Abduljabbar, The effect of the activation functions on the classification accuracy of satellite image by artificial neural network. Energy procedia, 2019. 157: p. 164-170.
2. Mohammed, M.A., et al., Effect of Thermal Neutron Radiation Dose on Density of Local and Extended Energy States in Se55S20Sb15Sn10 Alloy. Iraqi Journal of Applied Physics, 2024. 20(2B): p. 393-398.
3. Mohammed, A.M., et al., A Comprehensive Literature Survey on Mineral Exploration Techniques Using Remote Sensing and GIS. Journal of Physics: CS (JPCS), 2024.
4. Alsajjad, A.Z.Y., M.A. Mohammed, and K.A. Jasim. Preparation of Ge− Se− Sb ternary alloys and study of the effect of antimony on electrical properties, extended and localized energy states. in AIP Conference Proceedings. 2023. AIP Publishing.
5. Lehmkoster, J., & Schroder, T., 2014 Oil and gas from the sea. Hamburg, Germany: World Ocean Review; Maribus gGmbH,.
6. Algeroy, J., Lovell, J., Tirado, G., Meyyappan, R., Brown, G., Greenaway, R., Carney, M., Meyer, J.H., Davies, J.E., & Pinzon, I.D., 2010 Permanent monitoring: Taking it to the reservoir. Oilfield Review, , 22, 34-41.
7. Zhang, Y., Xiao, L., Fu, J., Chen, H., & Zhao, X., 2005. The perspective of the permanent monitoring with an FBG sensor network in oil and gas production in China. International Society for Optical Engineering, , 6041, 60410X. [CrossRef]
8. Xu, X.-H., Peng, G., Liu, X.-F., Shao, Y.-L., Xiao-Hong, X., Gang, P., Xue-Feng, L., & Yan-Lin, S., 2012. Oil and gas exploration information integration management plan based on GIS technology. Proceedings of the Fourth International Conference on Computational and Information Sciences, Chongqing, China, 17-19 August 2012, 526-529. [CrossRef]
9. Akhondi, M.R., Talevski, A., Carlsen, S., & Petersen, S., 2010. Applications of wireless sensor networks in the oil, gas and resources industries. Advances in Information Networking and Applications, , 941-948.
10. Stalford, H., & Ahmed, R., 2014. Intelligent Casing-Intelligent Formation (ICIF) Design. Proceedings of the Offshore Technology Conference, Houston, TX, USA, 5-8 May [CrossRef]

11. Zhang, Y.Z., Xiao, L.Z., & Wang, J.Y., 2007. Oil well real-time monitoring with downhole permanent FBG sensor network. Proceedings of the 2007 IEEE International Conference on Control and Automation, Seoul, Korea, , 2591-2594.
12. Makhlouf, A.S.H., & Aliofkhazraei, M. (Eds.), 2015. Handbook of Materials Failure Analysis with Case Studies from the Oil and Gas Industries. Oxford, UK: Butterworth-Heinemann,
13. Gysling, D., & Bostick, F., 2002. Changing paradigms in oil and gas reservoir monitoring—The introduction and commercialization of in-well optical sensing systems. Proceedings of the 2002 15th Optical Fiber Sensors Conference, Portland, OR, USA, 6-10 May [CrossRef]
14. Meehan, N., 2012.Reservoir Monitoring Handbook. Contoocook, NH, USA: Elsevier Science & Technology Books,
15. Jones, F.E., 1988.Techniques and Topics in Flow Measurement. Boca Raton, FL, USA: CRC, 1995.
16. Cheremisinoff, N.P., Flow Measurement for Engineers and Scientists. New York, NY, USA: Marcel Dekker,
17. Collins, J., & Lee, A.P., 2013.Flow Rate Measurements, Methods. In Encyclopedia of Microfluidics and Nanofluidics. Boston, MA, USA: Springer,
18. Rasmussen, A., & Zaghloul, M.E., In the flow with MEMS. IEEE Circuits Devices Magazine, 1998, 14, 12-25. [CrossRef]
19. Kuo, J.T.W., Yu, L., & Meng, E., 2012 Micromachined Thermal Flow Sensors—A Review. Micromachines, , 3, 550-573. [CrossRef]
20. Oda, S., Anzai, M., Uematsu, S., & Watanabe, K., A 2003. silicon micromachined flow sensor using thermopiles for heat transfer measurements. IEEE Transactions on Instrumentation and Measurement, , 52, 1155-1159. [CrossRef]
21. Frazão, O., Caldas, P., Araújo, F.M., Ferreira, L.A., & Santos, J.L., 1976. Optical flowmeter using a modal interferometer based on a single nonadiabatic fiber taper. Optics Letters, 2007, 32, 1974-. [CrossRef] [PubMed]
22. Byrne, G.D., James, S.W., & Tatam, R.P., 2001.A Bragg grating based fibre optic reference beam laser Doppler anemometer. Measurement Science and Technology, , 12, 909-913.
23. Huang, C.Y., Chan, P.W., Chang, H.Y., & Liu, W.F., 2018. A Fiber Bragg Grating-Based Anemometer. Sensors, , 18, 2213. [CrossRef] [PubMed]
24. Dong, X., Zhou, Y., Zhou, W., Cheng, J., & Su, Z., 2012. Compact Anemometer Using Silver-Coated Fiber Bragg Grating. IEEE Photonics Journal, , 4, 1381-1386. [CrossRef]
25. Bolognini, G., & Hartog, A., 2013. Raman-Based Fiber Sensors: Trends and Applications. Optical Fiber Technology, , 19(6), 678-688.
26. Udd, E., & Spillman Jr, W.B., 2011. Fiber Optic Sensors: An Introduction for Engineers and Scientists. John Wiley & Sons,.
27. Jonghan, P., et al., 2006. Raman-based distributed temperature sensor with simplex coding and link optimization. IEEE Photonics Technology Letters, , 18(17), 1879-1881.
28. Haus, J., Optical Sensors: Basics and Applications. Wiley Online Library, John Wiley & Sons, 2010.
29. Bassan, F., et al., 2015.Raman-Based Distributed Temperature Sensor Using Simplex Code and Gain Controlled EDFA. In 24th International Conference on Optical Fiber Sensors,
30. Bolognini, G., Park, J., Kim, P., Lee, D., Di Pasquale, F., & Park, N., 2006. Performance Enhancement of Raman-Based Distributed Temperature Sensors Using Simplex Codes. In IEEE Optical Fiber Communication Conference and the 2006 National Fiber Optic Engineers Conference, OFC, 3.
31. Soto, M., et al., 2007. Distributed Temperature Sensor System Based on Raman Scattering Using Correlation-Codes. Electronics Letters, , 43(16), 862-864.
32. Baronti, F., et al., SNR Enhancement of Raman-Based Long-Range Distributed Temperature Sensors Using Cyclic Simplex Codes. Electronics Letters, 2010, 46(17), 1221-1223.
33. Tanner, M., Dyer, S., Baek, B., Hadfield, R., & Nam, S.W., 2011. High-Resolution Single-Mode Fiber-Optic Distributed Raman Sensor for Absolute Temperature Measurement Using Superconducting Nanowire Single-Photon Detectors. Applied Physics Letters, , 99(20), 201110.
34. Bolognini, G., Park, J., Soto, M., Park, N., & Di Pasquale, F., 2007. Analysis of Distributed Temperature Sensing Based on Raman Scattering Using OTDR Coding and Discrete Raman Amplification. Measurement Science and Technology, , 18(10), 3211.
35. BP., Energy consumption worldwide from 2000 to 2018, with a forecast until 2050. [Online]. Available: https://www.statista.com/statistics/222066/projected-globalenergyconsumption-by-source/
36. Inkpen, A., & Moffett, M.H., 2011. The global oil & gas industry: Management, strategy and finance. PennWell Books, LLC
37. Bentham, J., The scenario approach to possible futures for oil and natural gas. Energy Policy, 2014, 64, 87-92.

38. Saleh, T.A., & AL-Hammadi, S.A., 2018. Insights into the fundamentals and principles of the oil and gas industry: The impact of nanotechnology. In Nanotechnology in Oil and Gas Industries (pp. 1-35). Springer
39. Fanchi, J.R., & Christiansen, R.L., 2016. Introduction to petroleum engineering. John Wiley & Sons,
40. Hartog, A., Frignet, B., Mackie, D., & Clark, M., 2014. Vertical seismic optical profiling on wireline logging cable. Geophysical Prospecting, , 62(4), 693-70.
41. Constantinou, A., Farahani, A., Cuny, T., & Hartog, A., Improving DAS acquisition by real-time monitoring of wireline cable coupling. 2016 SEG International Exposition and Annual Meeting. OnePetro, 2016.
42. Veil, J.A., Puder, M.G., Elcock, D., & Redweik Jr, R.J., 2004. A white paper describing produced water from production of crude oil, natural gas, and coal bed methane. Argonne National Lab., IL (US),
43. Goodwin, R.W., Williams, J.R., & Leung, J.Y., 2014. The Current and Future Outlook for Hydraulic Fracturing in the United States. Journal of Petroleum Technology, , 66(12), 28-33.
44. Mohammed F G, Ali M H, Mohammed S G and Saeed H S 2021 "Forest Change Detection in Mosul Province using RS and GIS Techniques" Iraqi Journal of Science 3779-89.
45. Alatta H J, George L E, Behadili S F, Sayyid B H and Ali M H 2023 Geospatial Data Analysis of School Distribution in Baghdad City Iraqi Journal of Science 6675-85

Modern Technology for Encrypting Video Conversations

Baydaa Jaffer Al-Khafaji [1, a)], Abdul Monem S. Rahma [2, b)]

[1] *Iraqi Commission for Computers and Informatics, Informatics institute for postgraduate studies, Baghdad, Iraq*
[2] *Computer Science Department, Al-Maarif University College, Baghdad, Iraq*

Corresponding author: [a] Baydaa.j.s@ihcoedu.uobaghdad.edu.iq
[b] Monem.rahma@uoa.edu.iq

Abstract. Virtual meetings encryption is a very complex task as it requires a reliable encryption algorithm that should work efficiently on two different media types of video and audio. the algorithm needs to be complex enough to prevent attacks, it needs to be fast in order that the stream stays in real-time. During the last decade, video conferencing was widely used, and last year this problem becomes of particular interest due to the increased demand for virtual meetings. This paper proposes a secure system that targets encrypting the virtual meeting channels. For a video meet application in a conference room, want to consider a few factors when selecting a video compression technique. Implementing the system within the constraints of GF (2^8) and using inverted matrices has significantly enhanced the speed and complexity of the encryption process, making it viable for real-time applications without sacrificing security. The results underscore the efficacy of using parallel processing in reducing encryption times which is critical for real-time video encryption applications. The improved method not only accelerated the encryption process but also maintained high standards of video quality and integrity.

Keywords: video, AES, RSA, S-Box, HMAC, GF (2^8).

INTRODUCTION

Video is a series of images, or frames per second, that are displayed at a particular speed to provide the impression of movement. Every frame is a static image, much to the same extent as a picture which records a solitary point in time. When the frames are played consecutively at a sufficiently fast rate, they give the impression of movement [1]. Video can be captured using a variety of devices, such as digital cameras, camcorders, and smartphones. The video is captured as a series of frames, usually at a rate of 24, 30, or 60 frames per second (fps). The frame rate determines how smooth the video appears. Increased frames per second lead to enhanced movement fluidity, albeit necessitating greater storage capacity as well as processing capabilities [2,3]. Digital video refers to the scenario in which the initial image is created in the recording device as a collection of bytes. Upon perusing this, we may instinctively perceive that an image generated in this manner is of lesser quality compared to an analogue image. Analogue images possess seemingly limitless resolution, while digital images possess a fixed and finite resolution that cannot be enhanced without sacrificing image quality. However, in reality, the great level of detail of analogue images does not provide a benefit, as we typically watch them on a television screen or computer screen with a specific and unchanging resolution[4,5].There are several types of video compression techniques, including MPEG (Moving Picture Experts Group): MPEG is one of the most widely used video compression standards, and it includes several subtypes, such as MPEG-1, MPEG-2, MPEG- and MPEG-7. MPEG uses inter-frame prediction, which means that each frame is compressed based on the differences between it and the previous frame [6,7]. H.264/AVC (Advanced Video Coding) is a contemporary video encoding standard extensively employed in video with a high resolution. The compression of video data is achieved through the utilization of remainder. HEVC/H.265(High Efficiency Video Coding) is a more recent compressed video technology that provides superior reduction rates compared to H.264. It employs a more sophisticated compression technique and has the capability to decrease file sizes by up to 50% in comparison to H.264 [8]. VP9 is an open-source video compression standard developed by Google. It uses intra-frame and inter-frame prediction, and itis designed to provide high-quality video at low bitrates.AV1 is a newer open-source video compression standard that is designed to offer better compression rates than H.265. It uses a more advanced compression algorithm and can achieve a 30% reduction in file sizes compared to H.265[9]. For a video meet application in a conference room, want to consider a few factors when selecting a video compression technique. These factors include, Bandwidth Video meet applications require real-time streaming of video data, which can put a strain on

Technologies and Materials for Renewable Energy, Environment and Sustainability
AIP Conf. Proc. 3321, 020041-1–020041-8; https://doi.org/10.1063/5.0289625
Published under an exclusive license by AIP Publishing. 978-0-7354-5231-2/$30.00

bandwidth. You will want to select a compression technique that can deliver high-quality video at low bitrates to minimize the impact on network bandwidth [10]. Latency In a conference room setting, low latency is important for ensuring smooth communication between participants. select a compression technique that can deliver low-latency video data to minimize delays in the video stream [11]. Quality The video quality of the meet application is important for ensuring that participants can clearly see and communicate with each other. select a compression technique that can deliver high-quality video without introducing too much noise or distortion [12]. Given these factors, H.264/AVC or H.265/HEVC would be good choices for a video meet application in a conference room. Both of these compression techniques are widely used and offer good compression rates and video quality. They also support low-latency video encoding and decoding, which is important for real-time communication [13,14]. The Advanced Encryption Standard, also known as the AES, is widely regarded as a fundamental component of contemporary cybersecurity due to its exceptional combination of safety and efficacy [15]. AES demonstrates exceptional flexibility in meeting various security needs by utilizing stable block dimensions of 128 bits and supporting lengths for keys of 128, 192, or 256 bits. The AES algorithm utilizes a carefully designed functional framework consisting of four main changes: Sub Bytes, Shift Rows, Mix Columns, and Add Round Key. The Sub Bytes operation is a non-linear substitution step that changes every bit in the current block by utilizing an alternative list. (S-box), with the mathematical transformation $S(b) = A \times b^{-1} + C$ exemplifying its intricate nature. Here, A and C denote constants, while b^{-1} represents the multiplicative inverse of the byte within the finite field $GF(2^8)$ [16]. The use of asymmetric encryption, or public-key cryptography, is a cryptographic method that involves using two keys, one of which is a public key for encrypting data and a personal key for decrypting it. In contrast to symmetrical encryption, a common key can be openly shared with no loss of safety, as only the associated personal key, usually remains confidential, can decipher the information [17]. This method enhances Enhancing privacy by obviating the necessity of sharing a solitary secret code among multiple participants. Two widely used asymmetric encryption methods are the (RSA) algorithm and the (ECC). Asymmetric encryption is particularly useful for secure key exchange, digital signatures, and authentication processes, where ensuring the identity of the parties involved and the integrity of the information is crucial. However, asymmetric encryption This type of encryption is typically quicker and requires a greater number of computers compared to symmetrical encryption, which makes it a poor choice for encoding huge amounts of data. Amounts of data. Instead, it is often used in conjunction with symmetric encryption to balance security and performance [18]. The Rivest–Shamir–Adleman (RSA) algorithm stands as a cornerstone of modern asymmetric encryption, serving as a linchpin in securing data transmission and managing cryptographic keys. Unlike symmetric algorithms such as AES, RSA operates on A set of resources consists of a common key, which is used for encoding, & a personal key, which is used for decoding. The implementation of that dual-key method adds a vital level of protection., allowing for the distribution of encryption keys without compromising the integrity of the decryption process.[19]. This capability is especially vital in scenarios where secure key exchange is paramount, safeguarding sensitive information from unauthorized access. Grounded in the principles of number theory, RSA relies on the formidable challenge of factoring large integers to uphold its security guarantees [20], Cryptographic key management includes generating, distributing, storing, using, and replacing keys; it is one of the most critical components of encryption as it is directly responsible for the safety of information. Indeed, the most important concern regarding key management is the need to keep the keys secure, as they are the secrets used to encrypt/decrypt the data [21,22]. For instance, should the keys be easily accessible due to improper generation practices or insecure storage, the information may be accessed by malicious actors. Subsequently, if the confidentiality of information is compromised, other defining features of secure systems become irrelevant due to the fact that the result of the encryption process can be seen by unwanted viewers [23,24].

METHODOLOGY

The paper aims to design System outlines a secure method for video encryption and decryption using a combination of RSA and AES encryption algorithms, coupled with HMAC for integrity verification. This methodology is suitable for a paper on secure video transmission and involves several key steps in both the sender's and receiver's actions. The aforementioned is a hybrid encryption system that integrates the strengths of two predominant cryptographic algorithms RSA and AES along with HMAC for integrity checks. This model is designed to address the pressing needs for secure video transmission over potentially insecure networks, especially in scenarios where real-time performance and data integrity are paramount. Below, we delve into the rationale behind selecting these components and the synergistic benefits they provide in securing video communications. RSA is utilized primarily for its capability in secure key distribution, which is critical in the public-key infrastructure (PKI). In our model, RSA encrypts the AES keys, ensuring that only the intended receiver can decrypt them with their corresponding private RSA key. This setup effectively prevents unauthorized access to the AES keys during Transmisiones is renowned for its efficiency and speed, which are essential for real-time video encryption. Unlike RSA, AES can quickly encrypt and decrypt large volumes of data with minimal performance overhead, making it ideal for streaming high-definition video without lag. Figure 1.

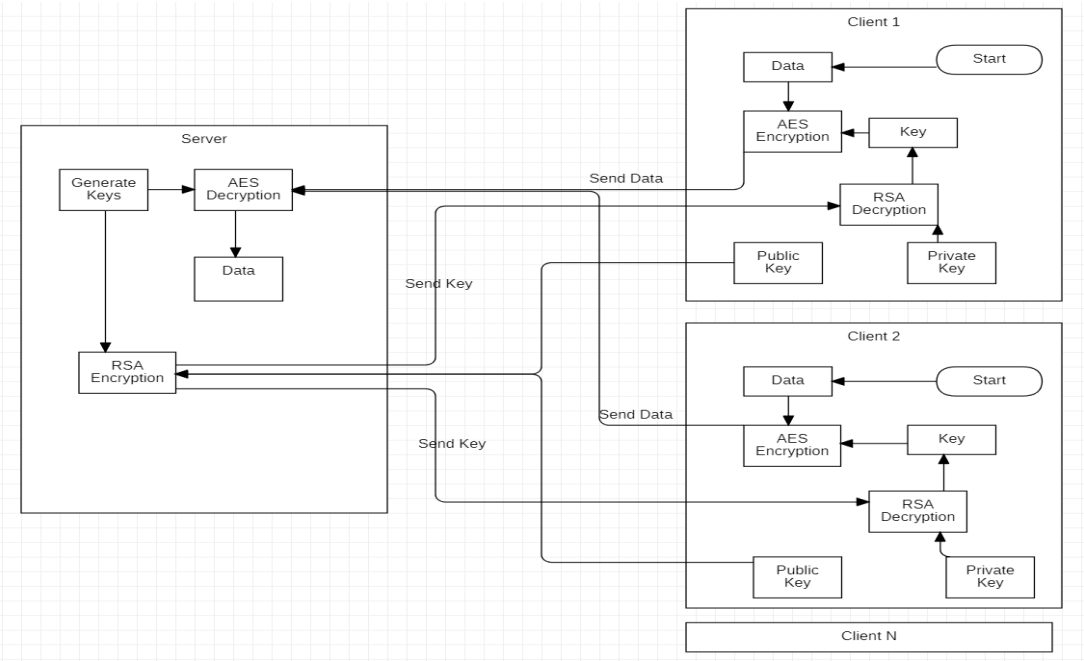

Figure 1. proposal system for secure meeting

RESULT AND DISCUSSION

In the contemporary landscape of digital communication, encryption plays a pivotal role in securing data transmissions, particularly in video communications used in virtual conferencing, telemedicine and online education. This section presents comprehensive comparison of two encryption methodologies. implemented to enhance the security of video data. Our objective is to thoroughly assess the impact of these methods on encryption time, video integrity, and computational efficiency. To rigorously evaluate the encryption schemes, we employed both an original AES-GCM encryption method and an improved method leveraging parallel processing. The assessment criteria were primarily focused on:

Encryption Time Efficiency: Measuring the time taken to encrypt the entire video file.

Video Data Integrity: Assessing the fidelity of video content post-decryption by analyzing frames for color distribution and brightness variations. Computational Resource Utilization: Observing the CPU and memory utilization during the encryption process, providing insights into the scalability of each method.

The experiment involved encrypting a 15-second video, consisting of 450 frames, at a frame rate of 30 FPS. The video featured varied color profiles and brightness levels to comprehensively test the encryption's impact on data integrity. The experiment involved encrypting a 15-second video, consisting of 450 frames, at a frame rate of 30 FPS. The video featured varied color profiles and brightness levels to comprehensively test the encryption's impact on data integrity.

Two encryption schemes were compared: Original Method: Utilizing a single-threaded AES-GCM encryption Improved Method: Implementing a multi-threaded approach where the video data was divided into four segments, each encrypted concurrently. Encryption Time The original encryption method recorded a time of 0.01849 seconds to encrypt the video. The improved method significantly reduced the encryption time to 0.00787 seconds, indicating a performance improvement of 57%. Figure 2.

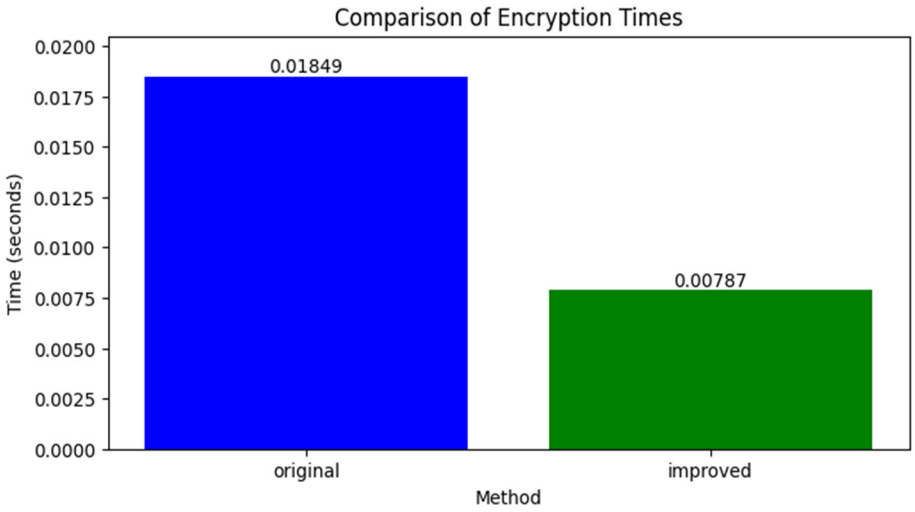

Figure 2. Comparison of Encryption Times

The bar chart, titled "Comparison of Encryption Times," visually represents the performance of two encryption methodologies: the original and the improved. The original method is depicted with a blue bar, showing an encryption time of 0.01849 seconds, while the improved method is represented by a green bar, which demonstrates a reduced encryption time of 0.00787 seconds.

This graphic effectively highlights the efficiency gains achieved with the improved method, showing a 57% reduction in encryption time compared to the original. The chart serves as a clear and concise presentation of comparative performance data, essential for evaluating the effectiveness of enhancements made to the encryption process. Video Metrics Analysis, the analysis confirmed no loss in the total frames and frame rate, indicating that the encryption did not introduce any temporal distortions or frame drops. The uniform frame rate ensured that the encryption process was smooth and did not affect the playback quality. Color Distribution and Brightness Detailed histograms for frames 50, 150, and 300 showed consistent color integrity across all RGB channels, confirming that the encryption and decryption processes did not alter the visual content.

Brightness analysis revealed a slight increase in luminance across the frames, suggesting minimal impact on the video's exposure and contrast settings during encryption. Frame 50: This histogram illustrates a pronounced peak at the lower end of the pixel intensity range, particularly visible in the red channel. This suggests a predominance of darker values in this frame, which is consistent with the unaltered state of a video containing shadows or nighttime scenes. Figure 3.

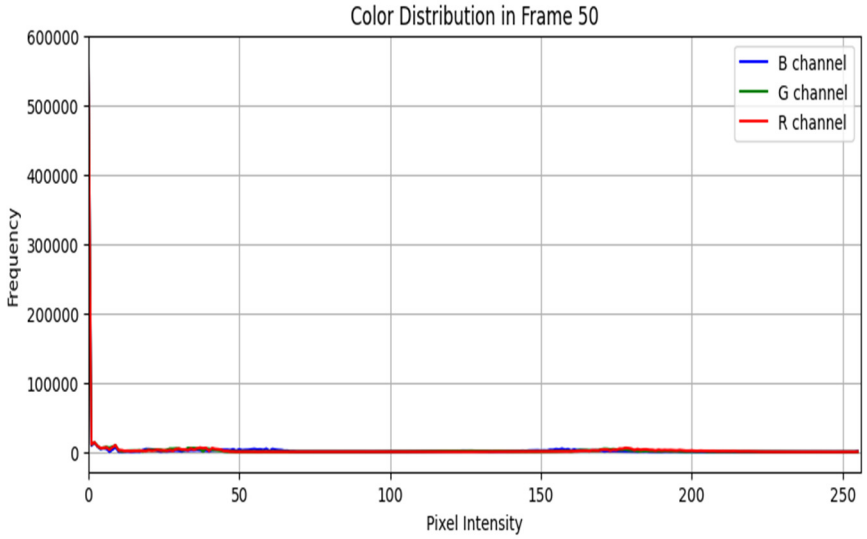

Figure 3. Color distribution in frame 50

Frame 150: The color distribution in this frame shows a more spread-out intensity across the spectrum with notable peaks in the lower intensities for all channels. This distribution can indicate a frame with a more balanced mix of light and dark areas, illustrating the encryption's ability to handle varied visual content without bias. Figure 4.

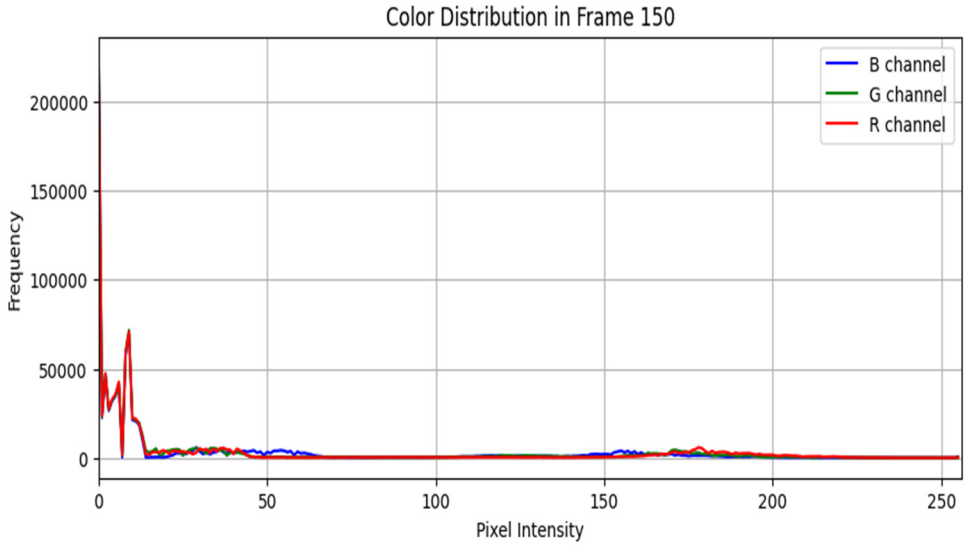

Figure 4. Color distribution in frame 150

Frame 300: Similar to Frame 150, this histogram also displays balanced intensity distribution but with fewer spikes in higher intensities. The relatively flat line across the higher pixel values suggests minimal presence of very bright or washed-out areas, aligning with a consistent visual output post-decryption. Figure 5.

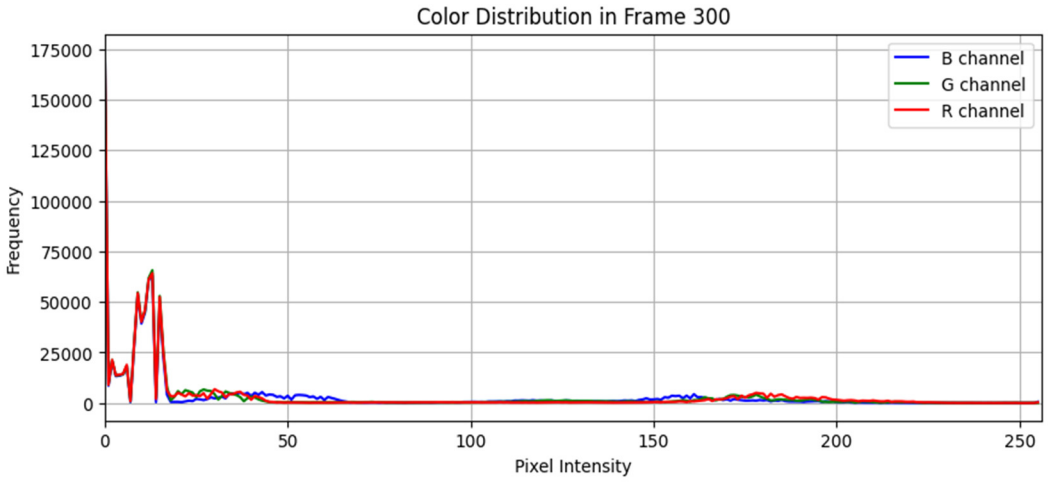

Figure 5. Color distribution in frame 300

The color distribution histograms for Frames 50, 150, and 300 from the encrypted video provide empirical data on the fidelity of the video content through the encryption and decryption processes. Analyzing the RGB channels in these histograms demonstrates how the encryption algorithm preserves the integrity of visual data across different segments of the video. Figure 6.

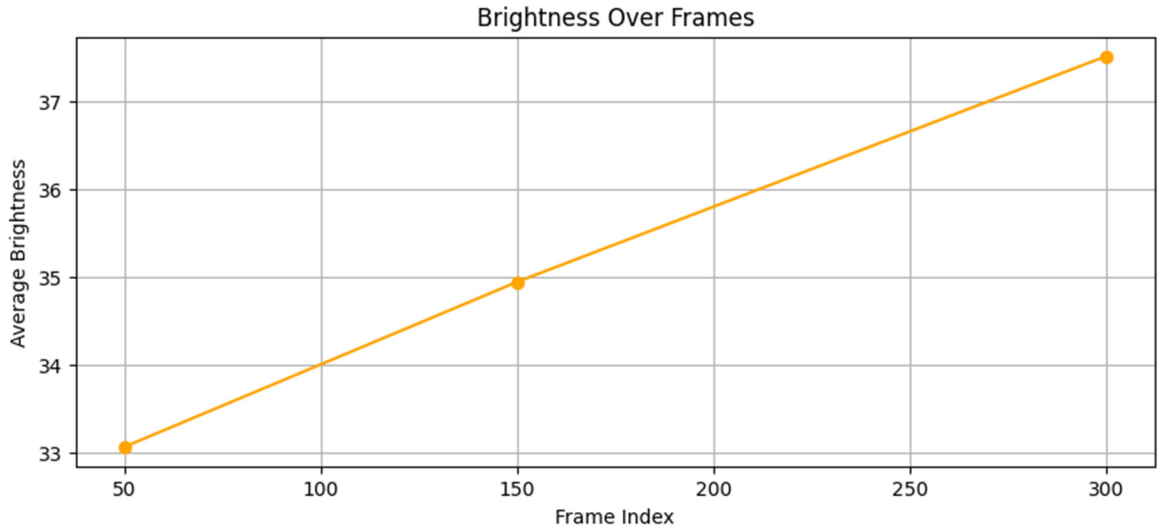

Figure 6. Brightness Over Frames

The slight variations in the peaks of these histograms underscore the encryption's robustness, showing negligible alteration in the color properties of the video. This level of consistency is crucial for applications where the visual accuracy of encrypted video data is paramount, such as in telemedicine and secure communications. Key Length and Security the RSA encryption utilized keys where the private key was significantly longer than the public key, adhering to cryptographic standards for secure key exchange Figure 7**.** illustrates the significant difference in byte length between the private and public RSA keys used in the secure video encryption system. The graph highlights the private key's substantially greater length compared to the public key, reflecting a typical characteristic of asymmetric encryption methods where the private key contains more data to maintain its confidentiality and complexity.

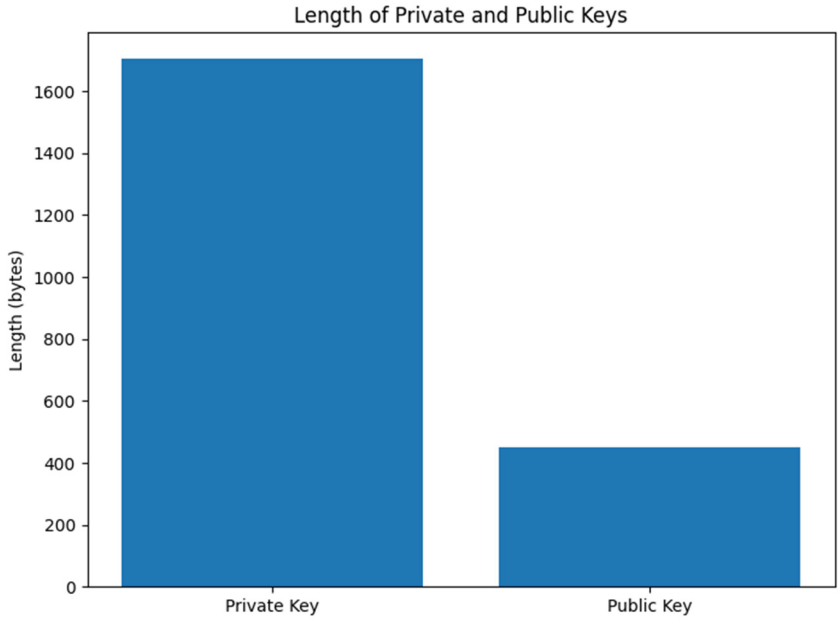

Figure 7. Length of private and public keys

Private Key: Shown in the graph with a considerable length of over 1400 bytes, the private key's size is crucial for the encryption's security. The larger size of the private key includes not only the modulus and exponent but also additional parameters that allow for secure private key operations and enhance cryptographic strength against brute force or cryptographic attacks.

Public Key: The public key, significantly shorter at around 400 bytes, consists mainly of the modulus and a smaller public exponent. The size is adequate to perform encryption tasks while ensuring that the key can be publicly shared without compromising the overall security system.

CONCLUSION

The results underscore the efficacy of using parallel processing in reducing encryption times which is critical for real-time video encryption applications. The improved method not only accelerated the encryption process but also maintained high standards of video quality and integrity.

However, it is crucial to address potential security concerns that arise from parallel processing, such as the management and synchronization of multiple encryption keys and the potential for increased vulnerability to side-channel attacks, this comparative analysis reveals that integrating parallel processing techniques in video encryption significantly enhances encryption speed and efficiency. This finding is instrumental for applications requiring real-time encryption of high-definition video streams. Further exploration into adaptive encryption algorithms that dynamically adjust based on available system resources and network conditions could pave the way for more resilient and flexible video encryption solutions in the future. Key Management, implement a secure key management system. Explore techniques for key distribution, key exchange, and key storage to ensure the overall security of the encryption system.

REFERENCES

1. Hove, D. P., & Watson, B. (2022). The Shortcomings of Video Conferencing Technology, Methods for Revealing Them, and Emerging XR Solutions. PRESENCE: Virtual and Augmented Reality, 31, 283–305. Doi: 10.1162/pres_a_00398
2. Hasan, R., & Hasan, R. (2021, January). Towards a threat model and security analysis of video conferencing systems. In 2021 IEEE 18th Annual Consumer Communications & Networking Conference (CCNC) (pp. 1-4). IEEE.
3. Fatima, S., Rehman, T., Fatima, M., Khan, S., & Ali, M. A. (2022). Comparative Analysis of Aes and RSA Algorithms for Data Security in Cloud Computing. Eng. Proc., 20(1), 14. Doi: 10.3390/engproc2022020014
4. Zhu, D., Zheng, J., Zhou, H., Wu, J., Li, N., & Song, L. (2022). A Hybrid Encryption Scheme for Quantum Secure Video Conferencing Combined with Blockchain. Mathematics, 10(17), 3037. Doi: 10.3390/math10173037
5. Isobe, T., & Ito, R. (2021). Security Analysis of End-to-End Encryption for Zoom Meetings. IEEE Access, 9, 90677–90689. Doi: 10.1109/ACCESS.2021.3091722
6. Alsaidi, Bushra Kh, Baydaa Jaffer Al-Khafaji, and Suad Abed Al Wahab. "Content Based Image Clustering Technique Using Statistical Features and Genetic Algorithm." Engineering, Technology & Applied Science Research 9.2 (2019).
7. BJ Al-Khafaji, AMS Rahma A Modern Encryption Approach to Improve Video Security as an Advanced Standard Adopted(2024) Ibn AL-Haitham Journal for Pure and Applied Sciences 37 (2), 475-485.
8. B.J Alkhafaji, M Salih, S Shanin, Z Nabat improved technique for hiding data in a colored and a monochrome image,2020, Periodicals of Engineering and Natural Sciences 8 (2), 1000-1010
9. B.J Alkhafaji, MA Salih, SAH Shanin, OA Rashid, AA Rashid, MT Hussein,2021,Applying the Artificial Neural Networks with Multiwavelet Transform on Phoneme recognition , Journal of Physics: Conference Series 1804 (1), 012040.
10. RAHMA, A.M.S., RAHMA, M.A.S., and RAHMA, M.A.S. (2015) Automated analysis for basketball free throw. In: Proceedings of the 7th International Conference on Intelligent Computing and Information Systems, Cairo, December 2015. Piscataway, New Jersey: Institute of Electrical and Electronics Engineers, pp. 447-453.
11. B.J Alkhafaji, M Salih, S Shanin, Z Nabat, segmenting video frame images using genetic algorithms,2020 Periodicals of Engineering and Natural Sciences 8 (2), 1106-1114
12. Abdulsalam WH, Alhamdani RS, Abdullah MN. Facial emotion recognition: A survey. International Journal of Advanced Research in Computer Engineering & Technology (IJARCET). 2018 Nov;7(11)
13. Ali RH, Abdulsalam WH. The prediction of COVID 19 disease using feature selection techniques. In Journal of Physics: Conference Series 2021 May 1 (Vol. 1879, No. 2, p. 022083). IOP Publishing.
14. B.J Alkhafaji Steganography techniques using tunes and Discrete Cosine Transform (DCT) Journal of Xi'an University of Architecture & Technology, S. (2020). Volume XII, Issue IV, - 5234- 5244

15. B.J Alkhafaji, Image Improvement Using the Combination of Wavelet and Multiwavelet Transform 2010 - Ibn AL-Haitham Journal for Pure and Applied Science VO L.23 (3).
16. Baydaa Jaffer Al-Khafaji, Abdul Monem S Rahma, (2023). Proposed new modification of AES algorithm for data security, Global Journal of Engineering and Technology Advances, *Vol. 3, No. 12, pp* 117–122
17. Al-Khafaji, Baydaa Jaffer. "Proposed speech analyses method using the multiwavelet transform." Ibn AL-Haitham Journal for Pure and Applied Science 27.1 (2017): 394-401.
18. Abdulsalam WH, Alhamdani RS, Abdullah MN. Speech emotion recognition using minimum extracted features. In2018 1st Annual International Conference on Information and Sciences (Amicis) 2018 Nov 20 (pp. 58-61). IEEE
19. Al-Khafaji, Baydaa Jaffer. "Proposed speech analyses method using the multiwavelet transform." Ibn AL-Haitham Journal for Pure and Applied Science 27.1 (2017): 394-401.
20. Baydaa Jaffer Al-Khafaji Color image analyses using four deferent transformations (FFT-DCT-DWT-DMWT). (2014) Computer Engineering and Intelligent Systems www.iiste.org ISSN 2222-1719 Vol.5, No.10, *pp* 16–24
21. Baydaa-Jaffer Al-Khafaji Abdul Monem S. Rahma, Wisam Abed Shukur New technology for advanced results for security wireless sensor networks (2024) Wasit Journal for Pure sciences, Vol. 3 No. 1 p. 83-89.
22. Majeed Ban Hassan, Wisal Hashim Abdulsalam, Zainab Hazim Ibrahim, Rasha H Ali, Shahla Mahadhan, Digital Intelligence for University Students Using Artificial IntelligenceTechniques, international Journal of Computing and Digital Systems, University of Bahrain, Volume 6, Issue 1
23. Al-Khafaji, Baydaa Jaffer. "Steganography techniques using tunes and Discrete Cosine Transform (DCT)." JOURNAL OF XI'AN UNIVERSITY OF ARCHITECTURE & TECHNOLOGY 12 (2020)
24. Baydaa J Al-Khafaji, Detect the Infected Medical Image Using Logic Gates." Ibn AL-Haitham Journal for Pure and Applied Science Vol. 27.2 (2014): p.260-267.
25. Baydaa-Jaffer Al-Khafaji Abdul Monem S. Rahma, Optimizing Symmetric vs. Asymmetric Image encryption mathematically, International Journal of Advances in Engineering and Management (IJAEM) Volume 4, Issue 9 Sep. 2022.
26. Iptehaj Al-Hakam, Nassir H Salman (*2022*), An Improved Probability Density Function (PDF) for Face Skin Detection, *Iraqi Journal of Science, Vol. 63, No.* 10, pp: 4460-4473, DOI: 10.24996/ijs.2022.63.10.31
27. Wisal Hashim Abdulsalam, Security For Three – Tired Web Application, IBN AL-HAITHAM JOURNAL For Pure and Applied Science, Vol. 28.2 (2015): p. 193-199.
28. Baydaa Jaffer Al-Khafaji, Zanbaq Hikmet Thonon, Wasan alaaal Hamami, hiding information in edges of image by using encryption and decryption techniques, International Journal of Advances in Engineering and Management (IJAEM) Volume 3, Issue 10 Oct 2021, pp: 510-512.
29. W. H. Abdulsalam, R. S. Alhamdani, and M. N. Abdullah, "Emotion recognition system based on hybrid techniques," International Journal of Machine Learning and Computing, vol. 9, 2019.
30. Baydaa Jaffer Al-Khafaji, Bushra Kh. Alsaidi, Suad abed al Wahab, Cryptography and Steganography whit using Edge detection (Cumin operator), Journal of Xi'an University of Architecture & Technology, Volume XII, Issue V, 2020, pp: 544-548.

The effect of the percentage of doping with silver and zinc oxide on the properties of the coating layer for nickel and copper

Mina S. Nsaif [a] Iman Adnan Annon [b] and Ahmed. S. Abbas [c]

Production Engineering & Metallurgy Department - University of Technology- Iraq, Baghdad, Iraq

[a] Corresponding author: menaalbaiaty06@gmail.com.
[b] *mimanadnanannon2001@gmail.com.*
[c] *ahmedsabbas2006@gmail.com.*

Abstract. Low carbon steel is widely used in oil and gas applications. In this research multilayers of Nickel (Ni) and Copper (Cu) have been deposited on low carbon steel substrate using the electroplating process (ELP).The first layer of Ni is coated to be followed by a layer of Cu . ELP was implemented using Watts bath containing (300 g/l) of $NiSO_4$. $6H_2O$, (30 g/l) of ($NiCl_2.6H_2O$), (40 g/l) of H_3BO_3 and (30 g/l) of (NaCN), (30 g/l) of (CuCN), (10 g/l) of ($NaOH.6H_2O$). First bath parameters were temperature is (59 - 60 °C), current density in the range of (3-5 A/dcm^2), voltage was holed at (8V), for Ni, and temperature was between (50-51°C), current density in the range of (1-2 A/dcm^2), voltage was holed at (4 V), while the plating time (10 minutes) for both Ni and Cu. The results refer to metallurgical tests were achieve including the micro hardness of DC sputtering, Vickers micro hardness results showed improvement in hardness values compared, with steel substrate, and in the presence of Low carbon steel- electroplating (Ni)- DC sputtering (ZnO 95%- Ag 5%) 383.15 Hv, Low carbon steel- electroplating (Ni)- DC sputtering (ZnO 90%- Ag 10 %) 313.175 and Low carbon steel- electroplating (Ni- Cu)- DC sputtering (ZnO 85%- Ag 15 %) 302. 15 Hv. The roughness was measured using surface roughness measurement device. The average surface roughness (Ra) depicted a satisfying values as a result of Low carbon steel- electroplating (Ni- Cu)- DC sputtering (ZnO 95%- Ag 5 %) layer coating, which gave uniform surface distribution with Ra 0.180 μm, Low carbon steel- electroplating (Ni)- DC sputtering (ZnO 90%- Ag 10 %) Ra (μm). X-ray 0.388 μm Low carbon steel- electroplating (Ni- Cu)- DC sputtering (ZnO 85%- Ag 15 %) 0.2043. Diffraction pattern (XRD) test examinations are adopted as a good evidence for the presence of Ni, and Cu in both internal and external finish layers, respectively. Corrosion examinations were carried out in seawater solution (3.5 NaCl gm) the corrosion behavior tends to be more resistance, with layers of in sea water environment, which is considered an important criterion to increase the part life. Low carbon steel- electroplating (Ni- Cu)- DC sputtering (ZnO 95%- Ag 5 %) layer coating 1.2905E-03, Low carbon steel- electroplating (Ni)- DC sputtering (ZnO 90%- Ag 10 %) 7.444 and Low carbon steel- electroplating (Ni)- DC sputtering (ZnO 85%- Ag 15 %) 5.1.

Keywords: *DC Sputtering, Mixing ratio, ZnO-Ag, electroplating, roughness*.

INTRODUCTION

The increasing demand for new materials in various engineering applications has led many researchers to explore surface engineering methods and techniques to impart new properties and characteristics to material surfaces, distinct from their basic substrates [1]. Electroplating is a widely used electrodeposition process that produces dense, uniform, and adherent metal or alloy coatings on surfaces using electric current. These coatings serve decorative, protective, or property-enhancing purposes [2]. Nickel electroplating technology, extensively developed over the past five decades, enables the efficient production of a broad range of industrial coatings for both decorative and functional applications [3]. Nickel coatings are used to enhance physical properties such as wear resistance, heat resistance, and corrosion resistance [4]. They often serve a dual role by providing a bright decorative finish and improved corrosion resistance or other functional properties [5]. Copper-nickel alloys offer significant advantages due to their durability [6]. They are highly resistant to corrosion and rust, making them ideal for outdoor applications such as roofing or gutters [7]. Copper-nickel alloys do not corrode when exposed to saltwater or other marine environments, making them suitable for boat construction and coastal structures [8]. Additionally, these alloys have excellent electrical conductivity, making them perfect for wiring systems and electrical components [9]. Their aesthetic appeal, available in various colors and finishes, makes them suitable for decorative items such as

Technologies and Materials for Renewable Energy, Environment and Sustainability
AIP Conf. Proc. 3321, 020042-1–020042-17; https://doi.org/10.1063/5.0289759
Published under an exclusive license by AIP Publishing. 978-0-7354-5231-2/$30.00

coins or jewelry [10]. Furthermore, copper-nickel can be polished to a high shine and is recyclable, making it an environmentally friendly choice for many applications [11]. For the electroplating process to be effective, the surface must be cleaned of organic materials like greases and oils [12]. This can be achieved using conventional solvents or by cleaning with alkaline or inorganic chemicals such as oxides [13]. The advantages of electroplating include its simplicity, ease of control, and operation under ambient pressure conditions [14]. This environmentally friendly technique involves low material consumption [15]. The electroplating mechanism comprises three stages. The first stage involves discharging metal ions to form adsorbed atoms, which migrate towards the cathode under the influence of applied potential through convection and diffusion. The second stage involves the transfer of electrons at the cathode surface, allowing the ions to enter the diffusional layer and be adsorbed onto the cathode surface [15]. The third stage, called incorporation, involves moving these adsorbed atoms to the growth point at the cathode, building up the metal lattice layer.

NORMAL DISTRIBUTION

In probability and statistics, the normal distribution bell curve is one of the most important continuous probability distributions. The normal distribution is defined as the probability density function f(x) for the continuous random variable x, in the system. A normal distribution is a very important statistical data distribution pattern occurring in many natural phenomena, such as height, blood pressure, lengths of objects produced by machines, etc [24, 25].

Material and equipment

Preparation for low carbon steel substrate examinations

To implanted microstructure examinations and hardness test, low carbon steel sample should be prepared. The following steps have been followed in this work. First, low carbon steel samples are cut into small pieces of dimension (2×2) cm. Secondly, brass samples were cold mounted in order, to make easy handling during the preparation operations, such as, grinding, polishing and etching.

Nickel electroplating

The electroplating (ELP) process began by drilling holes in the specimens and connecting them to the cathode using copper wires, while the nickel was connected to the positive pole. The specimens were then immersed in the electrolyte. Appropriate plating current was applied to the electrolyte to achieve a stable state and ensure a high-quality plating layer. The temperature of the bath was controlled using a thermometer to maintain it within the required range, and the pH was measured and maintained at a value of 10.

Copper electroplating

The same rectangular specimens, with identical dimensions, were plated with copper.
The components of the electroplating bath included 30 g/l of NaCN, 30 g/l of CuCN, and 10 g/l of NaOH·6H2O.
Electroplating bath made of Pyrex glass.
Insoluble electrodes (two electrodes), made of stainless steel.
Distilled water

DC Sputtering System

The method was used in an argon discharge using a low-pressure gas apparatus made up of an anode (silver-doped zinc in different ratios of 5%, 10%, and 15%), a target (cathode), and an evacuated chamber. A 4 kV DC power source drove the gas discharge, which the cathode faced. The electrodes of the cathode were contained in a quartz tube and protected by a ceramic disk, and the anode was positioned to sustain the discharge [19]. The top electrodes had a diameter of 14.5 cm, an effective cathode dark space area of 7.5 cm, and were spaced 4 cm apart. Argon was supplied to the plasma chamber at the appropriate flow rate and pressure via a gas source-flow controller system [20]. The system included argon tubes, fittings, and dual-step controls, with a two-stage needle valve

regulating flow pressure to the plasma hollow [21]. The vacuum setup featured a Blazer rotary pump (60 m^3/h) and a Variant V-1000HT turbo pump. Discharge gas pressures were monitored in the plasma chamber [22-23].

Thermal Treatment of ZnO doping 5%, 10%, and 15% Ag Thin Film on Lcs , Ni& Cu Substrates

The crystallization of the as-sputtered multilayer morphology was stabilized in a Carbolite furnace to enhance the adhesion between the ZnO-doped Ag thin film and the LCS, Ni, and Cu substrates. The annealing process was conducted in an argon gas atmosphere to prevent or minimize oxidation or contamination of the samples. The specimen was subjected to a temperature of 400 °C for 2 hours [24]. The specimen was placed in the furnace to undergo the process of cooling until it reached the ambient temperature of the room.

Steps to prepare the powder

The powder is mixed according to the equation [25-27]:

W= molecular weight of first substance × doping ratio + molecular weight of second substance × doping ratio

$$\text{Wight of first substance} = \frac{\text{molecular wight of first substance} \times \text{doping ratio}}{\text{w}} \times \text{the total wight of the pullet to be pressed}$$

$$\text{Wight of second substance} = \frac{\text{molecular wight of second substance} \times \text{doping ratio}}{\text{w}} \times \text{the total wight of the pullet to be pressed}$$

The mixture is mixed using a vibrating device until it is homogeneous and then pressed by applying a load 8 ton (see Figure 1).

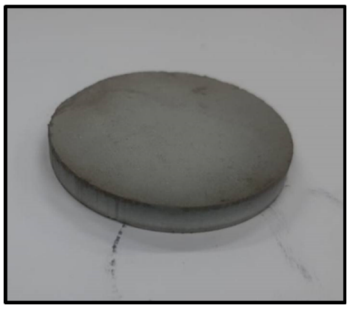

FIGURE 1. Compressed powder of ZnO doping Ag

Corrosion inspection

Specimens measuring 40 x 20 mm, including low carbon steel, low carbon steel electroplated with nickel, low carbon steel electroplated with copper, and low carbon steel electroplated with both nickel and copper, each had a small hole with a 3 mm diameter. A corrosion solution comparable to seawater was prepared by dissolving 3.5 grams of NaCl in one liter of distilled water at room temperature, creating a 3.5 wt.% NaCl solution. For the testing process, a polarization cell was set up, consisting of the electrolyte solution, a reference electrode, a counter electrode(s), and the metal sample of interest, which was connected to a specimen holder and referred to as the working electrode. The electrodes were connected to a potentiostat. The working, reference, and counter electrodes were placed in the electrolyte solution, which closely resembled the actual application environment of the material being tested. In the solution, an electrochemical potential (voltage) was generated between the various electrodes. This test was conducted in the Department of Nanotechnology [28-30].

Roughness inspection

A portable surface roughness gage instrument (pocket surf) manufactured by Mahar Federal Inc. USA with an accuracy of (0.001) μm is used to test the surface roughness of nickel and copper. The measures lab in the department of production engineering and metalworking is where these tests are carried out.

Results and Discussion

Thin films made of nickel and copper are plated on a low carbon steel substrate. In this research the surface quality were studied the results show.

XRD analysis

Figure 2 depicts the XRD after electroplating and DC sputtering methods for the prepared samples

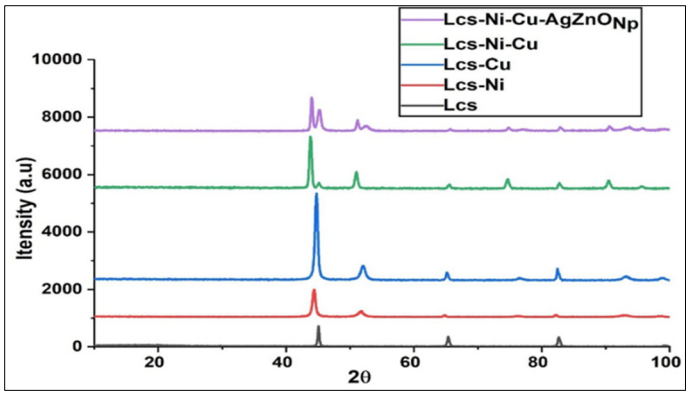

FIGURE 2. The XRD after electroplating and DC sputtering methods for the prepared samples

The X-ray diffraction (XRD) pattern of low carbon steel typically exhibits peaks corresponding to the crystallographic planes of the iron (Fe) and iron carbide (Fe3C or cementite) phases present in the steel microstructure. Here are the common peaks observed in the XRD pattern of low carbon steel: Alpha Iron (Ferrite) Peaks: (110) Plane: Around 44.5° 2θ, (200) Plane: Around 65.0° 2θ, (211) Plane: Around 82.0° 2θ. For Copper (Cu) Peaks: (111) Plane: Around 43.3° 2θ, (200) Plane: Around 50.5° 2θ, (220) Plane: Around 74.1° 2θ. For Nickel (Ni) Peaks: (111) Plane: Around 44.5° 2θ, (200) Plane: Around 51.8° 2θ, (220) Plane: Around 76.3° 2θ [28-35].

Microhardness after Electroplating and DC sputtering techniques

The hardness values after using electroplating and DC sputtering techniques, Time 15 min, load 100 g

Table 1 provided outlines the hardness values of various coatings applied to low carbon steel samples using both electroplating and DC sputtering techniques. The coatings were deposited for 15 minutes under a load of 100 grams, and the hardness was measured using the Vickers hardness test (Hv) (see Figure 3).

Table 1. Result of Vickers hardness test for substrate and different types of coating 95%ZnO doping 5%Ag.

No. of samples	Type of Coating	The hardness values after deposition (Hv) using Vickers
1	Low carbon steel-Pure	335.2
2	Low carbon steel- DC sputtering (ZnO 95%- Ag 5%)	182.75
3	Low carbon steel- electroplating (Ni)- DC sputtering (ZnO 95%- Ag 5%)	383.15
4	Low carbon steel- electroplating (Cu)- DC sputtering (ZnO 95%- Ag 5%)	236.6
5	Low carbon steel- electroplating (Ni- Cu)- DC sputtering (ZnO 95%- Ag 5%)	275.35

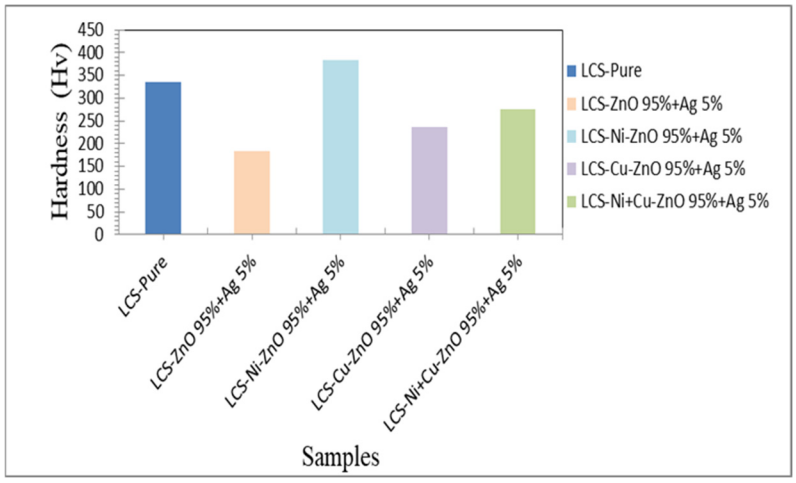

FIGURE 3. The hardness values after electroplating and DC sputtering methods using Vickers

The hardness value of the untreated low carbon steel is 335.2 Hv. This serves as the baseline for comparison with the coated samples. Low carbon steel, known for its ductility and malleability, has a relatively low hardness value, representing the inherent properties of the material without any surface modifications. The hardness value for low carbon steel coated with ZnO (95%) and Ag (5%) using the DC sputtering technique is 182.75 Hv. This value is significantly lower than the baseline hardness of the pure low carbon steel (335.2 Hv). The reduction in hardness indicates that the ZnO-Ag coating softens the surface of the steel. Both zinc oxide and silver are softer materials compared to the base steel, leading to a decrease in overall hardness when they form the coating. The hardness value for low carbon steel coated first with nickel via electroplating and then with ZnO (95%) and Ag (5%) using DC sputtering is 383.15 Hv. This represents an increase in hardness compared to both the pure steel and the ZnO-Ag coating alone. Nickel, known for its hardness and ability to enhance surface properties, significantly improves the surface hardness when used as a base layer before applying the ZnO-Ag coating. The hardness value for low carbon steel coated first with copper via electroplating and then with ZnO (95%) and Ag (5%) using DC sputtering is 236.6 Hv. This value is lower than the pure low carbon steel but higher than the ZnO-Ag coating alone. Copper, while not as hard as nickel, still contributes to a modest increase in hardness over the ZnO-Ag coating, but the effect is not as pronounced as with nickel. The hardness value for low carbon steel coated with a combination of nickel and copper via electroplating, followed by ZnO (95%) and Ag (5%) using DC sputtering is 275.35 Hv. This value is higher than the copper-only electroplated sample but lower than the nickel-only electroplated sample. The combination of nickel and copper provides an intermediate hardness, indicating that nickel's hardness enhancement is partially offset by the softer copper. Comparing the results, it is evident that the type of coating significantly influences the hardness of the low carbon steel samples. The pure low carbon steel has a baseline hardness of 335.2 Hv. Coating with ZnO-Ag alone using DC sputtering reduces the hardness to 182.75 Hv, showing that this coating softens the steel surface. The combination of electroplating with nickel followed by ZnO-Ag sputtering results in the highest hardness increase (383.15 Hv), demonstrating that nickel is highly effective in enhancing surface hardness, even when followed by a softer ZnO-Ag coating. Electroplating with copper followed by ZnO-Ag sputtering results in a hardness of 236.6 Hv, indicating that copper provides some improvement but not as much as nickel. The combination of nickel and copper electroplating followed by ZnO-Ag sputtering results in a hardness of 275.35 Hv. This intermediate value suggests a balance where nickel's hardening effect is moderated by the presence of copper, resulting in a less pronounced increase in hardness.

The hardness values after using electroplating and DC sputtering techniques, Time 15 min, load 100 g, ZnO 90%, Ag 10%

Table 2 and Figure 4 presents the hardness values of low carbon steel samples after deposition with different types of coatings using electroplating and DC sputtering techniques.

TABLE 2. Result of Vickers hardness test for substrate and different types of coating ZnO doping 10%Ag

No. of samples	Type of Coating	The hardness values after deposition (Hv) using Vickers
1	Low carbon steel-Pure	335.2
2	Low carbon steel- DC sputtering (ZnO 90%- Ag 10%)	164.2
3	Low carbon steel- electroplating (Ni)- DC sputtering (ZnO 90%- Ag 10%)	313.175
4	Low carbon steel- electroplating (Cu)- DC sputtering (ZnO 90%- Ag 10%)	253.175
5	Low carbon steel- electroplating (Ni- Cu)- DC sputtering (ZnO 90%- Ag 10%)	288.75

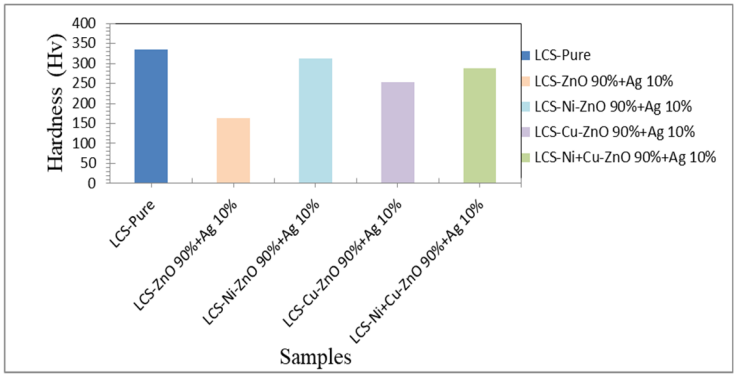

FIGURE 4. The hardness values after electroplating and DC sputtering methods using Vickers

This represents the baseline hardness of untreated low carbon steel. The relatively high hardness value indicates the inherent properties of low carbon steel, known for its ductility and moderate hardness. The hardness significantly decreases when the low carbon steel is coated with ZnO 90%-Ag 10% using DC sputtering. This reduction indicates that the ZnO-Ag coating is softer compared to the pure low carbon steel, possibly due to the nature of the ZnO-Ag composite, which may be less hard than the steel substrate .Electroplating with nickel followed by DC sputtering with ZnO 90%-Ag 10% results in a significant increase in hardness compared to the ZnO-Ag coating alone. Nickel is known for its hardness, and its presence enhances the overall hardness, though it is still slightly lower than the pure low carbon steel. Electroplating with copper followed by DC sputtering with ZnO 90%-Ag 10% also increases the hardness compared to the ZnO-Ag coating alone. Copper's addition improves the hardness, but not as effectively as nickel. The resulting hardness is lower than that of the pure Lcs and the nickel-plated sample. The combination of nickel and copper electroplating followed by DC sputtering with ZnO 90%-Ag 10% yields a hardness value higher than copper alone but lower than nickel alone. This suggests a synergistic effect where both metals contribute to an overall increase in hardness, though it remains below the pure low carbon steel's hardness.

Baseline vs. Coated Samples: All coated samples exhibit varying hardness values compared to the pure low carbon steel. The ZnO-Ag coating alone significantly reduces the hardness, indicating the softness of the composite layer.

Nickel vs. Copper Coatings: Nickel electroplating results in a higher hardness increase than copper when combined with ZnO-Ag sputtering. This highlights nickel's superior hardness enhancement properties.

Combination Coating (Ni-Cu): The dual electroplating of nickel and copper provides an intermediate hardness value, suggesting that the combination of both metals offers balanced properties but does not surpass the pure low carbon steel's hardness.

The highest hardness value of 302.15 Hv is observed in Sample 5, which combines electroplating with both nickel and copper before applying the ZnO 85%-Ag 15% sputtering. This multi-layered coating approach appears to provide a synergistic effect, resulting in a surface hardness closer to the original low carbon steel, albeit slightly reduced.

The hardness values after using electroplating and DC sputtering techniques, Time 15 min, load 100 g

Figure 5 and Table 3 depicts the hardness values after using electroplating and DC sputtering techniques.

Table 3. Result of Vickers hardness test for substrate and different types of coating ZnO doping 15%Ag

No. of samples	Type of Coating	The hardness values after deposition (Hv) using Vickers
1	Low carbon steel-Pure	335.2
2	Low carbon steel- DC sputtering (ZnO 85%- Ag 15%)	145.65
3	Low carbon steel- electroplating (Ni)- DC sputtering (ZnO 85%- Ag 15%)	243.2
4	Low carbon steel- electroplating (Cu)- DC sputtering (ZnO 85%- Ag 15%)	269.75
5	Low carbon steel- electroplating (Ni- Cu)- DC sputtering (ZnO 85%- Ag 15%)	302.15

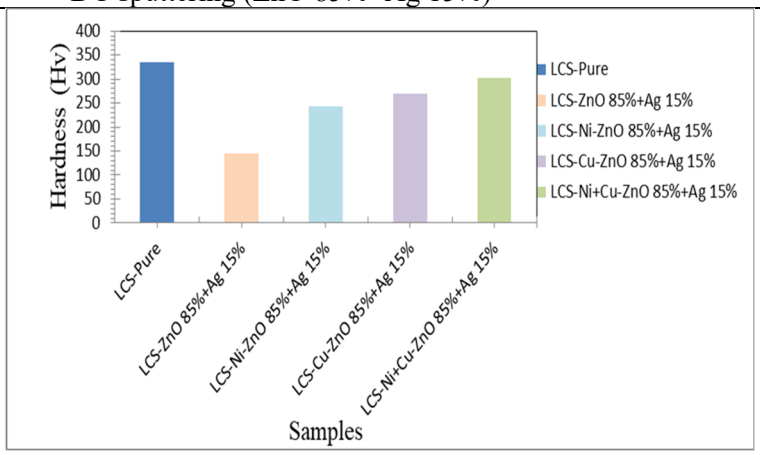

FIGURE 5. The hardness values after electroplating and DC sputtering methods using Vickers

Surface roughness

The roughness values after using electroplating and ZnO doping 5% silver DC sputtering techniques

Table 4 and Figure 6 provided lists the roughness values of low carbon steel samples after applying various coating techniques, including electroplating and DC sputtering, with roughness measured using the average roughness (Ra) metric. The table compares the roughness values of pure low carbon steel, the same steel after a prolonged exposure, and different coatings.

TABLE 4. Roughness measurement after electroplating and ZnO doping 5% Ag DC Sputtering

No. of samples	Type of Coating	Time of coating (hrs)	Roughness (Ra)
1	Low carbon steel-Pure	-	0.876
2	Low carbon steel- DC sputtering (ZnO 95%- Ag 5%)	2	0.709
3	Low carbon steel-Ni DC sputtering (ZnO 95%- Ag 5%)	2	0.572
4	Low carbon steel- electroplating (Cu)- DC sputtering (ZnO 95%- Ag 5%)	2	0.775
5	Low carbon steel- electroplating (Ni- Cu)- DC sputtering (ZnO 95%- Ag 5%)	2	0.180

The roughness value of the untreated low carbon steel after 10 minutes is 0.876 Ra. This value represents the baseline roughness of the material in its natural state without any surface treatment. The roughness value of the untreated Lcs after 2 hours is 0.709 Ra. The reduction in roughness compared to the 10-minute measurement (0.876 Ra) suggests that prolonged exposure or natural oxidation may slightly smooth the surface, possibly due to the settling of surface irregularities over time. The roughness value for Lcs coated with ZnO (95%) and Ag (5%) using DC sputtering for 2 hours is 0.572 Ra. This value is significantly lower than both untreated samples, indicating that the DC sputtering process effectively smooths the surface. The ZnO-Ag coating creates a uniform layer, filling in surface imperfections and reducing roughness. The roughness value for low carbon steel first coated with nickel via electroplating and then with ZnO (95%) and Ag (5%) using DC sputtering for 2 hours is 0.775 Ra. This value is higher than the roughness achieved with DC sputtering alone (0.572 Ra) but lower than the pure untreated steel after 10 minutes (0.876 Ra). The initial nickel layer adds some roughness to the surface, which is then partially smoothed by the subsequent ZnO-Ag sputtering layer. When comparing the results, it is evident that the application of coating techniques significantly impacts the surface roughness of Lcs. The untreated Lcs has the highest roughness value after 10 minutes (0.876 Ra), while prolonged exposure without treatment reduces the roughness to 0.709 Ra, suggesting some natural smoothing over time. The DC sputtering of ZnO-Ag alone achieves the lowest roughness value (0.572 Ra), indicating that this technique is highly effective in creating a smooth surface. The uniform deposition of ZnO and Ag particles fills in surface imperfections, resulting in a significant reduction in roughness compared to the untreated samples. The combination of electroplating with nickel followed by DC sputtering with ZnO-Ag results in a roughness value of 0.775 Ra. Although this is an improvement over the initial untreated surface (0.876 Ra), it is not as effective as DC sputtering alone. The initial nickel electroplating likely introduces some surface irregularities that are not entirely smoothed out by the subsequent ZnO-Ag sputtering.

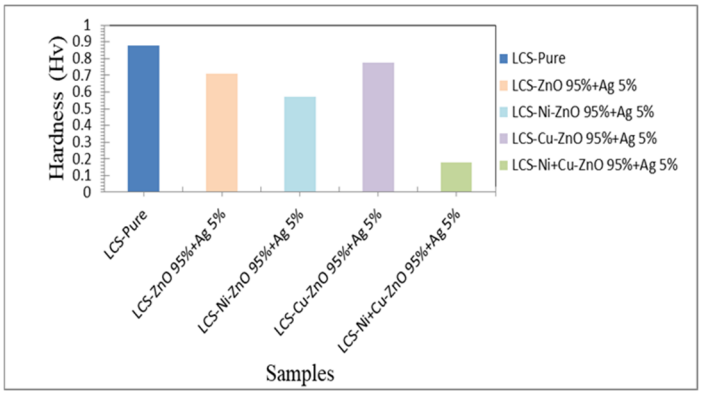

FIGURE 6. The roughness values after electroplating and DC sputtering methods

The roughness values after using electroplating and ZnO doping 10% silver DC sputtering techniques, and after anneling 400 ºC for 2 hours, (Time 15 min, load 100 g)

Roughness, denoted as Ra, is a measure of the surface's texture and is an important factor in determining the material's suitability for various applications.The pure low carbon steel sample (Sample 1) serves as the baseline with a roughness value of 0.876 Ra. This value represents the inherent surface texture of the untreated steel. Sample 2, which involves DC sputtering with a coating composition of ZnO 90%-Ag 10%, shows a roughness value of 0.589 Ra. This reduction in roughness compared to the pure steel indicates that the sputtering process smoothens the surface, possibly due to the deposition of the fine ZnO-Ag particles that fill surface irregularities. When electroplating with nickel is added before the ZnO 90%-Ag 10% sputtering (Sample 3), the roughness further decreases to 0.388 Ra. This significant decrease suggests that the nickel layer effectively smoothens the surface prior to the sputtering, leading to an even finer texture. Sample 4 involves electroplating with copper before the ZnO 90%-Ag 10% sputtering and results in a roughness value of 0.643 Ra. Even though it's lower than the pure steel, this number is greater than the nickel-plated sample. This indicates that the copper layer contributes to surface smoothening but not as effectively as the nickel layer. Sample 5 repeats the copper electroplating followed by ZnO 90%-Ag 10% sputtering but shows a roughness value of 0.459 Ra. This is an improvement over Sample 4 and suggests some variation in the coating process or layer uniformity, leading to a smoother surface than initially

achieved with copper electroplating. Table 5 and Figure 7 outlines the roughness values (Ra) of low carbon steel samples after undergoing different coating processes and annealing at 400 °C for two hours.

TABLE 5. Roughness measurement after electroplating and DC Sputtering ZnO doping 10% Ag

No. of samples	Type of Coating	Time of coating (hrs)	Roughness (Ra)
1	Low carbon steel-Pure	-	0.876
2	Low carbon steel- DC sputtering (ZnO 90%- Ag 10%)	2	0.589
3	Low carbon steel- electroplating (Ni)- DC sputtering (ZnO 90%- Ag 10%)	2	0.388
4	Low carbon steel- electroplating (Cu)- DC sputtering (ZnO 90%- Ag 10%)	2	0.643
5	Low carbon steel- electroplating (Cu)- DC sputtering (ZnO 90%- Ag 10%)	2	0.459

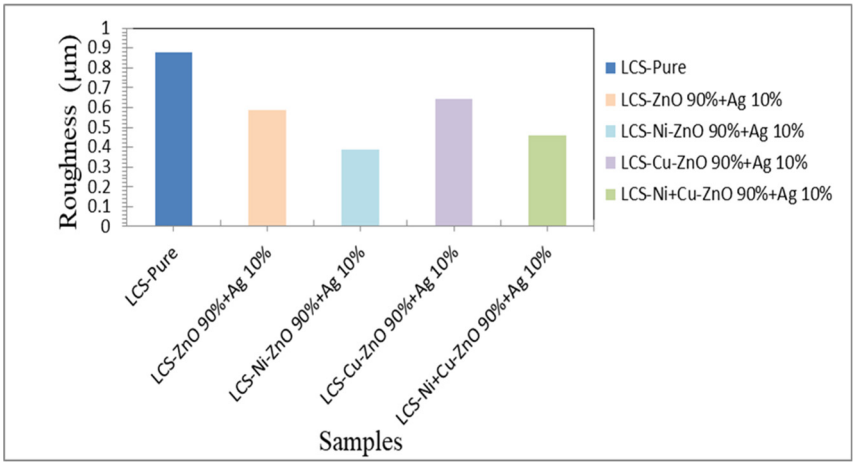

FIGURE 7. The roughness values after electroplating and DC sputtering methods

The roughness values after using electroplating and ZnO doping 15% silver DC sputtering techniques, and after anneling 400 °C for 2 hours, (Time 15 min, load 100 g)

Table 6 and Figure 8 provided lists the roughness values of low carbon steel samples after applying various coatings using electroplating and DC sputtering techniques, with roughness measured using the average roughness (Ra) metric.

TABLE 6. Roughness measurement after electroplating and DC Sputtering ZnO doping 15% Ag

No. of samples	Type of Coating	Time of coating (hrs)	Roughness (Ra)
1	Low carbon steel-Pure	-	0.876
2	Low carbon steel- DC sputtering (ZnO 85%- Ag 15%)	2	0.4696
3	Low carbon steel- electroplating (Ni)- DC sputtering (ZnO 85%- Ag 15%)	2	0.5113
4	Low carbon steel- electroplating (Cu)- DC sputtering (ZnO 85%- Ag 15%)	2	0.2043
5	Low carbon steel- electroplating (Cu)- DC sputtering (ZnO 85%- Ag 15%)	2	0.7373

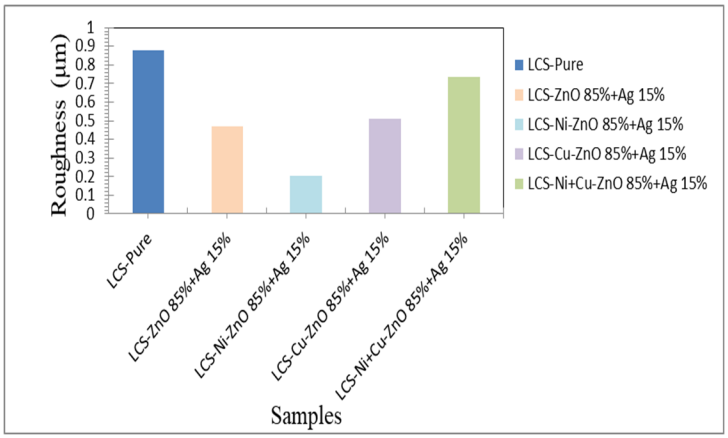

FIGURE 8. The roughness values after electroplating and DC sputtering methods

The roughness value of the untreated low carbon steel after 10 minutes is 0.876 Ra. This serves as the baseline for comparison with the coated samples. The relatively high roughness value indicates that the surface of the pure Lcs is rougher compared to the coated samples. The roughness value for low carbon steel coated with ZnO (85%) and Ag (15%) using DC sputtering for 2 hours is 0.4696 Ra. This value is significantly lower than the baseline roughness of the pure low carbon steel (0.876 Ra). The ZnO-Ag coating effectively smooths the surface, filling in surface imperfections and reducing roughness. The combination of ZnO and Ag creates a uniform, smooth layer that significantly improves the surface finish. The roughness value for low carbon steel coated first with nickel via electroplating and then with ZnO (85%) and Ag (15%) using DC sputtering for 2 hours is 0.5113 Ra. This value is lower than the baseline roughness but slightly higher than the ZnO-Ag sputtering alone. The initial nickel electroplating provides a relatively smooth base, which is then further smoothed by the ZnO-Ag sputtering, although not as effectively as sputtering alone. The roughness value for low carbon steel coated first with copper via electroplating and then with ZnO (85%) and Ag (15%) using DC sputtering for 2 hours is 0.2043 Ra. This is the lowest roughness value among all the samples tested. Copper electroplating provides an exceptionally smooth base layer, which is then further smoothed by the ZnO-Ag sputtering, resulting in the most significant reduction in surface roughness. Interestingly, another sample with the same combination of copper electroplating followed by ZnO-Ag sputtering shows a higher roughness value of 0.7373 Ra. This discrepancy suggests variability in the coating process or sample preparation, highlighting the importance of process control and consistency in achieving the desired surface finish. Comparing the results, it is evident that the application of coating techniques significantly impacts the surface roughness of Lcs. The pure Lcs has the highest roughness value of 0.876 Ra, indicating a rougher surface compared to the coated samples. The ZnO-Ag sputtering alone achieves a roughness value of 0.4696 Ra, demonstrating its effectiveness in smoothing the surface. The combined electroplating and sputtering techniques generally result in lower roughness values, with copper electroplating followed by ZnO-Ag sputtering achieving the lowest roughness value of 0.2043 Ra. This indicates that copper provides an excellent base for further smoothing by ZnO-Ag sputtering. However, the variability seen in the two samples with the same combination of coatings (samples 4 and 5) suggests that process control is crucial. The higher roughness value of 0.7373 Ra in the second sample indicates potential inconsistencies in the coating process, such as variations in coating thickness, deposition rates, or surface preparation.

Corrosion test

The corrosion values of the samples after electroplating and DC sputtering deposition with ZnO and 5% Ag NP

Table 7 presents the corrosion values of samples after a combination of electroplating and DC sputtering deposition with zinc oxide (ZnO) and 5%silver (Ag) Np.

TABLE 7. The corrosion values for the prepared samples

Samples	$I_{corr} \times 10^{-6}$ (mA/cm^2)	Corrosion Rate (mpy)	Corrosion resistance
Low carbon steel- DC sputtering (95% ZnO- 5% Ag)	1.0541	0.012	0.084
Low carbon steel- electroplating (Ni)- DC sputtering (95 % ZnO- 5% Ag)	4.023	0.05	0.02
Low carbon steel- electroplating (Cu)- DC sputtering (95% ZnO- 5%Ag)	5.0867	0.06	0.016
Low carbon steel- electroplating (Ni+Cu)- DC sputtering (95% ZnO- 5% Ag)	6.1906	0.0726424	1.2905E-03

The value indicates that the addition of ZnO and Ag nanoparticles significantly improves the corrosion resistance of Lcs, both in its pure form and after electroplating with Ni, Cu, or a combination of both. The trend shows a marked reduction in the corrosion current (Icorr) and corrosion rate across all samples, reflecting the protective effect of the ZnO-Ag nanoparticle layer. The Ni-Cu electroplated sample with ZnO-Ag deposition demonstrates the best overall corrosion resistance, followed closely by the Ni and Cu electroplated samples with ZnO-Ag. The pure ZnO-Ag coating on low carbon steel also shows significant improvement over the uncoated steel.

Corrosion Resistance: The sample, which underwent electroplating with a combination of nickel and copper followed by DC sputtering with ZnO 95%-Ag 5% nanoparticles, exhibits a corrosion rate of 1.2905×10-3 mpy. This value suggests a relatively low level of corrosion, indicating effective corrosion resistance provided by the combined coating.

The corrosion rate observed in the sample subjected to the combined electroplating and DC sputtering process is notably low, indicating effective corrosion protection. While direct comparison with other samples is not provided in the given data, it can be inferred that the corrosion resistance achieved in this sample is promising, especially considering the multi-step coating process involving both electroplating and DC sputtering with ZnO/Ag NPs. The combination of electroplating with a dual Ni+Cu layer followed by DC sputtering deposition with ZnO 95%-Ag 5% nanoparticles demonstrates promising corrosion resistance for low carbon steel.

This approach highlights the potential benefits of combining different deposition techniques and materials to enhance the protective properties of coatings against corrosion. Further optimization and characterization of such multi-layered coatings could lead to improved corrosion protection for various applications (see Figure 9).

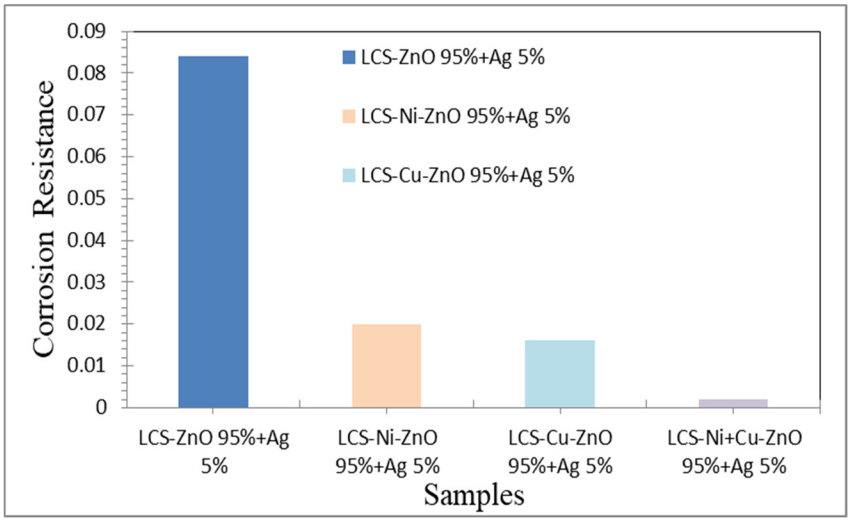

FIGURE 9. The corrosion resistance values for the samples in this work

The corrosion values of the samples after electroplating and DC sputtering deposition with ZnO and 10% Ag NP

Table 8 and Figure 10 presents the corrosion values of samples after a combination of electroplating and DC sputtering deposition with zinc oxide (ZnO) and 10% silver (Ag) nanoparticles.

TABLE 8. The corrosion values for the prepared samples

Samples	$I_{corrx}10^{-6}$ (mA/ cm^2)	Corrosion Rate (mpy)	Corrosion resistance
Low carbon steel- DC sputtering (ZnO 90%-Ag 10%)	1.6924	0.00019854	5.036
Low carbon steel – electroplating (Cu)-DC sputtering-(ZnO 90%-Ag 10%)	3.9677	0.0046546	2.148
Low carbon steel- electroplating (Ni)- DC sputtering (ZnO 90%-Ag 10%)	1.1451	0.013433	7.444
Low carbon steel - electroplating (Ni-Cu)-DC sputtering (ZnO 90%-Ag 10%)	2.2079	0.25901	0.4529

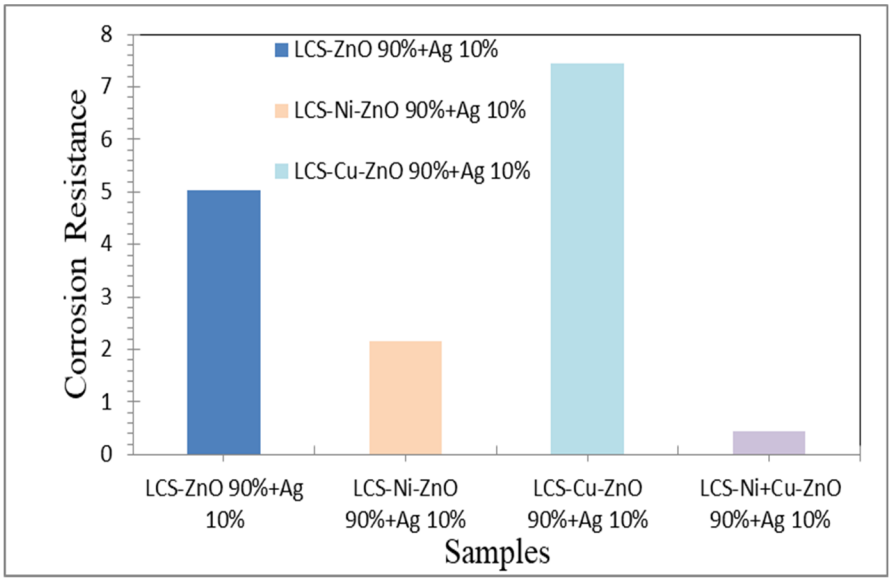

FIGURE 10. The corrosion resistance values for the samples in this work

Corrosion Resistance: This sample shows a relatively low corrosion current and corrosion rate, indicating good corrosion resistance. The addition of ZnO and Ag nanoparticles via DC sputtering provides a protective barrier that enhances the corrosion resistance of low carbon steel.

Corrosion Resistance: This sample has a higher corrosion current and rate compared to the pure ZnO-Ag sputtered sample, suggesting that while Cu electroplating followed by ZnO-Ag sputtering improves corrosion resistance, it is not as effective as the ZnO-Ag sputtering alone. The combined layers do provide better protection than untreated low carbon steel.

Corrosion Resistance: This sample exhibits the lowest corrosion current and highest corrosion resistance, indicating superior corrosion protection. Ni electroplating combined with ZnO-Ag sputtering significantly enhances the corrosion resistance, making it the best-performing sample in this set.

This sample shows the highest corrosion current and corrosion rate among the samples tested, indicating the lowest corrosion resistance. The combination of Ni-Cu electroplating followed by ZnO-Ag sputtering does not perform as well as the other treatments. This suggests that the synergistic effect of Ni and Cu electroplating may not

be as effective in conjunction with ZnO-Ag sputtering, possibly due to issues such as galvanic corrosion between the different metals.

The corrosion values of the samples after electroplating and DC sputtering deposition with ZnO and 15% Ag NP

Table 9 and Figure 11 presents the corrosion values of samples after a combination of electroplating and DC sputtering deposition with zinc oxide (ZnO) and silver (Ag) nanoparticles.

TABLE 9. The corrosion values for the prepared samples

Samples	$I_{corrx}10^{-6}$ (mA/cm^2)	Corrosion Rate (mpy)	Corrosion resistance
Low carbon steel- 85% ZnO 15%Ag	5.2	0.0615	4.2
Low carbon steel- electroplating (Ni)- DC sputtering (85% ZnO+ 15% Ag	6.3	0.0735	5.1
Low carbon steel- electroplating (Cu)- DC sputtering (85% ZnO+ 15% Ag)	7.7765	0.00091228	2.8162
Low carbon steel- electroplating (Ni-Cu)- DC sputtering (85% ZnO+ 15% Ag)	5.5	0.064	4.8

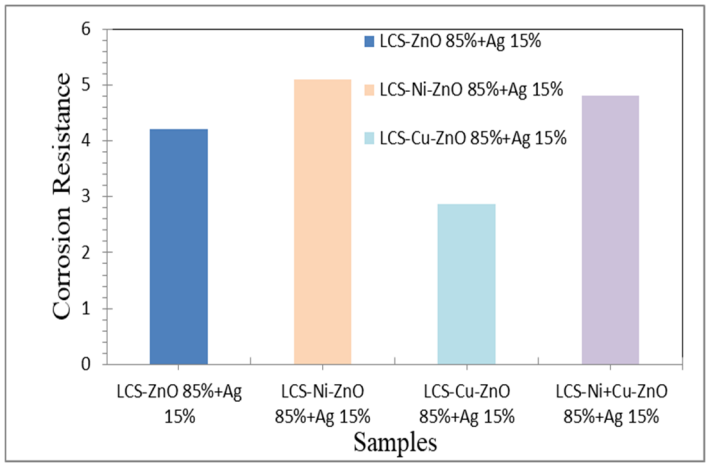

FIGURE 11. The corrosion resistance values for the samples in this work

The Figure shows that adding ZnO and Ag nanoparticles significantly improves the corrosion resistance of Lcs. Among the samples, the combination of electroplating with Ni and Cu followed by DC sputtering with ZnO and Ag provides the highest corrosion resistance. The electroplating (Cu) combined with DC sputtering (85% ZnO + 15% Ag) showed slightly higher corrosion current density but still maintained a relatively low corrosion rate, indicating a good overall resistance. The effectiveness of these coatings is evident from the reduced corrosion rate and improved corrosion resistance values. The presence of both Ni and Cu in the coating enhances the protective qualities, likely due to better surface coverage and reduced porosity, which is crucial in protecting the underlying steel from corrosive environments.

Energy dispersion spectrometry (EDX)

Containing zinc an investigation was conducted on a silver thin film that was coated with many layers of nickel and copper and then placed on an Lcs substrate. The process involves both quantitative and qualitative investigation into the micromultilayer composition of thin films. The chemical composition analysis of the produced system low carbon steel-Ni-Cu and Zn doping Ag is shown in Figure (5-16), which shows the EDS analysis of each layer element. This analysis is a good indicator for the existence of Ni, Cu, Zn, and Ag elements in this system.

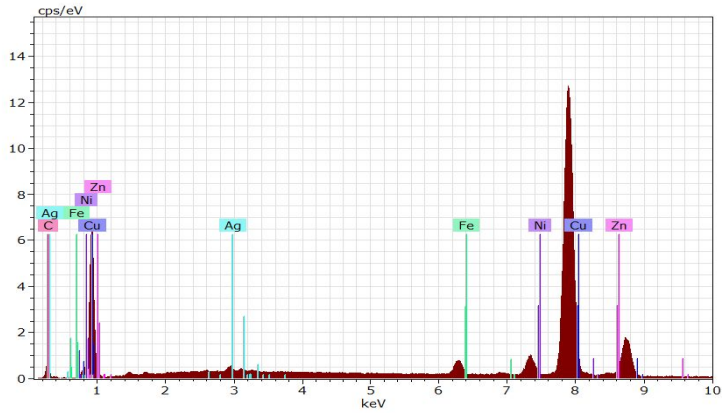

FIGURE 12. EDX of Ni-Cu-Zn doping Ag on Lcs

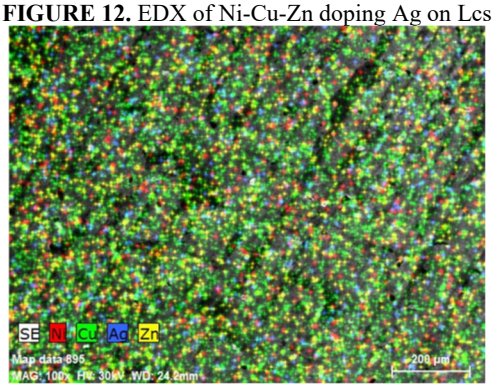

FIGURE 13. The EDS for deposit of Ni- Cu- Zn-Ag on low carbon steel substrate

The sample refers to Ni-Cu-Zn-Ag NP as shown in Figure 13 and Table 10.

TABLE 10. The results of EDX spectra

Element	Weight percentage (wt.%)	Atomic weight (at. (%))
O	10.22414183	6.355444607
Ni	7.174974001	4.207180119
Cu	4.600884171	2.058915622
Zn	22.05603546	37.61714192
Ag	55.94396454	49.76131773

The material analyzed through EDX consists predominantly of silver and zinc, with smaller amounts of oxygen, nickel, and copper. The high percentages of Ag and Zn suggest a material likely engineered for enhanced conductivity and corrosion resistance, with the presence of Ni and Cu potentially contributing to improved mechanical properties.Table 10 presents the results of EDX spectra, showing the weight percentage and atomic percentage of different elements (O, Ni, Cu, Zn, Ag) in a sample. Here is an interpretation and comparison of the data:

Weight Percentage (wt.%)

Oxygen (O): 10.22%, Nickel (Ni): 7.17%, Copper (Cu): 4.60%, Zinc (Zn): 22.06%, Silver (Ag): 55.94%. Silver (Ag) has the highest weight percentage at 55.94%, indicating that it is the predominant element in the sample by mass. Zinc (Zn) is the second most abundant element by weight at 22.06%, which aligns with its significant presence in the sample. Oxygen (O) constitutes 10.22% by weight, suggesting the presence of oxides or oxygen-containing compounds in the sample. Nickel (Ni) and Copper (Cu) are present in lower amounts, with weight

percentages of 7.17% and 4.60%, respectively. This indicates their relatively smaller contribution to the overall mass of the sample. The EDX analysis reveals that silver and zinc are the major components of the sample, with silver being the most abundant both by weight and by atomic percentage. Zinc follows, contributing significantly in both metrics but with a much higher atomic percentage due to its lower atomic mass compared to silver. Oxygen, nickel, and copper are present in smaller quantities. Oxygen's presence indicates possible oxide formation or contamination. Nickel and copper, while essential components, contribute minimally to the overall composition.

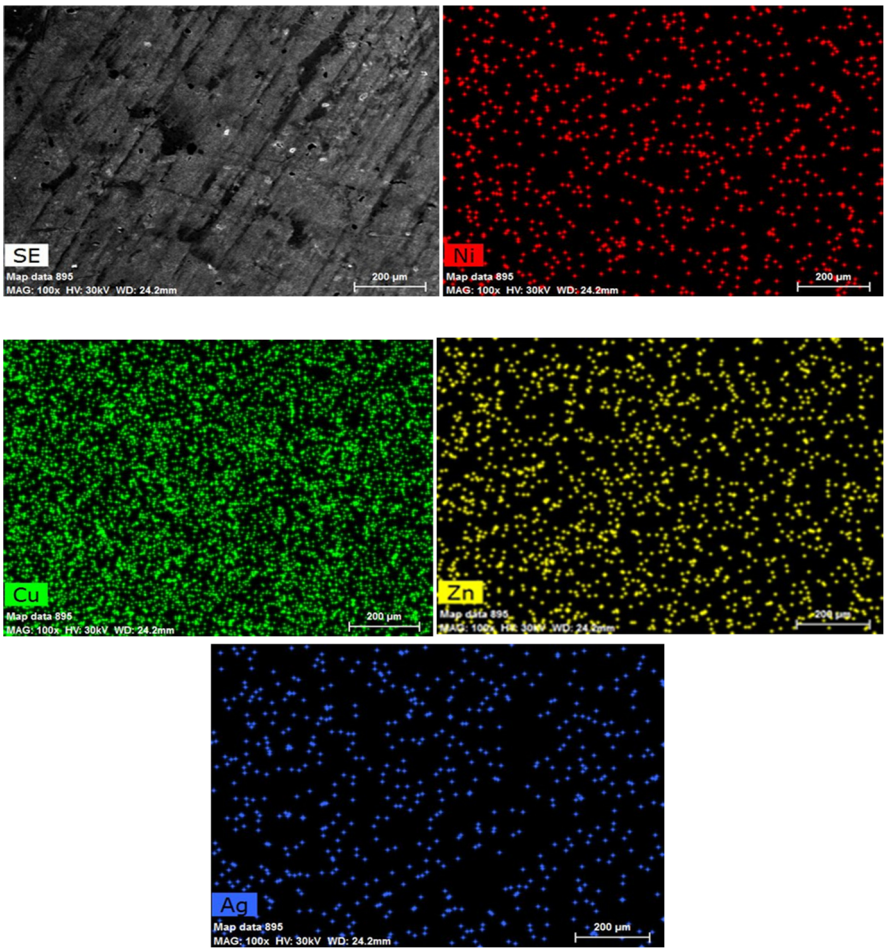

FIGURE 14. EDX images of samples Lcs, Ni, Cu, ZnO and Ag

Figure 14 shows the results of the EDX analysis for each layer element; this system's chemical composition analysis provides a good indicator for the existence of Na, Zn, and Ag elements.

Conclusions

The study highlights the significant effects of various coating techniques on the properties of low carbon steel. Initially, pure low carbon steel exhibits a baseline hardness value of 335.2 Hv. Coating with ZnO-Ag via DC sputtering reduces hardness, indicating a softer composite layer. Nickel electroplating followed by ZnO-Ag sputtering significantly enhances hardness, while copper electroplating followed by ZnO-Ag sputtering increases hardness but less effectively than nickel. Combining nickel and copper electroplating before ZnO-Ag sputtering offers a balanced hardness increase. In terms of roughness, untreated low carbon steel's baseline roughness of 0.876 Ra decreases to 0.709 Ra after 2 hours. DC sputtering with ZnO (95%) and Ag (5%) for 2 hours further reduces roughness to 0.572 Ra, indicating a smooth surface. Nickel electroplating followed by ZnO (95%) and Ag (5%) sputtering achieves a roughness of 0.775 Ra. ZnO (90%) and Ag (10%) sputtering results in a roughness of 0.589

Ra, with nickel electroplating followed by the same sputtering reducing it to 0.388 Ra. Copper electroplating followed by ZnO (85%) and Ag (15%) sputtering achieves the lowest roughness of 0.2043 Ra, although variability is noted, emphasizing the need for process control.

In corrosion resistance, ZnO and Ag nanoparticles significantly enhance low carbon steel's resistance, reducing corrosion current and rate. Nickel electroplating followed by ZnO 90%-Ag 10% sputtering shows the lowest corrosion current and highest resistance, outperforming other samples. Copper electroplating followed by ZnO-Ag sputtering improves resistance but is less effective than ZnO-Ag sputtering alone. Combining electroplating with Ni and Cu followed by ZnO-Ag sputtering significantly enhances corrosion protection, highlighting the importance of coating material and process selection.

REFERENCES

1. N. Assoudi et al., "Comparative examination of the physical parameters of the sol gel produced compounds La0.5Ag0.1Ca0.4MnO3 and La0.6Ca0.3Ag0.1MnO3," Optical and Quantum Electronics, vol. 54, no. 9, Jul. 2022, doi: https://doi.org/10.1007/s11082-022-03927-x.
2. H. Wang, B. Xu, and J. Liu, "Micron-nano MoS2 Solid Lubrication Film," Springer eBooks, pp. 207–264, Jan. 2012, doi: https://doi.org/10.1007/978-3-642-23102-5_5.
3. A. K. Singh, None Lipika, and Reeta Rani Singhania, "Nature-Inspired Sustainable Superhydrophobic/Superoleophobic Coatings for Emulsified Oil/Water Separation," pp. 338–364, Feb. 2024, doi: https://doi.org/10.1002/9781394207305.ch12.
4. R. Rajesh, M. V. Kulkarni, B. R. Vergis, P. Sampathkumaran, and S. Seetharamu, "Copper nickel alloys made using direct metal laser sintering method for assessing corrosion resistance properties," Materials Today: Proceedings, vol. 49, pp. 703–713, 2022, doi: https://doi.org/10.1016/j.matpr.2021.05.178.
5. Liu, X., Jin, P., Shu, Z., Yang, Y., Gui, B., Cui, Q., ... & Zheng, J. (2024). Regulating the structure and performance of amorphous carbon-based films by introducing different interlayers for applications in PEMFC bipolar plates. Surface and Coatings Technology, 131000.
6. Ijaodola, O., Ogungbemi, E., Khatib, F. N., Wilberforce, T., Ramadan, M., El Hassan, Z., ... & Olabi, A. G. (2018). Evaluating the effect of metal bipolar plate coating on the performance of proton exchange membrane fuel cells. Energies, 11(11), 3203.
7. J. Halling, "The Tribology of Surface Coatings, Particularly Ceramics," Proceedings of the Institution of Mechanical Engineers, Part C: Journal of Mechanical Engineering Science, vol. 200, no. 1, pp. 31–40, Jan. 1986, doi: https://doi.org/10.1243/pime_proc_1986_200_091_02.
8. Dini, J. W. (1997). Properties of coatings: Comparisons of electroplated, physical vapor deposited, chemical vapor deposited, and plasma sprayed coatings. Material And Manufacturing Process, 12(3), 437-472.
9. Mwema, F. M. (2019). Thin Film Coating: Characterizing the Evolving Properties of Aluminium Thin Films Prepared via RF Magnetron Sputtering (Master's thesis, University of Johannesburg (South Africa)).
10. Pathan, T. S. (2017). Development and Characterisation of Functionally Coated Steel as a Bipolar Plate Material for Polymer Electrolyte Membrane Fuel Cells (Doctoral dissertation, UCL (University College London)).
11. M. Rasheed, Suha Shihab, O. Alabdali, and H. H. Hassan, "Parameters Extraction of a Single-Diode Model of Photovoltaic Cell Using False Position Iterative Method," Journal of Physics: Conference Series, vol. 1879, no. 3, p. 032113, May 2021.
12. S. Wannarumon, E. L. J. Bohez, and K. Annanon, "Aesthetic evolutionary algorithm for fractal-based user-centered jewelry design," Artificial Intelligence for Engineering Design, Analysis and Manufacturing, vol. 22, no. 1, pp. 19–39, Dec. 2007, doi: https://doi.org/10.1017/s0890060408000024.
13. Valova, E., Georgieva, J., Armyanov, S., Avramova, I. V. A. L. I. N. A., Dille, J., Kubova, O., & Delplancke-Ogletree, M. P. (2010). Corrosion behavior of hybrid coatings: Electroless Ni–Cu–P and sputtered TiN. Surface and Coatings Technology, 204(16-17), 2775-2781.
14. N.-W. Li, Y.-X. Yin, S. Xin, J.-Y. Li, and Y.-G. Guo, "Methods for the Stabilization of Nanostructured Electrode Materials for Advanced Rechargeable Batteries," Small methods, vol. 1, no. 6, pp. 1700094–1700094, May 2017, doi: https://doi.org/10.1002/smtd.201700094.
15. Wang, Z., & Zhang, S. (2023). Research and application progress of high-entropy alloys. Coatings, 13(11), 1916.
16. M. Rasheed, S. Shihab, O. Y. Mohammed, and A. Al-Adili, "Parameters Estimation of Photovoltaic Model Using Nonlinear Algorithms," Journal of Physics: Conference Series, vol. 1795, no. 1, p. 012058, Mar. 2021.

17. X. Chen et al., “Influence of cutting speed on fretting wear properties of UVAM-processed NAB alloy,” Materials characterization, vol. 185, pp. 111711–111711, Mar. 2022, doi: https://doi.org/10.1016/j.matchar.2021.111711.

A comparison of some robust methods and quantile regression

Rabab Abdulrida Saleh [(a)], Iqbal Mahmood alwan [(b)]

Department of Statistics, College of Administration and Economics, University of Baghdad, Baghdad, Iraq

[(a)] Corresponding Author Email: rabab.saleh@coadec.uobaghdad.edu.iq
[(b)] Iqbal.alwan@coadec.uobaghdad.edu.iq

Abstract. Regression analysis is considered one of the most important statistical methods in analyzing data. It builds a statistical model to estimate the relationship between the response variable and a variable or a group of explanatory variables. To estimate the regression model, basic assumptions must be available so that the estimator can be the best unbiased linear estimate and that the data does not include outliers. if they exist It affects the estimation and makes the estimates incorrect, making them useless. In this research, some robust methods were used, including (the M-estimation; S-Estimation, and Quantile regression) methods. The above techniques have been applied to yellow corn production data in Iraq, which contained some outliers. It was found that the M method is the best because it has the least Sum Squared Error.

Keywords: Regression; Robust Methods; M-Estimation; S-Estimation; Quantile regression

INTRODUCTION

The ordinary least squares method is an important application in regression analysis. It depends on minimizing the sum of the squares of the deviations between the expected values and the actual values. The application of this method depends on basic assumptions that must be fulfilled, which are that the error is normally distributed with a mean of zero and a constant variance, and there is no correlation between the random errors and the explanatory variables are not related to each other, that is, the variables are orthogonal. Also, there are no outliers, and if one of these hypotheses is missing, estimating coefficients using ordinary least squares becomes useless, because it gives unreliable estimates. In the case of the presence of outliers, we resort to using robust methods. We can show some similarity between outliers and skewed normal distribution, although they represent different concepts in statistics and data analysis. Outliers are where some values of the data are very far from the rest of the data, leading to deviation from the normal shape. The normal distribution is skewed, it is skewed (to the right or left) from the standard normal distribution, which leads to distortion of the standard normal shape. Therefore, we cannot use methods that rely on certain assumptions, such as the error is normally distributed. In 2021, researchers Al-Khafaji and Saleh presented a study on the skewed normal distribution, through which they explained The symmetrical normal distribution is the most common in theory, but in practice, we find that the data is not normally distributed, and the reason is that the presence of a deviation in the data or the presence of extreme values causes the data to deviate from the normal distribution, and this deviation is responsible for the shape Distribution, and most life phenomena contain a percentage of deviation. In 2022, researchers Rasheed and Saleh studied robust methods using an exponential regression model with three parameters, and the methods were compared (MOM, forward search, least absolute). Combine them with ordinary least squares, using simulations and different sample sizes, and apply them to data that contain outliers. In the same year, researchers Bahez and Rasheed used some non-parametric methods to estimate the semi-parametric robust regression model, and a comparison was made between the methods (S-estimation -local smoothing, M- Estimation - local smoothing, S-Estimation-Nadarya - Watson Smoothing, M-Estimation-Nadarya-Watson Smoothing) using

Technologies and Materials for Renewable Energy, Environment and Sustainability
AIP Conf. Proc. 3321, 020043-1–020043-7; https://doi.org/10.1063/5.0289814
Published under an exclusive license by AIP Publishing. 978-0-7354-5231-2/$30.00

simulations of different dimensions and sizes. The results showed that the strong S-estimation -local smoothing method is better for large sample sizes and the M- M-estimation -local smoothing method is better for small sample sizes. In this research, a comparison will be made between some powerful methods (M estimation, S estimation, and quantile regression). For real data on yellow maize crop production in Iraq, it turns out that M methods are the best using statistical criteria.

Robust M-estimation

This method is one of the most used impregnable methods due to the high efficiency of the estimators obtained with the method of least squares, which is a strong method for the presence of outliers in the values of the dependent variable (variable response) [3],[9]. Still, it is not vulnerable to the presence of lifting points, and I have described the M estimators as an extension of the greatest potential estimates. The following relationship describes the multiple linear regression model [2]:

$$Y_i = \beta_0 + \beta_1 X_{i1} + \beta_2 X_{i2} + \ldots + \beta_k X_{ik} + \varepsilon_i \quad (1)$$
$$i = 1,2,3,\ldots,n$$

The process of estimating the model is based on the least square's method according to the method of matrices and the following relationship [6]:

$$\hat{\beta} = (X'X)^{-1}X'Y \quad (2)$$

x: matrix of independent variables whose first column is equal to one with $n\ x\ p$
y: is the dependent variable vector and is with dimensions n x 1
The general M estimator minimizes the objective function described for the model errors in the following formula:

$$\sum_{i=1}^{n} \rho(r_i) = \sum_{i=1}^{n} \rho(Y_i - X_i' b) \quad (3)$$

In the case of using the Ordinary least squares method to estimate the parameters of the above model, the error function is described

$$\rho(r_i) = r_i^2 \quad (4)$$

This function is differentiable according to ρ′=ψ, and the derivation of the target function is relative to the parameters of the model by placing partial derivatives equal to zero, resulting in a system of estimated equations for the parameters of the model:
Let the weight function be W(ui) = ψ (ui)/ ui which is: ui =r_i/s
And W (ui) A weight function with model errors, and let it be Wi=W(ui) Therefore, the estimated equations can be written in terms of weights as follows [4]:

$$\sum_{i=1}^{n} W_i((Y_i - X_i' b)/S)X_i' = 0 \quad (5)$$

The solution of estimated equations is through the method of iteratively reweighted least-squares (IRLS), and requires the implementation of the estimation process with a set of repetitive steps according to the following:

$$b^{(\wedge)} = [X'W^{(t-1)}X]^{-1}X'W^{(t-1)}Y \quad (6)$$

After adopting the least squares estimates as prime values for the parameters and depending on the repetition, the weights are adjusted according to multiple selected functions, meaning that the calculation of the matrix of country weights is as follows [10]:

$$W^{(t-1)} = diag[W_i^{(t-1)}] \quad (7)$$

Robust S-estimation

The estimators: were described by (Rousseeuw, Yohai) in 1984 in the following form [11]:

$$\hat{\theta}_S = \underset{\theta}{argmin} S(\theta) \quad (8)$$

where S(θ) represents the dispersion and in terms of parameters are described as:

$$\frac{1}{n-p}\sum_{i=1}^{n} X\left(\frac{Yi - X'i\theta}{S}\right) = \beta \quad (9)$$

The breakpoint to S(θ) is estimated by:

$$\frac{\beta}{max_s X(s)} \quad (10)$$

Where there are several functions to choose χ from the following Tukey function: [5]

$$Xk_0(s) = \begin{bmatrix} 3(\frac{s}{k_0})^2 - 3(\frac{s}{k_0})^4 + (\frac{s}{k_0})^6 & if|s| \le k_0 \\ 1 & otherwise \end{bmatrix} \quad (11)$$

Where k_0 represents the cut-off point and its initial value and controls the nature of the S estimators

Quantile regression models

Quantile regression models represent the relationship between a set of explanatory variables and specific percentages (or "quantiles") of the response variable, often the mediator. They have two main advantages over ordinary least squares regression models [7]:

a- Quantile regression makes no assumptions about the distribution of the response variable.

b- It resists the presence of the influence of extreme observations.

Quantile regressions are widely used in health, environmental, agricultural, industrial, and financial economics research. The main advantage of quantile regressions over ordinary least squares regressions is that they are resistant to extreme values in response measures. However, they are useful when conditional quantile functions are of interest. Different measures of central tendency and statistical dispersion can be used to analyze the relationship between variables more comprehensively. The linear regression model for calculating the mean takes the form of Equation (1): [8], [1]. The mean square error is with the equation:

$$MSE = \frac{1}{n}\sum_{i=1}^{n}(Y_i - \hat{Y})^2 \quad (12)$$

For quantile regression, the median can calculate any quantile (percentage) for a particular value in the feature's variables. Taking a similar structure to the linear regression model, the quantile regression model equation for the τth quantile is:

$$Q_r(Y_i) = \beta_0(\tau) + \beta_1(\tau)X_{i1} + \ldots + \beta_p(\tau)X_{ip} \quad (13)$$

This means that the beta coefficients now operate in percentage terms rather than being constants. Finding the values of these betas at a given quantity involves roughly the same process as in regular linear quantization, except that we now have to minimize the mean absolute deviation.

$$MAD = \frac{1}{n}\sum_{i=1}^{n}\rho_\tau\,(\,Y_i - (\beta_0(\tau) + \beta_1(\tau)X_{i1} + \ldots + \beta_p(\tau)X_{ip})) \quad (14)$$

Here the function ρ is the check function which gives asymmetric weights to the error depending on the quantile and the overall sign of the error. Mathematically, ρ takes the for

$$\rho_\tau(u) = \tau\, max(\,u, 0) + (1 - \tau)\, max(\,-u, 0) \quad (15)$$

In this case, u is the error of a single data point and the max function returns the largest value between the parentheses. If the error is positive, the check function multiplies the error by τ, and if the error is negative, the check function multiplies the error by (1-τ).

The practical side

In this aspect, data were taken from the Central Statistical Organization from 1949 to 2019 about the production yield rate of the maize crop in Iraq represented by the dependent variable, and the area harvested by the explanatory variable to estimate the production yield rate. Some robust methods were used, represented by M-estimation; S-estimation; and Quantile regression. A test was conducted on existing outliers' values of the dependent variable using the box plot, and after confirming the existence of the outliers, the methods mentioned above were applied

RESULTS ANALYSIS AND DISCUSSION

The data was analyzed using some robust methods and quantitative regression to estimate the yield rate of maize production. A comparison was made between the methods using R-squared, S.E. of regression, Sum squared error, and the results were as follows; -

The Result of Robust M-estimation and Discussion

In this method use the weight = Bi Square, tuning =4.685, scale=median centered.
and the results in Table (1).

Table (1) Robust estimates for M method

Variable	*Coefficient*	St. Error	Z-Statistic	Prob.
B0	*273.7542*	25.76610	10.62459	0.0000
the area harvested(B1)	*0.000679*	7.70E-05	8.810534	0.0000
R-squared	*Adjusted R-squared*	S.E. of regression	Sum Squared Error	F
0. 411128	*0.402593*	229,4147	3631547	46.499

Through the table above, it is clear that the harvested area, if increased by one unit, will lead to an increase in production by 0.000679, and the significance of both the marginal slope and the fixed limit is shown, where the probability value was 0.0000, which is less than 0.05, and the value of the determination coefficient was 0.411128, which means that the independent variable (Harvested area (explained by 0.411128 of the total changes in the rate of production yield)

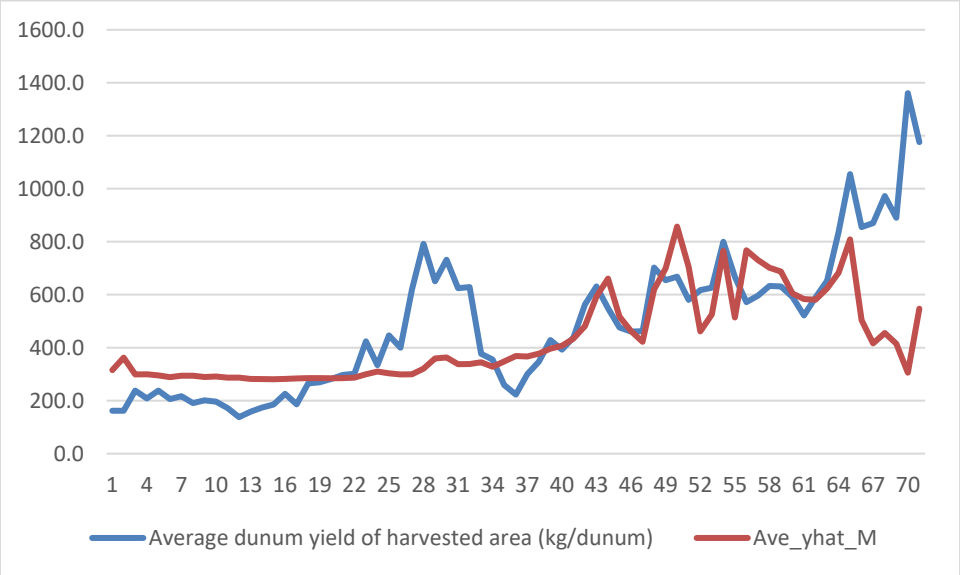

Figure (1) shows the real and estimated value of the production yield rate variable for the M method

The Result of Robust S-estimation and Discussion

In this method use the S settings: tuning=1.547645, breakdown=0.5, trials=200, subsmpl=2, refine=2, compare=5 Random number generator: rng=kn, seed=325418823 and the results are as in Table (2).

Table 2: Robust estimates for the S method

Variable	*Coefficient*	St. Error	Z-Statistic	Prob.
B0	*214.5232*	22.08052	9.715499	0.0000
the area harvested(B1)	*0.000761*	6.60E-05	11.52853	0.0000
R-squared	*Adjusted R-squared*	S.E.of regression	Sum squared Error	F
0.561291	*0.554933*	244.4969	4124734	86.03

Through the table above, it is clear that the harvested area, if increased by one unit, will lead to an increase in production by 0.000761, and the significance of both the marginal slope and the fixed limit is shown, where the probability value was 0.0000, which is less than 0.05, and the value of the determination coefficient was 0.561291, which means that the independent variable (Harvested area (explained by 0.561291 of the total changes in the rate of production yield)

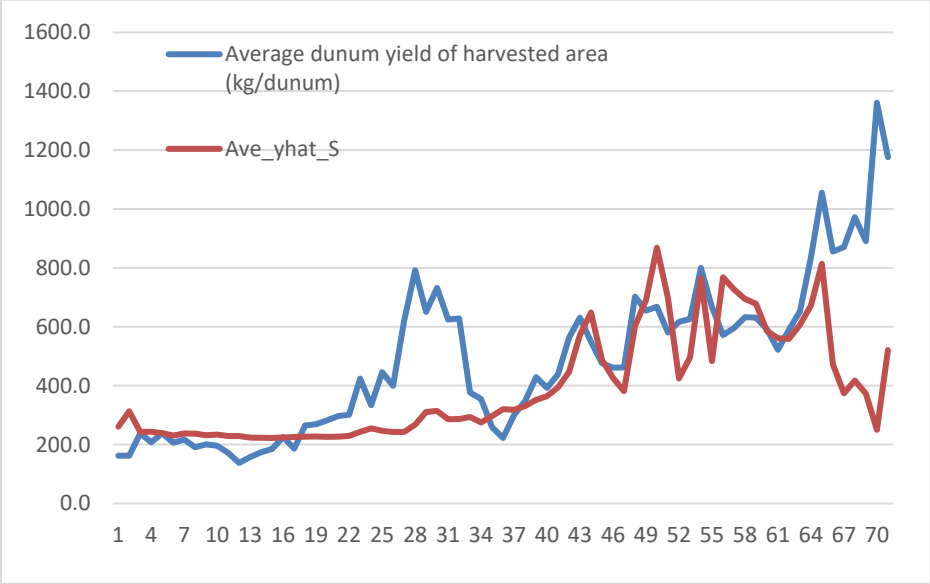

Figure No. (2) shows the real and estimated value of the production yield rate variable for the S method

The Result of Quantile Regression and Discussion

In this method, Quantile Regression (Median) Sparsity method: Kernel (Epanechnikov) using residuals Bandwidth method: Hall-Sheather, bw=0.23463, and the results were as in Table 4.

Table (3) Robust estimates for the Quantile Regression method

Variable	*Coefficient*	St. Error	Z-Statistic	Prob.
B0	*256.7814*	33.92616	7.568832	0.0000
the area harvested(B1)	*0.000736*	0.000119	6.188346	0.0000
Pseudo R-squared	*Adjusted R-squared*	S.E.of regression	Sum squared Error	F
0.333406	*0.323745*	231.5013	9758873	33.03

Through the table above, it is clear that the harvested area, if increased by one unit, will lead to an increase in production by 0.000736, and the significance of both the marginal slope and the fixed limit is shown, where the probability value was 0.0000, which is less than 0.05, and the value of the determination coefficient was 0.333406, which means that the independent variable (Harvested area (explained by 0.333406 of the total changes in the rate of production yield)

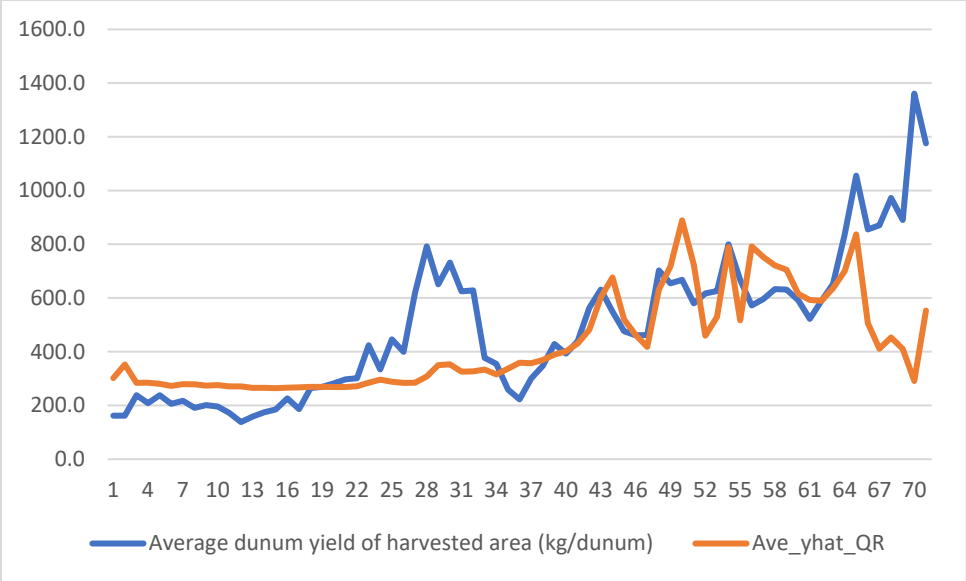

Figure No. (3) shows the real and estimated value of the production yield rate variable for the QR method

CONCLUSION

Through the above results, it was confirmed that there are outliers' values in the data of the dependent variable, and the robust methods were applied with Quantile regression.

It turned out that the best method was the robust M method due to obtaining the least sum of squares error and the least values for the standard deviation of the regression coefficients estimates in the model.

All modalities had significant regression coefficients which means that the assumed linear relationship of the maize yield rate is significant,

It is clear from the graphic forms of the estimated and real values that all the methods were similar and close to the real values, and the best way for the robust M method, and this confirms the provision of accurate and reliable estimates for estimating the rate of maize production yield. then the S methods, and the last Quantile regression.

From the results, it was found that the explanatory power of the S model was the best because it had the highest coefficient of determination

REFERENCES

1. 1-ALkhafaji, A.A. and Saleh, R.A. (2021) (A statistical study on the parameters of the Skew Normal distribution depending on the use of the genetic algorithm using the simulation method. Journal of physics conference series, doi:10.1088\1742-6596\1879\3\032017.
2. 2--Bahez,KH.Zahraa and Rasheed,H.A.(2022)(comparing some of robust the non-parametric methods for semi-parametric regression models estimation. journal of economics and administrative sciences (JEAS), vol .28(no.132), pp 105-117.
3. 3-De Menezes, Diego Q.F. (2021). "A review on robust M-estimators for regression analysis". Computers & Chemical Engineering. 147 (1): 107254. doi: 10.1016/j.compchemeng.2021.107254. S2CID 232328341.
4. 4-Huber, P.J. (1964)."Robust Estimation of location parameter.Ann.Math.Statist., 35,73-101.
5. 5-HUBER, P.J. (1981). Robust Statistics. Wiley, New York.
6. 6-Irashyyid, and Saleh. A.,2022. (Robust Estimation for one–parameter exponential Regression Model). journal of economics and administrative sciences (JEAS), vol .28(no.134), pp 147-159.
7. 7-Khadijah Iddrisu, Joshua Yindenaba Abor, Kannyiri T. Banyen. **2022.** Fintech, foreign bank presence and inclusive finance in Africa: Using a quantile regression approach. *Cogent Economics & Finance.*
8. 8-Koenker, Roger and Kevin F. Hallock. (2001) "Quantile Regression". Journal of Economic Perspectives, Volume 15, Number 4, Pages 143–156.

9. 9-Maronna, R. A., Martin, R. D. and Yohai, V. J. (2006), Robust Statistics. John Wiley.
10. 10-Montgomery, D. C., Peck, E. A. and Vining, G.G., (2001)," Introduction to Linear Regression Analysis", 3rd ed, Wiley, New York.
11. 11-Rousseeuw, P.J., and A. Leroy, (1987)" *Robust Regression and Outlier Detection",* Wiley, New York, 1987.

A study of sustainable polyester composites incorporating recycled materials

Khulood Ibrahim Dawood, Atheed Habeeb Taha Al-Temimi, Nuha Hadi Jasim Al Hasan [a)], Haider Maath Mohammad, Safaa A. S. Almtori

Department of Engineering Materials, College of Engineering, University of Basrah, Basrah, Iraq.

[a)] Corresponding author: nuha.jasim@uobasrah.edu.iq

Abstract. This research aimed to produce composite materials using three distinct base of a polyester- Poly(methyl methacrylate) and Poly(methyl methacrylate) PMMA in order to enhance their mechanical properties by blend with different weight ratios of glass fibers and steel mesh. The study focuses on evaluating the hardness, elastic modulus and thermal properties of the samples and comparing their properties. Hardness tests demonstrated an increase in hardness with higher doping ratios. Polyester reinforced with glass fibers, steel mesh, and a combination of both demonstrates improved an increase in hardness with higher ratios additions of glass fiber and steel mesh in different number of layers. Similarly, PMMA reinforced with glass fibers and steel mesh provides increased harness and elastic modulus, with a hybrid combination offering optimal performance.

INTRODUCTION

Composite materials are used in a wide range of applications, due to their mechanical and thermal properties. Different materials used as a reinforcement such as fibers continuous, fiber discontinuous, and particles which can randomly arranged or in adding as layers. Hybrid composites of different addition E-glass in resin are significant because of their durability and impact resistance, [1-3].

Zhang, et al. [4] developed a composite of unsaturated polyester resin, reinforced in order to enhance the toughness of a novel hybrid.

Sezavar, et al. [5] improved mechanical properties of PMMA with alumina nanoparticles. Hasan, et al.[6] observed that tensile strength, impact resistance, and thermal conductivity of an polyester-E-glass mix increased with using gamma radiation. El-Wazery et al. [7] studied polyester composites reinforced with glass fibers, finding improved mechanical properties of glass fiber at 60 wt.% of fabricated composites.

Singh and Rajamurugan [8] noted increased flexural strength in polyester composites with steel mesh. Rahman et al. [9] reported enhanced impact resistance in PMMA-glass fiber composites. Aranha et al. [10] found improved mechanical properties glass fiber Polyester composites, while jute fiber polyester composites demonstrated decrease in mechanical properties. Ravishankar et al. [11] observed improved impact properties in PMMA with polypropylene fibers. Gad et al. [12] enhanced PMMA with various nanoparticles and fibers, improving mechanical properties. Zhang [13] and Jagger et al. [14] reported improved Young's modulus and reduced crack propagation in PMMA with glass beads and carbon fibers.

Aykaç [15] improved bone cement with carbon fibers, noting increased tensile strength and impact performance. Shi et al. [16] enhanced fracture toughness in PMMA with aramid fibers.

Tomar and Gope [17] used metal fibers to reinforce PMMA, achieving significant tensile strength improvements.

Demir et al. [18] reported improved mechanical properties in polyester and epoxy composites with glass fibers and alumina particles. Nemati et al. [19] developed polymer-reinforced composites in order to study thermal properties. Abbas et al. [20] improved mechanical properties of PMMA nanocomposites.

This study investigates the hardness, elastic modulus and thermal properties of polymer matrix composites reinforced with glass fiber and steel mesh. Additionally, the research aims to compare these properties across different reinforcement ratios to gain improvement into their performance characteristics.

Technologies and Materials for Renewable Energy, Environment and Sustainability
AIP Conf. Proc. 3321, 020044-1–020044-15; https://doi.org/10.1063/5.0289771
Published under an exclusive license by AIP Publishing. 978-0-7354-5231-2/$30.00

EXPERIMENTAL WORK

Materials

i- PMMA resin which is a transparent viscous liquid at room temperature. It solidifies by adding the hardener, which is a powder that is added to the resin at a ratio of (0.01) grams per (1 gram) of PMMA. was used due to its properties of hardness and resistance to scratching.
ii- Polyester Resin is a sticky transparent liquid material with a yellow color, as every (75 grams) of resin is added to it (0.45 grams) of hardener, and they are mixed at room temperature. It was used due to its properties of low cost and resistance to weathering and aging
iii- Glass Fiber is a completely natural material, ecologically clean and harmless to human health, used in the form of a continuous fiber which were cut into pieces with dimensions of (24 cm, 1.5 cm). It used due to its properties of resistance to chemical and biological effects.
iv- Mineral Fibers (Steel meshes) were also used in the form of a continuous fiber with the same dimensions as the glass fibers.

Wood Mold Preparation

The preparation of the mold requires a time if the container must be provided for the material because the material is in a liquid state and it is not easy to handle it because this results in the loss of part of the weight of the material during its transfer from one container to another, so the mold is prepared before starting the process of processing the composite material for the purpose of unloading it directly from the container to the mold, and therefore the preparation of the mold is as following steps:
i. Put the mold on a fixed table.
ii. Cut an appropriately sized piece of aluminum foil for the purpose of wrapping the mold to prevent the composite material from sticking to the mold.
iii. Gluing the outer edges of the aluminum foil used to wrap the mold to the mold to prevent the movement of wrapping paper during casting by using electric tape black or any available adhesive reinforcement Preparation.

Preparing the composite specimens

Which were used in the form of continuous fibers, and therefore it requires a cutting process with dimensions suitable for the internal dimensions of the mold and be less than its dimensions by 1mm for the purpose of entering it freely and avoiding contact between the walls of the mold and the reinforcement, which results in difficulty in introducing the reinforcement into the mold.

Table 1. Description of specimens

item	Composites	No. of layer	Descriptions
1PG	Polyester reinforced with glass fibers	0	38g resin + 0.22g hardener, mix, pour into mold, solidify, remove from mold, clean edges with sandpaper
2PG		One	38g resin + 0.22g hardener, mix, pour part into mold, insert 2g glass fiber, pour remaining mixture, solidify, weigh, calculate fiber percentage
3PG		Two	38g resin + 0.22g hardener, mix, pour part into mold, insert 3g glass fiber, pour remaining mixture, solidify, weigh, calculate fiber percentage
4PG		Three	38g resin + 0.22g hardener + 9g fiberglass, mix, pour into mold with 6 pieces of fiber, solidify, weigh, calculate fiber percentage
5PG		four	38g resin + 0.22g hardener + 10.17g fiberglass, mix, pour into mold with 8 pieces of fiber, solidify, weigh, calculate fiber percentage
1PS	Polyester reinforced	0	38g resin + 0.22g hardener, mix, pour into mold, solidify, remove from mold, clean edges with sandpaper

2PS	with steel mesh	One	38g resin + 0.22g hardener, mix, add 1.81g mineral fiber, pour into mold, solidify, remove appendages, weigh, calculate fiber percentage
3PS		Two	38g resin + 0.22g hardener, mix, pour part into mold, insert 2.13g metallic fiber, pour remaining mixture, solidify, weigh, calculate fiber percentage
1PGS	Polyester reinforced with combination glass fibers and steel mesh	0	38g resin + 0.22g hardener, mix, pour into mold, solidify, remove from mold, clean edges with sandpaper
2PGS		One layer of glass fiber and steel mesh	38g resin + 0.22g hardener, mix, cut 1.43g steel mesh, 1.81g fiber, pour into mold with fiber, solidify, weigh
3PGS		Two layer of glass fiber and steel mesh	38g resin + 0.22g hardener, mix, cut 3g steel mesh, 1.5g fiber, pour into mold with fiber, solidify, weigh
1PMG	PMMA reinforced with glass fibers	0	19g PMMA resin + 0.11g and 0.19g hardener
2PMG		One layer of glass	38g resin + 0.38g hardener, mix, pour part into mold, insert 1.5g fiber, pour remaining mixture, solidify, weigh, calculate fiber percentage
3PMG		One layer of glass	38g resin + 0.38g hardener, mix, pour part into mold, insert 3.29g fiber, pour remaining mixture, solidify, weigh, calculate fiber percentage
4PMG		One layer of glass	38g resin + 0.38g hardener, mix, pour part into mold, insert 10.38g fiber, pour remaining mixture, solidify, weigh, calculate fiber percentage
1PMS	PMMA reinforced with steel mesh	One	19g PMMA resin + 0.11g and 0.19g hardener
2PMS		Two	38g resin + 0.38g hardener, mix, cut 1.43g mineral fiber, pour into mold, solidify
3PMS		Three	38g resin + 0.38g hardener, mix, cut 2.60g mineral fiber, pour into mold, solidify
1PMGS	PMMA reinforced with combination glass fibers and steel mesh	0	19g PMMA resin + 0.11g and 0.19g hardener
2PMGS		One layer of glass fiber+ One layer of steel	38g resin + 0.38g hardener, mix, cut 1.43g steel mesh and 1.5g fiber glass, pour into mold, solidify

3PMGS		Two layer of steel	38g resin + 0.38g hardener, mix, cut 2.86g steel mesh and 3g fiber glass, pour into mold, solidify
1POPMG	Composite material made from (polyester +PMMA) reinforced with glass fibers	0	19g polyester resin + 19g PMMA resin + 0.11g and 0.19g hardener respectively, mix, pour into mold
2POPMG		One layer of glass fiber	19g polyester resin + 0.11g hardener + 19g PMMA resin + 0.19g hardener, mix, cut 1.29g fiber, pour into mold, solidify
3POPMG		Two layer of glass fiber	19g polyester resin + 0.11g hardener + 19g PMMA resin + 0.19g hardener, mix, cut 2.74g fiber, pour into mold, solidify
4POPMG		Six layer of glass fiber	19g polyester resin + 0.11g hardener + 19g PMMA resin + 0.19g hardener, mix, cut 8.89g fiber, pour into mold, solidify
1POPMS	Composite material made from (polyester +PMMA) reinforced with steel mesh		19g polyester resin + 19g PMMA resin + 0.11g and 0.19g hardener respectively, mix, pour into mold
2POPMS			19g PMMA resin + 0.19g hardener + 19g polyester resin + 0.11g hardener, mix, cut 1.17g fiber steel, pour into mold, solidify
3POPMS			19g PMMA resin + 0.19g hardener + 19g polyester resin + 0.11g hardener, mix, cut 5.39g steel mesh, pour into mold, solidify
1POPMGS	Composite material made from (polyester +PMMA) reinforced with combination glass fibers and steel mesh	0	19g polyester resin + 19g PMMA resin + 0.11g and 0.19g hardener respectively, mix, pour into mold
2POPMGS		One layer of glass fiber and steel mesh	19g polyester resin + 0.11g hardener + 19g PMMA resin + 0.19g hardener, mix, cut 1.58g fiber, cut 1.34g steel mesh, pour into mold, solidify
3POPMGS		Two layer of glass fiber and steel mesh	19g polyester resin + 0.11g hardener + 19g PMMA resin + 0.19g hardener, mix, cut 2.94g fiber, cut 2.13g steel mesh, pour into mold, solidify

Hardness test

Durometer measures the depth of an indentation made by a given force on a material. This depth depends on the material's hardness, viscoelastic properties, presser foot shape, and test duration. ASTM D2240 durometers assess initial hardness or indentation hardness over time.

The force applied should be 5 kg ±0.5 kg, without shock, and the material must be at least 6 mm thick. Hardness readings are taken after about three seconds, with at least three measurements on different specimen areas. Shore-D device measures hardness on a scale of 0 to 100, with higher numbers indicating harder materials.

Figure1 shore D device

Tension Test

Tensile testing of plastics and composites, following ASTM and ISO methods, measures the force to break a sample and its elongation. This generates stress-strain diagrams to determine tensile modulus. The test involves placing the specimen in a tensioning device until breakage. Data from these tests help optimize material selection, design, and quality control, Figure 2.

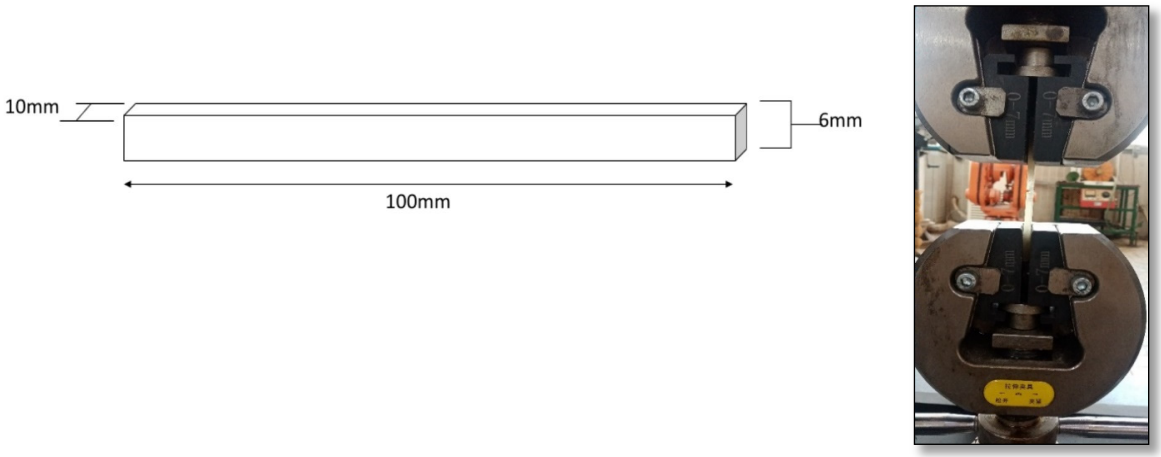

Figure 2 a. test specimen dimensions for tension test, b. tension test device

The modulus of elasticity for each sample was calculated according to the following equation:

$$S_{D=100-}\frac{20(-78.188+\sqrt{6113.36+781.88E})}{E}$$

Where: S_D is the ASTM D2240 type D harness, and E is in MPa.

Thermal conductivity

The test in the Department of Materials Engineering used a homemade device per British specification BS 4745 to calculate the thermal conductivity coefficient of pure and reinforced specimens.

Using Lee's disc method, the specimen was placed between two metal heat conductors to determine the coefficient of thermal conductivity, as shown in Figure 2.

$$K = \frac{k * d(T_2 - T_0)(T_1' - T_2')\acute{A}}{\acute{d}(T_2' - T_0')(T_1' - T_2)A}$$

Where: K = coefficient of thermal conductivity, T_o=23.6°C, k=0.23 w/m*k,,À=625 mm^2 , D'=2.6 mm^2
T'_2=62°C , T'_1=100°C , T'_o=28°C, A=Length*width*high , D=thickness of specimen

The specimen is an insulator. It is in the form of a thin rectangular with large cross-sectional area (A = L*W*H) compared to the area exposed at the edge in order to reduce the energy loss. The specimen used in the test with dimensions as shown in Figure 3.

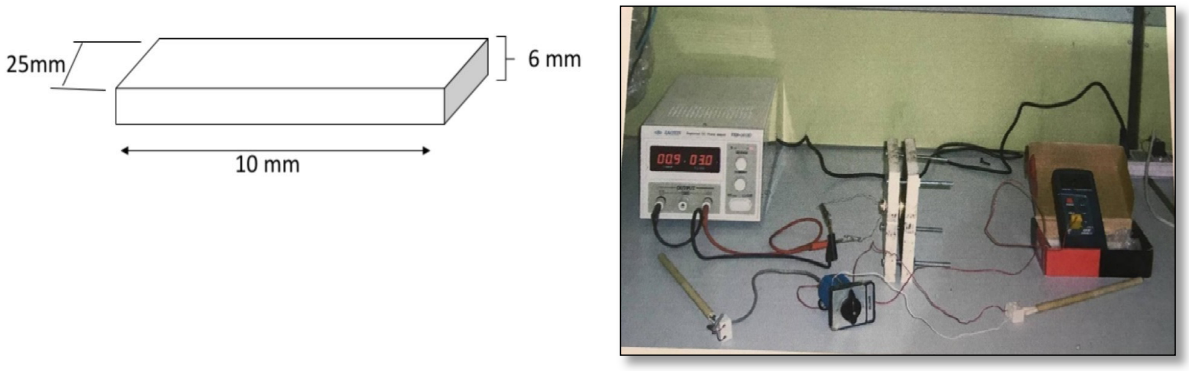

Figure 3. a. thermal conductivity testing device, b. Test specimen dimensions for thermal conductivity test

Results and discussions

Hardness test results

Polyester reinforced with glass fibers

Through the research, we notice that the hardness values have improved after reinforcing the polyester with the fibers, and this is due to the increase in crosslinking and stacking resulting from the crosslinking between the polyester and the glass fibers, which reduces the movement of the polymer particles and thus increases their hardness, which leads to an increase in their resistance.

For deformation, the hardness of the superimposed material increases with the increase in the percentage of added fibers , as shown in Figure 4a. The hardness values calculated at room temperature 25 m improved after polyester reinforcement.

The properties of glass fibers have high hardness and their ability to withstand the bulk of the stresses. This is because increasing the temperature leads to an increase in the ductility of the material due to the movement of the primary units and the loosening of the bonds between them, and this leads to a weakening of its resistance to scratching as shown in Figure 4a., it is clear that the highest value of hardness appeared in the sample reinforced with eight pieces of fiberglass.

Polyester reinforced with steel mesh

The hardness values have improved after reinforcing the polyester with steel. The hardness of the reinforced material increases with the increase in the percentage of added steel, as shown in Figure 4b.

The hardness values when reinforced with steel are much higher than the values of reinforcement using glass fibers, due to the high hardness values of steel compared to glass fibers. From the Figure 4b, it is clear that the highest value of hardness appeared in the sample reinforced with two pieces of steel mesh.

Polyester reinforced with combination glass fibers and steel mesh

The hardness values have improved after reinforcing the composite with combination of steel and glass fibers. The hardness increases with the increase in the percentage of added fibers, as shown in Figure 4c. From the Figure 4c, it is clear that the highest value of hardness appeared in the sample reinforced with two pieces of combination of 2(fiberglass and steel mesh).

PMMA reinforced with glass fibers

The hardness values have improved after reinforcing the PMMA with the fibers. The hardness of the reinforced material increases with the increase in the percentage of added fibers , as shown in Figure 4d . From the table it is clear that the highest value of hardness appeared in the sample reinforced with six pieces of fiberglass.

PMMA reinforced with steel mesh

The hardness of the reinforced material increases with the increase in the percentage of added fibers , as shown in Figure 4e. The hardness values improved after PMMA reinforcement The properties of steel have high hardness Higher than glass fibers and their ability to withstand the bulk of the stresses also Therefore, the hardness in the case of using steel is greater than in the case of using glass fiber
We also notice from the diagrams that the value of PMMA hardness is higher than polyester and therefore the increase in its hardness is much higher than in polyester.
We also notice from the diagrams that the value of PMMA hardness is higher than polyester and therefore the increase in its hardness is much higher than in polyester. From the Figure 4e, the highest value of hardness appeared in the sample reinforced with two pieces of steel mesh.

PMMA reinforced with combination glass fibers and steel mesh

The hardness values have improved after reinforcing the composite with combination of steel and glass fibers. The hardness increases with the increase in the percentage of added fibers, as shown in Figure 4f., it is clear that the highest value of hardness appeared in the sample reinforced with eight pieces of combination of 2(glass fiber +steel mesh).

Composite material made from (polyester +PMMA) reinforced with glass fibers

The hardness of the superimposed material increases with the increase in the percentage of added fibers, as shown in Figure 4g. The hardness values improved after composite reinforcement; it is clear that the highest value of hardness appeared in the sample reinforced with six pieces of fiberglass.

Composite material made from (polyester +PMMA) reinforced with steel mesh

The hardness of the composite material increases with the increase in the percentage of added steel mesh, as shown in Figure 4h. The hardness values improved after composite reinforcement; it is clear that the highest value of hardness appeared in the sample reinforced with two pieces of steel mesh.

Composite material made from (polyester +PMMA) reinforced with combination glass fibers and steel mesh

The hardness values have improved after reinforcing the composite with combination of steel and glass fibers. The hardness of the composite material increases with the increase in the percentage of added fibers , as shown in Figure 4i. The hardness values improved after composite reinforcement.
The properties of steel and glass fibers which are characterized by high hardness and their ability to withstand the bulk of the stresses gave unprecedented hardness results in all previous alloys. From the Figure 4i, the highest value of hardness appeared in the sample reinforced with eight pieces of combination of 2(glass fiber +steel mesh).

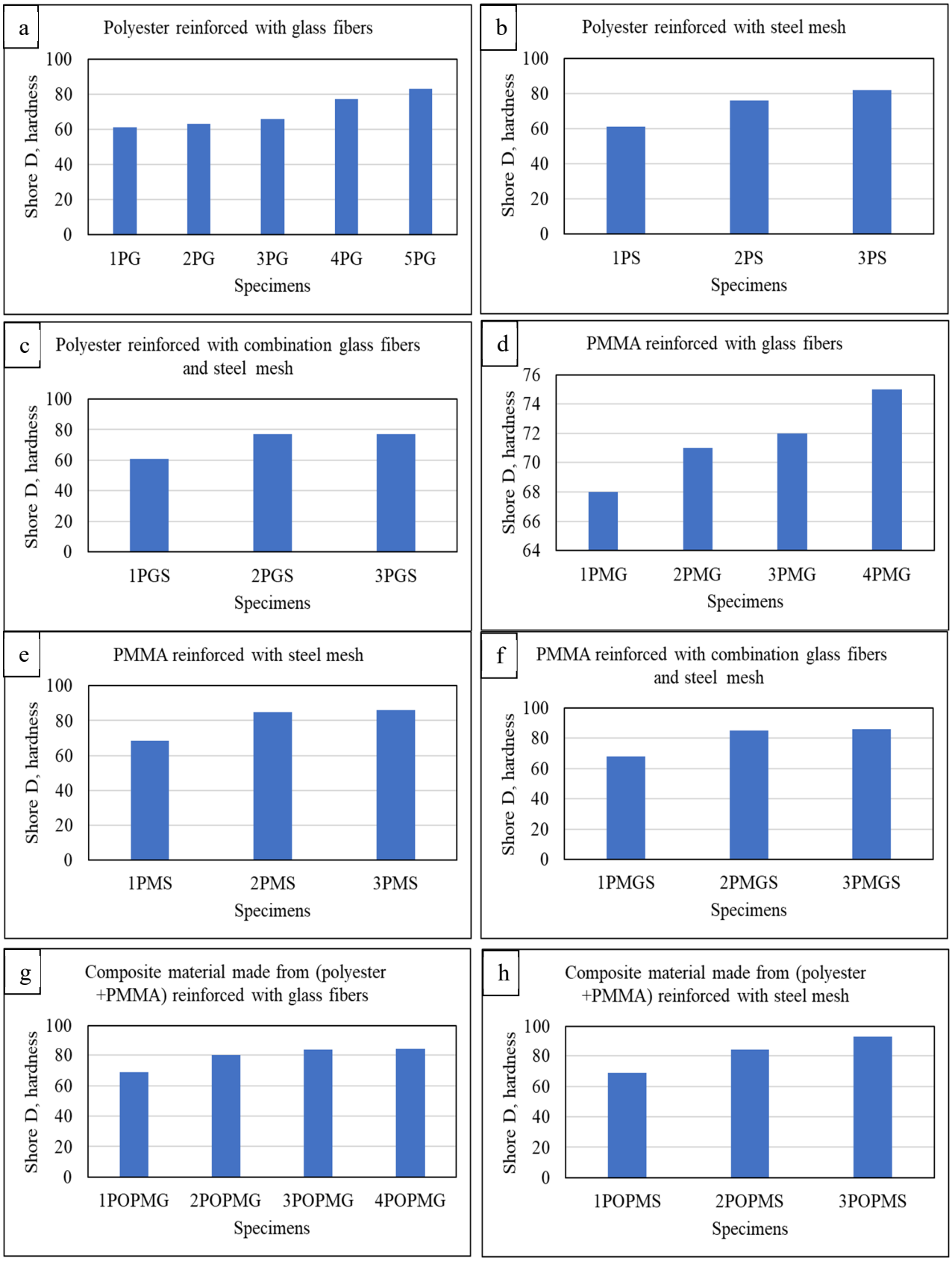
a
Polyester reinforced with glass fibers
Shore D, hardness
100
80
60
40
20
0
1PG
2PG
3PG
4PG
5PG
Specimens
b
Polyester reinforced with steel mesh
Shore D, hardness
100
80
60
40
20
0
1PS
2PS
3PS
Specimens
c
Polyester reinforced with combination glass fibers and steel mesh
Shore D, hardness
100
80
60
40
20
0
1PGS
2PGS
3PGS
Specimens
d
PMMA reinforced with glass fibers
Shore D, hardness
76
74
72
70
68
66
64
1PMG
2PMG
3PMG
4PMG
Specimens
e
PMMA reinforced with steel mesh
Shore D, hardness
100
80
60
40
20
0
1PMS
2PMS
3PMS
Specimens
f
PMMA reinforced with combination glass fibers and steel mesh
Shore D, hardness
100
80
60
40
20
0
1PMGS
2PMGS
3PMGS
Specimens
g
Composite material made from (polyester +PMMA) reinforced with glass fibers
Shore D, hardness
100
80
60
40
20
0
1POPMG
2POPMG
3POPMG
4POPMG
Specimens
h
Composite material made from (polyester +PMMA) reinforced with steel mesh
Shore D, hardness
100
80
60
40
20
0
1POPMS
2POPMS
3POPMS
Specimens

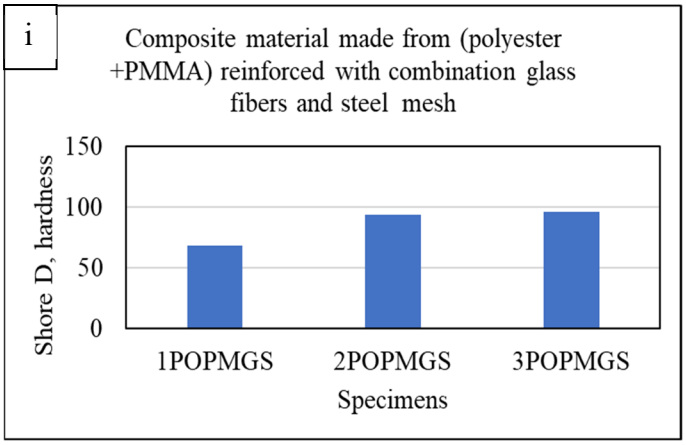

Figure 4. shows the shore hardness of specimens

Elastic modulus results

The linear modulus of elasticity (or Young's modulus) expresses the elasticity of the material and shows how the material behaves under the influence of forces and it is a linear relationship

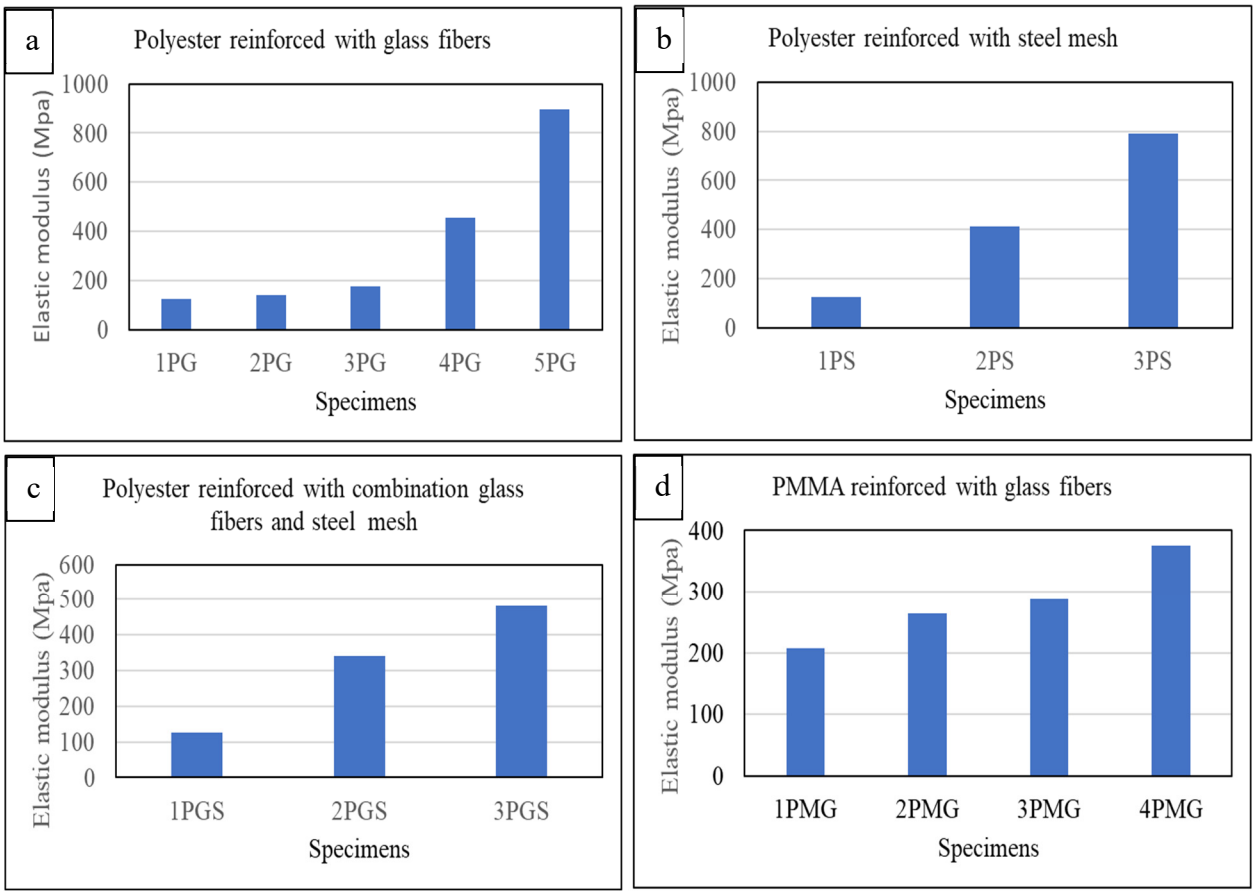

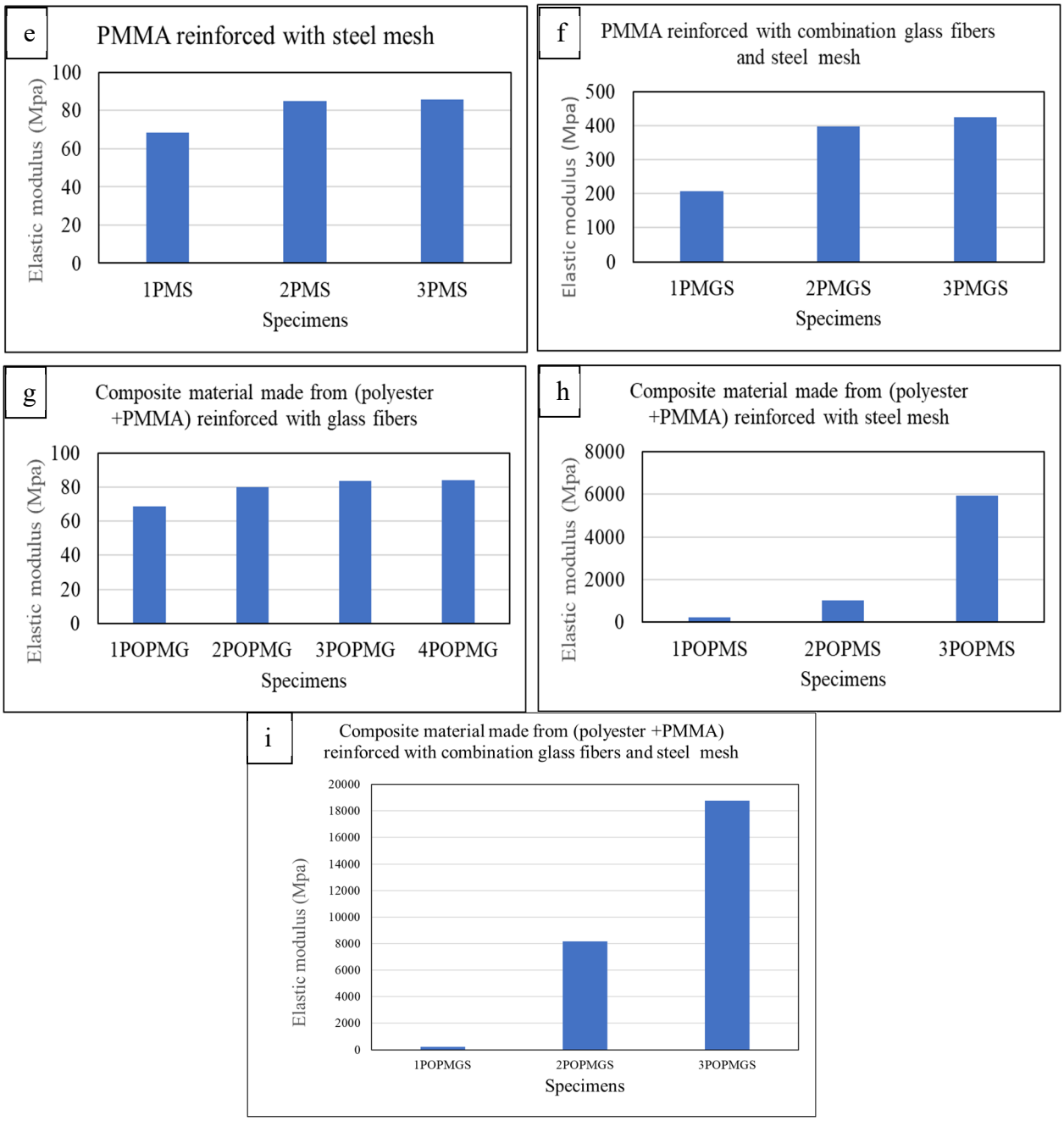

Figure 5. show the elastic modulus of specimens

Polyester reinforced with glass fibers

Figure 5a, shows the modulus of elasticity increases when adding glass fibers in polyester, and by using 8 layers of glass the modulus of elasticity reaches highest value.

Polyester reinforced with steel mesh

Figure 5b, shows the coefficient of elasticity increases by adding steel mesh to polyester, and by using 2 layers the highest value, which is equal to 791 MPa.

Polyester reinforced with combination glass fibers and steel mesh

Figure 5c, shows the modulus of elasticity increases by adding of glass fiber and steel mesh in polyester, and the coefficient of elasticity reaches highest value by using 2 layers, equal to 483 MPa.

PMMA reinforced with glass fibers

Figure 5d, shows the modulus of elasticity increases by adding glass fibers to PMMA in a semi-linear fashion, and the highest value reached when using six pieces in the current research, which is equal to 375MPa.

PMMA reinforced with steel mesh

Figure 5e, shows the modulus of elasticity increases by adding steel mesh to PMMA in a semi-linear fashion, and the highest value reached when using 2 pieces in the current research, which is equal to 1372 MPa.

PMMA reinforced with combination glass fibers and steel mesh

Figure5f, shows the modulus of elasticity increases by adding of glass fiber and steel mesh in PMMA in a semi-linear fashion, and the highest value reached when using 2 layers from each, equal to 424 MPa.

Composite material made from (polyester +PMMA) reinforced with glass fibers

From the Figure 5g, shows the modulus of elasticity increases by adding glass fiber to (PMMA +polyester) matrix in a semi-linear fashion, and the highest value reached when using 6 pieces in the current research, which is equal to 1026 MPa .

Composite material made from (polyester +PMMA) reinforced with steel mesh

From the Figure 5h, shows the modulus of elasticity increases by adding steel mesh to PMMA +polyester) matrix in a semi-linear fashion, and the highest value reached when using 2 pieces in the current research, which is equal to 5953 MPa.

Composite material made from (polyester +PMMA) reinforced with combination glass fibers and steel mesh

Figure 5i, shows the modulus of elasticity increases by adding combination of (glass fiber +steel mesh) to (PMMA +polyester) matrix in a semi-linear fashion, and the highest value reached when using 2 pieces from each in the current research, which is equal to 18765 MPa.

Thermal conductivity results

Polyester reinforced with glass fibers

Figure 6a, shows a significant increase in thermal conductivity after adding 2, 6 pieces of glass fibers, and the reason for this is that the doping materials have thermal conductivity higher than the thermal conductivity of the base material (polymer), and the increase was for (polyester), (two pieces of glass fibers /polyester) and (Six pieces of glass fibers /polyester) in sequence. However, specimens reinforced with one piece of glass fiber and eight pieces show a decrease in the values of the conductivity coefficient compared to the rest of the values, and perhaps the reason is due to the exposure of the specimen to high temperature during the finishing of the edges or scraping a large percentage of the fibers, which led to a change in the properties

Polyester reinforced with steel mesh

Figure 6b, shows a significant increase in thermal conductivity after adding materials doping of steel mesh, and the reason for this is that the doping materials have thermal conductivity higher than the thermal conductivity of the base

material (polymer), and the increase was for (polyester), (one piece of steel /polyester) and (two pieces of steel mesh /polyester) in sequence. There are several reasons, including minerals contain moving electrons have a high thermal conductivity in addition to the vibration of the lattice (the so-called Phonons). polymers contain localized electrons, so they can conduct Heat in it only by vibrating the grate.

Polyester reinforced with combination glass fibers and steel mesh

Figure 6c, shows a significant increase in thermal conductivity after adding materials doping of steel mesh + glass fibers , when adding one piece from each and the reason for this is that the doping materials have thermal conductivity Higher than the thermal conductivity of the base material (polymer), and the increase was for (PMMA), (two pieces of (steel mesh + glass fibers) /composite) and drop in value for (two pieces of (steel mesh+ glass fiber) /PMMA) in sequence.

PMMA reinforced with glass fibers

Figure 6d, shows a significant increase in thermal conductivity after adding materials doping of glass fibers , and the reason for this is that the doping materials have thermal conductivity Higher than the thermal conductivity of the base material (polymer), and the increase was for composite (pmma) , (one piece of glass fiber /(PMMA)), (Six pieces of glass fibers / composite alloy) in sequence but there are decrease in thermal conductivity value of composite contain two pieces of glass fibers.

PMMA reinforced with steel mesh

Figure 6e, shows a significant increase in thermal conductivity after adding materials doping of steel mesh, and the reason for this is that the doping materials have thermal conductivity higher than the thermal conductivity of the base material (polymer), and the increase was for (PMMA), (one piece of steel /PMMA) and (two pieces of steel mesh /PMMA) in sequence. There are several reasons, including minerals contain moving electrons have a high thermal conductivity in addition to the vibration of the lattice (the so-called Phonons). polymers contain localized electrons, so they can conduct heat in it only by vibrating the grate.

PMMA reinforced with combination glass fibers and steel mesh

Figure 6f, shows a significant decrease in thermal conductivity after adding materials doping of steel mesh, and the reason for this is that the doping materials make large gap between the pmma molecules, and the decrease was for (pmma), (two pieces of steel+ glass fibers / pmma) and (one piece of steel mesh + glass fiber /pmma) in sequence.

Composite material made from (polyester +PMMA) reinforced with glass fibers

Figure 6g, shows a significant increase in thermal conductivity after adding materials doping of glass fibers , and the reason for this is that the doping materials have thermal conductivity Higher than the thermal conductivity of the base material (polymer), and the increase was for composite (pmma +polyester) , (one piece of glass fiber /(PMMA +polyester)), (two pieces of glass fibers /(PMMA+ polyester)), (Six pieces of glass fibers / composite) in sequence.

Composite material made from (polyester +PMMA) reinforced with steel mesh

Figure 6h, shows a significant increase in thermal conductivity after adding materials doping of steel mesh, and the reason for this is that the doping materials have thermal conductivity higher than the thermal conductivity of the base material (polymer), and the increase was for (composite), (one piece of steel /composite) and (two pieces of steel mesh /composite) in sequence. There are several reasons, including minerals contain moving electrons have a high thermal conductivity in addition to the vibration of the lattice (the so-called phonons). polymers contain localized electrons, so they can conduct heat in it only by vibrating the grate.

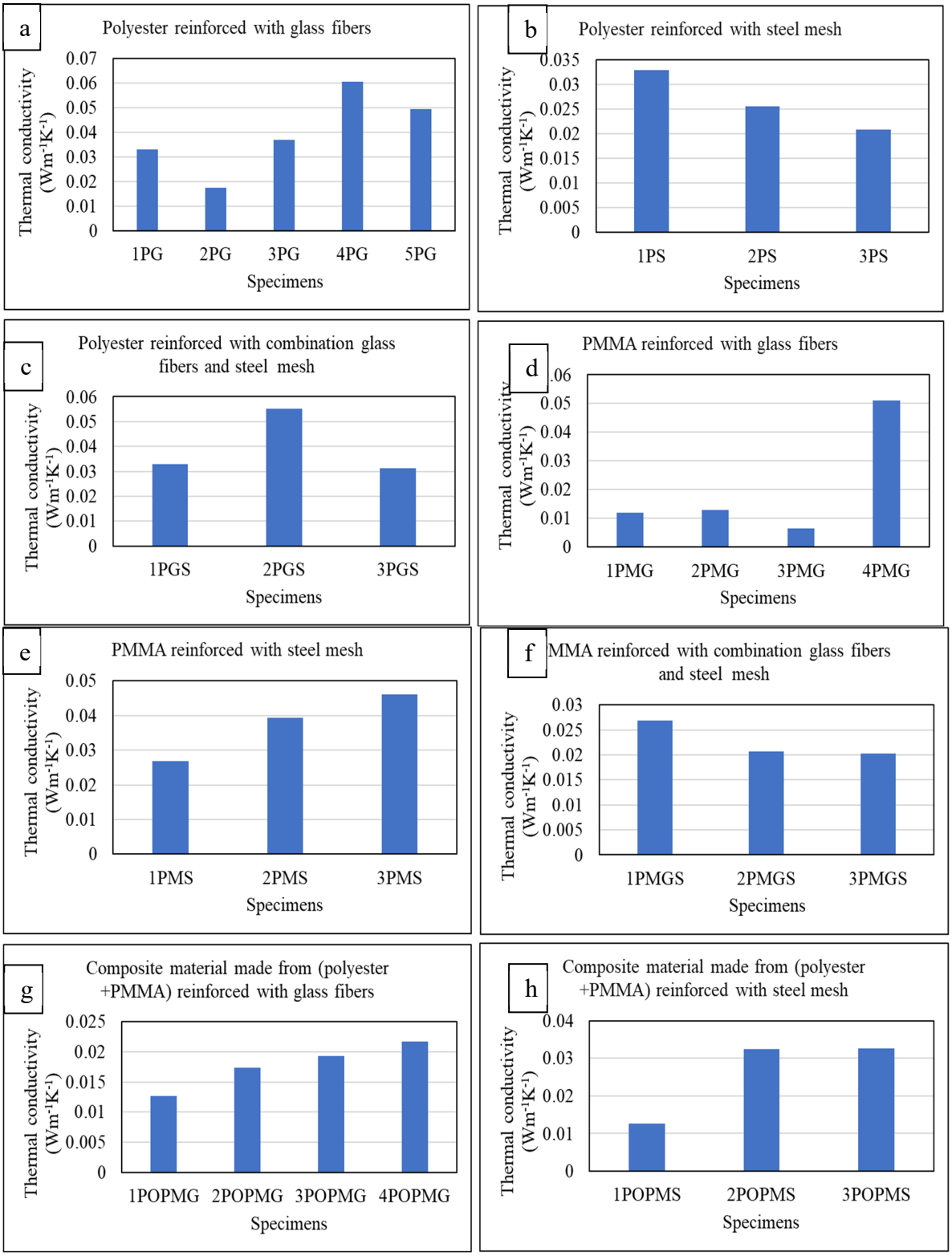
a
Polyester reinforced with glass fibers
Thermal conductivity (Wm-1K-1)
0.07
0.06
0.05
0.04
0.03
0.02
0.01
0
1PG
2PG
3PG
4PG
5PG
Specimens
b
Polyester reinforced with steel mesh
Thermal conductivity (Wm-1K-1)
0.035
0.03
0.025
0.02
0.015
0.01
0.005
0
1PS
2PS
3PS
Specimens
c
Polyester reinforced with combination glass fibers and steel mesh
Thermal conductivity (Wm-1K-1)
0.06
0.05
0.04
0.03
0.02
0.01
0
1PGS
2PGS
3PGS
Specimens
d
PMMA reinforced with glass fibers
Thermal conductivity (Wm-1K-1)
0.06
0.05
0.04
0.03
0.02
0.01
0
1PMG
2PMG
3PMG
4PMG
Specimens
e
PMMA reinforced with steel mesh
Thermal conductivity (Wm-1K-1)
0.05
0.04
0.03
0.02
0.01
0
1PMS
2PMS
3PMS
Specimens
f
MMA reinforced with combination glass fibers and steel mesh
Thermal conductivity (Wm-1K-1)
0.03
0.025
0.02
0.015
0.01
0.005
0
1PMGS
2PMGS
3PMGS
Specimens
g
Composite material made from (polyester +PMMA) reinforced with glass fibers
Thermal conductivity (Wm-1K-1)
0.025
0.02
0.015
0.01
0.005
0
1POPMG
2POPMG
3POPMG
4POPMG
Specimens
h
Composite material made from (polyester +PMMA) reinforced with steel mesh
Thermal conductivity (Wm-1K-1)
0.04
0.03
0.02
0.01
0
1POPMS
2POPMS
3POPMS
Specimens

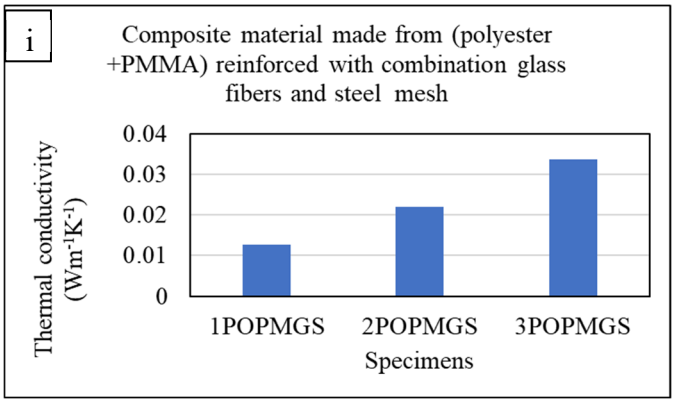

Figure 6. shows the thermal conductivity of specimens

Composite material made from (polyester +PMMA) reinforced with combination glass fibers and steel mesh

Figure 6i, shows a significant increase in thermal conductivity after adding materials doping of steel mesh, and the reason for this is that the doping materials have thermal conductivity higher than the thermal conductivity of the base material (polymer), and the increase was for (PMMA), (one piece of (steel + glass fiber) /composite) and (two pieces of (steel mesh+ glass fibers) /PMMA) in sequence. There are several reasons, including minerals contain moving electrons have a high thermal conductivity in addition to the vibration of the lattice (the so-called phonons). polymers contain localized electrons, so they can conduct heat in it only by vibrating the grate.

CONCLUSIONS

The values of hardness, elastic modulus and thermal properties increase with the increase in the addition of glass fibers and steel mesh, both separately and together.

The addition of steel mesh to materials hybrid overlays prepared from polyester, PMMA, or a mixture of polyester and PMMA, reinforced with glass fibers, led to an increase in the values of hardness, elastic modulus and thermal properties.

The values of hardness and elastic modulus mentioned increase with the volumetric fraction of steel, except for the thermal conductivity values of polyester reinforced with steel mesh.

The values of hardness, elastic modulus, and thermal conductivity are higher for hybrid overlays supported by both steel mesh and glass fibers compared to those reinforced with either steel mesh or glass fibers alone.

REFERENCES

1. Clyne T W and Hull D 2019 *An Introduction to Composite Materials* (Cambridge: Cambridge University Press)
2. Swolfs Y, Gorbatikh L and Verpoest I 2014 Fibre hybridisation in polymer composites: A review Compos. Part A Appl. Sci. Manuf. 67 181-200
3. Alagesan P K 2020 Recent advances of hybrid fiber composites for various applications Hybrid Fiber Composites: Materials, Manufacturing, Process Engineering 381-404
4. Zhang H, Zhu K, Liu F and Kang H 2024 Development and performance of a novel hybrid toughened unsaturated polyester resin (UPR) composite for crack repair of asphalt pavement Constr. Build. Mater. 416 135274
5. Sezavar A, Zebarjad S M and Sajjadi S A 2015 A study on the effect of nano alumina particles on fracture behavior of PMMA Technologies 3 94-102
6. Hasan K F, Islam M, Morshed M N, Iqbal M I I and Wu J H W 2016 Dynamic mechanical behavior and analysis of the jute-glass fiber reinforced polyester hybrid composites Am. J. Appl. Phys. 1 1-12
7. El-Wazery M S, El-Elamy M I and Zoalfakar S H 2017 Mechanical properties of glass fiber reinforced polyester composites Int. J. Appl. Sci. Eng. 14 121-131

8. Singh C Q J and Rajamurugan G 2021 Effect of resin on mechanical and wear performance of wire mesh-reinforced hydrophilic fiber composite Trans. Indian Inst. Met. 74 2853-2867
9. Rahman S S, Mahmud M B, Salehi A, Monfared A R, Islam M A, Filleter T and Park C B 2024 Mechanically strong and fully transparent PMMA composite with greatly improved toughness and impact strength incorporating PEBA nanofibrils Chem. Eng. J. 480 148311
10. Aranha R, Filho M A A, Santos C D L, de Andrade T H F, Fonseca V M, Rivera J L V, dos Santos M A, de Lima A G B, de Amorim W F Jr and de Carvalho L H 2024 Effect of water absorption and stacking sequences on the tensile properties and damage mechanisms of hybrid polyester/glass/jute composites Polymers 16 925
11. Oleiwi J K, Salih S I and Fadhil H S 2018 Study compression and impact properties of PMMA reinforced by natural fibers used in denture Eng. Technol. J. 36 652-655
12. Gad M M, Fouda S M, Al-Harbi F A, Näpänkangas R and Raustia A 2017 PMMA denture base material enhancement: a review of fiber, filler, and nanofiller addition Int. J. Nanomed. 12 3801-3812
13. Zhang Y 2015 The effect of inkjet printed polymer on the mechanical properties of carbon fibre reinforced plastic (Sheffield: University of Sheffield) PhD Thesis
14. Jagger D C, Harrison A and Al-Marzoug K 2000 Effect of the addition of poly (methyl methacrylate) beads on some properties of acrylic resin Int. J. Prosthodont. 13 451-456
15. Aykaç A and Akkaş E Ö 2023 Enhancement of mechanical and thermal properties of poly methyl methacrylate composite bone cements with zinc oxide nanostructures modified carbon fibres additives J. Adhes. Sci. Technol. 37 2729-2753
16. Shi M, Takahashi S, Takeno A and Nakai A 2023 Nanofiber veil applied in toughness enhancement of thermoplastic carbon fiber composites J. Thermoplast. Compos. Mater. 36 1631-1650
17. Tomar P and Gope P C 2024 Effect of glass fiber and nylon fiber reinforcement on the mechanical and thermal properties of styrene butadiene rubber mixed PMMA denture base material J. Mech. Behav. Biomed. Mater. 150 106308
18. Demir T N, Yilmaz A N Y and Bedeloglu A C 2023 Investigation of mechanical properties of aluminum–glass fiber-reinforced polyester composite joints bonded with structural epoxy adhesives reinforced with silicon dioxide and graphene oxide particles Int. J. Adhes. Adhes. 126 103481
19. Nemati N H, Moghadam K R and Afra N 2024 Optical, morphological, and thermal properties of polymer nanocomposite films and coatings Polymer Nanocomposite Films and Coatings (Woodhead Publishing) pp 71-101
20. Abbas A F, AL-Kawaz A E and Mezaal Z K 2024 Studying the tribological and mechanical properties of the PMMA nano composite coating JJMIE 81 2

Bibliometric-statistical study: biopolymer trend

Segundo Rojas Flores[1(a)], Santiago M. Benites[1], Magaly De La Cruz-Noriega[1], Renny Nazario-Naveda[1]

[1] *Vicerrectorado de Investigación, Universidad Autónoma del Perú, Villa el Salvador, Peru.*

[a)] Corresponding author: segundo.rojas.89@*gmail.com*

Abstract. Polymers of petrochemical origin used in industries have caused different damages to nature. For this reason, more environmentally friendly ways have been sought to replace them, with biopolymers being the ideal replacement. This research reports statistical data on the research carried out in this area in a synthesized manner so that new researchers can direct their work in a specific area. From 2016 to 2023, it has been found that 1,292 documents of original articles have been published; of Reviews were 207, and of conference Papers were 80 documents. Among these, the researcher Selvasekarapandian S. stands out, with 30 documents published in the Scopus database, the most significant reach, and an H-index of 13. His contributions serve as a testament to the potential impact of new research in this field. The document with the most significant number of citations was titled "Natural emulsifiers—Biosurfactants, phospholipids, biopolymers, and colloidal particles: Molecular and physicochemical basis of functional performance" with a total of 486 citations, and the journal with the highest number of publications was International Journal of Biological Macromolecules from the Elsevier publishing house. It was also observed that the preferred languages for publishing are English, Russian, Chinese, and Spanish. On the other hand, India is the country that does the most research on biopolymers, and University Putra Malaysia has the highest number of publications. Likewise, it was observed that the curve of documents published during the period above is exponential, demonstrating the importance of this topic, which will be reported in 2023 alone, with 553 original research documents published in Scopus.

1. INTRODUCTION

Biopolymers are a new generation of alternative materials to those produced from petroleum derivatives because they are renewable, low-cost, and biodegradable raw materials, becoming an environmentally friendly alternative [1]. These characteristics make biopolymers sustainable and attractive materials for use in different fields of science, such as in the biomedical and pharmaceutical industries [2,3]. However, their use has spread to the food industry and in clean technologies to mitigate environmental pollution [2,4]. In the field of medicine, the use of biopolymers is more extensive due to their versatility. They are highly compatible with cells, tissues, and cellular compartments and have low immunogenicity and toxicity [5,6]. Advances have been made in wound healing, where biopolymers such as polysaccharides and enzymes are being investigated, within the first group, alginates, chitosan, pectin, hyaluronic acid, and gellan gum stand out, have attracted attention for this medical purpose, while on the protein side, gelatin and collagen are being tested [3]. On the other hand, in the pharmaceutical industry, the use of biopolymers such as bacterial exopolysaccharides are being investigated, which can be used as three-dimensional carriers (hydrogels, aerogels, liposomes, micro and nanoparticles, films, etc.) for a controlled release of active ingredients of drugs such as antimicrobials, anti-inflammatory and antitumor agents at specific sites of cells or tissues in animal models [7]. Without a doubt, medicine and the pharmaceutical industry go hand in hand. Therefore, the advances made in using biopolymers in one field will be applied in the other; for example, the pharmaceutical industry is investigating pain management and regenerative biomaterials using biopolymers, which have applications in therapeutic medicine [8]. In the same way, progress is being made in stem cell therapy by incorporating biopolymers as carriers [9].

The food industry is an area that is increasingly drawn to the potential of biopolymers, particularly in food packaging, with the aim of partially or completely replacing the use of plastic containers [2,10]. The biodegradability and low cost of these materials make them particularly attractive. Various renewable sources are being explored, with those of animal and vegetable origin being the most commonly used [6,11]. However, there is a growing interest in marine biopolymers, such as proteins (muscle proteins, collagen and gelatine) and polysaccharides (chitin, chitosan, alginate,

Technologies and Materials for Renewable Energy, Environment and Sustainability
AIP Conf. Proc. 3321, 020045-1–020045-10; https://doi.org/10.1063/5.0289616
Published under an exclusive license by AIP Publishing. 978-0-7354-5231-2/$30.00

agar and carrageenan), which can be used for coating and as biodegradable films for food [12]. Another exciting application of biopolymers is as carriers of antimicrobial and antioxidant materials [6]. This research is not only essential for preserving food quality, improving safety and nutrition aspects, and extending the shelf life of products, but also for the ecological and sustainable future of the food industry [11,13].

In environmental science, biopolymers stand out for their impressive performance and low carbon footprint. They have emerged as a viable solution for industrial wastewater treatment, effectively eliminating heavy metals, organic dyes, and oils. Notably, biopolymers like proteins, cellulose, chitosan, and keratin are already used for wastewater treatment [4]. Furthermore, a wide range of biopolymers, including cellulose, chitin, chitosan, alginate, gelatine, guar gum, keratin, silk fibroin, zein, albumin, lignin, and starch, have been successfully integrated into advanced oxidation processes for the treatment of organic dyes in industrial effluents [14]. The recent exploration of biopolymers in nanotechnology (nanocomposites) has led to their incorporation into matrices (e.g., silicate sheets) based on biopolymers like cellulose and chitin, with promising applications in agriculture for the treatment of water and soil contaminated with xenobiotics [15-18]. On a different note, microalgae and cyanobacteria have demonstrated their potential in the production of bioplastics based on biopolymers such as polyesters and biodegradable aliphatic polyesters. Among these, the most well-known biopolymer is polyester, 3-hydroxybutyrate. These bioplastics hold great promise as alternatives. However, they are still undergoing extensive research to address their limitations [19,20]. Bibliometric techniques are a powerful tool for visualizing the trends and evolution of research in any field of study, including the exciting field of biopolymers. They quantify the different techniques, scientific impact, and direction of ideas and concepts, paving the way for future research. The scientific community has embraced this methodology to map foci and trends of studies linked to countries, institutions, and authors [21,22]. In this context, the Scopus database is the most recognized worldwide, hosting many documents published in various areas. Researchers often choose it as a platform to showcase their work and gain global exposure [23].

This research has as its primary objective to report the bibliometric analysis on biopolymers to make a general mapping of all the research carried out from 2016 to 2023 in the Scopus database. While this analysis provides a comprehensive overview, it is important to note that it may not capture all relevant research due to limitations in data availability and search terms. Nevertheless, this study will provide a kind of abbreviated database where researchers from all over the world will access information on the current trends and gaps to provide a solution to the lack of existing knowledge. The purpose is to direct new research towards the existing gaps in knowledge on this topic, improving and evolving towards new, renewed research trends.

2. MATERIALS AND METHODS

A specific bibliometric analysis of articles and reviews indexed under the topic biopolymer OR biopolymers AND KEY ("Biocompatibility" OR "Biopolymer Electrolyte" OR "Biopolymer Composites" OR "Biodegradability" OR "Biodegradable Polymers" OR "Biomaterial" in the primary collection of Scopus between 2016 and 2023, updated to December 31, 2023; only in the English language. Scopus, a widely used catalog renowned for its comprehensive coverage of journals of recognized relevance and its minimal errors in metadata registration, was the primary source. The downloaded files were pre-processed to improve data quality and reorganized in Microsoft Excel 16, a reliable tool for data management, considering titles, years, journals, categories, authors, affiliated institutions, countries, keywords (KEY), and received citations. The author and keywords assigned by Scopus were standardized using a thesaurus (bioenergy, renewable energy, biomass) that allowed the unification of equivalent terms and safeguarded their consistency in the different records and computer tools used for processing. The production indicators, the number of documents, their percentages and distribution, as well as the number of large producers with ten or more documents in the area were quantified; (b) impact indicators, such as citations received in Scopus, the H index (HI), the quartile of the journals in which the documents were published according to Journal Citation Reports and the citation structure by years, countries and supraregions obtained by grouping the articles according to the ranges of citations received. The analysis and the visualization of the thematic network were performed with VOSviewer 1.6.15, a trusted tool for network analysis, normalizing the graph according to the strength of association.

3. RESULTS AND DISCUSSION

In the initial mapping carried out on polymers, Figure 1 (a) was made, which shows the most used types of documents for publications in the biopolymers area between the years 2016 and 2023, showing that research articles have a 77.1% representation with 1292 documents, followed by Reviews with 12.4% (with 207) and the third with a considerable percentage were the Conference Paper with 4.8 % (80 documents); This shows that the area of research articles has a significant presence in the subject of biopolymers.

In Figure 1 (b), the publication trend of the documents is observed, observing that only from the year 2016 to 2021 a substantial increase from 155 to 349 in the years above, although in the year 2023, 745 documents are observed this value will increase because there is still time to finish this year; Thus, the accumulation of documents published during the mentioned period is also observed, going from 155 to 1675 in just five years, which would indicate to us that this area of research will continue to increase in the coming years, mainly due to various applications that are being worked on and its high capacity to replace mainly plastic materials [24,25].

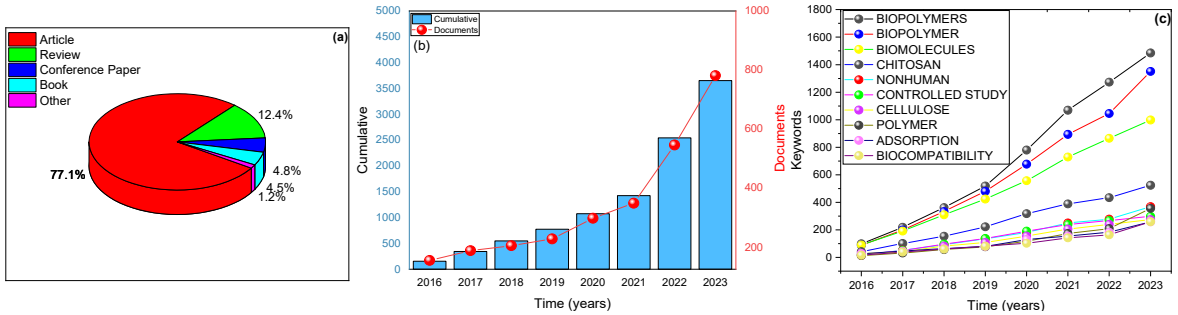

FIGURE 1. (a) percentage of document type, (b) number of documents and (c) the 10 most used keywords in documents published in Scopus from 2016 to 2023.

Likewise, it was observed in the search for information that English (1654), Russian (7), Chinese (5), Spanish (5), and Korean (2) are the languages most used to communicate the results obtained in the different types of research, with English being the language that stands out above the languages used by the scientific community.

In Figure 1 (c), the keywords used with greater frequencies in the different types of documents from 2016 to 2023 are observed, managing to observe that the ten main keywords have had an increase, but the first three (biopolymers, biopolymer, and biomolecules) have managed to obtain an exponential form in their graphs with 1273, 1045 and 865 occurrences for the keywords of biopolymers, biopolymer and biomolecules (see Table 1), although the keywords are considered the most important by the authors in the published documents, these are a vital part for the bibliometric analysis due to the impulses that it gives in the thematic areas giving new bibliometric indicators/approaches [26,27]

TABLE 1. Top 5 keywords with the highest number of occurrences.

KeyWords	Occurrences
biopolymers	1273
biopolymer	1045
biomolecules	865
chitosan	434
chemistry	401
nonhuman	278

In Table 2, the first 10 articles with the highest number of citations are shown; the document published by McClements D. and Gumus C. in 2016 with 33.12 % (486 citations in total) more citations than the one received by Zhao et al. in 2018 (325 citations in total) which was in second place, these publications were made in the journal Advances in Colloid and Interface Science and Angewandte Chemie International Edition; respectively.

The work carried out by McClements D. and Gumus C. focused on the replacement of synthetic surfactants with natural emulsifiers, amphiphilic proteins, polysaccharides, biosurfactants, phospholipids, and bioparticles, analyzing the physicochemical bases of the formation and stabilization of emulsions with natural emulsifiers comparing the benefits and limitations of different natural emulsifiers [28].
The document published by Zhao et al. investigated biopolymer aerogels, focusing on their broad applications as thermal insulators and for emerging applications in filtration, oil-water separation, CO2 capture, catalysis, and medicine [29].
On the other hand, the paper by Bilal M. and Iqbal H. in 2019 and published in the International Journal of biological macromolecules managed to obtain 170 citations, 71.19% less than that obtained by McClements D. and Gumus C.
In the work carried out by Bilal M. and Iqbal H., a systematic review was carried out on biopolymers and their advanced compounds as support carriers for the immobilization of a variety of different enzymes to develop biocatalysts with the desired catalytic activity and stability characteristics for emerging applications [37].
In the literature review, biopolymers' use in enzymatic immobilization has begun to generate significant interest in the scientific community, highlighting it as one of the most promising fields for scientific research.

TABLE 2. Top 10 most cited articles during 2016 to 2023.

Ranking	Articulo	Año	Autores	TC	TC per Year	Revista	Editorial	Ref.
1	Natural mulsifiers—Biosurfactants, phospholipids, biopolymers, and colloidal particles: Molecular and physicochemical basis of functional performance	2016	McClements D. and Gumus C.	486	69.43	Advances in Colloid and interface Science	Elsevier	[28]
2	Biopolymer aerogels and foams: Chemistry, properties, and applications	2018	Zhao et al.	325	65	Angewandte Chemie International Edition	Wiley Online Library	[29]
3	Biopolymer nano-particles and natural nano-carriers for nano-encapsulation of phenolic compounds	2016	Esfanjani A. and Jafari S.	305	43.57	Colloids and Surfaces B: Biointerfaces	Elsevier	[30]
4	Hydrophilic Multitemplate Molecularly Imprinted Biopolymers Based on a Green Synthesis Strategy for Determination of B-Family Vitamins	2018	Ostovan et al.	252	50.40	ACS Applied Materials	ACS Publications	[31]
5	Improving the integrity of natural biopolymer films used in food packaging by crosslinking approach: A review	2017	Garavand et al.	251	41.83	International Journal of Biological Macromolecules	Elsevier	[32]
6	Bacterial cellulose: a versatile biopolymer for wound dressing applications	2019	Portela et al.	206	51.50	Microbial biotechnology	Wiley Online Library	[33]
7	Biopolymer-based functional composites for medical applications	2017	Park et al.	195	32.50	Progress in Polymer Science	Elsevier	[34]
8	Introduction of Microbial Biopolymers in Soil Treatment for Future Environmentally-Friendly and Sustainable Geotechnical Engineering	2016	Chang et al.	181	25.86	Sustainability	MDPI	[35]
9	Three-dimensional force microscopy of cells in biopolymer networks	2016	Steinwachs et al.	176	25.14	Nature methods	Nature	[36]
10	Naturally-derived biopolymers: Potential platforms for enzyme immobilization	2019	Bilal M. and Iqbal H.	170	42.50	International journal of biological macromolecules	Elsevier	[37]

TC= Total Citations;

In Table 3, the authors with the highest number of publications registered since 2016 can be observed, and it can be observed that Selvasekarapandian S. published 30 documents in the Scopus database, ranking as the researcher with the most production in the area of biopolymers; his most cited article (58 citations) being the one that synthesized electrolytes from biopolymers based on tamarind seed polysaccharide, whose electrolytes have potential use in lithium batteries [38].

Likewise, Chang I. managed to publish 23 documents, ranking second in Table 2, his most published document (181 citations), being the one that made an introduction to the treatment and improvement of soil, performing an analysis of the implementation of biopolymers in joint cement seeing its economic feasibility, so that in the future biopolymers can replace joint cement [39-41]. The one that made the most minor publications within Table 2 was Aziz, S.B., who published ten documents, the most cited one (35 citations) being the one who worked on the fabrication of polyvinyl alcohol (PVA) polymeric electrolytes with chitosan (CS) plasticized using a solution casting technique [42,43]. In the realization of the study of central studies, there is a strong tendency in the production of research in generating electrolytes based on or mixing different types of biopolymers for use in batteries, clearly to reduce the different polluting chemical references that are generated in the production and generation of these sources of electrical energy [44,45].

In Figure 2, can see the collaborations carried out between the most influential authors in the field of biopolymers from 2016 to 2023; with the VOSviewee Program, it could be observed that Chang I. (second place in Table 2) has a more significant number of collaborations, his most frequent collaborators being researchers Smitha S., Li X. Zhang I., and others; While the author Selvasekarapandian S. who published the most significant number of documents in Table 2, has a strong collaboration with researchers Liu Y., Shi J., Zhang X., and others, but the collaborations that Chan I. and McClements Dj have; it may be that in the coming years, these researchers will surpass the documents published by Selvasekarapandian S. and will be ranked higher than the current ones. Likewise, it was observed that Smitha S. and Guo C. are the authors who, in 2021, had more collaborations than the authors mentioned above.

TABLE 3. Top 10 authors with the highest number of documents published in Scopus between 2016 and 2023.

	Autores con mayor cantidad de documentos publicados.					
Ranking	Autor	Número de articulos	Articulo mas citado	Citas	H-Index	G-Index
1	Selvasekarapandian S.	30	Synthesis and characterization of biopolymer electrolyte based on tamarind seed polysaccharide, lithium perchlorate and ethylene carbonate for electrochemical applications [15].	58	13	21
2	Chang I.	23	Introduction of microbial biopolymers in soil treatment for future environmentally-friendly and sustainable geotechnical engineering [12].	181	12	23
3	Cho G-C.	19	Introduction of microbial biopolymers in soil treatment for future environmentally-friendly and sustainable geotechnical engineering [12].	181	8	17
4	Mcclements Dj	15	Natural emulsifiers — Biosurfactants, phospholipids, biopolymers, and colloidal particles: Molecular and physicochemical basis of functional performance [5].	489	10	15
5	Im, J.	14	Introduction of microbial biopolymers in soil treatment for future environmentally-friendly and sustainable geotechnical engineering [12].	181	8	14
6	Isa, M.I.N.	14	Structural and ionic transport properties of protonic conducting solid biopolymer electrolytes based on carboxymethyl cellulose doped with ammonium fluoride [16].	71	9	14
7	Samsudin, A.S.	13	Investigation on the effect of NH4Br at transport properties in k–carrageenan-based biopolymer electrolytes via structural and electrical analysis [17].	40	9	13
8	Monisha, S.	11	Proton-conducting I-Carrageenan-based biopolymer electrolyte for fuel cell application [18].	48	9	11
9	Sapuan, S.M.	11	Biopolymers and biocomposites: Chemistry and technology [19].	61	6	11
10	Aziz, S.B.	10	The study of the degree of crystallinity, electrical equivalent circuit, and dielectric properties of polyvinyl alcohol (PVA)-based biopolymer electrolytes [20].	35	7	10

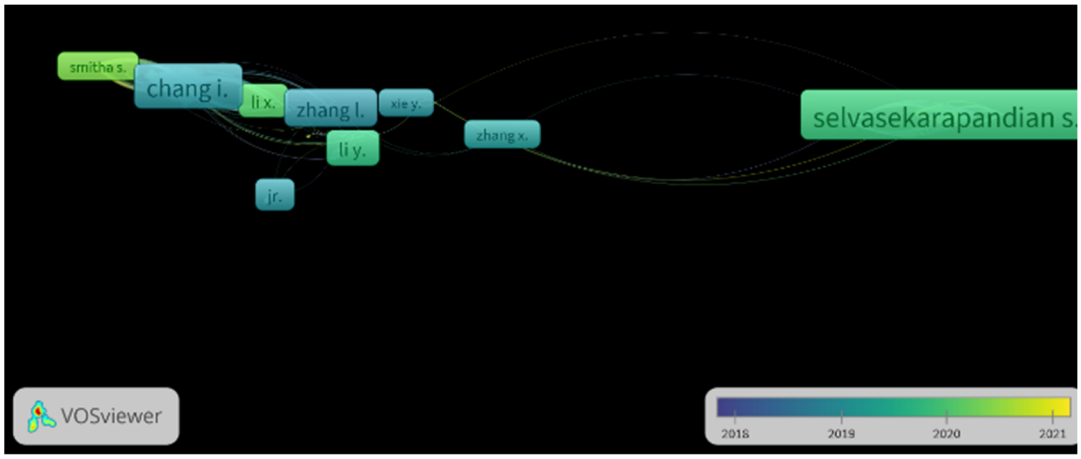

FIGURE 2. Collaborations carried out between researchers from 2016 to 2023.

Table 4 shows the ten countries with the highest number of published documents, observing India as the country with the highest number of published articles (222) with a difference of 5 articles, second place belonging to China (with 217). However, China has obtained more citations than India, with 3628 and 2710, respectively. Likewise, it can also be observed that countries that have managed to have a large number of collaborations between researchers within the same countries have generated a more significant number of published articles; for example, India has an SCP of 179, which indicates a high level of self-citation, and a MCP of 43, which suggests a strong level of international collaboration. Similarly, China, in the second place, has an SCP of 150 and USA in the third place with 136 published articles has a SCP of 103. On the other hand, Poland was the last country in this report observed, with 23 documents and 259 citations obtained with an SCP and MCP of 20 and 3, respectively [46-48]. Figure 3 shows a map of the foremost collaborations carried out between countries, showing that India mainly has strong collaborations with China and the USA and some collaborations with Malaysia, Indonesia, Japan, and others. In contrast, China strongly collaborates with the USA and, to a lesser extent, with India, Iran, South Korea, Germany, and others. On the other hand, Poland has collaborations with the USA and China, but in a smaller amount than those mentioned above, with Brazil, Spain, and Portugal being the countries with the highest number of collaborations. While Figure 4 (a) shows the affiliations with the highest number of publications, it can be observed that Universiti Putra Malaysia is the institution that published the most documents in 2023. As can be seen in Table 4, the country is located in the fourth position. In contrast, BHARATHIAR UNIVERSITY, belonging to India, is located in second place with 48 documents published only in the year 2023, but in 2016, it had no publications on the subject. Likewise, it was observed that the only university in South America is SÃO PAULO STATE UNIVERSITY (UNESP), with 32 documents published in 2023, placing it as the pioneer university in this area in Latin America.

TABLE 4. The 10 countries with the highest number of publications in the area from 2016 to 2023.

Ranking	Country	Articles	SCP	MCP	TC
1	India	222	179	43	2710
2	China	217	150	67	3628
3	Usa	136	103	33	2633
4	Malaysia	109	75	34	1428
5	Brasil	57	49	8	526
6	Korea	74	48	26	1274
7	Iran	61	46	15	1921
8	Germany	51	36	15	627
9	Italy	33	20	13	597
10	Poland	23	20	3	259

Intra-country (SCP)
Inter-country (MCP)
TC=citaciones totales

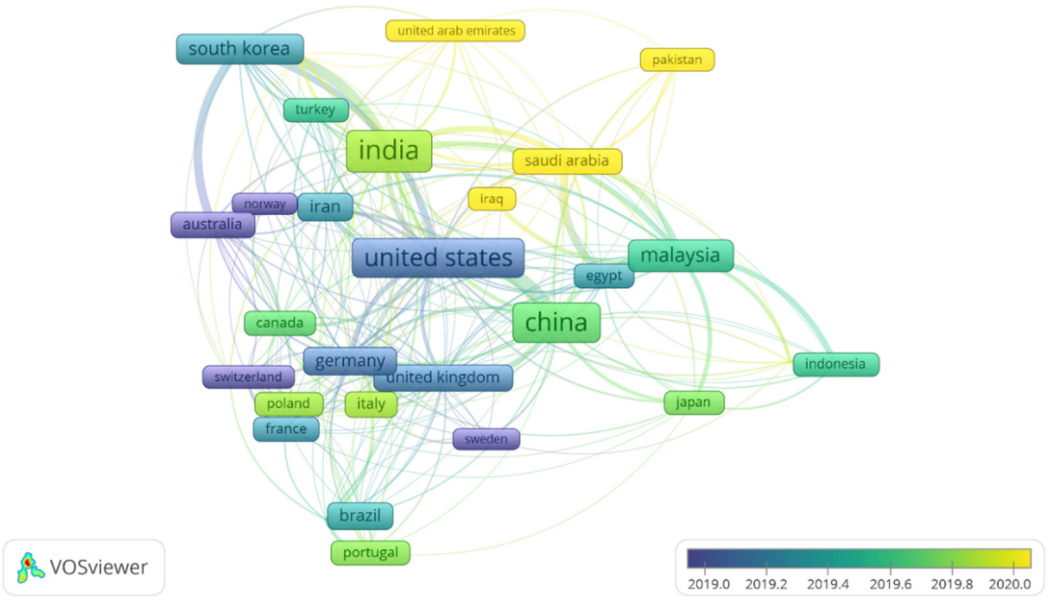

FIGURE 3. Map of collaborations of the main producers of scientific documents on biopolymers.

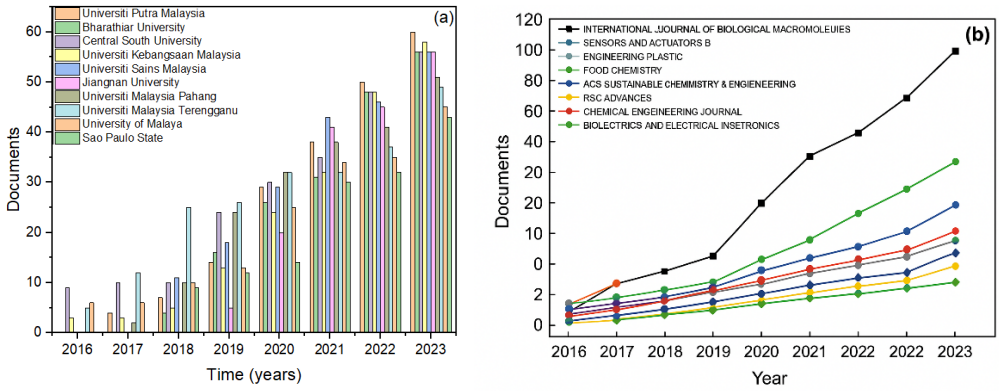

FIGURE 4. (a)Top 10 universities with the highest number of published documents and (b) Increase in publications on biopolymers in the top 10 journals with the highest number of documents.

Figure 4 (b) shows the increases in documents published in the last seven years of the 10 journals with the highest production. As can be seen, in 2023, the International Journal of Biological Macromolecules published 74 documents on biopolymers. However, in 2016, it only published 5 documents, noting the increase in this journal area, which is why it is positioned as the journal with the highest number of publications in 2016-2023, with 274 documents. In 2016, the Biomacromolecules journal was the one that published the most documents (8 documents), but in 2023, it only published 16 documents, this number being the same as last year (2021). Another journal that shows a substantial increase in publications is Polymer, with 58 documents published this year (2023), which, unlike in 2016, had no publications on the subject [49].

4. CONCLUSION

This research highlights the importance of biopolymers, with the number of publications increasing exponentially in recent years, reaching approximately 553 documents in 2023 alone. The three most used keywords are biopolymers, biopolymers, and biomolecules. The article with the highest number of citations was the one titled “Natural emulsifiers—Biosurfactants, phospholipids, biopolymers, and colloidal particles: Molecular and physicochemical basis of functional performance,” by McClements D. and Gumus C., with a total of 486 citations. India has the highest

number of articles published, with 2,710 citations obtained, demonstrating the importance that this country dedicates to using these materials to replace conventional plastic. Similarly, University Putra Malaysia has the most significant number of documents published in this area, and the International Journal of Biological Macromolecules is the most used journal for publications on biopolymers, with a total of 202 citations obtained from 2016-2023. It is noteworthy that the trend in the use of biopolymer has shifted towards macromolecules, which are currently the most used due to their ability to increase the resistance of different products, keeping our audience abreast of the latest developments.

ACKNOWLEDGMENTS

This research was funded under a project from the Universidad Autonoma del Peru.

REFERENCES

1. Rendón-Villalobos, R.; Ortíz-Sánchez, A.; Tovar-Sánchez, E.; Flores-Huicochea, E. The Role of Biopolymers in Obtaining Environmentally Friendly Materials. In *Composites from Renewable and Sustainable Materials*; Poletto, M., Ed.; InTech: London, England, 2016 ISBN 9789535127932.
2. Baranwal, J.; Barse, B.; Fais, A.; Delogu, G.L.; Kumar, A. Biopolymer: A Sustainable Material for Food and Medical Applications. *Polymers (Basel)* **2022**, *14*, 983, doi:10.3390/polym14050983.
3. Smith, A.M.; Moxon, S.; Morris, G.A. Biopolymers as Wound Healing Materials. In *Wound Healing Biomaterials*; Ågren, M.S., Ed.; Elsevier, 2016; pp. 261–287 ISBN 9781782424567.
4. Zubair, M.; Ullah, A. Biopolymers in Environmental Applications. In *Biopolymers and their Industrial Applications*; Thomas, S., Gopi, S., Amalraj, A., Eds.; Elsevier, 2021; pp. 331–349 ISBN 9780128192405.
5. Kumar, S.S.D.; Houreld, N.N.; Abrahamse, H. Biopolymer-Based Composites for Medical Applications. In *Encyclopedia of Renewable and Sustainable Materials*; Hashmi, S., Choudhury, I.A., Eds.; Elsevier, 2020; pp. 20–28 ISBN 9780128131961.
6. Wankhade, V. Animal-Derived Biopolymers in Food and Biomedical Technology. In *Biopolymer-Based Formulations*; Pal, K., Banerjee, I., Sarkar, P., Kim, D., Deng, W.-P., Dubey, N.K., Majumder, K., Eds.; Elsevier, 2020; pp. 139–152 ISBN 9780128168974.
7. Saha, I.; Datta, S. Bacterial Exopolysaccharides in Drug Delivery Applications. *J. Drug Deliv. Sci. Technol.* **2022**, *74*, 103557, doi:10.1016/j.jddst.2022.103557.
8. Gu, X.; Carroll Turpin, M.A.; Romero-Ortega, M.I. Biomaterials and Regenerative Medicine in Pain Management. *Curr. Pain Headache Rep.* **2022**, *26*, 533–541, doi:10.1007/s11916-022-01055-5.
9. Stowers, R.S. Advances in Extracellular Matrix-Mimetic Hydrogels to Guide Stem Cell Fate. *Cells Tissues Organs* **2021**, 1–18, doi:10.1159/000514851.
10. Matos Fonseca, J.; Koop, B.L.; Trevisol, T.C.; Capello, C.; Monteiro, A.R.; Valencia, G.A. An Overview of Biopolymers in Food Packaging Systems. *Nanotechnology-Enhanced Food Packaging* **2022**, 19–53. https://doi.org/10.1002/9783527827718.ch2
11. Abdullah; Cai, J.; Hafeez, M.A.; Wang, Q.; Farooq, S.; Huang, Q.; Tian, W.; Xiao, J. Biopolymer-Based Functional Films for Packaging Applications: A Review. *Front. Nutr.* **2022**, *9*, 1000116, doi:10.3389/fnut.2022.1000116.
12. Mahmud, N.; Islam, J.; Tahergorabi, R. Marine Biopolymers: Applications in Food Packaging. *Processes (Basel)* **2021**, *9*, 2245, doi:10.3390/pr9122245.
13. Khalid, M.Y.; Arif, Z.U. Novel Biopolymer-Based Sustainable Composites for Food Packaging Applications: A Narrative Review. *Food Packag. Shelf Life* **2022**, *33*, 100892, doi:10.1016/j.fpsl.2022.100892.
14. Peramune, D.; Manatunga, D.C.; Dassanayake, R.S.; Premalal, V.; Liyanage, R.N.; Gunathilake, C.; Abidi, N. Recent Advances in Biopolymer-Based Advanced Oxidation Processes for Dye Removal Applications: A Review. *Environ. Res.* **2022**, *215*, 114242, doi:10.1016/j.envres.2022.114242.
15. Manju, P.; Santhana Gopala Krishnan, P. Biodegradable Polyvinyl Alcohol/Starch/Halloysite Nanotube Bionanocomposite: Preparation and Characterization. In *Biodegradable and Environmental Applications of Bionanocomposites*; Springer International Publishing: Cham, **2023**; pp. 221–236 ISBN 9783031133428.
16. Martín, J.; del Mar Orta, M.; Medina-Carrasco, S.; Santos, J.L.; Aparicio, I.; Alonso, E. Biodegradable Polymers and Their Bionanocomposites Based on Layered Silicates: Environmental Applications. In *Biodegradable and Environmental Applications of Bionanocomposites*; Springer International Publishing: Cham, **2023**; pp. 1–30 ISBN 9783031133428.

17. Zhang, R.; Xu, H. Environmental Properties and Applications of Cellulose and Chitin-Based Bionanocomposites. In *Biodegradable and Environmental Applications of Bionanocomposites*; Springer International Publishing: Cham, **2023**; pp. 99–140 ISBN 9783031133428
18. Muthukumaran, P.; Suresh Babu, P.; Shyamalagowri, S.; Aravind, J.; Kamaraj, M.; Govarthanan, M. Polymeric Biomolecules Based Nanomaterials: Production Strategies and Pollutant Mitigation as an Emerging Tool for Environmental Application. *Chemosphere* **2022**, *307*, 136008, doi:10.1016/j.chemosphere.2022.136008.
19. Mastropetros, S.G.; Pispas, K.; Zagklis, D.; Ali, S.S.; Kornaros, M. Biopolymers Production from Microalgae and Cyanobacteria Cultivated in Wastewater: Recent Advances. *Biotechnol. Adv.* **2022**, *60*, 107999, doi:10.1016/j.biotechadv.2022.107999.
20. Calijuri, M.L.; Silva, T.A.; Magalhães, I.B.; Pereira, A.S.A. de P.; Marangon, B.B.; Assis, L.R. de; Lorentz, J.F. Bioproducts from Microalgae Biomass: Technology, Sustainability, Challenges and Opportunities. *Chemosphere* **2022**, *305*, 135508, doi:10.1016/j.chemosphere.2022.135508.
21. Donthu, N., Kumar, S., Mukherjee, D., Pandey, N., & Lim, W. M. (2021). How to conduct a bibliometric analysis: An overview and guidelines. *Journal of Business Research*, *133*, 285-296.
22. Moral-Muñoz, J. A., Herrera-Viedma, E., Santisteban-Espejo, A., & Cobo, M. J. (2020). Software tools for conducting bibliometric analysis in science: An up-to-date review. *Profesional de la Información*, *29*(1).
23. Venegas, C. N. (2022). The importance of publishing in journals that are not yet indexed in Scopus, PubMed or WOS. *World Journal of Advanced Research and Reviews*, *14*(3), 629-633.
24. Awasthi, S. K., Kumar, M., Kumar, V., Sarsaiya, S., Anerao, P., Ghosh, P., ... & Awasthi, M. K. (2022). A comprehensive review on recent advancements in biodegradation and sustainable management of biopolymers. *Environmental Pollution*, 119600.
25. Ariyadasa, S., Daear, W., Abeysekera, G., Billington, C., Fee, C., Prenner, E., & Pang, L. (2022). Evaluation of Biopolymer Materials and Synthesis Techniques to Develop a Rod-Shaped Biopolymer Surrogate for Legionella pneumophila. *Polymers*, *14*(13), 2571.
26. Wang, M., & Chai, L. (2018). Three new bibliometric indicators/approaches derived from keyword analysis. *Scientometrics*, *116*(2), 721-750.
27. Pesta, B., Fuerst, J., & Kirkegaard, E. O. (2018). Bibliometric keyword analysis across seventeen years (2000–2016) of intelligence articles. *Journal of Intelligence*, *6*(4), 46.
28. McClements, D. J., & Gumus, C. E. (2016). Natural emulsifiers—Biosurfactants, phospholipids, biopolymers, and colloidal particles: Molecular and physicochemical basis of functional performance. *Advances in Colloid and interface Science*, *234*, 3-26.
29. Zhao, S., Malfait, W. J., Guerrero-Alburquerque, N., Koebel, M. M., & Nyström, G. (2018). Biopolymer aerogels and foams: Chemistry, properties, and applications. *Angewandte Chemie International Edition*, *57*(26), 7580-7608.
30. Esfanjani, A. F., & Jafari, S. M. (2016). Biopolymer nano-particles and natural nano-carriers for nano-encapsulation of phenolic compounds. *Colloids and Surfaces B: Biointerfaces*, *146*, 532-543.
31. Ostovan, A., Ghaedi, M., Arabi, M., Yang, Q., Li, J., & Chen, L. (2018). Hydrophilic multitemplate molecularly imprinted biopolymers based on a green synthesis strategy for determination of B-family vitamins. *ACS Applied Materials & Interfaces*, *10*(4), 4140-4150.
32. Garavand, F., Rouhi, M., Razavi, S. H., Cacciotti, I., & Mohammadi, R. (2017). Improving the integrity of natural biopolymer films used in food packaging by crosslinking approach: A review. *International Journal of Biological Macromolecules*, *104*, 687-707.
33. Portela, R., Leal, C. R., Almeida, P. L., & Sobral, R. G. (2019). Bacterial cellulose: A versatile biopolymer for wound dressing applications. *Microbial biotechnology*, *12*(4), 586-610.
34. Park, S. B., Lih, E., Park, K. S., Joung, Y. K., & Han, D. K. (2017). Biopolymer-based functional composites for medical applications. *Progress in Polymer Science*, *68*, 77-105.
35. Chang, I., Im, J., & Cho, G. C. (2016). Introduction of microbial biopolymers in soil treatment for future environmentally-friendly and sustainable geotechnical engineering. *Sustainability*, *8*(3), 251.
36. Steinwachs, J., Metzner, C., Skodzek, K., Lang, N., Thievessen, I., Mark, C., ... & Fabry, B. (2016). Three-dimensional force microscopy of cells in biopolymer networks. *Nature methods*, *13*(2), 171-176.
37. Bilal, M., & Iqbal, H. M. (2019). Naturally-derived biopolymers: Potential platforms for enzyme immobilization. *International journal of biological macromolecules*, *130*, 462-482.
38. Sampathkumar, L., Christopher Selvin, P., Selvasekarapandian, S., Perumal, P., Chitra, R., & Muthukrishnan, M. (2019). Synthesis and characterization of biopolymer electrolyte based on tamarind seed polysaccharide, lithium perchlorate and ethylene carbonate for electrochemical applications. *Ionics*, *25*(3), 1067-1082.

39. Ramlli, M. A., & Isa, M. I. N. (2016). Structural and ionic transport properties of protonic conducting solid biopolymer electrolytes based on carboxymethyl cellulose doped with ammonium fluoride. *The Journal of Physical Chemistry B*, *120*(44), 11567-11573.
40. Ramlli, M. A., & Isa, M. I. N. (2016). Investigation on the effect of NH4Br at transport properties in k–carrageenan based biopolymer electrolytes via structural and electrical analysis. *The Journal of Physical Chemistry B*, *120*(44), 11567-11573.
41. Karthikeyan, S., Selvasekarapandian, S., Premalatha, M., Monisha, S., Boopathi, G., Aristatil, G., ... & Madeswaran, S. (2017). Proton-conducting I-Carrageenan-based biopolymer electrolyte for fuel cell application. *Ionics*, *23*(10), 2775-2780.
42. Ilyas, R. A., & Sapuan, S. M. (2020). Biopolymers and biocomposites: chemistry and technology. *Current Analytical Chemistry*, *16*(5), 500-503.
43. B. Aziz, S., S. Marf, A., Dannoun, E. M., Brza, M. A., & Abdullah, R. M. (2020). The study of the degree of crystallinity, electrical equivalent circuit, and dielectric properties of polyvinyl alcohol (PVA)-based biopolymer electrolytes. *Polymers*, *12*(10), 2184.
44. Singh, R., Polu, A. R., Bhattacharya, B., Rhee, H. W., Varlikli, C., & Singh, P. K. (2016). Perspectives for solid biopolymer electrolytes in dye sensitized solar cell and battery application. *Renewable and Sustainable Energy Reviews*, *65*, 1098-1117.
45. Lizundia, E., & Kundu, D. (2021). Advances in natural biopolymer-based electrolytes and separators for battery applications. *Advanced Functional Materials*, *31*(3), 2005646.
46. Song, W., Gao, B., Xu, X., Xing, L., Han, S., Duan, P., ... & Jia, R. (2016). Adsorption–desorption behavior of magnetic amine/Fe3O4 functionalized biopolymer resin towards anionic dyes from wastewater. *Bioresource Technology*, *210*, 123-130.
47. Reddy, M. S. B., Ponnamma, D., Choudhary, R., & Sadasivuni, K. K. (2021). A comparative review of natural and synthetic biopolymer composite scaffolds. *Polymers*, *13*(7), 1105.
48. Liu, J., Sun, L., Xu, W., Wang, Q., Yu, S., & Sun, J. (2019). Current advances and future perspectives of 3D printing natural-derived biopolymers. *Carbohydrate polymers*, *207*, 297-316.
49. Ramezanzade, L., Hosseini, S. F., & Nikkhah, M. (2017). Biopolymer-coated nanoliposomes as carriers of rainbow trout skin-derived antioxidant peptides. *Food Chemistry*, *234*, 220-229.
50. Luo, S., Cao, J., & McDonald, A. G. (2016). Interfacial improvements in a green biopolymer alloy of poly (3-hydroxybutyrate-co-3-hydroxyvalerate) and lignin via in situ reactive extrusion. *ACS Sustainable Chemistry & Engineering*, *4*(6), 3465-3476.
51. Kownacka, A. E., Vegelyte, D., Joosse, M., Anton, N., Toebes, B. J., Lauko, J., ... & Wilson, C. J. (2018). Clinical evidence for use of a noninvasive biosensor for tear glucose as an alternative to painful finger-prick for diabetes management utilizing a biopolymer coating. *Biomacromolecules*, *19*(11), 4504-4511.
52. Kasturi, P. R., Ramasamy, H., Meyrick, D., Lee, Y. S., & Selvan, R. K. (2019). Preparation of starch-based porous carbon electrode and biopolymer electrolyte for all solid-state electric double layer capacitor. *Journal of colloid and interface science*, *554*, 142-156.
53. Abhilash, M., & Thomas, D. (2017). Biopolymers for biocomposites and chemical sensor applications. In *Biopolymer composites in electronics* (pp. 405-435). Elsevier.

Mapping of Rn-222 gas concentrations in Baghdad governorate by using (CR-39) detector and remote sensing

Imad H. Ahmed [1, a], Mahmood S. Karim[2]

[1]*Department of Physics, College of Science, University of Mustansiriyah, Baghdad, IRAQ*
[2] *Department of Physics, College of Education, University of Mustansiriyah, Baghdad, IRAQ.*

[a] Corresponding author: emadhameed321@uomustansiriyah.edu.iq

Abstract In this research, the concentrations of Rn-222 gas were measured in environmental samples (aerosols, water, and soil) for different regions of Baghdad governorate by using the technique of counting traces of alpha particles emitted from Rn-222 gas in a nuclear trace detector (CR-39). The first part included measuring the concentrations of Rn-222 gas in air aerosol samples in the Baghdad Governorate. The results showed that the highest rate of Rn-222 concentrations was in the Mahmoudiya region (4.35 ppm), and the average Rn-222 concentrations for ten regions of Baghdad ranged between (4.35-1.73 ppm) and average concentrations (3.135 ppm). The second part included determining the concentrations of Rn-222 gas in the Tigris water for regions of Baghdad, the results indicated that the highest rate of Rn-222 gas concentrations in the water was in the Mahmoudiya region (0.17 ppm), and the average Rn-222 concentrations for ten regions of Baghdad ranged between (0.17- 0.017 ppm) and average concentrations (0.0859 ppm). The third part included determining the concentrations of Rn-222 gas in the soil for regions of Baghdad, the results indicated that the highest rate of concentrations of Rn-222 gas in the soil was in the Mahmoudiya region (5.2 ppm) and the average Rn-222 concentrations for ten Baghdad regions ranged between (5.2 -1.5 ppm) and the average Rn-222 concentration (3.38 ppm). The fourth part includes mapping Rn-222 concentrations for the three samples using remote sensing technology and geographic information systems.

Keywords: Rn-222, Soil, aerosols, water, CR-39.

INTRODUCTION

Radioactive materials move naturally via the air, water, and soil, the three basic environmental components. They typically spread via various pathways to people, animals, and plants. Because the air is typically a moving medium with rapidly transmitted pollution and bodies of water and groundwater are medium-moving media with medium-speed transmission, the physical and chemical properties of the media carrying radioactive materials differ, which is reflected in the residence time of the radioactive materials in the medium and their transfer to humans. On the other hand, compared to air and water, soil is a relatively immobile medium, which can cause contamination over short and long terms. In this context, soil is significant because it is the last destination for radioactive elements. Its long-term function is to store these materials while also serving as a source of contamination for plants, animals, and water. [1,2]. The hazards associated with Rn-222 gas are not limited to its radioactivity; it can disperse over wide areas. After 3.83 days, Rn-222 transforms into polonium, which releases alpha particles and accumulates on homes and plants, endangering the local population. A particular kind of radiation released by radioactive materials is known as radioactivity. According to Warren's taxonomy of environmental factors, radioactivity is an everlasting phenomenon that has encircled the human environment and damaged water, air, and soil to varying degrees. Due to the existence of radioactive element nuclides that are susceptible to this phenomenon, it has also contaminated plant and animal food [3,4]. A species is considered polluted when its concentration exceeds the limits allowed by national and international environmental regulations and endangers both the environment and people. Since radioactivity affects environmental elements first, and because Baghdad has experienced more bombing and environmental neglect than other cities, second, and has a higher population density than other cities, third, the research will concentrate on the

Technologies and Materials for Renewable Energy, Environment and Sustainability
AIP Conf. Proc. 3321, 020046-1–020046-9; https://doi.org/10.1063/5.0289760
Published under an exclusive license by AIP Publishing. 978-0-7354-5231-2/$30.00

radioactive pollutants of environmental elements caused by the spread of radioactive materials in the air, water, and soil in the city [5,6].

DESCRIPTION OF STUDY AREA

The city of Baghdad (in English: Baghdad city) is the official capital of the Republic of Iraq; as shown in Figure 1The municipality is located on a broad alluvial plain at an altitude of 34 meters above sea level, and the Tigris River divides it into two halves, an eastern half called Rusafa and a western half known as Karkh, and Its lands are generally flat. Being of sedimentary origin, the region was exposed to periodic floods from the Tigris River. The population in Baghdad reaches (7,711,305) people, according to the latest estimates in (2023 AD) with an annual growth rate of about (2.65%) and the population is expected to reach (10,178,581) people in (2033 AD). It is worth noting that it is considered the largest governorate in Iraq in terms of number Population, followed by Mosul governorate, then Basra. Most of the city's residents are mainly Arabs, with a small group of Kurds and other ethnic groups and the dialect of the Arabic spoken by its residents differs from that found in other large urban centers in Iraq. It tends toward the Bedouin Arabic dialect [7,8].

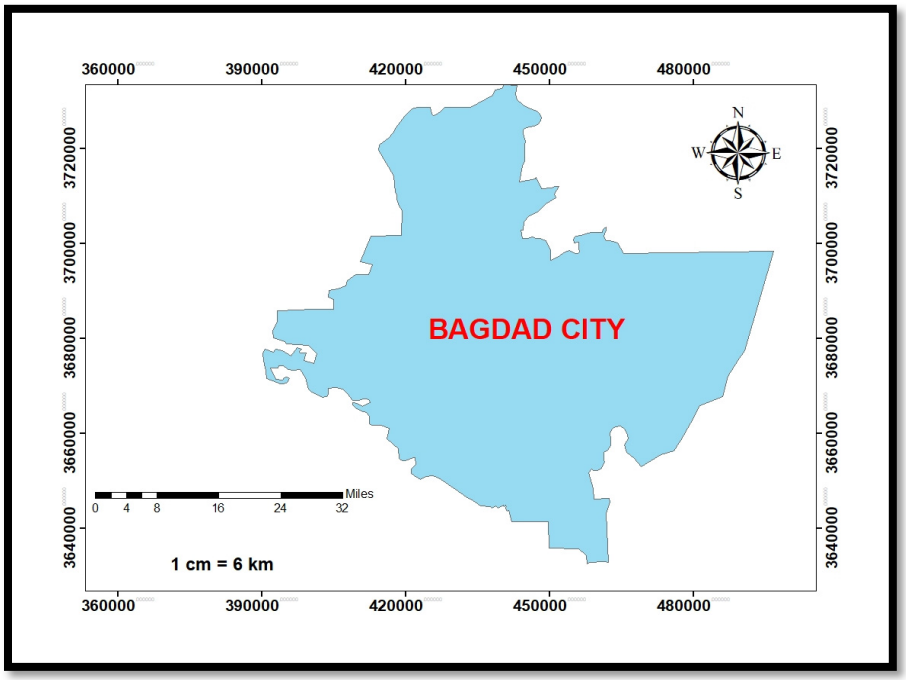

Figure1. Baghdad Governorate

EXPERIMENTAL PART

A- Calculating Rn-222 concentrations in the air

1- Samples of air aerosols (plankton, dust, liquid, and solid bodies, etc.) were collected using an air blower at a speed (3000 rpm) and at a height of (165 cm) (the height represents the average height of an Iraqi person) for 7 days.
2- Air aerosols were collected from several regions of Baghdad and then sieved with a sieve of size (70 µm).
3-To record alpha particles from the radioactive Rn-222 gas in the aerosol, 20 gm of air aerosol was placed in a tightly sealed plastic cup and the nuclear trace detector (CR-39) was attached to a region (11 cm2) with adhesive tape. The detector was left for a month. Air, as shown in Figure (2), represents the cup used for irradiation to obtain Rn-222 concentrations, and the dimensions of the cup are ideal, as the separation between Rn-222 gas and thoron gas is based on the half-life, where Rn-222 has (3.8 d.) and thoron (55 s.), and the emission from the air aerosol sample. It takes longer time than the detector's half-life to reach the detector, hence a beaker with a minimum length of 10 cm is preferred [9].

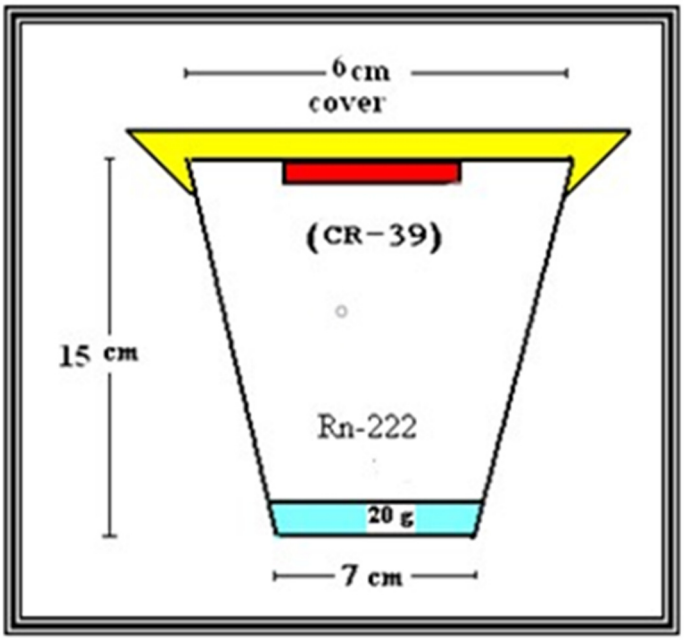

Figure 2. The process of detector exposure to Rn-222 using the mug technique for air aerosol samples.

B- Calculating Rn-222 concentrations in water

1- Water samples were collected from different regions of Baghdad, and (1/4) liter of water was placed in a plastic container as in Figure (3).
2- A nuclear trace detector (CR-39) with a region (2×2 cm^2) was placed in the container lid for a month to ensure the recording of alpha particles emitted from radioactive Rn-222 gas present in water samples.

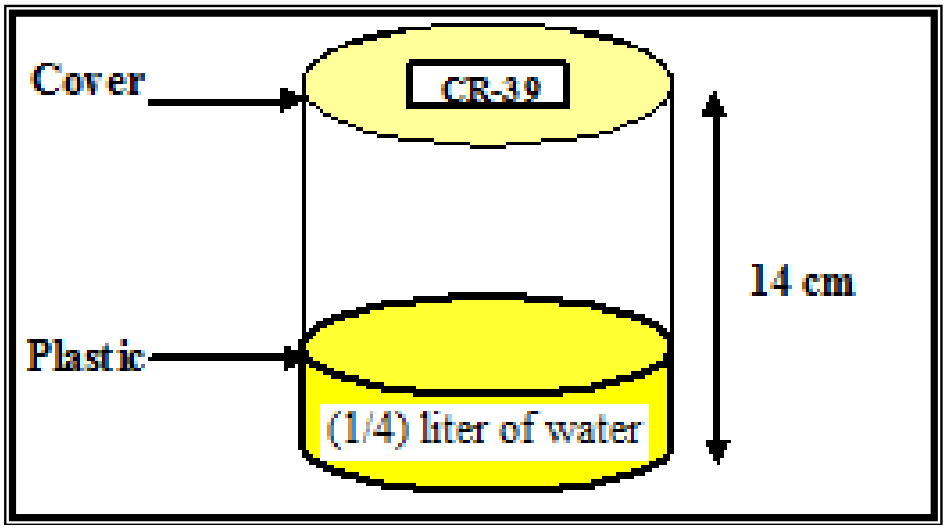

Figure 3. The container for exposing the reagent (CR-39) to water samples.

C- Calculating Rn-222 concentrations in the soil

1- Soil samples were collected from specific regions of Baghdad governorate, and then the samples were dried and sieved to obtain homogeneous samples.

2- (25 gm) of soil was placed in plastic cups. The nuclear trace detector (CR-39) with a region of (1×1 cm^2) was attached to the lid of the cup with adhesive tape and left for a month to ensure the recording of alpha particles on the detector resulting from the dissolution of Rn-222 emitted from the soil as in Figure (4).

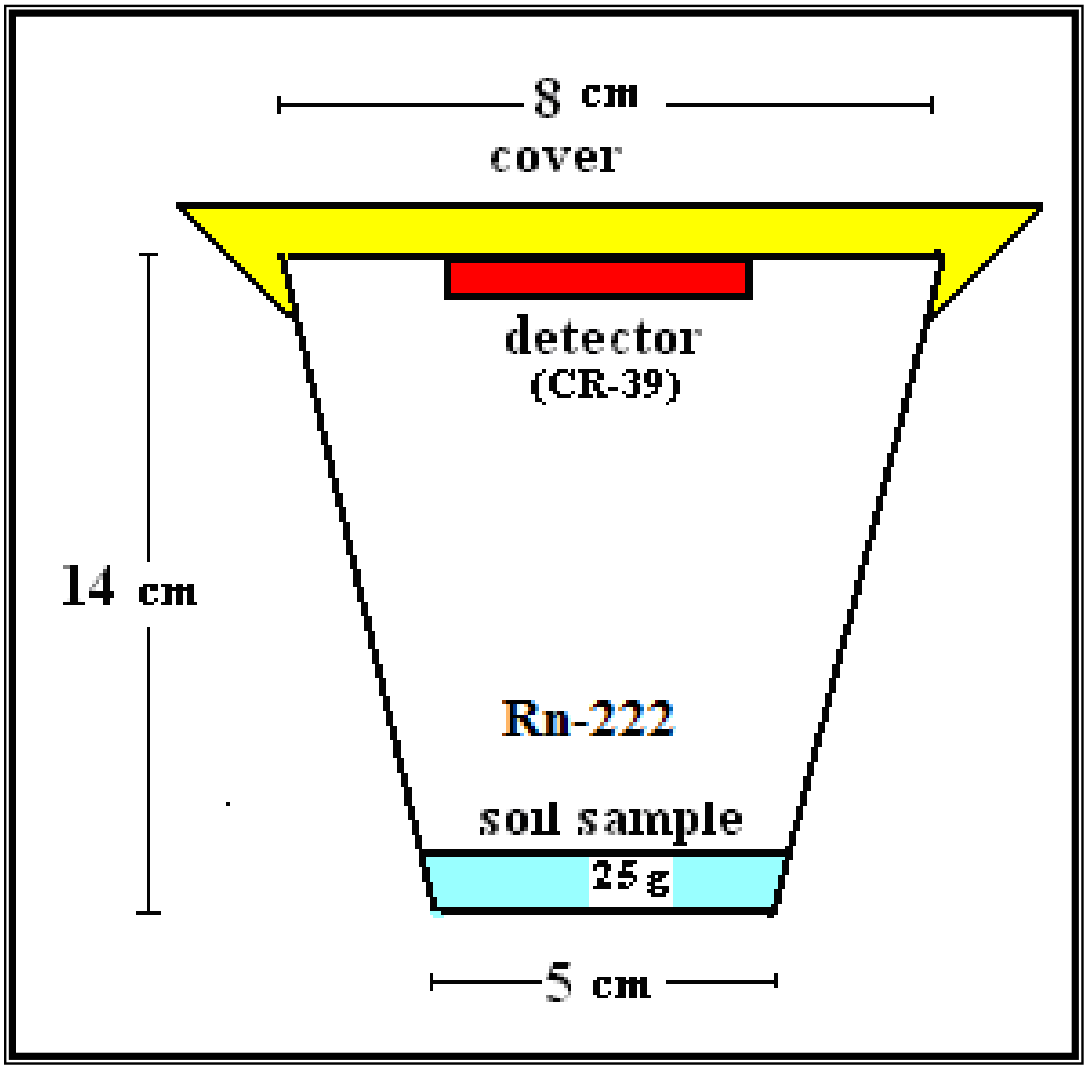

Figure 4. The process of detector exposure to Rn-222 using the mug technique for soil samples.

D- The reagents were raised after irradiation for (A, B, and C) and a chemical scraping process was carried out using the scraping solution (NaOH) and appropriate scraping conditions with a standard of (6.25) and a temperature of (70 C^o) for four hours [10]. Calibration was done by exposing the detector to soil samples. The standard contains known concentrations of U-238 that are internationally approved and manufactured by the International Atomic Energy Agency (IAEA). The trace density of the soil (Tx) and the standard soil (Ts) formed on the detector were calculated using an optical microscope, and the graphical relationship was drawn between the known concentrations of the standard samples (Es) and the trace density. The standard (Ts) for the study samples (air, water, and soil) and the relationship was linear as in Figures (5), (6), and (7) respectively, and the Rn-222 concentrations for the unknown samples (Ex) were calculated from the relationship [11].

$$Ex = \left(\frac{Es}{Ts}\right) * Tx = \frac{Tx}{slop} \text{ ,.....} \quad \text{.....} (1)$$

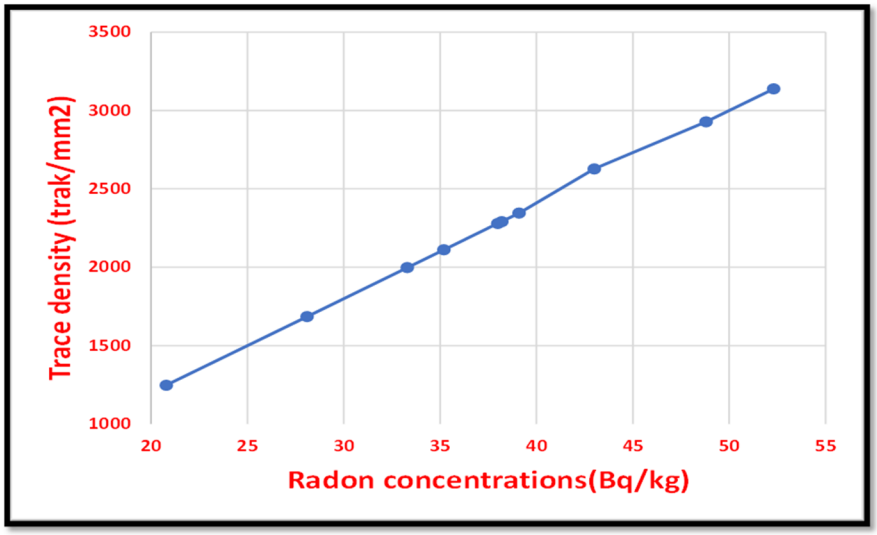

Figure 5. Trace density (Ts) and Rn-222 concentrations (Es) for air samples.

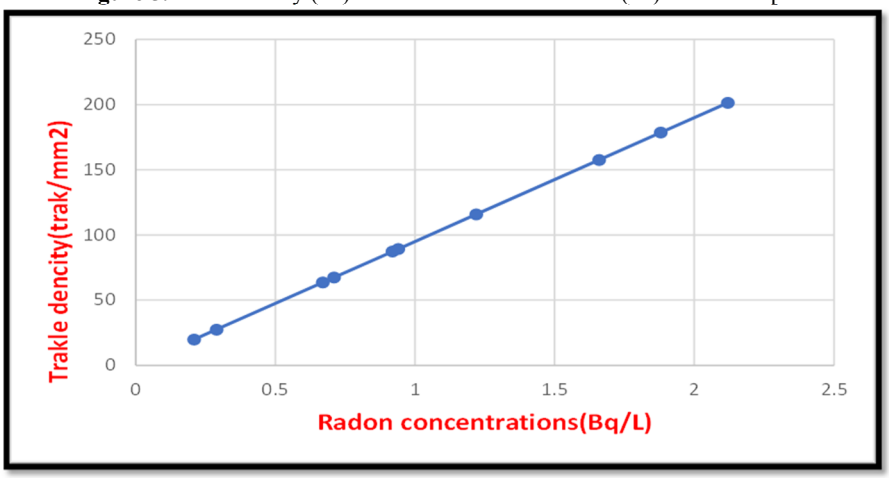

Figure 6. Trace density (Ts) and Rn-222 concentrations (Es) for water samples.

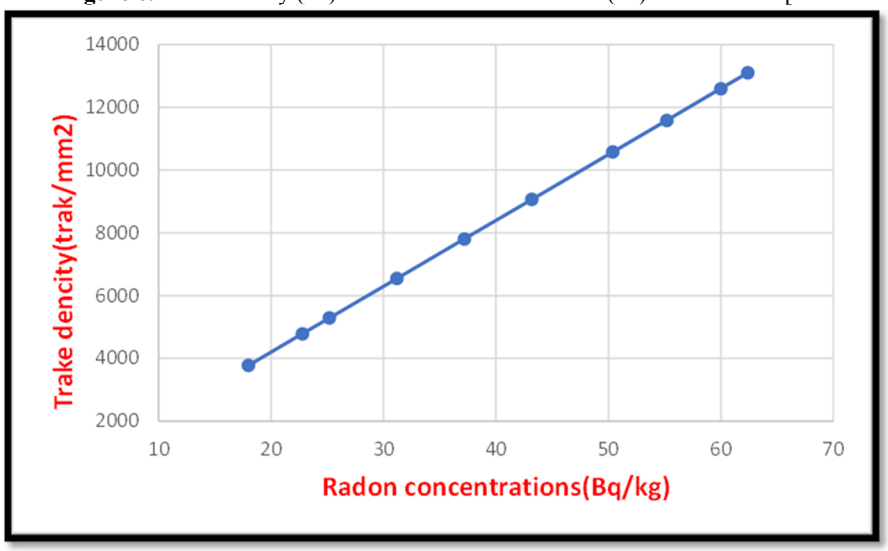

Figure 7. Trace density (Ts) and Rn-222 concentrations (Es) for soil samples.

RESULTS AND DISCUSSION

Concentrations of radioactive Rn-222 gas were determined for different regions of Baghdad governorate, using the technique of counting traces of alpha particles emitted from radioactive Rn-222 gas using a (CR-39) detector. The research includes Rn-222 concentrations for different samples of the environment (air, water, and soil) for the regions (Wardiya. New Baghdad, Talbiyah, Jadriya, Adhamiya, Mahmoudiyah, Rashidiya, Yusufiyah, Taji and Zaafaraniyya) and as follows:- Rn-222 concentrations for air aerosol samples were collected for ten different regions of Baghdad governorate, as in Table (1), where the average concentrations were (37.68 Bq/kg), equivalent to (3.135 ppm), where each (12 Bq/kg) of lower U-238 equivalent to one part per million (ppm). The highest concentration of Rn-222 in the air was in the Mahmoudiyah region (52.31 Bq/kg), the lower concentration in the New Baghdad region was (20.8 Bq/kg), and the average concentrations were (37.68 Bq/kg).

1- Rn-222 concentrations for water samples were collected from the Tigris River, well water, irrigation canals for crops and ponds, and different regions of Baghdad, where the highest concentration of Rn-222 in units (Bq/L) in the water in the Mahmoudiyah region was (2.12 Bq/L), equivalent to (2.12 Bq/L). 0.17 ppm and the lower concentration of Rn-222 in the New Baghdad region is (0.21 Bq/L), which is equivalent to (0.017 ppm), and the average concentration is (1.06 Bq/L), as in Table (2). When comparing the results with international measurements, which represent the permissible dose of Rn-222 in water, some international organizations, including the Environmental Protection Agency (E.P.A), recorded a maximum permissible value in water, which is (0.148 Bq/L). The International Commission (ICRP) also recorded Radiation Protection) has a value of (0.5994 Bq/L), as a limit. It is allowed in household water, representing evidence of danger [12]. From the above, we find that Rn-222 concentrations in water are higher than global concentrations, which poses a danger to residents in these regions.

2- Rn-222 concentrations for soil samples were taken for different regions of Baghdad, and the highest concentration of Rn-222 in the soil was in the Yusufiyah region (62.4 Bq/kg), equivalent to (5.2 ppm), and the lower concentration in the Jadriyah region was (18 Bq/kg), equivalent to (1.5 ppm), we find that the rates of Rn-222 contamination in the soil vary from one region to another, noting that the study regions have different terrains, some of which are agricultural or residential, the present results show that the radon gas concentration in soil samples is below the allowed limit (11.7 ppm) recommended by (UNSCEAR, 1993) [13].

3- Rn-222 radioactivity maps were drawn for all the samples mentioned above for the study region using remote sensing and geographic information systems, as shown in Figures (8), (9), and (10), respectively [14].

Table (1) Rn-222 concentrations in air aerosol for different regions in Baghdad.

No.	Name of region	Trace density (track/mm^2)	Rn-222 con. (Bq/kg)	Rn-222 con. (ppm)
1	Alwahda	3138.6	52.31	4.35
2	AL-Mahmudi	2928	48.8	4.06
3	AL-Rashidia	2629	43.0	3.58
4	AL-Youssoufia	2375	39.1	3.25
5	AL-Adamya	2278	38.2	3.18
6	Sader City	2256	38.0	3.16
7	AL-Tagi	2168	35.2	2.93
8	AL-Madain	1989	33.3	2.77
9	Bagdad algidida	1675	28.1	2.34
10	AL-Mamoun	1261	20.8	1.73
Average		**2256.33**	**37.67**	**3.135**

Table (2) Rn-222 concentrations in water for different regions in Baghdad.

No.	Name of regions	Trace density (track/mm^2)	Rn-222 con. (Bq/L)	Rn-222 con. (ppm)
1	AL-Mahmudi	201.4	2.12	0.17
2	Alwahda	178.6	1.88	0.15
3	AL-Rashidia	157.7	1.66	0.13
4	AL-Youssoufia	115.9	1.22	0.1
5	AL-Adamya	89.3	0.94	0.078

6	Sader City	87.4	0.92	0.076
7	AL-Tagi	67.45	0.71	0.059
8	AL-Madain	63.65	0.67	0.055
9	AL-Mamoun	27.55	0.21	0.024
10	Bagdad algidida	19.95	0.21	0.017
Average		**100.89**	**1.06**	**0.0859**

Table (3) Rn-222 concentrations in soil for different regions in Baghdad.

No.	Name of regions	Trace density (track/mm^2)	Rn-222 con. (Bq/kg)	Rn-222 con. (ppm)
1	AL-Mahmudi	13104	62.4	5.2
2	Alwahda	12600	60.0	5.0
3	AL-Rashidia	11592	55.2	4.6
4	AL-Youssoufia	10584	50.4	4.2
5	AL-Adamya	9072	43.2	3.6
6	Sader City	7812	37.2	3.1
7	AL-Tagi	6552	31.2	2.6
8	AL-Madain	5292	25.2	2.1
9	Bagdad algidida	4788	222.8	1.9
10	AL-Mamoun	3780	18.0	1.5
Average		**8517.6**	**40.56**	**3.38**

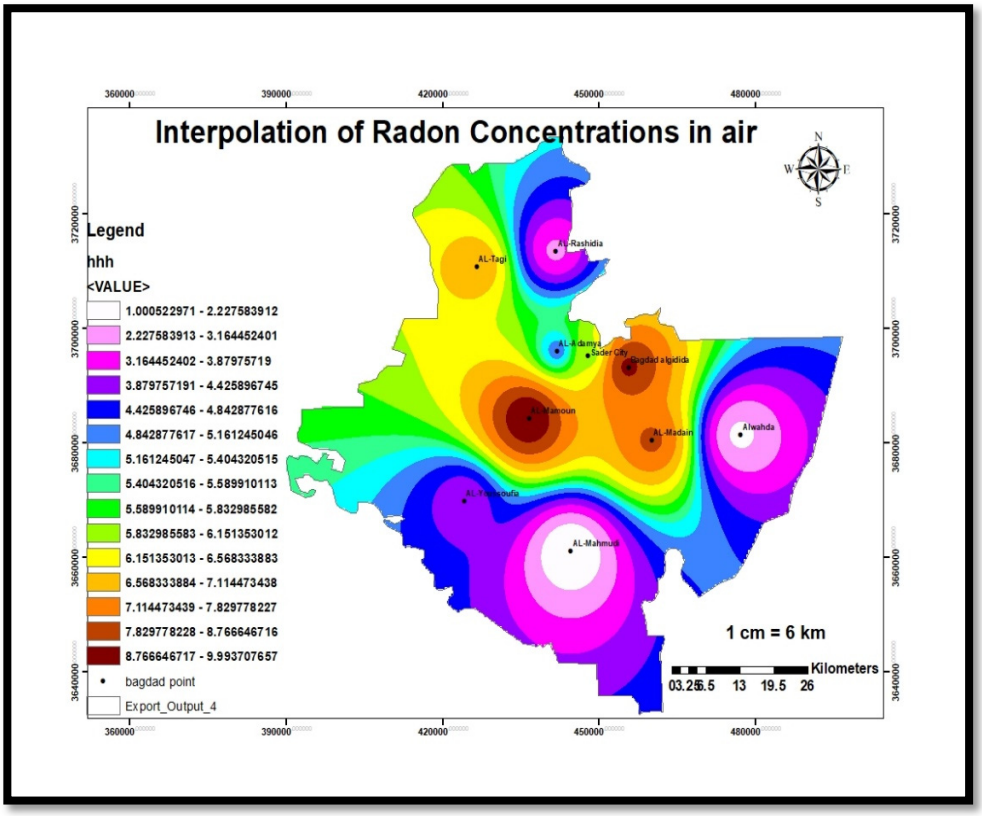

Figure 8. Distribution map of Rn-222 concentrations for the study regions in air

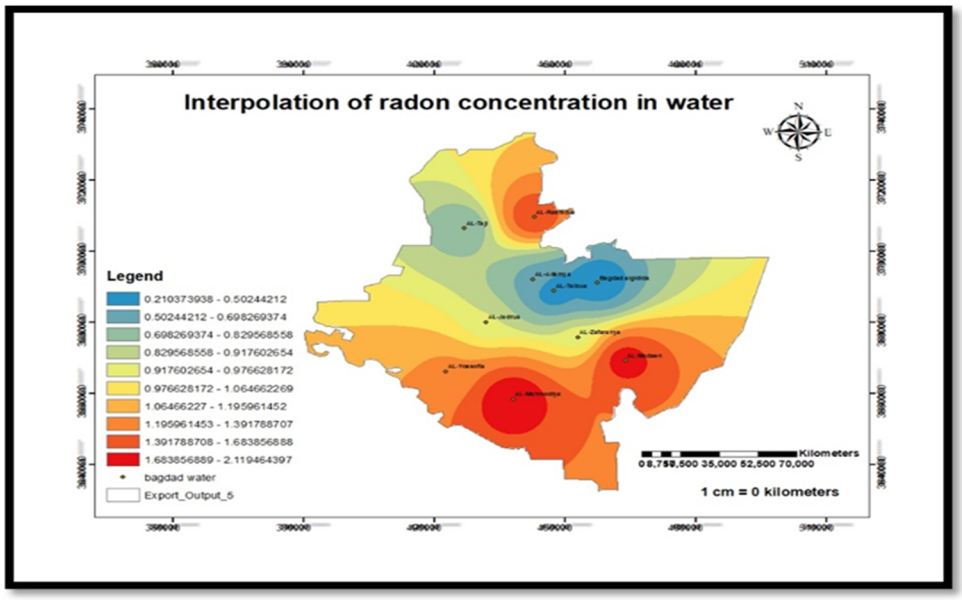

Figure 9. Distribution map of Rn-222 concentrations for the study region in water.

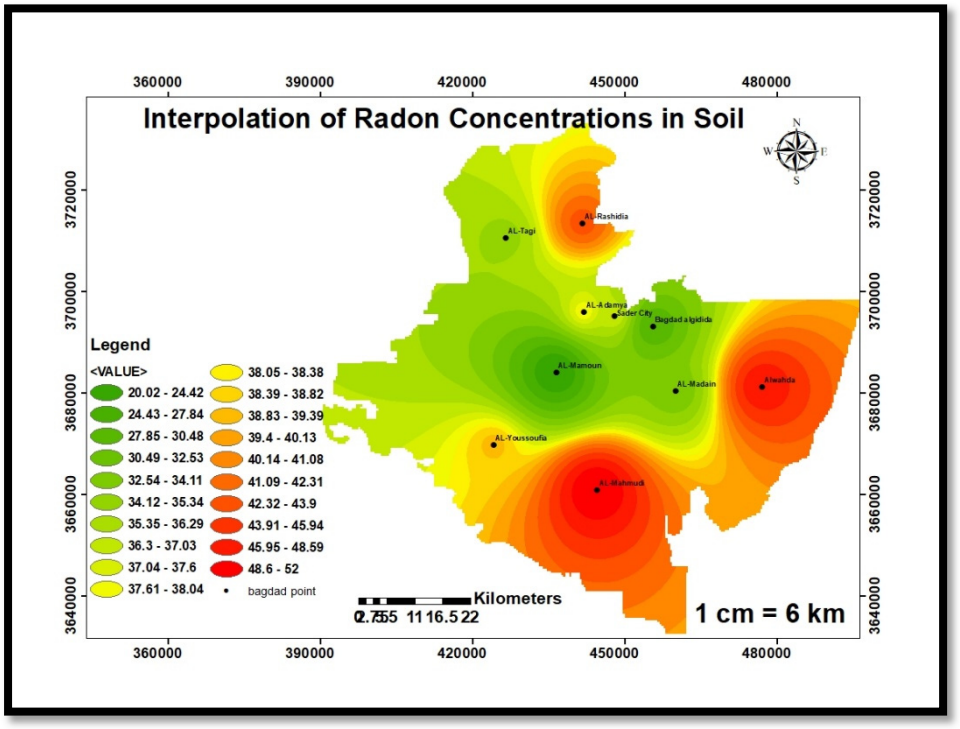

Figure 10. Distribution map of Rn-222 concentrations for the study region in the soil

CONCLUSIONS

The first part of the article tested the amounts of the gas Rn-222 in air aerosol samples from the Baghdad Governorate. The results showed that the greatest rate of Rn-222 concentrations (4.35 ppm) was found in the Mahmoudiya region. The second section's task was to determine the Rn-222 gas concentrations in the Tigris water for the different Baghdad regions. The results indicated that the greatest rate of Rn-222 gas concentrations in the water (0.17 ppm) was found in the Mahmoudiya region. The third part involved determining the concentrations of Rn-222 gas in the soil for

different parts of Baghdad. The results indicated that the greatest rate of Rn-222 gas concentrations in the soil (5.2 ppm) was found in the Mahmoudiya region. The amounts of Rn-222 gas in all samples (soil, water, and aerosols) for every area of the Baghdad governorate are below the permitted level as reported by the ICRP and UNSCEAR (1993). As a result, we conclude that Baghdad's radon gas pollution rate is extremely low and within acceptable bounds.

REFERENCES

1. Hadeel T. Hamad, Mahmood S. Karim, Nada F. Kadhim, "Assessment of Rn-222 gas concentrations in Educational laboratories of Department Physics in the College of Sciences, Al-Mustansiriya University" Journal of Physics: Conference Series, Vol.1879, Issue 3, pp. 32067- 32073 (2021).
2. Warren C.E., "Biology and Water Pollution Control", W.B. Sanders Company, London, p.434 (1971).
3. Sameera A. Ebrahiem, Esraa H. Falih, Hind Abdul Majeed Mahdi, Auday H. Shaban, Indoor 222Rn measurement and hazards indices in houses of Al-Najaf province – Iraq, AIP Conf. Proc. Vol.1968, pp: 030003-1–030003-5, 2018.
4. Taghreed K. Hameed, Auras M. Omron, Mahmood S. Karim "Measurement of Rn-222 gas Concentrations and Rn-222 Exhalation Rates in Some Cigarettes Tobacco Samples" Iraqi Journal of Science, pp. 4300-4303 (2021).
5. Charles H Briscoe, Kenneth Finlayson, Robert W Jones Jr, Cherilyn A. Walley, A Dwayne Aaron Michael, R Mullins James, A Schroder, "All Roads Lead to BAGHDAD" Army Special Operations Forces in Iraq, UNIVERSITY OF ILLINOIS URBANA CHAMPAIGN, (2006).
6.] Abojassim, A. A., & Rasheed, L. H. "Natural radioactivity of soil in the Baghdad governorate", Environmental Earth Sciences, 80(1), 1-13. (2021).
7. Tawfiq N.F., Mansour H.L. Karim M.S., " Measurements of Radon-222 concentrations in dwellings of Baghdad Governorate " Indian Journal of Applied Research,4, Issue:2, pp.35-39, (2014).
8. Karim M. S."Study of radioactivity and radon gas emanation in some Iraqi governorates" Ph.D.Thesis, Al-Mustansiriyah University College of Education. (2015).
9. Ghayb D.H., "Measurement of Alpha Emitters concentration in Tigris River water in Baghdad city using CR-39 plastic track detector". M.Sc. Thesis, Al-Nahrain University, College of Science, (2002).
10. A. A. Hasan, I. T. Al-Alawy, and H. G. Daway, "Estimate the Relationship Between Track Density and Radon Concentration: Hazard Effects in Euphrates River of Karbala-Iraq," Al-Mustansiriyah Journal of Science, vol. 34, no. 4, pp. 116-122. (2023).
11. United Nations Scientific Committee on the Effects of Atomic Radiation, "Sources and Effects of Atomic Radiation", Report to General Assembly, UNSCEAR, United Nations, (1993).
12. Fouad K. Mashee, Gheidaa S. Hadi, "Study the Wet Region in Anbar Province by Use Remote Sensing (RS) and Geographic Information System (GIS) Techniques", Iraqi Journal of Science, 58(3A), 1333-1344. DOI: 10.24996/ijs. (2017).
13. Emad H. Ahmed, Mahmood S. Karim, Fouad K. Mashee Al-Ramahi," Choosing the best locations to establish a nuclear power plant in Iraq with respect to radioactivity in those areas", Journal of Physics, Conference Series 2857 (2024) 012012, (2024).
14. Fouad K. Mashee, Muaid J. Rasheed, Ali K. Mohammed Ali, Abdulrahman B. Ali, "Dem Imagery for Investigation and Verification Najaf-Karbala Hill Formation by Using Remote Sensing Techniques", Iraqi Geological Journal, 56(1C), 191-201. DOI: https://doi.org/10.46717/igj.56.1C.13ms-2023-3-24.

Simulation Investigations of Physical Docking of Drug Developed With Nanomaterial for Cancer Tumor Treatment

Iman M. Kadhim [a)], Bahjat B. Kadhim [b)]

Department of Physics, College of Science, Mustansiriayah University, Baghdad, Iraq.

[a)] eman.muslim@uomustansiriyah.edu.iq
[b)] Corresponding author E-mail: sci.phy.bbk@uomustansiriyah.edu.iq

Abstract. In this research, the electronic and thermodynamic properties that are essential for understanding molecular interactions, especially in the context of drug effect discovery, were analyzed using Gaussian 09 for all calculations and Gauss View 6.0.16 for visualization to gain a deeper understanding of material behavior was used. This study calculated the electronic and thermodynamic properties by combining the B3LYP computational level with the basis set (6-311g(d,p)), which yielded accurate results for molecular properties. The main factors studied included energy gap, ionization energy, electron affinity, cohesive binding energy, and interaction energy, along with Gibbs free energy (ΔG), enthalpy (ΔH), and entropy (ΔS). Structural models were developed for the docking interactions between deoxyhemoglobin and letrozole, $(Fe_2O_3)_2$ and deoxyhemoglobin, as well as the docking models of $(Fe_2O_3)_2$ and letrozole with progesterone. The results showed that the docking interaction between $(Fe_2O_3)_2$ and letrozole is characterized by high stability and safety for human health. In contrast, the interaction of letrozole with progesterone showed the highest (ΔG) value (0.649 eV), making it the least stable interaction. The docking of $(Fe_2O_3)_2$ with progesterone showed a (ΔG) value of (0.505 eV), indicating its greater stability and spontaneity, making it a promising candidate for nano therapy in combating breast cancer.

Keywords: progesterone, docking, breast cancer, Simulation, DFT, $(Fe_2O_3)_2$, letrozole.

INTRODUCTION

The emergence of nanoparticles (NPs) as a medical rule-changing tool has improved therapeutic efficacy and patient outcomes by tackling issues such as medication resistance and non-specific dispersion. The nano system facilitates the delivery of specific drugs. According to [1], NPs help with the targeted distribution of chemotherapeutics, which reduces harm to healthy tissues. According to [2], polymeric nanoparticles make drugs like paclitaxel more effective in aggressive types of breast cancer, like triple-negative breast cancer (TNBC), by making the tumor more permeable and allowing the drug to stay in the body for longer. Photothermal and photodynamic therapies make use of nanoparticles, which, when coupled with more conventional methods, produce even more impressive synergistic results[3]. By modulating the tumor microenvironment, Mukherjee and Raikwar [4] found that designing nanocarriers can improve drug concentration at the target site. Oehler et al. [3] note that there are still obstacles to overcome, including concerns about biodistribution, safety, and regulations. Although recent developments in nanomaterials have opened up exciting new possibilities for treating breast cancer, it is essential to overcome their drawbacks and make sure they are safe for clinical application on a large scale [5].

Iron oxide nanoparticles $(Fe_2O_3)_2$ have recently made their way into cancer treatment. These nanoparticles enhance the efficacy of treatment while minimizing damage to healthy cells by making use of their unique properties. Grancharova et al. [6] found that the unique properties of IONPs, such as their ability to convert light into heat and boost cell membrane permeability, enable them to enhance medicine accumulation within tumors.

The discovery of progesterone role in breast cancer led to the development of letrozole and other aromatase inhibitors (AIs) as targeted therapies[7]. One important alternative for treating estrogen receptor-positive (ER+) breast cancer is letrozole, which is known for its highly effective progesterone production inhibitor. This review will

Technologies and Materials for Renewable Energy, Environment and Sustainability
AIP Conf. Proc. 3321, 020047-1–020047-9; https://doi.org/10.1063/5.0289830
Published under an exclusive license by AIP Publishing. 978-0-7354-5231-2/$30.00

focus on letrozole's role in breast cancer treatment, including its clinical consequences, comparative effectiveness, and action mechanisms.

Aromatase is an enzyme that mainly occurs in the periphery of the body and is responsible for converting androgens into progesterone [8]. One of the most important aspects of treating ER+ breast cancer is lowering serum progesterone levels, which letrozole accomplishes by specifically inhibiting aromatase[9].

The specific characteristics and interactions of hemoglobin (HB) with different medicines allow it to play a pivotal role in the targeted delivery of therapeutic chemicals to tumor cells. New methods that use hemoglobin as a therapeutic agent or carrier improve this capability, which in turn improves the effectiveness of cancer treatment while reducing adverse effects. To increase the effectiveness of anti-cancer treatments, hemoglobin-based oxygen carriers (HBOC) were created to boost oxygen transport in hypoxic tumor environments [10].

THEORETICAL CONCEPTS

Simulation and modeling all possible drug interactions between hemoglobin (HB) and breast cancer therapeutics allows one to examine the thermodynamic and electronic properties of drugs used to treat this condition, ultimately leading to the selection of the most effective and safe drug for them. Atoms, molecules, solid states, chemistry, biology, and even nuclear physics can benefit from density functional theory (DFT), a popular computational approach to finding solutions to quantum mechanical problems. Similar to our findings, many density functional calculations involving biomolecules rely on dispersion changes [11-13].

The electronic spectrum is divided into two types of bands: valence bands and conduction bands. The valence shell is the most outer region of an atomic or molecular electronic configuration and orbitals. This region is prone to encounters with outside electrons. These molecular orbitals are commonly known as HOMOs, which stands for highest-occupied molecular orbits. Connected to the nucleus are electrons in this band. In addition, the valence band and the higher energy level, which is called the conduction band or occupied molecular orbits lowest unoccupied molecular orbits LUMO, are clearly separated. It denotes a region called an orbital where excited valence band electrons can go. When it comes to the electron-free conduction band, the LUMO is considered the gold standard. A molecular orbital's significance is best illustrated by its (HOMO) and (LUMO) values. The prohibited energy gap, often known as the band gap, is the difference in energy levels between the low- and high-level operators [14]:

$$E_g = (\varepsilon_{LUMO} - \varepsilon_{HOMO}) \dots\dots\dots \quad \dots\dots\dots (1)$$

The ionization potential (*IP*) is the energy needed to liberate an electron from a system at the ground state reference geometry [15]:

$$IP = -\varepsilon_{HOMO} \dots\dots\dots\dots \quad \dots\dots (2)$$

The quantity of energy released when an electron is connected to a system is called electron affinity (*EA*) [16]:

$$EA = -\varepsilon_{LUMO} \dots\dots\dots\dots\dots \quad \dots\dots (3)$$

Energy of the highest occupied molecular orbital (HOMO) in the valence band at 0K was considered the Fermi level. However, the Fermi energy which is determined from the HOMO and LUMO, known as the mid gap level [17, 18]:

$$E_F = -\frac{IP + EA}{2} \dots\dots\dots\dots \quad \dots\dots (4)$$

The energy difference between the vacuum level (LUMO) and the Fermi level (chemical potential) is the work function, which is represented as the lowest energy needed to remove an electron from the Fermi level [19]:

$$\Phi_m = LUMO - E_F \dots\dots\dots\dots \quad \dots\dots (5)$$

The term "electronegativity" refers to the calculated propensity of a system to undergo electron bonding. The electronegativity describes the electrons' tendency to escape from the equilibrium state [15]:

$$\chi = \frac{IP + EA}{2} \dots\dots\dots\dots \quad \dots\dots (6)$$

The stability of a system's energy levels in response to external charges is quantified by the electrophilicity index [15, 20]:

$$\omega = \frac{\chi^2}{2\eta} \dots\dots \quad \dots\dots (7)$$

Chemical hardness is a way to quantify the charge transport impedance. If the external potential V(r) is constant, the chemical hardness can be known theoretically as the second derivative of electronic energy with respect to the number of electrons. It can be calculated chemical hardness right away using this formula [15]:

$$\eta = \frac{IP - EA}{2} \dots\dots\dots\dots \quad \dots\dots (8)$$

The chemical reactivity range is measured by the global chemical softness, *S*, which is a property of molecules. The chemical hardness η is reversed [15]:

$$S = \frac{1}{2\eta} = \left(\frac{\partial^2 N}{\partial E^2}\right)_{V(r)} = \left(\frac{\partial N}{\partial \kappa}\right)_{V(r)} \ldots\ldots\ldots\ldots\ldots \quad \ldots . (9)$$

Thermodynamic characteristics and the nature of the binding forces allow for the docking of any pharmacological substance containing deoxyhemoglobin (DHB) via one of four distinct types of binding forces. These include electrostatic interactions, hydrogen bonding, hydrophobic interactions, and Van der Waals forces. Thermodynamic characteristics can be utilized to ascertain the first contact forces. All combinations utilized in this research utilized Van der Waals forces, with the presence of cations ensuring charge equilibrium. This was done to preserve the structural formula of the compounds under investigation and to keep the drug's physical or chemical properties unchanged [21]. Each of the many possible topological configurations has its own set of advantages and disadvantages. Consider pore systems; their topologies determine the number of dimensions per channel, which in turn determines the reaction or entrapment potential of materials within internal cages [22]. Another possible use for these channels is to encase certain metal nanoparticles [23].

The structural configurations of letrozole, $(Fe_2O_3)_2$, and progesterone, and diluted hemoglobin were analyzed using the most relevant measures, thermodynamic quantities. It was performed analytical calculations using enthalpy, Gibbs free energy, and entropy to evaluate the affinity of diluted hemoglobin for antidiabetic drugs in the context of diabetes etiology. Free energy, defined as the amount of heat exchanged during thermodynamic processes, and entropy, a measure of the disorder or unpredictability of a system, are both parameters of this concept. It can be calculated the Gibbs free energy as follows [24]:

$$\Delta G = \Delta H - T\Delta S \ldots \quad . (10)$$

Equation 10 represents (*G*), enthalpy, entropy energy, and temperature. These two mechanisms, which depend on the reaction rate constant, can be shown by letrozole and $(Fe_2O_3)_2$ docking with progesterone or letrozole and $(Fe_2O_3)_2$ nano conjugated with deoxyhemoglobin. [24]:

Docking has been considered a related physical parameter, particularly in terms of thermal stability, where a complete understanding of the dependence of pharmaceutical and nanostructured materials on cohesive energy and interaction energy may be achieved [35]. Both the pre- and post-docking stages of this example have had their intrinsic electron binding energies (E_B) assessed [25, 26]:

$$E_B = [(N\,E_{Drug} + M\,E_{DHB}) - E_{Docking}]/(N + M) \ldots \quad \ldots\ldots . . (11)$$

Calculating the interaction and reaction energy weakens the surface's residual forces. Consequently, the thermal energy shows that the surface energy is also decreasing [27]. This mechanism contributes to the exothermic features of interaction, as demonstrated by the following equation [25]:

$$E_{int} = E_{Docking} - \left(E_{DHB} + E_{Drug}\right) \ldots\ldots \quad (12)$$

Where E_B, E_{int}, $E_{Docking}$, E_{DHB} and E_{Drug} stand for the binding energy, total interaction energy, DHB, and drug molecule energies, respectively. The total energy needed to dock DHB with the medication is also represented by this symbol. The letters *N* and *M* stand for the system's atoms, respectively.

MATERIALS AND COMPUTATIONS

Density functional theory (DFT) is a useful theory for determining the ground state properties of materials such as metals, conductors, insulators, and biomaterials. It is a comprehensive theory that studies the behavior of a single electron and then generalizes it to all atoms in a molecule, allowing it to evaluate the electronic and thermodynamic properties and determine the optimum structural stability of materials. Gaussian 09 for all calculations and Gauss View 6.0.16 for visualization to gain a deeper understanding of material behavior was used. This study calculated the electronic and thermodynamic properties by combining the B3LYP computational level with the basis set (6-311g(d,p)), which yielded accurate results for molecular properties.

Furthermore, it can be considered electrostatic potentials to investigate the most beneficial aspects of heme docking. It can be generated and prepared the molecular structure of hemoglobin for drug loading and targeting to specific areas in the body, including malignant tumors and progesterone, using Gauss View 6.0.16, density functional theory at the B3LYP level, and the basis set 6-311G(d,p). In order to understand the nanomaterial's effects on the human body and its impact on breast cancer relative to the drug letrozole, which is recognized by the World Health Organization, a structural model was created for the docking interactions between deoxyhemoglobin and letrozole, $(Fe_2O_3)_2$ and deoxyhemoglobin, and both letrozole and progesterone.

RESULTS AND DISCUSSION

The results show the optimization of the optimal structures at the lowest energy as shown in Figures 1, 2, 3, and 4 for deoxyhemoglobin (DHB), oxyhemoglobin (OHB), letrozole, $(Fe_2O_3)_2$, and progesterone, respectively.

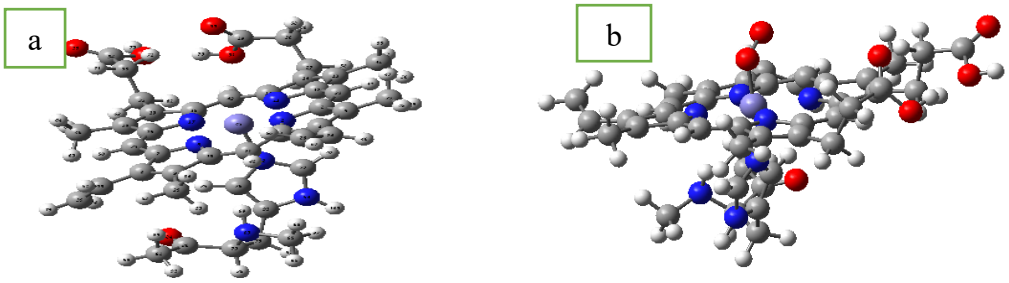

Fig. 1 The optimized structure for: (a) DHB, (b) OHB.

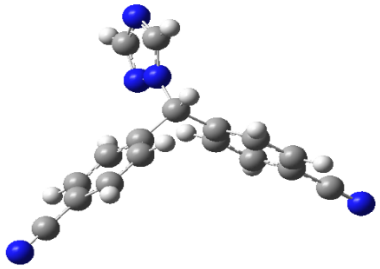

Fig. 2 The optimized structure of Letrozole molecule.

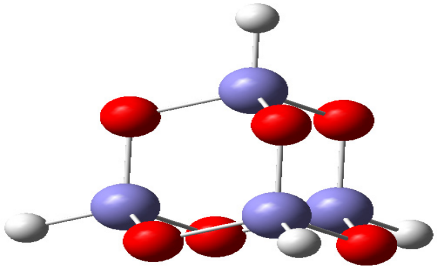

Fig. 3 The optimized structure of $(Fe_2O_3)_2$ molecule.

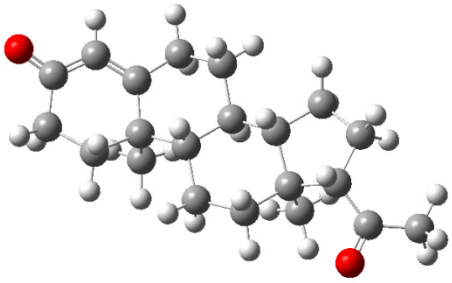

Fig. 4 The optimized structure of progesterone.

Figures 5 and 6 illustrate the optimization docking process between Letrozole and deoxyhemoglobin, as well as the docking of $(Fe_2O_3)_2$ with deoxyhemoglobin, respectively, to assess the impact of the drug and nanomaterial on human health and determine their safety.

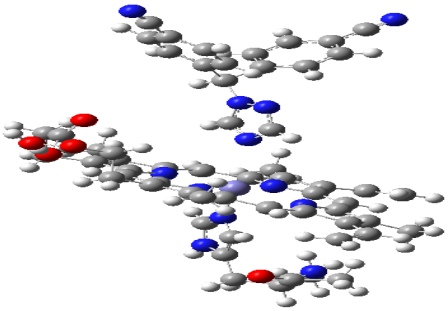

Fig. 5: Docking of deoxyhemoglobin with Letrozole.

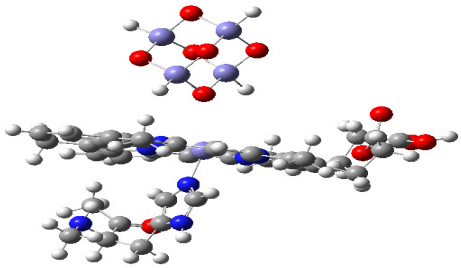

Fig. 6 Docking of deoxyhemoglobin with $(Fe_2O_3)_2$.

Figures 7 and 8 show the optimal docking process between letrozole and progesterone, as well as the docking of $(Fe_2O_3)_2$ with progesterone, respectively, to evaluate the effect of the drug and the nanomaterial on progesterone to find out which drug is better for treating breast cancer.

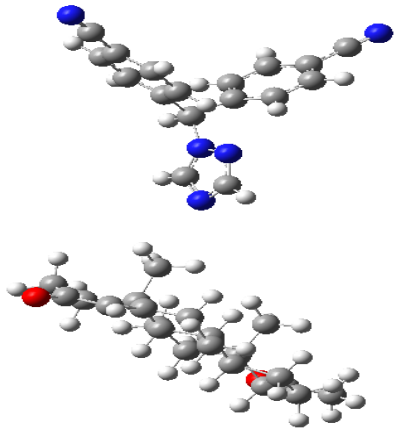

Fig. 7 Docking of Letrozole with progesterone.

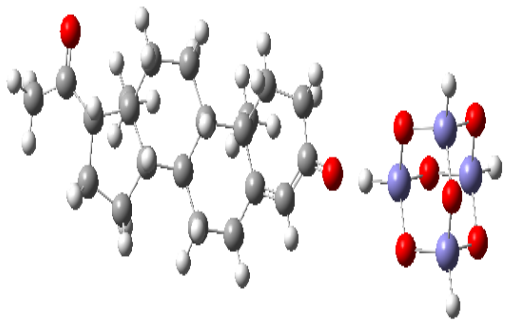

Fig. 8 Docking of $(Fe_2O_3)_2$ with progesterone.

It is possible to discuss the interpretation of the structural results as follows, where the studies of electronic and thermodynamic factors provide a wide spectrum of features important for comprehending molecule interactions, especially in the context of medication discovery. Essential for describing the behavior of chemicals are key factors like energy gap, ionization potential, and electron affinity. Calculations of cohesive binding energy and interaction energy also shed light on how medicinal substances interact with biological targets, such as hemoglobin. Critical thermodynamic and electronic characteristics disparity in energy, it affects reactivity and conductivity by showing how much energy an electron needs to move from the valence band into the conduction band. Electron affinity and ionization potential, these factors are crucial for predicting chemical behavior as they reveal the energy alterations that transpire upon the removal or addition of electrons. Energy and Fermi level, they affect the electronic characteristics of materials by defining the energy levels at which electrons occupy zero-energy states. Issues related to heat and mass calculating the Gibbs free energy, entropy, and enthalpy. To comprehend the spontaneity and stability of reactions involving medicinal substances, these thermodynamic factors are crucial. Energy of cohesive binding, it gauges the intensity of molecular interactions, a critical factor in assessing a medicine's effectiveness. Although it can be primarily focused on the electronic and thermodynamic parameters, it's important to remember that alterations in environmental conditions can significantly influence these features, potentially altering drug interactions and their efficacy.

In this study, it was looked closely at the hemoglobin structure's heme component. By using the optimized hemoglobin structure, it was led to study how docking affects the electronic and thermodynamic properties of various breast cancer medicines. Since $(Fe_2O_3)_2$ docks only to tumors, it is an ideal nanomaterial for the treatment of breast cancer [28].

Table 1 shows the electronic properties of four substances: deoxyhemoglobin, progesterone, letrozole, and $(Fe_2O_3)_2$. It can be analyzed these properties based on the HOMO and LUMO values. Low HOMO values indicate higher stability in electron donation, with letrozole and $(Fe_2O_3)_2$ showing low values, meaning that they are more stable in terms of electron donation compared to progesterone and deoxyhemoglobin. On the other hand, $(Fe_2O_3)_2$ has the lowest LUMO value, indicating its high ability to accept electrons. As for the energy gaps, progesterone and letrozole are larger, making them more stable and less reactive compared to deoxyhemoglobin and $(Fe_2O_3)_2$, which have smaller energy gaps and are more reactive. In addition, $(Fe_2O_3)_2$ shows the highest electron affinity values, indicating its stability in accepting electrons, while deoxyhemoglobin shows the lowest value. In terms of hardness and ductility, letrozole and progesterone are considered to be the most rigid and less susceptible to chemical reactions, while $(Fe_2O_3)_2$ and deoxyhemoglobin are the most ductile and more susceptible to reactions. Finally, $(Fe_2O_3)_2$ shows the highest value of chemical function and work potential, making it the most attractive to electrons, and also shows the highest value of chemical stability index ω, indicating that it is the most reactive of these compounds.

Table 1: The electronic proprieties in (eV).

Properties	Deoxyhemoglobin	progesterone	Letrozole	$(Fe_2O_3)_2$
HOMO	-4.780	-6.276	-7.520	-7.585
LUMO	-1.945	-1.524	-2.299	-4.600
IP	4.780	6.276	7.520	7.585
EA	1.945	1.524	2.299	4.600
E_g	2.835	4.751	5.220	2.985
E_f	-3.363	-3.900	-4.909	-6.092
Φ_m	1.417	2.375	2.610	1.492
χ	3.363	3.900	4.909	6.092
Hard	1.417	2.375	2.610	1.492
S	0.352	0.210	0.191	0.335
ω	3.989	3.202	4.616	12.435
SCF	-99365.4	-26366.2	-25263.9	-176257.7

In Table 2, the HOMO values indicate the stability of the compounds in donating electrons; both letrozole with progesterone and $(Fe_2O_3)_2$ with progesterone show the lowest HOMO values (-6.222 and -6.530 eV), reflecting greater stability. In contrast, $(Fe_2O_3)_2$ with DHB shows the highest HOMO value (-4.978eV), making it more capable of donating electrons. As for the LUMO values, letrozole with DHB shows the lowest value (-7.409 eV), making it more stable in accepting electrons, while $(Fe_2O_3)_2$ with DHB has the highest LUMO (-4.227 eV), indicating its less ability to accept electrons.

The energy gap (E_g) reflects the reactivity and stability of the compounds, as letrozole with DHB shows a negative gap (-2.382 eV), indicating high reactivity and instability, while letrozole with progesterone shows a larger gap (3.850 eV), indicating greater stability. The chemical potential (χ) indicates the ability to attract electrons, as letrozole with DHB and $(Fe_2O_3)_2$ with progesterone show the highest values (6.218 and 5.050eV, respectively), meaning that they have a high ability to attract electrons. As for hardness, letrozole with DHB shows high softness with negative hardness values (-1.191 eV), making it more susceptible to reactivity, while letrozole with progesterone shows a higher hardness (1.925 eV), making it more resistant to reactions. Finally, $(Fe_2O_3)_2$ with DHB shows the highest value of chemical stability index (ω) (28.232 eV), reflecting its high reactivity, while letrozole with DHB shows a negative value (ω = -16.231 eV), indicating obvious instability.

Table 2: The electronic proprieties in (eV) for docking reactions.

Properties	OHB	Letrozole with deoxyhb	$(Fe_2O_3)_2$ with deoxyhb	Letrozole with progesterone	$(Fe_2O_3)_2$ with progesterone
HOMO	-5.026	-5.027	-4.978	-6.222	-6.530
LUMO	-2.882	-7.409	-4.227	-2.371	-3.570
IP	5.026	5.027	4.978	6.222	6.530
EA	2.882	7.409	4.227	2.371	3.570
$E_{.g.}$	2.144	-2.382	0.750	3.850	2.960
E_f	-3.954	-6.218	-4.603	-4.296	-5.050
Φ_m	1.072	-1.191	0.375	1.925	1.480
χ	3.954	6.218	4.603	4.2968	5.050
Hard	1.072	-1.191	0.375	1.925	1.480
S	0.466	-0.419	1.332	0.259	0.337
ω	7.292	-16.231	28.232	4.794	8.617
SCF	-103457	-124615.9	103463.2	-51628.0	-176257.7

In Table 3, we note that the Gibbs free energy (*G*) values indicate the thermal stability of the system. It is shown that DHB has the highest value (19.525 eV), which means that it is less thermodynamically stable, while $(Fe_2O_3)_2$ shows the lowest value (0.418 eV), which reflects higher stability. As for the enthalpy (*H*) values, DHB also has the highest value (23.485 eV), which indicates that it has the highest change in thermal energy, while $(Fe_2O_3)_2$ shows the lowest value (1.755 eV).

Entropy (*ST*) plays a role in determining how random or chaotic the system is, and it is noted that DHB has the highest value (3.959 eV), which means that it is more chaotic, while $(Fe_2O_3)_2$has the lowest value (1.336 eV), which means that it is more organized. As for the binding energy (E_B), it is noted that Letrozole and DHB show large negative values (-1162.751 eV and -975.352 eV, respectively), which means that they may be more stable at the molecular level in interactions with other systems, while $(Fe_2O_3)_2$ shows a positive binding energy (12.930 eV), which indicates that it is more difficult to form bonds compared to other systems.

Table 3: Thermodynamic proprieties.

Energies (eV)	progesterone	Letrozole	$(Fe_2O_3)_2$	deoxyhb
G	11.515	5.454	0.418	19.525
H	13.270	7.195	1.755	23.485
ST	1.755	1.740	1.336	3.959
E_B	3.493	-1162.751	12.930	-975.352

In Table 4, the Gibbs free energy (*G*) shows variation between the systems. The highest value for Letrozole with deoxyhemoglobin (25.606 eV) indicates that it is less thermodynamically stable, while the lowest value for $(Fe_2O_3)_2$ with progesterone (12.439 eV) reflects a relatively higher stability.

Letrozole with deoxyhemoglobin has the highest enthalpy (*H*) value (29.727 eV), which means that the thermodynamic energy changes the most. On the other hand, $(Fe_2O_3)_2$ with progesterone has the lowest energy change (15.035 eV). In terms of (*TS*), which expresses the effect of entropy on the system, the values are close, but Letrozole with deoxyhemoglobin records the highest value (4.120 eV), indicating a more random system, while $(Fe_2O_3)_2$ docking with progesterone has the lowest value (2.596 eV), indicating that it is more organized.

In comparison, systems containing letrozole tend to be less stable and more affected by thermodynamic factors compared to systems containing $(Fe_2O_3)_2$ and progesterone, which appear to be more stable and less affected by changes in entropy and temperature.

Table 4: Thermodynamic and pharmacodynamics proprieties.

Energies (eV)	OHB	Letrozole with deoxyhb	$(Fe_2O_3)_2$ with deoxyhb	$(Fe_2O_3)_2$ with progesterone	Letrozole with progesterone
G	19.677	25.606	20.363	12.439	17.619
H	23.739	29.727	24.275	15.035	20.440
TS	4.062	4.120	3.911	2.596	2.821
ΔG	0.566	0.626	0.420	0.505	0.649
ΔH	0.063	-0.953	-0.965	0.010	-0.025
TΔS	-0.502	-1.580	-1.385	-0.495	-0.674
E_B	-996.235	642.004	-511.175	2.457	-1330.746
E_{int}	-1.717	-198717.328	-198707.817	-52732.568	-52730.397

Gibbs free energy (ΔG) values express the stability of a chemical reaction; the lower the (ΔG) value, the more stable and less reactive the reaction is. Table 4 reveals that the docking of $(Fe_2O_3)_2$ with DHB has the lowest (*G*) value (0.420 eV), suggesting that it is the most stable, non-spontaneous, safe, and does not negatively impact the body's health. In contrast, the reaction between letrozole and deoxyhemoglobin shows the highest (ΔG) value (0.626 eV), indicating that it is also a non-spontaneous reaction but safer. Letrozole docking with progesterone, on the other hand, has the highest (ΔG) value (0.649 eV), which means it is less stable. On the other hand, $(Fe_2O_3)_2$ docking with progesterone has a (ΔG) value (0.505 eV), which means it is more spontaneous and more stable, making it a good candidate for use in nanomaterial-based breast cancer treatment.

Negative values for enthalpy (ΔH) mean that the reaction is exothermic. For example, the docking of letrozole with deoxyhemoglobin (-0.953 eV) and docking $(Fe_2O_3)_2$ with DHB (-0.965 eV) shows that they give off energy and might work well in chemical docking. While the docking $(Fe_2O_3)_2$ with progesterone shows a small change in energy (0.010 eV), which means that it is a slightly endothermic reaction.

We can see that the docking of trozole with deoxyhemoglobin has the highest negative value (-1.580 eV), which means it is more organized and less random. On the other hand, the system of docking $(Fe_2O_3)_2$ with progesterone has the lowest negative value (-0.495 eV), which means it is less organized and more random. Finally, the binding energy (E_B) indicates the stability of the system, where large negative values, as in the interaction between $(Fe_2O_3)_2$ and progesterone (-511.175 eV) and OHB (-996.235 eV), reflect great stability.

CONCLUSIONS

The study analyzed the stability of various chemical reactions, including letrozole with deoxyhemoglobin and $(Fe_2O_3)_2$ with progesterone. Letrozole with deoxyhemoglobin showed the highest Gibbs free energy (G) value, indicating less thermodynamic stability. Letrozole with deoxyhemoglobin had the lowest enthalpy (H) value, indicating the most significant thermodynamic energy changes. The system's (TS) (transformation state) values were close, but letrozole with deoxyhemoglobin was more random. The docking of $(Fe_2O_3)_2$ with DHB showed the lowest (G) value, suggesting stability and safety. The docking of letrozole with deoxyhemoglobin showed the highest (ΔG) value, indicating a non-spontaneous, safe reaction. The docking of trozole with deoxyhemoglobin had the highest negative value, indicating more organization. The binding energy (E_B) indicated system stability. It can be analyzed the electronic properties of the substances using HOMO and LUMO values. The Gibbs free energy (G) values indicated thermal stability, with DHB having the highest value. Entropy (ST) indicated the system's chaotic or chaotic nature.

REFERENCES

1. S. Jaishree, K. Selvaraj, S. Prakash, D. Vineesh, Innovative Nanoscale Drug Delivery Strategies for Breast Carcinoma: A Comprehensive Exploration, Current drug metabolism.
2. M.A. Bazzazan, P. Fathollazadeh, S.K. Shahbaz, N. Rezaei, Polymeric nanoparticles as a promising platform for treating triple-negative breast cancer: Current status and future perspectives, International Journal of Pharmaceutics 664 (2024) 124639.
3. J.B. Oehler, W. Rajapaksha, H. Albrecht, Emerging Applications of Nanoparticles in the Diagnosis and Treatment of Breast Cancer, Journal of personalized medicine 14(7) (2024) 723.
4. D. Mukherjee, S. Raikwar, Recent Update on Nanocarrier (s) as the Targeted Therapy for Breast Cancer, AAPS PharmSciTech 25(6) (2024) 153.
5. S.R. Baddam, S. Ganta, S. Nalla, C. Banoth, B. Vudari, P.C. Akkiraju, E. Srinivas, R.S. Tade, Polymeric nanomaterials-based theranostic platforms for triple-negative breast cancer (TNBC) treatment, International Journal of Pharmaceutics (2024) 124346.
6. T. Grancharova, P. Zagorchev, B. Pilicheva, Iron Oxide Nanoparticles: Parameters for Optimized Photoconversion Efficiency in Synergistic Cancer Treatment, Journal of Functional Biomaterials 15(8) (2024) 207.
7. A.S. Bhatnagar, The discovery and mechanism of action of letrozole, Breast cancer research and treatment 105(Suppl 1) (2007) 7-17.
8. S. Janowska, S. Holota, R. Lesyk, M. Wujec, Aromatase Inhibitors as a Promising Direction for the Search for New Anticancer Drugs, Molecules 29(2) (2024) 346.
9. N. Bhatia, S. Thareja, Aromatase inhibitors for the treatment of breast cancer: An overview (2019–2023), Bioorganic Chemistry (2024) 107607.
10. H. Bu, X. Xu, J. Chen, Y. Cui, L.-Q. Wang, Synthesis of a hemoglobin-conjugated triblock copolymer for oxygen carrying and specific recognition of cancer cells, RSC advances 7(76) (2017) 48166-48175.
11. B. Huang, G.F. von Rudorff, O.A. von Lilienfeld, The central role of density functional theory in the AI age, Science 381(6654) (2023) 170-175.
12. S. Vuckovic, A. Gerolin, K.J. Daas, H. Bahmann, G. Friesecke, P. Gori-Giorgi, Density functionals based on the mathematical structure of the strong-interaction limit of DFT, Wiley Interdisciplinary Reviews: Computational Molecular Science 13(2) (2023) e1634.

13. B. Singha, K. Ray, Density functional theory insights on photocatalytic ability of CuO/TiO2 and CuO/ZnO, Materials Today: Proceedings 72 (2023) 451-458.
14. K.I. Williamson, D.J. Herr, Y. Mo, Mapping the correlations between bandgap, HOMO, and LUMO trends for meta substituted Zn-MOFs, Journal of Computational Chemistry (2024).
15. B.B. Kadhim, A. Al-Rubaiee, M.T. Matrood, Structural and electronic properties of InGaP nanocrystal diamantane drug carrier, Am J Mater Sci 7 (2017) 12-17.
16. S. Vadhel, P. Vinodkumar, M. Vinodkumar, Theoretical Investigation of Dissociative Electron Attachment of Acrylonitrile, The Journal of Physical Chemistry A 127(21) (2023) 4734-4742.
17. C.D. Hallock, M.J. Rose, Electrochemical Impedance of Well-Passivated Semiconductors Reveals Bandgaps, Fermi Levels, and Interfacial Density of States, Journal of the American Chemical Society 146(28) (2024) 18989-18998.
18. F. Hu, M. Berteau-Rainville, H. Hase, Y. Zhang, Q. Wang, I. Salzmann, S. Duhm, Energy-Level Alignment Governs Doping-Related Fermi-Level Shifts in Polymer Films, ACS Applied Electronic Materials 5(10) (2023) 5687-5695.
19. S.A. Marye, R.R. Kumar, A. Useinov, N. Tumilty, Thermal stability, work function and Fermi level analysis of 2D multi-layered hexagonal boron nitride films, Microelectronic Engineering 283 (2024) 112106.
20. B.B. Kadhim, H.O. Muhsen, Structural and electronic properties of SWGaPNT drug carrier, Nanoscience and Nanotechnology 7(1) (2017) 9-13.
21. V. Aiassa, C. Garnero, A. Zoppi, M.R. Longhi, Cyclodextrins and their derivatives as drug stability modifiers, Pharmaceuticals 16(8) (2023) 1074.
22. K. Berijani, A. Morsali, H. Garcia, Synthetic strategies to obtain MOFs and related solids with multimodal pores, Microporous and Mesoporous Materials 349 (2023) 112410.
23. J.-H. Li, H.-Y. Zhang, Q.-W. Shi, J. Ying, C. Janiak, Encapsulated Pt-based nanoparticles for catalysis, Progress in Materials Science (2024) 101335.
24. M.A. Abdulsattar, N.M. Almaroof, H.R. Jabbar, Interaction thermodynamics of human hemoglobin with environmental and toxic gases: A density functional theory study, Journal of Physics: Conference Series, IOP Publishing, 2021, p. 012132.
25. Z. Mahdavifar, R. Moridzadeh, Theoretical prediction of encapsulation and adsorption of platinum-anticancer drugs into single walled boron nitride and carbon nanotubes, Journal of Inclusion Phenomena and Macrocyclic Chemistry 79 (2014) 443-457.
26. X. Hu, I. Maffucci, A. Contini, Advances in the treatment of explicit water molecules in docking and binding free energy calculations, Current medicinal chemistry 26(42) (2019) 7598-7622.
27. K. Zhou, J. Chen, T. Wang, Y. Su, L. Qiao, Y. Yan, Effect of surface energy on protein adsorption behaviours of treated CoCrMo alloy surfaces, Applied Surface Science 520 (2020) 146354.
28. H. Hosseinkazemi, S. Samani, A. O'Neill, M. Soezi, M. Moghoofei, M.H. Azhdari, F. Aavani, A. Nazbar, S.H. Keshel, M. Doroudian, Applications of iron oxide nanoparticles against breast cancer, Journal of Nanomaterials 2022(1) (2022) 6493458.

Enhancement and analysis of x-ray images to diagnose pulmonary inflammation

Hawraa Hadi[1a] and Dhufr Hadi[2b]

[1] *Department of Anesthesia, College of Health and Medical Techniques/Kufa, Al_Furat Al_Awsat Technical University, 31003 Al-Kufa, Iraq*

[2]*Department of Physics, College of Education for Pure Sciences, University of Kerbala, Karbala, Iraq*

[a)]Corresponding author: hawraaalwaelly@gmail.com
[b)]dhufrhadi@gmail.com

Abstract: Many respiratory system patients are examined daily to determine the level of inflammation in the lung to receive appropriate treatment. so it is necessary to choose medical examination devices that are accurate, quick, effective, and reliable in determining the level of pneumonia that are inexpensive and with a low radiation dose. This research proposes to enhance and analyze chest X-ray images to detect a percentage of pneumonia using MATLAB and ImageJ processing software. The research results showed that the number of healthy alveoli in the patient is small and their size is large compared to the alveoli of a healthy person. It also showed that the percentage of the damaged area of the lung is considerable, which indicates that the lung is infected with inflammation and is damaged to some extent according to the degree of infection. The results also show that the percentage of agreement with the clinical diagnosis varies after image enhancement.

Keywords: X-ray, ImageJ, MATLAB, Image processing and Image analysis

INTRODUCTION

A computed tomography (CT) scan is a series of multiple x-ray images. For taking a cross-sectional image of a very thin section of the body, up to 0.3 mm wide, [1] X-rays are emitted and pass through the patient's body from multiple angles and then received by detectors placed on the opposite side of the X-ray emitting device then the thin sections of the body processed by a computer connected to the device to create detailed images [2]. To perform a CT scan of the chest, the area of the body that is usually examined when evaluating pneumonia, several cross-sectional images are required to cover the entire chest area. CT scanners are more sophisticated, expensive, and less widely available than X-ray machines [3]. They are also more difficult to decontaminate, taking more than 20 minutes. They are used to provide very detailed information and this requires more radiation than an X-ray machine. Therefore, they should only be used when appropriate for the patient's condition.

In X-ray imaging technology, the device emits a low-dose beam of X-rays that can pass through the body without the patient seeing or feeling them. Parts of the body absorb these rays at different rates based on their density, dense parts of the body, such as bones, pass less of the rays and appear white, while less dense parts (soft parts) pass more of the rays and appear gray, a detector on the other side captures the rays after they have passed and converts them into an image. Some X-ray machines are lightweight and easy to handle and disinfect, which is critical in any pandemic [4] [5].

X-ray imaging is used in patients with respiratory symptoms to monitor the progression of the disease and make decisions about treatment and follow-up, such as hospitalization [6]. It is also used to evaluate the condition of the organs and components inside the chest, such as the lungs, bronchi, heart wall, and chest wall, and to diagnose the cause of shortness of breath, cough, chest pain, or injuries and fractures of the ribs and collarbone. It is also used to

Technologies and Materials for Renewable Energy, Environment and Sustainability
AIP Conf. Proc. 3321, 020048-1–020048-5; https://doi.org/10.1063/5.0289833
Published under an exclusive license by AIP Publishing. 978-0-7354-5231-2/$30.00

diagnose a variety of lung diseases, such as emphysema, pneumonia, fluid accumulation, and to detect tuberculosis. X-rays also allow us to see any foreign body in the airway that has been inhaled [7].
Image processing techniques can be used to improve the quality of medical images taken by different imaging devices. This is done in many ways, for example, by removing distortions and noise in the images, which are then used to classify the severity of the disease, which helps doctors see details better and make treatment decisions [8] [9]. Singh et al. used deep learning technology on lung X-ray images to determine the severity of the disease and classify lung images as infected or non-infected. The results achieved a success rate of approximately 96% [10]. Another study by Thyagachandran et al. used some image processing algorithms to extract features and apply them to the ImageNet EfficientNetB5pre-trained model, then classified the images into three categories (COVID-infected, pneumonia, and normal) using a neural network from machine learning on chest CT images to classify the level of lung damage [11]. In addition, a study to detect lung cancer was presented by Abdillah et al, in their study, they found that the best method for detecting lung cancer is based on segmenting CT images using control watersheds and area growth and then enhancing the images using a Gabor filter. [12] Image processing techniques have proven their potential to enhance the accuracy and reliability of lung disease severity analysis.

METHODOLOGY

The presence of pneumonia is confirmed by some blood tests so that they can receive appropriate treatment, self-isolate, and inform those who have been in close contact with them to take the necessary measures. To determine the extent and location of the infection, this is done by chest CT scan or X-rays to determine the extent of lung damage.
In this research, a system based on ImageJ and MATLAB was proposed using chest X-rays to determine the extent of damage and compare it with the incidence rate. In medical images, pre-processing is a particularly delicate and challenging task. This research used MATLAB R2019b program for pre-processing contrast using the adaptive histogram equalization technique (AHE)for X-ray images as the first step.
The figure 1 shows the steps that follow to calculate the pneumonia percentage using the ImageJ software and compare it with the actual results of the doctors' diagnosis.

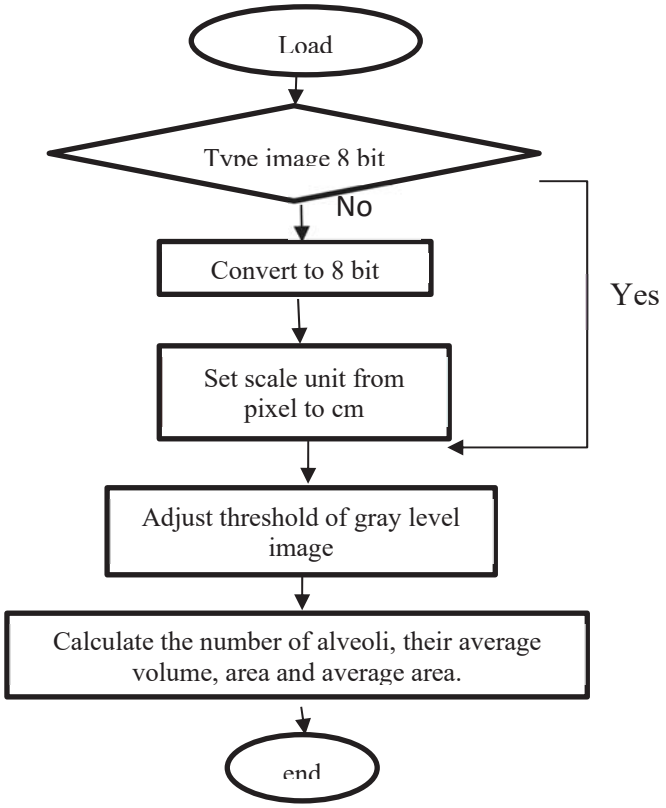

Figure1: steps for calculate the number of alveoli, their average volume, area and average area.

RESULTS AND DISCUSSION

The result of pre-processing contrast using the adaptive histogram equalization technique (AHE) for X-ray images is shown in table (1) below.

Table (1) The result of pre-processing

	Unhealthy 1	Unhealthy 2	healthy
original	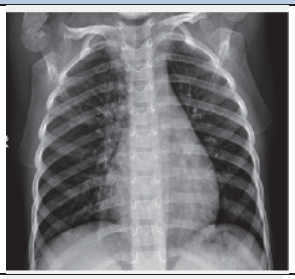		
Pre-processing	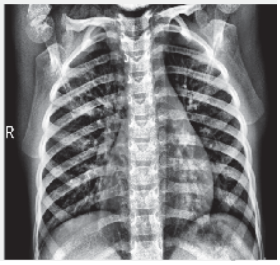		
RMS	125	138	185
SNR	6	5	3
PSNR	30	29	27

Table 1 shows the results of the pre-processing, where the first image is of a healthy person and the other two images are of patients with pneumonia. It was shown that the preprocessing by using the adaptive histogram equalization (AHE) technique greatly enhanced the contrast of the X-ray images.

The steps mentioned in flowchart (1) in the previous topic were applied to two images of infected patients and one image of an uninfected persons. The number of alveoli, their area, their average area, and the mean were calculated. Tables (2) and (3) below show the results for the original image before pre-processing and after pre-processing respectively.

Table (2) result for an original image

Slice	Count	Total Area	Average Size	%Area	Mean
Unhealthy 1	130	191	1.470	8.314	55
Unhealthy 2	43	136	3.171	7.255	90
healthy	152	110	0.728	4.768	103

Table (3) result for pre-processing image

Slice	Count	Total Area	Average Size	%Area	Mean
Unhealthy 1	211	435	2.063	20.568	66
Unhealthy 2	57	232	4.075	12.223	94
healthy	205	197	0.962	8.497	95

From the data shown in Tables (2) and (3), it is clear that the number of alveoli compared to the average area they occupy for uninfected persons is within the normal limits for healthy people, as they are small in size due to not being infected. While for infected patients, it is clear that their size is large compared to healthy people due to the accumulation of fluids inside them as a result of pneumonia. We also note that the percentage of the damaged area of the lung is very large, which indicates that the lung is infected and damaged according to the degree of infection.
When comparing the results, we obtained with the clinical diagnosis results, we found that the percentage of agreement is 45% regarding the images before the pre-processing, while the percentage of agreement increases to 67% in the images after the pre-processing.
Table (4) below shows the images after the approximate identification of the alveoli using the ImageJ program.

Table (4) image after calculating the threshold.

	Unhealthy 1	Unhealthy 2	healthy
Original		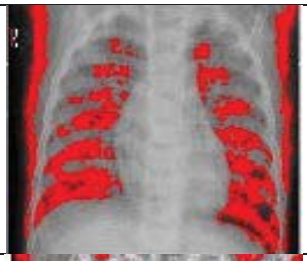	
Pre-processing			

where we notice from figures in above table (4) that the red color in the lung image of a healthy person shows the alveoli that are within the normal distribution and normal size. In the lung images of infected people, we notice that the size of the alveoli is very large compared to their size in healthy people, where the red color shows the damage that has occurred, which has taken up a large area of the lung.

CONCLUSION

The unhealthy chest X-ray image was further examined and compared with the clinical parameters considered in predicting the severity of lung disease. The experimental results using the Matlab and ImageJ software indicated that it provides a rapid and cost-effective examination in places where conventional large-scale testing is not possible. The research results showed that the number of healthy alveoli in the patient is small and their size is large compared to the alveoli in a healthy person. It also showed that the percentage of damaged area of the lung is large, indicating that the lung is infected with inflammation and is damaged to some extent depending on the degree of infection. The results also showed that the percentage of agreement with the clinical diagnosis varies after image enhancement.

REFERENCES

1. H. Hadi, E. A. Al-Hilo, S. M. Alshrefi and D. Hadi, "Improving fractal compression technique for CT scan images," in Technologies and Materials for Renewable Energy, Environment and Sustainability (AIP Conference Proceedings), Athens, Greece, 2022.

2. X. Ou ،x. chen ،X. Xu ،L. Xie ،X. chen ،Z. Hong ،H. Bai ،X. Liu ،Q. Chen ،L. Li و H. Yang ،"Recent Development in X-Ray Imaging Technology: Future and Challenges،" research a science partner journal ،p. 1826 ، 12 2021.
3. H. H. Al-waelly and H. M. Abduljabbar ،"The Interpolation Effect on the Spare Sinogram for 3D Image Reconstruction،" Technologies and Materials for Renewable Energy, Environment and Sustainability (AIP Conference Proceedings) ،Athens, Greece2019 ،.
4. R. Sharma ،S. D. Sharma ،S. Pawar ،A. Chaubey ،S. Kantharia و D. A. R. Babu ،"Radiation dose to patients from X-ray radiographic examinations using computed radiography imaging system،" Journal of Medical Physics 40(1):p 29-37, Jan–Mar 2015. | DOI: 10.4103/0971-6203.152244 ،pp. 29-373 ، 2015.
5. H. H. AL-waelly and H. M. Abduljabbar ،"3D image reconstruction from its 2D projection – a simulation study،" Progress in Industrial Ecology ،Vol. 14, No. 1 2020.
6. J. E. Aldrich ،E. Duran ،P. Dunlop and J. R. Mayo ،"optimization of dose and image quality for computed radiography and digital radiography،" Journal of Digital Imaging ،p. pages 126–1318 ، march 2006.
7. J. A. Rowlands ،"The physics of computed radiography،" Physics in Medicine & Biology ،pp. Volume 47, Number 2320 ، November 2002.
8. S. M. Islam و H. S. Mondal ،"Image Enhancement Based Medical Image Analysis،" 2019 10th International Conference on Computing, Communication and Networking Technologies (ICCCNT) ،Kanpur, India2019 ،.
9. N. Salem ،H. Malik و A. Shams ،"Medical image enhancement based on histogram algorithms،" Procedia Computer Science ،pp. 300-31122 ، January 2020.
10. A. Singh ،B. Lall ،B. K. Panigrahi ،A. Agrawal ،A. Agrawal ،B. Thangakunam و D. J. Christopher ،"Deep Learning based Diagnostic and Severity Assessment Framework for Lung Diseases using Chest Radiographs،" 2023 IEEE 36th International Symposium on Computer-Based Medical Systems (CBMS) ،L'Aquila, Italy24-22 ، June 2023.
11. A. Thyagachandran, A. Balachandran and H. A. Murthy, "Identification and Severity Assessment of COVID-19 Using Lung CT Scans," IEEE Access, no. 11, pp. 124542 - 124555, 06 November 2023 .
12. B. Abdillah ،A. Bustamam و D. Sarwinda ،"Image processing based detection of lung cancer on CT scan images،" p. 893(1):012063 ،October 2017.

Simulation of Physical Properties for Biomaterials Docking Mechanism with the Gouty Articular Cartilage

Sarah A. K. Athari [a)], Bahjat B. Kadhim [b)]

Department of Physics, College of Science, Mustansiriayah University, Baghdad, Iraq

[a)] sarah.a.athari@uomustansiriyah.edu.iq
[b)] Corresponding author E-mail: sci.phy.bbk@uomustansiriyah.edu.iq

Abstract: There is a problem with injury to multiple organs in the human body, in the joint areas, including injury to the knee joint, whether it occurs in the cartilage or tearing and cutting the knee tissue, and there is a possibility of analyzing it physically. In this study it was used the case, that the Gout arthropathy is represented by sodium urate monohydrate crystals that accumulate in synovial membranes, articular cartilage, causing articular cartilage degradation. Especially, Triamcinolone Corticosteroid injections is frequently utilized for treatment administration intra-articular. Gaussian View 6.0.16 program was used in conjunction with the Gaussian 09 program in employing density functional theory at the (B3LYP) level and with the help of the basis set (6-311G(d,p)), taking into account the case of dispersion and scattering. The tests included simulations of the thermodynamic properties represented by the Gibbs free energy, enthalpy and entropy, while the electronic properties included (energy gap, (HOMO) and (LUMO) energy, ionization potentials, electron affinities, chemical potential, global hardness, softness, and electrophilicity index). It was shown, through thermodynamic results and pharmacodynamics effects, that the metabolic processes depend mainly on the values of Gibbs free energy, if they are negative or positive values, in addition to their dependence on the values of the total energy after the docking processes, and the values of the binding energy and the interaction energy.

Keywords: Gout, Uric Acid, Articular Cartilage, Density Functional Theory, Osteoarthritis.

INTRODUCTION

Nanomaterials have indeed revolutionized various fields of science and technology due to their unique properties and applications. The size range of nanomaterials, typically defined as having at least one dimension between 1 and 100 nanometers, gives rise to distinctive physical, chemical, and biological characteristics compared to their bulk counterparts [1]. For biomedical applications, nanoparticles are very appealing due to their special qualities, such as their high surface area-to-volume ratio [2]. Nanomaterials' improved reactivity and size-dependent features have made them promising for use in various fields such as tissue engineering, drug delivery, and imaging. However, the incorporation of nanomaterials into the human body raises questions about their long-term impact, safety, and biocompatibility [3].

Sudden injuries that affect multiple joint areas in the human body are important to address their causes and the various treatment methods that are followed in rebuilding these joints, especially those related to rebuilding articular cartilage. Articular cartilage (AC), a layer of connective tissue, measures 1-4 mm in thickness. Collagen, proteoglycans (PG), sulfated glycosaminoglycans (GAGs), water, and a small quantity of chondrocytes make up its major constituents. Together, these elements give cartilage the strength it needs to resist pressure and mechanical forces. In the field of regenerative medicine, researchers have created nanocomposites based on collagen and polymers generated from acrylates to modify the mechanics and characteristics of collagen matrices for uses such as tissue engineering and controlled medication release. These developments emphasize the importance of comprehensive research, as well as the opportunities and difficulties that nanomaterials in biomedical applications present [4].

The popular disease that attacks the joints is inflammatory arthritis [5], known as "osteoarthritis". Gout is one of most common illness in adults, which is a result of uric acid crystals (Monosodium-urate (MSU) crystal) deposition

Technologies and Materials for Renewable Energy, Environment and Sustainability
AIP Conf. Proc. 3321, 020049-1–020049-8; https://doi.org/10.1063/5.0291636
Published under an exclusive license by AIP Publishing. 978-0-7354-5231-2/$30.00

in synovial fluid cavity due to either underexcretion or overproduction, leading to persistent hyperuricemia and being the end product of abnormal purine metabolism [6].

Purines are the primary metabolic substrates for all living creatures, serving as vital components for DNA and RNA production. Purines not only serve as DNA and RNA building components, but they also offer the energy and cofactors required for cell survival and proliferation. Increasing the ratio of production leads to gouty arthritis, which arises when deposition in joints results from hyperuricemia exceeding the local solubility [7].

Simulation is used to obtain results that optimize the accuracy of real outcomes and to learn how to compare them in order to achieve congruence, as is widely known and scientifically validated. With the use of Gaussian 09W, which makes use of a number of potent algorithms, scientists can accurately study molecules' electrical structures, energetics, and spectroscopic characteristics. It can simulate complex molecular dynamics and predict the geometries of molecules and reaction pathways [8]. Gaussian 09W is a vital tool in areas including drug design development, materials research, and catalysis since scientists use it to study a variety of molecular modeling issues. Because of the software's strong computational foundation and user-friendly interface, scientists can run complex simulations that deepen our understanding of molecular behavior and spur creativity in a variety of scientific domains. Using density functional theory, electronic, structural, and vibrational properties were investigated. The B3LYP hybrid functional was used to do DFT computations utilizing the usual 6-311G (d,p) basis sets [9 -12].

THEORETICAL CONSIDERATIONS

Quantum mechanics' basic equation, the Schrödinger equation, explains how a physical system's quantum state varies over time. Most commonly, it is spelled as [13]:

$$E = E_T + E_v + E_J + E_{XC} \quad \ldots \quad \ldots\ldots (1)$$

E_v: electron nuclear interaction energy; E_T: electronic kinetic energy, the term E_{XC} represents the exchange correlation, while E_J represents the electron-electron repulsion energy.

The Schrödinger equation is utilized in the context of the study you outlined to determine the system's total energy, which takes into account the electronic structure of the materials being studied.The electronic characteristics of the materials, including their energy levels, wave functions, andelectron concentrations, can be obtained by solving the Schrödinger equation [14]. Solid-state physics concepts describe the atomic arrangement, bond lengths, angles, and other geometric features of the materials' structure. Without this information, the system's Hamiltonian operator, which contains terms for electron kinetic energy, potential energy resulting from interactions between electrons and nuclei, and any external potentials, cannot be constructed [15]. By solving the Schrödinger equation, researchers can compute a variety of electronic properties, including band structures, densities of states, and electronic transport parameters, as well as the ideal structure of the materials they are studying in the context of solid state physics. The electronic properties of materials help us understand how they behave in many situations, for example in pharmacodynamics, where the interactions between drugs and living systems depend on things like molecular orbitals and charge distributions [16].

In fact, one of the most important electrical characteristics in quantum chemistry and materials science is the energy gap, sometimes known as the band gap. The band gap represents the energy difference between the lowest unoccupied molecular orbital (*LUMO*) and the highest occupied molecular orbital (*HOMO*) in crystalline materials or molecular systems. After finding the lowest possible total energy using quantum mechanical calculations, finding the *HOMO-LUMO* gap would reveal important details about the electronic properties of the materials being studied. This is necessary to fully understand their behavior and possible uses, such as in drug delivery and pharmacodynamics. The formula provided for the energy gap is [17]:

$$E_g = -(-\varepsilon_{LUMO} + \varepsilon_{HOMO}) \quad \ldots\ldots\ldots\ldots \quad \ldots\ldots (2)$$

Ionization potential (*IP*) is the energy needed to release an electron from the system at the ground state reference geometry [18], whereas electron affinity (*EA*) is the energy released when an electron is associated with the system [19]. Additionally, we represent a work function as the minimal energy required to remove an electron from the Fermi level, which we calculate as the energy difference between the Fermi level (chemical potential) and the vacuum level (*LUMO*). [20].

$$\Phi_m = LUMO - E_F \quad \ldots\ldots \quad \ldots\ldots\ldots (3)$$

Electronegativity is a fundamental concept in chemistry that describes the tendency of an atom to attract electrons towards itself when it forms a chemical bond with another atom. It's important to clarify that electronegativity is not about the "escape inclination" of electrons from a system, but rather about the relative ability of an atom to attract and hold onto electrons in a chemical bond [21]:

$$\chi = \frac{IP + EA}{2} \quad \ldots \qquad \ldots (4)$$

The electrophilicity index is indeed a concept used in theoretical chemistry to quantify the ability of a molecule to accept electrons or to act as an electrophile in a chemical reaction. However, its definition is more nuanced than simply measuring the stabilization in energy when a system acquires an additional electronic charge from the environment [22].

$$\omega = \frac{\chi^2}{2\eta} \qquad \ldots\ldots\ldots \qquad (5)$$

while chemical hardness does describe a molecule's resistance to changes in its electron density, it's not directly related to the impedance to transport charge. Instead, it's a measure of the stability and reactivity of a molecule based on its electronic structure [23]:

$$\eta = \frac{(IP - EA)}{2} \quad \ldots\ldots\ldots\ldots\ldots \qquad (6)$$

The global chemical softness (ζ) is indeed a property of molecules that measures the range of chemical reactivity. It is related to the chemical hardness (η) and is defined as the reciprocal of the chemical hardness [24]:

$$\zeta = \frac{1}{2\eta} = \left(\frac{\partial^2 N}{\partial E^2}\right)_{v(r)} = \left(\frac{\partial N}{\partial \kappa}\right)_{v(r)} \quad \ldots\ldots\ldots \qquad \ldots\ldots (7)$$

It might have a negative or positive value. In a negative state, the drug acts as an electron donor, transferring charge from the drug to the Gouty AC. In a positive state, the drug acts as an acceptor, transferring charge from the Gouty AC to the drug.

In fact, one of the most important ideas in thermodynamics is Gibbs free energy, sometimes known as Gibbs energy. Under constant pressure and temperature, it represents the most beneficial work that a system can extract. It is also essential for figuring out whether certain processes like chemical reactions are feasible under these circumstances. The formula represents Gibbs free energy (G) [25,26]:

$$\Delta G = -(-\Delta H + T\Delta S) \quad \ldots\ldots \qquad \ldots (8)$$

where S is the system's entropy, T is its temperature, and H is the system's enthalpy. In the field of pharmacodynamics, effective medication design and development depend on an understanding of how pharmaceuticals interact with the human body. Docking simulations are a useful tool for investigating these interactions at the molecular level. Two molecules, like a medication and its target receptor, release or absorb energy when they bind together. We refer to this as binding energy. Docking simulations, along with factors like binding energy, adsorption energy, and thermal stability, can help researchers learn important things about the pharmacodynamics properties of drugs and nanomaterial's. This thorough approach allows for a deeper comprehension of the interactions between these systems and the potential for therapeutic behavior optimization. [27]:

$$E_B = [(N\,E_{CS} + M\,E_{uric\ acid\ and\ Tria}) - E_{docking}]/(N + M) \quad \ldots\ldots\ldots \qquad \ldots (9)$$

Where E_B represent the binding energy, $E_{docking}$ refers to the total energy of the docking atoms of chondroitin sulfate CS with uric acid and triamcinolone. The E_{CS} and $E_{\ uric\ acid\ and\ Tria}$ energies of atoms of chondroitin sulfate CS, uric acid and triamcinolone respectively. N and M are the number of atoms of chondroitin sulfate CS and uric acid with triamcinolone present in the structure of the system respectively. The nature of the interaction energy between two materials, such as a ligand and a receptor, is crucial for understanding the stability and feasibility of their binding. The interaction energy, often denoted as interaction (E_{int}), represents the total energy change associated with the formation of the complex between the two materials [28]:

$$E_{int} = E_{docking} - (E_{CS} + E_{\ uric\ acid\ and\ Tria}) \quad \ldots\ldots \qquad \ldots\ldots (10)$$

Where E_{int}, $E_{docking}$, E_{CS} and $E_{\ uric\ acid\ and\ Tria}$, , the total energies of the interaction, chondroitin sulfate CS, and uric acid with Triamcinolone, are molecules respectively.

MATERIALS AND COMPUTATIONS

Major composed AC is of proteoglycans, known as aggrecan, that make up the infrastructure of cartilaginous tissues. It is composed of a variety of sulfated glycosaminoglycans (GAGs)[29], which are un branched polysaccharides consisting of a repeating disaccharide unit. Like chondroitin sulfate (CS, 100–150 per aggrecan monomer) and keratan sulfate (KS, 30–60 per aggrecan monomer) [30]. Around that, aggrecans consist of link proteins connected with long chains of GAGs. Collectively, aggrecan molecules form a "brush-like" architecture, It is crucial to maintain cartilage integrity and flexibility [31].

Chondroitin sulfate (CS) is the major component found in aggrecan. With age, the length of chondroitin sulfate decreases due to various diseases. Despite decades of research on the causes of cartilage degeneration, including

declining nutrition, loss of viable cells, accumulation of degraded matrix molecules, and post-translation modification of matrix proteins, a fundamental understanding of the process remains elusive [32].

The most common cause was an inflammatory disease. When unexpected crystals start gathering in the synovial cavity, it causes the cartilaginous tissue to swell and the immune system to be motivated, which, as a result, degradation and will reduce the function of the cartilage. As well as the component of cartilage, this research focuses on gout arthropathy disease [33].

As mentioned, the major component of cartilage is CS so that when the uric acid crystals deposition in synovial cavity [34]. Triamcinolone (TA) known as Corticosteroids are effective anti-inflammatory medicines, and intra-articular injections have been used treating symptomatic arthritis, which is a regularly utilized corticosteroid due to its low solubility, injectability inside joints, and greater anti-inflammatory efficacy through extended drug release [35].

In the present work, it shall build up Articular cartilage (AC) represented by Chondroitin Sulfate CS and docking with the smallest sodium urate monohydrate crystals molecules representing (Gouty AC) and Triamcinolone as drug (complex). Gaussian 09 is used to illustrate molecular modeling, these molecules included Chondroitin Sulfate of molecular with formula ($C_{19}H_{33}NO_{14}S$)[36], meanwhile, uric acid is a substituted purine with the formula ($C_5H_4N_4O_3$), also known as "1H-Purine-2,6,8(3H)-trione,7,9-dihydro-" with Triamcinolone molecular with formula ($C_{21}H_{27}FO_6$) [37].

The structures of these molecules are by utilization density functional theory (DFT) at the level B3LYP (beck three-parameter hybrid functional mixed with Lee-Yang-Parr correlation functional). A 6-311G(d,p) standard basis set, have been employed can be characterized as a split valence basis, since the core orbitals are a contraction of 6 primitive Gaussian type orbital's (GTOs), the inner portion of the valence orbitals is a contraction of 3 primitive GTOs, and the outside part of the valence is represented by one primitive GTO_S [38].

RESULTS AND DISCUSSION

Using density functional theory (DFT) implemented in Gaussian 09 and visualized by Gauss View 6.0.16 is a common and powerful approach for studying the electronic and thermodynamic properties of materials, including metals, semiconductors, and insulators, which is agreement with many studier [10]. DFT is a computational quantum mechanical modeling method used to investigate the electronic structure (ground state properties) of atoms, molecules, and solids. It approximates the electronic density of a system and solves the Schrödinger equation to determine the total energy (*SCF*) as well as electronic energy to get the required properties. DFT is widely used due to its efficiency and accuracy for a wide range of systems, and that is compatible with recent studies [40].

The simulation to obtain the optimal structures was done through the use of density functional theory at the level (B3LYP), in accordance with the basis set (6-311G(d,p)), for the components of the knee joint cartilage tissue represented by chondrite sulfide and for the substance that causes the deterioration and erosion of articular cartilage represented by urea, in addition to, it is one of the most important medical drugs used in treating swelling, tearing, and deterioration of the cartilage of the knee joint.

The individual and the docking of optimum structures, as these structures were obtained after the total energy was obtained at its lowest value, as it is considered one of the basic conditions for obtaining the optimum structures in their state. Optimum structure, as it is important and governing, in obtaining the electronic and thermodynamic properties of any system under study, and this is consistent with a number of recent studies, based on simulation computed using DFT computation and the 6-311G (d, p) standard basis set. Structure of Gouty AC, represented as a result of docking CS with uric acid and Triamcinolone (As a complex). Table(1) display properties values, where *HOMO*, *LUMO* and E_g investigate the chemical activity and stability of structure. A reduction in the energy gap enables electrons to be simply excited from their ground state. The ionization potential (*IP*) represent the least amount of energy needed to separate an electron from a molecule in the ground state case. Otherwise, electron affinity (*EA*) is the variation in energy of a balanced atom in the ground state case when an electron added to the atom. Chemical potential is negative amount of electronegativity.

For docking structure electronegativity greater is extremely reactive because of its ability to collect electrons from the environment, which is led to increased (*EA*) value. This high value implies that it provides a stable negative ion. Hardness is a crucial factor for measuring molecule stability and reactivity; a decrease in hardness is the key feature as an indicator for the band gap becoming more flexible and lowering species' resistance to losing electrons. The softness behavior indicates that drug binding increases the softness of the AC. a lower hardness, an increase in softness, and an extremely high electrophilicity index.

Table 1: Structural and electronic properties of Chondroitin Sulfate CS with uric acid and Triamcinolone.

Property (eV)	Chondroitin sulfate	Uric Acid	Triamcinolone	Docking
E_g	6.409	0.794	4.887	2.603
IP	6.936	8.883	6.375	6.993
EA	0.526	8.089	1.488	4.390
Ω	-3.731	-8.486	-3.932	-5.691
χ	3.731	8.486	3.932	5.691
η	3.204	0.397	2.443	1.301
S	0.156	1.259	0.204	0.384
ω	0.301	3.668	0.405	0.916
SCF	-56867.106	-17283.516	-37228.162	-111317.261

Table 2: Thermodynamic proprieties.

Structure	Gibbs, eV	Enthalpy, eV
Chondroitin sulfate CS	8.969	11.433
Uric Acid	0.625	1.783
Triamcinolone	11.071	13.240
Docking	2.264	2.602

Table 3: Thermodynamic and pharmacodynamics proprieties.

Energy (eV)	CS +Uric Acid	Docking (CS , uric acid and Tria)
ΔG	- 5.968	- 18.402
ΔH	- 5.966	- 23.856
E_B	2.624	-13.738
E_{int}	-5.249	-6.152

CONCLUSION

From the current study it can be found out the mechanism of docking that occurs between the medical drugs used to treat the deterioration of the cartilage of the knee joint, with the components of this cartilage, through the use of simulations based on diagnosing the structural, electronic and thermodynamic properties of the docking process between the tissues of the knee joint and the medical drugs used. The study findings on the interaction between chondroitin sulfate, uric acid, and triamcinolone provide valuable insights into their thermodynamic properties and potential interactions. Here's a breakdown of the conclusions drawn from the study, Chondroitin sulfate exhibits a favorable Gibbs free energy index, indicating a spontaneous reaction and facilitating the docking process. Its Gibbs

free energy is higher than that of uric acid and triamcinolone, suggesting a thermodynamically favorable interaction. All compounds exhibit positive entropy numbers, indicating that the interactions release heat and are thermodynamically favorable. The total energy of the system is more stable than that of chondroitin sulfate alone. The docking of uric acid with chondroitin sulfate is higher compared to triamcinolone, indicating a weaker coupled reaction with chondroitin sulfate. This suggests that the uric acid gradually affects chondroitin sulfate significantly, potentially through non-spontaneous interactions. Triamcinolone is identified as effective in eliminating the negative effects of uric acid on chondroitin sulfate. This indicates that triamcinolone could serve as a remedy to counteract the adverse effects of uric acid on chondroitin sulfate.

REFERENCES

1. Cho, Seongkoo, Steven F. Buchsbaum, Monika Biener, Justin Jones, Michael A. Melia, Jamie A. Stull, Hector R. Colon-Mercado, Jonathan Dwyer, and S. Roger Qiu. 2024. "True Active Surface Area as a Key Indicator of Corrosion Behavior in Additively Manufactured 316L Stainless Steel." Materials & Design 237 (January): https://doi.org/10.1016/J.MATDES.2023.112559112559.
2. Abdulsattar, Mudar Ahmed, Bahjat B. Kadhim, and Huda M. Jawad. 2015. "Electronic, Structural and Vibrational Properties of GaP Diamondoids and Nanocrystals: A Density Functional Theory Study." Nanomaterials and Nanotechnology 5 (1): 1–10. https://doi.org/10.5772/60577.
3. Agarwal, Shivang, and Amartya S. Banerjee. 2024. "Solution of the Schrödinger Equation for Quasi-One-Dimensional Materials Using Helical Waves." Journal of Computational Physics 496 (January): 112551. https://doi.org/10.1016/J.JCP.2023.112551.
4. Athari, Sarah A.K., and Bahjat B. Kadhim. 2023. "Physical Properties for Biomaterials Docking with Bones and Articular Cartilage." AIP Conference Proceedings 3018 (1). https://doi.org/10.1063/5.0171972.
5. Bagayoko, Diola. 2014. "Understanding Density Functional Theory (DFT) and Completing It in Practice." AIP Advances 4 (12): 0–12. https://doi.org/10.1063/1.4903408.
6. Bar Oz, Michal, Ashok Kumar, Jinan Elayyan, Eli Reich, Milana Binyamin, Leonid Kandel, Meir Liebergall, Juergen Steinmeyer, Veronique Lefebvre, and Mona Dvir-Ginzberg. 2016. "Acetylation Reduces SOX9 Nuclear Entry and ACAN Gene Transactivation in Human Chondrocytes." Aging Cell 15 (3): 499–508. https://doi.org/10.1111/acel.12456.
7. Barreto, Goncalo, Mikko Manninen, and Kari K. Eklund. 2020. "Osteoarthritis and Toll-like Receptors: When Innate Immunity Meets Chondrocyte Apoptosis." Biology 9 (4): 1–15. https://doi.org/10.3390/biology9040065.
8. Boeth, Heide, Peter C. Raffalt, Aoife MacMahon, A. Robin Poole, Felix Eckstein, Wolfgang Wirth, Frank Buttgereit, et al. 2019. "Association between Changes in Molecular Biomarkers of Cartilage Matrix Turnover and Changes in Knee Articular Cartilage: A Longitudinal Pilot Study." Journal of Experimental Orthopaedics 6 (1): 1–10. https://doi.org/10.1186/s40634-019-0179-3.
9. Chattaraj, Pratim Kumar, Utpal Sarkar, and Debesh Ranjan Roy. 2006. "Electrophilicity Index." Chemical Reviews 106 (6): 2065–91. https://doi.org/10.1021/cr040109f.
10. Chen, Mengqian, Yanan Li, and Guangrong Huang. 2020. "Potential Health Functions of Collagen Bioactive Peptides: A Review." American Journal of Biochemistry and Biotechnology 16 (4): 507–19. https://doi.org/10.3844/ajbbsp.2020.507.519.
11. Duan, Wangping, Yu Zhao, Xiaochun Ren, Ruipeng Zhao, Qi Li, Zhenwei Sun, Wenjie Song, Yanfei Yang, Pengcui Li, and Xiaochun Wei. 2021. "Combination of Chondrocytes and Chondrons Improves Extracellular Matrix Production to Promote the Repairs of Defective Knee Cartilage in Rabbits." Journal of Orthopaedic Translation 28 (June 2020): 47–54. https://doi.org/10.1016/j.jot.2021.01.004.
12. Fleischhauer, Lutz, Dominique Muschter, Zsuzsanna Farkas, Susanne Grässel, Attila Aszodi, Hauke Clausen-schaumann, and Paolo Alberton. 2022. "Nano-Scale Mechanical Properties of the Articular Cartilage Zones in a Mouse Model of Post-Traumatic Osteoarthritis." Applied Sciences (Switzerland) 12 (5). https://doi.org/10.3390/app12052596.
13. Flores-Gallegos, N., and L. Flores-Gómez. 2023. "An Approach to Chemical Hardness through Shannon's Entropy." Journal of Mathematical Chemistry 61 (8): 1726–38. https://doi.org/10.1007/S10910-023-01488-2/METRICS.
14. Hasan, Fatima A., and Mohammed T. Hussein. 2021. "Study of Some Electronic and Spectroscopic Properties of ZnO Nanostructers by Density Functional Theory." Materials Today: Proceedings 42: 2638–44. https://doi.org/10.1016/j.matpr.2020.12.593.
15. Hayes, Anthony J., and James Melrose. 2020. "Aggrecan, the Primary Weight-Bearing Cartilage Proteoglycan, Has Context-Dependent, Cell-Directive Properties in Embryonic Development and Neurogenesis: Aggrecan

Glycan Side Chain Modifications Convey Interactive Biodiversity." Biomolecules 10 (9): 1–38. https://doi.org/10.3390/biom10091244.
16. Huovinen, Jere, Maija Haj Hussain, Markus Niemelä, Sakari Laaksonen, Hanna Marja Voipio, Juha Jyrkäs, Janne Mannila, et al. 2019. "Pharmacokinetics of Intra-Articular Vitamin D Analogue Calcipotriol in Sheep and Metabolism in Human Synovial and Mesenchymal Stromal Cells." Journal of Steroid Biochemistry and Molecular Biology 188: 172–84. https://doi.org/10.1016/j.jsbmb.2018.12.006.
17. Hussein, Mohammed T., and Hanan A. Thjeel. 2019. "Vibration Properties of ZnS Nanostructure Wurtzoids: ADFT Study." Journal of Physics: Conference Series 1178 (1): 0–9. https://doi.org/10.1088/1742-6596/1178/1/012015.
18. Joudeh, Nadeem, and Dirk Linke. 2022. "Nanoparticle Classification, Physicochemical Properties, Characterization, and Applications: A Comprehensive Review for Biologists." Journal of Nanobiotechnology 20 (1). https://doi.org/10.1186/S12951-022-01477-8.
19. Kruszewska, Natalia, Adam Mazurkiewicz, Grzegorz Szala, and Małgorzata Słomion. 2022. "Characterization of Synovial Fluid Components: Albumin-Chondroitin Sulfate Interactions Seen through Molecular Dynamics." Materials 15 (19). https://doi.org/10.3390/ma15196935.
20. Mandal, Arkajit, Michael A.D. Taylor, and Pengfei Huo. 2023. "Theory for Cavity-Modified-State Reactivitiesvia Electron–Photon Interactions." The Journal of Physical Chemistry. A 127 (32): 6830. https://doi.org/10.1021/ACS.JPCA.3C01421.
21. Middelburg, Jack J. 2024. "The Gibbs Free Energy," 35–46. https://doi.org/10.1007/978-3-031-53407-2_4.
22. Mihajlovic, Marko, Margot Rikkers, Milos Mihajlovic, Martina Viola, Gerke Schuiringa, Blessing C. Ilochonwu, Rosalinde Masereeuw, et al. 2022. "Viscoelastic Chondroitin Sulfate and Hyaluronic Acid Double-Network Hydrogels with Reversible Cross-Links." Biomacromolecules 23 (3): 1350–65. https://doi.org/10.1021/acs.biomac.1c01583.
23. Molloy, Rachael G.E., Weihao Sun, Jialu Chen, and Wuzong Zhou. 2019. "Structure and Cleavage of Monosodium Urate Monohydrate Crystals." Chemical Communications 55 (15): 2178–81. https://doi.org/10.1039/C8CC10050K.
24. Muhsen, Haider O, Bahjat B Kadhim, and Ali O Muhsen Almayyali. 2017. "Electronic Properties of InPNT Drug Carrier." J. Chem. Pharm. Sci. 10 (3): 1414–18.
25. Patra, Chandra N. n.d. "Interdisciplinary R & D Theoretical Chemistry : An Overview on Modern Trends."
26. Pomin, Vitor H. 2015. "Keratan Sulfate: An up-to-Date Review." International Journal of Biological Macromolecules 72: 282–89. https://doi.org/10.1016/j.ijbiomac.2014.08.029.
27. Rubin, Shiri, Orly Ohana, Ori Goldberg, Orit Peled, Yulia Gendler, Zohar Habot-Wilner, Yoel Levinsky, Rotem Tal, Liora Harel, and Gil Amarilyo. 2022. "The Efficacy and Safety of Intra-Articular Injection of Triamcinolone Acetonide versus Triamcinolone Hexacetonide for Treatment of Juvenile Idiopathic Arthritis." Pediatric Rheumatology 20 (1): 1–7. https://doi.org/10.1186/s12969-022-00666-x.
28. Salahshoori, Iman, Mahdi Golriz, Marcos A.L. Nobre, Shahla Mahdavi, Rahime Eshaghi Malekshah, Afsaneh Javdani-Mallak, Majid Namayandeh Jorabchi, et al. 2024. "Simulation-Based Approaches for Drug Delivery Systems: Navigating Advancements, Opportunities, and Challenges." Journal of Molecular Liquids 395 (February): 123888. https://doi.org/10.1016/J.MOLLIQ.2023.123888.
29. Scherer, Justin, K. D. Rainsford, Colin A. Kean, and Walter F. Kean. 2014. "Pharmacology of Intra-Articular Triamcinolone." Inflammopharmacology 22 (4): 201–17. https://doi.org/10.1007/s10787-014-0205-0.
30. Schwabl, Christoph, Mihra Taljanovic, Gerlig Widmann, James Teh, and Andrea S. Klauser. 2021. "Ultrasonography and Dual-Energy Computed Tomography: Impact for the Detection of Gouty Deposits." Ultrasonography 40 (2): 197–206. https://doi.org/10.14366/usg.20063.
31. Shang, Jinxiang, Chao Zhou, Chanyi Jiang, Xiaogang Huang, Zunyong Liu, Hengjian Zhang, Jiayi Zhao, Wenqing Liang, and Bin Zeng. 2023. "Recent Developments in Nanomaterials for Upgrading Treatment of Orthopedics Diseases." Frontiers in Bioengineering and Biotechnology 11: 1221365. https://doi.org/10.3389/FBIOE.2023.1221365.
32. Siddiqui, Sharmin, Faisal Ameen, Ishrat Jahan, Shahid M. Nayeem, and Mohammad Tabish. 2019. "A Comprehensive Spectroscopic and Computational Investigation on the Binding of the Anti-Asthmatic Drug Triamcinolone with Serum Albumin." New Journal of Chemistry 43 (10): 4137–51. https://doi.org/10.1039/C8NJ05486J.
33. Soltani, Alireza, Mohammad T. Baei, E. Tazikeh Lemeski, Sara Kaveh, and Hanzaleh Balakheyli. 2015. "A DFT Study of 5-Fluorouracil Adsorption on the Pure and Doped BN Nanotubes." Journal of Physics and Chemistry of Solids 86: 57–64. https://doi.org/10.1016/j.jpcs.2015.06.008.

34. “Understanding Gibbs Free Energy - Testbook.” n.d. Accessed May 15, 2024. https://testbook.com/physics/gibbs-free-energy.
35. Xiao, Huimin, Xin Chen, Xuanzhe Liu, Gen Wen, and Yaling Yu. 2023. “Recent Advances in Decellularized Biomaterials for Wound Healing.” Materials Today Bio 19 (February): 100589. https://doi.org/10.1016/j.mtbio.2023.100589.
36. Yin, Jie, Wenkai Ren, Xingguo Huang, Jinping Deng, Tiejun Li, and Yulong Yin. 2018. “Potential Mechanisms Connecting Purine Metabolism and Cancer Therapy.” Frontiers in Immunology 9 (July): 1–8. https://doi.org/10.3389/fimmu.2018.01697.
37. Yoon, Hojong, Justine C. Rutter, Yen Der Li, and Benjamin L. Ebert. 2024. “Induced Protein Degradation for Therapeutics: Past, Present, and Future.” The Journal of Clinical Investigation 134 (1). https://doi.org/10.1172/JCI175265.
38. Zare, Karim, Nasim Shadmani, and Elham Pournamdari. 2013. “DFT/NBO Study of Nanotube and Calixarene with Anti-Cancer Drug.” Journal of Nanostructure in Chemistry 3 (1). https://doi.org/10.1186/2193-8865-3-75.
39. Zhang, Shuye, Xiangyu Xu, Tiesong Lin, and Peng He. 2019. “Recent Advances in Nano-Materials for Packaging of Electronic Devices.” Journal of Materials Science: Materials in Electronics 30 (15): 13855–68. https://doi.org/10.1007/s10854-019-01790-3.
40. Zhao, Xiaoduo, Weiyi Zhao, Yunlei Zhang, Xiaoqing Zhang, Zhengfeng Ma, Rui Wang, Qiangbing Wei, Shuanhong Ma, and Feng Zhou. 2022. “Recent Progress of Bioinspired Cartilage Hydrogel Lubrication Materials.” Biosurface and Biotribology, no. June: 225–43. https://doi.org/10.1049/bsb2.12047.

The possibility of electrical transition $B(E2; 0_1^+ \rightarrow 2_1^+)$ and determining the shape of the nuclei of iron

Reem Gani Abdulrazak Mohammed [a] , Sameera Ahmed Ebrahiem [b]

Department of Physics, College of Education for pure science Ibn Al-Haitham, University of Baghdad, Bagdad, Iraq

[a] Corresponding author: Reem.Mohammed1704d@ihcoedu.uobaghdad.edu.iq
[b] sameera.a.i@ihcoedu.uobaghdad.edu.iq

Abstract: This study included the calculation of the distortion coefficient δ derived from the electric quadrupole moments Q_o and the distortion coefficients β_2, which arise from low electrical transition potential (B (E_2) ↑ in e^2 b^2 unit, based on the excitation energy +2 specifically for the even-even nuclei of the element iron-26 and for mass numbers between 52-. Since the distortion parameter β2 is a model based on quantum mechanics, considering that it describes the interaction of a nucleon Along with all the other nucleons in the nucleus, it can be calculated from the low electrical transition potential (B (E_2) ↑ in e^2 b^2 unit, which depends on the gamma energy, which is measured in units the KeV and the mass number. In general, the shape of the nucleus is spherical when the nucleus is stable, as this voltage reduces the surface energy of the nucleus, as shown in the declared values for nucleons with magic numbers. The root mean square of the radius was calculated and compared with previous studies, and the major and minor axes (b, a) were calculated... The values of ΔR were calculated, which indicates the deviation between the minor semi-axis b and the major semi-axis a is included in the calculation of the delta distortion coefficient.

Keyword: nuclei, shell model, quadrupole moments, possibility of electrical transition, excitation energy, half-life.

INTRODUCTION

In this model, parts of the nucleus move independently of one another, while the liquid drop model indicates exactly the opposite, as a drop. The fluid is incompressible, and the movement of any part of it is related to movement, all adjacent pairs. Another model that explains the shape of the nuclei is the collective model that combines both the shell and liquid droplet model. We assume that all nuclei have similar mass densities for the liquid drop model and that their Similar to a drop of charged liquid, energies are roughly proportional to their mass.... The SEMF, which is the model's output, provides a useful explanation of the binding energies and average masses. The Schrödinger equation is solved by the shell model, a quantum mechanical model [1]. The nucleus is seen as spherical. Although a substantial spin-orbit term is added, it is predicated on the same premises as the Fermi gas model. It makes highly accurate predictions about the spin, parity, and nuclear magic numbers of the ground state nucleus as well as the coupling term of the SEMF. The collective model, which is a quantum mechanical model, is capable of predicting both electric and magnetic dipoles. However, it is permitted to experience distortions of the spherical shape that is employed in the shell model within the current potential. N-even, Z-odd, Z-even and N-odd configurations are all possible for even nuclei; however, for reasons that will be discussed below, practically just a few odd and odd varieties of even-mass nuclei are known to exist, and all that are stable against decay are of the even type. [1].

Theory: In the empty shell of the nucleus, it is the arrangement of valence nucleons that causes nuclear distortion, and hence distortion occurs only when both protons (p) and neutrons (n) are not full [2]. Quadrilateral aberrations are one of the basic types of distortions; In these deformities, the nucleus can take on either an ovoid or oblate shape [3]. their liquid drop model of the nucleus is supple and soft, thus permitting them to detect considerable distortions in its shape from a perfect sphere. Anywhere the number of neutrons (N) had a high frequency, a considerable number of nuclei were identified (N) and protons (P) were markedly distant from the magnetic values, exhibiting a distorted charge distribution [4]. The distortion parameter β2 is a model based on quantum mechanics [5]. Considering that

Technologies and Materials for Renewable Energy, Environment and Sustainability
AIP Conf. Proc. 3321, 020050-1–020050-4; https://doi.org/10.1063/5.0290408
Published under an exclusive license by AIP Publishing. 978-0-7354-5231-2/$30.00

these probabilities describe the interactions of nucleons with all other nucleons in all remainder nucleons in the nucleus [5]:

$$\beta_2 = 4\pi / 3ZR_o^{\,2} [\ B(E2)\uparrow e^{\,2} b^{\,2}/ e^{\,2}]^{\,1/2} \quad (1)$$

$$\text{Where} \quad R_o = 0.0144\, A^{\,1/3} \quad (2)$$

$$\text{And} \quad B(E2)\uparrow = 2.6\, E\gamma^{\,-1} Z^{\,2} A,^{\,-2/3} \quad (3)$$

In this context, A denotes the mass number of a nucleus, Z represents the atomic number, and $E\gamma$ signifies the gamma-ray transition energy, measured in kilo electrinos (KeV).

To calculate the deformation parameter δ, we rely on the internal electric quadrupole Q_o because it provides information on deformation and shape, measuring the distortion and spherical symmetry of the charge distribution. [6]. The quadrilateral deformation coefficient (the degree of variation in the spherical shape) can be calculated using the quadrilateral moments Q_o [6].

$$\delta = 0.75Q_o / (< r^2 > Z) \quad (4)$$

$$\text{Where} \quad Q_o = [(16\,\pi/5)\, B(E2)\, e^{\,2} b^{\,2}/e^{\,2}]^{\,½} \quad (5)$$

The average radius $< r2 >$ can be calculated:

$$< r^2 > = 0.63R_o^{\,2} (1+10/3(\pi\, a_o/R_o)^{\,2})/(1+(\pi\, a_o/R_o)^{\,2}) \ (\text{À} \leq 100) \quad (6)$$

Whence the Ro: radial Woods-Saxon parameters are, Ro=1.07A1/3 fm and ao=0.55(fm), with ao from fast electron scattering information [7] [8].

In general, the shapes of nuclei are approximately spherical when a nucleus is stable since it lowers the surface energy of the nucleus [8][9]. Hence, small sections of spheres are seen, as with the region 150<A<190

$$\boldsymbol{\delta} = \Delta \boldsymbol{R} / \boldsymbol{R} \quad (7)$$

Where: ΔR denotes the difference between the semi-major and semi-minor axes.

The average of the nuclear radius is represented by R, due to, as assumed,

$$\Delta \boldsymbol{R} = (\boldsymbol{b} - \boldsymbol{a}) \quad (8)$$

The subsequent equations provide the semi-axes (a) and (b) [9].

$$a = \sqrt{< r2 > (1.66 - \frac{2\delta}{0.9})} \quad (9)$$

$$b = \sqrt{5 < r2 > -2a^2} \quad (10)$$

RESULT AND DISCUSSIONS

In the present study, the shape of the cores has been assessed by computing the deformation parameters $\beta 2$ and δ . β values have been computed for even-even iron isotopes for all masses in the range (52-62) from the gamma energy of Fristoe. The values of The possibility of electrical transition $B(E2; 0_1^+ \rightarrow 2_1^+)$ were taken from Global [12] as it was shown in Table No. 2 that the values of deformation parameter β_2 range between (0.2555-0.3095) and that the values decrease with increasing mass number, that is, with increasing neutrons, where the relationship is inverse. The calculated values are somewhat close to the values calculated by Global, except for the deformation parameter β_2 value at the mass number (54) , where the deformation parameter β_2 value is lower because the number of neutrons is (28) , which is a magic number, as shown in Figure 1. As for the values of the deformation parameter δ, which depend on the values of quadrilateral moments Q_o and shown in Equation No. 4 , the values decrease with the increase in the number of neutrons, and the values range between (0.2141 - 0.1813) , as shown in Table No. 1. The values of he possibility of electri; transition $B(E2; 0_1^+ \rightarrow 2_1^+)$ were also calculated and compared with the theoretical values calculated by Global. It was found that the values are very close.

In Table No. 3, The average radius $< r2 >$was calculated and compared with the theoretical values announced in reference [13] and included in calculating the values of the **δ** deformation parameters for mass numbers less than 100, To calculate ΔR which represents the variance between the semi-major axes and semi-minor, as indicated in Equation No. 8, illustrated in Figure 1.

Table 1. Average half-life t (s) for iron (Fe) isotopes, neutron numbers N, gamma energy to the first state, probability T of transition, and A represent mass numbers.

Z	A	N	E_i(KeV) [14]	Eγ (KeV)[14]	$t_{1/2}$ (s) [14]	T (s)	τ (s)
26	52	26	849	849.6	0.7ps*10^{-13}	1.0101*10^{-13}	9.9000*10^{12}

	54	28	1408	1408.19	$0.80*10^{-13}$	$1.1544*10^{-13}$	$8.6625*10^{12}$
	56	30	846	846.776	$6.07*10^{-13}$	$8.7590*10^{-13}$	$1.1417*10^{12}$
	58	32	810	810.784	$6.54*10^{-13}$	$9.4372*10^{-13}$	$1.0596*10^{12}$
	60	34	823	823.63	$8.0*10^{-13}$	$1.1544*10^{-12}$	$8.66225*10^{11}$
	62	36	876	876.8	$68*10^{-13}$	$9.8124*10^{-12}$	$1.0191*10^{12}$

Table 2. Additionally, it includes the mass numbers (A), the major and minor axes (b, a), neutron counts (N), the root mean square of the radius $<r^2>^{(1/2)}$, as well as their separation (ΔR) for the isotopes of iron, described in two distinct ways.

Z	A	N	A theoretical value	Present work						
			$< r^2 >^{\frac{1}{2}}$ Fm [13]	$< r^2 >$fm	$< r^2 >^{\frac{1}{2}}$ Fm (p.w)	a (fm)	b (fm)	ΔR_1	ΔR_2	ΔR_3
26	52	26	……..	16.4652	4.0577	2.1983	3.2593	0.8549	1.0610	1.3115
	54	28	3.6933	16.7893	4.0974	2.3158	3.1243	0.6512	0.8085	0.9934
	56	30	3.7377	17.1087	4.1362	2.2458	3.2549	0.8241	1.0092	1.2503
	58	32	3.7745	17.4237	4.1741	2.2594	3.2651	0.8270	1.0057	1.2482
	60	34	…….	17.7345	4.2112	2.2843	3.2589	0.8061	0.9747	1.2108
	62	36	……..	18.0414	4.2475	2.3168	3.2408	0.7680	0.9240	1.1481

Table 3. Quadrupole moment Tetrapolar electrode (Q_o) in barns, gamma energy to the first level E^γ, low electrostatic transition potential B(E2)↑ in e^2 b^2 units, average nuclear radius (Ro^2), number of neutrons (N), mass numbers of isotopes (A) Iron and parameters of deformation (β2, δ) for iron F

Z	A	N	The Theoretical Values		A present Work					
			E_γ (KeV) [14]	B(E2)↑ (e^2b^2) for Global Best Fit[12]	β_2 for Global Best Fit	δ	β_2	Qo (b)	B(E2)↑ (e^2b^2)	R_O^2
26	52	26	849.6	0.147	0.3079	0.2141	0.3095	1.2218	0.1485	20.06
	54	28	1408.19	0.086	0.3002	0.1610	0.2315	0.93716	0.0874	20.57
	56	30	846.776	0.140	0.2860	0.2013	0.2876	1.1940	0.1418	21.08
	58	32	810.784	0.143	0.2824	0.1997	0.2840	1.2060	0.1447	21.58
	60	34	823.63	0.137	0.2702	0.1924	0.2724	1.1831	0.1392	22.07
	62	36	876.8	0.126	0.2535	0.1813	0.2555	1.1342	0.1280	22.56

CONCLUSIONS

The analysis of the previous data results and results observed for the given nuclei at rest reveal that the energy of the first 2+ state varies smoothly with A. It was noted that the nucleons are lying on outside partial or full oscillation conditions which polarize in one direction and thus give rise to a permanent deformation of the nucleus. Thus, these nuclei would then take up stable no spherical shapes barring the gauge factor B2 at A=54, where the gauge factor is depressed since n=28, a magic number, shows that if there is a magic number deviation, the movement of the nucleons will be just outside the closed shell; as the magic number comes closer, it is highly stable in particular and increases in rotational motion as well as the deformation of the nucleus.

REFERENCES

1. Martin, B. R. (2006). Nuclear and particle physics: An introduction. John Wiley & Sons. Ltd. ISBN: 0-470-01999-9.
2. Alyaa Abdulkad, "The Probability of Electric Transition the Square of Rotational Energy and the Moment of Inertia for Cm (A=246) Isotope" Journal of Science and Arts. 37 (4) (2016):417- 426.
3. Ali Abdulwahab Ridha, "Deformation parameters and nuclear radius of Zirconium (Zr) isotopes using the Deformed Shell Model ', 2009, Wasit Journal for Science & Medicine, 2 (1): (115 - 125)
4. Salim, D.A., Ebrahiem, S.A. (2022). Study of nuclear properties for the carbon (C) and oxygen (O) isotopes: Deformation parameters and root mean square radii. (AIP Conference Proceedings).
5. Zghaier, Haider A; Ebrahiem, Sameera A; Abdul_Jabbar, Hadeel, "Study the Shapes of Nuclei for Heavy Elements with Mass Number Equal to (226≤ A≤ 252) Through Determination of Deformation Parameters for two Elements (U&Cf) " , Ibn AL-Haitham Journal For Pure and Applied Science , 2018 .
6. Boboshin I. and et al. (2007). Investigation of quadrupole deformation of nucleus and its surface dynamic vibrations, international conference on nuclear data for science and technology, Russia, p.65:
7. Bariq H. Walya, Sameera A. Ebrahiemb , " Study of the nuclear properties of an aluminum isotope in the production of third cycle elements" AIP Conference Proceedings 2437, 020087 (2022).
8. F. Ertugrala, E. Guliyevb, A.A. Kulievc" "Quadrupole Moments and Deformation Parameters of the 166-180Hf, 180-186W and 152-168Sm Isotopes" Special issue of the International Conference on Computational and Experimental Science and Engineering, Acta Physica Polonica A 128(2B) (2015).
9. Ibrahim, Z.H., Ibrahim, S.A., Shaban, A.H., Jasim, K.A., Mohammed, M.K., Radiological Dose Assessments for Workers at the Italian Fuel Fabrication Facility at Al-Tuwaitha Site, Baghdad - Iraq with Aid of GIS Techniques, Energy Procedia, 2017, 119, pp. 709–717.
10. Ebrahiem, Sameera A; Zghaier, Haider A, "Estimation of geometrical shapes of mass-formed nuclei (A= 102-178) from the calculation of deformation parameters for two elements (Sn & Yb) ", Journal of Physics: Conference Series, 2018.
11. Jasim, K.A., Alwan, T.J., Mahdi, K.H., Mansour, H.L., The effect of neutron irradiation on the properties of Tl 0.6Pb0.3Cd0.1Ba2Ca 2Cu3O9-δ superconductors, Turkish Journal of Physics, 2013, 37(2), pp. 237–241. https://doi.org/10.3906/fiz-1203-16.
12. Raman S., Nestor C.W., and Tikkanen JR. "Transition Probability From The Ground to the First-Excited 2+ State of Even–Even Nuclides" Atomic Data and Nuclear Data Tables.78 (2001):1-128.
13. Angeli. a. I; Marinova. K.P. Table of experimental nuclear ground state charge radii; An update. Atomic Data and nuclear Data Table 99, Elsevier Inc: 2013, 69-95.
14. Firestons R. B. and Shirley V. S. Table of Isotopes eighth edition, John Wiley and Sons , New York (1999).
15. Ibrahim SM, Ebrahiem SA, Rhaiem A Ben. Calculating of the electric transition forces and radii of even-even-nuclei of cadmium (100-12448cd) cd isotopes. Ibn AL-Haitham Journal For Pure and Applied Sciences 2024;37:215–22.
16. Mohammed SJ, Aobaid AK, Ebrahiem SA. Calculation of protons stopping power in Yttrium-90 and Iodine-131 radioactive isotopes. AIP Conf Proc, vol. 3018, AIP Publishing; 2023.

Investigation of Coated Nanofibers Based on Sodium Alginate Loaded With Antimicrobial Agents

Hanan M. Khudir [a], Akram R. Jabur [b], Ishraq A. Kadhim [c]

Department of Materials Engineering, University of Technology, Baghdad, Iraq

[a] Corresponding author: *mae.22.009@grad.uotechnology.edu.iq,*
[b] *akram.r.jabur@uotechnology.edu.iq*
[c] *aishraq.a.kadhim@uotechnology.edu.iq*

Abstract. Polymeric scaffolds loaded with antibacterial nanoparticles have been a significant advancement in the field of biomedical applications. Our study aims to prepare an antimicrobial scaffold from collagen and polycaprolactone loaded with silver nanoparticles (AgNPs) and titanium dioxide(Tio2NPs) using electrospinning technology these fibers were deposited on sodium alginate films. These nanoparticles were added in three different ratios, the amount of (AgNPs) was variable in each ratio, while the amount of (Tio2NPs) remained constant. The scaffolds were analyzed using Field emission scanning electron microscopy (FESEM), Fourier transformtion infrared spectroscopy (FTIR), and wettability measurements. Through the results of the FESEM, we notice a decrease in the average fiber diameter with an increase in the amount of AgNPs, as it was 76.34±0.62 nm in ALg-D scaffold, which contains the amount of AgNPs is (0.3 g) , and 63.23±0.85 nm in ALg-E scaffold, which contains the amount of AgNPs is (0.5 g), and the average fiber diameter reached 58.30±2.12 nm in ALg-E scaffold, which contains the highest amount of AgNPS (0.7 g) . that the wettability results showed that the water contact angle decreased when nanoparticles were added and the scaffold became very hydrophilic. The antibacterial results showed significant activity against Gram-positive and Gram-negative bacteria in all scaffolds loaded with nanoparticles, and the ALg- E1 scaffold was the one that showed the highest bacterial resistance. In conclusion, ALg-E1 scaffold may be a promising scaffold for wound dressing application.

INTRODUCTION

The skin, being the biggest organ of the human body, acts as a protective barrier that separates the body from the surrounding environment. It provides immunity against diseases and germs [1]. Nevertheless, the skin is susceptible to a multitude of different forms of injury [2]. This is a significant health issue. Due to the impact on the body's natural defence mechanism, skin injuries might compromise its ability to protect against pathogens, leading to a delay in the wound healing process [3]. Therefore, it is crucial to promptly dress a wound when it has occurred [4]. traditional wound dressings. such as gauze and bandages were the most widely used to cover wounds due to their low cost and easy accessibility ,which can shield the wound from external factors [5], but they generate a localised dry environment , which can result in issues such as infections, stimulation of bacterial development, and potential reinjury of the regenerated epithelium when the gauze is taken off [6], [7].Therefor , engineering of tissue has prioritised the development of these dressings into bioactive wound dressings that enhance the wound healing process instead of merely serving as a covering[8], By creating biomaterial-based scaffolds, to offer stable structure that can support cellular regeneration and mimic the functionality of natural tissue [9]. It functions as a base for cellular attachment, growth, and proliferation [10]. Therefore, an effective scaffold must possess both biological and mechanical qualities. The desired characteristics include optimal strength, compatibility with biological systems, suitable porosity, and the ability to mimic the extracellular matrix (ECM)[11], [12] . Electrospun nanofibers are well-suited for use in wound dressing applications because they closely resemble the structure of the extracellular matrix (ECM)[13], have significant surface area to their size ratio [14], and suitable porosity [15]. Electrospinning is an uncomplicated and cheap method for fabricating fibrous porous mats that can mimic the structural features of the extracellular matrix (ECM) [16]. Nevertheless, the many materials utilised in this domain nevertheless necessitate some enhancements. The sluggish wound healing process is a significant obstacle in the field of wound treatment. Common reasons that can impede the wound healing process include bacterial infection, underlying physiological disorders, malnutrition, extended periods of bed rest, and the natural process of ageing [17],[18]. The majority of currently utilised wound dressings exhibit several limitations, including inadequate anti-inflammatory and antibacterial activities, inability to absorb excessive wound exudates, necessitating frequent dressing changes, and subpar mechanical characteristics [19]. The careful choice of materials is crucial in the development of dressings with bioactive properties, enabling them to effectively absorb excess exudate and preserve the absorbed volume. This promotes a moist environment that facilitates the healing

Technologies and Materials for Renewable Energy, Environment and Sustainability
AIP Conf. Proc. 3321, 030001-1–030001-11; https://doi.org/10.1063/5.0289598
Published under an exclusive license by AIP Publishing. 978-0-7354-5231-2/$30.00

of wounds [20].These bioactive wound dressing are also loaded with antibiotics and nanomaterials, which enhances its ability to resist bacteria. Additionally, it is biodegradable, reducing the need for frequent dressing changes. Furthermore, it is non-toxic and biocompatible [21]. Biopolymers are highly regarded as suitable materials for manufacturing wound dressings due to their distinctive characteristics that render them valuable in this application. These attributes include biodegradability, exceptional biocompatibility, lack of toxicity, absence of antigenicity and immunogenicity, as well as easy accessibility [7]. Among them, Sodium alginate is a naturally occurring polymer that is obtained from the cell wall of brown seaweed [22],[23], Alginate has been extensively utilised in wound dressing due to its high hydrophilicity, allowing alginate-based dressings to effectively absorb wound fluids and provide a moist environment [24]. In addition to preventing bacterial contamination of wounds, it enhances the process of re-epithelialization and the creation of granulation tissue, leading to faster wound healing [25]. Collagen type I (Col_1) is a prominent protein found in mammals [26]. It is found in around 70% of the extracellular matrix (ECM) in the skin, bone, and cartilage [27],[28] . Collagen is crucial in all stages of skin regeneration, including the inflammatory, proliferative, and remodelling phases. Typically, the naturally occurring collagen within the body can effectively perform its function during the process of regular wound healing [29]. The utilisation of collagen-based dressings is essential for enhancing and expediting the healing process. This is because exogenous collagen generates a chemotactic signal that attracts macrophages, granulocytes, and fibroblasts, hence promoting the formation of new tissue and facilitating wound healing [30]. Although collagen possesses favourable characteristics such as high biodegradability, biocompatibility, non-antigenicity, and cell adhesion properties, but its quick degradation and limited electrospinning ability may restrict its application as a scaffold material [31]. In order to address this limitation, collagen can be blended with additional synthetic polymers to generate hybrid structures possessing superior characteristics compared to any of its individual components [32], [33]. Polycarbolactone (PCL) is a synthetic polymer that has found extensive use in medical applications [34]. PCL is a semi-crystalline linear polyester with advantageous properties including biocompatibility, biodegradability, and mechanical strength [35]. Poly(caprolactone) (PCL) exhibits drawbacks such as poor interaction with the biological fluids and its inherent hydrophobicity, resulting in reduced effectiveness of cell proliferation and adhesion [36]. Blending collagen with PCL has become highly regarded as a promising option for creating nanofibrous scaffolds for skin tissue engineering applications. This approach combines the advantages of both natural and synthetic polymers [37]. Bacterial infections provide significant risks, and if not properly treated, can have potentially lethal consequences depending on the location of the injury [38]. Therefore, the activity of bactericidal against positive- gram and negative- gram bacteria cells is a critically significant characteristic in scaffold production. Gram-negative Pseudomonas aeruginosa (P. aeruginosa), and gram-positive Staphylococcus aureus (S.aureus) are two of the most prevalent bacteria that have demonstrated strong resistance to antibiotics. These bacteria have the potential to induce severe infections in skin tissue, including pneumonia, endocarditis, and septicaemia [39]. So Researchers have integrated nanoparticles (NPs) with antibacterial properties into scaffolds in order to enhance their antibacterial activity [40]. The presence of nanoparticles (NPs) in scaffolds enhances their quality by serving as both antibacterial agents and reinforcements. To produce a scaffold with both antibacterial characteristics and excellent mechanical capabilities [41]. Metal-based nanoparticles (NPs) with broad-spectrum antibacterial activity and no drug resistance are commonly utilised as antibacterial agents in wound dressings, such as AgNPs [42].

The antibacterial activity of silver nanoparticles (Ag NPs) was observed to be strong against both Gram-positive and Gram-negative bacteria. The antibacterial activity of silver nanoparticles is attributed to the strong interaction between silver nanoparticles and the surfaces of bacterial cells. This interaction leads to a localised breakdown of the inner membrane, ultimately resulting in the death of the bacterial cells [43].

TiO2 is a type of nanoparticles utilised as antibacterial agents. It is a chemically stable and biocompatible compound with excellent photocatalytic activity. Furthermore, it exhibits superior bactericidal activity against both Gram-positive and Gram-negative bacteria when compared to chemically synthesised nanoparticles [44]. The usage of TiO2 nanoparticles (NPs) as a dopant in a polymeric matrix is significant because TiO2 NPs are chemically inactive and their ability to hinder the growth of microorganisms makes them ideal for biological applications [45]. The uses of TiO2 NPs are greatly influenced by their physical properties. It exists in three distinct forms, namely brookit, anatase, and rutile. Anatase nanoparticles are frequently utilised for various purposes out of a selection of three options [46].

The aim of the research is to develop wound dressings from simple wound dressings that cover the wound only to bioactive anti-bacterial wound dressings by fabrication a polymeric scaffold loaded with anti-bacterial nanoparticles to efficiently stimulate the wound healing process and regenerate damaged skin tissue.

EXPERIMENTAL

MATERIALS

Collagen that is laboratory extracted from bovine skin by the modified acid-enzymatic method , sodium Alginate (SA) from Sigma-Aldrich (china) and, polycaprolactone (PCL) (Mn 80,000) from Sigma-Aldrich (United Kingdom), acetic acid (99.5%) with molecular weight (60.05) from THOMAS BAKER (India), glycerine with molecular weight (92.10) from Panreac (Barcelona) spain ,Nano Silver Powder (AgNPs) with particle size (20 nm),from HONGWUNEWAM TERIAL (China)and Nano Titanium dioxide powder(TIO2) (Anatase) with particle size (10 nm),from HONGWUNEWAM TERIAL (China).

METHOD

PREPARATION OF SODIUM ALGINATE FILMS

A(4%w/v) sodium alginate solution was prepared by dissolving sodium alginate in 45ml of distilled water using magnetic stirring at 1400 rpm for one hour. Subsequently, 5 ml of glycerine was introduced into the solution and allowed to undergo magnetic stirring for a duration of thirty minutes. Afterwards, 5 ml of glycerine was added to the solution and subjected to magnetic stirring for a period of thirty minutes. Ultimately, the solutions were placed in petri dishes and left to dry at the temperature of the electric heater for a duration of two days. This film will function as a base for the electrospinning process.

PREPARATION OF ELECTROSPINNING SOLUTION

Collagen, polycaprolactone (PCL), and a mix of collagen and PCL were individually prepared. A 6% w/v collagen solution was made by dissolving freeze-dried collagen isolated from bovine skin in acetic acid at room temperature for one day, using a magnetic stirrer. A 12% w/v solution of Pcl was prepared by stirring it magnetically for 2 hours at room temperature. The Pcl also dissolved in acetic acid. The mixture was prepared at a ratio of 4 :1.PCL: COL and was then placed on a magnetic stirrer for a duration of two hours at room temperature.

ADDING ANTIBACTERIAL NANOPARTICLES

Antibacterial agents titanium dioxide (Tio2 NPs) and silver nanoparticles (Ag NPs) were added together to the electrospinning solution but in three different ratios: D, E, and F. The amount of (Tio2) was constant in all ratios, which was (0.5g), while the amount of (Ag) was in different quantities it was (0.3g) in first ratio (D), (0.5g) in the second ratio (E) and (0.7g) in the third ratio (F). Each ratio was individually added to the collagen/PCL (blend) solution to obtain three different solutions and left on the magnetic stirrer for 3 hours, then each solutions was sonicated in ultrasonic bath for 30 min.

Table 1. (ALg , ALg-A, ALg-B, ALg-C, ALg-D, ALg-E and ALg-F) concentrations.

N	Samples	Concentrations of scaffolds
1-	ALg	Alginate (4%w/v)
2-	ALg- A	Alginate + collagen (6%)
3-	ALg- B	Alginate + polycaprolactone (12%)
4-	ALg- C	Alginate + collagen (6%) + polycaprolactone (12%)
5-	ALg- D	Alginate + collagen (6%) + polycaprolactone (12%) + (o,5g) from (Tio2) and (o.3g) from (Ag NPs)
6-	ALg- E	Alginate + collagen (6%) + polycaprolactone (12%) + (o,5g) from (Tio2) and (o.5g) from (Ag NPs)
7-	ALg- F	Alginate + collagen (6%) + polycaprolactone (12%) + (o,5g) from (Tio2) and (o.7g) from (Ag NPs)

ELECTROSPINNING PARAMETERS

10 mL from each solution resulted were injected into a Teflon syringe using a G22 gauge needle connected to the high voltage cathode of the uniaxial electrospinning apparatus, and fibres were placed onto the Alg films at a distance of 15 cm from the collector to the needle. The flow rate and voltage were optimised at 2 mL/h and 20 kV, respectively, for all scaffolds. The electrospinning process was conducted at a temperature of 23 ± 2 ◦C, which corresponds to the commonly accepted normal room temperature.

CHARACTERIZATION OF SCAFFOLD

FIELD EMISSION SCANNING ELECTRON MICROSCOPY (SEM)

The acquisition of field emission scanning electron microscopy (FESEM) images was performed using a MIRA3-XMU instrument. A 10 nm thick layer of gold was applied to all samples using fine coat ion sputter in order to prevent discharge during FESEM testing. The diameters, porosity, and morphology of the fibres were analysed using the Image J programme.

FOURIER TRANSFORM INFRARED SPECTROSCOPY

The chemical bonding of the produced scaffolds was assessed using Fourier Transform Infrared Spectroscopy (FTIR) with a BRUKER TENSOR-27 instrument. The spectrometer is outfitted with a mid-infrared source that functions within the range of 4000 to 400 cm^{-1}.

WETTABILITY

The contact angle of the scaffold was measured using a goniometer (CAM 110, Germany). Each scaffold was treated with a 5 microliter volume of water, and photographs were taken after a 2-second interval.

ANTIBACTERIAL ACTIVITY

The antibacterial efficacy of nanoparticle-loaded scaffolds and a bare Alg-Blend-C1 scaffold against Gram-negative Pseudomonas aeruginosa (P. aeruginosa) and gram-positive Staphylococcus aureus (S.aureus) bacteria was evaluated using the Inhibition Zone approach. The spread plate approach was used to inoculate nutrient agar plates with 1 mL of a bacterial solution containing 108 CFU/mL. A circular layer of the produced scaffolds, measuring 1.5 cm in diameter, was placed on the plates. The plates were then incubated at a temperature of 37°C for a duration of 24 hours. The inhibition zones were found by quantifying the cleareareas that surrounded each scaffold.

RESULT AND DISCUSSION

FESEM OF THE SCAFFOLD

'Figure 1,' displays the Field Emission Scanning Electron Microscopy (FESEM) picture of the Alg-A scaffold. From this view, it is evident that the scaffold exhibits a fibers-free morphology. This is because collagen, being a natural polymer, cannot be electrospun on its own due to its inherent properties. The use of collagen as a scaffold material is limited due to its low electrospinning capability and rapid degradation [47]. In regards to the Alg-B scaffold depicted in **'**Figure 2(A),' it was noted that there were fibres present on the surface of the alginate film. These fibres had an average diameter of 56.99 ± 1.15 nm with average pore size of 609.35 ± 17.9 nm in 'Figure 2 (B),(C)**,'** it should be noted that these fibres were irregular in shape and exhibited slight crosslinking. Conversely, the Alg-C scaffold in 'Figure 3(A),' fibres demonstrated enhanced morphology, characterised by increased regularity, homogeneity, continuity, strong crosslinking, and absence of beads. We observed a reduction in the average fibre diameter for Alg-C to 44.97 ± 1.61 nm in 'Figure 3 (B)'. This drop can be attributed to the decrease in the viscosity of the solution caused by the addition of collagen to the PCL and their combination. As a result, the fibres were produced with a reduced diameter and increased crosslinking, leading to a decrease in pore size to 333.223±25.9 nm, as shown in 'Figure 3 (C),' [48]. 'Figure 4(A),' displayed a FESEM image of the ALg-D scaffold, revealing smooth and bead-free fibre morphology. The average diameter of the fibres in these scaffolds loaded with nanoparticles was much larger than that of the nanoparticle-free scaffold. The observed increase in average fibre diameter may be attributed to an increase in the viscosity of polymer solutions caused by the addition of nanoparticles, as depicted in 'Figure 4 (B),(C)'. The mean fibre diameter measured 76.34 ±0.62 nm, whereas the pore size was 318.85 ±15.9 nm [49]. The FESEM image of ALg- E nanofiber scaffolds in 'Figure 5 (A)' clearly demonstrate that the fibres formed were both smooth and uniform. Additionally, a minor agglomeration of the nanoparticles was found. This is attributed to the high surface energy of the nanoparticles, In addition, there may be a distribution in the size of the powder nanoparticles, which leads to their agglomeration and overcoming the surface tension [41]. a decrease in the average fiber diameter of this scaffold was observed compared to the ALg-D scaffold, due to the increase in the amount of AgNPs to 0.5 in this scaffold. The increase in the amount of AgNPs in the solution led to an increase in the electrical charge and conductivity, which led to

a thinner diameter of the fibers, it was about of 63.23±0.85 nm with the pore size 151.57 ±9.65 nm in 'Figure 5(B),(C)' [39]. As for the ALg-F-scaffold in 'Figure 6 (A)', the fibers were uniform, regular, and more intertwined, with a lower average diameter of 58.30±2.12 nm in 'Figure 6(B)' This is because this scaffold contains the highest percentage of AgNPs , which may reach (0.7g) Which led to an increase in the electrical conductivity of the solution further, thus facilitating the stretches of the polymer jet and the production of thinner nanofibers [50].

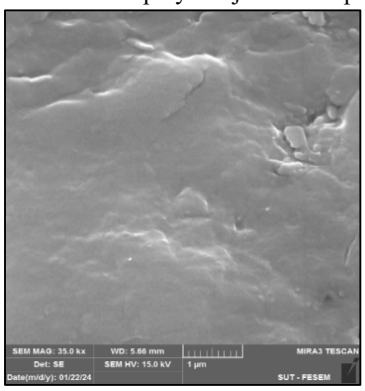

FIGURE 1. FESEM of ALg-A

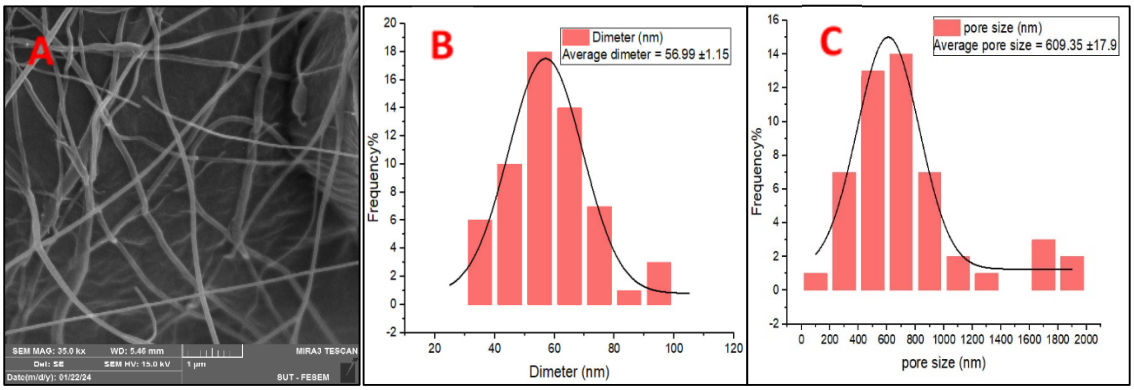

FIGURE 2. (A) FESEM of ALg- B scaffold (35 KX); (B) average fiber dimeter in ALg- B scaffold ; (C) avreage pore size in ALg- B scaffolds.

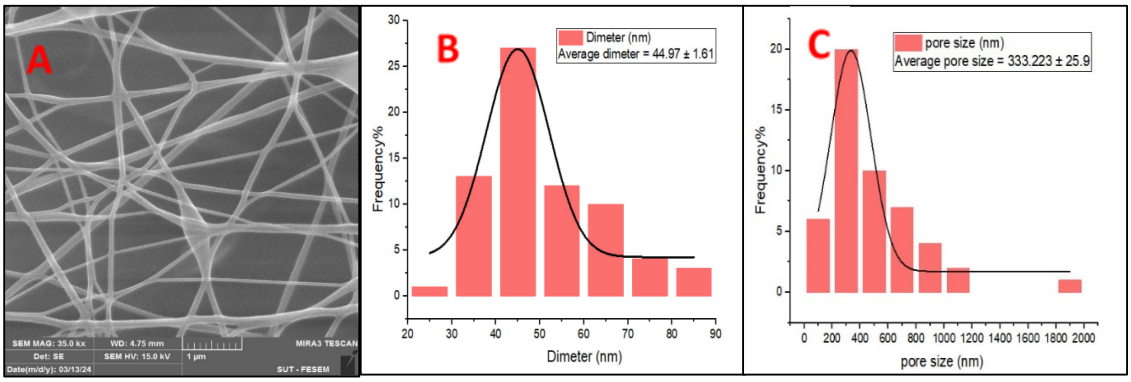

FIGURE 3. (A) FESEM of ALg-C scaffold (35 KX); (B) average fiber dimeter in ALg-C scaffold; (C) avreage pore size in ALg-C scaffolds.

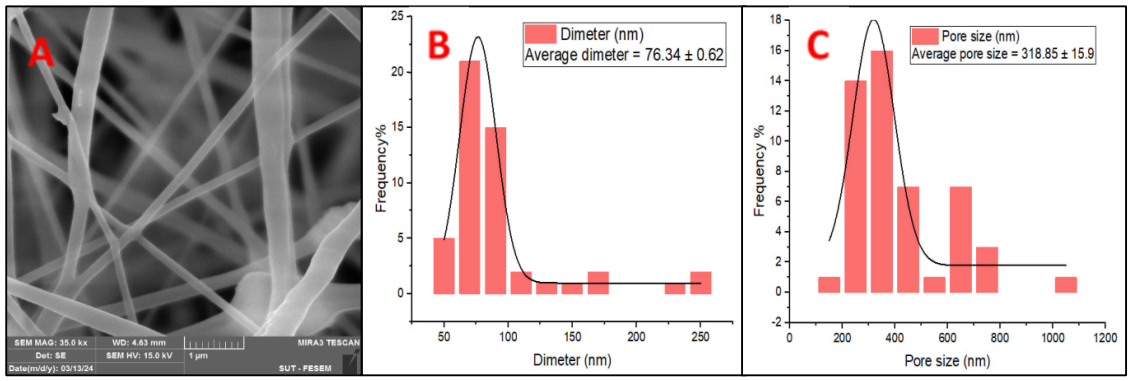

FIGURE 4. (A) FESEM of ALg-D scaffold (35 KX); (B) average fiber dimeter in ALg-D scaffold; (C) avreage pore size in ALg-D scaffolds

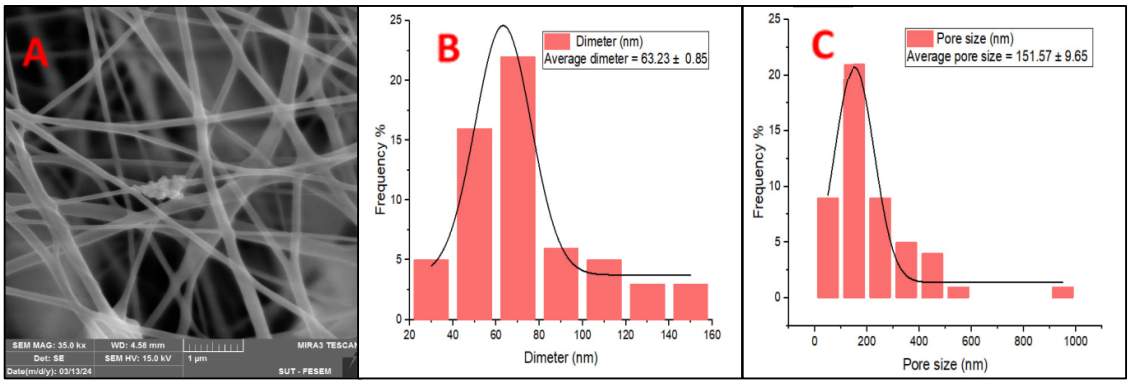

FIGURE 5. (A) FESEM of ALg-E scaffold (35 KX); (B) average fiber dimeter in ALg-E scaffold; (C) avreage pore size in ALg-E scaffold.

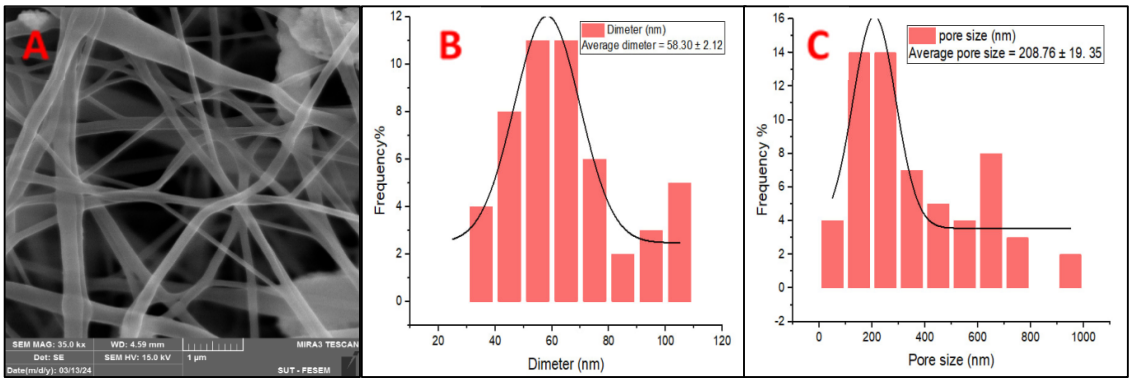

FIGURE 6. (A) FESEM of ALg-F scaffold (35 KX); (B) average fiber dimeter in ALg-F scaffold ; (C) average pore size in ALg-F scaffold.

FTIR RESULT

'Figure 7,' displays the FTIR spectra of scaffolds. The absorption peaks (O–H) in the sodium alginate film (ALg) were seen at a stretching vibration frequency of 3275 cm^{-1}. The peak found at 2933 cm^{-1} can be attributed to the stretching vibrations of (C-H) bonds in aliphatic chains, including both symmetric and asymmetric vibrations. In addition, a peak at 1032 cm^{-1} is attributed to the stretching vibrations of the (C-O-C) groups. The peaks seen at 1605 and 1412 cm^{-1} are attributed to the stretching vibrations of carbonyl groups. Specifically, the peak at 1605 cm^{-1} corresponds to the symmetric stretching vibration, while the peak at 1412 cm^{-1} corresponds to

the asymmetric stretching vibration [51]. Regarding the ALg- A scaffold, the amide A is seen at the specific wavenumber of 3275cm^{-1}. Amide B has absorption peaks at 2923 and 2880 cm^{-1}. The Amide I peak is detected at a wavenumber of 1619 cm-1, whilst the Amide II peaks are recorded at wavenumbers of 1544 cm^{-1} and 1411 cm^{-1}. The Amide III peak is observed at a wavenumber of 1235 cm^{-1} [42] The ALg-B scaffold displayed a distinct presence of an asymmetric CH^2 bond at 2936 cm^{-1} and a symmetric CH_2 bond at 2868 cm^{-1}. The carbonyl bond (C=O) has been shifted to a frequency of 1723 cm^{-1}. The band at 1616 cm^{-1} corresponds to the stretching of the CH_2 bond. The (C-O) band is detected at a wavenumber of 1294 cm-1, whereas the (C-O-C) bands are found at 1240 and 1144 cm^{-1}[52]. We observe amide A change position in the ALg-C scaffold to 3331 cm^{-1}. Furthermore, there is a clearly noticeable existence of an asymmetrical CH_2 bond at 2944 cm-1 and a symmetrical CH_2 bond at 2867 cm^{-1}. The amide I peak is observed at a wavenumber of 1724 cm^{-1}, whereas the peak at 1616 cm^{-1} corresponds to the stretching of the CH_2 bond. The Amide II peak was identified at a wavenumber of 1470 cm^{-1}, while the Amide III peak was located at a wavenumber of 1294 cm^{-1}. The peaks detected at 1240 and 1173 cm^{-1} were attributed to the (C-O-C) bands. We observe a minor shift in the peak positions of the Alg when Col and Pcl are deposited upon it [53]. Also, the transmission peaks of nanoparticles-loaded scaffolds are very close to those of ALg-C scaffold. The characteristic peaks of nanoparticles were not apparent in the spectra of all nanoparticles-loaded scaffolds, without any extra absorption peaks appearing. The results indicated that there was no chemical interaction between the nanoparticles (AgNPs, Tio2 NPs) and polymers during the fabrication process of the scaffolds. This suggests that the original components did not undergo any chemical changes.

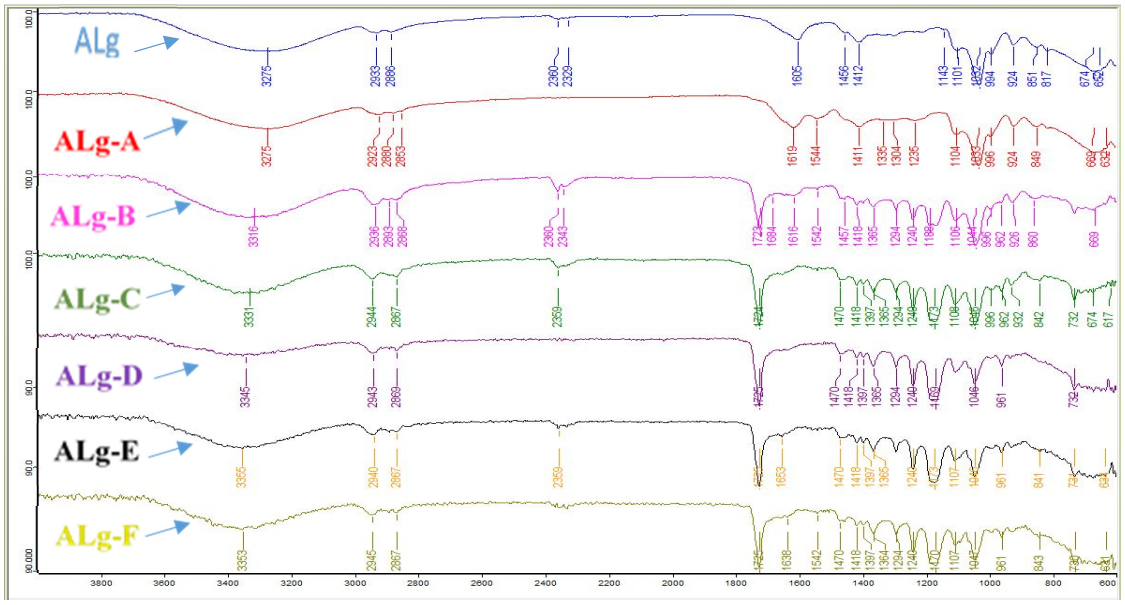

FIGURE 7. FTIR analysis of all scaffolds (free of nanoparticles and loaded with nanoparticles).

WETTABILITY RESULT

The wettability of the scaffold is an essential characteristic that impacts the capacity of cells to adhere to the scaffold. The hydrophilicity of the scaffold was assessed by measuring its water contact angle [54]. Figure 8 (A, B, C, D, E, F, G) depicts the water contact angle measurements for all scaffolds. The film Alg in Figure 8 (A) had a hydrophilic characteristic, as indicated by a contact angle of (30.744°) [55]. the Alg-A scaffold shown in 'Figure 8 (B),' has a contact angle of (32.890°), which is quite similar to the contact angle of the alginate film. This suggests that the Alg-A scaffold also has a hydrophilic nature. While the Alg-B scaffold, as depicted in 'Figure 8 (C),' exhibited a hydrophobic nature with a contact angle of (112.101°). The hydrophilic nature of the ALg-C nanofiber scaffold 'Figure 8 (D),' is a result of the incorporating of collagen in the scaffold. This led to the water contact angle of the nanofibers reaching (66.66°). The incorporating of collagen in the scaffold resulted in a reduction in the water contact angle and an enhancement in the hydrophilic nature of the scaffold, attributable to its hydrophilicity [56]. Regarding the scaffolds that are loaded with nanoparticles, we see a more significant reduction in the water contact angle. The value decrease to (42.668°) in the ALg-D scaffold, (37.517°) in the ALg-E scaffold, and reached a value of (33.219°) in the ALg-F scaffold. We can conclude that the the presence of nanoparticles resulted in a notable reduction in the water contact angle and an enhancement in hydrophilicity [57],

Because of their significant surface area to volume ratio, scaffolds loaded with nanoparticles have thinner fibres. This results in an increased total surface area available for interaction with water molecules. The high surface to volume ratio leads to a greater uptake of water and hydrophilicity, which in turn causes high degradation rates [50].

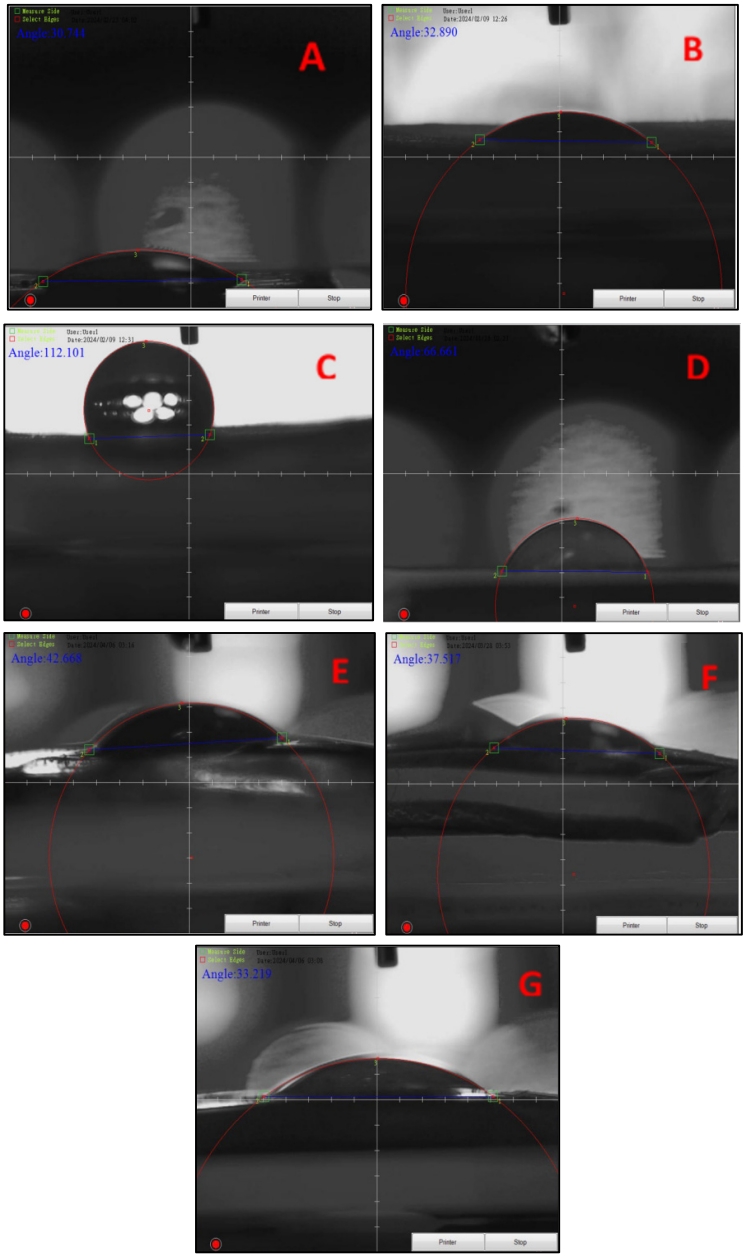

FIGURE 8. Show the scaffolds contact angle; (A) ALg, (B). ALg-A, (C). ALg-B , (D). ALg-C, (E) ALg-D, (F) ALg-E, (G) ALg-F.

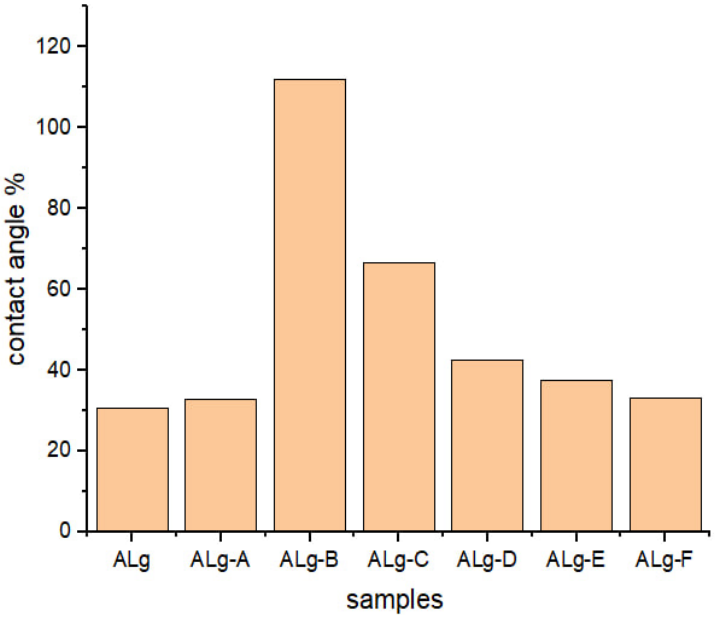

FIGURE 9. Shows the scaffolds contact angle percentage for all scaffolds.

ANTIBACTERIAL ACTIVITY RESULT

The scaffolds were employed against Gram-positive Bacteria Staphylococcus aureus (S.aureus) and Gram-negative Pseudomonas aeruginosa (P. aeruginosa) are pathogenic organisms. In the antimicrobial activity assay. The findings indicated that the sample without nanoparticles exhibited no bacterial resistance, so heightening the vulnerability to bacterial colonisation and consequently elevating the likelihood of illness [52]. The scaffolds loaded with nanoparticles exhibited antibacterial properties against both Gram-positive and Gram-negative bacteria, as demonstrated in the 'Figure 10,' and 'Table 2'. The sample ALg-E exhibited the highest level of inhibition zone for both type of bacteria, in which the mount of AgNPs is equal to Tio2NPs. We can conclude that this ratio is the most effective as a result of an ideal balance between (AgNPs) and (Tio2NPs), as they interact synergistically to enhance antibacterial activity. This ratio may be optimal to achieve intense interactive effects without reaching excessively inhibitory or toxic concentrations. Increasing the concentration of silver may lead to excessive toxic effects that harm bacterial cells in ineffective ways [58].

Table 2. Bacterial Inhibition zone

Sample	Inhibition zone (S.aureus) (mm)	Inhibition zone (mm) (P. aeruginosa)
control	0	0
ALg-C (C1)	0	0
ALg-D (D1)	21	23
ALg-E (E1)	23	25
ALg-F (F1)	22	23

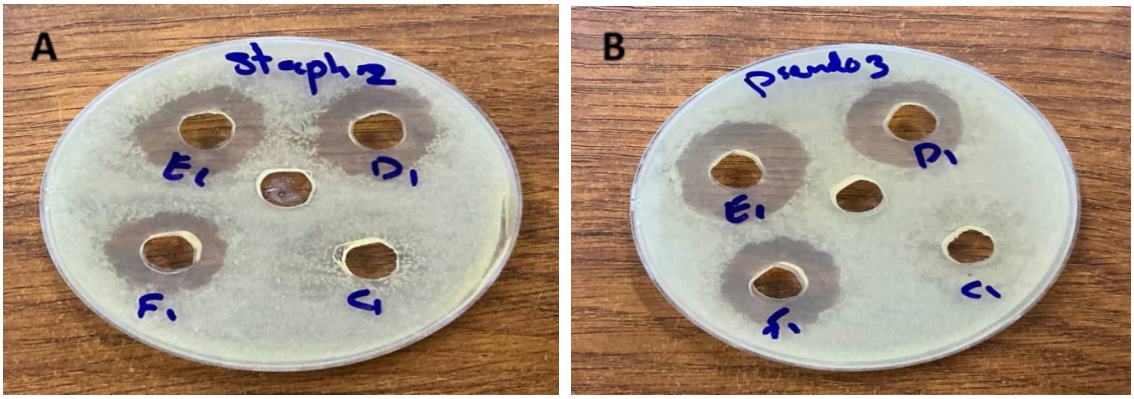

FIGURE 10. Shows the inhibition zone of scaffolds without nanoparticles , The scaffolds loaded with nanoparticles and control in (A) Staphylococcus aureus (S.aureus) and (B) Pseudomonas aeruginosa (P. aeruginosa) .

CONCLUSION

This study involved the fabrication of a polymeric scaffold using collagen and polycaprolactone. The scaffold was loaded with silver nanoparticles and titanium dioxidenanoparticles by using the electrospinning process these fibers were deposited on sodium alginate films for promoting wound healing. The nanoparticles were added in three different ratios, the amount of silver nanoparticles (AgNPs) was variable in each ratio, while the amount of titanium dioxide nanoparticles (Tio2 NPs) was constant. These scaffolds were studied to evaluate their suitability as a suitable biomaterial for wound healing, as the FESEM results demonstrated that the average diameter of the nanofibers was in contradiction with the increase in the amount of silvernanoparticles in the scaffold. The results of the wettability property also showed that the addition of nanoparticles led to a decrease in contact angles, and the scaffolds loaded with nanoparticles became more hydrophilic than the scaffolds devoid of nanoparticles. As for the antibacterial results, they showed that the scaffolds devoid of nanoparticles did not show any bacterial resistance, while all the scaffolds loaded with nanoparticles showed bacterial resistance against Gram-positive and Gram-negative bacteria. ALg-E Scaffold was the scaffold that showed the highest bacterial resistance. Consequently, this newly scaffold is suited for use in skin tissue engineering because of its favourable characteristics, including excellent antibacterial activity, as well as a surface that promotes cell proliferation and adherence.

REFERENCES

1. B. Zeybek and M. Duman, *J. Mater. Sci.,* **3**(1), 121–134 (2014).
2. J.M. Anaya Mancipe, L.C. Boldrini Pereira, P.G. de Miranda Borchio, M.L. Dias, and R. M. da Silva Moreira Thire, *J. Biomed. Mater. Res. Part B Appl. Biomater.,* **111**(2), 366–381 (2023).
3. T.T.P. Ho et al., *Mater. Sci. Eng. C,* **120,** 111724 (2021).
4. A. Hernández-Rangel and E.S. Martin-Martinez, *J. Biomed. Mater. Res. Part A,* **109**(9), 1751–1764 (2021).
5. B. Azimi et al., *J. Funct. Biomater.,* **11**(3), 67 (2020).
6. A. Memic, T. Abdullah, H.S. Mohammed, K. Joshi Navare, T. Colombani, and S.A. Bencherif, *ACS Appl. Bio Mater.,* **2**(3), 952–969 (2019).
7. H. Bi, T. Feng, B. Li, and Y. Han, *Polymers*,**12**(4), 839, (2020).
8. Y. Dong et al., *Adv. Fiber Mater.,* **2**, 212–227, (2020).
9. I. Negut, G. Dorcioman, and V. Grumezescu, *Polymers*, **12**(9), 2010 (2020).
10. Y.D. Nokoorani, A. Shamloo, M. Bahadoran, and H. Moravvej, *Sci. Rep.,* **11**(1), 16164 (2021).
11. I.A.U. Kadhim, *J. Biomimetics, Biomater. Biomed. Eng.,* **59,** 11–20 (2023).
12. T.Y. Jasim, M.A. Najim, and A.R. Jabur, "Improving the mechanical properties of (chitosan/polyurethane) electrospun blend scaffold used for skin regeneration," in *AIP Conference Proceedings,* AIP Publishing, 2019.
13. A. Ehterami et al., *Int. J. Biol. Macromol.,* **117**, 601–609 (2018).
14. S.A. Moosa, A.R. Jabur, and E.S. Al-Hassani, "Effect of different polycaprolactone scaffolds concentration on metoprolol tartrate release ratio," in *AIP Conference Proceedings*, AIP Publishing, 2022.
15. S.A. Moosa, A.R. Jabur, and E.S. Al-Hassani, *Key Eng. Mater.,* **886**, 183–188 (2021).
16. A.R. Jabur, E.S. Al-Hassani, A.M. Al-Shammari, M.A. Najim, A.A. Hassan, and A.A. Ahmed, *Energ Proced,* **119**, 61–71 (2017).

17. E.M. Tottoli, R. Dorati, I. Genta, E. Chiesa, S. Pisani, and B. Conti, *Pharmaceutics,* **12**(8), 735 (2020).
18. S. Fahimirad and F. Ajalloueian, *Int. J. Pharm.,* **566,** 307–328 (2019).
19. Z. Mbese, S. Alven, and B.A. Aderibigbe, *Polymers,* 13(24), 4368 (2021).
20. C.D. Weller, V. Team, and G. Sussman, *Front. Pharmacol.,* **11,** 495485, (2020).
21. V. Vivcharenko and A. Przekora, *Appl. Sci.,* **11**(9), 4114, (2021).
22. T.C. Mokhena, M.J. Mochane, A. Mtibe, M.J. John, E.R. Sadiku, and J.S. Sefadi, *Materials*, **13**(4), 934 (2020).
23. M.A.S. Abourehab et al., *Int. J. Mol. Sci.,* **23**(16), 9035 (2022).
24. M. Summa et al., *Eur. J. Pharm. Biopharm.,* **122**, 17–24 (2018).
25. A.R. Abbasi et al., *Int. J. Biol. Macromol.,* **155**, 751–765 (2020).
26. A.M.E. Matinong, Y. Chisti, K.L. Pickering, and R.G. Haverkamp, *Biology*, **11**(6), 905 (2022).
27. A. Terzi et al., *Macromol. Biosci.,* **20**(5), 2000017 (2020).
28. H. Jafari et al., *Polymers,* **12**(10), 2230 (2020).
29. S.S. Mathew-Steiner, S. Roy, and C.K. Sen, *Bioeng,* **8**(5), 63 (2021).
30. S. Sharma, V.K. Rai, R.K. Narang, and T.S. Markandeywar, *Life Sci.,* **290**, 120096 (2022).
31. E. Türker, Ü.H. Yildiz, and A.A. Yildiz, *Int. J. Biol. Macromol.*, **139**, 1054–1062 (2019).
32. B. Safari, M. Aghazadeh, L. Roshangar, A. Aghanejad, and S. Davaran, *Eur. Polym. J.,* **171**, 111220 (2022).
33. S. I. Salih, A. R. Jabur, and T. A. Mohammed, "The effect of PVP addition on the mechanical properties of ternary polymer blends," in *IOP Conference Series: Materials Science and Engineering*, IOP Publishing, 2018, p. 12071.
34. G. El Fawal, H. Hong, X. Mo, and H. Wang, *J. Drug Deliv. Sci. Technol.,* **63**, 102501 (2021).
35. A. Al-Khateeb, E.S. Al-Hassani, and A.R. Jabur, Int. J. Biomater., **2023,** (2023).
36. A. Dewle, P. Rakshasmare, and A. Srivastava, *ACS Appl. Bio Mater.,* **4**(2), 1238–1251 (2021).
37. D. Mondal, M. Griffith, and S.S. Venkatraman, *Int. J. Polym. Mater. Polym. Biomater.,* **65**(5), 255–265 (2016).
38. A. J. Hassiba et al., *Nanomed,* **11**(6), 715–737 (2016).
39. E. Pazos-Ortiz et al., *J. Nanomater.,* **2017**(1), 4752314 (2017).
40. N. Eghbalifam, S.A. Shojaosadati, S. Hashemi-Najafabadi, and A.C. Khorasani, *Int. J. Biol. Macromol.,* **155**, 119–130 (2020).
41. A. Saatchi, A.R. Arani, A. Moghanian, and M. Mozafari, *Ceram. Int.,* **47**(7), 9447–9461 (2021).
42. E. Matei et al., *Coatings,* **11**(2), 121 (2021).
43. G. Rath, T. Hussain, G. Chauhan, T. Garg, and A.K. Goyal, *J. Drug Target.,* **24**(6), 520–529 (2016).
44. C.L. de Dicastillo, M.G. Correa, F.B. Martínez, C. Streitt, and M.J. Galotto, A*ntimicrob. Resist. One Heal. Perspect.*, 2020.
45. K. del Ángel-Sánchez, N.A. Ulloa-Castillo, E. Segura-Cárdenas, O. Martinez-Romero, and A. Elías-Zuñiga, *MRS Commun.,* **9**(1), 390–397 (2019).
46. H.A. Alhadrami et al., *Am. J. Nanomater,* **5**(1), 31–42 (2017).
47. N. Munir and A. Callanan, *Biomed. Mater.,* **13**(5), 51001 (2018).
48. V. Perez-Puyana et al., *J. Biomed. Mater. Res. Part A,* **109**(9), 1600–1612 (2021).
49. S.A. Moosa, A.R. Jabur, E.S. Al-Hassani, and A.M. Al-Shammari, *Eng. Technol. J.,* **40**(12), 1671–1682 (2022).
50 S. Ahmadian, M. Ghorbani, and F. Mahmoodzadeh, *Int. J. Biol. Macromol.*, **162**, 1555–1565 (2020).
51. I.A.U. Kadhim, *Key Eng. Mater.,* **900,** 26–33 (2021)
52. A. Al-khateeba, E.S. Al-Hassania, A.R. Jabur, and S.B.A. Bakar, *Eng. Technol. J.,* **41**(06), 845–859 (2023).
53. Q. Zhang, S. Lv, J. Lu, S. Jiang, and L. Lin, *Int. J. Biol. Macromol.,* **76**, 94–101 (2015).
54. P. Sobhanian, M. Khorram, S.S. Hashemi, and A. Mohammadi, *Int. J. Biol. Macromol.,* **130**, 977–987 (2019).
55. I. A. U. Kadhim, *J. Biomimetics, Biomater. Biomed. Eng.,* **59**, 11–20 (2023).
56. P. Prabu, N. Dharmaraj, S. Aryal, B.M. Lee, V. Ramesh, and H.Y. Kim, *J. Biomed. Mater. Res. Part A* **79**(1), 153–158 (2006).
57. B. Samavati, E. Tamjid, M.A. Khalili, and K. Khajeh, "3D-Printing and Biofunctionalization of PCL-Based Nanocomposite Scaffolds for Osteogenic Differentiation," 2024.
58. T. Bruna, F. Maldonado-Bravo, P. Jara, and N. Caro, *Int. J. Mol. Sci.,* **22**(13), 7202 (2021).

Isolating the prolidase enzyme and studying some pharmaceutical compounds for people with thyroid

Vian Ismael Mohammed[1, a], Sayran Sattar Saleh[2, b]

[1]*Department of Chemistry, College of Science, University of Kirkuk, Kirkuk, Iraq.*
[2]*Department of Chemistry, College of Education for Pure Sciences, University of Kirkuk, Kirkuk, Iraq*

[a)] Corresponding author: vyanismael@uokirkuk.edu.iq
[b)] Sayran.2017@uokirkuk.edu.iq

Abstract. The study examined the impact of levothyox, carbamazol, nebivolol, and glimepiride on the effectiveness of prolidase. This was done after the enzyme was extracted from people with thyroid glands using the G-100 gel filtering procedure. Prolidase was extracted from a thyroid patient's serum for the investigation, utilizing various biochemical methods. Following dialysis, sephadex (G-100) was prepared by ammonium sulfate precipitation (70%) and used for gel filtering to retrieve a single proteinous peak. The enzyme's specific activity was 2533 units/mg protein with a 56-fold purification level using gel filtration chromatography (G-100). According to the findings, the best conditions for extracting enzyme from the serum of a thyroid patient were (40) µg/ml of protein as the source of the enzyme and 60 mM/L of Tris-HCl buffer solution at pH (8.0) at 37°C. The maximal velocity (Vmax) and Michaelis constant (Km) utilizing Gly-Pro as a substrate were found to be (4.81000 U/L) and (3.62289 mol/L), respectively, using a Line Weaver-Burk plot. Lastly, included the investigation of how pharmacological chemical compounds affected the activity of the enzyme; the findings indicated that the medication chemical compounds for type : Levothyox and Carbamazol give the inhibition type non-competitive, with constant in Km value to (40 mM/L) and decreased Vmax value (100 U/L) for each drug respectively. The effect of Nebivolol and Glimepiride on prolidase efficiency was activated because the enzyme efficiency without any drug was (350.6) but addition of Nebivolo and Glimepirid was effective (488-426.9) (508.7-428.7), respectively.

INTRODUCTION

The thyroid gland an endocrine gland with a butterfly-like form under the Adam's apple in the neck, consists of two lobes, the right and the left, which are joined by a thin isthmus of tissue. Adult thyroid glands weigh 25 grams, with 5 cm long, 3 cm wide, and 2 cm thick lobes, as well as an isthmus that is 1.25 cm high and wide. The thyroid gland, which is typically larger in women than in men and grows larger during pregnancy, generates thyroid hormones (TRs), which control a number of essential bodily functions [1] . The term "thyroid" comes from the Greek word "thyrion," which means shield [2]. Triiodothyronin (T3) and thyroxine (T4) are key hormones that it is thought to be the only gland to produce, emit, and store. These two hormones are crucial for the development, growth, and regulation of the body's metabolism [3]. Thyroid-stimulating hormone (Tsh), which is generated by the anterior pituitary gland, controls thyroid hormone secretion. Thyroid-releasing hormone (TRH), which is produced by the hypothalamus, controls Tsh [4,5].Prolidase [E.C. 3.4.13.9] is an enzyme that belongs to the class of enzymes that catalyze the hydrolysis of basic substances. It is the only enzyme that can hydrolyze dipeptides that have proline or hydroxyproline derivatives at the terminal end of the carbon group to produce free proline. Finally, free proline is important in the last stages of the catabolism of proteins rich in proline amino acids and hydroxyproline like collagen catabolism. The enzyme participates in the remodeling of tissue material. The visceral matrix is located between cells and contributes to cell growth by regulating growth and transcription factors. The enzyme has important roles in many physiological aspects and pathological processes such as wound healing, inflammation, and angiogenesis that cause cancer and its spread. Since collagen is the main component of the extracellular matrix, the connection between the cell and extracellular proteins is through collagen gene expression, and it also has a role in the process of cell differentiation and growth in addition to its role in the formation of tumors. Therefore, any change that occurs in collagen metabolism can affect In cell metabolism and development, it is known that good external collagen can be degraded by a series of enzymatic

Technologies and Materials for Renewable Energy, Environment and Sustainability
AIP Conf. Proc. 3321, 030002-1–030002-10; https://doi.org/10.1063/5.0290622
Published under an exclusive license by AIP Publishing. 978-0-7354-5231-2/$30.00

reactions of collagenase enzymes, but the final step to complete the decomposition takes place only in the presence of the enzyme prolidase. Consequently, any alteration in collagen metabolism has the potential to It is known that good exterior collagen can be broken down by a series of enzymatic reactions of collagenase enzymes on cell metabolism and development, but the last step to finish the breakdown only occurs in the presence of the enzyme prolidase [6,7].This enzyme can be found in the brain, heart tissue, uterine tissue cells, spleen, intestines, red blood cells, white blood cells, blood plasma, and both mono- and multinucleated cells [8]. When osteoporosis and liver diseases arise, the enzyme has been shown to have aberrant activity; this can be exploited to The enzyme can be used as a marker to identify several kinds of cancerous tumors, including breast cancer, which is characterized by a reduction in collagen deposition,as well as carcinoma. The final piece of knowledge is one of his most significant academic retirements—no collagenases. Only when prolidase is present can hydrolysis take place [9,10] .The enzyme primarily functions on imidopeptides, which are byproducts of the breakdown of collagen, the most abundant structural protein in the human body (collagen accounts for approximately 33% of total protein mass, of which proline and hydroxyproline make up more than 20%) percentage of collagen [5]. Consequently, the degradation of collagen generates a substantial amount of peptides that contain proline and hydroxyproline [9]. In order to create collagen, the enzyme breaks down these peptides and recycles the proline. der to create collagen, the enzyme breaks down these peptides and recycles the proline .There are two isoenzymes of prolidase: prolidase I and prolidase II. The dominant form, the first isotope, has a molecular weight of 56 kDa and a strong affinity for the dipeptides Gly-Pro and Ala-Pro. With a molecular weight of 95 kDa, the second isotope exhibits a poor affinity for Gly-Pro and a high affinity for Met-Prol [11]. Hydrophilic amino acid residues and residues are present in prolides. Two chains of hydrophilic amino acid residues In a number of disorders, enzyme activity has also been linked to oxidative stress .Additionally, enzyme activity has been linked to oxidative stress in a number of diseases [12] . Prolipidase activity and inflammation have also been found to be related to one another during the course of pulmonary fibrosis [13]. As shown in the placental tissue of women who have aborted has a higher enzyme effectiveness than that of women who have not aborted, and this could be because of accelerated collagen turnover, which can lead to placental pathology and miscarriage [14]. Manganese serves as the enzyme's catalyst. At the terminal end of the alpha carbon, prolina or hydroxyprolina derivatives are produced to yield free prolina. It is the sole enzyme capable of catalyzing the breakdown of dipeptides [15,16].

EXPERIMENTAL PART

Materials and Methods

Thyroid gland patients had their blood drawn into a volume of (15 ml), put in a gel tube, and submerged in a water bath at (37°C) until the blood coagulated. (10 ml) of serum was then extracted after it was centrifuged for ten minutes at (3500 xg) speed. Serum and apply it directly to the object to carry out purifying processes.

Determination of prolidase activity

The prolidase enzyme reacts with the dipeptide (glycine - proline), distinct types of the enzyme to give the amino acid proline and glycine in free form [17]. The amount of proline released is measured colorimetrically after its reaction with ninhydrin, wavelength (515) when coordinated, based on prolidase as a standard substance.

Solutions used

1. Dilution solution: 1.0 mmol of MnCl2 in 6 mmol of pH (7.8–8) Buffer Tris HCl. The solution for the regulating gear was made. 2. Standard proline solution: L-proline solution was made and dissolved in 0.45 mol/L of trichloroacetic acid solution at a concentration of 650 micromol/L. 3.Glycyl-L-Proline matrix solution :0.05 mol/L of Tris HCl solution containing 1 mmol/L of Mncl2 and 94 mmol/L of Glycyl-L-Proline were made, with a pH of 7.8 to 8.0. 4. Chinard's reagent: Mix 120 cm3 of glacial acetic acid, 80 cm3 of orthophosphoric acid (6 mol/L), and 25 g of ninhydrin to make the reagent. Thoroughly mix the solution in a water bath at 70 °C.

The Solutions used

Make a trichloro acetic acid (TCA) solution with a concentration of 0.45 mol/L. Prior to creating Chinard's reagent, which is 6 moles per liter of orthophosphoric acid made by dissolving 203.5 cm^3 of the acid in 296.5 cm3 of distilled water, the mixture was melted at 70°C in a water bath.

Procedure

The following steps were relied upon to estimate the effectiveness of the enzyme: The serum was diluted six times using 250 microliters of dilution solution for every 50 microliters of blood serum, and then the mixture was incubated for 24 hours at 37°C. I prepared test tubes as shown in Table 1.

TABLE.1 The prepared test tubes.

Solution	Test	Control
Substrate solution	100 µl	-
Dilutionserum solution	100 µl	100 µl

After 30 minutes of incubation at 37 degrees Celsius, the reaction was halted by adding 1 cm^3 of a TCA solution with a concentration of 0.45 mol /L. (100 µl) of the diluted, un-incubated serum solution was added to the control tube after the reaction was halted. After the tubes were centrifuged for five minutes at 2000 rpm, 0.5 cm^3 of the clear solution was taken out of each tube. Examine and regulate. I prepared four tubes as shown in Table 2.

TABLE.2 The prepared test tubes

No	Solution	Test	Control	Standard	Blank
1	Chouinard's reagent	1 Ml	1 ml	1 ml	1 ml
2	Glacial acetic acid	1 Ml	1 ml	1 ml	1 ml
3	Clear solution	0.5 Ml	0.5 ml	-	-
4	Standard proline solution	-	-	0.5 ml	-
5	stopping solution	-	-	-	0.5 ml

The synthesis of the colored complex in the four tubes above was allowed to be completed for ten minutes at 90°C in a water bath. Following the device's zeroing with the buffer solution, the absorbance of each tube was measured at 515 nm. The following equation [18]. Was then used to compute the enzyme's activity [19]:

$$\textbf{Prolidase Activity} = \frac{\text{Abs of test-Abs of control}}{\text{Abs of standarad}} \text{x2.4x (S)}$$

S=94 mol/L Concentration of the matrix in mmol/L (1)

Isolation and partial purification of Prolidase

From serum specimens. Prolidase is isolated from serum and partially purified in this section of the investigation using samples of serum extract. Different steps are used for partial purification, and they will be explained as follows:

Ammonium sulfate precipitation

The solid form of ammonium sulfate is gradually added to 10 ml of serum, stirring continuously with an electric stirrer for 60 minutes at 4 °C. After that, the mixture is placed in a microcentrifuge for 15 minutes. The ammonium sulfate was added at 30% saturation. Both a filtrate and a precipitate were produced. The filtrate was obtained, and the head was disposed of. After that, 10 milliliters of serum were gradually mixed with ammonium sulfate at a rate of 70% saturation percent using an electric stirrer for 60 minutes at 4 °C. The sample was then left for 24 hours at 4 °C to finish the sedimentation process, as indicated in figure 3.4.Given that ammonium sulfate precipitation is one of the initial phases of partial purification, during which the proteins in the sample are deposited according to the sample's saturation level with ammonium sulfate [20].

Dialysis procedure

Preparation of Dialysis bag

Prepare all of the reagents (0.01M) before using the dialysis tube, which is constructed of virgin wood pulp and regenerated cellulose. The tubing is flat and clear. To produce EDTA solution, dissolve 1.4612 g of EDTA in 0.5 L of D.W. (0.2M). To create a sodium bicarbonate solution, dissolve 8.4003g of NaHCO3 in the reagent (1). One can create a sodium azide solution by dissolving 0.01g of sodium azide in 100 ml of D.W. After the dialysis tube was broken up, it was immersed in one liter of D.W. and brought to a boil for three minutes. Following a 30-minute boil, the dialysis tube was reboiled in one liter of reagent (2) and then immersed in reagent (3) for two hours. first After being in the D.W. for thirty minutes, the dialysis tube was rinsed multiple times with D.W. until the pH of the solution was attained (at which point the dialysis tube was ready for use). After being kept in reagent (3), the tube was retained at 4°C and used for dialysis against buffer. The ammonium sulfate fraction was collected and dialyzed against a 0.1M phosphate buffer (pH = 7.4), with the buffer solution changed every 8 hours, overnight at 4 °C [21] .

Gel filtration chromatography

Separating substances based on variations in molecular weight and size is known as gel filtration chromatography. Additionally, the gel filtration technique is employed in the following phases of column preparation for gel filtration chromatography to estimate the approximate molecular weight of protein molecules [22] employing Sephadex G-100 for gel filtration chromatography. Gel Sephadex G-100 (Solarbio) prepared a slurry in the equilibration buffer for three days at room temperature (~25±1Co). The gel was then loaded onto the glass column bed (30×1.5) cm, which had been pre-equilibrated with (0.1 M) Tris-HCl buffer, pH 7.4. The gel preparation and fractionation procedures were carried out as previously mentioned [23]. The column's dimensions were chosen using the subsequent computations [24, 25].

The effect of some medications on the effectiveness of the prolidase

The efficacy of the prolidase enzyme after its final purification process was tested using the methodology of researchers Befani and others [26]. Additionally, the quality of inhibition was studied using varying concentrations of chemicals involved in the particular enzyme reaction to measure the effectiveness of the enzyme after determining the ideal conditions for it.

RESULTS AND DISCUSSION

Gel filtration technology was used in the process of separating the protein compounds obtained through the dialysis process. A separation column containing sephadex G-100 was used, and it was observed that highly effective band was observed, as in fig.1. The peak was at the volume of 162 ml, where the molecular weight of the enzyme was 53703.2, using standard materials with known molecular weight using the standard curve as shown in fig. 2. Comparing the specific activity of the enzyme during the purification processes of the precipitate resulting from the precipitation process to its effectiveness in serum crude (44.7 enzyme units/mg protein), the results presented in Table 3 show that the enzyme's specific activity increased to a value of (53.25 enzyme units/mg protein). It also rose further following the membrane sorting procedure (dialysis) as a result of the elimination of protein molecules of low

molecular weights (less than 14,000 Daltons) [27]. After utilizing the separation column, it rose and reached 57.3 enzyme units/mg protein. To separate substances with differing molecular weights, use Sephadex G-100.

TABLE.3 The Steps to purify the prolidase enzyme from the serum of people with thyroid

Purification step	Serum cruds	Purification ammonium sulphate (70%)	Dialysis	Test	G-100
Size(ml)	10	8.5	7.5	1 Ml	10
Total protein concentration (mg/ml)	52	26.3	13.5	1 Ml	1.5
Activityenzyme (*E unit / ml)	501	426	401	0.5 Ml	380
Total efficiency Units of enzymes	5.010	3.621	3.007	-	3.800
Qualitative effectiveness (EU/mg protein)	9 6.3	137.6	222.7	-	2533
The number of times purification	1	1.4	5	-	56
Yield%	100	72.2	60	-	75

Enzyme unit: The amount of enzyme required, under the given measurement conditions, to convert one micromole of the base material (Gly-Pro) into proline per minute per milliliter.

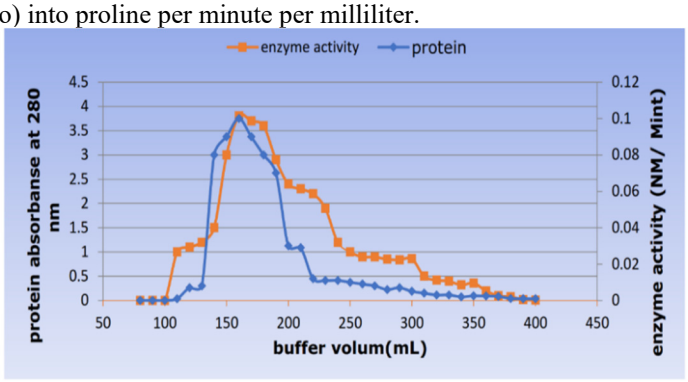

FIGURE 1. Profile showing the prolidase protein band emerging from the separation column G-100 and returned to serum fluid using gel filtration technology.

TABLE .4 Molecular weights and sizes of the standard materials used in the gel filtration technique using a type of gel Sephadex G-100

Standard material name	Molecular Weight(Daltone)	Log Molecular Weight	Elute
Blue dextran (V0)	2000000	94	solution
Urease	480000	100	6.30
Hexokinase	100000	126	5.62
Bovine serum albumin	67000	159	5
Amylase	58000	174	4.9
Egg albumin	45000	217	4.7
Pepsin	36000	243	4.65
Insulin	5750	285	4.3
Tryptophan (Vi)	204	432	3.75
The unknown(highly effective peak)	53703.2	162	2.3

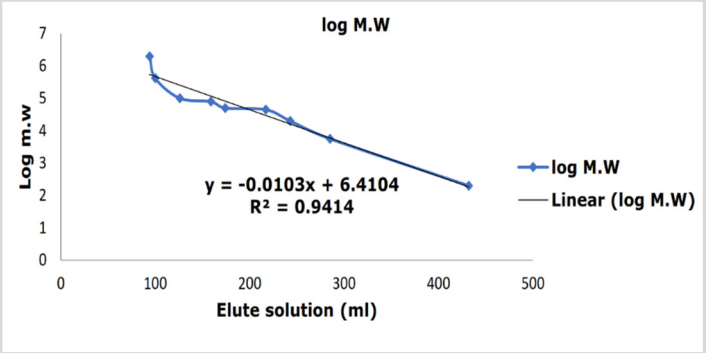

FIGURE 2. Standard curve for determining molecular weight by gel filtration technique using a separation column Sephadex G-100.

The effect of pharmaceutical chemical compounds on the effectiveness of the prolidase enzyme

A multitude of chemical substances influence the prolidase enzyme's efficacy, either by raising or decreasing it. The rate of the enzymatic process. The impact of several medicinal chemical substances on the enzyme's efficacy has been studied. separated from patients' serum who have thyroid disease[28] . A number of pure medicines were used specified (it does not contain any additives) and will be obtained from the General Company for Pharmaceutical Manufacturing and Pioneer to manufacture medicines and medical supplies in Sulaymaniyah Governorate and learn their effect on the effectiveness of the prolidase enzyme. He describes Table 4. Outcomes acquired by applying varying doses within a substance's concentration the foundation used to calculate the enzyme's ideal conditions (5*00*, *5*0, *5*,0.5,0.005 and 0.0005 mmol/L) for each. In line with researcher Befan and colleagues' methodology [25]. it is a commonly used medicine and has various therapeutic benefits. For example, a formulation applied to the body to treat an Hypothyroidism, such as levothyrox and Carbamazol to treat an Hyperthyroidism.

Nebivolol it is used to treat high blood pressure, heart failure, and angina finally Glimepiride are used for Diabetes . The results also indicate that there is an inhibition of the enzyme's effectiveness when using the compounds .The selected medicinal chemical in different proportions when using the concentration (5*00*, *5*0, *5*,0.5,0.005 and 0.0005 mmol/L) compared with the effectiveness the last standard for the enzyme is(390.6 IU/L). Two pharmaceutical substances were shown to have a proportionately diminishing effect on the prolidase enzyme's activity.There were differences in the percentage of decreased enzyme effectiveness levothyrox and carbamazol. This can help lower the risk of developing certain illnesses or their sequelae, which impact several essential physiological processes in the body. There is a rare condition that has been reported to cause the body's enzyme production to decline, potentially affecting connective tissue It has been noted that certain treatments can be substituted with pure enzymes from various sources. Additionally, stay away from some drugs that may make the enzyme less potent and less effective overall to lessen its impact on the body.

Previous research has observed that certain drugs contribute to the inhibition of collagen's metabolic processes by reducing the prolidase enzyme's capacity to produce collagen in cells [23,29-31]. On the other hand, it has been observed that there is an increase in enzyme efficiency activity, as the percentage of activity is activated.The enzyme between (39.2-21.8 and 45-22.3) (in the use of Nebivolol and Glimepiride) (Table *5*) is also observed in the D-Rasat. Previously on There's Some Medicine. It's been activated in prolidase enzyme like a mellivalin-type chemical [31,32] . The prolidase enzyme is not very effective at breaking down harmful organic phosphorus compounds. It was therefore necessary to work on finding an enzyme with good purity and high efficiency relative to its quantity as well as to find chemical compounds that are active in pharmaceutical compounds in order to support the degradation of those toxic compounds from chemical nerve agents and insecticides such as di isopropyl fluorophosphates (DFP) or neuroactive compounds used in warfare and inhibiting enzyme colline assers Additionally, the technology of enzyme genetic engineering could be used to develop the process of enzyme synthesis [33].

Table 5.The effect of some pharmaceutical chemical compounds on the effectiveness of the prolidase.

Pharmacological formula	Chemical Structure of Pharmacological	Pharmacological conc (mg/ml)	The effectiveness of the enz-prolidase (U/L)	(-)Inhibitor (+)activator %
Levothyrox	$C_{15}H_{11}I_4NO_4$	500	183.5	(-)47.7
		50	187.7	(-)46.5
		5	190.7	(-)45.6
		0.5	220.9	(-)37.0
		0.05	224.6	(-)35.9
		0.005	230.8	(-)34.2
		0.0005	183.5	(-)19.4
Carbamazol	$C_7H_{10}N_2O_2S$	500	182.9	(-)47.8
		50	201.2	(-)42.6
		5	205.3	(-)41.4
		0.5	207.9	(-)47.0
		0.05	218.8	(-)37.6
		0.005	221.4	(-)36.8
		0.0005	235.7	(-)32.8
Nebivolol	$C_{22}H_{25}F_2NO_4$	500	488	(+)39.2
		50	475.5	(+)35.6
		5	471.3	(+)34.4
		0.5	460.4	(+)31.3
		0.05	445.3	(+)27.0
		0.005	428.3	(+)22.1
		0.0005	426.9	(+)21.8
Glimepiride	$C_{24}H_{34}N_4O_5S$	500	508.7	(+)45.0
		50	507.7	(+)44.8
		5	490.5	(+)39.9
		0.5	473.9	(+)35.2
		0.05	470.8	(+)34.3
		0.005	459.3	(+)31.0
		0.0005	428.7	(+)22.3

Determining the type of inhibition exhibited by the pharmaceutical substances (Carbmazol and Levothyrox) found in the investigation

The results shown in Fig. 3 and 4 indicated that the two pharmaceutical compounds Levothyrox and Carbamazol give a non-competitive type of inhibition, If these types of inhibitors have the advantage that the composition of the inhibitor is not similar to or may be slightly similar to the composition of the base material, and the non-competitive inhibitor is usually associated with the enzyme at another location different from the active location, i.e. there is no competition between the inhibitor and the base material on the union with the active location of the enzyme, so the increased concentration of the base material does not eliminate the effect of the functioning of these inhibitors [26] . He recognizes both forms. The maximum velocity Vmax1 for Levothyrox and Carbamazol is (50,66.66) respectively while the(Km)value remains constant. Any substance that reduces the prolidase enzyme's efficacy and, in varying degrees, inhibits the collagen-building process has an impact on the body's various tissues and functions. Additionally,

the prolidase plays a significant role in construction. Since prolaides enzyme is primarily involved in the formation of collagen and because collagen increases the flexibility of ligament tissues in many organs, including skin, bones, cartilage, and strings, any substance that reduces the effectiveness of prolidase enzyme and, in varying amounts, inhibits the process of collagen building will have an effect on different body functions and tissues [34-37].

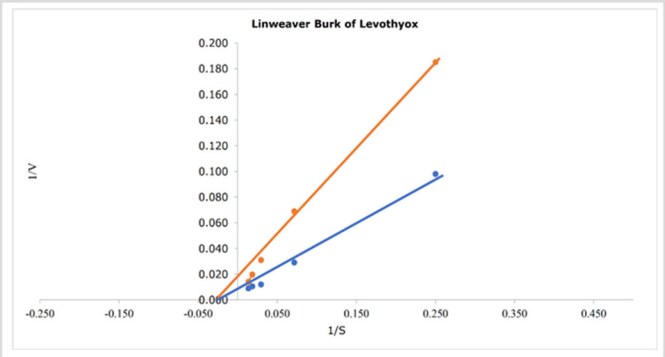

FIGURE 3. Lainwevre-Brack drawing when using a compound Levothyox, which has given a non-competitive inhibition.

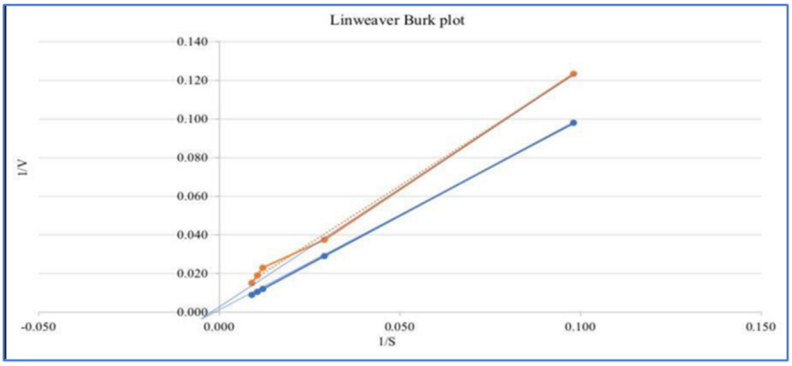

Figure 4. Lainwevre-Brack drawing when using a compound Carbamazol, who has given a non-competitive inhibition.

CONCLUSIONS

The present study comes out with the following conclusions:

1. The findings indicated that the medication chemical compounds for type: Levothyox and Carbamazol give the inhibition type non-competitive, with decrease in *K*m value to (40 mM/L) Vmax value (100 U/L) for each drug respectively.
2. The effect of Nebivolol and Glimepiride on prolidase efficiency was activated because the enzyme efficiency without any drug was (350.6) but addition of Nebivolo and Glimepirid was effective (488-426.9) (508.7-428.7), respectively
3. The Prolidase specific activity was found to be 2533 units/mg protein with a 56-fold purification level using gel filtration chromatography (G-100) of serum thyroid patients.

REFERENCES

1. A. M. Sawka, S. E. Carty, B. R. Haugen, J. V. Hennessey, P. A. Kopp, E. N. Pearce, J. A. Sosa, R. P. Tufano, and J. Jonklaas, "American Thyroid Association Guidelines and Statements: Past, Present, and Future: American Thyroid Association Guidelines Policy and Procedures Task Force", ***Thyroid***, 28(6), 692-706, (2018).
2. K. D. Liyanarachchi, and M. Debono, " Physiology of the pituitary, thyroid, parathyroid and adrenal glands", ***Surgery (Oxford)***, 35(10), 542-55, (2017).

3. S. Baksi, and A. Pradhan, " Thyroid hormone: sex-dependent role in nervous system regulation and disease", ***Biol Sex Differ***, 12(1), 25, (2021).
4. C. Aguayo-Mazzucato, A. M. Zavacki, A. Marinelarena, J. Hollister-Lock, I. El Khattabi, A. Marsili, **and** S. Weir, " Thyroid hormone promotes postnatal rat pancreatic β-cell development and glucose-responsive insulin secretion through MAFA", ***Diabetes***, 62(5), 1569-1580. (2013).
5. J. F. Silva, N. M. Ocarino, and R. Serakides, " Thyroid hormones and female reproduction. Biology of reproduction ", ***Biol Reprod***, 99(5), 907-21, (2018).
6. R. L. Kitchener, and A. M. Grunden, " Prolidase function in proline metabolism and its medical and biotechnological applications", ***J Appl Microbio***, l113(2), 233-47, (2012).
7. M. Cechowska-Pasko, J. Pałka, and M. Z. Wojtukiewicz, "Enhanced prolidase activity and decreased collagen content in breast cancer tissue," ***Int. J. Exp. Pathol.***, 87(4), 289–296, (2006).
8. G. Zanaboni, K. M. Dyne, A. Rossi, V. Monafo, and G. Cetta, "Prolidase deficiency: biochemical study of erythrocyte and skin fibroblast prolidase activity in Italian patients," ***Haematologica***, 79(1), 13–18, (1994).
9. I. Eni-Aganga, Z. M. Lanaghan, M. Balasubramaniam, C. Dash, and J. Pandhare, "PROLIDASE: A review from discovery to its role in health and disease," ***Front. Mol. Biosci.***, 8, 723003, (2021).
10. P. S. Cox, D. A. Denton, D. R. Mouw, and E. Tarjan, "Natriuresis induced by localized perfusion within the third cerebral ventricle of sheep," ***Am. J. Physiol. Regul. Integr. Comp. Physiol.***, 252(1), R1–R6, (1987).
11. H. S. Duong, Q.-Z. Zhang, A. D. Le, A. P. Kelly, R. Kamdar, and D. V. Messadi, "Elevated prolidase activity in keloids: correlation with type I collagen turnover: Prolidase activity and collagen turnover in keloids," ***Br. J. Dermatol.***, 154(5), 820–828, (2006).
12. R. Segal, W. Evans, D. Johnson , J. Smith, S. Colletta, J. Gayton, S. Woodard, G. Wells, and R. Reid,"Structured exercise improves physical functioning in women with stages I and II breast cancer: Results of a randomized controlled trial," ***J. Clin. Oncol.***, 19(3), 657–665, (2001).
13. A. Toker, H. Aksoy, B. Börekçi, and A Özkan, " Correlations of Serum IL-6 Levels andProlidase Activity Between Bone Turnover Markers and Bone Mineral Density inPostmenopausal Women With and Without Osteoporosis", ***Turk J Med Sci***, 37(3), 129–134, (2007).
14. A. Surazynski, Y. Liu, W. Miltyk, and J. M. Phang, "Nitric oxide regulates prolidase activity by serine/threonine phosphorylation," ***J. Cell. Biochem.***, 96(5), 1086–1094, (2005).
15. I. Gecit, M. Aslan, M. Gunes, N. Pirincci, R. Esen, H. Demir, and K. Ceylan,"Serum prolidase activity, oxidative stress, and nitric oxide levels in patients with bladder cancer," ***J. Cancer Res. Clin. Oncol.***, 138(5), 739–743, (2012).
16. A. Cakmak, D. Zeyrek, A. Atas, H. Celik, N. Aksoy, and O. Erel, "Serum prolidase activity and oxidative status in patients with bronchial asthma," ***J. Clin. Lab. Anal.***, 23(2), 132–138, (2009).
17. V. Şen, Ü. Uluca, A. Ece, İ. Kaplan, F. Bozkurt, F. Aktar, S. Bağlı, and R. Tekin. "Serum prolidase activity and oxidant–antioxidant status in children with chronic hepatitis B virus infection," ***Ital. J. Pediatr.***, 40(1), 1-8, (2014).
18. A. K. Verma, S. Chandra, R. G. Singh, T. B. Singh, S. Srivastava, and R. Srivastava, "Serum prolidase activity and oxidative stress in diabetic nephropathy and end stage renal disease: A correlative study with glucose and creatinine," ***Biochem. Res. Int.***, 2014(1), 1–7, (2014).
19. J. M. Savitt, V. L. Dawson, and T. M. Dawson, "Diagnosis and treatment of Parkinson disease: molecules to medicine," ***J. Clin. Invest.***, 116(7), 1744–1754, (2006).
20. R. C. Bollineni, I. J. Guldvik, H. Grönberg, F. Wiklund, I. G. Mills, and B. Thiede, "A differential protein solubility approach for the depletion of highly abundant proteins in plasma using ammonium sulfate," ***Analyst***, 140(24), 8109–8117, (2015).
21. S. Xu, Y. Shen, and Y. Li, "Antioxidant activities of sorghum kafirin Alcalase hydrolysates and membrane/gel filtrated fractions," ***Antioxidants (Basel)***, 8(5), 131, (2019).
22. Yamama Z. Hani1 , Israa G. Zainal1,* , Firyal W. Asker2 , Luban H. Jasim2.Study of Some Heterocyclic Compounds Made from a New 4(3*H*)- Quinazolinone and Their Biological and Antioxidant Activities. Chemical Methodologies 7(2023) 372-382
23. L. A. L. Al-Helaly, S. S. Saleh, and L. F. Bdaiwi, "Studying the enzymes levels in cerebrospinal fluid for children with acute lymphoblastic leukemia," ***World J. Pharm. Pharm. Sci.***, 231–244, (2017).
24. X. Wu, R. Li, Y. Zhao, and Y. Liu, "Separation of polysaccharides from Spirulina platensis by HSCCC with ethanol-ammonium sulfate ATPS and their antioxidant activities," ***Carbohydr. Polym.***, 173, 465–472, (2017).
25. Ali Rahmman , Sayran Saleh and, Wassan Nazhan. Partial Purification and Molecular Weight Determination Of Glutathione S-transferase Enzyme By Gel filtration Method In Patient With Beta Thalassemia Major2023. Journal of Namibian Studies History Politics Culture.

26. O. Befani, E. Grippa, L. Saso, P. Turini, and B. Mondovi, “Inhibition of monoamine oxidase by metronidazole,” ***Inflamm. Res***., 50(2), 136–137, (2001).
27. Nelson, D.L., Cox, M.M. "Lehninger, Principles of Biochemistry". 17th ed. W.H.freeman, New York., pp.600,617, 286, 289, (2017).
28. W. L. Mock and P. C. Green, “Mechanism and inhibition of prolidase,” ***J. Biol. Chem***., 265(32), 19606–19610, (1990).
29. K. Chrzanowski, A. Bielawska, K. Bielawski, J. Pałka, and S. Wołczyński, “Acetylsalicylic acid as a potential regulator of prolidase-convertible pro-drugs in control and neoplastic cells,” ***Farmaco***, 59(9), 679–684, (2004).
30. W. Miltyk, E. Karna, and J. Pałka, “Inhibition of prolidase activity by non-steroid antiinflammatory drugs in cultured human skin fibroblasts,” ***Pol. J. Pharmacol***., 48(6), 609–613, (1996).
31. L. Al-Helaly, “Isolation of prolidase from amniotic fluid and study of its kinetic and affinity properties towards pharmacological compounds,” ***J.Edu.Sci***., 28(3), 52–72, (2019).
32. S. Raha and B. H. Robinson, “Mitochondria, oxygen free radicals, and apoptosis,” ***Am. J. Med. Genet***., 106(1), 62–70, (2001).
33. A. Lupi, R. Tenni, A. Rossi, G. Cetta, and A. Forlino, “Human prolidase and prolidase deficiency: an overview on the characterization of the enzyme involved in proline recycling and on the effects of its mutations,” ***Amino Acids***, 35(4), 739–752, (2008).
34. A. Sorushanova, L. M. Delgado, Z. Wu, N. Shologu, A. Kshirsagar et al.. “The collagen suprafamily: From biosynthesis to advanced biomaterial development,” ***Adv. Mater***., 31(1), 180165, (2019).
35. A. Przylipiak, M. Donejko, E. Rysiak, K. Gluszuk, and A. Surażyński, “Influence of caffeine and hyaluronic acid on collagen biosynthesis in human skin fibroblasts,” ***Drug Des. Devel. Ther.***, 1923, (2014).
36. S. M. Ng, M. A. Turner, and A. M. Weindling, “Neurodevelopmental outcomes at 42 months after thyroxine supplementation in infants below 28 weeks’ gestation: A randomized controlled trial,” ***Thyroid***, 30(7), 948–954, (2020).
37. M. Spodenkiewicz, M. Spodenkiewicz, M. Cleary, M. Massier, G. Fitsialos, V. Cottin et al., “Clinical genetics of prolidase deficiency: An updated review,” ***Biology (Basel)***, 9(5), 108, (2020).

Detection of polymorphisms and level for the IL-20 cytokine in psoriasis patients

GR Schneiter [a], AAN Dhabaan, QN Raddam

Department of Biology, College of Education, Al-Iraqia University, Baghdad, Iraq

[a] Corresponding author: anwar.a.nasser@aliraqia.edu.iq

Abstract. The study included 40 blood samples taken from patients with psoriasis whose average age ranged from 7-66 years, with an average age of 9.4 ± 0.34 years, in addition to 40 samples for healthy people that were considered as normal samples and their average age was 10.9 ± 0.38 years. An immunological and genetic study was conducted on blood samples taken from the infected and the normal sample. Levels of cytokinesis Interleukin 20 (IL-20) were measured by ELISA, as the concentration in the patients' blood serum was 1358.33 pg/mL, while its concentration in the normal sample was 757.52 pg/mL Genetic polymorphism of the IL-20 -1053 T/G gene was studied in the studied samples using the Amplification refractory mutation system (ARMS-PCR). The results of the electrophoresis of the amplified IL-20 -1053 T/G I gene with this technology shown the presence of two alleles, namely T and G, as the G allele recorded a higher percentage than the T allele in the infected sample, which was 47.50 %, while the T allele recorded a higher percentage in the healthy sample, which was 70%. The G allele also appeared as an Etiological faction (EF) allele associated with disease. The TT genotype shown a higher percentage in the normal sample compared to the infected sample, which was 62.50%. The TT genotype appeared as a protective genotype against the risk of psoriasis, while the GT and GG genotypes shown a higher percentage in the infected sample compared to the normal sample was 35% and 30 respectively, and shown the GT and GG genotypes associated with developing psoriasis risk.

Keywords: polymorphisms, Interleukin 20, psoriasis.

INTRODUCTION

Psoriasis: psoriasis is a chronic, long-term disease in which the immune system becomes overactive, which leads to the multiplication of skin cells rapidly. In 2014, the World Health Organization identified psoriasis as a chronic, non-infectious, disfiguring, and disabling disease, with no known cure. [2]

Symptoms: Psoriasis usually causes patches of dry, patchy skin on brown, black, and white skin. Some people find their psoriasis itchy or painful. Many instances of psoriasis exhibit cyclical patterns, resulting in periods of exacerbation lasting a few weeks or months before subsiding or ceasing altogether. [3]

The causes of disease: The cause of psoriasis appears to be the abnormal formation of keratin, epidermal proliferation, immune system activity, and genetic factors, which play a role in causing psoriasis. [4]

Psoriasis affects all ages in all countries, where the reported prevalence of psoriasis in countries ranges from 0.09% to 11.43%. In Iraq, the incidence of psoriasis ranges from 0.5% to 0.7%, which makes psoriasis a serious global problem, affecting at least 100 million people all over the world. [5]

Cytokines are kinetic mediators consisting of soluble proteins with low molecular weight peptide chains ranging from 5-20 kilo Daltons. Cytokinesis are important mediators involved with the manifestations of immune responses before and after the occurrence of inflammation in order to induce cells to interact permanently against pathogens. [6]

Cytokines are produced by large numbers of leukocytes and non-leukocytes and work to facilitate communication between cells and can differentiate and multiply for active immune cells, and their action may be Autocrine on the cell itself or on neigh boring cells Paracrine action or its action may be hormonal Endocrine action on cells and at long distances [7].

Technologies and Materials for Renewable Energy, Environment and Sustainability
AIP Conf. Proc. 3321, 030003-1–030003-7; https://doi.org/10.1063/5.0291118
Published under an exclusive license by AIP Publishing. 978-0-7354-5231-2/$30.00

T cells play a major role in the production of cellular motility, and in 1986 AD, Mossman and Coffman introduced a concept of differentiated T cell types and Th helper cells depending on what these T cells produce from cellular drives during stimulation to differentiation, and T cells are the source of many kinetics In addition, Th1 helper cells and Th2 cells, as well as Th17 cells, are an important source in the production of cytokinesis, organizing and stimulating them for an immune response against pathogens and foreign bodies [8].

Interleukin 20

a protein encoded by the IL20 gene in humans, is situated near the IL-10 gene on chromosome 1q32. It belongs to the IL-20 subfamily, which is part of the broader IL-10 family. Alongside IL-20, this subfamily comprises cytokines such as IL-19, IL-20, IL-22, and IL-24. [9]

Psoriasis has been associated with IL-20

as studies have revealed the presence of both IL-20 and its receptor in human skin. IL-20 is implicated in processes such as proliferation, angiogenesis, and chemotaxis, all of which are characteristic features of psoriasis. Research has demonstrated that IL-20 can induce thickening of the human epidermis in vivo. Elevated levels of both IL-20 and its mRNA in psoriatic skin lesions suggest a potential role for this cytokine in the development of psoriasis. An imbalance in the receptor and IL-20 complexes could contribute to the suspected pathogenic effects observed in psoriasis. [10]

MATERIALS AND METHODS

Collect samples of blood from patients with psoriasis

Forty blood samples were collected from patients with psoriasis and 40 samples from healthy subjects (the normal group) from some hospitals in Baghdad-Iraq for the period from October of 2022 until December of the same year, and the ages of children ranged from 7-66 years. Blood was drawn into specialized 5-milliliter blood collection tubes without anticoagulant for cytokine concentration determination using the ELISA device. Additionally, 2.5-milliliter tubes containing EDTA as an anticoagulant were used for DNA extraction. Subsequently, samples were evaluated by specialists in the hospital's Dermatology Unit. A special form was organized in which information was collected about sick and healthy children.

Interleukin 20 kits

I used a diagnostic kit for cytokinesis IL-20 I mini-ELISA development kit manufactured by the American company Peprotech.

PCR mix

Go Taq® Green Master Mix (2X) was was employed in the anti-replication system experiments utilizing ARMS-PCR technology, following the guidelines provided in the accompanying leaflet from the American company Promega.

Primers

Three specialized primers were custom-made by Canadian company Alpha DNA, according to demand, in the detection of the IL-20 gene -1053 T/G, according to the source [1]. Specific G (Forward inner primer) is 5`-CAAGATAAAAATATTTTAGTGCAATGTC -3`, Specific T (Reverse inner primer) is 5`-TTGTCATAAGCTTTTTTAATTCATTCTT -3`, and forward outer primer is 5` - ACTCATCAATAATATTTTCATCATATGCT - 3, and the Reverse outer primer: 5` - AGTTTTAAGATAAAATAATAATGGGCTG -3. All primers above were dissolved using Nuclease-Free water and according to the leaflet attached by the manufacturer.

A DNA molecular weight marker

It produced by Promega was employed, with a total size of 1.5 kb (1500 base pairs), segmented into increments of 100 base pairs.

The concentration of cytokinesis IL-20 was determined using an ELISA apparatus.

1. Isolate serum from the studied samples

2.5 milliliters of each freshly drawn blood sample were placed in anticoagulant-free tubes and centrifuged in a centrifuge at a speed of 1500 rpm for 10 minutes. Serum was isolated from all patients with psoriasis and healthy subjects (the normal sample) who were included in the study, and placed the serum in clean, new, well-sealed tubes and stored at -20ºC until use.

2. The concentration of cytokinesis IL-20 in the serum of infected and healthy samples was measured using an ELISA device, and the working method was followed based on the calibration prepared by the American Biotech Company and according to the leaflet attached to the kit. Before conducting the determination of cytokinesis IFN-γ concentrations, the solutions and samples were placed at room temperature 25 ºC for 30 minutes before starting the measurement with the ELISA device. The optical density (O.D) of the cytokinesis IFN-γ studied in the sera of patients with diabetes mellitus - type 1 and normal samples was measured using the ELISA device. The results of the samples were recorded by projecting the readings onto the standard curve to extract the concentration of IFN-γ included in this study, Figure (1) shows the standard curve and its rates used to extract IL-20 cytokinetic concentrations.

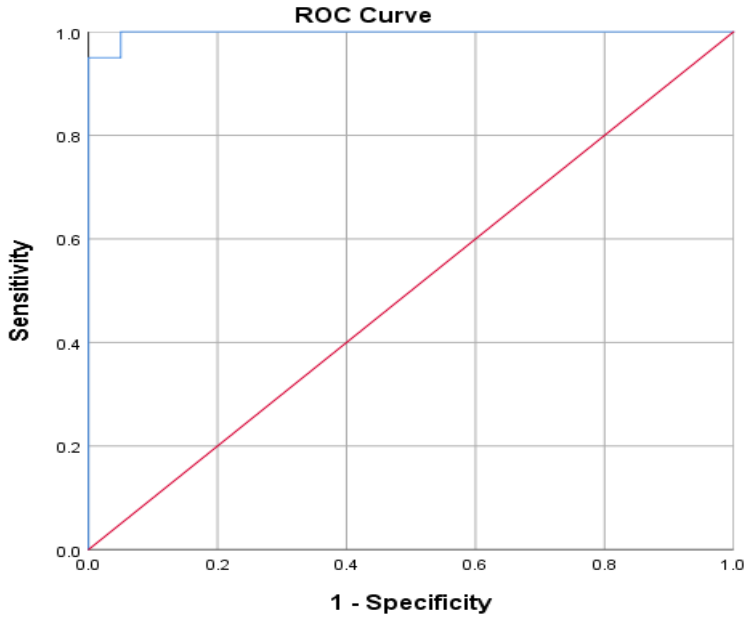

Figure 1. The standard curve for measuring IFN-γ concentration

Extraction of total DNA from blood samples of infected patients and the normal sample

Isolation of DNA from blood samples taken from children with diabetes mellitus - type 1 and the normal sample using the ReliaPrepTM Blood gDNA Miniprep System kit by Promega, following the manufacturer's instructions provided in the accompanying leaflet. The extracted DNA concentration and purity were assessed using the NanoDrop device, by determining the ratio of A260/A280. Pure DNA typically exhibits an absorbance value of 1.8 ± 0.1 [20]. Subsequently, the samples were stored at -20°C until further use.

Detection of the IL-20 gene

In this study, the TARMS-PCR method was employed to detect the IL-20 gene. The master mix of the primers utilized was prepared according to the method of [11] with some modifications. Go Taq® Green Master Mix was used from the American company Promega with a volume of 12.5 µl at a concentration of 1X, a primer with a volume of 1 µl with a concentration of 1 µm for each primer, and a DNA template with a volume of 2 µl and a concentration of 100 ng, and the total volume of the reaction was 25 µl. In this experiment, specific G and T primers were utilized to detect the G and T alleles, respectively. Following the detection of the outer primer, the samples were subjected to amplification of DNA in a thermocycler. The device program was adjusted to achieve the required reaction conditions. During the experiment, the denaturation phase of the template was conducted at 95ºC for 3 minutes, followed by the initial denaturation step at 95ºC for 15 seconds. Subsequently, the first annealing step was performed at 65ºC for 50 seconds, and finally, the first elongation occurred at 72ºC for 40 seconds.

The stages of primary deformation, initiator fusion and first elongation were for 35 cycles. Final elongation at 72ºC for 7 minutes. The amplification products of the DNA resulting from the use of the above primers for DNA samples

of children with diabetes mellitus - type 1 and the normal sample were loaded in the designated place in the Agarose gel at a concentration of 1.5% (the agarose gel was prepared by dissolving 0.6 g of Agarose in 40 ml of Tris-borate buffer (TBE).) at a concentration of 1X. Heat the mixture at a temperature of 60 ºC using a hot plate until the mixture melts and pour into a (dedicated migration basin). He carried the molecular genetic marker according to the attached leaflet, which had a size of 1.5 kilobases. The loading dye bromophenol blue for electrophoresis was added to each sample in a volume of 3 µm (the loading dye was prepared by dissolving 25 mg of bromophenol blue in 6.7 ml of distilled water. 25 mg of Xylene cyanole FF and 3.3 ml of glycerol were added to make the volume Final 10 ml. The tincture was kept below -20°C for long-term use). The samples were electrophoresed from the negative black electrode towards the positive red electrode under an electric voltage of 75 volts for a period of 3-4 hours and using a Tris-borate buffer (TBE) (10X of this buffer was prepared for the purpose of using it in the electrophoresis process by melting 108 grams of Tris base, 55 grams of boric acid, and 40 milliliters of ethylene diamine tetra acetic acid (EDTA) at a concentration of 0.5 M. Sterile distilled water was added up to 1 later with the pH adjusted to 8). The agarose gel was stained with Ethidium bromide (EtBr) for 15 minutes. The Ethidium bromide dye was prepared from a stock solution with a concentration of 10 mg/ml, diluted in distilled water to achieve a concentration of 0.5 µg/ml. Following staining, the enlarged DNA segments were visualized and photographed using a gel documentation system equipped with a specialized camera.

STATISTICAL ANALYSES

The data underwent analysis to assess polymorphisms and IL-20 levels utilizing the Statistical Package for Social Sciences (SPSS). Significant differences among means were determined employing Mann-Whitney U and Fisher's tests, with a significance threshold set at $P < 0.05$. Genotype and allele frequencies, along with odds ratios (OR) and confidence intervals (CI), were evaluated using Compare 2 Ver.3.04 software developed by J. H. Abramson between 2003 and 2013. Furthermore, the results were subjected to Hardy-Weinberg equilibrium analysis using a tool available on the website www.had2know.com.

RESULTS AND DISCUSSION

Psoriasis samples were the normal sample

The study encompassed 40 blood samples procured from individuals diagnosed with psoriasis, with ages spanning from 7 to 66 years. Additionally, 40 blood samples (ranging from 11 to 75 years) were obtained from ostensibly healthy individuals, designated as the control group, with an average age of 10.9 ± 0.38 years. Immunological and genetic analyses were carried out on blood samples collected from both the affected individuals and the control group.

Set the concentration of IL-20

The levels of cytokinesis IL-20 in the studied samples were estimated using the ELISA instrument. Table (1) demonstrates a notable elevation in the IL-20 concentration within the serum of individuals with infection compared to the control sample (healthy individuals), as the concentration in the blood serum of infected people reached 1358.33 pg/mL, while its concentration in the normal sample was 757.52 pg/mL (Figure 2). The statistical analysis employing the Mann-Whitney U test revealed significant variances in the IL-20 concentration between individuals afflicted with psoriasis and the control group, with a probability level of $P < 0.05$. The calculated probability value was 0.035, indicating statistically significant differences. The results of this study show that there are high levels in the concentration of IL-20 in patients with psoriasis and the extent of the role that it plays in the response directed against skin cells in people with psoriasis. Psoriasis patients, where the results indicate that there is a correlation between IL-20 and patients with psoriasis, where the results show that there is a difference in levels between patients with psoriasis and healthy people, where the results show that there is a significant difference at and below $P<0.05$.

Cytokinesis stimulates the immune response, and the mechanism of destruction of cells is either directly or indirectly. The direct degradation mechanism induces Th1 cellular kinetics to produce inflammatory kinetics, whose effects appear either primarily in macrophage cells, leading to increased infiltration of these lymphocytes at sites of infection, or through increased filtration of CD8+T cells within the tissue [8].

Table 1. IL-20 concentration in the serum of the studied samples

probability P	95% confidence level		(40 samples) Mean ± standard error pg/mL	95% confidence level		(40 samples) Mean ± standard error pg/mL	cytokinesis
	Highest value	Lowest value		Highest value	Lowest value		
--31333#	1004.06	589.22	98.87±757.52	4136#	318<#	90.88±1358.33	ID053#

* = significant difference at P<0.05 using the Mann-Whitney U test.

Polymorphism of the IL-20 gene

The study investigated genetic polymorphism of the IL-20 gene in psoriasis patients compared to healthy individuals (normal samples) using TARMS-PCR technology. Electrophoresis results of the IFN-γ T/A +874 gene amplified by this method indicated the presence of two alleles, T and G, and three genotypes, TT, GT, and GG, in both psoriasis and control samples.

Frequency distribution analysis of the T and G alleles of the IL-20 gene, employing the Hardy-Weinberg equilibrium, revealed distinct patterns between psoriasis patients and the normal sample. In the psoriasis sample, the G allele accounted for 47.50% compared to the T allele at 52.50%. Conversely, in the normal sample, the T allele constituted 70% compared to the G allele at 52.50% (Table 1).

Table (1) also indicates a significant disparity in frequency distribution between the infected and normal samples. The analysis revealed that the G allele exhibited a notably higher frequency in the infected sample compared to the normal sample, as determined by Fisher's test. The critical Odds ratio (OR) was calculated at 2.60, with Confidence Intervals (CI) under 95% ranging from 1.11 to 4.02. The allele's ratio as an Etiological faction (EF), indicating association with the disease, stood at 2.11. Conversely, the T allele exhibited a noteworthy frequency in the normal sample, showing higher ratios compared to the infected sample, as determined by Fisher's test. The critical Odds ratio was computed at 0.47, with a confidence interval under 95% ranging from 0.25 to 0.90. Its ratio as a Preventive faction (PF), suggesting a protective effect against the disease, amounted to 36.8% [12].

Table 2. presents the outcomes of the statistical and genetic scrutiny concerning the frequency of the T and G alleles of the IL-20 -1053 T/G gene in both psoriasis patients and the normal sample.

P value	(95%CI) OR	Normal sample The number is 60 (%)	affected sample The number is 100 (%)	Allele	gene
*0.017	0.47(0.25 to 0.90)	(%70.00)56	(%52.50)24	*t*	IL-20 -1053 T/G
	%36.8			P.F	
	2.11(1.11 to 4.02)	(%30.00)38	(%47.50)42	*G*	
	%25			E.F	

OR= Odds ratio, CI= Confidence Intervals, P.F= Preventive faction, E.F= Etiological faction,
* = significant difference at P<0.05 using Fisher's test.

The results of genetic analysis of ARMS-PCR for the TGF-β (+869*G/T) gene, assessed against the Hardy-Weinberg equilibrium, revealed three genotypes in both psoriasis patients and the normal sample: TT, GT, and GG. The analysis indicated a variation in genotype frequencies between the psoriasis patient sample and the normal sample. Specifically, the TT genotype exhibited a higher percentage in the normal sample compared to the patients, with percentages of 62.50% and 35%, respectively. This difference was statistically significant ($p < 0.05$), with a probability value of 0.012 using Fisher's test. The critical ratio (OR) value was calculated as 0.32, with a confidence interval ranging from 0.0 to 0.8. The TT genotype appeared to confer protection against the development of psoriasis, with a rate of 42.3%. Conversely, the GT genotype illustrated a higher percentage among the psoriasis patients compared to the normal sample, with percentages of 35% and 15%, respectively. This difference was statistically significant ($p < 0.05$), with a probability value of 0.035. The critical ratio (OR) value for the GT genotype was 1.85, with a confidence interval between 1.05 and 8.80. The GT genotype was associated with an elevated risk of psoriasis development, accounting for 23.5% of cases.

Furthermore, the GG genotype exhibited a higher percentage in the psoriasis patient sample compared to the normal sample, with percentages of 30% and 22.50%, respectively. However, this disparity was not statistically significant. The critical ratio value for the GG genotype was 1.48, with a confidence interval between 1.55 and 3.98. The GG genotype was also associated with an increased risk of developing psoriasis, with a ratio of 9.7. These findings are summarized in Table (2).

Based on the aforementioned findings, it is evident that both the heterozygous genotype GT and the homozygous genotype GG are correlated with the risk and onset of psoriasis among the patient cohort. However, the correlation between the genotype GT and the risk of developing psoriasis appears to be stronger compared to the association observed with the genotype GG. Therefore, the GT genotype emerges as a reliable indicator for assessing the likelihood of developing the disease. These outcomes may be linked to the observed immunological findings, particularly the notable and significant elevation in IL-20 concentration levels in the blood serum of psoriasis patients relative to the normal sample. In general, the genetic and immunological results underscore the significance of the IL-20 gene in relation to the susceptibility to psoriasis development. Additionally, the results demonstrate that the homozygous genotype TT poses a lower risk among psoriasis patients, highlighting its potential role as a protective genetic variant against the disease. Conversely, the genotype GT is identified as a genotype associated with an increased risk of psoriasis development. These insights emphasize the intricate relationship between genetic factors, notably variations in the IL-20 gene, and immunological processes underlying psoriasis pathogenesis. Such understanding is pivotal for advancing tailored therapeutic interventions and personalized management strategies for individuals affected by psoriasis [14].

Table 3. illustrates the outcomes of the statistical and genetic analysis of the observed genotypes of the mutant gene IL-20 -1053 T/G in a sample of people with psoriasis and a normal sample.

P value	(95%CI) OR	Normal sample Number 30 (%)	affected sample Number 50 (%)	genotype	Gene
*0.012	0.32(0.0 to 0.80)	25(62.50%)	14(35%)	TT	IL-20 -1053 T/G
	%42.3			P.F	
*0.035	1.85(1.05 to 8.90)	6(15%)	12(35%)	GT	
	%23.5			E.F	
0.306	1.48(1.55 t0 3.98)	9(22.50%)	14(30%)	GG	
	%9.7			E.F	

OR = Odds ratio, CI = Confidence Intervals, P.F = Preventive faction, E.F = Etiological faction,
* = significant difference at P<0.05 level using Fisher's test.

CONCLUSIONS

This study investigated the genetic polymorphism of the IL-20 gene -1053 T/G in the analyzed samples using amplification resistance mutation system (ARMS-PCR). Electrophoresis results of the IL-20 -1053 T/G gene amplified via this technique revealed the presence of two alleles, T and G. The G allele exhibited a higher frequency

than the T allele in the infected sample, accounting for 47.50%, whereas the T allele predominated in the healthy sample at 70%. Notably, the G allele emerged as a pathogenicity-associated allele linked to the disease.
Furthermore, the TT genotype was more prevalent in the normal sample compared to the affected sample, comprising 62.50% of cases. The TT genotype appeared to confer protective effects against the risk of developing psoriasis. Conversely, the GT and GG genotypes exhibited higher frequencies in the affected sample relative to the normal sample, comprising 35% and 30%, respectively. These genotypes, GT and GG, were associated with an increased risk of developing psoriasis.

REFERENCES

1. Parisi, R.; Iskandar, I.Y.K.; Kontopantelis, E.; Augustin, M.; Griffiths, C.E.M.; Ashcroft, D. 2020 National, regional, and worldwide epidemiology of psoriasis: Systematic analysis and modelling study. BMJ : 369, 1590.
2. World Health Organization. Global report on psoriasis. World Health Organization`2021 .
3. Afifi, L; Danesh, MJ; Lee, KM; et al. 2017 *Dietary behaviors in psoriasis* : patient-reported outcomes from a U.S. national survey. Dermatol Ther (Heidelb).7:227-242.
4. Parisi ,R; Symmons ,DPM; Griffiths ,CEM; Ashcroft, DM. 2013 *the Identification and Management of Psoriasis and Associated Comorbidity project team*. Global epidemiology of psoriasis: a systematic review of incidence and prevalence. Journal of Investigative Dermatology, 133:377–385.
5. Danielsen , K; Olsen ,A,O; Wilsgaard, T; Furberg , AS. 2013 *Is the prevalence of psoriasis increasing?* A 30–year follow-up of a population–based cohort. Br J Dermatol.;168:1303–10.
6. Dinarello, C. A. 2007. Historical Review Cytokines. J. Immunol. 37(suppl 1):S34-S45
7. Doan, T., Melvold, R., Viselli, S. and Waltenbaugh, C.. 2008. Lppincotts IIIustrated Review: Immunology, Lippincott Williams and Wilkins. pp 67.
8. Miossec, P., Korn, T. and Kuchroo,V. 2009. Interleukin-17 and 17 Helper T cell. J. Medicin. 361(9):888-898
9. .9 Lee ,S-J; Cho ,S-C; Lee ,E-J; Bok Lee ,K-S; Lim ,J-H; Choi ,Y-H; Kim ,W-J; Moon,S-K. 2013. *Interleukin-20 Promotes Migration of Bladder Cancer Cells through Extracellular Signal-regulated Kinase (ERK)-mediated MMP-9 Protein Expression Leading to Nuclear Factor (NF-κB) Activation by Inducing the Up-regulation of p21WAF1 Protein Expression*.Journal of Biological.288.(8):5539-5552 .
10. Otkjaer ,K; Kargballe ,A,T; Funding ,J,T; Clausen .P.L ;Noerby ,t; Steiniche,L; Iversen . 2005 *The dynamics of gene expression of interleukin*-19 and interleukin-20 and their receptors in psoriasis British Journal of Dermatology.153(5):911-918.
11. Kingo ,K., Ko, S. , Nikopensius, T., Silm, H., and Vasar, E. 2004.*Polymorphisms in the interleukin-20 gene: relationships to plaque-type psoriasis*. Genes and Immunity 5, 117–121.
12. Sabat ,R; Wallace ,E; Endesfelder, S; Wolk ,K. 2007 IL-19 and IL-20: two novel cytokines with importance in inflammatory diseases. Expert Opin Ther Targets. 11:601-612
13. Akalin, E. and Murphy, B. 2001. *Gene polymorphisms and transplantation*. J. Curr. Opin. Immunol. 13(5):572-6.
14. Lowes, MA; Kikuchi ,T; Fuentes-Duculan, J; Cardinale ,I; Zaba ,LC; Haider AS; et al. 2008 *Psoriasis vulgaris lesions contain discrete populations of Th1 and Th17 T cells*. J Invest Dermatol;128:1207-11.

Histomorphometric and histochemical study of the adrenal gland in adult males of the Iraqi pin-tailed sandgrouse bird (*Pterocles alchata*)

Wafaa Barghash Obaid and Nahla A Al-Bakri [a)]

Department of Biology, College of Education for Pure Science (Ibn Al-Haitham), University of Baghdad, Baghdad, Iraq

[a)] Corresponding author: nahla.ar.s@ihcoedu.uobaghdad.edu.iq

Abstract. The adrenal gland is a vital endocrine gland that secretes many important hormones in the daily life of birds. It is located in the Iraqi Pterocles alchata bird on both sides of the aorta in the front and side of the cranial lobe of the kidney at the caudal end of the lungs, triangular shape with a creamy yellow color. The statistical analysis showed no significant differences between the weight and length of the right and left glands. Histologically the gland of the sandgrouse bird capsule contains autonomic nodes consisting of nerve cells and the average thickness of the capsule is 42.69±1.81µm, the parenchyma of the gland is divided into two areas; the cortex and medulla in addition to the blood sinuses. The cortex area is divided into an area under the capsule and the central area, the cortex areas are made up of columnar cells with small nuclei and acidophilic cytoplasm, while the medulla area has appeared in the form of small irregular islands or an intertwined network between the cortical tissues and the tissues under the capsule and are concentrated near the blood sinuses and polygonal cells with a basicity cytoplasm and a large, spherical central nucleus containing two or more nucleoli. The statistical analysis showed significant differences in the average diameters of the adrenal parenchyma nuclei. Histochemical tests showed a strong interaction of the components of the capsule and the gland parenchyma with Periodic acid Schiff, Periodic acid Schiff & Alcian blue compound, Verhoeff and Masson's stains.

Keywords. Adrenal gland, Adrenal cortex, Adrenal medulla, Pterocles alchata.

INTRODUCTION

There are more than 8,755 species of birds distributed around the world, and there are about 10,000 known species of birds, which vary by their species, environments, and nature of food [1]. Birds are considered one of the economically important animal wealth rings because they provide meat, eggs, and feathers that are used for various purposes, and they are also very important in the biological control of harmful insects and rodents [2, 3]. The *Pterocles alchata* bird belongs to the order Columbiforms, family Pteroclidae includes wild birds that inhabit desert areas. It has many different types of colors and shapes. The Iraqi large pin-tailed sandgrouse *Pterocles alchats* was Iraq's most common sandgrouse species. This species is characterized by the length of the two central tail feathers and their needle shape and feed on grains [4]. The adrenal gland is a complex endocrine gland that regulates multiple vital functions, such as response to stress, metabolism, and immune functions [5, 6]. The adrenal glands work by producing a range of hormones, which are produced from the cortex zone that produces glucocorticoids (corticosterone) and mineralocorticoids (aldosterone) [7, 8]. The adrenal glands are as important in birds as they are in mammals, as the removal of the glands in birds eventually leads to the death of birds that suffer from gland removal within 60 hours [9, 10]. The adrenal glands are double organs located in front of or in the middle of the cephalic lobe and their shape is flat and close to each other until they merge into some species [11]. Studies have indicated distinct differences in shape, weight and size of the adrenal gland between different species of vertebrate animals [12]. Birds have a pair of adrenal glands that are located on the cranial lobe of the kidneys and play important roles in the bird's body; the histological structure of the adrenal gland shows a variation in birds that is not similar to other vertebrates. The adrenal

Technologies and Materials for Renewable Energy, Environment and Sustainability
AIP Conf. Proc. 3321, 030004-1–030004-12; https://doi.org/10.1063/5.0289926
Published under an exclusive license by AIP Publishing. 978-0-7354-5231-2/$30.00

gland in other vertebrate species is made up of two distinct regions, where the medulla always occupies the central part and is surrounded by the adrenal cortex with its three zones (glomerulosa, fasciculate and reticularis zone) [13]. In birds, the internal tissue of the gland is not divided into the outer cortex and the inner medulla, but consists of two areas or two glandular parts that differ morphologically and physiologically interacting with each other, one of which secreted the steroid-secretion called adrenocortical tissues and the other part is called chromaffin (Adrenomedullary) tissues [14]. Many studies conducted on birds did not report the description of the adrenal gland of the Iraqi pin-tailed sandgrouse, so the current article aims to provide a detailed study of the anatomical and histological structure of the adrenal gland in the Iraqi pin-tailed sandgrouse bird with the help of histochemical examinations to determine the histological and anatomical characteristics of the gland because of its importance in scientific research.

MATERIALS AND METHODS

Sample collection

The study samples were collected from 6 adult male animals of the Iraqi pin-tailed sandgrouse bird *Pterocles alchats* obtained from the local markets (Ghazal Market, Baghdad). All samples were classified according to the taxonomic key located in the Natural History Museum in Baghdad and the animal was sacrificed by inhaling chloroform, dissecting it, locating the gland, and removing it, and the samples were fixed in a 10% formalin solution and used in the histological study [15]. The adrenal gland was photographed in its place in the body with the rest of the viscera, and then it was separated and cleaned using dissecting forceps, both the right and left glands were weighed and their length was measured [16].

Histological preparations

paraffin sections were prepared according to the method of Bancroft and Stevens [17], where the samples were passed to the dehydration an ascending series of alcohol starting with a concentration of 70% and ending with an absolute alcohol concentration of 100%, xylene was used to clear the samples and embed with paraffin wax with a high melting point, then the wax blocks containing the samples were cut using rotary microtome and a thickness of 5 microns, the tissue sections were then colored using the Harris hematoxylin-eosin stains. For the histochemical study, Periodic acid Schiff (PAS), Alcian blue (AB), Verhoeff's and Masson's stains were used, and the sections were molted using DPX. Finally, the tissue slides were photographed after being examined with a light microscope with a Canon imaging camera to image the tissue slides of the gland. The statistical package for the social science (SPSS, 20) was used to find significant differences in the average of the study measurements using the T-test and one-way analysis of variance (ANOVA), and the results were presented in the form of mean± standard error and the significant differences of less than $p \leq 0.05$ in statistical analyses.

RESULTS AND DISCUSSION

Location and shape of the adrenal gland

Anatomical examination of the Iraqi pin-tailed sandgrouse showed that it has a pair of small adrenal glands located in the abdominal cavity on both sides of the aorta in the front and behind the cranial lobe of the kidney Cranial lob at the end of the lungs, and the glands appeared partially covered with testes, the two glands are triangular shape. The right gland was slightly shorter, both glands were creamy-yellow, and it was also noted that the left gland rises slightly above the level of the right gland (Figure 1).

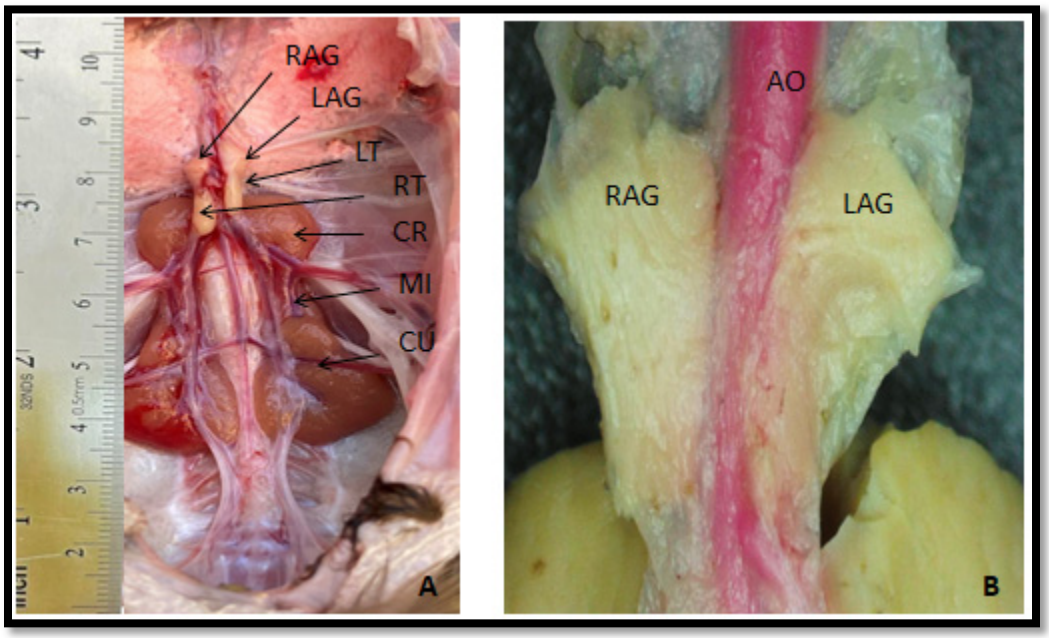

Figure 1. The general appearance of the urinary system of the Iraqi pin-tailed sandgrouse, noted: aorta (AO), cranial lobe (CR), caudal lobe (CU), left adrenal gland (LAG), left testis (LT), median lobe (MI), right adrenal gland (RAG), right testis (RT).

The statistical analysis to find the average weight and length of the right and left adrenal glands showed that there were no significant differences between the average weight and length of the two glands at the p>0.05 probability level (Table 1 and Figure 2).

Table 1. Average weight and length of the right and left adrenal glands of the Iraqi pin-tailed sandgrouse bird.

Character / Adrenal	Weight g Average±Standard error	Length cm Average±Standard error
Right gland	0.00±0.015	0.37±5.20
Left gland	0.00±0.014	0.24±3.60
P value#	0.557**	0.447**

T-test**No significant differences at probability level p>0.05.

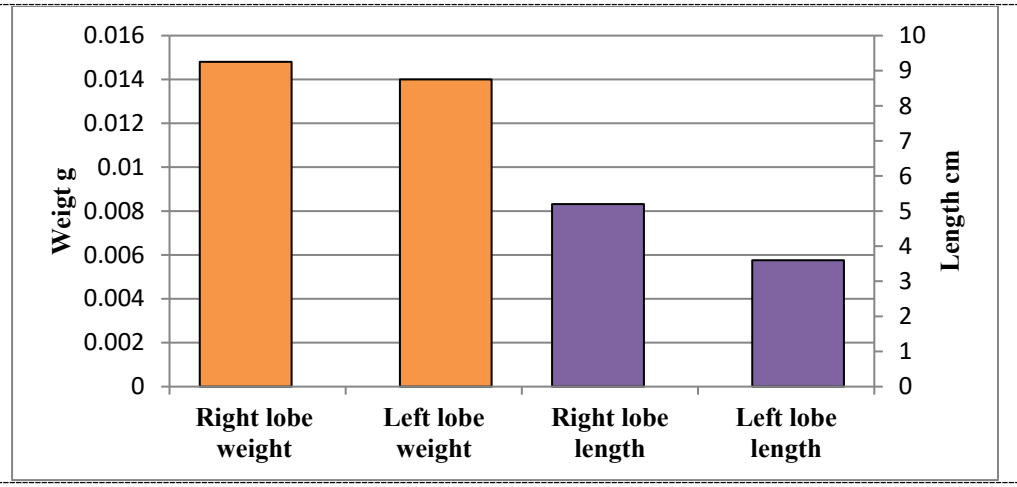

Figure 2. Weights and lengths of the right and left adrenal glands of the Iraqi pin-tailed sandgrouse bird.

Histological structure of the adrenal gland

The adrenal gland in males of the Iraqi pin-tailed sandgrouse is surrounded by a thin capsule of dense connective tissue rich in collagen fiber and reticular fiber containing several blood vessels. Short thin trabeculae of connective tissue of the capsule penetrating the cortex area of the capsule were observed, and many autonomic ganglia nodes containing many ganglion neurons were observed to link with the capsule and their presence was observed in the cranial and caudal poles of each gland (Figure 3), and statistical analysis showed that the average thickness of the capsule was 42.69±1.81 µm.

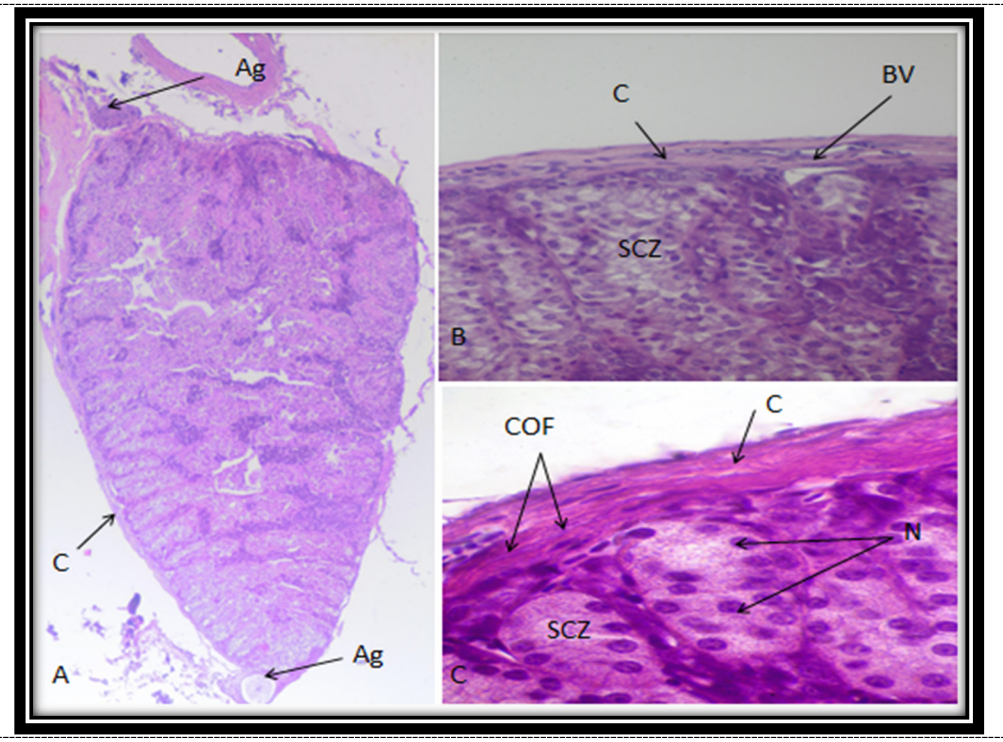

Figure 3. A cross section of the right adrenal gland of the Iraqi pin-tailed sandgrouse, noted: autonomic ganglia (Ag), blood vessels (BV), capsule (C), collagen fiber (COF), nucleus (N), subcapsular zone (SCZ), A: 4x, B: 100x, C: 40X, H&E stain.

The histochemical result showed a strong interaction towards the color of the Periodic acid-Schiff stain (PAS), and with the Periodic acid-Schiff reagent and the Alcian blue (Ab) compound indicating the presence of neutral and acidic mucopolysaccharide compounds, and the reaction was concentrated in the nerve ganglia. The tissue showed a strong interaction towards these stains and showed a positive interaction with the Mason tricolor Masson's trichrome, and Verhoeff's stains indicating the presence of collagen and elastic fibers. These fibers were spread in varying proportions, the elastic fibers were more than the collagen fibers in the capsule sheath during the use of Masson's and Verhoeff's stains, and also the interaction was positive towards the Periodic acid-Schiff stain (PAS), and with the Periodic acid-Schiff reagent and the Alcian blue (Ab) compound in the capsule (Figure 4).

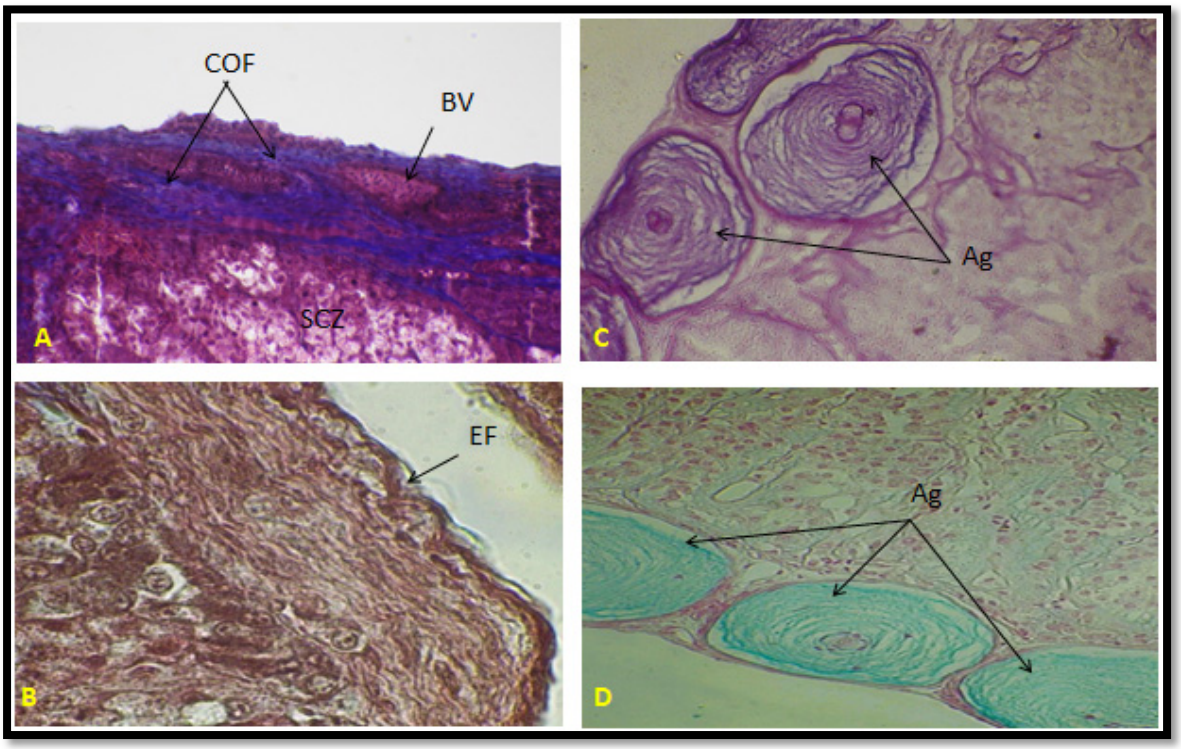

Figure 4. A cross section of the adrenal gland of the Iraqi pin-tailed sandgrouse bird, noted: the collagen fibers (COF), blood vessels (BL), elastic fibers (EF), autonomic ganglia nodes (Ag), A: Masson's stain, 40x, B: Verhoeff's stain, 100x, C: Alcian blue, 40x, D: Alcian blue and PAS compound, 40x.

Internal tissue of the adrenal gland

The result of a microscopic examination of the histological sections of the adrenal gland in males of the pin-tailed sandgrouse bird showed that the parenchyma tissue of the gland consists of cortex and medulla interacting with each other, the cortex area consists of two areas; the subcapsular zone or called the peripheral zone and the central zone or called the inner zone (Figure 5).

The subcapsular zone (SZ) consists of groups of cells located just below the capsule consisting of curved cords arranged vertically on the capsule consisting of two rows of large polyhedral to columnar cells and an acidophilic cytoplasm containing numerous vacuoles and small spherical to oval nuclei-based on a basement membrane (Figure 6).

The central zone has the cells of this zone in the form of straight and curved cords, each consisting of double rows of columnar cells with small nuclei, a few vacuoles acidic cytoplasm a small nucleus, and many small blood pockets, and a few connective tissues between the cortical cords were observed (Figure 7).

The medulla area appeared in the histological sections in the form of small irregular islets or an interlocking network between the cortical and sub-capsular tissues and concentrated near the blood pockets are polygonal cells with a basal cytoplasm and a large central spherical nucleus containing two nuclei or more, and chromaffin cells are large and few compared to the cells of the inner zone, towards the periphery of the gland in the subcapsular zone chromaffin cells tend to become small and cytoplasm contains fewer granules (Figure 8).

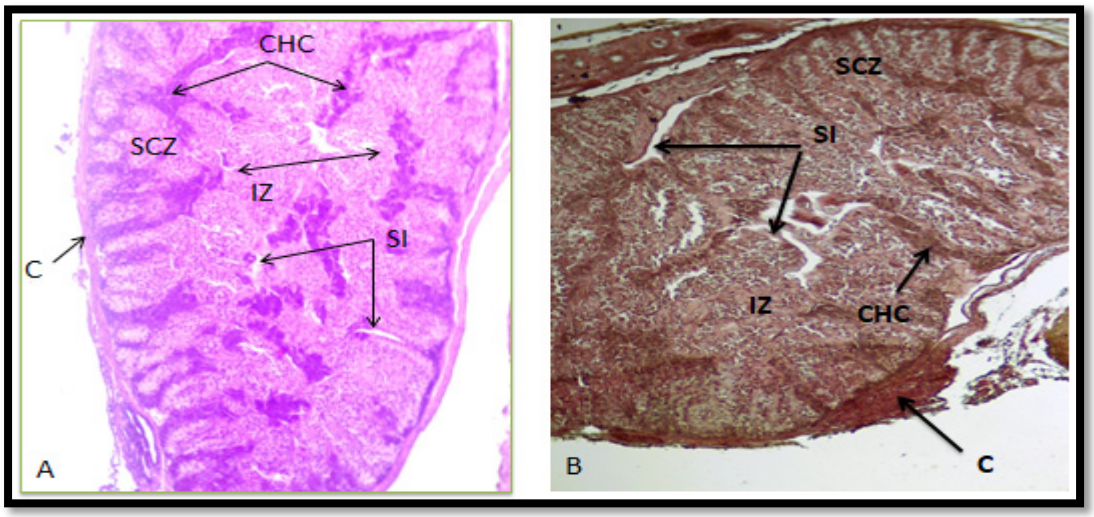

Figure 5. A cross section of the adrenal gland of the Iraqi pin-tailed sandgrouse bird, the zones of the gland, capsule (C), Chromaffin cells (CHC), Inner zone (IZ), Sub Capsular Zone (SCZ), blood sinuses (Si), H&E stains, A: 10x, B: Verhoeff's stain, 10x

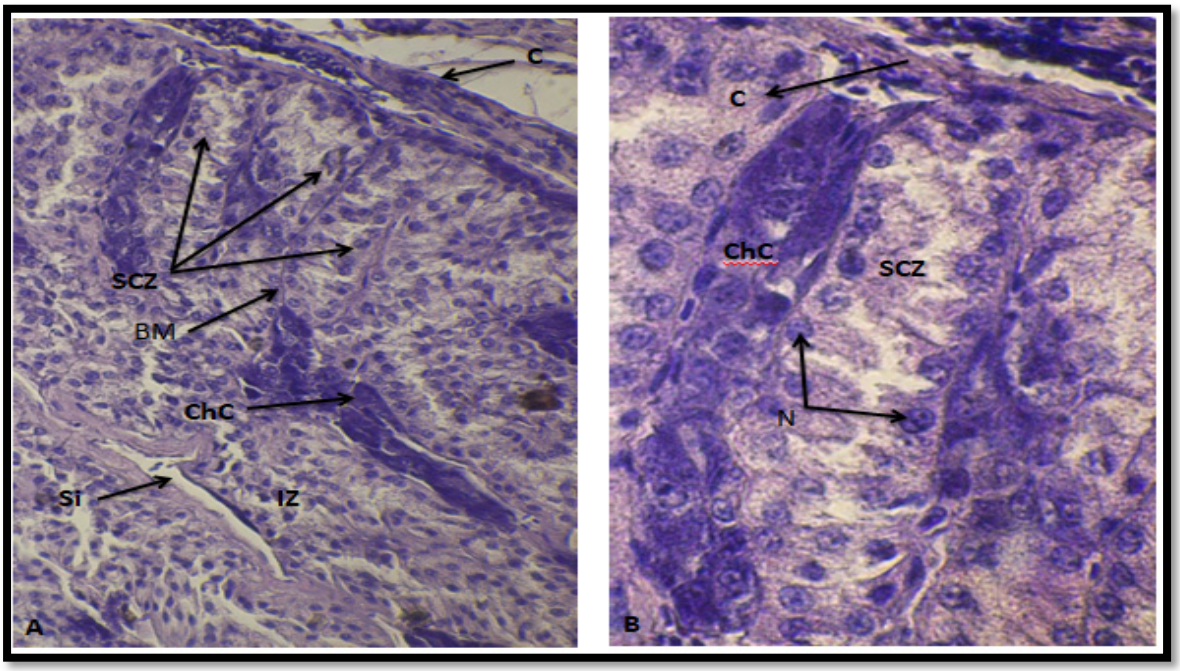

Figure 6. A cross section of the adrenal gland of the Iraqi pin-tailed sandgrouse bird, noted: Basement Membrane (BM), Capsule (C), Chromaffin Cells (Ch), Inner Zone (IZ), nucleus (N), blood sinuses (Si), A: H&E stain, 40x, B: 100x. H&E stain, 40x.

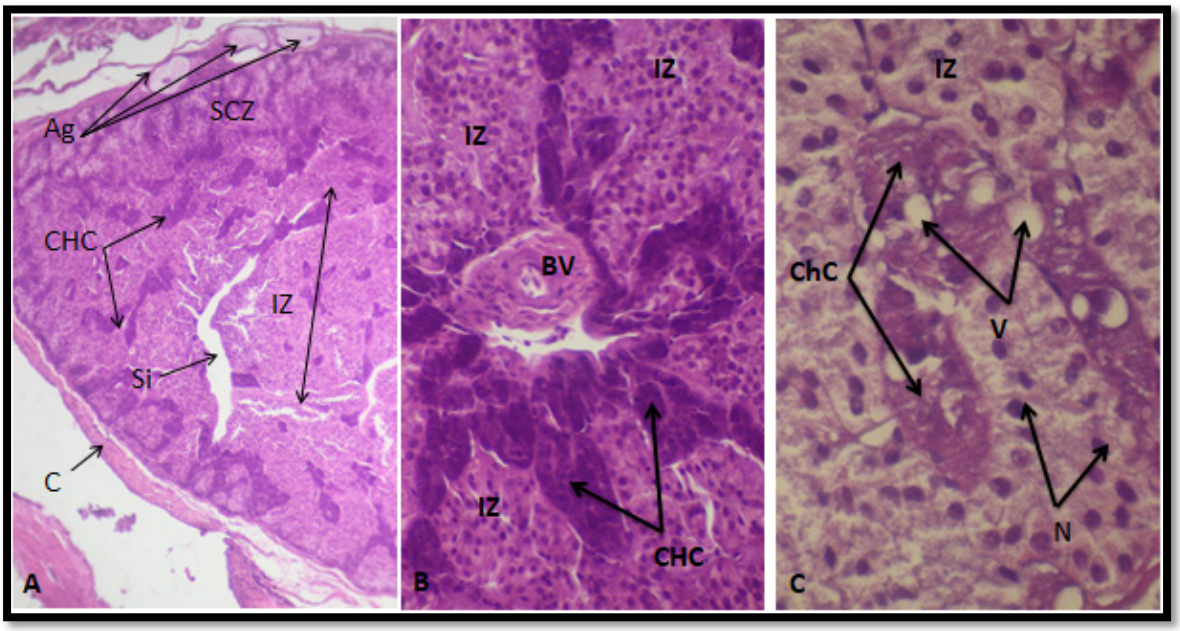

Figure 7. A cross section of the adrenal gland of the Iraqi pin-tailed sandgrouse bird, noted: autonomic ganglia nodes (Ag), blood vessels (BV), Capsule (C), Chromaffin Cells (CHC), Inner zone (IZ), Nucleus (N), Subcapsular zone (SCZ), Vacuoles (V), H&E stain, A: (10x), B: (40x), C: (100x)..

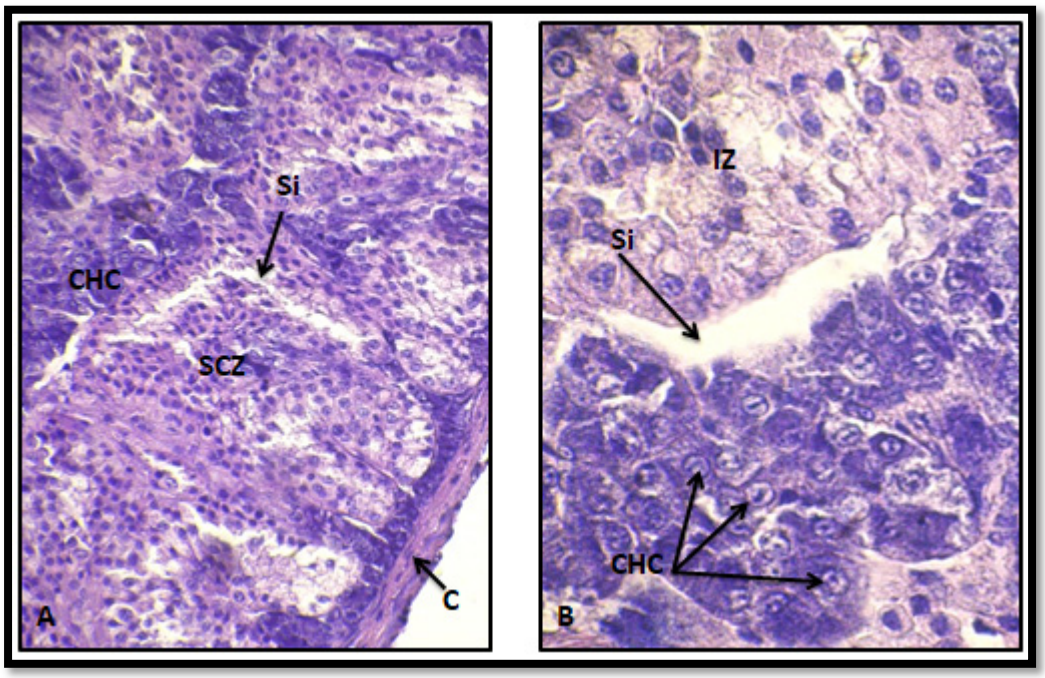

Figure 8. A cross section of the adrenal gland of the Iraqi pin-tailed sandgrouse bird, Chromaffin Cells (CHC), Capsule (C), Inner Zone (IZ), blood Sinuses (Si), Sub Capsular Zone (SCZ), A: H&E stain, (40x), B: (100x).

The statistical analysis showed significant differences in the average diameters of the nuclei of the cells of the adrenal zones, where the average diameters of the cells of the subcapsular zone were 7.60±0.63, while the average diameters of the central (internal) zone cells were 4.94±0.40 µm, and the average diameters of chromaffin cells in the medulla area was 0.40±6.84 µm with significant differences at the $p \leq 0.050$ probability level (Table 2 and Figure 9).

Table 2. Diameters of cell nuclei in the adrenal gland of the Iraqi pin-tailed sandgrouse bird.

Measurement Type	Average±Standard error (µm)	P value
Cell nuclei in subcapsular zone	7.60±0.63	
Cell nuclei in the central zone	4.94±0.40	0.002*
Chromaffin cells	6.84±0.40	

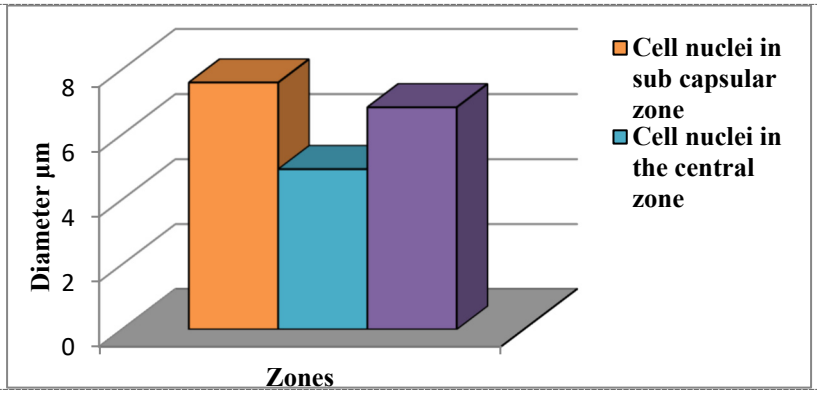

Figure 9. Diameters of the nuclei of cells in the adrenal gland of the Iraqi pin-tailed sandgrouse bird.

The histochemical results showed a strong reaction to the periodic acid-Schiff stains (PAS) and the periodic acid-Schiff stain and Alcian blue (Ab) compound of the basement membrane of the cells of the gland parenchyma indicating the presence of acidic and neutral mucopolysaccharide compounds (Figure 10) and a strong reaction of Verhoeff stain appeared in the stroma of the gland indicating the presence of elastic fibers in the parenchyma tissue of the gland (Figure 11).

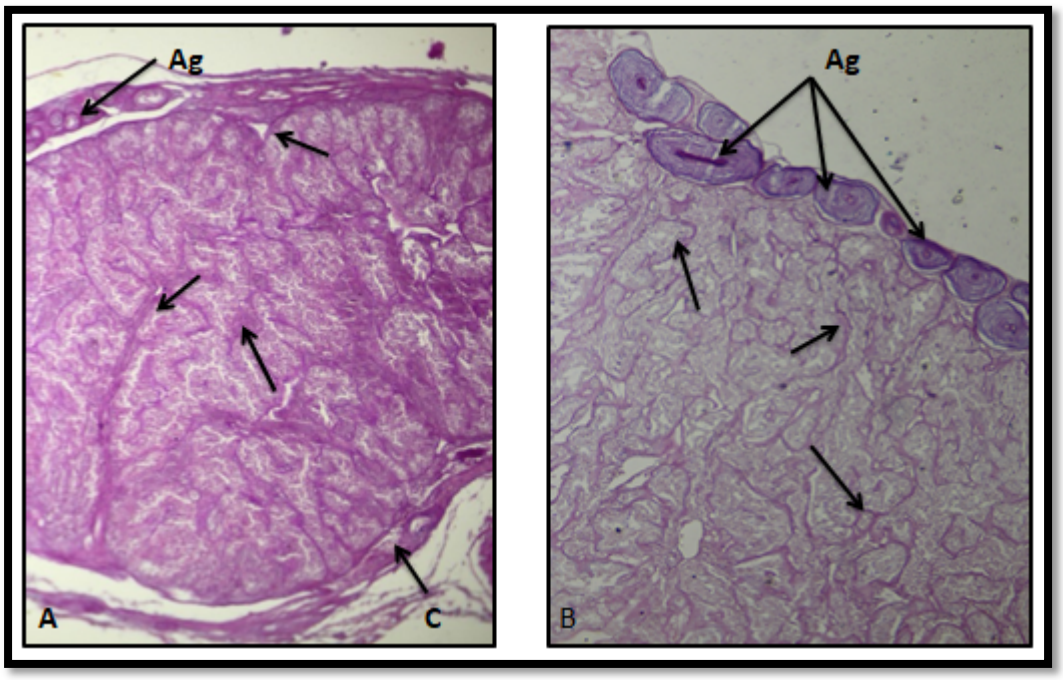

Figure 10. A cross section in the adrenal gland of the Iraqi pin-tailed sandgrouse bird, noted: autonomic ganglia nodes (Ag), capsule (C), positive interaction with PAS and PAS with Ab compound (arrow), A: PAS stain 10x, B: PAS& Ab compound stains 10x.

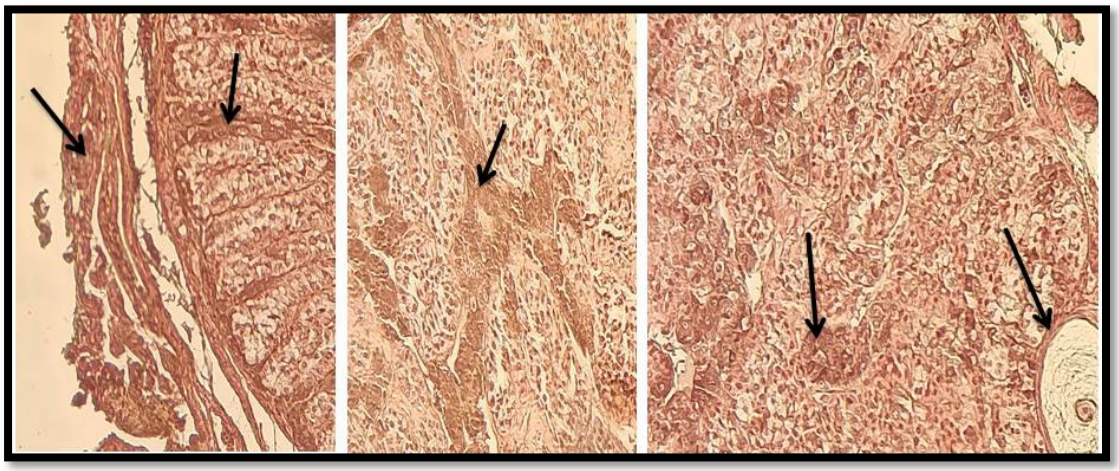

Figure 11. A cross section in the adrenal gland of the Iraqi pin-tailed sandgrouse bird, showing the presence of elastic fibers in the capsule of the gland and the stroma densely (arrow) Verhoeff's stain, 40x.

In this study, the general shape and histological structure of the adrenal gland in the Iraqi pin-tailed sandgrouse bird was examined, and it was found that the location of the adrenal gland in this study is consistent with Sadoon [18] when studying the adrenal gland in the local pigeon *Columba livia domestica*, where the study indicated that the adrenal gland in the small pigeon is located in the abdominal cavity in the anterior pole of the kidneys with a creamy color. It also agrees with the study of Ahmed and Dauod [10] on the Iraqi *Francolinus francolinus*, where they indicated that *Francolinus francolinus* birds have a pair of small adrenal glands located in the abdominal cavity near the upper edge of the kidneys, oval located on the cranial lobe of the kidneys and partially covered by the gonads and on the sides of the aorta and the posterior vena cava.The result of the current study is consistent with the study of Tang et al. [9] on African ostriches and Jabbar et al. [19] on Guinea fowl, Muscovy ducks, and Fathima and Iucy [20] in female ducks *Anas platyhynchas domesticus* one day after hatching to 24 weeks after hatching, that the glands were very small in adult duck, and El-Zoghby [21] in Egyptian geese, as well as Kober et al. [22] in chickens indicated that the right gland showed an oval or triangular shape, while the left one was an elongated oval. Moawad and Randa [14] reported through their study of male breeds of domestic chickens *Gallus gallus domedticus*, that the adrenal gland is located on both sides of the median line at the front of the cranial pole of the kidney and is yellow in color and the right gland is elongated in shape while the left is triangular in shape and the ventral surface of the glands is located at the testes. Da'aj et al. [23] when studying the adrenal gland in quails Coturnix coturnix stated that the adrenal gland was in the form of small double organs located within the abdominal cavity at the anterior end of the cranial pole of the kidney with a yellow-brown color and flat shape. Al-Jebori et al. [24] observed when studying the adrenal gland in female ducks Anas platyrhynchos that it has a pair of adrenal glands located in the ventral cavity at the anterior end of the kidneys, ranging in color from yellowish gray to reddish-yellow and the right gland was pyramidal and the left gland was triangular. The result of the current study also showed that there were no significant differences between the dimensions of the right and left adrenal gland, and this is not consistent with the study of Al-Jebori et al. [24] when studying local duck females, which showed significant differences in the weights of the right and left gland, where the weight of the left gland was 0.41±0.017 g while the right gland was 0.39±0.01 g. Humayun et al. [12] also indicated that the weight of the right gland in male chickens was 98.3±1.9 g and in females 96.0±1.4 g, while the left one was 107.0±1.4 g in males and in females it was 101.3±0.4 g, adding that the weight of the adrenal glands varies greatly depending on different species and breeds, the age of birds, their health status and various environmental factors. Ahmed and Dauod [10] when studying the adrenal gland in the Iraqi black pheasant Francolinus francolinus indicated that the average length of the right gland was 6.167±0.60 mm and its weight was 0.044±0.002 g, while the average length of the left gland was 7.33±0.760 mm and its weight was 0.052±0.009 g. Additionally, Tang et al. [9] noted in their study of African ostriches that the average length of the left and right glands after 40 days of hatching ranged from 2.0 to 3.0 cm, was 0.6 cm wide and 0.3 cm thick. Jabbar et al. [19[when studying the adrenal gland in Guinea fowl (*Numida meleagris*) and Muscovy ducks (*Cairina moschata*) reported that significant differences were recorded in Guinea fowl about the length of the right and left gland, where the lengths of the right gland ranged from 5.201-6.67 mm, while the length of the left gland ranged between 6.11-7.15 mm, while no significant difference was shown for the thickness and weight of the two glands. Prokopenko and Kot [25] indicated during their study on poultry that the left gland is larger than the right gland, and Kober et al. [22] indicated that the average mass of the right and left

gland in domestic chickens was 97.2±1.2 and 104.1±1.4 respectively, while the length was 0.8 cm for the right gland and 0.9 cm for the left gland, and the width of the right gland was 0.6 cm and the left gland was 0.5 cm wide. Fathima and Lucy [20[mentioned during their study on the adrenal gland in Kutt and Duck birds (*Anas platyrhynchos domesticus*) during different age periods, where the study showed that the left gland recorded a higher weight than the right gland in all age groups, and the average weight of the gland gradually increased from the age of one day, where its weight reached (0.011±0.001) g to the age of 12 weeks, where its weight increased to 0.093±0.002 g. Microscopic examination of the histological sections of the adrenal gland in males of the Iraqi *Pterocles alchata* bird showed that the average thickness of the capsule was 42.69±1.81 µm, and Kot and Prokopento [26] indicated that the thickness of the capsule in male chickens amounted to 18.14±1.82 µm, while in females it was larger which was 29.09±2.17 µm, and this result was similar to what was found in this study. In Pigeon pigeons, the thickness of the capsule did not exceed 143.46±0.67 µm [27], Kot and Prokopenko [28] stated that the thickness of the wallet depends mainly on body weight by studying different types of birds.

The histochemical result showed a strong interaction towards the PAS stains, PAS with Alcian blue (Ab) compound, Masson's trichrome, and the Verhoeff's stain, this result is consistent with Moawod and Rauda [14] when studying the histological and chemical characteristics of the adrenal gland, where the results of the chemical study showed a positive reaction of collagen fibers in the capsule with Masson's trichrome. As well as Basha et al. [29] mentioned that during their study on Japanese quails and when using PAS and Ab compound stains the percent of a positive reaction to the gland capsule is evidence of the presence of neutral mucopolysaccharide compounds. This result showed agreement with histochemical studies of the adrenal gland in terms of the presence of positive reactions using special stains and different vertebrates as indicated by Batah [13] when studying the adrenal gland in Guinea pigs and Albino rats and Kadhim [30] on male squirrel and hamsters. The results of the chemical study showed a positive interaction of the Masson's trichrome, Periodic acid-Schiff (PAS) and Verhoeff's stains with the gland capsule containing collagen, carbohydrates and elastic fibers. The adrenal parenchyma in the male Iraqi *Pterocles alchata* under study was completely different from that of the mammals, because of the latter showed an outer cortex and an inner medulla, but the former has cortical tissues intertwined with medulla tissue, and this result is consistent with most birds as in Moawad and Randa [14] in chickens *Gallus gallus domesticus*, and the study of Ghosh et al. [31] and Gulmez et al. [32] in goose, and the study of Al-Jebori et al. [24] in female ducks *Anas platyhynchos*, and the studies by Humayun et al. [12] for the study of domestic chickens Gallus domesticus and the study of Jabbar et al. [19] on Guinea fowl and Muscovy ducks, Tang et al. [9] on African ostrich chicks and El-Desoky and Mustafa [33] on Japanese quail Coturnix japonica support the results of the current study. The current study is consistent with the study by Tang et al. [9] where it was stated that cortical tissue is dominant in the gland, and this finding is also consistent with Mikami et al. [34] in Japanese quails and Humayun et al. [12] in chickens where they indicated that the ratio of cortex tissue to medulla was 3:1 and 1.6:1 respectively, and Aire [35] stated that the ratio of cortex tissue in the chicken breeds; Rhode Island and red island was 52%. The functional importance of the high percentage of cortical tissue can be attributed to the high production of cortical hormones, in birds living in dry areas where water preservation is necessary, the hormones glucocorticoid and mineral corticoids are very important, so the *Pterocles alchata* bird had a high percentage of cortical tissue because water preservation is necessary. This bird is one of the migratory birds exposed to stress, when exposed to stress, the adrenal gland secretes corticosteroids that are produced from the cortex and catecholamine, which includes the hormone epinephrine and norepinephrine, which is produced from the marrow to the blood, which helps the bird to adapt to its new environmental conditions, and therefore there is a clear variation in the proportions of cortical and medullary tissues. Mikami et al. [34] stated during their study on Japanese quail that the proportion of cortical tissue is greater because quail is a migratory bird and needs to preserve water, while Humayun et al. [12] in chickens, the ratio of cortex to medulla was close because chickens are domestic birds and the water retention process is unnecessary. The diameters of the nuclei of the gland zones also showed significant differences among themselves, and this is consistent with the study of Kot and Prokopenko [28] on species of birds that the diameters of the cell nuclei of the subcapsular zone, the inner region, and the diameters of the chromaffin cells showed significant differences between bird species, which the cell diameters of quails reached (11.83, 17 and 25.3) µm respectively, in domestic chickens (18.5, 18.66, 20.83) µm, in domestic turkeys (20, 22, 22.17) µm and Muscovy ducks (20, 19, 20.83) µm. Humayun et al. [12] in their study of the adrenal gland in domestic chickens *Gallus gallu*s indicated that the diameters of the nuclei of the cells of the subcapsular zone, the central zone, and the chromaffin cells in the medulla area were (5.1±0.0, 5.0±0.0, 5.1±0.0) µm respectively. Tang et al. [9] also indicated in African ostriches that the average diameter of chromaffin cell nuclei was approximately 8 µm and the average diameter of these cells was 6.7 µm in domestic hens in the study by Hodges [36]. The histochemical results agree with Basha et al. (29) on the Japanese quail and El-Zoghby [21] on Egyptian geese ducks, where the study showed a positive interaction with PAS and PAS & AB compounds with acidic and neutral mucopolysaccharides and the interaction included the capsule and trabeculae, internal tissues and basement membrane. Kot et al. [37] reported that numerous

histochemical studies of wild bird species during the mating season, such as *Columba livia*, *Passer domesticus*, *Corvus splendens*, *Acridotheres tristis*, *Acridotheres ginginianus* and *Bubulcus ibis*, showed that the internal tissue of the adrenal gland is characterized by the highest content of alkaline phosphatase, glycogen, mucopolysaccharides and lipids, while the subcapsular zone observed moderate content of ascorbic acid. It was also observed that the histochemical properties of chromaffin cells remain unchanged throughout the year except phosphatase enzyme, the amount of which increases with the sexual activity of birds, Basha et al. [38] reported on quails birds that internal tissues are rich in glycogen, fat, cholesterol, mucopolysaccharides and ascorbic acid, and Moawad and Randa [14] during their study on domestic chickens reported that the use of Sudan black B and Sudan 111 stains helped in estimating the maximum amount of fat in the subcapsular zone of the gland. It must be pointed out the importance of studies related to organs that have a role in hormonal regulation and their role in body metabolism, which were conducted on different types of animals, whether anatomical, histological, physiological, or other, including [39, 40, 41].

REFERENCES

1. Al-Taai SAH and Nasif RH 2020 Comparative histomorphological study of kidneys in pigeon (Columba livia) and starling birds (*Sturnus valguris) Indian J. Foren. Med. Toxicol*. 14 1707.
2. Al-Hamawandy DH and Al-Bakri NA 2019 Analysis of fatty acids of liver in the embryo and adult of domesticated chicken *Gallus gallus domesticus J. Global Pharma Technol.* 11 62.
3. Alkafagy SM Ghazi J and Alhaaik.AG 2019 Micromorphological study of kidney in adult kestrel, *Falco tinnunculus Biochem. Cell. Arch*. 19 3927.
4. Al-Loos B 1062 Birds of Iraq Three volumes, Al-Rabia Press, Baghdad 279.
5. Taher IA and Arrak JK 2016 The effect of melatonin on adrenal gland and pancreas function in alloxan-induced diabetes in adult female rabbits *Iraqi J. Vet. Med* 40 38.
6. Kadhim AB and Khaleel IM 2022 Comparative morphological and morphometrically study of the adrenal gland in adult males' squirrel (*Sciurus anomalous*) and hamster (*Mesocricetus auratus*) *Iraqi J. Vet. Sci*. 36 725.
7. Alwan AF 2014 Fetal adrenal cortex development with maternal serum Cortisol profiles in relation to estrous induction, laparoscopical insemination in Iraqi goats out breeding season *Iraqi J. Vet. Med*. 38 129.
8. Kadhim AB and Khaleel IM 2021 Comparison of Histomorphometric Study of Chromaffin Cells in Adult Males Squirrel (*Sciurus anomalus*) and Hamster (*Mesocricetus auratus*) *Iraqi J. Vet. Med*. 45 46.
9. Tang L Peng KM Wang JX Luo HQ and Cheng JY 2009 The morphological study on the adrenal gland of African ostrich chicks *Tissue Cell*. 412 231.
10. Ahmed NA and Dauod HAM 2016 Morphological description and histological structure of adrenal gland in black Iraqi partridge *Francolinus francolinus Iraqi J. Sci.* 57 330.
11. Ritchie MBA 2008 The anatomy and physiology of avian endocrine system *Vet. Clin. Exot. Anim.* 11 1.
12. Humayun KAKM Aoyama M and Sugita S 2012 Morphological and histological studies on the adrenal gland of the chicken (*Gallus domesticus*) *J. Poultry Sci*. 49 39.
13. Batah AL and Mirhish SM 2019 Histomorphological and histochemical study of adrenal gland in adult male of guinea pigs (*Cavia porcellus*) *Iraqi J. Vet. Med*. 43 59.
14. Moawad UK and Randa MH 2017 Histocytological and histochemical features of the adrenal gland of adult Egyptian breeds of chicken (*Gallus gallus domesticus*) *Beni-Suef Univ. J. Basic Appl. Sci.* 6 199.
15. Al-Bakri NA and Al-Zuheri JJ 2021 Anatomical and histological structure of the cerebellum in the Iraqi frog *Rana ridibunda ridibunda J. Physics: Conf. Ser*. 1879 1.
16. Al-Zuheri JJS and Al-Bakri NA 2020 Morphological study of the brain and spinal cord of the Iraqi frog, *Rana ridibunda ridibunda Biochem. Cell. Arch*. 20 0000.
17. Bancroft JD and Stevens A 2010 *Theory and practice of histological techniques* 4th ed. Churchill Living state London 726.
18. Sadoon AH 2018 Morphological and histochemical study of adrenal gland in local domestic pigeons (*Columba livia domestica*) in Basrah province. *Basrah J. Vet. Res*. 17 74.
19. Jabbar AI Alshammary HKA and Al-Agele RAGA 2021 Histomorphological comparative study of the adrenal gland in local Guinea fowl (*Numida meleagris*) and mascovy duck (*Caorina moschata domestica*) *Ann. Roman. Soc. Cell Biol*. 25 4360.
20. Fathima R and Lucy KM 2014 Morphological studies on the adrenal gland of kutt and duck (*Anas platyrhynchos domesticus*) during post hatch period J. *Agric. Vet. Sci*. 7 58.
21. EL-Zoghby IM 2010 Light and Electron microscopic studies of the adrenal gland of the Egyption Geese (*Alopochena egyptiacus*) *Lucrări Ştiiţifice-seria Med. Vet*. 06/53 221.

22. Kober A, Aoyama M and Sugitta S 201. Morphological and histochemical studies on the adrenal gland of the chicken (*Gallus domesticus*) *J. Poultry Sci*. 49 39.
23. Da'aj SA Ali MA and. Shehan NA 2020 Anatomical and histological study of adrenal gland in the quail (*Coturnix coturnix*) *Biochem. Cell. Arch*. 20 000.
24. Al-Jebori JGA, Al-Jebori AKH Hossain AO and Al-Tamimi ZSM 2016 Histomorphological study of adrenal gland in local adult female duck (*Anas platyrhynchos*) *Basrah J. Vet. Res*. 15 164.
25. Prokopenko VS and Kot TF 2021 Macroscopic characteristics of the avian adrenal gland *Bull. Suny Nat. Agrarian Univ. The Series: Vet. Med*. 4 17.
26. Kot T and Prokopenko V 2020 Peculiarities of the morphology of the adrenal gland of chicken *Scient. Horizon*. 5 8.
27. Prokopenkto VS 2022 Morphology of the adrenal gland blue rock pigeon (*Columba livia* L) *Scient MessLUN of Veterinary Med Biotechnol*. *Series. Vet. Sci.* 24 67.
28. Kot, T. and V. Prokopenko. Micromorhpometric characteristics of the adrenal gland in birds. Ukrainian J. Vet. Sci. 13(4): 25-34.
29. Basha SH Venkatensan S and Remesh G 2008 Histochemical reactions of the adrenal gland in Japanese quail (*Coturnix coturnix japonica*) *Indian J. Anim. Sci*. 78 47.
30. Kadhim AB 2022 Comparative histomorphological and histochemical study of adrenal gland in adult males squirrel (Sciurus anomalus) and hamster (Mesocricetus auratus) PhD. Thesis College of Veterinary Medicine, University of Baghdad, 450.
31. Ghosh A. Carmichael SW and Mukherjee M 2001 Avian adrenal medulla: cytomorphology and function *Acta Biologica Szegediensis*. 45 1.
32. Gulmes N Kocamis H Liman N and Kukner A 2004 Internal cell zonation in the adrenal gland of the goose (*Ansea Anser*) *Growth Dev. Aging*, 68 11.
33. El-Desoky SMM and Mustafa FZA 2020 Morphological and histological studies of the adrenal gland in the Japanese quail (*Coturnix japonica*) *Microsc Res. Tech*.1.
34. Mikami SI Takagi T and Farner DS 1980 Cytological differentiation of the internal tissue of the Japanese quail, *Coturnix coturnix Cell Tissue Res*. 208 353.
35. Aire TA 1980 Morphometric study of the avian adrenal gland *J. Anat*. 131 19.
36. Hodges RD 1974 The adrenal glands In: the histology of the fowl Academic Press, London, 464.
37. Kot T Tkachuk S. Usenko S and Prokopenko V 2023 Adrenal Gland of Poultry: Anatomy, Microscopy, Morphometry, and Histochemistry *J. World's Poultry Res*. 13 20.
38. Basha S Kannan TA and Ramesh G 2009 Age-related changes of the adrenal gland in Japanese Quail (*Coturnix coturnix japonica*) *Tamilnadu J. Vet. Anim. Sci*. 5 198
39. Bayram EN, Al-Bakri NA and Al-Shmgani HS 2023 Zinc chloride can mitigate the alterations in metallothionein and some apoptotic proteins induced by cadmium chloride in mice hepatocytes: A histological and immunohistochemical study *J. Toxicol.*1 2200539.
40. Lafta IA AL-Bakri NA and Abdulhameed WA 2022 Expression of urotensin ii of human placental tissues and in serum in gestational diabetic mellitus in Iraqi woman *IJDDT* 12 70.
41. Bayram, N Al-Shmgani HS and Al-Bakri NA 2022 Comprehension of the zinc chloride's ameliorative apoptotic and genotoxic effects on mice with cadmium-induced hepatotoxicity *J Anim Behav Biometeorol* 10 2235.

Study the immunological and hematological parameters of rabbits infected by different *Klebsiella pneumoniae* antigens

Mariam Esam Hamed [a)], Khalid Mahmood Hammadi [b)]

Department of Biology, College of Education, Al-Iraqia University, Baghdad, Iraq

[a] mariam.essam19981998@gmail.com
[b] Corresponding author: khalidmh0@gmail.com

Abstract. This study included collecting approximately 130 clinical samples from sheep diagnosed with mastitis during the period from 1/9/2022 to 15/12/2022, and the results reported that only 2 isolates belonging to the *Klebsiella Pneumonia* bacteria had been isolated. This study was conducted in two experiments. The first experiment included detection of the infective dose of LPS antigen, as it was injected into five groups of rabbits at different concentrations (900 - 1000 – 1200- 1800- 2000 µg/kg of body weights of rabbits). The second experiment was done to assess the rabbits' haematological and immunological parameters (cellular and humoral) with two different *Klebsiella Pneumonia* antigens: the lipopolysaccharide antigens (by use selected concentration) and the formaldehyde-killed antigens. 15 rabbits were divided into 3 groups, with 5 rabbits in each group, the first group (group A) was immunized orally (PO) with 3 × 10 CFU/animal of killed *Klebsiella Pneumonia.* The second group (group B) were given 1800µg of LPS /animal, while the 3rd group were drenched by sterile PBS (pH=7.2) and consider as control negative group. The results of the blood count tests at 24 hrs. showed that there were significant differences for the two infected groups (killed and LPS) in both the numbers of white blood cells and lymphocytes at a significant level of 0.001 when compared with the zero time for the same time or with a control group. The results of the IL-6 and IgG ELISA test showed that there was an increase in the value starting from the second week after injection in the two infected groups (A and B), especially in the group injected with the killed antigens, and it began to significant increase ($P \leq 0.001$), and this percentage began to increase in the third week. This was for the group injected with the killed vaccine, while for those who were injected with the LPS, their forgetfulness in the third week.

Keywords: *Klebsiella pneumoniae*, *antigens, Rabbits*, immunological, hematological

INTRODUCTION

Klebsiella pneumoniae bacteria is one of the most important types of bacteria that belong to the Enterobacteriaceae family. This bacterium was discovered for the first time by the German scientist Edwan Klebs in 1834. Therefore, it was named after him, but it was diagnosed for the first time by the scientist Fried Landers, and therefore it was called Fried Landers Bacilli. It was considered one of the important types of bacteria that pollute soil and water, which consequently leads to many diseases that affect humans, animals, and plants [1]. Because it belongs to the Enterobacteriaceae family, which is one of the most important and widespread groups of microorganisms, its natural habitat is the intestinal tract of humans and animals. It was considered one of the Gram-negative bacilli [2]. This type of bacteria causes many diseases in humans and animals, as it can cause acquired pneumonia, in addition to urinary tract infections and septicemia [3]. This bacterium mostly targets the elderly who suffer from incurable diseases such as diabetes or respiratory diseases, because the immune system They are weak, and they also affect newborns. Birth or premature infants who are immunologically compromised [4].

In animals, it causes many pathological conditions, such as urinary tract infections in sheep, and also a special condition called mastitis, which is represented by the presence of these bacteria in the udder of cattle, which makes it hard and fossilized [5].

Technologies and Materials for Renewable Energy, Environment and Sustainability
AIP Conf. Proc. 3321, 030005-1–030005-7; https://doi.org/10.1063/5.0291627
Published under an exclusive license by AIP Publishing. 978-0-7354-5231-2/$30.00

MATERIALS AND METHODS

Bacterial isolation

The bacteria *Klebsiella pneumonia* was identified in sheep that had developed clinical mastitis. Milk samples (n=120) from clinical cases were collected after antisepsis and cultured in Brain Heart Infusion broth. The recovered bacteria were grown overnight in BHIB at 37°C for 48 hours before being streaked onto MacConkey agar and blood agar plates. he inoculum-containing plates underwent aerobic incubation. Each and every colony was identified using a variety of techniques, including colony morphology, Gram staining, lactose, glucose, mannitol, and sucrose fermentation, as well as biochemical assays (catalase, urease, TSIA, indole, and citrate). The diagnosis was verified using the Vitek-2 system., The isolation process was made by the biology lab at the University of Al-Iraqia, college of Education, Baghdad, Iraq.

Experimental animals

35 healthy rabbits of both sexes were collected from local markets (20 rabbits to study the infective dose and (15) to study the hematological and immunological (cellular and humoral) tests. Their weights ranged from 900 gm to 1500 gm. They were fed with various types of green grass (jet) and placed inside iron cages in the temperature of the room that rang (25+_2). The floor was covered with sawdust, which was changed weekly, and it was brought two months before the start of the experiment to monitor its health condition and for its adaptation.

Lipopolysaccharide extraction and purification

Klebsiella pneumonia lipopolysaccharide was extracted using the hot EDTA method as outlined by [6]. The purified lipopolysaccharide was then purified using sephadox B6 column gel filtration chromatography [7]. Purified LPS was then chemically analyzed to determine its protein and carbohydrate contents [8,9].

Killed vaccine preparation

According to a killed whole-cell vaccine was created [10]. After being grown on Brain heart infusion broth at 37 C for 24 hours, *Klebsiella pneumonia* was harvested using PBS pH 7.2 and then killed with 5% formalized PBS pH 7.2. After being incubated at 37 C for an entire night, the bacterial suspension was diluted with PBS pH 7.2 by McFarland tube (3×10^9 CFU/ml) and then washed three times using PBS pH 7.2 with centrifugation at 3000 rpm for fifteen minutes [11].

The experimental study designs

In the experimental study, the rabbits were divided into three groups and each of the three groups included 5 rabbits. The rabbits of the first group (A) were immunized by (3×10^{10}) CFU/animal of killed *Klebsiella pneumonia*, while those of the second group (B) were immunized by 1800µg/ Kg of LPS /animal, while the 3rd group were drenched by sterile PBS (pH=7.2) and consider as control negative group. Using a cardiac puncture technique, blood samples were obtained on days 0, 15, 30, 45, and 60 of the experiment for serological purposes. The serum was obtained after centrifugation (2000 rpm) for 15 minutes, liquated, and frozen at (-20) C until use.

The animals were clinically examined after immunization, including measuring blood parameters, the Blood tests were conducted for all groups of rabbits for a period of five days. white blood cell count, lymphocytes and granulocytes were measured, and a comparison was made between the three groups based on what was stated in [12]

The Immunological tests were also done for the detection of cellular immune response (Interleukin IL-6 test) and humoral immune response (IgG immunoglobulin). The concentration of interleukin 6 and IgG in the blood serum of rabbits was calculated by using the Enzyme-linked Immunosorbent Assay technology for all three groups.

THE RESULT AND DISCUSSION

blood parameters

The increase in the numbers of white blood cells, lymphocytes, and granulocytes appeared clearly on the second day after the injection in LPS and killed antigens, when compared to the control group. The results revealed that there was significant increase for the two infected groups (A and B) of white blood cells, lymphocytes and granulocytes at a significant level of 0.001, when compared with the zero time or with a control group as for measuring proportion. This study is consistent with a study conducted by reference [15] on rabbits that were experimentally injected with Klebsiella pneumoniae. The white blood cells are active cells in performing the functions of the immune system. The results have shown that the injection The pathogenic dose of *Klebsiella pneumoniae* bacteria had a clear effect on the white blood cell count Specifically in lymphocytes, which represent the cellular and humoral arms of a specific immunity, while Neutrophils and monocytes are mainly involved in the phagocytosis process, while.Eosinophils in allergic reactions and parasitic infections, as for cells Basophils release histamine, heparin, and some defensive mediators of reactions Immunology [14]. As shown in Figure (1) and Figure (2), Figure (3).

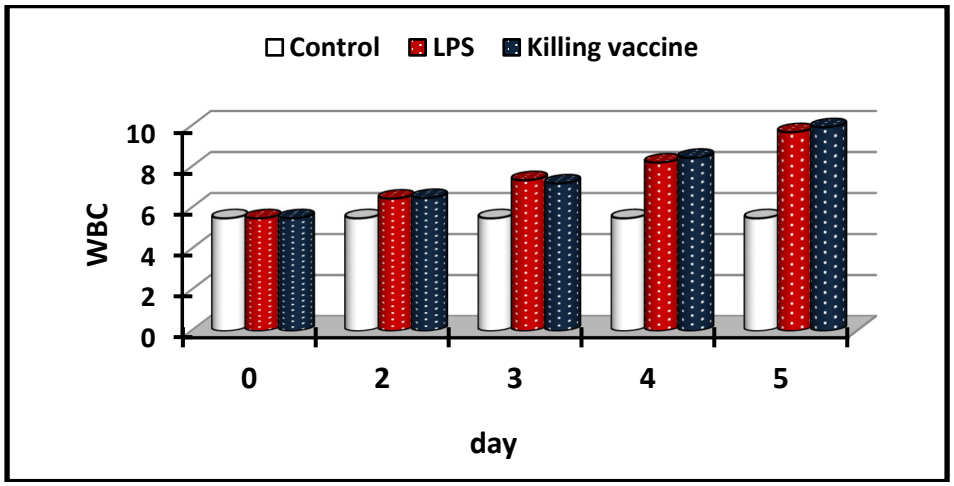

FIGURE (1) SHOWS THE DIFFERENCE IN THE WHITE BLOOD CELL MEASUREMENT RATE FOR THE THREE GROUPS, (KILLED, LPS AND CONTROL GROUP).

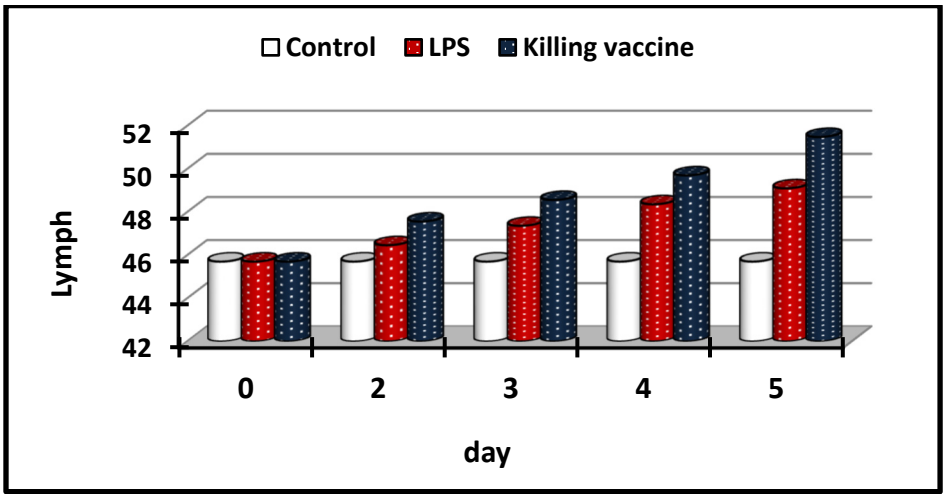

FIGURE (2): SHOWS THE DIFFERENCE IN THE LYMPHOCYTE MEASUREMENT RATE FOR THE THREE GROUPS ,(KILLED, LPS AND CONTROL GROUP).

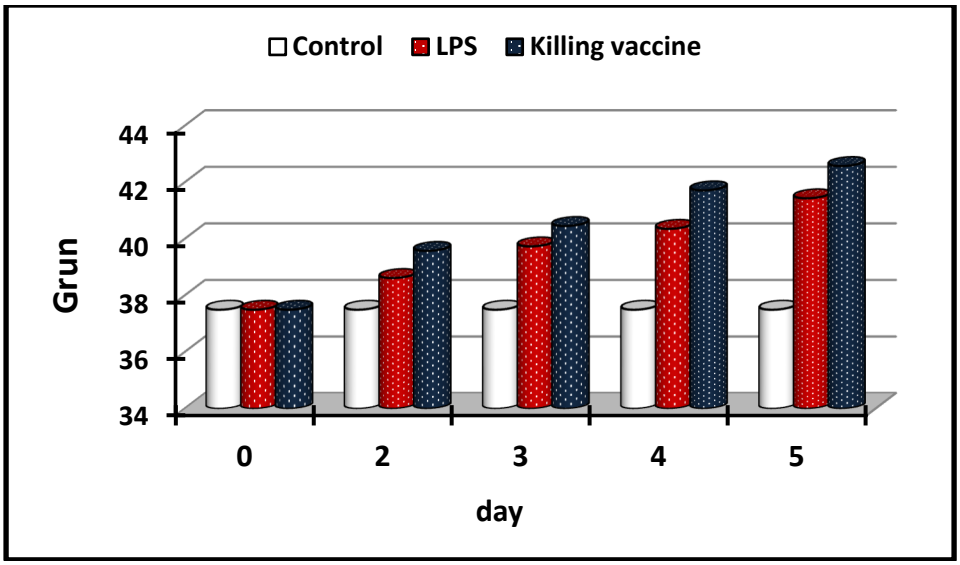

FIGURE (3) SHOWS THE DIFFERENCE IN THE GRANULOCYTE MEASUREMENT RATE BETWEEN THE THREE GROUPS, (KILLED, LPS AND CONTROL GROUP).

RESULTS OF IMMUNOLOGICAL TESTS

Results of cellular immunity tests

Results of the interleukin type VI (IL-6) test in the blood serum of rabbits using the ELISA technique ؛The results of the IL-6 test showed that there was an increase in the value of starting from the second week after injection in the two infected groups (A and B), especially in the group injected with the killed vaccine (20.86 ± 0.39).
It began to significantly increase ($P \leq 0.001$), and this percentage began to increase in the third week, reaching (22.71+_0.39). This was for the group injected with the killed vaccine, while for those who were injected with the LPS, their forgetfulness in the third week reached (20.96±10.49), with a significant difference.

The fifth week recorded the highest measurement rates, in which the killed vaccine group reached (24.6+_0.06), while the group injected with the LPS also recorded (22.79+- 0.34), with a significant difference of ($P \leq 0.001$). As for the control group, no changes appeared in its readings starting from the first week and throughout the duration of the experiment. As shown in Figure (4)

The reason for the increase in interleukin-6 levels is due to the occurrence of internal inflammation in rabbits after dosing them with killed antigen and LPS, which led to an increase in temperature and thus led to an increase in respiratory and heart rates, as the increase in interleukin-6 led to a reduction in albumin production in the liver [16] in addition to its production of hepcidin, which has a role in obstructing the work of iron and zinc transporters in the body, thus leading to a reduction in iron levels in the body.

This is the reason for seeing the rabbits in a constant state of lethargy during the experiment period [17]. Increasing the rate of interleukin-6 leads to excessive production of autoantibodies thus causing an autoimmune response to the bacteria *Klebsiella pneumoniae*.

We also notice that the rate of interleukin-6 increases starting from the third week and throughout the duration of the experiment, and that interleukin-6 has a role in stimulating inflammation or disease, and this agrees with the study [18] in a study conducted on genetically modified mice on the role of interleukin 6 in myositis.

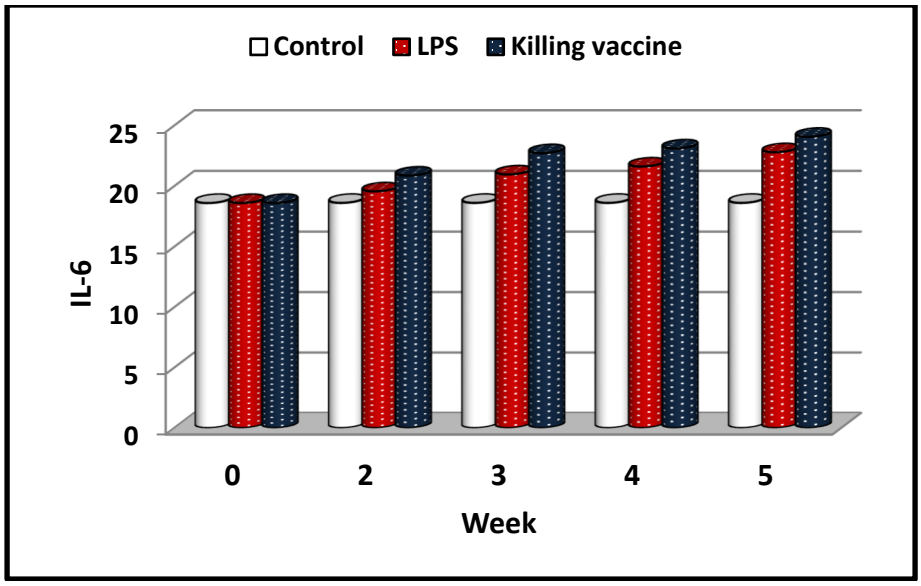

FIGURE (4) SHOWS THE MEASUREMENT RATES OF IL-6 IN RABBIT BLOOD SERUM FOR THE THREE PATHOGENIC GROUPS, THE KILLED VACCINE, AND THE CONTROL.

RESULTS OF HUMORAL IMMUNITY TESTS

Results of the IgG immunoglobulin test in rabbit blood serum using the ELISA technique زAll experimental animals (LPS, killed, and control groups) had low levels of antibody titers before immunization. Group A showed an increase in serum antibody titer at day 14 after immunization (252±1.58) , and this increase persisted until the fifth week when the peak antibody titer was reached (248.80 ±3.27). The serum antibody titer in Group B was (273.40± 3.05) on day 14 post-immunization compared to zero-day; the group's antibody titer peaked at day 42 post-immunization and then began to decline until the study ended. In contrast, the control group had low antibody titer throughout the study period, which was unchanged from the baseline titer at zero days. as shown in Figure (5). During the study period, group A showed a significantly higher antibody titer at ($P \leq 0.05$) than that recorded in groups B and C. Additionally, group B demonstrated higher significance at ($P \leq 0.05$) than that of group-C. Overall, the experiment's results showed that group A exhibited the best behavior and the highest serum antibody titer.

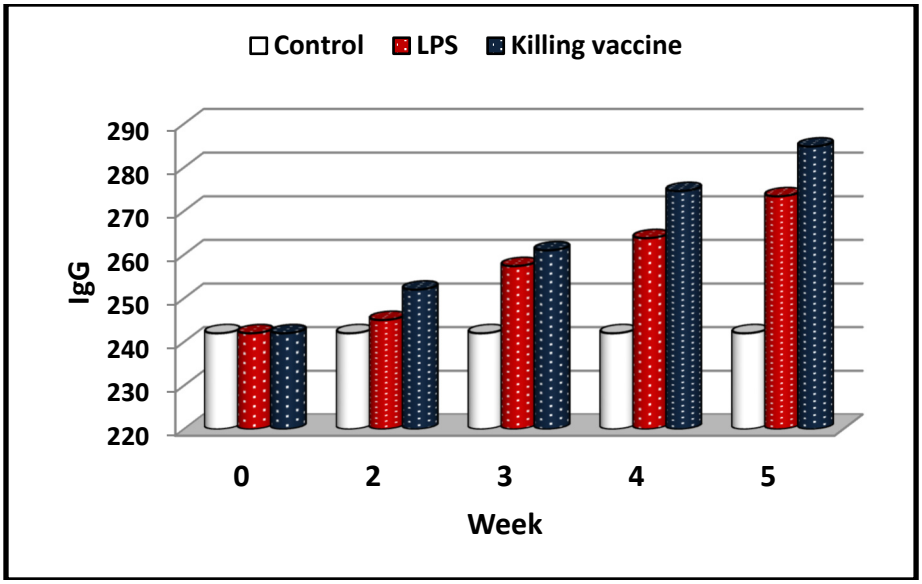

FIGURE (5) SHOWS THE IGG MEASUREMENT RATES FOR THE THREE PATHOGENIC GROUPS, THE KILLED VACCINE, AND THE CONTROL

Explained that the reason for the increase in the rate of immunoglobulin (IgG) measurement in the two injected groups was due to the increased production of lymphocytes, as the injected rabbits could cause a humoral immune response through their production of antibodies to the Klebsiella pneumoniae bacteria, as we observed [15,]. This production began to increase from the first week until the fifth week of injection, and it is consistent with a study conducted by reference [19,-22] on mice that were injected with salmonella mangaka bacteria, which belong to the Enterobacter family, and which recorded a clear increase in the percentage of immunoglobulin (IgG) in the fourth week and began It decreased in the eighth week, and this differs from the study where he studied immunoglobulin [21] on a group of patients suffering from typhoid using ELISA technology, starting from four weeks to two years, where he concluded that the highest percentage of increase in immunoglobulin (IgG)) I reached it peaked in the fourth week and then began to decline successively.

CONCLUSIONS

The two extracted antigens (LPS and killed antigens) were activating the immune response (humoral and cellular) there it can be a promising result for developing a safe, effective, vaccine for protection against *Klebsiella pneumoniae* infection, especially in cases of mastitis or another type of infection. About 130 clinical samples from sheep afflicted with mastitis were collected for this investigation between January 9, 2022, and December 15, 2022. The findings showed that only two isolates of the Klebsiella pneumoniae bacterium had been identified. This investigation was conducted in two experiments. In the initial trial, the infectious dose of LPS antigen was determined by injecting it into five groups of rabbits at varying concentrations (900, 1000, 1200- 1800, and 2000 µg/kg of body weight). In the second experiment, two distinct Klebsiella pneumoniae antigens were used to evaluate the rabbits' cellular and humoral immune and hematological parameters: the lipopolysaccharide antigens (using a chosen concentration) and the formaldehyde-killed antigens.

REFERENCES

1. Chan, Y.; Liu, J.; Pociask, D.; Zheng, M.; Mietzner, T. and Berger, T. (2009) Lipocalin 2 is required for pulmonary host defense against Klebsiella infection. J Immunol. 182(8) 47-56
2. Hammadi. K. M. (2023). Evaluation of liver and renal function tests together with histopathological alterations in rabbits infected with a virulent strain of Proteus vulgaris. Biomedicine:; 43(5): 1613-1620
3. Lee,C.R.; Lee,J.H.; Park,K.S.; Jeon,J.H.; Kim, Y.B.; Cha, C.J.; Jeong, B.C. and Lee,S.H.(2017).Antimicrobial Resistance of Hypervirulent Klebsiella pneumoniae: Epidemiology, Hypervirulence-Associaated Determinants, and Resistance Mechanisms front.Cell.Infect.Microbial.13-1:(483)7
4. Umeh, O.; Berkowitz, L.; shepp, D.; Talavera, F.; King, J.; Mylonakia, E. and cunha, B. (2006). Infectious disease, Klebsiella infection. J. Med. 27.(1)
5. Hammadi. K. M. The liver and renal function test in experimentally immunized rabbits with sonicated antigens of Klebsiella pneumoniae. Iranian Journal of Ichthyology. 2023; (Special Issue 1): 112-117.
6. Subhi, I. M., Zgair, A. K., & Ghafil, J. A. (2016). Extraction and Purification of Pseudomonas aeruginosa Lipopolysaccharide Isolated from Wound Infection. World Journal of Experimental Biosciences, 5(1), 5–8.
7. Naser, H. H.; Salih, S. M. and Al-shaibani, A. B. (2013). Protective Humoral Immunity Induced by Lipopolysaccharide Incorporated Liposome in Mice Against Shigella flexneri Infection. Journal of Al-Nahrain University, 16(3), 205–213.
8. Bradford, M.(1976). A rapid and sensitive method for the quantitation of microgram quantities of protein utilizing the principle of protein-dye binding; J. Annu.Biochem.;Vol. 72;pp 248-254.12- Coles C. F. (1998). U.S. Patent No. 5,712,679. Washington, DC: U.S.Patent and Trademark Office
9. Dubios,M.K.,Gilles K.A.,Hamilton J.K.,Rebers P.A. And Smith F. (1956). Colorimetric method for determination of sugers and related substance. Anal. Chem. 28:350-356
10. paton, J.C.; Rogers,T.J.; Morona,R.; And Paton, A.W.(2001). Oral Administration of Formaldehyde-Killed Recombinant Bacteria Expressing a Mimic of the Shiga Toxin Receptor Protects Mice from Fatal Challenge with Shiga-Toxigenic Escherichia coli. Infection and Immunity; Vol. 69; No. 3;p.1389–1393.
11. Paton, A. W.; Morona, R. and Paton, J. C. (2000). A new biological agent for treatment of Shiga toxigenic Escherichia coli infections and dysentery in humans. Nature Medicine; 6(3); 265–270. https://doi.org/10.1038/73111
12. Coles C. F. (1998). U.S. Patent No. 5,712,679. Washington, DC: U.S.Patent and Trademark Office
13. Itrat, M. and Zarnigr.(2013). Aloe vera: a review of it's clinical effectiviness, Int. Res. J. Pharm., 4(8):75-95

14. Mahdi, S.H., Jassim, W.H., Hamad, I.A., Jasima, K. A., Epoxy/Silicone Rubber Blends for Voltage Insulators and Capacitors Applications, Energy Procedia, 2017, 119, pp. 501–506
15. Al-Anbaki, Jassim Hadi Musa (2020). Isolating and distinguishing the most common bacteria in terms of common diseases in meat and meat products, while studying the pathogenesis of the most common bacteria. Master's thesis / College of Veterinary Medicine / University of Diyala
16. Fung, C. P.; Hu, B. S.; Chang, F. Y.; Lee, S. C.; Kuo, B. I.; Ho, M.; Siu, L. K. and Liu, C. Y. (2000). A 5-year study of the seroepidemiology of Klebsiella pneumoniae: High prevalence of capsular serotype K1 in Taiwan and implication for vaccine efficacy. J. Infect. Dis. 181(6):2075-2079.
17. Gillmore JD,Lovat LB, persey MR, pepys MB, Hawkins PN 2001.Amyloid load and Clinical Outcome in AA amyloidosis to circulating concentration of serum amyloid A Protein .Lancet 358:24-29
18. Nemeth E, Rivera S, Gabayan V, Keller C, Taudorf S, Pedersen BK, Ganz T 2004. IL-6 mediates hypoferremia of inflammation by inducing the synthesis of the iron regulatory hormone hepcidin. J Clin Invest 113: 1271-1276.
19. Jasim, K.A., Journal of Superconductivity and Novel Magnetism, 2013, 26(3), pp. 549–552.
20. Omar, B.A., , AIP Conference Proceedings, 2018, 1968, 030047.
21. OkiyamaN, Sugihara T, Iwakura Y,Yokozeki H ,Miyasaka N, KohsakaH 2009.Therapeutic effects of interleukin-6 blockade in amurine model of Polymyositis that dose not require interleukin-17A . Arthritis Rheum 60:2505-2512
22. Shalal, Zeina Shaker. (2011). Clinical and immunological study of Salmonella mbandaka bacteria isolated from humans in mice. Master's thesis/Faculty of Medicine Veterinary/University of Diyala
23. Sarasombath, S.; Banchuin, N.; Sukosol, T. Rungpitarangsi, B. and Manasatit, S. (1987)." Systemic and Intestinal Immunities after Natural Typhoid Infection". Journal of clinical microbiology, June, p. 1088- 1093

A comparative study of some mechanical and thermal properties of single and hybrid composites of polyester and agricultural waste powders

Abdulraheem Dheyaa Ibrahim [1,a)], Suaad H Aleabi [1,b)]

[1)]*Department of Physics, College of Education for Pure Science (Ibn-AL-Haitham), Baghdad University, Baghdad, Iraq*

[a)] Corresponding author Abd.Ali2204p@ihcoedu.uobaghdad.edu.iq
[b)] soaad.h.l@ihcoedu.uobaghdad.edu.iq

Abstract This research included taking advantage of agricultural waste powders (sawdust and walnut shells) to prepare Single and hybrid wood-plastic composites(WPC) consisting of (UP+ sawdust), (UP+ sawdust+ walnut shell) with different weight fractions (5, 10, 15)% and with a particle size of(75)µm. The study included some mechanical properties represented by tensile strength, hardness, impact and modulus of elasticity as well as thermal conductivity. The results demonstrated an improvement in the mechanical properties of several of the proportions studied, as well as single and hybrid materials. As for thermal conductivity, Thermal conductivity values decreased for both single and hybrid composites, as well as all proportions. This is due to the insulating properties of reinforced materials.

Keywords: mechanical properties, tensile strength, hardness, impact and modulus of elasticity

INTRODUCTION

Wood-based renewable composites have received a lot of interest in recent years, both scientifically and commercially, because of its lightweight, eco-friendliness, and low cost, as well as global environmental consciousness. Natural fibers are regarded possible alternatives to glass or carbon fibers in fiber-reinforced thermoplastic composites because of their environmental friendliness, recyclability, biodegradability, and inexpensive cost when compared to mineral fillers [1]. Although wood has many benefits, there are certain drawbacks that must be considered when using wood. As a building material, these drawbacks can be summarized as: It visibly expands and contracts in response to air humidity, and the substance does not cease. At this point, even high humidity causes decomposition and rot, as well as breakdown over time by bacteria, while insects induce erosion and degradation. This is in addition Its ability to combust It can be said that these disadvantages are considered negative Home to work on The properties of wood vary Technology such as stabilization of wood against moisture and wood working plastic [2]. The importance of particle-supported polymeric materials has led scientists and researchers to conduct numerous investigations and research. In 2018, Mohammed Al-Saadi and colleagues studied the effect of pistachio husks on the mechanical properties of polyester matrix. It obtained the highest tensile, flexural, and impact strength by distributing pistachio husk particles in the polymer matrix.[3] In 2021, researchers Yahya Hısman Celik and colleagues studied the effect of hazelnut shells, pistachio skins, and Apricot kernel peel on unsaturated polyester composites. It was discovered that adding more reinforcements to polyester increases its compressive strength, stiffness, specific weight, and thermal conductivity qualities. [4]. In 2012, S. Nitin investigated and applied walnut shell particles reinforced polyester composites with wt.% 0 to 40% to improve mechanical strength and wear characteristics. The particle size of 1.00 mm was attained by employing two sieves, 0.5 mm and 1 mm, in succession. According to studies, when the percentage of walnut shell particles increases, the density falls. Porosity/voids would be present, which decreases the density because no pressure was exerted. [5].

Technologies and Materials for Renewable Energy, Environment and Sustainability
AIP Conf. Proc. 3321, 030006-1–030006-8; https://doi.org/10.1063/5.0289906
Published under an exclusive license by AIP Publishing. 978-0-7354-5231-2/$30.00

Meysam Zahedi et al. investigated the properties of walnut shell/PP composites and compared them with wood flour/PP composites. The effects of organo-montmorillonite (OMMT, 0, 3 and 5 wt.%) as a reinforcing agent and MAPP as a coupling agent (4 and 6 wt.%) on mechanical and physical properties were also studied. Composites are created by melting and then hot pressing. The resultant composites had acceptable and equivalent qualities to wood flour properties, and the greatest improvement in mechanical properties was achieved at 3% organoclay loading and 6% MAPP [6].

Polyester is a synthetic textile made from coal, air, water, and petroleum. It is used in a variety of goods, including apparel, home furnishings, industrial fabrics, computer and recording tapes, car bumpers, and electrical insulation. Polyester offers various advantages over conventional materials like cotton. Polyester is the ideal fabric for applying water-, soil-, and fire-resistant treatments since it absorbs oil but not moisture [7]. However, polyester has some drawbacks, such as excessive thermal expansion, poor weathering resistance, susceptibility to stress cracking, difficulty bonding and poor temperature capability, low tensile strength, and brittleness. These constraints can be addressed by including natural fiber into the product during manufacture. This would improve its qualities including impact strength, flexural strength, tensile strength and hardness, and water adsorption property [8]. Natural fibers such as sisal, coir, jute, ramie, pineapple leaf, and banana leaf fiber have been promoted as alternatives to glass or other traditional reinforcement materials in composites. Natural fiber is appealing because of its environmental benefits, such as abundance, low cost, low density, bio compatibility, flexibility during processing, low health risk, availability, and flexural high modulus [9].The research goal is to create and investigate the mechanical and thermal properties of unsaturated polyester single and hybrid composites reinforced with sawdust and walnut shells.

EXPERIMENTAL MATERIALS AND METHODS:

In this investigation, polyester was employed Saudi saturator produced by the industrial Resins Company Ltd. as a basis material in the prepared composite materials. It is a viscous liquid with good properties as it is made. Oligomers are low-molecular-weight polymers. Therefore, this material can be converted into an oligomer .The solid state when it is solidified by adding the solidifying material (Methyl ethyl ketone peroxide) type (Hardener) It is a liquid substance with a light consistency and a transparent color (MEKP).It is added to the resin at a weight rate of (2%), noting that These solidification reactions occur at room temperature. As for the reinforcement materials used in the research, they are powders from agricultural waste, represented by sawdust wood, in addition to powder from walnut shells, whose particle sizes were measured using a sieving analysis, where the particle size was 75µm. Composites were prepared from polyester and agricultural waste powders by (Hand lay – up molding technique) according to the following steps:

A Preparing a special mold made of galvanized iron with dimensions 10x10x1)cm3 for the casting process, which is cleaned properly (Flour after the conditioning process, then followed by a drying process, to complete Later, apply Vaseline to prevent adhesion .The resin is applied to the mold in an attempt to facilitate the extraction process Castings after the solidification process is completed.

B Collecting wood industry waste and walnut shells in all their shapes and sizes, then crushing these wastes, then sifting them through a mesh sieve, passing through granules with a grain size of (75 µm). On the other hand, the coarse parts are broken into small parts. Using an electric grinding machine enables us to smooth it to Required granular size. Sawdust and walnut shell powders are dried in an electric dryer at temperature (50) Cº for the purpose of removing moisture and to ensure that a separating surface does not form between base material and support material.

C Weigh the amount of unsaturated polyester and the material Hardened with a weight percentage of (2%) per (100) gm. of unsaturated polyester and thus mix these materials Weighed in a plastic container using a glass rod Gradually followed by mechanical mixing process Electric mixer. During the mechanical mixing process Pour small amounts of the cementing material gradually to prevent clumping non-homogeneous, where the mixing process continues in this manner until all the powder used in it is exhausted The mixture usually takes about three minutes. Therefore, the mixture of unsaturated polyester with the hardener The reinforcement materials resulting from the mixing process are placed in the prepared meld Prepare slowly until it fills, then leave these castings for (24) hours at room temperature. The casting is then taken from the mild and heated in an oven for two hours at a temperature of to increase crosslinking. Following that, the casting (50) Cº s are cut according to the standard specifications for the tests that will be conducted.

EXPERIMENTAL TEST

A Impact Test: Charpy impact experiment equipment manufactured by testing machines in Amityville, New York, was used to test the performance of the prepared samples. The instrument's major components are the pendulum and the energy normal gauge.

The Charpy impact test consists of a standard test portion that fractures during one flow of the hammer swing. The instrument's performance is obtained by raising the hammer to its highest point, securing it in place, and introducing the samples.

Swing motion turns potential energy to kinetic energy, however the amount in broken samples is underestimated. As a result, the quantity of broken energy will be displayed on an indication scale, and the sample impact strength will be calculated using the relation (1). [10].

$$I.S = U/A \ (KJ/m^2) \quad (1).$$

Where: I.S, the impact strength, U, the energy fracture (kilojoules) , A : the cross-section area Measured by (m2).

B Tensile Test: The method used to determine the tensile strength of the sample was in accordance with ASTMD 3039-76 specifications.

A universal testing machine was utilized to conduct the test at a loading rate of 10 mm/min, and the highest load was recorded to determine the tensile strength of the neat polyester and composite samples. During the initial stage of the test, the specimen experienced elongation and the specimen resistance increased, which was detected by a load cell. This value was recorded until the specimen ruptured [12].

C *Thermal Conductivity:* The method used in this study to calculate the factor thermal conductivity of all samples is (Disk Lee). This method is dependent on specific equations.

$$Q = -K \ dT/dx \quad (2)$$

dT/dx: heat grade in (^{o} C/ m), The symbol indicates the movement of heat from high to low temperatures.

The following equations can be used to calculate the quantity of thermal conductivity [13].

$$k[T_B - T_A/d_s] = e[T_A + 2/r(d_A + 1/4d_s)T_A + 1/2rd_sT_B] \quad (3)$$

$$IV = \pi r^2 e(T_A + T_B) + 2\pi re[d_A T_A + d_s(T_A + T_B/2) + d_B T_B + d_c T_c] \quad (4)$$

When (e) represents the quantity of heat energy transient by disc material space the unit per second, unit (w/m2^{o}C).

I: denoted a current pass through convector coil.

TA, TB, TC, represent heat for disc A, B, C. (^{o}C).

ds: the thickness for samples(mm).

RESULTS AND DISCUSSION

Impact Strength: The impact test is very important and therefore it is possible to calculate the absorbed energy required for destruction. The sample fraction is used in research, as this value is given directly from the pen device, which can be calculated from the equation (1).

Due to its fragility, unsaturated polyester is usually considered unsuitable for use in composite materials. However, by incorporating agricultural waste powders to reinforce both single and hybrid composite samples, we observed significant improvements in the results, as depicted in Figures (1,2), which shows the relationship between impact strength and the weight fractions of sawdust powder and walnut shell, which represents the single composite material (Up+ sawdust).

An increase in the impact strength value, as the highest value reached (0.4 KJ/m2) for percentage 15% compared to the pure polyester sample, which reached (0.25K J/m2).

For the hybrid composite sample (Up + sawdust + walnut shell), the 10% sample had the highest impact strength value, reaching (0.35 KJ/ m2) compared to the pure sample.

This is due to the increased impact strength of the single and hybrid composite materials due to the small size of sawdust and walnut shell powders which enables it to spread well within the matrix material and thus has the ability to resist impact and thus increase the durability of the impact, and this is consistent with what the researcher reported [14,15] .

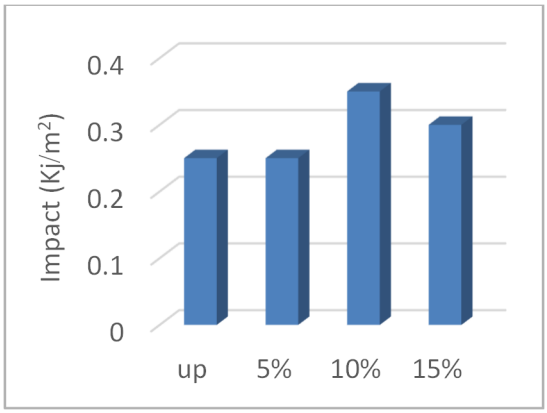

Figure 1. represents the relationship between impact strength and the weight fraction of the single composite material (Up+ sawdust).

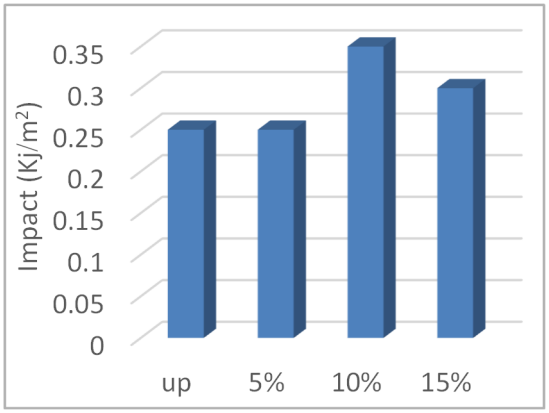

Figure 2. represents the relationship between impact strength and the weight fraction of the hybrid composite material (Up+ sawdust + walnut shell).

Mount of stress that a material can withstand before breaking, cracking, becoming distorted, or otherwise failing.Representation of Figures(3, 4): The relationship between stress and strain for single and hybrid composites of unsaturated polyester .Figure (5) shows the maximum strength values for unsaturated polyester and its single and hybrid composites .From the curve that describes the relationship between maximum strength and the weight fraction used for both single and hybrid composites of unsaturated polyester, the figure shows that there is a variation in the values of tensile strength, as it is noted that the highest value of tensile strength for the single composite materials was for the percentage of 10%, reaching (42 Mpa) compared to the sample For the pure polyester sample, it reached(50 Mpa). As for the hybrid composites materials, the highest tensile strength value reached (68 Mpa) compared to the pure polyester sample, the reason can be attributed to the increase in tensile strength for the single and hybrid samples, The sawdust and walnut shell form a strong interfacial connection with the polyester matrix. The increase in tensile strength caused by the integration of wood sawdust and walnut shell is due to the intrinsic adhesion of the wood sawdust, walnut shell, and matrix interface. This adherence allows good stress transmission from the polymer matrix to the particles during stressing, resulting in an increase in tensile strength up to the optimal levels. [16]. The rise in tensile strength with an increase in the wood sawdust weight percent demonstrates that the inclusion of the wood sawdust and walnut shell into the matrix provides efficient reinforcing [17].

The reason for the decrease in tensile strength observed in samples of alone and hybrid composite materials could be because of large stress concentration points caused by filler molecule agglomeration and polymer removal in the interphase, which exacerbates the problem by creating stress concentration points, and weak interfacial bonding that results in areas of The smaller ones split somewhat between the polymer matrix, walnut shell, and sawdust. [18].

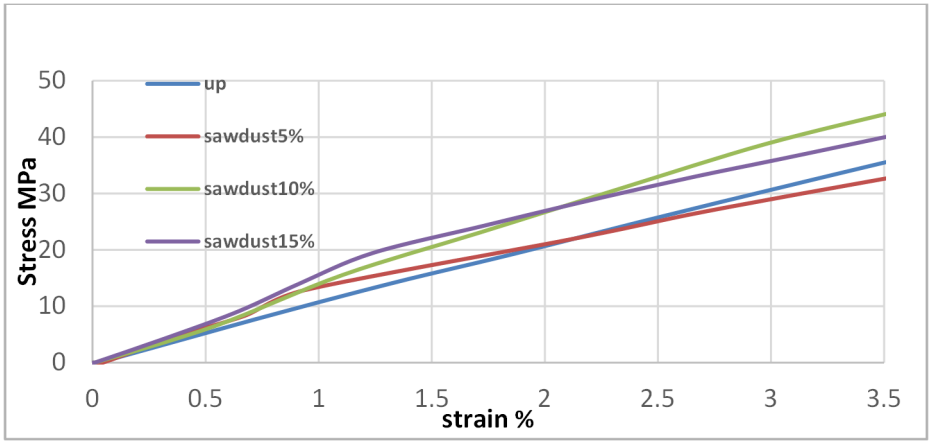

Figure 3. represents the relationship between stress - strain for the single composite material (Up+ sawdust) for all weight fractions

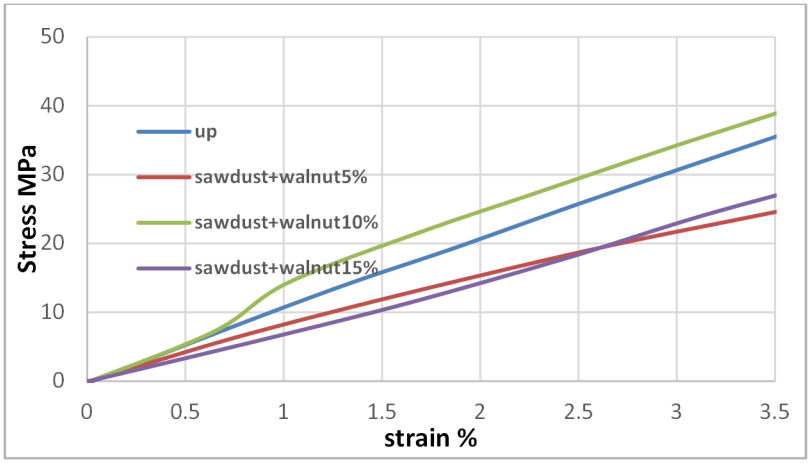

Figure 4. represents the relationship between stress - strain for the single composite material (Up+ sawdust + walnut) for all weight fractions.

Figures (6) shows the relationship between the tensile modulus of elasticity and the weight percentages for both the single and hybrid sample models, where one can notice the variation in the elastic modulus values for both the single and hybrid samples. For the single materials, the highest value of the modulus of elasticity for the sample with a concentration of 10% was (11.739) Mpa compared to the the elasticity of the pure polyester sample reached (9.7425) Mpa, and for the hybrid composite materials, the highest value of the modulus of elasticity reached (10.404) Mpa for the sample with a concentration of 10% compared to the pure polyester sample. The modulus of elasticityIt increases in a non-linear relationship with increasing weight percentages of sawdust powder and walnut shells for both single and hybrid composites the reason for this may be attributed to reducing the movement of particles, which then leads to a reduction in strain, i.e. an increase in the fragility of the polymeric material, as...There are several factors that may affect the elastic modulus values of the composite material, namely, the aggregation or accumulation of fillers the quality of adhesion, elastic properties, and viscosity of the base material [19].

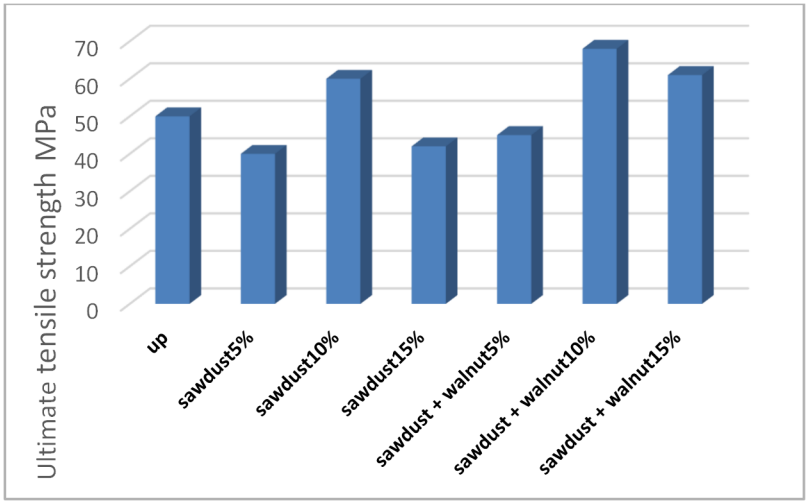

Figure 5. represents the relationship between Ultimate tensile strength and weight fractions of unsaturated polyester and its single and hybrid.

Hardness

Hardness is defined as the material's resistance to penetration or scratching. There are a number of different overall standards to determine the hardness of plastic materials. The utmost common of which is the hardness of the Shore D. The penetration occurs at sluggish rate on the surface of sample through the effects of force, lead to a local creep. After the vanish of the influence force, relatively slow retrieval occurs, which changes the dimensions. Hardness

depends on factors such as particle size, particle content and shape, degree of adhesion between particles and the polymer material, and dispersion of particles within the matrix[20]. From Figure (7,8) which shows the relationship between hardness and weight percentages of sawdust and walnut shell powders for un saturated polyester and alone and hybrid composite material , the figure shows that there is an increase in the hardness value for the single and hybrid composites, as the highest hardness value for the single composite material with a percentage of 10% was (83) compared to the pure polyester material, which is equal to (72). As for the hybrid composite material, the highest value was for the percentage of 5%, amounting to (82) compared to the pure sample. The reason can be attributed to the increase in hardness values for both the single and hybrid composites because of the cohesion strength between the matrix and the reinforcing material as well as the uniform distribution of sawdust and powdered walnut shell between unsaturated polyester resin chains [21].
The increase in hardness values causes the overlap and stack to increase once again, which reduces the movement of polymer molecules and increases the materials' resistance to scratching and plastic deformation. [22].

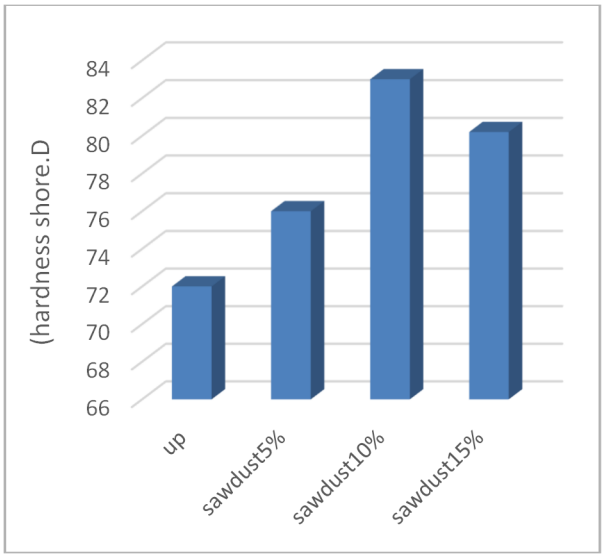

Figure 6. symbolizes the relationship between hardness and weight fractions for unsaturated polyester and alone composite material.

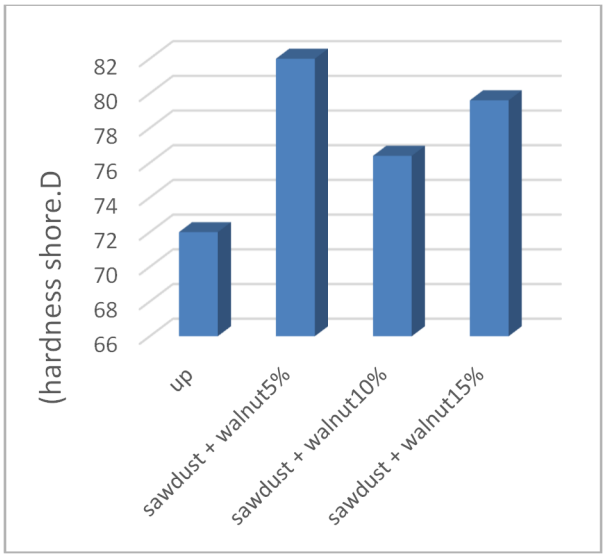

Figure 7. symbolizes the relationship between hardness and weight fractions for unsaturated polyester and hybrid composite material.

Thermal Conductivity

Energy can be transported through heat, which moves from hotter areas to cooler areas using different methods such as conduction, convection, and radiation. Heat can be transferred using one or more of these methods, where conduction and convection are slower than radiation due to the speed of radiation is equal to the speed of light [23,24]. Figures (9,10) displays the correlation between the thermal conductivity and the weight percentage of unsaturated polyester, as well as its single and hybrid composites., it is clear that there is a decrease in the value of the thermal conductivity of unsaturated polyester after reinforcement with agricultural waste powders, walnut shells and sawdust, For both single and hybrid composites, the reason can be attributed to the decrease in thermal conductivity after reinforcement to The increased number of micro-voids present in the composite material is a result of a larger amount of poorly bonded areas between sawdust, walnut shells, and the polymer matrix. When thermal energy is transferred through the matrix material, it does so by the vibratory motion of the atoms. As the atoms reach the interface region, the medium through which they move changes, causing an obstruction to the transition of thermal energy. This leads to a decrease in the values of transmitted thermal energy and a drop in thermal conducting values. [25,26].

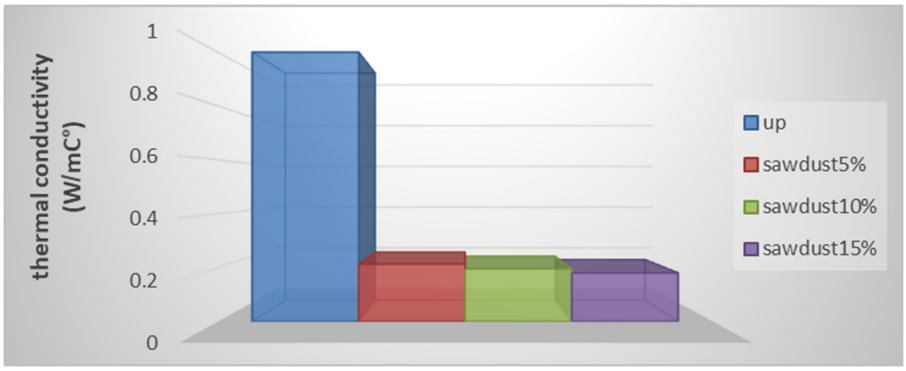

Figure 8. represents the relationship between thermal conductivity and weight fractions for unsaturated polyester and single composite material.

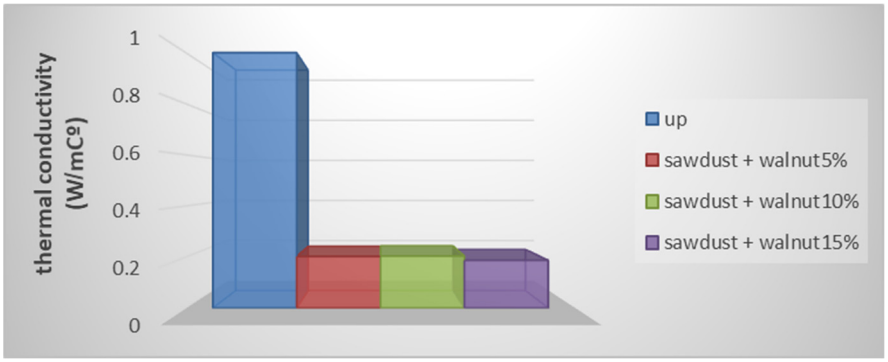

Figure 9. represents the relationship between the thermal conductivity of unsaturated polyester and hybrid composites

CONCLUSIONS

The results obtained from the research show that mechanical properties of both the single composite material and the hybrid material have been enhanced by 10%, as the highest value was reached for the tensile strength, hardness, and modulus of elasticity for the single composite material at this rate. As for the impact test, the highest value was reached at the rate of 15%, and for the hybrid composite material the highest values were reached for the tensile and impact strength, the modulus of elasticity at the same rate was 10%, while for the hardness test, its highest value was at 5%. The research indicated that both the single and hybrid composite materials exhibited reduced thermal conductivity values when analyzed. The reason for this can be attributed to the nature of the reinforced materials (sawdust and walnut shells), as they are insulating materials.

REFERENCES

1. Ashori, A. 2008. Wood–plastic composites as promising green-composites for automotive industries! *Bio resource Technol*. **99**, 4661–4667.
2. Ndiaye, D., Fanton, E., Therias, S., Vidal, L., Tidjani, A. and Gardett ,J. (2008) "Durability of Wood Polymer Composites". Comp. Sci. Tech. 68, 2779–2784.
3. Mohamad Alsaadi1; Ahmet Erkli; Khamis Albu-khaleefah Effect of Pistachio Shell Particle Content on the Mechanical Properties of Polymer Composite, Arabian Journal for Science and Engineering, 2018, 43, 4689–4696, https://doi.org/10.1007/s13369-018-3073-x,.
4. Yahya Hısman Celik; et al, Effects of natural hard-shell particles on physical, chemical, mechanical and thermal properties of composites, Polymers and Polymer Composites, 29 (9S), (2021) S667–S677, DOI: 10.1177/09673911211020717.
5. Chillab, R.K., Jahil, S.S., Wadi, K.M., Jasim, K.A., Shaban, A. H. Fabrication of ge30te 70-xsbx glasses alloys and studying the effect of partial substitution on d.C electrical energy parameters, Key Engineering Materials, 2021, 900, pp. 163–171. https://doi.org/10.4028/www.scientific.net/kem.900.163.

6. Meysam Zahedi, Hossein Khanjanzadeh, Hamidreza Pirayesh and Mohammadali Saadatnia.Utilization of natural montmorillonite modified with dimethyl, dehydrogenated tallow quaternary ammonium salt as reinforcement in almond shell flour–polypropylene bio-Nano composites. Composites Part B Engineering. 2014.
7. Jassim, K.A., Jassim, W.H., Mahdi, S.H., The effect of sunlight on medium density polyethylene Water pipes, Energy Procedia, 2017, 119, pp. 650–655. https://doi.org/10.1016/j.egypro.2017.07.091
8. Mahdi, H.A., Jasim, K.A., Shaban, A.H., Manufacturing and improving the characteristics of the isolation of concrete composites by additive Styrofoam particulate, Energy Procedia, 2019, 157, pp. 158–163.
9. Oladele I. O., Daramola O. O., Adewole A. T., Comparative Study of the Reinforcement Efficiency of Cow Bone and Cow Bone Ash in Polyester Matrix Composites for Biomedical Applications, Acta Technica Corviniensis - Bulletin of Engineering, 2014, 4, p. 27-34.
10. Mohammed M. Yahyaa , Suad H. Aleabi " Enhancing Some Mechanical Properties (Compression, Impact, Hardness, Young modulus) and Thermal Conductivity, Diffusion Coefficient of Micro Epoxy Composites" , Ibn Al-Haitham Journal for Pure and Applied Sciences, 2022.
11. Mohammed M. Yahyaa , Suad H. Aleabi , "Comparison between some mechanical (Tensile , wear rate , hardness, Roughness) and thermal conductivity of epoxy Nano and micro-composites ", AIP Conf. Proc. 2769, 020059-1–020059-8; https://doi.org/10.1063/5.0129376 , 2023.
12. Zinah Abdulateef Abbas, and Suad H. Aleabi, " Studying some of mechanical properties (tensile, impact, hardness) and thermal conductivity of polymer blend reinforce by magnesium oxide" , AIP Conference Proceedings 2123, 020036 (2019); https://doi.org/10.1063/1.5116963.
13. Aleabi, S.H., Watan, A.W., Salman, E.M.-T., kareem Jasim A.,Shaban, A.H., Alsaadi, T.M., The study effect of weight fraction on thermal and electrical conductivity for unsaturated polyester composite alone and hybrid, AIP Conference Proceedings, 2018, 1968, 020019.
14. Abed, R. A., Al-sarraf, A. R., ; Al-maamori, M. "Preparation and Study Some of The Mechanical Properties for Wood- Plastic Composites", Journal of Mechanical Engineering Research and Developments ISSN: 1024-1752. 2020,43,4, 01-13.
15. Kadhim, B.B., Risan, R.H., Shaban, A.H., Jasim, K.A., Electrical characteristics of nickel/epoxy - Unsaturated polyester blend nanocomposites, AIP Conference Proceedings, 2019, 2123, 020062.
16. E. Agnantopoulou, V. Tserki, S. Marras, J. Philippou, and C. Panayiotou, “Development of biodegradable composites based on wood waste flour and thermoplastic starch,” Journal of Applied Polymer Science, vol. 126, no. S1, pp. E273–E281, 2012.
17. M. S. Huda, L. T. Drzal, M. Misra, and A. K. Mohanty, “Wood-fiber-reinforced poly (lactic acid) composites: evaluation of the physicomechanical and morphological properties,” Journal of Applied Polymer Science, vol. 102, no. 5, pp. 4856–4869, 2006.
18. M. H. Alzuhairi, K. M. Shabbeb, and S. A. H. Alsaedy, “Heat and chemical treatments for sawdust/UPE composites,” Engineering and Technology Journal, vol. 34, no. 8, pp. 1624–1635, 2016.
19. Suad H. Aleabi,Mahmood Radhi Jobayr, et.al " Properties Evaluation of a Composite of Unsaturated Polyester Resin Reinforced with Mullet ", Solid State Technology ISSN: 0038-111X Vol. 63, No. 1, (2020)
20. Jasim, K.A., Fadhil, R.N., The Effects of micro Aluminum fillers in Epoxy resin on the thermal conductivity, Journal of Physics: Conference Series, 2018, 1003(1), 012082.
21. Shatha H Mahdi et al, “Preparation of unsaturated polyester/Nano ceramic composite and study electric, thermal and mechanical properties”, Iraqi Journal of Physics, 2017,15, 188-201,.https://doi.org/10.30723/ijp.v15i35.67.
22. Suad. H. Aleabi, " The effect of using Al2O3 additives on some mechanical properties of unsaturated polyester", College of Education for Pure Sciences Ibn Al-Haitham, 27.2014.
23. Anwar M. Ahmed , Ebtahag Z. Sulyman, " Improving Mechanical and Thermal Properties for Unsaturated Polyester Resin by Adding Sisal Fibers", College of Basic Education Researchers Journal. ISSN: 7452-1992 Vol. (19), No.(1), (2023).
24. Suad H. Aleabi, " Study of the effect of wear on Unsaturated polyester resin reinforced with rice husk “, Ibn Al-Haitham Journal for Pure and Applied sciences, 2012.
25. Mohammed H. Alzuhairi, KadhumM. Shabbeb, Sally A. Hussain Alsa,edy " Heat and Chemical Treatments for Sawdust/UPE Composites " , Eng. &Tech.Journal, Vol.34,Part (A), No.8,2016.
26. Shihab A. Zaidan; Amani Z. Mohammed, Study the electromechanical Strength Properties for Epoxy Dispersed Silica Powder Composite, Ibn Al-Haitham Journal for Pure and Applied sciences, 2017, 30(1), 339-354.

Manufacturing of high-quality plastic chairs from (unsaturated polyester/ glass fiber) reinforced by nano chicken eggshell particles

Rana Jamal Mizban[a], Widad Hamdi Jassim[b]

Department of physics, College of Education for Pure Science, Ibn-Haitham, University of Baghdad, Baghdad, Iraq

[a] Corresponding author: rana.jamal2104p@ihcoedu.uobaghdad.edu.iq
[b]Widad.h.j@ihcoedu.uobaghdad.edu.iq

Abstract. To manufacture plastic chairs with high mechanical properties and low cost, unsaturated polyester reinforced by glass fibre s with different weight fraction (2.5, 5, 7.5 and 10%) have been used. Unsaturated polyester reinforced by 7.5% of glass fibres was selected as optimal composite according to the improvement in mechanical properties as impact strength, tensile strength, flexural strength and hardness. By adding 7.5% of glass fibres to Unsaturated polyester, it's impact strength will improves by the (~ 148 %), the tensile strength improved by (~ 238 %), the flexural strength improved by (35.79%) and the hardness improved by (5.26%).To a achieved more improvement in tensile strength and flexural strength, chicken eggshells powder with nanoparticles size partials and small amount (1% wt.) was added to (unsaturated polyester / 7.5% glass fibres) composite. Scanning electron microscope (SEM) has been utilized to interpretation the results of Unsaturated Polyester mechanical properties before and after reinforcing by glass fibres and eggshell particles.

Keywords: Unsaturated Polyester, glass fibres, eggshell powder, mechanical properties, Scanning electron microscope.

INTRODUCTION

Unsaturated polyesters is one the most important thermosetting polymers that easily molded and have important applications in many industry's as in painting, aircraft and marine coatings, in Electric field unsaturated polyester used in electrical wires and cables as insulators to insulating high voltages [1].This unsaturated polyester strengthens by different fillers to made a composite with new mechanical and physical properties, the chemical properties of this polymer composite depend on degree of its polymer matrix cross- linking and the reinforcement fillers, also The final composite qualities are influenced by many factors, including the kind and quantity of the materials used, the distribution and orientation of the fibers, the amount of voids present, the nature of the connections between the different components, and the processes of load transmission at the interface between the matrix and filler. These factors have been shown to have a significant impact on the overall performance of the composite [2-5]. The thermal conductivity of a resin matrix is influenced by factors such as the chemical structure of the resin, the kind of fillers used, and the level of bonding between the fillers and the matrix [6, 7]. Unsaturated polyester resin, when reinforced with glass fiber, is being used as a substitute for steel in some applications due to its favorable mechanical qualities. These attributes are influenced by the characteristics of the fiber and matrix, as well as the strength of the bond or adhesion between the fiber and matrix [8]. Polymer /Glass fiber (GF) composites have low weight to high strength ratio, low density and high stiffness; these composites have many applications, such as marine fields and automotive industries. The performance of these composites depending on the kinds of Glass fiber, matrices and glass fiber-polymer matrix interface [9]. The most commonly utilized type of glass fiber that used to reinforce unsaturated polyester to improving physical, mechanical, and electrical properties is the 'E' type of glass fiber [10, 11]. Many researchers have been used different fillers to enhance the mechanical characteristics of pure polyester.

Technologies and Materials for Renewable Energy, Environment and Sustainability
AIP Conf. Proc. 3321, 030007-1–030007-9; https://doi.org/10.1063/5.0289612
Published under an exclusive license by AIP Publishing. 978-0-7354-5231-2/$30.00

S. T. wicaksono in (2019) have been used the calcium carbonate particles with different weight percentages (2.5%, 5%, 7.5%, 10% and 20%) to reinforced (polyester/kenaf) composite, the highest tensile strength (43.38 MPa) was showed for (polyester /kenaf +5 wt.% calcium carbonate) hybrid composite [12].
L. Shin in (2020), examines the mechanical durability of composites made of unsaturated polyester and glass fiber, which are filled with chicken eggshell in different weight percentages ranging from 10 wt.% to 40 wt.%. The results show that the addition of 10 wt.% of eggshell powder increases the tensile strength by 18% and the compressive strength by 30% in the hybrid composite [13].
F. Muhammed in (2022) examines the impact of different sizes and percentages of eggshell particles on the tensile and flexural properties of glass fiber-reinforced epoxy composites. Two sizes of eggshell powder fillers, 53 micrometers and 150 micrometers, were used at loading percentages of 0%, 10%, 25%, and 40% by weight. The optimal loading percentage was found to be 10% for both filler sizes [14].
In this research the mechanical properties of unsaturated polyester that reinforced with glass fibers by different weight percentages (2.5,5,7.5 and 10) wt.% have been investigated, the best weight percentage of class fibers has been selected based on the optimal values of impact strength, tensile strength, hardness, and flexural strength chicken eggshells powder with small weight (1%) was used to reinforce the best (Unsaturated polyester/glass fibers) composite to enhance all mechanical properties of this composite.

PREPARATION METHODS

Understand Polyester resin reinforced by E-glass fibres with proportions (2.5, 5, 7.5 and 10 wt.%), the mixtures remain for (24 hours) in silicone meld that prepared with dimensions according to mechanical test that carried out on samples. Chicken eggshells powder with low weight ratio (1%) and density of (1.85 gm/ cm^3) was mixed with the optimal (UPE/ E-glass fibres) composite based on the superior mechanical qualities such as impact, tensile, and flexural strength, as well as the enhancement in hardness measured by shore (D) of the composite.

Measurements

Mechanical test

Impact Test

An impact test was conducted on composites made of unsaturated polyester and glass fiber, as well as on hybrid composites made of unsaturated polyester, glass fiber, and nano eggshell fillers. The test was done using a Charpy impact instrument, following the international standard ISO-179.

Tensile Test

Tensile test was carried out on samples at room temperature using microcomputer controlled electronic universal testing machine (WDW-200E) made in China, this test carried out on samples that casting according to (ASTM D-368).

Flexural Test

To ascertain the flexural strength of composites made from unsaturated polyester and glass fibers and (unsaturated polyester/ glass fibre+ nano eggshell fillers) hybrid composite, three-point bending test was carried out on samples that casting according to (ASTM-D790).

Hardness Shore (D)

hardness test was performed on the composites using the device (TH2IO, Italy). Five measurements of hardness have been taken at different positions on composite surfaces to get the average hardness value.

RESULTS AND DISCUSSION

Impact test

Figure 1 shows the variation of impact strength values of the unsaturated polyester that reinforced with glass fibre by the weight percentages (2.5, 5, 7.5 and 10 wt.%). It was found that the impact strength increases by increasing the glass fibre content [2]. the impact strength values vary from lower value (8.74 MPa) for pure unsaturated polyester reaching to higher value (21.68 MPa) for unsaturated polyester reinforced with 7.5% glass fibres, this because, the good interconnection between glass fibres and unsaturated polyester and also because the glass fibers will bear the majority of the impact energy, which is consistent with our findings [4].

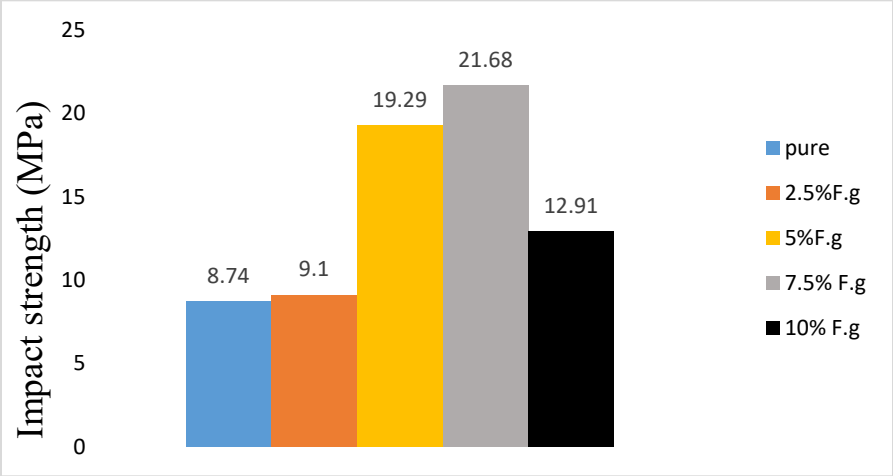

Figure 1. The effect of glass fibre content on impact strength of unsaturated polyester

Figure 2 shows that pure unsaturated polyester have lower impact strength (8.74 MPa), but the impact strength values will increase to (10.33 MPa) by adding eggshells powder with small weight percentage (1 wt.%) and increase to higher value (21.64 MPa) for (UPE/ 7.5 glass fibres /1 wt.% eggshell powder) hybrid composite, this is because the presence of nano eggshell particles which leads to a strong the bonding between the unsaturated polyester and the glass fibres, also, the uniformly shaped of eggshell particles will leading to decreases in stress concentration of the unsaturated polyester, these results are agreed with the research's [15, 16].

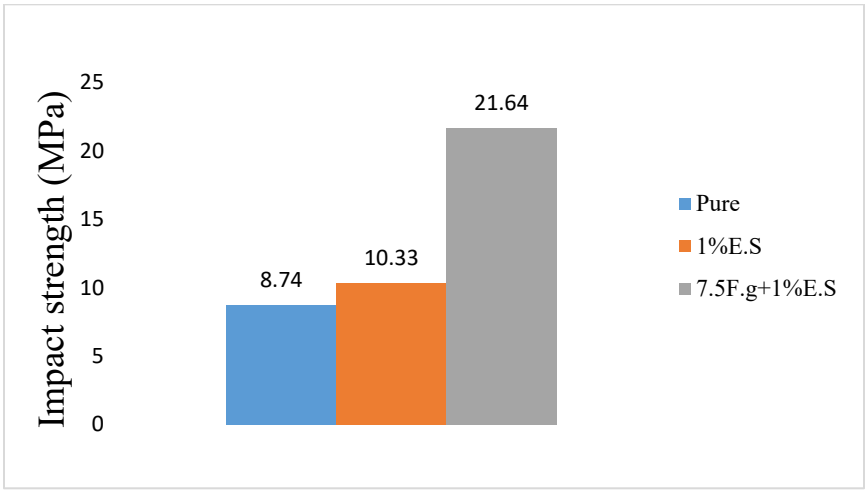

Figure 2: The comparative in impact strength values of unsaturated polyester

Tensile test

Figure 3 demonstrates a significant increase in tensile strength, from 7.698 MPa for pure unsaturated polyester, to 26.06 MPa for the composite material with a glass fiber percentage of 7.5 wt.%. This improvement can be attributed to the strong interfacial bonding between the matrix and reinforcement, where the glass fibers bear the majority of the applied loads. Furthermore, the inclusion of a higher proportion of fibers will result in an increase in the tensile strength. These fibers will be evenly distributed across a larger surface area inside the composite matrix [13]. The addition of 10 wt.% of glass fibers to the composite resulted in a decrease in tensile strength (8.14MPa). This might be attributed to the poor transfer of the load from the matrix to the fibers via the interface area.

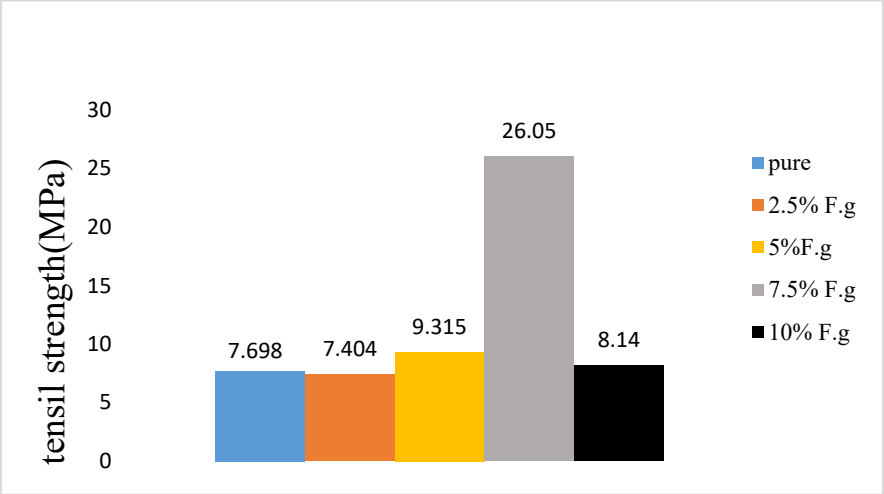

Figure 3: Tensile strength values of unsaturated polyester reinforced by glass fibres with different weight percentages

Figure 4 shows that with addition of eggshell powder in unsaturated polyester, the impact strength is increased to (14.58 MPa) this indication of change in properties of unsaturated polyester; from brittle to tough, similar findings were reported by [16].

The hybrid composite (UPE/7.5% glass fibres +1%E.S) have the highest tensile strength, this may due to the presence of glass fibres and eggshell particles in unsaturated polyester matrix which gives the hybrid composite (UPE/7.5% glass fibres +1%E.S) the ability of carrying the external stress from the unsaturated polyester matrix to glass fibres and eggshell powder, this results good agreements with [15, 16].

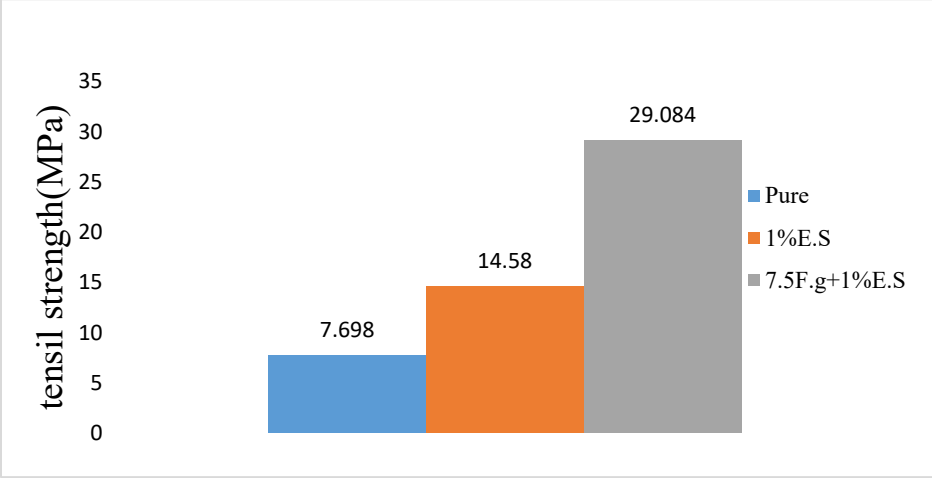

Figure 4: Tensile strength values of unsaturated polyester and there composites

Flexural test

Figure 5 the flexural strength values of glass fibres reinforced unsaturated polyester composites in different weight percentages of glass fibres (0%, 2.5%, 5%, 7.5% and 10% step 2.5%) was presented, the flexural strength varied from (63.4MPa) to (47 MPa) with glass fibres that varied from (0 wt.%) to (10 wt.%), the maximum value of flexural strength reached to (86.14MPa) at the glass fibres percentage (7.5 wt.%).

The Unsaturated polyester is brittle; therefore, its bending strength value was low before adding the glass fibres, but after loadings the glass fibres with optimal ratio in unsaturated polyester the bending strength will be increased to higher value, this because the high elasticity of glass fibres in this fixed ratio which helps to carrying a large number of externals loads, these results agreed with [4, 17].

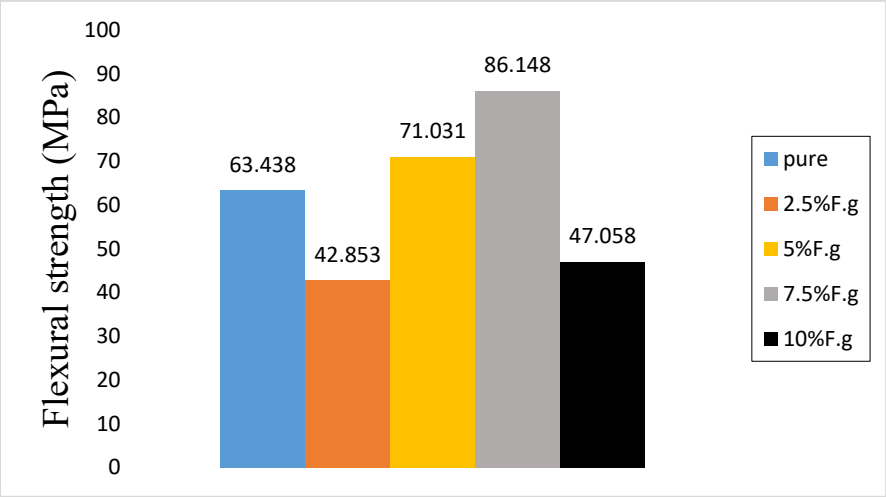

Figure 5: Flexural strength values of unsaturated polyester reinforced by glass fibres with different weight percentages

To increase the improvement in flexural strength of (unsaturated polyester/ 7.5% glass fibres) hybrid composite , eggshells powder with small weight percentage (1 wt.%) was added, Figure 6 presents the flexural strength of fabricated composite (unsaturated polyester/ 7.5%% glass fibres +1% eggshell powder) composite increased to (93.797 MPa), this improvement may be due the good diffusion of the nanoparticles of eggshell powder in matrix of (unsaturated polyester/7.5% glass fibres) composite, which leads to carrying more external bending stress on this hybrid composite.

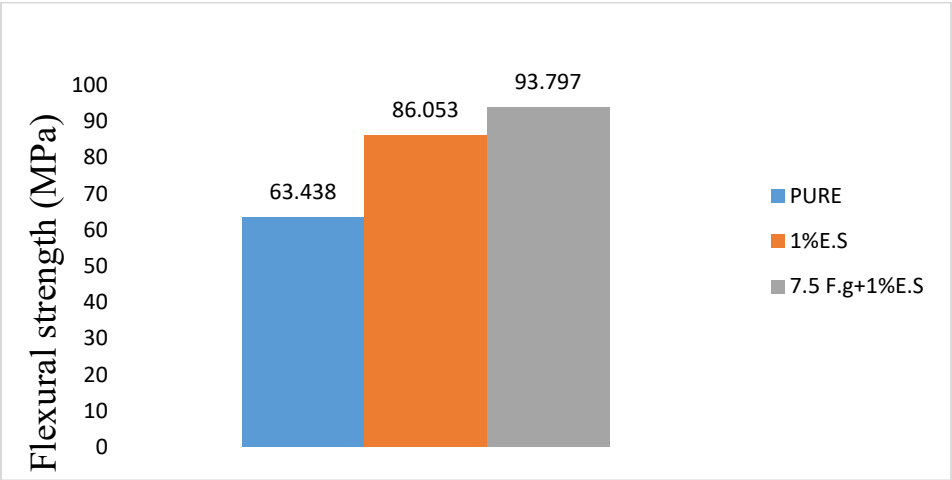

Figure 6: flexural strength values of unsaturated polyester and their composites

Hardness shore (D)

The hardness values of the (unsaturated polyester/ glass fibres) composite is shown in the Figure 7. The addition of glass fibres improves the hardness values of brittle unsaturated polyester ,this due to the highest level of hardness values of glass fibres as compared to pure unsaturated polyester resin and the bonding between the unsaturated polyester and glass fibres leading to the restricting in the movement of the unsaturated polyester chains towards the external stress that is applied on the composite [18], hardness values increase with increasing glass fibres content in unsaturated polyester, this because the glass fibres distribution in matrix resin, which decrease the penetration of the composite surface [4]. The hardness shore (D) value improved from (82.23) for pure unsaturated polyester to higher value (86.56) for (UPE/ 7.5% glass fibres) composite because the compatibility between glass fibres and unsaturated polyester, these results agree with [2].

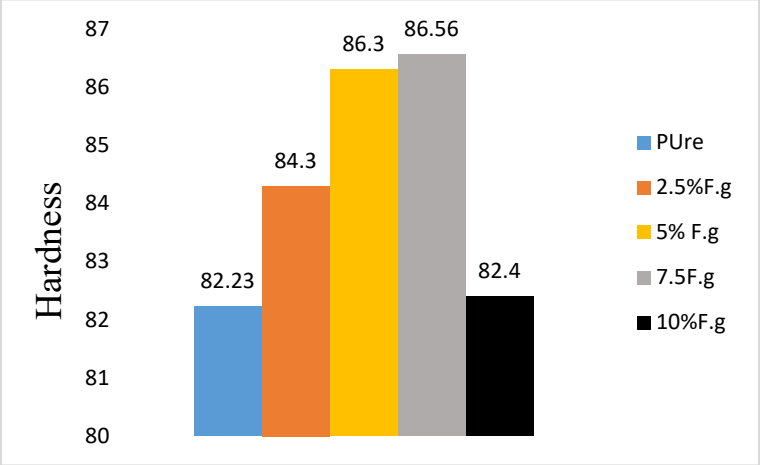

Figure 7: Hardness values of unsaturated polyester reinforced by glass fibres with different weight percentages.

Figure 8 shows the hardness value of pure unsaturated polyester (82.23) that increased to (83.83) by adding eggshells powder with small weight percentage (1 wt.%) to unsaturated polyester, and slightly achievements in hardness value (83.86) can be get by adding this ratio of eggshells powder to (Unsaturated Polyester/ 7.5% glass fibres) composite, this may due good dispersion of nano particles eggshell between the matrix chains and glass fibres.

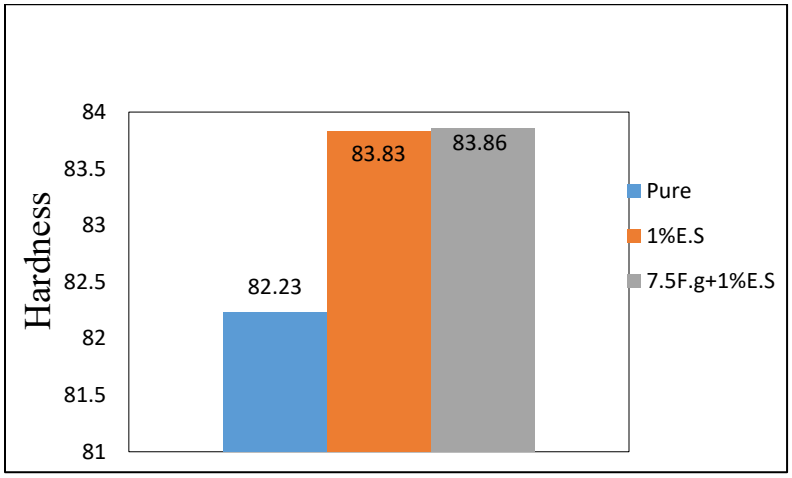

Figure 8: Hardness values of unsaturated polyester and their composites

Surface Morphology

The interpretation of Scanning electron microscopy (SEM) is very important in fabrication of composite, Figures 9 to 11 show the Scanning electron microscope (SEM) of the fractured surfaces of pure unsaturated polyester, (unsaturated

polyester/ 1 wt.% eggshell powder) composite and (unsaturated polyester/ 1% eggshell powder+7.5% glass fibres) hybrid composite with three magnification forces (50, 100 and 150%).
Figure 9 shows the cracks in unsaturated polyester surface, this because the brittleness of this resin. Figure 10 shows small fragments of eggshell particles in resin matrix that causes the compatibility between the eggshell powders and the resin matrix, and indicate good adhesion between eggshell powder and resin matrix.
Figure 11 shows the dispersion of eggshell particles in the cavities between the resin matrix and reinforced glass fibres, which leads to higher mechanical properties of the (unsaturated polyester/ 1% eggshell powder+7.5% glass fibres) hybrid composite, these results agreed with research [19-25].

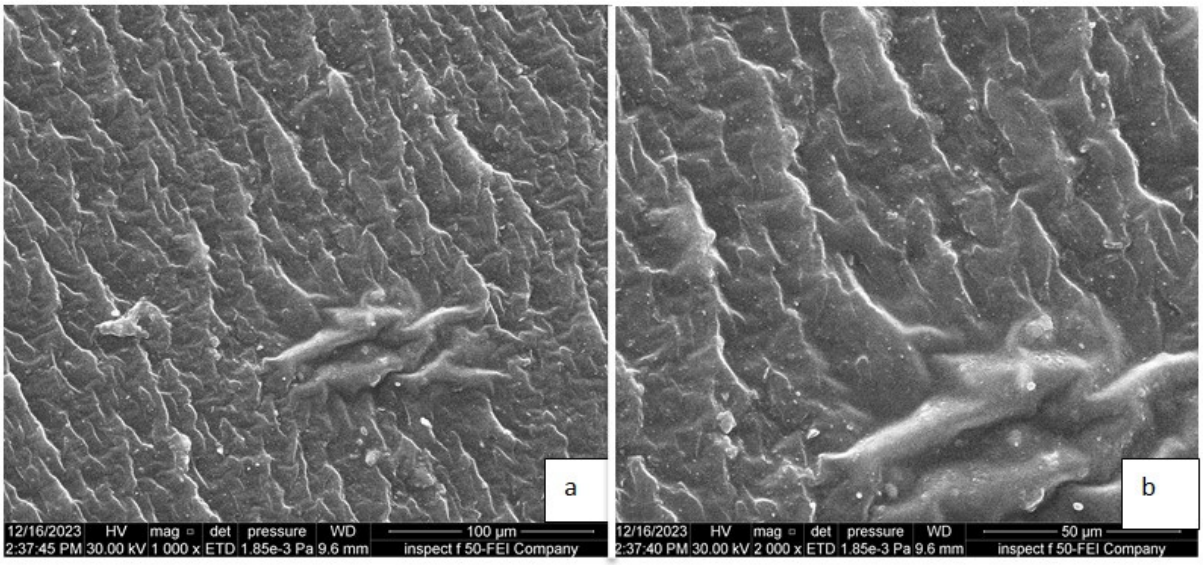

Figure 9: SEM micrographs of pure unsaturated polyester with force magnification a) 1000x b) 2000x

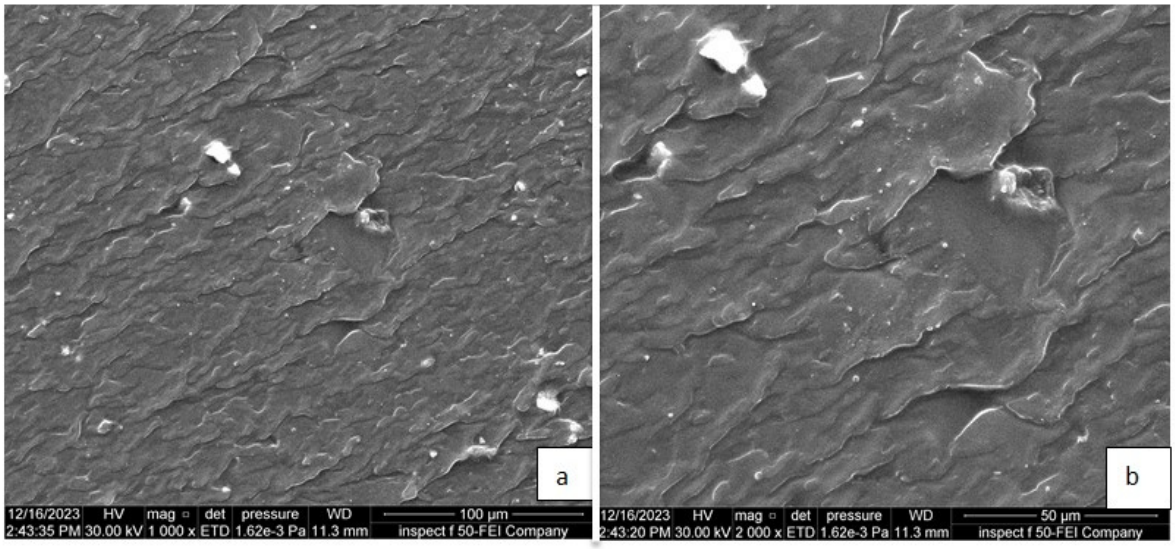

Figure 10: SEM micrographs of (UPE/ eggshell) with force magnification a) 1000x b) 2000x

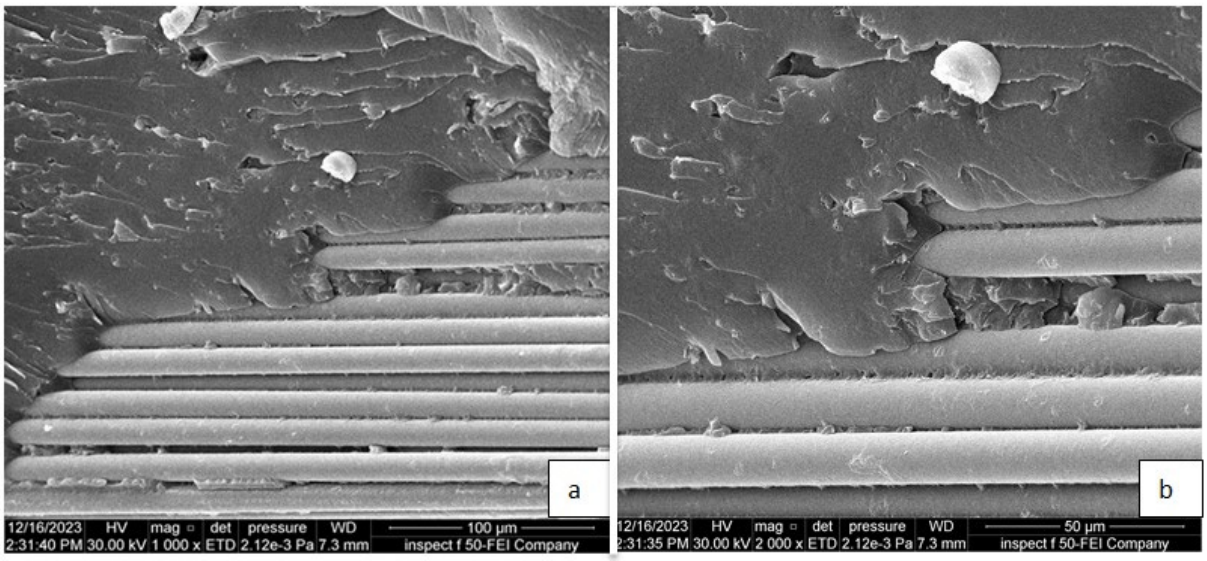

Figure 11: SEM micrographs of (UPE/ glass fibres + eggshell powder) with force magnification a) 1000x b) 2000x

CONCLUSIONS

Unsaturated polyester resin has lower value of impact strengths, before reinforcement with (E-chopped glass fibres), where the presence of glass fibres needs more absorbent energy for the fracture. The improvement was achieved in impact strength, tensile strength, flexural strength and hardness by adding (7.5% glass fibres) to unsaturated polyester resin. Adding of small amount (1 wt.%) of eggshells powder to glass fibres in resin matrix has a positive effect on the impact strength, tensile strength, flexural strength of unsaturated polyester, thus mean the (UPE/ 7.5% glass fibres /1% eggshell powder) hybrid composite can be used to manufacture plastic chairs with a good performance in service work. (SEM) micrographs shows microstructure of unsaturated polyester before and after reinforcing, these micrographs explain the reasons of the improvement in mechanical properties of the (UPE / 7.5%glass fibres /1% eggshell powder) hybrid composite, where the nano sized eggshell particles with small amounts play a good binding factor between glass fibres and resin matrix.

REFERENCES

1. Mahdie, Sh. H. (2017). Preparation of unsaturated polyester/nano ceramic composite and study electric, thermal and mechanical properties. Iraqi Journal of Physics 15.35, 188-201.
2. Younis, Sudad, Jawad K. Oleiwi, & Reem A. Mohammed. (2018). ome mechanical properties of polymer matrix composites reinforced by nano silica particles and glass fibers. Engineering and Technology Journal 36.12 , 1283-1289.
3. Hameed, H. K., & W. H. Jassim. (2020). Comparison Study of Some Mechanical Properties of Epoxy Composites usinguncarbonized Orange peel and Carbonized Orange peel." IOP Conference Series: Materials Science and Engineering. Vol. 757. No. 1. IOP Publishing.
4. El-Wazery, M. S., M. I. El-Elamy, & S. H. Zoalfakar. (2017) . Mechanical properties of glass fiber reinforced polyester composites. International journal of applied science and engineering 14.3 ,121-131.
5. Jasim, K.A., Fadhil, R.N., The Effects of micro-Aluminium fillers in Epoxy resin on the thermal conductivity, Journal of Physics: Conference Series, 2018, 1003(1), 012082.
6. Hamdi, W. J., & Nadir, F. H., (2018). Preparation of epoxy chicken eggshell composite as thermal insulation." Journal of the Australian Ceramic Society 54.2, 231-235.
7. Jassim, K.A., Jassim, W.H., Mahdi, S.H., The effect of sunlight on medium density polyethylene Water pipes, Energy Procedia, 2017, 119, pp. 650–655. https://doi.org/10.1016/j.egypro.2017.07.091.
8. Elahi, A. H. F., et al. (2014) Study on the mechanical properties of glass fiber reinforced polyester composites. International Conference on Mechanical Industrial and Energy Engineering, vol ICMIEE-PI.
9. Kulkarni, M. B., & Hussein, A. A., (2015). Studies on Thermal and Mechanical Properties of Glass Fiber-Reinforced Unsaturated Polyester/Benzoxazine Composites.

10. Kowshik, Suhas, et al. (2023). Mechanical Properties of Post-Cured Eggshell-Filled Glass-Fibre-Reinforced Polymer Composites." Journal of Composites Science 7.2, 49.
11. Jassim, A. N., & Widad. H. J., (2023). Preparation of Polyester/Micro Eggshell Fillers Composite as Natural Surface Coating." Ibn AL-Haitham Journal for Pure and Applied Sciences 36.1 ,88-99.
12. Wicaksono, S. T., A. H. Laksana, & Hosta A., (2019) . Effect of calcium carbonate on the tensile and density properties of kenaf/polyester hybrid composite." IOP Conference Series: Materials Science and Engineering. Vol. 546. No. 4. IOP Publishing,
13. Shin, Lee Jie, et al. (2020). Tensile and compressive properties of glass fiber-reinforced polymer hybrid composite with eggshell powder. Arabian Journal for Science and Engineering 45, 5783-5791.
14. Muhammad, A. F., et al. (2022). Effect of eggshell fillers on the tensile and flexural properties of glass fiber reinforced polymer composites. Materials Today: Proceedings 66 , 2938-2942.
15. Kadhim, B.B., Risan, R.H., Shaban, A.H., Jasim, K.A., Electrical characteristics of nickel/epoxy - Unsaturated polyester blend nanocomposites, AIP Conference Proceedings, 2019, 2123, 020062.
16. Nayak, S. Y., et al. (2015). Use of egg shell particulate as fillers in e-glass/epoxy composites. Proceedings of international conference on mechanical engineering and industrial automation.
17. Saadon, A.K., Shaban, A.H., Jasim, K.A., Effects of the Ferrits addition on the properties of Polyethylene Terephthalate, Baghdad Science Journal, 2022, 19(1), pp. 208–216.
18. Aleabi, S.H., Watan, A.W., Salman, E.M.-T., kareem Jasim A.,Shaban, A.H., Alsaadi, T.M., The study effect of weight fraction on thermal and electrical conductivity for unsaturated polyester composite alone and hybrid, AIP Conference Proceedings, 2018, 1968, 020019.
19. Adekomaya, O., A. A. Adediran, & K. Adama. (2018). Characterization and morphological properties of glass fiber reinforced epoxy composites fabricated under varying degrees of hand lay-up techniques. Journal of Applied Sciences and Environmental Management 22.1 ,110-114
20. Enneffatia, M., Rasheed, Louatia, M., B., Guidaraa, K., Shihab, S., Barillé R., Investigation of structural, morphology, optical properties and electrical transport conduction of Li0.25Na0.75CdVO4 compound, Journal of Physics: Conference Series, 2021, 1795(1), pp. 012050.
21. Rasheed, M., Mohammed, O. Y., Shihab, S., Al-Adili, A., Explicit Numerical Model of Solar Cells to Determine Current and Voltage, Journal of Physics: Conference Series, 2021, 1795(1), pp. 012043.
22. Rasheed, M., Shihab, S., Alabdali O., Hassan, H. H., Parameters Extraction of a Single-Diode Model of Photovoltaic Cell Using False Position Iterative Method, Journal of Physics: Conference Series, 2021 1879(3), pp. 032113.
23. Rasheed, M., Shihab, S., Mohammed, O. Y., Al-Adili, A., Parameters Estimation of Photovoltaic Model Using Nonlinear Algorithms, Journal of Physics: Conference Series, 2021, 1795(1), pp. 012058.
24. Sarhan, M. A., Shihab, S., Kashem, B. E., Rasheed M., New Exact Operational Shifted Pell Matrices and Their Application in Astrophysics, Journal of Physics: Conference Series, 2021 1879(2), pp. 022122.
25. Shihab, S., Rasheed, M., Alabdali, O., Abdulrahman A. A., A Novel Predictor-Corrector Hally Technique for Determining the Parameters for Nonlinear Solar Cell Equation, Journal of Physics: Conference Series, 2021, 1879(2), pp. 022120.

Investigating air pollution and its relationship to geographic and demographic data in Karbala

Khalid H. Abbas Al-Aarajy [1,a], Kareem Hassan Alwan [2], Mohammed A. Mohammed [1,b], Zainab H. Mohammed Hassan [2] and Kareem A. Jasim [3,c]

[1] *Department of Remote Sensing and GIS, College of Science, University of Baghdad, Lab. of Seismology and Spatial Data Analysis, Baghdad, Iraq*
[2]*Center for Urban and Regional Planning, University of Baghdad, Baghdad, Iraq*
[3]*Department of Physics, College of Education for Pure Science, University of Baghdad, Baghdad, Iraq*

[a] Corresponding author: khaled.h@sc.uobaghdasd.edu.iq
[b] mohammed.a.m@sc.uobaghdad.edu.iq
[c] kareem.a.j@ihcoedu.uobaghdad.edu.iq

Abstract. The purpose of conducting this study in the city of Karbala, specifically on the day of the Arabian visit, is to determine the effect of increasing the concentrations of polluting gases on the health of visitors to the city. This study investigates the changes in the levels of ozone (O3), sulfur dioxide (SO2), and carbon monoxide (CO) in the city of Karbala. These gases are considered among the gases that are believed to threaten human health and cause suffocation and other problems resulting from the increase in their concentration. The Sentinel-5 tropospheric monitoring instrument (Sentinel-5P TROPOMI) was used to find SO2, O3, and CO to monitor local air quality and pollution using relatively high-resolution satellite data and to investigate the relationship between the pollutants and the demographic and geographic information of the study area. Geospatial analyses were performed using demographic data and numerical elevation models and vegetation cover for this purpose. The results showed that the district of Al-Hur showed a greater increase in the concentration of carbon dioxide gas compared to other regions, while the amount of ozone gas increased in the canter of the Karbala region, especially near the road used by tourists traveling from Najaf to Imam. The shrine, while the increase in sulfur dioxide is distributed in each of the districts of Al-Husseinah, Al-Hur and the western strip. The overall conclusions of the study showed that local air quality and pollution levels can be monitored using Sentinel-5P TROPOMI data.

Keywords: concentrations, polluting gases, health, sulfur dioxide and high-resolution satellite data

INTRODUCTION

The problem of air pollution is getting worse as the world's population is growing so quickly. Urbanization, energy use, transportation, and motorization are some of the major contributors to air pollution. Additionally, the environment's quality and people's health are negatively impacted by population increase and exposure to air pollutants [1].

Using satellite-based equipment, the atmosphere's concentration of SO2, O3, and CO can be determined. TROPOMI (TROPO spheric Monitoring Instrument), the only payload on board the Sentinel-5 Precursor (S5P) satellite of the European Space Agency (ESA), was launched in October 2017. Due to its unprecedented spatial resolution (3.5 7 km at the beginning of the mission and 3.5 5.5 km since 6 August 2019) and high signal-to-noise ratio, TROPOMI is expected to revolutionize the way we monitor air pollution from space [2].

At the same time, recent years have seen a significant expansion in the possibilities for remote observations of the status of the atmosphere.

Particularly, several satellites have been put into orbit above the Earth with the primary objective of detecting the vertical distribution of several atmospheric chemicals, such as ozone, nitrogen dioxide, methane, carbon monoxide, water vapor, and aerosols [3].

Technologies and Materials for Renewable Energy, Environment and Sustainability
AIP Conf. Proc. 3321, 030008-1–030008-9; https://doi.org/10.1063/5.0289726
Published under an exclusive license by AIP Publishing. 978-0-7354-5231-2/$30.00

Another gas released by the coal mining industry is CO. CO is a key component in the creation of ground-level ozone (O3) and has a brief atmospheric lifespan (days to a few weeks).

In the atmosphere, CO and OH interact and lower each other's concentrations. Meanwhile, powerful greenhouse gases like methane have a shorter lifetime because of OH radicals. As a result, the decrease in (OH) enhances the indirect global warming potential of these gases [5].

STUDY AREA

study area is located within Karbala city, as it includes all of the sub-districts of Al-Husayniyyah and part of Al-Hur sub-district within the Karbala district, and the sub-districts of Al-Khairat and Al-Jaddol Al-Gharbi within the Al-Hindiyah district, in addition to the canter of the Karbala district, with an area of approximately (1491.048) km2, as it lies between (43.93 - 44.48) longitudes, and latitudes (32.18 - 32.96).

As it passes through the study area three of the main roads used by visitors heading to visit the Arbaeen, so it was necessary to study the air quality within the study area. As for the spatial boundaries of the study, the data were taken on September 17, 2022.

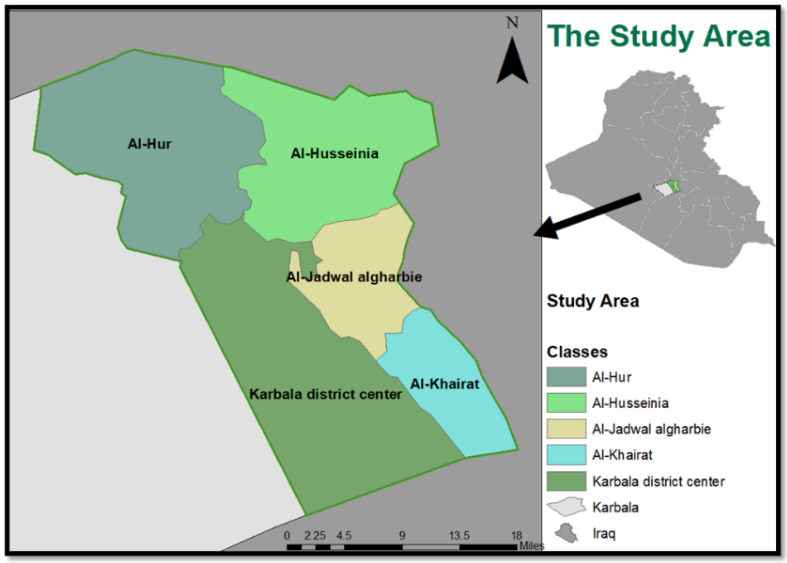

Figure (1): Represent the study area

DATA AND METHODS:

The single payload of the Sentinel-5p spacecraft, which was launched into Low-Earth orbit on October 13, 2017, is TROPOMI, a space-borne spectrometer that covers wavelength bands between the ultraviolet and the shortwave infrared.

It was funded jointly by the Netherlands Space Office and the European Space Agency (ESA). The information is freely available for download via the ESA Copernicus Open Access Hub. [1] The data used in this study from the Sentinel 5 satellite are satellite images that have been processed and corrected by Q GIs and Arc Map software as they provide information on the concentrations of carbon monoxide, sulfur dioxide and ozone gas.

The study area passes through three of the main roads that visitors use to travel from the city limits of Karbala to the shrine of the two Imam.

Several stations distributed along the three roads were chosen to measure the concentration of gases at each station, using spatial analysis tools from Arc Map software to study the distribution and identify areas of high concentration and areas of low concentration, as shown in Table (1). which shows the location of each station and the concentration of those gases in each station.

Table (1) The concentration of gases in stations

Stations	longitude	latitude	SO2 mol/m^2	O3 mol/m2	CO mol/m2
0	44° 2' 19.444" E	32° 37' 16.632" N	-2.6E-05	0.127139	0.034329
1	44° 2' 41.379" E	32° 38' 6.384" N	-0.00056	0.12678	0.034329
2	44° 3' 11.892" E	32° 39' 7.017" N	0.000506	0.125964	0.034329
3	44° 4' 15.096" E	32° 40' 6.714" N	0.000506	0.125964	0.032866
4	44° 5' 7.044" E	32° 41' 0.030" N	0.000506	0.125964	0.032866
5	44° 7' 2.002" E	32° 41' 25.231" N	0.000506	0.125964	0.032866
6	44° 2' 7.822" E	32° 36' 48.351" N	-2.6E-05	0.127139	0.034329
7	44° 3' 27.676" E	32° 36' 21.693" N	-0.00056	0.12678	0.034329
8	44° 6' 47.608" E	32° 35' 57.537" N	-0.00056	0.12678	0.034329
9	44° 8' 37.191" E	32° 35' 13.637" N	0.000329	0.127027	0.034425
10	44° 11' 59.306" E	32° 34' 23.293" N	-1.8E-05	0.127829	0.031757
11	44° 12' 51.884" E	32° 32' 39.966" N	0.000436	0.12822	0.031757
12	44° 16' 1.408" E	32° 32' 36.753" N	0.000436	0.12822	0.031757
13	44° 18' 29.708" E	32° 32' 24.831" N	-7.7E-05	0.127302	0.031757
14	44° 20' 37.038" E	32° 32' 9.351" N	-7.7E-05	0.127302	0.032769
15	44° 1' 51.012" E	32° 35' 40.533" N	-2.6E-05	0.127139	0.034425
16	44° 3' 16.093" E	32° 34' 5.764" N	-0.00071	0.127566	0.034425
17	44° 6' 59.052" E	32° 31' 24.774" N	-0.00071	0.127566	0.033514
18	44° 8' 23.886" E	32° 29' 46.905" N	0.000365	0.127101	0.033514
19	44° 9' 56.021" E	32° 27' 22.140" N	0.000365	0.127101	0.034239
20	44° 11' 8.912" E	32° 25' 28.427" N	-0.00032	0.127942	0.033652
21	44° 13' 12.082" E	32° 22' 39.404" N	0.000626	0.128382	0.031459
22	44° 15' 8.735" E	32° 20' 10.874" N	0.000626	0.128382	0.032276

RESULT AND DISCUSSION

NDVI and UHI of study area **Figures (2, and 3)**

Carbon monoxide (CO)

CO is an odorless and colorless gas that may be emitted from the incomplete incineration of any carbonaceous materials. The major sources of CO are tobacco smoke, gas stoves and pilot lights, wood stoves and fireplaces, and usage of kerosene-fueled vehicles and gasoline engines in general, the movement of automobiles is the most productive source of CO concentration in the air [6].

Figures (4, and 5) show the distribution intensity of carbon monoxide gas within the study area, as well as the distribution along the three roads (Baghdad-Karbala, Babylon-Karbala, Najaf-Karbala) Respectively. Where it is noticed that the concentration of gas increases in the district of Al-Hur, where it reaches the highest value (0.034425) mol/m^2, while the concentration decreases as we go out towards the district of Al-Hussainiya, the western stream, Al-Khayrat and the center of Karbala district, where it witnessed the lowest value (0.031459) mol/m^2.

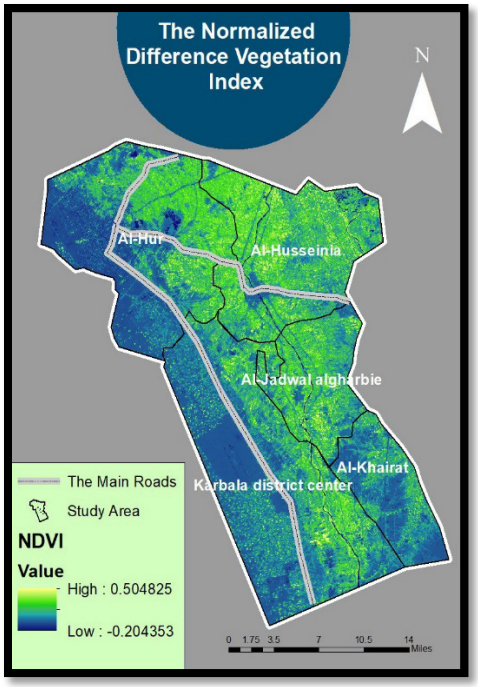

Figure (2) the NDVI of the study area

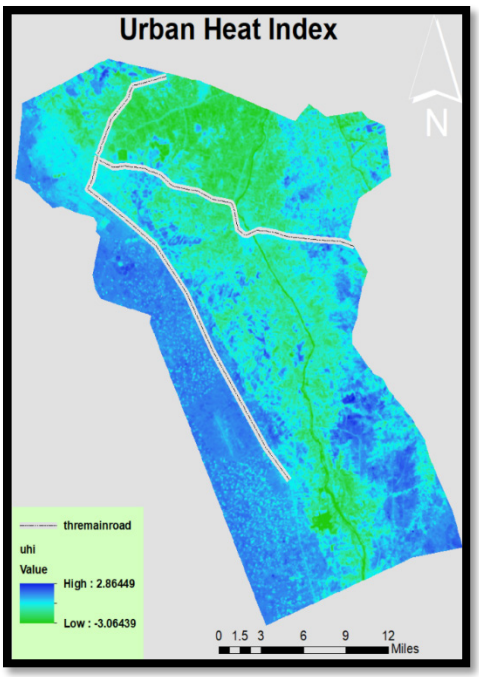

Figure (3) the UHI of the study area

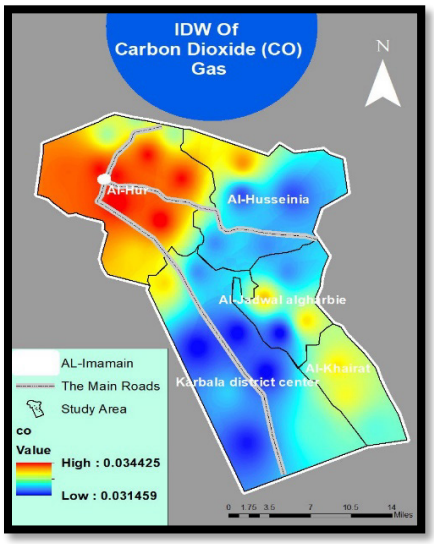

Figure (4) CO concentration of study area

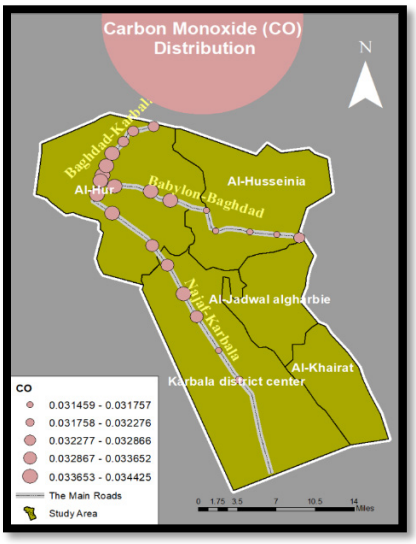

Figure (5) CO concentration of three roads

Ozone gas O_3

O3 is one type of gas that is formed due to photoreaction with existing air pollutants such as oxides of nitrogen (NOx) and volatile organic compounds (VOCs). The 8-hour mean concentration of O3 is 100 µg/m3. At ground level, the O3 is the pollutant in the air that causes severe health effects on the human body[7]. Figure (6,7) shows that the eastern portion of the Al-Hussainiya district and the two sub-districts of Al-Khairat, Al-Jaddol Al-Gharbi, are the areas with the highest concentrations of ozone gas, with a maximum concentration of (0.1 29 141) mol/m2. While the ozone gas concentration falls in Al-Hur and the northern parts of the Al-Husseiniya district, where it achieved the lowest value (0.12538) mol/m2, the gas concentration rises elsewhere.

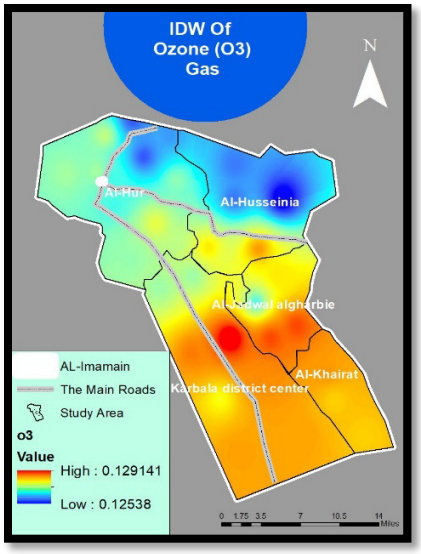

Figure (6) O3 concentration of study area

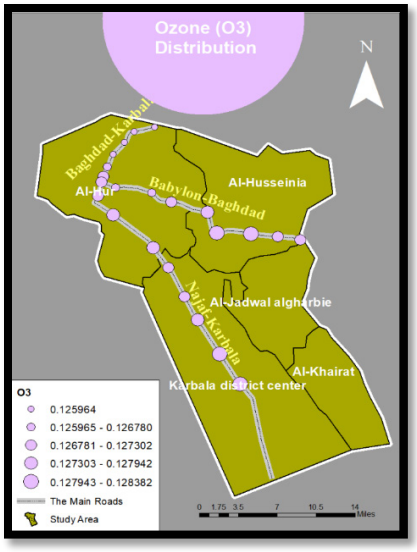

Figure (7) O3 concentration of three roads

Sulfur dioxide SO_2

SO2 is colorless, has a bad odor and is a toxic natural pollutant in the air. The natural source of SO2 in air is due to the action of volcanic activity. The other sources are fossil fuel, coal, oil, diesel, power plants, metals processing industries, smelting facilities and diesel vehicles and SO2 is also released from atmospheric secondary pollutants, such as sulphur aerosols, PM 2.5 and 10. [8]. Figures 8 and 9 show the distribution of sulfur dioxide gas across most of the study area, with the highest concentration occurring in Al-Husayniyyah, Al-Jaddol Al-Gharbi, and the southern part of the Al-Hur area (0.00147697) and the lowest concentration occurring in Al-Khairat and the Central offal-Hur side (0.00105495).

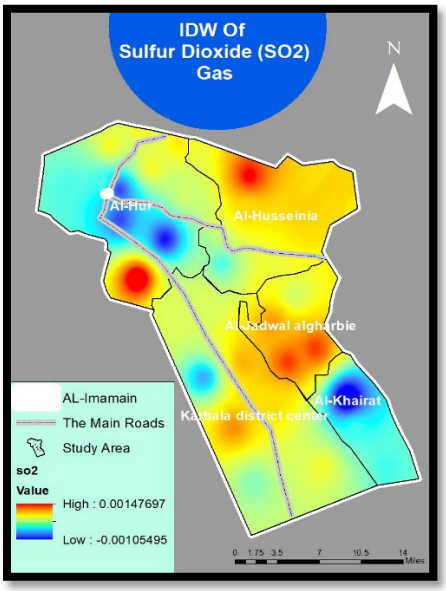

Figure (8) CO concentration of study area

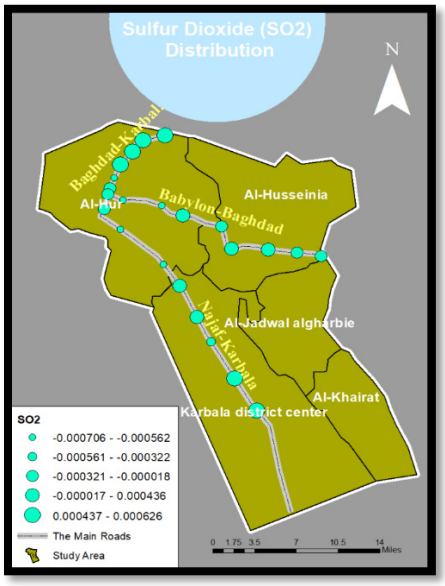

Figure (9) CO concentration of three roads

The mean and standard deviation value

In this study, satellite measurements of the HUI, SO2, CO, and O3 levels were made over the province of Karbala. As a result, the MA of the values derived inside the Karbala province's boundaries and displayed in the Figures above. Based on the results (Figs. 4, 5, 6, 7,8 and 9), it is visually clear that the Karbala metropolis has high mean concentrations of CO, SO2, and O3, but that the distribution of concentrations within the study area is irregular [14, 15]. This irregularity may be caused by the area's built-up areas, population density, and central business district. Table (2) shows the average concentrations of gases and the standard deviation in each of the study areas.

Table (2): Impact of LULC on the UHI, SO_2, CO, and O_3. (MOL/M^2)

Name	Type	MEAN	MAX	MIN	STD
Al-Husseinia	CO	0.032465537	0.033848975	0.031757001	0.0004913
	SO2	0.000562281	0.001202987	-1.80E-05	0.000207113
	O3	0.126709963	0.128219992	0.125380024	0.00063067
	UHI	-0.65412233	2.149443865	-2.81633353	0.829764981
Al-Hur	CO	0.033834	0.034425	0.032321	0.000391
	SO2	0.000159	0.001477	-0.00071	0.000359
	O3	0.12692	0.127616	0.125964	0.000297
	UHI	-0.19978	2.225457	-2.62713	1.012424
Al-Jadwal algharbie	CO	0.032504524	0.033651955	0.031459015	0.000441194
	SO2	0.000681369	0.001089995	0.000313191	0.000187482
	O3	0.127977939	0.128618002	0.126822039	0.000406403
	UHI	-0.271248874	2.611011982	-2.747430563	0.784671817
Al-Khairat	CO	0.03297057	0.03346098	0.0323929	0.00023657
	SO2	-0.0001221	0.00063657	-0.001055	0.00027882
	O3	0.12811463	0.12839732	0.12797099	0.00010421
	UHI	0.79774262	2.86448812	-1.7479323	0.58271136
Karbala district center	CO	0.032187066	0.033513997	0.031459004	0.000429205
	SO2	0.000384749	0.000856984	-0.000287996	0.000198917
	O3	0.128046779	0.129140973	0.127101004	0.000365943
	UHI	0.433524402	2.502089977	-3.064390659	0.888765171

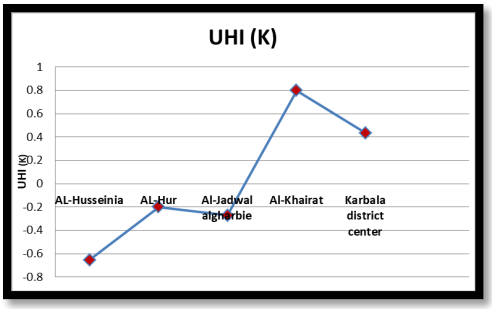

Figure (10) the mean of urban height index

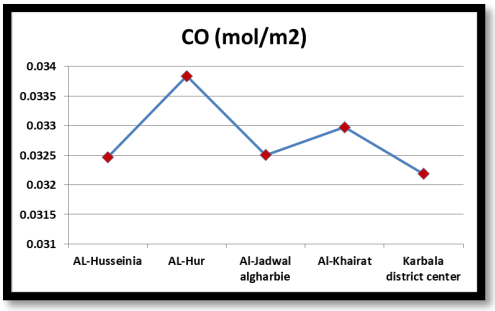

Figure (11) the mean of CO concentration

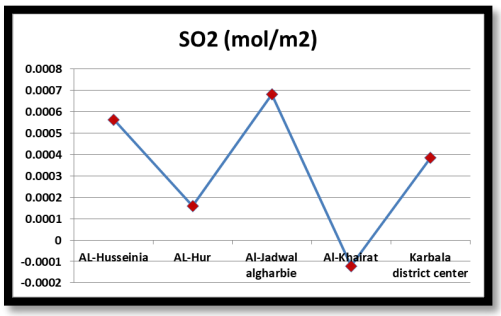

Figure (12) the mean of SO2 concentration

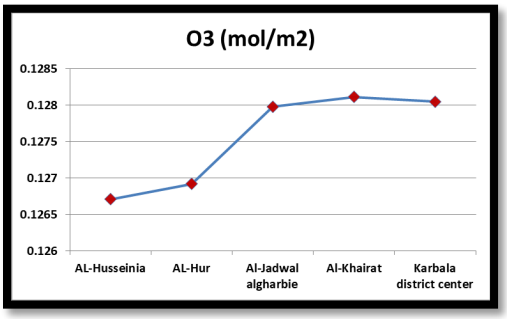

Figure (13) the mean of O3 concentration

Figure (10- 13) shows that the concentration of gases varies from one region to another and at the same region. Because the data was collected on September 17, 2022, the day of the Arbaeen visit, where the areas around the imam are densely populated and here the need for fuel and energy means for cooking and other purposes increases, the district of Al-Hur had the highest concentration of carbon monoxide gas [16, 17], While the least concentration of it was in the center of Karbala district, on the road of visitors coming from Najaf, almost. As for sulfur dioxide gas, the Al-Jadwal algharbie district ranked first with the highest concentration of 0.000681369 mol /m^2, while the Al-Khairat district recorded the lowest concentration among other regions, amounting to 0.0001221 mol/ m^2. While the highest concentration of ozone gas was in the district of Al-Khairat and the lowest concentration of gas in the district of the Al-Husseinia.

Concentration of pollutants in some international countries

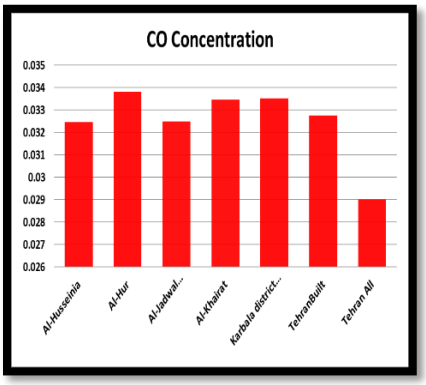

Figure (14) CO concentration on global cities

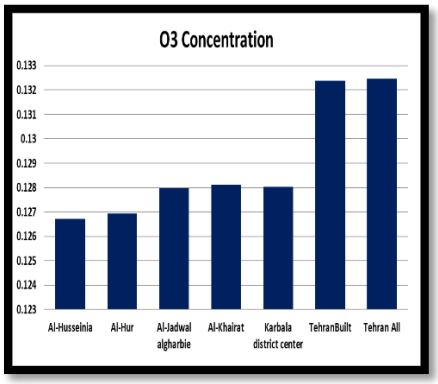

Figure (15) O3 concentration on global cities

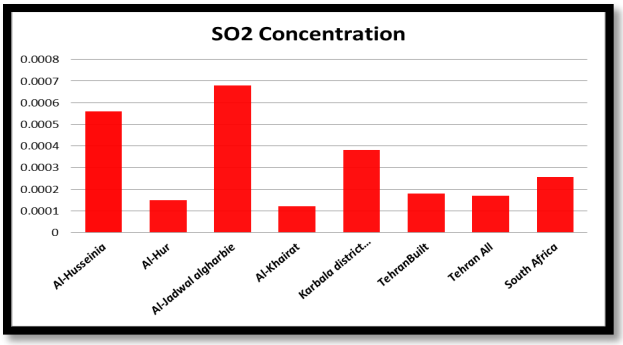

Figure (16) SO2 concentration on global cities

Figure 14 shows that the concentration of CO gas is high compared to the results of the city of Tehran, and the reason is that our data was collected on a day when the city of Karbala was densely populated, so the use of fuel, coal, car smoke, and the like increases from the sources.[9,10] . The results of works in the city of Tehran and South Africa were also taken into consideration to compare the results obtained with the global research that depended on the same satellite. As for ozone gas, see it to be present in great quantities above Tehran's sky due to the city's status as an industrial hub with numerous oil, mining, and other enterprises. Figure 16: The quantities of SO2 show convergence with South Africa and Tehran, except a pronounced increase in each of the western table and Al-Husseiniyah, which we will discuss in the conclusions.

CONCLUSION

Since millions of people visit Karbala on this day for Arbaeen, evidence of the concentration of several pollutants in the air was collected on 9/17/2022, making it necessary to investigate the amounts of such pollutants because they have an impact on human health. The impact of the LULC shift on the makeup of urban air pollution and LST has so far been established. However, the current study's use of remote sensing and GIS recognizes the vital link between the study area's vegetation and LST (which is naturally UHI). Additionally, the research methodology demonstrated that Kerala's city center and the urban region as a whole have the highest average concentrations of CO, SO2, and O3. And so on. Positive connections between CO, O3, and LST show the reciprocal impacts of LST, CO, and O3 values in the Karbala Governorate. The presence of large quantities of O3 gas in the southwestern side of the Karbala district center due to the presence of the Karbala refinery in that area, which in turn affects the area of Al-Hussainiya and the western stream due to the prevailing winds in the region. As for the SO2 foci, they are the result of the gas stations (the Al-Khairat station in the western stream and the Al-Hur station) and the presence of many brick factories in Al-Hussainiya. The overall conclusions of the study showed that local air quality and pollution levels can be monitored using Sentinel-5P TROPOMI data.

REFERENCES

1. Kaplan, G., & Yigit Avdan, Z. (2020). Space-Borne Air Pollution Observation from Sentinel-5P TROPOMI: Relationship Between Pollutants, Geographical and Demographic Data. International Journal of Engineering and Geosciences (IJEG), 5(3), 130-137.
2. Ialongo, I., Virta, H., Eskes, H., Hovila, J., & Douros, J. (2020). Comparison of TROPOMI/Sentinel-5 Precursor NO2 observations with ground-based measurements in Helsinki. Atmospheric Measurement Techniques, 13, 205-218.
3. N. E. (2022). Integral Assessment of Atmospheric Air Quality in the Largest Cities of Russia Based on TROPOMI (Sentinel-5P) Data for 2019–2020. Cosmic Research, 60(Suppl. 1), S57–S68.
4. Huda Jamal Jumaah, Mohammed Hashim Ameen, Shakeel Mahmood & Sarah Jamal Jumaah. (2023). Study of air contamination in Iraq using remotely sensed Data and GIS. Geocarto International, 38(1), 2178518.
5. Trenchev, P., Dimitrova, M., & Avetisyan, D. (2023). Huge CH4, NO2 and CO Emissions from Coal Mines in the Kuznetsk Basin (Russia) Detected by Sentinel-5P. Remote Sensing, 15(6), 1590.
6. Sharma, S., Zhang, M., Anshika, Gao, J., Zhang, H., & Kota, S. H. (2020). Effect of restricted emissions during COVID-19 on air quality in India. Science of The Total Environment, 728, 138878.

7. Zhou, C., Su, F., Pei, T., Zhang, A., Du, Y., Luo, B., Cao, Z., Wang, J., Yuan, W., Zhu, Y., Song, C., Chen, J., Xu, J., Li, F., Ma, T., Jiang, L., Yan, F., Yi, J., Hu, Y., Liao, Y., & Xiao, H. (2020). COVID-19: Challenges to GIS with Big Data. Geography and Sustainability, 1(1), 77–87.
8. Zhu, S., Sun, J., Liu, Y., Lu, M., & Liu, X. (2020). The air quality index trend forecasting based on improved error correction model and data preprocessing for 17 port cities in China. Chemosphere, 252, 126474.
9. Fuladlu, K., & Altan, H. (2021). Examining land surface temperature and relations with the major air pollutants: A remote sensing research in case of Tehran. Urban Climate, 39, 100958.
10. Shikwambana, L., Mhangara, P., & Mbatha, N. (2020). Trend analysis and first time observations of sulphur dioxide and nitrogen dioxide in South Africa using TROPOMI/Sentinel-5 P data. International Journal of Applied Earth Observation and Geoinformation, 91, 102130.
11. Khalid H. Abbas Al-Aarajy, 2023 "Land Surface Temperature investigation of Babylon city between (2002 2022) using Remote Sensing and GIS Technique" , Iraqi Journal of Science, 2023, Vol. 64, No. 12, pp: 6686-6693.
12. Khalid A , Ahmed Z ,2023 "Spectrum Analyzing X-ray Data Image (FITS) Using Ds9 Program" , Journal of Survey in Fisheries Sciences,Vol.10(3S),pp.6512-6521.
13. Khalid H, Ahmed A., Khaleel I, 2024 "Supervised Classification Accuracy Assessment Using Remote Sensing and Geographic Information System", TEM Journal. Vol. 13, , pp. 396-403.
14. Jaafar S. Muhammad1, Kareem A. Jasim, Auday H. Shaban, Determining Heavy Metals and other Elements Concentrations in the Soil at Baquba-Iraq, Key Engineering Materials, 2021, ISSN: 1662-9795, Vol. 886, pp 273-280.
15. Al ZahraaYaseen Alsajjad Mohammed A MohammedShow, Yaseen Alsajjad, Preparation of Ge -Se -Sb ternary alloys and study of the effect of antimony on electrical properties, extended and localized energy states, AIP Conf. Proc. 3018, 020037 (2023. DOI: 10.1063/5.0171583 .
16. Wadi, K.M., Jasim, K.A., Shaban, A.H., Kamil, M.K., Nsaif, F.K., The effects of sustainable manufacturing pressure on the structural properties of the pb2ba2ca2cu3o9+σ compound, Journal of Green Engineering, 2020, 10(9), pp. 6052–6062.
17. Jaafar S. Muhammad1, Kareem A. Jasim, Auday H. Shaban, The Concentration of the Toxic Elements (Cd, Hg, As) in Diyala Governorate Soil Utilizing GIS Techniques, Journal of Physics: Conference Series 1879 (2021) 03206,doi:10.1088/1742-6596/1879/3/032063.

The bacterial effectiveness and cytotoxicity of the polymer loaded with the nano silver nitrate

Mohamed Khalil Alioui [1,a)] , Adnan Raad Ahmed [1] , Randa Kamil Hossain [2], Ahmed Hussein Ali[3]

[1] *Department of physics, Collage of Education for Pure Science, Tikrit University, Tikrit, Iraq.*
[2] *Department of physics, Collage of Science, Mustansiriyah University, Baghdad, Iraq.*
[3] *Department of Medical physics, Collage of Applied Sciences, Fallujah University, Anbar, Iraq.*

[a)] Corresponding author: mohammedkhalil905@ gmail.com

Abstract. This study concentrates on evaluating the cytotoxicity and the anti- bacterial activity of the mixture of polymer consisting of PEG, PVA and chitosan by adding different concentrations of the Nano silver nitrate and antibiotic Augmentin. The study also deals with the structural properties (XRD, FTIR) and visual properties (UV-Vis), after that the anti- bacterial activity is tested against the Gram positive and negative bacteria. The findings clarify that the Nano silver nitrate has a significant and active role in inhibition the growth of cell, and the maximum of inhibition diameter in concentration (100%) ranging between 30-38 mm. The toxicity is evaluated by using (L929). By testing the cytotoxicity, it is found that the Nano silver nitrate does not appear as having a posinuous effect in the low concentrations but it has a poisonuous effect on the cells if there are high concentrations

Keywords: Nano silver nitrate, cytotoxicity, Bactria, PVA, PEG

INTRODUCTION

The Nano technique is employed in developing structures and systems having regulatory traits on the middle level among the individual molecules about (100nm). This case makes the researchers pay attention to create the Nano particles from the noble minerals as gold and silver with several applications in sciences [1]. The Nano particles has an important role in several applications because of their little toxicity and they are very stable due to the existence of protein and also they are active in costs [2]. Microbial infections are a major concern especially in the healthcare institutions, and exposure to the Nano particulate matter is a constant risk[3] . This is necessary because the public perception of nanotechnology can be exposed to danger because of the fear of nanotechnology. The Nano silver particles have gained importance due to their antibacterial and antifungal activity, and this has led the researchers to find new ways to create Nano particles [4] . Polymer blend plays an important role because of their simple preparation methods and diverse properties [5]. The interest in polymers has increased significantly because of the industrial applications[6] . As for human health, studies have shown that the Nano particles have a fundamental impact on the cellular levels such as genes and proteins[7] . It has been observed that the Nano sliver particles lead to an increase in ROS associated with DNA damage and apoptosis programmed cell death [8] , and that chitosan has gained an important role as a biomaterial due to biological properties such as biocompatibility , biodegradability , antibacterial activity and wound[9], and ketone is one of the most common polymers in nature and an essential part of bone structure and cell surfaces[10]. The properties of chitosan make it very useful in many applications, for example , in the medical, chemical end ecological fields[11] . Chitosan has a solid crystalline structure due to hydrogen bonding within the molecules[12] . PEG has been used in a large range of polymers because of its molecular weight , water solubility , biocompatibility and low toxicity[13] . PVA is also non-toxic, having high dielectric strength, good charge storage capacity and visual and electrical properties[14] . PVA has a wide range of applications in the industrial sector and having different fields of science and technology[15] . Chitosan and PVA have been evaluated as the best well-known

Technologies and Materials for Renewable Energy, Environment and Sustainability
AIP Conf. Proc. 3321, 030009-1–030009-9; https://doi.org/10.1063/5.0291377
Published under an exclusive license by AIP Publishing. 978-0-7354-5231-2/$30.00

types of environmentally friendly polymers. These materials are used in many areas of applications as medicines and pharmaceutical materials as a result of their biocompatibility , capability to bio analysis , low toxicity or even the complete absence of toxicity[16] . The new properties of the material that have Nano size may have a toxicological role because the same properties that make these secondary particles interesting for a wide group of applications may impact on their toxicity[17] .

EXPERIMENTAL PART

In this part of study , a mixture of polymer consisting of PVA,PEG,CH is prepared by adding different blends of Nano silver nitrate and anti-material .

1. Nano silver nitrate is prepared using the method of chemical reduction that uses sodium citrate ($C_6H_5O_7Na_3$) as a reducing agent , silver nitrate solution (A1) then is prepared by dissolving (0.24 g) of silver nitrate in 100 of non-ionic distilled water, and then prepared sodium citrate solution (A2) by dissolving (0.3 g) of sodium citrate in 100 ml distilled water .
2. Chitosan preparation : we take (1.5 g) of chitosan powder dissolved in (100 ml) of distilled water with addition of (2 ml) of 2% acetic acid that is a good solvent for chitosan . The mixture is stirred at room temperature at a moderate speed for 35 minutes using a magnetic stirrer .
3. In the preparation of polyethylene glycol (PEG) and polyvinyl alcohol (PVA) , 5g of each of PVA and PEG polymers are dissolved in (100 ml) individually to produce 5% concentration of each agent of them . The PVA solution is prepared at 85^0C for 15 minutes with continuous stirring while PEG is dissolved at room temperature for 5 minutes and then stored in tightly sealed container.

Table (1) : The amount of the used material

Material	M(g)	Water (ml)	Acetic acid
PEG	5	100	
PVA	5	100	
CH	1.5	100	2%

RESULT AND DISCUSSION

XRD

In the Figure (1) , the X-ray diffraction spectrum of the samples is shown. The results show that the broad value is located at the diffraction angle (2θ=20°) corresponding to PVA and chitosan polymers at specific angles (2θ) , and it shows diffraction at angles (38.5 , 44.5 63) returning to Nano silver corresponds to peaks (111),(200) and(220). These peaks confirms the presence of AgNPS in the samples , and these agree with the reference card JCPD (96-901-2962). This result is also consistent with previous studies[18].

Moreover , it is noted that intensity of the peaks shows improvement with the increase of silver particles in the Nano composite, as it indicates an improvement in crystallinity. Additional small peaks with low relative intensity appeared within the range of 25 to 45 degrees which may be associated with the crystalline nature of the added components [11] . When AgNPS is added to PVA and PEG , it may lead to repulsion between the added molecules and that in turn leads to an increase in the character of the chain arrangement, on the other hand it indicates a decrease in the integrated density and particle size [19]. This means that the crystalline structure has been destroyed due to cross-linking .We notice from the figure that when AgNPS increases, it leads to an expansion of the diffraction peak.

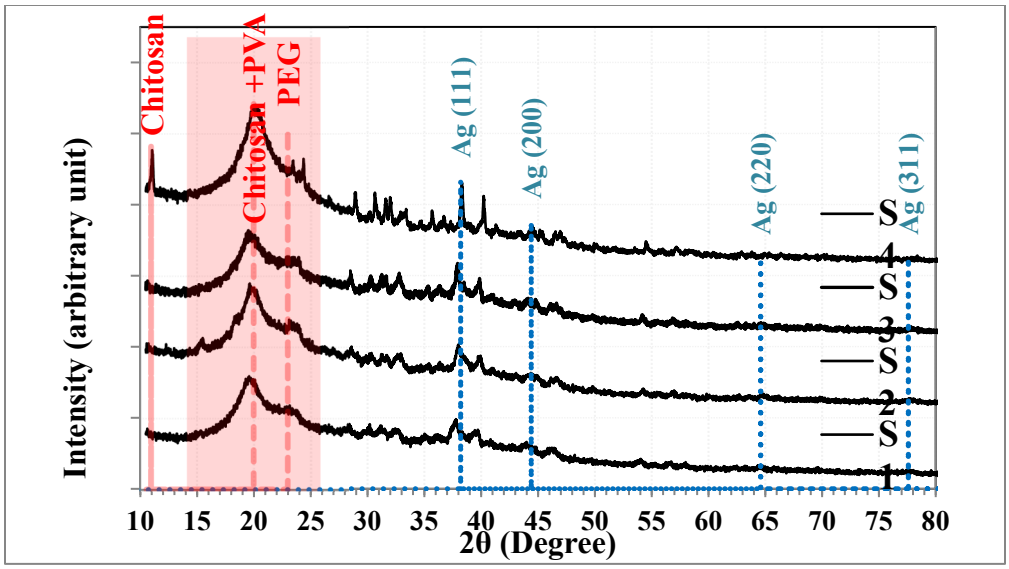

Figure (1) : The XRD pattern of samples S1,S2,S3,S4 .

UV-Visible

We may notice in figure (2) that the first sample (S1) shows an absorptive value at (0.022) with a wavelength (504 nm) , while the sample (S4) has the highest value of absorption as compared with the other values that amounted (0.34) with a wavelength (470nm) . The figure shows that the samples (S1 ,S2 ,S3 ,S4) with different concentrations and a wavelength ranging from (200-1100 nm) , we may notice the higher concentration of silver nanoparticles, the greater the absorbance.

To understand that, we should know the mechanism of the interaction between UV-Vis and the material especially the nanoparticles: when UV Ultraviolet rays are shed on the material, it excites collective vibration in it on the free electrons, and this vibration is called Plasmon, it is either surface or size[20] .

The resonance of the surface Plasmon plays on important role in determining the visual absorption spectra of nanoparticles which shift to a higher wavelength as the size of the particles increases [21] .

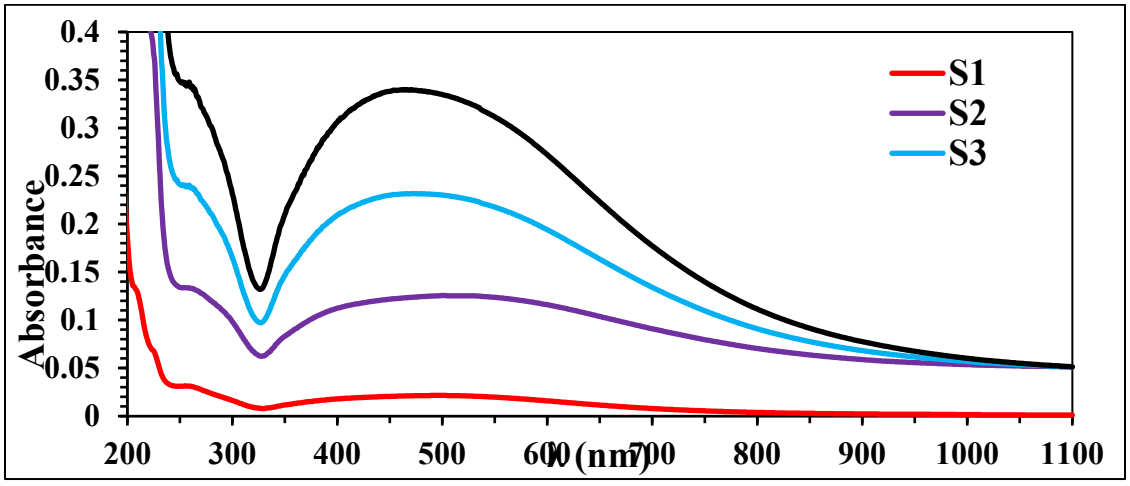

Figure (2): UV spectrum of the samples : (S1, S2, S3, S4)

FTIR

It may be recorded an determined the date of the spectrum of infrared ray in a group of main areas. The most important of these areas is the one that locates between (2892-3410) cm^{-1} for it is attributed to the carbon bond or to (O-H) bond

and also to vibration (O-H). The bond (C=C) represents the ketone bond, while the second area that locates between (1473-1647) cm^{-1} we may notice in which (O-H),(C-H),(-NH2).

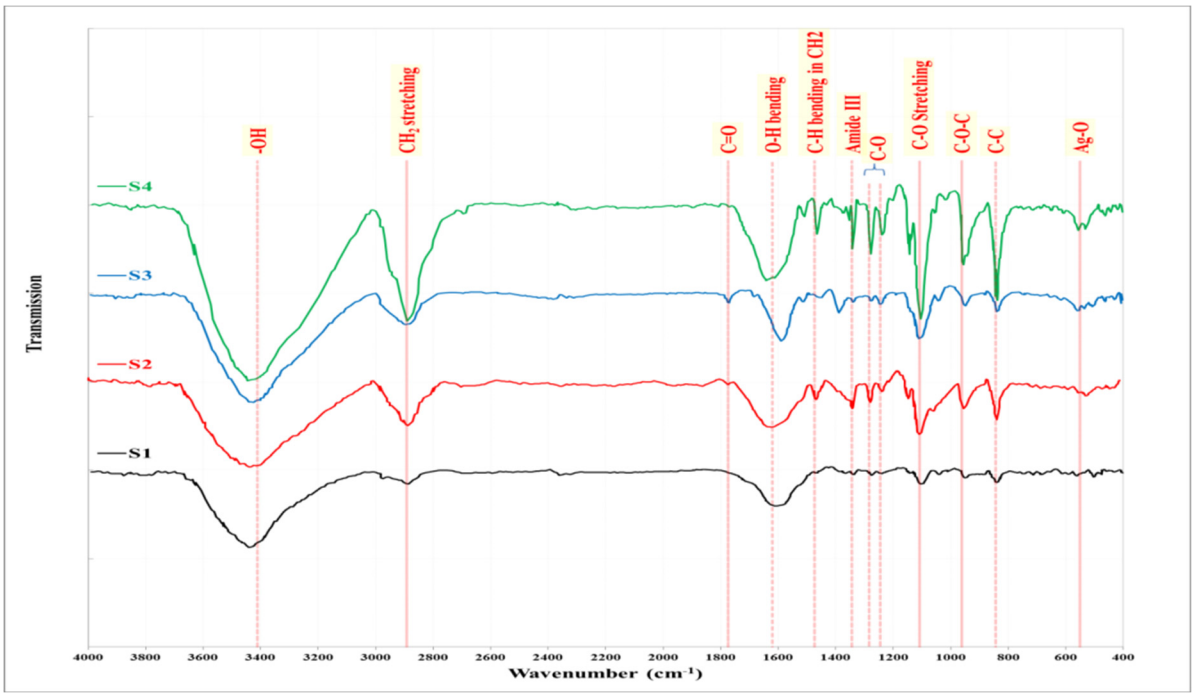

Figure (3) shows the spectrum of infrared ray for the sectors of polymers for the samples (S1,S2,S3,S4) respectively

.

Table (2) : FTIR bands of polymer composite

Band Type	S1	S2	S3	S4
O-H	3410.17	3410.17	3410.17	3410.17
CH_2 stretching	2892.66	2892.66	2892.66	2892.66
C=O	1724.29	1724.29	1724.29	1724.29
O-H bending	1647.46	1647.46	1647.46	1647.46
-NH_2 bending	1568.36	1568.36	1568.36	1568.36
C-H bending in CH2	1473.45	1473.45	1473.45	1473.45
Amide III	1344.63	1344.63	1344.63	1344.63
C-O	1283.62	1283.62	1283.62	1283.62
	1245.20	1245.20	1245.20	1245.20
C-O stretching	1109.60	1109.60	1109.60	1109.60
C-O-C	962.71	962.71	962.71	962.71
C-C stretching	845.20	845.20	845.20	845.20
Ag-O	-	545.00	548.00	550.00

The bacterial examinations

By using the technique of diffusion , the counter activity of bacteria for the following samples (S1,S2,S3,S4) is tested which is prepared by adding the polymer consisting of (PVA,PEG and CH) and Nano silver nitrate with adding the antibiotic Augmentin . The used bacteria in this study is (S.aureus) and (E.coli) which was Gram negative and positive which was one of most dangerest bacteria for which this technique used to stand against it.

The number of the prepared samples is five samples that represent different mixture proportions with different concentrations as follows (25% , 50% , 100%) for each sample after gaining the results , it is clear that the better sample of all five samples is the sample (S4) with concentration proportion (100%).

It is the most effective in influence , while the other samples have a large role in inhibiting the bacteria , but the most effective is (S4). It is clear through the gained results that the prepared samples has an important role in inhibiting the

growth of bacteria with different degrees according to the kind of bacteria and the proportion of concentration , and this is attributed to the entering of Nano silver particles in to the cell and that may lead to severals influences : the Nano silver particles may penetrate the cell membrance and entering in cytoplasm, the molecules of DNA may lose their ability to reproduce when silver nitrate , and that may be one of the reasons of bacteria cell death. This results are consistent with the researcher's[22] .

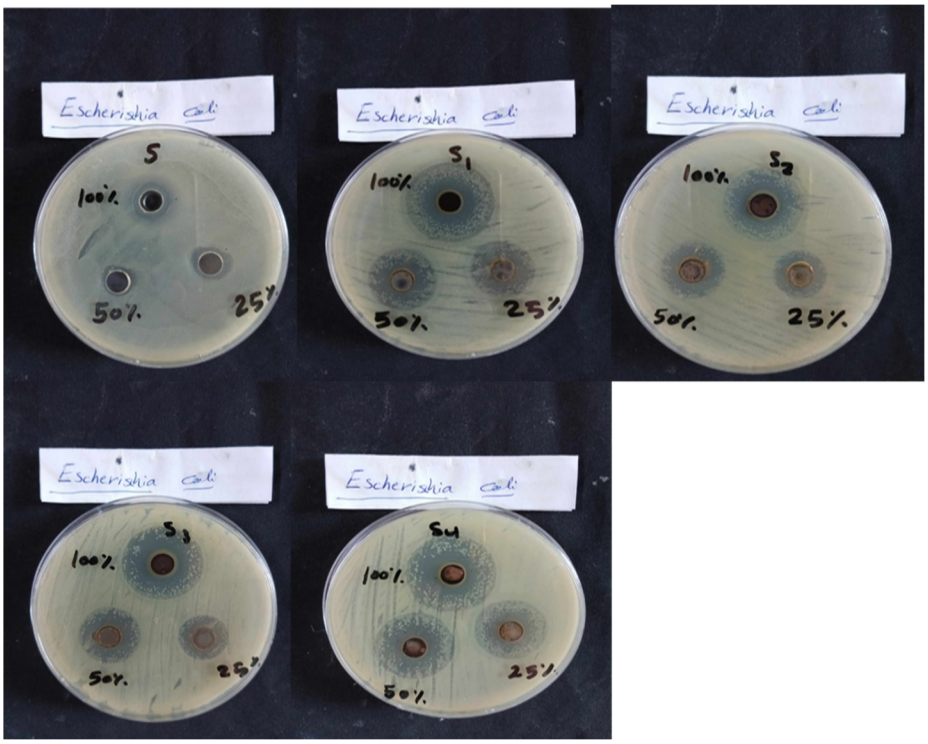

Figure (4) shows a picture of the inhibition of (E. coli) bacteria with different concentrations

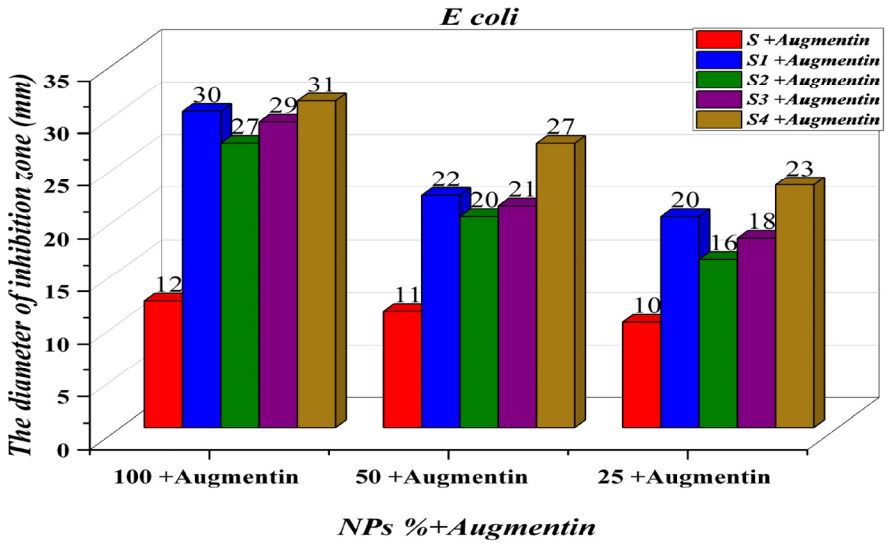

Figure (5) shows the diameter of the inhibition zone (mm) for (E. coil) bacteria of silver nanoparticles with the antibiotic

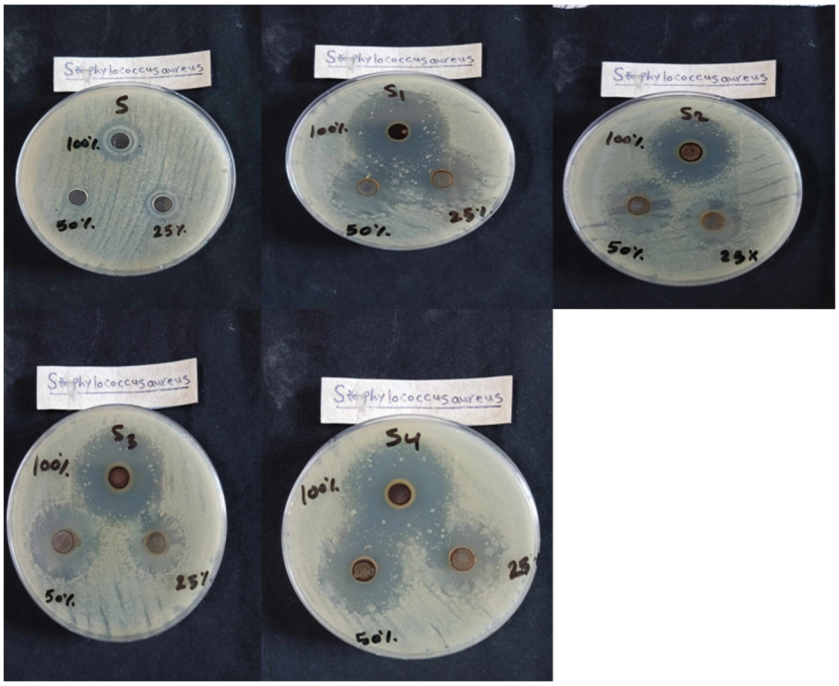

Figure (6) shows a picture of the inhibition of (S. aureus) bacteria with different concentrations

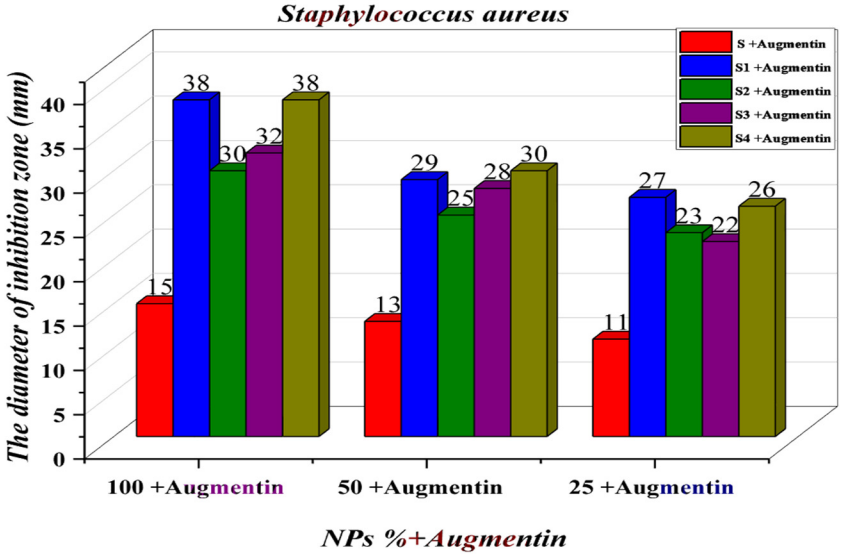

Figure (7) shows the diameter of the inhibition zone measured in (mm) for the bacteria (S. aureus) of silver nanoparticles with the antibiotic.

Cytotoxicity

The analysis of the counter influences is conducted for the polymer with the Nano silver nitrate with different concentrations on the fibroblasts (L929) by examining MTT, then planting cells in 96 well can with density 10^4 cell, well in a size amounted to (200µl) after 24 hours, and adding (10µl) of the solution MTT (5µL) to each well and put then on (37^0C) for three hours . After that the floating medium is removed and adding (100µl) from DMSO to melt the blue crystals. Finally the absorption is measure by using a board at 570 nm . Through examining MTT , it was clear that the proportion of the cell remaining shows a lowness with an increase in concentration of Nano silver

particles where the average of cell survival between (62%) at concentration (100%) , (100%) at concentration(0 %) . In the figure , it is shown that the proportion of the first three employed concentration , the proportion of remaining is less than 13% and that consider non-toxin for the cell. However , the last concentration includes a proportion of remaining 38% . This proportion is evidence indicating the toxicity of this concentration on the employed cells. The reason behind the death of cells may be attributed to several reasons , one of these reasons is the Nano silver particles at a high concentration affects the structure and functions of cell [23] , probably , AgNPS may cause an oxidative stress in the cell at a high concentration and that means it generates free roots that cause a damage in DNA, and that in turn leads to apoptosis death of cells [24].

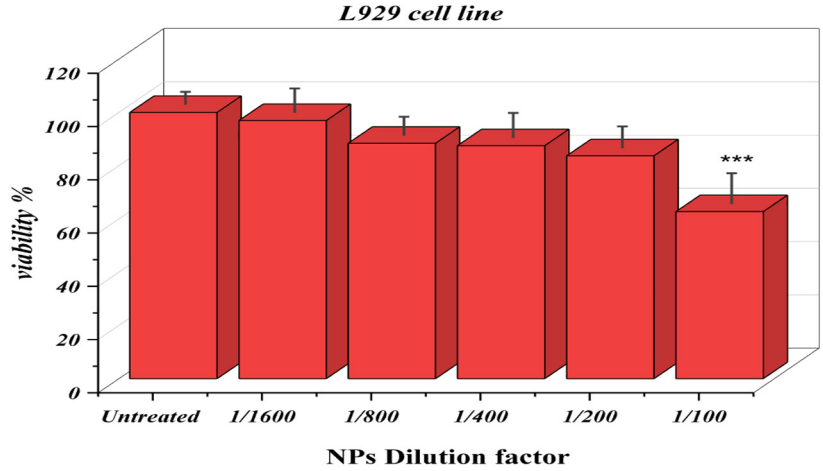

Figure (8) shows the percentage of cell survival of L929 fibroblasts for each concentration within 24 hours

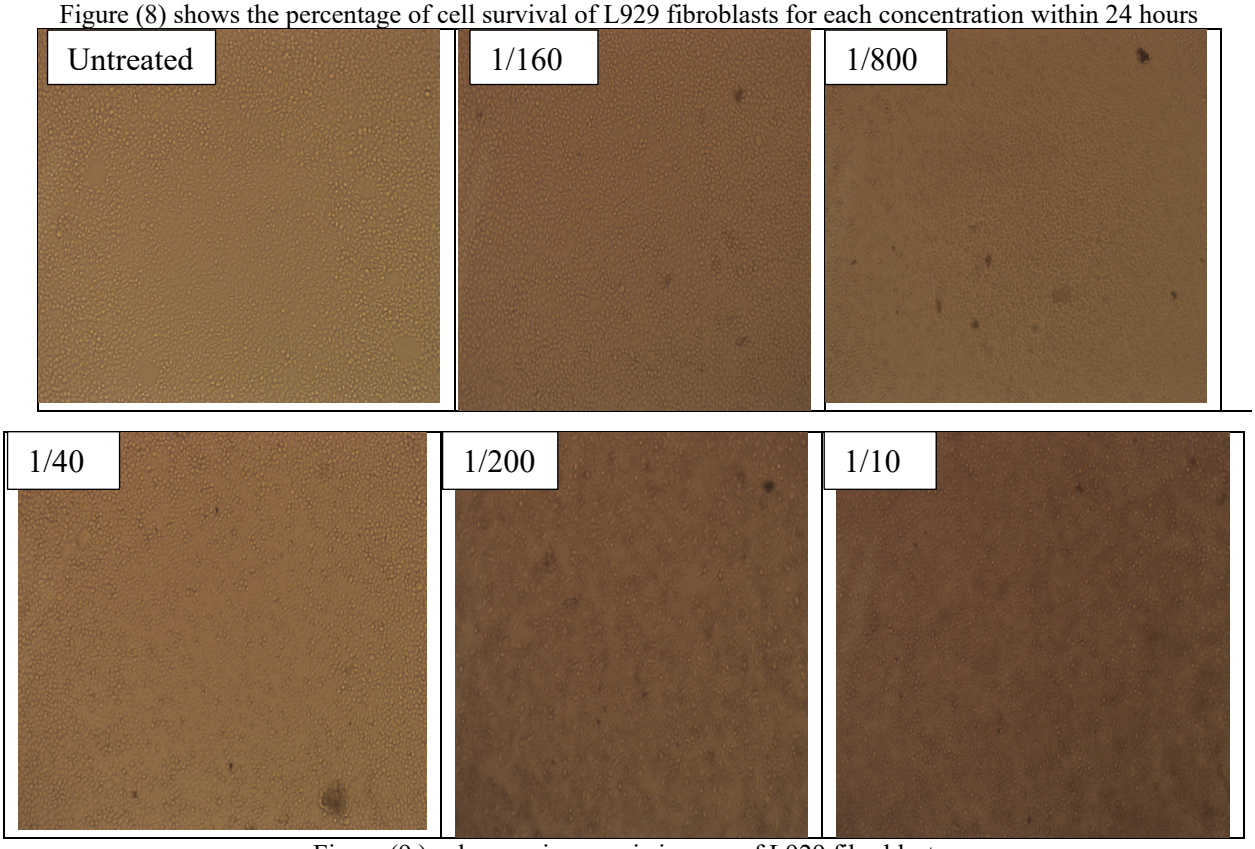

Figure (9) : shows microscopic images of L929 fibroblasts

CONCLUSIONS

In our nowadays, the Nano materials are regarded as a good means to eliminate the bacteria inflammations and an activity against bacteria , in addition , they are used as incentives and vital treatment elements .
The study showed that a mixture of polymer and Nano silver nitrate has important role in inhibiting the growth of cell and the evaluation of cytotoxicity showed that the Nano silver nitrate has no toxin effect.

REFERENCES

1. Rai, M. K., Deshmukh, S. D., Ingle, A. P., & Gade, A. K. (2012). Silver nanoparticles: the powerful nanoweapon against multidrug-resistant bacteria. *Journal of applied microbiology*, *112*(5), 841-852.
2. Ventola, C. L. (2015). The antibiotic resistance crisis: part 1: causes and threats. Pharmacy and therapeutics, 40(4), 277.
3. Syed, A., & Ahmad, A. (2012). Extracellular biosynthesis of platinum nanoparticles using the fungus Fusarium oxysporum. Colloids and Surfaces B: Biointerfaces, 97, 27-31.
4. Gopinath, P. M., Narchonai, G., Dhanasekaran, D., Ranjani, A., & Thajuddin, N. (2015). Mycosynthesis, characterization and antibacterial properties of AgNPs against multidrug resistant (MDR) bacterial pathogens of female infertility cases. asian journal of pharmaceutical sciences, 10(2), 138-145.
5. Wolinsky, H. (2006). The battle of Helsinki: two troublesome paragraphs in the Declaration of Helsinki are causing a furore over medical research ethics. EMBO reports, 7(7), 670-672.
6. Mohammed, A., Suhail, M. H., & Ghazi, M. (2017). Structural and optical properties for PVA-PEG-MnCl2 composites. Iraqi Journal of Physics, 15(32), 99-113.
7. O'brien, J., Wilson, I., Orton, T., & Pognan, F. (2000). Investigation of the Alamar Blue (resazurin) fluorescent dye for the assessment of mammalian cell cytotoxicity. European journal of biochemistry, 267(17), 5421-5426.
8. Ahamed, M., Karns, M., Goodson, M., Rowe, J., Hussain, S. M., Schlager, J. J., & Hong, Y. (2008). DNA damage response to different surface chemistry of silver nanoparticles in mammalian cells. Toxicology and applied pharmacology, 233(3), 404-410.
9. Bakshi, P. S., Selvakumar, D., Kadirvelu, K., & Kumar, N. S. (2020). Chitosan as an environment friendly biomaterial–a review on recent modifications and applications. International journal of biological macromolecules, 150, 1072-1083.
10. Barbosa, M., & Martins, M. C. L. (Eds.). (2017). Peptides and proteins as biomaterials for tissue regeneration and repair. Woodhead Publishing.
11. Tan, H., Chu, C. R., Payne, K. A., & Marra, K. G. (2009). Injectable in situ forming biodegradable chitosan–hyaluronic acid based hydrogels for cartilage tissue engineering. Biomaterials, 30(13), 2499-2506.
12. El-Hefian, E. A., NASEF, M., Yahaya, A. H., & Khan, R. A. (2010). Preparation and characterization of chitosan/agar blends: rheological and thermal studies. Journal of the Chilean Chemical Society, 55(1), 130-136.
13. Li, Q., Dunn, E. T., Grandmaison, E. W., & Goosen, M. F. (2020). Applications and properties of chitosan. In Applications of Chitan and Chitosan (pp. 3-29). CRC Press.
14. Knop, K., Hoogenboom, R., Fischer, D., & Schubert, U. S. (2010). Poly (ethylene glycol) in drug delivery: pros and cons as well as potential alternatives. Angewandte chemie international edition, 49(36), 6288-6308.
15. Sarada, B. A., Bhargav, P. B., Sharma, A. K., & Rao, V. V. R. N. (2011). Studies on (PEO+ PVA+ KIO3) polymer blend electrolyte films for electrochemical cell applications. Materials Research Innovations, 15(6), 394-400.
16. Watanabe, M., Nagano, S., Sanui, K., & Ogata, N. (1987). Structure-conductivity relationsihp in polymer electrolytes formed by network polymers from poly [dimethylsiloxane-g-poly (ethylene oxide)] and litegum perchlorate. Journal of Power Sources, 20(3-4), 327-332.
17. Chen, J., Wei, D., Gong, W., Zheng, A., & Guan, Y. (2018). Hydrogen-bond assembly of poly (vinyl alcohol) and polyhexamethylene guanidine for nonleaching and transparent antimicrobial films. ACS applied materials & interfaces, 10(43), 37535-37543.
18. Kim YS, Kim GS, Cho HS, RHA DS, Kim GM, Park JD, Choi BS, Lim R, Chang HK, Chung YH, Kwon IH, Han BS, Yu AG. 2008. Twenty-eight-day oral toxicity, genotoxicity, and gender-specific tissue distribution of silver nanoparticles in Sprague-Dawley rats. inhale. Toxicol. 20:575–583
19. Tommalieh, M. J., Zihlif, A. M., & Ragosta, G. (2011). Electrical and thermal properties of polyimide/silica nanocomposite. Journal of Experimental Nanoscience, 6(6), 652-664.

20. .2 Bonsak, J. (2010). Chemical synthesis of silver nanoparticles for light trapping applications in silicon solar cells (Master's thesis).
21. 3 Shrivastava, S., Bera, T., Roy, A., Singh, G., Ramachandrarao, P., & Dash, D. (2007). Retracted: Characterization of enhanced antibacterial effects of novel silver nanoparticles. Nanotechnology, 18(22), 225103.
22. Streetman, B. G., & Banerjee, S. (2000). Solid state electronic devices (Vol. 4, pp. 202-203). New Jersey: Prentice hall.
23. Sotiriou, G. A., Diaz, E., Long, M. S., Godleski, J., Brain, J., Pratsinis, S. E., & Demokritou, P. (2012). A novel platform for pulmonary and cardiovascular toxicological characterization of inhaled engineered nanomaterials. Nanotoxicology, 6(6), 680-690.
24. Ahamed, M., AlSalhi, M. S., & Siddiqui, M. K. J. (2010). Silver nanoparticle applications and human health. Clinica chimica acta, 411(23-24), 1841-1848.

Acetylcholine Esterase and Antioxidative Markers: A Study of Autism Spectrum Disorder Individuals

Ako Saber Kaky [1,a], Sayran Sattar Saleh [1,b]

[1] *Department of Chemistry, College of Science, University of Kirkuk, Kirkuk, Iraq*
[a] Corresponding author: ako.kaky@uokirkuk.edu.iq
[b] sayran.2017@uokirkuk.edu.iq

Abstract. This study looked at possible biomarkers in autism spectrum disorder (ASD). It compared levels of different biomarkers in 96 ASD patients to 96 healthy kids. The study showed kids with ASD had lower activity of an enzyme called acetylcholinesterase (AChE) and this enzyme is involved in a neurotransmitter system called cholinergic. Having less of this enzyme working suggests changes in this brain system, which has been tied to ASD before. In addition, ASD patients had higher levels of thiol groups, which relate to oxidative stress. Oxidative stress is an imbalance between free radicals and antioxidants in the body. So, the increased oxidative stress seen here may play a role in ASD. The study also found ASD patients had lower free amino acids compared to the healthy participants. Especially branched-chain amino acids were decreased. Overall, these results give information into cholinergic neurotransmission and oxidative stress in ASD. They suggest oxidative stress could contribute to how ASD starts or continues. Interesting though, no big differences existed in total protein or albumin between groups. But free amino acids and amines were markedly higher in ASD. This research ought to keep going to see if them higher levels really affect ASD. In conclusion - this study spots possible biomarkers and causes tied to ASD. It shows we need more studies to get better tests and treatments for this disorder and the results promises that these measures could help as markers to detect ASD.

INTRODUCTION

Autism spectrum disorder (ASD) is a condition characterized by challenges, in social interaction speech difficulties and repetitive behaviors. While significant progress has been made in understanding ASD, the causes and mechanisms behind this condition are still not fully understood. Autism spectrum disorder is known to be a syndrome influenced by both genetic factors. Researchers have explored pathways linked to the onset of ASD, such as the role of acetylcholinesterase (AChE), in its pathophysiology [2].

Acetylcholinesterase is an enzyme known for its role, in stopping communication by breaking down the neurotransmitter acetylcholine (ACh) in synapses. Its function is crucial for ensuring neuron communication and avoiding overstimulation of receptors. Besides its role in transmission AChE has garnered attention for its possible involvement, in autisms underlying mechanisms [3].

When the levels of antioxidants are low, in a living system, oxidants, also known as oxygen species (ROS) can lead to oxidative stress. The central nervous system (CNS) is particularly vulnerable to stress due to its oxygen consumption and lipid concentration. Conditions, like Parkinsons disease (PD) Alzheimers disease (AD) Huntingtons disease (HD) and amyotrophic lateral sclerosis (ALS) have been associated with macromolecule damage caused by processes [4]

A pretty thorough review of past research was done to clarify and evaluate the link between blood biomarkers connected to oxidative stress and autism spectrum disorder (ASD). For every study they found on this, they compared the typical levels of biomarkers between ASD cases and folks without ASD. This gave them one main ratio estimate for each biomarker that showed how much higher or lower it was for ASD versus non-ASD [5].

Studies have also looked at markers of oxidative stress in the blood of kids with autism. One big analysis published in the journal Translational Psychiatry examined a bunch of these markers. They found that levels of oxidized glutathione (GSSG), malondialdehyde, homocysteine, S-adenosylhomocysteine nitric oxide, and copper were higher in autistic children compared to healthy kids. On the flip side, levels of reduced glutathione (GSH), total glutathione

Technologies and Materials for Renewable Energy, Environment and Sustainability
AIP Conf. Proc. 3321, 030010-1–030010-7; https://doi.org/10.1063/5.0289601
Published under an exclusive license by AIP Publishing. 978-0-7354-5231-2/$30.00

the ratios of GSH/GSSG and total GSH/GSSG, as well as methionine, cysteine, vitamins B9 D, B12, and E, S-adenosylmethionine/S-adenosylhomocysteine and calcium were significantly lower in autistic kids [6]
Another study published in Front Psychiatry [7] suggested that oxidative stress might play a role in the development of ASD. The study found that oxidative stress in ASD could be caused by protein post-translational changes (e.g., carbonylation), abnormal metabolism (e.g., lipid peroxidation), and toxic buildup (e.g., reactive oxygen species (ROS)) [7].
Currently, there has been a noticeable increase in scientific research focused on examining the influence of oxidative stress on the development and progression of autism spectrum condition. Oxidative stress is intimately linked to the organism's ability to counteract the impact of reactive oxygen species (ROS) by utilizing antioxidants [8]. Rossignol and Frye (2020) conducted an experiment to investigate the correlation between oxidative stress, mitochondrial dysfunction, and inflammation in the brain regions of persons diagnosed with autism [9]. This study highlights the importance of oxidative stress in autism spectrum disorder (ASD) and also shows potential connections between acetylcholinesterase (AChE) activity and neurological impairment.
Research into potential treatments, like whether antioxidant supplements help, has gotten some notice for people with autism spectrum disorder. A 2020 study by Gvozdjakova and others checked out if taking L-carnitine could cut down oxidative stress [10]. They didn't look just at autism exactly, but more generally at antioxidants and oxidative stress. Seems like antioxidants could maybe help reduce oxidative stress for people with autism according to what they found and it's also possible it could help control AChE levels [11].
A paper published in 2010 by EB Mukaetova-Ladinska looked closely at how problems with acetylcholine are connected to autism spectrum disorder. The research suggested that an enzyme called acetylcholinesterase (AChE), as well as other parts of the body's cholinergic system, might play a role in causing ASD and another paper, this one by KOEVOET D., talks about using animal models to understand the complicated interactions between brain chemicals like neurotransmitters and oxidative stress. The animal research helps explain what's going on in the human brain in autism [13].
The studies shed light on a complex connection between oxidative damage, antioxidants, AChE enzyme, and autism disorders. Science is finding this unique link but kind of slowly. Anyways, it seems like oxidative stress could form a crucial role in how people get autism diseases, right? It possibly affects how the AChE enzyme works in us. The main point is that oxidative damage may connect to autism, but like through this intricate series of reactions along with AChE. Furthermore, there is current investigation into the potential utilization of antioxidant therapy as a method to mitigate oxidative stress in individuals diagnosed with Autism. Additional research is necessary to clarify the exact processes that explain these interactions. This will provide new possibilities for innovative therapy methods that could help persons with autism and improve our comprehension of this intricate neurodevelopmental illness [14,15].

MATERIALS AND METHODS

Study case and Subjects

The study had a cohort of 96 patients who were diagnosed with autism spectrum disorder and ranged in age from 3 to 12 years. In addition, the study involved 96 individuals in good health whose age ranges closely matched those of the patients. Blood samples were collected at Kirkuk Pediatric Hospital in Kirkuk, Iraq. A skilled pediatrician conducts the diagnosis of patients. The patient group and control group were asked a range of questions regarding medical history, parental consanguinity, age of ASD diagnosis, administered per, as well as weight and height measurements.

Biochemical assays

The quantification of total protein was performed using absorbance measurements at a wavelength of 660 nm, following the Lowry technique [16]. Bovine serum albumin was utilized as a reference for calibration purposes. The concentration of albumin was evaluated utilizing the bromo cresol green reagent (BCG) technique, as described in reference [17]. The quantification of free amino groups was carried out using spectrophotometric methods as described in reference [18]. The analysis for thiol groups was conducted using the Ellman technique [19]. Utilizing the method suggested by *Levine et al.*, the carbonyl group of the protein was quantified [20]. The AChE activity was assessed using Ellman's standard method [21]. Globulin are calculated by minus albumin from total protein. AGR is the ratio of albumin to globulin.

Blood collection

A venipuncture technique was employed to obtain a volume of 5 ml of blood using a disposable syringe. The blood was thereafter transferred into gel tubes for separation. The tubes underwent centrifugation for a duration of 10 minutes. The serum was isolated from the cells and thereafter kept at a temperature of -20°C.

Statistical analysis

This study presents the results in terms of Mean ± SD and reports the significant differences (p value) seen between the groups. The identification of significant disparities was established by a statistical examination, in which a p-value of 0.05 or below was deemed indicative of significance. The statistical analysis was performed with the GraphPad Prism software.

RESULTS AND DISCUSSION

Table 1 displays the enzyme activity and specific activity (enzyme activity divided by total protein) of serum AChE, presented as the mean value plus or minus the standard deviation in U/ml and U/mg, respectively. The measures were acquired from individuals who have been diagnosed with ASD and were then compared to the measurements of persons who are in good health.

Table 1. the (activity and specific activity) of the serum AChE for all studied groups.

Parameters	Controls (n=96)	Patients (n=96)	P value
Serum AChE U/ ml	5.023 ± 0.883	4.224 ± 1.160*	0.0369
S.A in Serum U/mg	0.722±0.151	0.57 ± 0.145*	0.001

***Significant (p≤0.05)**

The findings in Table 1 indicated that the patients group exhibited notably reduced levels of acetylcholine esterase activity and specific activity of ASD patients' serum in comparison to the healthy individuals. Furthermore, the findings align with prior research that has demonstrated a decrease in the activity of acetylcholinesterase (AChE). The research revealed a significant decrease in acetylcholinesterase (AChE) activity among individuals diagnosed with neurological disorders [22]. The decline in AChE activity has been correlated with the presence of despair, anxiety, boredom, and sadness, hence further substantiating the connection between this condition and mental health and psychiatric issues [23]. Estrogen's effect on brain function, particularly in improving choline uptake and acetylcholine synthesis, could explain the rise in acetylcholinesterase activity [24]. The observed decrease in specific activity might be due to certain impurities, achieved by dividing the activity of AChE by the concentration of TP in the serum. The specific function of an enzyme can serve as a dependable indicator of its purity [25]. The findings indicated above align with the research undertaken by which investigated the parameters in children diagnosed with autism [26].
Table 2 Investigating the serum levels of various components in individuals diagnosed with autism spectrum disorder compared to a control group of healthy individuals. The data is presented as the Mean ± Standard Deviation (SD).

Table 2. represent the serum concentration of some antioxidant markers in patient groups of autism spectrum disorder (ASD) as compared to control.

Parameters	Control (n=96)	Patients (n=96)
TP gm/dl	7.03 ±0.774	7.42 ±0.910
Albumin gm/dl	4.273 ±0.738	4.035 ± 0.572*
Globulin gm/dl	2.888±0.958	3.395 ± 1.097
AGR	1.673 ±1.098	1.45 ±0.978
Thiol µmol/L	19.92±8.026	18.791 ± 8.045*
Thiol /TP µmol /gm	2.86 ±1.183	2.57± 1.152
Free amino mmol/L	0.271 ±0.129	0.73 ± 0.477*
Free amino/TP mmol/gm	0.042±0.019	1.00 ± 0.532
Carbonyl nmol/ml	0.783 ±0.414	0.890 ±0.404
Carbonyl / T.P nmol/gm	7.03 ±0.774	7.42 ±0.910

***Significant (p≤0.05)**

The particular activity of an enzyme can be utilized as a reliable measure of its purity [27]. The findings indicated above align with the research undertaken by [26], which investigated the parameters in children diagnosed with autism [27]. Albumin makes up over 50% of the total protein found in serum. Albumin is synthesized by the liver and performs various important roles in the body, including maintaining osmotic pressure, transporting nutrients, fatty acids, bilirubin, cholesterol, medications in the circulation, and eliminating waste materials [27]. Research has demonstrated that albumin plays a crucial role in the antioxidant capacity of blood serum against reactive oxygen species (ROS) [28]. The measurement of the albumin globulin ratio (AGR) was also conducted, which can provide insights into physiological abnormalities [29]. Additionally, representative measures were employed to assess the extent of systemic inflammation. Moreover, this metric may be readily measured with simplicity and at a little expense. Hepatic cells are primarily responsible for the synthesis of albumin and globulin. [30]. The findings pertaining to the concentrations of TP, albumin, globulin, and AGR were consistent with the study conducted by Ayaydın, H. [31], which examined these parameters in individuals with autism. The inquiry findings revealed a statistically significant increase ($p \leq 0.05$) in the concentrations of unbound amino acids and the ratio of unbound amino acids to total protein in the ASD group compared to the non-ASD group. The findings on the amounts of free amino acids and the ratio of free amino acids to total protein align with the data provided by the cited authors, Ayaydın, H. [31], Which researcher investigated these specific criteria in individuals diagnosed with autism. Several research initiatives have suggested using the concentration of "free amino and free amino/TP" as indications in sick states [32]. There is a hypothesis that the increase in the concentration of amino groups and the ratio of free amino acids to total protein may be connected to elevated levels of circulating branched-chain amino acids (BCAAs) and central nervous system (Acyl CNsO) associated with fatty acids in the group of patients [33]. A possible reason for the increased amounts of branched-chain amino acids (BCAAs) could be due to the increased breakdown of BCAAs, leading to higher levels of propionyl carnitine (C3) and iso-valerylcarnitine (C5) in the bloodstream [34]. The study findings indicate a significant rise in the patient groups compared to the control group, with statistical significance ($p \leq 0.05$). Nevertheless, there was no significant decline observed among the patient groups ($p \geq 0.05$). The observed results of carbonyl/TP may be linked to the existence of oxidative stress and inflammation in the persons being studied [35]. The probable association between the increase in serum protein carbonyl concentration and many variables, including excessive hydration, sarcopenia, and the serum concentration of pre-albumin, has been suggested [36]. The findings of the carbonyl study were consistent with those of a previous study conducted by Ayaydın, H. [31], which examined the same parameters in individuals with autism. Carbonylation has garnered significant interest and scrutiny in several academic and clinical investigations because to its predominantly irreversible and irreparable nature. Consequently, it has emerged as the most dependable biomarker for the cumulative assessment of severe oxidative protein damage [38]. In addition, it has been observed that the amounts of protein carbonyls are significantly higher compared to other forms of oxidative alterations [39]. The study's findings indicated that there was no statistically significant ($p > 0.05$) decline in thiol and thiol/TP concentrations in patients when compared to the control group. Thiol groups have substantial nucleophilic characteristics and exhibit more nucleophilicity at healthy pH levels than amine and carbonyl groups found in the side chains of Arginine (Arg) and Lysine (Lys) [40], [41]. The findings of the thiol and thiol / TP analyses were consistent with the research conducted by the authors referenced as Ayaydın, H. [31], who investigated the aforementioned parameters in the context of autism. The term "serum" denotes a residual constituent of bloodstream that remains subsequent to the analysis of total thiols, which serves as an indicator of oxidative stress. Investigating this characteristic has been carried out in various systemic conditions such as ischemic heart disease, lung diseases, diabetes, Alzheimer's disease, renal disorders, preeclampsia, and alcoholism [42], [43]. Research indicates that oxidative stress could be a factor in the development of specific diseases, highlighting the increasing significance of thiol chemistry. Thiols are essential in the antioxidation process due to the presence of sulfhydryl (-SH) groups. Sulfhydryl groups has the ability to facilitate electron reduction, so affording protection to organisms against oxidative damage instigated by reactive oxygen species (ROS). Di-sulfides are produced through the conversion of thiols via this chemical process. Throughout history, this double-sided balance has been utilized to measure only one side. Nevertheless, the levels of both variables were evaluated both individually and collectively in accordance with the procedure described in [44], which enabled a thorough assessment of the condition [44].

CONCLUSION

This study suggests potential alterations in the cholinergic and antioxidant systems in individuals with autism spectrum disorder. Compared to controls, the ASD group displayed significantly lower activity of both acetylcholinesterase (AChE), crucial for cholinergic neurotransmission. The research showed a no significant differences were observed in total protein, AGR, globulin, and carbonyl levels, the research showed a significant increase ($p \leq 0.05$) in thiol level and a significant decrease in albumin and free amino level in the ASD patients compared to the healthy subjects.

Further research required to understand their potential role in the autism spectrum disorder. These findings warrant further investigation to elucidate their potential contributions to the pathophysiology of ASD and explore their suitability as potential biomarkers for diagnosis or monitoring.

Acknowledgment

The following people and organizations have provided significant assistance to our research effort, for which the authors are really grateful: the parents who participated in the study, the personnel and management of the Pediatric Hospital in Kirkuk, and our respected supervising physicians.

REFERENCES

1. LONGO, F., & KLANN, E. (2021). Reciprocal control of translation and transcription in autism spectrum disorder. *EMBO reports*, 22. https://doi.org/10.15252/embr.202052110.
2. SHINOTOH, H., HIRANO, S., & SHIMADA, H. (2020). PET Imaging of Acetylcholinesterase. *PET and SPECT of Neurobiological Systems*. https://doi.org/10.1007/978-3-030-53176-8_7.
3. KAMARUDDIN, M., MARZUKI, I., BURHAN, A., & AHMAD, R. (2020). Screening acetylcholinesterase inhibitors from marine-derived actinomycetes by simple chromatography. IOP Conference Series: *Earth and Environmental Science*, 679. https://doi.org/10.1088/1755-1315/679/1/012011.
4. SINGH, A., KUKRETI, R., SASO, L., & KUKRETI, S. (2019). Oxidative Stress: A Key Modulator in Neurodegenerative Diseases. Molecules (Basel, Switzerland), 24(8), 1583. https://doi.org/10.3390/molecules24081583.
5. FRUSTACI, A., NERI, M., CESARIO, A., ADAMS, J. B., DOMENICI, E., DALLA BERNARDINA, B., & BONASSI, S. (2012). Oxidative stress-related biomarkers in autism: systematic review and meta-analyses. Free radical biology & medicine, 52(10), 2128–2141. https://doi.org/10.1016/j.freeradbiomed.2012.03.011.
6. CHEN, L., SHI, X. J., LIU, H., MAO, X., GUI, L. N., WANG, H., & CHENG, Y. (2021). Oxidative stress marker aberrations in children with autism spectrum disorder: a systematic review and meta-analysis of 87 studies (N = 9109). Translational psychiatry, 11(1), 15. https://doi.org/10.1038/s41398-020-01135-3.
7. LIU, X., LIN, J., ZHANG, H., KHAN, N. U., ZHANG, J., TANG, X., CAO, X., & SHEN, L. (2022). Oxidative Stress in Autism Spectrum Disorder-Current Progress of Mechanisms and Biomarkers. Frontiers in psychiatry, 13, 813304. https://doi.org/10.3389/fpsyt.2022.813304.
8. PANGRAZZI, L., BALASCO, L., & BOZZI, Y. (2020). Natural Antioxidants: A Novel Therapeutic Approach to Autism Spectrum Disorders?. *Antioxidants*, 9. https://doi.org/10.3390/antiox9121186.
9. FRYE, R. E., ROSSIGNOL, D. A., SCAHILL, L., MCDOUGLE, C. J., HUBERMAN, H., & QUADROS, E. V. (2020, October). Treatment of folate metabolism abnormalities in autism spectrum disorder. In Seminars in pediatric neurology (Vol. 35, p. 100835). WB Saunders. https://doi.org/10.1016/j.spen.2020.100835
10. GVOZDJÁKOVÁ, A., SUMBALOVÁ, Z., KUCHARSKÁ, J., KOMLÓSI, M., RAUSOVÁ, Z., VANČOVÁ, O., ... & MOJTO, V. (2020). Platelet mitochondrial respiration, endogenous coenzyme Q10 and oxidative stress in patients with chronic kidney disease. Diagnostics, 10(3), 176. https://doi.org/10.3390/diagnostics10030176
11. PRUTHI, S., KAUR, K., SINGH, V., & SHRI, R. (2021). Improvement of cognitive function in mice by Citrus reticulata var. kinnow via modulation of central cholinergic system and oxidative stress. *Metabolic Brain Disease*, 36, 901 - 910. https://doi.org/10.1007/s11011-021-00687-7.
12. MUKAETOVA-LADINSKA, E.B., WESTWOOD, J., PERRY, E.K. (2010). Cholinergic Component of Autism Spectrum Disorder. In: Blatt, G.J. (eds) The Neurochemical Basis of Autism. *Springer*, Boston, MA. https://doi.org/10.1007/978-1-4419-1272-5_9.
13. HALLADAY, A. K., AMARAL, D., ASCHNER, M., BOLIVAR, V. J., BOWMAN, A., DICICCO-BLOOM, E., ... & THREADGILL, D. W. (2009). Animal models of autism spectrum disorders: information for neurotoxicologists. Neurotoxicology, 30(5), 811-821. https://doi.org/10.1016/j.neuro.2009.07.002.
14. MEMBRINO, V., PAOLO, A., ALIA, S., PAPIRI, G., & VIGNINI, A. (2023). The Role of Oxidative Stress in Autism Spectrum Disorder: A Narrative Literature Review. *Oxygen*. https://doi.org/10.3390/oxygen3010004.
15. SANTOS, J., ARAÚJO, C., ROCHA, C., COSTA-FERRO, Z., & SOUZA, B. (2023). Modeling Autism Spectrum Disorders with Induced Pluripotent Stem Cell-Derived Brain Organoids. Biomolecules, 13. https://doi.org/10.3390/biom13020260.
16. ANGLIN, D. M., S. ERESHEFSKY, M. J. KLAUNIG, M. A. BRIDGWATER, T. A. NIENDAM, L. M. ELLMAN, J. DEVYLDER, G. THAYER, K. BOLDEN ET C. W. MUSKET (2021). « From womb to

neighborhood: a racial analysis of social determinants of psychosis in the United States », *American Journal of Psychiatry*, vol. 178, n° 7, p. 599-610. https://doi.org/10.1176/appi.ajp.2020.20071091.
17. MASSICOT, F., G. HACHE, L. DAVID, D. CHEN, C. LEUXE, L. GARNIER-LEGRAND, P. RAT, O. LAPREVOTE ET F. COUDORE (2013). « P2X7 cell death receptor activation and mitochondrial impairment in oxaliplatin-induced apoptosis and neuronal injury: cellular mechanisms and in vivo approach», *PloS one*, vol. 8, n° 6, p. e66830. https://doi.org/10.1371/journal.pone.0066830
18. POHANKA, M. (2012). « Alpha7 nicotinic acetylcholine receptor is a target in pharmacology and toxicology », *International journal of molecular sciences*, vol. 13, n° 2, p. 2219-2238. https://doi.org/10.3390/ijms13022219.
19. CHAOUBAH, A. (2021). The important role played by Biostatistics in Health professionals' training. *Revista Brasileira de Oftalmologia*. https://doi.org/10.5935/0034-7280.20210016.
20. LEVINE, R. L., GARLAND, D., OLIVER, C. N., AMICI, A., CLIMENT, I., LENZ, A. G., ... & STADTMAN, E. R. (1990). [49] Determination of carbonyl content in oxidatively modified proteins. *In Methods in enzymology* (Vol. 186, pp. 464-478). Academic Press. https://doi.org/10.1016/0076-6879(90)86141-H.
21. POHANKA, M., HRABINOVA, M., KUCA, K., & SIMONATO, J. P. (2011). Assessment of acetylcholinesterase activity using indoxylacetate and comparison with the standard Ellman's method. *International journal of molecular sciences*, 12(4), 2631-2640. https://doi.org/10.3390/ijms12042631.
22. PIENIAZEK, A., L. GWOZDZINSKI, Z. ZBROG ET K. GWOZDZINSKI (2018). « Alterations in conformational state of albumin in serum in chronic hemodialyzed patients », *Plos one*, vol. 13, n° 3, p. e0192268. https://doi.org/10.1371/journal.pone.0192268.
23. TAVERNA, M., A.-L. MARIE, J.-P. MIRA ET B. GUIDET (2013). « Specific antioxidant properties of human serum albumin », Annals of intensive care, vol. 3, n° 1, p. 1-7. https://doi.org/10.1186/2110-5820-3-4.
24. KAUR, D., BEHL, T., SEHGAL, A., SINGH, S., SHARMA, N., CHIGURUPATI, S., ... & BUNGAU, S. (2021). Decrypting the potential role of α-lipoic acid in Alzheimer's disease. *Life Sciences*, 284, 119899. https://doi.org/10.1016/j.lfs.2021.119899.
25. OKI, S., Y. TOIYAMA, Y. OKUGAWA, T. SHIMURA, M. OKIGAMI, H. YASUDA, H. FUJIKAWA, Y. OKITA, S. YOSHIYAMA ET J. HIRO (2017). « Clinical burden of preoperative albumin- globulin ratio in esophageal cancer patients », The American Journal of Surgery, vol. 214, n° 5, p. 891-898. https://doi.org/10.1016/j.amjsurg.2017.04.007.
26. SUZUKI, K., SUGIHARA, G., OUCHI, Y., NAKAMURA, K., TSUJII, M., FUTATSUBASHI, M., ... & MORI, N. (2011). Reduced acetylcholinesterase activity in the fusiform gyrus in adults with autism spectrum disorders. Archives of general psychiatry, 68(3), 306-313. https://doi.org/10.1001/archgenpsychiatry.2011.4.
27. ALT, N., J. A. CARSON, N. L. ALDERSON, Y. WANG, R. NAGAI, T. HENLE, S. R. THORPE ET J. W. BAYNES (2004). « Chemical modification of muscle protein in diabetes », *Archives of biochemistry and biophysics,* vol. 425, n° 2, p. 200-206. https://doi.org/10.1016/j.abb.2004.03.012.
28. MIHALIK, S. J., S. F. MICHALISZYN, J. DE LAS HERAS, F. BACHA, S. LEE, D. H. CHACE, V. R. DEJESUS, J. VOCKLEY ET S. A. ARSLANIAN (2012). « Metabolomic profiling of fatty acid and amino acid metabolism in youth with obesity and type 2 diabetes: evidence for enhanced mitochondrial oxidation », *Diabetes care*, vol. 35, n° 3, p. 605-611. https://doi.org/10.2337/DC11-1577.
29. LIBERT, D. M., A. S. NOWACKI ET M. R. NATOWICZ (2018). « Metabolomic analysis of obesity, metabolic syndrome, and type 2 diabetes: amino acid and acylcarnitine levels change along a spectrum of metabolic wellness », *PeerJ*, vol. 6, p. e5410. https://doi.org/10.7717/peerj.5410.
30. ODETTI, P., S. GARIBALDI, G. NOBERASCO, I. ARAGNO, S. VALENTINI, N. TRAVERSO ET U. M. MARINARI (1999). « Levels of carbonyl groups in serum proteins of type 2 diabetes mellitus subjects », *Acta diabetologica*, vol. 36, n° 4, p. 179-183. https://doi.org/10.1007/s005920050164.
31. AYAYDIN, H., KILIÇASLAN, F., KOYUNCU, I., ÇELIK, H., ÇALIK, M., GÜZELÇIÇEK, A., & KIRMIT, A. (2021). Impaired Thiol/Disulfide Homeostasis in Children Diagnosed with Autism: A Case–Control Study. *Journal of Molecular Neuroscience*, 71, 1394 - 1402. https://doi.org/10.1007/s12031-021-01790-1.
32. ZOU, M., LI, D., WANG, L., LI, L., XIE, S., LIU, Y., XIA, W., SUN, C., & WU, L. (2020). Identification of Amino Acid Dysregulation as a Potential Biomarker for Autism Spectrum Disorder in China. *Neurotoxicity Research*, 38, 992 - 1000. https://doi.org/10.1007/s12640-020-00242-9.
33. SALEH, S.S. AND SARHAT, E.R., 2019. Effects of ethanolic Moringa oleifera extract on melatonin, liver and kidney function tests in alloxan-induced diabetic rats. *Indian Journal of Forensic Medicine & Toxicology*, *13*(4), pp.1015-1019. https://doi.org/10.5958/0973-9130.2019.00431.6
34. STADTMAN, E. R., et R. L. LEVINE (2003). « Free radical-mediated oxidation of free amino acids and amino acid residues in proteins », Amino acids, vol. 25, n° 3-4, p. 207-218. https://doi.org/10.1007/s00726-003-0011-2.

35. ZENG, J., et M. J. DAVIES (2005). « Evidence for the formation of adducts and S-(carboxymethyl) cysteine on reaction of α-dicarbonyl compounds with thiol groups on amino acids, peptides, and proteins », *Chemical research in toxicology*, vol. 18, n° 8, p. 1232-1241. https://doi.org/10.1021/tx050074u.
36. THORPE, S. R., et J. W. BAYNES (2003). « Maillard reaction products in tissue proteins: new products and new perspectives », Amino acids, vol. 25, n° 3-4, p. 275-281. https://doi.org/10.1007/s00726-003-0017-9.
37. ATES, I., M. KAPLAN, M. YUKSEL, D. MESE, M. ALISIK, Ö. EREL, N. YILMAZ et S. GULER (2016). « Determination of thiol/disulphide homeostasis in type 1 diabetes mellitus and the factors associated with thiol oxidation », *Endocrine*, vol. 51, n° 1, p. 47-51. https://doi.org/10.1007/s12020-015-0784-6.
38. GUMUSYAYLA, S., G. VURAL, H. BEKTAS, O. DENIZ, S. NESELIOGLU et O. EREL (2016). « A novel oxidative stress marker in patients with Alzheimer's disease: dynamic thiol–disulphide homeostasis », *Acta neuropsychiatrica*, vol. 28, n° 6, p. 315-320. https://doi.org/10.1017/neu.2016.13.
39. ALWAHAB, A., MOHAMMED, R., & ZAINAL, I. G. (2021). Measurement of Protein Oxidation Levels in Serum of Women with Pregnancy Complications. *Egyptian Journal of Chemistry*, *64*(11), 6449-6455. 10.21608/ejchem.2021.72125.3685
40. Jiang, S., & Yang, J. (2022). Association of insulin-like growth factor-1 and insulin-like growth factor-binding protein-3 with estimated glomerular filtration rate in patients with type 2 diabetes mellitus. *Global Translational Medicine*. https://doi.org/10.36922/gtm.v1i2.62.
41. GUTTERIDGE, J. M. C., et B. HALLIWELL (2018). « Mini-review: oxidative stress, redox stress or redox success? », *Biochemical and biophysical research communications*, vol. 502, n° 2, p. 183-186. https://doi.org/10.1016/j.bbrc.2018.05.045.
42. Onat, T., Kırmızı, D., Başer, E., Ercan, M., Çaltekin, M., Yalçın, S., Kara, M., Esinler, D., & Yalvaç, E. (2020). The relationship between oxidative stress and preeclampsia. The serum ischemia-modified albumin levels and thiol/disulfide homeostasis. *Turkish Journal of Obstetrics and Gynecology*, 17, 102 - 107. https://doi.org/10.4274/tjod.galenos.2020.23682.
43. PÉREZ-TORRES, I., M. E. SOTO, V. CASTREJÓN-TELLEZ, M. E. RUBIO-RUIZ, L. MANZANO PECH et V. GUARNER-LANS (2020). « Oxidative, reductive, and nitrosative stress effects on epigenetics and on posttranslational modification of enzymes in cardiometabolic diseases », *Oxidative Medicine and Cellular Longevity*, vol. 2020. https://doi.org/10.1155/2020/8819719.
44. SUZUKI, Y. J., M. CARINI et D. A. BUTTERFIELD (2010). « Protein carbonylation », *Antioxidants & redox signaling*, vol. 12, n° 3, p. 323-325. https://doi.org/10.1089/ars.2009.2887.

Blood variations of male albino mice treated with the antibiotic (cefoperazone)

Hussein Ali Salman AlAmiri [a], Hanan Y.Muhsin [b]

Department of Biology, College of Education for Pure Science / Ibn Al-Haitham, University of Baghdad, Baghdad, Iraq.

[a] Corresponding author: hussein.hasan1602a@ihcoedu.uobaghdad.edu.iq
[b] hanan.y.m@ihcoedu.uobaghdad.edu.iq

Abstract. The effect of the antibiotic cefoperazone was examined. The experiment was conducted on white male mice. The experiment was divided into three groups, 11-12 mice were allocated to each group to conduct different experiments, It was injected Intraperitoneal into the groups for 7 consecutive days. The control group was given distilled water throughout the experimental days. The second group was given the antibiotic cefoperazone at a dose of 500 mg/kg/day. The third group was given the antibiotic cefoperazone 800 mg/kg/day. Cefoperazone affects blood components, causing a noticeable increase in the total number of blood cells, a slight increase in the number of red blood cells, and an increase in hemoglobin and hematocrit. It also caused an increase, but it did not constitute a significant difference in blood counts. As for white blood cells, there was a significant difference for lymphocytes and eosinophils, and there was an increase in neutrophils, while for Basophil cells there was no significant increase.

Keywords: cefoperazone. red blood cells. white blood cells, CBC, Lymphocyte, Neutrophile

INTRODUCTION

During the past decade, studies conducted on antibiotics mainly targeted the activity of Gram-negative and Gram-positive bacteria, while maintaining international drug safety standards. Previous studies have shown that Cefime antibiotics do not lead to clear effects on the immune system, but it has been shown that repeated injections of Cefime antibiotics in large quantities lead to different immunological effects, whether in humans or animals [1]. Cefoperazone is a semi-synthetic third-generation cephalosporin used to treat respiratory tract infections, bacterial septicemia, skin infections, intra-abdominal infections and urinary tract infections. Cefoperazone acts on intestinal bacteria, Pseudomonas aeruginosa, bacilli, *Staphylococcus aureus*, and others. It has a broad spectrum against bacteria. [2, 3]. Bacterial flora is found in both humans and animals and are also known as opportunistic pathogens [4]**.** For example, human skin and mucous microbes contain Staphylococcus aureus, which is common but opportunistic and causes major diseases and infections [5]. Approximately 20-25% of healthy people are carriers of Staphylococcus aureus bacteria [6]. There is also Candida albicans, a yeast found as part of the normal microbial flora in most healthy humans. It is found on mucous surfaces as a usually harmless colonizer [7]. In cases of weak immunity, it can cause harm, there are more than 100 different species, but only a few can infect humans. For example, Candida spp is of continuing medical importance, and may also be life-threatening with systemic infections and chronic mucocutaneous infections. Patients with weak immunity [8]. While the study conducted on some bacterial isolates from burn wound infections showed their high sensitivity against some beta-lactam antibiotics [9]. On the other hand, many studies have found that strains of bacteria producing beta-lactamases are more common and that Staphylococcus aureus bacteria have increased their resistance to beta-lactam antibiotics. Many cephalosporins and penicillin's have become ineffective for treatment due to beta-lactamase enzymes [10]**.** Cefoperazone works by penetrating the outer layers of the bacterial cell wall, so it acts as a bactericide [11]. Matsubara, (1980) mentioned that Cefoperazone has antimicrobial activity because it has an affinity for penicillin-binding proteins. It has a high ability to bind to penicillin-binding proteins 1B, 1A, and 2A, which contribute to the initiation of cell wall elongation [12]. Third-generation cephalosporins selectively

Technologies and Materials for Renewable Energy, Environment and Sustainability
AIP Conf. Proc. 3321, 030011-1–030011-9; https://doi.org/10.1063/5.0289592
Published under an exclusive license by AIP Publishing. 978-0-7354-5231-2/$30.00

inhibit the synthesis of mucin polypeptides in the bacterial cell wall. It is unique in its ability and the presence of the beta-lactamase enzyme to remain stable [13]. All cephalosporins are expected to cross the placenta and are thought to be excreted into breast milk [14]. all non -steroidal anti -inflammatory drugs are offered from the body of the liver and kidneys [15].

MATERIALS AND METHODS

Experimental animals:

Thirty-five male mice were obtained from the Iraqi Ministry of Health/National Center for Pharmaceutical Control and Research. At 12 weeks of age, animals were fed a regular diet and water ad libitum in a controlled room at 23°C humidity .Whole blood was collected and placed in a tube containing clean ethylenediaminetetraacetic acid (EDTA) to measure the number of white blood cells (WBCs) and differential cell counts [16]

Animal Breeding:

This study was conducted on healthy, adult male white mice. The mice were cared for throughout the duration of the study in terms of cleanliness, ventilation, lighting, temperature, and continuous provision of feed and water to the mice [17].

Cefoperazone Antibiotic

Cefoperazone from Smart (New Delhi, India) is a commercial product.

Treatments

Initially, 11-12 mice were allocated to each group to conduct different experiments. The first and second groups were injected intraperitoneally with a dose of 500 mg/kg/day and 800 mg/kg/day, respectively, of the antibiotic, while the third group was injected with distilled water (control). The experiment lasted for seven days. At the end of the experiments, blood was drawn from the heart for examination.

Statistical Analysis

The Statistical Analysis System- SAS (2018) program was used to detect the effect of different groups in study parameters. The least significant difference- LSD was used to significantly compare between means. Estimate of the Correlation coefficient between different parameters in this study the complete blood count [18].

3. Results and Discussion

Intraperitoneal injection of cefoperazone was therapeutic at a dose of (500 and 800 mg/kg body weight) in male mice, where the antagonist cefoperazone was given at doses of 180 and 360 mg/kg body weight for 7 days.

Table 1: Comparison between different groups in WBC, RBC, HGB and HCT

Group	Mean ±SE				
	WBC ($x10^9$/L)	RBC ($x10^{12}$/L)	HGB (g/dl)	HCT (%)	PLT ($x10^9$/L)
Control	5.64 ±0.07 b	7.91 ±0.85	12.87 ±0.37 a	38.27 ±0.61 a	795.25 ±84.27
Conc. 1	9.82 ±0.67 a	7.20 ±0.60	10.67 ±0.90 b	35.50 ±3.04 ab	912.00 ±48.53
Conc. 2	6.87 ±0.25 b	7.97 ±0.23	11.00 ±0.57 ab	32.52 ±1.60 b	877.00 ±36.71
LSD	1.334 **	1.970 NS	2.096 *	5.452 *	191.88 NS
P-value	0.0002	0.631	0.0487	0.0491	0.406
Means having with the different letters in same column differed significantly. * ($P \leq 0.05$). ** $p < 0.01$ versus saline-treated controls.					

Table 2 presents a comparison between the different groups in terms of white blood cell (WBC) differential. The table shows the mean ± standard error (SE) values for the number of neutrophils, lymphocytes, monocytes, eosinophils, and basophils in each group..

Table 2: Comparison between different groups in the differential of White blood cells.

Group	Mean ±SE			
	Neutrophil	Lymphocyte	Eosinophil	Basophil
Control	0.108 ±0.004 b	5.39 ±0.11 c	0.00 ±0.00 c	0.055 ±0.006
Conc. 1	0.195 ±0.034 a	8.79 ±0.28 a	0.165 ±0.01 a	0.045 ±0.011
Conc. 2	0.160 ±0.012 ab	6.50 ±0.24 b	0.050 ±0.009 b	0.060 ±0.009
LSD	0.0691 *	0.718 **	0.025 **	0.0282 NS
P-value	0.0498	0.0001	0.0001	0.499
Means having with the different letters in the same column differed significantly. * (P≤0.05), ** (P≤0.01).				

The results that were conducted to analyze the average values of the white blood cell (WBC), red blood cell count (RBC), hemoglobin concentration (HGB), hematocrit level (HCT), and platelets (PLT) showed between three different groups: control, and the two concentrations. the first and the second. The results are presented in Table 1, where mean values with standard errors (SE) are shown..

1- white blood cell (WBC): In the control group, the average number of white blood cells was (5.64 x 10^9)/liter, which is significantly lower compared to the two groups treated with the antibiotic, as the first concentration represented the highest value, as it rose to (9.82 x 10^9)/liter, while the second concentration: It decreased from the first concentration, but remained higher than the control group, so that its value represented (6.87 x 10^9)/litre, as shown by different letters in the same column as in Figure (1)

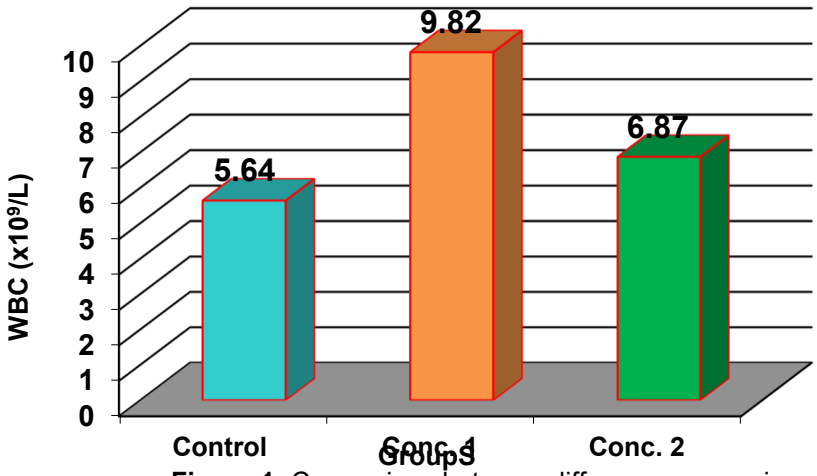

Figure 1: Comparison between difference groups in WBC

2- Red blood cell count (RBC): The average number in the control group was 7.91 x 1012/L. There was a slight increase, but there was no significant difference from the rest of the treated groups as shown in Figure (2).

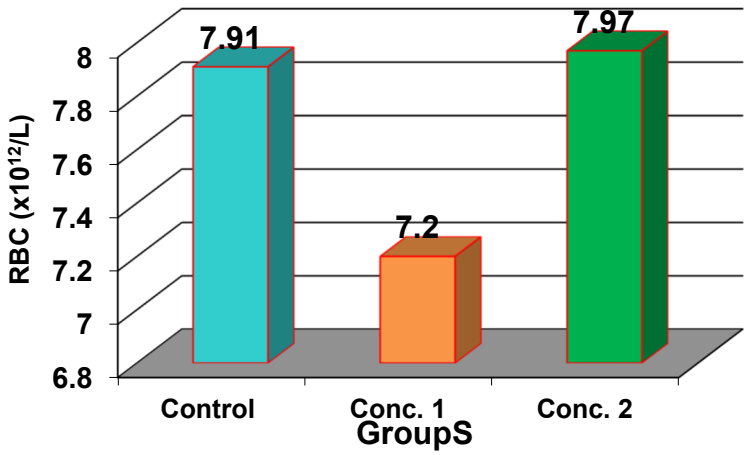

Figure 2: Comparison between difference groups in RBC

3- Hemoglobin) HGB) : the average hemoglobin concentration in the control group increased to 12.87 g/dL, which is much higher compared to the two concentrations for the control groups as shown in Figure(3).

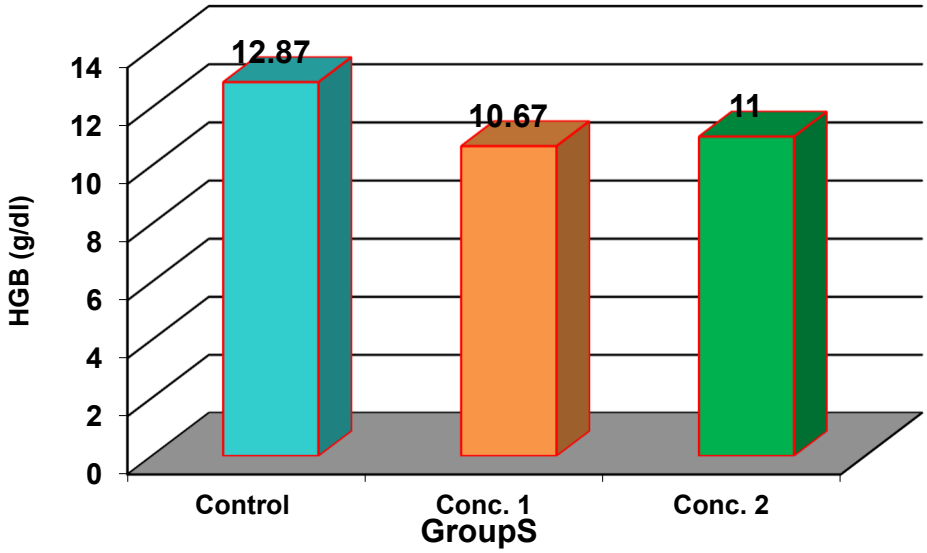

Figure 3: Comparison between difference groups in HGB

4- hematocrit level (HCT): the mean HCT level in the Control group was 38.27%, which was significantly higher compared to the other two groups as shown in Figure(4).

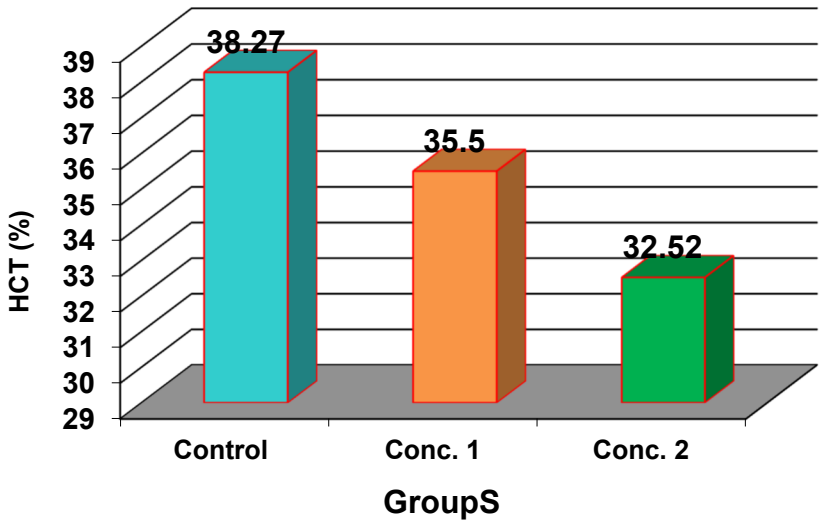

Figure 4: Comparison between difference groups in HCT

5- platelets (PLT) : In the control group, the average number was (795.25 x 10^9)/liter, which is lower compared to the two groups treated with the antibiotic, as the first concentration represented the highest value, as it rose to (912.00) ×10^9)/L. As for the second concentration: it decreased from the first concentration, but remained higher than the control group, so that its value represents (877.00 ×10^9)/L, as in Figure 1) as in Figure (5)

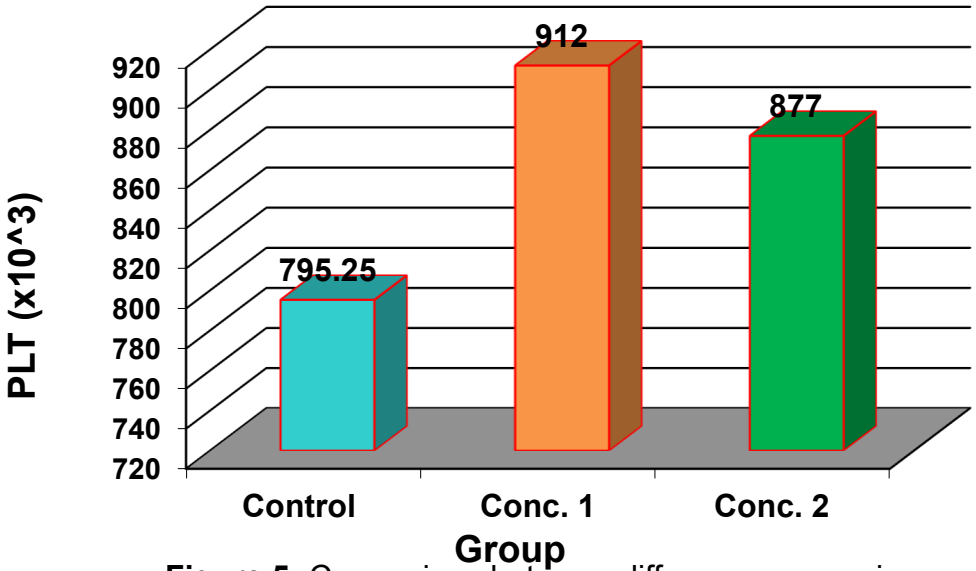

Figure 5: Comparison between difference groups in PLT

6- Table 2 presents a comparison between the different groups in terms of white blood cell (WBC) differential. The table shows the mean ± standard error (SE) values for the number of neutrophils, lymphocytes, monocytes, eosinophils, and basophils in each group..

The mean values in the control group were 0.108 ± 0.004 for neutrophils, 5.39 ± 0.11 for lymphocytes, 0.00 ± 0.00 for eosinophils, and 0.055 ± 0.006 for basophils. In comparison, in the group labeled "Conc. 1," the mean values were significantly higher for neutrophils (0.195 ± 0.034), lymphocytes (8.79 ± 0.28), and eosinophils (0.165 ± 0.01), but remained the same for basophils (0.045). ±0.011). The "Conc.2" group also showed that the mean values were found

to be lower than Conc. 1 for neutrophils (0.160 ± 0.012) and lymphocytes (6.50 ± 0.24) but similar for eosinophils (0.050 ± 0.009) and basophils (0.060 ± 0.009).
The p values for each comparison were. Neutrophils ($p = 0.0498$) and lymphocytes ($p = 0.0001$) showed significant differences between groups, while eosinophils ($p = 0.0001$) and basophils ($p = 0.499$) did not show significant differences. .
The results highlight differences in white blood cell differentiation between different groups Cefoperazone is a broad-spectrum cephalosporin antibiotic that was first developed in the 1970s. It is commonly used to treat a variety of bacterial infections, including pneumonia, sepsis, and urinary tract infections. The drug works by inhibiting cell wall synthesis in susceptible bacteria, leading to their death or inability to replicate.
The use of broad-spectrum antibiotics to treat infectious bacteria diseases to improve human health [19, 20]. However, heavy use of these antibiotics can lead to significant changes in the gut microbiome [21, 22] . Gu , (2020) mentioned that Exposure to β-Lactam Antibiotics on Mice for 4 days reduced the alpha and beta diversity of intestinal bacteria and produced an increase in the blood for inflammatory cytokines [23] . The changes persisted for a long time, but the bacterial community tended to return to its normal level after stopping treatment. The effect of four antibiotics on immunity and intestinal microbes was evaluated in mice, and it was concluded that short-term use on healthy mice could lead to disruption of the diversity and biomass of intestinal microorganisms, leading to long-term effects resulting in inflammatory response and the deficient resilience of microbiota[24].
After reviewing the literature and scientific research, I did not find research conducted on mice. On the other hand, a study was conducted on humans. Drug-induced hemolytic anemia (DIHA) is a rare drug complication most commonly caused by second- and third-generation cephalosporins. Cefoperazone/sulbactam is a combination preparation of cefoperazone, a third-generation cephalosporin, and sulbactam sodium, a beta-lactamase inhibitor) Iakovlev VP).
Another study indicated that it has been repeatedly reported that cefoperazone/sulbactam may lead to abnormal coagulation function resulting from it. However, only two reports of DIHA associated with cefoperazone/sulbactam were available. It indicated the presence of a case of abdominal infection in a patient who was prescribed treatment with intravenous cefoperazone/sulbactam (3 g, q. 12 hours) and resulted in an adverse reaction, namely hemolytic anemia. As treatment was discontinued, the condition began to improve and the negative effects decreased The research that took place about a 93 -year -old woman who had abdominal pain, nausea and vomiting for 3 days with fever at 38.5 ° C for two days. After accepting the hospital, its vital signs were normal. The full number of blood showed the number of white blood cells (WBC) 11.72 x 109/l (normal 3.5-9.5 x 109/l), the number of neutrophils (NE) 86.0 % (normal 40 % - 75 %), the number of red blood cells (RBC (3.24 x 1012/L) 3.8-5.1 x 1012/L), hemoglobin (HB) 110 g/l (normal 115-150 g/l), hematocrit (HCT) 32.8 % (normal 35-45 %) and platelet (PLT) 225 × 10^9/L (normal 125–350 × 10^9/L). It has been diagnosed with abdominal infection, abnormal liver function, jaundice and post -bile. On the day of acceptance, it was given by the doctors of Sevroberzon/Solbachamam as an anti -infection treatment (3.0 g, Q12H, IVGTT [Guttae intravenously]. On the third day, RBC, HB and HCT decreased a little bit and PLT showed a trend of fluctuation, which corresponds to our study on cefoperazone, and values were 3.10 x 1012/L, 108 g/l, and 31.8 %, respectively. After one month of anti -infection therapy, the infection improved, WBC and NE also fell. Meanwhile, RBC, HCT and HB continued to decline. The results of the laboratory test excluded the possibility of anemia caused by anemia, iron anemia or other types of anemia, and the tomography did not show any bleeding in the abdomen, so it was diagnosed with hemolytic anemia on the day 34. Medicines given before a decrease in RBC, HCT and HB (on the first day and day 2) are cefoperazone/sulbactam, omeprazole for injections, phosphatidil colin, glutamine, nadroprin calcium, aspolol, and potassium chloride. cefoperazone/sulbactam has been given only 34. At the same time, we searched for stickers and considered that it might be associated with cefoperazone/sulbactam. We stopped cefoperazone/sulbactam immediately on the day 34. Although anemia was 3 degrees as evaluated. Because we considered it a reaction to drugs, we stopped the medicine for monitoring. WBC was on the height while it is compatible with our studies, After pulling cefoperazone/sulbactam, RBC, HCt and HB levels recovered and returned to normal after 20 days[25].
The antibiotic caused changes in the shape and structure of red blood cells, including increased fragility and altered hemoglobin content. Side effects of cefoperazone/sulbactam include diarrhea, abdominal pain, bruising, congestion of the skin and mucous membranes, bleeding, blood clotting disorders, blood in the urine, and hemoptysis) [26] . Activated partial thrombin time (APTT), prolongation of prothrombin time (PT), and coagulation disorders have also been shown. Cefoperazone is characterized by the presence of the N-methylthiotetrazolium side chain, the molecular structure of which is similar to the chain found in glutamate. In liver microsomes, glutamate carboxylase competitively binds to vitamin K1, forming a complex. The defect in the clotting process within the body is the result of the effect of this structure on the synthesis of clotting factors, as clotting factors depend on the group of vitamins II, VII, IX, and X . Cephalosporins also contain a COOH group located on the 7C atom substituent, which causes bleeding because

it hinders platelet aggregation. [27]. In another study, it was shown that 25.8% of patients treated with cefoperazone/sulbactam for 3-12 days showed a blood clotting defect [28].
Due to the morphological changes, the red blood cells' ability to transport oxygen throughout the body was significantly reduced. Cefoperazone was associated with the development of hemolytic anemia. Hemolytic anemia results in a decreased ability to carry oxygen due to low levels of hemoglobin and the number of red blood cells. To ensure that adequate oxygen reaches the tissues during treatment, hemoglobin levels must be monitored [29][30] .
On the other hand, our study agreed with a study on mice that showed that cefoperazone increased IgM production in serum. In addition, cefoperazone has never been shown to activate germinal centers in the spleen. Thus, the discrepancy between the data on the immunostimulatory activity of cefoperazone reported by Gilesen and Pusztay-Marcus and our data may be due to differences in the assay methods between the reverse and direct PFC and in the rat strains used. The clinical relationship between the immunostimulatory and antibacterial activities of ceftisol should be investigated further, as the antibiotic is likely to require much higher doses than usual to demonstrate its immunostimulatory activity.

CONCLUSION

It was clearly obvious that Cefoperazone caused morphological changes in the red blood cells' which led to affect their ability to transport oxygen throughout the body Cefoperazone was associated with the development of hemolytic anemia. Hemolytic anemia results in a decreased ability to carry oxygen due to low levels of hemoglobin and the number of red blood cells. To ensure that adequate oxygen reaches the tissues during treatment, hemoglobin levels must be monitored. Also, Cefoperazone found to elict and improved the immunity of the body by increased the numbers of WBC. The study found a significant difference in white blood cell count, Hgb concentration, and HCT level between the three groups. However, no statistically significant differences were observed for the number of red blood cells and the number of platelets. These results indicate that the concentration of the antibiotic cefoperazone affected blood cell counts and hemoglobin levels in the groups tested.

REFERENCES

1. J. Descotes , " Immunotoxicology of Drugs and Chemicals, ed 2," ***Amsterdam, Elsevier,*** vol.1 ,no1, pp.31-48 , 1988.
2. S. Mitsuhashi , S . Minami, N. Matsubara , A . Yotsuji , S. Kurashige , I "Saikawa ,. In vitro and in vivo antibacterial activity of cefoperazone" ***Clinical Therapeutics***, vol.1 ,no3 ,1980 ,pp. 1-13,1980, PMID: 6446381.
3. A.E.Czeizel , M. Rockenbauer, H.T. Sorensen , and J. Olsen, "Use of cephalosporins during pregnancy and in the presence of congenital abnormalities: a population-based, case-control study" ***American journal of obstetrics and gynecology***, vol.*184*,no.6, pp.1289-1296 , 2001, https://doi.org/10.1016/S0002-9378(02)70079-3 .
4. A.W. Anwer, G.M. Saleh , M.E.Ahmed, "Antimicrobial Susceptibility of Enterococcus faecium Isolated from Bee-gut on PhzMGene of Pseudomonas aeruginosa Isolates from Infected Wounds**"** ***bn Al-Haitham Journal for Pure and Applied Sciences (IHJPAS)***, vol.37, no.2,pp.39-48, **2023, https://doi.org/10.30526/37.2.3379 .**
5. A.M. Abd Zaid, and N.J. Kandala, IRAQI *JOURNAL OF AGRICULTURAL SCIENCES*, Vol.52, No.6, pp. 1356-1364, 2021, 10.36103/ijas.v52i6.1475.
6. A.A.I. Al-Halaq, and N.M. Utba, "Prevalence of Methicillin-resistant Staphylococcus aureus Carrying lukS-lukF Gene in Iraqi Patients with Furunculosis" ***Iraqi Journal of Science***, pp.3323-3329, 2023, http://dx.doi.org/10.24996/ijs.2023.64.7.13 .
7. S.R.M. AL-Rubaie, and S. A. Al-Qaysi, " Detection of Some Virulence Factors in Candida albicans Obtained from Different Clinical Specimens of Iraqi Patients" Departmentof Biology, *Ibn AL-Haitham Journal For Pure and Applied Sciences,* vol.37,no.2,pp.1-11, 2024, doi.org/10.30526/37.2.3315 .
8. K.I.Othman, S.M. Abdullah , and A.M. Majid, " Isolation and Identification Candida spp. from Urine and Antifungal Susceptibility Test" *Iraqi Journal of Science*,vol.59, no.4B , pp.1981-1988 ,2018 , http://dx.doi.org/10.24996/ijs .
9. M. Al-Azzawi, & I. Alkhalifawi, "Detection of Bacteria Causing Burn Infection Isolated from Several Hospitals in Baghdad" *Ibn AL-Haitham Journal For Pure and Applied Sciences.* Vol.36, no.3, pp.1-8 , 2023,doi.org/10.30526/36.3.3090 .
10. E.D. Salman, A.J. AL-Saedi, A.G.M. AL-Kazzaz, and S. S. Yahya, "The Effect of Aqueous Extract and Essential Oils of the Leaves of Eucalyptus incrassate on β-Lactam Resistant Staphylococcus aureus" *Ibn AL-Haitham Journal For Pure and Applied Science*, vol.*27,*no.1, pp.76-82, 2014.

11. W. Zimmermann, 1979 "Penetration through the Gram- negative cell wall: a co – determinant of the efficacy of B- lactam antibiotics" International *journal of clinical pharmacology and biopharmacy*, vol.*17*,no.3,pp. 131–134, 1979, PMID: 107128
12. N.Matsubara, S. Minami, M. Matsuhashi, M. Takaoka, , & S.Mitsuhashi, "Affinity of cefoperazone for penicillin binding proteins*"* *Antimicrobial agents and chemotherapy*, vol.*18,*no.1, pp.195–199,1980, https://doi.org/10.1128/AAC.18.1.195
13. B. A. Cunha, & A. M. Ristuccia, "Third generation cephalosporins" *The Medical clinics of North America*, vol.*66*, no.1,pp. 283–291,1982, https://doi.org/10.1016/s0025-7125(16)31460-2
14. R.Elzoghby, "TERATOLOGICAL AND PATHOLOGICAL STUDIES OF CEFOPERAZONE IN FEMALE ALbino rats" *Lucr ST.USAMV Iasi Med Vet Series*, vol 53,no.12,pp.236-248, 2010.
15. I.M. Mnati, and B.H. Mutlak, "Histopathological Changes in Liver Induced by Piroxicam Administration in Adult Male Albino Mice Mus musculus". *Indian Journal of Forensic Medicine & Toxicology*, vol.14, no.3,pp.1535-1541, 2020.
16. R.A. Salih, , Z.H. Kadri, &, H.M. Al-Abassi "Study of the Immunomodulatory Properties of Pistacia khinjuk Extract on Rats" *INTERNATIONAL JOURNAL OF DRUG DELIVERY TECHNOLOGY,*vol.12,no.2 , pp.918-923, 2022, DOI: 10.25258/ijddt.12.2.79
17. B.Al-Musawiu, and N. Al-Bakri, " Effect of Hydroxychloroquine Drugs on Amino Acids in the Kidneys of White Mice (Mus musculas)" *INTERNATIONAL JOURNAL OF DRUG DELIVERY TECHNOLOGY*,vol. 12,no.4,pp.1590-1594, 2022,DOI: 10.25258/ijddt.12.4.18
18. SAS, "Statistical Analysis System, User's Guide. Statistical" *Version 9.6th ed. SAS. Inst. Inc. Cary. N.C. USA*. 2018
19. K. Nicolaou, S. A. Rigol, "brief history of antibiotics and select advances in their synthesis"*The Journal of antibiotics*, vol.71,no.2, pp.153–184. ,2018, https://doi.org/10.1038/ja.2017.62
20. R.Benkő, , M.Gajdács, M. Matuz, , G. Bodó, , A. Lázár, , E.Hajdú, , E.Papfalvi, , P.Hannauer, P. Erdélyi, & Z. Pető, "Prevalence and Antibiotic Resistance of ESKAPE Pathogens Isolated in the Emergency Department of a Tertiary Care Teaching Hospital in Hungary: A 5-Year Retrospective Survey" *Antibiotics (Basel, Switzerland)*, vol.*9*(9), 624 ,2020, https://doi.org/10.3390/antibiotics9090624 .
21. L. Dethlefsen, D.A. Relman ,"Incomplete recovery and individualized responses of the human distal gut microbiota to repeated antibiotic perturbation" Proceedings of the National Academy of Sciences of the United States of America, vol. 108 ,(Suppl 1), pp.4554–4561, 2011, https://doi.org/10.1073/pnas.1000087107 .
22. J. C. Clemente, L. K. Ursell, L. W. Parfrey, & R. Knight, (). "The impact of the gut microbiota on human health: an integrative view" *Cell,* vol.*148*,no.6, pp.1258–1270 , 2012, https://doi.org/10.1016/j.cell.2012.01.035
23. S. L. Gu, , Y.Gong, J. Zhang, Y. Chen, , Z. Wu, , Q.Xu, , Y.Fang, , J.Wang, , & L. L. Tang, "Effect of the Short-Term Use of Fluoroquinolone and β-Lactam Antibiotics on Mouse Gut Microbiota" *Infection and drug resistance*, vol.13, pp.4547–4558 ,2020, https://doi.org/10.2147/IDR.S281274 .
24. K. Korpela, A. Salonen, L. J.Virta, R. A.Kekkonen, K. Forslund, P. Bork, & W. M.de Vos, "Intestinal microbiome is related to lifetime antibiotic use in Finnish pre-school children" *Nat Communications*, vol.7,no.1,pp.1-8,10410, 2016, doi:10.1038/ncomms10410 .
25. X. M.Sun, L. H. Liu, Q.Wu, & H. G. Wang, "Cefoperazone/sulbactam-induced hemolytic anemia" *Journal of postgraduate medicine*, vol.*69*,no.1, pp.46–49, 2023, https://doi.org/10.4103/jpgm.JPGM_1335_20
26. L. J.Chen, F. Y.Hsiao, L. J. Shen, F. L. Wu, W. Tsay, C. C.Hung, & S. W. Lin, "Use of Hypoprothrombinemia-Inducing Cephalosporins and the Risk of Hemorrhagic Events" *A Nationwide Nested Case-Control Study*, *PloS one* , vol.*11*,no.7,pp,1-11, e0158407,2016, https://doi.org/10.1371/journal.pone.0158407
27. R. S.Wong, G. Cheng, , N. P.Chan, W. S. Wong, & , M. H.NG, "Use of cefoperazone still needs a caution for bleeding from induced vitamin K deficiency" *American journal of hematology*, vol.*81*,no.1,pp. 76-80 ,2006, https://doi.org/10.1002/ajh.20449 .
28. X.Shao, Y. Ren, N. Xie, K.Fan, H.Sun, J. Lu, J. Wei, & X. Tian, "Effect of Cefoperazone/Sulbactam on Blood Coagulation Function in Infected Emergency Department Patients and the Necessity of Vitamin K1 (VK1) Preventive Intervention: A Single-Center, Retrospective Analysis. *Medical science monitor" international medical journal of experimental and clinical research*, *29*, e939203. 2023, https://doi.org/10.12659/MSM.939203
29. E. J.Favaloro, G.McCaughan, &, L. Pasalic "Clinical and laboratory diagnosis of heparin induced thrombocytopenia: an update" *Pathology*, vol.*49*,no.4, pp.346–355,2017, https://doi.org/10.1016/j.pathol.2017.02.005 .

30. Zhou, L., Bao, J., & Ma, J. (2019). Hemolytic Anemia and Reactive Thrombocytosis Associated With Cefoperazone/Sulbactam. *Frontiers in pharmacology*, vol. *10*, pp.1-4, 1342, https://doi.org/10.3389/fphar.2019.01342 .
31. K.Akahane, K.Furuhama, M.Kato, T.Une, & T. Onodera, "Influences of cephem antibiotics on the immune response in mice" *Chemotherapy*, vol.*36*, no.4 , pp.300–307,1990, https://doi.org/10.1159/000238781 .

Blood electrolyte levels and renal functions in the regulation of blood pressure

Safa N. Ali [a)], Mouruj A. Alaubydi [b)]

Department of Biotechnology, College of Science, University of Baghdad, Baghdad, Iraq

[a)] Corresponding author: Safa.ali2306@sc.uobaghdad.edu.iq
[b)] mourujrabea@gmail.com

Abstract. Hypertension is defined as having a systolic blood pressure (SBP) of 140 mmHg or higher and/or a diastolic blood pressure (DBP) of 90 mmHg or higher hypertension, also known as high blood pressure. Osmotic pressure within a kidney function by (Urea, Creatinine, and Uric acid) can maintain fluid homeostasis through the excretion of fluids and the concentration of electrolytes such as (Calcium, Potassium, and Sodium). These parameters are used as serum markers to find their role in inducing hypertension. As stated by the results, the study involved 94 human subjects, both sex groups were divided into three subgroups (patients with medications, patients with no medications, and dialysis patients). The results of urea conc. showed a highly significant difference among patient groups in males as well as in females. Whilst, creatinine conc. were non-significant variation between both sexes in all groups of study, but significantly different were contradicted in the statistical level in males and females. Whereas uric acid results recorded in general non-significant differences between male and female groups. But a significant differences are found between female patient groups As well as, Ca recorded significant differences only in female patient groups, While Na and K conc. revealed non-significant differences between sexes as well as among different study groups.Results show that the choosing of biochemical markers has had no direct effects on Iraqi patients.

Keywords: Hypertension, Blood pressure, Renal function.

INTRODUCTION

Hypertension (high blood pressure) is a major worldwide public health challenge, defined as having a systolic blood pressure (SBP) of 140 mmHg or higher and/or a diastolic blood pressure (DBP) of 90 mmHg or higher hypertension. In 2010, it was estimated that 1.39 billion adults worldwide had hypertension, and this number is expected to rise to 1.56 billion by 2025 [2]Blood pressure (BP) level is determined by only two variables: peripheral vascular resistance and cardiac output, and based on the principle of identifying genes and genetic variants that influence the regulatory or counter-regulatory pathways of BP control will lead to the development of novel drugs and targeted treatments that will reduce high BP effectively without any adverse effects [3]. The kidneys are essential organs that help maintain normal body functions by regulating fluid, electrolyte, and acid-base balance. This helps to create a balanced environment for cell and tissue metabolism. Additionally, the kidneys help regulate blood pressure and produce erythrocytes. The nephrons are the basic functional units of the kidneys, and each kidney has approximately 1.2 million nephrons. The nephron consists of a glomerulus, which is the filtration unit, and a tubule [31]. The net effect of a multitude of independent factors, each with a small cumulative effect, this can be extended to hypertension [3]. The kidneys regulate fluid reabsorption from the glomerular filtrate. Human body fluids can divide into intracellular and extracellular fluid compartments and the regulation of fluid homeostasis in the body depends on the excretion of fluids and the concentration of electrolytes, which generate osmotic pressure. This process is called osmoregulation [4]. Previous findings suggest that potassium may be more effective in lowering blood pressure at higher levels of sodium intake [32]. Therefore, this study was aimed to find the real correlation among factors such as some essential electrolyte serum levels and the strong relationship with renal functions in hypertension occurrence, by improving the

Technologies and Materials for Renewable Energy, Environment and Sustainability
AIP Conf. Proc. 3321, 030012-1–030012-8; https://doi.org/10.1063/5.0290406
Published under an exclusive license by AIP Publishing. 978-0-7354-5231-2/$30.00

find their effect on patients with hypertension who take medications, and patients with no-medications by the filtration and reabsorption of mechanical action of the kidney function units by glomerular filtration rate (GFR).

MATERIAL AND METHODS

Study acceptance

Ethical approval from University of Baghdad/ college of science (no. CSEC/0124/0016) was obtained for the study from accredited individuals for requesting blood samples.

The subjects

A group of 59 patients involved (patients administered hypertension medications, non-medicated patients, and dialysis patients) were collected from private Clinics, which were selected according to the advice of a specialist physician, and other 36 apparently healthy individuals as control.

Confirmative Bio test

All patients and control subjects' serums were analyzed for several biochemical parameters including Renal function (Urea, *Creatinine*, Uric acid sodium, potassium, and calcium) in serum using Cobase c311, Roche Hitachi/ Germany. All the biochemicals normal range depend on the instruction of the kits of the same device. Urea is 15 – 40 mg/dl , creatinine in female is 0.6-1.1 mg/dl, whereas in male 0.7-1.3mg/dl, uric acid is 2.6 – 6.0 mg/dl in adult female and, 3.5-7.2 in adult male, calcium is 8.41 - 11.6 mg/dl, K is 3.5 – 5.1 mmol/L, and Na is 135 – 148 mmol/L.

Statistical analysis

The data were analyzed using the following software, Microsoft excel, and IBM SPSS V26. The results reported in this study were expressed as mean ± SD. Independent t-test were used to test between males and females. One-way ANOVA were used to test between study groups. Probability values less than 0.05 and 0.01 were considered significantly.

RESULTS AND DISCUSSION

The study was conducted on 94 human subjects, males and females, with age ranging from 35 to 60 years old. These people were divided into two groups, Hypertensive patients, which included 58 patients, 25 (43.1%) males and 33(56.9%) females with mean age 51.9, and 52 respectively, both sex groups are divided into three subgroups (patients with medications, patients with no medications, and dialysis patients). Another apparently healthy control, which included 36 people, 15(41.7%) males and 21(58.3%) females.

The results in Table 1 revealed there is a non-significant variation between males and females' patients in all studied groups. These results were incompatible with Jane, (2001) who reviewed that some studies by using the 24-hour technique of blood pressure monitoring have revealed that blood pressure is higher in men than in women at the same ages. While beyand menopause, blood pressure rises in females to levels more than in males. And found that hormone supplement therapy in most cases does not meaningfully decrease hypertension in postmenopausal females, signifying that the loss of estrogens hormone may not be the only reason component involved in the hypertension in females beyand menopause. In contrast, androgens hormone may decline slightly, in most postmenopausal females. As well as, He found that in animal studies showed, there is a reducing of the pressure-natriuresis correlation in male naturally hypertensive rats and in ovariectomized female spontaneously hypertensive rats treated with testosterone chronically. The key factor in adjusting the pressure-natriuresis association is the renin-angiotensin system (RAS). The probability that androgens elevate blood pressure via the RAS is discovered, and the chance that the RAS also stimulates oxidative stress leading to produce of vasoconstrictor materiales and reduction in nitric oxide accessibility is suggested.

Table 1. The baseline of the patient's number

	Total NO.	Patients	Patients-no-medications	Dialysis	P. Value¥
Male	25	14 (56%)	9 (36%)	2 (8%)	0.0407*
Female	33	22 (66.7%)	9 (27.3%)	2 (6%)	
P- value	0.134	0.428 N.S	0.479 N.S	0.777 N.S	
Total No.	58	36 (62.1%)	18 (31%)	4 (6.9%)	

¥: Chi square goodness of fit test was used *and were indicated to significant at (P≤0.05) and (P≤0.01)**

As well as, Paul *et al*.,(2022) elucidated that in spite of hypertension is overall more common in males, females involvement a much sharper gradient in BP from the 3rd decade of life and subsequently the occurrence of hypertension become faster comparatively with age. The responsible mechanisms for these BP may include the continued vascular influence of BP disorders of sex hormones, pregnancy, interactions between the renin–angiotensin–aldosterone system and or even psychosocial sex factors such as socioeconomic deprivation. Additionally, the impact of increase BP is not uniform and women are at higher risk of increasing a multitude of antagonistic cardiovascular effects at lower BP thresholds.

On the same context, the recent results showed significant variation among study groups (medicated, nonmedicated, and dialysis) between males (14(56%),9(36%),and 2(8%)) and females(22(66.7%), 9(27.3%), and 2(6%)) respectively.

As Hikari *et al*., (2020) explained the mechanism of Blood pressure medicines which can keep BP at a healthy level throughout: Producing the body to get rid of H_2O, which declines the amount of H_2O and salt in the body to a good and suitable level. Relaxing state in the blood vessels, that making the heart beat with less force, and the obstructive of the nerve activity that can control the blood vessels. Because of all previous advantages, the recent results showed most hypertensive people are medicated with the percentage more than other groups.

Urea level in serum

The following results in table 2 revealed that, there was a non-significant variation between both sexes in all groups of study, these results confirmed to that documented in another local research done by AL – Hamdani, (2010). While Xiaoyun *et al*., (2019) observed a significant increasing occurrence of hypertension and hyperuricemia in males than in females. Males with hyperuricemia (mainly those in middle age) had a significant susceptibility of hypertension, whilst this significant relationship was not detected in females.

On the other hand, the current results showed a high significant difference among patients groups in males (54.17 ± 43.16,46.96 ± 49.90, 116.50 ± 53.03)mg/dL, as well as in females (41.08 ± 18.04,30.28± 13.15, 135.90 ± 28.14)mg/dL. These results were significantly different in comparable with the control group 33.54 ± 13.03 mg/dL and 27.03 ± 7.30 mg/dL respectively. These results are confirmed to all researches studies with this subject and they explained this increasing may be related to the decrease Glomerular Filtration Rate (GFR) as a result of influence the increasing of blood pressure on renal function (decrease in renal blood flow as a sequence of increasing renal vascular resistance) . The decrease in the blood flow of renal leads to a reduction of GFR, consequently lead to a drop in distal tubular flow rate then increase the reabsorption of urea and declined in the secretion which may be explained the increases of serum urea concentration as Xiaoyun *et al*., (2019) mentioned.

Table 2. The urea serum level differences among study groups

Urea mg/dl					
Sex	**Study groups**				**P-value**
	Patient (medications)	**Patients (No-medication)**	**Dialysis patients**	**Control**	
Male	54.17 ± 43.16	46.96 ± 49.90	116.50 ± 53.03	33.54± 13.03	0.038 *
Female	41.08 ± 18.04	30.28 ± 13.15	135.90 ± 28.14	27.03 ± 7.30	0.001*
P-value	0.209	0.374	0.693	0.064	

Data presented as Mean ± SD, © * significant (P<0.05)

Creatinine level in serum

The following results in Table 3 elucidated that, as before, there was a non-significant variation between both sexes in all groups of study, but the results of different groups were contradicted in the statistical level that appeared between males (1.66 ± 1.76, 1.26 ± 1.31, and 5.05 ± 0.07) mg/dL and females (0.90 ± 0.60,0.87 ± 0.36, and 11.05 ± 7.85) mg/dL comparable with the control group (0.94 ± 0.48, and 0.64 ± 0.13) mg/dL.

Table 3. The Creatinine serum level differences among study groups

Creatinine level mg/dL					
Sex	**Study groups**				**P-value**
	Patients with medication	**No-medication**	**Dialysis**	**Control**	
Male	1.66 ± 1.76	1.26 ± 1.31	5.05 ± 0.07	0.94 ± 0.48	0.010*
Female	0.90 ± 0.60	0.87 ± 0.36	11.05 ± 7.85	0.64 ± 0.13	0.001*
P-value	0.067	0.424	0.393	0.011*	

Data presented as Mean ± SD, * significant (P<0.05)

The normal range of creatinine in blood serum is 0.7-1.3 mg/dLfor male and 0.6-1.1 mg/dL for female. Female frequently have a lower blood creatinine level than male, because female predominantly have less muscle mass than male. Creatinine level differences based on individual's size and muscle mass (Hsieh *et al*.,2008). The recent results were occurred within the normal range for both medicated and nonmedicated groups regardless of sex. While dialysis group, inspite of nonsignificant difference between male and female, but this group showed decreases in the level of creatinine in male than female which revealed increases in the level of creatinine in the blood. These results are expected because most females had increase in body mass index incomparable to males and most males are presomokers as Shabankhani *et al*., (2015) reviewed that serum creatinine had a significant effect on the work of kidneys, and the characterization of differences that affected the creatinine blood level was highly suggested in regulatory the kidneys performance. The results of most global studies showed on hemodialysis patients conducted that by determining and adjusting variables like weight, tobacco consumption, and monitoring of correlated diseases like hyper and hypotension could expect and control creatinine variation accurately. Additionally, Xiaoyun *et al*., (2019) found the elevation of serum creatinine concentration may be attributed to get down in creatinine clearance due to the decrease in the GFR

Uric acid level in serum

Uric acid a waste materials normaly produce in the blood. It is yielded as a result of natural substance found in the body called purines were break down. They are also found in many foods and drinks (Jessica et al., 2016). Regardless of the normal range 3.5 to 7.2 mg/dL, the results in Table 4 recorded in general no significant differences between males and females' groups. But a significant differences are found between females patients (5.71 ± 1.61,4.73 ± 1.14, 6.55 ± 2.47) mg/dL groups in comparable with control group 5.78 ± 1.73 mg/dL, these results are compatible with a study done by Kuwabara *et al.*, (2014), depended on the regression analyses were performed in the overall group, showed there were significant differences between HT and normal BP groups with respect to several variables, including age, sex, weight, height, BMI, eGFR, SUA, and prevalence of smoking, dyslipidemia, and diabetes.
In addition,Yoshiaki *et al*., (2019) study was certified that Uric Acid was strongly related with the occurrence of hypertension in the multivariable modle in all experiment subjects. In age-stratified analysis, the subjects below 50 years of age in males had the significant suggestion of Uric acid with occurrence of hypertension, while subjects above 50 years did not. In females, contributors above 40 years had the significant relationship, whilst those below 40 years did not. The data suggested that Uric acid level is an independent predictor for occurrence hypertension among middle aged of males below 50 years old and middle aged and the elderly females above 40 years, as the current study found.

Table 4. The Uric acid serum level differences among study groups

Uric acid mg/dL					
Sex	**Study groups**				**P-value**
	Patient	**Non-medication**	**Dialysis**	**Control**	
Male	5.86 ± 1.70	5.98 ± 1.53	7.20 ± 2.69	5.78 ± 1.73	0.742
Female	5.71 ± 1.61	4.73 ± 1.14	6.55 ± 2.47	4.51 ± 1.31	0.028*
Mean	0.796	0.071	0.825	0.018*	

Data presented as Mean ± SD, * significant (P<0.05)

As well as, the current results are compatible with a study done by Kuwabara *et al*., (2014) reported that, Hyperuricemia, can independently increase the risk of cardiovascular events, metabolic syndrome, and renal failure. However, these observations were made in hypertensive patients who were undergoing treatment with antihypertensive agents that can influence uric acid levels. Calcium antagonists usually decrease uric acid levels, while thiazide diuretics, β-blockers, angiotensin-converting enzyme inhibitors, and angiotensin II receptor antagonists often increase uric acid levels. Hyperuricemia is a risk factor for vascular disease, hypertension, and metabolic syndrome. The study has also shown that hyperuricemia hinders arterial dilation, which are dependent on endothelium. In addition, UA has been found to inhibit NO expression over time and increase the expression of inflammatory cytokines IL-6, IL-8, and TNF-α in vitro, especially at high doses (Zhen and Gui, 2017).

Calcium level in serum

Calcium is one of the essential biochemical marker related with heart vescular and kidney diseases, throughout intracellular Ca^{++} plays a vital role in the directive of cardiovascular occupations: An elevated influx of Ca^{++} into the cells of vascular smooth muscle leads to a develop muscular tone and therefore to an amplified vascular resistance and increase in blood pressure (Simonetti and Mohaupt, 2007).

The result in Table 5 recorded significant differences only in females' patient's groups (8.94 ± 0.91, 9.63 ± 0.78, 5.75 ± 0.07) mg/dL comparable with the control group (9.34 ± 0.91) mg/dL. While the male groups showed no significant differences (9.28 ± 1.20, 9.14 ± 0.88, 8.40 ± 2.40) mg/dL, compared with the control group (9.27 ± 0.60) mg/dL. These results are compatible with a study done in the North American Journal of Medical Sciences (2012) demonstrated that, one of the important ions present in the serum is calcium. The current study indicates that there is no significant difference in serum calcium levels between the hypertensive and normotensive groups, which is in line with the findings of Kosch *et al.*, (2001).

Table 5. the Calcium serum level differences among study groups

Ca mg/dL					
Sex	**Study groups**				**Mean**
	Patient	**No-medication**	**Dialysis**	**Control**	
Male	9.28 ± 1.20	9.14 ± 0.88	8.40 ± 2.40	9.27 ± 0.60	0.686
Female	8.94 ± 0.91	9.63 ± 0.78	5.75 ± 0.07	9.34 ± 0.91	0.001**
P-value	0.346	0.239	0.260	0.739	

Data presented as Mean ± SD, * significant (P<0.05) and highly significant (P<0.01)

However, the results are contradictory with those of others who reported a significant decrease in serum calcium was observed in patients with essential hypertension when compared to normotensive individuals (Reichel *et al*., 1992; Hazari *et al*., 2012) also they reported a reduction occurance in calcium serum level in males with elevated DBP.

Haruki and his coworkers (2019) demonstrated that the orderly consumption of Ca may play a role to the inhibition and treatment of hypertension in individuals with a non-vit D deficiency, as well as that dietary vit D intake may efficiently avoids this deficiency. This reason may be explained the current results, in spite of most patiants serum Ca levels are within the normal ranges except those of dialysis, are suffered from hypertension due to most Iraqis are suffered from vit D deficiency (Salim *et al*., 2023)

Potassium and sodium levels in serum

Table 6, showed the level of K^+ in experimental subjects which were revealed a non-significant differences ($P<0.05$) in all studied groups, either in females (4.13 ± 0.64, 4.08 ± 0.434.40 ± 1.70) mg/dL or males (3.88 ± 0.43, 3.68 ± 0.44, 3.65 ± 0.78) mg/dL compared to control (4.08 ± 0.43, 4.11 ± 0.41) mg/dL. This recent results were agreed with a Chinese study that reviewed a non-significant difference between males and females in the statistical data (Xi *et al*., 2015).

Whereas, the current results disagreed with Krogager *et al.,* (2017) documantion how they found that males more often had hyperkalemia, whereas females were generally more susceptible to hypokalemia.

However, the normal range of K^+ in both hypertension or normal control individuals in this study is indicated to the regulatory mechanisms preserve the serum K^+ concentration within fitted limits, and there is still little data about BP properties of vairations within or close the normal serum K^+ range (McDonough and Youn , 2017). Vasan *et al*., (2004) observed that decline of serum K^+ concentration has been associated to salt-sensitivity and salt-sensitive hypertension by hyperaldosteronism. Krogager *et al*., (2017) found that, renin–angiotensin–aldosterone system inhibitors and diuretics are essential in the treatment of hypertension, but may lead to serum potassium abnormalities. And they concluded, K^+ levels outside the range of 4.1–4.7 mmol/L were related with rised mortality risk in hypertension individuals.

On the same context, Amie *et al*., (2022) elucidated an important note which included a data improve electrolytes are have unstable ranges among individuals. Throughout, the differences in mean of K^+ in serum among Ghanaian populations living in diverse locations in Ghana and Europe, the different suggestions with hypertension between sites.

Table 6. Potassium serum level differences among study groups

K (mg/dL)					
Sex	**Study groups**				**Mean**
	Patient	**No-medication**	**Dialysis**	**Control**	
Male	3.88 ± 0.43	3.68 ± 0.44	3.65 ± 0.78	4.11 ± 0.41	0.111
Female	4.13 ± 0.64	4.08 ± 0.43	4.40 ± 1.70	4.08 ± 0.43	0.897
P-value	0.224	0.073	0.627	0.867	

On another hand the level of Sodium (Na) is association with the level of potassium in blood serum. Table 4-6 revealed the non-significant differences in the level of Na^+ between female serum groups (139.29 ± 4.58, 142.35 ± 2.55,140.50 ± 2.12) mg/dL and males' groups (138.79 ± 5.56,139.19 ± 2.76,137.50 ± 0.71) mg/dL compared with control (143.50 ± 7.26,141.65 ± 4.06) mg/dL respectively.

These results are compatible with the results of K^+, both ions serum levels are within the normal range, this due to Na/K balance mechanism as Vanessa and Ellen (2014) reviewed, the Na/K ratio appears to be more strongly related with BP outcomes than either Na or K alone in hypertensive adult populations. The data from the clinical studies provide the importance of this ratio in the evaluation of BP outcomes and occurance of hypertension. But it remains unclear whether this is fact in normotensive individuals and in children and for associated outcomes including the arterial stiffness, the augmentation index, renin-angiotensin system, and endothelial dysfunction.

As well as, Huan et al., (2021) concluded that an elevated in the level of Na in the serum was related with an improved risk of emerging hypertension, suggesting that serum Na could be a possible risk factor for increasing of blood pressure.

Table 7. The Sodium serum level differences among study groups

Na mg/dL					
Sex	**Study groups**				**Mean**
	Patient	**No-medication**	**Dialysis**	**Control**	
Male	138.79 ± 5.56	139.19 ± 2.76	137.50 ± 0.71	141.65 ± 4.06	0.259
Female	139.29 ± 4.58	142.35 ± 2.55	140.50 ± 2.12	143.50 ± 7.26	0.102
P-value	0.775	0.024*	0.198	0.378	

The communication between the blood vessels and tubules within the kidney plays a crucial role in regulating the reabsorption of salt and water, which affects the intravascular filling pressure. If blood pressure rises, a process called pressure natriuresis takes place, which leads to an increase in salt excretion through urine. This results in a decrease in extracellular fluid volume and ultimately causes a drop in blood pressure. However, in cases of chronic hypertension, the kidneys retain salt excessively, leading to volume expansion and increased blood pressure. High blood pressure, in turn, triggers natriuresis, which helps to restore salt balance and lower blood pressure. This means that hypertension is a slow response to chronic salt retention, even in individuals with an inherited genetic predisposition. It can take years for the increase in blood pressure to develop (Murillo-de-Ozores *et al*., 2019). Thus this regulatory mechanism may explain the normal K/Na serum levels in patients of hypertension in the current study, and may occurred throughout using hypertension drugs.

CONCLUSIONS

In general, High blood pressure is commonly seen in people with chronic kidney diseases. The kidney plays a significant role in regulating blood pressure. However, when kidney function is impaired, maintaining balance in hormones, electrolytes, adrenergic activity, and endothelial function becomes difficult. This is especially true in the presence of other conditions like diabetes and cardiovascular disease and can contribute significantly to hypertension, and also ADH is a hormone that plays a crucial role in maintaining the balance of water, osmolarity, and blood pressure in the body by Calcium, phosphate, magnesium, sodium, potassium, and chloride all play important roles in maintaining good body fluids balancing, so for example, if increased potassium intake can lead to a reduction in blood pressure, on another hand sodium intake is linked with a decrease in both systolic and diastolic blood pressure; but in our finding results from Clinical experimental examinations have been carried out to observe the effects of renal function biochemical parameters and electrolyte serum levels had no direct effect on inducing hypertension in Iraqi individuals for all these biomarkers.

REFERENCES

1. Su, Wen, et al. "Aquaporins in the kidney: physiology and pathophysiology." American Journal of Physiology-Renal Physiology 318.1 (2020): F193-F203.
2. Zhu, Xu, et al. "Inverse association of serum carotenoid levels with prevalence of hypertension in the general adult population." Frontiers in Nutrition 9 (2022): 971879.
3. Padmanabhan, Sandosh, Mark Caulfield, and Anna F. Dominiczak. "Genetic and molecular aspects of hypertension." Circulation research 116.6 (2015): 937-959.
4. Chen, J., Sarah Sabir, and Yasir Al Khalili. "Physiology, osmoregulation and excretion." (2019).
5. Schultheiss, Ulla T., et al. "Thyroid function, renal events and mortality in chronic kidney disease patients: The German Chronic Kidney Disease study." Clinical Kidney Journal 14.3 (2021): 959-968.
6. Basu, Gopal, and Anjali Mohapatra. "Interactions between thyroid disorders and kidney disease." Indian journal of endocrinology and metabolism 16.2 (2012): 204-213.
7. Isra'a, H. A. "Estimation of serum uric acid, urea and creatinine in essential hypertensive patients." Tikrit Medical Journal 16.1 (2010): 152-158.
8. Lin, Xiaoyun, et al. "Gender-and age-specific differences in the association of hyperuricemia and hypertension: a cross-sectional study." International journal of endocrinology 2019 (2019).
9. Perneger, Thomas V., et al. "A prospective study of blood pressure and serum creatinine: results from the'Clue'study and the ARIC study." Jama 269.4 (1993): 488-493.
10. Yadav, Dhananjay, et al. "Association between urine albumin-to-creatinine ratio within the normal range and incident hypertension in men and women." Yonsei medical journal 57.6 (2016): 1454.

11. Kuwabara, Masanari, et al. "Relationship between serum uric acid levels and hypertension among Japanese individuals not treated for hyperuricemia and hypertension." Hypertension Research 37.8 (2014): 785-789.
12. Zhen, Haitao, and Fen Gui. "The role of hyperuricemia on vascular endothelium dysfunction." Biomedical reports 7.4 (2017): 325-330.
13. Hazari, Mohammed Abdul Hannan, et al. "Serum calcium level in hypertension." North American Journal of Medical Sciences 4.11 (2012): 569.
14. Minisola, Salvatore, et al. "Epidemiology, pathophysiology, and genetics of primary hyperparathyroidism." Journal of Bone and Mineral Research 37.11 (2020): 2315-2329.
15. Yalçin, Siddika Songül, et al. "Association of urine phthalate metabolites, bisphenol A levels and serum electrolytes with 24-h blood pressure profile in adolescents." BMC nephrology 23.1 (2022): 141.
16. Van der Wijst, Jenny, et al. "Effects of a high-sodium/low-potassium diet on renal calcium, magnesium, and phosphate handling." American Journal of Physiology-renal Physiology 315.1 (2018): F110-F122.
17. Krogager, Maria Lukacs, et al. "Short-term mortality risk of serum potassium levels in hypertension: a retrospective analysis of nationwide registry data." European heart journal 38.2 (2017): 104-112.
18. Murillo-de-Ozores, Adrián Rafael, Gerardo Gamba, and Maria Castañeda-Bueno. "Molecular mechanisms for the regulation of blood pressure by potassium." Current Topics in Membranes 83 (2019): 285-313.
19. Danzi, Sara, and Irwin Klein. "Thyroid hormone and blood pressure regulation." Current hypertension reports 5.6 (2003): 513-520.
20. Berta, Eszter, et al. "Hypertension in thyroid disorders." Frontiers in endocrinology 10 (2019): 482.
21. O'Shea, P. M., T. P. Griffin, and M. Fitzgibbon. "Hypertension: the role of biochemistry in the diagnosis and management." Clinica Chimica Acta 465 (2017): 131-143.
22. Trepanier, Lauren A. "Medical management of hyperthyroidism." Clinical Techniques in Small Animal Practice 21.1 (2006): 22-28.
23. Fitzgerald, Stephen Paul, and Nigel Geoffrey Bean. "Thyroid stimulating hormone (TSH) autoregulation reduces variation in the TSH response to thyroid hormones." Temperature 5.4 (2018): 380-389.
24. Åsvold, Bjørn O., et al. "Association between blood pressure and serum thyroid-stimulating hormone concentration within the reference range: a population-based study." The Journal of Clinical Endocrinology & Metabolism 92.3 (2007): 841-845.
25. Jiang, F., et al. "Change in serum TSH levels within the reference range was associated with variation of future blood pressure: a 5-year follow-up study." Journal of Human Hypertension 31.4 (2017): 244-247.
26. Chaulin, Aleksey M., et al. "Experimental modeling of hypothyroidism: principles, methods, several advanced research directions in cardiology." Russian Open Medical Journal 10.3 (2021): 311.
27. Bayram, Saja Muhanad, Lina A. Salih, and Samia A. Eleiwe. "The Study the correlation between Human Chorionic Gonadotropin Hormone and Some Biochemical Parameters in Iraqi Women with Pregnancy-Induced Hypertension." Iraqi Journal of Science (2018): 1786-1791.
28. Allawi, Ahmed Fallah, Ferial A. Al-Mahdawi, and Abdul-Karim Y. Al-Samerraie. "Study the Effect of Hyperthyroidism on Heart Function by Using BNP as Indicator." Iraqi Journal of Science (2014): 1541-1546.
29. Hasan, Mustafa R., Satar M. Kadam, and Samar I. Essa. "Diffuse Thyroid Uptake in FDG PET/CT Scan cCan Predict Subclinical Thyroid Disorders." Iraqi Journal of Science (2022): 2000-2005.
30. Abed, R. M. "Osteocalcin level and its association with vitamin D receptor gene polymorphisms (taqi and apai) in Iraqi obese type 2 diabetes mellitus in." International Journal of Science and Research (IJSR) December 6.12 (2017): 1599-1604.
31. McDuffie, James E. "Brief overview: assessment of compound-induced acute kidney injury using animal models, biomarkers, and in vitro platforms." Toxicologic Pathology 46.8 (2018): 978-990.
32. Ekmekcioglu, Cem, et al. "The role of dietary potassium in hypertension and diabetes." Journal of physiology and biochemistry 72 (2016): 93-106.

A comparative study of the effectiveness of prolidase, proline dehydrogenase and some hormones in patients with immune and non-immune thyroid disease

Vian Ismael Mohammed [a] and Sayran Sattar Saleh [b]

Department of Chemistry, College of Science, University of Kirkuk, Kirkuk, Iraq.

[a] Corresponding author: vyanismael@uokirkuk.edu.iq
[b] sayran.2017@uokirkuk.edu.iq

Abstract. In studies that examined the relationship between the effectiveness of prolidase, proline dehydrogenase, and some hormones in patients with autoimmune and non-immune thyroid disease. First, we did some blood tests to diagnoses type of thyroid disease such as (TSH , T3, T4, anti Tpo, anti TG, TSH receptor Ab) This study was conducted on 50 healthy people and 200 patients, including 100 with non-immune thyroid disease (50 hyperthyroidism and 50 hypothyroidism). There was a decrease in the TSH percentage and a increase in the T3 and T4 percentage for hyperthyroidism, and a increase in the TSH percentage and an decrease in T3 and T4 for the underactive thyroid. As for the thyroid, the immune tests were normal for (anti Tpo, anti TG, TSH receptor Ab) . And 100 patients with an immune thyroid gland (including 50 Graves, in which there was a decrease in TSH and an increase in T3, T4, and 50 Hashemito, in which there was an increase in TSH and a decrease in T3, T4) and there was an increase in immune tests anti Tpo, anti TG, Tsh receptor Ab) . There may be a peripheral association between thyroid hormones and leptin in addition to the proposed central relationship, although this effect is unclear. Since both thyroxine and triiodothyronine are implicated in the starvation-induced decrease in thermogenesis, thyroid hormones and leptin may be engaged in adaptive thermogenesis through mitochondrial uncoupling proteins and heat production. Studies on leptin in humans and rodents have not consistently shown a connection between serum leptin concentrations and thyroid function. However, given that thyroid hormone plays a part in thermogenesis and the control of uncoupling proteins, leptin may play a significant role in thyroid pathophysiology. We have concentrated on the role of leptin in thyroid pathophysiology in this review.

INTRODUCTION

Autoimmune thyroid diseases (AITD) are the most common organ-specific autoimmune disorders (ADs), impacting 2–5% of the population and showing significant gender differences (i.e., women 5–15% and males 1–5%). AITD include Graves' Disease (GD) and Hashimoto Thyroiditis (HT), among others (44) . For hypothyroidism and hyperthyroidism, respectively, the main causes are HT and GD . As a result of reactive T cell and B cell infiltration, autoantibody production, loss of immunological tolerance, and the emergence of a humoral and cellular immune response to thyroid gland antigens, they are reflective of the development of clinical symptoms [1] . Hashimoto thyroiditis: It is the most prevalent autoimmune cause of hypothyroidism, when lymphocytes invade its thyrocyte and, in certain cases, produce cell lysis and a response of inflammation that destroys the follicle and lowers thyroid hormone levels. To diagnose HD, thyroid antibodies TgAb and TPOAb have been employed. Hashimoto's thyroiditis is believed to be caused by a confluence of environmental and hereditary variables. People who have a family history of autoimmune diseases Hashimoto's thyroiditis is more common in people with thyroid disorders[2] [3]. Graves' disease (GD)This type of hyperthyroidism, known as Graves' autoimmune disease, is most common and is caused by autoantibodies in the bloodstream called thyroid stimulating immunoglobulins (TSIs), which are directed against the thyroid gland's TSH receptors. These autoantibodies bind to TSH receptors (TSHRs) and mimic the action of pituitary TSH by inducing thyroid growth and function, which leads to over function of the thyrocyte and increases the rate at which thyroid hormones are released. TSH release is inhibited by the increased level of TH secretion brought on by TSI. TSH levels are therefore below normal—often nil—in nearly all Graves' disease patients, rather than improved.

Technologies and Materials for Renewable Energy, Environment and Sustainability
AIP Conf. Proc. 3321, 030013-1–030013-9; https://doi.org/10.1063/5.0290902
Published under an exclusive license by AIP Publishing. 978-0-7354-5231-2/$30.00

It's quite likely that autoimmunity against thyroid tissue developed into the antibodies that cause hyperthyroidism. Eyeball protrusion affects most hyperthyroidism sufferers to some extent. Ophthalmopathy, also known as Graves' orbitopathy, is a disorder marked by edema, upper eyelid retraction, and swelling in the soft tissue surrounding the orbit of the eye. There are cases when it gets so bad that the protrusion of the eyeball stretches the optic nerve to the point of eyesight damage. The eyelids of a patient sometimes don't close all the way when they blink or sleep, which can lead to excessive tearing, double vision, gritty and dry eyes, and photophobia—all conditions that can harm the eyes [4]. Non-autoimmune thyroid diseases clinically shown as non-autoimmune hypothyroidism or destructive thyroiditis.Destructive thyroiditis was the diagnosis made for patients who acquired clinical TD, which is characterized by an initial hyperthyroid phase followed by a progressive remission (sometimes with a hypothyroid phase) in the absence of thyroid antibodies. A reduced or blocked uptake of radioiodine served as confirmation. Non-autoimmune hypothyroidism was defined as hypothyroidism in those without thyroid antibodie who had clinical symptoms and laboratory evidence of the condition.

The hepatologist's analysis of the virus genotype, viral response, and side effects determined how long an HCV treatment would last[5].In the event that TD was discovered during IFNα therapy, the patient was kept under observation or received thyroid medication. IFNα therapy should not be stopped. Following a three-month break from IFNα therapy, thyroid function tests were used to assess the patients clinically. In order to ascertain if the patient's TD was temporary or permanent, testing was done on them twelve months after the therapy was stopped if they had experienced one[6]. Prolidase [E.C. 3.4.19.9] is an enzyme that belongs to the class of enzymes that catalyze the hydrolysis of basic substances. It is the only enzyme that can hydrolyze dipeptides that have proline or hydroxyproline derivatives at the terminal end of the carbon group in order to produce free proline. Finally, free proline is important in the last stages of the catabolism of proteins rich in proline amino acids and hydroxylprolineis like collagen catabolism At the terminal end of the alpha carbon, prolina or hydroxyprolina derivatives are produced to yield free proline. It is the sole enzyme capable of catalyzing the breakdown of dipeptides the equation [7][8].

An enzyme that is present in all living things is proline dehydrogenase (ProDH), also referred to as proline oxidase (POX). It works as a catalyst to oxidize L-proline to delta1-pyrroline-5-carboxylate, which releases electrons that can be transported to molecular oxygen or other electron transfer systems. Apart from being crucial for the breakdown of proline, proDH also performs important functions in energy supply, transferring redox potential between different parts of the cell, and producing reactive oxygen species. Sequence similarities allow for the extension of structural studies of prokaryotic ProDHs to eukaryotic ProDHs, providing more insights into the biochemical activity and biological roles of this enzyme. This article presents the findings from the most current studies on the biochemistry and transcriptional, post-transcriptional, and translational control of ProDH[9]

The hormone leptin, a protein hormone with 167 amino acids, is one of the most significant hormones produced and secreted by adipose tissue. Its release and production are enhanced in large adipocytes, even after the formation of adipose cell volume, and its regulation is comparable to that of inflammatory immune adipocytes in these cells.Leptin regulates endocrine function, reproduction, and other bodily processes. It acts through the hypothalamus, which causes a decrease in hunger and an increase in energy expenditure, which in turn controls body weight.

MATERIALS AND METHODS

Study case and Subjects

The study included (250) blood samples from both sexes, their ages ranged between (20-60) years. These samples involved healthy individuals and patients with hyperthyroidism and hypothyroidism the diagnosis depending on clinical symptoms and hormonal diagnosis of thyroid function tests (T4, T3 and TSH), and were divided into three groups:

- Control group: include 50 healthy individuals
-non-immune thyroid disease (including 50 hyperthyroidism and 50 hypothyroidism).
-an immune thyroid disease including 100 patients (50 Graves and 50 Hashemito)

Biochemical assays

the prolidase activity was measured using manual method as well as the proline dehydrogenase and leptin concentration was measured using the enzyme-linked immunosorbent (ELESA) technique, as well as the concentration of some hormone (TSH , T3, T4, anti Tpo, anti TG, Tsh receptor Ab) in human serum. The electrochemiluminescence immunoassay “ECLIA” is intended for use on cobas e 411 immunoassay analyzers. In this

study, the SPSS program was used in the statistical analysis, and the Word 2016 program was also used in writing this research, all for the Windows operating system, and the data is expressed through arithmetic mean value.

Blood collection

The samples were collected 5 ml of pink blood was drawn and placed in (Gel tub) tubes free of coagulant and left at room temperature until the blood froze. After that, it was separated by a centrifuge During 3000 cycles for 10 minutes, then it was placed in special tubes for keeping samples in the refrigerator at a temperature of 20 C^0

Statistical analysis

This study presents the results in terms of Mean ± SD and reports the significant differences (p value) seen between the groups. The identification of significant disparities was established by a statistical examination, in which a p-value of 0.05 or below was deemed indicative of significance. The statistical analysis was performed with the GraphPad Prism software.

RESULTS AND DISCUSSION

The study`s results indicated that the characteristics of immunological hypothyroidism in two groups: a control group and patients with hypothyroidism. TSH levels were measured in both groups, indicating a functioning thyroid. In the patient group, TSH levels were significantly higher, suggesting hypothyroidism. Patients with hypothyroidism had elevated TSH levels, decreased T3 and T4 levels, and comparable levels of anti-thyroid antibodies. They also displayed lower concentrations of PDH, which is involved in thyroid hormone production, and higher levels of leptin, a hormone related to energy balance. Both the control and patient groups exhibited Anti TPO and Anti TG antibodies, with higher levels observed in the patient group. Lower PDH levels in the patient group suggest potential alterations in pituitary hormone secretion, potentially affecting thyroid hormone production regulation. Furthermore, the patient group displayed higher leptin levels, indicating potential disturbances in appetite and energy regulation associated with hypothyroidism. Thyroid hormone levels in circulation determine the amount of TSH that the anterior pituitary gland produces, which is influenced by small changes in T4 concentration. Low TSH levels typically indicate hyperthyroidism disease, while high TSH levels typically indicate hypothyroidism. This is due to the inverse correlation between TSH and THs levels or the negative regulatory relationship between THs and the pituitary gland[10]

Table 1: Non-immunological Hypothyroidism

Groups	TSH mIU/L	T3 ng/ml	T4 n mol/l	Anit TPO mIU/ml	Anti TG mIU/ml	Tsh receptorAb	PDH	liptin
Control	2.36±0.85	1.85±0.56	117.38 ±23.02	6.52±1.55	2.19±0.76	0.76±0.49	1030.62± 218.03	5.89±0.51
Patients	29.61±14.18	0.55±0.27	16.68± 4.96	5.5±1.79	2.19±0.88	0.74±0.30	520.62±98.25	18.79±0.72

Table 1 shows the measurements for various parameters in two groups (a control group and a group of patients with hypothyroidism). The pituitary gland secretes a hormone called TSH (thyroid-stimulating hormone) mIU/L, which causes the thyroid to generate thyroid hormones. TSH values in the control group are within the usual range (0.27-4.2 mIU/L), suggesting a thyroid that is working normally. On the other hand, the TSH levels in the patient group are substantially higher (29.61±14.18 mIU/L), indicating hypothyroidism, which is typified by an underactive thyroid. The active thyroid hormone T3 (triiodothyronine) is essential for controlling metabolism. The T3 levels in the control group are between 1.2 and 3.5 ng/ml, which is the usual range. Nonetheless, the T3 levels in the patient group are significantly lower (0.55±0.27 ng/ml), which adds more evidence to the hypothyroidism diagnosis. Another thyroid hormone, T4 (thyroxine) nmol/l, is transformed into T3 by the body. The T4 levels in the control group are within the normal range, which is 58.1–181 nmol/l. On the other hand, the patient group has much lower T4 levels (16.68±4.96 nmol/l), which is in line with hypothyroidism. Overall, the data show that, in comparison to the control group, the

hypothyroid patient group has higher TSH levels, lower T3 and T4 levels, and similar levels of anti-thyroid antibodies (Anti-TPO and Anti-TG). Individuals with hypothyroidism also have increased levels of the hormone leptin, which is linked to energy balance, and decreased amounts of PDH, a protein involved in the synthesis of thyroid hormones. The slight variations in antibody concentrations (anti-TSH receptor, anti-TG, and anti-TPO) raise the possibility that immune-mediated processes may not be the main cause of hypothyroidism in this particular situation.

Table 2. Immunological Hypothyroidism

Groups	TSH mIU/L	T3 ng/ml	T4 nmol/l	Anit TPO mIU/ml	Anti TG mIU/ml	Tsh receptorAb	PDH	liptin
Control	2.39±0.83	1.85±0.56	117.48±24.9	6.52±1.55	2.19±0.76	0.76±0.49	1030.62±218.	5.89±0.51
Patients	49.87±22.3	0.34±0.09	14.42±2.98	35.5±11.02	12.26±3.5	5.44±1.84	538.45±47.2	25.64±4.7

The table (2) provides comprehensive data on various parameters measured in the control group and the patient group with immunological hypothyroidism. Firstly, thyroid function is greatly influenced by TSH (thyroid-stimulating hormone) levels. The patient group has considerably high TSH levels (49.87±22.30 mIU/L), while the control group has TSH levels within the normal range (2.39±0.83 mIU/L). Higher TSH levels imply the body's attempt to stimulate the underactive thyroid gland, which is why these results point to hypothyroidism in the patient group.
Secondly, , the main thyroid hormones in charge of controlling metabolism are T3 (triiodothyronine) and T4 (thyroxine). The patient group had considerably lower levels of both hormones (T3: 0.34±0.09 ng/ml, T4: 14.42±2.98 nmol/l) than the control group, which shows normal T3 (1.85±0.56 ng/ml) and T4 (117.48±24.97 nmol/l) levels. The patient group's hypothyroidism is further confirmed by these decreased values, which show inadequate thyroid hormone synthesis.

Table 3. Non-immunological Hyperthyroidism

Groups	TSH mIU/L	T3 ng/ml	T4 nmol/l	Anit TPO mIU/ml	Anti TG mIU/ml	Tsh receptorAb	PDH	liptin
Control	2.39±0.83	1.85±0.56	117.48±24.97	6.52±1.55	2.19±0.76	0.76±0.49	1030.62±218.03	5.89±0.51
Patients	0.25±0.14	5.6±1.42	224.41±22.9	5.49±1.64	2.40±0.81	1.05±0.36	416.06±54.6	8.03±0.52

It's also critical to evaluate the antibodies linked to autoimmune thyroid disorders. Anti-TG and Anti-TPO antibodies are present in both the control and patient groups, with the patient group exhibiting greater levels (Anti-TG: 12.26±3.50 mIU/ml, Anti-TPO: 35.55±11.02 mIU/ml). These results imply the presence of autoimmune activity in both groups, which is frequently linked to hypothyroidism. The presence of antibodies that target the TSH receptor can be inferred from the TSH receptor/I levels. The sick group exhibits significantly higher levels (5.44±1.84) compared to the control group, which has levels within the predicted range (0.76±0.49). This suggests the existence of antibodies that could obstruct the TSH receptor's normal function and hasten the onset of hypothyroidism.
In addition, PDH levels in the patient group are lower (538.45±47.26) than in the control group (1030.62±218.03), which may indicate changes in pituitary hormone secretion. This discovery raises the possibility of a communication breakdown between the thyroid and pituitary glands, which may have an impact on the control of thyroid hormone production. Finally, leptin levels are greater in the sick group (25.64±4.74) than in the control group (5.89±0.51).

Energy balance and appetite control are influenced by leptin. The patient group's higher leptin levels suggest that hypothyroidism may be causing problems with appetite and energy balance. All things considered, the findings emphasize the distinctive qualities of immunological hypothyroidism. These consist of increased TSH levels, decreased T3 and T4 levels, Anti-TG and Anti-TPO antibodies, possible TSH receptor interruption, changed pituitary hormone output, and abnormalities in the regulation of appetite.

Data on the several parameters measured in the patient group with non-immunological hyperthyroidism and the control group are shown in Table (3). TSH (thyroid-stimulating hormone) mIU/L states: TSH levels in the control group are 2.19±0.85 mIU/L. The patient group exhibits hyperthyroidism, as seen by their significantly lower TSH values of 0.25±0.14 mIU/L. These readings fall short of the typical range. TSH levels are lowered in non-immunological hyperthyroidism because the thyroid gland overproduces thyroid hormones. Because the sick group produces too many thyroid hormones, their TSH levels are lower.Triiodothyronine (T3) ng/ml indicates that the control group's T3 levels are 1.8±0.52 ng/ml.The patient group exhibits hyperthyroidism, as evidenced by their considerably higher T3 levels of 5.6±1.42 ng/ml. These values are higher than typical. Increased thyroid hormone synthesis is shown by elevated T3 levels in the patient group, which supports the hyperthyroidism diagnosis. T4 (thyroxine) nmol/l: T4 levels in the control group are 121.23±22.46 nmol/l, which falls within the usual range of 58.1–181 nmol/l. The T4 levels of the patient group are 224.41±22.94 nmol/l, which is substantially higher and indicates hyperthyroidism. These values are higher than typical. The patient group's elevated T4 levels provide additional evidence of the hyperthyroidism-related overproduction of thyroid hormones.
The control group contains identical amounts of Anti TPO (6.63±1.160 mIU/ml) and Anti TG (2.21±0.82 mIU/ml) antibodies, according to Anti TPO (Antithyroid Peroxidase) mIU/ml and Anti TG (Antithyroglobulin) mIU/ml. Anti-TG (2.40±0.81 mIU/ml) and Anti-TPO (5.49±1.64 mIU/ml) antibody levels are likewise comparable in the patient group. Comparable amounts of anti-TG and anti-TPO antibodies are seen in both groups, indicating that autoimmune mechanisms are not the cause of the hyperthyroidism seen in the patient group. TSH receptor/I (<1.85): TSH receptor/I levels in the control group are 0.78±0.49, which is within the predicted range (<1.85). At 1.05±0.36, the patient group's TSH receptor/I levels are marginally greater.
Pituitary Derived Hormones (PDH) show that the control group's PDH levels are 1057.12±175.74. PDH levels in the patient group are lower, at 416.06±54.6. The patient group's reduced PDH levels raise the possibility of pituitary hormone secretion changes, which could be connected to the dysregulation of thyroid hormone synthesis. Leptin states that the leptin levels in the control group are 5.85±0.56. The leptin levels of 8.03±0.52 are marginally higher in the patient group. The patient group's elevated leptin levels raise the possibility of changes in appetite and energy control linked to hyperthyroidism.

Table 4 Immunological Hyperthyroidism\

Groups	TSH mIU/L	T3 ng/ml	T4 nmol/l	Anit TPO mIU/ml	Anti TG mIU/ml	Tsh receptorAb	PDH	liptin
Control	2.39±0.83	1.85±0.56	117.48±24.97	6.52±1.55	2.19±0.76	0.76±0.49	1030.62±218.03	5.89±0.51
Patients	0.11±0.06	5.62±1.05	232.11±16.5	23.21±6.08	7.98±1.39	4.73±1.90	347.15±50.90	11.52±0.82

Overall, the results indicate that in comparison to the control group, the patient group with non-immunological hyperthyroidism has reduced TSH levels, increased T3 and T4 levels, and similar levels of anti-TG and anti-TPO antibodies. Additionally, the patient group has slightly elevated leptin levels, slightly decreased PDH levels, and slightly elevated TSH receptor/I levels. Collectively, these data point to non-immunological hyperthyroidism's overproduction of thyroid hormone and possible changes in hormone regulation. The patient group's raised TSH receptor/I level suggest that the TSH receptor may have been mildly activated or stimulated, which could have contributed to the increased synthesis of thyroid hormones associated with hyperthyroidism. reduced TSH immune-positive cell counts in their anterior pituitary glands and low levels of TSH in circulation [11]. Approximately 50-60% of T3 binding to the Nuclear Receptors TRs in the rat pituitary gland is achieved via the conversion of T4 to T3 by

the D2 enzyme. The human pituitary gland has the same D2 receptor, whose activity is increased in hypothyroidism and decreased in hyperthyroidism [12]. Higher thyroid hormone levels, or hyperthyroidism, result in hypermetabolism, which raises resting energy expenditure, weight loss, cholesterol reduction, enhanced gluconeogenesis, and lipolysis [13].

Table (4) provides data on various parameters measured in the control group and the group of patients with immunological hyperthyroidism TSH states: TSH levels in the control group are 2.45±0.70 mIU/L, At 0.11±0.06 mIU/L, the patient group's TSH levels are considerably lower, indicating hyperthyroidism. These readings fall short of the typical range. The patient group's reduced TSH values are indicative of hyperthyroidism, which is characterized by an overabundance of thyroid hormones. Triiodothyronine (T3) ng/ml indicates that the control group's T3 levels are 1.94±232.11 ng/ml, considerably higher than the typical range of 1.2-3.5 ng/ml. A severe outlier or a mistake in data entry could be to blame for this. T3 levels in the patient group are 5.62±1.05 ng/ml, which is within the normal range. T3 levels in the patient group are within normal limits, suggesting that high T3 levels are not indicative of abnormal thyroid hormone synthesis in immunological hyperthyroidism: T4 levels in the control group are 116.83±25.3 nmol/l, which falls within the usual range of 58.1-181 nmol/l. The patient group exhibits hyperthyroidism, as evidenced by their significantly higher T4 levels of 232.11±16.55 nmol/l. These values are higher than typical. The patient group's elevated T4 levels attest to the hyperthyroidism-related overproduction of thyroid hormones. Anti TPO (Antithyroid Peroxidase) mIU/ml and Anti TG (Antithyroglobulin) mIU/ml show that the control group contains 6.61±1.6 mIU/ml of Anti TPO and 2.20±0.73 mIU/ml of Anti TG. The anti-TG (7.98±1.39 mIU/ml) and anti-TPO (23.21±6.08 mIU/ml) antibody levels are considerably greater in the patient group. The patient group's elevated levels of anti-TG and anti-TPO antibodies suggest that immunological hyperthyroidism is accompanied with autoimmune activity. Thyroid hormone production goes into overdrive as a result of these antibodies' targeting and assault of thyroid gland elements. TSH receptor/I (<1.85) indicates that the control group's TSH receptor/I levels are within the predicted range (<1.85), at 0.73±0.46. TSH receptor/I levels are greater in the patient group (4.73±1.90). The patient group's raised TSH receptor/I levels indicate a significant stimulation or activation of the TSH receptor, which may have contributed to the increased production of thyroid hormones observed in immunological hyperthyroidism. Pituitary Derived Hormones (PDH): PDH values in the control group are 974.56±215.63. PDH levels are greater in the sick group (347.15±50.90). The patient group's higher PDH levels suggest possible changes in pituitary hormone secretion, which may have an impact on the generation of thyroid hormone. Leptin states that the control group's "leptin" levels have a mean value of 5.88; the patient group's "leptin" levels have a mean of 11.52. Overall, the patient group with immunological hyperthyroidism is shown to have decreased TSH levels, increasing T4 levels, greater TSH receptor/I levels, elevated levels of anti-TPO and anti-TG antibodies, and possibly altered pituitary hormone secretion, according to the overall results. Since the patient group's T3 levels are within the normal range, this particular form of hyperthyroidism may have no effect on T3. Together, these results highlight the features of autoimmune-driven hyperthyroidism and shed light on the underlying processes and clinical presentations of immunological hyperthyroidism.

Table 5. Regression analysis for control cases between prolidase enzyme and other thyroid- parameters

B	(t) statics	F	R2	R	Sig	P- value
8.740	11.124	123,746	0.502	0.708	0.01	0.32

Table 5 presents a regression analysis comparing the prolidase enzyme and thyroid parameters. Prolidase has a coefficient estimate (B) of 8.740, and a t-statistic of 11.124 suggests a stronger correlation. With an F-value of 123,746 the F-statistic evaluates the regression model's overall significance. The prolidase enzyme can account for roughly 50.2% of the variation in thyroid parameters, according to the R-squared value. A relatively high positive correlation is shown by the correlation coefficient of 0.708. The coefficient estimate might not be statistically significant at the specified significance level of 0.05, according to the p-value of 0.32.

Table 6. Regression analysis for patients between prolidase enzyme and other thyroid- parameters

B	(t) statics	F	R2	R	Sig	P- value
10.750	31.988	143.709	0.539	0.734	0.01	0.002

The results in Table 6 represent the regression analysis for patients between prolidase enzyme and other thyroid parameters. The estimated impact of the independent variable (prolidase enzyme) on the dependent variable (thyroid parameters) in the regression model is represented by the coefficient estimate (B). The prolidase enzyme's coefficient

estimate in this instance is 10.750. The significance of the coefficient estimate is determined by the t-statistic. By dividing the coefficient estimate by its standard error, it may be computed. The prolidase enzyme's t-statistic in this instance is 31.988. A stronger correlation between the independent and dependent variables is shown by a greater absolute value of the t-statistic. The regression model's overall significance is evaluated using the F-statistic. It ascertains whether there is a statistically significant link between the independent variables and the dependent variable. In this instance, the F-value is 143.709.

The degree and direction of the linear link between the independent and dependent variables are measured by the correlation coefficient (R). The prolidase enzyme and the thyroid parameters have a relatively significant positive link in this instance, as indicated by the correlation value of 0.734. These data allow us to draw the conclusion that prolidase enzyme and patient thyroid parameters have a statistically significant direct association. A significant correlation coefficient, positive coefficient estimate, an overall statistical significance suggest that patients' elevated thyroid parameter values are correlated with prolidase enzyme levels.

The results indicate that there is a statistically significant direct relationship between prolidase enzyme and thyroid parameters in patients. A positive coefficient estimate, positive correlation coefficient, and overall statistical significance indicate that higher levels of prolidase enzyme are associated with higher values of the thyroid parameters in patients.

Prolidase exhibits clinical significance in addition to its biological effects, as evidenced by the condition known as prolidase deficiency. Prolidase activity is also known to be impacted by metabolic, oncological, and diseases related to collagen metabolism [8]The majority of scientific reports focus on the biological properties of proline. Enzymatic activity of PEPD is necessary for the turnover of collagen as the main component of the extracellular matrix, participating in the proteolysis of di- and tripeptide derived from degradation of collagen and proline-containing proteins. At the cellular level, the biological processes dependent on the enzymatic activity of prolidase result from the biological activity of enzymatic reaction products: proline or hydroxyproline (Pro or Hyp, respectively) [14] [15].An enzyme called prolidase catalyzes the breakdown of dipeptides that have proline or hydroxyproline at their C-terminus. Since prolidase-mediated catalysis is the rate-limiting step in collagen biosynthesis, it is important to note that these dipeptides are largely synthesized during collagen turnover. Proline is produced and then recycled during the synthesis and turnover of collagen. Numerous physiological and pathological systems depend on this mechanism. Thus, changes in prolidase activity are linked to multiple clinical disorders as well as prolidase deficiency, an uncommon hereditary ailment. The oxidant-antioxidant balance within the body is linked to thyroid hormones. Reduced collagen turnover is linked to hypothyroidism. The oxidative and anti-oxidative states of the body are related to thyroid hormones [16] [17]. Reduced rates of collagen catabolism have been linked to hypothyroidism. Simultaneously, the degree of oxidative stress is directly associated with the suppression of collagen synthesis, and there is evidence linking elevated oxidative stress with SH. Prolidase is regarded as a target enzyme for the synthesis of collagen because it is crucial to the recycling of proline for collagen synthesis. On the other hand, no research has been done on the prolidase activity (SPA) in serum in SH patients [18] [19] [20].

CONCLUSION

In summary, immunological tests were normal in patients with autoimmune hypothyroidism (low TSH and elevated T3 and T4) and in 50 patients with Hashimoto's syndrome (high TSH and decreased T3 and T4). There were also elevated immunological tests (anti-Tpo, anti-TG, and Tsh receptor Ab). There may be a peripheral association between thyroid hormones and leptin in addition to the proposed central relationship, although this effect is unclear. Since both thyroxine and triiodothyronine are implicated in the starvation-induced decrease in thermogenesis, thyroid hormones and leptin may participate in adaptive thermogenesis through mitochondrial uncoupling proteins and heat production. Studies on leptin in humans and rodents have not consistently shown a link between serum leptin concentrations and thyroid function. However, since thyroid hormone plays a role in thermogenesis and the control of unconjugated proteins, leptin may play an important role in thyroid pathophysiology. In this review, we focused on the role of leptin in the pathophysiology of the thyroid gland.

Recognition

The following people and organizations have provided great assistance to our research efforts, for which the authors are truly grateful: parents who participated in the study, staff and management of Kirkuk Public Health Hospital and Laboratory, and our respected supervising physicians.

Declaration of authors

There is no conflict of interest. We confirm ownership of all figures and tables in the manuscript. In addition, all figures and images included in the manuscript have the required permission for republication attached. The project received approval from the local ethics committee at Kirkuk University and the Kirkuk Health Directorate

REFERENCES

1. Anaya JM, Castiblanco J, Rojas-Villarraga A, Pineda-Tamayo R, Levy RA, Gómez-Puerta J, et al. The multiple autoimmune syndromes. A clue for the autoimmune tautology. Clin Rev Allergy Immunol. 2012;43:256–64. DOI: 10.1007/s12016-012-8317-z
2. Bhakat B, Pal J, Das S, Charaborty SK, SircarMedical NR. A Prospective Study to Evaluate the Possible Role of Cholecalciferol Supplementation on Autoimmunity in Hashimoto's Thyroiditis. J Assoc Physicians India. 2023;71(1):1. PMID: 37116030
3. Shoenfeld Y, Cervera R, Gershwin ME. Diagnostic criteria in autoimmune diseases. Vol. 543. Springer; 2008. DOI:10.1007/978-1-60327-285-8
4. Heufelder AE, Wenzel BE, Gorman CA, Bahn RS. Detection, cellular localization, and modulation of heat shock proteins in cultured fibroblasts from patients with extrathyroidal manifestations of Graves' disease. J Clin Endocrinol Metab. 1991;73(4):739–45. DOI: 10.1210/jcem-73-4-739
5. Lowenstein A, Fainboim H, Reyes A, Lutzky C, Ameigeiras B, Schroder T, et al. Autoimmune and non-autoimmune thyroid dysfunction in HCV infected and HCV–HIV co-infected patients before and after interferon alpha therapy: A prospective study. Endocrinol Diabetes y Nutr. 2020;67(4):263–71. doi: 10.1016/j.endinu.2019.04.012.
6. Cakmak A, Zeyrek D, Atas A, Celik H, Aksoy N, Erel O. Serum prolidase activity and oxidative status in patients with bronchial asthma. J Clin Lab Anal. 2009;23(2):132–8. doi: 10.1002/jcla.20303.
7. Eni-Aganga I, Lanaghan ZM, Balasubramaniam M, Dash C, Pandhare J. PROLIDASE: A Review from Discovery to its Role in Health and Disease. Front Mol Biosci. 2021;8:723003. doi: 10.3389/fmolb.2021.723003
8. Liu Y, Borchert GL, Surazynski A, Hu CA, Phang JM. Proline oxidase activates both intrinsic and extrinsic pathways for apoptosis: the role of ROS/superoxides, NFAT and MEK/ERK signaling. Oncogene. 2006;25(41):5640–7. doi: 10.1038/sj.onc.1209564.
9. Mortimer RM. Abnormal laboratory results: Thyroid function tests. Aust Prescr. 2011;34(1):12–5. https://doi.org/10.18773/austprescr.2011.011
10. Yamada M, Saga Y, Shibusawa N, Hirato J, Murakami M, Iwasaki T, et al. Tertiary hypothyroidism and hyperglycemia in mice with targeted disruption of the thyrotropin-releasing hormone gene. Proc Natl Acad Sci. 1997;94(20):10862–7. https://doi.org/10.1073/pnas.94.20.10862
11. ITAGAKI Y, YOSHIDA K, IREDA H, KAISE K, KAISE N, YAMAMOTO M, et al. Thyroxine 5′-deiodinase in human anterior pituitary tumors. J Clin Endocrinol Metab. 1990;71(2):340–4. doi: 10.1210/jcem-71-2-340
12. Bartalena L, Tanda ML. Graves' ophthalmopathy. N Engl J Med. 2009;360(10):994–1001. doi: 10.1056/NEJMcp0806317.
13. Karna E, Szoka L, Huynh TYL, Palka JA. Proline-dependent regulation of collagen metabolism. Cell Mol Life Sci. 2020;77:1911–8. https://doi.org/10.1007%2Fs00018-019-03363-3
14. Palka J, Oscilowska I, Szoka L. Collagen metabolism as a regulator of proline dehydrogenase/proline oxidase-dependent apoptosis/autophagy. Amino Acids. 2021;53(12):1917–25. doi: 10.1007/s00726-021-02968-y.
15. Chainy GBN, Sahoo DK. Hormones and oxidative stress: an overview. Free Radic Res. 2020;54(1):1–26. doi: 10.1080/10715762.2019.1702656.
16. Liyanarachchi KD, Debono M. Physiology of the pituitary, thyroid, parathyroid and adrenal glands. Surgery (Oxford). 2017 Oct 1;35(10):542- doi.org/10.1016/j.mpsur.2017.07.002
17. Spodenkiewicz M, Spodenkiewicz M, Cleary M, Massier M, Fitsialos G, Cottin V, et al. Clinical genetics of prolidase deficiency: an updated review. Biology. 2020 May 21;9(5):108. Available from .doi: 10.3390/biology9050108.
18. Ng SM, Turner MA, Weindling M. Neurodevelopmental Outcomes at 42 Months After Thyroxine Supplementation in Infants Below 28 Weeks' Gestation: A Randomized Controlled Trial. Thyroid (2020) 30:948. doi: 10.1089/thy.2019.0293.
19. I lona Zareba , Jerzy Palka Prolidase-proline dehydrogenase/proline oxidase-collagen biosynthesis axis as a potential interface of apoptosis/autophagy . 2016 Jul 8;42(4):341-8. doi: 10.1002/biof.1283. Epub 2016 Apr 4.

20. Surazynski A., Miltyk W., Palka J., Phang J.M. Prolidase-dependent regulation of collagen biosynthesis. Amino Acids. 2008;35:731–738. doi: 10.1007/s00726-008-0051-8.

Effect of Fish Collagen and Natural Extracts on Burn Wound Healing

Rusul Alani[1, a], Fatimah J. Al-Hasani [2,b] Emad S. Al-Hassani[2,c]

[1]*Environmental Research Center, University of Technology , Iraq, Baghdad*
[2]*Materials Engineering Department, University of Technology , Iraq , Baghdad*
Corresponding author: [a]mae.22.002@grad.uotechnology.edu.iq
[b]fatimah.j.alhasani@uotechnology.edu.iq
[c]Emad.S.Alhassani@uotechnology.edu.iq

Abstract. This work aims to prepare a simple comfort with high degree of antimicrobial activity burn cream compared with commercial one (MEBO CREAM) aid to enhance the healing process as well as skin renewing. the extraction of herbal material (moringa oleifera and hypericum perforatum) by water and glycerin in addition to fresh plants serum okra (Abelmoschus esculentus) were added to main burn cream component that was prepared by mixing the oil phase and water phase after heating them to 70C°. the herbs were added after cooling the cream to 40C° . high degree of microbial resistance to S. aureus and P. aeruginosa bacteria observed for burn cream samples. Animals were divided into 7 groups. each group contains two rats. The animals were treated with several topical creams, including collagen 20%, CH (collagen and hypericum perforatum both 10%), CM (collagen and moringa oleifera both 10%), CO (collagen & okra each 10%), and MS mebo cream. The sixth group served as the control and did not receive any therapy and the last group was M (master which is the cream base). Burn injury was generated by exposing the rats to boiling water for 15 seconds. Over the course of twenty-one days, in accordance with the study protocol, the size of the injury was calculated. On the 21st day, the average wound sizes were 0.8, 0.6±0.1, 0.2 , 0.2±0.1 , 0.1±0.1, 0.05 and 0.3±0.1in the control positive, C, CO, CH, CM, MS, and M groups, respectively. The injury dimension in the CM and MS group was notably less compared to the other groups.

Keywords: fish collagen, burn cream, moringa oleifera , hypericum perforatum , rats , fresh plant

INTRODUCTION

As biological materials get increasing attention, they provide advantages such as preservation of the environment, enhanced biological compatibility, and lower prices.[1] Skin wound dressings derived from natural sources have always been a research hotspot in the field of regenerative medicine and traumatology.[2] A burn is characterized as the harm inflicted onto the skin due to an excessive amount of heat or corrosive substances. Burn injuries typically arise from the exposure to high temperatures or corrosive substances. Burn injury is defined as an inflammation occurring beneath the outermost layer of the skin, known as the stratum corneum. The outcome of this injury can either lead to self-healing or get worse and result in additional tissue death, depending on the treatment technique. Various types of burn injuries are prevalent in different regions of the world. However, burns caused by heat and associated injuries continue to be the most often documented cause of burn-related fatalities and disability [3] The primary approach for treating wounds typically involves using medication topically to promote wound healing, reduce inflammation, and prevent infection from occurring often linked with serious injuries. [4] Materials from nature are frequently utilized in the recovery and regrowth of human tissues due to their compatibility in addition to their ability to be easily disposed of within the body. [5] The primary objective of utilizing biomaterials is to enhance human health by reinstating the functionality of innate biological tissues and organs within the body.[6] Medicinal herbs have garnered significant interest as alternative remedies that are beneficial for the treatment or prevention of illnesses associated with lifestyle choices. Herbs are a natural gift bestowed upon humans to promote a disease-free and healthy life.[7] Fish-derived collagen has emerged as a viable substitute for commercially available gelatin sourced from pigs and cows, particularly for the production of membranes in tissue engineering applications. fish skin collagen was

Technologies and Materials for Renewable Energy, Environment and Sustainability
AIP Conf. Proc. 3321, 030014-1–030014-17; https://doi.org/10.1063/5.0289596
Published under an exclusive license by AIP Publishing. 978-0-7354-5231-2/$30.00

responsible for improving the wound healing rate and the process of reepithelization and collagen deposition. [8] Moringa contains around 46 antioxidants and is one of the most potent natural sources of antioxidants. Antioxidants provide the necessary free radicals to the human system and prevent the impact of free radicals. M. oleifera includes bioactive components such as flavonoids, tannins, saponins, alkaloids, phenolics, and triterpenoids that have antibacterial properties. Therefore, it can be utilized as an affordable and safe plant-based antimicrobial agent. The leaves of Moringa oleifera contain a significant amount of minerals and proteins. This plant has a long-standing history as a traditional remedy for various disorders. Previous research has explored its potential in treating diverse oral soft tissue diseases.[9] Seeds of okra is full in protein and unsaturated fatty acids such as linoleic acid [10] Okra has been used to enhance skin health and improve blood circulation. One hundred grams of okra contain around 27 percent of the recommended daily intake of vitamin-C and 50 percent of the RDI of vitamin K. Vitamin C is an important antioxidant that facilitates the development and restoration of body tissues. Consuming a greater quantity of okra might have the beneficial effect of revitalizing our skin and hair, while also providing protection against degenerative ailments linked to prolonged exposure to free radicals.[11] Hypericum perforatum is a member of the Hypericaceae family and is classified as a herb. It exhibits anticancer, antiviral, antimicrobial, antibacterial, analgesic, and hepatoprotective properties. The extracted form of Hypericum perforatum suppresses the production of free radicals, as well as the activities of myeloperoxidase (7), cyclooxygenase-1, 5-lipoxygenase (8), inducible cyclooxygenase, and nitric oxide synthase.[12] Nevra Seyhan et al this study was about using curcumin and Hypericum perforatum on burns on a group of 24 male Sprague-Dawley rats that had second-degree burns and it found that these herbals was effective in the healing of burns [13]Duta Indriawan et al this study was to see the ability of Moringa oleifera to enhance the healing of burn wounds in humans and it found that using a mixture of silver sulfadiazine and Moringa oleifera resulted increase in the quantity of fibroblasts and a decrease in PMN cells within burn tissue[14].Mohammadreza akhoondinasab meibodi et al did a study about seeing the difference aloevera and silver sulfadiazine in burn injury healing and it found that The aloe vera group showed more pronounced wound healing. Furthermore, the rate of healing in the group treated with aloe vera was higher than that in the group treated with silver sulfadiazine. [15]. Hence, there is a perpetual demand for alternatives that are environmentally friendly.[16]. this research also concentrated on developing a novel product that is not only safe for application to the skin but also devoid of any adverse effects, achieved through the utilization of locally sourced materials to maintain cost-effectiveness and maintaining sustainable development. Also the herbs used before in the ancient medicine. The different between this research and others is using different herbs and fresh plant mixed with fish collagen to make a cream with multiple benefits.

EXPERIMENTAL WORK

Preparation of burn cream samples involves herbal ingredients extraction process as well as plants serum extraction with addition to main cream ingredient with additions of main burn cream ingredients (liquid paraffin 5.5g, solid paraffin 9 g, stearyl alcohol 9.5 gm, sodium lauryl sulfate 3g, propylene glycol 12ml, water 40ml and phenoxyethanol 0.6ml) and the fish collagen which was bought online from CLC cosmetic page.

Herbal Material Extraction

50 gm from every herbal substance (moringa oleifera, hypericum perforatum) where weighted, 105 gm of water, 345 gm of glycerin, mixing all the ingredient and placed in a water bath in temperature is below 60 c for 15 minutes, then filter the mixture and take the filtrate, and then 3 gm from a preservative (potassium sorbate) was added to the filtrate. Last step is to leave it about 24 hours.

Extraction of Fresh Plants Serum

Fresh okra was bought from a store in Baghdad, washed and dried in the shadow for 24 hours. after that it was dried in the oven and stored in airtight container then stored in cool dark place. 50 g of the dried okra were grinded in a grinder then extracted like the dried herbs in the previous method. Finally, there are three phases of burn-cream preparation (water phase, oil phase and cold phase).

Preparation of Burn Cream

It contains three phases. Water phase contains these additions (water, sodium lauryl sulfate, propylene glycol) on a magnetic stirrer and heated the mixture until it reaches 70°C. Oil phase contains these additions (solid paraffin, liquid paraffin, stearyl alcohol) on a water bath until the temperature reach 70°C then the oil phase and the water phase are mixed and blended until the texture became creamy. Cold phase is the addition of the herbal extracts (moringa oleifera, hypericum perforatum, Okra (Abelmoschus esculentus) and fish collagen and the preservative(phenoxyethanol) then they are added when the temperature of the water and oil phases mixture reaches 40 c. Finally, 5 burn cream samples and a commercial one as shown in table 1 and figure 1 were prepared.

Table (1) burn cream samples.

Symbol sample	Name	Main ingredient
MS	Commercial burn cream	Beta sitosterol
M	Master burn cream	No additives
C	Master with collagen	20% fish collagen
CH	Master with collagen + hypericum perforatum	10% of each one
CO	Master with collagen + Okra	10% of each one
CM	Master with collagen + moringa oleifera	10% of each one

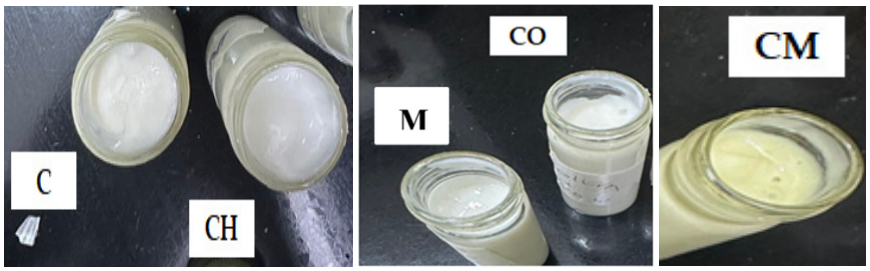

Fig. 1 commercial and prepared burn cream samples

CHARACTERIZATIONS

Viscosity test

Burn cream consistency is an important parameter. Viscosity is a type of rheological tests that used for creams. The viscosity of the samples was calculated in different angular velocities using a viscometer with different spindles (S05,S04) It was done at Material Engineering Department at University of Technology .Viscosity is a measure of how much a fluid resists flowing. The viscosity is a crucial factor in deciding the way the prepared burn cream mixture will be spread.

Ph determination

Checking the pH level during storage is an essential part of burn cream production in relation to emulsion stability, as pH fluctuations indicate the presence of potential chemical reactions. Considering the pH range of human skin falls between 4.5 to 6.0, it is essential for skincare products to possess a pH value that falls within this range.[17]. As figure 2 shows , the ph was measured by using ph strips by diluting 2 grams of the cream with 20 ml of distilled water and then immerse the strip in the mixture and see the color of it.

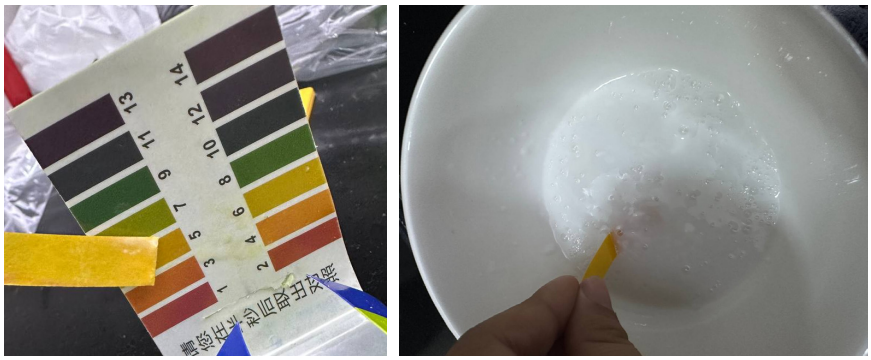

Fig. 2 ph measurement

Spreadability test

The cream foundation should have a smooth and effortless spreading ability, with little resistance and without causing excessive friction during the applying procedure.[18] Measuring spreadability involved the use of a glass slide. Another glass slide was placed on top of the cream, and then 0.5 g of burn cream was poured on top, resulting in a sandwich-like arrangement. A weight of 500 g was placed on the plate on top and measured for a duration of 5 minutes. The stress was eliminated after a duration of 5 minutes, and the rise in diameter of the burn cream was evaluated.as shown in figure 3. [19]

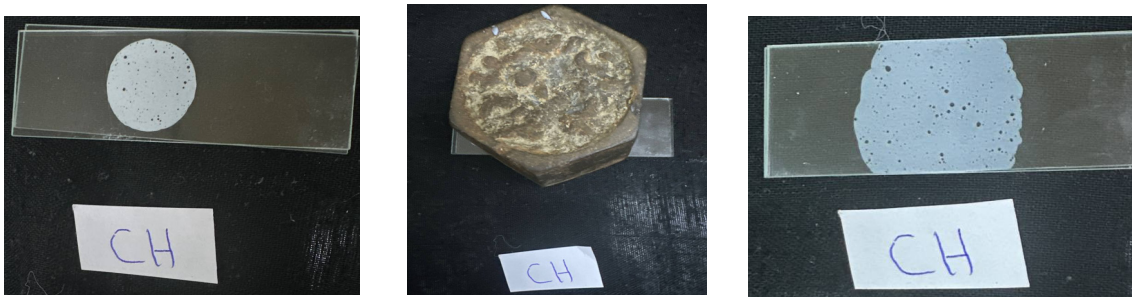

(a)Before load diameter (b) during load (c) after load diameter

Fig. 3 Spreadability test

Extrudeability test

The cream's extrudability was assessed using a customized extrudability tools to determine its suitability for use and consumer satisfaction. The duration required for the entire expulsion of 10 grams of cream from a 60-milliliter feeder syringe, under a pressure of less than 1 kilograms per square centimeter, was recorded. As it was seen in figure 4 . [20]

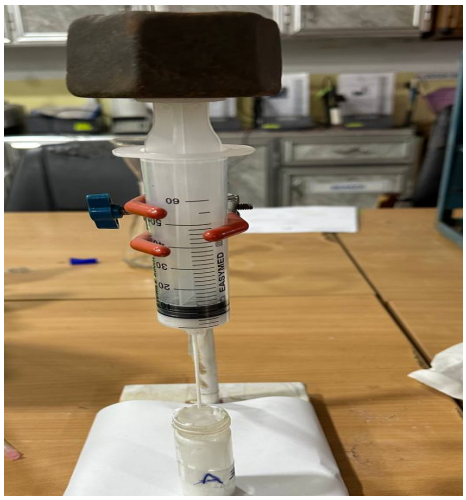

Fig. 4 extrudeability test

Total phenolic and flavonoid content test

Herbs are used in medicines and cosmetic due to its benefits. The anti-oxidant action of plant-based products is mostly related to phenolic and flavonoid components.[21].

Total phenolic content

Polyphenols have a wide range of functions, including. The quantification of phenolic components was conducted in the extract of ethanol using a standardized Folin-Ciocalteu reagent. The experimental solution consisted of 100 micro-litter of the concentrate, 500 micro-litter of the Folin-Ciocalteu reagent, and 1.5 milli-litter of a 20% solution of sodium-carbonate. Subsequently, the sample was stirred using a vortex mixer and then diluted with water that was distilled until reaching a final volume of 10 ml. The absorbance at 765 nm was measured after a 2-hour reaction then utilized to calculate the phenolic content. [22].

Total flavonoid content

The quantification of the overall flavonoid concentration in the crude extract was conducted using the aluminium chloride-colorimetric technique. Concisely, 50 micro-litter of crude concentrate (1 mg/mL ethanol) were diluted to 1 milli-litter with methanol, combined with 4 mL of distilled water, and after that mixed with 0.3 milli-litter of 5% NaNO2 solution. After 5 minutes of incubation, 0.3 mL of 10% AlCl3 solution was included, and the mixture stayed undisturbed for six minutes. Subsequently, 2 mL of a 1 mol/L NaOH solution were introduced, and the resulting volume of the combination was adjusted to 10 mL using double-distilled water. The solution was left undisturbed for a duration of 15 minutes, and the degree of absorption was quantified at a wavelength of 510 nanometers.[23]

Antibacterial test

The diffusion technique using agar wells was employed to assess the antibacterial effects of burn cream opposing staphylococcus aureus and Pseudomonas aeruginosa bacteria. Every isolate of bacteria was cultured in nutritional broth and then kept at 37 degrees Celsius for 18 to 24 hours.
. Following the time for incubation, 0.1 ml for every suspended bacterium was placed on the top layer of nutritional agar and incubated at 37 degrees Celsius for twenty-four hours.
.One colony of bacteria was transferred into a test container containing 5 milliliters of normal saline to create the suspension of bacteria with a moderate level of cloudiness comparable to the standard turbidity fluid, which is approximately equivalent to 1.5x10^8 CFU/milli litter. A portion of bacterial dispersion was carefully transferred onto Mueller-Hinton agar substrate using a cotton swab that was sterile and evenly dispersed, then allowed to stand for 10 minutes. The preceding agar layer was created with three wells per plate, each measuring five millimeters in diameter. The agar plates were extracted, and 50 micro-litter of the material was dispensed into every well using a micropipette.

Distilled water was added to the central well as a control. The plates were placed in an incubator at 37 degrees Celsius for a period of 18 hours, and then the size of inhibitory zones was measured as figure 5 and 6 shows.[24]

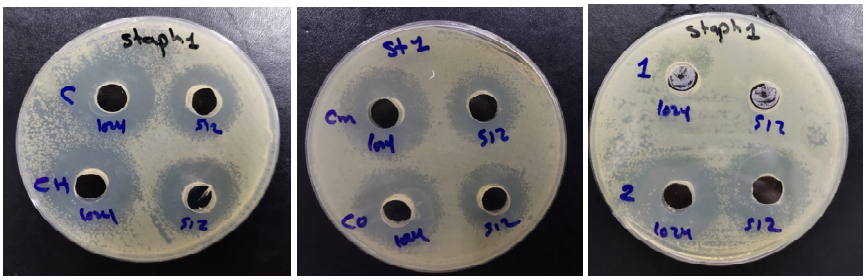

Fig. 5 staphylococcus aureus bacteria for burn-cream samples

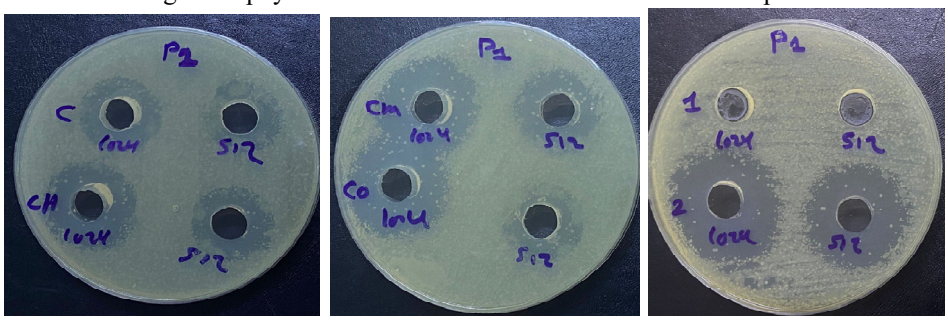

Fig. 6 Pseudomonas-aeruginosa bacteria for burn-cream samples
(1) M sample , (2) MS sample , (C) collagen , (CH) collagen + hypericum perforatum , (CM) collagen + moringa , (CO) collagen + okra

Fourier transform infrared spectroscope (FTIR) test.

The utilization of mid infrared spectroscopy is being extensively employed for the characterization of organic molecules. This test is utilized to comprehensively characterize collagen and the herbs employed in the present study [25]

Animals test

The animals used were 22 white rats weight from (128 -341) g. they were divided to 7 groups; each group has 2 rats. The animals underwent shearing on either their right or left thighs, followed by a subcutaneous injection of 0.1 mL of 2% lidocaine into the designated area. The lidocaine was left there for a duration of 5 minutes. Injury is inflicted by placing a 2 cm rectangular metal plate, which has been disinfected by dipping it in hot water (100°C) and then cooling it for a period and then put it again in the boiling water and put it, onto the sheared thigh of the rats for a duration of 15 seconds. the first group was (positive control) which was subjected to burn but left without healing), G2(C), G3(CO), G4(CH), G5(CM), G6(MS) , G7(M) . the creams were used daily to all categories uniformly. [26] the evaluation of wound contraction and epithelialization period was conducted in this test. Wound contraction was quantified as the percentage of contraction at 5-day intervals following wound formation. The wound size area was measured by a ruler .figure 7 shows the intervals healing .

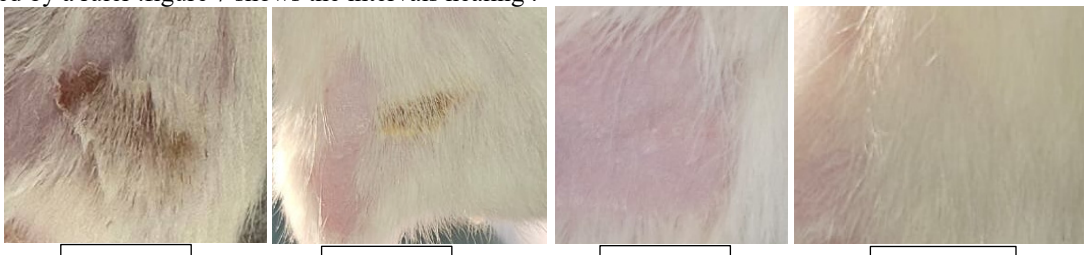

Fig. 7 burn wound healing of CM group

Statistical Analysis

The data was shown as mean ± standard deviation and were analyzed using R program to evaluation utilizing a one-way examination of variance (ANOVA), following Tukey's post-hoc analysis. A significance level of $p<0.05$, $P<0.01$, $P<0.001$ was used to determine the significance of all data.

RESULTS AND DISCUSSION

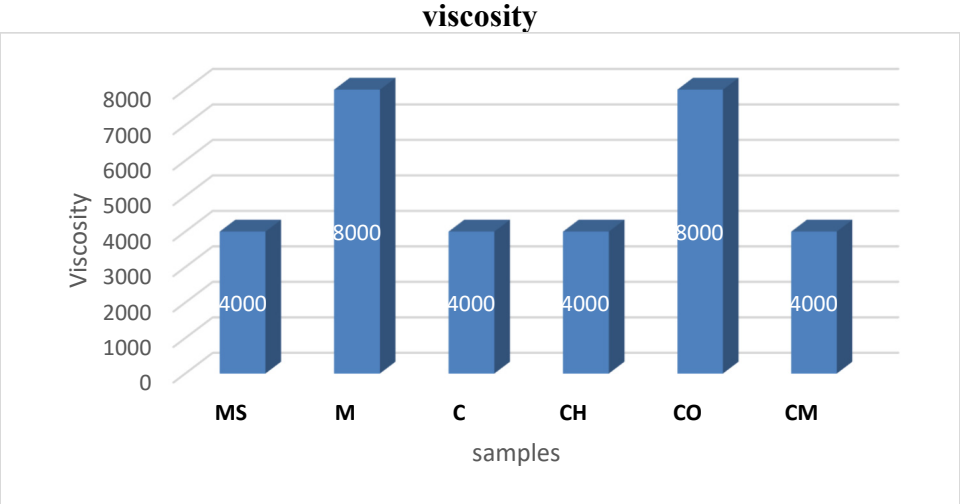

Fig. 8 The Viscosity for burn cream samples at Room Temperature

As shown in the figure 8 all the prepared burn cream samples have convergent results. Okra polysaccharides displayed desirable rheological characteristics, including shear thinning and gelling behaviors, within a specific concentration range. It has been demonstrated that okra polysaccharides have significant technical value as viscosity improvements, gelling substances, and thickeners. They are utilized in the food and healthcare sectors [27]. CO had a higher value due to the thickening agent of okra and master sample (M) showed the same value as CO which means the collagen and the herbs decreased the viscosity and it had the same value of the commercial burn cream (MS).

Ph results

From table (2) PH of prepared burn cream samples ranged from 4.5-6 which is acceptable and suitable for skin behavior [16]. no deviation in PH values of prepared samples compared with commercial one. PH value for master cream was 6, addition of collagen decreased the PH of the cream samples to 4.5 this is due to low ph value of fish collagen that range from 2 to 6 since collagen consist of amino acid bound together to from triple helix. it is mostly found in connective tissue such bone, skin [28] collagen addition support skin renewing as well as cells regeneration. when okra was added the value still the same cause okra has a ph value 3 since it's contain mucilage polysaccharides [29]moringa oleifera addition increased the ph due to its ph of 5.8 to 6 and it's component of flavonoid and that was seen also in total phenolic and flavonoids content test [30] hypericum perforatum also increased the ph due to its ph value of 6 to 7 since it contains high concentration of flavonoids [31]

Table (2) PH values of burn cream samples

PH	Value
MS	5.5
M	6
CM	5
CH	5
CO	4.5
C	4.5

spreadability results

From table (3) it was seen that CO sample and master (M) sample showed closed result and have the lowest spreadability due the thickening property of the okra, but the other samples and the commercial one have highest spread ability due to the light consistency of the liquid collagen and herbs affects and this gives close results for the viscosity test.

Table (3) Spreadability value of burn cream samples

Samples	Diameter of the spread circle – initial diameter
Commercial burn cream (MS)	1.5
Master burn cream (M)	1
Collagen burn cream (C)	1.5
Collagen + hypericum perforatum burn cream (CH)	1.4
Collagen + okra burn cream (CO)	1.1
Collagen + moringa oleifera burn cream (CM)	1.4

Extrudeability results

The process of extrusion is influenced by the characteristics and concentration of the material. Table 4 provides evidence of variations in extrusion time, which may be attributed to the specific properties of each cream specimen.as shown that the more viscous sample the less extrusion it has and as the viscosity test showed that CO and M samples have higher viscosity, so they have longer extrusion time comparing with the other samples. other collagen samples and the commercial burn cream have shorter time.

Table (4) extrudeability time of burn cream samples

Samples	Time in minutes
Commercial burn cream (MS)	1:30
Master burn cream (M)	1:50
Collagen burn cream ©	1:30
Collagen + hypericum perforatum burn cream(CH)	1:32
Collagen + okra burn cream (CO)	2:13
Collagen + moringa oleifera burn cream (CM)	1:40

Total phenolic and flavonoid content results

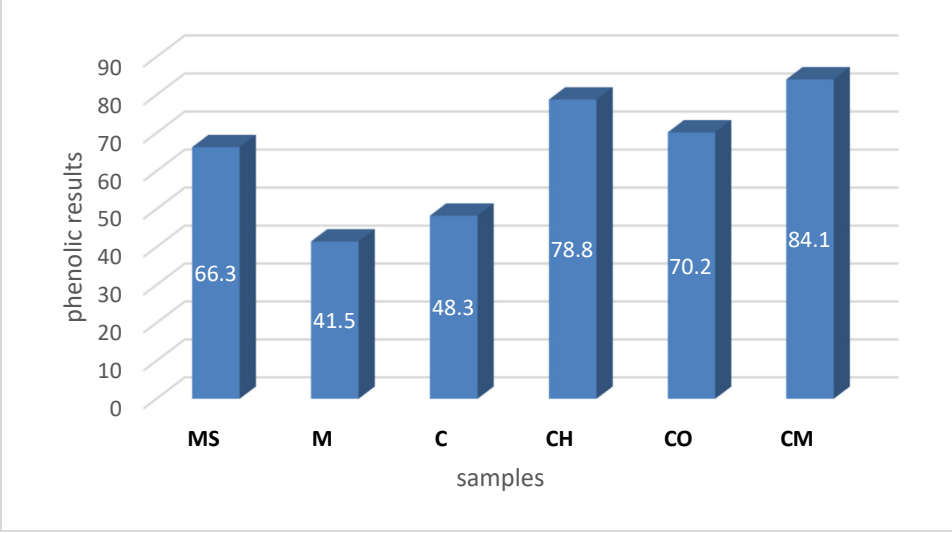

Fig. 9 phenolic content of burn cream samples

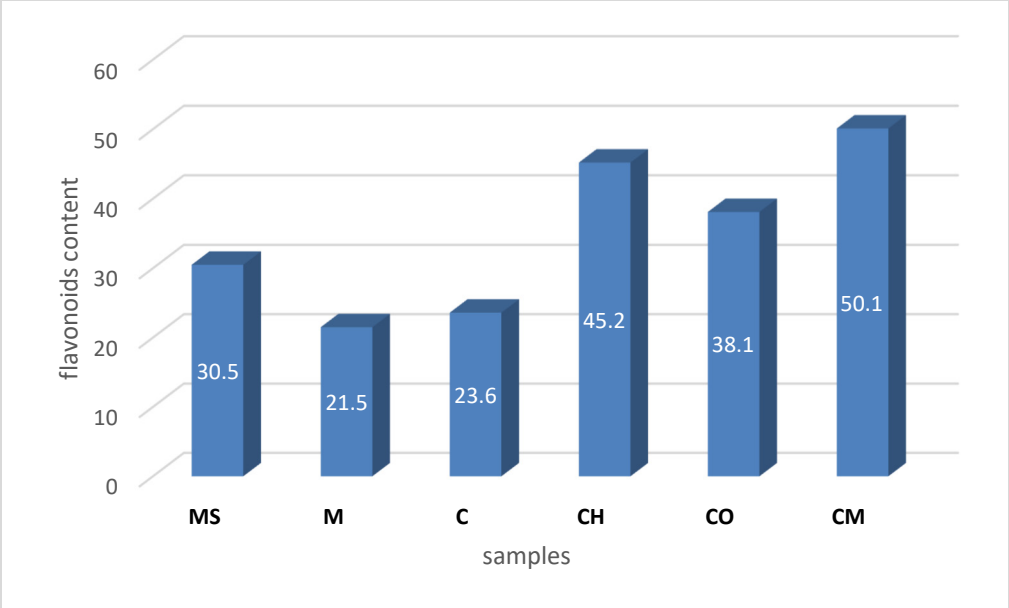

Fig. 10 flavonoids content of burn cream samples

as shown in the figures 9 and 10 that (CM) has the highest phenolics and flavonoids content compare with the other samples which is why moringa oleifera are known of their highly antioxidant and highly inflammatory properties. (CH) sample also gave a good value comparing with the other samples while the sample (M) has the lowest content because it doesn't contain any additives.

Antibacterial test

Figure 11 and 12 shows that the master sample didn't have any inhibition zone of the two bacterias since it doesn't contain any additives, for S.aureus the samples CH and C demonstrated exceptional antibacterial efficacy and showed a much more pronounced inhibition region, measuring 18 mm and 19 mm, respectively, when compared to the rest of the specimens. CO and the commercial one gave inhibition region of 17mm which gives good indication for the success of the prepared sample. CM gave 16mm inhibition region, all the sample's result were similar. for P. aeruginosa bacteria in comparison to S. aureus. Commercial and C sample gave the highest inhibition region measuring 22mm and 21mm, respectively, but the other samples gave less inhibition region. Therefore, the resulting product is suitable for purposes that necessitate defense against S. aureus bacteria, which commonly cause skin infections. The variation in antibacterial effectiveness is contingent upon the primary constituent of each extract. [32-35]

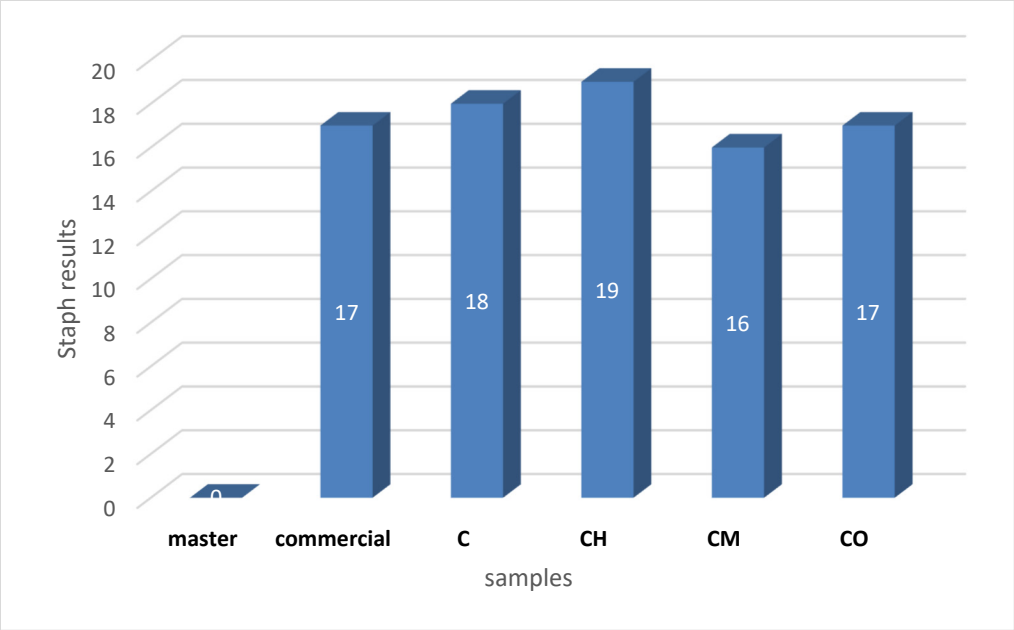

Fig. 11 Antibacterial behavior of staphylococcus-aureus bacteria

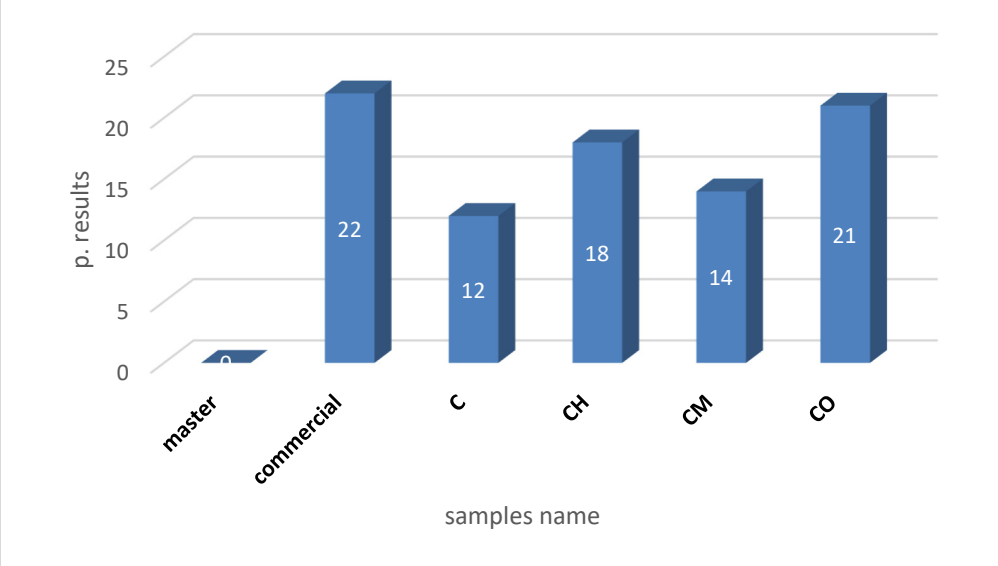

Fig. 12 Antibacterial behavior of Pseudomonas-aeruginosa bacteria

FTIR results

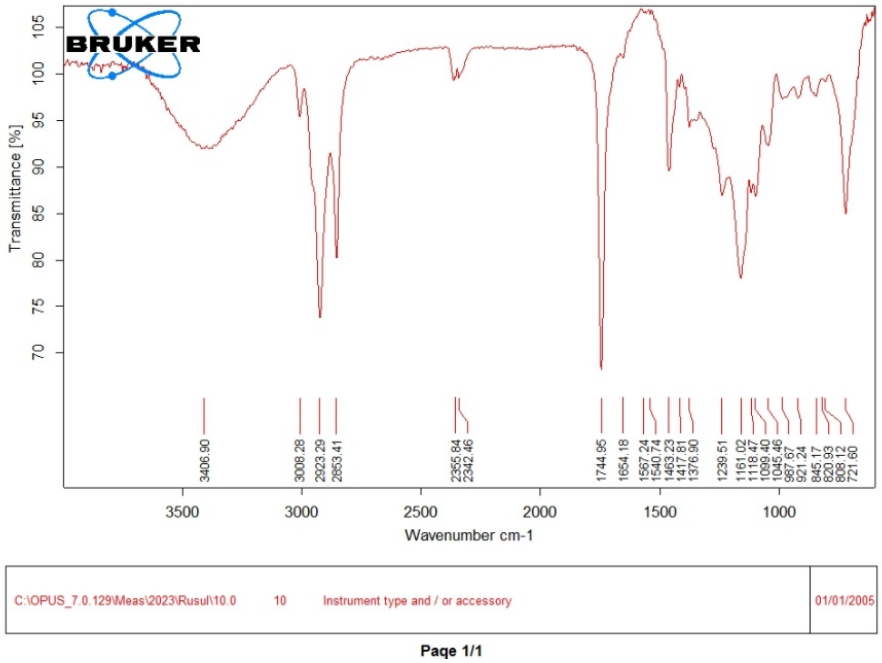

Fig. 13 FTIR Chart of commercial burn cream sample

Structural analysis of commercial burn cream (MEBO) showing the functional groups and composition listed in table 5 and showed in figure 13 . From FTIR figure many bands appears indicating to the inherent constituents of cream. strong (O-H) band appears at 3406 cm-1 corresponded to many cream ingredients as result to their chemical composition such as (beta sitosterol) ingredient ($C_{29}H_50O$) , scutellaria baicalensis and phellodendron amurense that contains a protoberberine alkaloid (C20H18NO4), which belongs to a category of fundamental organic compounds found in nature that have at least one nitrogen atom. so, C=N band is the more characteristic band appears at 1654cm-1 [36]. a broad peak band in the region of approximately 3200-3600 cm^-1, stretching vibration of hydroxyl groups (O-H) corresponding to the scutellaria baicalensis contains flavonoids. The flavonoids baicalin and baicalein are derived from the root of the and they are the most prominent bioactive compounds. baicalin structure is C21H18O11 [37] 1744cm-1 peak band which is belongs to C=O of scutellaria baicalensis, sesame oil which was also observed at 1161.02cm-1, 2923.29cm-1 and 3008.28cm-1. The other component that belongs to 1744cm-1 is Beeswax and 1463.23cm-1which belongs to hydrocarbon vibration is also belongs to beeswax [38] .

Table (5) Bands information's of sample (MS)

Ingredient	Peak no	Wave no	Appearance	Functional group	Compound class
Beeswax	1 5	1463.23cm-1 1744cm-1	medium strong	-C-H -C=O	alkanes esters
Sesame oil	2 5 6 7	1161.02cm-1 1744cm-1 2923.29cm-1 3008.28cm-1	strong strong strong strong	-C-O -C=O -CH2 -CH	esters esters Aliphatic methylene Unsaturated

phellodendron amurense	3 8	1654cm-1 3406cm-1	medium Strong - board	-C=N -OH	imine -Alcohol
scutellaria baicalensis	4 8	1744cm-1 3406cm-1	strong Strong - board	-C=O -OH	Carbonyl group -Alcohol
Beta sitosterol	8	3406cm-1	Strong - board	-OH	-Alcohol

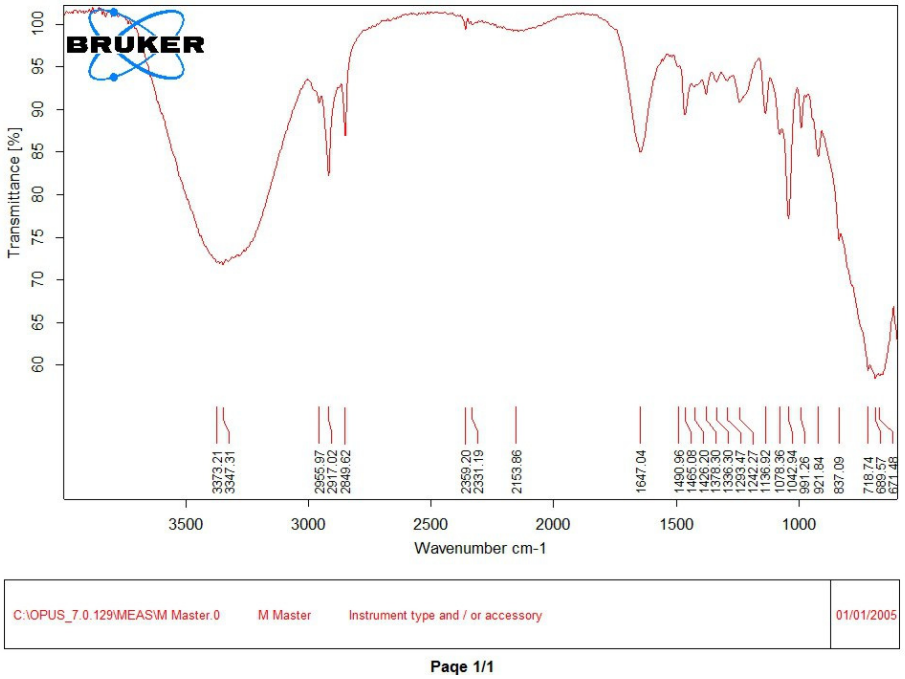

Fig. 14 FTIR Chart of master burn cream sample

Structural analysis of Master sample is simpler than the commercial one due to the simple components.as shown in figure 14.

Table (6) Bands information's of sample (M)

Ingredient	Peak no	Wave no	Appearance	Functional group	Compound class
Water	1	3373.21	Strong - board	OH stretching vibration	Alcohol
Propylene glycol	1	3373.21	Strong - board	OH stretching vibration	Alcohol
Paraffin wax	3	2849.62cm-1	strong	C-H	alkanes
Stearyl alcohol	4 3	1647.04cm-1 2849.62cm-1	strong strong	-C=O -C-H	-Amide -alkanes
Sodium lauryl sulfate	5	1242.27cm-1	strong	S=O	
Liquid paraffin	3	2849.62cm-1	strong	C-H	alkanes

In this sample the table 6 showed a peak number 3373.21cm-1 belongs to O-H group is of Propylene glycol and water [39]. paraffin wax, was observed at 2849cm-1 which belongs to C-H [40]. Stearyl alcohol was also observed in the same peak number in addition to 2917.02cm-1[41]. the CH2 and CH3 peaks was at 1464 cm-1 (hydrocarbons). peak 1647.04cm-1 belongs to S=O of sodium lauryl sulfate [42]

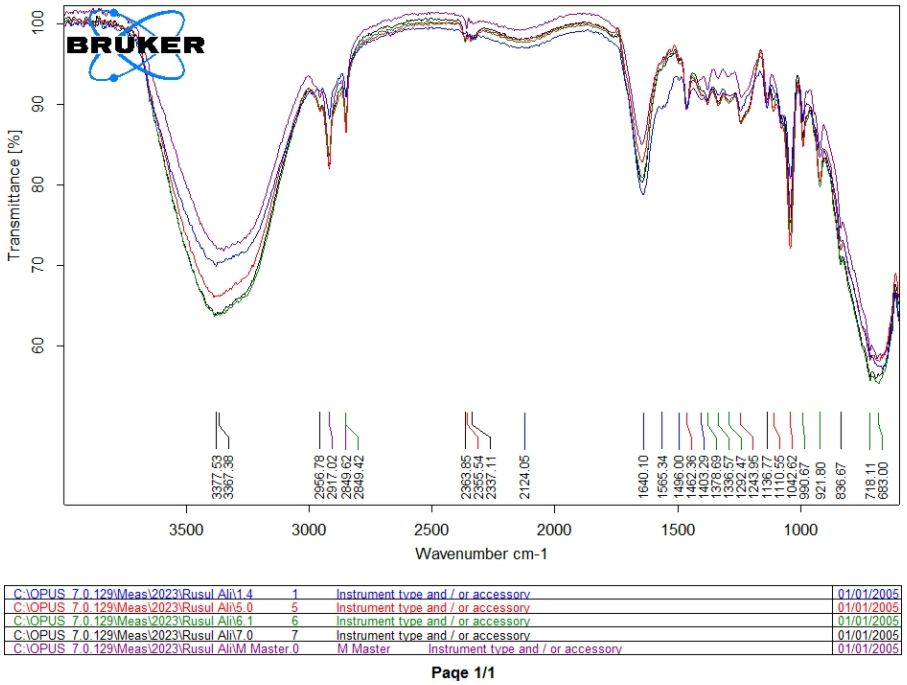

Fig. 15 FTIR Chart of merged charts of samples (M-C-CH-CM-CO)

(1) Only collagen sample (C)
(5) CH (Collagen + hypericum perforatum sample)
(6) CM (collagen + moringa oleifera sample)
(7) CO (collagen + okra sample)
(0) M (master sample)

Table (7) Bands information's of merged charts of samples (M-C-CH-CM-CO)

Main ingredients					
Ingredient	Peak no	Wave no	Appearance	Functional group	Compound class
Water	1	3373.21	Strong - board	OH stretching vibration	Alcohol
Propylene glycol	1	3373.21	Strong - board	OH stretching vibration	Alcohol
Paraffin wax	3	2849.62cm-1	strong	C-H	alkanes
Stearyl alcohol	4 3	1647.04cm-1 2849.62cm-1	strong strong	-C=O -C-H	-Amide -alkanes
Sodium lauryl sulfate	5	1242.27cm-1	strong	S=O	
Liquid paraffin	3	2849.62cm-1	strong	C-H	alkanes

Additives					
Collagen	5	1243.95cm-1 1640.01cm-1 2917.02cm-1 3377.53cm-1		C-Stretching C=O N-H stretching CH2	-Amide II -amide III Amide 1 Amide B Amide A
-Moringa		3377.53cm-1 2917.02cm-1 1565.34cm-1		-O-H -C-H -C=C	hydroxyl -alkanes -cyclic alkene
-Hypericum perforatum		2917.02cm-1 3377.53cm-1 1042.62cm-1		-C-H -O-H -C-O	-alkanes -alcohol -ether
Okra		1403.29cm-1 3377.53cm-1 3377.53cm-1		-C-H -N-H -O-H	 Aliphatic primary amine -alcohol

The using of natural ingredients extraction (moringa oleifera, okra (Abelmoschus esculentus), hypericum perforatum) and fish collagen in the preparation of burn cream samples aid to enhancing the structure as well as hydration rate of cream which has a preferable effect on general cream performance. figure (15) illustrated the effect on the functional group bands in comparison with master sample. The table 7 showed that collagen has many functional groups which are amide-A band which relates to N–H stretching positions at 3377.53cm-1 cm-1. The amide-B band of was observed at 2917.02 cm-1. amide I was observed at C=O stretching vibration was observed in 1640.01cm-1. Amide-II and amide-III were also observed at 1243.95cm-1 cm-1, O-H was observed at 3377.53cm-1[43]. 3377 cm-1 which is assigned to O-H stretching of all the additions and also represent N-H (Aliphatic primary amine) . The absorption peak at 2917.02cm-1 is caused by C-H that belongs to alkanes and it's assigned to hypericum perforatum and moringa and also observed at 1403.29cm-1 which is assigned to okra. C-O (ether) was approximately at 1042.62cm-1, C=C was at 1565.34cm-1. From the figure it was clear all ingredients present same functional group bands. No new bands appeared for unwanted material. there increasing in the intensity of O-H band when the natural ingredients were added, due to glycerin effects.it enhances the role and effectiveness of the presence of collagen to improve healing and activate the role of other substances in the work.

Animal test results

Table (8) Effect of the creams on percentage of wound contraction in many animal groups during the study period of 21 days after the injury

Animals group	N	Day5	Day 10	Day 15	Day 21
		Mean ± S.D	Mean ± S.D	Mean ± S.D	Mean ± S.D
G1 control	2	1.6±0.1	1.4	1.2	0.8
G2 C	2	1.3	1±0.1	0.8	0.6±0.1
G3 CO	2	1.3±0.2a**	1±0.2	0.7±0.2	0.2
G4 CH	2	1.1±0.7a***	0.9±0.5	0.5±0.1	0.2±0.1
G5 CM	2	1.5	1.4	0.7	0.1±0.1
G 6 MS	2	1.5±0.2	1.3±0.2	0.9±0.2	0.05
G 7 M	2	1.4	1.2±0.1	1.2	0.3±0.1

a-significantly different from control, b- significantly different from C, c-significantly different from CO, d-significantly different from CH , e- significantly different from CM , f- significantly different from MS ($p<0.05$), g-significantly different from M.
-*$p<0.05$, **$p<0.01$, ***$p<0.001$

as shown in the table 8. a better wound healing was observed in MS and CM group in comparison with control group. On day 5, the difference was statistically significant between CH and CO group when compared with control ($P < 0.01$ & $p<0.001$). on the other days no statistically significant differences were observed throughout the groups in terms of the wound size. after day 15 the percentage of wound size contraction increased in CM and MS groups and almost completely healed as we can see in day 21. Figure 16 shows the comparisons between the samples.

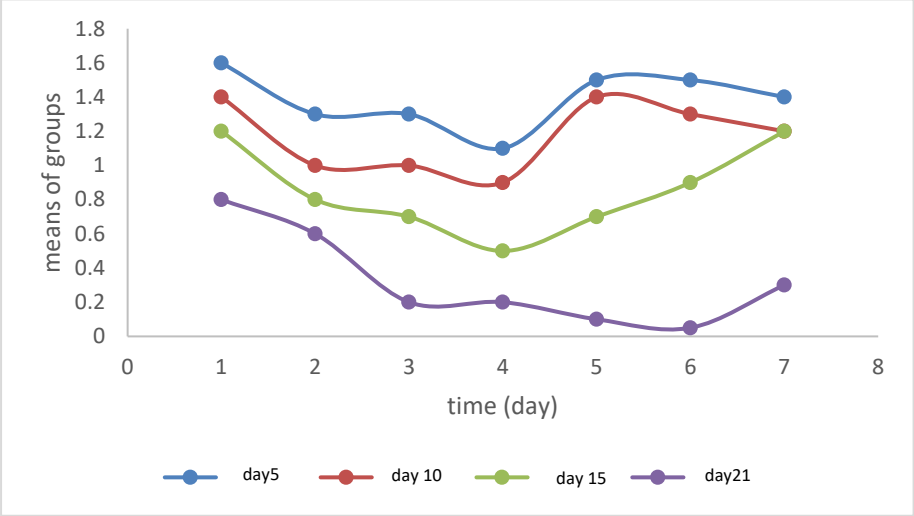

Fig. 16 comparisons between means of groups through the calculated period

table (9) effect of groups on wound contraction in a period of 21 days

Animals group	N	Period of epithelialization
G1 control	2	17.5 ± 0.7
G2 C	2	15.5 ± 0.7
G3 CO	2	16.5 ± 0.7
G4 CH	2	16±1.4
G5 CM	2	14 ±1.4
G 6 MS	2	14 ±1.4
G 7 M	2	16.5 ± 1.4

As shown in the table 9 and figure 17 that CM and MS group took 14 days for complete epithelization comparing with control group that took 17 days. while the other groups almost had the same day of healing.

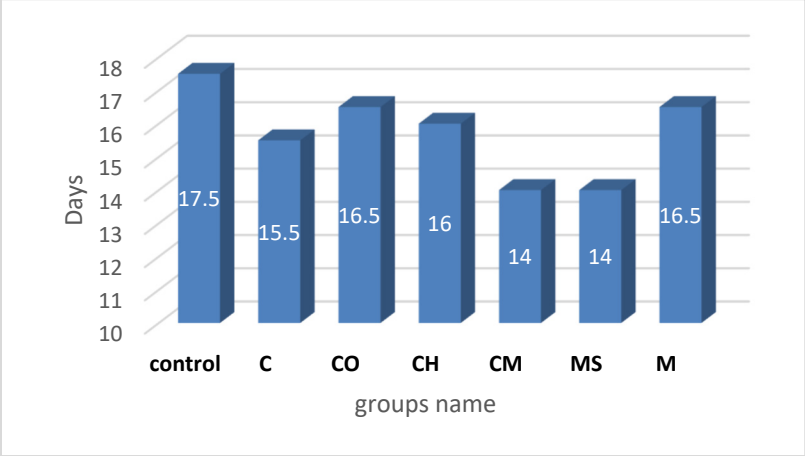

Fig. 17 epithelization period

CONCLUSION

Based on the current results, it can be inferred that the herbal cream formulation demonstrated significant efficacy in promoting wound healing in cases with thermal burn injuries. The designed herbal cream's anti-burn effect can be linked to the healing power of its key components, which are derived from the extraction of these plant-based medicines. CM and MS were the groups that had the highest percentage of healing due to the huge advantages of moringa oleifera components which gave these results. Other researchers can use other herbs related to burns and enable them to apply the cream for purposes other than burns due to the many benefits of these herbs. Other tests can be performed regarding creams not mentioned in their research.

REFERENCES

1. N. Mohammed, A. B AL-Zubaidi, and F. J. Al-Hasani, “Synthesis, characterization, of natural hybrid composite matrix for antibacterial and antifungal application,” in AIP Conference Proceedings, AIP Publishing, 2022.
2. Zhou, T., et al. (2017). "Multifunctional and biomimetic fish collagen/bioactive glass nanofibers: Fabrication, antibacterial activity and inducing skin regeneration in vitro and in vivo." International journal of nanomedicine: 3495-3507.
3. McGill V., Kowal-Vern A., Fisher S.G., Kahn S., Gamelli R.L., The impact of substance use on mortality and morbidity from thermal injury. J. Trauma. 1995; 38:931-934.
4. Bhatia, N., et al. (2014). "Evaluation of burn wound healing potential of aqueous extract of Morus alba based cream in rats." J Phytopharm 3(6): 378-383.
5. Al-Hasani, F. J., et al. (2023). "Enhancing the Cell Viability and Antibacterial Properties of Composite Layer by Active Particulate Additions."
6. Hamad, Q. A., et al. (2022). "Comparative study of biotin and hydroxyapatite on biological properties of composite coating." International Journal of Biomaterials 2022.
7. Parkash, J., et al. (2018). "Herbs as traditional medicines: a review." Journal of Drug Delivery and Therapeutics 8(5): 146-150.
8. de Souza, A., et al. (2022). "Fish collagen for skin wound healing: a systematic review in experimental animal studies." Cell and Tissue Research 388(3): 489-502.
9. Dhiman, J. (2023). "A Review on Medicinal uses of Moringa oleifera." Journal of Drug Delivery and Therapeutics 13(11): 197-201.
10. Oyelade, O.J., Ade-Omowaye, B.I.O., and Adeomi, V.F. (2003). Influence of variety on protein, fat contents and some physical characteristics of okra seeds. J. Food Eng., 57: 111-114
11. Gemede, H. F., et al. (2015). "Nutritional quality and health benefits of okra (Abelmoschus esculentus): A review." J Food Process Technol 6(458): 2.
12. Kıyan, S., et al. (2015). "Investigation of acute effects of Hypericum perforatum (St. John’s Wort-Kantaron) treatment in experimental thermal burns and comparison with silver sulfadiazine treatment."
13. Seyhan, N. (2020). "Evaluation of the healing effects of Hypericum perforatum and Curcumin on burn wounds in rats." Evidence-Based Complementary and Alternative Medicine 2020.
14. Indriawan, D., et al. (2022). "The Effectiveness of Moringa oleifera Burn Healing: In Vivo Study." Bioscientia Medicina: Journal of Biomedicine and Translational Research 6(11): 2342-2346.
15. Akhoondinasab, M. R., et al. (2014). "Comparison of healing effect of aloe vera extract and silver sulfadiazine in burn injuries in experimental rat model." World journal of plastic surgery 3(1): 29.
16. E. Al-Hassani, F. Al-Hassani, and M. Najim, “Effect of polymer coating on the osseointegration of CP-Ti dental implant,” in AIP Conference Proceedings, AIP Publishing LLC, 2018, p. 030022.
17. S. Alani, F. J. Alhasani, and E. S. Al Hassani, “Enhanced the Structure of Ophthalmic Implants (Rigid Contact Lenses) by Aloe Vera Addition,” in Key Engineering Materials, Trans Tech Publ, 2022, pp. 13–23.
18. Sabale, V., et al. (2011). "Formulation and in vitro evaluation of the topical antiageing preparation of the fruit of Benincasa hispida." Journal of Ayurveda and integrative medicine 2(3): 124.
19. N. A. H. Abou Youssef, A. A. Kassem, R. M. Farid, F. A. Ismail, E.-M. Magda Abd Elsamea, and N. A. Boraie, “A novel nasal almotriptan loaded solid lipid nanoparticles in mucoadhesive in situ gel formulation for brain targeting: Preparation, characterization and in vivo evaluation,” Int J Pharm, vol. 548, no. 1, pp. 609–624, 2018.
20. E. S. Farboud, S. A. Nasrollahi, and Z. Tabbakhi, “Novel formulation and evaluation of a Q10-loaded solid lipid nanoparticle cream: in vitro and in vivo studies,” Int J Nanomedicine, pp. 611–617, 2011.

21. Mahmoudi, M., et al. (2009). "Antidepressant and antioxidant activities of Artemisia absinthium L. at flowering stage." African journal of Biotechnology 8(24).
22. Laouini, S. E. and M. R. Ouahrani (2017). "Phytochemical screening, in vitro antioxidant and antibacterial activity of Rumex vesicarius L. extract." Scientific Study & Research. Chemistry & Chemical Engineering, Biotechnology, Food Industry 18(4): 367-376.
23. Sahgal, G., et al. (2009). "In vitro antioxidant and xanthine oxidase inhibitory activities of methanolic Swietenia mahagoni seed extracts." Molecules 14(11): 4476-4485.
24. Lewus, C. B. and T. J. Montville (1991). "Detection of bacteriocins produced by lactic acid bacteria." Journal of microbiological methods 13(2): 145-150.
25. Salih, S., et al. (2017). "Study the Effect of adding Natural Rubber and Polymethyl Methacrylate to the Epoxy Resin on the Quantitative Analysis and its Mechanical Properties." Engineering and Technology Journal 35(2A): 163-171.
26. Hasri, N. M. and N. Zebua (2020). "Test of burn wounds healing effects of collagen from snakehead fish (Channa striata) bone in the preparation of cream on male white rats (Rattus norvegicus)." Indonesian Journal of Pharmaceutical and Clinical Research 3(1): 62-75.
27. Ding, M., et al. (2021). "Polysaccharides from the lignified okra: Physicochemical properties and rheological properties." Bioactive Carbohydrates and Dietary Fibre 26: 100274.
28. Lu, Wen-Chien, et al. "Characterization and biological properties of marine by-product collagen through ultrasound-assisted extraction." Aquaculture Reports 29 (2023): 101514.
29. Ghori, Muhammad U., et al. "Okra extracts in pharmaceutical and food applications." Food Hydrocolloids 42 (2014): 342-347.
30. Widiantara, Tantan, et al. "Chemical properties of moringa milk powder used rotary vacuum drying." Food Science and Technology 43 (2023): e116322.
31. Calapai, Gioacchino, et al. "Effects of Hypericum perforatum on levels of 5-hydroxytryptamine, noradrenaline and dopamine in the cortex, diencephalon and brainstem of the rat." Journal of Pharmacy and Pharmacology 51.6 (1999): 723-728.
32. Shalaby, M., et al. (2020). "Fish scale collagen preparation, characterization and its application in wound healing." Journal of Polymers and the Environment 28: 166-178.
33. Saddiqe, Zeb, Ismat Naeem, and Alya Maimoona. "A review of the antibacterial activity of Hypericum perforatum L." Journal of ethnopharmacology 131.3 (2010): 511-521.
34. Rahman, M. Mashiar, et al. "Antibacterial activity of leaf juice and extracts of Moringa oleifera Lam. against some human pathogenic bacteria." CMU J Nat Sci 8.2 (2009): 219.
35. Rahman, M. Mashiar, et al. "Antibacterial activity of leaf juice and extracts of Moringa oleifera Lam. against some human pathogenic bacteria." CMU J Nat Sci 8.2 (2009): 219.
36. Manske, R. H. F. (12 May 2014). The Alkaloids: Chemistry and Physiology, Volume 8. Vol. 8. Saint Louis: Elsevier. pp. 683–695.
37. Long, H.L., Xu, G.Y., Deng, A.J., Li, Z.H., Ma, L., Lu, Y., ... & Qin, H.L. (2015). Two new flavonoids from the roots of Scutellaria baicalensis. Journal of Asian Natural Products Research, 17(7), 756-760.
38. Zimnicka, B. and A. Hacura (2006). "An Investigation of molecular structure and dynamics of crude beeswax by Vibrational Spectroscopy." Polish Journal of Environmental Studies 15(4): 112-114.
39. Shinzawa, H., et al. (2017). "Non-equilibrium behavior of polyethylene glycol (PEG)/polypropylene glycol (PPG) mixture studied by Fourier transform infrared (FTIR) spectroscopy." Vibrational Spectroscopy 88: 49-55.
40. Špaldoňová, A., et al. (2021). "Analysis of beeswax adulteration with paraffin using GC/MS, FTIR-ATR and Raman spectroscopy." Journal of Apicultural Research 60(1): 73-83.
41. Fahmy, H., et al. (2016). "An innovative SA/PVP hybrid for attaining water repellent cotton/polyester blended fabric." International Journal of ChemTech Research 9(3): 215-227.
42. Peretz, S., et al. (2013). "Chitosan microparticulate systems prepared by polymer-surfactant interaction." Rev Roum Chim 58(2–3): 275-281.
43. Riaz, T., et al. (2018). "FTIR analysis of natural and synthetic collagen." Applied Spectroscopy Reviews 53(9): 703-746.

The Role of Acetylcholinesterase (AChE) in Autism Spectrum Disorder (ASD): Partial Purification and Evaluation of Inhibitory Compounds

Ako Saber Kaky [1,a], Sayran Sattar Saleh [1,b]

[1] *Department of Chemistry, College of Science, University of Kirkuk, Kirkuk, Iraq*
[a] Corresponding author: ako.kaky@uokirkuk.edu.iq
[b] sayran.2017@uokirkuk.edu.iq

Abstract. This study aimed to purify acetylcholinesterase (AChE) from the serum of autism spectrum disorder (ASD) patients and investigate its molecular properties and inhibition by various compounds. AChE was successfully purified through a series of steps, including ammonium sulfate precipitation, dialysis, and gel filtration chromatography, resulting in a highly purified enzyme with a specific activity of 4.26 U/mg. The molecular weight of the purified AChE was estimated to be approximately 231,800 Da by gel filtration and 57,000 Da for its subunit by SDS-PAGE, consistent with previous reports on AChE structure. To assess the potential therapeutic implications, the inhibitory effects of ten compounds on AChE activity were evaluated. Results indicated varying degrees of inhibition, with Donepezil demonstrating potent competitive inhibition. Other compounds, such as Isocarboxazid and Duloxetine, exhibited non-competitive inhibition. However, the precise mechanisms of action for many compounds require further investigation. The successful purification of AChE from ASD patients and characterization of its molecular properties provides valuable insights into the enzyme's role in this condition. The identification of potential AChE inhibitors offers promising avenues for the development of novel therapeutic strategies targeting cholinergic dysfunction in ASD and related neurodegenerative disorders. Further studies are warranted to elucidate the underlying mechanisms of inhibition and to explore the clinical efficacy of these compounds.

INTRODUCTION

Autism spectrum disorder (ASD) is a disease marked by difficulty in social interaction, speech impairments, and repetitive behaviours. Although there has been significant progress in comprehending ASD, the precise origins and processes of this disorder remain incompletely known [1]. Autism spectrum disorder is a condition that is impacted by hereditary factors. Scientists have investigated the mechanisms associated with the development of autism spectrum disorder (ASD), including the involvement of acetylcholinesterase (AChE), in its underlying physiological processes [2].

Acetylcholinesterase is an enzyme that functions by degrading the neurotransmitter acetylcholine (ACh) at synapses, hence halting transmission. The role of this is vital for facilitating neuronal transmission and preventing excessive activation of receptors. In addition to its function in transmission, Acetylcholinesterase (AChE) has attracted interest for its potential participation in the underlying processes of autism [3].

Oxidative stress may occur in a biological system when the quantities of antioxidants are insufficient, causing an increase in oxidants, sometimes referred to as reactive oxygen species (ROS). The central nervous system (CNS) is very susceptible to stress because of its high oxygen demand and lipid content. Conditions such as Parkinson's disease (PD), Alzheimer's disease (AD), Huntington's disease (HD), and amyotrophic lateral sclerosis (ALS) have been linked to macromolecule damage resulting from various mechanisms [4]

Acetylcholinesterase (AChE; EC 3.1.1.7), sometimes referred to as AChE or acetylhydrolase, is a vital enzyme in the human body that plays a fundamental role in facilitating communication between nerve cells and muscles. Located at the intersection of these cells, AChE functions as a chemical toggle, deactivating the signal that instructs a muscle to contract. It does this by decomposing a molecule known as acetylcholine (ACh), the primary neurotransmitter

Technologies and Materials for Renewable Energy, Environment and Sustainability
AIP Conf. Proc. 3321, 030015-1–030015-14; https://doi.org/10.1063/5.0289600
Published under an exclusive license by AIP Publishing. 978-0-7354-5231-2/$30.00

responsible for starting muscle action. Acetylcholinesterase (AChE) breaks down acetylcholine (ACh), guaranteeing that the signal is transient and allowing the muscle to relax [3].
This delicate balancing act is essential for everything from blinking your eyes to coordinating complex movements. AChE is present not only at neuromuscular junctions but also in other areas of the nervous system, highlighting its broad influence on various bodily functions [5].
A study conducted by Pardo et al. (2017) investigated the levels of AChE activity in the brain tissue of individuals with ASD. The study found that the levels of AChE activity were significantly higher in the brain tissue of individuals with ASD compared to controls. The authors suggested that the increased AChE activity may be related to the abnormal cholinergic activity observed in ASD [6].
Research indicates alterations in acetylcholinesterase levels in individuals with ASD. These changes may contribute to disruptions in cholinergic signaling, potentially influencing cognitive and behavioral aspects associated with ASD. The dysregulation of acetylcholinesterase in ASD has implications for the cholinergic system's overall functioning. Understanding how changes in enzyme activity may affect cognitive processes provides insights into the neurobiological underpinnings of ASD. Genetic variations and polymorphisms in genes related to acetylcholinesterase can influence its activity. Exploring these genetic influences is essential for understanding individual differences in the cholinergic system and susceptibility to ASD. Prenatal exposures to environmental factors can impact the cholinergic system's development and function. Investigating how environmental influences interact with genetic factors sheds light on the complex interplay contributing to ASD risk [7].
The regulation of AChE activity is crucial for maintaining normal neurotransmission. AChE activity can be modulated by various factors, including its own inhibitors, such as neostigmine, physostigmine, and edrophonium. Additionally, the AChE enzyme's activity is regulated by a variety of endogenous molecules, including calcium, zinc, and various peptides [8].
Acetylcholinesterase inhibitors are widely used in the treatment of various diseases, including Alzheimer's disease, myasthenia gravis, and glaucoma. In Alzheimer's disease, AChE inhibitors such as donepezil, galantamine, and rivastigmine are used to increase the levels of ACh in the brain, thereby improving cognitive function. In myasthenia gravis, AChE inhibitors such as pyridostigmine are used to increase the levels of ACh at the neuromuscular junction, thereby improving muscle function. In glaucoma, AChE inhibitors such as physostigmine are used to reduce intraocular pressure by increasing the levels of ACh in the eye [8,9].
Studies have shown that AChE plays a critical role in regulating neurogenesis, neuronal differentiation, and synaptic development. AChE is involved in the modulation of cell proliferation and migration, as well as the regulation of cell survival and differentiation. AChE has also been shown to play a role in the regulation of synapse formation and maturation, including the development of dendritic spines and the establishment of synaptic contacts [10,11].
Studies have also shown that disruption of AChE activity during development can lead to abnormal brain development and cognitive deficits. For example, exposure to AChE inhibitors during gestation has been shown to impair synaptic development and lead to cognitive deficits in animal models. In humans, prenatal exposure to AChE inhibitors has been associated with increased risk of developmental delays and cognitive deficits [12].
Acetylcholinesterase inhibitors, designed to increase acetylcholine levels by inhibiting acetylcholinesterase activity, have been explored for various neurological conditions. Understanding their mechanism of action and potential applications in ASD treatment provides insights into novel therapeutic avenues. Studies investigating the use of cholinesterase inhibitors in ASD treatment suggest potential benefits for specific cognitive and behavioral symptoms. Evaluating the effectiveness, safety, and long-term implications of these medications is crucial for their integration into ASD therapeutic strategies [13].
A study conducted by Schneider (2000) investigated the effects of a cholinesterase inhibitor, tacrine, on the behavioral symptoms of ASD. The study found that the administration of tacrine led to significant improvements in communication and social interactions in children with ASD. The authors suggested that the therapeutic effects of tacrine may be related to its ability to increase the levels of ACh in the synapse [14].

MATERIALS AND METHODS

Study case and Subjects

The study had a cohort of 96 patient who were diagnosed with autism spectrum disorder and ranged in age 3-12 years old. In addition. Blood samples was collected at Kirkuk Paediatric Hospital in Kirkuk, Iraq. A skilled paediatrician conducts the diagnosis of patient. The patients were asked a range of questions regarding medical history, parental consanguinity, age of ASD diagnosis, administered per, as well as weight and height measurements.

Biochemical assays

The activity of acetylcholinesterase was evaluated using the approach outlined in the reference. The quartz cuvette contains a reaction mixture of 3 mL and has a route length of 1 cm. The solution is composed of 0.075 M of ATI, 0.01 M of DTNB, and 0.1 M phosphate buffer with a pH of 7.4. The optical density was evaluated at a wavelength of 412 nm during a duration of 3 minutes, with data recorded at 30-second intervals. The enzyme activity was measured using the extinction coefficient ΔA × D.F ×106 /13600 ×3 ×103 μmol/min/ml and was expressed as μmoles of acetylthiocholine hydrolysed per mL per minute or units (U) [15]. The enzymatic activity was measured and expressed as units per milligramme (U mg−1). The protein content was determined using the Lowry method and Ciocalteu's Phenol reagent. In addition, protein quantification was conducted using the Folin phenol reagent. The research used bovine serum albumin as the benchmark. The absorbance of the blue-colored complex was measured at a wavelength of 620 nm 16].

Blood collection

A venipuncture technique was employed to obtain a volume of 5 ml of blood using a disposable syringe. The blood was thereafter transferred into gel tubes for separation. The tubes underwent centrifugation for a duration of 10 minutes. The serum was isolated from the cells and thereafter kept at a temperature of -20°C.

Salting Out

Precipitation, and "salting – out "is a relatively inexpensive way to concentrate and purify molecules, including proteins. In this process, at high Salt concentration protein solubility decreases as ionic strength increases. Ammonium Sulphate [$(NH4)_2SO_4$] is often used for this purpose because of its high solubility in water. Eight milliliter of crude serum was first brought to (30 -70) % saturation with solid ammonium sulphate, with mobilization for 60 min at 4C°, then allow for 24 hr at (4°C) in order to complete the precipitation, the precipited protein was regimented by cooling centrifuge at (14600xg) for 20 min at (4°C), redissolved in 1ml of D.W. Both enzyme activity and protein content were determined for each separate fraction. The remaining solution was kept and stored in refrigerator [17,18].

Dialysis against Buffer

Dialysis is the process of separating smaller molecules from larger one in a solution using a semipermeable cellophane dialysis membrane with M.Wt. cut off (<30000) Dalton. When this is placed in a significantly larger volume of a buffered solution with the right level of ions, the membrane permits the transfer of salt and buffer, but not proteins. Dialysis is a process that keeps big proteins inside a bag or tube while allowing other solutes in the protein preparation to adjust their concentration until they reach a balance with the solution outside the membrane. Dialysis might be used, for example, to remove ammonium sulfate from the protein preparation [19].
After the sample solution has been poured into the sac, it was closed just above the top of the solution, air was removed, and the sac was tightly knotted at the end and tied with stirring. The dialysis sac containing the suspension in (Step I) was dialyzed against 0.015M The obtained ammonium sulfate precipitate (enzyme solution) was dialyzed in the presence of (0.1 M Tris-HCL) pH (7.6) The solution was stirred with a magnetic stirrer overnight at (4^o C). The buffer solution was changed each 6 hours during dialysis. Then the supernatant solution containing the enzyme was estimated by (modified Lowry method) (650nm) as described before, enzyme activity (412 nm) as described in section (2.1), and then stored for the next step.

Size – exclusion chromatography (SEC) - Gel filtration on Sephadex G-200

1- Sephadex G- 200 solution:
Four grams of Sephadex G - 200 was swollen in120 mL of phosphate working buffer solution (0.2 M, pH 7.4) then left for (24 - 48) hour in 4 ^{o} C and buffer solution exchanged continuously by (Decantation)
2- phosphate buffer solution (pH = 7.3 ,0.2 M)
Dissolved (2.84 gm) 0f (Na2HPO4, MW =141.69) in distilled water, then the pH was adjusted with few drops of hydrochloric acid, and then the volume was made up to 100 ml with distilled water [20,21].
Procedure:

Preparation of the column:

Gel filtration was carried out with a (1.5 x 50) cm glass column used and put in the end of column small amounts of glass wool to prevent losing gel particles outside, the dimensions of the column were determined according to the following formulas: Diameter = 3 m / 10 cm where m is the amount of protein in mg. Length = 30 x diameter.
The gel was allowed to swell in an excess of 0.2 M phosphate buffer solution, pH 7.4 (30 mL / gm gel) and left for 48 hours at 4 ° C, fine particles were removed by decantation before packing the column. The matrix suspension should be adjusted to a thick slurry usually about 75% of settled matrix the suspension must be carefully mixed before pouring. Then the slurry was carefully poured into a vertical glass column down the wall using a glass rod. After the gel had settled, the column was equilibrated with phosphate buffer pH 7.4 for 24 hours.

Application of the Sample

A 5 ml sample of the proteinaceous material, produced according to the instructions in section (2.2), was placed on top of a Sephadex G-200 bed, and then a phosphate buffer solution was added. The proteinaceous components were separated by passing them through a phosphate buffer solution at a rate of 24 ml/hour. Approximately 2 mL fractions were taken at 5-minute intervals. Each fraction's protein content and acetylcholinesterase (AChE) activity were measured using the techniques detailed in section (2.1). Using a UV/Visible Spectrophotometer, the absorbance at a 280 nm wavelength revealed the protein components in every obtained fraction.

Estimation of the Molecular Weight

Estimation of the Molecular Weight of Partially Purified AChE by Sodium dodecyl sulfate -Polyacrylamide Gel Electrophoresis (SDS-PAGE) [22].

In vitro inhibition assay of acetylcholinesterase

This study examined the *in vitro* inhibitory effect of Isocarboxazid, Alprazolam, Methylphenidate, Fluoxetine, Duloxetine, Vitamin C, Vitamin E, Selenium, Magnesium and Donepezil on acetyl choline esterase activity, by using different concentrations (0.02, 0.04, 0.06, 0.08, 0.1, 0.2, 0.4 and 0.6) M from each compound [23].
Reagents
1- The reagent (1) is created by dissolving 1 gramme of the medication in 5 millilitres of a 0.1 molar phosphate buffer at a pH of 7.4, resulting in a stock solution.
2- The buffer solution was used to get the mixture volume to 50µl after the reagent (1) solution had been diluted to reach concentrations of (0.02, 0.04, 0.06, 0.08,0.1,0.2,0.4, and 0.6) M.
Eight test tubes containing 50µl of medications and supplements were filled with previously prepared solutions and 15µl of partly purified serum was added. The tubes were then stored at 4° C for an hour.
3- The process was carried out under ideal circumstances, just as the stages in section (2.1) indicated. The activity of the control cuvette was confirmed to be 100% when the inhibitor was absent.
4- As shown in table (3-42) various inhibitor concentrations (maximum and lowest inhibition) were evaluated for each sample in order to ascertain the values of the kinetic constants. In this work, eight distinct doses of acetyl choline iodide (0.02, 0.04, 0.06, 0.08,0.1,0.2,0.4, and 0.6) g/ml were used as the substrate. The activity in the crude and partly purified samples for individuals with autism spectrum disorder was compared with the activity in the presence of an inhibitor using the Lineweaver-Burk plot. Additionally, the following equation was used to get the inhibition %.

Statistical analysis

$$\text{The percentage of inhibition} = \frac{\text{activity without inhibitor} - \text{activity with inhibitor}}{\text{activity without inhibitor}} * 100$$

This research highlights the significant differences (p value) observed between the groups and offers the data in terms of Mean ± SD. A statistical analysis was used to determine whether differences were significant, with a p-value of 0.05 or less being considered significant. The program GraphPad Prism was used to carry out the statistical analysis.

RESULTS AND DISCUSSION

Table 1 presents the mean value and standard deviation of the enzyme activity and specific activity (enzyme activity divided by total protein) of serum AChE. The enzyme activity is measured in U/ml and the specific activity is measured in U/mg. The measurements were obtained from people diagnosed with autism spectrum disorder (ASD) and were then compared to the measurements of individuals in a state of good health.

Table 1. The (activity and specific activity) of the serum AChE for all studied groups.

Parameters	Controls (n=96)	Patients (n=96)	P value
Serum AChE U/ ml	5.023 ± 0.883	4.224 ± 1.160*	0.0369
S.A in Serum U/mg	0.722±0.151	0.57 ± 0.145*	0.001

**Significant ($p \leq 0.05$)*

The results presented in Table 1 demonstrate a significant decrease in acetylcholine esterase activity and specific activity of ASD patients' blood in comparison to the control group. Moreover, the results are consistent with previous studies that have shown a decline in the activity of acetylcholinesterase (AChE).

The study found a significant reduction in acetylcholinesterase (AChE) function in patients who have been diagnosed with neurological diseases. The decrease in AChE activity has been linked to the existence of despair, anxiety, boredom, and unhappiness, therefore providing more evidence for the association between this state and mental health and psychiatric problems [23].

The impact of oestrogen on brain function, namely its ability to enhance the absorption of choline and the production of acetylcholine, may account for the increase in acetylcholinesterase activity [24]. The reduction in specific activity seen may be attributed to particular impurities, obtained by dividing the activity of AChE by the concentration of TP in the serum. The precise role of an enzyme may operate as a reliable predictor of its purity [25]. The aforementioned results are consistent with the study conducted by [26], which examined the parameters in children diagnosed with autism.

Table 2 examines the blood levels of several components in persons with autism spectrum disorder in comparison to a control group of healthy individuals. The data is shown in the format of the Mean ± Standard Deviation (SD).

Table 2. Purification Step of AChE Enzyme for ASD patients

Purification Step	Volume (ml)	Protein Conc. (gm/dl)	Total Protein (gm)	Enzyme Activity U/ml	Total Activity IU	Specific Activity U/mg	Fold of Purification	Yield 100%
Serum	**8**	**71**	**568**	**5.2**	**41.6**	**0.07**	**1**	**100**
precipitation by Ammonium sulphate 70%	**5**	**23.4**	**117**	**5.8**	**29**	**0.248**	**3.38**	**69.71**
Dialysis	**3.5**	**9**	**31.5**	**6.3**	**22.05**	**0.70**	**9.56**	**53.00**
Gel Filtration Sephadex G – 200	**9**	**1.55**	**13.95**	**6.6**	**59.4**	**4.26**	**58.14**	**142.7**

This table outlines the purification process for the enzyme Acetylcholinesterase (AChE) in autism spectrum disorder, commonly found in serum. Each row represents a different purification step, with key parameters measured to assess the efficiency of the process. Our goal is to isolate and concentrate the AChE enzyme while removing impurities.

The initial state is represented by the "Serum" row. We had 100 units (U) of total AChE activity in a volume of 8 ml. This translates to a relatively low specific activity of 0.07 U/mg protein, indicating the presence of many other proteins besides AChE.

Ammonium Sulfate Precipitation: The first purification step utilizes ammonium sulfate precipitation. This technique leverages the different solubility properties of proteins at varying ammonium sulfate concentrations. Here, the yield (percentage of initial activity retained) is 69.71%, which means we lose some AChE, but also see a significant

improvement in fold purification (3.38-fold). This indicates some separation from other proteins. The specific activity increases to 0.248 U/mg, showing that AChE is being enriched relative to total protein.
Dialysis: This step removes the ammonium sulfate salts introduced in the previous step. While the yield remains good at 53%, the fold purification increases impressively to 9.56-fold. Notably, the specific activity also increases substantially to 0.7 U/mg, indicating a highly purified enzyme preparation.
Gel Filtration Chromatography (Sephadex G-200):
This final step involves separating proteins based on their size. By collecting 3 fraction (3 ml) which equal to 9 ml (from 131 to 140 elution volume), the yield increased to 142.79%, suggesting some increasing in volume during separation (fraction). However, the fold purification remains very high at 58.14-fold compared to the dialyzed sample. This significant jump suggests successful removal of a large portion of contaminating proteins while retaining a good amount of AChE. Most importantly, the specific activity reaches a remarkable 4.26 U/ml, signifying a highly purified AChE preparation with minimal contamination from other proteins.
This data demonstrates a successful purification process for AChE. While enzyme activity is kept at the same value throughout the steps, the substantial increase in specific activity signifies a progressive enrichment of AChE relative to other proteins. The final product obtained through gel filtration is a highly purified AChE preparation with minimal contamination, making it suitable for further studies.

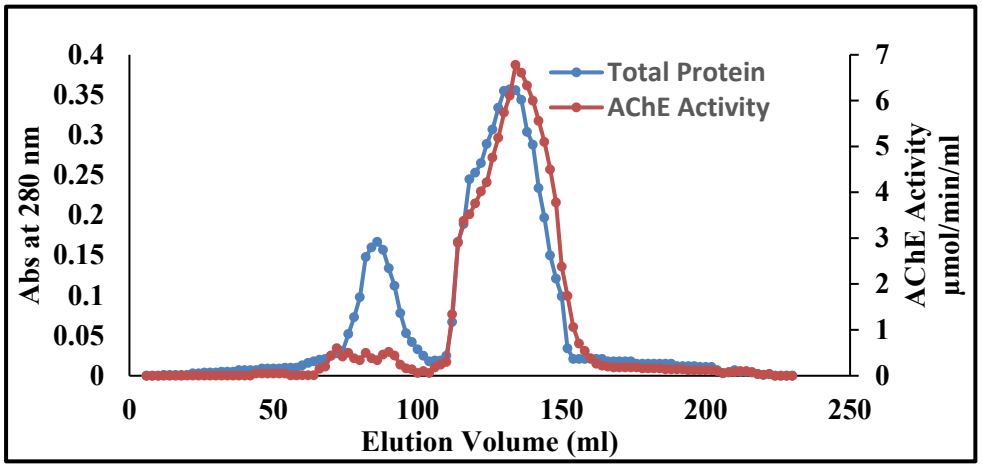

Figure 1. The Elution Profile of AChE from Autism Spectrum Disorder Patient by Using Gel Filtration Method on Sephadex G – 200.

Standard proteins with known molecular weights were used to estimate the molecular weight of AChE as described in section (2.6). The elution volume Ve for each protein was estimated from figure 1.
Measure the approximate molecular weight of the partially aspirated from the serum of ASD patients onto the separation column containing sephadex G -200, which found a distinctive peak of protein, that have highest specific activity equal to (4.26 U/mg) fold of purification was equal to (58.14). Eluted fractions were followed by measuring absorbance of protein content at 280 nm the elution volume of AChE solution, collected from this technique is (9 ml) and this volume was used in the estimation of the approximate molecular weight of the enzyme, this volume correspond to a molecular weight of (231800) Da when using the standard curve that have been drawn between elution volume against molecular wight logarithm as shown in table 3 and figure 2.
This was in agreement with study by Kaya, H.B in (2013) [27]. The findings were consistent with the molecular weight of the enzyme obtained from red blood cell walls, which was determined to be 70,000 Daltons for each individual subunit using electrophoresis. It is also associated with the research conducted by Lelas F. B in 2017 [28] who used gel filtration to determine the molecular weight of the enzyme isolated from cerebral spinal fluid, which has a molecular weight of 163,606 Dalton, and who is involved in a study by Geoffrey Webb (1978) [29] that determined the molecular weight of the enzyme isolated from electric organ tissue, which has a molecular weight of 55000 Dalton.
The proteins were observed to move a distance of 4.0 cm towards the positive electrode, forming a distinct protein peak. This measurement was made from the point of origin, as depicted in figure 3. The distance was calculated by estimating the molecular weight of the protein to be 57000 Dalton, using the standard curve provided in table 3 and figure 3.
The results were consistent with the molecular weights of the enzyme isolated from serum, which were determined to be 70,000 Daltons for each subunit using electrophoresis. The researcher also observed that the electrophoresis

approach revealed a molecular weight of around 60,000 Daltons for the enzyme's component.
The researchers discovered that the enzyme exists in several configurations, with the quadruple shape being predominant in the human brain. Consequently, the estimated molecular weight of the enzyme falls within the range of 240,000 to 280,000. Dalton.
Multiple researchers have approximated the molecular weight of the enzyme that has been dissolved in a solvent from various sources to be 260000 Dalton. Furthermore, detergents and other chemicals that break apart substances have been used to confirm the presence of a subunit with a molecular weight ranging from 50000 to 80000 Daltons. Evidence has been provided suggesting that the actual molecular weight is 57000, and that these species consist of four to six subunits. Additional findings indicate that the enzyme's structure in the membrane consists of a single unit with a molecular weight of around 75000. Furthermore, various forms of the enzyme found in solubilised preparations are composed of aggregates of this single unit [30,31]

Table 3. Standard material that used to Estimate the Approximate Molecular Weight of AChE and the distance it moved from the point of origin.

Standard material	Molecular weight (Dalton)	Distance from point of origin(cm)
Glycogen phosphor	97000	3.6
Phosphofructokinase	82000	3.7
Bovine serum albumin	67000	3.9
Egg albumin	45000	4.1
Pepsin	36000	4.3
Trypsin anhydrase	20000	4.6
AChE	57000	4.0

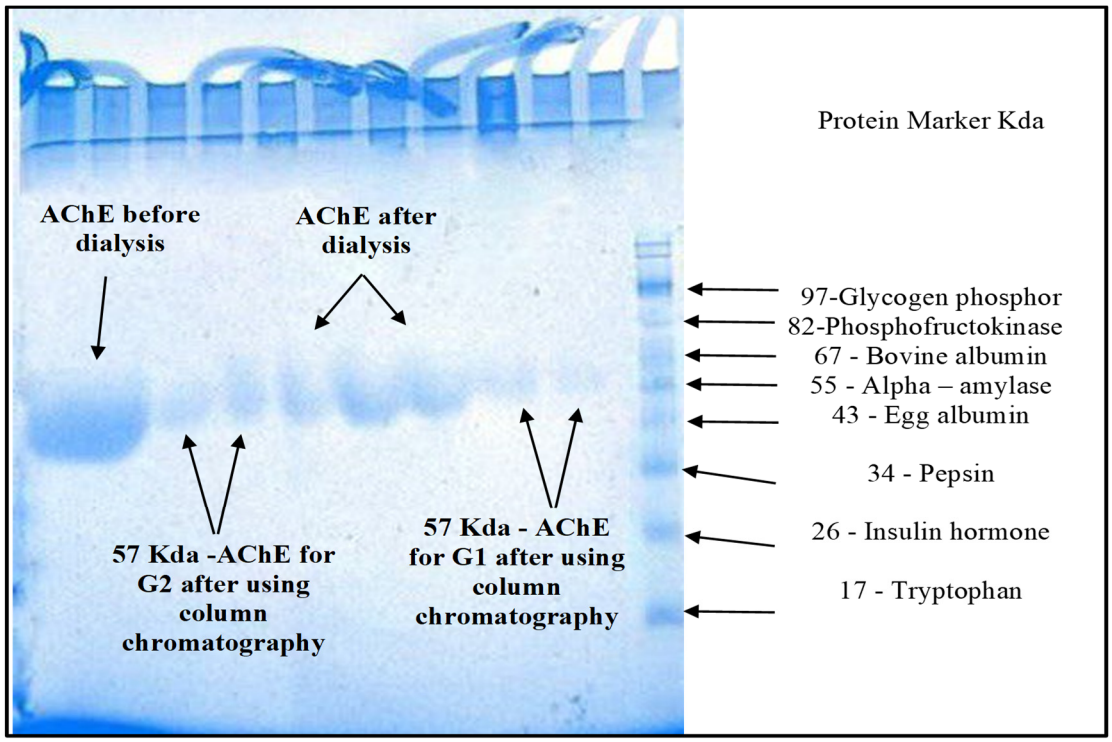

Figure 2. SDS-PAGE Analysis bands of the purified acetylcholinesterase and the standard proteins.

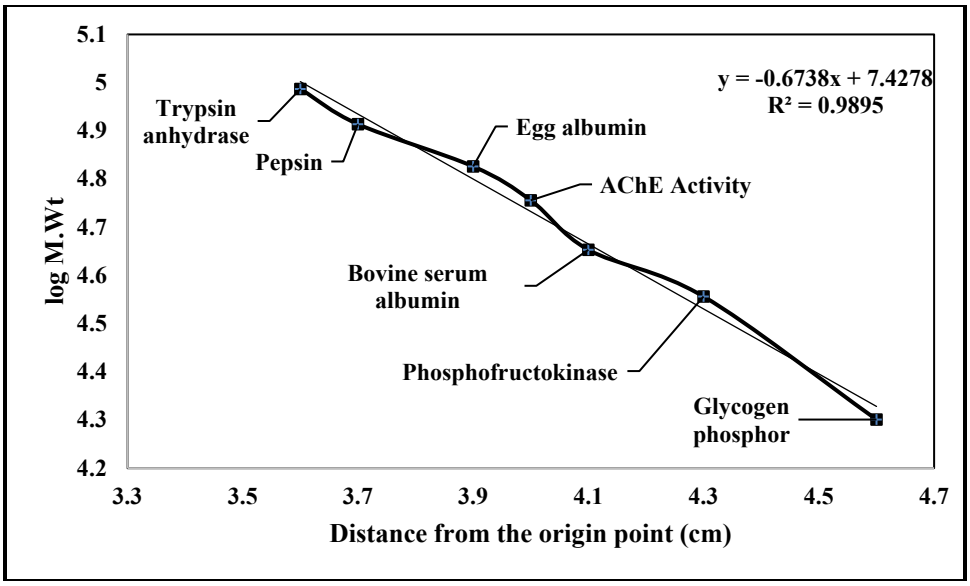

Figure 3. Calibration Curve Used to Determine the Approximate Molecular Weight of Acetylcholinesterase Using SDS-Page Polyacrylamide Electrophoresis.

The table 4 shown the effect of inhibitors (D1-D10) to isolated and purified AChE. Inhibitor is a substance that reduces the activity of another substance. For each drug, the table shown the concentration of the drug that add to the sample, and calculate AChE activity without inhibitor and after adding the inhibitors. The percent inhibition (%Inhibition) calculate be dividing the AChE activity after adding the inhibitor by AChE activity before adding the inhibitors. The AChE activity, Km and Vmax before adding the inhibitor were (6.5), (0.034) and (6.78) respectively.
Below is a breakdown of the results for each drug (D1-D10):

- **D1 (Alprazolam)**: The inhibitor caused a small inhibition of AChE activity, ranging from 8% to 18%. The ChE activity after adding inhibitor remained relatively high, ranging from 5.2 to 5.9. The $Km_{inhibitor}$ (7.303) is close to the Km (6.784) before adding the inhibitor while the $Vmax_{inhibitor}$ (0.075) was lower than the Vmax (0.034) which means Alprazolam concentration effect on V and competitive with the substrate, which means the drug is a competitive inhibitor, this deals with the reference [32].
- **D2 (Ascorbic Acid)**: The inhibitor caused a small inhibition of AChE activity, ranging from 9% to 22%. The AChE activity after adding inhibitor remained relatively high, ranging from 5.1 to 5.9. The $Km_{inhibitor}$ (5.798) is close to the Km (6.784) before adding the inhibitor while the $Vmax_{inhibitor}$ (0.041) was decreased compared to the Vmax (0.034) which means Ascorbic Acid might a non-competitive inhibitor, this deals with the if this small effect counts as inhibition [33].
- **D3 (Magnesium)**: The inhibitor not caused a significant inhibition of AChE activity, ranging from 9% to 11%. The AChE activity after adding inhibitor remained relatively high, ranging from 5.8 to 6.78. The $Km_{inhibitor}$ (5.581) is close to the Km (6.784) before adding the inhibitor while the $Vmax_{inhibitor}$ (0.041) was slightly higher than the Vmax (0.034) which means Magnesium act as a non-competitive inhibitor [34].
- **D4 (Isocarboxazid)**: The inhibitor caused a significant inhibition of AChE activity, ranging from 34% to 38%. The AChE activity after adding inhibitor was lower than for most other drugs, ranging from 4 to 4.3. The $Km_{inhibitor}$ (4.346) is slightly lower compared to the Km (6.784) before adding the inhibitor while the $Vmax_{inhibitor}$ (0.034) was same as the Vmax (0.034), which means Isocarboxazid act as a non-competitive inhibitor, this deals with the reference [35].
- **D5 (Methylphenidate)**: The inhibitor caused a small inhibition of AChE activity, ranging from 26% to 29%. The AChE activity after adding inhibitor remained relatively high, ranging from 4.6 to 5. The $Km_{inhibitor}$ (4.805) is lower to the Km (6.784) before adding the inhibitor while the $Vmax_{inhibitor}$ (0.062) was significantly higher than the Vmax (0.034) which means Methylphenidate tend to be a non-competitive inhibitor, this deals with the reference [36].
- **D6 (Selenium)**: The inhibitor caused a no significant inhibition of AChE activity, ranging from 23% to 25%. The AChE activity after adding inhibitor remained relatively high, ranging from 4.9 to 5.25. The $Km_{inhibitor}$ (5.254) is lower compared to the Km (6.784) before adding the inhibitor while the $Vmax_{inhibitor}$ (0.062) was higher compared to the Vmax (0.034) [37].
- **D7 (Duloxetine)**: The inhibitor caused a significant inhibition of AChE activity, ranging from 54% to 62%.

The AChE activity after adding inhibitor was lower than for most other drugs, ranging from 2.5 to 3. The $Km_{inhibitor}$ (6.518) similar to the Km (6.784) before adding the inhibitor while the $Vmax_{inhibitor}$ (0.060) was higher than the Vmax (0.034) which means Duloxetine act as a non-competitive inhibitor, this deals with the reference [38].

- **D8 (Fluoxetine)**: The inhibitor caused a small inhibition of AChE activity, ranging from 34% to 35%. The AChE activity after adding inhibitor remained relatively high, ranging from 4.2 to 6.78. The $Km_{inhibitor}$ (5.301) is slightly lower than the Km (6.784) before adding the inhibitor while the $Vmax_{inhibitor}$ (0.060) was higher than the Vmax (0.034) [39].
- **D9 (alpha-tocopherol)**: The inhibitor caused a significant inhibition of AChE activity, ranging from 58% to 62%. The AChE activity after adding inhibitor was lower than for most other drugs, ranging from 2.4 to 2.7. The $Km_{inhibitor}$ (6.625) is not differ to the Km (6.784) before adding the inhibitor while the $Vmax_{inhibitor}$ (0.035) was same value compared to the Vmax (0.034), it's not clear how it works [40].
- **D10 (Donepezil)**: The inhibitor caused a significant inhibition of AChE activity, ranging from 58% to 63%. The AChE activity after adding inhibitor was lower than for most other drugs, ranging from 2.4 to 2.7. The $Km_{inhibitor}$ (2.704) is less than the Km (6.784) before adding the inhibitor while the $Vmax_{inhibitor}$ (0.031) was slightly lower than the Vmax (0.034) which means Donepezil act as a competitive inhibitor, this deals with the reference [41].

Table 4. Shows the effect of the inhibitor concentrations, the percentage of inhibition, Km and Vmax for (D1-D10).

Compound	Inhibitor Conc.	AChE Activity after adding the inhibitor	Inhibition %	Km for AChE after adding inhibitor	Vmax for AChE after adding inhibitor
D1 D1 D1 D1 D1	0.01	6	8%	0.0749	7.304
	0.02	5.9	9%		
	0.05	5.8	11%		
	0.1	5.7	12%		
	0.15	5.6	14%		
D2 D2 D2 D2 D2	0.01	5.3	18%	0.0406	5.799
	0.02	5.2	20%		
	0.05	5.2	20%		
	0.1	5.1	22%		
	0.15	5.1	22%		
D3 D3 D3 D3 D3	0.01	5.9	9%	0.0409	5.582
	0.02	5.9	9%		
	0.05	5.8	11%		
	0.1	5.8	11%		
	0.15	5.8	11%		
D4 D4 D4 D4 D4	0.01	4.3	34%	0.0335	4.346
	0.02	4.3	34%		
	0.05	4	38%		
	0.1	4	38%		

	0.15	4	38%		
D5 D5 D5 D5 D5	0.01	4.8	26%	0.0345	4.805
	0.02	4.7	28%		
	0.05	4.7	28%		
	0.1	4.6	29%		
	0.15	4.6	29%		
D6 D6 D6 D6 D6	0.01	5	23%	0.0615	5.254
	0.02	5	23%		
	0.05	5	23%		
	0.1	4.9	25%		
	0.15	4.9	25%		
D7 D7 D7 D7 D7	0.01	3	54%	0.0644	6.519
	0.02	2.8	57%		
	0.05	2.6	60%		
	0.1	2.5	62%		
	0.15	2.5	62%		
D8 D8 D8 D8 D8	0.01	4.2	35%	0.0603	5.301
	0.02	4.2	35%		
	0.05	4.2	35%		
	0.1	4.2	35%		
	0.15	4.2	35%		
D9 D9 D9 D9 D9	0.01	4.3	34%	0.0347	6.625
	0.02	4.2	35%		
	0.05	4.2	35%		
	0.1	4.1	37%		
	0.15	4	38%		
D10 D10 D10 D10 D10	0.01	2.7	58%	0.0314	2.704
	0.02	2.6	60%		
	0.05	2.5	62%		
	0.1	2.4	63%		
	0.15	2.4	63%		

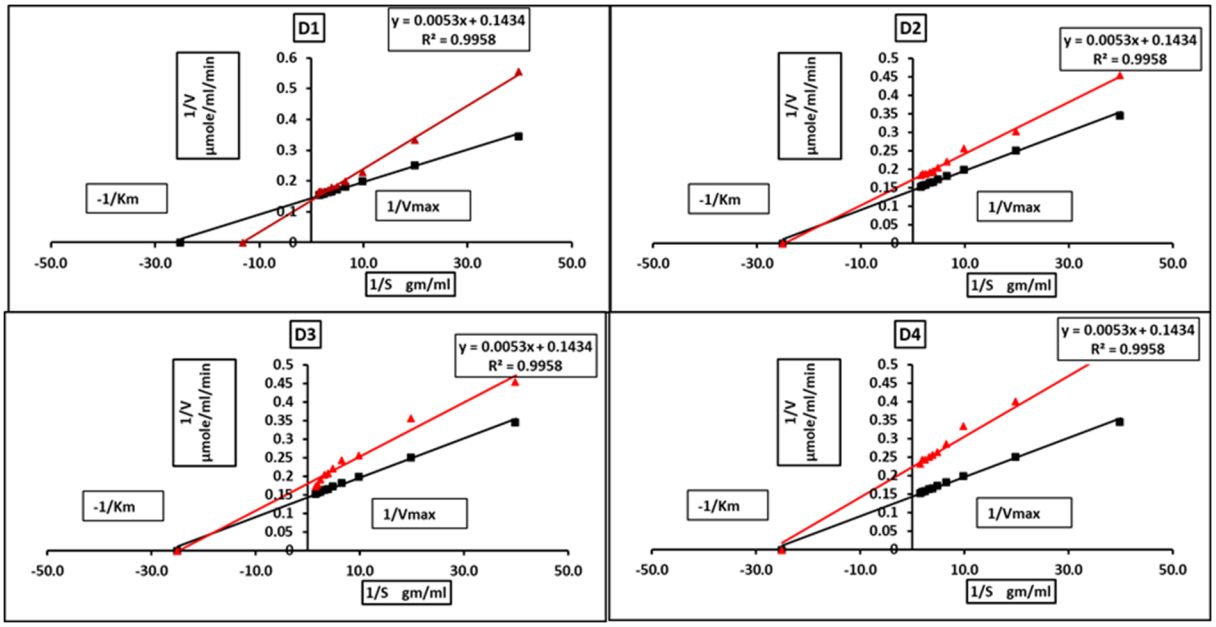

Figure 4 Lineweaver - Burk plot for each inhibitor (D1-D4)

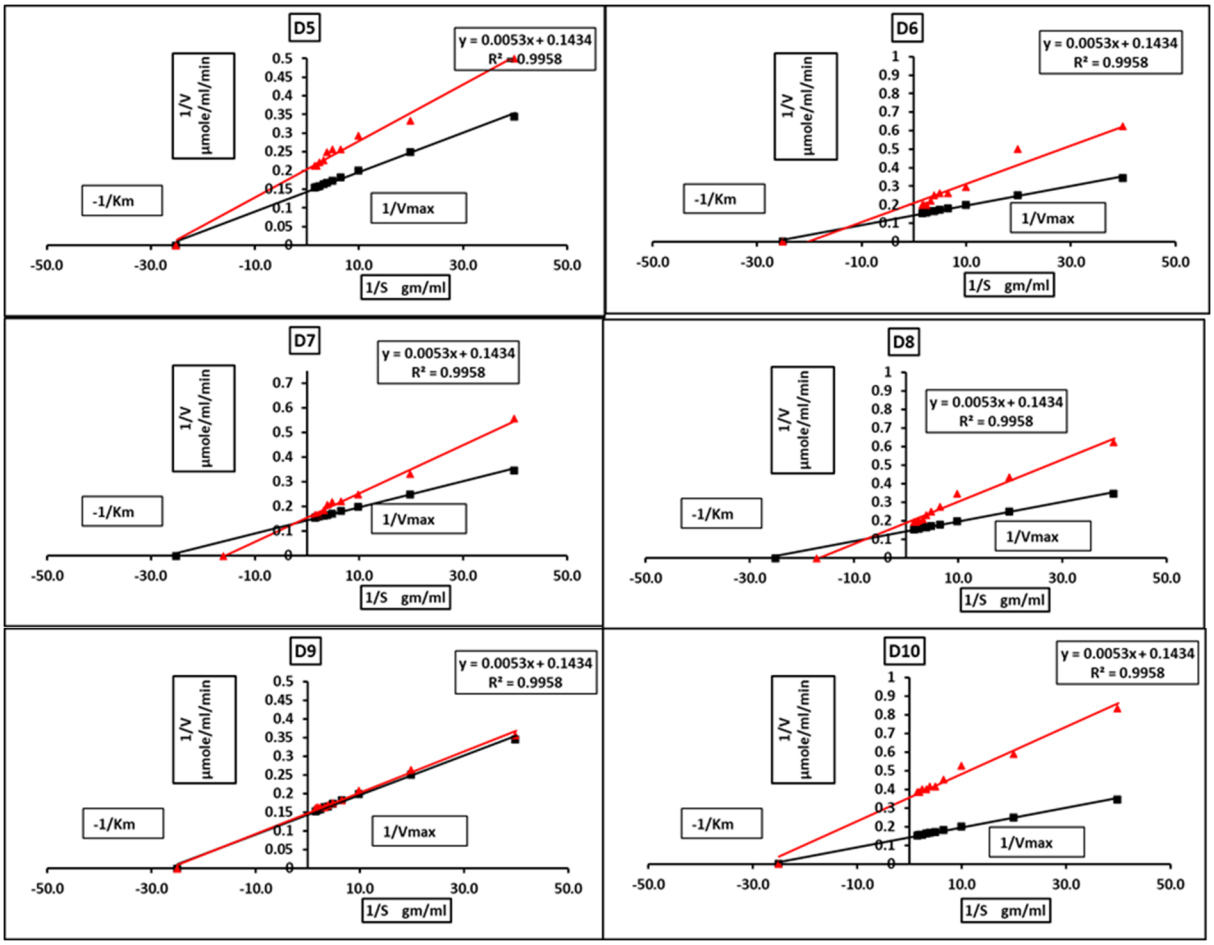

Figure 5 Lineweaver - Burk plot for each inhibitor (D5-D10)

CONCLUSION

The present study successfully isolated and purified acetylcholinesterase (AChE) from the serum of ASD patients, achieving a high degree of purity as evidenced by the significant increase in specific activity throughout the purification process. Gel filtration chromatography determined the approximate molecular weight of AChE to be around 231,800 Da, which aligns with previous findings suggesting a multimeric structure. SDS-PAGE analysis further indicated a subunit molecular weight of approximately 57,000 Da, consistent with the known subunit composition of AChE. The inhibitory effects of ten compounds on AChE activity were evaluated. Results showed varying degrees of inhibition, with some compounds demonstrating significant inhibitory potential. Notably, Donepezil exhibited potent competitive inhibition, aligning with its established role as an AChE inhibitor. Other compounds, such as Isocarboxazid and Duloxetine, displayed non-competitive inhibition. However, the precise mechanisms of action for many of the tested compounds require further investigation. These findings contribute to the understanding of AChE in the context of ASD and provide a foundation for future studies exploring the potential therapeutic implications of AChE modulation. Identifying effective AChE inhibitors may offer novel avenues for the development of treatments for ASD and other neurodegenerative disorders characterized by cholinergic dysfunction.

Acknowledgment

The following people and organizations have provided significant assistance to our research effort, for which the authors are really grateful: the parents who participated in the study, the personnel and management of the Pediatric Hospital in Kirkuk, and our respected supervising physicians.

REFERENCES

1. Longo, F., & Klann, E. (2021). Reciprocal control of translation and transcription in autism spectrum disorder. *EMBO reports*, 22. https://doi.org/10.15252/embr.202052110.
2. Shinotoh, H., Hirano, S., & Shimada, H. (2020). PET Imaging of Acetylcholinesterase. PET and SPECT of Neurobiological Systems. https://doi.org/10.1007/978-3-030-53176-8_7.
3. Kamaruddin, M., Marzuki, I., Burhan, A., & Ahmad, R. (2020). Screening acetylcholinesterase inhibitors from marine-derived actinomycetes by simple chromatography. IOP Conference Series: Earth and Environmental Science, 679. https://doi.org/10.1088/1755-1315/679/1/012011.
4. Singh, A., Kukreti, R., Saso, L., & Kukreti, S. (2019). Oxidative Stress: A Key Modulator in Neurodegenerative Diseases. Molecules (Basel, Switzerland), 24(8), 1583. https://doi.org/10.3390/molecules24081583.
5. Small, G. A., Rana, S., & Aloi, M. (2023). Peripheral Nerve and Neuromuscular Disorders. Handbook of Emergency Neurology, 295. https://doi.org/10.1017/9781316338513.
6. Wong-Guerra, M., Jiménez-Martin, J., Pardo-Andreu, G. L., Fonseca-Fonseca, L. A., Souza, D. O., de Assis, A. M., ... & Nuñez-Figueredo, Y. (2017). Mitochondrial involvement in memory impairment induced by scopolamine in rats. Neurological research, 39(7), 649-659. https://doi.org/10.1017/9781316338513.
7. Vallés, A. S., & Barrantes, F. J. (2021). Dysregulation of neuronal nicotinic acetylcholine receptor–cholesterol crosstalk in autism spectrum disorder. Frontiers in Molecular Neuroscience, 14, 744597. https://doi.org/10.3389/fnmol.2021.744597.
8. Marucci, G., Buccioni, M., Dal Ben, D., Lambertucci, C., Volpini, R., & Amenta, F. (2021). Efficacy of acetylcholinesterase inhibitors in Alzheimer's disease. Neuropharmacology, 190, 108352. https://doi.org/10.1016/j.neuropharm.2020.108352.
9. Akıncıoğlu, H., & Gülçin, İ. (2020). Potent acetylcholinesterase inhibitors: potential drugs for Alzheimer's disease. Mini reviews in medicinal chemistry, 20(8), 703-715. https://doi.org/10.2174/1389557520666200103100521
10. Fronza, M. G., Alves, D., Praticò, D., & Savegnago, L. (2023). The neurobiology and therapeutic potential of multi-targeting β-secretase, glycogen synthase kinase 3β and acetylcholinesterase in Alzheimer's disease. Ageing research reviews, 102033. https://doi.org/10.1016/j.arr.2023.102033
11. Luo, X., Lauwers, M., Layer, P. G., & Wen, C. (2021). Non-neuronal role of acetylcholinesterase in bone development and degeneration. Frontiers in cell and developmental biology, 8, 620543. https://doi.org/10.3389/fcell.2020.620543

12. Sarailoo, M., Afshari, S., Asghariazar, V., Safarzadeh, E., & Dadkhah, M. (2022). Cognitive impairment and neurodegenerative diseases development associated with organophosphate pesticides exposure: a review study. Neurotoxicity Research, 40(5), 1624-1643. https://doi.org/10.1007/s12640-022-00552-0
13. Moss, D. E. (2020). Improving anti-neurodegenerative benefits of acetylcholinesterase inhibitors in Alzheimer's disease: are irreversible inhibitors the future?. International journal of molecular sciences, 21(10), 3438. https://doi.org/10.3390/ijms21103438.
14. S. Schneider, L. (2000). A critical review of cholinesterase inhibitors as a treatment modality in Alzheimer's disease. Dialogues in clinical neuroscience, 2(2), 111-128. https://doi.org/10.31887/DCNS.2000.2.2/lschneider
15. Singh, S., Tiwari, R. K., & Pandey, R. S. (2019). Acute toxicity evaluation of triazophos, deltamethrin and their combination on earthworm, Eudrilus eugeniae and its impact on AChE activity. Chemistry and ecology, 35(6), 563-575. https://doi.org/10.1080/02757540.2019.1600679
16. Assink Junior, E. J., de Jesus, P. C., & Borges, E. M. (2023). Whey Protein Analysis Using the Lowry Assay and 96-Well-Plate Digital Images Acquired Using Smartphones. Journal of Chemical Education, 100(6), 2329-2338. https://doi.org/10.1021/acs.jchemed.2c00830
17. Liu, S., Li, Z., Yu, B., Wang, S., Shen, Y., & Cong, H. (2020). Recent advances on protein separation and purification methods. Advances in Colloid and Interface Science, 284, 102254. https://doi.org/10.1016/j.cis.2020.102254
18. SALEH, S.S. AND SARHAT, E.R., 2019. Effects of ethanolic Moringa oleifera extract on melatonin, liver and kidney function tests in alloxan-induced diabetic rats. Indian Journal of Forensic Medicine & Toxicology, 13(4), pp.1015-1019. https://doi.org/10.5958/0973-9130.2019.00431.6.
19. Liu, S., Li, Z., Yu, B., Wang, S., Shen, Y., & Cong, H. (2020). Recent advances on protein separation and purification methods. Advances in Colloid and Interface Science, 284, 102254. https://doi.org/10.1016/j.cis.2020.102254
20. Bravo, R. K. D., Angelia, M. R. N., Uy, L. Y. C., Garcia, R. N., & Torio, M. A. O. (2022). Isolation, purification and characterization of the antibacterial, antihypertensive and antioxidative properties of the bioactive peptides in the purified and proteolyzed major storage protein of pigeon pea (Cajanus cajan) seeds. Food Chemistry: Molecular Sciences, 4, 100062. https://doi.org/10.1016/j.fochms.2021.100062
21. ALWAHAB, A., MOHAMMED, R., & ZAINAL, I. G. (2021). Measurement of Protein Oxidation Levels in Serum of Women with Pregnancy Complications. Egyptian Journal of Chemistry, 64(11), 6449-6455. 10.21608/ejchem.2021.72125.3685.
22. Yıldız, S., Bilen, Ç., & Karakuş, E. (2021). Purification and Characterization of Polyphenol Oxidase Enzyme from Damson Plum (Prunus insititia) by Spectrophotometrically. https://doi.org/10.21203/rs.3.rs-803684/v1
23. Pant, D. R., Aryal, B., Pun, D., Sharma, S., & Joshi, G. P. (2021). Inhibition of α-amylase and α-glucosidase activities in vitro by extracts of selected medicinal plants. Biodiversitas: Journal of Biological Diversity, 22(3). https://doi.org/10.13057/biodiv/d220314.
24. Kaur, D., Behl, T., Sehgal, A., Singh, S., Sharma, N., Chigurupati, S., ... & Bungau, S. (2021). Decrypting the potential role of α-lipoic acid in Alzheimer's disease. Life Sciences, 284, 119899. https://doi.org/10.1016/j.lfs.2021.119899.
25. Oki, S., Y. Toiyama, Y. Okugawa, T. Shimura, M. Okigami, H. Yasuda, H. Fujikawa, Y. Okita, S. Yoshiyama Et J. Hiro (2017). « Clinical burden of preoperative albumin- globulin ratio in esophageal cancer patients », The American Journal of Surgery, vol. 214, n° 5, p. 891-898. https://doi.org/10.1016/j.amjsurg.2017.04.007.
26. Suzuki, K., Sugihara, G., Ouchi, Y., Nakamura, K., Tsujii, M., Futatsubashi, M., ... & Mori, N. (2011). Reduced acetylcholinesterase activity in the fusiform gyrus in adults with autism spectrum disorders. Archives of general psychiatry, 68(3), 306-313. https://doi.org/10.1001/archgenpsychiatry.2011.4.
27. Kaya HB, Ozcan B, Ozdemir H. Purification of Acetylcholinesterase by 9-Amino-1,2,3,4-tetrahydroacridine from Human Erythrocytes. Appl Biochem Biotechnol. 2013;170:198-209. doi:10.1007/s12010-013-0177-3. https://doi.org/10.1007/s12010-013-0177-3
28. Bdaiwi LF, Al-Helaly LA, Saleh SS. Isolation of Acetylcholinesterase Enzyme from Cerebrospinal Fluid of Healthy and Hydrocephalus Disease Patients' Children in Mosul City. Rafidain J Sci. 2018;27(4):374-387. https://doi.org/doi:10.33899/rjs.2018.159372.
29. Webb G. Acetylcholinesterase: characterization of native and proteolytically derived forms and identification of structural protein components. Can J Biochem. 1978;56(12):1124-1132. doi:10.1139/o78-177. https://doi.org/10.1139/o78-177
30. Abubakar MU, Abubakar D. Characterization of Acetylcholinesterase from Various Sources: A Mini Re. J Environ Bioremediation Toxicol. 2021;4(1):24-30. doi:10.54987/jebat.v4i1.581. https://doi.org/10.54987/jebat.v4i1.581

31. Webb G. Molecular Properties of Acetylcholinesterase. University of British Columbia; 1978. Accessed May 20, 2024. https://doi.org/10.14288/1.0059491
32. Jana, S., Nasreen, T., & Singh, S. K. (2023). Discovery of reversible selective monoamine oxidase B inhibitors with anti-acetylcholinesterase activity derived from 4-oxo-N-4-diphenyl butanamides. Future Medicinal Chemistry, 15(2), 189-210. https://doi.org/10.4155/fmc-2022-0169
33. Mudgal, R., Sharma, S., Singh, S., & Ravichandiran, V. (2023). The neuroprotective effect of ascorbic acid against imidacloprid-induced neurotoxicity and the role of HO-1 in mice. Frontiers in Neurology, 14, 1130575. https://doi.org/10.3389/fneur.2023.1130575
34. Boumezzourh, A., Ouknin, M., Merzouki, M., Dabbous-Wach, A., Hammouti, B., Umoren, P. S., ... & Majidi, L. (2023). Acetylcholinesterase, tyrosinase, α-Glucosidase inhibition by Ammodaucus leucotrichus Coss. & Dur. fruits essential oil and ethanolic extract and molecular docking analysis. Moroccan Journal of Chemistry, 11(04), 11-4. https://doi.org/10.48317/IMIST.PRSM/morjchem-v11i04.43316
35. Coşar, E. D., Dincel, E. D., Demiray, S., Sucularlı, E., Tüccaroğlu, E., Özsoy, N., & Ulusoy-Güzeldemirci, N. (2022). Anticholinesterase activities of novel indole-based hydrazide-hydrazone derivatives: design, synthesis, biological evaluation, molecular docking study and in silico ADME prediction. Journal of Molecular Structure, 1247, 131398. https://doi.org/10.1016/j.molstruc.2021.131398
36. Foschiera, L. N., Schmitz, F., & Wyse, A. T. (2022). Evidence of methylphenidate effect on mitochondria, redox homeostasis, and inflammatory aspects: Insights from animal studies. Progress in Neuro-Psychopharmacology and Biological Psychiatry, 116, 110518. https://doi.org/10.1016/j.pnpbp.2022.110518
37. Samad, N., Rao, T., Rehman, M. H. U., Bhatti, S. A., & Imran, I. (2021). Inhibitory effects of selenium on arsenic-induced anxiety-/depression-like behavior and memory impairment. Biological Trace Element Research, 1-10. https://doi.org/10.1007/s12011-021-02679-1
38. Meejuru, G. F., Somavarapu, A., Danduga, R. C. S. R., Nissankara Roa, L. S., & Kola, P. K. (2021). Protective effects of duloxetine against chronic immobilisation stress-induced anxiety, depression, cognitive impairment and neurodegeneration in mice. Journal of Pharmacy and Pharmacology, 73(4), 522-534. https://doi.org/10.1093/jpp/rgaa003
39. Nadeem, M. S., Khan, J. A., & Rashid, U. (2021). Fluoxetine and sertraline based multitarget inhibitors of cholinesterases and monoamine oxidase-A/B for the treatment of Alzheimer's disease: Synthesis, pharmacology and molecular modeling studies. International Journal of Biological Macromolecules, 193, 19-26. https://doi.org/10.1016/j.ijbiomac.2021.10.102
40. Zueva, I., Lushchekina, S., Shulnikova, P., Lenina, O., Petrov, K., Molochkina, E., & Masson, P. (2021). α-tocopherol, a slow-binding inhibitor of acetylcholinesterase. Chemico-Biological Interactions, 348, 109646. https://doi.org/10.1016/j.cbi.2021.109646
41. Ahmad, M. (2020). Donepezil: A review of the recent structural modifications and their impact on anti-Alzheimer activity. Brazilian Journal of Pharmaceutical Sciences, 56, e18325. https://doi.org/10.1590/s2175-97902019000418325

Extraction of Invertase From Baker's Yeast Utilizing PEG8000 With Potassium Phosphate and Potassium Citrate in Aqueous Two-Phase Systems

Meaad H. Kadhim [a] and Khalid W. Hameed [b]

Biochemical Engineering Department, University of Baghdad, Al-Khwarizmi College of Engineering, Baghdad, Iraq

[a] *Corresponding author: miad.abadi2205@kecbu.uobaghdad.edu.iq.*
[b] *kwhameed@kecbu.uobaghdad.edu.iq.*

Abstract. An aqueous two-phase system (ATPS) extraction method that uses liquid-liquid is a potent technique for extracting and isolating mixtures of biomolecules. In this study, due to the capacity of invertase to convert sucrose into simpler sugars, it is frequently utilized in the food field, was extract from Baker's yeast. The specific activity of the crude extract was found to be 21.64 U/mg. Two ATPS systems were utilized: first, polyethylene glycol 8000/ Potassium Phosphate (PEG8000/PPH), and second, polyethylene glycol 8000/ potassium citrate (PEG8000/PC). The behavior of the recovery percentage (%Rec) and partition coefficient (K_E) of the invertase enzyme in ATPS was studied during the research. The influence of four parameters was studied: temperature, concentration of PEG8000, concentration of potassium phosphate or potassium citrate and pH. In both systems, the maximum %Rec and K_E were for the first system 96.07% and 24.44 at 30°C, PEG8000 concentration 2.1 g/10 ml, Potassium Phosphate concentration 1.8 g/10 ml and pH 9, whereas, for the second system were 98.73% and 77.74 at 20°C, PEG8000 concentration 2.4 g/10 mL, concentration of potassium citrate 1.8 g/10 ml, and pH 10. In this study no supporting agent was added such as NaCl or $MgSO_4$ a high extraction rate was got without it.

Keywords: *Aqueous two-phase extraction, invertase, fermented source, polymer/salt, partitioning.*

INTRODUCTION

Invertase, which is also referred to as β-fructofuranosidase (E.C. 3.2.1.26), is an enzyme that breaks down sucrose into glucose and fructose in equal amounts, resulting in a substance called invert sugar. Fructose is preferred over sucrose because it is sweeter and doesn't crystallize as quickly [1, 2]. This is why invertase is mostly used in the food industry, in things like candy, condensed milk, syrups, meals for kids, and drinks. This enzyme is also used to make fake honey and plasticizing agents that are used in the paper, makeup, and drug industries. It is also used in the scientific field to make sugar biosensors [1-6]. As a result, there is a continuous quest for both highly efficient manufacturers of invertase and enhanced cost-effective techniques for enzyme synthesis. The invertase existence in many yeasts, including *Saccharomyces cerevisiae*, *Candida utilis*, *Pichia anomola* and a few *fungus*, mostly *Aspergillus niger* and *Neurospora sp.* [7-11]. A lot of plants, like potato, carrot, tomato, tobacco, sugar cane, and bamboo, also make a lot of invertases [12-15]. There are several isoforms of plant invertases, each with unique subcellular localization and metabolic characteristics [16-20]. The ideal pH range for acid invertases is typically 3.5–5.0, whereas the ideal pH range for alkaline invertases is 7.0–8.0 [21-25]. In this research, we tried to isolate invertase from baker's yeast (*S. cerevisiae*). Several researchers have devised methods for isolating and purifying invertase [26-29]. However, almost all of these invertase methods involve more than one step, such as gel filtration, ion-exchange chromatography, ultrafiltration, and others. It is well known that the more steps there are, the more product output is lost [30-33]. Additionally, the expansion of these methodologies is both costly and challenging. It is worth noting that the purification stages account for 50–90% of the production cost [34, 35]. Therefore, there is a requirement for large-scale bioseparation methods that are both efficient and cost-effective, yield while keeping the biological activity of the compounds. Aqueous two-phase system (ATPS) is one such purification procedure that satisfies all of these criteria. In comparison to current methods, this technique provides benefits such as ease of scaling up, the ability to run constantly, and a shortening of the time needed to separate, isolate, and purify certain macromolecules, like proteins and enzymes, especially in the beginning stages of processing [36-40]. The Aqueous Two-Phase System (ATPS) was serendipitously discovered. By Martinus Willem Beijerinck in 1896, however, it

Technologies and Materials for Renewable Energy, Environment and Sustainability
AIP Conf. Proc. 3321, 030016-1–030016-10; https://doi.org/10.1063/5.0289633
Published under an exclusive license by AIP Publishing. 978-0-7354-5231-2/$30.00

wasn't actually used till the 1970s [41, 42]. In recent years, ATPS systems have been developed and extensively researched. It is composed of several kinds of chemicals, such as systems of polymer-polymer and polymer-salt such as PEG-dextran, and PEG-dipotassium phosphate (K_2HPO_4)/ Potassium citrate ($C_6H_5K_3O_7$) that can be combined, and it serves a number of functions [43, 44]. Still, there are two-phase systems that are made up of ionic liquids and short-chain alcohols [45, 46]. This process is superior to alternative extraction methods because of its affordability, environmental friendliness, and versatility in extracting a wide range of compounds [47, 48]. Water aids in the stabilization and separation of biomolecules' structure in the two phases of ATPS [49, 50], whereas additional liquid-liquid extraction (LLE) methods can harm biological products since the organic solvents and process conditions are frequently severe [51]. Researchers have examined several forms of ATPS to analyze and comprehend their capacity to segregate, remove, and refine biomolecules and particles [52]. Although salt ATPS offer numerous advantages, there is a limited comprehension of the partitioning of biomolecules in these systems, making it challenging to anticipate their behavior. To obtain two phases, the concentration of polymer/salt must be higher than the critical concentration, below which two phases cannot be attained [53]. The amount of a certain chemical, like phosphate, and the surface features of the biomolecules being targeted, like proteins, are both very important in figuring out how biomolecules act in a system [54, 55]. In addition, the way proteins interact with system factors like pH and temperature is also very important [56, 57]. The aim of the present work is to find the optimal operating conditions for the extraction of invertase enzyme from Baker's Yeast by ATPS and using the Taguchi method as an experimental design. The parameters that were studied on the effect of the extraction of invertase from Baker's Yeast are: temperature (10–40 ^oC), pH (7–10), concentrations of potassium phosphate, potassium citrate, and PEG4000 (1.5–2.4 g/10 ml).

Materials and methods

Materials

Sucrose, Peptone, polyethylene glycol (PEG8000), 3, 5-Dinitrisalicylic acid (DNS), NaOH, $FeSO_4$, $ZnSO_4$, Folin-reagent, serum albumin from cows (BSA) were purchased from HIMEDIA Laboratories Pvt. Ltd., India. Cupric sulfate ($CuSO_4$), Sodium Potassium tartrate ($C_4H_4O_6KNa{\cdot}4H_2O$), sodium carbonate (Na_2CO_3), Potassium Phosphate (K_2HPO_4), Potassium Citrate ($C_6H_5K_3O_7$) were purchased from Central Drug House Ltd., India, Yeast Extract was purchased from BDH (BDH, England), Baker's yeast (*Saccharomyces cerevisiae*) was obtained from local market/Baghdad/Iraq. This study used water that had been deionized and double-distilled. It came from the biochemical engineering department's lab.

Methodolody

Yeast Activation and production conditions

The yeast is activated by dissolved 1.5g in 100 ml of Yeast extract broth media and incubated in a rotary shaking incubator at 30^oC for 24hr at 150 rpm. After yeast activation, 5ml of the yeast culture was transferred to the individual 250 ml of production media containing (Sucrose 30g/L, Peptone 1g, K_2HPO_4 1g/l, MgSO4 0.3g/l, FeSO4 0.3g/1, $ZnSO_4$ 0.3g/1, Yeast Extract 5g/1), pH adjusted to 5. The medium incubated in a rotary shaking incubator at 30^oC for 72hr (The agitation rate was kept at 150 rpm). After 72hrs, the production broth culture was filtrate by using cooling centrifuge at 6000 rpm and 4°C for 10min to obtain supernatant, this supernatant used as Invertase crude [33].

Aqueous Two Phase Partitioning

First system: the stock solutions of dipotassium phosphate (1.5–2.4 g) per 10 ml of crude extract and (1.5–2.4 g), PEG8000 per 10 ml of distilled water. Second system:

The stock solutions of Potassium Citrate (1.5–2.4 g) per 10 ml of distilled water and (1.5–2.4 g) of PEG8000 per 10 ml of crude extract are prepared previously. From the experimental study, it was found that mixing of dipotassium phosphate with the crude extract and PEG8000 with distilled water for the first system gave a greater recovery percentage than if we mixed them vice versa, while for the second system, the mixing of PEG8000 with crude extract gave more recovery. It is mixed 5 ml of dipotassium phosphate or potassium citrate solution with 5 ml of PEG8000 solution using vortex for 2 min. To obtain the two phases, the mixture can be left for 2–3 hours under

gravity force, but to exceed the process, the mixture is separated into two phases using centrifugation at 6000 rpm for 10 min. The top phase is the PEG8000 solution, while the bottom phase is the salt solution. After the extraction and at equilibrium, the phase that loses the enzyme is called the raffinate phase (R_f), while the phase that gains the enzyme is called the extract phase (Ex). On the basis of earlier studies, the system parameters were chosen [34, 35, 36, 37]. The top phase was precisely isolated from the bottom phase using a Pasteur pipette. Parts of the stages were looked at to measure the amount of protein and enzymes present. Formulas from previous research were used to figure out the partition factors, including the specific activity, partition coefficient, and return percentage [35, 38]. The enzyme activity (K_E) or protein content (K_P) is the definition of the invertase partition coefficient in aqueous two-phase systems. When everything is equal, as shown in Equations (1) or (2) and (3), this coefficient tells us the ratio of the amount of enzyme in the extract phase to the amount in the raffinate phase [38].

$$\mathrm{K_p} = \frac{\mathrm{C_{Ex}}}{\mathrm{C_{Rf}}} \tag{1}$$

$$\mathrm{K_E} = \frac{\mathrm{A_{Ex}}}{\mathrm{A_{Rf}}} \tag{2}$$

$$\text{or } \mathrm{K_E} = \frac{\%\mathrm{Rec}}{1-\%\mathrm{Rec}} \tag{3}$$

where CEx and CRf are the total protein concentrations in mg/mL of the extract and raffinate phases respectively, AEx and ARf are the enzyme activities in U/mL of the extract and raffinate phases, respectively.

In order to judge the efficiency of the cleansing procedure, it is essential to quantify the effectiveness of the catalyst, particularly known as the enzyme's specific activity (SA, shown in units per milligram of protein), recovery % and partition coefficient of enzyme (KE) additionally; the calculations were performed based on the provided equations [39].

$$\text{Invertase activity (U/ml)} = \frac{\mathrm{A\ x\ V}}{€\ \mathrm{x\ t\ x\ v}} \tag{4}$$

where: A: absorbency at 540 nm, V: Total volume of reaction mixture in (2 ml), €: Enzyme constant (0.01), t: incubation time (30 min), and v: volume of crude used in (0.2 ml)

$$\mathrm{SA} = \frac{\text{Invertase activity}}{\mathrm{C_{Rf}}} \tag{5}$$

$$Recovery\ (\%) = \left(1 - \frac{A_{Rf}}{A_{in}}\right) \times 100 \tag{6}$$

where $\mathrm{A_{in}}$ is the initial activity of enzyme in U/mL.

Invertase activity assessment

The Miller method, which was first outlined in 1959, was used to measure invertase activity. The test mixture was 0.8 ml of substrate (50 mM sucrose in 50 mM pH 4.5 buffer citrate) and 0.2 ml of enzyme that had been diluted properly. For 30 minutes, the mixture was kept at 37°C. Adding 1 ml of DNS (3, 5-dinitrosalicylic acid) solution and heating it in a hot water bath for 5 minutes stopped the process. After putting the solution in an ice bath to cool it down to room temperature, spectrophotometry at 540 nm was used to find out how many reducing sugars were present [38]. One unit of invertase activity is the amount of enzyme that can change one mole of sucrose into glucose in one minute at 37°C and a pH of 4.5. The exact activity is found by counting how many units are present per milligram of protein when sugar is used as a substrate.

Determining Concentration of protein

The protein concentration was determined using the Lowry method [40], which involved the use of specific solutions for protein measurement.

Solution (1): 2% Sodium carbonate: To make it, 10 grams of Na_2CO_3 were mixed with 500 milliliters of a 0.1-molecular-solution of NaOH. Solution (2): 2% Sodium Potassium tartrate was prepared by dissolving 2 g of sodium potassium tartrate in a small volume of distilled water, then distilled water should be added to achieve a volume of 100 ml. Solution (3): One gram of CuSO4 was mixed with one hundred milliliters of pure water to make 1% CuSO4. Solution (4): was prepared immediately via mixing 98 ml of solution (l) with 1 ml of solution (2) and l ml of solution (3). Solution (5): Bovine Serum Albumin (BSA) was made by slowly soaking 0.01 g of BSA in distilled water and then adding more distilled water to make the amount 100 ml. Solution (6): Folin-reagent was prepared by diluting 1 ml of Folin in 2 ml of distilled water (1:2 v/v).

The protein concentration was measured by the Lowry method, as described via Lowry et al. in 1951. The previously produced solutions were utilized, and the protein was determined as follows: The necessary dilution was made from the initial concentration of BSA, which was 0.10 mg/ml. Each tube was supplemented with 4.0 ml of solution 4 and subsequently allowed to incubate for a duration of 10 minutes. 0.4 millilitres of folin reagent (solution 6) was added to each tube, vigorously mixed, and then allowed to sit for 30 minutes. The absorbance was measured at a wavelength of 600 nm, with tube number 1 serving as the reference. Fig. 1 depicts the standard curve of BSA utilizing the Lowry method.

RESULTS AND DISCUSSION

Minitab 17.0 software was used to design the number of experiments using Taguchi method, where each parameter has four levels. The study initially focuses on examining the effect of four factors: temperature, pH, PEG8000 concentration, and K_2HPO_4 (PPH) or $C_6H_5K_3O_7$ (PC) concentration. Once the ideal conditions that produce the highest extraction rate are determined, neutral salts (NaCl or MgSO4) will be introduced as supporting agent to improve the result if the extraction rate is low. In this study, no supporting agent was added because a high extraction rate was obtained. It is used equal volumes of the extracting solvent and feed. The number of tests done with System 1's (PEG8000/K_2HPO_4) settings is shown in Tables 1 and 2. and System 2 (PEG8000/$C_6H_5K_3O_7$), respectively, and the results of %Rec and partition coefficient K_E.

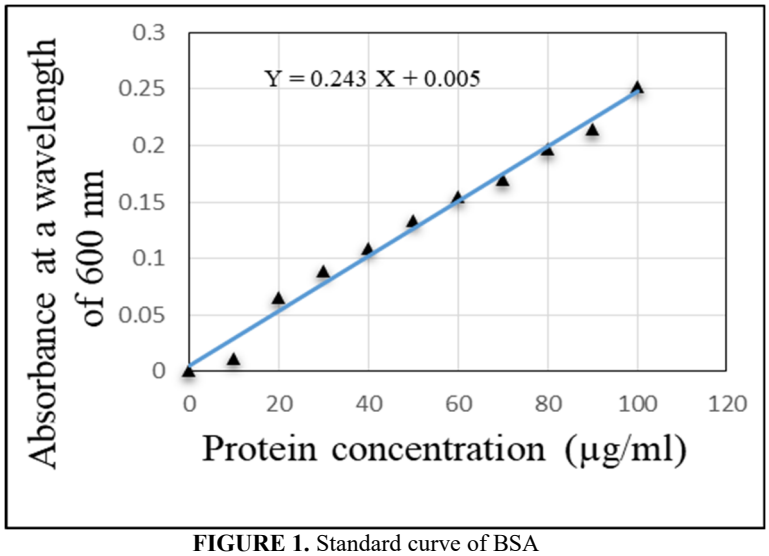

FIGURE 1. Standard curve of BSA

TABLE 1. Tests were done on system-1 (PEG8000/K2HPO4) using the Taguchi method and the percentage of recovery (%Rec) and partition coefficient (KE) that were found

Run No.	Temp °C	pH	K_2HPO_4 (PPH) g/10 ml	PEG 4000 g/10 ml	% Rec	K_E
1	10	7	1.5	1.5	90.63	9.67
2	10	8	1.8	1.8	91.26	10.44
3	10	9	2.1	2.1	92.7	12.69
4	10	10	2.4	2.4	91.5	10.76
5	20	7	1.8	2.1	94.03	15.75
6	20	8	1.5	2.4	94.53	17.28
7	20	9	2.4	1.5	94.26	16.42
8	20	10	2.1	1.8	94.73	17.97

9	30	7	2.1	2.4	93.7	14.87
10	30	8	2.4	2.1	95.36	20.55
11	30	9	1.5	1.8	94.3	16.54
12	30	10	1.8	1.5	94.6	17.51
13	40	7	2.4	1.8	91.83	11.23
14	40	8	2.1	1.5	92.73	12.75
15	40	9	1.8	2.4	95.3	20.27
16	40	10	1.5	2.1	94.43	16.95

TABLE 2. The number of tests of system-2 (PEG8000/ $C_6H_5K_3O_7$) according to Taguchi method with their findings of Recovery percent (%Rec) and partition coefficient (K_E)

Run No.	Temp ^oC	pH	$Na_3C_6H_5O_7$ (PPH) g/10 ml	PEG 4000 g/10 ml	% Rec	K_E
1	10	7	1.5	1.5	95.36	20.55
2	10	8	1.8	1.8	96.86	30.84
3	10	9	2.1	2.1	97.13	33.84
4	10	10	2.4	2.4	97.9	46.61
5	20	7	1.8	2.1	98.1	51.63
6	20	8	1.5	2.4	96.7	29.3
7	20	9	2.4	1.5	98.3	57.82
8	20	10	2.1	1.8	97.43	37.91
9	30	7	2.1	2.4	98.46	63.93
10	30	8	2.4	2.1	96.3	26.02
11	30	9	1.5	1.8	97.03	32.67
12	30	10	1.8	1.5	97.5	39
13	40	7	2.4	1.8	96.5	27.57
14	40	8	2.1	1.5	97	32.33
15	40	9	1.8	2.4	97.63	41.19
16	40	10	1.5	2.1	97.86	45.72

Temperature Effect

Fig. 2 and 4a of System-1 show that the percentage recovery (%Rec) increases as the temperature increases. Specifically, at temperatures ranging from 10 to 30 degrees Celsius, the enzyme recovery and K_E (partition coefficient) increase from 91.5% to 94.5% and from 10.76 to 17.18, respectively. There is a slight decrease in %Rec from 94.5 – 93.6% in the temperature range 30 – 40^{o}C. In Fig. 3 and 4b of System-2, both the %Rec and K_E of the enzyme increase from 96.8 – 97.65% and 30.25 – 41.6 respectively in the temperature range 10 – 20^{o}C, then start reduced slightly after temperature of 20^{o}C. The effect of temperature on the behaviour of a liquid mixture is complex because of the interaction between its individual components, including electrostatic and hydrophobic forces. Various temperature-activity and temperature-stability patterns of invertase have been seen. These depend on things like where the enzyme came from, how long it was incubated, the temperature, and the medium that was utilized [41]. The optimum temperature for maximum activity of invertase obtained from different sources of plant is typically 37 ^{o}C [42, 43, 44]. Karkaş and Önal, 2012 demonstrated that yeast exogenous invertase exhibited its highest level of activity at an ideal temperature of 60 °C. Most of the time, invertase enzymes from different types of microbes have very high activity between 50 and 90 °C [41, 45]. In this research, it is examined the temperature range of 10 to 40 degrees Celsius for the salts potassium phosphate and potassium citrate, in combination with polyethylene glycol having a molecular weight of 8000. It is discovered that the optimal temperature for maximum activity was observed at 30 and 20 degrees Celsius for the system-1 and system-2 respectively. Furthermore, It was noted that increasing the temperature further had no significant effect on activity.

pH Effect

In several industrial applications, pH stability is another important consideration when selecting enzymes as biocatalysts, where the pH range of the medium is taken from 7.0 to 10.0 for system-1 and system-2 at room temperature. Bioproduct can be divided into two phases based on the surface characteristics and charges that each one possesses. The pH of the watery fluid can change this. Protein molecules with a positive net charge try to pull electrons from other proteins, which makes an electric push. However, if the pH is higher than the pI (which stands for "pH-indicator" or "Potential Isoelectric point"), the electric force is weaker and the proteins will have a net

negative charge. If it is lower than the pI, it will become positive, and if they are equal, there will be no net charge [46]. In Fig. 2 and 4a of system-1, when the pH change from 7 to 9, the partition coefficient increases and then recovery percent (%Rec), indicating that additional enzymes will be recovered for the PEG/PPH system. In pH range of (7 – 9) the %Rec increases from 92.5 – 94.2%, after pH 9, the %Rec reduced to 93.8%. These results are agreed with [47, 48, 49, 50]. For the PEG/PC of system-2, Fig. 3 and 5a show the effect of pH on the %Rec and then K_E. In pH range of (7 – 8), the %Rec decreases from 97.1 – 96.7%, after pH 8, the %Rec improved to 97.7%. The studies of Akardere et al., 2010 noted a decrease in the partition coefficient as the pH increased [51]. Rao and Nair, 2011; Pirdashti et al, 2021; Kee et al, 2021, they mentioned in their studies, the appearance of the two phases disappears as the pH increases above 10.0. [49, 50, 52].

Concentration Effect of salt

Another major factor affecting enzyme partitioning in two-phase systems is the concentration of salt used. Through experiments, it was found that the amount of dipotassium phosphate and potassium citrate in the solution has an effect on the amount of enzyme extracted in ATPS and how well it is broken down. Based on the work of Baskaran et al. (2018) and Pirdashti et al. (2021), they discovered that when the salt content goes up, the recovery percentage and partition coefficient go up too [50, 53]. When examining Fig. 2 and 4b of system-1, it is clear that the recovery percentage little increases (93.5% to 93.8%) when K_2HPO_4 (PPH) salt is added between the ranges of 1.5 – 1.8 g/10 ml, this enhances the extraction process and increases the concentration of the solution, and thus the partition coefficient increases. as the amount of PPH salt went from 1.8 g/10 ml to 2.4 g/10 ml, the recovery rate of enzyme reduced from 93.8 – 93.2%. This mean the PPH salt concentration has little effect on the recovery of enzyme. For the PEG8000/$C_6H_5K_3O_7$ (system-2), it was observed that the recovery rate rose from 96.7% to 97.5% and the partition coefficient improved from 29.3 to 42.47 when the $C_6H_5K_3O_7$ (PC) concentration increased from 1.5 g/10 ml to 2.1 g/10 ml, as shown in Fig. 3 and 5b. Additionally, there was a modest decline observed of the %Rec with a value of 97.25%, when the salt content increased to 2.4 g/10 ml.

Concentration Effect of PEG

The influence of PEG8000 concentration on phase formation was further examined, revealing that the concentration of PEG8000 has a substantial effect on the rate and uniformity of invertase enzyme partitioning. This, in turn, influences the amount of recoverable invertase. The impact of the concentration of polyethylene glycol (PEG) on the systems PEG8000/K_2HPO_4 and PEG8000/$C_6H_5K_3O_7$ is described in Fig. 2 and 4b plus 3 and 5b, respectively. In the range of 1.5 – 1.8 g/10 ml of PEG8000 concentration of system-1, there is very slightly negative effect on the %Rec, in range of 1.8 – 2.1 g/10 ml of PEG8000 concentration, the percentage of invertase enzyme recovered increased from 93% to 94.4% then a slight decrease occurs to become 93.7% at 2.4 g/10 ml. This is in agreement the results that Shad et al. (2018) found, which is that the amount of enzyme restored drops when there is a lot of PEG because proteins move from the lower phase to the upper phase in ATPS, as a result, the partition coefficient increases automatically [54].

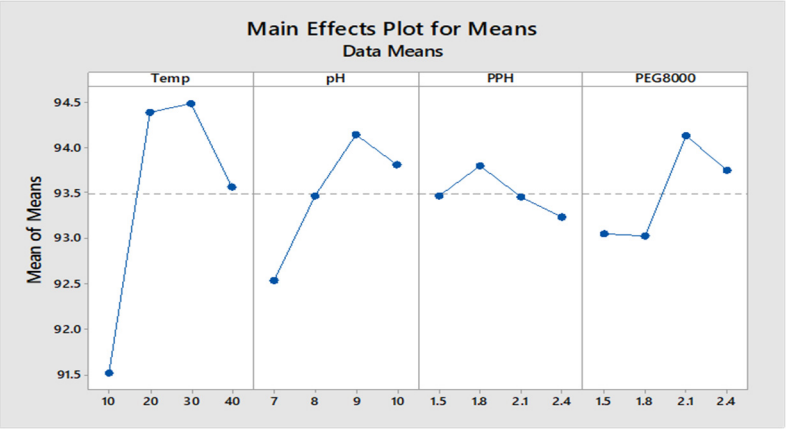

FIGURE 2. Effect of the parameters (temperature, pH, concentrations of PEG8000 and dipotassium phosphate) on the recovery% and then on K_E of the system-1 without adding the supporting agents

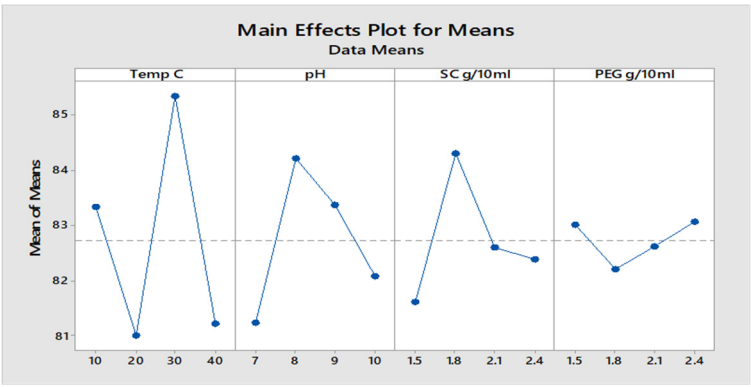

FIFURE 3. Effect of the parameters (temperature, pH, concentrations of PEG8000 and potassium citrate) on the recovery% and then on K_E of the system-2 without adding the supporting agents

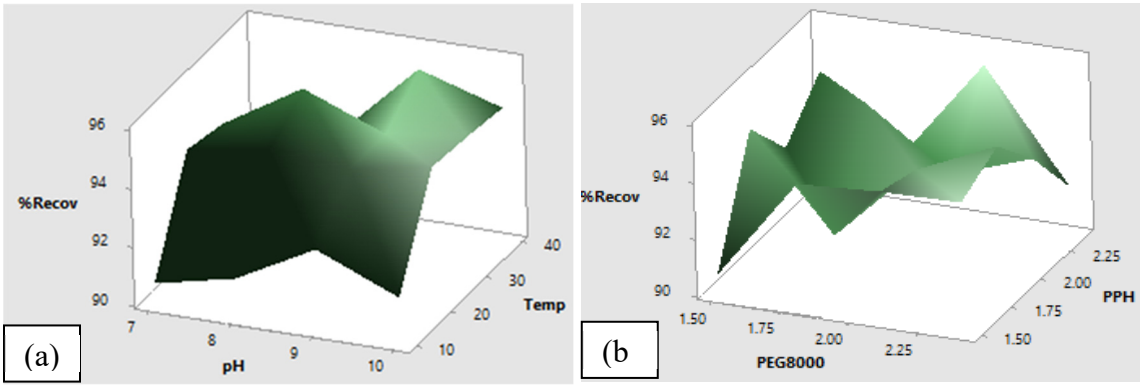

FIGURE 4. (a) Recovery percent of system-1 as a function of temperature and pH and (b) Recovery percent of system-1 as a function of concentration of K2HPO4 and PEG8000

For system-2 (PEG8000/$C_6H_5K_3O_7$), the %Rec reduced slightly when the concentration of PEG (1.5 – 1.8 g/10 ml), then increased from 96.9 – 97.7% at (1.8 – 2.4 g/10 ml) of PEG. This finding is consistent with Fravash et al., 2007; Antelo et al., 2015 when they determined that the concentration of PEG had a favorable impact on %Rec and K_E, which increased in response to the increase in PEG [48, 55].

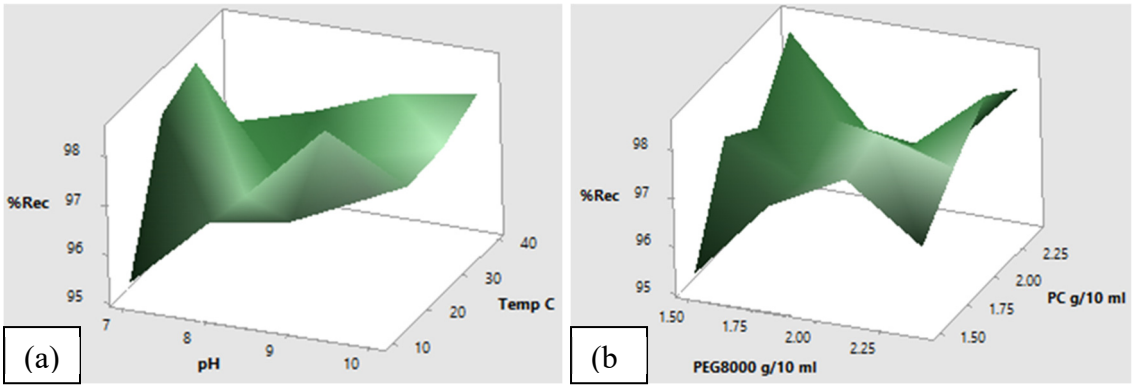

FIGURE 5. (a) Recovery percent of system-2 as a function of temperature and pH and (b) Recovery percent of system-2 as a function of concentration of C6H5K3O7 and PEG8000

Statistical Analysis

After conducting the statistical analysis, using statistica v.12, the equations (7) and (8) were obtained that describe the recovery rate as a function of four parameters of the first and second systems respectively:

Rec (%)= 42.4 + 24.8×X1 – 86.9×X2 + 2905×X3 – 2624.2×X4 + 0.05×X1×X2 +0.07×X1×X3 + 0.01×X1×X4 - 175.7×X2×X3 + 196.3×X2×X4 – 67×X3×X4 – 0.58×X12 + 2.7×X22 – 328.7×X32 + 291.8×X42 (7)

The correction factor, R2 = 99.0%

Rec (%)= 54.51 + 27.62×X1 - 98.75×X2 + 3167×X3 – 2911.5×X4 -0.02×X1×X2 -0.28×X1×X3 + 0.04×X1×X4 -191.4×X2×X3 + 212.2×X2×X4 – 73×X3×X4 – 0.62×X12 + 3.42×X22 – 356.6×X32 + 320.1×X42 (8)

The correction factor, R2 = 99.96%.

where X1 is the temperature, oC, X2 is the pH, X3 is the concentration of K2HPO4 or C6H5K3O7 salt, g/10 ml, and X4 is the PEG8000 concentration, g/10 ml.

CONCLUSION

In this study, the extraction of invertase enzyme from Baker's yeast using aqueous two-phase system was effective and efficient. There is different behavior of %Rec and then K_E with parameters of the system-1 (PEG8000/K_2HPO_4) and system-2 (PEG8000/$C_6H_5K_3O_7$). The distribution pattern of invertase in PEG8000/K_2HPO_4 demonstrated that it is possible to extract the enzyme into the salt-concentrated bottom phase, but in PEG8000/$C_6H_5K_3O_7$, the enzyme was extracted into the upper phase rich in polymers. 96.0% was the highest %Rec and 24 was the highest partition coefficient for system-1 at optimum operating condition of a temperature 30 °C, pH 9, K_2HPO_4 concentration 1.8 g/10 ml, and PEG8000 concentration 2.1 g/10 ml, whereas for the system-2 were 97.7% and 42.5 respectively at optimum operating condition of a temperature 20°C, pH 10, K_2HPO_4 concentration 1.8 g/10 ml, and PEG8000 concentration 2.4 g/10 ml. From the above obtaining results, it can be say there is no need to adding supporting agents such as NaCl, KCl, or $MgSO_4$, no need to extraction by another stages or using volume of extracting solvent greater than the feed.

REFERENCES

1. J. Arnau, D Yaver, CM Hjort, "Strategies and challenges for the development of industrial enzymes using fungal cell factories", Grand Challenges Fungal Biotechnol, 179–210, 2019.R. D. Batista et al., "Optimization of β-fructofuranosidase production from agrowaste by Aspergillus carbonarius and its application in the production of inverted sugar", Food Technol. Biotechnol. 59(3), 306–313, 2021.
2. S. M. Kotwal, V. Shankar, "Immobilized invertase", Biotechnol Adv; 27:311–22, 2009.
3. C. Aranda A. Robledo, O. Loera, J. C. Contreras-Esquivel, R. Rodríguez, C. N. Aguilar, "Fungal invertase expression in solid-state fermentation", Food Technology & Biotechnology, 44(2), 2006.
4. Andjelković, U., Pićurić, S., & Vujčić, Z. "Purification and characterisation of Saccharomyces cerevisiae external invertase isoforms", Food Chemistry, 120(3), 799-804, 2010.
5. H. Manoochehri, N.F. Hosseini, M. Saidijam, M. Taheri, H. Rezaee, and F. Nouri, "A review on invertase: Its potentials and applications" Biocatalysis and Agricultural Biotechnology, 25, p.101599, 2020.
6. H. S. Lee and A. Sturm, Purification and characterization of neutral and alkaline invertase from carrot. Plant Physiology, 112(4), 1513-1522, 1996.
7. C. C. Liu, L. C. Huang, C. T. Chang, & H. Y. Sung, "Purification and characterization of soluble invertases from suspension-cultured bamboo (Bambusa edulis) cells" Food chemistry, 96(4), 621-631, 2006.
8. M. C. Madhusudhan, & K. S. M. S. Raghavarao, "Aqueous two phase extraction of invertase from baker's yeast: Effect of process parameters on partitioning", Process biochemistry, 46(10), 2014-2020.
9. A. Sturm, "Invertases. Primary structures, functions, and roles in plant development and sucrose partitioning", Plant physiology, 121(1), 1-8, 1999.
10. M. Nakamura, M. Hagimori, & T. Matsumoto, "Purification and characterization of acid invertase from cultured tobacco cells" Agricultural and biological chemistry, 52(12), 3157-3158, 1988.
11. A. C. Santana de Almeida, L. Costa de Araújo, A. Mendes Costa, C. A. Moraes de Abreu, M. A. Gomes de Andrade Lima, & M. D. L. A. Perez Fernandez Palha, "Sucrose hydrolysis catalyzed by auto-immobilized invertase into intact cells of Cladosporium cladosporioides" Electronic Journal of Biotechnology, 8(1), 54-62, 2005.
12. A. Basu, P. Chaudhuri, D. Malakar, & A. K. Ghosh, Co-purification of glucanase with acid trehalase–invertase aggregate in Saccharomyces cerevisiae. Biotechnology letters, 30, 299-304, 2008.
13. B. A. Shoushtari, G. Pazuki, J. R. Shahrouzi, S. Shahriari, & N. Hadidi, "Separation of erythromycin using aqueous two-phase system based on acetonitrile and carbohydrates" Fluid Phase Equilibria, 505, 112360, 2020.

14. Z.M., Jaffer, K.W. Hameed, and S.G. Imran, 2021, February. "Extraction of prodigiosin using aqueous two phase system". In IOP Conference Series: Materials Science and Engineering (Vol. 1076, No. 1, p. 012026). IOP Publishing.
15. M. C. Madhusudhan, & K. S. M. S. Raghavarao, "Aqueous two phase extraction of invertase from baker's yeast: Effect of process parameters on partitioning", Process biochemistry, 46(10), pp 2014-2020, 2011.
16. P. A. Albertsson, "Partition of cell particles and macromolecules"., 3rd ed. Wiley, New York. 1959.
17. A. L., Grilo, M. Raquel Aires-Barros, & A. M. Azevedo, "Partitioning in aqueous two-phase systems: fundamentals, applications and trends", Separation & Purification Reviews, 45(1), 68-80, 2016.
18. R. Hatti-Kaul editor. "Aqueous two-phase systems: methods and protocols" Springer Science & Business Media; 2008 Feb 5.
19. H.A. Mahdi, K.W. Hameed, and A.J.A. Ali, "Application of Aqueous Two-Phase Systems in the Extraction of Bovine Serum Albumin", Journal of Polymer & Composites, 11(1), pp.55-65p, 2023.
20. J.V.D. Molino, D.D.A. Viana Marques, A.P. Júnior, P.G. Mazzola, and M.S.V. Gatti, "Different types of aqueous two-phase systems for biomolecule and bioparticle extraction and purification", Biotechnology Progress, 29(6), pp.1343-1353, 2013.
21. A. G. Teixeira, R. Agarwal, K. R. Ko, J. Grant-Burt, B. M. Leung, and J. P. Frampton, "Emerging biotechnology applications of aqueous two-phase systems" Advanced healthcare materials, 7(6), 1701036, 2018.
22. S. G. Mugaddas "The Influence of Different Molecular Weights of Polyethylene Glycol (Peg) to the Formation of the Aqueous Two-Phase System Peg-Natrium Salt of Citric Acid-Water" Journal of Baku Engineering University, 18, 2020.
23. H. Walter (Ed.) "Partitioning in aqueous two–phase system: theory, methods, uses, and applications to biotechnology". Elsevier, 2012.
24. R. Hatti-Kaul, "Aqueous two-phase systems: A general overview. Molecular biotechnology", 19, 269-277, 2001.
25. E. Espitia-Saloma, P. Vázquez-Villegas, O. Aguilar, & M. Rito-Palomares, "Continuous aqueous two-phase systems devices for the recovery of biological products", Food and Bioproducts Processing, 92(2), 101-112. (2014).
26. J. A. Asenjo, & B. A. Andrews, "Aqueous two-phase systems for protein separation: a perspective", Journal of Chromatography A, 1218(49), 8826-8835. 2011.
27. W.T. Mohammed, and A.S. Mahdi, "Liquid-Liquid Extraction of Metal Ions Using Aqueous Biphasic Systems", Journal of Engineering, 18(09), pp.989-998, 2012.
28. Y. Zhang, Y. Luo, J., Zhao, W. Zheng, J. Zhan, H. Zheng, and F. Luo, "Emerging delivery systems based on aqueous two-phase systems: A review" Acta Pharmaceutica Sinica B, 2023.
29. H.A. Mahdi, K.W. Hameed, and A.J.A., Ali, "Extraction of Bovine Serum Albumin by Aqueous Two-Phase System Using PEG4000/Sodium Citrate and PEG8000/Sodium Phosphate", Al-Khwarizmi Engineering Journal, 19(2), pp.39-51, 2023.
30. Y. K. Yau, C. W. Ooi, E. P. Ng, J. C. W. Lan, T. C., Ling & P. L. Show, "Current applications of different type of aqueous two-phase systems", Bioresources and Bioprocessing, 2, 1-13, 2015.
31. J. F. Pereira, M. G. Freire, & J. A. Coutinho, "Aqueous two-phase systems: Towards novel and more disruptive applications", Fluid Phase Equilibria, 505, 11234, 2020.
32. A.J.R. AL-Sa'ady, "Optimization of invertase production from Saccharomyces cerevisiae by solid state fermentation". Curr Res Microbiol Biotechnol, 2, pp.373-377, 2014.
33. S. Klomklao, S. Benjakul, W. Visessanguan, B. K. Simpson, & H. Kishimura, "Partitioning and recovery of proteinase from tuna spleen by aqueous two-phase systems", Process Biochemistry, 40(9), 3061-3067, 2005.
34. C. K. Su, & B. H. Chiang, "Partitioning and purification of lysozyme from chicken egg white using aqueous two-phase system", Process Biochemistry, 41(2), 257-263, 2006.
35. Z. Gu, & C. E. Glatz, "Aqueous two-phase extraction for protein recovery from corn extracts" Journal of Chromatography B, 845(1), 38-50, 2007.
36. D. F. Coelho, E. Silveira, A. Pessoa Junior, & E. B. Tambourgi, "Bromelain purification through unconventional aqueous two-phase system (PEG/ammonium sulphate)", Bioprocess and biosystems engineering, 36, 185-192, 2013.
37. T. Karkaş, & S. Önal, "Characteristics of invertase partitioned in poly (ethylene glycol)/magnesium sulfate aqueous two-phase system", Biochemical Engineering Journal, 60, 142-150, 2012.

38. N. Assoudi et al., "Comparative examination of the physical parameters of the sol gel produced compounds La0.5Ag0.1Ca0.4MnO3 and La0.6Ca0.3Ag0.1MnO3," Optical and Quantum Electronics, vol. 54, no. 9, Jul. 2022, doi: https://doi.org/10.1007/s11082-022-03927-x.
39. Y. Ghasemi, M. Mohkam, A. Ghasemian, and S. Rasoul-Amini,. Experimental design of medium optimization for invertase production by Pichia sp. Journal of Food Science and Technology, 51, pp.267-275, 2014.
40. O. H. Lowry, N. J., Rosebrough, A. L., Farr, & R. J. Randall, "Protein measurement with the Folin phenol reagent" J biol Chem, 193(1), 265-275, 1951.
41. W. Liebl, D. Brem, & A. Gotschlich, "Analysis of the gene for β-fructosidase (invertase, inulinase) of the hyperthermophilic bacterium Thermotoga maritima, and characterisation of the enzyme expressed in Escherichia coli" Applied Microbiology and Biotechnology, 50, 55-64, 1998.
42. M. B. Singh, & R. B. Knox, "Invertases of Lilium pollen: characterization and activity during in vitro germination", Plant Physiology, 74(3), 510-515, 1984.
43. H. B. Krishnan, J. T. Blanchette, & T. W. Okita, "Wheat invertases: characterization of cell wall-bound and soluble forms", Plant Physiology, 78(2), 241-245, 1985.
44. H. S. Lee, & A. Sturm, "Purification and characterization of neutral and alkaline invertase from carrot", Plant Physiology, 112(4), 1513-1522., 1996.
45. A. Belcarz, G. Ginalska, J. Lobarzewski, & C. Penel, "The novel non-glycosylated invertase from Candida utilis (the properties and the conditions of production and purification)", Biochimica et Biophysica Acta (BBA)-Protein Structure and Molecular Enzymology, 1594(1), 40-53, 2002.
46. S. Raja, V. R. Murty, V. Thivaharan, V. Rajasekar, and V. Ramesh, "Aqueous Two Phase Systems for the Recovery of Biomolecules – A Review," Sci. Technol., vol. 1, no. 1, pp. 7–16, 2012.
47. M. Rasheed, S. Shihab, O. Y. Mohammed, and A. Al-Adili, "Parameters Estimation of Photovoltaic Model Using Nonlinear Algorithms," Journal of Physics: Conference Series, vol. 1795, no. 1, p. 012058, Mar. 2021, doi: https://doi.org/10.1088/1742-6596/1795/1/012058.
48. S. Saravanan, J. R. Rao, T. Murugesan, B. U. Nair, & T. Ramasami, "Partition of tannery wastewater proteins in aqueous two-phase poly (ethylene glycol)-magnesium sulfate systems: effects of molecular weights and pH". Chemical engineering science, 62(4), 969-978, 2007.
49. R. S. Faravash, H. Modarress, & B. Nasernejad, "Structural and partitioning studies of bovine serum albumin in mixture of (poly (ethylene glycol)+ K2HPO4+ H2O)" Journal of Chemical & Engineering Data, 52(1), 71-76, 2007.
50. P. E., Kee, J. C. W. Lan, H. S. Yim, Y. H. Chow, P. T. Chen, & H. S. Ng, "Efficiency of polymer/salt aqueous two-phase electrophoresis system for recovery of extracellular Kytococcus sedentarius TWHKC01 keratinase", Process Biochemistry, 100, 199-206, 2021.
51. M. Pirdashti, Z. Heidari, N. Abbasi Fashami, S. M. Arzideh, & I. Khoiroh, "Phase equilibria of aqueous two-phase systems of PEG with sulfate salt: effects of pH, temperature, type of cation, and polymer molecular weight", Journal of Chemical & Engineering Data, 66(3), 1425-1434, 2021.
52. E. Akardere, B. Özer, E. B. Çelem, & S. Önal, "Three-phase partitioning of invertase from Baker's yeast" Separation and Purification Technology, 72(3), 335-339, 2010.
53. J. R. Rao, & B. U. Nair, "Novel approach towards recovery of glycosaminoglycans from tannery wastewater", Bioresource technology, 102(2), 872-878., 2011.
54. D. Baskaran, K. Chinnappan, R. Manivasagan, & D. K. Mahadevan, "Partitioning of crude protein from aqua waste using PEG 600-inorganic salt Aqueous Two-Phase Systems" Chemical Data Collections, 15, 143-152, 2018.
55. Z. Shad, H. Mirhosseini, A. S. M. Hussin, B. Forghani, M. Motshakeri, & M. Y. A. Manap, "Aqueous two-phase purification of α-Amylase from white pitaya (Hylocereus undatus) peel in polyethylene glycol/citrate system: Optimization by response surface methodology", Biocatalysis and agricultural biotechnology, 14, 305-313. 2018.
56. F. S. Antelo, J. A. V. Costa, and S. J. Kalil, "Purification of C-phycocyanin from Spirulina platensis in aqueous two-phase systems using an experimental design", Brazilian Archives of Biology and Technology, vol. 58, pp. 1-11, 2015.
57. M. Rasheed, SuhaShihab, O. Alabdali, and H. H. Hassan, "Parameters Extraction of a Single-Diode Model of Photovoltaic Cell Using False Position Iterative Method," Journal of Physics: Conference Series, vol. 1879, no. 3, p. 032113, May 2021, doi: https://doi.org/10.1088/1742-6596/1879/3/032113.

Extraction of Invertase Enzyme From Potato Tubers by Aqueous Two-Phase System

Meaad H. Kadhim [a] and Khalid W. Hameed [b]

Biochemical Engineering Department, University of Baghdad, Al-Khwarizmi College of Engineering, Baghdad, Iraq.

[a] *Corresponding author: miad.abadi2205@kecbu.uobaghdad.edu.iq.*

[b] *kwhameed@kecbu.uobaghdad.edu.iq.*

Abstract. An aqueous two-phase system (ATP) is a liquid-liquid separation technique in which two immiscible aqueous phases are formed. It works well for getting biomolecules out of mixes and sorting them. In this study, invertase enzyme was extracted from potato tuber using ATP. Two ATP systems were used: first, polyethylene glycol 4000/dipotassium phosphate (PEG4000/PPH) and second, polyethylene glycol 4000/sodium citrate (PEG4000/SC). During the study, the behavior of the recovery rate (%rec) and distribution coefficient (ke) of the invertase enzyme in ATP was investigated. The temperature, the amount of PEG4000, the amount of dipotassium phosphate or sodium citrate, the pH, and the addition of sodium chloride or magnesium sulfate as support agents all had an effect. In both systems, the maximum %rec and ke were 92.56% and 12.44, respectively, for the first system at a temperature of 40 °C, a PEG4000 concentration of 2.1 g/10 ml, a dipotassium phosphate concentration of 2.4 g/10 ml, and a pH value of 9.4. Meanwhile, the maximum %rec and ke for the second system are 88.74% and 7.88, respectively, for a temperature of 30 °C, a PEG4000 concentration of 2.4 g/10 ml, a sodium citrate concentration of 1.8 g/10 ml, and a pH value of 8. After adding neutral salt, in the first system as the better system, under the same optimum conditions and MgSO4 concentration of 0.5 g/10 ml, the maximum %rec and Ke were 97.96% and 48.01, respectively.

Keywords: *ATPS, Enzymes, glycol, parameters, PEG4000.*

INTRODUCTION

Extraction of bioproducts from downstream using commercial methods such as liquid-liquid extraction (Aqueous-organic system) lead to lose some properties of these bioproduct. One of the alternative methods is to use aqueous two-phase system; this method is environment friendly and didn't affect the bioproducts [1-5]. In 1896, Martinus Willem Beijerinck serendipitously discovered Aqueous Two-Phase System (ATPS), yet it wasn't put to use until the 1970s [6-10]. In recent years, ATPS systems have been developed and extensively researched. It is composed of several kinds of chemicals, such as systems of polymer-polymer or polymer-salt that can be combined, and it serves a number of functions [11-13]. This process is superior to alternative extraction methods because of its affordability, environmental friendliness, and versatility in extracting a wide range of compounds [14-18]. Water aids in the stabilization and separation of biomolecules' structures in the two phases of ATPS [19-21], while other liquid-liquid extraction (LLE) techniques might be detrimental to biological products due to the harsh process conditions and use of organic solvents [22-25]. ATPS consist of a combination for two distinct materials. They may consist of either a salt plus polymer, such as dipotassium phosphate (K_2HPO_4), or sodium citrate ($Na_3C_6H_5O_7$) and PEG, or two polymers, such as PEG and dextran. To obtain two phases, the concentration of polymer/salt must be higher than the critical concentration, below which two phases cannot be attained. The critical concentrations depend on molecular weight of polymer and type of salt [26-30]. Nevertheless, biphasic systems exist, consisting of short-chain alcohols and ionic liquids [31-35]. Researchers have examined several forms of ATPS to analyze plus comprehend their capacity to separate, eliminate, and cleanse particles and biomolecules [36-38]. Although ATPS offer numerous advantages, there is a limited comprehension of the partitioning of biomolecules in these systems, making it challenging to anticipate their behavior. The amounts of a certain chemical, like phosphate, and the properties of the proteins being studied are what are being looked at, such as proteins, are both crucial elements in determining the behavior of biomolecules in a system. Furthermore, the interplay between a system and biomolecules factors such as pH and temperature is also of significant importance [39-41]. The target enzyme in this research is Invertase Enzyme. Invertase, also known as beta-fructofuranosidase, is a glycoprotein that breaks down the end portions of beta-fructofuranoside molecules. It is from enzymes, which are important in the food industry and responsible for sucrose

Technologies and Materials for Renewable Energy, Environment and Sustainability
AIP Conf. Proc. 3321, 030017-1–030017-11; https://doi.org/10.1063/5.0289636
Published under an exclusive license by AIP Publishing. 978-0-7354-5231-2/$30.00

inversion by producing D-fructose and D-glucose. It functions best at a pH of 4.5 and is stable at a temperature of 50 °C. It has a broad distribution across the biosphere, particularly in plants and microbes [42-45]. The food industry mostly uses invertase to convert sucrose, which has a harsh taste and easily crystallizes, into fructose syrup. It is also utilized in the manufacturing of sucrose biosensors and in the paper, pharmaceutical, and cosmetic industries [15, 16]. invertase is produced by various types of plants such as potatoes, carrots, tomatoes, tobacco, sugar cane, and bamboo [46-50]. Additionally, reports of its existence in many yeasts, including *Saccharomyces cerevisiae* [51], *Candida utilis* [52], *Pichia anomola* [53], and a few fungi, mostly *Aspergillus niger* and *Neurospora sp*. [54-60]. There are several isoforms of plant invertase, each with unique subcellular localization and metabolic characteristics [60]. The ideal pH range for acid invertase is typically 3.5–5.0, whereas the ideal pH range for alkaline invertase is 7.0–8.0 [44]. Fresh potato has invertase activity, which has been demonstrated to increase under cold storage [30], which indicates a useful source for researching the characterization and purification of invertase would be potato tubers. While there are a number of ways to purify invertase from various plant sources, these techniques are thought to be costly and time-consuming [20]. The traditional procedure often includes four steps or more, each of which causes a loss in product and activity recovery to varying degrees. Consequently, the utilization of cost-effective techniques that offer superior purification outcomes with less procedural steps has resulted in a recent upsurge in enthusiasm for protein purification. A popular technique made for this purpose is the aqueous two-phase system (ATPS). Albertson created it initially in the 1950s to distinguish between proteins, nucleic acids, and cells [10]. The method provides several advantages, including effectiveness, rapid separation with minimal damage, excellent mass transfer, selective partitioning, and affordability. It is used in a variety of biotech industries [12].

The aim of the present work is to find the optimum operating condition for the extraction of invertase enzyme from local Iraqi potato tuber using Taguchi method as an experimental design. The parameters that studied on the effect of extraction of invertase from potato are: Temperature (10 – 40 ^{o}C), pH (8 – 10) for first system and (7 – 10) for second system, concentration each of potassium phosphate, sodium citrate, and PEG4000 (1.5 – 2.4 g/10 ml), and concentration of supporting agents, NaCl or MgSO4, (0 – 2 g/10 ml).

Materials and methods

Materials

Sucrose, polyethylene glycol (PEG4000), 3, 5-Dinitrisalicylic acid (DNS), sodium hydroxide (NaOH) and serum albumin from cows (BSA) were purchased from HIMEDIA Laboratories Pvt. Ltd., India. Dipotassium phosphate (K_2HPO_4), cupric sulfate ($CuSO_4$), sodium carbonate (Na_2CO_3) and tri-sodium citrate ($Na_3C_6H_5O_7$) were gotten from Central Drug House Ltd., India, and sodium chloride (NaCl) was supplied by Alpha Chemika, India. Folin-reagent from Sisco Research Laboratories Pvt. Ltd. (Srl) in India. Potato was obtained from local markets of Iraq, and reagents of the highest quality were employed in the analysis. The water utilized in this research was deionized and double-distilled, sourced from the laboratory of the biochemical engineering department.

METHODOLOGY

Crude extract preparation

The peels were removed from the fresh potato roots after they had been carefully cleansed with distilled water. Subsequently, twenty grams of roots were chopped into little pieces and mixed in fifty millimoles of ice-cold citrate buffer with a pH of 4.5 for one minute at a temperature of 4 oC. The homogeneous solution was filtered through five layers of cheesecloth, then separate the remaining solids by centrifugation at 6000 revolutions per minute for twenty minutes at 4 oC. The clear supernatant is considered a crude enzyme extract. It was found that the crude extract had a specific activity of 18.11 U/mg.

Aqueous Two Phase Partitioning

First system: the stock solutions of dipotassium phosphate (1.5–2.4 g) per 10 ml of crude extract and (1.5–2.4 g) of PEG4000 per 10 ml of distilled water. Second system: The stock solutions of sodium citrate (1.5–2.4 g) per 10 ml of distilled water and (1.5–2.4 g) of PEG4000 per 10 ml of crude extract are prepared previously. From the experimental study, it was discovered that the blending of dipotassium phosphate with crude extract for the initial system, whereas for the second system, the fusion of PEG4000 with crude extract resulted in higher retrieval. It is

mixed with 5 ml of dipotassium phosphate or sodium citrate solution with 5 ml of PEG4000 solution using vortex for 2 min. To obtain two phases, the mixture can be left for 2–3 hrs under gravity force, but to exceed the process, the mixture is separated into two phases using centrifugation at a speed of 6000 revolutions per minute for 10 min. The top phase is PEG4000 solution, while the bottom phase is the salt solution. After the extraction and at equilibrium, the phase that loses the enzyme is called the raffinate phase (Rf), while the phase that gains the enzyme is called the extract phase (Ex). On the basis of earlier studies, the system parameters were chosen [33-36]. The upper stage was accurately separated from the lower stage using a Pasteur pipette. The dimensions for the capacities of the different stages were recorded. Portions of the stages were evaluated for protein measurement and enzyme scrutiny. The division factors, like the partition coefficient, yield percentage, and unique efficacy, were calculated using equations derived from past investigations [36-39]. The content of protein (KP) or the partition coefficient (KE) is the definition of the invertase partition coefficient in aqueous two-phase systems. This coefficient denotes the concentration ratio of enzyme in the extract phase to that of the raffinate phase when the system is in equilibrium, as demonstrated in Eqs. 1, 2, or 3 [39, 40].

$$K_p = \frac{C_{Ex}}{C_{Rf}} \tag{1}$$

$$K_E = \frac{A_{Ex}}{A_{Rf}} \tag{2}$$

$$\text{or } K_E = \frac{\%Rec}{1-\%Rec} \tag{3}$$

where CEx and CRf are the total protein concentrations in mg/mL of the extract and raffinate phases respectively, AEx and ARf are the enzyme activities in U/mL of the extract and raffinate phases, respectively.

In order to judge the efficiency of the cleansing procedure, it is essential to quantify the effectiveness of the catalyst, particularly known as the enzyme's specific activity (SA, shown in units per milligram of protein), recovery % and partition coefficient of enzyme (KE) additionally; the calculations were performed based on the provided equations [39].

$$\text{Invertase activity (U/ml)} = \frac{A \text{ x } V}{€ \text{ x } t \text{ x } v} \tag{4}$$

where: A: absorbency at 540 nm, V: Total volume of reaction mixture in (2 ml), €: Enzyme constant (0.01), t: incubation time (30 min), and v: volume of crude used in (0.2 ml)

$$SA = \frac{\text{Invertase activity}}{C_{Rf}} \tag{5}$$

$$\%Rec = \left(1 - \frac{A_{Rf}}{A_{in}}\right) \times 100 \tag{6}$$

where A_{in} is the initial activity of enzyme in U/mL.

Determining Invertase activity

Miller in 1959 detailed the Miller procedure for measuring plant-invertase activity. The testing combination contained 0.8 mL of substrate, 50 millimoles sucrose in a pH 4.5 citrate buffers, and 0.2 ml of enzyme diluted to the desired concentration. Then the combination was placed in an incubator at 37 °C for 30 minutes. The reaction was then finished by adding 1 ml of DNS (3,5-dinitrosalicylic acid) reagent and heated for five minutes, then chilled the solution to room temperature by submerging it in an ice bath and quantified the reducing sugars using spectrophotometry at a 540 nm wavelength [41]. One unit of invertase activity is the amount of enzyme that can change one mole of sugar into glucose in one minute at a pH of 4.5 and a temperature of 37 oC. Utilizing as the substrate, it is measuring the quantity of units per milligram of protein to ascertain the specific activity.

Finding the Protein Concentration

The Lowry technique was utilized to figure out the protein concentration [42], and including solutions used for protein determination:

Solution (1): 2% Na2CO3: The solution was prepared by dissolving 10 g of Na2CO3 in 500 ml of 0.1M NaOH. Solution (2): 2% Sodium Potassium tartrate: Two grams of sodium potassium tartrate were dissolved in a small amount of purified water. Then, 100 milliliters of distilled water were added to make the full volume. Solution (3): 1% CuSO4: One gram of CuSO4 was mixed with 100 milliliters of pure water to make the solution. Solution (4): It was prepared immediately by mixing 98 ml of solution (1) with 1 ml of solution (2) and 1 ml of solution (3). Solution (5): Bovine Serum Albumin (BSA): To make the solution, 0.01 g of BSA was slowly dissolved in distilled water, and then 100 ml of distilled water was added to make the right amount. Solution (6): Folin-reagent: The reagent was prepared by diluting 1 mL of Folin in 2 mL of distilled water (1:2 v/v).

The protein concentration was determined according to Lowry method [42]. Aqueous Two-Phase System (ATPS) is a liquid-liquid separation technique that has been identified as a potent approach for the extraction and separation of biomolecule mixtures. This technique entails the formation of two immiscible aqueous phases. ATPS was employed to extract the Invertase enzyme from potato tubers in this investigation. Two ATPS systems were employed: polyethylene glycol 4000/dipotassium phosphate (PEG4000/PPH) and polyethylene glycol 4000/sodium citrate (PEG4000/SC).

RESULTS AND DISCUSSION

The protein amount and specific activity of the crude extract were measured to be 4.711 mg and 18.11 U/mg, respectively. It has been used Minitab 17.0 software to design the number of experiments by Taguchi method, where each parameter has four levels. The study initially focuses on investigating the influence of four parameters: temperature, pH, concentration of PEG4000 and K2HPO4 (PPH) or Na3C6H5O7 (SC). Once the optimal conditions that yield the highest percentage recovery are determined, neutral salts (NaCl or MgSO4) will be introduced to observe their influence. Figure 1, Tables 1 and 2 show the number of experiments with the parameters of system 1 (PEG4000/K2HPO4) and system 2 (PEG4000/Na3C6H5O7) respectively, and the results of recovery percent (%Rec) and partition coefficient (KE).

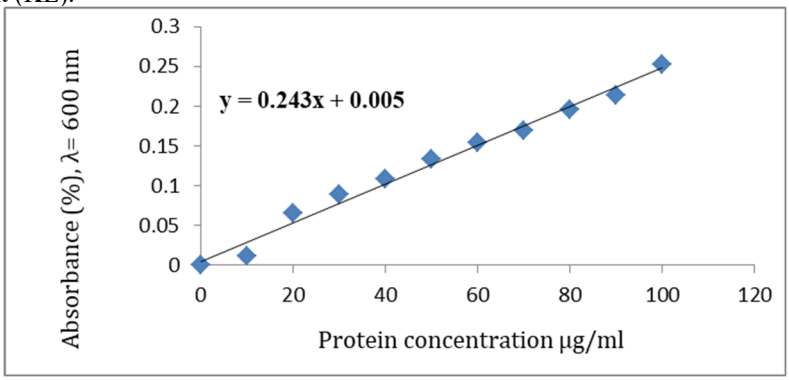

FIGURE 1. Standard curve of BSA

TABLE 1. Experiments of system-1 (PEG4000/PPH) according to Taguchi method with their results of %Rec and KE

Run No.	Temp °C	pH	K_2HPO_4 (PPH) g/10 ml	PEG 4000 g/10 ml	% Rec	K_E
1	10	8	1.5	1.5	77.1	3.37
2	10	8.7	1.8	1.8	86.8	6.58
3	10	9.4	2.1	2.1	89.1	8.17
4	10	10	2.4	2.4	88.9	8
5	20	8	1.8	2.1	84.2	5.33
6	20	8.7	1.5	2.4	83.0	4.88
7	20	9.4	2.4	1.5	89.0	8.09
8	20	10	2.1	1.8	86.2	6.25
9	30	8	2.1	2.4	85.9	6.1
10	30	8.7	2.4	2.1	91.1	10.24
11	30	9.4	1.5	1.8	83.2	4.95

12	30	10	1.8	1.5	84.8	5.58
13	40	8	2.4	1.8	89.1	8.17
14	40	8.7	2.1	1.5	87.0	6.69
15	40	9.4	1.8	2.4	88.1	7.4
16	40	10	1.5	2.1	84.2	5.33

TABLE 2. Experiments of system-2 (PEG4000/SC) according to Taguchi method with their results of %Rec and KE

Run No.	Temp ^{o}C	pH	$Na_3C_6H_5O_7$ (PPH) g/10 ml	PEG 4000 g/10 ml	% Rec	K_E
1	10	7	1.5	1.5	82	3.04
2	10	8	1.8	1.8	84.53	6.46
3	10	9	2.1	2.1	83.18	5.94
4	10	10	2.4	2.4	83.63	6.1
5	20	7	1.8	2.1	81.93	5.53
6	20	8	1.5	2.4	81.14	5.3
7	20	9	2.4	1.5	80.24	5.06
8	20	10	2.1	1.8	80.69	5.17
9	30	7	2.1	2.4	82.72	5.78
10	30	8	2.4	2.1	87.35	7.9
11	30	9	1.5	1.8	85.32	6.81
12	30	10	1.8	1.5	86	7.14
13	40	7	2.4	1.8	78.32	4.61
14	40	8	2.1	1.5	83.85	6.19
15	40	9	1.8	2.4	84.76	6.56
16	40	10	1.5	2.1	78	3.4

Temperature Effect

Enzyme's recovery, described in the above Tables 1 and 2. As the temperature increased, causing enzymes to undergo alterations in their form, structure, and stability. Therefore, the temperature range was set between 10 – 40 oC. To determine the percent relative activities, the enzyme activities at various temperatures were divided by the enzyme activity with the highest activity, and the resulting quotient was multiplied by 100. A study has been conducted to investigate temperature affects the invertase enzyme return rate and partition coefficient as illustrated in Figures 2 and 3 for systems 1 and 2, individually, without adding supporting salts (NaCl or MgSO4). The enzyme's temperature activity and stability profile are crucial considerations for industrial applications. It is seen from Figure 2 (System-1), that %Rec increases with increasing of temperature, where from (10 – 20 oC) the recovery of enzyme and then KE are almost stable (%Rec = 85.5%) and not affected by temperature, from (20 – 40 oC) the %Rec increases from (85.5 – 87.1%), while in Figure 3 (System-2), the %Rec of enzyme reduced from (10 – 20 oC), increased from (20 – 30 oC), and then decreased from (30 – 40 oC). The influence of temperature on the behavior of an aqueous composition is intricate due to the interplay of its constituent parts, namely electrostatic and hydrophobic forces. The results exhibit a favorable comparison to the previous reports. Typically, invertase derived from various plants exhibit their greatest level of activity at a temperature of 37 oC [18, 43, 44]. Following the treatment of enzyme samples at different temperatures for a duration of 1 hour, a rise in activity was observed, specifically at a temperature of 40 oC. Temperature's effect on the activity and stability of invertase has been investigated plus discovered to be highly dependent on the enzyme's location and the temperature itself. According to reports, the soluble invertase found in wheat coleoptiles exhibited its highest level of activity at a temperature of 37 oC. Additionally, the enzyme maintained 60% of its maximal activity after being exposed to a temperature of 50 oC for a duration of 4 minutes [43]. Another investigation into plant invertase was revealed by Singh and Knox, 1984 [44], where they discussed the differences in the heat stability of various plant forms of invertase.

pH Effect

pH was adjusted using HCl or NaOH. In many industrial applications, pH stability is another important consideration when selecting enzymes as biocatalysts. The range of pH value was taken from 8.0 to 10.0 for PEG/K2HPO4 system and from 7.0 to 10.0 for the PEG/SC system. In Figure 2, the %Rec rises from (83.8 – 87.2%) when the pH increases from 8 – 9.4. It indicates that more enzymes will be retrieved for the PEG/K2HPO4 system. The %Rec and KE values reached their peak at a pH of 9.4, with values of 87.2% and 6.81, respectively. For the

PEG/SC system in Fig. 3, more enzymes recovered when pH changed from 7 – 8, %Rec and KE increased from (81.3 – 84.2%) and (4.35 – 5.33) respectively. These results are agreed with results of Singh and Knox, 1984, Pirdashti et al, 2021, Saravanan et al, 2007, Kee et al, 2021 [44, 45, 46, 47]. After pH 9.4 for system-1 and pH 8 for system-2, the %Rec reduces significantly. It is noted that the two phases disappear as the pH increases after 10, this phenomenon is agreement with Rao and Nair, 2011; Vijaya Santhi, 2020 [48, 49].

Concentration Effect of Potassium phosphate or Sodium citrate

The concentration of salt used in two-phase system is important factor influencing enzyme partitioning. Through experimentation, the quantity of dipotassium phosphate and sodium citrate in the solution has an effect on the amount of enzyme extracted in ATPS and how well it is broken down. In accordance to the results of Pirdashti et al, 2021; and Baskaran et al, 2018, they found in the PEG/salt system that the recovery percentage and partition coefficient increase when the salt concentration rises [45, 50]. Upon examining Figure 2 of system-1, it becomes evident that the rising of salts concentrates in the solution, enhances the extraction process, and increases the partition coefficient. For the PEG/PPH (system-1), increasing the PPH salt concentration from 1.5 g/10 ml to 2.4 g/10 ml resulted in an increase in the enzyme %Rec from 81.5% to 89.4% and an increase in the partition coefficient from 4.40 to 8.43, and for the PEG/SC (system-2), increasing the SC salt concentration from 1.5 to 1.8 g/10 ml led to a rise in the %Rec from 81.5% to 84.4% and an improvement in the partition coefficient from 4.40 to 5.41 as shown in Fig.3. But more contents of SC salt led to reducing the %Rec to 82.2%.

Concentration Effect of PEG

The concentration effect of PEG 4000 on phase creation was further investigated, revealing that the concentration of PEG4000 has a substantial effect on the rate and uniformity of invertase enzyme partitioning. This, in turn, influences the amount of recoverable invertase. The influence of the concentration of PEG on the system-1 and 2 are shown in Figures 2 and 3, individually. For the system-1, when the concentration of PEG4000 increased from 1.5 – 2.1 g/10 ml, the percentage of invertase enzyme recovered increased from 84.3% - 87.1% (Fig. 2) without adding NaCl or MgSO4, and for system-2, the percentage recovery increased from 82.2% to 83.4% without adding NaCl or MgSO4 (Figure 3). These results are consistent with Antelo et al, 2015 [51], where they came to the conclusion that increasing the concentration of PEG was good for both %Rec and KE. It was found that the %Rec of the invertase enzyme slightly dropped from 87.2 to 86.4 when PEG increased from (2.1 – 2.4 g/10 ml) for system-1, while for system-2, the %Rec increased slightly from (82.2 – 83.1%) when PEG increased from (1.8 – 2.4 g/10 ml. For the two systems, the PEG's concentration has little effect on the recovery of enzyme. Shad et al, 2018; and Mahdi et al, 2023, who found that increasing the PEG concentration leads to a decrease in the percentage of enzyme recovered, confirmed that the recovery percentage decreased as the polymer concentration increased. Proteins migrate from the lower phase to the upper phase in ATPS, resulting in an automatic increase in the partition coefficient [52, 53].

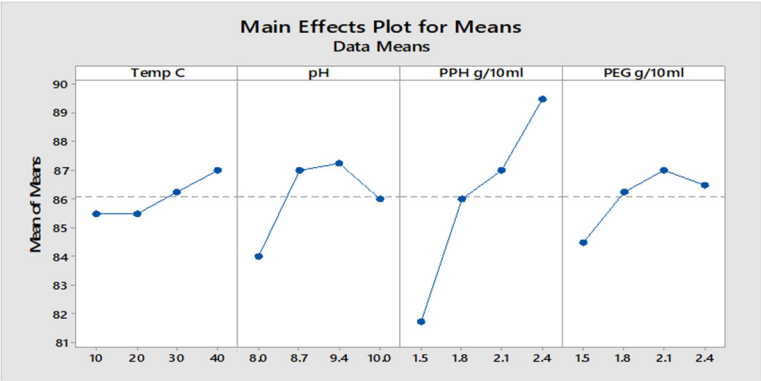

FIGURE 2. Effect of the parameters (temperature, pH, concentrations of PEG4000 and dipotassium phosphate) on the recovery% and then on KE of the system-1 without adding the supporting agents

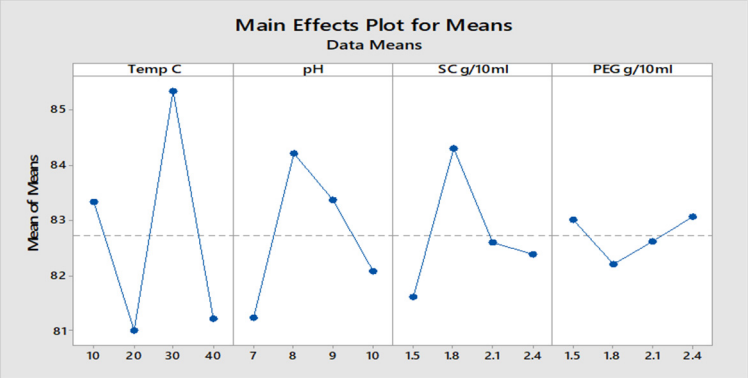

FIFURE 3. Effect of the parameters (temperature, pH, concentrations of PEG4000 and sodium citrate) on the recovery% and then on KE of the system-2 without adding the supporting agents

The maximum values obtained of %Rec and KE for the system-1 (PEG/PPH) are 92.56% and 12.44 respectively, at a temperature of 40 °C, pH 9.4, PPH concentration 2.4 g/ 10 ml, and PEG4000 concentration 2.1 g/10 ml, and for and system-2 (PEG/SC), the %Rec and KE are 88.74% and 7.88 respectively, at temperature of 30 oC, pH 8, SC concentration 1.8 g/ 10 ml, and PEG4000 concentration 2.4 g/10 ml.

Effect of NaCl and $MgSO_4$

This is a final step to show the influence of adding supportive agents as a strategy for boosting protein partitioning and enzyme recovery rate. The first system was chosen to study the effect of adding supporting salts, as it achieved a greater recovery percent than the second system. Typically, the hydrophobic phase contains proteins with a higher concentration of hydrophobic anions or cations, and the opposite is also true [35]. Figure 4 shows the effect of adding two different types of salts, NaCl and MgSO4, on the %Rec of enzyme of system-1 at optimum conditions (temperature = 40 oC, pH 9.4, PEG4000 concentration = 2.4 g/10 ml, and K2HPO4 concentration = 2.1 g/10 ml). The function these salts as agents that enhance the separation process, the salts comprise ions that vary in their hydrophobicity, with some ions being more hydrophobic than others. This difference in hydrophobicity enables ions with opposite hydrophobicities to be separated. One phase concentrates the more hydrophobic ions, while another phase concentrates the less hydrophobic ions [54, 55]. It can be seen from Figure 4, that the %Rec and then KE varied with the addition of NaCl and MgSO4 significantly, where %Rec increases from 92.1 – 93.56% and from 92.1 – 97.96% for NaCl and MgSO4 respectively when these salts increases their concentration from 0 – 0.5 g/10 ml. Then the %Rec and then KE start to reduce with increasing concentrations of both salts, these findings are in agreement with results of Ferreira et al, 2014, and Hameed, 2016 [56, 57], whereas the system comprised of neutral salts and the partition coefficients exhibited a linear decrease as the electrostatic potential between the phases varied.

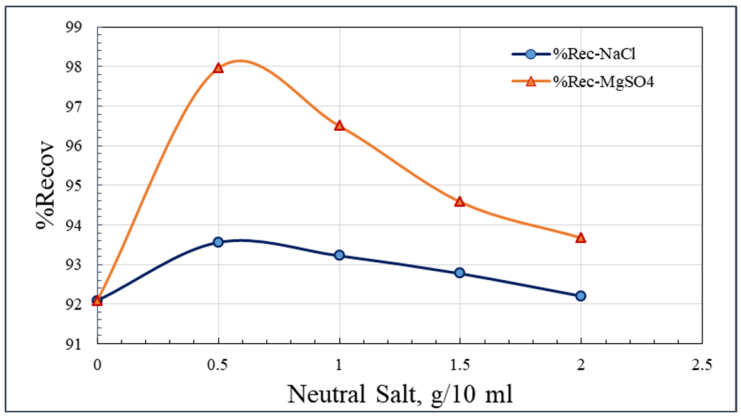

FIGURE 4. Effect of Nacl and $MgSO_4$ concentration on the %Rec and K_E of the system-1 at T = 40°C; conc. of PEG and K_2HPO_4 are 2.1 and 2.4 g/10 ml, individually, pH 9.4

CONCLUSION

The distribution pattern of invertase in PEG4000/PPH demonstrated that it is possible to extract the plant enzyme into the salt-concentrated bottom phase, but in PEG4000/SC, the plant enzyme was extracted into the upper phase rich in polymer. The concentration of PEG, type and concentration of salt, temperature, pH, and the addition of natural salts were observed to significantly impact the partitioning of invertase. This resulted in a recovery percent and partition coefficient of enzyme up to 97.96% and 48.01, respectively. The most effective system for invertase recovery was a combination of PEG4000 (2.1 g/10 ml), K2HPO4 (2.4 g/10 ml) at a pH of 9.4 and a temperature of 40 oC, and included a concentration of 0.5 g/10 ml of MnSO4. ATPS is a cost-effective, uncomplicated, secure, and remarkably efficient approach for purifying proteins, especially when compared to other traditional purification techniques. For the high recovery percent of invertase in a single stage, it can be said there is no need to more stages to extraction. When subjected to purification using the aqueous two-phase extraction procedure, the enzyme exhibited a high level of activity and exceptional stability; these qualities make potato invertase a desirable biocatalyst for various industrial applications.

REFERENCES

1. Albertsson P. Å.: Partition of Cell Particles and Macromolecules in Polymer Two-Phase Systems. Advances in protein chemistry, vol. 24, pp. 309-341 (1970) https://doi.org/10.1016/S0065-3233(08)60244-2.
2. Grilo A. L., Raquel Aires-Barros M. and Azevedo A. M.: Partitioning in Aqueous Two-Phase Systems: Fundamentals, Applications and Trends. Separation & Purification Reviews, vol. 45, pp. 68-80 (2016) doi: 10.1080/15422119.2014.983128.
3. Hatti-Kaul R. , "Aqueous two-phase systems: methods and protocols," Springer Science & Business Media, vol. 11 (2008)
4. Iqbal M., Tao Y., Xie S., Zhu Y., Chen D. and Yuan Z.: Aqueous two-phase system (ATPS): an overview and advances in its applications," Biological procedures online, vol. 18, pp. 1-18 (2016).
5. Asenjo J. A. and Andrews B. A.: Aqueous two-phase systems for protein separation: A perspective. Journal of Chromatography A 1218, vol. 49, pp. 8826-8835 (2011) doi: 10.1016/j.chroma.2011.06.051
6. Mendes, M.S., Rosa, M.E., Ramalho, F., Freire, M.G. and e Silva, F.A..: Aqueous two-phase systems as multipurpose tools to improve biomarker analysis. Separation and Purification Technology, p.123875. (2023) https://doi.org/10.1016/j.seppur.2023.123875.
7. Espitia-Saloma E., Vázquez-Villegas P., Aguilar O. and Rito-Palomares M.: Continuous aqueous two-phase systems devices for the recovery of biological products. Food and Bioproducts Processing, vol. 92, pp. 101-112 (2014) doi: 10.1016/j.fbp.2013.05.006
8. Molino J. V. D., Marques D. D. A., Júnior A. P., Mazzola P. G. and Gatti M. S. V.: Different types of aqueous two-phase systems for biomolecule and bioparticle extraction and purification. Biotechnology Progress, vol. 29, pp. 1343-1353 (2013)
9. Teixeira A. G., Agarwal R., Ko K. R., Grant-Burt J., Leung B. M. and Frampton J. P.: Emerging biotechnology applications of aqueous two-phase systems. Advanced healthcare materials, vol. 7, p. 1701036 (2018) doi: 10.1002/adhm.201701036
10. Mohammed W.T., and Mahdi A.S.: Liquid-Liquid Extraction of Metal Ions Using Aqueous Biphasic Systems. Journal of Engineering, 18(09), pp.989-998, (2012).
11. Shahbazova, G.M. and Masimov, E.A.: Effect of a Various Additivies to the Formation of Aqueous Biphasic System Polyetylenglycole (Peg)/Sodium Citrate/Water. Open Access Library Journal, 9(1), pp.1-9. (2022) DOI: 10.4236/oalib.1108142
12. Yau Y. K., Ooi C. W., Ng E. P., Lan J. C. W., Ling T. C. and Show P. L.: Current applications of different type of aqueous two-phase systems. Bioresources and Bioprocessing, vol. 2, pp. 1-13 (2015) doi: 10.1186/s40643-015- 0078-0
13. Pereira J. F., Freire M. G. and Coutinho J. A.: Aqueous two-phase systems: Towards novel and more disruptive applications. Fluid Phase Equilibria, vol. 505, p. 112341 (2020) doi: 10.1016/j.fluid.2019.112341
14. Kulshrestha S., Tyagi P., indhi V. and Yadavilli K. S.: Invertase and its applications–a brief review. Journal of pharmacy research, vol. 7, pp. 792-797 (2013) https://doi.org/10.1016/j.jopr.2013.07.014
15. Bagal D. S., Vijayan A., Aiyer R. C. Karekar R. N. and Karve M. S.: Fabrication of sucrose biosensor based on single mode planar optical waveguide using co-immobilized plant invertase and GOD. Biosensors and Bioelectronics, vol. 22, pp. 3072-3079 (2007)

16. Kumar S., Chauhan V. S. and Nahar P.: Invertase embedded-PVC tubing as a flow-through reactor aimed at conversion of sucrose into inverted sugar. Enzyme and microbial technology, vol. 43, pp. 517-522 (2008) DOI: 10.1016/j.enzmictec.2008.08.002
17. Ahiakpa, J.K., Karikari, B., Magdy, M., Munir, S., Mumtaz, M.A., Li, F., Wang, Y., Shang, L. and Zhang, Y., Regulation of invertase and sucrose for improving tomato fruit flavor: A review. Vegetable Research, 1(1), pp.1-13 (2021) https://doi.org/10.48130/VR-2021-0010
18. Lee H. S. and Sturm A.: Purification and characterization of neutral and alkaline invertase from carrot. Plant Physiology, vol. 112, pp. 1513-1522 (1996) https://doi.org/10.1104/pp.112.4.1513.
19. Liu C. C., Huang L. C., Chang C. T. and Sung H. Y.: Purification and characterization of soluble invertases from suspension-cultured bamboo (Bambusa edulis) cells. Food chemistry, vol. 96, pp. 621-631 (2006).
20. Madhusudhan M. C. and Raghavarao K. S. M. S.: Aqueous two phase extraction of invertase from baker's yeast: Effect of process parameters on partitioning. Process biochemistry, vol. 46, pp.2014-2020 (2011) doi:10.1016/j.foodchem.2005.02.044.
21. Andjelković U., Pićurić S. and Vujčić Z.: Purification and characterisation of Saccharomyces cerevisiae external invertase isoforms. Food Chemistry, vol. 120, pp. 799-804 (2010) doi:10.1016/j.foodchem.2009.11.013
22. Nadeem, H., Rashid, M.H., Siddique, M.H., Azeem, F., Muzammil, S., Javed, M.R., Ali, M.A., Rasul, I. and Riaz, M.: Microbial invertases: a review on kinetics, thermodynamics, physiochemical properties. Process Biochemistry. 50(8), pp.1202-1210 (2015) http://dx.doi.org/10.1016/j.procbio.2015.04.015.
23. Rodriguez J., Perez J. A., Ruiz T. and Rodriguez L.: Characterization of the invertase from Pichia anomala. Biochemical journal, vol. 306, pp. 235-239 (1995) https://doi.org/10.1042/bj3060235.
24. Nguyen Q. D., Rezessy-Szabó J. M., Bhat M. K. and Hoschke Á.: Purification and some properties of β-fructofuranosidase from Aspergillus niger IMI303386. Process Biochemistry, vol. 40, pp. 2461-2466 (2005) DOI:10.1016/J.PROCBIO.2004.09.012
25. Valencia-Hernández, L.J., Wong-Paz, J.E., Ascacio-Valdés, J.A., Contreras-Esquivel, J.C., Chávez-González, M.L., Martínez-Pérez, A., Castillo-Olvera, G. and Aguilar, C.N.: Kinetic study of fungal growth of several tanninolytic strains using coffee pulp Procyanidins. Fermentation, 8(1), p.17 (2021) https://doi.org/10.3390/fermentation8010017
26. Sturm A.: Primary structures, functions, and roles in plant development and sucrose partitioning. Plant physiology, vol. 121, pp. 1-8 (1999) https://doi.org/10.1104/pp.121.1.1
27. Draffehn A. M., Meller S., Li L. and Gebhardt C.: Natural diversity of potato (Solanum tuberosum) invertases. BMC Plant Biology, vol. 10, pp. 1-15 (2010) doi:10.1186/1471-2229-10-271
28. Zhang K, Wu Z, Wu X, Han H, Ju X, Fan Y, Yang C, Tang D, Cao Q, Wang J, Lv C.: Regulatory and functional divergence among members of Ibβfruct2, a sweet potato vacuolar invertase gene controlling starch and glucose content. Frontiers in Plant Science 14, 1192417 (2023) https://doi.org/10.3389/fpls.2023.1192417
29. Li R, Li J, Liao X, Wang Y.: Purification and characterisation of soluble acid invertase from mango fruits. International Journal of Food Science & Technology. Apr;52(4): 906-15 (2017) https://doi.org/10.1111/ijfs.13354
30. Gan Q, Li X, Zhang X, Wu L, Ye C, Wang Y, Gao J, Meng Y.: D181A site-mutagenesis enhances both the hydrolyzing and transfructosylating activities of BmSUC1, a novel β-fructofuranosidase in the silkworm Bombyx mori. International Journal of Molecular Sciences. Feb 28;19(3):683 (2018) https://doi.org/10.3390/ijms19030683
31. Fisher, D.: The separation of cells and organelles by partitioning in two-polymer aqueous phases. Biochemical Journal, 196(1), p.1. (1981) doi: 10.1042/bj1960001
32. Raja S., Murty V. R., Thivaharan V., Rajasekar V. and Ramesh V.: Aqueous two phase systems for the recovery of biomolecules–a review. Science and Technology, vol. 1, pp. 7-16 (2011) doi: 10.5923/j.scit.20110101.02
33. Mohd Salleh, M.H., Fitri Peli, A., Ngalimat, M.S. and Sim, K.J.: A mini literature review on current advancements in protein purification techniques. In Biology and Life Sciences Forum Vol. 20, No. 1, p. 12 (2022) https://doi.org/10.3390/IECBM2022-13507
34. Mendes, M.S., Rosa, M.E., Ramalho, F., Freire, M.G. and e Silva, F.A.: Aqueous two-phase systems as multipurpose tools to improve biomarker analysis. Separation and Purification Technology, p.123875 (2023) https://doi.org/10.1016/j.seppur.2023.123875
35. Sripokar, P., Chaijan, M., Benjakul, S., Yoshida, A. and Klomklao, S.: Aqueous two-phase partitioning of liver proteinase from albacore tuna (Thunnus alalunga): application to starry triggerfish (Abalistes stellaris) muscle hydrolysis. International journal of food properties, 20(sup2), pp.1600-1612 (2017) https://doi.org/10.1080/10942912.2017.1350705

36. Gandolfi, O.R.R., de Sousa Castro, S., Gonçalves, G.R.F., Muniz, I.D.C.B., Fontan, R.D.C.I., Pimentel, J.G. and Bonomo, R.C.F.: Thermodynamic modelling of the partitioning of lysozyme in aqueous two-phase systems composed of polyethylene glycol and salt at different temperatures. Chemical Engineering Journal Advances, 16, p.100556 (2023) https://doi.org/10.1016/j.ceja.2023.100556
37. Da Silva, C.A.S., Coimbra, J.D.R., Rojas, E.E.G. and Teixeira, J.A.C.: Partitioning of glycomacropeptide in aqueous two-phase systems. Process Biochemistry, 44(11), pp.1213-1216 (2009) https://doi.org/10.1016/j.procbio.2009.06.016
38. Coelho D. F., Silveira E., Pessoa Junior A. and Tambourgi E. B.: Bromelain purification through unconventional aqueous two-phase system (PEG/ammonium sulphate). Bioprocess and biosystems engineering, vol. 36, pp. 185-192 (2013) DOI: 10.1007/s00449-012-0774-5
39. Karkaş T. and Önal S.: Characteristics of invertase partitioned in poly (ethylene glycol)/magnesium sulfate aqueous two-phase system. Biochemical Engineering Journal, vol. 60, pp. 142-150 (2012) https://doi.org/10.1016/j.bej.2011.11.005
40. Jaffer, Z.M., Hameed, K.W. and Imran, S.G.: February. Extraction of prodigiosin using aqueous two phase system. In IOP Conference Series: Materials Science and Engineering (Vol. 1076, No. 1, p. 012026). IOP Publishing (2021) DOI 10.1088/1757-899X/1076/1/012026
41. Gusakov, A.V., Kondratyeva, E.G. and Sinitsyn, A.P.: Comparison of two methods for assaying reducing sugars in the determination of carbohydrase activities. International journal of analytical chemistry, (2011) https://doi.org/10.1155/2011/283658
42. Lowry O. H., Rosebrough N. J., Farr A. L. and Randall R.: Protein measurement with the Folin phenol reagent. J biol Chem, vol. 193, pp. 265-275 (1951)
43. Chugh, V., Kaur, N., Gupta, A.K. and Rai, A.: The seed biochemical signature as a potent marker for water logging tolerance in maize. Plant Stress, 4, p.100085 (2022) https://doi.org/10.1016/j.stress.2022.100085
44. Singh M. B. and Knox R. B.: Invertases of Lilium pollen: characterization and activity during in vitro germination. Plant Physiology, vol. 74, pp. 510-515, (1984) doi:10.1104/pp.74.3.510
45. Pirdashti M., Heidari Z., Abbasi Fashami N., Arzideh S. M. and Khoiroh I.: Phase equilibria of aqueous two-phase systems of PEG with sulfate salt: effects of pH, temperature, type of cation, and polymer molecular weight. Journal of Chemical & Engineering Data, vol. 66, pp. 425-1434 (2021) doi: 10.1021/acs.jced.0c01029
46. N. Assoudi et al., "Comparative examination of the physical parameters of the sol gel produced compounds La0.5Ag0.1Ca0.4MnO3 and La0.6Ca0.3Ag0.1MnO3," Optical and Quantum Electronics, vol. 54, no. 9, Jul. 2022, doi: https://doi.org/10.1007/s11082-022-03927-x.
47. Saravanan S., Rao J. R., Murugesan T., Nair B. U. and Ramasami T.: Partition of tannery wastewater proteins in aqueous two-phase poly (ethylene glycol)-magnesium sulfate systems: effects of molecular weights and pH. Chemical engineering science, vol. 62, pp. 969-978 (2007) doi:10.1016/j.ces.2006.10.025
48. Kee P. E. Lan J. C. W., Yim H. S. Chow Y. H. Chen P. T. and Ng H. S.: Efficiency of polymer/salt aqueous two-phase electrophoresis system for recovery of extracellular Kytococcus sedentarius TWHKC01 keratinase. Process Biochemistry, vol. 100, pp. 199-206 (2021) doi: 10.1016/j.procbio.2020.10.005
49. Rao J. R. Nair U.: Novel approach towards recovery of glycosaminoglycans from tannery wastewater," Bioresource technology, vol. 102, pp. 872-878 (2011)
50. Vijaya Santhi L., Hrishikesh A. T. Richa S. Prabhakar G. and Raghavarao K. S. M. S.: Differential partitioning of coconut whey proteins and fat using aqueous two phase extraction. Fluid Phase Equilibria, vol. 503, p. 112314 (2020) https://doi.org/10.1016/j.fluid.2019.112314
51. Baskaran D., Chinnappan K., R. Mahadevan K.: Partitioning of crude protein from aqua waste using PEG 600-inorganic salt Aqueous Two-Phase Systems. Chemical Data Collections, vol. 15, pp. 143-152 (2018) https://doi.org/10.1016/j.cdc.2018.05.004
52. M. Rasheed, S. Shihab, O. Y. Mohammed, and A. Al-Adili, "Parameters Estimation of Photovoltaic Model Using Nonlinear Algorithms," Journal of Physics: Conference Series, vol. 1795, no. 1, p. 012058, Mar. 2021, doi: https://doi.org/10.1088/1742-6596/1795/1/012058.
53. Antelo F. S., Costa J. A. V. and Kalil S. J.: Purification of C-phycocyanin from Spirulina platensis in aqueous two-phase systems using an experimental design. Brazilian Archives of Biology and Technology, vol. 58, pp. 1-11 (2015) doi: 10.1590/S1516- 8913201502621
54. Shad Z., Mirhosseini H., Hussin A. S. M., orghani B. Motshakeri M. and Manap M. Y. A.: Aqueous two-phase purification of α-Amylase from white pitaya (Hylocereus undatus) peel in polyethylene glycol/citrate system: Optimization by response surface methodology. Biocatalysis and agricultural biotechnology, vol. 14, pp. 305-313 (2018) https://doi.org/10.1016/j.bcab.2018.01.014

55. Mahdi H.A., Hameed K.W., and Ali A.J.A.: Application of Aqueous Two-Phase Systems in the Extraction of Bovine Serum Albumin Journal of Polymer & Composites, 11(1), pp.55-65p, (2023) DOI: 10.37591/JoPC
56. M. Rasheed, Suha Shihab, O. Alabdali, and H. H. Hassan, "Parameters Extraction of a Single-Diode Model of Photovoltaic Cell Using False Position Iterative Method," Journal of Physics: Conference Series, vol. 1879, no. 3, p. 032113, May 2021, doi: https://doi.org/10.1088/1742-6596/1879/3/032113.
57. Raja S., Murty V. R. Thivaharan V., Rajasekar V.: Aqueous two phase systems for the recovery of biomolecules–a review," Science and Technology, vol. 1, pp. 7-16 (2011) doi: 10.5923/j.scit.20110101.02
58. Shad Z., Hussin A. S. M. Akbari-Adergani B.: A Primary Approach for Separation and Characterization of Î±-Amylase from White Pitaya (Hylocereus Undatus) Peels by Polymer/Salt Two Phase System. Journal of microbiology, biotechnology and food sciences, vol. 11, pp. e3467-e3467 (2022) DOI: https://doi.org/10.55251/jmbfs.3467
59. Ferreira L. Fan X., Mikheeva L. M. Madeira P. P., L., Uversky V. N. and Zaslavsky B. Y.: structural features important for differences in protein partitioning in aqueous dextran–polyethylene glycol two-phase systems of different ionic compositions. Biochimica et Biophysica Acta (BBA)-Proteins and Proteomics, vol. 1844, pp. 694-704 (2014) DOI: 10.1016/j.bbapap.2014.01.016
60. Hameed R. M.: The application of aqueous two phase systems to the analysis of protein isoforms of importance in clinical biochemistry and biopharmaceutical production. Doctoral dissertation, Brunel University London (2016).

Optimizing Biogas Production Through Co-Digestion of Cow Dung and Chicken Droppings

Basirat Kikelomo Odunola[1,a], Wunuken Carlos Solomon[1,b], Sani Umar Mohammed[1,c], Aisha Sa'ad[1,d], Aimé Claude Nyoungue[2,e], and Nkague Nkamba Leontine[3,f].

[1] *Department of Mechanical Engineering, Nigerian Defence Academy, Kaduna State, Nigeria*
[2]*LGIPM, Université de Lorraine, F-57000, Metz, France*
[3]*Higher Teachers Training College (HTTC), University of Yaounde, Yaounde Cameroon*

[a] Corresponding author: bkodunola@nda.edu.ng
[b] Scwunuken@nda.edu.ng, [c]sumuhammed@nda.edu.ng, [d]a.saad@nda.edu.ng
[e] Aime.nyoungue@univ-lorraine.fr
[f] lnkague@gmail.com

Abstract. This paper explores the utilization of animal wastes, specifically cow dung and chicken droppings, to generate biogas as a sustainable alternative to fossil fuels. The study involves design and construction of laboratory scaled biodigesters using re-used plastic bottles, incorporating biogas upgradation devices. The experimentation includes five different slurry ratios (CCH_{100}, CCH_{75}, CCH_{50}, CCH_{25}, and CCH_{0}) duplicated under two temperature conditions (ambient and elevated). Gas analysis and graphical representation of the results reveal that the CCH_{100amb} blend produced the highest methane yield at ambient temperature (19℃-28.1℃), while CCH_{75amb} demonstrated the optimum methane yield among co-digested blends. Furthermore, the study highlights total elimination of moisture content and Hydrogen Sulphide in the generated gas, emphasizing the potential of co-digestion as a sustainable and efficient method for biogas production.

Keywords: Biogas, cow dung, chicken droppings, co-digestion, elevated temperature.

INTRODUCTION

The escalating population in Nigeria has led to the daily production of substantial amounts of waste from diverse human activities. From kitchen residues, sewage, and remnants of food in various settings like offices, markets, business centers, schools, to the waste generated in slaughterhouses, cattle ranches, and farmyards, these byproducts find their way to disposal sites. Beyond being unsightly, these dumpsites emit foul odors, compromising the aesthetics of the environment and posing health risks through the action of bacteria on the accumulated waste. Harnessing this bacterial action, which is responsible for the unpleasant odors, presents an opportunity to convert these wastes into a valuable resource: clean energy. Energy, as the primary and universal measure of work, has been an integral part of human civilization since prehistoric times. From the use of wood as fuel by Homo erectus to the present day, where fuels derived from plants and animal fats continue to play a crucial role, energy consumption has evolved significantly [1].

Nigeria is endowed with vast energy resources, including petroleum, coal, and renewables, but faces a disparity between resource availability and effective utilization. Despite Nigeria's abundance of energy resources, a significant portion of the Nigerian population, especially in rural areas, still rely on solid biomass fuels derived from wood, crop residues, bagasse, and animal dung for cooking. This dependence on solid biomass fuels, particularly in indoor cooking, gives rise to indoor air pollution (IAP), characterized by harmful pollutants like carbon monoxide, benzene, formaldehyde, and more [2], [3]. Prolonged exposure to these pollutants contributes to respiratory ailments and mortality, with IAP accounting for 1.5 to 2 million deaths globally each year [4]. Additionally, solid biomass fuels contribute significantly to greenhouse gas emissions, with adverse effects on the environment. Conversely, urban centers in Nigeria favour kerosene, liquefied petroleum gas (LPG) and electricity as domestic fuels. However, each of these options has its challenges, ranging from safety concerns and accessibility to environmental impact. Therefore, there is a critical need to explore alternative fuels that are both environmentally friendly and economically viable [5].

Technologies and Materials for Renewable Energy, Environment and Sustainability
AIP Conf. Proc. 3321, 040001-1–040001-11; https://doi.org/10.1063/5.0289631
Published under an exclusive license by AIP Publishing. 978-0-7354-5231-2/$30.00

Aligning with global energy sustainability practices, promoting the use of eco-friendly renewable fuels, such as biogas, is imperative for the socio-economic and environmental well-being of Nigeria. This study delves into the potential of utilizing biogas generated from animal wastes, specifically cow dung and chicken droppings, to address energy challenges and contribute to the nation's sustainable development. Several studies have investigated factors influencing biogas production, optimal feedstock mixing ratios, and biogas upgrading techniques. Notably, [6] explored optimal cow dung and poultry droppings mixing ratios under tropical conditions, providing valuable insights. While [6] provides insights into optimal mixing ratios, variations in environmental conditions and experimental timing with the present study warrant further investigation. Ray et al. [7] digester design inspired the present study, but the main difference is in the upgrading devices and experimental conditions which necessitate additional research. The establishment of mesophilic and thermophilic temperature conditions in the present study sets it apart from other studies conducted solely under mesophilic conditions.

Having studied these literatures, this paper aims to present biogas as a potential solution to greenhouse gas emission challenge. Biogas, generated through the anaerobic decomposition of organic waste, offers a renewable and sustainable energy source that is considered carbon neutral. It primarily consists of methane (CH_4), carbon dioxide (CO_2), and trace amounts of other gases. The utilization of biogas can mitigate the adverse health and environmental impacts associated with traditional cooking fuels, making it a promising candidate for diversifying Nigeria's energy mix. Therefore, this research contributes significantly to understanding co-digestion strategies, optimizing biogas production for sustainable energy and waste management, positioning biogas as a promising avenue for a cleaner and more sustainable future.

STATE OF THE ART

Simeon et al [8], in a study compared the rate and amount of gas produced from the co-digestion of two different substrates of cow dung and poultry droppings under anaerobic conditions. Biogas production from three (3) cylindrical bio-digesters containing cow dung, poultry dropping, and a mixture of cow dung and poultry droppings under an average temperature of 28ºC was examined. In each case, the feedstock was diluted with equal volume of water to form slurry. The digestion took place for a period of 35 days. The biogas produced during this period was collected by balloon method and subsequently measured and recorded. The results obtained from the study showed that the co-digestion of cow dung and poultry droppings yielded a maximum volume of 2.62 cm^3, while poultry dropping yielded 2.50 cm^3 and cow dung yielded 1.78 cm^3. Thus, the co-digestion of the feedstock gave a better gas production and the mean biogas yield was found to be 2.62 cm^3.

An experiment was performed by Moses et al [9] on the Quality of optimized biogas yields from co-digestion of cattle dung with fresh mass of sunflower leaves, pawpaw and potato peels. The study emphasized that the conversion of wastes to energy needs serious attention to boost energy supply and reduce environmental pollution. Biogas yields were obtained from co-digestion of cattle dung with sunflower leaves, pawpaw and potato peels at different compositions in four biogas digesters (A, B, C and D). The substrates were mixed with water in ratio 1:2 and left for a 40-day retention time. Proximate analysis of the substrates, volume and quality of the biogas was determined. Analysis of variance was carried out to show significance of time and temperature over biogas yield. Retention time and temperature, were found to be significant in biogas production. Also, there was high methane contents in the biogas produced.

Mangibo et al [10], carried out laboratory scale research on co-digestion of cow dung with rice husk for biogas production. The study was conducted at ambient temperature range of between 26ºC-29°C for a period of 52 days with a total solid concentration of 8% in each slurry. Water displacement method was used to collect the biogas produced which was subsequently measured. The slurry ratios considered were 50:50, 25:75 and 0:100 for cow dung and rice husk respectively. Blend 50:50 showed a cumulative biogas yield of 161.5 ml at the end of the 38th day of the experiment after which there was no further gas production. The gas production from blend 25:75 was not significant, while there was no gas production from blend 0:100.

Chomini et al [11], carried out a study on the effects of co-digestion of cow dung and poultry manure on biogas yields. Five mix ratios of cow dung and poultry manure were subjected to anaerobic co-digestion. The mixture are in the ratio 100:0, 0:100, 50:50, 75:25 and 25:75 respectively. These were separately loaded into 13.6 L digesters locally fabricated and kept for an eight weeks retention period. The average biogas yields obtained ranged from 2961.0 to 2031.1 ml, in the order of the following mix ratios, 50:50, 25:75, 0:100, 100:0, 75:25 respectively.

Otun et al [12], investigated the anaerobic digestion and co-digestion of three different types of biodegradable wastes (food waste, fruit waste and cow dung) to generate biogas for energy consumption. A digester was constructed using a 25 Litres capacity plastic keg. The experiment was batch operated and daily gas yield from the plant was monitored for 30 days. The slurry temperature was monitored and presented. The digester was charged with these wastes in the ratio of 1:1, of waste to water respectively. The mesophilic temperatures range attained during the test period were between 25ºC-28.4ºC and a slurry temperature range of between 24.4ºC and 28.4ºC. It was found from the results obtained that the co-digestion of cow dung and food waste had the highest

biogas yield of 164.8%, this was followed by the co-digestion of the three wastes (cow dung, fruit waste and food waste) with a percentage of 91.0%. The co-digestion of cow dung and fruit waste had 83.9%, while cow dung, food waste and fruit waste had 79.8%, 77.4% and 76.4% respectively within the retention period. The results showed that co-digestion of multiple substrates produced more biogas than anaerobic digestion of single substrate. The study concluded that biogas is not just a renewable energy source but also an appropriate way of managing waste, having the potential to replace fossil fuel.

Babatola [13], experimentally investigated biogas yield pattern in household and some animal wastes in the laboratory. The study parameters included dilution and concentration of substrates, the effect of available space in the digester and the comparative biogas yield from different wastes. The methodology involved keeping all other parameters constant and just vary one for accurate experimental results. The ambient temperature, weight of substrate, volume of digester, were kept constant, while the ratio of water dilution was varied until optimum dilution ratio was achieved. Also, other parameters were kept constant while the digester volume was varied until optimum digester space was achieved. The results obtained showed that the optimum dilution and concentration were 2 ml/g and 500 mg/l respectively and the more airtight the digester is, the more the volume of biogas produced. It was found from the results that rabbit waste produced the highest volume of biogas followed by pig waste.

Ukpai and Nnabuchi [14], experimentally investigated a batch operated anaerobic co-digestion of wastes and compared the biogas yield from the co-digestion of cow dung, cowpea and cassava peel. A constructed 45 litres capacity metallic prototype biodigester was used to digest the wastes and the daily biogas yield was noted throughout the 30 days retention period. The slurry and ambient temperatures were also noted and presented. The digester was charged in the ratio 1:2, 1:5 and 1:5 of waste to water respectively. The mesophilic ambient temperatures range attained within the retention period was between 20^{o}C-32^{o}C and a slurry temperature range of 22^{o}C and 36^{o}C. It was shown from the results obtained that cowpea produced the highest methane content of 76.2%, followed by cow dung with 67.9% content and cassava peeling had the least methane content of 51.4%. The cow dung had the highest cumulative biogas yield of 124.3 L/total mass of slurry (TMS) while cow pea had 87.5 L/TMS and cassava peeling with lowest cumulative biogas yield of 87.1 L/TMS within the retention period. Also, on the conduct of a flame test, the generated gas was found flammable at different period during the digestion. Cow pea had the highest volume of flammable gas and flamed on the 7th day. These results showed that these wastes could be a source of renewable gas if managed properly since each of the waste sluggishly continued gas production after the 30 days retention time.

Ray et al [15], designed and developed a biogas production, purification and storage system suitable for use in the rural households. The biogas system was modelled after a floating drum type digester and fed with kitchen wastes and the gas collected by an elastic balloon. In addition, upgrading devices were also incorporated in the design to remove water vapour and hydrogen sulphide from biogas produced using two containers one with silica gel and the other steel wool.

Riyadi et al [16], in a study identified the characteristics of steel wool and efficiency of Hydrogen Sulphide (H_2S) concentration reduction from raw biogas. Biogas was allowed to pass through upgrading device containing steel wool. It was found from the result that steel wool media containing iron (Fe) and zinc (Zn) elements spread evenly on the media surface with about 97.5% mass. Hydrogen Sulphide (H_2S) concentration at inflow ranged from 68 to 111 ppm while it was reduced to between 0 to 21.2 ppm at the outflow at a mesophilic temperature range of between 29^{o}C and 33^{o}C. The result showed an average optimal hydrogen Sulphide removal efficiency of 97%, obtained at a flow rate of 0.1 L/min and a column height of 100 cm. It was concluded that steel wool can reduce Hydrogen Sulphide content in biogas at ambient temperature condition.

Chukwuma et al [17], investigated the optimal mixing ratio of cow dung and poultry droppings for biogas generated under tropical condition. The blends of cow dung and poultry droppings used were in the ratios 100:0, 75:25, 50:50, 25:75 and 0:100 respectively. Five locally fabricated 30 L digesters were used for the investigation. The obtained result showed the biogas yield in the order of, 25:75, 100:0, 50:50, 0:100 and 75:25 cow dung and poultry droppings respectively. The study suggested an optimum mixing ratio of 25:75 cow dung and poultry dropping which had 16.35 L/total mass of slurry (TMS) within the retention period.

STATEMENT OF THE PROBLEM

The fuel of choice for domestic applications whether for lighting, heating, cooking, etc are still fossil based because of their availability and accessibility. Nonetheless its use is not without adverse repercussions on the environment, plant life, and human health such as emission of pollutants and greenhouse gases (GHGs) which contribute to global warming and related environmental challenges. Thus, there is a strong interest by the world community for a switch from fossil fuels usage to sustainable ones like biogas. Though biogas is not an entirely new, clean and renewable energy, its production has traditionally been from a single animal feedstock such as cow dung, pig feces, chicken droppings etc. However, in most traditional African settings, animal farms consist of a combination of animals. Even though some of the feces from these farms are repurposed as feed for other

animals or used as fertilizer, direct application to fields can lead to the release of methane -a potent greenhouse gas. Therefore, co-digesting these feces for biogas will not only serve as source of clean fuel, but the effluent from its generation could also be used as manure, and hence the motivation for the study.

METHODOLOGY

This section explains in details the steps followed to achieve the results as follows:

Design Consideration

In order to design for the biodigester, factors such as quantity of raw material available, quantity of gas per day, hydraulic retention time (HRT), total solid (TS), volume of digester and gas holder volume were put into consideration. Also, the quantity of total solid (TS) value of a certain amount of material is pegged at 8% as adopted from most literature [3, 8, 9]. This value was found as most favorable indicator for biogas production rate [8] and [9]. The design is mathematically presented as follow [8]:

Total digester volume;

$$V_T = V_{gc} + V_{sl} + V_f + V_{gs} \quad (1)$$

Where:

Vgc - volume of gas collecting chamber
Vsl - volume of sludge layer
Vgs - volume of gas storage chamber
Vf - volume of fermentation

From which the working volume of the digester is expressed as

$$V_w = V_{gs} + V_f \quad (2)$$

Accordingly, the working volume, (V_w) is equally the product of quantity of feed (litres/day) and hydraulic retention time (day) often represented as:

$$V_w = V_{gs} + V_f \quad \text{and} \quad V_w = Q \times HRT \quad (3)$$

The following assumptions are considered in this study:

$$V_{gc} \leq 5\% V_T \quad (4)$$

$$V_{sl} \leq 15\% V_T \quad (5)$$

$$V_{gs} + V_f = 80\% V_T \quad (6)$$

$$V_{gs} = 0.5 \left(V_{gs} + V_f + V_{sl}\right) K \quad (7)$$

Where K = 0.4 $m^3/m^3/d$. (gas production rate per m3 of digester volume per day).

For the purpose of the research work and considering the assumptions above, the following dimensions were adopted:

$$V_{sl} = 15\ \% V_T \quad (8)$$

And

$$V_{gs} + V_f = 80\% V_T \quad (9)$$

Experimental set-up

The study employed an experimental methodology presented above, focusing the production of various ratios of the mixture of cow dung and chicken droppings for co-digestion followed the biodigester fabrication. Fresh cow dung and fresh chicken droppings without sawdust residue were obtained from an animal farm herder at Mahuta, Mando and a commercial poultry farm, Ajayi KE Poultry at kamazo Sabo both in Kaduna State, Nigeria. The experiment was performed at the Department of Mechanical Engineering, Nigerian Defence Academy, Permanent Site, Afaka Kaduna. The set up included ten 1.5 litre capacity laboratory scaled biodigesters, which were labeled and charged with different ratios of cow/chicken dung and water that made up 1kg of slurry per

digester. Each of the charged biodigester was replicated for each ratio, five of the charged biodigesters were kept at thermophilic (an elevated ambient) temperature of above 35℃ while the remaining five biodigesters were kept at mesophilic (ambient (room)) temperature of between 19℃ and 28℃. An elevated temperature was obtained by keeping the five digesters in an enclosed cupboard incorporated with 2 100watts bulbs to maintain constant temperature.

Production of the varying Mixtures of Feedstock

Fresh cow dung was obtained from an animal farm herder at Mahuta Mando in Kaduna State, while fresh chicken droppings without sawdust residue was gotten from a commercial poultry farm, Ajayi KE Poultry at kamazo Sabo Kaduna state. The digital electronic weigh balance was used to weigh the required quantity of dung and water to make the required slurry (feed). The ratio of cow dung to chicken droppings and water added was as shown in Table 1.

Table 1. Ratios of cow-chicken dung blends and water charged at elevated and ambient temperatures.

S/N	Digester	Qty of Blends (%)		Qty of Blends (kg)		Qty of Water added (kg)	Temp. Condition
		Cow Dung	Chicken Dropping	Cow Dung	Chicken Dropping		
1	CCH_{100amb}	100	0	0.500	0	0.500	$19^{O}C$-$28.1^{O}C$
2	CCH_{75amb}	75	25	0.375	0.125	0.500	$19^{O}C$-$28.1^{O}C$
3	CCH_{50amb}	50	50	0.250	0.250	0.500	$19^{O}C$-$28.1^{O}C$
4	CCH_{25amb}	25	75	0.125	0.375	0.500	$19^{O}C$-$28.1^{O}C$
5	CCH_{0amb}	0	100	0	0.500	0.500	$19^{O}C$-$28.1^{O}C$
6	CCH_{100elv}	100	0	0.500	0	0.500	$42.8^{O}C$-$9.6^{O}C$
7	CCH_{75elv}	75	25	0.375	0.125	0.500	$42.8^{O}C$-$9.6^{O}C$
8	CCH_{50elv}	50	50	0.250	0.250	0.500	$42.8^{O}C$-$9.6^{O}C$
9	CCH_{25elv}	25	75	0.125	0.375	0.500	$42.8^{O}C$-$9.6^{O}C$
10	CCH_{0elv}	0	100	0	0.500	0.500	$42.8^{O}C$-$9.6^{O}C$

RESULTS AND DISCUSSION

Composition of methane from the mixture slurry

The findings in this study are explained in figures 1 to 8. In figure 1, the percentage of methane generation per cow dung-chicken droppings slurry blend at both ambient (19℃-28.1℃) and elevated temperatures (27℃-59.6℃). Methane yield ranged from 45% to 82.59% for 0.000432 m³ volume of biogas. The highest methane yield was observed in CCH_{100amb} at ambient temperature (82.59%), followed by CCH_{75amb} (80.14%). At an elevated ambient temperature, CCH_{75elv} exhibited a methane yield of 75.06%. CCH_{25amb}, CCH_{50amb}, CCH_{100elv}, and CCH_{0amb} showed yields of 63.92%, 50%, 47.84%, and 45%, respectively. Blends CCH_{50elv}, CCH_{25elv}, and CCH_{0elv} at elevated temperatures did not generate gases, possibly due to the dominance of mesophiles that struggle under thermophilic conditions. Interestingly, CCH_{75} consistently yielded significant methane amounts at both mesophilic and thermophilic conditions, possibly indicating the presence of both types of bacteria. The study supports the synergistic effect of co-digestion in biogas production reported by Chukwuma et al [6].

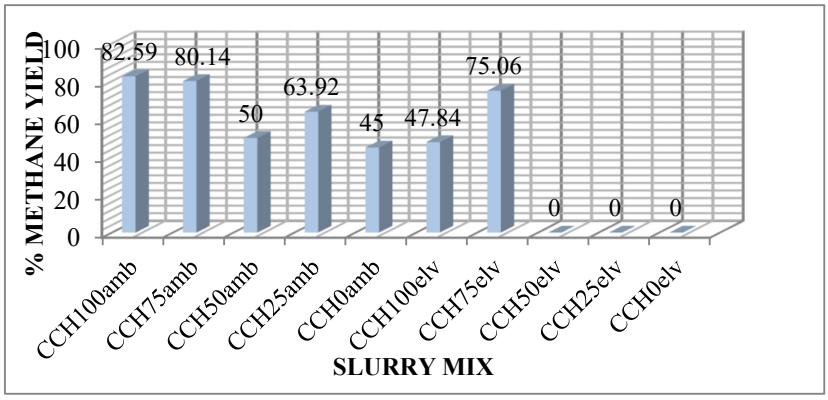

FIGURE 1. Percentage Methane (CH_4) Generations per Slurry Blend

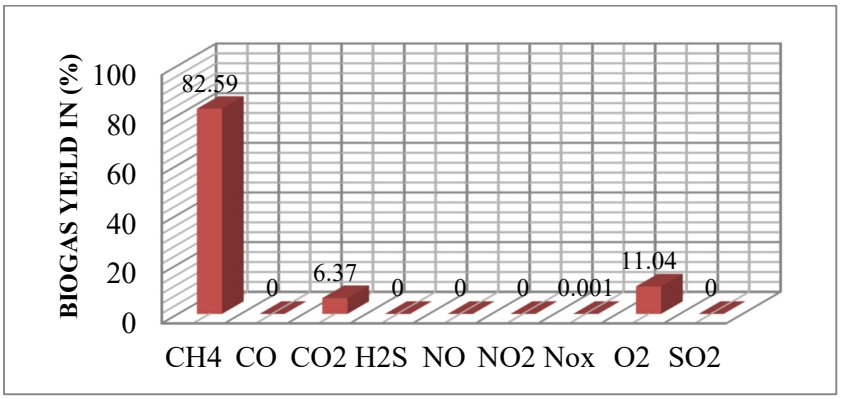

FIGURE 2. Percentage Compositions of Constituents in Slurry Blend CCH_{100amb}

In figures 3 to 7, the percentage compositions of biogas constituents in individual slurry blends $CCH_{100amb,}$ $CCH_{75,}$ $CCH_{50,}$ CCH_{25}, and CCH_0 investigated at ambient temperature. As described by Welink et al [10], biogas is a mixture of gases with methane as the desired component, and CO_2, H_2S, and moisture considered impurities. It can be observed from the graphs that the percentage of CO_2 and O_2 present were very small, 6.37% and 11.04% respectively when compared to CH_4 with 82.59%. Also, the quantity of, NO, NO_2 and NO_x were negligible, having 0.001, 0.0005 and 0.001 respectively. The incorporated scrubber in the biogas system design may account for this outcome in line with findings by Ryckebosch et al [11]. Traces of H_2S was absent in the generated gases from the slurry blend CCH_{100amb}, perhaps this is owing to the steel wool incorporated in the biodigester design.

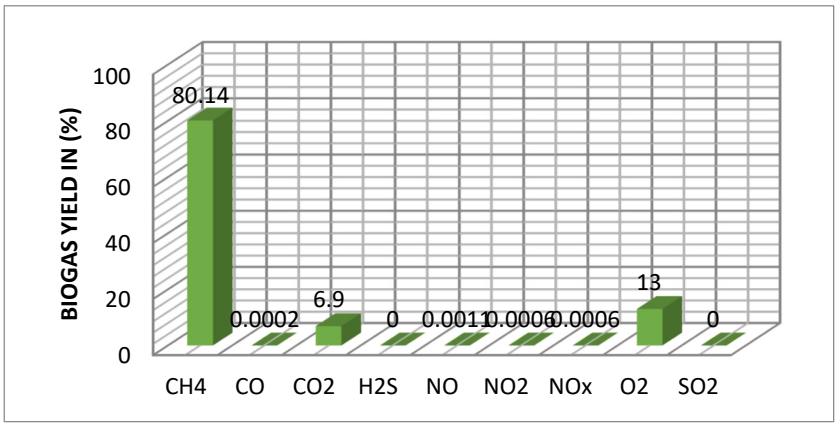

FIGURE 3. Percentage Compositions of Constituents in Slurry Blend CCH_{75amb}

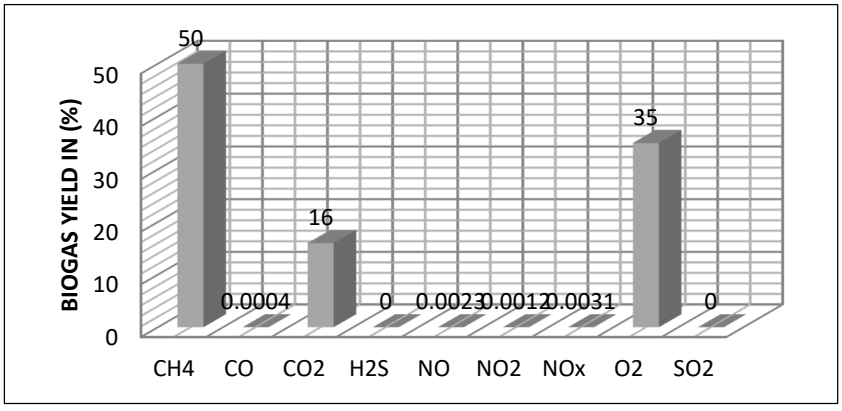

FIGURE 4. Percentage Compositions of Constituents in Slurry Blend CCH_{50amb}

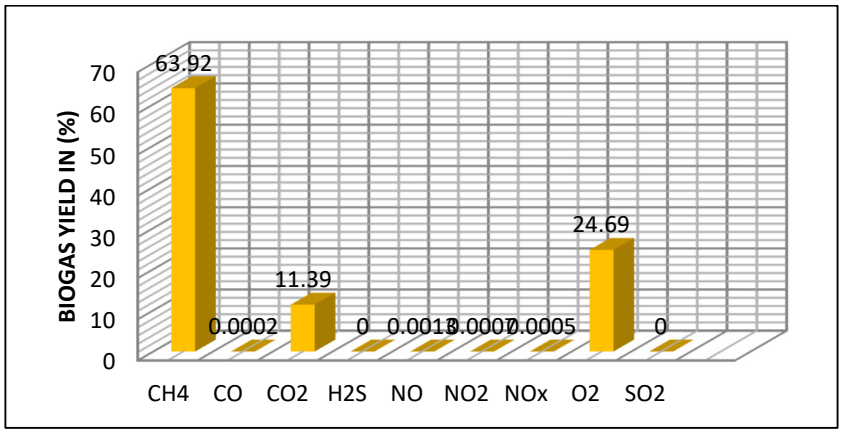

FIGURE 5. Percentage Compositions of Constituents in Slurry Blend $CCH25_{amb}$

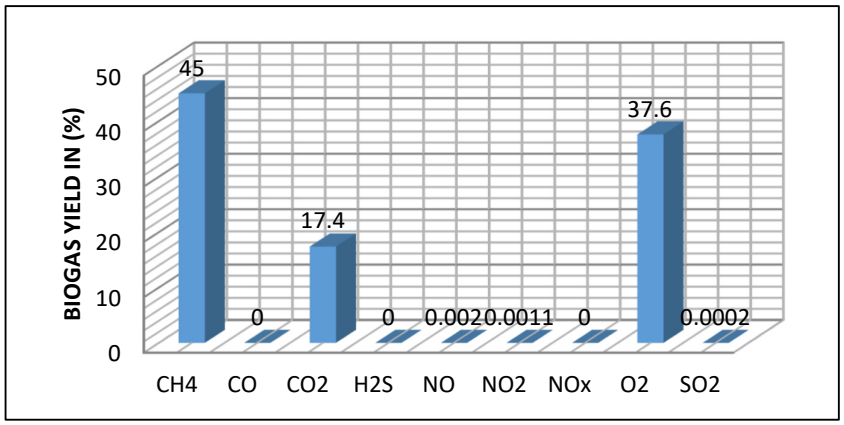

FIGURE 6. Percentage Compositions of Constituents in Slurry Blend CCH_{0amb}

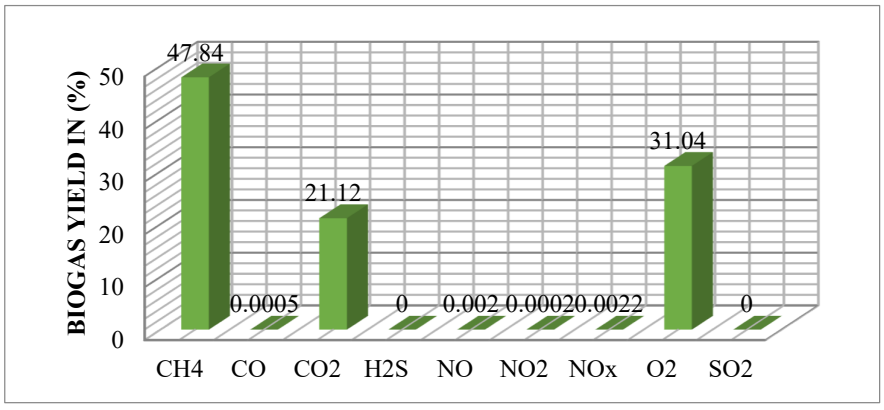

FIGURE 7. Percentage Compositions of Constituents in Slurry Blend CCH_{100elv}

Figures 8 and 9 present the percentage compositions of biogas constituents in slurry blend CCH_{100elv} investigated at elevated temperature. It reveals similarly that the percentage of CO_2 was small compared to percentage of methane generated. This outcome may be attributed to the incorporated scrubber in the biogas system design. H_2S traces were also absent in the gases generated from the slurry blend, due to the steel wool in the biodigester design, which traps H_2S also reported by [12].

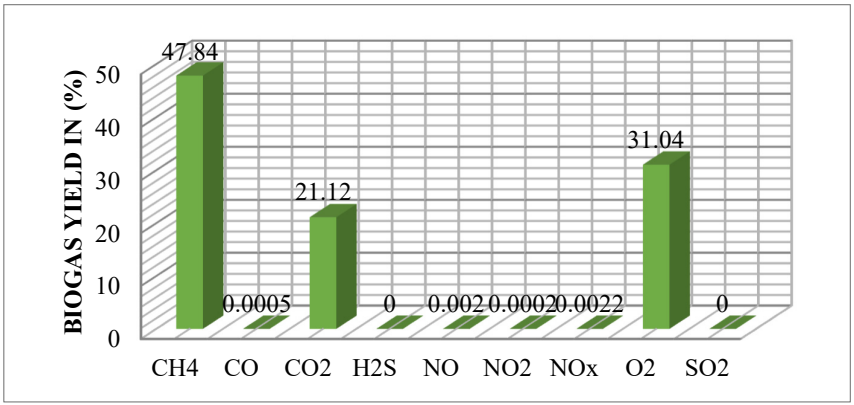

FIGURE 8. Percentage Compositions of Constituents in Slurry Blend CCH_{75elv}

Temperature profiling

We also determined the mean lowest slurry temperature on different days in order to understand the influence of the least temperature on the feedstock on different days from the first day of the test until 14 days. The results are presented as:

Variation of mean lowest slurry temperature on day 2

The variation of mean lowest slurry temperature on day 2 for the different slurry mix obtained at average elevated temperature of 27oC is presented in Figure 9.

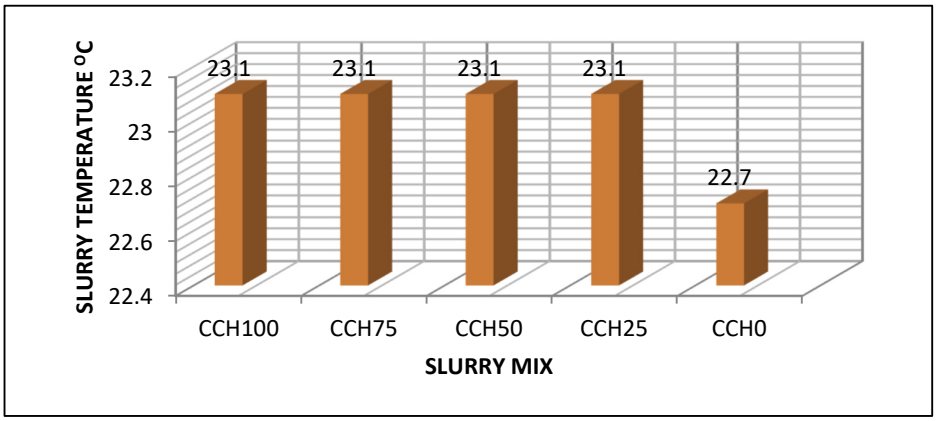

FIGURE 9. Variation of mean lowest slurry temperature on day 2.

From the graph above, it is observed from that the slurry temperatures vary between a minimum of 22.7°C and a maximum of 23.1°C. It is also observed that there was no significant change in the slurry blends temperatures as the blends CCH_{100}, CCH_{75}, CCH_{50} and CCH_{25} recorded the same temperature values of 23.1°C respectively, while blend CCH_0 recorded the least temperature value of 22.7°C. On day 2 of the study, there was epileptic power supply and the alternative solar power standby too failed. This could account for the insignificant change in slurry temperature as insignificant digestion might have taken place. This is in agreement with the reports of [18, 19, and 20], that the specific growth of the methanogenic bacteria during digestion process is directly proportional to the biogas production rate in batch condition which is a function of the operating temperature range as indicated in the study, [17] it is well known that temperature fluctuation is a major factor in biogas production and this could affect the action of the bacteria adversely.

Variation of mean lowest slurry temperature on day 8

The variation of mean lowest slurry temperature on day 8 obtained at average ambient Temperature of 19ºC is presented in Figure 10.

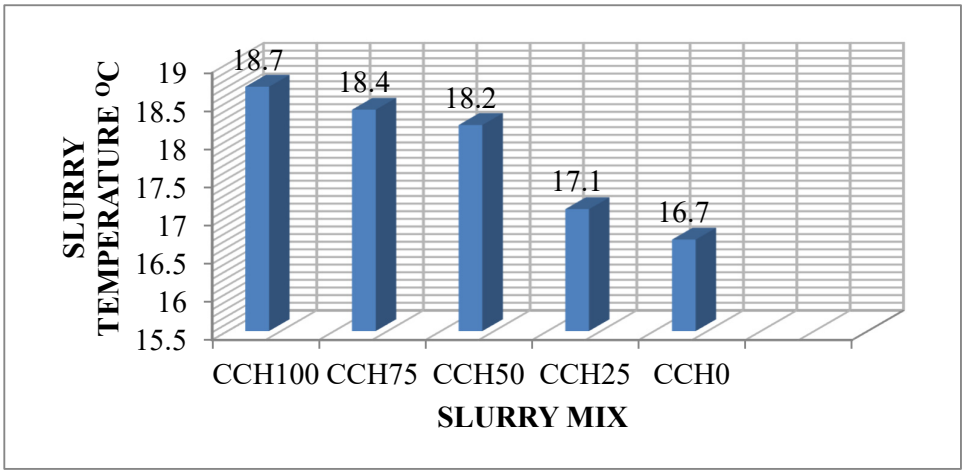

FIGURE 10. Variation of mean lowest slurry temperature on day 8.

It is observed from the above figure that the slurry temperatures generally vary between a minimum of 16.7ºC and a maximum of 18.7ºC. The blend CCH_{100} recorded the highest temperature of 18.7ºC. Next to it was blend CCH_{75} with a temperature of 18.4ºC, then CCH_{50} 18.2ºC, blend CCH_{25} 17.1ºC and blend CCH_0 with the least temperature record of 16.7ºC as expected from the literature [21]. It was also observed during the investigation that the temperature of the blend CCH_{100} under the mesophilic temperature condition throughout the investigation period recorded the highest temperature. The reason for this could be as reported by Babalola [13], and Ukpai and Nnabuchi [14] that the decomposition of cow dung takes longer period before generation of biogas could be achieved because cows feed on fibers which require longer period to be digested by the microorganism. This accounts for the high rise of temperature recorded because the more work is done by the microorganism the higher the energy or heat produced. It was also observed during the investigation that with increase in chicken mixture ratio in the blends, the slurry temperatures drop. The reason for this could be as reported by Marchaim [22] that poultry droppings digest faster than cow dung. As can be seen in the figure, the addition of chicken droppings into the blends, boosted decomposition.

Variation of mean slurry temperature on day 14

The variation of the mean slurry temperature on day 14 obtained at average ambient temperature of 23.8oC is presented in figure 11.

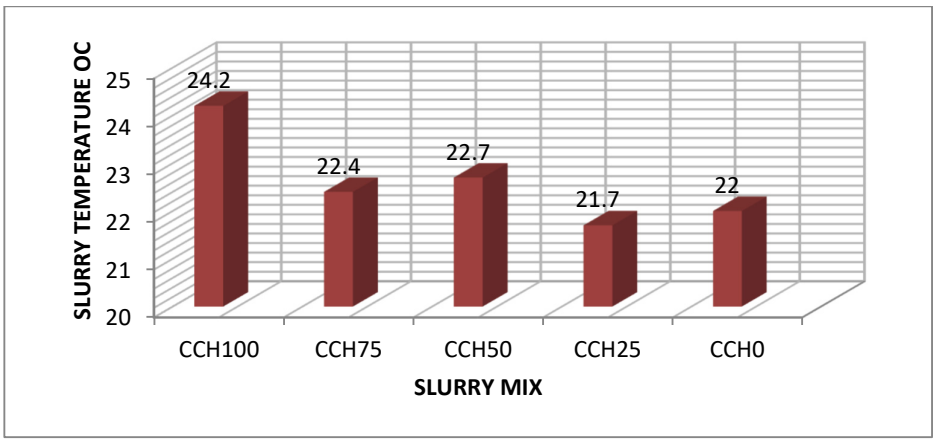

FIGURE 11. Variation of Mean Slurry Temperature on Day 14

The slurry temperatures were observed to vary between a minimum of 21.7ºC and a maximum of 24.2ºC as seen from figure 11. The blend CCH_{100} recorded the highest temperature of 24.2ºC, followed by blend CCH_{50} with a temperature of 22.7ºC. This was closely followed by blend CCH_{75} with a temperature of 22.4ºC, and then blend CCH_0 with a temperature record of 22.0ºC, while blend CCH_{25} recorded the least slurry temperature of 21.7ºC. As earlier noted by Jepma and Nakicenovic [21], that anaerobic digestion is a heat generating process, this may account for the variation in the slurry temperatures. The observed results are in agreement with those in the literatures [3, 14 and 22] as earlier stated.

CONCLUSION

In this study, methane yield composition from a slurry of the mixture of cow dung and chicken slurry was evaluated. Five different combinations of the mixture were considered; a ratio comprising of 100% cow dung, then a 75% cow dung:25% chicken droppings, followed by 50%-50% of each, a 25% cow dung to 75% chicken slurry and lastly, a 100% chicken slurry. It was observed that the best ratio for optimal biogas yield was blend CCH_{75}. The biogas generated was devoid of impurities such as H_2S and moisture. The study's noteworthy contribution lies in identifying CCH_{75} as the optimal blend for methane yield among the co-digested ratios. This finding adds valuable insights to the field of biogas production, affirming the significance of blend composition in enhancing methane generation. The study further supports existing knowledge on the synergistic effects of co-digestion in biogas production, emphasizing the importance of bacterial types in the digestion process. In conclusion, this study contributes valuable insights into the design, operation, and optimization of laboratory-scaled biodigesters for efficient biogas production.

REFERENCES

1. M. Hazirika, "Homo Erectus/Egoster and Out of Africa: Record Developments in Palloantropology Prelubttres Archaelogy". *Intensive course in Biological Anthropology,* EAA Summer School ebook 1:35-41'16 – 30 June, 2007.
2. J. Grab, C. Meyer, I. Weeks, R. Collett, I. Galball, J. Todd, F. Carnovate, R. Joynt, A. Hinwood, H. Berko and S. Brown, S. "Emissions from Domestic Solid Fuel Burning Appliances (Wood-heaters, open fire places*)" Technical Report,* No.5, Environment Australia, March, 2002.
3. R. Edwards, R. "Review 21 Emissions of Health-Damaging Pollutants from Household stoves" WHO Indoor Air Quality Guidelines: Household Fuel Combustion. Accessed February 2018.
4. O.O. Desalu, O.O. Ojo, E.A. Ariyibi, T.F. Kolawole and A.F. Ogunleye, Pan African Med J, **12**(2) (2012)
5. Global Alliance for Clean Cook stoves, "Comparative Analysis of Fuels for Cooking: Life Cycle Environmental Impacts and Economic and Social Considerations" Eastern Research Group (ERG). Accessed February 2018.
6. E.C. Chukwuma, I.C.E. Umeghalu, L.C. Orakwe, E.E. Bassey and J.N. Chukwuma, African J Agricult Res, **8**(18), 1940-1948 (2013)
7. N.H.S. Ray, M.K. Mohanty and R.C. Mohanty, Int J Renew Energ Res, **6**(2) (2016)
8. M.I. Simeon, J. Edache, and D.A. Eyeowa, Biogas Production from the Co-digestion of Cow Dung and Poultry Droppings using a Plastic Cylindrical Digester, Proceedings of the 2017 Annual Conference of the School of Engineering and Engineering Technology (SEET), The Federal University of Technology, Akure, Nigeria, 11-13 July, 2017.
9. A.O. Moses, O. Oyetola and A.A. Noor, J Chem Pharmaceutical Res, **8**(4), 112-118 (2016)
10. A. Mangibo, T. Elijah, I. Ibifuro, and S.M. Yahaya, Sci Res Essays, **4**(9), 861-866 (2009)
11. M.S. Chomini, C.I.C. Ogbonna, B.C. Falemara and P. Micah, IOSR J Agricult Veterinary Sci, **8**(11), Ver. I 48-56 (2015)
12. T.F. Otun, O.M. Ojo, F.O. Ajibade and J.O. Babatunde, Int J Energ Environ Res, **3**(3), 12-24 (2015)
13. J.O. Babatola, African Res Rev, **2**(4), 54-68 (2008)
14. P.A. Ukpai and M.N. Nnabuchi, Advanc Appl Sci Res, **3**(3), 1864-1869 (2012)
15. N.H.S. Ray, M.K. Mohanty and R.C. Mohanty, Int J Energ Environ Res, **6**(2) (2016)
16. U. Riyadi, G.A. Kristanto and C.R. Priadi, "Utilization of Steel Wool as Removal Media of Hydrogen Sulfide in Biogas". 2nd International Tropical Renewable Energy Conference (i-TREC) IOC Conf. Series: Earth and Environmental Science 105, 012026, 2017
17. E.C. Chukwuma, I.C.E. Umeghalu, L.C. Orakwe, E.E. Bassey and J.N. Chukwuma, African J Agricult Res, **8**(18), 1940-1948 (2013)
18. A. Gupta, R. Chandra, P.M.V. Subbarao and V.K. Vijay, J Sci Ind Res, **68**, 624-629 (2009)
19. A.B.,Rabah, A.S. Baki, L.G. Hassan, M. Musa and A.D. Ibrahim, Sci World J, **5**(4), 2010 (2010)
20. A. Nopharatana, P.C. Pullammanappallil and W.P Clarke, Waste Manage, **27**, 595-603 (2007)

21. C.J. Jepma, and N. Nakicenovic, “Sustainable Development and the Role of Gas”, EDReC/IIASA/IGU (2006),
22. U. Marchaim, Biogas Processes for Sustainable Development. Publication Division, Food and Agriculture Organization of the United Nations. Viale delle Terme Di Caracalla, Rome, Italy. http//www.fao.org/docrep/t0541e/t0541e06.htm. (1992),

Simulation of Misalignment Induced by Sun Tracking Errors in High-Concentrator Photovoltaic Systems Across Different Regions

Ourraoui Imane [1,a] and Ahaitouf Ali[1]

[1]*Laboratory of Intelligent System Georessources and renewable energies, Faculty of science and technology, Sidi Mohammed ben Abdallah university, B.P. 2202 – Imouzzer Road,Fez ,3000, Morocco.*

[a)] Corresponding author: *imane.ourraoui@usmba.ac.ma.*

Abstract. The purpose of this study is to test our prototype sun tracking system for CPV in strong condition and assess the structural misalignment and deformation induced sun tracking error caused by weight and wind loads for the proposed structure system in different loading scenarios namely Madrid Spain and Ifrane Morocco. The wind load on the tracker decreases as the elevation angle increases, and a large recirculation zone and suction pressure field are identified on the tracker's leeward side. The maximum wind load is always located on the tracker's pedestal. As the elevation angle decreases, the wind load on the pedestal increases. The wind load distribution on the CPV modules and tracker was used as a load input for analyzing the structural deformation of the entire system (CPV modules and tracker). Based on the von Mises criterion, the maximum simulated misalignment under the given loading conditions which is acceptable to obtain a high accuracy for these two regions.

INRODUCTION

The rapid growth of photovoltaics (PV) has spurred the development of various types of solar cells, including silicon-based cells, thin-film cells, and III-V multi-junction cells, which may become the most promising power generation technologies over the next 30 years. Among these, concentrator photovoltaics (CPV) stand out, as they use optics to focus sunlight onto a small solar cell, thereby reducing the cell's size. CPV technology, which has been developed over the past 30 years and is now at the commercial operation stage, holds the record for the highest power output per solar cell area [1-4]. To maintain the high conversion efficiency, CPV only absorbs direct normal irradiation (DNI) and requires accurate sun-tracking of the solar tracker. The two-sun tracking system with its azimuth-elevation axes is the most common configuration. The sun tracking system tracker must meet two major requirements: first, it must be able to maintain an overall stiffness within sub-degree accuracy so that acceptance-angle losses of the CPV module are not reduced. Next, it can provide maximum service for high wind loads. Several research has dealt with this subject [5]. Beginning by J. C. Wu et al studied who analyzed the wind load and identified the effects of elevation angle and wind speed on the structural strength of the tracker. Such wind load distribution on the CPV modules induced structural deformation of the whole system. This deformation induced different levels of off-set angle on the CPV module which may reduce the tracking accuracy and degrade the electricity output of CPV system [6]. M. Yamamoto et al developed a bio-mimetic strategy using a Kalman filter that rapidly detects and rectifies any installation errors. This innovation method attempted to optimize the collection of energy using solar panels and performed wind stability for a concentrated photovoltaic tracker's complete system based on 1.4, Kw CPV panel and consists of the process controller with Kalman filter, After the Kalman filter learns the installation position, the errors are automatically counteracted by the control software, the system's tracking accuracy is evaluated using an additional sensor. A CCD camera is attached to the CPV panel, and the sun image is pattern-matched to confirm the sun's positions, the wind velocity on the three days, which sometimes exceeds 10 m/s, is simultaneously recorded. The tracking accuracy deteriorates very little under these conditions, showing the system to have good wind resistivity. The simulation test confirmed that it can reduce wind by 20%.[7]. C. K. Lin and J. Y. Fang investigated the effects of wind loadings on structural deformation in high concentrator photovoltaic (HCPV) using finite element analysis. The authors analyzed wind pressure distribution under a wind speed of 12 m/s, The largest maximum concentrator misalignment for all the calculated conditions was 0.142° which is far below the acceptance angle of 0.5° [8].

Technologies and Materials for Renewable Energy, Environment and Sustainability
AIP Conf. Proc. 3321, 040002-1–040002-7; https://doi.org/10.1063/5.0289794
Published under an exclusive license by AIP Publishing. 978-0-7354-5231-2/$30.00

Imane and Ali proposed a new design for CPV sun tracking system and simulate the misalignment-induced sun tracking error in high concentrated photovoltaic in Fez Morocco. The simulation results showed that the maximum simulated misalignment still negligeable, and is estimated to 4.6×10-6°, for a wind speed of 3.3m/s. it is anticipated that the examined high CPV system (HCPV) will work safely under these effects [9,10]. Developing CPV trackers with high precision sun movement tracking is still a challenging problem to be taken up. Besides more reliable tracking depends also on the site of use given that the meteorological conditions are not equivalent very where. Hence this study aims to test the reliability of our own design of CPV sun tracking system in a different region which is Madrid Spain and Ifrane Morocco. In addition to analyze the misalignment of our own sun-tracking system in these regions. Wind load is then calculated and input into a parallel study's structural analysis. by finite element analysis (FEA) approach. This paper is organized as follows.in Section 2. The requirement of the Sun tracking system is discussed. In section.3 we described the new prototype design before listing the approach used to calculi the misalignment of the system in the new regions. In the fourth section, the results and some remarques are presented putting an end with a conclusion.

PERFORMANCES ISSUES IN CPV TRACKING

The main reasons behind the sun tracking performance decline can be either related to the precision of pointing the tracker. Or related to the acceptance angle. On the one hand, losses resulting from tracking accuracy, are basically the exactness of the sun position coordinates. In fact, even if the sun ephemeris is very precise they can lose their reliability once mounted in the field by many error sources, which can highly degrade their final tracking accuracy. These errors are as follows: the geographical positioning error of the sun tracker and the clock error of the controller unit. The great disadvantage of the closed loop strategy is that they do not perform well on cloudy days and it needs maintenance of the solar sensor, it is necessary also to perform a precise installation of the camera. The precision can also be influenced by the tracking drive and its control system, which essentially depends on the performance of tracking speed control and on the mechanical backlash introduced by the drive's gearings. there can be errors related to a bad adjustment of the zero of the encoders or due to the aging of the mechanical installation.

Concerning acceptance angle losses these are due to the precision of sun tracking. The higher the tracking precision, the wider the acceptance angle becomes. When the solar modules are not sufficiently well aligned among themselves their capturing surfaces are not in the same plane (or parallel planes). It results in a decrease in the global acceptance angle of the set of modules, which will produce a decrease in the optical performance every time the pointing vector of the sun tracker lies outside the reduced acceptance angle. More the deformation of the tracker structure plays an important role in enhancing the performance of the accuracy, it also causes the decrease of acceptance angle [10] as shown in Figure 1.

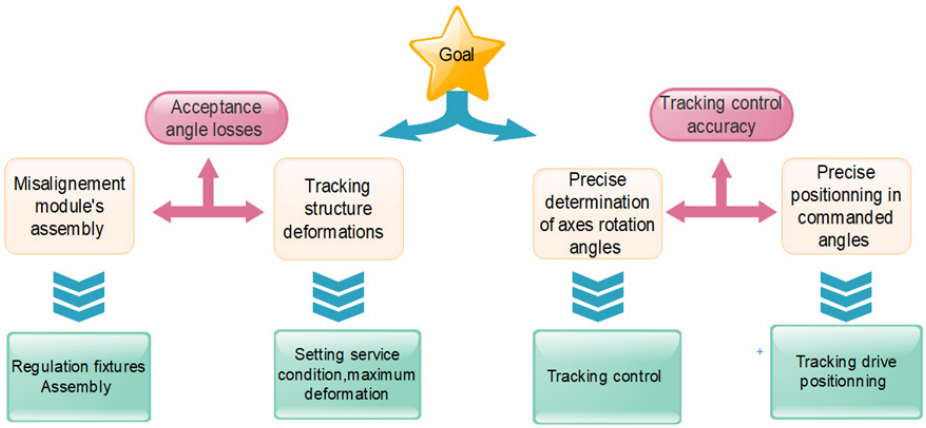

FIGURE 1. Requirements of CPV Sun Tracking System

WIND-RESISTANT SUN TRACKING SYSTEM: SYSTEM DESCRIPTION AND THEORICAL APPROACH FOR WIND LOADS ANALYSIS

Figure 2 presents a photograph of the Concentrated Photovoltaic (CPV) unit utilized in this experimental study. This unit was engineered and manufactured by Magpower and was provided as part of the LOUCOUM project, a Moroccan initiative aimed at advancing solar energy technologies. Currently, the module is deployed and operational at the SIGER laboratory within the Sidi Mohamed Ben Abdellah University (USMBA), where it serves both research and performance validation purposes. The key electrical characteristics and specifications of the CPV module are outlined in Table 1 for reference. Structurally, the module is composed of six identical compartments. Each compartment integrates a high-efficiency triple-junction solar cell, which is thermally coupled to an aluminum-based heat spreader to ensure adequate dissipation of thermal energy under high solar concentration. In addition, a secondary optical element (SOE) is incorporated in each compartment to enhance and homogenize the irradiance distribution received by the photovoltaic cell, thereby improving overall conversion efficiency. To concentrate sunlight onto the active cell area, each compartment is equipped with a square Fresnel lens made of polymer optical element (POE), measuring 350 mm × 350 mm. These lenses focus incoming solar radiation onto the smaller surface area of the high-efficiency cells. The optical design of the system yields a nominal geometric concentration ratio of 800 suns, which allows for efficient use of expensive semiconductor materials while maximizing energy yield. The full assembly of the CPV module has a total length of approximately 2.1 meters and a height of 35 centimeters, as illustrated in Figure 3. This compact form factor, combined with modular scalability and advanced thermal management, makes the system particularly suitable for high-insolation regions such as North Africa, where solar resource availability is abundant and consistent.

FIGURE 2. Concentrated photovoltaic (CPV) units located in our laboratory in Fez Morocco.

TABLE 1. Characteristic of the used CPV module (according to the data sheet of the supplier).

Characteristic	Value
Peak Power (Pm)	110w
Open Circuit Voltage (V_{oc})	17.70 V
Short Circuit Current (I_{sc})	7.70 A
Maximum Power Voltage (V_{mp})	15.27 V

The first step is to estimate and measure the wind velocity since the focus is on the wind load and velocity distribution effects on the tracker's strength. Using Retscren software, the greatest wind speed for Madrid Spain, is 5 Km/h, and for Ifrane Morocco which is 20 km/h. The wind force, that the wind exerts on the Sun tracker, is composed of the drag force, which is the horizontal component, and the lift force, the vertical one. The definition and calculation of these components are shown in [9].The proposed architecture of the solar tracker with the CPV module specific to this investigation is depicted in Figure 3 and also is described in [9].Catia Software is used for design as well as wind flow modeling on the tracker's surface. A thorough finite element (FE) study was conducted over the whole tracker structure with the CPV unit, as described in Figure 4. Three different configurations were simulated. The first panel was set at 0° with respect to the horizontal plane, whereas the plates in the second and third are slanted at 45° and 90° with respect to the horizontal plane, respectively. The finite element method was used to investigate the structural deformation of the CPV module and solar tracker because of wind load spreading on the used module and tracker structure. The mesh used is the same in which is described in Table 2.

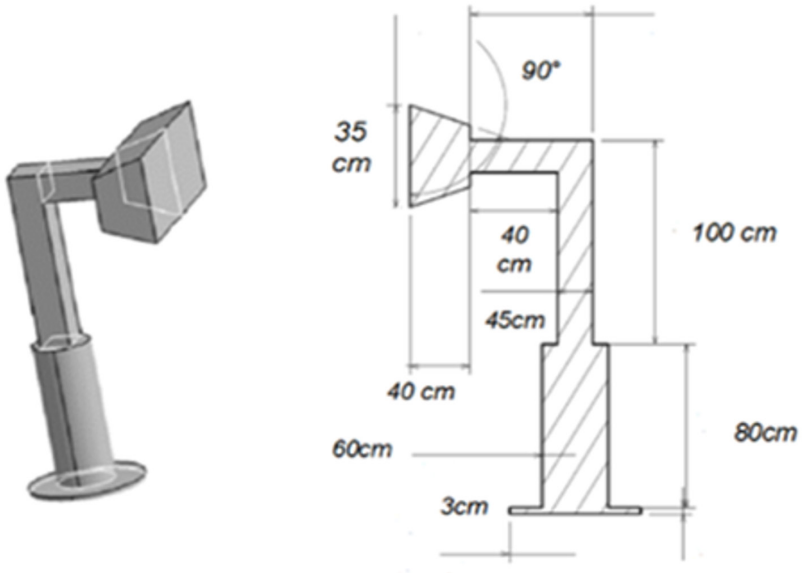

FIGURE 3. Model of the tracker with the CPV unit in Catia software.

TABLE 2. Mesh information of the proposed design.

	Proposed Design
Element size	284.45 - 1422.26 mm
Number of elements	69032
Number of knots	117254
Degree of freedom	381564

RESULTS AND DISCUSSION

Figure 4 illustrates the wind pressure distribution on the CPV module at different panel orientation angles (0°, 45°, and 90°). The surface pressure maps provide insights into the areas experiencing the highest wind loads and allow evaluation of the resulting misalignments on both the CPV module and the tracker structure.
In the case of Ifrane (Figure 5), the misalignment is approximately 1.94×10−3° at 0°, increases to 2.47×10-3° at 45°, and reaches a maximum of 4.55×10-3° at 90°. Although the wind load appears to be more evenly distributed between the structure and the CPV unit at 90°, the simulations reveal that the CPV unit itself is more exposed due to the strong winds commonly observed in this region. This highlights a critical point: even when the mechanical design ensures balanced distribution, extreme wind conditions can directly impact the CPV unit. In such cases, it is recommended to halt system operation temporarily to prevent damage and preserve system integrity.

For Madrid, Spain (Figure 6), the misalignment remains significantly lower: 4.21×10−4° at 0 °, 2.62×10−4°at 45 °, and 9.2×10−4° at 90 ° elevation angles, respectively. The most critical wind loads are concentrated on the upper section of the pedestal and on the CPV unit. The analysis also confirms that as the elevation angle increases, the distribution of the CPV module's weight becomes more symmetric across the horizontal axis, reducing the combined effects of torque and bending moments. Conversely, at lower angles, the wind force exerts a greater moment due to the less favorable load distribution.

Simulation results confirm that across all tested elevation angles, the misalignment remained below 0.1°, ensuring reliable structural behavior under typical operating conditions. This finding is particularly relevant for the design of trackers in moderate-wind regions like Fez, where lighter structural materials could be used without compromising system stability. However, in wind-intensive areas such as Ifrane, special attention must be paid to the CPV unit's direct exposure to avoid potential degradation.

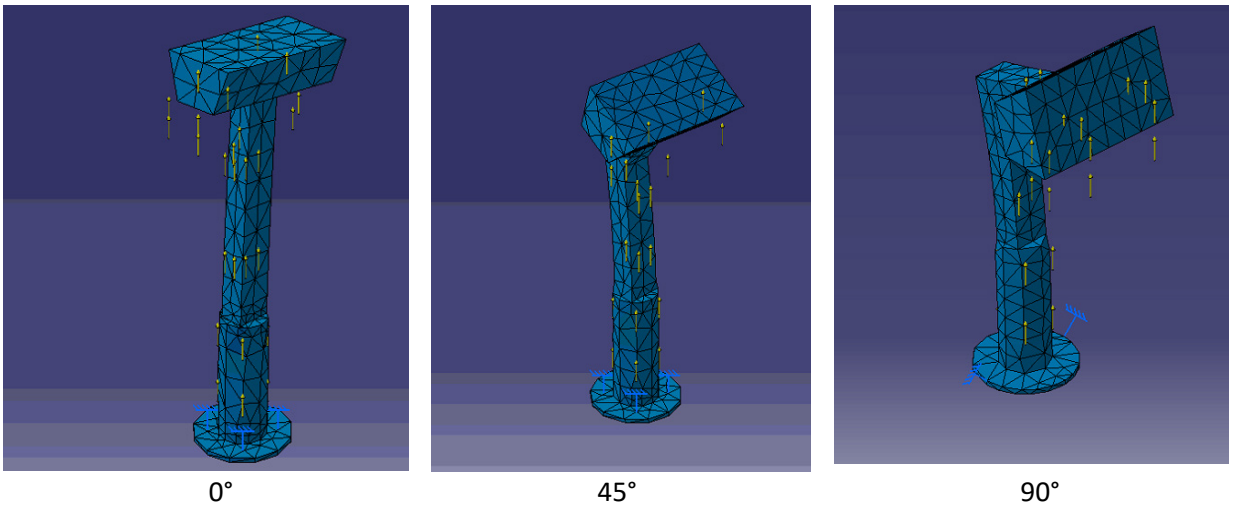

FIGURE 4. Three Configurations designed by Catia software to calculate the misalignment of CPV tracking system.

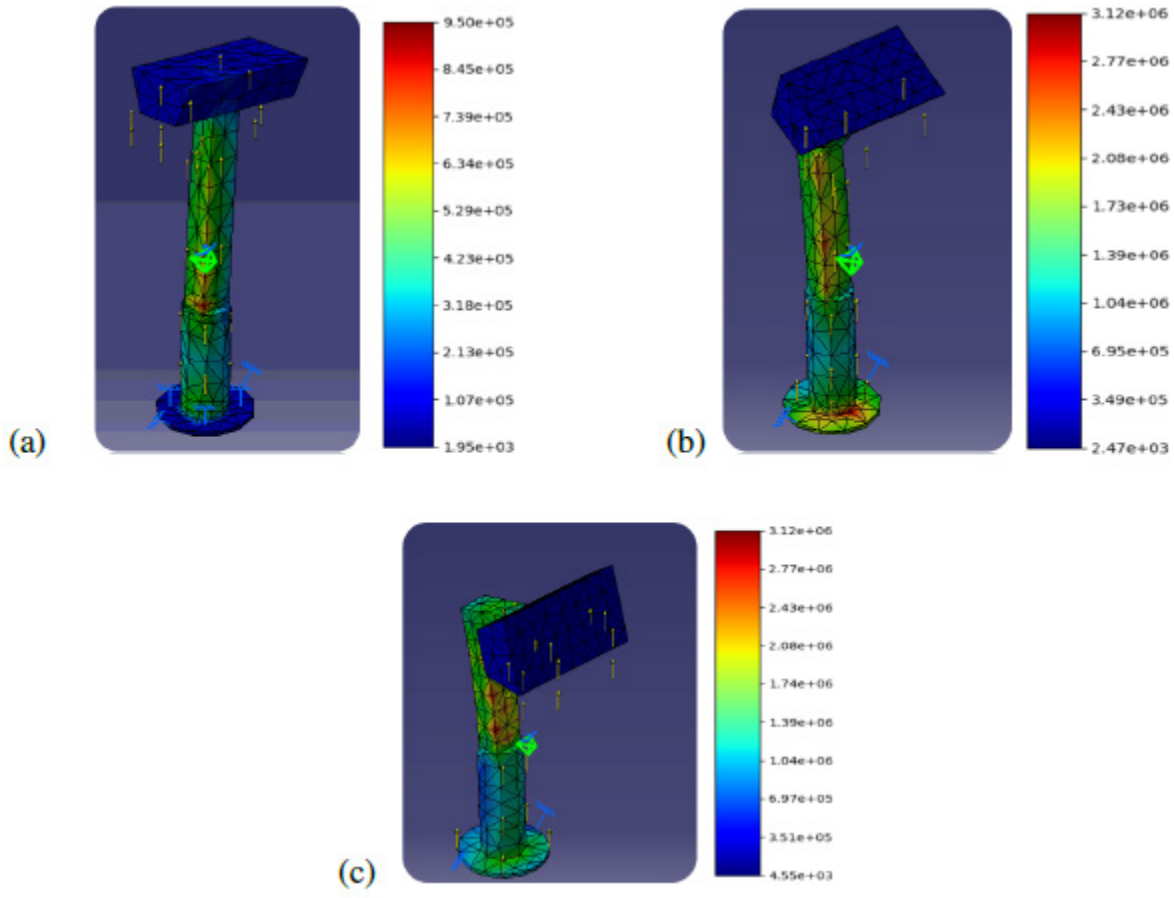

FIGURE 5. Pressure distribution (wind load) and observed deformations on the CPV module, as well as the streamline pattern of the side view of the solar tracker windward at different elevation angles (0° , 45° , 90°) in Ifrane Morocco.

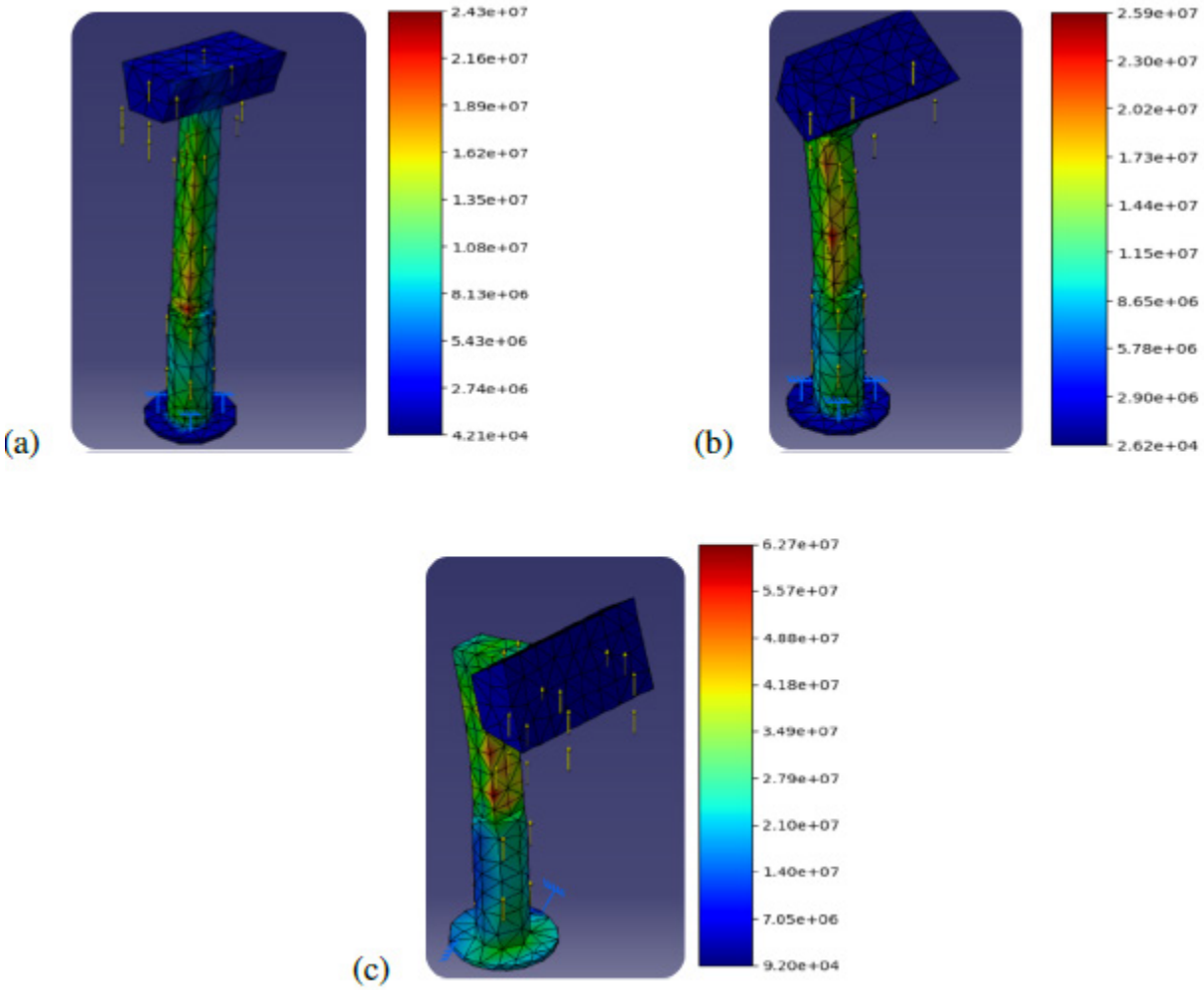

FIGURE 6. Pressure distribution (wind load) and observed deformations on the CPV module, as well as the streamline pattern of the side view of the solar tracker windward at different elevation angles (0°, 45°, 90°) in Madrid Spain.

CONCLUSION

We defined the key requirements for deploying a CPV sun tracking system, emphasizing the need for a compact, lightweight structure to facilitate installation, maintenance, and transportation. To ensure the system's reliability, structural simulations were conducted under demanding environmental conditions, specifically those of Madrid and Ifrane. These analyses confirmed the system's robustness and adaptability across varying weather scenarios. The finite element method (FEM) applied in this study proved effective in assessing structural deformation and angular misalignment across different geographical settings. Simulations revealed that the highest wind pressure is consistently concentrated on the front face of the CPV modules. Furthermore, the tracker's pedestal is identified as a critical area that must be monitored closely, as it bears significant mechanical stress. The wind load distribution served as the primary input for evaluating overall structural deformation. The maximum recorded misalignment was 4.55×10^{-3}°, which remains well below the critical threshold for ensuring high-efficiency operation in HCPV systems.

REFERENCES

1. M. Wiesenfarth, I. Anton and A.W. Bett, *Appl Phys Rev*, **5**(4), (2018).
2. P. Pérez-Higueras, JP. Ferrer-Rodríguez, F. Almonacid and E.F. Fernández, *Renew Sustain Energ Rev*, **94**, 143–153 (2018).
3. M. Burhan, S.J. Oh, K.J.E. Chua and K.C. Ng, *Solar Energ,* **137**, 352–363, (2016).
4. I. Luque Heredia, P.h.D. Thesis.Control de seguimiento solar de alta precisión con autocalibracion, Universidad Politécnica de Madrid, pp. 1–305 (2010).
5. C. Algora and I. Rey-Stolle, Handbook of Concentrator Photovoltaic Technology. (2016).
6. J.C. Wu, K.H. Lin and C.K. Lin, *AIP Conf Proc,* **1277**, 145–148 (2010).
7. M. Yamamoto et al., A biomimetic strategy for designing easily-installable CPV tracking system with high wind resistivity, Conference Record of the IEEE Photovoltaic Specialists Conference, 1766–1769, (2013).
8. C.K. Lin and J.Y. Fang, *AIP Conf Proc*, **1556**, 210–213 (2013).
9. Ourraoui, Imane, and Ali Ahaitouf. "Investigation of the feasibility and potential use of sun tracking solutions for concentrated photovoltaic Case study Fez Morocco." *Energy Reports* 8 (2022): 1412-1425.
10. Imane, Ourraoui, and Ahaitouf Ali. "Modelling of Control Strategy for Sun Tracking of Concentrated Photovoltaic (CPV) Systems and Performance Analysis of Optical Losses Due to Tracking Errors." *Journal of Physics: Conference Series*. Vol. 2857. No. 1. IOP Publishing, 2024.

Bioethanol Production From Corn Straw via Steam Explosion Pretreatment and Fed-Batch Enzymatic Hydrolysis

Tatiana Ramírez-Contreras[1,a)], Laura Camila Porras Borja[1,b)], Yineth Piñeros-Castro[1,c)]

[1]*Faculty of Natural Sciences and Engineering, Universidad Jorge Tadeo Lozano, 110311 Bogotá, Colombia.*

[a)]tatiana.ramirezc@utadeo.edu.co
[b)]laurac.porrasb@utadeo.edu.co
[c)]Corresponding author: yineth.pineros@utadeo.edu.co

Abstract. The growing global energy demand and depletion of fossil fuel reserves necessitate the development of alternative, clean energy sources. Agro-industrial residues, such as corn straw (CS), are abundant wastes that, due to their lignocellulosic nature, can be u This study evaluates bioethanol production from corn straw (CS) through steam explosion (SE) pretreatment followed by enzymatic hydrolysis (EH). SE was conducted at severities of 3.0, 3.4, and 3.8, with optimal results at 11 minutes and 180°C (Severity 3). The pretreatment improved the accessibility of cellulose and hemicellulose for hydrolysis. Subsequent EH using the fed-batch method achieved a yield of 200 mg reducing sugars per gram of biomass. Fermentation with *Saccharomyces cerevisiae* yielded 41.57 mg ethanol per gram of CS. The results indicate that SE and EH treatments, combined with the fed-batch methodology, enhance fermentable sugar production and bioethanol conversion efficiency. Additionally, this process minimizes the formation of microbial inhibitors, demonstrating its potential for sustainable bioethanol production from agro-industrial residues like corn straw. Further optimization could increase yields and improve the economic viability of this approach.

INTRODUCTION

The use of fossil fuels, particularly oil, currently accounts for the majority of global power generation. According to the International Energy Agency, Colombia consumed 32 million tons of oil in 2023, while the United States consumed 2200 million tons in the same year [1]. Consequently, the search for alternative energy sources has become crucial to meet global demand and reduce pollution levels.

One viable alternative is the use of agro-industrial waste, which holds potential for the production of sugars that can be converted into ethanol for industrial use. This approach offers a sustainable solution for fuel production without competing with food crops. Lignocellulosic materials are particularly abundant and renewable, forming a structural component of plants. It is estimated that the annual global production of lignocellulosic biomass is approximately 181.5 billion tonnes. This significant quantity underscores its potential as a sustainable source for biofuel production and other value-added products, emphasizing the importance of efficient biomass utilization in addressing global energy needs [2]. Ethanol derived from lignocellulosic biomass has gained significant attention due to its potential to produce biofuels from agricultural waste. However, the biological conversion of various lignocellulosic feedstocks faces economic and technical challenges [3]. Key factors for reducing costs include efficient raw material utilization for high productivity, high ethanol concentration during distillation, recovery of co-products, and process integration to reduce energy demand [4].

Straw has commonly been used for bioethanol production, with wheat straw, rice straw, canola, rye, and barley being the most utilized in various countries [5]. Straws typically contain 30-50% glucan, 34-40% cellulose, and 14-17% lignin [6]. Corn crops produce substantial biomass, of which only about 50% is harvested as grain. The residual biomass can be categorized into stover, cobs, and husks, generating significant amounts per hectare annually [7]. Post-harvest, corn crops yield substantial waste, including stalks, husks, and straw, amounting to 20-25 tons per hectare [8]. The lower lignin content in corn plant residues makes them more digestible and richer in soluble sugars, thus more accessible for cellulose conversion.

To utilize the sugars present in these materials, initial fractionation is required to remove physical and chemical barriers impeding the conversion of cellulose and hemicellulose to fermentable sugars [9]. Various pretreatment methods, including chemical, physical, or combinations thereof, have been studied [10]. However, many pretreatments

Technologies and Materials for Renewable Energy, Environment and Sustainability
AIP Conf. Proc. 3321, 040003-1–040003-7; https://doi.org/10.1063/5.0289605
Published under an exclusive license by AIP Publishing. 978-0-7354-5231-2/$30.00

involve high energy costs or significant environmental pollution and generate inhibitors that affect the fermentation process.

Several studies have investigated pretreatment methods for corn straw capable of yielding high sugar concentrations. These include chemical treatments with calcium hydroxide [11], sulfuric acid [12], acetone and phosphoric acid [13], lactic and acetic acid [14], and ionic liquids [12]. Biological pretreatments have recovered significant amounts of sugars [15], while hydrothermal treatments have achieved high yields [16]. Steam explosion (SE) is the most common and effective pretreatment for biomass fractionation, inducing structural alterations due to high temperature and pressure [17]. This treatment has been successfully applied at high severities to various biomass types [18-24].

SE pretreatment is considered effective and sustainable, requiring no reactive or contaminating agents, thus offering a profitable process. This pretreatment aims to solubilize hemicellulose, making cellulose more accessible for enzymatic hydrolysis and avoiding inhibitor formation [25]. Consequently, high concentrations of fermentable sugars can be obtained for bioethanol production.

By other hand, fed-batch enzymatic hydrolysis (EH) is a methodology designed to increase yield and enhance volumetric productivity. Compared to solids-recycling and sequential hydrolysis, fed-batch hydrolysis prevents the accumulation of enzyme activity, potentially reducing the required equipment size [26]. Studies indicate that fed-batch simultaneous saccharification and fermentation (SSF) of pretreated substrates demonstrates excellent fermentability and higher ethanol yield compared to batch processes [27]. Overall, fed-batch SSF processes show superior volumetric productivity, ethanol yield, and maximum ethanol concentration [28]. The objective of this paper is to evaluate the bioethanol production process from corn crop residues in a fed-batch simultaneous saccharification and fermentation (SSF).

MATERIALS AND METHODS

RAW MATERIALS

Yellow corn (Zea mays) from the Biosystems Center of Jorge Tadeo Lozano University was used in this study. Characterization included the quantification of moisture, lignin, ash, cellulose, and hemicellulose following the methodology of the National Renewable Energy Laboratory (NREL) [29].

STEAM EXPLOSION PRETREATMENT

The material was ground and sieved to obtain particle sizes between 2.5 and 1.0 mm, then impregnated with water for 24 hours before undergoing steam explosion (SE) pretreatment. Severity of the SE treatment was defined using a mathematical model based on first-order kinetics and the Arrhenius law, accounting for the combined effect of temperature and residence time [30]. Experiments varied biomass residence time (5, 11, and 28 minutes), registering severities of 3.0, 3.4, and 3.8, respectively, with a temperature of 180°C. The experiments were conducted in a 10L reactor, coupled to an expansion tank and reboiler. After treatment, the solid and liquid fractions were separated for characterization. The efficiency of the steam explosion treatment was determined by calculating the overall yield of sugars produced during the enzymatic hydrolysis. Enzymatic hydrolysis (EH) was performed using Celluclast (15 FPU/g substrate), β-glucosidase (NS50010 - 12.6 IU/g substrate), Novozyme (NS 50010), stirred 150 rpm, at 50°C with an initial concentration of 50 g/L of solids in 0.05 M citrate buffer at pH 4.8. Hexokinase assays, and HPLC chromatography were conducted for sugar quantification.

FED-BATCH SIMULTANEOUS SACCHARIFICATION AND FERMENTATION

Fermentation was performed for both the solids and liquids from the pretreatment using the enzyme complex mentioned above, at 250 rpm and 50°C. For solids, a suspension of 50 g/L of solids was started, adding 50% of the initial mass every 12 hours for 56 hours to reach a final concentration of 125 g/L. After enzymatic hydrolysis (fed-batch), fermentation was carried out with the Ethanol Red strain, activated 24 hours before with 20 g/L glucose and a broth containing yeast extract (2.5 g/L), NH4Cl (2 g/L), KH2PO4 (1 g/L), and MgSO4*7H2O (0.3 g/L). The hydrolysate was supplemented with the same salts and 5 mL of inoculum (final biomass concentration 1 g/L). Fermentation was conducted at 100 rpm and 30°C for 24 hours, with monitoring every 6 hours. The liquids from

pretreatment were hydrolyzed (24 hours, 50°C, 250 rpm) and fermented (48 hours, 30°C, 100 rpm) using the same enzymes, salts, and yeast. Ethanol quantification was performed by HPLC.

RESULTS

The chemical composition of the untreated starting material was determined to be 34.33% cellulose, 16.60% lignin, 25.84% hemicellulose, and 22.02% ash.

STEAM EXPLOSION PRETREATMENT

This stage involves physically altering the complex structures of the material to facilitate enzymatic hydrolysis (EH) by fractionating the major components of the cell wall. This process increases the surface area and makes the material highly accessible to enzymatic attack, thereby reducing carbohydrate degradation. The alteration of the lignocellulosic matrix is evidenced by changes in the texture and appearance of the material, as shown in the photographs in Figure 1.

(a) (b) (c) (d)

FIGURE 1. Photographs of evidence. (A) Original PM; (B) Severity 3.0; (C) Severity 3.4; (D) 3.8 Severity.

The analysis indicates that increasing the severity of steam explosion pretreatment decreases solid recovery, with values dropping from 63% at severity 3.0 to 56% at severity 3.8. This trend suggests that higher severity levels cause greater biomass degradation and solubilization. Optimizing pretreatment conditions is crucial to balance effective biomass breakdown while maximizing solid recovery for subsequent enzymatic hydrolysis.

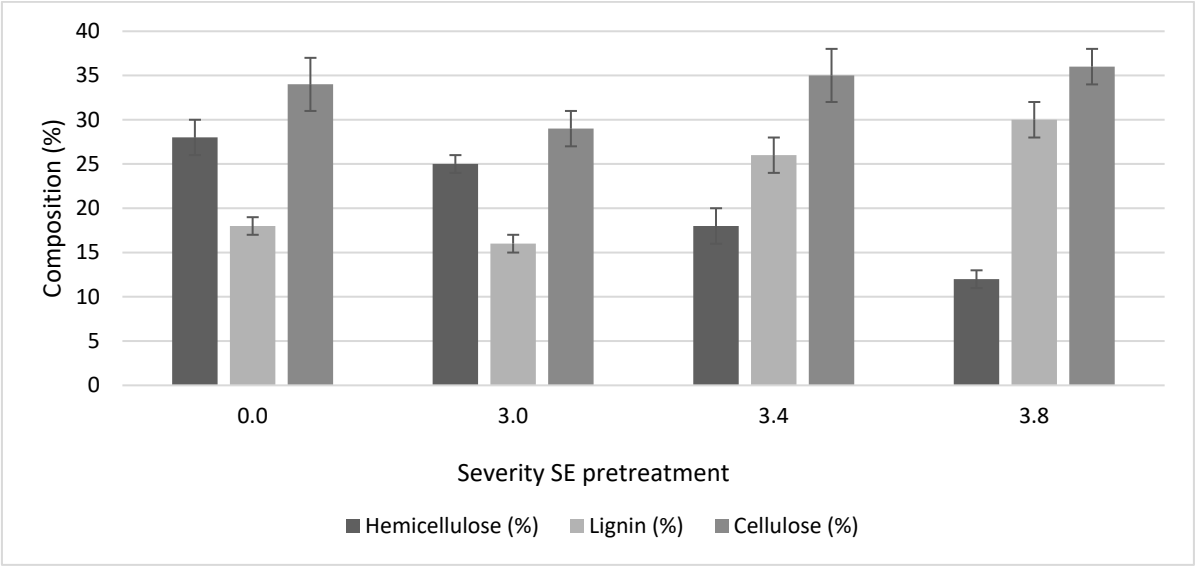

FIGURE 2. Composition of original and pretreated material at different severities

Figure 2 present the composition data of materials. With increasing severity, cellulose and lignin concentrations slightly increase, while hemicellulose decreases. As severity increases from 0.0 to 3.8, hemicellulose decreases from 28% to 12%, while cellulose and lignin increase from 34% to 36% and 18% to 30%, respectively. This occurs because lignocellulosic biomass releases organic acids like acetic acid under severe conditions, leading to acidic auto-hydrolysis. In the liquid fraction, the solubilization of the hemicellulosic fraction increased from 15.1% at a severity of 3.0 to 24.5% at a severity of 3.8.

During the enzymatic hydrolysis (EH) stage, cellulose and hemicellulose polymers are broken down into their respective monomers. This type of hydrolysis has advantages over chemical hydrolysis, including reduced corrosion, low enzyme consumption, and low toxicity of hydrolysates. Additionally, it requires less costly equipment since it is performed at atmospheric pressure and near-ambient temperature and, does not require chemical agents. However, it has some drawbacks, such as long reaction times, high enzyme costs, and the inhibition of hydrolysis by products like cellobiose and glucose [31]. In Figure 3, the overall yield of reducing sugars (RS) obtained from each treatment is shown. The yields were 9.16% for the 5-minute treatment, 15.39% for the 11-minute treatment, and 19.71% for the 28-minute treatment. These data indicate that longer steam explosion (SE) pretreatment times increase the RS yield during enzymatic hydrolysis (EH), as the material becomes more delignified, making cellulose and hemicellulose more accessible for hydrolysis.

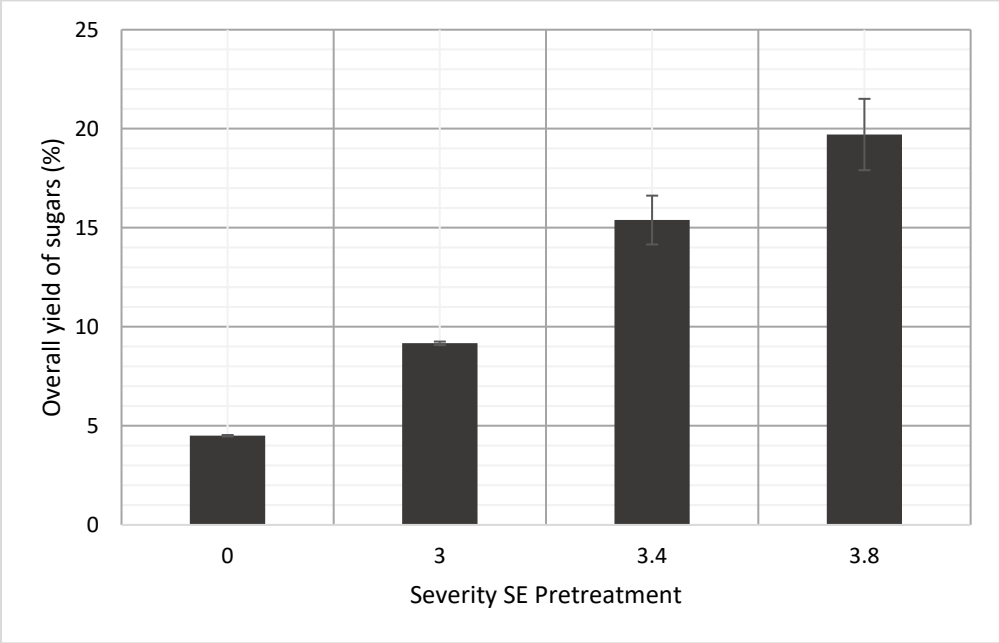

FIGURE 3. Overall yield of sugars of original and pretreated material at varying severity levels

For this fed-batch hydrolysis, the 11-minute (Severity 3) pretreated material was chosen because it showed good performance in EH. Additionally, higher severity treatments, such as the 28-minute duration, were more likely to generate microbial inhibitors during pretreatment [31]. Conversely, the lowest severity treatment resulted in low sugar yields, which were not conducive to ethanol production.

FED-BATCH SIMULTANEOUS SACCHARIFICATION AND FERMENTATION

One of the variables to modify in enzymatic hydrolysis (EH) is the biomass load in the process, as it promotes an increase in fermentable sugar concentration and subsequently ethanol concentration in the following fermentation. However, this same biomass load can affect EH efficiency [32], as high biomass concentrations decrease the hydrolysis rate [33], resulting in low glucose yield.

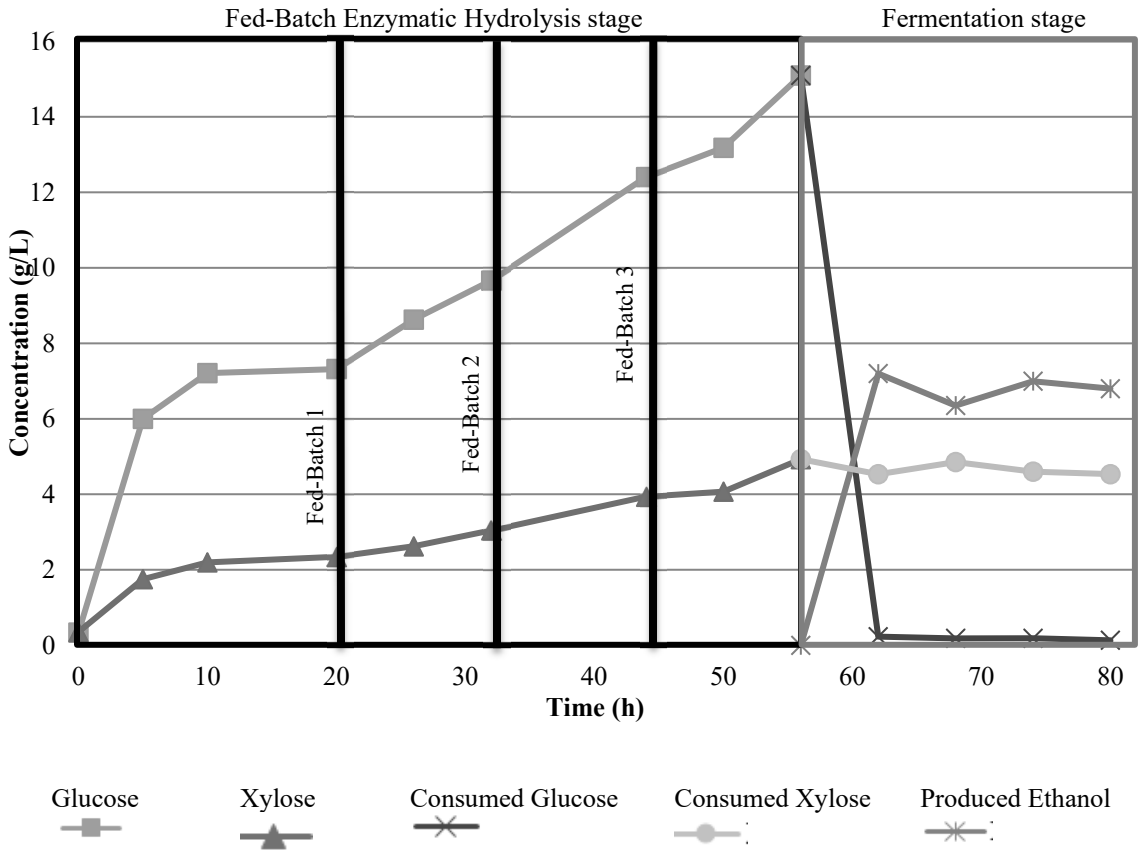

FIGURE 4. Fed batch enzymatic hydrolysis (Stage with 3 fed batch of substrate) and Fermentation

Figure 4 illustrates the behavior of EH and fermentation over a total of 80 hours, showing an increase in fermentable sugar concentration over time in EH and ethanol production after the inoculation of *Saccharomyces cerevisiae* at 56 hours of EH. By the end of the process, 32.08 g/L of reducing sugars were obtained, consisting of 46.2% glucose, 15.15% xylose, and 38.64% other sugars (cellobiose and arabinose).

EH monitoring revealed that glucose concentration increased significantly during the first 10 hours, then remained constant until the first biomass load, after which glucose concentration increased again. This is because higher solid concentrations lead to increased reaction yield and rate [33]. Each time biomass was added to the hydrolysis, the corresponding amount of enzymes was also added to maintain the enzyme-substrate ratio.

It is clearly evident that glucose concentration decreases as ethanol concentration increases. The most drastic change in concentrations occurs within the first 6 hours of fermentation, as the highest fermentative activity takes place during the initial 24 hours. Subsequently, it was found that the concentrations of glucose and ethanol remain constant. This is because there are no more fermentable sugars available for the yeast, ending the fermentative activity. Approximately 7 g/L of ethanol and 15 g/L of glucose were obtained from enzymatic hydrolysis, with a total of 44 g/L of reducing sugars. The fermentation of sugars derived from lignocellulosic material is mostly carried out with *Saccharomyces cerevisiae.* However, this yeast cannot ferment pentoses derived from hemicellulose, as evidenced in Figure 4.

The yield (Yps) obtained in this study was 0.4769, which is very close to the theoretical value of 0.5114 reported in the literature [34]. This indicates that the process achieved satisfactory yields. Additionally, no inhibitors were generated during the steam explosion (SE) pretreatment that could affect this final stage. The fermentation efficiency was found to be 93.24%, indicating a high conversion rate of glucose to ethanol with the strain and operating conditions used. However, the ethanol yield based on the pretreated material (PM) was 41.57 mg ethanol/g PM, which is low compared to the 251 mg ethanol/g PM reported in the literature [35]. Therefore, it is necessary to improve the enzymatic hydrolysis process, considering that the fermentation achieved high yield levels.

CONCLUSIONS

This study demonstrates that steam explosion (SE) pretreatment effectively fractionates the main chemical components of corn straw, with the 11-minute treatment (Severity 3) preventing the generation of fermentation inhibitors. This pretreatment enhances enzymatic hydrolysis and fermentation, resulting in higher glucose yields compared to the 5-minute treatment. Additionally, a biomass load of 31.5 g resulted in an ethanol production of 41.57 mg ethanol/g CS, although this is lower than literature values of 251 mg ethanol/g PM, indicating the need for improved EH processes. Despite this, a high theoretical yield of 93.24% was achieved, compared to the 86.8% yield from other studies using SE pretreatment. These results highlight the potential of SE and EH for efficient bioethanol production from corn straw, emphasizing the importance of optimizing pretreatment and hydrolysis conditions to enhance overall yields and reduce costs. Further research should focus on refining EH processes and exploring the use of genetically engineered strains to improve ethanol production.

ACKNOWLEDGMENTS

The authors would like to thank Jorge Tadeo Lozano University for funding this project.

REFERENCES

1. International Energy Agency, Oil Market Report - September 2023, IEA, 2023. Available at: IEA Oil Market Report
2. I. Haq, K. Qaisar, A. Nawaz, F. Akram, H. Mukhtar, X. Zohu, Y. Xu, M. W. Mumtaz, U. Rashid, and W.A.W. A.K. Ghani, *Catalysts* **11**(3), 309 (2021).
3. M. Broda, D. J. Yelle, and K. Serwańska, *Molecules* **27**(24), 8717 (2022).
4. M. Galbe and G. Zacchi, *Biochem. Eng. Biotechnol,* **108**, 41–65 (2007).
5. S. Saval, *Biotecnol,* **16**(2), 14–46 (2012).
6. M. Ramos, E. Laveriano, and L. San Sebastián, *Trends Food Sci. Technol.* **131**, 14–27 (2023).
7. H. Escalante Hernández, et al., Atlas del potencial energético de la biomasa residual en Colombia (2008).
8. H. Zhang, W. Jia, and R. Feng, *Sustainability* **15**(14), 11362 (2023).
9. A.M. Sánchez Riaño, et al., *Revista Tumbaga* **1**, 61–91 (2010).
10. R. Singh, et al., *Renew. Sust. Energ. Rev.* **32**, 713–728 (2014).
11. W.E. Kaar and M. T. Holtzapple, *Biomass Bioenerg.* **18**(0), 189–199 (2000).
12. R.M. Pezoa Conte, Estudio del pretratamiento con ácido diluido y líquidos iónicos en residuos agrícolas para la producción de bioetanol de segunda generación. Santiago de Chile, Chile: Universidad de Chile (2010).
13. A.S. Amarasekara, Feedstocks for cellulosic ethanol production. Handbook of cellulosic ethanol. Texas, USA: Scrivener Publishing LLC; Wiley (2014).
14. H. Xu, M.H. Thomsen, and A.B. Thomsen, *J. Biotechnol.* **139**(4), 300–305 (2009).
15. C. Wan and Y. Li, *Bioresour. Technol.* **101**(16), 6398–6403 (2010).
16. B. C. Saha, et al., *Ind. Crops Prod.* **44**(0), 367–372 (2013).
17. G. Li and H. Chen, *Biomass Bioenerg.* **67**(0), 1–7 (2014).
18. M. Jurado, et al., *Bioresour. Technol*. **100**(24), 6378–6384 (2009).
19. A. D. Moreno, et al., *Biochem. Eng. J.* **79**(0), 94–103 (2013).
20. C. Cara, et al., *Fuel* **87**(6), 692–700 (2008).
21. M. C. Fernandes, et al., *Bioresour. Technol.* **186**(0), 309–315 (2015).
22. M. D. Ferro, et al., *Biochem. Eng. J.* (2015).
23. E. Viola, et al., *Biomass Bioenergy.* **32**(7), 613–618 (2008).
24. M. Boluda Aguilar, et al., *Bioresour. Technol.* **101**(10), 3506–3513 (2010).
25. A. Pandey*, et al.,* Biofuels: Alternative feedstocks and conversion processes (2011).
26. V. Pihlajaniemi, *et al., Bioresour. Technol.* **153**(0), 15–22 (2014).
27. X. Zhao, et al., *Bioresour. Technol*. **135**(0), 350–356 (2013).
28. E. Tomás-Pejó, et al., *Fuel* **88**(11), 2142–2147 (2009).
29. A. Sluiter, B. Hames, R. Ruiz, C. Scarlata, J. Sluiter, D. Templeton, and D. Crocker, Natl. Renew. Energy Lab. (2008). Determination of structural carbohydrates and lignin in biomass. Available at: http://www.nrel.gov/biomass/pdfs/42618.pdf.

30. Y. Liu, L. Chen, and F. Sun, *Biomass Bioenerg.* **164,** 106458 (2023)
31. E.P. Dagnino, E.R. Chamorro, S.D. Romano, F.E. Felissia, and M.C. Area, *Renew Energ.* **74**, 1–9 (2015).
32. A.A. Modenbach and S.E. Nokes, *Biotechnol. Bioeng.* **110,** 1527–1540 (2013).
33. O. J. Rojas, *Bioresour. Technol.* **102**, 4499–4510 (2011).
34. J. Choi, S. Jang, J. Kim, et al., *Renew. Energ.* **130,** 952–960 (2019).
35. J. Xu, M.H. Thomsen, and A.B. Thomsen, *J. Biotechnol.* **139,** 300–305 (2009).

Potential use of banana waste as fuel for the generation of electrical current

Segundo Rojas Flores[1,a)], Santiago M. Benites[1,b)], Magaly De La Cruz-Noriega[1,c)], Renny Nazario-Naveda[1,d)]

[1] Vicerrectorado de Investigación, Universidad Autónoma del Perú, Lima, Perú.
a) Corresponding author: srojasfl@autonoma.edu.pe
b) santiago.benites@autonoma.edu.pe
c) mdelacruzn@autonoma.edu.pe
d) rnazario@autonoma.edu.pe

Abstract. The demand for electrical energy has suffered a significant increase since industrialization, and currently, humanity can only carry out its daily activities if it has this supply. By 2024, an electricity supply of 1,614 TWh will be needed. Currently, efforts are being made to sustainably generate electrical energy through non-conventional alternatives to stop depending on fossil sources. In this sense, microbial fuel cells are presented as a promising alternative because they use a wide variety of wastes as a fuel source (MFCs). This research uses banana waste, which is abundant in the north and east of Peru; 4 kg of banana waste was used as fuel in single-chamber MFCs. The electrical current and maximum voltage shown were 3.591 ± 0.474 mA and 0.925 ± 0.087 V on the twelfth day, where they showed an optimal pH of 5.87 ± 0.34 whose electrical conductivity was 264.67 ± 24.72 mS/cm. The electrical power density shown was 2.571 ± 0.097 mW/cm^2 at a current density of 0.475 A/cm^2, with a $R_{int.}$ of 89.244 ± 9.747 Ω and a maximum oxidation-reduction potential of 247.63 ± 29.54 mV.

INTRODUCTION

Banana is one of the most essential fruits consumed in the subtropical and tropical areas of the planet; a 120-gr flat fruit contains approximately 70% water and 30% dry matter [1]. Its appearance varies from yellow to red, depending on its ripeness; in 2019, approximately 120 million tons were produced, and annual growth of 4.3% was forecast due to its high demand [2,3]. The high demand for this fruit is due to the variety of foods that can be tasted, such as dessert or baked, dried, roasted, and fried [4]. However, it has been estimated that 30-40% of this fruit is rejected for export due to failing to meet quality standards because they decompose in ripe fruits easily and quickly [5]. These high waste values have been reported as an excellent problem for companies and society because many are thrown into inappropriate landfills, causing environmental pollution [6,7]. On the other hand, MFCs (microbial fuel cells) are electronic devices that contain an innovative technology because they take advantage of the ability of microorganisms to generate electric current from carbon sources in organic waste [8]. MFCs produce electricity and water in their operation process, achieving a favorable approach for the ecosystems present in the environment [9]. The technology consists of two chambers (anodic and cathodic) that contain two electrodes (anodic and cathodic), which are responsible for capturing the electrons generated in the waste used as fuel; the electrons travel from one chamber to the other through an external circuit generating a flow of electrons and thus generating the electric current [10,11]. One of the main phenomena within microbial fuel cells is the exoelectrogenetic oxidation processes in the substrates used as fuel; this process occurs in the anodic chamber in the presence of protons and electrons produced by microorganisms [12,13].

Fruit waste has started to gain relevance in the field of renewable energy and microbial fuel cells, for example, Kalagbor et al. (2020) used papaya waste (12 Kg) as fuel in their microbial fuel cells, generating peaks of 22.9 mV and a power density of 0.2452 mW/cm^2 [14]. Pineapple waste has also been reported as fuel in single-chamber MFCs, managing to generate maximum peaks of voltage, power density and electric current of 0.99 ± 0.03 V, 513.99 ± 6.54 mW/m^2 and 4.95667 ± 0.54775 mA, using zinc and copper as electrodes [15]. Likewise, Kebaili et al. (2021) used fermented fruit juices as substrates in their MFC, where they included 6 ml of sucrose, generating voltage peaks of 0.140 V and a power density of 20 mW.m^{-2} [16]. One of the critical factors for generating adequate electrical energy in microbial fuel cells is the materials for the manufacture of electrodes [17]. Although materials such as carbon, graphite, carbon felt, and other derivatives have had an essential role in their development in recent decades, metallic materials have begun to be considered for their manufacture [18]. Metallic materials

Technologies and Materials for Renewable Energy, Environment and Sustainability
AIP Conf. Proc. 3321, 040004-1–040004-7; https://doi.org/10.1063/5.0289618
Published under an exclusive license by AIP Publishing. 978-0-7354-5231-2/$30.00

have a high electrical conductivity, thus generating a good flow of electrons and reducing losses or electricity leaks in this process [19]. However, one of the characteristics they lack is a high porosity in the process of capturing electrons, which is why research is being done on metallic-based electrodes to take advantage of the high carbon porosity and the high conductivity of metallic materials [20].

The primary aim of this research is to assess the electrical potential of a single-chamber microbial fuel cell, using banana waste and carbon and zinc electrodes as fuel, over a period of 25 days. To achieve this, we will monitor parameters such as power density, current density, voltage, chemical oxygen demand, internal resistance, electrical conductivity, oxidation-reduction power, and electric current. The potential benefits of this research are hopeful-it could provide a second, more productive use for silver waste, such as energy generation. This could lead to significant cost reductions for companies when this technology is scalable. Moreover, it could contribute to new knowledge in the field of biomass utilization for environmentally sustainable electricity generation.

MATERIALS AND METHODS

A. PREPARATION OF BANANA WASTE IN MICROBIAL FUEL CELLS

The microbial fuel cells were made of a cubic shape with polyethylene, with a capacity of 5 liters. A circular hole of 15 cm in diameter was made in the cube, where the zinc electrode used as a sample was placed, while the carbon electrode (area = 300 cm) used as an anode was placed in the center. Both electrodes were connected on the outside through a 50 Ω resistor, as shown in Figure 1. On the other hand, banana waste (4 kg) was collected from the Zonal Palermo market, Trujillo, Peru. The selection was carried out by the market merchants, who collected them in hermetic bags (adequately sealed) and took them to the laboratory. The waste in the laboratory was washed repeatedly to eliminate traces of impurities acquired from the environment. The banana waste was ground into a paste and placed in equal parts in the three microbial fuel cells.

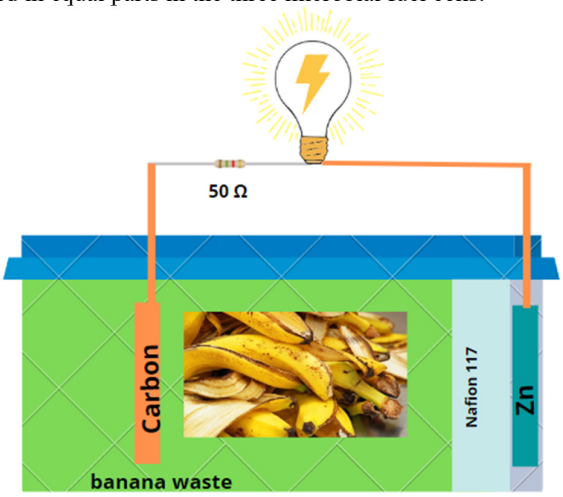

FIGURE 1. Design of the prototype used as MFC.

OBTAINING THE MONITORED PHYSICAL-CHEMICAL PARAMETERS

The current and voltage values were monitored for 25 days using a mustimeter (Prasek Premium PR-85, USA), while the cd (current density) and pd (power density) values were measured using the method described by Rojas-Flores et. (2022) whose external resistances were 15 ± 0.1, 30 ± 1.5, 60 ± 2.2, 120 ± 2.5, 240 ± 3.5, 400 ± 4.5, 550 ± 5.5, 620 ± 6.5, 720 ± 8.5, 1000 ± 20.5 Ω [21]. In this sense, the internal resistance was found using the power sensor (Vernier- ± 30V & ± 1000 mA, USA) and Ohm's law. Likewise, the pH and electrical conductivity values were monitored with a pH meter (110 Series Oakton, USA) and a conductivity meter (DC-4301, USA) during the 25 days of operation. The COD (chemical oxygen demand) values were measured using the closed reflux colorimetric method according to the NTP 360.502:2016 standard [22].

RESULTS AND DISCUSSION

The voltage values observed during the monitoring of the microbial fuel cells can be seen in Figure 2 (a), where the values increased from the first day (0.075 ± 0.005 V) to the 12th day (0.925 ± 0.087 V) and then showed a continuous decrease until the last day (0.466 ± 0.141 V). The successive increase in the voltage values is due to the minor electrochemical reactions in the substrate used, which generate a potential differential between the anodic and cathodic electrodes [23]. In the literature, it has been found that small values shown in the first days are due to the acclimatization period of the electrochemical compounds that occur over time [24]. In their research, Cheng et al. (2024) mentioned that the stabilization of the voltage values is due to the fact that the microorganisms have a better adhesion to the anodic electrode [25]. Rokhim et al. (2024) mention in their research that there is a relationship between the acidity of the substrate fruits and the voltage: the more alkaline the substrate, the voltage values will decrease, and the more acidic the fruit, the voltage values will increase [26]. The current values shown by the microbial fuel cells can be seen in Figure 2 (b); the MFCs showed an increase from the first day (0.820 ± 0.049 mA) to day 12 (3.591 ± 0.474 mA) and then slowly decreased until day 25 (1.509 ± 0.723 mA). The progressive increase in the electric current values is due to the gradual formation of the anodic biofilm, which is responsible for the capture of electrons generated in the metabolic process of microorganisms, while the decrease in electrical values is due to the loss of carbon sources during the elapsed time [27,28]. Zafar et al. (2023) mention that the design of the MFC interferes with the uptake of electrons by the electrodes because it does not allow degradation of the substrate or it does not allow the contents of the substrate to be mixed homogeneously [29]. Yaakop et al. (2023) obtained an electricity curve similar to our research, mentioning that the decrease in the electric current values is due to the final life cycle of microorganisms due to a lack of carbon sources in the substrate [30].

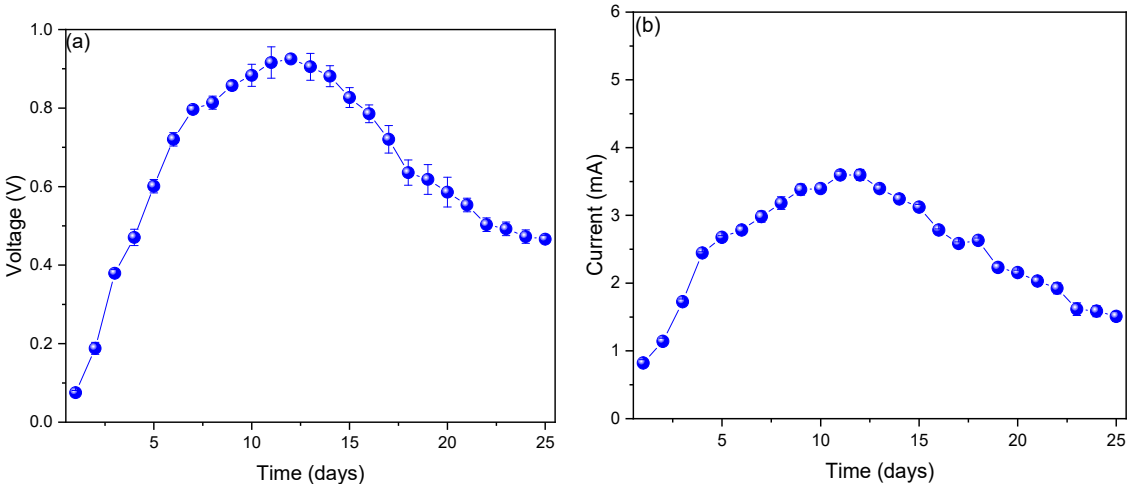

FIGURE 2. Report of (a) voltage and (b) electric current of the MFCs.

Microbial fuel cells showed levels from slightly acidic (4.721) to slightly alkaline from the first to the last day (7.770 ± 0.668) of monitoring, with the optimal operating pH on day 12 being 5.87 ± 0.34. pH values in microbial fuel cells are vital since many electron-generating bacteria proliferate at established pH, and the variations existing during monitoring directly affect their growth, thus harming the performance of MFCs [31]. Banerjee et al. (2023) mention in their research that the decomposition of organic waste produces acids that reduce pH and oxygen levels, which puts aquatic ecosystems at risk [32]. Microbial fuel cells showed progressive increases in their electrical conductivity values from the first day (86.41 ± 1.73 mS/cm) to the twelfth day (264.67 ± 24.72 mS/cm) and then showed a decrease until the twenty-fifth day (1444.31 ± 2.08 mS/cm). In the fermentation processes of organic waste, ions are released that help to increase the electrical conductivity values. In the first days, the increases in ions helped to increase the increase, but in the last days, sedimentation of organic matter was observed, generating a decrease in the values [33]. Zhao et al. (2023) showed the importance of electrical conductivity in the resistance values of MFCs, mentioning that increasing conductivity decreased the resistance values of the MFC [34]. The chemical oxygen demand values are observed in Figure 3 (c); the observed values decreased from the first day (1654.11 ± 8.54 mg/L) to the last day (440.15 ± 31.25 mg/L), showing a reduction of 73.397%. The chemical oxygen demand values decrease because the metabolism of microorganisms and redox reactions that occur within

the MFCs consume the organic matter present in the substrate [35]. In their research, Aleid et al. (2023) used Sugarcane Waste as a substrate in their MFCs, mentioning that they managed to reduce it by 90% and showing the potential that this type of waste also has to reduce heavy metals [36]. In Figure 3 (d), the values of the oxidation-reduction potential (ORP) can be observed, showing a progressive increase from day 1 (71.90 ± 1.21 mV) to day 12 (247.63 ± 29.54 mV) and then showing a successive decrease until the last day (147.538 ± 35.24 mV). In their research, Tong et al. (2023) mentioned that the intracellular ORP is of utmost importance because it controls the synthesis of enzymes and the genetics of electroactive microorganisms, affecting the process of their metabolisms [37].

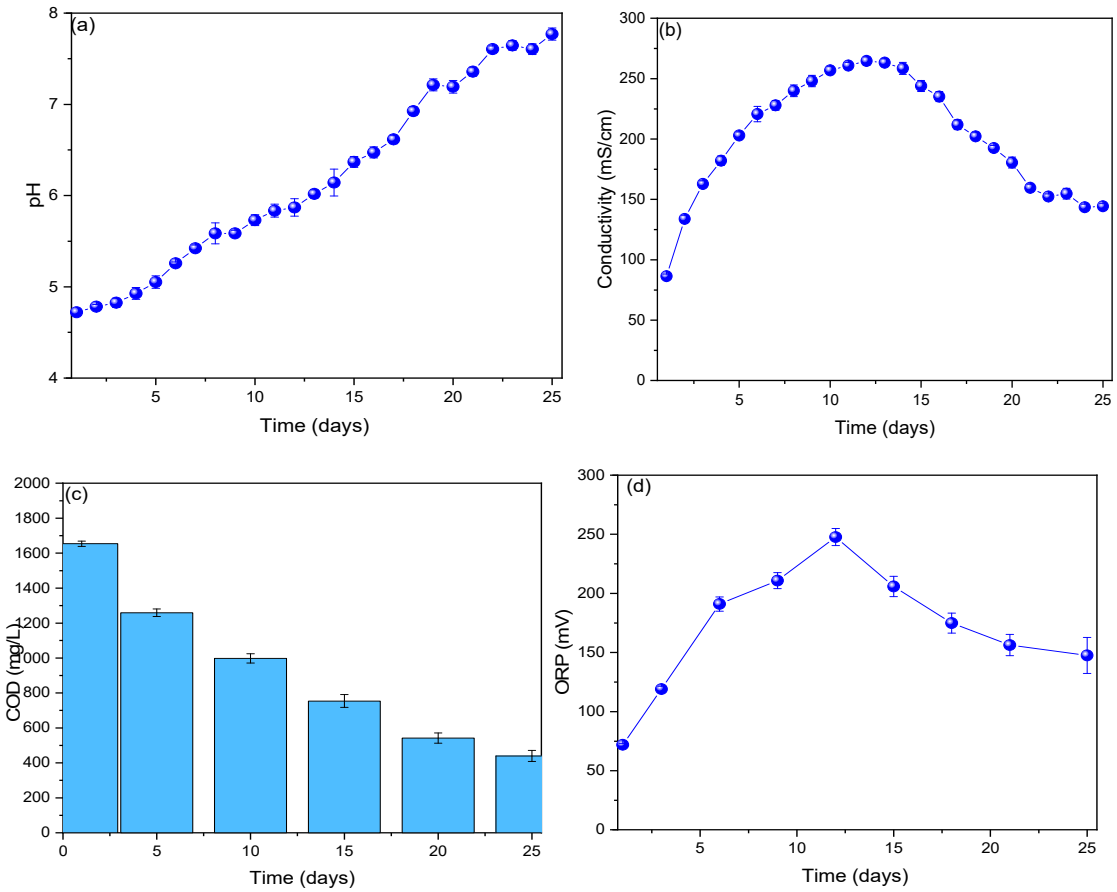

FIGURE 3. Monitoring of (a) pH, (b) conductivity, (c) COD and (d) ORP values of microbial fuel cells.

Microbial fuel cells showed an average internal resistance of 89.244 ± 9.747 Ω on the twelfth day, see Figure 4 (a). This value was obtained with the slope of the linear fit obtained from Ohm's Law (V=IR), where the values of voltages and electric current were fitted to the "y" and "x" axes, respectively. Electrodes made from metallic materials considerably reduce the values of the internal resistance of MFCs due to their high electrical conductivity. However, it has been reported that these metals, when not coated, can adversely affect the performance of MFCs because they are harmful to certain electron-generating microorganisms [38,39]. In addition, it has been reported that the internal resistance values depend on the areas of the electrodes and their separation [40]. Moqsud et al. (2023) showed an internal resistance of approximately 100 Ω using corn waste as a substrate, reporting that the position (vertical or horizontal) of the electrode directly indicates the values of the internal resistance and the voltage of the MFC [41]. The power density values as a function of the current density are observed in Figure 4 (b), where a power density of 2.571 ± 0.097 mW/cm^2 was shown with a current density value of 0.475 A/cm2. Verma et al. (2023), in their research on cellulosic waste and used motor oil as fuel, managed to report a power density of 16.00 ± 0.32 mW/m^2 in a 163.3 ± 1.66 mA/m^2, mentioning that carbon electrodes with metallic nanoparticles help to enhance the power density values [42]. Likewise, Din et al. (2023) reported a power density of 0.3714 mW/cm^2 at a current density of 0.235 mA/cm^2 and a peak voltage of 1.58 V, using potato waste as

substrates in their single-chamber MFCs mentioning that the high activity of the bacteria present in their substrate is mainly responsible for their high reported values [43]. Likewise, Erazo S. and Agudelo E. (2023) reported a power density of 900 mW/cm^2 for a current density of 22 mA/cm^2 using coffee waste as a substrate, mentioning that microbes have a great electrogenic potential associated with the oxidation-reduction reaction of organic matter is an essential point for the generation of power density values [44]. Figure 5 shows the schematic of generating electrical energy from banana waste, observing that banana waste has great potential to be used as fuel at the laboratory prototype scale.

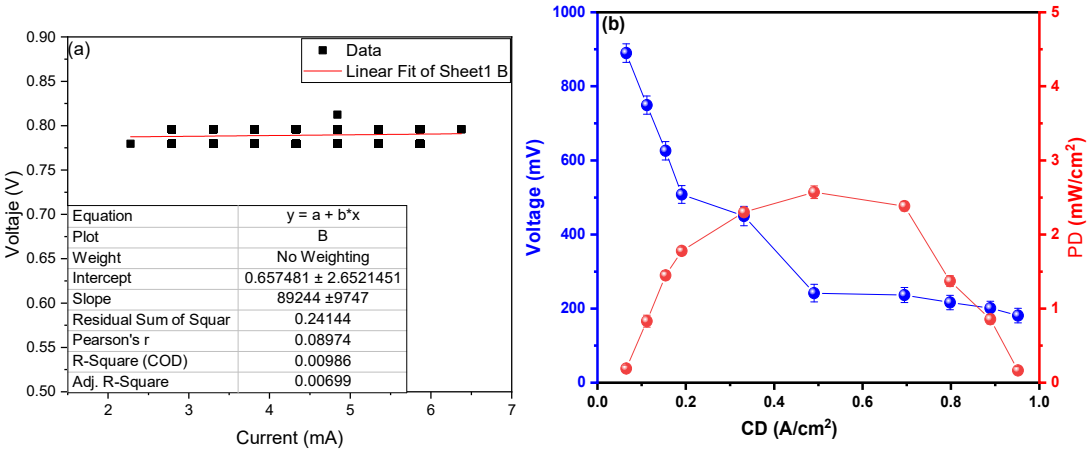

FIGURE 4. Values of (a) internal resistance and (b) power density as a function of current density.

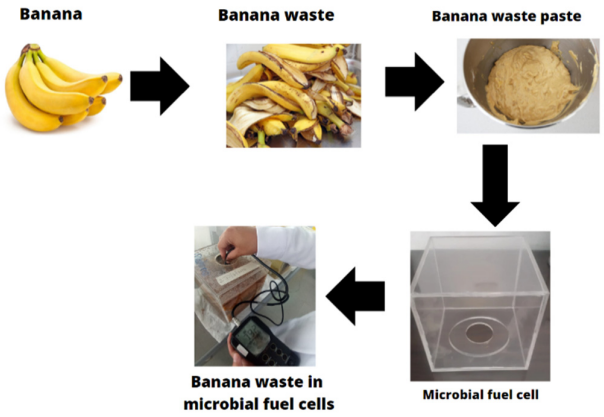

FIGURE 5. Schematic of the process of generating electrical energy using banana waste.

CONCLUSION

The low-cost microbial fuel cells, a breakthrough in renewable energy research, were fabricated using banana waste and zinc-carbon electrodes. These cells demonstrated excellent electric current values (3.591 ± 0.474 mA) and voltage (0.925 ± 0.087 V) on the twelfth day. These values were achieved from an optimum operating pH of 5.87 ± 0.34 with an electrical conductivity of 264.67 ± 24.72 mS/cm. The microbial fuel cells showed an internal resistance of 89.244 ± 9.747 Ω with a density of 2.571 ± 0.097 mW/cm^2, whose current density value was 0.475 A/cm^2, while the maximum oxidation-reduction potential shown was 247.63 ± 29.54 mV. This research not only demonstrates the potential of banana waste as fuel in microbial fuel cells but also highlights its role in the generation of alternative energy in an environmentally sustainable manner, contributing to the global efforts in combating climate change.

Looking ahead, our research opens up exciting possibilities for further advancements in microbial fuel cells. We recommend exploring the use of nanoparticles embedded in the electrons to enhance the

values of electric currents. Additionally, the coating of the electrodes could significantly reduce corrosion, a common issue with metallic electrodes. Furthermore, the introduction of biocatalysts holds promise for increasing the voltage and electric current values in microbial fuel cells. These potential avenues for future work inspire us to continue pushing the boundaries of renewable energy and environmental sustainability.

ACKNOWLEDGMENTS

This research was funded under a project from the Universidad Autonoma del Peru.

REFERENCES

1. W.M. Hikal, S.A. Ahl, A.H. Hussein, A. Bratovcic, K.G., Tkachenko, J. Sharifi-Rad, and M. Atanassova, *Evidence-Based Complementary and Alternative Medicine,* (2022).
2. S. Alzate Acevedo, Á.J. Díaz Carrillo, E. Flórez-López, and C.D. Grande-Tovar, *Molecules,* **26**(17), 5282 (2021)
3. A.N., Sawarkar, N. Kirti, A. Tagade, and S.P. Tekade, *Bioresour Technol Rep,* **18**, 101092 (2022).
4. N.J. Mim, M.M. Meraz, M.H. Islam, E.N. Farsangi, M.T. Mehedi, S.A.K. Arafin and R.K. Shrestha, *J Build Eng,* **64,** 105581 (2023).
5. C. Pongsuwan, P. Boonsuk, D. Sermwittayawong, P. Aiemcharoen, J. Mayakun, and K. Kaewtatip, *Ind. Crops Prod,* **180**, 114731 (2022).
6. S. Deb, Y. Kumar, and D.C. Saxena, *Food Chem*, **X**(13), 100205 (2022).
7. M. Mago, A. Yadav, R. Gupta, and V.K. Garg, *Bioresour Technol,* **326**, 124742 (2021).
8. J. Arun, P. SundarRajan, K.G. Pavithra, P. Priyadharsini, S. Shyam, R. Goutham, and A. Pugazhendhi, *Fuel,* **355,** 129530 (2024).
9. A.V. Sonawane, S. Rikame, S.H. Sonawane, M. Gaikwad, B. Bhanvase, S.S. Sonawane, and R. Gaikwad, *Chemosphere,* 141127 (2024).
10. S. Kunwar, N. Pandey, P. Bhatnagar, G. Chadha, N. Rawat, N.C. Joshi, and P.A. Gururani, Environ Sci Pollut Res, **31**(5), 6723-6737 (2024).
11. N.N.M., Noor, N.I. Oktavitri, and K. Kim, *Fuel,* **367**, 131438 (2024).
12. E.T. Sayed, H. Rezk, M.A. Abdelkareem, and A.G. Olabi, *Int J Hydrogen Energ,* **52**, 1015-1025 (2024).
13. K. Tamilarasan, S. Shabarish, J.R., Banu, and V.G. Sharmila, J Environ Manage, **351**, 119777 (2024).
14. A. Kalagbor Ihesinachi, and A.I. Stephen*, Int. J. Energ Inf. Commun,* **11**, 11-20 (2020).
15. S. Rojas-Flores, R. Nazario-Naveda, S.M. Benites, M. Gallozzo-Cardenas, D. Delfín-Narciso, and F. Díaz, *Molecules,* **27**(21), 7389 (2022).
16. H. Kebaili, M. Kameche, C. Innocent, F.Z. Ziane, S.A. Sabeur, T. Sahraoui, T., and M.A. Charef, *Acta Ecologica Sinica*, **41**(2), 97-105 (2021).
17. X. Huang, C. Duan, W. Duan, F. Sun, H. Cui, S. Zhang, and X.Chen, J Clean Prod, **301,** 126951 (2021).
18. R. Kaur, A. Marwaha, V.A. Chhabra, K.H. Kim, and S.K. Tripathi, *Renew Sust Energ Rev,* **119,** 109551 (2020).
19. J. Zhou, M. Li, W. Zhou, J. Hu, Y. Long, Y.F. Tsang, and S. Zhou, *Sci Total Environ*, **748**, 141425 (2020).
20. M.S. Hamed, H. S. Majdi, and B.O. Hasan, *ACS Omega,* **5**(18), 10339-10348 (2020).
21. S. Rojas-Flores, S.M. Benites, M. De La Cruz-Noriega, L. Cabanillas-Chirinos, F. Valdiviezo-Dominguez, M.A. Quezada Álvarez, and L. Angelats-Silva, L. *Processes,* **9**(8), 1301 (2021).
22. R. Agüero-Quiñones, Z. Ávila-Sánchez, S. Rojas-Flores, L. Cabanillas-Chirinos, M.D.L. Cruz-Noriega, J. Cruz-Monzón, and R. Nazario-Naveda, *Sustainability,* **15**(19), 14513 (2023).
23. Y.A. Attia, M. Samer, M.S. Mohamed, E. Moustafa, M. Salah, and E.M. Abdelsalam, Biomass Convers Bioref, **14**(1), 847-858 (2024).
24. J. Arun, P. SundarRajan, K.G. Pavithra, P. Priyadharsini, S. Shyam, R. Goutham, R., and A. Pugazhendhi, *Fuel,* **355**, 129530 (2024).
25. G. Cheng, Y. Yang, E. Luo, D.K. Suthar, Y. Zhao, X. Luan, and C. Dong*, J Power Sour,* **591**, 233841 (2024).
26. D.A. Rokhim, I.Y. Vitarisma, S. Sumari, Y. Utomo, and M.R. Asrori, *J Renew Mater,* **12**(2) (2024).
27. M. Hassan, S. Kanwal, R.S. Singh, M.A. Sa, M. Anwar, and C. Zhao, *Int J Hydrogen Energ.* (2023).
28. G.L. Garbini, A. Barra Caracciolo, and P. Grenni, *Microorganisms,* **11**(5), 1255 (2023).
29. H. Zafar, N. Peleato, and D. Roberts, *Bioresour Technol*, **374**, 128778 (2023).

30. A.S. Yaakop, A. Ahmad, F. Hussain, S.E. Oh, M.B. Alshammari, and R. Chauhan, *Int J Chem Eng*, 1-10 (2023).
31. F. Ding, H. Liu, X. Jiang, Y. Jiang, J. Cheng, Y. Tu, and X. Yan, *Electrochim Acta,* **438**, 141548 (2023).
32. A. Banerjee, R.K. Calay and S. Das, *Water,* **15**(19), 3472 (2023).
33. J. Ma, J. Zhang, Y. Zhang, Q. Guo, T. Hu, H. Xiao, and J. Jia, *J Power Sour,* **556**, 232486. (2023).
34. Y. Zhao, L. Duan, and S.W. Hermanowicz, *J Molecular Liquids,* **380**, 121704 (2023).
35. N. Terbish, S.R. Popuri, and C.H. Lee, *Fuel,* **332**, 126167 (2023).
36. G.M. Aleid, A.S. Alshammari, A.D. Alomari, H. Almukhlifi, A. Ahmad, and A.A. Yaqoob, *Processes,* **11**(4), 1060 (2023).
37. K.T.X. Tong, I.S. Tan, H.C.Y. Foo, P.L. Show, M.K. Lam, and M.K. Wong, *Bioeng*, **14**(1), 246-289 (2023).
38. G. Pasternak, A. de Rosset, and P. Rutkowski, *Energ Convers Manage*, **281**, 116807 (2023).
39. M.B. Alshammari, and A. Ahmad, *Biomass Conver Bioref,* 1-15 (2024).
40. S. Rajesh, and A.S. Kumawat, *Ionics,* **29**(11), 4417-4435 (2023).
41. M.A., Moqsud, and T. Okamoto, *Bioresour Technol Rep,* 24, 101611. (2023).
42. M. Verma, V. Singh, and V. Mishra*, J Environ Chem Eng,* **11**(5), 110566 (2023).
43. M. I. Din, M. Ahmed, M. Ahmad, M. Iqbal, Z. Ahmad, Z. Hussain, and A. Samad, *J Chem*, (2023).
44. S. Erazo, and L.M. Agudelo-Escobar, *Processes,* **11**(2), 373 (2023).

Sustainable Electrical Energy Generation Using Tangerine Waste in Microbial Fuel Cells

Segundo Rojas Flores[1,a)], Santiago M. Benites[1,b)], Magaly De La Cruz-Noriega[1,c)], Renny Nazario-Naveda[1,d)]

[1] Vicerrectorado de Investigación, Universidad Autónoma del Perú, Lima, Perú.

a) Corresponding author: srojasfl@autonoma.edu.pe
b) santiago.benites@autonoma.pe
c) mdelacruzn@autonoma.edu.pe
d) rnazario@autonoma.edu.pe

Abstract. The agroindustry in Peru has increased exponentially in recent years, registering an export value during January-August 2023 of approximately 5,045 million dollars, which represents 28.56% (3,604 million dollars) more than what was registered in 2018. This has generated an increase in agricultural waste, the problem of which is increasing in markets, crop fields, and areas with few inhabitants because fruit or vegetable waste is thrown away around these places, contaminating the environment. Recently, agricultural waste has emerged as a promising fuel for sustainably generating alternative electrical energy through microbial fuel cells (MFCs). This research used 5 kg of mandarin waste as a substrate in single-chamber MFCs with carbon and zinc electrodes, where the physical-chemical parameters were monitored for 25 days. Generating maximum values of voltage (0.751 ± 0.049 V) and electric current (4.672 ± 0.154 mA) on the tenth day, operating at an optimal pH of 6.59±0.24 showing a maximum electrical conductivity of 184.74±19.17 mS/cm. The COD was reduced by 92.51%, and the maximum ORP shown was 199.25 ± 16.84 mV, with an internal resistance of 58.844 ± 6.517 Ω. The PD observed on the tenth day was 4.512±0.151 mW/cm^2 at a CD of 0.359 A/cm^2.

Keywords: tangerine waste, organic waste, microbial fuel cells, electricity, sustainability.

INTRODUCTION

The importance of a healthy diet has surged in recent years, leading to a significant increase in the demand for fruits and vegetables [1]. This surge in demand has prompted agro-exporting companies to ramp up their investments. The economic contribution of agro-industrial companies in Peru, accounting for a substantial 46% of its economy [2], underscores the significance of this trend. It's worth noting that the demand has been growing at an annual rate of 2.8 to 3.2% (over the past 20 years, it has seen a staggering growth of 16.97%) [2]. This robust demand, however, has also led to a substantial amount of waste, particularly during harvest and sale [3]. This issue is more pronounced in developing countries, where fruit waste is often discarded on the streets near these supply centers, posing environmental and health risks for the local communities [4,5]. Conversely, the consumption of electric energy has skyrocketed as a result of the universal use of electricity in our daily lives [6,7]. For instance, in Peru, consumption has reached a staggering 57,639 GWh, with an estimated CO_2 emission of approximately 61,610 Mt [8], which is posing significant and urgent environmental challenges for society. Despite these alarming figures, a significant portion of the population still lacks a reliable electricity supply, primarily due to their distance from major cities where their homes are located [9,10]. As a response, the installation of environmentally friendly electricity generation systems has seen a 60% increase in the past decade [11].

In Peru, the production of citrus fruits has emerged as a promising fruit for export due to the existing demand for this type of fruit. It has been recorded that the consumption of citrus fruits worldwide is 18% of all fruits consumed [12]. Countries such as China, Brazil, India, and Mexico are the leading exporters of this fruit worldwide, with 28.2, 12.20, 8.82, and 5.60 %, respectively [13]. One of the most consumed fruits is tangerine because it contains a high content of vitamins; it is estimated that the total production of this fruit is approximately

Technologies and Materials for Renewable Energy, Environment and Sustainability
AIP Conf. Proc. 3321, 040005-1–040005-7; https://doi.org/10.1063/5.0289619
Published under an exclusive license by AIP Publishing. 978-0-7354-5231-2/$30.00

10 million tons per year. If the production and consumption of this fruit continue to increase, the amount of waste will also increase, becoming a potential problem that needs to be addressed [14,15].

Microbial fuel cells (MFCs) are presented as an innovative solution to solve the problem of fruit waste and the generation of electric energy sustainably. This type of technology comprises two electrical elements (cathodic and anodic), which are inside chambers separated by a membrane [16]. The process of generating electric energy in this type of technology starts with the generation of electrons in chemical processes, primarily reduction-oxidation processes that occur inside the chambers (anodic and cathodic); the electrons are captured by the electrodes and transported through a circuit from one chamber to the other, thus generating the electric current [17,18]. Recently, potato waste has been used as a substrate (fuel) in MFC, generating voltage peaks of 1.12 V and an electric current of 12.45 mA, using zinc and copper electrodes in its MFC [19]. Onion waste has also been used as fuel in single-chamber MFC using zinc and copper as electrodes, generating electric current peaks of 4.459 ± 0.0608 mA and power density of 595.69 ± 15.05 mW/cm^2 with a pH of 6968 ± 0.286 [20]. Likewise, food waste has been reported as fuel in MFC, showing an internal resistance of 117 Ω, with a power density of 0.1047 mW/m^2 and a peak voltage of 110 mV [21]. Tangerine production in Peru in recent years has been increasing due to the high demand registered; it has been reported that in 2022, the production of mandarin was 38.7% of the total citrus fruits produced, which presented a harvest of approximately 20,859 hectares [22]. In addition, it has been recorded that 639 thousand tons of Tangerine were harvested in 2022, and in 2023, an increase in production of 8.3% was observed [23]. The production increases recorded in recent years have also generated an increase in agricultural waste, leading to significant losses for companies and expenses for properly disposing of the same fruits [24].

Due to this, this research's main objective is to observe the potential of Tangerine waste in MFC for 25 days. The potential of these wastes will be verified by monitoring the parameters of power density, current density, voltage, chemical oxygen demand, internal resistance, electrical conductivity, oxidation-reduction power, and electric current of the MFCs. This research will give a sustainable way to generate electrical energy using Tangerine waste, making agro-industrial companies take an interest in financing these types of research for a short-term scaling of this technology.

MATERIALS AND METHODS

PREPARATION OF TANGERINE WASTE IN MICROBIAL FUEL CELLS.

Single-chamber MFCs were manufactured using cubic polyethylene containers with a volume of 4L. Holes of 15 cm diameter were made in one of the cubes to place the Zn electrode (zinc, catalytic) and in the center (inner part) of the cube, the carbon electrode used as anode electrode was placed; both electrodes were separated on the outside through an external resistance of 50 Ω, see Figure 1. On the other hand, Tangerine waste was collected from the Ex-Palermo market in Trujillo, Peru. The same merchants selected the waste, managing to collect 5 kg. The collected waste was taken to the laboratory and underwent a rigorous washing process several times until any waste acquired from the environment was eliminated. The waste was then placed in an extractor (Labtron, LDO/B10), obtaining approximately 9 liters of waste, divided into three parts and placed in each single-chamber MFC.

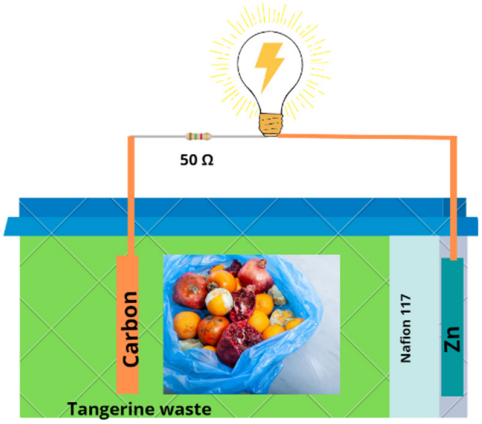

FIGURE 1. Design of the prototype used as MFC.

OBTAINING THE MONITORED PHYSICAL-CHEMICAL PARAMETERS

The current and voltage values were meticulously monitored for 25 days using a high-precision multimeter (Prasek Premium PR-85, USA). The power density and current density values were measured using the well-established method described by Rojas-Flores et al. (2022), with external resistances of 15 ± 0.1, 30 ± 1.5, 60 ± 2.2, 120 ± 2.5, 240 ± 3.5, 400 ± 4.5, 550 ± 5.5, 620 ± 6.5, 720 ± 8.5, 1000 ± 20.5 Ω [25]. The internal resistance was determined using the power sensor (Vernier- ± 30V & ± 1000 mA, USA) and Ohm's law. The pH and electrical conductivity values were monitored with a high-accuracy pH meter (110 Series Oakton, USA) and a conductivity meter (DC-4301, USA) throughout the 25 days of operation. The COD (chemical oxygen demand) values were measured using the closed reflux colorimetric method according to the NTP 360.502:2016 standard [26].

RESULTS AND ANALYSIS

The voltage values increased progressively from the first day (0.109 ± 0.005 V) of monitoring until the tenth day, where they showed a value of 0.751 ± 0.049 V, and then gradually decreased until the last day (0.374 ± 0.105 V), see Figure 2 (a). It has been reported in the literature that successive voltage increases in microbial fuel cells are due to the presence of redox reactions that produce a potential differential between the electrodes; the redox reactions increase in the first ones due to the rich content of organic matter that the substrate used may have and as the organic matter decreases the redox reactions also and consequently the voltage values also decrease [27,28]. Similar research has been carried out using banana waste in a single-chamber MFC, where they managed to generate voltage peaks of 0.286 V, where it was mentioned that the voltage values also depend on the anaerobiosis in which the substrate is found during its operation in the MFC [29]. In Figure 2 (b), the values obtained from the monitoring carried out during the 25 days are shown to observe that the values of the electric current increase from the first day (1.637 ± 0.049 mA) until the tenth day (4.672 ± 0.154 mA) and then an electric loss is observed until the 25th day (2.528 ± 0.723 mA). The generation of electrons in the fermentation process of the substrate or the metabolic process of the microorganisms present in the waste used as substrates are the leading causes of the generation of electric current [30]. The generated electrons are attached to the anodic electrode, which transports the electrons to the cathodic electrode; chemical oxidation-reduction reactions occur [31]. At the beginning of the monitoring, the microorganisms contain a high organic content and carry out their metabolism without any problem. However, as the carbon sources decrease, the electric current values decrease [32].

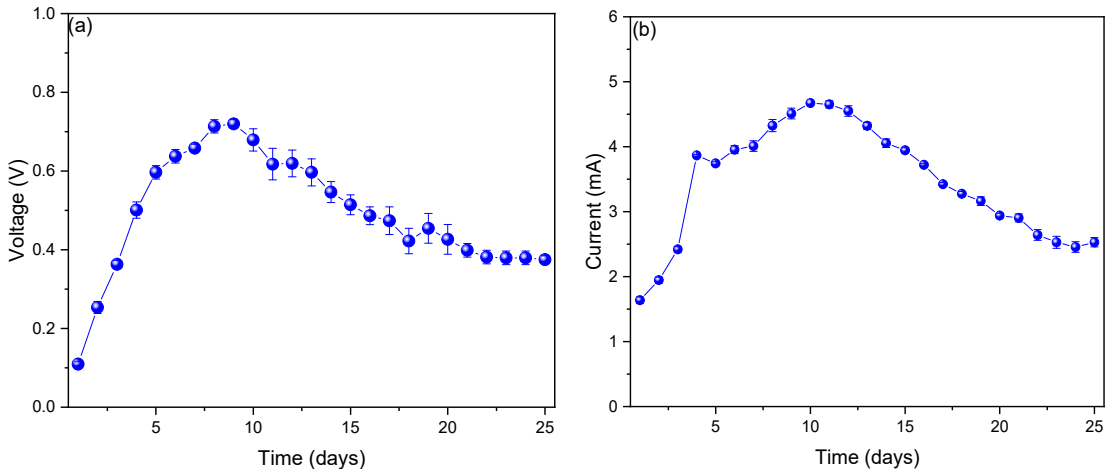

FIGURE 2. Monitoring of (a) voltage and (b) electric current values of microbial fuel cells.

The pH values shown by the MFCs during monitoring can be seen in Figure 3 (a); the values increased from a slightly acidic level on the first day to slightly alkaline on the last day, with its optimal operating pH of 6.59 ± 0.24 on day 10. This optimal operating pH is crucial for MFC performance as it is the pH at which the microorganisms that are the main electron generators within the MFC thrive. When the pH deviates from this optimal value, the microorganisms' growth and, consequently, the MFC's performance are affected [33]. For example, Li et al. (2021), in their research, managed to generate power density peaks of 1196 ± 25 mW / m^2 at a pH of 9.5, and as the pH of the substrate varied, the power density values varied [34]. Likewise, in Figure 3 (b), the values obtained from the

monitoring carried out on the MFCs can be observed, showing successive increases from the first day (86.406 ± 0.012 mS/cm) to the tenth day (184.74±19.17 mS/cm) and then showing losses of electrical conductivity values until day 25 (109.128 ± 23.84 mS/cm). In the fermentation process, ions are released, which, when their concentration increases, causes the conductivity values to increase as well; these processes are repeated until the fermentation decreases at the end of the monitoring [35]. It has also been mentioned that as the electrical conductivity values increase, the internal resistance values of the MFC decrease [36]. The values of the chemical oxygen demand can be observed in Figure 3 (c), where a considerable reduction of these values is observed; the observed reduction was 92.51 % from the first day (1350.842 ± 4.314 mg/L) to the last day (101.115 ± 31.258 mg/L). The decrease of the COD reinforces those mentioned in Figure 1 (a) and (b) because it observes a decrease of the organic matter from the first day; the decomposition of the organic matter is originated by the redox reactions and metabolisms of the microorganism's present [37]. The ORP values are shown in Figure 3 (c), showing a progressive increase from the first day (127.843 ± 1.211 mV) to the ninth day (199.251 ± 16.843 mV) and then a sharp drop until the 25th day (60.684 ± 13.554 mV). The potential differential released that originates in the energy generation process generates the ORP values. It has been reported that ORP values higher than 100 mV are due to the substrate's anaerobic conditions. In comparison, values below 100 mV are due to aerobic conditions, which can indicate the medium in which the substrate is found [38].

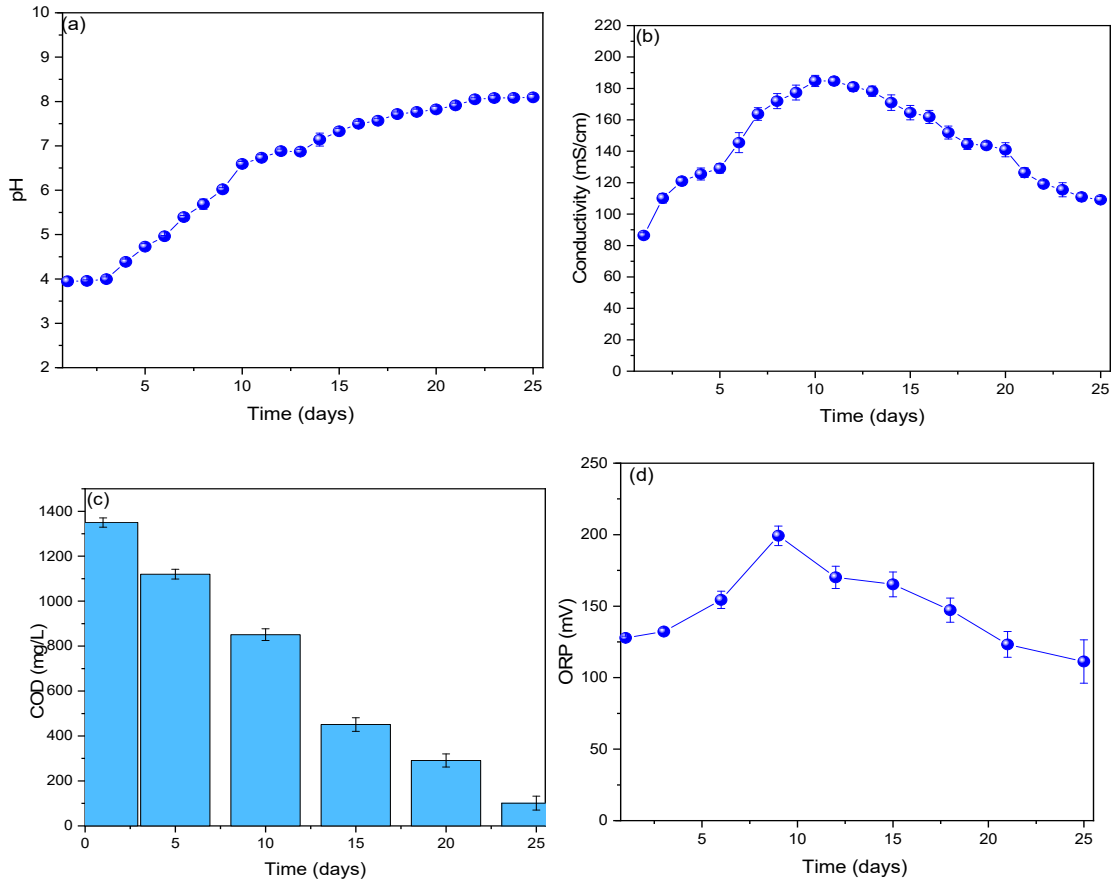

FIGURE 3. Monitoring of (a) pH, (b) conductivity, (c) COD and (d) ORP values of microbial fuel cells.

The calculated internal resistance was 58.844 ± 6.517 Ω, which was calculated using Ohm's Law, for which the values of the voltage and electric current were adjusted to the "x" and "y" axis, respectively, whose slope of the linear fit represents the internal resistance of the system, see Figure 4 (a). The values of the internal resistance of the MFC depend on the conductivity shown by the cells; a low resistance reveals that the electrons flowed more freely from the anodic to the cathodic chamber [39]. Lawson et al. (2020) studied the importance of the cathodic electrode in the internal resistance of the MFC, showing an internal resistance of 51 ± 1 Ω using carbon paper as a cathodic electrode, mentioning that this type of electrode has a greater capacity to adhere electrons due to the

porosity it shows [40]. The power density values as a function of current density are shown in Figure 4 (b), showing a maximum power density of 4.512 ± 0.151 mW/cm^2 for a current density of 0.359 A/cm^2 whose peak voltage observed was 726.887 ± 25.974 mV. They have also reported that the good formation of the anodic biofilm helps improve the performance of the PD values in the MFC because the electrons can flow with less energy loss during their journey to the cathodic electrode [41]. Choudhury et al. (2021) managed to generate a maximum PD of 50 mW/m2 in a DC 143.3 mA/m2, mentioning that the variations in the electrode distances influence the generation of PD because a shorter distance means less loss of electric current due to the current leaks existing in the circuit [42]. Tangerine has excellent potential as fuel in MFC. Figure 5 shows the schematization process for the generation of bioelectricity.

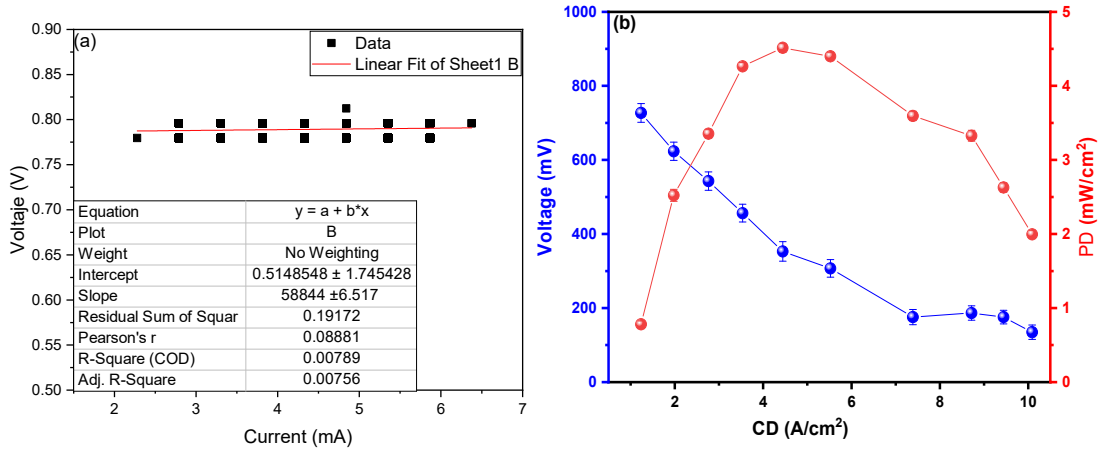

FIGURE 4. Values of (a) internal resistance and (b) power density as a function of current density.

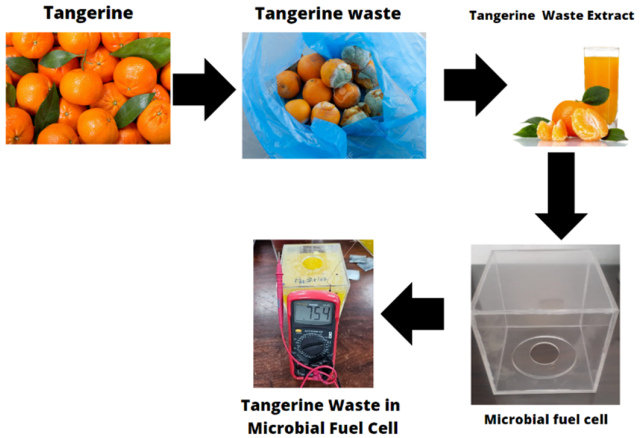

FIGURE 5. Schematic of the process of generating electrical energy using Tangerine waste.

CONCLUSION

Using tangerine waste in single-chamber microbial fuel cells, employing Zn and carbon electrodes, yielded consistently impressive electrical results throughout the monitoring. The experiment's findings underscore this waste type's immense potential and provide robust evidence of its efficacy. The waste demonstrated a rapid generation of electric current (4.672 ± 0.154 mA) and peak voltage (0.751 ± 0.049 V) on the tenth day, with MFCs operating at a pH of 6.59 ± 0.24, an electrical conductivity of 184.74 ± 19.17 mS/cm, and a maximum ORP of 199.25 ± 16.84 mV. Furthermore, the waste managed to reduce the chemical oxygen demand by a staggering 92.51% over 25 days, showcasing a maximum power density of 4.512±0.151 mW/cm2 for a current density of 0.359 A/cm2, with an internal resistance of the MFC calculated to be 58.844 ± 6.517 Ω.

The exploration of agricultural waste as a potential energy source is a burgeoning field of research, with significant gaps yet to be filled. In light of this, it is highly recommended for future investigations to explore the

incorporation of bacteria or fungi in the waste used as fuel. This approach could serve as biocatalysts and potentially enhance the electricity generation of the MFC, opening up new avenues for research and innovation.

ACKNOWLEDGMENTS

This research was funded under a project from the Universidad Autonoma del Peru.

REFERENCES

1 C.S. Arbaiza, H.V. Huerta, and C.R. Rodriguez, *Int J E-Adoption (IJEA)*, ***13***(1), 1-17 (2021).
2 G. Damonte, and R. Boelens, R. Hydrosocial territories, agro-export and water scarcity: capitalist territorial transformations and water governance in Peru's coastal valleys. In *Rural–Urban Water Struggles.* pp. 126-143, Routledge. (2020).
3 H. Ramos-Leon, G. Montoya-Valdiviezo, J. Castillo, and L. Cardenas, L. *AIP Conf Proceed,* **2613**(1), (2023).
4 X. Esteve-Llorens, D. Ita-Nagy, E. Parodi, S. González-García, M.T. Moreira, G. Feijoo, and I. Vázquez-Rowe, *Sci Total Environ*, **818,** 151686 (2022).
5 L.T. Raynolds, and A. Ipsen, *J Agrarian Change*, e12565 (2023).
6 Guyol, N. B. (2023). *The World Electric Power Industry*. Univ of California Press.
7 A. Pramuanjaroenkij, and S. Kakaç, *Int J Hydrogen Energ*, **48**(25), 9401-9425 (2023).
8 H. Ritchie, P. Rosado, and M. Roser, Electricity mix. *Our World in Data*. (2024).
9 M. M. H., Sifat, S. M., Choudhury, S. K., Das, M. H., Ahamed, S. M., Muyeen, M. M., Hasan, and P. Das, Towards electric digital twin grid: Technology and framework review. *Energy and AI*, **11,** 100213 .
10 J. Zhang, Z. Wang, E.J. Miller, D. Cui, P. Liu, & Z. Zhang, *J Energ Storage*, **57,** 106294 (2023).
11 L. Laureti, A. Massaro, A. Costantiello, and A. Leogrande, *Sustainability*, **15**(3), 2160 (2023).
12 Y. Li, W. Zhao, M. Qian, Z, Wen, W. Bai, X. Zeng, and H. Dong, *Food Chem,* 13853 (2024).
13 S. Rojas-Flores, L. Cabanillas-Chirinos, R. Nazario-Naveda, M. Gallozzo-Cardenas, F. Diaz, D. Delfin-Narciso, and W. Rojas-Villacorta, *Sustainability*, ***15***(4), 3559 (2023).
14 L. Luo, M. Wang, W. Su, J. Zhuo, L. Zhang, W. Zhu, and J. Wang, *J Agricult Food Chem*, **72**(3), 1756-1767 (2024).
15 F. Yue, F. Zhang, Q. Qu, C. Wang, Y. Qin, L. Ma, and X. Wang, *Food Chem*, **417**, 135812 (2023).
16 W.H. Tan, S. Chong, H.W. Fang, K.L. Pan, M. Mohamad, J.W. Lim, and T.C.K. Yang, *Processes*, ***9***(6), 985 (2021).
17 W.H. Tan, S. Chong, H.W. Fang, K.L. Pan, M. Mohamad, J.W. Lim, and T.C.K. Yang, *Processes*, ***9***(6), 985 (2021).
18 A.S. Jatoi, F. Akhter, S.A. Mazari, N. Sabzoi, S. Aziz, S.A. Soomro, and S. Ahmed, *Environ Sci Pollut Res,* **28,** 5005-5019 (2021).
19 M.I. Din, M. Iqbal, Z. Hussain, and R. Khalid, *Energ Sour, Part A: Recov, Util Environ Effects*, 1-11 (2020).
20 R.F. Segundo, M. De La Cruz-Noriega, N. Milly Otiniano, S.M. Benites, M. Esparza, and R. Nazario-Naveda, *Molecules*, ***27***(3), 625. (2022).
21 A.S. Yaakop, A. Ahmad, F. Hussain, S.E. Oh, M.B. Alshammari, and R. Chauhan, *Int J Chem Eng*, ***2023*****,** 1-10 (2023).
22 L.E.D.O. Aparecido, G.B. Torsoni, R.F.D. Lima, A.C.C. Baratti, M.F.D.M. Rossi, A.F. Dos Santos, and P.M. Peche, *Pest Manage Sci,* (2024).
23 M.A.M. Condori, M.E.V. Gutierrez, R.D.N. Oviedo, & and F.J. Choix, *J Appl Phyco,l* **36**(1), 101-111. (2024).
24 F.K.F. Dos Santos, I.G.C. Barcellos-Silva, O. Leite-Barbosa, R. Ribeiro, Y. Cunha-Silva, and V.F. Veiga-Junior, *Biomass*, ***4***(2), 217-242 (2024).
25 S. Rojas-Flores, S.M. Benites, M. De La Cruz-Noriega, L. Cabanillas-Chirinos, F. Valdiviezo-Dominguez, M.A. Quezada Álvarez, and L. Angelats-Silva, *Processes*, 9(8), 1301 (2021).
26 R. Agüero-Quiñones, Z. Ávila-Sánchez, S. Rojas-Flores, L. Cabanillas-Chirinos, M.D.L. Cruz-Noriega, J. Cruz-Monzón, and R. Nazario-Naveda, *Sustainability*, **15**(19), 14513 (2023).
27 Y. Fan, A. Janicek, H. and Liu, *European Chem Biotechnol J*, 1, 47-57 (2024).
28 J. Guo, J. Cheng, J. Wang, J., Z. Zhang, X. Xie, and P. Chu, *Water Sci Technol*, **81**(9), 1972-1982 (2020).
29 N.I. Rincón-Catalán, A. Cruz-Salomón, P.J. Sebastian, S. Pérez-Fabiel, M.D.C. Hernández-Cruz, R.M. Sánchez-Albores, and H.A. Nájera-Aguilar, *Processes*, **10**(8), 1552 (2022).
30 R. Suresh, S. Rajendran, P.S. Kumar, K. Dutta, and D.V.N. Vo, *Chemosphere*, **287**, 132186 (2022).
31 A.A. Yaqoob, M.N.M. Ibrahim, and C. Guerrero-Barajas, *Environ Technol Innov*, **23**, 101579. (2021).

32 M.S. Hamed, H.S. Majdi, and B.O. Hasan, *ACS Omega*, **5**(18), 10339-10348. (2020).
33 S. Malekmohammadi, and S. Ahmad Mirbagheri, *Water Sci Technol*, **84**(6), 1309-1323 (2021).
34 X. Li, Y. Lu, H. Luo, G. Liu, C.I. Torres, and R. Zhang, *Chemosphere*, **265,** 129088 (2021).
35 N.N.M. Noor, N.I. Oktavitri, and K. Kim, *Fuel*, **367,** 131438 (2024).
36 H. Wang, X. Song, H. Zhang, P. Tan, and F. Kong, *J Hazard Mater*, **384,** 121459. (2020).
37 H.D. Nguyen, and S. Babel, *Environ Res*, *204*, 112095 (2022).
38 S.M. Tan, S.A. Ong, L.N. Ho, Y.S. Wong, W.E. Thung, and T.P. Teoh, *J Environ Health Sci Eng*, **18,** 793-807 (2020)
39 R. Rossi, and B.E. Logan, *Electrochimica Acta*, **348,** 136291 (2020).
40 K. Lawson, R. Rossi, J.M. Regan, and B.E. Logan, *Bioresour Technol*, **316**, 123919 (2020).
41 A. Khamis, N.A.M. & Zulfakar, *Int J Environ Waste Manage*, **33**(4), 465-478. (2024).
42 P. Choudhury, R.N. Ray, T.K. Bandyopadhyay, B. Basak, M. Muthuraj, and B. Bhunia, *Int J Hydrogen Energ*, **46**(4), 3171-3182 (2021).

Improving Energy Management and Thermal Comfort in Office Buildings: A Comparative Study of AI Models for Temperature Prediction

Amal Azzi [1,2, a)] ,Mohamed Tabaa[1] Asmae Chakir[1], Badr Chegari[3], Hanaa Hachimi[2]

[1] *Multidisciplinary Laboratory of Research and Innovation, Moroccan School of Engineering Sciences, Casablanca 20250, Morocco*
[2] *Laboratory of Advanced Systems Engineering, National School of Applied Sciences, Ibn Tofail Univesity Campus, Kenitra 14000, Morocco.*
[3] *TIMA, CNRS, Grenoble INP, Institute of Engineering, Université Grenoble Alpes, 38000, Grenoble, France*

[a)]Corresponding author *:* amal.azzi@uit.ac.ma

Abstract. The rapid increase in human population and the development of technologies have greatly increased energy consumption in today`s world. Since the building sector is a major consumer of energy, a new concept called Home Energy Management Systems (HEMS) has gained in importance. These systems use various techniques and technologies to reduce energy consumption and ensure thermal comfort. This study explores the potential of machine learning for intelligent temperature prediction in office buildings. Focusing on a case study in Casablanca, Morocco. Accurate temperature forecasting is crucial for optimizing Heating, Ventilation, and Air Conditioning (HVAC) systems, leading to significant energy savings and improved thermal comfort for occupants. Building modeling was simulated using the EnergyPlus engine, and the results built a database that was used to predict the temperature of the treated zone using artificial intelligence. We evaluate six machine learning models for their effectiveness in predicting temperature (Gated Recurrent Units, Long-Short Term Memory with Convolutional Neural Network, Extreme Gradient Boosting, Random Forest, Support Vector Regression, and Long-Short Term Memory) The results showed that XGBoost, Random Forest and GRU performed well, giving predictions of the order of 0.95, 0.9, 0.83, respectively.

Keywords: artificial intelligence; forecasting model; long short-term memory; machine learning

HEMS	Home energy management
HVAC	Heating Ventilation and air conditioning systems
GRU	Gated recurrent unit
LSTM	Long Short-Term memory
SVR	Support vector regression
CNN	Convolutional Neural Network
XGBoost	Extreme Gradient Boosting
AI	Artificial Intelligence
RF	Random Forest

INTRODUCTION

Climate change has become a serious issue that must be faced by all countries side by side. This change has influenced human living by causing several disasters, we can note among others: heat waves, tropical storms, and forest fires. Moreover, these accidents are becoming more and more frequent. In fact, a site where 3.6 billion people currently reside is no longer suitable because of the risk of new events occurring that threaten the comfort and quality of life of its residents [1]. Among the most notable contributors to climate change is the use of conventional types of energy, namely oil, coal and gas, to satisfy human needs, so the degradation of life in a location is caused by its inhabitants themselves, so finding solutions to find a compromise has become a necessity, not a choice [2]. In 2021, fossil fuels accounted for approximately 81% of total U.S primary energy [3]. In 2022 the production, transportation, and processing of oil and gas resulted in 5.1 billion tonnes $C0_2$ equivalent, accounting for little less than 15% of worldwide energy sector greenhouse gas emissions [4]. Reducing greenhouse gas emissions is crucial to mitigate these effects and reserve global health. This means making more environmentally-friendly decisions about energy use, food production and transportation.

Technologies and Materials for Renewable Energy, Environment and Sustainability
AIP Conf. Proc. 3321, 040006-1–040006-14; https://doi.org/10.1063/5.0289602
Published under an exclusive license by AIP Publishing. 978-0-7354-5231-2/$30.00

Buildings are one of the main contributors to excessive energy consumption and carbon emissions[5]. This sector plays a critical role in the energy context and contributes significantly to both overall greenhouse gas emissions and global energy consumption, according to the EIA[5]. it was responsible for 37% of world CO2 emissions and 36% of global energy consumption in 2020 [6]. A considerable portion of a building's energy consumption is attributed to its heating and cooling systems, represent around 40% of the total energy used in building [7] , making them potential sources of carbon emissions. As a result, A number of studies have suggested several approaches[8], such as the creation and use of sophisticated control techniques, for maximizing the energy usage of HVAC systems while preserving occupant comfort[9]. The objective of these techniques is to maximize the amount of energy utilized in building systems, including lighting [10] , HVAC[11] and other electrical appliances. Including renewable energy sources into building energy usage through the use of solar panels[12], wind turbines[13], and other technologies is another potential strategy. More importantly, the development of artificial intelligence (AI) has created new avenues for improving building energy management[14]. This integration can lessen reliance on fossil fuels.

Artificial intelligence (AI) has recently undergone a revolution in terms of its utilization. This discipline is currently used in a wide range of fields known for their complexity [15]. It is also known for its ability to process multiple systems that involve a variety of parameters while making the system correlated to a number of external constraints. Among these areas we find automation, optimization of processes, decision support and data processing [16]. All these fields of application are characterized by the data available, which is the fundamental driver behind artificial intelligence algorithms. The energy field, a data-rich field, has also begun to take advantage from this intelligence to facilitate various tasks within the national electricity network, along with satisfying human comfort inside their living environment [17]. Indeed, within the field of energy, and thanks to artificial intelligence, we're already capable of predicting weather conditions, predicting the electrical behavior of inhabitants, forecasting the intermittent production of renewable systems, or even predictively controlling energy systems.

AI techniques could be used for prediction or regression and classification. In the energy field the application is dominated by prediction and forecasting challenges. In this sense, various AI algorithms have been used. In [18] authors have compared GRU, LSTM and FFNN performance for PV energy production prediction of 300 randomly selected solar customers in the Ausgrid power grid area. Others in [19] ,compare various machine learning models (FFNN, CNN, LGBM, LSTM, RF, SVR, XGBoost) to anticipate the heating demand of a heating system. Authors in [20], has been developed a model based on LSTM neural network for an energy load forecasting.

In this work, we focused on accurate temperature prediction for an office building in Casablanca, Morocco. To ensure thermal comfort and reduce energy consumption, the EnergyPlus engine was used to simulate the modeling. We used the modeling results to build a database for temperature prediction. With the aim of improving temperature prediction, we trained six models and then evaluated their effectiveness. Extreme Gradient Boosting performed exceptionally well in terms of accuracy, as evidenced by its 95% performance and root mean square error (RMSE) of 1.42. In addition, random forests have an accuracy of 90% and an RMSE of 1.70. Finally, with a training time of 13.60 seconds and a prediction time of 0.02 seconds, Extreme Gradient Boosting offers solid performance that strikes a balance between accuracy and time savings.

This article is structured in the following way: Section 2 we will discuss the state of the art concerning Energy Management for Smart Buildings, and we illustrate several applications of IA models in energy efficiency in the building sector. Section 3 discusses the approach for modeling techniques such as white box, black box, and gray box. Section 4 investigates the findings of AI models and discusses them. Finally, section 5 summarizes the test findings and presents different views.

BACKGROUND

Demographic growth in a country activates several parameters that need to be checked at different points in time, especially when it comes to population lifestyle changes [21]. This increase must be balanced against the need for satisfaction, to avoid impacting on people's human rights and guaranteeing them a life in line with standards [22]. Therefore, any country capable of guaranteeing this satisfaction is a country that has already modified several aspects to reach this target [23]. The most important thing is the energy source that will be used, which must be available to satisfy demand and environmentally friendly so that it does not contribute to climate change, which is one of the drawbacks of conventional energy sources. Consequently, the integration of renewable energies is the subject of a primordial step by countries around the world [24], aimed at satisfying the electricity needs of citizens and protecting the environment at the same time. The sectors that will initially benefit from this integration are those that consume the most energy, namely the residential sector, followed by the transport sector [25]. The identification of these areas has involved other sector-dependent decisions. For the residential sector, which is the main energy-consuming sector in a country, we find: the integration of small-scale renewable energy installations, the transition from a conventional

electricity grid architecture to another with an intelligent structure, the integration of data and information systems and the control of energy on both the demand and production sides[26], [27]. This last point, energy management, is seen as a key element in ensuring good control of the energy produced and consumed at the same time, particularly for smart building[28], [29].

The main aim of building energy management is to reduce energy waste, maximize efficiency, and maintain thermal comfort using various techniques and technologies, such as consumption control and optimization. Building energy management is an essential component of smart cities and smart buildings. The smart city network relies on residential and commercial buildings as nodes, and these buildings incorporate intelligent energy management systems. To improve efficiency and reduce energy consumption, these systems use renewable energy sources, wireless sensor systems, and other elements of the Internet of Things (IoT) framework, as well as artificial intelligence, which plays a very interesting role in managing the different techniques used and even in interpreting consumption, thus facilitating management. Several research works have concentrated on energy management to improve sustainability by predicting temperature and/or electricity consumption [30] .Artificial intelligence technologies are essential for optimizing energy use and enhancing energy management in buildings [31] The objective of the authors in this study[32] ,is to improve the accuracy of indoor load forecasting in an office building by proposing a new approach that combines the LSTM model with PQR. The study offers a comprehensive analysis over a period of a year, comparing the proposed LSTM-PQR model with standard models such as BPNN, SVM and random forest. The evaluation covers both point prediction and interval prediction performance. The results showed that the MPC-PQR model outperforms reference models in daily interval load forecasting.it shows enhancements in the range of 6.4%to 20.9%for Prediction interval coverage probability. Furthermore, various machine learning techniques, namely SVM, ANN, DT, and RF, are utilized in [33], to forecast the electricity usage of a hotel building. These models are compared based on their efficacy in predicting power consumption for a building use case. Artificial Neural Networks (ANN) have demonstrated the most favorable outcomes. In the same concept, the authors in[34], examine the efficacy of four ML algorithms, decision tree, SVM, RF and VR in forecasting energy usage in a chemistry building based on limited data. The findings demonstrate that DT, RF, and VR provide more accurate estimates of building energy usage than SVM. This study[35], introduces a neural network-based predictor designed to forecast a building's HVAC power usage with a one-day lead time. The authors found that the model, which utilizes LSTM, achieves impressive test error and correlation coefficients. In addition, the results show great potential for accurately predicting. Another work [36] aims to create an LSTM-based model for forecasting the daily energy consumption of a Teatro real building´s HVAC system. It focuses on determining optimal time lags, turning hyperparameters, and analyzing the impact of dropout and early stopping regularization techniques. As a result, evaluation metrics show an acceptable level of accuracy. In [37], the authors utilize a CNN-LSTM model to improve the accuracy and efficiency of forecasting residential energy consumption.

BUILDING MODELING TECHNIQUES:

There are several approaches to building modeling discussed in the literature for exploiting and analyzing its thermal and energy behavior[38]. Three main objectives guide this modeling: long-term load forecasting for system planning, medium-term forecasting for system maintenance, and finally, short-term modeling for day-to-day operations. Short-term modeling of existing buildings can be divided into three categories: purely empirical models (black box)[39], purely physical models (white box)[40], and those that combine the two (gray box)[41]. Black-box models are empirical and data-driven, focusing on input-output relationships without detailed physical descriptions. They rely on statistical or machine-learning techniques to predict building performance based on historical data. Black-box models are empirical and data-driven, focusing on input-output relationships without detailed physical descriptions. They rely on statistical or machine-learning techniques to predict building performance based on historical data[42]. White-box models are based on fundamental physical principles and require in-depth knowledge of the building's physical properties[43]. These models describe thermal phenomena using detailed mathematical equations that take into account heat transmission, heat storage and heat flow. They can be static or dynamic, linear or non-linear, and are generally represented by differential equations[44]. In article [45], the authors separate simulation tools into black-box and white-box models, depending on the techniques and improvements used in energy modeling. The article mentions several white-box software packages, such as the leading EnergyPlus used in the field of building energy performance based on fundamental principles of physics and engineering. This study [46] , presents white-box models based on detailed building parameters and heat balance equations. It cites EnergyPlus as a simulation tool commonly used to create physical energy models that accurately represent building thermal dynamics. EnergyPlus [5], developed by the U.S.Departement of Energy is a popular building energy simulation tools mustly used in the field of building thermal modeling and energy modeling ,Energyplus used to simulate a building’s energy

consumption for heating , ventilation, air conditioning , lighting , electrical equipment , people activity and other energy flows, and thermal behaviors by defining the surfaces and sub surfaces like wall floor ground and door , windows defining the materials used in the constructions for this surfaces in order to define the heat flow and the thermal behaviors, that means that EnergyPlus is a white-box model , relies on detailed physical equations and engineering principles to simulate building energy performance[47]. Grey-box model [48] ,combine elements of the white-box and black-box approaches, based on physical laws and empirical data. They use simplified physical equations complemented by data-driven techniques, striking a balance between accuracy and complexity. The gray box modeling technique combines the advantages of physical (white box) and data-driven (black box) modeling. It exploits the known physical properties and governing equations of the HVAC system to provide a solid foundation, while leveraging empirical data to improve the accuracy and predictive performance of the model[49]. Figure 1 presents different building modeling techniques. needs and principles.

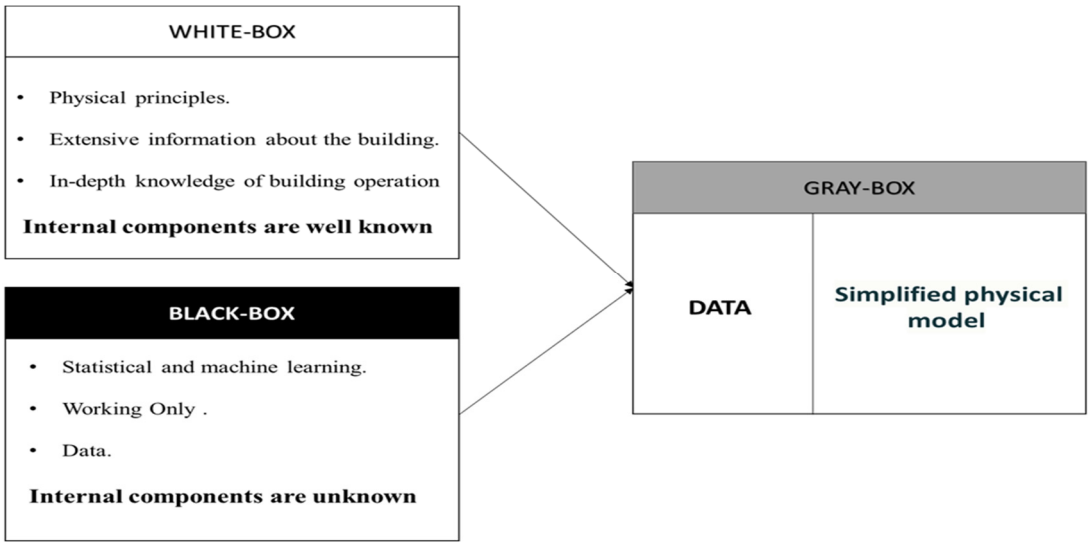

FIGURE 1: The different approaches to building modeling

METHODOLOGY

DATASET DESCRIPTION

The building in question is a typical commercial building in Casablanca, Morocco. The building has three facades: north, east, and west. With a surface area of 80 m^2, a height of 2.75 m, and a thermal zone, as shown in Figure 3, the building envelope and materials are designed to reproduce typical construction practices in the region as presented in Table 1. Walls, roofs, and floors are modeled with specific thermal properties to simulate realistic heat transfer dynamics. The thermophysical characteristics collected were captured from AMEE's BINAYAT software [50]. The area is occupied by 18 people. This study aims to explore the use of artificial intelligence models in conjunction with the widely used building energy simulation software, EnergyPlus, to model and analyze the thermal dynamics of a defined area.

The main objective of this research is to select the most appropriate algorithm from several options for predicting the temperature of the simulated zone. To achieve this goal, we first modeled the building using EnergyPlus to generate accurate data on the zone's thermal conditions. To start the simulation process, it is necessary to have an input data file (IDF) that contains detailed information about the building, including its geometry, materials, construction, thermal zone distribution, position, energy consumption devices, and HVAC subsystems. A weather data file refers to the country or city of the building, as presented in figure 2. After the simulation is completed, the spreadsheet file will include the chosen output data in the csv file. This data was then used to train different prediction algorithms to assess which offered the best accuracy. The resulting temperature prediction will then be used as a setpoint to control HVAC (heating, ventilation, and air conditioning) systems, a crucial factor in maintaining thermal comfort and optimizing energy consumption

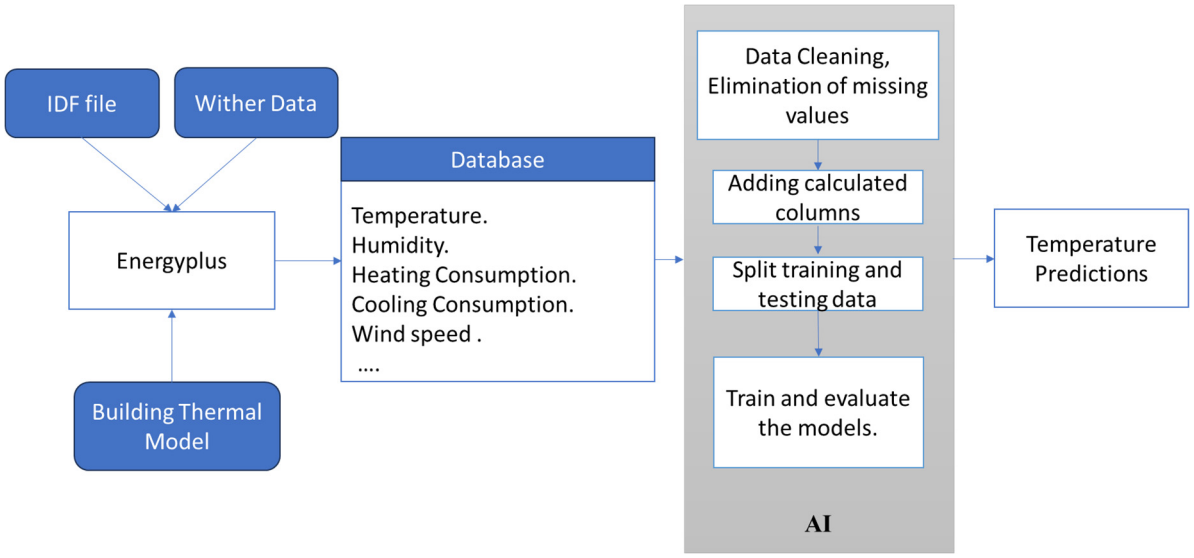

FIGURE 2: Our research approach.

The calculation of cooling/heating loads may be done in different ways. Energy and moisture balances for the zone's air are created, and the ensuing ordinary differential equations are solved using a predictor-corrector method as the foundation of the computations for EnergyPlus [51], The zone air's heat balance comes first in this:

Where:

$$C_z \frac{dT_z}{dt} = \sum_{i=1}^{Nsl} \dot{Q}_i + \sum_{i=1}^{Nsurfaces} h_i A_i (T_{si} - T_z) + \sum_{i=1}^{Nzones} \dot{m}_i C_p (T_{zi} - T_z) + \dot{m_{inf}} C_p (T_\infty - T_z) + \dot{Q_{sys}} \quad (1)$$

$\sum_{i=1}^{Nsl} \dot{Q}_i$ Sum of the convective internal loads.

$\sum_{i=1}^{Nsurfaces} h_i A_i (T_{si} - T_z)$ Convective heat transfer from the zone surfaces.

$\dot{m_{inf}} C_p (T_\infty - T_z)$ heat transfer due to infiltration of outside air.

$\sum_{i=1}^{Nzones} \dot{m}_i C_p (T_{zi} - T_z)$ heat transfer due to interzone air mixing.

$\dot{Q_{sys}}$ air systems output.

$C_z \frac{dT_z}{dt}$ energy stored in zone air.

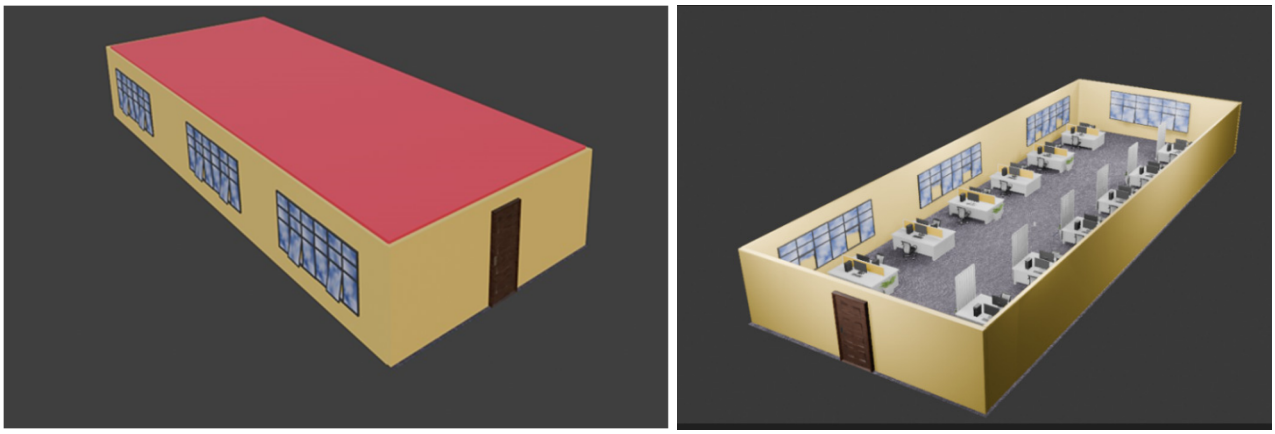

FIGURE 3: The office building modeled in our case.

DATA PRE-PROCESSING

We carried out a number of systematic pre-processing procedures to prepare our dataset for analysis. Using the Python package Pandas, we first imported the dataset, which included our simulated data and meteorological information. We eliminated unused spaces and formatted the date column to make it clearer. Duplicate timestamps were detected and dealt with. To maintain consistency, the next hour's timestamp was used to fill in the missing data. We determined the NaN values in each column, numbered them, and processed them. Associations between variables were studied by calculating a correlation matrix. Some of the columns have been rearranged for improved organization. Commas were used as decimal separators in numerical columns, which were then cleaned up and transformed to floating-point values. Ultimately, a new CSV file called "data.csv" included the cleaned and pre-processed dataset. An accurate and dependable analysis requires a clean, well-structured, and homogenous dataset, which was produced by this thorough pre-processing method.

The dataset, which covered a year, was captured hourly. The goal is to develop models that enable us to forecast temperature values using the six models GRU, SVR, CNN-LSTM ,LSTM, RF, and XGBoost. We have to prepare our data in sequence format for this, so we create sequences. We then divide our dataset into 75% for training, 5% for validation, and 20% for testing. We used RMSE, MAE, and R^2as our evaluation metrics, and we selected the model that returned the lowest value for both MAE and RMSE.

Table 1:Thermal properties of the building's materials.

Construction	Material	Thickness [mm]	Conductivity [W/m-k]	Density [Kg/m3]	Specific heat [kJ/Kg-k]
Exterior Wall	Ciment	15	1,8	2500	1
	Raw earth	100	1,04	2300	1
	Layer of air	50	R=0,18m^2k/W		
	Raw earth	100	1,04	2350	1
	Ciment	15	1,8	2500	1
Internal wall	Ciment	15	1,8	2500	1
	Concrete agglo 6 holes	120	0,56	768	0,83
	Ciment	15	1,8	2500	1

Table 2: Thermal properties of the building's materials. (Continuation).

Construction	Material	Thickness[mm]	Conductivity [W/m-k]	Density [Kg/m3]	Specific heat[kJ/Kg-k]
Roof	Plaster	20	0,56	1350	1
	Hourdis	200	1,32	1327	1
	Concrete	50	2	2450	1
	Ciment	15	1,8	2500	1
	Floor tile	15	1,3	2300	0,84
Ground floor	Ciment	15	1,8	2500	1
	Hourdis	160	1,18	1372	1
	Concrete	40	2	2450	1
	Ciment	15	1,8	2500	1

AI MODELS

In the study that we conducted, we used artificial intelligence models with a particular emphasis on temperature prediction. In order to effectively estimate temperature, these models have undergone intensive training to understand the complex relationships between meteorological elements, energy use, and building models.

GATED RECURRENT UNITS

Because they can capture long-term dependencies better than other recurrent designs, Gated Recurrent Units (GRUs) and Long Short-Term Memory (LSTMs) have drawn a lot of attention.

Gated Recurrent Units (GRUs), a relatively modern recurrent design, are closely related to the well-known Long Short-Term Memory (LSTM) networks. GRUs, like LSTMs, use gates to control the flow of information, allowing the network to selectively keep or discard data as needed. This gating mechanism is a critical element that allows recurrent models to handle complex sequential data like language usage and time series[52]. Figure 4 present the architecture of a GRU cell with a reset gate and an update gate [53].

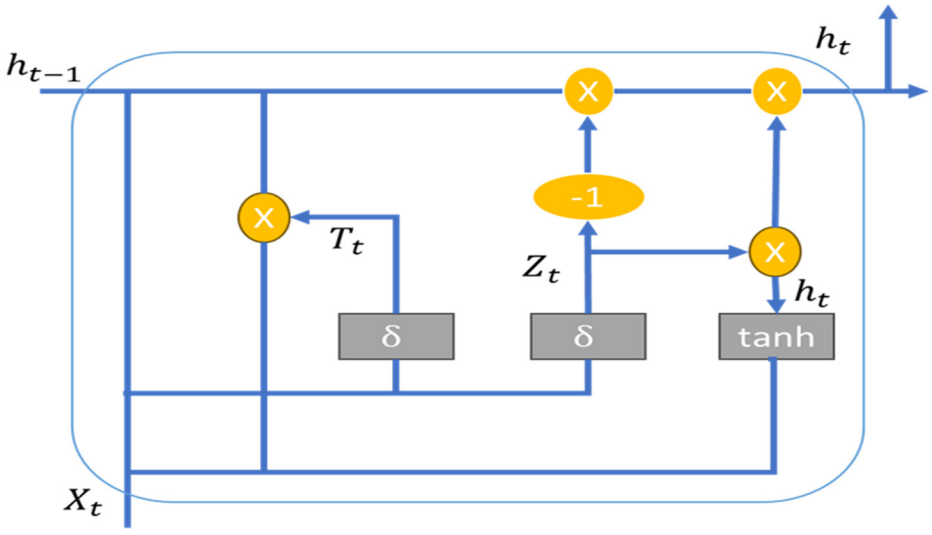

FIGURE 4:The architecture of a GRU cell

The GRU-based formula is as follows[54]:

$$z_t = \sigma(W_z x_t + U_z h_{t-1} + b_z) \quad (2)$$

$$r_t = \sigma(W_r x_t + U_r h_{t-1} + b_r) \quad (3)$$

$$\acute{h_t} = \tanh(W_h x_t + U_h(r_t \odot h_{t-1}) + b_h) \quad (4)$$

$$h_t = (1 - z_t) \odot h_{t-1} + z_t \odot \acute{h_t} \quad (5)$$

The input is represented by x_t in this instance, the hidden state at the previous time is represented by h_t−1, the update gate and reset gate are represented by z_t and r_t , respectively, the temporary hidden state is represented by $\acute{h_t}$ in this instance, and the hidden state is represented by h_t in this instance. The parameters W_z, W_r, W_h, U_z, U_r, U_h, b_z, b_r, and b_h must be ascertained by training. σ stands for the sigmoid function, while ⊙ denotes the element's product.

LONG-SHORT TERM MEMORY

Recurrent Neural Network (RNN) is a traditional algorithm used to predict and process sequential data that has been developed to multiple variants. Among others, we note Long-Short Term Memory (LSTM) that uses some mechanisms to capture long range dependencies which represent one of RNN algorithm limitations. The idea is that the LSTM has a memory cell that stores the variable information for the longest possible time.

The LSTM captures the information that needs to be kept for a long time to make accurate forecasts and also eliminates any information that may lead to errors being transmitted during the prediction process. To do that, the process combines three components, namely: cell state (Ct), hidden state (ht) and gates (ft, it, ot). The system starts by deciding the information that the system should forget for the next prediction using the forget gate by respecting the following equation:

$$f_t = \sigma \times (W_f \times [h_{t-1}, x_t] + b_f) \quad (6)$$

Where h_{t-1} is the hidden state from the previous step and x_t is the input vector at the current step. σ is the sigmoid activation function and W_f, b_f are weight matrices and bias vectors, respectively. The information that get value close to zero should be discard from Ct-1 and those with values close to one should be kept. Right after the process determines the values that should be updated using Eq. (7) and creates new Ct candidates' values following Eq. (8).

$$i_t = \sigma \times (W_i \times [h_{t-1}, x_t] + b_i) \quad (7)$$

$$c'_t = \tanh (W_c \times [h_{t-1}, x_t] + b_c) \quad (8)$$

Once the two previous steps have been completed, the system proceed to update the cell state.

$$c_t = f_t \odot c_{t-1} + i_t \odot c'_t \quad (9)$$

Finally, the output gate is calculated, and the hidden state is also updated using the following equations.

$$o_t = \sigma \times (W_o \times [h_{t-1}, x_t] + b_o) \quad (10)$$

$$h_t = o_t \odot \tanh (c_t) \quad (11)$$

EXTREME GRADIENT BOOSTING

The XGBoost (Extreme Gradient Boosting) algorithm[55], a powerful machine learning technique, has emerged as a promising tool for predicting thermal comfort and energy consumption in buildings [56][57] . XGBoost, introduced in 2014, is an enhanced algorithm based on GBD[58]. The core principle behind XGBoost is the use of the Newton method to solve the extreme value of the loss function, which is then expanded to the second-order derivatives to obtain an analytic solution as the gain to establish trees [59]. This article aims to examine the application of the

XGBoost algorithm in this field, highlighting its advantages and limitations, as well as its potential for integration with passive design strategies to achieve optimal building energy performance[60]. The XGBOOST method is used in this article to determine interior occupancy based on ambient temperature, humidity, and CO2 levels. With this information, energy consumption may be optimized while maintaining thermal comfort [61].

RANDOM FOREST

The ensemble learning method known as random forests has shown great promise in providing accurate predictions of building thermal comfort and energy consumption[62]. Since these methods don't rely on strict assumptions about the underlying data structure, they can be used to find complex links within high-dimensional data. The energy consumption patterns of buildings can be quite complicated and impacted by a wide range of factors, such as system operations, occupancy patterns, weather, and structure attributes. These models match a collection of data to a set of decision trees. To increase the target's predictability, each tree recursively splits the data into more homogeneous pieces known as nodes. The values of the predictor variables which are regarded as significant explanatory variables provide the foundation for the division points. Different decision trees are fitted by random forests to a predetermined number of bootstrap data sets[63]. As illustrated in Fig., the adjusted mean of every single response that comes from each bootstrap sample is the projected value for a continuous response.

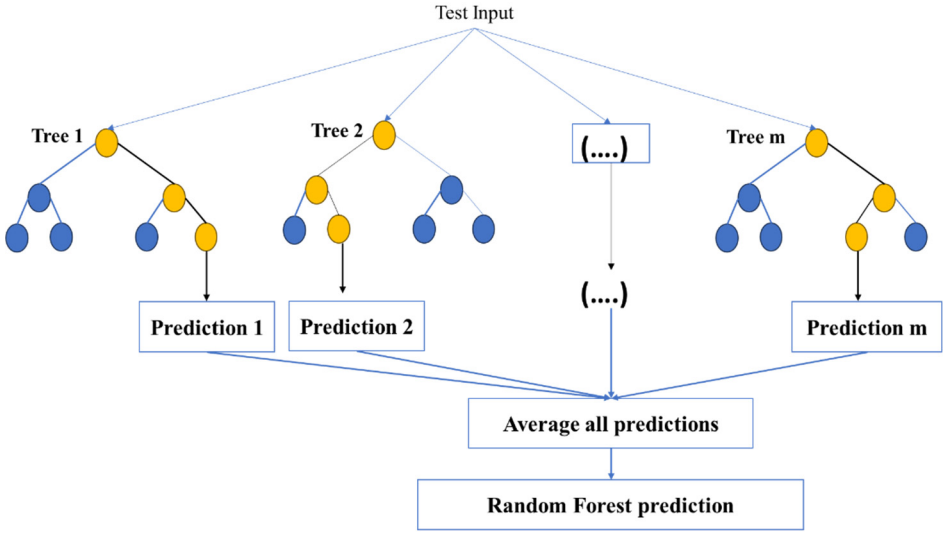

FIGURE 5:RF prediction algorithm.

SUPPORT VECTOR REGRESSION

The concepts of Support Vector Machines (SVMs) are extended to the field of regression analysis by the potent machine learning technique known as Support Vector Regression (SVR). While decreasing the model's complexity, SVR looks for the ideal hyperplane that best matches the training set of data, in contrast to classic regression techniques that seek to reduce the sum of squared errors. Regression using Support Vector Machines primarily involves the introduction of a kernel function that may nonlinearly map the input space into a hyper-dimensional feature space. This function then formulates an optimum hyperplane to achieve linear regression (LR) in the feature space [64]. Equation () expresses the SVR function.

$$f(x) = W^{T}\varphi(x) + b \tag{12}$$

The prediction outputs are denoted by f (x), W is the weight factor, b is the adjustable factor, and $\varphi(x)$ is the map function that maps the input space to a high-dimensional feature space.

EVALUATION METRICS

Every AI model employed in our investigation was trained on a system with an i7-11700 @ 2.50GHz (16 CPU), or around 2.5GHz processor. The findings in Table 2 detail the temperature prediction performance of six different models: random forests (RF), support vector regression (SVM), Extreme gradient boosting XGBoost, Long-short term memory (LSTM), Long-short term memory with Convolutional Neural Network (LSTM-CNN), gated recurrent units. This study evaluates their predictive accuracy using three common measures: root mean square error (RMSE), coefficient of determination (R^2) and mean absolute error (MAE). These measures are essential for comparing and evaluating the predictive capabilities of each model.

The Root Mean Square Error (RMSE) represents the square root of the mean of the squared differences between predicted and observed values[65]. RMSE is determined as follows:

$$\mathrm{RMSE} = \sqrt{\frac{1}{n}\sum_{i=1}^{n}(y_i - \hat{y}_i)^2} \tag{13}$$

Compared to other widely used metrics, including the Root Mean Square Error (RMSE), the Mean Absolute Error (MAE) offers a number of advantages. Since the MAE is a linear measure as opposed to the RMSE, it is less susceptible to outliers and offers a more easily understood representation of the average error . Furthermore, the RMSE is a function of three characteristics, whereas the MAE is a function of only one characteristic of the error distribution[65]. . MAE is determined as follows:

$$\mathrm{MAE} = \left|\frac{1}{n}\sum_{i=1}^{n}(y_i - \hat{y}_i)\right| \tag{14}$$

R^2 quantifies a model's goodness of fit. A high R^2 value means that the observed values and the anticipated values fit perfectly[65]. R^2 is determined as follows:

$$R^2 = 1 - \frac{\sum_{i=1}^{n}(y_i - \hat{y}_i)^2}{\sum_{i=1}^{n}(y_i - \bar{y})^2} \tag{15}$$

RESULTS AND DISCUSSION

According to a number of parameters, such as efficiency R^2, RMSE and MAE, the Extreme Gradient Boosting model appears to be the best option compared to the other models. The Extreme Gradient Boosting model has the lowest RMSE (1.42) and MAE (0.69), demonstrating very good predictive accuracy. In addition, the model's amazing fit to the data is highlighted by its high R^2 of 0.95, indicating an impressive overall performance. However, it has substantially faster prediction speeds (0.02 seconds) than Random Forests. This makes XGBoost an excellent model for real-time temperature prediction in cases where speed is crucial.

Randow forests, with strong performance in terms of accuracy and efficiency (RMSE (1.70), MAE (0.92), R^2 (0.90)), and gated recurrent units, which offer a balance between accuracy, model fit, and high efficiency (RMSE (2.19), MAE (1.48), R2 (0.90), and prediction time (1.56 s), are the next models in the ranking.

Sub-figures 6(a), 6(b) and 6(c) confirm the previous analysis by showing that there is a strong correspondence between predicted and actual values, with the majority of predicted points placed around the actual point , (blue line) following the actual temperature trend (red line). This finding validates the good performance of all three models. However, as sub-figures 6(e) show, the long-term memory model predicts values far removed from the actual values, leading to significant errors in these predictions.

When compared to LSTM and SVR, GRU has the lowest RMSE (2.19), meaning that it has the lowest mean error among the three models. With the greatest R-squared of any model, SVR appears to account for 89% of the variation in the data. SVR has the biggest RMSE (2.55) and the highest R-squared (0.89), suggesting an imbalance between model complexity and accuracy. GRU maintains a reasonably low error rate while achieving a decent balance between RMSE and R-squared, indicating that it can identify underlying variations in the data. However, while SVR is often better suited to short-term predictions, LSTM has the lowest R-squared of the three (0.68), indicating that it may not be able to capture temporal correlations in data in this case.

When compared to the previous set of models' assessment metrics, the LSTM-CNN and Long-Term Memory models performed comparatively less accurately.

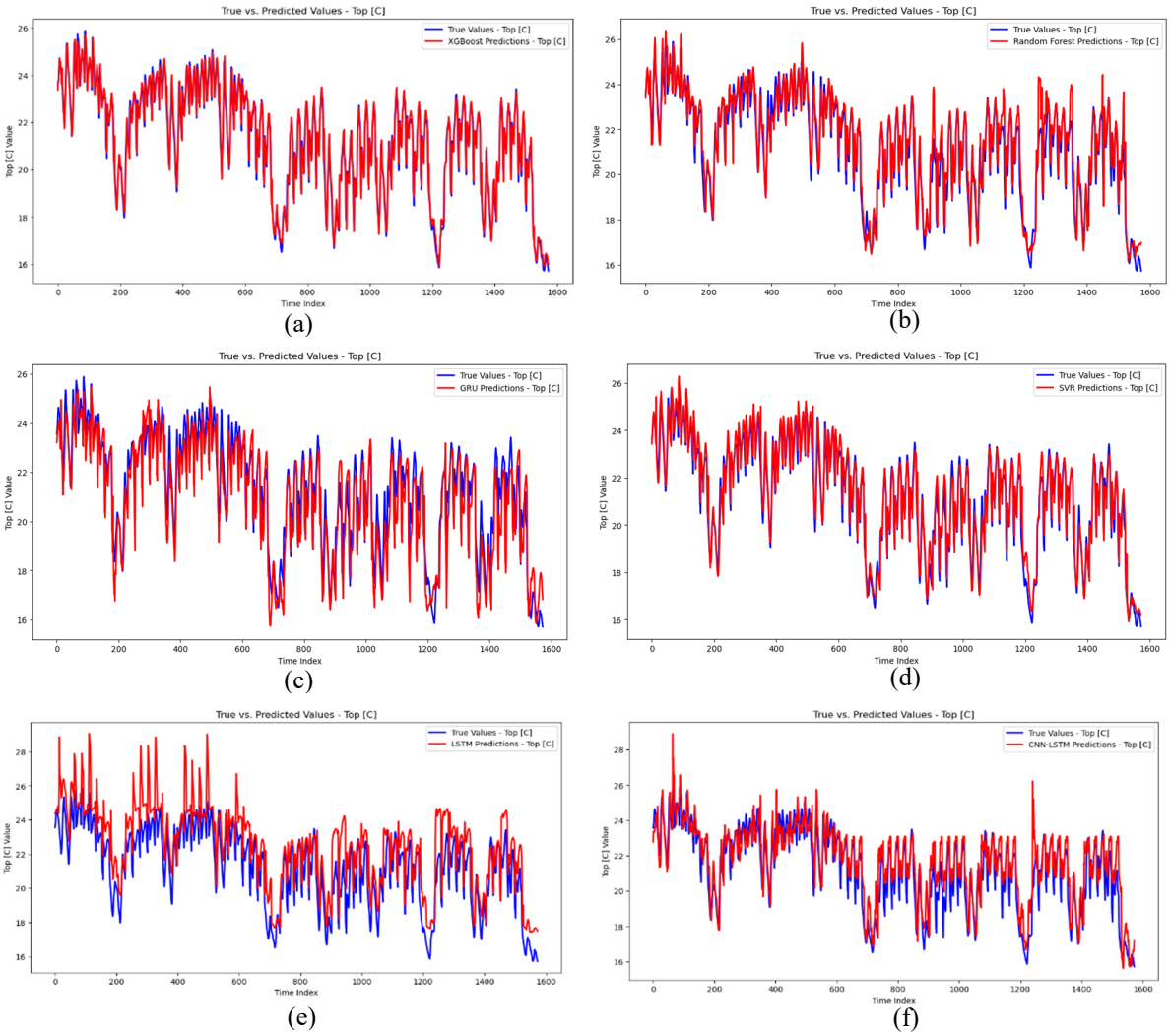

FIGURE 6 :Predicted vs.correct values for all AI models evaluated: (a): XGBoost predictions, (b): Random Forest predictions , (c):GRU predictions, (d):SVR prediction, (e):LSTM predictions, (f):CNN-LSTM predictions.

Table 3: Results of artificial intelligence model evaluation.

AI models	Performance metrics				
	RMSE	MAE	R-Squared	Training time (s)	Predicting time (s)
GRU	2.19	1.48	0.83	447.29	1.56
LSTM	2.44	1.88	0.68	506.63	2.01
CNN-LSTM	2.79	1.98	0.73	3098.78	3.74
SVR	2.55	1.30	0.89	13.58	5.91
Random_Forests	1.70	0.92	0.90	73.55	0.03
XGBOOST	1.42	0.69	0.95	13.60	0.02

CONCLUSION AND PERSPECTIVES

This study emphasizes how crucial artificial intelligence is for ensuring thermal comfort and energy savings. We can better regulate the heating, ventilation, and air conditioning system when we can anticipate temperatures accurately. This saves a significant amount of energy and guarantees occupant comfort. By analyzing six artificial intelligence models (Gated Recurrent Units, Long-Short Term Memory with Convolutional Neural Network, Extreme Gradient Boosting, Random Forest, Support Vector Regression, and Random Forest), the goal of this work is to predict temperature as an important control parameter. The database, an entire year of time series from an EnergyPlus simulation of an office building in Casablanca, Morocco. The database includes meteorological data, such as temperature, humidity and wind speed, as well as simulated data by zone, such as operating temperature and relative humidity, air temperature, power consumption, etc. XGboost is notable for its outstanding accuracy, with an RMSE of 1.42, an MAE of 0.69, a good forecast of 0.02 seconds, and an R-squared of 0.95. Random Forests comes closely behind XGboost in terms of performance, with an RMSE of 1.70 and an R-squared value of 0.90. The ability to accurately anticipate temperature has several advantages. Using these forecasts, we can dynamically alter HVAC system settings, ensuring that energy is utilized effectively while providing ideal thermal comfort to occupants. This results in considerable financial savings, lower environmental impact, and improved occupant well-being. For the future, we plan to extend our study by including many temperature zones in the building simulation, which would result in a more complex dataset that would capture the complexity of the real environment. In addition, increasing the dataset to include many years of data would enhance the learning capabilities of the models.

In the next phase of our research, we plan to incorporate these temperature forecasts directly into HVAC management algorithms. This creates a closed-loop system that continuously analyzes and modifies temperature conditions, ensuring both comfort and energy savings. Temperature prediction with AI promises to revolutionize building management practices.

REFERENCES

1. Hausfather, « State of the climate: How the world warmed in 2021 », Carbon Brief. Consulté le: 28 juin 2024. [En ligne]. Disponible sur: https://www.carbonbrief.org/state-of-the-climate-how-the-world-warmed-in-2021/
2. U. Nations, « What Is Climate Change? », United Nations. Consulté le: 28 juin 2024. [En ligne]. Disponible sur: https://www.un.org/en/climatechange/what-is-climate-change
3. « U.S. energy facts explained - consumption and production - U.S. Energy Information Administration (EIA) ». Consulté le: 28 juin 2024. [En ligne]. Disponible sur: https://www.eia.gov/energyexplained/us-energy-facts/
4. « Fossil Fuels - Energy System », IEA. Consulté le: 28 juin 2024. [En ligne]. Disponible sur: https://www.iea.org/energy-system/fossil-fuels
5. « Global Status Report for Buildings and Construction 2019 – Analysis », IEA. Consulté le: 28 juin 2024. [En ligne]. Disponible sur: https://www.iea.org/reports/global-status-report-for-buildings-and-construction-2019
6. H. Shi and Q. Chen, J Build Eng, **33**, 101869 (2021)
7. A. Kusiak, M. Li, and F. Tang, Appl Energ, **87**(10),. 3092-3102 (2010)
8. A. Colmenar-Santos, L.N. Terán de Lober, D. Borge-Diez, and M. Castro-Gil, Energ Build, 56, 66-77 (2013)
9. T. Salsbury, P. Mhaskar, and S.J. Qin, Comput Chem Eng, **51**, 77-85 (2013)
10. « The performance of occupancy-based lighting control systems: A review - X. Guo, DK Tiller, GP Henze, CE Waters, 2010 ». Consulté le: 28 juin 2024. [En ligne]. Disponible sur: https://journals.sagepub.com/doi/abs/10.1177/1477153510376225
11. E.H. Mathews, C.P. Botha, D.C. Arndt, and A. Malan, Energ Build, **33**(8), 853-863 (2001)
12. A. Chel and G. Kaushik, Alexandria Eng J, 57(2), 655-669 (2018)
13. M. Casini, « Small Vertical Axis Wind Turbines for Energy Efficiency of Buildings », … 2016,
14. H. Farzaneh, L. Malehmirchegini, A. Bejan, T. Afolabi, A. Mulumba,and P. P. Daka, Appl Sci, **11**(2), 2 (2021)
15. Z. Ullah, F. Al-Turjman, L. Mostarda, and R. Gagliardi, Comput Commun, **154**, 313-323 (2020)
16. R. Cioffi, M. Travaglioni, G. Piscitelli, A. Petrillo, and F. De Felice, Sustainability, **12**(2), 492 (2020)
17. Z. Liu, Y. Qiu, and S. Jafarinejad, « Artificial intelligence application to the nexus of renewable energy, water, and the environment », in The Renewable Energy-Water-Environment Nexus, Elsevier, 2024, p. 399-422. Consulté le: 26 juin 2024.[En ligne]. Disponible sur: https://www.sciencedirect.com/science/article/pii/B9780443134395000120
18. S. Souabi, A. Chakir, and M. Tabaa, Energ Rep, **9**, 90-105 (2023)
19. J. Runge and E. Saloux, Energy, **269**, 126661 (2023)
20. Q. Wu, H. Ren, S. Shi, C. Fang, S. Wan, and Q. Li, Energ Rep, **9**, 395-402 (2023)
21. L.F. Schlindwein and C. Montalvo, Energy Policy, **180**, 113662, (2023)
22. M. Laskari, R.F. de Masi, S. Karatasou, M. Santamouris, and M.N. Assimakopoulos, Energy Build, **255**, 111657 (2022)
23. K. Choukri, A. Naddami, and S. Hayani, Energ Sustain Soc, **7**(1), 25, (2017).
24. J. Żywiołek, J. Rosak-Szyrocka, M.A. Khan, and A. Sharif, Energies, **15**(4), 4 (2022)
25. Y. Geng et al., J Clean Prod, **159**, 301-316, (2017)
26. Z. Liu et al., Energy and AI, **10**, 100195 (2022)
27. J. El Mostafa, D. Zejli, and N. Komendantova, « Dynamics of Energy Transition in Morocco: Centralized versus Decentralized Options ». Consulté le: 26 juin 2024. [En ligne]. Disponible sur: https://iiasa.dev.local/
28. P.H. Shaikh, N.B.M. Nor, P. Nallagownden, I. Elamvazuthi, and T. Ibrahim, Renew Sustain Energ Rev, **34**, 409-429 (2014)
29. Chr. Lamnatou, D. Chemisana, and C. Cristofari, Renew Energ, **185**, 1376-1391 (2022)
30. S.F. Rafique and Z. Jianhua, IET Generat Transmission Distrib, **12**(3), 519-530 (2018)
31. M. Nutakki and S. Mandava, Eng Appl Artif Intell, **119**, 105721 (2023)
32. « Sustainability | Free Full-Text | A Novel Interval Energy-Forecasting Method for Sustainable Building Management Based on Deep Learning ». Consulté le: 26 juin 2024. [En ligne]. Disponible sur: https://www.mdpi.com/2071-1050/14/14/8584
33. « Smart Energy Management System: A Comparative Study of Energy Consumption Prediction Algorithms for a Hotel Building | IEEE Conference Publication | IEEE Xplore ». Consulté le: 26 juin 2024. [En ligne]. Disponible sur: https://ieeexplore.ieee.org/abstract/document/9815807
34. Q. Qiao, A. Yunusa-Kaltungo, et R. Edwards, « Predicting building energy consumption based on meteorological data », in *2020 IEEE PES/IAS PowerAfrica*, 1-5 (2020)
35. R. Sendra-Arranz and A. Gutiérrez, Energ Build, **216,** 109952 (2020)

36. L. Mendoza-Pittí, H. Calderón-Gómez, J.M. Gómez-Pulido, M. Vargas-Lombardo, J.L. Castillo-Sequera, and C.S. de Blas, Appl Sci, **11**(15), 15 (2021).
37. T.Y. Kim and S.B. Cho, Energy, **182**, 72-81 (2019)
38. « Control-Oriented Thermal Modeling of Multizone Buildings: Methods and Issues: Intelligent Control of a Building System | IEEE Journals & Magazine | IEEE Xplore ». Consulté le: 28 juin 2024. [En ligne]. Disponible sur: https://ieeexplore.ieee.org/abstract/document/7470638
39. D. Jacob, S. Dietz, S. Komhard, C. Neumann, and S. Herkel, J Build Perform Simulat, **3**(1), 53-62 (2010)
40. H.İ. Tol and H. B. Madessa, J Build Eng, **68**, 106038 (2023)
41. Y. Li, Z. O'Neill, L. Zhang, J. Chen, P. Im, and J. DeGraw, Renew Sustain Energy Rev, **146**, 111174 (2021)
42. T. Hauge Broholt, M. Dahl Knudsen, and S. Petersen, Energ Build, **275**, 112460 (2022)
43. G. Barone, A. Buonomano, C. Forzano, G. F. Giuzio, A. Palombo, and G. Russo, Renew Sustain Energ Rev, **173**, 113015 (2023)
44. F. Amara, K. Agbossou, A. Cardenas, Y. Dubé, and S. Kelouwani, Smart Grid Renew Energ, **6**(4), 4 (2015)
45. A. Shahcheraghian, H. Madani, and A. Ilinca, Energies, **17**, 376 (2024)
46. Y. Chen, M. Guo, Z. Chen, Z. Chen, and Y. Ji, Ener Rep, **8**, p. 2656-2671 (2022)
47. W. Liu et al., « Thermal modeling for energy-efficient smart building with advanced overfitting mitigation technique », In *21st Asia and South Pacific Design Automation Conference (ASP-DAC),* 417-422 (2016)
48. O.M. Brastein, D.W.U. Perera, C. Pfeifer, and N.O. Skeie, Energ Build, **169**, 58-68 (2018)
49. A. Azzi, M. Tabaa, B. Chegari, and H. Hachimi, Sustainability, **16**(5), 5 (2024)
50. B. Chegari, M. Tabaa, E. Simeu, F. Moutaouakkil, and H. Medromi, Energ Build, **239**, 110839 (2021)
51. « EnergyPlus ». Consulté le: 29 juin 2024. [En ligne]. Disponible sur: https://energyplus.net/documentation
52. S. Mohsen, Multimed Tools Appl, **82**(30), 47733-47749 (2023)
53. A. Chu, Y. Lai, and J. Liu, Secur Commun Networks, **2019**, 1-11 (2019).
54. X. Zhao and G. Liang, Front. Energy Res., **11,** (2023)
55. W. Li, Y. Yin, X. Quan, and H. Zhang, Front. Genet., **10,** (2019)
56. R. Wang, S. Lu, and Q. Li, Sustai Cities Soc, **49,** 101623 (2019)
57. S. Yaqian H. Zhijia and Z. Tao, Ahgydxxbzrkxb, **39**(1), 74-78, 99 (2022)
58. T. Chen and C. Guestrin, « XGBoost: A Scalable Tree Boosting System », in *Proceedings of the 22nd ACM SIGKDD International Conference on Knowledge Discovery and Data Mining, San Francisco California USA: ACM,* 785-794 (2016)
59. T. Chen and C. Guestrin, « XGBoost: A Scalable Tree Boosting System », in *Proceedings of the 22nd ACM SIGKDD International Conference on Knowledge Discovery and Data Mining, in KDD '16. New York, NY, USA: Association for Computing Machinery,* 785-794 (2016)
60. M. Lin, « Sustainable Building Performance through Improved Building-Occupant Interactions: An integrated Data Collection, Modeling and Analysis Approach », 2020, Consulté le: 25 juin 2024. [En ligne]. Disponible sur: https://khalifauniversity.elsevierpure.com/files/6822034/file
61. A. Mohammadabadi, S. Rahnama, and A. Afshari, Sustainability, **14**(21) 14644 (2022)
62. M.W. Ahmad, M. Mourshed, and Y. Rezgui, Energ Buildings, **147**, 77-89 (2017)
63. S.M. Basha, D.S. Rajput, J.J.R.S. Somula, and S. Ram, Scalable Comput: Pract Experien, **21**(4), 4 (2020)
64. V. Vapnik, The Nature of Statistical Learning Theory. Springer Science & Business Media, 2013.
65. Z. Wang, Y. Wang, R. Zeng, R S. Srinivasan, and S. Ahrentzen, Energ Build, **171**, 11-25 (2018)

Utilization of High Alcohol and Ferrocene for the Production of Carbon Nanotube From a Diesel Engine

Mohamed Almanzalawy[1,2, a)], Sameh Nada[1, b)], Ahmed Elwardany[3, c)] and Marwa Elkady[4, d)]

[1]*Energy Resources Engineering Department, Egypt-Japan University of Science and Technology (E-JUST), New Borg El-Arab City, Alexandria 21934, Egypt*
[2]*Mechanical Power Engineering Department, Faculty of Engineering, Mansoura University, El-Mansoura, 35516, Egypt*
[3]*Mechanical Engineering Department, Faculty of Engineering, Alexandria University, Alexandria 21544, Egypt*
[4]*Chemical and Petrochemicals Engineering Department, Egypt-Japan University of Science and Technology, Alexandria 21934, Egypt.*

[a)]Corresponding author: mohamed_manzalawy91@mans.edu.eg
[b)]sameh.nada@ejust.edu.eg
[c)]ahmed.elwardany@ejust.edu.eg
[d)]marwa.elkady@ejust.edu.eg

Abstract. This study used high-alcohol and ferrocene nanoparticles with a diesel/biodiesel blend (B30) to produce carbon nanotubes (CNT) from a diesel engine. The engine was operating at the optimum engine speed and full load. Five alcohols were used: butanol, pentanol, hexanol, heptanol, and octanol. Different concentrations were used to ensure a constant oxygen content in each blend. Based on the literature, the ferrocene concentration was optimized for CNT production. The combined impact of alcohol and ferrocene on engine and combustion characteristics was reported. In most cases, the additives reduce specific fuel consumption and increase thermal efficiency compared to B30. Ferrocene nanoparticles with high alcohol increased the pressure inside the combustion chamber, accelerated the heat release, and reduced the combustion period. Ultimately, CNT was detected using TEM imaging with high alcohols, from pentanol to octanol. However, butanol, with a lower carbon chain and smaller energy content, did not produce CNT.

INTRODUCTION

Projections indicate that there will be an increase in energy consumption in the transportation, industrial, and residential sectors in the following decades. Notwithstanding environmental concerns, it is projected that fossil fuels will provide around two-thirds of the energy demand [1]. Diesel engines are utilized by various industries, such as power generation, transportation, and construction, to convert chemical energy into mechanical energy. Compression ignition engines have higher thermal efficiency compared to spark ignition engines [2]. In addition, the product offers both durability and requires less maintenance.

Nevertheless, researchers face challenges in decreasing emissions from diesel engines. The revised environmental regulations render this task more challenging. The primary concerns of CI engines are around two types of pollutants. More precisely, nitrogen oxides (NO_x) and particulate matter (PM) [3]. Prolonged emissions from diesel engines have adverse effects on human health [4]. The use of biodiesel, alcohol, and nanoparticles is often reported to suppress engine pollution [5–8].

Carbon nanomaterials, such as carbon nanotubes (CNT), carbon nano-rods, carbon nano-onions, and fullerenes, are identified in the exhaust of compression ignition engines [9]. Three diesel engines were observed under typical running conditions, both with and without the presence of catalysts. Nevertheless, the exceptional thermal and chemical stabilities, electrical conductivity, and mechanical strength of CNTs render them highly valuable [10]. Therefore, numerous investigations have been conducted to examine the uses, characterization, and synthesis of CNT.

Using engines to produce CNT-like substances, such as multi-wall carbon nanotubes, can transform soot emissions into a lucrative asset. It is important to recall that combustion engines produce electricity. This study aims to develop a valuable product by addressing an environmental concern related to power and transportation equipment, specifically diesel engines.

Technologies and Materials for Renewable Energy, Environment and Sustainability
AIP Conf. Proc. 3321, 040007-1–040007-6; https://doi.org/10.1063/5.0289604
Published under an exclusive license by AIP Publishing. 978-0-7354-5231-2/$30.00

Utilizing diesel engines to generate carbon nanotubes transforms the problem of soot emissions into a valuable resource [11,12]. One must recognize that power production is one of the primary functions of combustion engines. This study seeks to enhance the primary product of power with a beneficial environmental impact. Production of carbon nanotubes involves three primary parameters: a carbon source, an energy source, and a catalyst. In this study, the carbon source is the fuel blend (comprising diesel, biodiesel, and alcohol), while the energy source is the heat of combustion. Ferrocene ($FeC_{10}H_{10}$) was used as a catalyst for synthesizing carbon nanotube and was applied to five blends at the same concentration.

EXPERIMENTAL METHODS

FIGURE 1 shows the used diesel engine for experiments in the current study. These experiments aimed to explore the potential of various fuel blends in producing carbon nanotubes. To ensure the fuel blends were homogeneous, a probe ultrasonicator BH-900N was utilized, which is known for its efficiency in creating uniform mixtures. The study identified B30 as the most effective base fuel. This blend was selected to study the impact of five different additives on engine performance and carbon nanotube production, both with and without the addition of Ferrocene nanoparticles. Ferrocene, a well-known catalyst for carbon nanotube synthesis, was incorporated into each blend at a concentration of 1770 ppm to facilitate the production process.

The alcohols chosen for this study were Butanol, Pentanol, Hexanol, Heptanol, and Octanol. Each alcohol was added to the base fuel in varying mass concentrations: Butanol at 7.095%, Pentanol at 8.735%, Hexanol at 10.495%, Heptanol at 12.389%, and Octanol at 14.432%. These specific concentrations were selected to ensure a comprehensive evaluation of each alcohol's effect on the engine's performance and the efficiency of carbon nanotube production. The use of these different alcohols aimed to identify the optimal blend that maximizes both the energy output of the engine and the production of carbon nanotubes. Introducing Ferrocene nanoparticles into these blends was expected to enhance the catalytic processes for forming carbon nanotubes. By investigating these parameters, the study aimed to provide valuable insights into improving fuel efficiency and reducing harmful emissions through the innovative use of diesel engines for carbson nanotube production. The corresponding blends were named B30Bu7F, B30Pen9F, B30Hex10F, B30Hep12F, and B30Oct14F, respectively, where F refers to Ferrocene in this study. The base blends

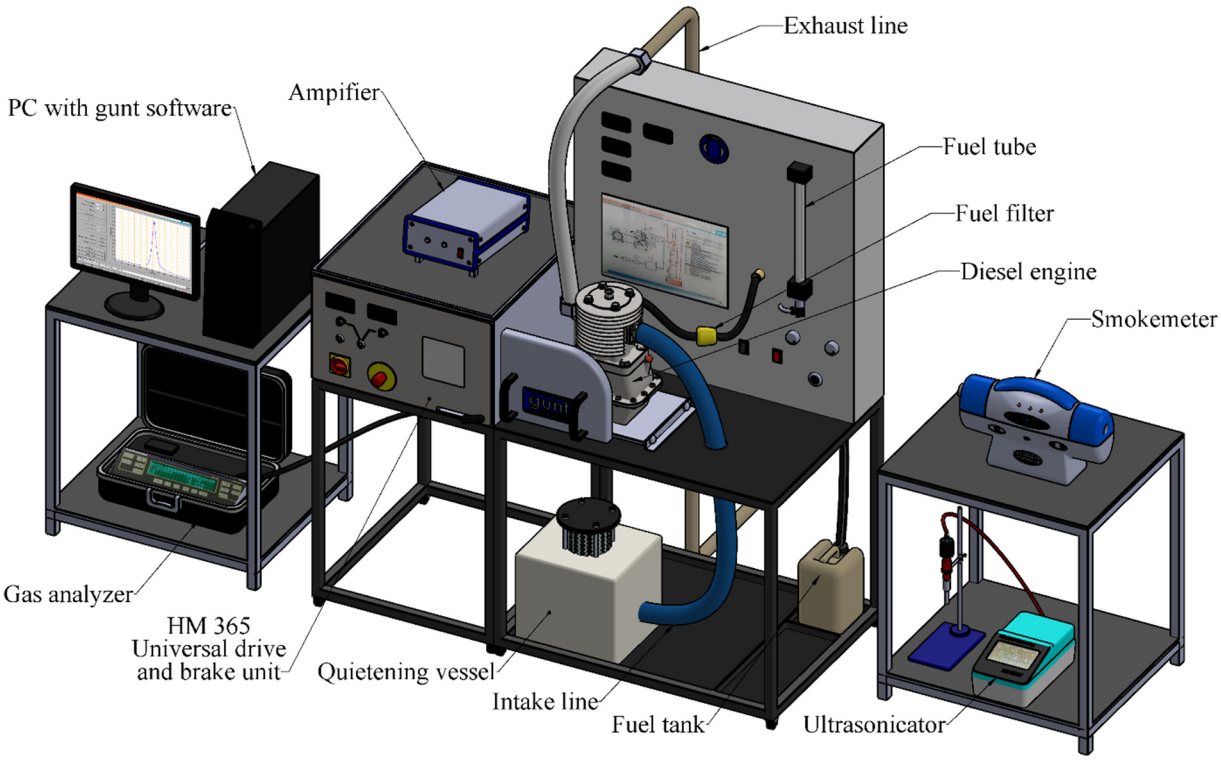

FIGURE 1. The experimental setup and equipment.

are neat diesel fuel (D100) and a blend of 30% biodiesel with 70% diesel fuel (B30). Butanol was investigated two times with and without Ferrocene nanoparticles.

Leveraging the previously identified optimal engine speed of 1750 rpm [13], all experiments were conducted at this setting for consistency. High temperatures are crucial for carbon nanotube (CNT) production, and the maximum in-cylinder pressure achievable during full engine load (6 Nm) was chosen for all tests. This study aimed to partially replace fossil fuels with a cleaner and renewable alternative: biodiesel. Based on prior research, B30 emerged as the optimal combination. Therefore, all investigated blends were prepared using B30 as the base fuel, and experiments were conducted using neat diesel fuel (D100) for comparison.

TABLE 1 summarizes the experiments conducted in the current study. The design of this experimental matrix was informed by a thorough review of previous literature and the newly obtained experimental data. The study aimed to build upon established methodologies and ensure a robust investigation by integrating historical research and current findings. This approach facilitated a meaningful comparison of new results with those reported in earlier studies, thus validating the current experimental outcomes and enhancing the overall understanding of the subject matter.

TABLE 1. Experiment matrix for the present study.

Blend	Alcohol additive	Mass % of A	Ferrocene
D100	–	–	–
B30	–	–	–
B30Bu7	Butanol	07.095%	–
B30 Bu7F	Butanol	07.095%	1770 ppm
B30Pen9F	Pentanol	08.735%	1770 ppm
B30Hex10F	Hexanol	10.495%	1770 ppm
B30Hep12F	Heptanol	12.389%	1770 ppm
B30Oct14F	Octanol	14.432%	1770 ppm

RESULTS AND DISCUSSION

FIGURE 2 illustrates the impact of alcohol and Ferrocene on engine performance. This figure comprehensively summarizes how adding these substances influences various engine parameters. Generally, incorporating alcohols or Ferrocene nanoparticles significantly enhances engine performance compared to B30 biodiesel alone. Specifically, these additives often result in a noticeable decrease in brake-specific fuel consumption (bsfc) and an increase in thermal efficiency, demonstrating their potential benefits.

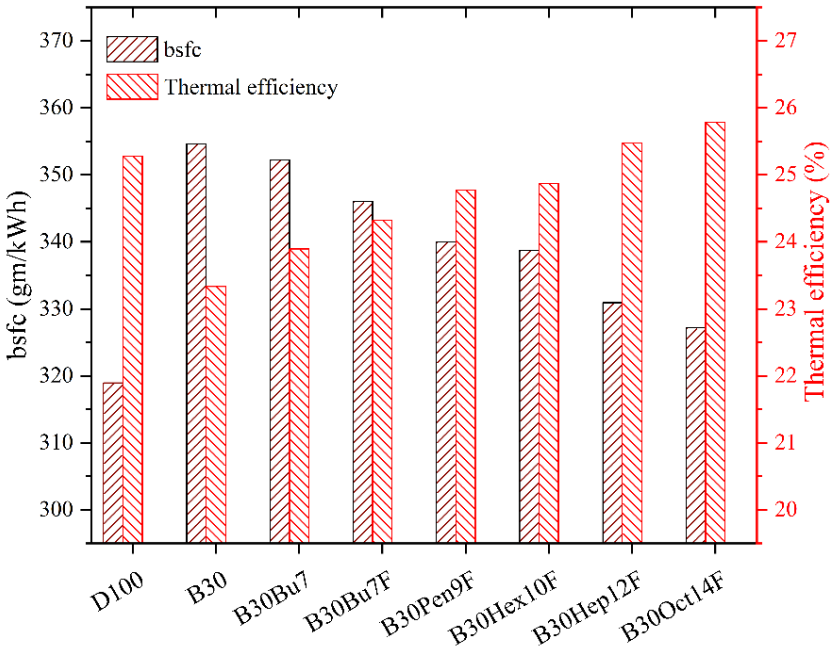

FIGURE 2. Engine performance for all blends at the full load.

In most instances, the addition of Ferrocene nanoparticles consistently reduced bsfc across all fuel blends. This reduction can be assigned to nanoparticles' improved atomization and evaporation of the fuel. These processes enable a more complete and efficient combustion, lowering the fuel required to generate the same load [14]. This effect is particularly evident in the data shown, where Ferrocene nanoparticles have been found to enhance the overall fuel combustion efficiency, thus validating their role in optimizing engine performance.

Moreover, the analysis indicates that high alcohol provides better fuel consumption rates compared to low alcohol. This improvement is primarily due to the higher energy content found in higher alcohols, which translates to more energy being released during combustion. Consequently, engines running on higher alcohol blends exhibit superior fuel efficiency. This relationship underscores the potential of higher alcohols as a viable alternative to traditional biodiesel, especially regarding energy output and consumption rates.

Additionally, the presence of Ferrocene nanoparticles not only reduced bsfc but also improved the overall combustion process. This improvement is evident in the enhanced thermal efficiency observed with these nanoparticles [15]. The data shown in Figure 2 clearly illustrates how Ferrocene nanoparticles contribute to a more efficient combustion process, leading to better thermal efficiency. This finding aligns with previous studies, reinforcing that Ferrocene nanoparticles benefit combustion enhancement.

Alcohols, particularly Octanol, also significantly improved thermal efficiency compared to B30 biodiesel. This can be attributed to several factors. Firstly, alcohols generally possess better viscosity characteristics than biodiesel, which facilitates better fuel atomization and mixing during combustion. Secondly, the functional groups in alcohols are more efficient in combustion, contributing to a more complete and efficient burn. This efficiency is particularly noticeable with higher alcohols, which offer better thermal efficiency due to their higher heating value [16]. The increased energy content in higher alcohols ensures that more energy is released during combustion, thereby enhancing the overall thermal efficiency of the engine.

In conclusion, the findings presented in Fig. 2 confirm that both alcohols and Ferrocene nanoparticles significantly enhance engine performance. These additives lead to reduced bsfc and improved thermal efficiency, thereby promoting a more efficient and effective combustion process inside diesel engines. This conclusion is supported by previous literature, which has consistently shown the positive effects of these substances on engine performance [17]. The enhanced atomization, evaporation, and combustion processes facilitated by these additives underscore their potential as valuable components in fuel formulation, paving the way for more efficient and sustainable engine operation.

FIGURE 3(a) provides a detailed summary of the variations in in-cylinder pressure observed across all tested fuel blends under full load conditions. The data show that including Ferrocene nanoparticles substantially increased in-cylinder pressure across all blends. This notable enhancement can be attributed to the catalytic properties of Ferrocene nanoparticles, which actively facilitate and promote more efficient combustion processes within the engine.

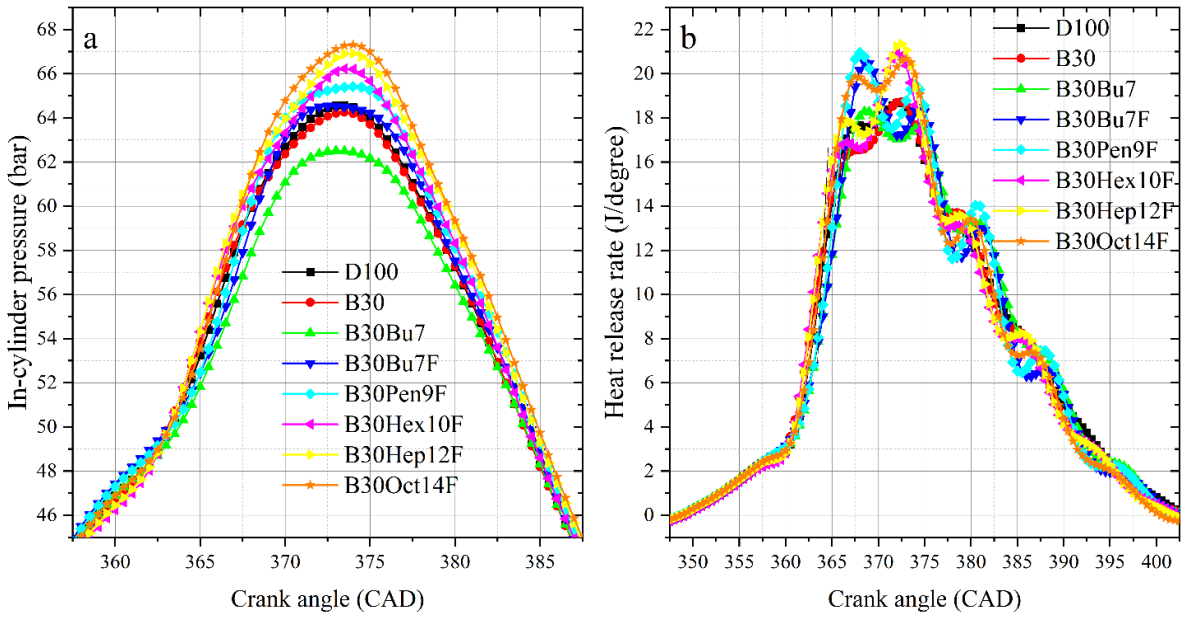

FIGURE 3. (a) In-cylinder pressure and (b) heat release rate for all blends at the full load.

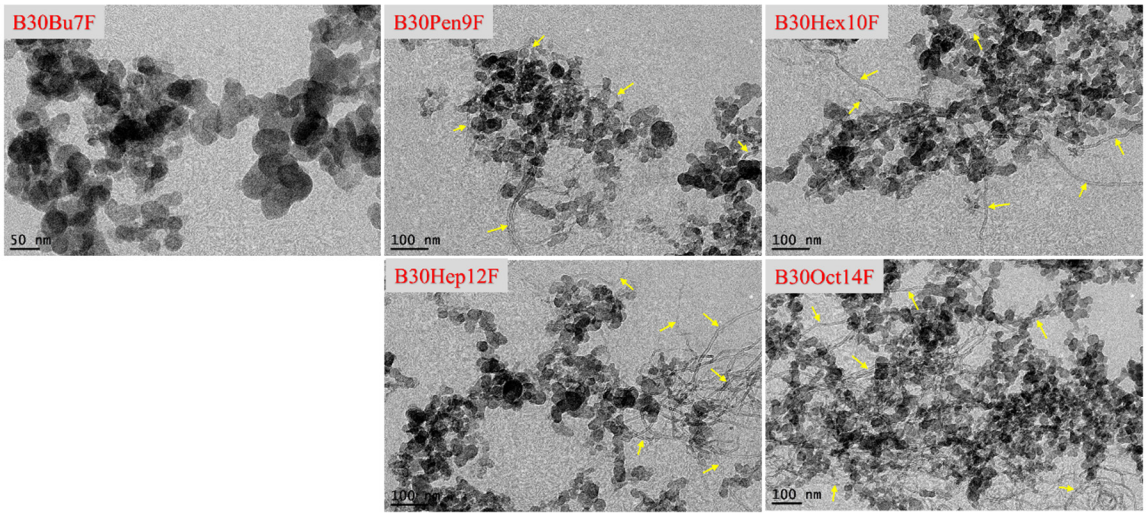

FIGURE 4. TEM images show the success of CNT production with high alcohol.

Metal nanoparticles, such as Ferrocene, are known for their catalytic activity, which accelerates the combustion reactions by providing active sites for the oxidation of fuel molecules. This catalytic effect increases the overall combustion efficiency and contributes to a more complete combustion process, thereby maximizing energy conversion from fuel to mechanical work. Furthermore, Ferrocene nanoparticles have been shown to reduce the time required for fuel evaporation within the cylinder, leading to more efficient and timely combustion.

These findings underscore the significant role of Ferrocene nanoparticles in enhancing engine performance by improving combustion dynamics and overall efficiency [18]. Such enhancements are crucial for achieving better fuel economy and reducing emissions, aligning with advancements reported in related research [19].

FIGURE 3(b) illustrates the heat release rate across all tested blends under full load conditions. Incorporating Ferrocene nanoparticles notably enhanced the heat release rate, consistent with findings reported in previous studies [19]. This enhancement can be attributed to the better atomization process and promoted combustion dynamics facilitated by nanoparticles [20].

Particulate matter from the diesel engine was sampled and imaged to detect traces of carbon nanotubes. Initially, particles were collected on the TEM grid using a thermophoretic approach for imaging. Unfortunately, no CNT traces were found with butanol, despite expectations that it would fulfill all conditions necessary for CNT synthesis. However, Fig. 4 shows that no CNT remnants were detected with B30Bu7F either. This outcome may be attributed to the low amount of butanol used, despite literature suggesting higher alcohol percentages are needed for noticeable CNT formation [21,22]. This challenge was addressed by utilizing higher alcohols with superior heating values and lower latent heat of vaporization [23]. Using longer carbon chain alcohols promoted CNT production within the diesel engine. Even with 7% butanol, CNT synthesis did not occur, whereas starting from around 9% Pentanol, traces of CNTs were successfully identified. Further investigations are necessary to determine the optimal conditions for enhancing CNT production in a diesel engine using higher alcohol blends.

CONCLUSION

A diesel engine was used in this work to evaluate the possibility of producing carbon nanotubes (CNT) through the utilization of high-alcohol and ferrocene nanoparticles. Butanol, pentanol, hexanol, heptanol, and octanol were utilized in this study. It was reported that alcohol and ferrocene had a combined influence on the performance of the engine and the characteristics of the combustion process. When compared to B30, the majority of cases resulted in a reduction in specific fuel consumption and an increase in thermal efficiency. As a result of the presence of ferrocene nanoparticles with high alcohols, the pressure inside the cylinder increased, the HRR increased, and the period of the combustion process decreased. The identification of CNT was ultimately accomplished through the utilization of TEM imaging while utilizing a variety of high alcohols, specifically pentanol to octanol. However, while having a shorter carbon chain and a lower energy content, butanol was not successful in producing carbon nanotubes.

ACKNOWLEDGMENTS

The work presented in this paper was funded by the Science and Technology Development Fund (STDF) under grant number STDF 43667.

REFERENCES

1. K. Nanthagopal, R.S. Kishna, A.E. Atabani, A.H. Al-Muhtaseb, G. Kumar, B. Ashok, Energy Convers. Manag. 203 (2020) 112244.
2. A.K. Wamankar, A.K. Satapathy, S. Murugan, Energy. 93 (2015) 511–520.
3. N. Wu, J. Phys. Conf. Ser. 2608 (2023).
4. U. States, Health Assessment Document For Diesel Engine Exhaust, 2002.
5. F.A. Zaher, M.S. Gad, Egypt. J. Chem. 61 (2018) 13–21.
6. H.H. Hamed, A.E. Mohammed, O.A. Habeeb, O.M. Ali, O.H.S. Aljaf, M.A. Abdulqader, Egypt. J. Chem. 64 (2021) 2827–2832.
7. E.E. Ebrahiem, Y.A. Hakim, T.M. Aboul-Fotouh, M.A. Elfattah, Egypt. J. Chem. 65 (2022) 349–355.
8. M.A. Fayad, A.O. Abd, M.T. Chaichan, H.A. Dhahad, A. Al Ezzi, IOP Conf. Ser. Earth Environ. Sci. 961 (2022).
9. H.S. Jung, A. Miller, K. Park, D.B. Kittelson, J. Air Waste Manag. Assoc. 63 (2013) 1199–1204.
10. M.F.L. De Volder, S.H. Tawfick, R.H. Baughman, A.J. Hart, Science (80-.). 339 (2013) 535–539.
11. T. Uchida, O. Ohashi, H. Kawamoto, H. Yoshimura, K.I. Kobayashi, M.T. Animura, N. Fujikawa, T. Nishimoto, K. Awata, M. Tachibana, K. Kojima, Jpn. J. Appl. Phys. 45 (2006) 8027–8029.
12. Y. Haik, S. Aldajah, System for producing carbon nanotubes from combustion engine exhausts, US 9,932,236 B2, 2018.
13. M.S. Almanzalawy, S. Mori, M.F. Elkady, A.E. Elwardany, J. Therm. Anal. Calorim. (2023).
14. A.E. Elwardany, M.N. Marei, Y. Eldrainy, R.M. Ali, M. Ismail, M.M. El-kassaby, Fuel. 270 (2020) 117574.
15. A. Suhel, N.A. Rahim, M.R.A. Rahman, K.A. Bin Ahmad, Y.H. Teoh, N.Z. Abidin, Symmetry (Basel). 13 (2021) 1–23.
16. C.L. Yaws, Wiliam Andrew, Texas, 2003.
17. P. Purushothaman, S. Masimalai, V. Subramani, Environ. Sci. Pollut. Res. 28 (2021) 11893–11903.
18. A.I. El-Seesy, A.M.A. Attia, H.M. El-Batsh, Fuel. 224 (2018) 147–166.
19. M. Nouri, A.H.M. Isfahani, A. Shirneshan, Clean Technol. Environ. Policy. 23 (2021) 2265–2284.
20. A.F. Chen, M. Akmal Adzmi, A. Adam, M.F. Othman, M.K. Kamaruzzaman, A.G. Mrwan, Energy Convers. Manag. 171 (2018) 461–477.
21. S. Suzuki, S. Mori, J. Chem. Eng. Japan. 50 (2017) 178–185.
22. S. Suzuki, S. Mori, J. Air Waste Manag. Assoc. 67 (2017) 873–880.
23. Y. Zhang, S. Gao, Z. Zhang, W. Li, T. Yuan, D. Tan, L. Duan, G. Yang, Fuel. 335 (2023) 127011.

Optical, Thermal and Electric Properties of PVC-C Thick Film Composites

Laheeb A. Mohammed [a], Khansaa Nasir Aklo [b], Shatha H. Mahdi [c], Kareem A. Jasim [d]

Department of Physics, College of Education for Pure Sciences Ibn Al-Haitham, University of Baghdad, Baghdad, Iraq

[a)] Corresponding author: laheeb.a.m@ihcoedu.uobaghdad.edu.iq
[b)] khansa.n.a@ihcoedu.uobaghdad.edu.iq
[c)] shatha.h@ihcoedu.uobaghdad.edu.iq
[d)] Kareem.a.j@ihcoedu.uobaghdad.edu.iq

Abstract. This paper aims to Study of the optical, thermal and electric properties of thermoplastic polyvinyl chloride and carbon composite. The optical properties of pure PVC and PVC-carbon composite thick films made utilizing the casting technique and have been investigated. In the spectral range (300-1100 nm), parameters like transmittance, Eg (energy gap), and α (absorption coefficient) were investigated, it was found that all of them are affected by adding carbon. The K (thermal conductivity) of the samples was calculated using a disk- Lee, and the results showed that the addition of the carbon leads to an improvement in the thermal conductivity. Further, thermogravimetric analysis differential scanning calorimetric (DSC) showed that the thick films exhibited melting and Glass transition temperatures increased after adding carbon.

INTRODUCTION

Since the 1930s, when polymer science was initially created, polymer materials have dominated the market in terms of their adaptability for product applications. These materials have been used as coatings, sheets, films, and fibers [1]. Our knowledge of the electrical and optical properties of these materials has undergone significant change since the discovery of semiconducting polymers [2]. Often used polymers include rubber, plastic, and resins. Proteins, natural rubber, silk, cellulose, and starch are examples of natural polymers. Semi-synthetic natural polymers include methylcellulose, hydrogenated natural rubber, and cellulosic cellulose nitrate. Synthetic polymers include PVC, polyethylene (PE), polyvinyl alcohol, and polystyrene (PS). They can be divided into thermosets and thermoplastics based on their heat reactivity. Polyolefin, linear polyesters, polyethers, and PVC are examples of thermoplastics whose properties can be repeatedly heated to create a plasticized or softening without significant modification. When heated, thermosets undergo chemical changes and become an infusible mass [3]. Modern synthetic polymer fibers find application in a wide range of items, such as clothing, carpets, ropes, and reinforcing elements [1]. Everyday use thermoplastic PVC has non-protonic polar C-Cl bonds in its macromolecules, making it more compatible with lignocellulose fillers than high-density polyethylene and polypropylene [4]. Poly (vinyl chloride) is utilized in stiff formulations for conduits, cable covers, cladding, gutters and downspouts, and water and sewage pipes. PVC is a plasticized material that is most commonly used for pipes and conduits. Moreover, flooring applications employ it, and consumer products packaging uses membrane roofing sheets [4-5]. New properties are often seen in composites composed of two materials with dissimilar physical properties. Composites can provide superior attributes than any original component and are used in a variety of industrial goods. Changes in the thickness, light source closeness, local film shape, optical interference, or microcavity effects can all be attributed to variations in self-absorption [2]. Transmission absorbance and optical band gap Eg of thin semiconductor films are two optical parameters that are needed for the production of thin-film devices and their development for different applications. The minimal energy difference between the lowest minimum of the conduction band and the greatest maximum of the valence band is the most precise representation (Eg) of the energy gap [6]. They are used in many different goods, including UV filters, visible laser diodes, coatings, solar cells, and infrared detectors. In order to create a PVC and C polymer composite and measure different characteristics, this research explained the casting technique [7]. For the manufacturing and use of polymers, thermo conductivity is a crucial attribute. Because polymers have intrinsic heat conductivities that are far lower than those of metals or ceramics, they make good thermal insulators. Polymers can be foamed to enhance their ability to withstand heat. Additional applications for enhanced thermal conductivity include electronic

Technologies and Materials for Renewable Energy, Environment and Sustainability
AIP Conf. Proc. 3321, 040008-1–040008-9; https://doi.org/10.1063/5.0289951
Published under an exclusive license by AIP Publishing. 978-0-7354-5231-2/$30.00

encapsulations and packaging, satellite devices, and locations where effective heat dissipation is required; for these uses, novel polymer composites, comprising polymers reinforced with either organic or inorganic fillers, are becoming more and more well-liked because of their low thermal expansion and lightweight nature [7, 8]. As a substance's temperature varies from one place to another (occurs in the direction in which the temperature decreases), thermal conductivity is a phenomenon of heat transfer in which energy is transferred from one location to another due to the oscillation of molecules accompanied by a change in temperature [9]. The optical, thermal, and electric properties of thermoplastic polyvinyl chloride and carbon composite are the focus of this work.

Experimental Part

Three samples (A1, A2, and A3) were prepared by mixing pure PVC with different weights (0.2 g, 0.3 g, and 0.4 g) with the addition of different proportions of dimethylamide DMF (20, 25, 30 ml) to each sample, respectively. Three other samples (A4, A5, and A6) were made y adding carbon to PVC by mixing (0.2 g + 0.015 g C in 20 ml MHF, 0.3 + 0.015 g in 25 ml MHF, 0.4 g + 0.015 g C in 30 ml MHF) as shown in table 1. on the thickness of films of pure PVC and Poly (vinyl chloride)-carbon composite. The components of each sample were mixed with a magnetic stirrer for 40 minutes until the mixture was homogeneous. Then it is poured into a glass dish with a diameter of 10 cm and left to dry at room temperature (25-30) °C for 72 hours[10,11]. The UV-VIS spectrophotometer type (UV-Visible 1800 Spectrometer) made in England was utilized to determine the transmission and absorption spectra in the range of (300-1100) nm wavelength. Thermal conductivities were checked using the Lee disk for all specimens, which consists of three metal discs (A, B, and C); the specimen is placed between them; and then the disc (C)) where the applied voltage to the heater's two ends (2.6 volts) and the current passing through it (2 Amp). Each is attached to a thermocouple. The device transforms electrical energy into heat energy for discs from the heater; the heat transfers from the heater disk to the next disk until you reach the disk at the end after an amount of time. The three discs measure their internal temperatures (TA, TB, and TC) on consecutive utilizing internally placed thermometers [12]. by using Differential scanning calorimetry (DSC) type (DSC 131 Evo), which gives a thorough survey of the specimen's temperature dependent on the heating rate[13,14]. The glass transitions of the amorphous polymers are characterized by the gradual change of thermal capacity with the temperature change and were included in the temperature survey of the specimen.

Table .1 shows the concentration of polyvinyl chloride and polyvinyl chloride-carbon composite

code	PVC [g]	C [g]
A 1	0.2	0
A 2	0.3	0
A 3	0.4	0
A 4	0.2	0.015
A 5	0.3	0.015
A 6	0.4	0.015

RESULTS AND DISCUSSION

Optical measurements

Studying the pure PVC and carbon-doped PVC optical properties is of great significance that allows for identifying the optical energy gap's value based on the specific preparation conditions and knowing the other absorbance constants, Transmission, absorption coefficient, and extinction coefficient. Fig.1. shows the Transmission spectrum as a function of the wavelength of the pure PVC and carbon-doped films.

Where noted from Figure 1 that a transmittance spectrum increases with an increase in wavelength. In addition, the transmittance drops as the amount of doped material carbon rises. This effect is explained by the fact that rising carbon concentrations raise the localized state density, which lowers transmittance values. The Transmission spectrum for the five samples A2, A3, A4, A5, and A6 compared with sample A1. For sample A2, Sample A3 showed a different behavior as the Transmission increased with the addition of carbon than sample A6 with increasing wavelength. This

is due to the change in the composition of the samples from the first sample, which led to a decrease in the Transmission, in addition to the fact that carbon can absorb electromagnetic radiation[14].

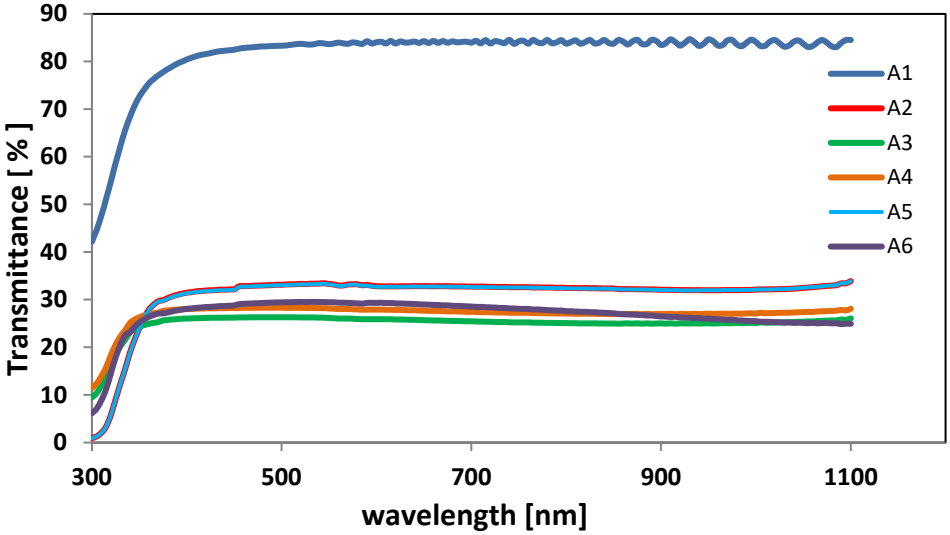

FIGURE 1. The transmittance spectrum as a function of the wavelength of the pure PVC and carbon-doped films

Absorption measurements

The absorption of radiation was measured as a function of the energy of the incident photon for the six samples under the experiment, shown in Figure 2. It is noted from this figure that the absorption of the samples prepared for pure and doped carbon generally begins to increase clearly with the increase with the increase in the energy of the incident photon (decrease in wavelength). This rapid optical energy increases for all fabricated films when the incident photon energy is equal to or greater than the gap value, indicating the occurrence of indirect electronic transitions. So the electronic change means that the impurity reduced the optical energy gap, thus decreasing the optical Transmission and increasing the absorption [15,16].

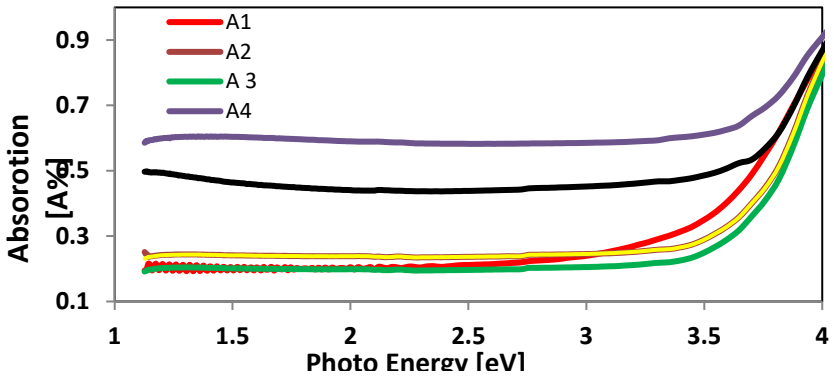

Figure 2. Shows the absorbance spectrum as a function of Photon of the pure PVC and carbon-doped films

To calculate the optical absorption coefficient, equation (1) is used, which represents the relationship between the intensity of the incident (I_o) rays on the sample and the intensity passing through the sample (I) [17-19].

$$I = I_o e^{-\alpha t} \quad (1)$$

Where (I_o) refers to incident intensities, transmitted light intensities is (I), opt. absorption coefficient α, t is the film thickness, and absorbance is defined by A. Substituting the logarithm value into the equation, we get Equation (2).

$$\alpha = 2.303A/t \quad (2)$$

The absorption coefficient, which is based on the energy of the incident photons (hυ) as well as the energy gap (Eg), indicates how much light a material can absorb[19]. Comparably speaking, Figure 3 shows the values of the absorption coefficient (α), showing large values of α above 104 cm-1. The absorbance of carbon-doped PVC films increases when the α value for both pure and carbon-doped PVC films rises. Figure 3 makes it evident that, by Beer's Law, the absorption coefficient increased with increasing photon energy for all films and with increasing carbon doping concentration for the doped films of samples A2, A3, A4, A5, and A6. The quantity of absorbing molecules and the interaction between PVC and carbon determine how much is absorbed [18]. As per Tauc's relation, which defines the absorption edge for direct and indirect transition. [17-18]:

$$\alpha(h\nu) = \beta\,(h\nu - Eg)^{n} \quad (3)$$

Which is used to compute the film optical energy band gap, where hν is the photon energy, β: is a constant, Eg: is the allowed or forbidden energy gap for direct and indirect transition, and exponential factor (n) depends on electronic transition and absorption coefficient α.

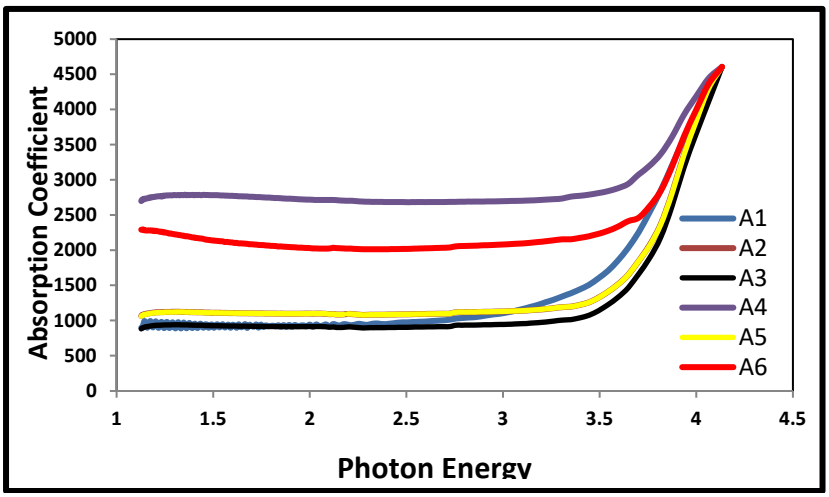

Figure 3. Shows the absorption coefficient of pure PVC and carbon doping as a function of Photon energy

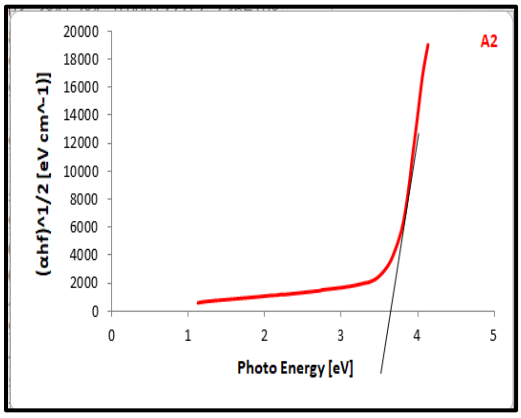

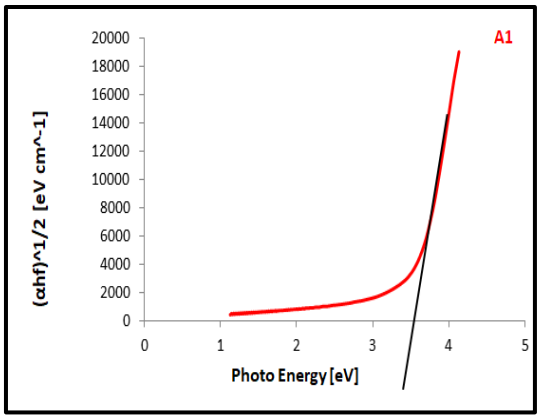

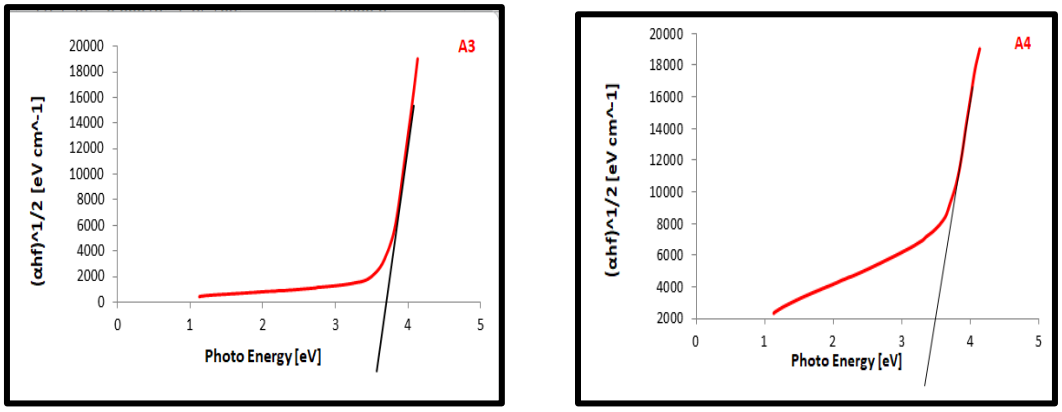

Fig . 4. Indirect allowed energy gap for$(\alpha h\nu)^{1/2}$ versus photon energy (hν)

The optical energy band gap of the films was determined by plotting $(\alpha h\nu)^{1/2}$ versus photon energy (hν) and by extrapolating the curve to αhν = 0[19]. From the absorption coefficient value of pure PVC and carbon doping PVC films, the indirect transition could happen at n=2. The energy gaps were measured by adopting the data of energy gap, as indicated in Table (2) and Fig. 4. It was found that the energy gap of the PVC samples in the presence of the additives decreased with the increase in the percentage of carbon addition. The energy gap's value decreased due to the carbon doping treatment, where the doping process led to new levels added near the valence band inside the energy gap. It creates bridges to cross electrons at low energies less than the pure substance value energy gap. The transition between the conduction and valence band increases, so the number of electronic transitions increases; a change occurred in the Fermi level position and its movement towards the material valence band. This increased the absorbance value. In general, the amplitude of the optical absorption region of low-energy photonic energies. Thus, the doping process improved optical properties [20,22].

Thermal conductivity

The Lee-Disk method was used to calculate the thermal conductivity of pure and doped specimens. The thermal conductivity coefficient (K) was calculated using equation (4) for specimens of thickness (ds) and radius (it seems that the thermal conductivity increases as the concentration of pure and doping PVC increases, based on the plotted curves [8].

$$(\frac{TB-TA}{ds}) = e[TA+\frac{2}{r}(dA+fourths)TA+\frac{dsTB}{2r}] \quad (4)$$

Where ds, dA, dB, dC: are the thickness of the specimen, disks A, B, C (mm), TA, TB, TC: are the temperature of the disks A, B, C (℃), and e: heat loss in (sec/cm^2)[8,11]. Fig. 5 illustrates Thermal conductivity K as a function of PVC concentration shows when an increase in the value of base matrix PVC, the thermal conductivity values fall respectively while Adding the percentage of doping with carbon led to an increase in the conductivity value while maintaining the same general behavior by decreasing its value with the increase of the base matrix PVC. It can be said that the reinforcement leads to an increase in the coefficient of thermal conductivity (K) when doping with carbon for all specimens, but it varies from one concentration to another; where the reason for this improvement is carbon is a heat-conductive material and has a high coefficient of thermal conductivity equal to (Kc=16.7 W/m.°K)[8,22,23].

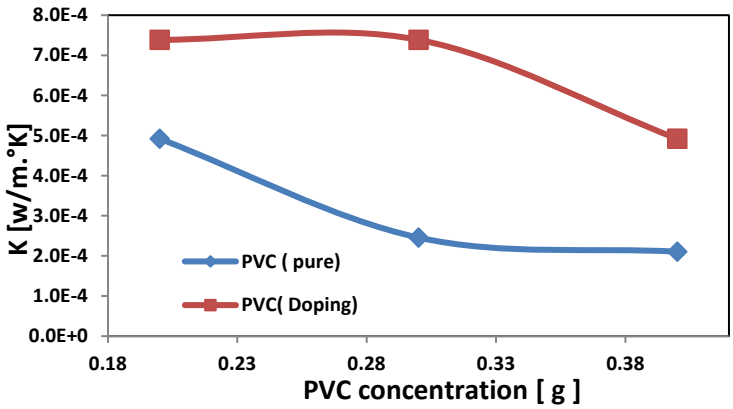

Figure 5. Thermal conductivity K as a function of PVC concentration for the PVC pure and composite PVC-C thick films

Differential scanning calorimetry studies(DSC)

The specimens that were used in the experiment underwent DSC thermal analysis. They were heated from room temperature to 350°C at a rate of 10°C per minute. Figure 6 shows the behavior of the DSC parameters, such as Tg and Cp, of composites made of PVC and C, I have a note regarding the curves on changing the temperature glass transition. It has been discovered that adding C composition to blend samples has caused the Tg value to increase to (186.332, 187.01, and 187.043) °C, and ΔCp (9.474, 5.009, and 7.745) μV due to the interaction between PVC and C through cross-linking. In contrast, the Tm value of the composite increased due to carbon's physical characteristics. Carbon remains solid at temperatures above the melting point of metals such as tungsten or rhenium [12, 24]. To create a typical thermogram using DSC, the difference in heat flow was plotted against temperature. This can be seen in Figure 6, which shows the melting temperatures of PVC at 192°C and 198°C. These temperatures were used during the manufacturing of composite laminates.

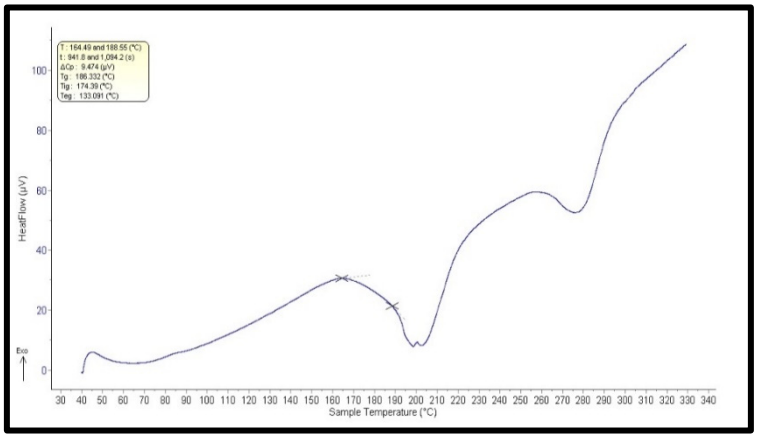

Figure 6-a. DSC diagram of A4 specimen

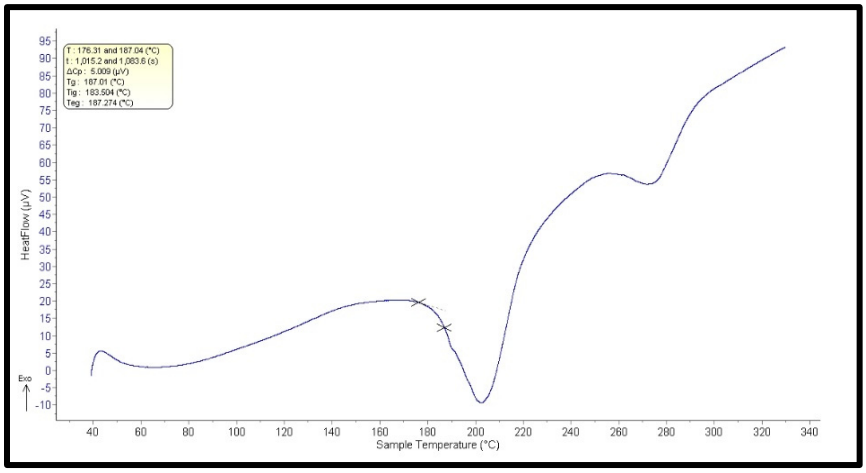

Figure 6-b. DSC diagram of A5 specimen

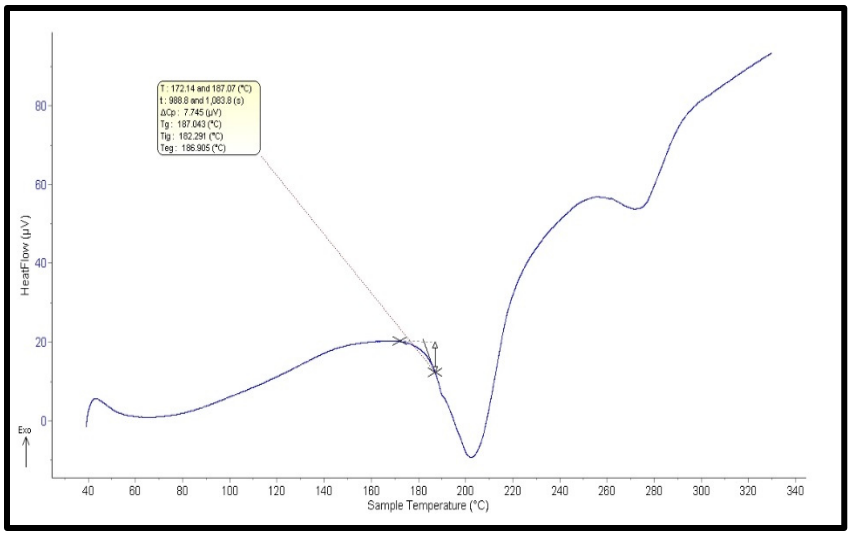

Figure 6-c. DSC diagram of A6 specimen

TABAL 2. The values of Energy gap and ΔCp, Tg for pure PVC and carbon doping

Code	PVC [g]	Carbon C [g]	Energy gap [eV]	ΔCp[μV]	Tg[°C]
A 1	0.2	0	3.542	4.193	210.266
A 2	0.3	0	3.647	3.928	210.266
A 3	0.4	0	3.701	11.396	191.449
A 4	0.2	0.015	3.444	9.474	186.332
A 5	0.3	0.015	3.594	5.009	187.01
A 6	0.4	0.015	3.642	7.745	187.043

CONCLUSIONS

In this research, PVC-C thick film composites were made by using the casting process, and the results of the optical and thermal insulation strength properties of new polymer composites were given. An improvement in optical properties was observed when carbon 0.015 g was added to polyvinyl chloride (0.2 g, 0.3 g, and 0.4 g). The results indicate that the impurity reduced the optical energy gap compared to pure specimens', reducing transmission and

increasing carbon absorption of carbon added to PVC polymer. Also, an increase in the thermal insulation strength of doped specimens was observed compared to pure specimens.

REFERENCES

1. Song. K, Zhang. Y, Meng. J, Green. E, Tajaddod. N., Li. H, & Minus. M, Structural polymer-based carbon nanotube composite fibers: Understanding the processing–structure–Performance relationship. Materials 6(6) (2013) 2543-2577. https://doi.org/10.3390/ma6062543.
2. Allen, P. B. Elementary solid state physics: Principles and Applications by M. A. Omar. American Journal of Physics, 43(10), (1975), 929-933. https://doi.org/10.1119/1.9980
3. Kadhim, B.B., Risan, R.H., Shaban, A.H., Jasim, K.A., Electrical characteristics of nickel/epoxy - Unsaturated polyester blend nanocomposites, *AIP Conference Proceedings*, 2019, **2123**, 020062.
4. Fidan. S, Volcanic ash reinforcement concentration effect on thermal properties of polyvinyl chloride composites. *Acta Physica Polonica A* **127**(4) (2015) 1002-1003. https://doi.org/10.12693/aphyspola.127.1002.
5. James E. Mark, Polymer Data Handbook, Second Edition, Oxford University Press, 22 May (2009).
6. Mulama. A. A, Mwabora. J. M , Oduor. A. O, Muiva. C. M, Muthoka. B, Amukayia. B. N, & Mbete. D. A, Role of Bismuth and Substrate Temperature on the Optical Properties of Some Flash Evaporated Se100-X BiX Glassy System; Glassy system. *New Journal of Glass and Ceramics* **05**(02) (2015) 16-24. https://doi.org/10.4236/njgc.2015.52003.
7. Jassim. K. A, Thejeel. M. A, Salman. E. M, & Mahdi. S. H ,Study characteristics of (epoxy–bentonite doped) composite materials. *Energy Procedia*, **119** (2017) 670-679. https://doi.org/10.1016/j.egypro.2017.07.094.
8. Borek. J, & Osoba. W ,Free volume in Plastified Poly(Vinyl chlorate). *Acta Physica Polonica A* 88(1) (1995) 91-95. https://doi.org/10.12693/aphyspola.88.91.
9. Kadhum. F. J, Saeed. A. A, AL-kadhemy.M. F, Al-Zuky, A. A, & Al- Saleh. A. H, Theoretical biosensor design for gold- PVA surface Plasmon resonance layers. *Iraqi Journal of Science* **62**(11) (2021) 4232-4239. https://doi.org/10.24996/ijs.2021.62.11(si).3.
10. Jassim. K. A, Jassim. W. H, & Mahdi. S. H , The effect of sunlight on medium density polyethylene water pipes. *Energy Procedia* **119** (2017) 650-655. https://doi.org/10.1016/j.egypro.2017.07.091.
11. Mahdi. S. H, Jassim. W. H, Hamad. I. A, & Jasim. K. A, Epoxy/Silicone rubber blends for voltage insulators and capacitors applications, *Energy Procedia* **119** (2017) 501-506. https://doi.org/10.1016/j.egypro.2017.07.059.
12. Jasim. K. A, Fadhil. R. N, Shaban. A. H , Jaafar. H. I, Maiyaly. B. K, Aleabi. S. H, & Salman. E. M, The effects of copper additives on the glass transition temperature and hardness for epoxy resin. *Progress in Industrial Ecology, An International Journal* ***13***(2) (2019) 163-172. https://doi.org/10.1504/pie.2019.099357.
13. Aleabi. S. H, Watan. A. W, Salman. E. M , Jasim. K. A, Shaban, A. H., & AlSaadi. T. M. The study effect of weight fraction on thermal and electrical conductivity for unsaturated polyester composite alone and hybrid. *AIP Conference Proceedings*(2018). https://doi.org/10.1063/1.5039178.
14. Jasim, K.A., Fadhil, R.N., The Effects of micro Aluminum fillers in Epoxy resin on the thermal conductivity, *Journal of Physics: Conference Series*, 2018, **1003**(1), 012082.
15. Elham Talib Abd AL-Hussein, Ban A. Yousif, Effect of silver nanoparticle on structural and some (optical, electrical) properties of poly (vinyl chloride) films. *AIP Conf. Proc*. **2213**, 020199 (2020). https://doi.org/10.1063/5.0000328.
16. Hammod. O. B, Thickness effect on the optical properties of PVC-methyldopa composite films. *Journal of Al-Nahrain University Science* **16**(3) (2013) 79-82. https://doi.org/10.22401/jnus.16.3.10.
17. Jasim, K.A., Mohammed, L.A., The partial substitution of copper with nickel oxide on the Structural and electrical properties of HgBa2 Ca2 Cu3xNix O8+δ superconducting compound, *Journal of Physics: Conference Series*, 2018, **1003**(1), 012071.
18. Widiastuti. I, Saputra. H. C, Wisnu Kusuma. S. S, & Harjanto. B. Mechanical and thermal properties of recycled high-density polyethylene/bamboo with different fiber loadings. *Open Engineering*, **12**(1) (2022)151-156. https://doi.org/10.1515/eng-2022-0010.
19. B. H. Hussein, S. H. Mahdi, S. A. Makki, B. K. Al-Maiyaly," Synthesis and Study the Structure, electrical and optical properties of Bi2-xCdxSr2Ca2Cu3O10+ δ thin film Superconductors . *Energy . Proc*., 157 (2019) 100-110; https://doi.org/10.1016/j.egypro.2018.11.169.
20. Jobayr, M.R., Al Razak, A.H.A., Mahdi, S.H., Fadhil, R.N., Study optoelectronic properties for polymer composite thick film. *AIP Conference Proceedings*, 2018, 1968, 030021.

21. W. Mahmoud, A. Al-Ghamdi, F. Al-Agel, *Polym Adv Technol*. **22**, 12, (2011) 2055–2061. https://doi.org/10.1007/s10854-017-7024-1.
22. Zainab, J.N., Jasim, K.A., Kadhum, F.J., Shaban, A.H., Heat treatment at different temperatures and its effect on the optical properties of pure pmma and pmma-coumarin Key Engineering Materials, 2021, 900, pp. 42–47.
23. Athab, Rana Hameed, and Bushra H. Hussein, Growth and Characterization of Vacuum Annealing AgCuInSe2 Thin Film, *Ibn AL-Haitham Journal For Pure and Applied Sciences*, **35**(4), (2022) 45-54. https://doi.org/10.30526/35.4.2868.
24. Hameed. M, Jasim. K. A, Study the effect of coating on the optical, insulation, thermal and structural properties of glass. *AIP Conference Proceedings* **2437**(1) (2022) 020007. https://doi.org/10.1063/5.0092701.
25. Chen.Z., Wei. W, Ni. B., & Chen. H., Plastic wastes derived carbon materials for green energy and sustainable environmental applications. *Environmental Functional Materials*, **1**(1) (2022) 34-48. https://doi.org/10.1016/j.efmat.2022.05.005.

Exploring Key Parameters Affecting Thermal Management of Lithium-Ion Batteries: A Numerical Investigation

Mohamed Kh. Saudi[1, 2, a)], Mohamed Emam[1, 2, b)], Hidetoshi Sekiguchi[3, c)], Ahmed S G Khalil[4, 5, d)], and Hamdy Hassan[1, 6, e)]

[1]*Department of Energy Resources Engineering, Egypt-Japan University of Science and Technology (E-JUST), Alexandria 21934, Egypt.*
[2]*Mechanical Engineering Department, Benha University, Shoubra Faculty of Engineering, 108 Shoubra Street, Cairo, Egypt.*
[3]*Chemical Science and Engineering Tokyo Institute of Technology, Tokyo, Japan*
[4]*Institute of Basic and Applied Sciences, Egypt-Japan University of Science and Technology (E-JUST), 21934 Alexandria, Egypt.*
[5]*Environmental and Smart Technology Group, Physics Department, Faculty of Science, Fayoum University, 63514 Fayoum, Egypt.*
[6]*Department of Mechanical Engineering, Assiut University, Assiut 71516, Egypt*

[b)] *mohamed.emam@ejust.edu.eg*
[c)] *hsekiguc@chemeng.titech.ac.jp*
[d)] *ahmed.s.khalil@ejust.edu.eg*
[e)] *hamdy.aboali@ejust.edu.eg*
[a)] *Corresponding author: mohamed.saudy@ejust.edu.eg*

Abstract. Electric and hybrid vehicles have become a promising solution to minimize the environmental impact related to traditional vehicles. However, to provide high power output, energy density, and to reduce charging time, these vehicles require an efficient and reliable energy storage system. Due to their high energy and power density, quick charging capabilities as well as their long cycle life, lithium-ion batteries have attracted considerable attention. Despite their advantages, safety concerns arise from the thermal energy generated during the operation process, which may cause combustion and explosions of the electric car battery system. To address this issue, a study was carried out on a three-dimensional battery pack containing 36 lithium-ion batteries. The study focused on evaluating how various parameters affect battery performance while using air cooling, specifically the impact of incorporating an Aluminum casing, employing various air inlet and outlet designs, utilizing a staggered array configuration, and varying air flow velocities and discharge rates. The results indicated that as the velocity of the air flow increased from 0.1ms–1 to value of 1ms–1, the maximum temperature within the Battery module decreased from 32.740˚C to 32.012˚C while discharging at a 4C rate. Furthermore, the implementation of air flow at a velocity of 1 m/s resulted in a significant decrease of 23% in the maximum temperature, when compared to pure natural convection cooling study. However, making modifications to the battery pack's configuration and air inlet and outlet designs had minimal impact on the cooling system.

INTRODUCTION

Combustion of liquid fossil fuels is responsible for supplying more than 99% of the energy required for transportation worldwide. However, this reliance on fossil fuels is causing major environmental issues [1]. Besides the destructive environmental consequences, the consumption of fossil fuels and other conventional sources of energy may lead to depletion within a few year [2]. Electric cars have been promising alternatives for fossil-fuel powered vehicles, with the potential to lessen greenhouse gas (GHG) emissions and reduce global warming. These eco-friendly vehicles have rapidly gained interest as symbols of the future of transportation and could soon become the dominant

Technologies and Materials for Renewable Energy, Environment and Sustainability
AIP Conf. Proc. 3321, 040009-1–040009-13; https://doi.org/10.1063/5.0289692
Published under an exclusive license by AIP Publishing. 978-0-7354-5231-2/$30.00

players in the automobile industry [3]. Despite their advantages, Electric cars encounter a major technological challenge in managing their energy storage system, particularly their battery packs, which can be heavy and expensive, also affecting their overall efficiency and affordability [4]. Batteries commonly have a shorter lifespan than other vehicle components. This leads to additional expenses for maintenance and replacement. Thus, lithium-ion batteries (LiBs) are considered as a practical solution to address these issues [5]. In contrast, lithium-ion batteries produce heat While the battery is being charged or discharged. This thermal energy gradually increases the battery's temperature, leading to thermal runaway and the risk of explosion [6]. Additionally, when the battery pack operates at low temperatures, dendrites can be formed, lithium plating. This reduces the electrolyte's conductivity and limits the amount of power and energy that the battery pack can produce [7]. Therefore, an effective thermal control system is vital to guarantee the protection and efficiency of the system. This helps regulate the excess heat produced during battery operation while keeping temperatures within the range of 20 to 45°C and ensuring that the highest temperature difference remains below 5°C [8]. The battery temperature control system (BTMS) can utilize various techniques to regulate the overheating of the battery. The techniques include both active, passive and hybrid methods, all previous methods can be used to regulate temperature and prevent potentially harmful temperature fluctuations during charging and discharging operations [9]. The air-cooling technique is a favourable option among the various BTMS methods due to several benefits. These include its simple design, low overall cost, easy maintenance, prolonged lifespan, and minimal power consumption. As a result, air cooling is popular among the various methods of cooling for BTMS and contributes significantly to the overall efficiency of electric vehicles [10,11]. Wang et al. [12] utilized Computational Fluid Dynamics CFD to simulate a two-dimensional (2D) design and investigated the impact of adding a parallel plate on the battery pack's cooling potential. The results of the study demonstrated that the incorporation of parallel plates led to a decrease of 3.26℃ in the highest temperature within the BTMs, Ruhani et al. [13] examined a 2D Battery assembly using COMSOL software, to analyse the temperature, pressure, and velocity values within a pack, by varying the Reynolds number between 80 and 140, and using air inlet sizes of 0.1, 0.15, and 0.2m. showing that increasing the intake size and Reynolds number resulted in improving the pack's pressure drop, which led to lower temperatures across all battery cells. Singh et al. [14] created a 2D model using COMSOL software to evaluate a BTMS according to the number of cells in the system. Although there was no notable change in the maximum temperature, increasing the number of cells adversely affected the cooling ability. Wu [15] utilized CFD to improve the effectiveness of a BTMS that follows a U-shape configuration, which contains a total of twelve prismatic batteries. The study achieved this by optimizing the tapered inlet/outlet and adjusting the battery spacing. The optimal model yielded a reduction in both the highest temperature to 38.2°C and the highest average temperature 0.3°C. Lee et al. [16] investigated the battery's module design with integrated thermal interface materials (TIM). The study found that of the TIM's parallel thermal conductivity played a significant role in promoting temperature distribution across the module. While vertical thermal conductivity was more related to the module's highest temperature and state of health.

Previous studies have examined various BTMS essential parameters. Nevertheless, only a few have been successful in maintaining the maximum temperature and temperature differences within an acceptable range while utilizing simple designs with minimal dimensions. This is often achieved by increasing the distance between cells and air velocity to ensure temperature uniformity. Additionally, most of the previous studies have adopted two-dimensional models for their research [17]. This paper employed a numerical simulation technique that utilizes the finite element method, coupled with a lumped battery model, in COMSOL Multiphysics software, focusing on a BTMS for a three-dimensional battery pack containing 36 LiBs connected as six series and six parallel (6S6P configuration), contained in an aluminium casing with a small thickness of 3mm and 1mm gap between cells. Various parameters such as air inlet/outlet geometries, staggered array, air velocity, and rate of discharge were investigated as it will be discussed through the study.

PHYSICAL MODEL DESCRIPTION

This study consisted of 36 battery cells arranged in a 6S6P configuration with a 1mm distance between cells. The performance of battery pack was assessed with and without Aluminum casing material during natural convection cooling. Then studying the impact of varying air inlet/outlet designs on cooling system, as follows: Case 1 had a middle rectangular inlet and outlet, Case 2 contained two rectangular inlets on the third top and third bottom face and a middle rectangular outlet, Case 3 featured a middle rectangular inlet and two rectangular outlets on the third top and third bottom face, Case 4 had two rectangular inclined inlets to the left with angle of 40º and a middle rectangular outlet, Case 5 had two rectangular vertical inlets which divided the inlet side face of the battery pack into three equal parts and a middle rectangular outlet, and Case 6 included a middle rectangular inlet and two rectangular vertical outlets, all previous cases were studied at different rate of discharge 1C and 4C at velocity of $0.1 ms^{-1}$. In addition, the

effect of a staggered array layout with a shift equal to the radius of the battery was studied, then finally studying the impact of changing air velocity. All geometries were outlined in figure 1, also the properties of the material that were used in the study as well as the main specifications of the selected battery were shown in table 1.

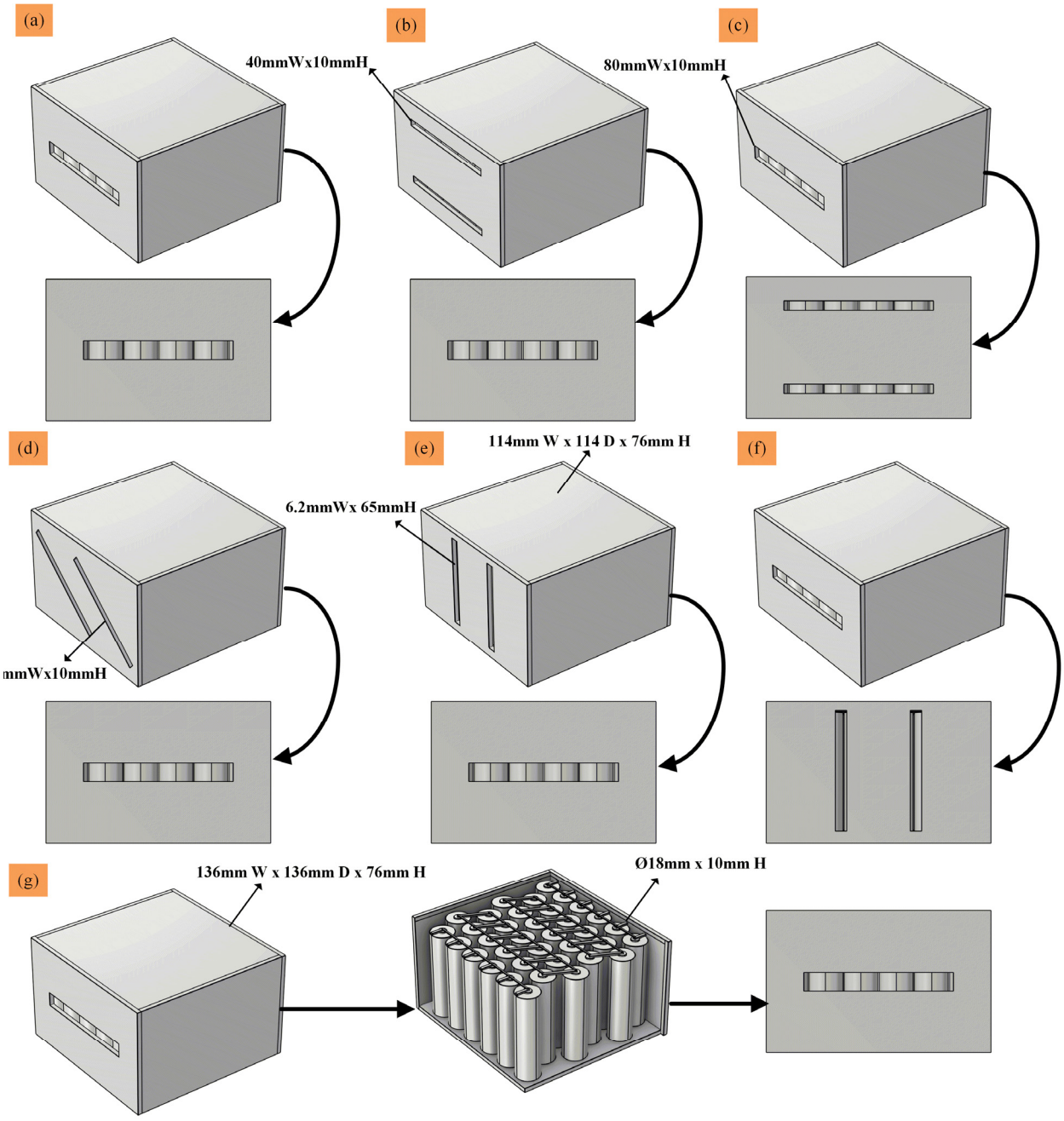

FIGURE 1. Represented the design of various cases: (a) Case 1, (b) Case 2, (c) Case 3, (d) Case 4, (e) Case 5, (f) Case 6, (g) staggered array.

Table 1. Material properties and battery specifications.

Material	Property/Specifications	Units	Values	Reference
Air domain	Specific-heat-ratio (γ)	—	1.4	
	Specific-heat-capacity (C_p)	($Jkg^{-1}K^{-1}$)	1012	—
	Density(ρ)	(kgm^{-3})	1.184	—
	Thermal-conductivity (k)	($Wm^{-1}K^{-1}$)	0.026	—
	Dynamic-viscosity (μ)	($kgm^{-1}s^{-1}$)	1.86×10^{-5}	—
Aluminium	Specific-heat-capacity (C_p)	($Jkg^{-1}K^{-1}$)	900	—
	Density(ρ)	(kgm^{-3})	2700	—
	Thermal-conductivity (k)	($Wm^{-1}K^{-1}$)	205	—
Battery cell	Specific-heat-capacity (C_p)	($Jkg^{-1}K^{-1}$)	1400	[18]
	Density(ρ)	(kgm^{-3})	2415	—
	Radial-thermal-conductivity $(k_{batt})_{rad}$	($Wm^{-1}K^{-1}$)	1	[18]
	Angular-thermal-conductivity $(k_{batt})_{rad}$	($Wm^{-1}K^{-1}$)	30	[18]
	Cell voltage (V)	(V)	3.6	—
	Cell capacity (Q)	(Ah)	2.5	—
	Material of Cathode	—	Li-Fe-PO4	—
	Material of Anode	—	Graphite.	—
	Material of Electrolyte	—	Carbonate.	—

THEORETICAL MODEL

Governing equations

Lithium-Ion batteries governing equations

lumped thermal model was employed to analyze the thermal characteristics of LiBs. This modelling approach was selected as the structure of an individual cylindrical cell had negligible impact upon overall performance [19,20]. The galvanostatic method was used to determine the current of the cell I_{cell} .

$$I_{cell} = (I_{1C}) \times C_{rate} \tag{1}$$

$$\eta_{IR,1C} = \eta_{IR,1C,ref} \exp\left[\frac{E_{\eta IR}}{R}\left(\frac{1}{T} - \frac{1}{T_{ref}}\right)\right] \tag{2}$$

$$J_0 = J_{0,\,ref} \exp\left[\frac{-E_{J0}}{R}\left(\frac{1}{T} - \frac{1}{T_{ref}}\right)\right] \tag{3}$$

$$\tau = \tau_{ref} \exp\left[\frac{E_{\tau}}{R}\left(\frac{1}{T} - \frac{1}{T_{ref}}\right)\right] \tag{4}$$

The symbol J_0 is used to represent the dimensionless exchange current, while the symbol R represents gas constant, T denotes the temperature and the activation energy term, $E_{\eta IR}$, whereas $\eta_{IR.1C.ref}$ refers to reference-ohmic-overpotential at 1C. $J_{0.ref}$ is the dimensionless reference-exchange-current, where the reference-diffusion-time

constant and a 20°C reference temperature was represented by τ_{ref} and T_{ref}, respectively. The total heat produced within the cell can be represented by the following equation:

$$q = I_{cell}(E_{OCV} - E_{cell}) - I_{cell}T\left(\frac{\partial E_{OCV}}{\partial T}\right) \tag{5}$$

Where the battery's open circuit voltage and cell voltage are represented as E_{OCV} and E_{cell} respectively.

Air domain

In this study, lumped model and heat transfer model were used in COMSOL software to analyze the system. The airflow was considered to be a Newtonian fluid with defined values for air density ($\rho_{air} = 1.184 kgm^{-3}$), air dynamic viscosity ($\mu_{air} = 1.86 \times 10^{-5} kgm^{-1}g^{-1}$), maximum selected velocity ($V = 1ms^{-1}$), and inlet cross-sectional area ($0.0008m^2$) with a hydraulic diameter ($d_h = 0.01778m$). The Reynolds number (Re) of 1131.6 indicated that the flow was steady, incompressible, and laminar.

$$Re = \frac{\rho_{air} u_i d_h}{\mu_{air}} \tag{6}$$

Equation of continuity:

$$\nabla \cdot \vec{V} = \left(\frac{\partial z}{\partial x} + \frac{\partial v}{\partial y} + \frac{\partial w}{\partial z}\right) = 0 \tag{7}$$

Equation of momentum conservation in x, y, z directions:

$$\rho\left(\frac{D\vec{V}}{Dx}\right) = \rho g - \nabla p + \mu \nabla^2 \vec{V} \tag{8}$$

$$\rho\left(\frac{\partial u}{\partial t} + u\frac{\partial u}{\partial x} + v\frac{\partial u}{\partial y} + w\frac{\partial u}{\partial z}\right) = \rho g_x - \frac{\partial p}{\partial x} + \mu\left(\frac{\partial^2 u}{\partial x^2} + \frac{\partial^2 u}{\partial y^2} + \frac{\partial^2 u}{\partial z^2}\right) \tag{9}$$

$$\rho\left(\frac{\partial v}{\partial z} + u\frac{\partial v}{\partial x} + v\frac{\partial v}{\partial y} + w\frac{\partial v}{\partial z}\right) = \rho g_y - \frac{\partial p}{\partial y} + \mu\left(\frac{\partial^2 v}{\partial x^2} + \frac{\partial^2 v}{\partial y^2} + \frac{\partial^2 v}{\partial z^2}\right) \tag{10}$$

$$\rho\left(\frac{\partial w}{\partial z} + u\frac{\partial w}{\partial x} + v\frac{\partial w}{\partial y} + w\frac{\partial w}{\partial z}\right) = \rho g_z - \frac{\partial p}{\partial z} + \mu\left(\frac{\partial^2 w}{\partial x^2} + \frac{\partial^2 w}{\partial y^2} + \frac{\partial^2 w}{\partial z^2}\right) \tag{11}$$

Energy conservation equation:

$$\rho C_p\left(\frac{\partial T}{\partial t}\right) + \rho C_p(\vec{\nabla} \cdot \nabla T) = \nabla \cdot [\nabla(kT)] + q \tag{12}$$

By substituting with equation (5) in equation (12).

$$\rho C_p\left(\frac{\partial T}{\partial f}\right) + \rho C_p(\vec{V} \cdot \nabla T) = \nabla \cdot [\nabla(kT)] + I_{cell}(E_{OCV} - E_{cell}) - I_{cell}\,T\left(\frac{\partial E_{OCV}}{\partial T}\right) \tag{13}$$

The resulting equation is linking between lumped battery model and laminar air flow, where C_p is specific heat at constant pressure.

Boundary conditions

The Reynolds number (Re) of 1131.6 indicated that the flow was steady, incompressible, and laminar. Including normal inlet flow velocity and 1atm pressure outflow boundary, while surrounding walls are configured with non-slip conditions.

Natural convection cooling was simulated with an external heat transfer applied to the outside boundaries. As the airflow inside the boundary layer was laminar, the y+ value was not considered. A two-stage lumped battery model was carried out, where a steady flow solution was evaluated first, followed by a time-dependent approach using a backward differentiation formula. The battery pack was discharged from an initial 100% state of charge to 20%, starting at an ambient temperature of 20 °C, utilizing air velocities varied from between 0.1ms^{-1} and 1ms^{-1}, through 1C and 4C rate of discharge. In addition, Lumped model electrochemical parameters were listed in table 2.

Table 2. Presented the electrochemical parameters.

Parameters	Symbols and units	Values	Reference
Current at 1C	I_{1C} (A)	2.5	—
Initial capacity of cell	Q_{cell0} (As)	9000	—
Reference-ohmic-overpotential at 1C	$\eta_{JR.1C.ref}$ (V)	0.0045	[18]
Reference-exchange-current	$J_{0.ref}$	0.85	[18]
Time constant	τ_{ref} (s)	1000	[18]
Energy activation related to η_{JR}	$E_{\eta IR}$ (Jmol^{-1})	24000	[18]
Energy activation related to J_0	E_{J0} (Jmol^{-1})	59000	[18]
Energy activation related to τ	E_{τ} (Jmol^{-1})	24000	[18]

NUMERICAL SOLUTION

Meshing

The study set out to attain a dual objective of independence in both the grid and time domains while preserving solution accuracy and maintaining a low runtime. That featured small grids near the battery cells and walls, as shown in figure 2. Mesh sizing was selected with care during simulation where the maximum temperature of the battery pack showed no significant difference. With this approach, the mesh elements of 436,683 were used for natural cooling without any casing. similar analyses were performed for other configurations such as Aluminium casing, and cases 1 through 6, as well as a staggered array configuration, resulting in the number of grids being set at 2216182, 2240489, 2240489, 2238094 and 2227693, 2227693, 4234502, respectively.

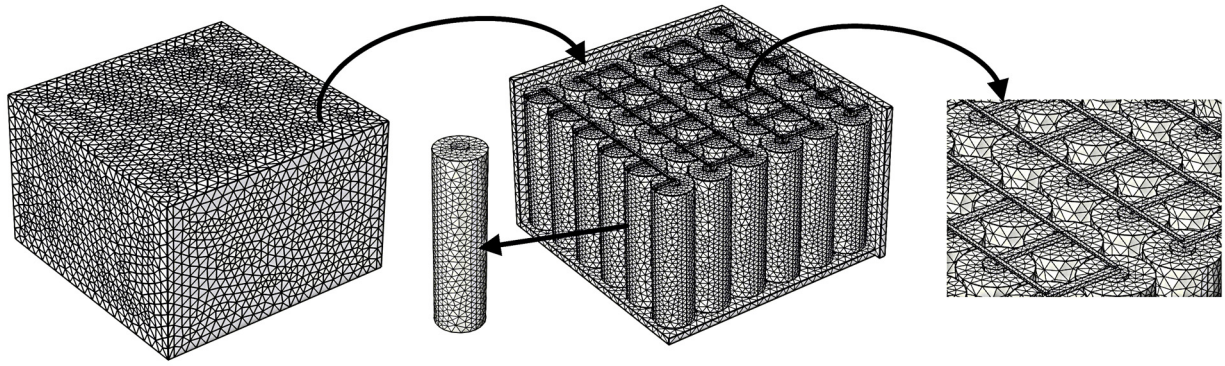

FIGURE 2. Represents the meshing quality for the battery pack.

Model validations

To ensure the simulation results' accuracy, the researchers carried out a comprehensive comparison with the findings of Kausthubharam et al. [21] who had conducted a study on battery packs using a commercially available thermal interface material (3M™).

The conducted comparison involved analyzing cell potential and temperature distribution contours. During 0.1ms^{-1} velocity of inlet flow and same initial temperature of 20˚C for both of air flow and batteries, a transient study was conducted for two scenarios as displayed in figure 3. one at 1C rate of discharge, and the other one at 4C. validation results displayed a small relative error within the accepted range as the maximum error was 4.8% as shown in table 3.

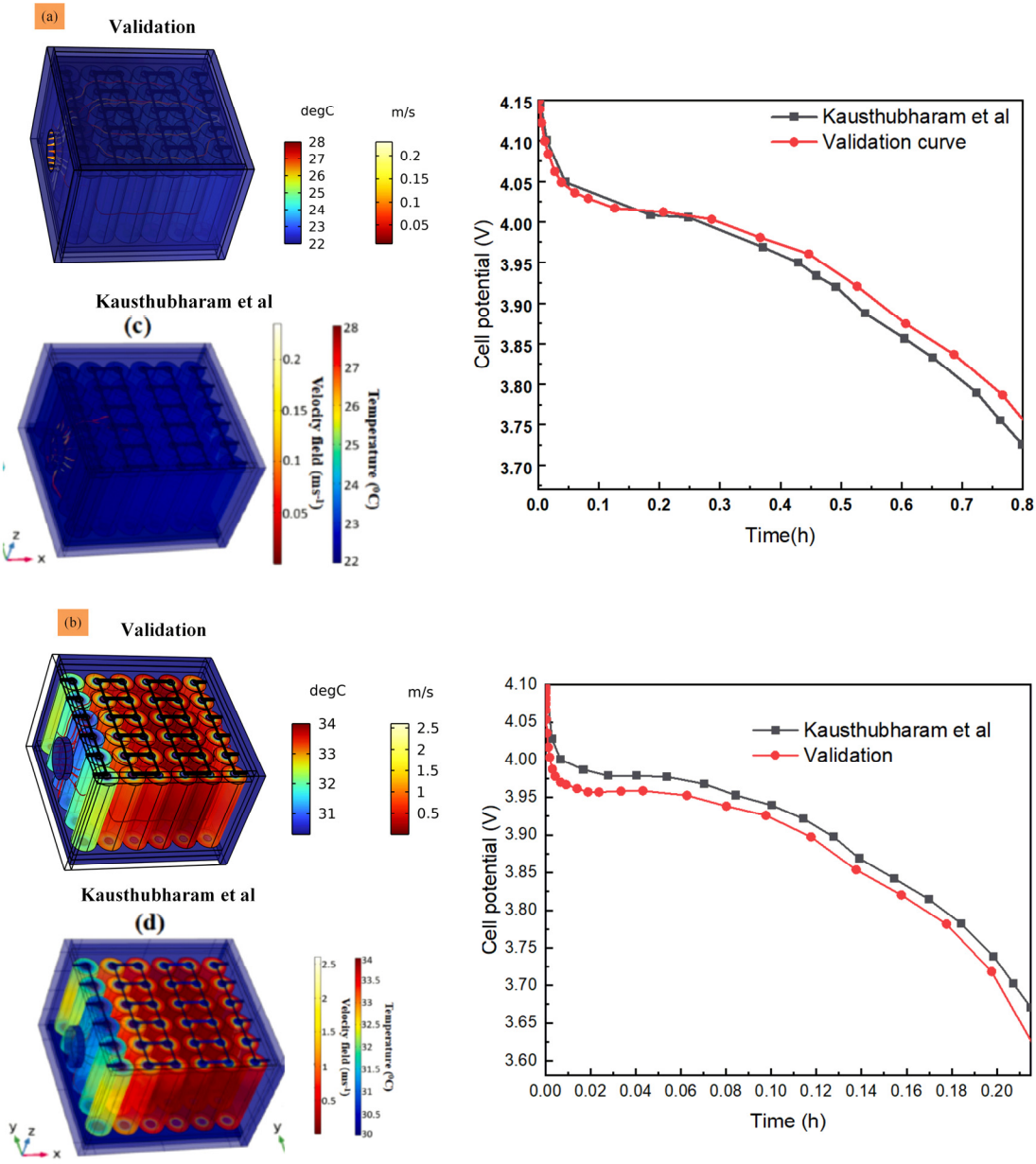

FIGURE 3. Temperature contours and cell potential at (a) 1C discharge rate, (b) 4C discharge rate.

Table 3. Showed the numerical results and the corresponding relative error for the validation.

Study	Case No.	Discharge rate	Velocity (ms^{-1})	T_{max} (˚C)	T_{min} (˚C)
Kausthubharam et al. [21]	Fig. 8. (c)	1C	0.1	22.4	21.5
Current study	—	1C	0.1	23.2	21.8
Error %	—	—	—	3.6	1.4
Kausthubharam et al. [21]	Fig. 9. (d)	4C	0.1	33.9	31.1
Current study	—	4C	0.1	34.3	29.6
Error %	—	—	—	1.2	4.8

RESULTS AND DISCUSSIONS

This paper forced cooling heat transfer model with lamped model for solving lithium-ion batteries utilized COMSOL Multiphysics software to investigate different parameters related to the battery pack, including air inlet/outlet geometries, staggered array, air velocity, and rate of discharge. These parameters were analysed and discussed throughout the study.

National convection cooling

The study aimed to assess how natural cooling affects the thermal behavior of a battery pack which was initially tested without any protective casing surrounding the batteries only pure national convection. However, it was found that the maximum temperature reached 41.523℃ which was not suitable for proper operation. As a result, an Aluminum casing was utilized to enhance the cooling performance as shown in figure 4. The study assessed both packs with an air domain at 20 ℃, 4C discharge rate, a cell-to-cell gap of 1 mm, and a casing thickness of 3 mm. Heat transfer cooling through natural convection was applied on the outer boundaries, using a coefficient of heat transfer value of 7.17 ($Wm^{-1}K^{-1}$). The results in table 4, showed that using an Aluminum casing reduced the highest temperature by 18.88% compared to natural convection alone from. This significant decrease was achieved due to the superior thermal conductivity of Aluminum.

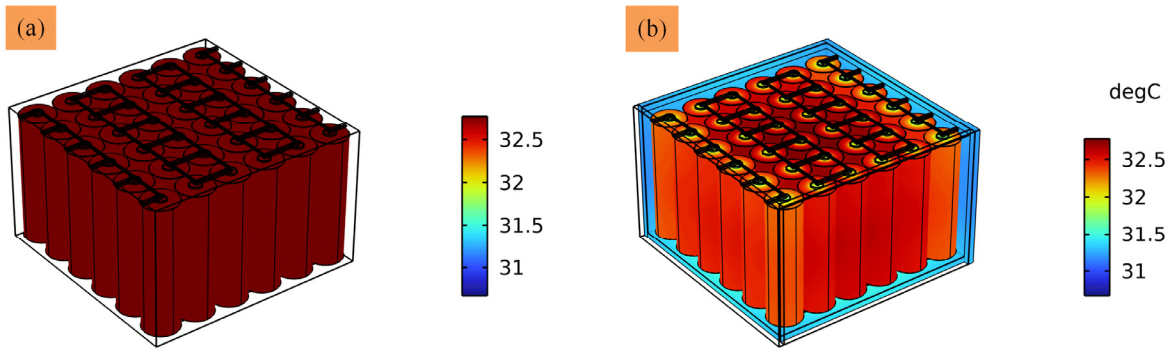

FIGURE 4. Natural convection cooling a) without casing, b) with Aluminum casing

Table 4. Effect of adding Aluminum casing.

casing material	T_{max} (˚C)	T_{min} (˚C)	ΔT (˚C)
No casing	41.523	38.362	3.161
Aluminum	33.685	31.793	1.892

Effects of changing Air inlet/outlet designs

The study aimed to analyze the thermal properties of batteries and how they are affected by the design of air inlet and outlet. The simulation parameters included 1C rate of discharge, $0.1ms^{-1}$ inlet flow velocity, and an initial temperature of 20°C for both the ambient temperature and batteries. Six different designs were examined to determine the Impact of changing the air pattern as shown in figure 5.

Then, the discharge rate was increased to 4C while maintaining the same air flow velocity as presented in figure 6. Although, the enhancement in the maximum temperature from one case to another was not significant almost 0.025°C at 1C and 0.059°C at 4C. At case 6 which represented the least enhanced study at 4C discharge rate, the highest temperature within the pack decreased by 2.6% and 21% compared to the Aluminum casing and free natural cooling cases, respectively. There was an increase in the maximum temperature of the battery pack as the discharge rate increased. This observation indicated a direct correlation between the rate of discharge and the battery's temperature.

Results indicated that altering the inlet and outlet designs did not have a significant impact on reducing the maximum temperature of the cells. However, it did result in a change in the distribution of heat within the battery pack. Based on these results, the researchers selected Case 1, which featured a rectangular inlet and outlet in the middle for further analysis. This case was found to have the best thermal management of the batteries in comparison to other cases, with maximum temperatures of 25.012°C at 1C and 32.740°C at 4C.

According to the data displayed in table 5, it was observed that altering the air flow inlet and outlet design alone was not enough to improve the air-cooling system's performance. Therefore, the staggered configuration of the air flow using a middle rectangular inlet and outlet was analyzed for better results.

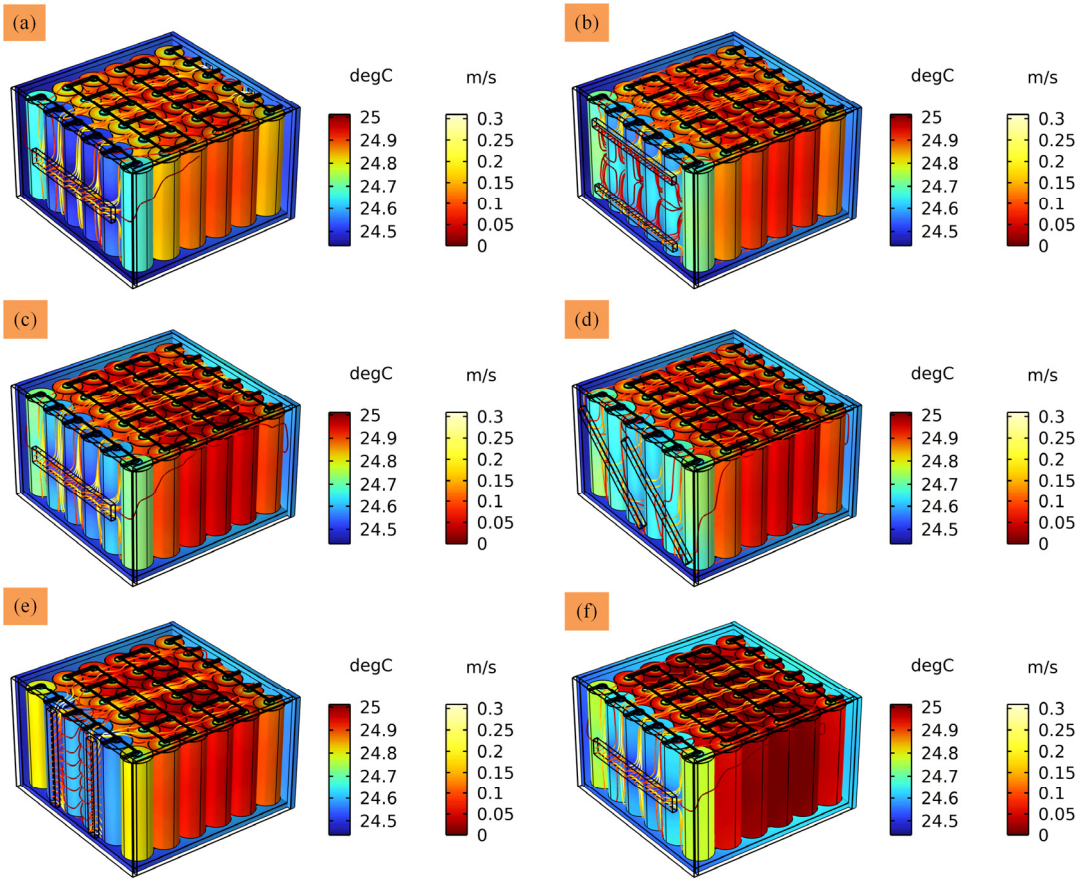

FIGURE 5. Discharge rate at 1C (a) Case 1, (b) Case 2, (c) Case 3, (d) Case 4, (e) Case 5, (f) Case 6

.

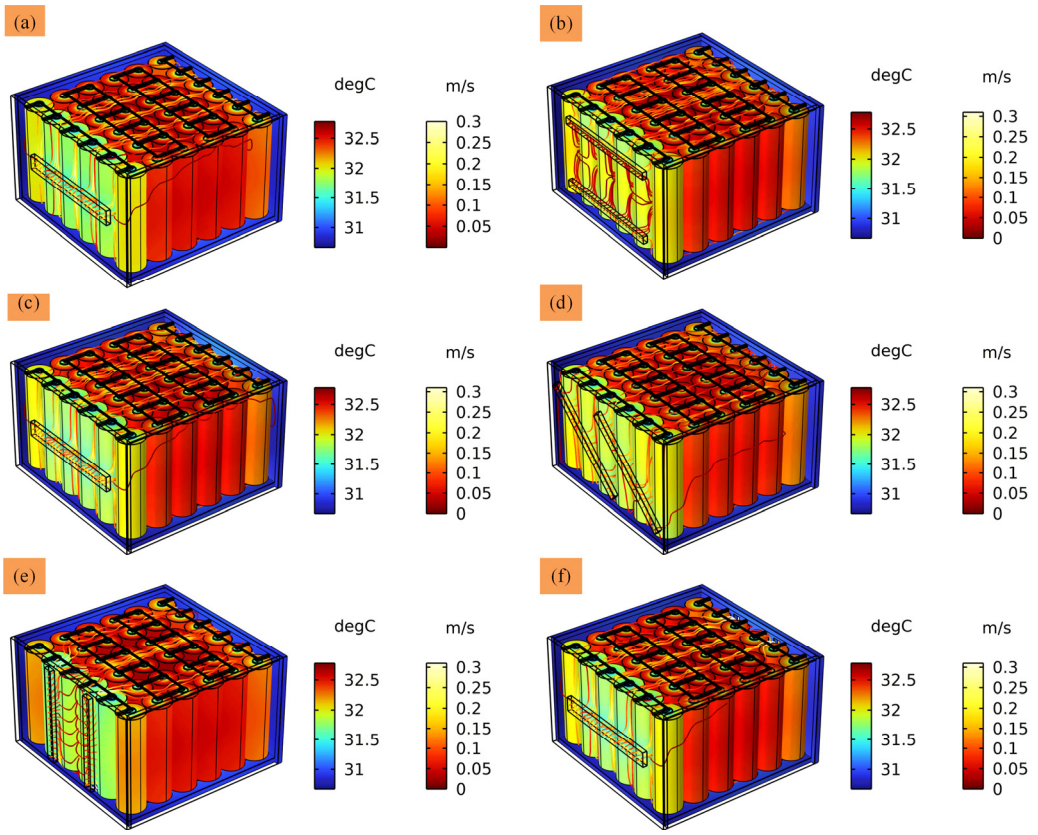

FIGURE 6. Discharge rate at 4C (a) Case 1, (b) Case 2, (c) Case 3, (d) Case 4, (e) Case 5, (f) Case 6.

Table 5. Effect of changing air inlet/outlet.

Case number	Rate of discharge (C)	T_{max} (˚C)	T_{min} (˚C)	ΔT (˚C)
Case 1.	1C	25.012	24.437	0.575
	4C	32.740	31.244	1.496
Case 2	1C	25.016	24.538	0.478
	4C	32.797	31.297	1.5
Case 3	1C	25.037	24.456	0.581
	4C	32.791	31.247	1.544
Case 4	1C	25.028	24.569	0.459
	4C	32.780	31.249	1.531
Case 5	1C	25.018	24.446	0.572
	4C	32.779	31.210	1.569
Case 6	1C	25.019	24.440	0.579
	4C	32.799	31.251	1.548

Staggered array configuration

A staggered array battery pack is a type of battery configuration in which the battery cells are organized in a staggered arrangement. Each cell is offset from the adjacent one by 1mm distance which is equal to the radius of the selected battery, form a zigzag pattern. This configuration was investigated at 20°C surrounding temperature, discharge rate at 4C, and air flowing at a speed of $0.1 ms^{-1}$. The study found that there was no significant reduce in the highest temperature of the batteries when the configuration was changed from an inline pattern 32.740°C to 32.815°C in a staggered pattern, in comparison with Case 1. The lack of improvement may be attributed to the fact that the staggered configuration did not provide sufficient airflow or thermal distribution between the cells, and because the cells were still packed densely together, thus not allowing for much improvement in heat dissipation as shown in figure 7. Nevertheless, Case 1, with a middle rectangular inlet and outlet, still proved to be one of the better designs in terms of thermal performance as presented in table 6.

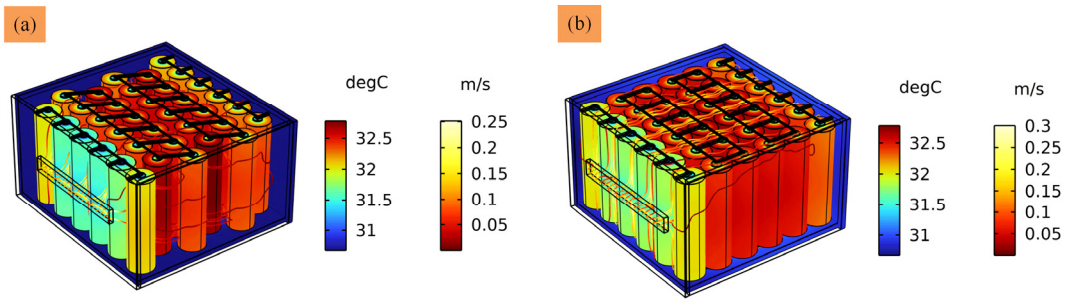

.FIGURE 7. A comparison between (a) staggered array, (b) case 1 inline configuration

Table 6. Effect of staggered configuration.

Configuration	T_{max} (˚C)	T_{min} (˚C)	ΔT (˚C)
Staggered	32.815	30.962	1.853
Inline	32.740	31.244	1.496

Air flow velocity

The air flow velocity can have a significant effect on the process of cooling a lithium-ion battery pack as in table7. When a battery is in operation, it generates heat that needs to be dissipated. Airflow is one of the parameters of dissipating heat from the battery. At low air flow velocities, heat transfer between the battery and the surroundings is limited, particularly during high discharge rates, resulting in a decrease in cooling rates.

The cell's temperature can then increase, leading to decreased battery capacity, accelerated degradation, and even safety concerns, such as the risk of thermal runaway. On the other hand, when the air flow velocity is high, the heat transfer rate increases, resulting in more effective cooling as shown in figure 8.

Changing the flow velocity from 0.1ms^{-1} to 1ms^{-1}, reduced the highest temperature from 25.012°C to 23.422°C during 1C discharge and from 32.740°C to 32.012°C during 4C discharge due to the modifications made.

Table 7. Comparison between different air velocities at different discharge rates

Velocity (ms^{-1})	discharge Rate (C)	T_{max} (˚C)	T_{min} (˚C)	ΔT (˚C)
0.1	1C	25.012	24.437	0.575
	4C	32.740	31.244	1.496
1	1C	23.422	21.901	1.521
	4C	32.012	28.560	3.452

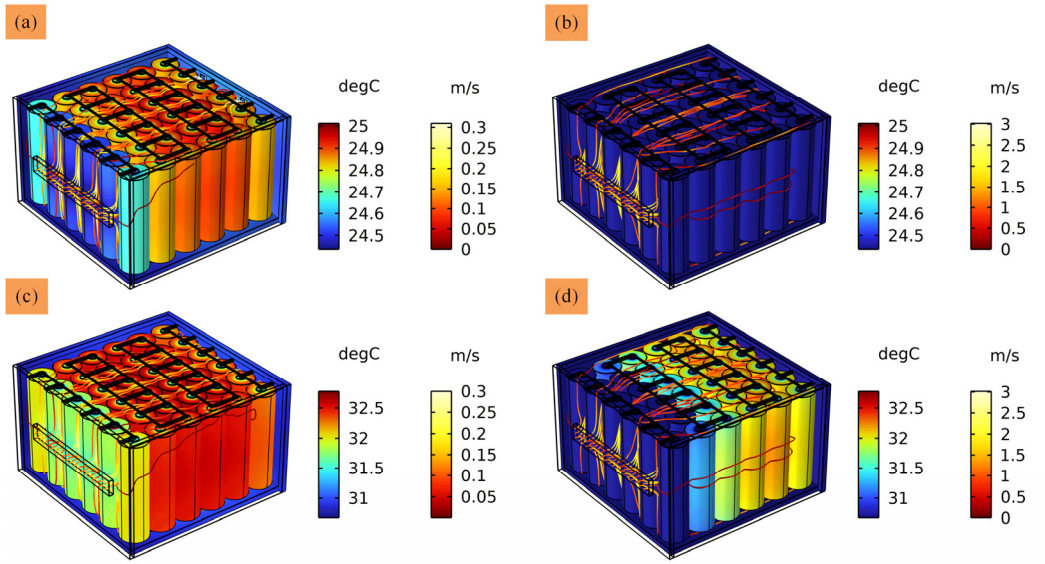

FIGURE 8. Effect of changing the flow velocity (a) 0.1ms^{-1} at 1C, (b) 1ms^{-1} at 1C, (c) 0.1ms^{-1} at 4C, (d) 0.1ms^{-1} at 1C.

CONCLUSION

The researchers utilized a numerical simulation method, employing the finite element method and a lumped battery model in the COMSOL Multiphysics software, to investigate a module consisting of 36 cylindrical battery cells arranged in a 6S6P configuration. The cells were contained in an aluminum casing with a small gap of 1mm between them and a thickness of 3mm. The study focused on various parameters including air inlet/outlet geometries, staggered array, air velocity, rate of discharge, their effects on the BTMS and showed that:

The natural cooling method for lithium-ion batteries has several drawbacks. Firstly, it was insufficient to dissipate heat generated during high-rate discharge. Secondly, natural cooling provides little flexibility to adjust the heat dissipation rate based on the battery's thermal needs, which can limit the efficiency of the battery. Finally, if it is exposed to high temperatures for a prolonged period due to inadequate cooling, it may cause severe hazards.

An aluminum casing added to a battery pack offers protection to the cells, acts as a thermal conductor, enhances the battery's performance, by reducing the maximum temperature by 18.88%.

Modifying the inlet and outlet design of a battery pack increased airflow and improved the thermal distribution within the pack. However, these modifications did not result in a significant decrease in the hightest temperature.

A study was carried out at $0.1 ms^{-1}$ inlet air flow and 4C rate of discharge indicated that the use of a staggered array battery pack configuration did not considerably reduce the maximum temperature of the battery pack, despite the potential benefits of improved air circulation and higher volumetric energy density. Less improvement may be due to insufficient space for airflow and thermal distribution between the cells despite the staggered configuration.

Air flow velocity plays a critical role in cooling. When air flows over the batteries, it carries away heat through forced convection heat transfer. This heat transfer process is directly proportional to the velocity of the air flow.

A higher flow velocity can result in a higher pressure drop and increased energy consumption in the cooling system. Thus, it is essential to improve the efficiency of airflow to achieve better results and minimize energy consumption.

The future study will be directed towards investigating how the spacing between cells affects thermal performance in battery packs. Additionally, there will be efforts to design innovative configurations that can achieve optimal operating conditions with minimal air flow velocity. This will involve identifying the best arrangement of inlet and outlet patterns to improve airflow and thermal distribution between the cells.

ACKNOWLEDGMENTS

The authors would like to show their appreciation and sincere gratitude for the Egyptian Ministry of Higher Education (MOHE) and Egypt-Japan University of Science and Technology (E-JUST) for providing the computational tools and the financial support to perform this study.

REFERENCES

1. G. Kalghatgi, H. Levinsky, M. Colket, Future transportation fuels, Prog. Energy Combust. Sci. 69 (2018) 103–105. https://doi.org/10.1016/j.pecs.2018.06.003.
2. M. Höök, X. Tang, Depletion of fossil fuels and anthropogenic climate change—A review, Energy Policy. 52 (2013) 797–809. https://doi.org/10.1016/J.ENPOL.2012.10.046.
3. The Global Electric Vehicle Market In 2023 – Virta, (n.d.). https://www.virta.global/en/global-electric-vehicle-market (accessed August 8, 2023).
4. M. Debert, G. Colin, G. Bloch, Y. Chamaillard, An observer looks at the cell temperature in automotive battery packs, Control Eng. Pract. 21 (2013) 1035–1042. https://doi.org/10.1016/J.CONENGPRAC.2013.03.001.
5. A. Tomaszewska, Z. Chu, X. Feng, S. O'Kane, X. Liu, J. Chen, C. Ji, E. Endler, R. Li, L. Liu, Y. Li, S. Zheng, S. Vetterlein, M. Gao, J. Du, M. Parkes, M. Ouyang, M. Marinescu, G. Offer, B. Wu, Lithium-ion battery fast charging: A review, ETransportation. 1 (2019) 100011. https://doi.org/10.1016/J.ETRAN.2019.100011.
6. Y. Saito, M. Shikano, H. Kobayashi, Heat generation behavior during charging and discharging of lithium-ion batteries after long-time storage, J. Power Sources. 244 (2013) 294–299. https://doi.org/10.1016/J.JPOWSOUR.2012.12.124.
7. C.R. Birkl, M.R. Roberts, E. McTurk, P.G. Bruce, D.A. Howey, Degradation diagnostics for lithium ion cells, J. Power Sources. 341 (2017) 373–386. https://doi.org/10.1016/J.JPOWSOUR.2016.12.011.

8. Y. Shi, S. Ahmad, H. Liu, K.T. Lau, J. Zhao, Optimization of air-cooling technology for LiFePO4 battery pack based on deep learning, J. Power Sources. 497 (2021) 229894. https://doi.org/10.1016/J.JPOWSOUR.2021.229894.
9. S. Lei, S. Xin, S. Liu, Separate and integrated thermal management solutions for electric vehicles : A review, J. Power Sources. 550 (2022) 232133. https://doi.org/10.1016/j.jpowsour.2022.232133.
10. X. Na, H. Kang, T. Wang, Y. Wang, Reverse layered air flow for Li-ion battery thermal management, Appl. Therm. Eng. 143 (2018) 257–262. https://doi.org/10.1016/J.APPLTHERMALENG.2018.07.080.
11. N.T. Tran, T. Farrell, M. Vilathgamuwa, S.S. Choi, Y. Li, A Computationally Efficient Coupled Electrochemical-Thermal Model for Large Format Cylindrical Lithium Ion Batteries, J. Electrochem. Soc. 166 (2019) A3059–A3071. https://doi.org/10.1149/2.1241913JES/XML.
12. M. Wang, S. Teng, H. Xi, Y. Li, Cooling performance optimization of air-cooled battery thermal management system, Appl. Therm. Eng. 195 (2021) 117242. https://doi.org/10.1016/J.APPLTHERMALENG.2021.117242.
13. B. Ruhani, A. Abidi, A.K. Hussein, O. Younis, M. Degani, M. Sharifpur, Numerical simulation of the effect of battery distance and inlet and outlet length on the cooling of cylindrical lithium-ion batteries and overall performance of thermal management system, J. Energy Storage. 45 (2022) 103714. https://doi.org/10.1016/j.est.2021.103714.
14. L.K. Singh, G. Mishra, A.K. Sharma, A.K. Gupta, A numerical study on thermal management of a lithium-ion battery module via forced-convective air cooling, Int. J. Refrig. 131 (2021) 218–234. https://doi.org/10.1016/J.IJREFRIG.2021.07.031.
15. M.S. Wu, Multi-objective optimization of U-type air-cooled thermal management system for enhanced cooling behavior of lithium-ion battery pack, J. Energy Storage. 56 (2022) 106004. https://doi.org/10.1016/j.est.2022.106004.
16. N. Lee, J. Choi, J. Lee, D. Shin, S. Um, Prognostic analysis of thermal interface material effects on anisotropic heat transfer characteristics and state of health of a 21700 cylindrical lithium-ion battery module, J. Energy Storage. 72 (2023) 108594. https://doi.org/10.1016/J.EST.2023.108594.
17. F.S. Hwang, T. Confrey, C. Reidy, D. Picovici, D. Callaghan, D. Culliton, C. Nolan, Review of battery thermal management systems in electric vehicles, Renew. Sustain. Energy Rev. 192 (2024) 114171. https://doi.org/10.1016/J.RSER.2023.114171.
18. B.Y. Liaw, E.P. Roth, R.G. Jungst, G. Nagasubramanian, H.L. Case, D.H. Doughty, Correlation of Arrhenius behaviors in power and capacity fades with cell impedance and heat generation in cylindrical lithium-ion cells, J. Power Sources. 119–121 (2003) 874–886. https://doi.org/10.1016/S0378-7753(03)00196-4.
19. Z. Lu, X. Yu, L. Wei, Y. Qiu, L. Zhang, X. Meng, L. Jin, Parametric study of forced air cooling strategy for lithium-ion battery pack with staggered arrangement, Appl. Therm. Eng. 136 (2018) 28–40. https://doi.org/10.1016/j.applthermaleng.2018.02.080.
20. W. Yang, F. Zhou, H. Zhou, Y. Liu, Thermal performance of axial air cooling system with bionic surface structure for cylindrical lithium-ion battery module, Int. J. Heat Mass Transf. 161 (2020) 120307. https://doi.org/10.1016/j.ijheatmasstransfer.2020.120307.
21. Kausthubharam, P.K. Koorata, N. Chandrasekaran, Numerical investigation of cooling performance of a novel air-cooled thermal management system for cylindrical Li-ion battery module, Appl. Therm. Eng. 193 (2021) 116961. https://doi.org/10.1016/j.applthermaleng.2021.116961.

Effect of the Inlet Nozzle on the Output Power of a Small-Scale Diffuser-Augmented Wind Turbine: Two- and Three-Dimensional Numerical Study

Ahmed T. Nile[1,2, a)], Mohamed Emam[1,3, b)], Shinichi Ookawara[1,4, c)] and Sameh Nada[1,5, d)]

[1] *Energy Resources Engineering Department, Egypt-Japan University of Science and Technology, E-JUST, Alexandria 21934, Egypt.*
[2] *Mechanical Power Engineering Department, Faculty of Engineering, Mansoura University, El-Mansoura 35516, Egypt.*
[3] *Mechanical Engineering Department, Benha University, Shoubra Faculty of Engineering, 108 Shoubra Street, Cairo, Egypt.*
[4] *Department of Chemical Science and Engineering, Tokyo Institute of Technology, Tokyo 152-8552, Japan.*
[5] *Mechanical Engineering Department, Benha Faculty of Engineering, Benha University Benha, Qalubia 13512, Egypt.*

[d)] Corresponding author: sameh.nada@ejust.edu.eg
[a)] ahmed.talaat@ejust.edu.eg or ahmed_nile@mans.edu.eg
[b)] mohamed.emam@ejust.edu.eg
[c)] ookawara.s.aa@m.titech.ac.jp

Abstract. This paper investigates the effect of attaching an inlet nozzle to the diffuser on the turbine output power. First, 2D and 3D numerical models are established and validated. Then, from the 2D results, the proper dimensions of the inlet nozzle are selected. After that, flow around the loaded diffusers with and without the inlet nozzle is simulated. For 2D simulations, a comprehensive axisymmetric model is adopted. The turbine is simulated by a uniform actuator disk with different load coefficients. For the 3D simulations, a periodical domain is developed. Also, the sliding mesh method is adopted for the turbine domain. ANSYS FLUENT 2020 R2 is used to solve the flow field for both studies. Reynolds-Averaged Navier-Stokes equations are integrated over the domains. While the turbulence model chosen is Shear-Stress Transport k-ω. The load (or turbine) power coefficient and the drag force acting upon the diffuser are the judging parameters used in the study. It is found that, for loaded diffusers, attaching the inlet nozzle has almost no effect on the turbine output power. Also, neglecting the change in the dynamic pressure across the load, in the 2D study, could lead to misleading outcomes.

INTRODUCTION

The world today faces a serious problem of global warming, which results because of the emissions of fossil fuels. So, it is important to depend on renewable energy sources such as solar energy and wind energy which could alleviate the harmful impact of fossil fuel on our world. Regarding the wind energy field, the Global Wind Energy Council (GWEC) stated that, in their report published in 2023, a wind power capacity of 77.6 GW was added in 2022 [1]. This added capacity offers 9 % year-over-year growth. However, it is still not sufficient to meet the global energy demand. According to [2], the only practical technique to enhance a turbine's output power is to increase its diameter. Yet, for a small-scale wind turbine, it is found to be efficient if this turbine is placed inside a diffuser, or a wind lens, as reported by [3]–[5]. This diffuser generates a low-pressure area downstream of the turbine. This induces a larger amount of air to flow through the turbine and subsequently, the turbine output power increases. This method is considered suitable for areas with low wind speeds. For some diffuser designs, there is a flange attached to the outlet section of the diffuser. This flange helps also in further decreasing the pressure downstream of the turbine. However, this flange could increase the drag force affecting the diffuser's structure.

Abe and Ohya [3] investigated numerically and experimentally the flow around empty and loaded diffusers. The load was a uniform actuator disk with variable load coefficients. It was used to simulate the turbine's existence. They stated that both the load's coefficient and the diffuser's open angle affect the diffuser's performance strongly. To

Technologies and Materials for Renewable Energy, Environment and Sustainability
AIP Conf. Proc. 3321, 040010-1–040010-11; https://doi.org/10.1063/5.0290414
Published under an exclusive license by AIP Publishing. 978-0-7354-5231-2/$30.00

calculate the power extracted by the load they derived an equation function of the axial flow velocity augmentation factor and load coefficient. However, they did not study the effect of adding an inlet nozzle to the diffuser. Ghajar and Badr [6] found that attaching a nozzle to a diffuser-augmented wind turbine increased its output power by about 11% and 83% under incoming air velocity of 12.3 and 16.6 m/s compared with the diffuser-augmented wind turbine, respectively. Their study was experimental, and they used an electrodynamometer to measure turbine output power. They attributed the high increment in the output at the higher air velocity to air turbulence and the closeness of the turbine to the fan blowing the air. Moreover, they mentioned that there is no need for a yaw mechanism in the case of using a nozzle with the diffuser. Based on Kosasih and Tondelli [7] experimental work, they found that attaching an inlet nozzle to the diffuser which surrounded the wind turbine increased the turbine output power coefficient by 63% compared to the bare turbine. Yet, utilizing the diffuser part only, without the inlet nozzle, to the turbine increased the output power by 60%. However, under yawed incoming flow, they found that attaching an inlet nozzle to the diffuser outperformed the one without the inlet nozzle. Kishore et al.[8] proposed a diffuser with an inlet nozzle to be used with a turbine of 39.4 cm rotor diameter. The turbine output power increased by 40% to 60% compared to the turbine without the diffuser. The inlet nozzle had a half cone angle of 15° and a length of 0.125 of diffuser diameter. They selected the dimensions of the inlet nozzle based on numerical simulations in the case of the empty diffuser. The maximum air flow velocity augmentation at the diffuser's axis was the parameter used to select the inlet nozzle dimensions and it was 1.2. However, they did not study the turbine performance in the case of using the diffuser part only. Mansour and Meskinkhoda[9] simulated the flow around a flanged diffuser proposed by Abe and Ohya[3] while it was empty and had an inlet nozzle. The air speed at the diffuser's axis reached about 1.6 times the incoming air flow velocity. However, they did not state the selected dimensions of the inlet nozzle. Mardiansah et al.[10] attached a flange and inlet nozzle to the diffuser proposed by Kannan et al.[11]. The dimensions of the flange and the inlet nozzle were altered through an optimization process to maximize the air flow velocity inside the empty diffuser. The optimal design increased air flow velocity by 67% compared to the incoming air flow velocity.

From the literature above, it is found that attaching an inlet nozzle to an empty diffuser demonstrates an increment in the air velocity flowing through the diffuser. However, it is important to investigate the effect of attaching the inlet nozzle to the loaded diffuser. Also, from the literature, the drag force experienced by the diffuser due to adding the inlet nozzle was not taken into consideration. Thus, the present study aims to widen the investigation of attaching an inlet nozzle to the diffuser when empty and loaded. Through the study, the drag force acting upon the diffuser structure will be considered in both cases.

This study is conducted in 2D and 3D flow domains. Based on the 2D study, the dimensions of the inlet nozzle will be selected. The parameters used to select the proper dimensions are the air mass flow rate through the diffuser and the drag force acting upon the empty diffuser. Then, a comparison between diffuser with and without an inlet nozzle will be established while the diffuser is loaded, in the 2D study. The load used to simulate the turbine is a uniform actuator disk with different load coefficients. The power extracted by the load and the diffuser's drag force are the parameters used in this comparison. Finally, 3D results will be presented for both cases but when a turbine is placed inside the diffuser instead of the load as in the 2D study.

PHYSICAL MODEL

Figure 1 presents a schematic diagram of the investigated diffusers. As shown in the figure, Case 1 represents a simple diffuser while in Case 2 an inlet nozzle is attached to the diffuser. The inlet nozzle is 20 mm in length with a half angle of 15°. The divergent part is 300 mm in length with a 4° half angle [3]. The load shown in the figure simulates the turbine. This load extended over 20 mm [3]. The load coefficient range used is from 0.2 to 2 [3]. However, in the 3D study, this load is replaced by a turbine. The turbine runs at different rotational speeds.

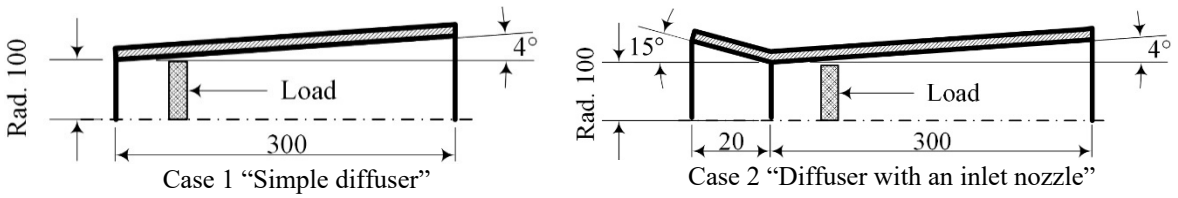

FIGURE 1. A schematic diagram of studied diffusers [Dimensions are in mm and diagrams are not to scale].

NUMERICAL SIMULATIONS

For the 2D simulations, the flow around the diffuser is assumed to be steady, incompressible, turbulent, and axisymmetric. On the other hand, for the 3D study, since the sliding mesh method is adopted for the turbine domain, the flow is considered to be transient. In both scenarios, the RANS equations are developed from the governing equations and the chosen turbulence model is Shear-Stress Transport *k-ω*. The selected model was assessed by previous researchers and attained a good agreement with measurements [12]–[15]. The governing equations can be found in [16]–[18].

The equation of the axial load force placed inside the diffuser, in the 2D calculations, can be written as follows [3]:

$$F_z = \frac{-1}{2}\rho\frac{C_{load}}{\Delta}U_z|U_z| \quad \left[\frac{N}{m^3}\right] \tag{1}$$

where C_{load} is defined as the load coefficient. This force is added as a source term in the axial momentum equation to be applied to each cell located in the load's domain.

Investigated Parameters

The augmentation factor is defined as the ratio between the flow velocity at any position, U, and the free stream velocity, U_0. It could be formulated as follows:

$$K = \frac{U}{U_0} \tag{2}$$

The pressure coefficient, C_{press}, is defined as the ratio between the gauge pressure at any location and the dynamic pressure of the free stream [19].

$$C_{press} = \frac{P - P_0}{\frac{1}{2}\rho U_0^2} \tag{3}$$

where P_0 is the static pressure of the free stream and ρ is the air density.

The normalized air mass flow rate through the diffuser is calculated at the throat section using the following equation:

$$Normalized\ air\ mass\ flow\ rate = \frac{\int_{A_{Throat}} \rho U_z\, dA}{\rho U_0 A_{Throat}} \tag{4}$$

where A_{Throat} equals the cross-sectional area of the throat.

The drag force experienced by the diffuser is a function of the pressure and shear stress acting in the flow direction [17]. Hence,

$$F_D = \int_{A_{Diffuser}} (-p\cos\theta + \tau_w \sin\theta)\, dA \ \ [N] \tag{5}$$

where p is the local static pressure at the diffuser wall, τ_w is wall shear stress at the diffuser wall, θ is the angle between the outer normal vector of the area dA and the positive direction of the flow, and $A_{Diffuser}$ is the surface area of the diffuser.

In the 2D simulations, the extracted power by the load is calculated via two different equations. The first one considers the change in the total pressure across the load. While the second one neglects the change in the dynamic pressure across the load so, it considers only the change in the static pressure across the load instead.

The first equation is applied to the three surfaces of the load:

$$Power(total_press) = \int_A \left(p + \frac{1}{2}\rho U^2\right)(U.n)\, dA \quad [W] \tag{6}$$

While the second equation, as reported by Bagheri-Sadeghi et al. [20], [21], is:

$$Power(static_press) = 2\pi \int_0^{0.5\, D_{Load}} U_z\, \Delta p\, r dr \quad [W] \tag{7}$$

where U_z is the axial flow velocity of air flowing through the load, Δp represents the static pressure difference across the load, and D_{Load} is the load's diameter.

The power coefficient for both equations, C_{power}, could be deduced as follows [5], [8]:

$$C_{power} = \frac{Power}{\frac{1}{2}\rho A_{load} U_0^3} \tag{8}$$

where A_{load} equals the cross-sectional area of the load.
While for the turbine, in the 3D study, the power coefficient is calculated by,

$$C_{power} = \lambda C_m \tag{9}$$

where λ is the turbine tip speed ratio and C_m is the turbine moment coefficient about its axis of rotation.

Computational Domains and Boundary Conditions

Figure 2 illustrates a representation of the layout of the adopted computational domains in the 2D and 3D studies. Also, the boundary conditions adopted for the current study are shown in the figure. Also, the figure gives the dimensions regarding the case used to validate the numerical model for the 2D study [3]. For the 2D study, a uniform air velocity, U_0, equals 5 m/s with a turbulence intensity of 3% was assumed at the inlet section [3]. But, for the 3D study, the air velocity is set to be 8 m/s [5]. The outlet pressure is set to be atmospheric.

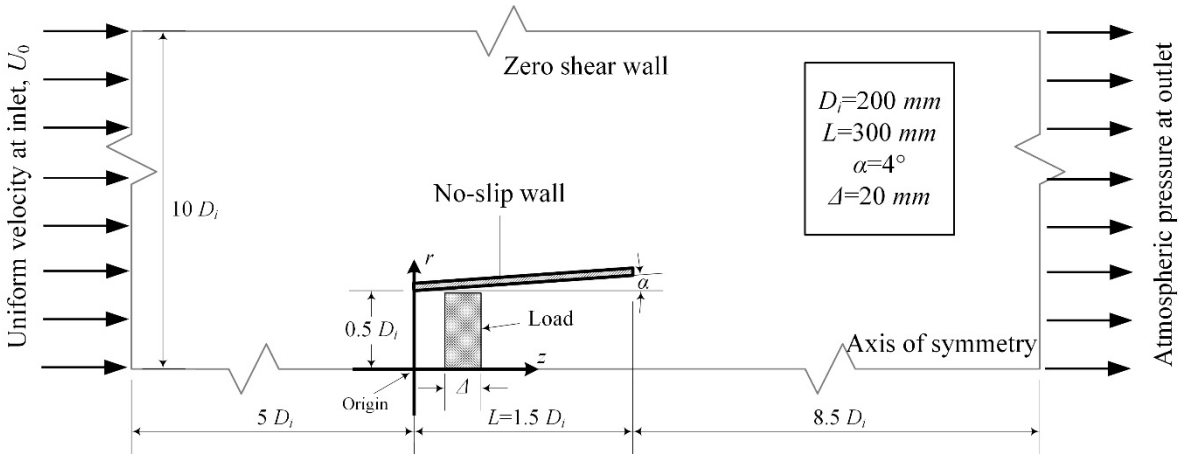

a) 2D study domain.

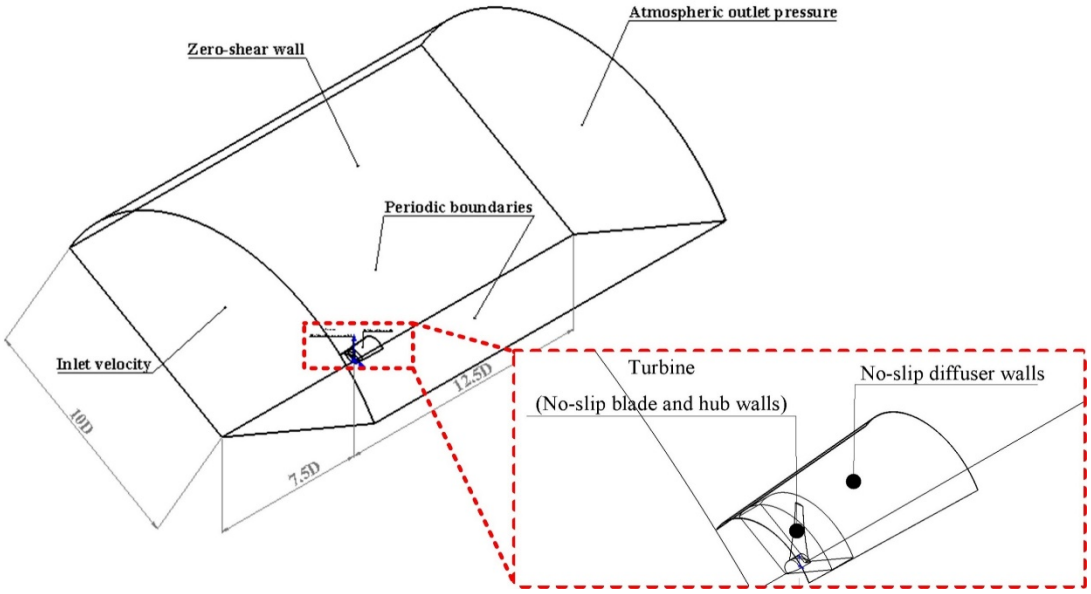

b) 3D study domain.

FIGURE 2. Computational domain representations.

NUMERICAL SOLUTION

The commercial software ANSYS FLUENT 2020 R2 is used to solve the governing equations along with the boundary conditions. The SIMPLE scheme is adopted for the pressure-velocity coupling. Moreover, the second-order upwind method is selected for both turbulent kinetic energy and specific dissipation rate. The convergence criteria are set as follows: the residuals of continuity and momentum equations are set to 10^{-5}. Besides, the change in air mass flow rate value at the diffuser's throat should equal 10^{-5} or less over 10 successive iterations.

Model Validation

Two sets of experimental and numerical results obtained by Abe and Ohya [3] are considered to validate the model used in this study. The first set is experimental measurements for an empty diffuser. The second set simulates a loaded diffuser with different load coefficients, C_{load}. The validation parameters are the augmentation factor, K, and the pressure coefficient, C_{press}, along the diffuser's axis. As shown in Fig. 3-a and -b, there is a fair agreement between the proposed model results and Abe and Ohya [3] experimental and numerical results. Figure 3-c presents the validation of the adopted three-dimensional model based on extracted experimental data of a diffuser-augmented wind turbine proposed by [5]. Full geometrical details of the diffuser can be found in [4].

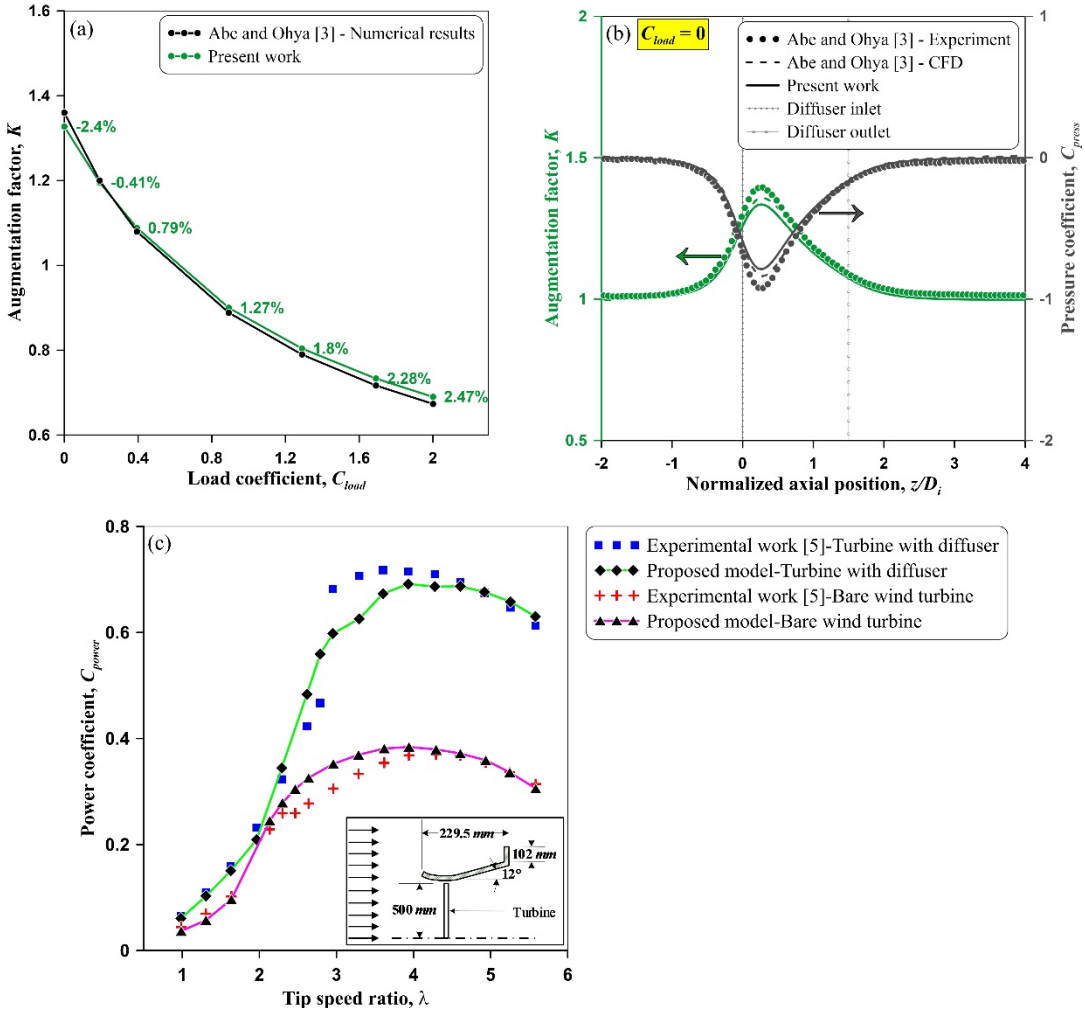

FIGURE 3. Numerical model validations. (a) Empty diffuser "For 2D study", (b) Augmentation factor just upstream the load at different load coefficients. [The given percentage at each point is the relative error of this point] "For 2D study", and (c) Power coefficient at different tip speed ratios. "For 3D study". The bottom-left figure is a schematic diagram for the diffuser.

RESULTS AND DISCUSSIONS

This section is divided into three subsections to present and discuss the outcomes of this study. Selecting the most proper dimensions of the inlet nozzle attached to the diffuser is discussed in the first section. Then moving to the second section, in which the effect of attaching the inlet nozzle is highlighted by setting a comparison with the diffuser without it. It is important to note that two different equations for calculating the extracted power by the load are adopted in that section. Finally, the effect of attaching the inlet nozzle on the turbine's power coefficient is presented in the last section.

The Most Suited Dimensions of the Inlet Nozzle "2D Study"

The most suited dimensions of the inlet nozzle are selected based on two parameters: ingested air mass flow rate through the diffuser and the drag force affecting the diffuser. It is required to have a large amount of air flowing through the diffuser in addition to a minimum drag force acting upon the diffuser as possible. The tested inlet nozzle angles and lengths range from 5° to 30° and from 10 mm to 60 mm, respectively. Figure 4 gives the values of air mass flow rate and drag force for the assorted designs. It is important to mention that the diffuser is empty in those cases. As shown, it is proven that adding an inlet nozzle to the diffuser increases the air mass flow rate and hence the air flow velocity as stated in the literature. This should enhance the performance of the wind turbine placed inside the diffuser. The most suited inlet nozzle dimensions are 60 mm length and 10° half angle. It induces the maximum amount of air to flow through the diffuser while applying the minimum drag force to it. However, an inlet nozzle with a length of 20 mm and half open angle of 15° is selected instead. This design reduces the total length of the diffuser and hence, it saves material and manufacturing costs. Also, it does not affect the air mass flow rate and the drag force so much. It is found that the air mass flow rate is reduced by less than 1% and the drag force is increased by about 3%. It is worth mentioning that the inlet nozzle angle is selected also by [8] but there is a difference in its length. In this study, the length to throat diameter equals 0.1 while in their study it was 0.125. Even though their divergent part dimensions are different from those used in this study.

Investigating the Effect of the Inlet Nozzle with A Loaded Diffuser in the 2D Domain

From the previous section, the selected inlet nozzle increases the air mass flow rate by about 14% when compared with a simple diffuser. This section illustrates the effect of the inlet nozzle when the diffuser is loaded. The load coefficient ranges from 0.2 to 2. The comparison is based on the extracted power from the flowing air by the load and the drag force acting upon the diffuser. The extracted power is calculated by equations (6) and (7).

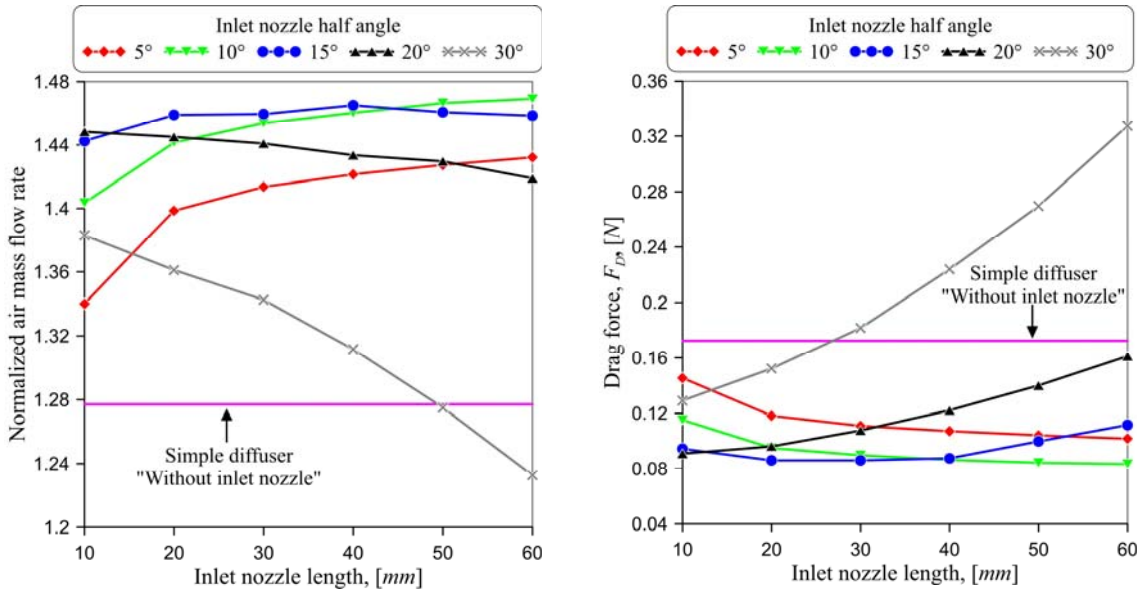

FIGURE 4. The normalized air mass flow rate (Left) and drag force acting on the diffuser (Right) at different half angles and lengths of the inlet nozzle.

As shown in Fig. 5, discarding the change in the dynamic pressure across the load, equation (7), gives a power coefficient lower than those calculated based on the total pressure, equation (6). Also, it is shown that, based on equation (6), there is no noticeable effect of adding the inlet nozzle to the diffuser on the power coefficient. On the other hand, when neglecting the change in the dynamic pressure through power calculation, equation (7), attaching the inlet nozzle to the diffuser outperforms the diffuser that has no inlet nozzle. Moving to the drag force, the diffuser without an inlet nozzle experiences a higher drag force at the minimum load coefficient. This is because of the low-pressure zone created at the diffuser's entrance in which a recirculation zone is formed. Figure 6-a depicts this recirculation zone. Adding the inlet nozzle part depletes this recirculation zone, as appears in Fig. 6-b.

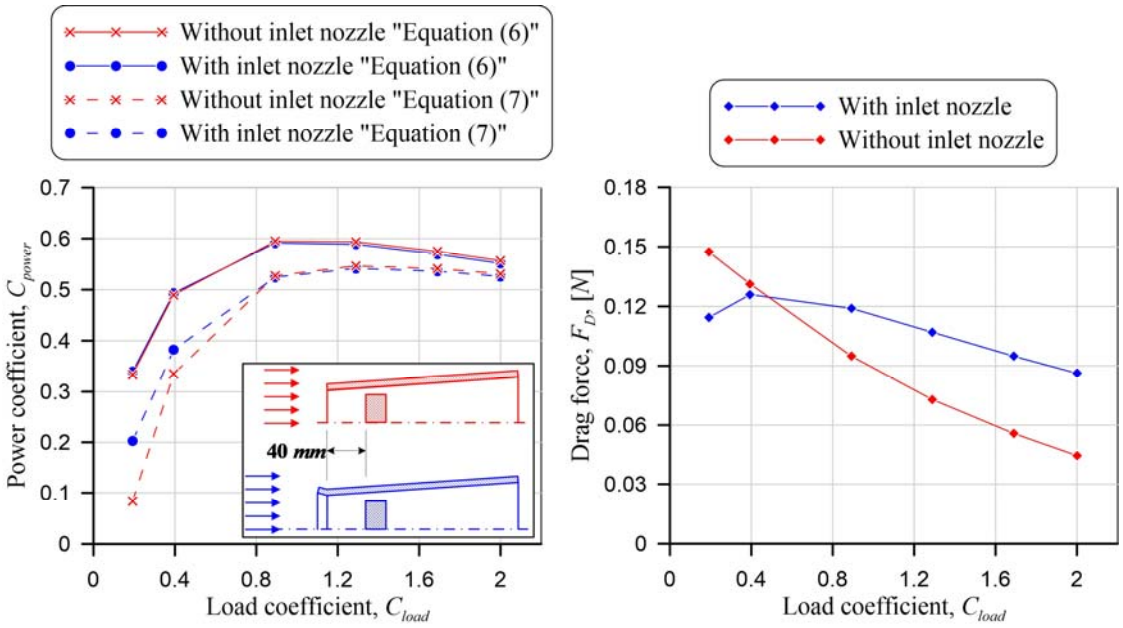

FIGURE 5. The power coefficient (Left) and the drag force (Right) at various load coefficients.

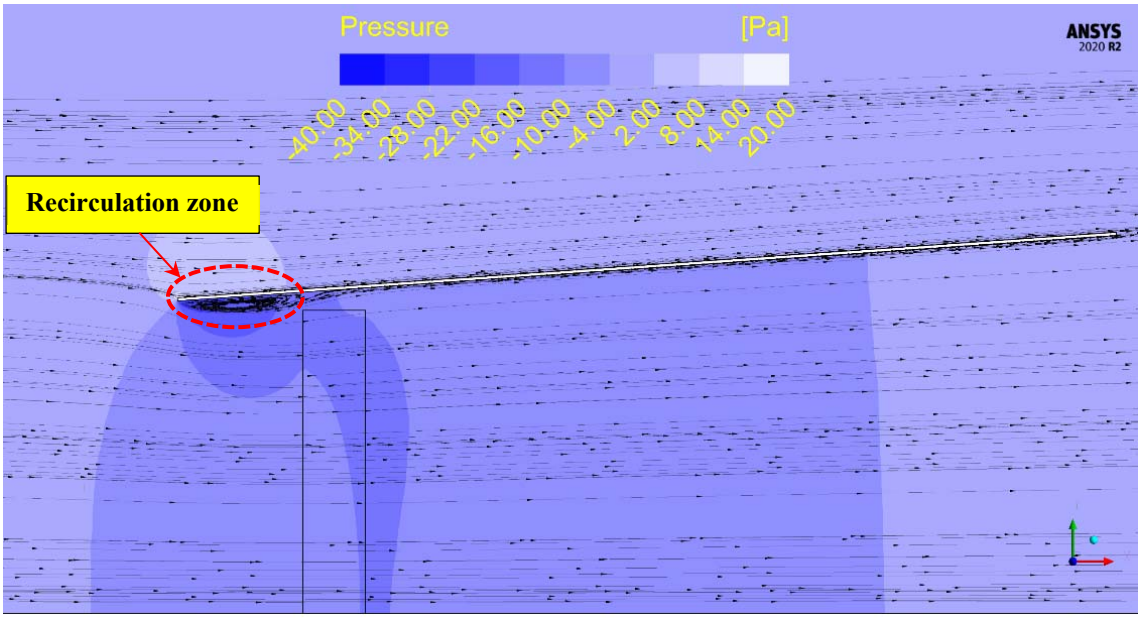

(a) Simple diffuser.

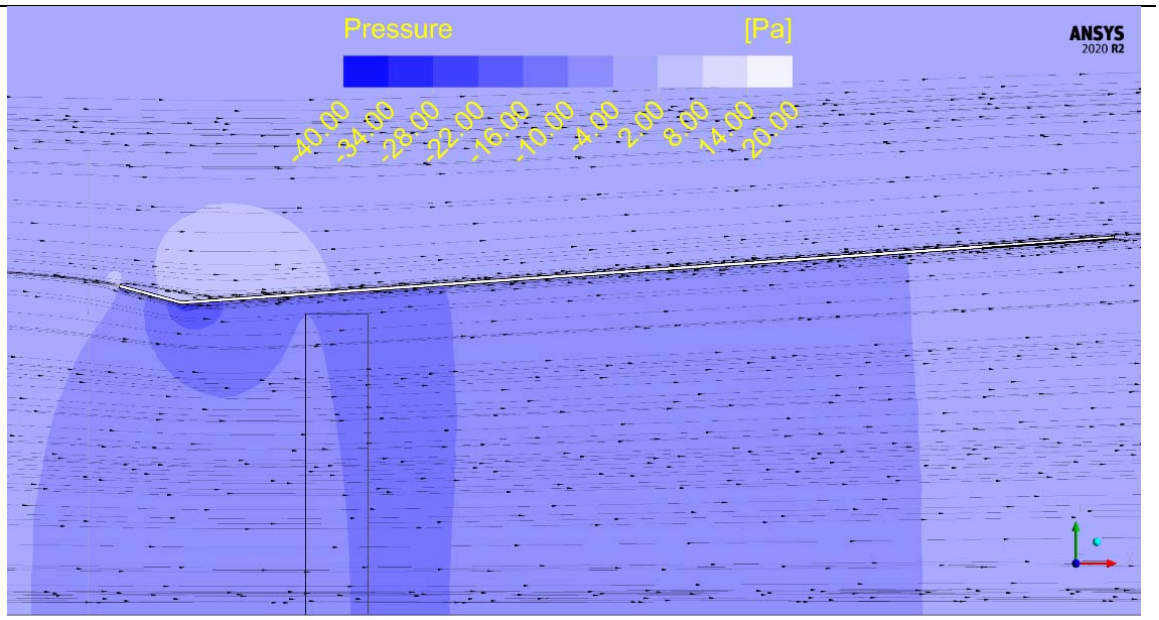

(b) Diffuser with inlet nozzle.

FIGURE 6. Pressure contours with velocity streamlines for simple diffuser (Top) and with inlet nozzle (Bottom) and the load is placed at 40 mm from the throat with C_{load} = 0.2

Inlet Nozzle Effect on Diffuser-Augmented Wind Turbine

In this section, the selected inlet nozzle from section 5.1 is attached to the diffuser. The turbine is scaled down by a factor of 1/5 of the one adopted by [5]. It is placed at a distance from the diffuser's throat so that the clearance between the inside wall of the diffuser and the blade tip equals 3 mm approximately. Figure 7 gives the values of the power coefficient and drag force acting on the diffuser at different turbine tip speed ratios. The turbine power coefficient is calculated by equation (9). As illustrated by Fig. 7, there is no noticeable enhancement in power coefficient when using the inlet nozzle. This is confirmed from the 2D study while considering equation (6) in calculating the extracted power. It is worth mentioning that [7] stated the same outcome regarding attaching the inlet nozzle to the diffuser. Moving to the drag force, the inlet nozzle alleviates the drag force acting on the diffuser structure at λ equal 1. This happens since attaching the inlet nozzle helps in depleting the low-pressure region formed at the diffuser's inlet section as shown in Fig. 8-a and -b. By comparing the change in the drag force values in the 2D and 3D studies, Fig. 5 and Fig. 7, there is a point at which the drag force acting on the simple diffuser becomes less than the force in case of attaching the inlet nozzle to the diffuser. However, the drag force is almost constant at the turbine tip speed ratio ranges from 3 to 5.

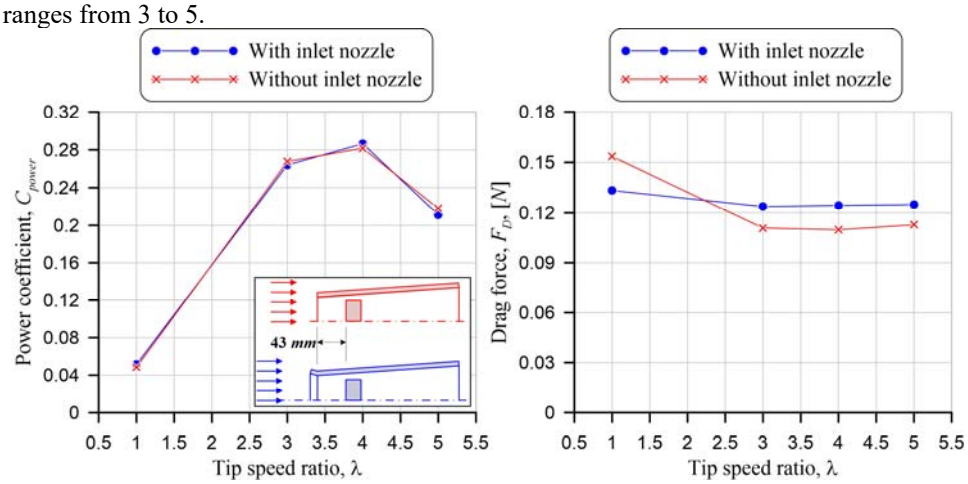

FIGURE 7. Turbine power coefficient (Left) and the drag force acts on the diffuser (Right) at different turbine tip speed ratios.

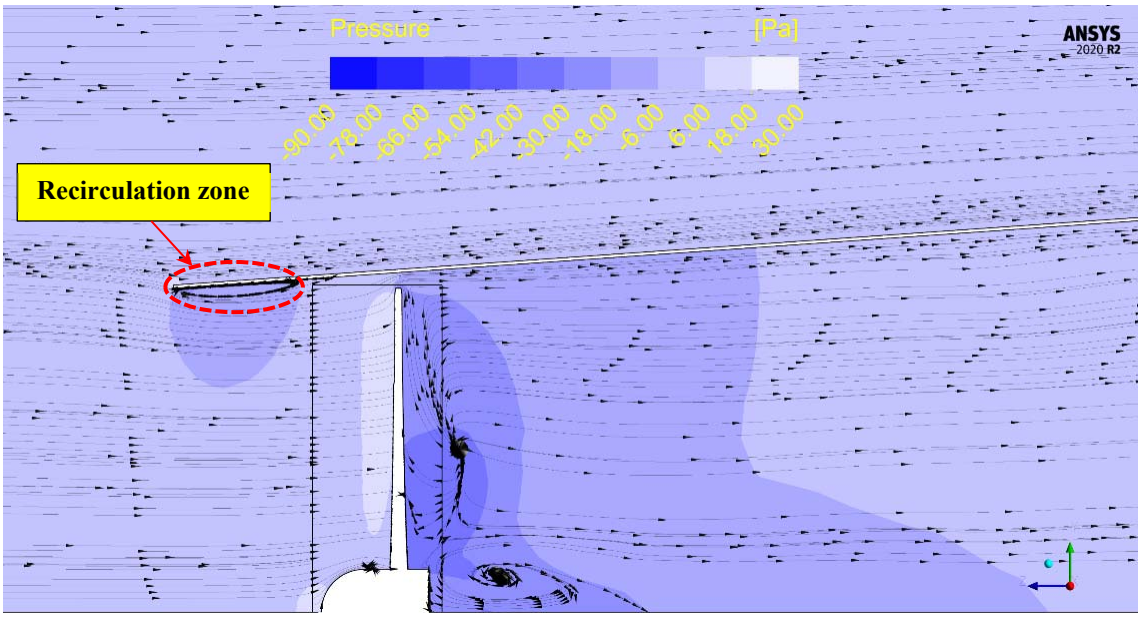

(a) Simple diffuser.

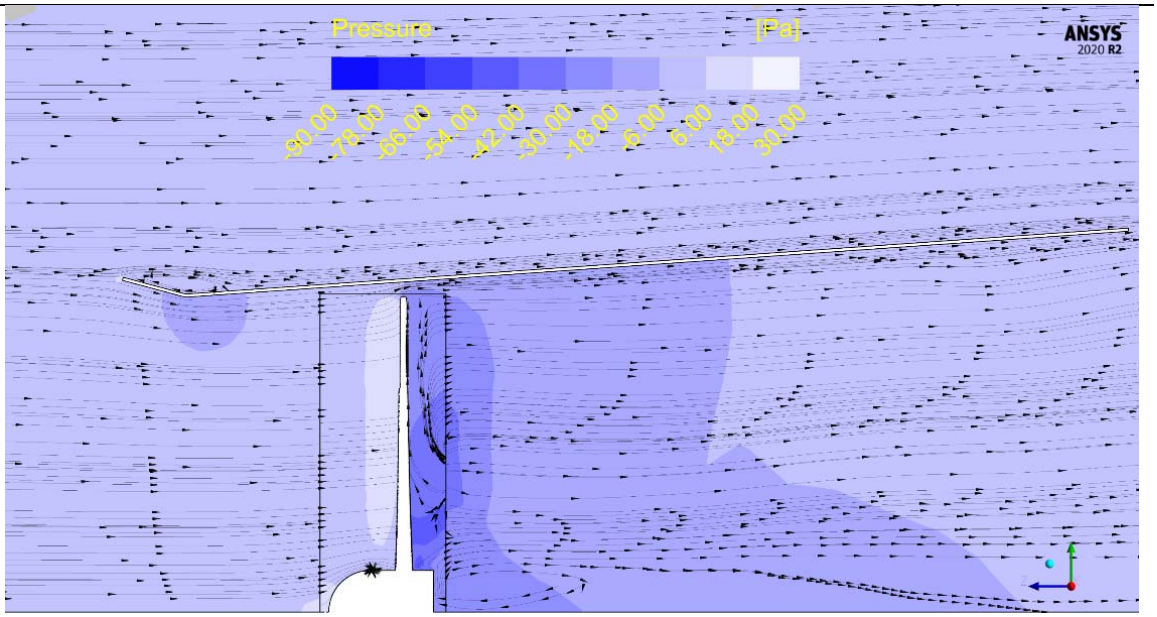

(b) Diffuser with inlet nozzle.

FIGURE 8. Pressure contours with velocity streamlines for simple diffuser (Top) and with inlet nozzle (Bottom) and the turbine domain's upstream side is placed at approx. 43 mm from the throat [at $\lambda = 1$].

CONCLUSION

Placing a small-scale wind turbine inside a diffuser helps in increasing the amount of air flowing through the turbine. Hence, the turbine's output power increases. Through this study, the effect of attaching an inlet nozzle to a diffuser on turbine output power coefficient was investigated. The study was conducted numerically in two- and three-dimensional flow domains. Through the 2D study, the turbine was simulated as a uniform actuator disk with a variable load coefficient. While a turbine was used in the 3D study. Load/Turbine power coefficients and drag force acts upon the diffuser were the judging parameters. The extracted power by the load in the 2D study was calculated via two equations, the first one considered the change in the dynamic pressure across the load. While the second one neglected this change. The inlet nozzle dimensions were selected based on how much the ingested air mass flow rate by the

diffuser increased while being empty, and the drag force experienced by the diffuser. The dimensions of the selected inlet nozzle were close to those in the literature. It was found that attaching the inlet nozzle to the diffuser increased the air mass flowing through the diffuser while being empty compared with the simple diffuser. Calculating the power coefficient in the 2D revealed that neglecting the change in the dynamic pressure across the load gave undervalued results compared with the equation that considered the change in the total pressure. Also, neglecting this dynamic pressure revealed misleading outcomes regarding the effect of the inlet nozzle. Since it was found that the inlet nozzle enhanced the extracted power by the load. However, both the 3D study and the power equation, which is a function of the total pressure, showed that there was no noticeable effect of the inlet nozzle on the output power of the turbine or the load. Also, this result agrees with what is found in the literature. This means that the two-dimensional study could be used for the sake of comparison between different diffuser geometries regardless of the values of the power coefficients in both cases. This could save the computational cost during the design phase. Finally, regarding the drag force, the 2D study could predict very well the force experienced by the diffuser either with an inlet nozzle or without as in the 3D study. Yet, this happens at minimum load coefficient and turbine tip speed ratio. Moreover, the 2D and 3D studies show that at some point the drag force affecting the simple diffuser became less than the one with an inlet nozzle.

ACKNOWLEDGEMENT

The financial support and computational resources provided by the Egyptian Ministry of Higher Education (MoHE) and the Egypt-Japan University of Science and Technology (E-JUST) for this research are gratefully acknowledged and appreciated. The first author also thanks Prof. Yuji Ohya (Kyushu University) for sharing turbine characteristics.

REFERENCES

1. GWEC, “Global Wind Report,” Brussels, Belgium, 2023.
2. M. M. Nunes, A. C. P. B. Junior, and T. F. Oliveira, “Systematic review of diffuser-augmented horizontal-axis turbines,” *Renewable and Sustainable Energy Reviews*, vol. 133, p. 110075, 2020.
3. K. Abe and Y. Ohya, “An investigation of flow fields around flanged diffusers using CFD,” *Journal of wind engineering and industrial aerodynamics*, vol. 92, no. 3–4, pp. 315–330, 2004.
4. Y. Ohya, T. Uchida, T. Karasudani, M. Hasegawa, and H. Kume, “Numerical studies of flow around a wind turbine equipped with a flanged-diffuser shroud using an actuator-disk model,” *Wind Engineering*, vol. 36, no. 4, pp. 455–472, 2012.
5. Y. Ohya and T. Karasudani, “A shrouded wind turbine generating high output power with wind-lens technology,” *Energies*, vol. 3, no. 4, pp. 634–649, 2010.
6. R. F. Ghajar and E. A. Badr, “An experimental study of a collector and diffuser system on a small demonstration wind turbine,” *International Journal of Mechanical Engineering Education*, vol. 36, no. 1, pp. 58–68, 2008
7. B. Kosasih and A. Tondelli, “Experimental study of shrouded micro-wind turbine,” *Procedia Engineering*, vol. 49, pp. 92–98, 2012.
8. R. A. Kishore, T. Coudron, and S. Priya, “Small-scale wind energy portable turbine (SWEPT),” *Journal of wind engineering and industrial aerodynamics*, vol. 116, pp. 21–31, 2013.
9. K. Mansour and P. Meskinkhoda, “Computational analysis of flow fields around flanged diffusers,” *Journal of Wind Engineering and Industrial Aerodynamics*, vol. 124, pp. 109–120, 2014, doi: 10.1016/j.jweia.2013.10.012.
10. F. Mardiansah, A. D. Putranto, and H. R. Hapsari, “Computational Fluid Dynamics Studies on the Wind Speed Characteristics of an Improved Diffuser Design,” in *2018 International Conference and Utility Exhibition on Green Energy for Sustainable Development (ICUE)*, 2018, pp. 1–4.
11. T. S. Kannan, S. A. Mutasher, and Y. H. K. Lau, “Design and flow velocity simulation of diffuser augmented wind turbine using CFD,” *Journal of Engineering Science and Technology*, vol. 8, no. 4, pp. 372–384, 2013.
12. H. A. Heikal, O. S. M. Abu-Elyazeed, M. A. A. Nawar, Y. A. Attai, and M. M. S. Mohamed, “On the actual power coefficient by theoretical developing of the diffuser flange of wind-lens turbine,” *Renewable energy*, vol. 125, pp. 295–305, 2018.
13. A. Alkhabbaz, H.-S. Yang, W. Tongphong, and Y.-H. Lee, “Impact of compact diffuser shroud on wind

turbine aerodynamic performance: CFD and experimental investigations," *International Journal of Mechanical Sciences*, vol. 216, p. 106978, 2022.
14. I. Hashem, A. A. Hafiz, and M. H. Mohamed, "Characterization of aerodynamic performance of wind-lens turbine using high-fidelity CFD simulations," *Frontiers in Energy*, pp. 1–22, 2020.
15. A. D. Paranjape, A. S. Bajaj, S. T. Palanganda, R. Parikh, R. Nayak, and J. Radhakrishnan, "Computational analysis of high-lift-generating airfoils for diffuser-augmented wind turbines," *Wind Energy Science*, vol. 6, no. 1, pp. 149–157, Jan. 2021, doi: 10.5194/wes-6-149-2021.
16. B. R. Munson, D. F. Young, and T. H. Okiishi, *Munson, Young and Okiishi - Fundamentals of Fluid Mechanics 8th edition*. Wiley, 2016.
17. Y. A. Çengel and J. M. Cimbala, *Fluid Mechanics: Fundamentals and Applications*. McGraw-Hill Higher Education, 2010.
18. H. K. Versteeg and W. Malalasekera, *An Introduction to Computational Fluid Dynamics: The Finite Volume Method*. Pearson Education, Limited, 2011. [Online]. Available: https://books.google.com.eg/books?id=mJS2uAAACAAJ
19. W. David, "Small Wind Turbines–Analysis, Design, and Application," *Introduction to Wind Turbine Technology*, 2011.
20. N. Bagheri-Sadeghi, B. T. Helenbrook, and K. D. Visser, "Wake comparison of open and ducted wind turbines using actuator disc simulations," in *Fluids Engineering Division Summer Meeting*, 2020, vol. 83730, p. V003T05A050.
21. N. Bagheri-Sadeghi, B. T. Helenbrook, and K. D. Visser, "Ducted wind turbine optimization and sensitivity to rotor position," *Wind Energy Science*, vol. 3, no. 1, pp. 221–229, Jan. 2018.

Standalone Hydrogen Production and Storage System Powered by Photovoltaic Under Different Climate Conditions

Mohamed G. Basiony [1,2, a)], Sameh Nada [1,3], Shinsuke Mori [4], Hamdy Hassan [1,5]

[1] *Energy Resources Engineering Department, Egypt-Japan University of Science and Technology (E-JUST), Alexandria, Egypt*
[2] *Mechanical Engineering Department, Faculty of Engineering, Suez University, Suez, Egypt*
[3] *Mechanical Engineering Department, Benha Faculty of Engineering, Benha University, Benha, Egypt*
[4] *Tokyo Institute of Technology, Tokyo, Japan*
[5] *Mechanical Power Engineering Department, Faculty of Engineering, Assiut University, Assiut, Egypt*

[a)] Corresponding author: mohamed.gamal@ejust.edu.eg

Abstract. Hydrogen is regarded as a promising solution for sustainable energy because it serves as both a carbon-neutral fuel and a practical storage medium for renewable energy sources (RES). So, this paper studies a standalone hydrogen production and storage system comprising a photovoltaic, proton exchange membrane (PEM) electrolyzer, reverse osmosis (RO) unit, electric heater, compressor, and storage tank. The mathematical model is developed and solved by Matlab/Simulink to assess the annual system's performance and overall efficiency under diverse Egyptian climates. The results indicate that the yearly hydrogen production equals 7.69, 8.17, and 8.42 kg/m^2 in Borg El-Arab, Assiut, and Aswan, respectively. Although Borg El-Arab experiences the lowest annual solar radiation of 2118.53 kWh/m^2, it achieves the highest overall system efficiency of 14.3%. Moreover, the PEM electrolyzer exploits 89.2% of the PV electricity to produce hydrogen.

INTRODUCTION

Hydrogen is recognized as a clean and efficient energy carrier that can substantially impact future energy security and sustainability [1]. The economic and environmental consequences of hydrogen production have been examined, focusing on methane's steam-reforming, which is currently the most cost-effective commercial process [2]. However, Norouzi [3] raises concerns about the sustainability of fossil fuel-based hydrogen production methods, citing limitations such as access to raw materials and greenhouse gas emissions. To tackle these issues, it is essential to adopt sustainable production methods, which can be accomplished by using renewable energy sources (RES) to produce hydrogen by splitting water in the electrolysis process.

Egypt is renowned for its abundant solar energy resources, characterized by an average yearly solar radiation between 2000 – 3200 kWh/m^2 [4]. Under such conditions, a photovoltaic (PV) system can capture solar energy and turn it into electricity that can be employed to operate a Proton exchange membrane (PEM) electrolyzer to ensure a sustainable source of hydrogen production with zero emissions. The PEM electrolyzer offers several advantages, including its rapid response time and the production of highly pure hydrogen [5]. For instance, Paul and Andrews [6] investigate the direct coupling between the PEM electrolyzer and PV panels in solar-hydrogen systems to achieve maximum power transfer and hydrogen production. The study reveals that a PV-electrolyzer system with direct coupling may achieve more than 94% of the theoretical maximum energy transfer, eliminating the demand for expensive electronic coupling systems. Gibson and Kelly [7] enhance the PV-electrolysis system performance by connecting the PEM electrolyzer directly to the PV panels at a voltage that corresponds to or slightly surpasses the electrolyzer working voltage, resulting in an efficiency of up to 12.4%. However, Ganeshan et al. [8] use a DC/DC converter in a solar hydrogen production system to provide a consistent rate of hydrogen synthesis, even when the solar irradiation fluctuates between 440 and 975 W/m^2.

On the other hand, Lopez et al. [9] utilize the particle swarm algorithm to optimize a PV-alkaline electrolyzer system. The optimization aims to find the PV plant's best configuration in terms of the azimuth and tilt angles of the

Technologies and Materials for Renewable Energy, Environment and Sustainability
AIP Conf. Proc. 3321, 040011-1–040011-12; https://doi.org/10.1063/5.0289634
Published under an exclusive license by AIP Publishing. 978-0-7354-5231-2/$30.00

panels, as well as the oversize factor. The objective is to reduce energy consumption, wasted energy, and hydrogen cost. The results reveal that oversizing the PV plant by a factor of 2.63 compared to the electrolyzer minimizes the cost. However, an additional 2% oversizing is required to achieve maximum efficiency. Meanwhile, Ghribi et al. [10] emphasize the significance of location. A mathematical model is developed to assess hydrogen production using a 60 W PV panel linked to a 50 W PEM electrolyzer system at seven locations in Algeria. Their research reveals that the annual hydrogen production in the southern region amounted to 29 m^3, whereas in the northern region, it was roughly 20 m^3. This variance highlights the significant reliance of hydrogen production on the amount of solar radiation that is accessible.

Currently, reverse osmosis (RO) is the main technique used for desalination, followed by multi-stage flash (MSF) and Multi-Effect Distillation (MED). Helal et al. [11] evaluated the economic viability of three RO desalination plant setups (diesel-assisted PV, fully diesel-driven, and fully PV) for remote areas in the UAE. The fully PV option is highly competitive, having a water cost of 7.34 \$/m^3, but motivators like reduced interest rates and land costs could further improve its cost-effectiveness. Qiblawey et al. [12] demonstrate the potential of renewable energy in addressing water scarcity in rural areas. The study evaluates a pilot plant in Jordan that combines RO and PV technology for water desalination. The system productivity varies between 9.3 and 53 L/h with SPC at 1.9 kWh/m^3, influenced by the water recovery rate and the operating pressure.

Thus far, several studies have examined the hydrogen production from PV through the electrolysis process; however, none include a desalination water system and a heater for supplying the electrolyzer with water at a suitable temperature. Therefore, a standalone system for hydrogen production and storage that contains PV panels, a PEM electrolyzer, an RO unit, a hydrogen storage tank, and an electric heater is studied. Three cities—Borg El-Arab, Assiut, and Aswan—are used in the study to illustrate the various climates in Egypt. A comprehensive mathematical model is constructed and computationally solved using Matlab/Simulink. Furthermore, the study investigates the system's performance and its overall efficiency.

SYSTEM DESCRIPTION AND SOLUTION STRATEGY

The proposed hydrogen production and storage system under various climate conditions in Egypt is depicted in Fig. 1. The system includes PV modules, a power controller, a PEM electrolyzer, a compressor, a hydrogen storage tank, an RO desalination unit, and an electrical heater. This system employs PV modules to generate electricity during daylight hours. This electricity is then utilized to power the RO unit, which produces sufficient water for the electrolyzer annually. The electrolyzer employs heated water supplied by the electric heater to produce hydrogen through the electrolysis process. Eventually, the generated hydrogen is compressed and stored in the storage tank. The power controller contains a DC/DC inverter and DC/AC converter to supply different system components with suitable. The system mathematical model is solved hourly by Matlab/Simulink, and Fig. 2 illustrates the methodology used to develop the solution.

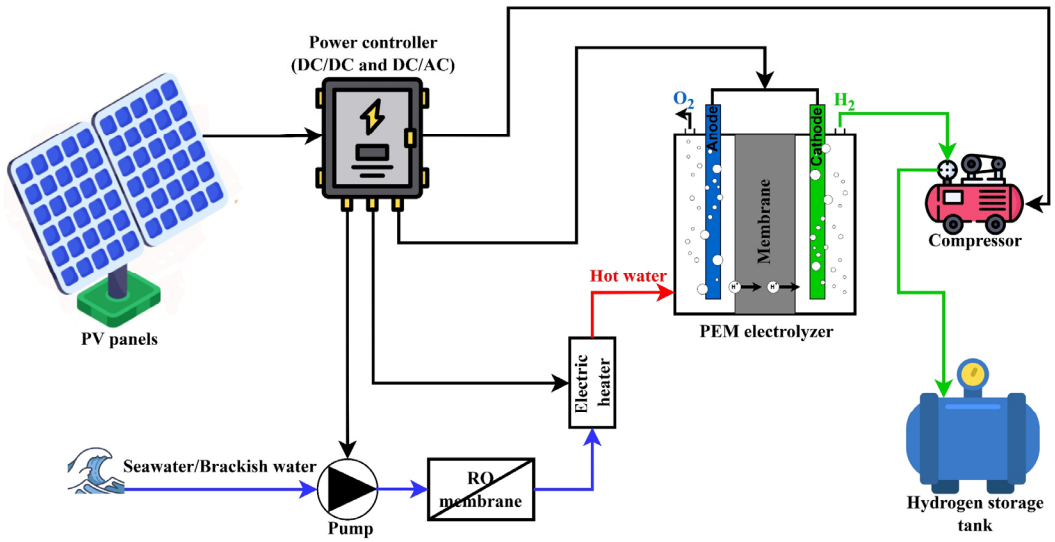

FIGURE 1. Proposed system layout.

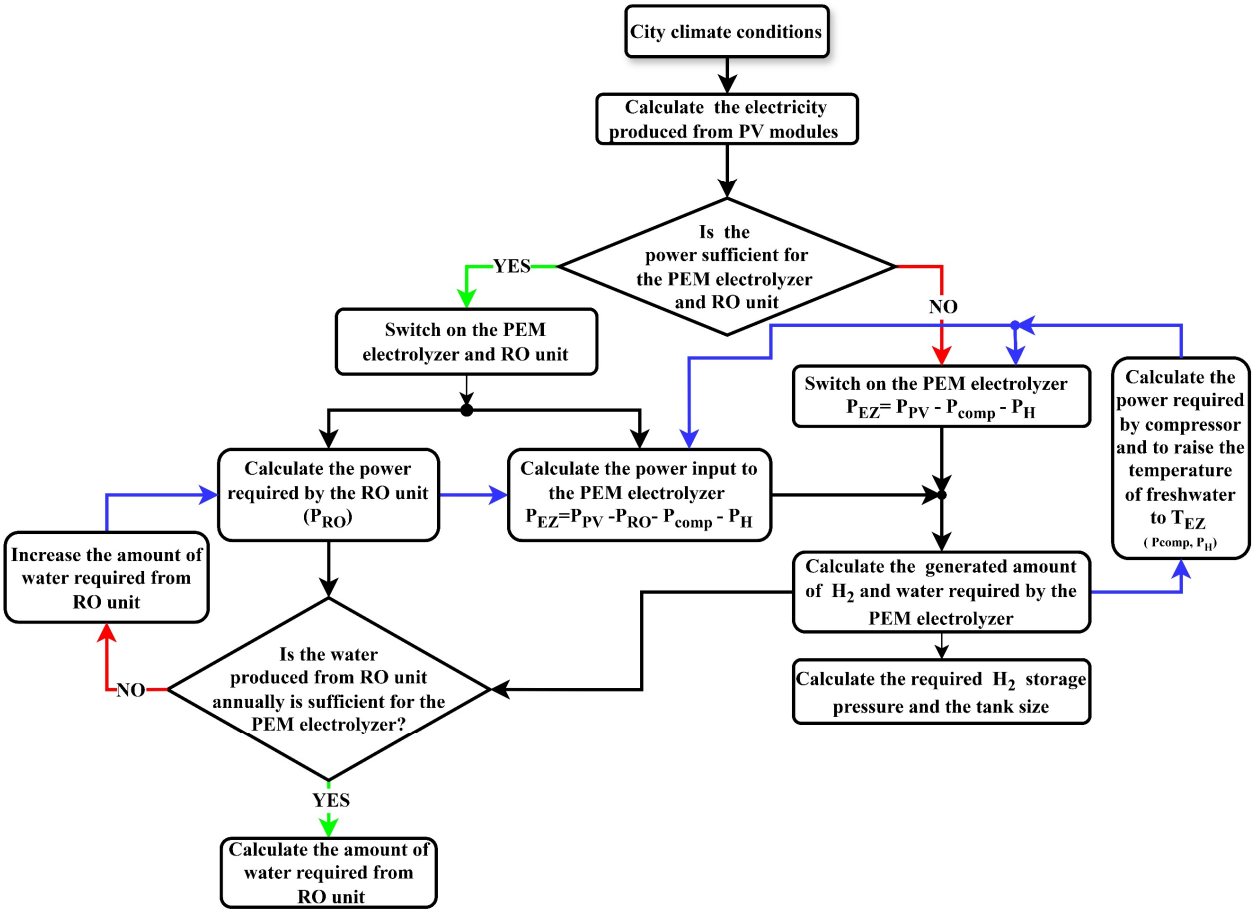

FIGURE 2. The system solution strategy.

MATHEMATICAL MODEL

In this section, the mathematical equations for each subsystem in the proposed system are outlined.

PV Model

The PV panels are installed with a 30° tilt angle to boost the quantity of solar energy captured. The following equation is employed to compute the power produced by the PV panels [13]:

$$\vec{W}_{PV} = N_{PV} \vec{W}_{PV,\max} \frac{G_I}{G_{I,ref}} [1 + \mu_p (t_{PV} - t_{PV,ref})] \quad (1)$$

$$t_{PV} = t_a + G_I \left[\frac{NOCT - 20}{800} \right] \quad (2)$$

where N_{PV}, t_{PV}, and G_I are the panels' number, the panel temperature (°C), and the solar insolation (W/m^2), respectively. The PV panel parameters are displayed in Table 1.

TABLE 1. PV module parameters [14].

Name	Parameter	Value
Reference solar irradiance	$G_{I,ref}$	1000 W/m^2
Maximum power of the PV panel	$\dot{W}_{PV,\max}$	430 W
Power thermal coefficient	μ_P	− 0.30 %/°C
Reference module temperature	$t_{PV,ref}$	25 °C
Nominal operating cell temperature	$NOCT$	45 °C
The area of the PV panel		1.955 m^2

PEM Electrolyzer Model

The present study chose the PEM electrolyzer because of its excellent handling of load changes, rapid responsive operation, and compact construction. The utilization of a PEM electrolyzer for hydrogen generation demonstrates significant potential for energy storage and management, especially when considering renewable energy sources (RES). The molar mass flow rate of the created hydrogen could be determined using the subsequent equation [15]:

$$\dot{n}_{H_2,gen} = \dot{n}_{H_2O,reacted} = \frac{J}{2F} \tag{3}$$

The electrolyzer input power is computed as follows:

$$\dot{W}_{EZ} = JV_{EZ} \tag{4}$$

where V_{EZ} and J refer to the electrolyzer voltage and its current density. The PEM electrolyzer voltage is computed as follows [16]:

$$V_{EZ} = V_0 + V_{ohm} + V_{act,ca} + V_{act,an} \tag{5}$$

where V_0 is the reversible voltage, V_{ohm} indicate the ohmic overvoltage, and $V_{act,ca}$ and $V_{act,an}$ are the cathode and anode activation overvoltage. The Nernest equation is utilized to calculate the reversible voltage as follows:

$$V_0 = 1.229 - 8.5\times10^{-4}(T_{EZ} - 298) \tag{6}$$

The membrane resistance to the passage of hydrogen ions is called the ohmic overvoltage, which is expressed as:

$$V_{ohm} = J\int_0^L \frac{dx}{\sigma_{EZ}\left[\lambda(x)\right]} \tag{7}$$

where σ_{EZ} is the local ionic conductivity. The activation overvoltage is given by:

$$V_{act,i} = \frac{RT_{EZ}}{F}\sinh^{-1}\left(\frac{J}{2J_{0,i}}\right) \tag{8}$$

$$J_{0,i} = J_i^{ref}\ \exp\left(-\frac{E_{act,i}}{RT_{EZ}}\right),\quad i = ca, an \tag{9}$$

In the former equation, $J_{0,i}$ represents the exchange current density, with the subscripts *ca* and *an* indicating the cathode and anode, respectively. The required electrical power of the heater can be determined by utilizing equation (10), which accounts for raising the water temperature to the designated temperature of the electrolyzer.

$$\dot{W}_H = \dot{m}_{EZ}C_P(T_{EZ} - T_{in}) \tag{10}$$

where $\dot{m}_{EZ}$ denotes the water mass flowrate consumed by the electrolyzer during the electrolysis process and T_{in} refers to the permeate water temperature provided by the RO unit, which is 298 K. Table 2 contains the PEM electrolyzer model parameters.

TABLE 2. PEM electrolyzer parameters [17].

Name	Parameter	Value
Electrolyzer temperature	T_{EZ}	353.15 K
Membrane thickness	L	50 μm
Cathode pre-exponential factor	J_{ca}^{ref}	4.609×10^{3} A/m^2
Cathode activation energy	$E_{act,ca}$	18 kJ/mol
Anode pre-exponential factor	J_{an}^{ref}	1.764×10^{6} A/m^2
Anode activation energy	$E_{act,an}$	76 kJ/mol
Faraday constant	F	96485 C/mol

Hydrogen Storage Model

The produced hydrogen is kept at a pressure of 200 bar in the storage tank after going through a three-stage compression to lessen the compressor power consumption. The power demanded by the compressor ($\dot{W}_{comp}$) can be calculated by [18]:

$$\dot{W}_{comp} = \frac{\dot{n}_{H_2}}{\eta_{comp}} \times \frac{n}{n-1} R T_{comp,in} [1 - r_{p,st}^{\frac{n-1}{n}}] \tag{11}$$

where R, n, and $r_{p,st}$ are the universal gas constant, the polytropic index, and the stage pressure ratio. Furthermore, the compressor efficiency (η_{comp}) is taken to be 90%.

RO Model

When high pressure is applied to saltwater in RO desalination, water molecules are compelled to go through a semi-permeable membrane, leaving the salt behind. The required pressure and, hence, the power depend upon the salinity of the water. The RO mathematical model is described in detail in [19,20]. The feed seawater mass flowrate ($\dot{m}_f$) can be determined from the permeate mass flowrate required from the RO unit ($\dot{m}_{p,RO}$), considering the recovery ratio (*RR*) as in the following equation:

$$\dot{m}_f = \frac{\dot{m}_p}{RR} \tag{12}$$

The net pressure difference within the membrane (Δp_{net}) in kPa is estimated as follows:

$$\Delta p_{net} = \frac{\dot{V}_p}{3600 \times TCF \times FF \times A_e n_e n_v K_w} + \Delta\Pi \tag{13}$$

where $\dot{V}_p$ is the permeate volume flow rate in m^3/h and $\Delta\Pi$ is the net osmotic pressure throughout the membrane, which is expressed as:

$$\Delta\Pi = \Pi_{avg,f} - 75.84 S_p \tag{14}$$

$$\Pi_{avg,f} = 37.92 (S_f + S_b) \tag{15}$$

where $\Pi_{avg,f}$ is the average osmosis pressure across the membrane on the feed side. The temperature correction factor (*TCF*) is expected from the following correlation:

$$TCF = \exp\left[2700\left(\frac{1}{t_f + 273} - \frac{1}{398}\right)\right] \tag{16}$$

where t_f is the feed temperature in °C. As for the membrane water permeability (K_w) is given by:

$$K_w = \frac{6.84\times10^{-8}\left(18.6865-0.177S_b\right)}{t_f+273} \tag{17}$$

The pump power consumption to overcome the membrane net pressure difference is:

$$\dot{W}_{pump,RO} = \frac{\Delta p_{net}\dot{V}_f}{3600\times\eta_p} \tag{18}$$

where $\dot{V}_f$ and η_p are the feed volume flow rate in m^3/h and pump efficiency. The specific power consumption (*SPC*) is expressed as:

$$SPC = \frac{\dot{W}_{Pump,RO}}{\dot{V}_p} \tag{19}$$

where *SPC* is in kWh/m^3. The RO unit modeling parameters are presented in Table 3.

TABLE 3. RO modeling parameters [20,21].

Name	Parameter	Value
Element type		FTSW30HR-380
Recovery ratio	*RR*	0.3
Fouling factor	*FF*	0.85
Salt rejection	*SR*	0.9944
Membrane area	A_e	35.3 m^2
Number of vessels	n_v	1
Number of membranes	n_e	1
Pump efficiency	η_p	80%

RESULTS AND DISCUSSION

This section provides a comprehensive analysis of the results of the suggested system in three cities in Egypt: Borg El- Arab, Assiut, and Aswan. These cities are located in the northern, middle, and southern of Egypt. The average ambient temperature and monthly solar radiation are shown in Fig. 3. According to Fig. 3a, Borg El-Arab consistently experiences the lowest temperatures, except from November to January, when Assiut has the smallest temperature. Conversely, Aswan experiences the highest average temperature during the entire year. Figure 3b illustrates that Aswan experiences the highest solar intensity for most of the year, except the summer months (June, July, and August), while Borg El-Arab has a higher solar intensity. Assiut witnesses the highest monthly solar radiation in August, with a value of 215.2 kWh/m^2.

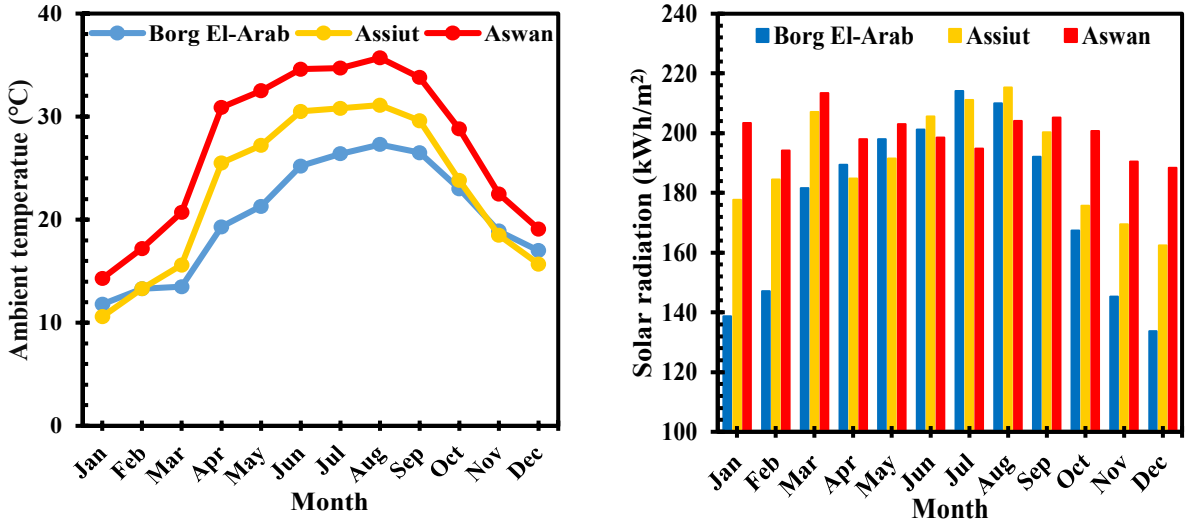

(a) (b)

FIGURE 3. (a) Monthly average ambient temperature and (b) Monthly solar radiation in Borg El-Arab, Assiut, and Aswan Cities.

The electrical power produced per unit area by PV modules in Borg El-Arab, Assiut, and Aswan is depicted in Fig. 4. The monthly power production in Borg El-Arab surpasses other cities from April to July, with its highest occurring in July at 43.32 kWh/m^2. Although Aswan experiences the highest solar intensity in April and May, its monthly electricity generation is lower than that of Borg El-Arab. This is primarily because of the rise in the temperature of PV panels, which negatively affects their performance. Moreover, the monthly electricity production from PV panels in Aswan is often higher than that of Assiut, except for the period from June to August, during which it is the lowest among these towns. Aswan achieved the greatest monthly power generation among all cities in March, valued at 43.5 kWh/m^2. Based on annual data, Aswan has the largest power generation, followed by Assiut and then Borg El-Arab, as demonstrated in Fig. 5, which corresponds to the yearly amount of solar radiation as 2394.34, 2285.33, and 2118.53 kWh/m^2, respectively.

In addition, Fig. 5 displays the yearly power usage of the PEM electrolyzer, compressor, heater, and RO unit, which represents only 95% of the PV-generated electricity due to the power controller efficiency. Furthermore, the electrolyzer is responsible for the most power consumption, with 89.2% of the energy used for hydrogen production in the electrolysis procedure. In contrast, RO has the lowest power consumption, amounting to only 0.07%. Meanwhile, the compressor and the heater consume about 4.73% and 1%, respectively.

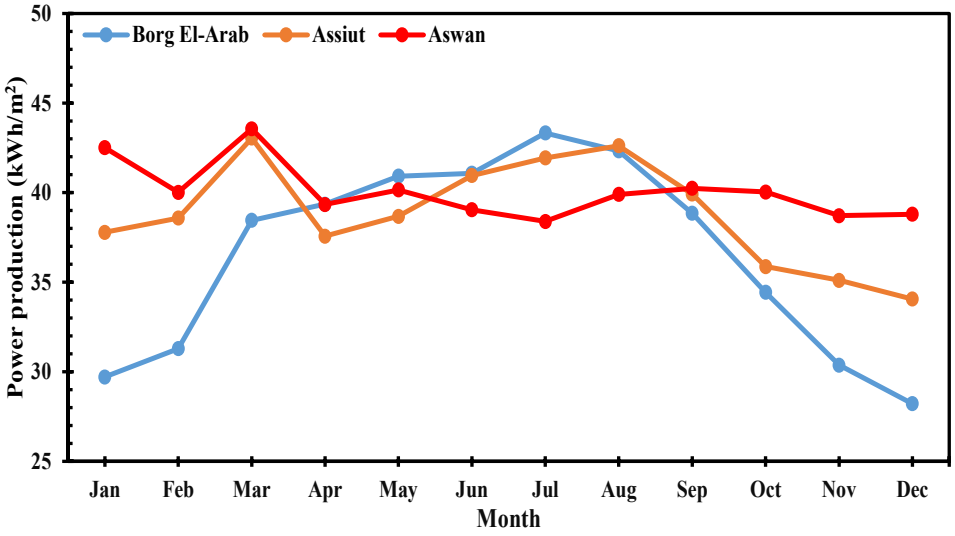

FIGURE 4. PV power production in Borg El-Arab, Assiut, and Aswan.

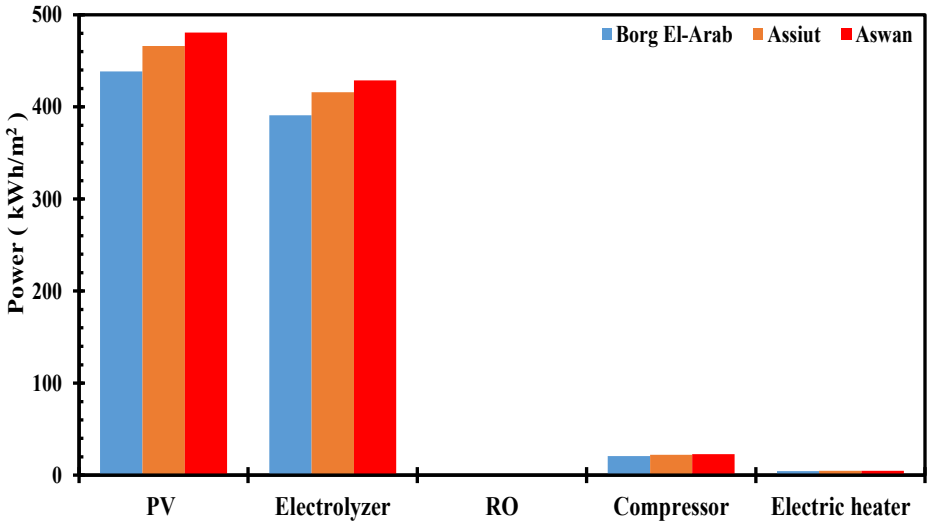

FIGURE 5. Annual power production and consumption within the system.

Given that the amount of hydrogen generated is directly proportional to the power supplied to the electrolyzer. Figure 6 illustrates the monthly quantity of hydrogen produced per unit area of PV panels, which follows the same pattern as the electricity generation from the PV panels seen in Fig. 4. The PV modules in Borg El-Arab, Assiut, and Aswan have an annual hydrogen production per unit area of 7.69, 8.17, and 8.42 kg/m^2, respectively. December witnesses the lowest level of hydrogen generation in these cities. Among them, Borg El-Arab has the lowest production rate, measuring 0.497 kg/m^2. The maximum monthly hydrogen production occurs in Aswan during March at 0.761 kg/m^2.

The RO unit produces the water supplied to the electrolyzer, guaranteeing that the permeate water is sufficient to fulfill the electrolyzer's needs for the entire year. The RO unit's specific power consumption (SPC) is 4.64 kWh/m^3 at a salt concentration of 45 ppt of the incoming feed water. Figure 7a displays the monthly water output per unit area of PV panels from the RO unit, which is used to meet the water requirements of the electrolyzer. This graph illustrates that Aswan consistently produces the highest monthly water volume yearly, while Borg El-Arab always has the lowest. Aswan has the highest water production among these cities, reaching a maximum of 7.13 L/m^2 in July. On the other hand, Borg El-Arab has the lowest water production, with a minimum of 4.71 L/m^2 in December. The monthly water consumption of the electrolyzer is illustrated in Fig. 7b. This graph and Fig.6 illustrate the direct connection between the electrolyzer's water consumption and the quantity of hydrogen produced. The difference between the water produced from the RO and water consumed by the electrolyzer is referred to as water accumulation, as depicted in Fig. 8. Borg El-Arab receives the lowest level of water accumulation due to the slight difference between water production and consumption.

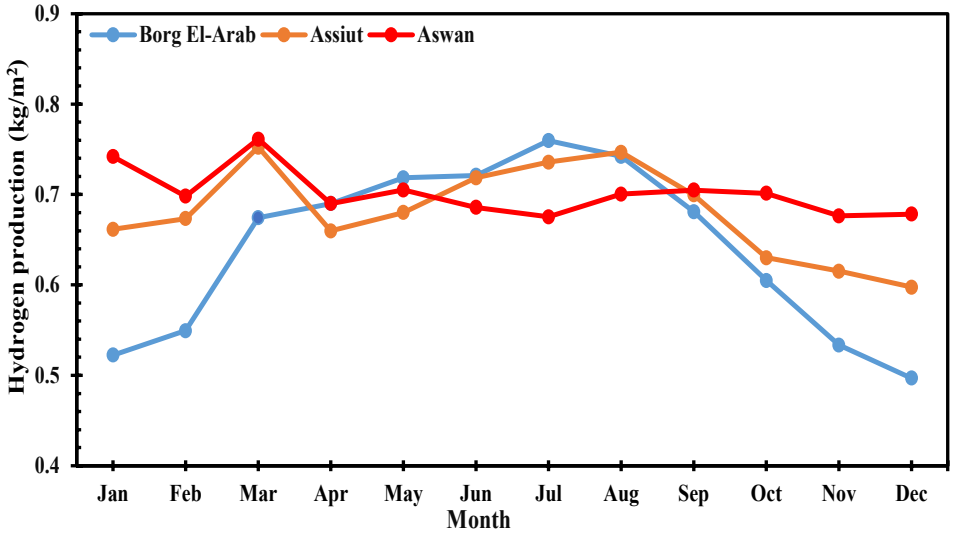

FIGURE 6. Monthly hydrogen production.

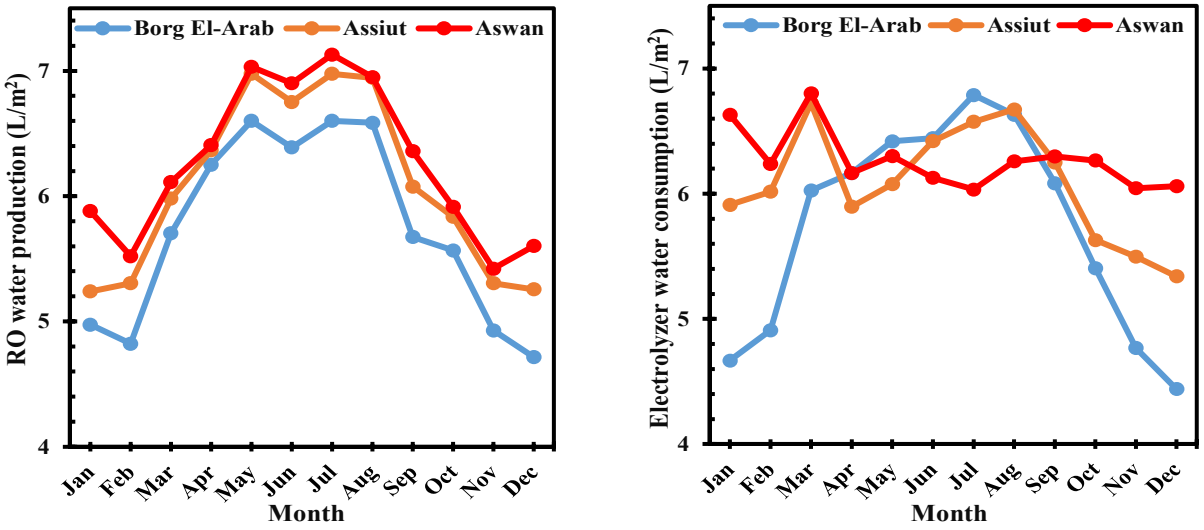

FIGURE 7. (a) RO water production and (b) Electrolyzer water consumption.

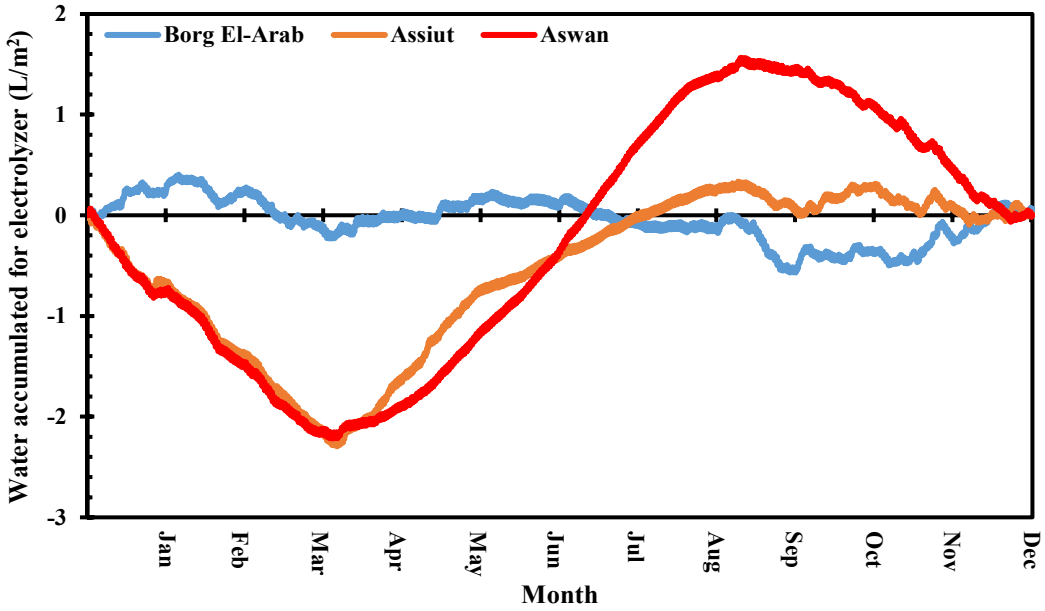

FIGURE 8. The change in water accumulation for the electrolyzer.

Figure 9 shows the average annual efficiencies of the PV panels, PEM electrolyzer, and the overall system in these three cities. The figure reveals that the PV efficiency is ranked in descending order as 20.69%, 20.40%, and 20.08% for Borg El- Arab, Assiut, and Aswan, respectively. Although Aswan has the highest solar intensity, the PV efficiency is the lowest due to the elevated temperature of the PV cells. The electrolyzer exhibits superior yearly efficiency compared to PV, with values of approximately 76.63% in Borg El-Arab, 76.53% in Assiut, and 76.46% in Aswan. The system efficiency is 14.30%, 14.08%, and 13.85% in Borg El-Arab, Assiut, and Aswan, respectively. This graph demonstrates that the system's overall efficiency is inferior in comparison to PV and electrolyzer due to the consideration of the impact of all system components on performance.

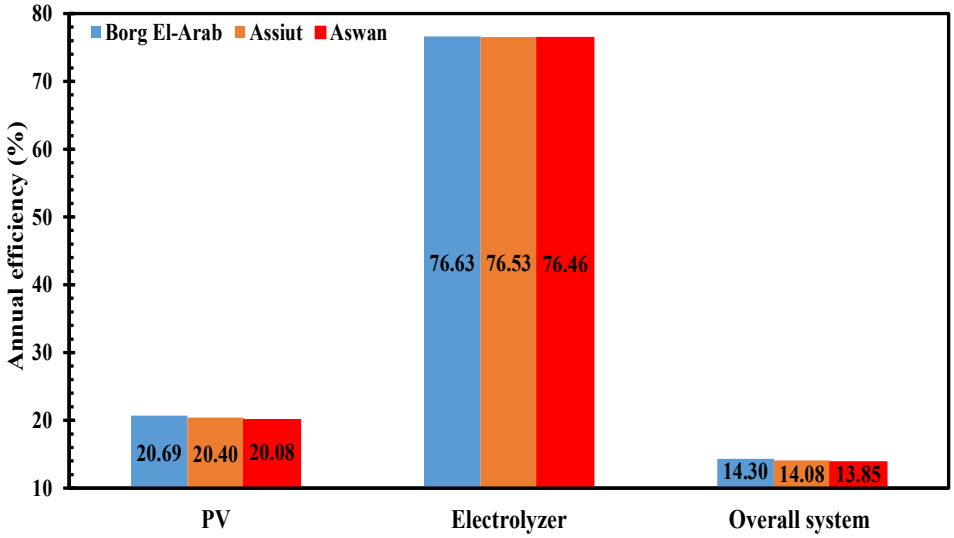

FIGURE 9. Annual efficiency of PV panels, PEM electrolyzer, and overall system.

CONCLUSION

This paper examines a hydrogen production and storage system that utilizes PV panels as a clean power source. The electrical power from the PV panels is employed to operate the electrolyzer, which produces hydrogen. It also powers the RO unit, which supplies water for the electrolysis process. Additionally, it is used to compress the produced

hydrogen gas for storage. This study is conducted in three Egyptian cities to exemplify the varied climatic conditions available in the country. The results show that the annual hydrogen production in Borg El-Arab, Assiut, and Aswan is 7.69, 8.17, and 8.42 kg/m^2, respectively. In addition, the electrolyzer exploits 89.2% of the generated power for hydrogen production, while RO only utilizes 0.07% to produce water that covers the electrolyzer needs. Although Aswan experiences the maximum solar radiation and produces more hydrogen per unit area of PV panels, it has the lowest overall system efficiency, about 13.85%, due to the increase in PV temperature. Finally, Borg El-Arab, representing northern Egypt in this study, is more efficient in producing hydrogen using PV panels at a rate of 7.69 kg/m^2 with an overall system efficiency of 14.30%.

ACKNOWLEDGMENTS

The authors express gratitude for the scholarship and facilities granted by the Egyptian Ministry of Higher Education (MOHE) and the Egypt-Japan University of Science and Technology (E-JUST).

REFERENCES

1. G. Bernardo, T. Araújo, T. da Silva Lopes, J. Sousa, and A. Mendes, "Recent advances in membrane technologies for hydrogen purification," Int. J. Hydrogen Energy, vol. 45, no. 12, pp. 7313–7338, May 2020, doi: 10.1016/j.ijhydene.2019.06.162.
2. M. Balat and M. Balat, "Political, economic and environmental impacts of biomass-based hydrogen," Int. J. Hydrogen Energy, vol. 34, no. 9, pp. 3589–3603, May 2009, doi: 10.1016/j.ijhydene.2009.02.067.
3. N. Norouzi, "Hydrogen production in the light of sustainability: A comparative study on the hydrogen production technologies using the sustainability index assessment method," Nucl. Eng. Technol., vol. 54, no. 4, pp. 1288–1294, May 2022, doi: 10.1016/j.net.2021.09.035.
4. "Ministry of Electricity and Renewable Energy - New and Renewable Energy Authority." Accessed: May 13, 2024. [Online]. Available: http://nrea.gov.eg/test/en/Technology/SolarIntro
5. B. Mohamed et al., "Hydrogen Production Methods Based on Solar and Wind Energy: A Review," Energies, vol. 16, p. 757, Jan. 2023, doi: 10.3390/en16020757.
6. B. PAUL and A. John, "Optimal coupling of PV arrays to PEM electrolysers in solar–hydrogen systems for remote area power supply," Int. J. Hydrogen Energy, vol. 33, no. 2, pp. 490–498, Jan. 2008, doi: 10.1016/j.ijhydene.2007.10.040.
7. T. Gibson and N. Kelly, "Optimization of solar powered hydrogen production using photovoltaic electrolysis devices," Int. J. Hydrogen Energy, vol. 33, no. 21, pp. 5931–5940, May 2008, doi: 10.1016/j.ijhydene.2008.05.106.
8. I. S. Ganeshan et al., "Regulated hydrogen production using solar powered electrolyser," Int. J. Hydrogen Energy, vol. 41, no. 24, pp. 10322–10326, May 2016, doi: 10.1016/j.ijhydene.2015.05.048.
9. V. A. Martinez Lopez, H. Ziar, M. Zeman, and O. Isabella, "Maximization of PV energy use and performance analysis of a stand-alone PV-hydrogen system," Int. J. Hydrogen Energy, vol. 48, no. 99, pp. 39298–39314, May 2023, doi: 10.1016/j.ijhydene.2023.09.072.
10. D. Ghribi, A. Khelifa, S. Diaf, and M. Belhamel, "Study of hydrogen production system by using PV solar energy and PEM electrolyser in Algeria," Int. J. Hydrogen Energy, vol. 38, no. 20, pp. 8480–8490, May 2013, doi: 10.1016/j.ijhydene.2012.09.175.
11. A. M. Helal, S. A. Al-Malek, and E. S. Al-Katheeri, "Economic feasibility of alternative designs of a PV-RO desalination unit for remote areas in the United Arab Emirates," Desalination, vol. 221, no. 1–3, pp. 1–16, May 2008, doi: 10.1016/j.desal.2007.01.064.
12. H. Qiblawey, F. Banat, and Q. Al-Nasser, "Performance of reverse osmosis pilot plant powered by Photovoltaic in Jordan," Renew. Energy, vol. 36, no. 12, pp. 3452–3460, May 2011, doi: 10.1016/j.renene.2011.05.026.
13. C. Darras et al., "Sizing of photovoltaic system coupled with hydrogen/oxygen storage based on the ORIENTE model," Int. J. Hydrogen Energy, vol. 35, no. 8, pp. 3322–3332, 2010, doi: 10.1016/j.ijhydene.2010.01.060.
14. "Atlas Topcon Double Glass 410-430W." Accessed: Sep. 15, 2023. [Online]. Available: https://www.eco-greenenergy.com/product/atlas-topcon-double-glass-108-cells-430w-module-10bb/
15. M. Nasser and H. Hassan, "Assessment of standalone streetlighting energy storage systems based on hydrogen of hybrid PV/electrolyzer/fuel cell/ desalination and PV/batteries," J. Energy Storage, vol. 63, p. 106985, 2023, doi: 10.1016/j.est.2023.106985.

16. M. G. Basiony, S. Nada, S. Mori, and H. Hassan, “Performance evaluation of standalone new solar energy system of hybrid PV/electrolyzer/fuel cell/MED-MVC with hydrogen production and storage for power and freshwater building demand,” Int. J. Hydrogen Energy, vol. 77, no. April, pp. 1217–1234, 2024, doi: 10.1016/j.ijhydene.2024.06.211.
17. E. Ozden and I. Tari, “Energy-exergy and economic analyses of a hybrid solar-hydrogen renewable energy system in Ankara, Turkey,” Appl. Therm. Eng., vol. 99, pp. 169–178, 2016, doi: 10.1016/j.applthermaleng.2016.01.042.
18. M. Nasser, T. F. Megahed, S. Ookawara, and H. Hassan, “Techno-economic assessment of clean hydrogen production and storage using hybrid renewable energy system of PV/Wind under different climatic conditions,” Sustain. Energy Technol. Assessments, vol. 52, p. 102195, 2022, doi: 10.1016/j.seta.2022.102195.
19. H. T. El-Dessouky and H. M. Ettouney, Fundamentals of Salt Water Desalination, 1st ed. Amsterdam ; New York: Elsevier, 2002. doi: 10.1016/B978-0-444-50810-2.X5000-3.
20. A. S. Nafey and M. A. Sharaf, “Combined solar organic Rankine cycle with reverse osmosis desalination process: Energy, exergy, and cost evaluations,” Renew. Energy, vol. 35, no. 11, pp. 2571–2580, Mar. 2010, doi: 10.1016/j.renene.2010.03.034.
21. DuPont, “FilmTec TM SW30HR-380 Element.” Accessed: Apr. 30, 2024. [Online]. Available: https://www.dupont.com/content/dam/dupont/amer/us/en/water-solutions/public/documents/en/RO-FilmTec-SW30HR-380-PDS-45-D00971-en.pdf

Hybrid Solar Photovoltaic With Vertical Axis Wind Turbine Grid-Connected System for Streetlighting Application in Egypt

Masoyi Sanda[1], Mohamed Emam[1], Shinichi Ookawara[2] and Hamdy Hassan[1, a)]

[1]*Department of Energy Resources Engineering, Egypt-Japan University of Science and Technology, Alexandria, Egypt*
[2]*Department of Chemical Science and Engineering, Tokyo Institute of Technology, Tokyo, Japan*

Corresponding author: [a)] hamdy.aboali@ejust.edu.eg

Abstract. Hybrid Solar Photovoltaic with Vertical Axis Wind Turbine Grid-Connected System for Streetlighting Application in Egypt. Performance and economic viability of using hybrid renewable energy systems consisting of solar photovoltaic and H-Darrieus vertical axis wind turbine at different land ratios for streetlighting application was assessed. Study shows solar photovoltaic is more economically viable than vertical axis wind turbine in the seven governorates.

INTRODUCTION

To achieve carbon neutrality, the use of renewable energy in reducing greenhouse gas emissions is important. This is important for countries planning to achieve clean and affordable energy in the sustainable development goals. As studies have shown the utilisation of renewable energy can significantly contribute to the economic growth of a country [1]. The use of microgrids provide flexibility in scaling up electric power generation and distribution. Also, it is an effective way of providing power to remote locations, as constructing infrastructures to expand the main electric grid can be expensive. Solar and wind are available natural energy resources, which can be used to generate energy for a microgrid for free. Both energy resources are intermittent due to dependency on climatic conditions. This intermittency can be partially mitigated by creating a hybrid system of both energy resources, as the wind turbine can supply energy when the solar irradiation is low or not available [2].

Previous work studied multiple methods of optimising the size and site selection of hybrid energy systems by using analytical, numerical, hybrid, software, artificial intelligence and geospatial analysis methods [3]. Most of the previous work are focused on using horizontal axis wind turbines in combination with solar photovoltaic panels for the hybrid systems. This shows there is a research gap in the research area of optimizing hybrid systems with vertical axis wind turbines and solar photovoltaic.

This paper aims to find the optimum size of Solar Photovoltaic (PV) and Vertical Axis Wind Turbine (VAWT) hybrid system for different land ratios by using numerical and analytical methods. The project capital, operating cost and payback period will be analysed for each land ratio. A grid connected system which uses the electric grid as energy storage will be assessed, it sends excess energy to the grid and receives energy from the grid when there is insufficient energy generation. The spacing of the solar panel rows to prevent shading will be considered in the analysis, as shading will lead to lower power output from the system. Also, the optimum spacing of wind turbines to minimise wake effect will be considered in the analysis. As, the wake effect reduces the speed of downwind and reduces power production of wind turbines downwind [4].

SYSTEM DESCRIPTION

The renewable energy hybrid system will consist of solar photovoltaic and vertical axis wind turbine. An Egyptian manufactured solar panel of 405 watts and a British manufactured 5 kilo-watt vertical axis wind turbine will be used for all the systems. The energy generated from the system will be converted to alternating current and transmitted to the electric grid when there is excess energy generation. The system will use energy from the electric grid when insufficient energy is being produced by the solar photovoltaic and wind turbine. Maximum power point tracking charge control techniques will be used to extract energy from the solar panels and the wind turbines for maximum efficiency.

Technologies and Materials for Renewable Energy, Environment and Sustainability
AIP Conf. Proc. 3321, 040012-1–040012-12; https://doi.org/10.1063/5.0289591
Published under an exclusive license by AIP Publishing. 978-0-7354-5231-2/$30.00

This study is carried out using the climatic conditions of Egypt for the year 2019. Geospatial analysis was used to merge the data of solar power potential and wind power density as shown in Fig. 1. The white colour represents the highest energy density, while dark gray colour represents minimum energy density. This was used to select the location of study in the governorates as shown in table 1. The study will assess land ratios of solar photovoltaic to vertical axis wind turbine of "0 to 1","1 to 0", "1 to 1", "33.3 to 66.7" and "66.7 to 33.3". Each location chosen in the governorates will be assessed with all the land ratios.

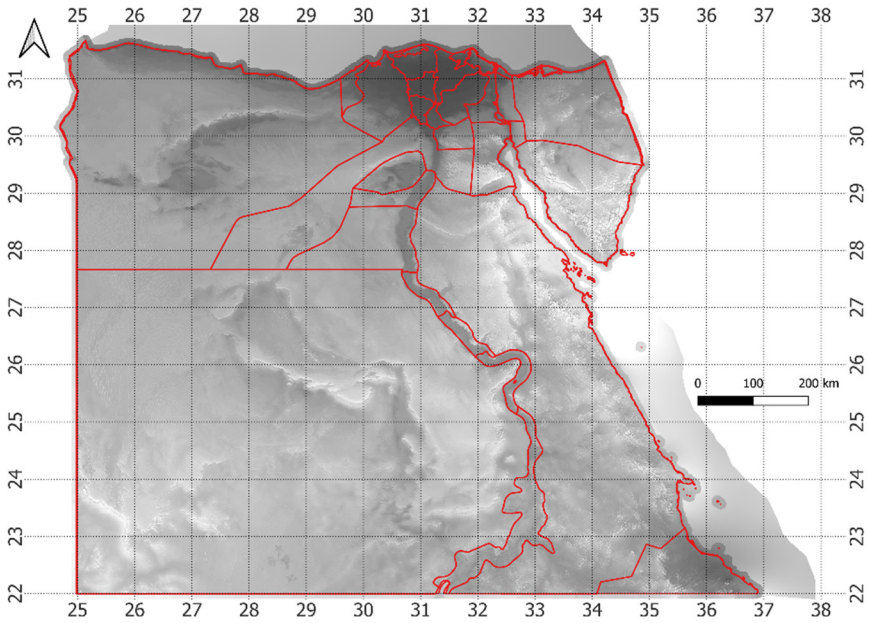

FIGURE 1. Geospatial analysis of solar power potential and wind power density.

TABLE 1. Study locations.

	Governorate Name	Latitude	Longitude
1	Red Sea Governorate	27.990	33.330
2	Asyut Governorate	27.426	30.929
3	South Sinai Governorate	29.047	33.586
4	Suez Governorate	29.244	32.320
5	Matrouh Governorate	30.440	28.310
6	The New Valley Governorate	25.390	29.890
7	Alexandria Governorate	30.375	29.628

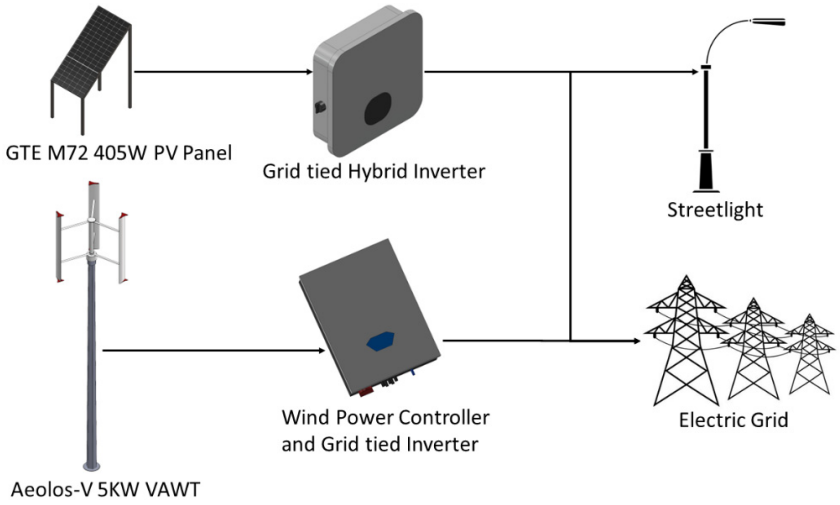

FIGURE 2. Grid connected system

SYSTEM MODELLING

This section contains the description of the mathematical equations used to model the hybrid energy system. The system contains solar photovoltaic panels (PV) and vertical axis wind turbines (VAWT).

Solar photovoltaic panels model

The power generated by the solar PV panel is dependent on the ambient temperature, solar irradiation, size of the solar panel and conversion efficiency of the PV module. The solar PV power generation is calculated on an hourly interval, as the weather conditions obtained were hourly [5].

$$P_{pv} = AI(t)\eta_{pv} \tag{1}$$

Where, P_{pv} is power generated by the solar PV panel, η_{pv} is the efficiency of the solar PV panel, A is the area of the solar PV panel and I(t) is the solar irradiance for a specific time.

$$\eta_{pv} = \eta_{pc}\eta_r[1 - \beta(T_c - NOCT)] \tag{2}$$

Where, η_{pc} is the power conditioning efficiency, η_r is the rated efficiency of the solar PV panel, β is the efficiency temperature factor, T_c is the cell temperature of the solar PV panel and NOCT is the normal operating cell temperature.

Vertical axis wind turbine model

The power produced by the VAWT depends on the rated power of the VAWT, wind velocity and the VAWT system efficiency. The maximum available power from the wind which can be converted to mechanical energy cannot exceed Betz limit.

$$Cp = \frac{16}{27} = 0.593 \tag{3}$$

$$A = rl \tag{4}$$

$$P_{available} = \frac{1}{2}\rho A v^3 Cp \tag{5}$$

Where r is radius of blades, l is length of blades, A is blades swept area, ρ is density of air, v is velocity of air and Cp is power coefficient. Therefore, the power generated by the wind turbine can be expressed as [6].

$$P_{wt}(t) = \begin{cases} \eta_{wt} Pr_{wt} \dfrac{V(t)^3 - {V_{ci}}^3}{{V_r}^3 - {V_{ci}}^3} & V \le V_r \\ \eta_{wt} Pr_{wt} & V_r \le V \le V_{co} \\ 0 & V > V_{co} \; or \; V < V_{ci} \end{cases} \tag{6}$$

Where Pr_{wt} is the rated power of the VAWT, η_{wt} is the VAWT efficiency, V_r is the rated wind velocity, V_{ci} is the cut-in wind velocity, V_{co} is the cut-out wind velocity and V is the wind velocity at the Vertical axis wind turbine height.

Computational fluid dynamics

The "Transition SST" turbulence model was used in ANSYS Fluent [7].

$$\frac{\partial}{\partial t}(\rho k) + \frac{\partial}{\partial x_j}(\rho u_j k) = \tilde{P}_k - \tilde{D}_k + \frac{\partial}{\partial x_j}\left((\mu + \sigma_k \mu_t)\frac{\partial k}{\partial x_j}\right) \tag{7}$$

Where, $\tilde{P}_k$ is the original production term and $\tilde{D}_k$ is the original destruction term for the model.

ECONOMIC AND ENVIRONMENTAL MODELLING

This section contains all the mathematical equations used for building the economic model of the system.

Levelised cost of electricity

The levelised cost of electricity (LCOE) is used to determine the hybrid energy system economic viability, which is the cost of selling electricity produced by the system for the system to break even before its end of lifetime. The

LCOE can be derived by dividing the total annual cost of the system by the total electrical load delivered by the system [8].

$$LCOE(D,d)_i = \frac{\sum_{t=1}^{n}\left(C_{ti} \times F_j\right) + OM_{ti}}{\sum_{t=1}^{n} E_{ti}} \quad (8)$$

Where, $LCOE_i$ is the levelised cost of electricity, C_t is Capital cost in year t, F_j is the fixed capital rate, OM_t is the operating and maintenance cost for year t and E_t is the annual energy generation in year t.

The portion of the capital costs which is set aside yearly to pay the cost of capital, interest on debt and return in equity is known as the fixed capital rate (F).

$$F = \frac{W}{1-(W+1)^{-n}} \quad (9)$$

Where, W is the weighted average cost of capital.

Payback period

The time it takes to recover the initial cash investment of the project is used to assess the present and future value of the hybrid energy system [9].

$$PBP = \frac{IC - NI}{(AEP \times RE) - OM} \quad (10)$$

Where, IC is the initial cost of installation, NI is the value of national incentives, AEP is the annual energy production, RE is the rate of electricity and OM is the annual operation and maintenance cost.

Enviro-Economic analysis

The renewable energy produced reduces the amount of carbon that would have been produced if fossil fuel was used to generate same quantity of energy. According to the United States Energy Information Administration, the electricity generation to carbon dioxide emission statistics in the year 2022 for coal is 1.04 Kg/KWh, natural gas is 0.44 Kg/KWh and petroleum is 1.08 Kg/KWh. Petroleum includes petroleum coke and petroleum liquids mainly composed of distillates and residual fuel oil [10]. The estimated quantity of carbon dioxide mitigation per annum is used to estimate the carbon credit value [11].

$$CO_{2.mit}(tonne) = \begin{cases} \frac{TE_{out} \times N \times CF_{petroleum}}{1000} \\ \frac{TE_{out} \times N \times CF_{nat.gas}}{1000} \end{cases} \quad (11)$$

Where, TE_{out} is the total amount of electrical energy generated by the PV and VAWT hybrid system. N is the hybrid energy system lifetime, $CF_{petroleum}$ is conversion factor for petroleum and $CF_{nat.gas}$ is conversion factor for natural gas.

The amount of carbon credit acquired by the hybrid energy system can be expressed as:

$$CC(\$) = CO_{2.mit}(tonne) \times Cost\ of\ CO_2(per\ tonne) \quad (12)$$

Where, CC is the carbon credit gained and $CO_{2.mit}$ is the amount of carbon dioxide mitigated.

MODEL AND SOLUTION VALIDATION

The mathematical model is simulated using MATLAB Simulink. The model simulates hourly data of wind speed and solar irradiation for a period of a year. The solar PV panel and wind turbine components were selected before designing the simulation. As the model is meant to determine the optimum sizing of land for each land ratio. The system working strategy and steps are illustrated in the Fig. 3. The weather data were obtained from "National Solar Radiation Database", "Photovoltaic Geographical Information System" and "NASA POWER" [12, 13, 14].

QGIS version 3.36 was used for the geospatial analysis. The output image in Fig. 1 was used to select the areas with the highest power generation potential in the selected governorates. Then, "ANSYS Fluent 2020 R2" was for the two-dimensional simulation of a single wind turbine to assess the length of the wake created downstream. The wake distance was used to create a simulation containing two wind turbines, so the effect of the wake on the second turbine will be assessed. This simulation was used to select the optimum distance between the turbines. A study to assess the average energy density of a land with the wind turbines using the optimum distance was carried out. Autodesk inventor was used to model the wind farm with an area of 100 meters by 100 meters. A similar study was done for the solar

panels to determine the land energy density using an optimum distance between the solar panels. Autodesk Revit was used for the solar analysis to determine the optimum distance to prevent shading of the solar panels on each other. MATLAB Simulink was used to build an energy model, which used the input of energy density, time, load pattern and land ratio. This model outputted the results for the study in the form of graphs and average values.

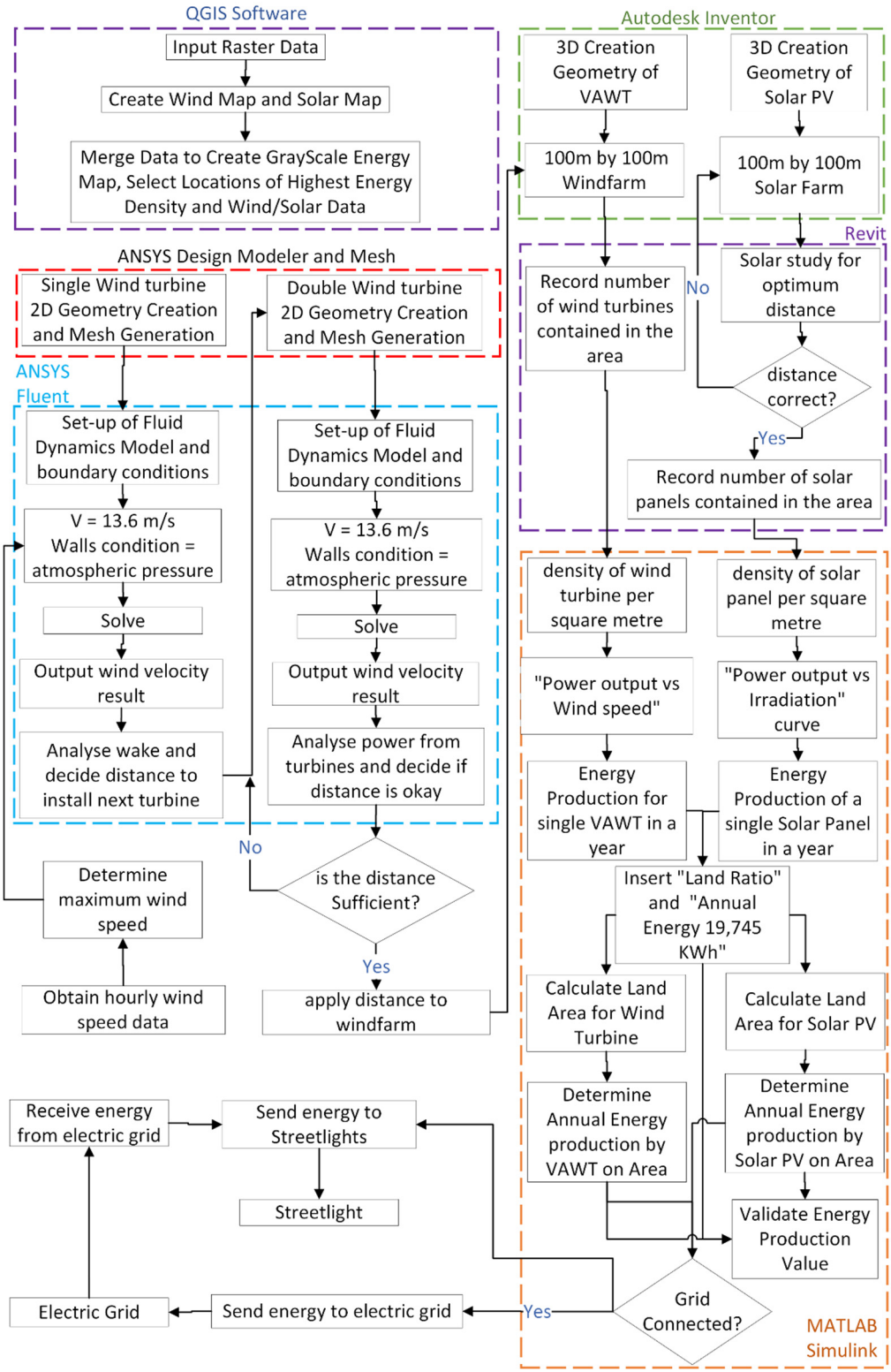

FIGURE 3. Process Flowchart.

Validation study

This is a two-dimensional computational fluid dynamics simulation of a three bladed NACA0015 profile vertical axis wind turbine. The simulation was executed on ANSYS Fluent with a "transition SST" model. The experimental results were obtained from literature which manufactured and tested the wind turbine in a wind tunnel. Also, a numerical study result which used "transition SST" model was obtained [15]. A comparison of the results in Fig. 4 shows the numerical study results being close to both literature results.

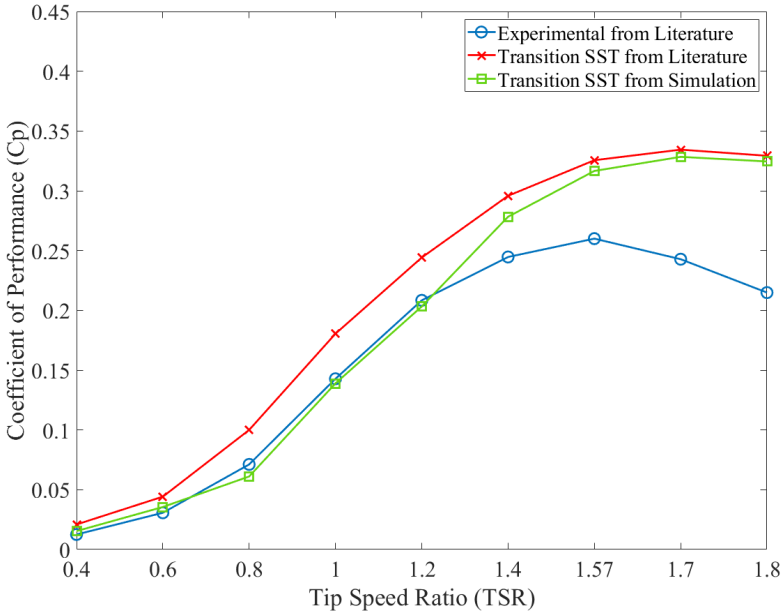

FIGURE 4. Validation study.

Computational fluid dynamics domain

The domain consists of a single constant velocity inlet, two symmetry boundaries and a pressure outlet to simulate real life conditions as shown in Fig. 5. The turbine was spinning at 150 rounds per minute, as this is the maximum allowable speed by the manufacturer. The inlet velocity was 13.6 meters per second, while the pressure outlet was at gauge pressure of zero. The turbine used was an "Aeolos V-5KW" with a power rating of 5 Kilo-Watts.

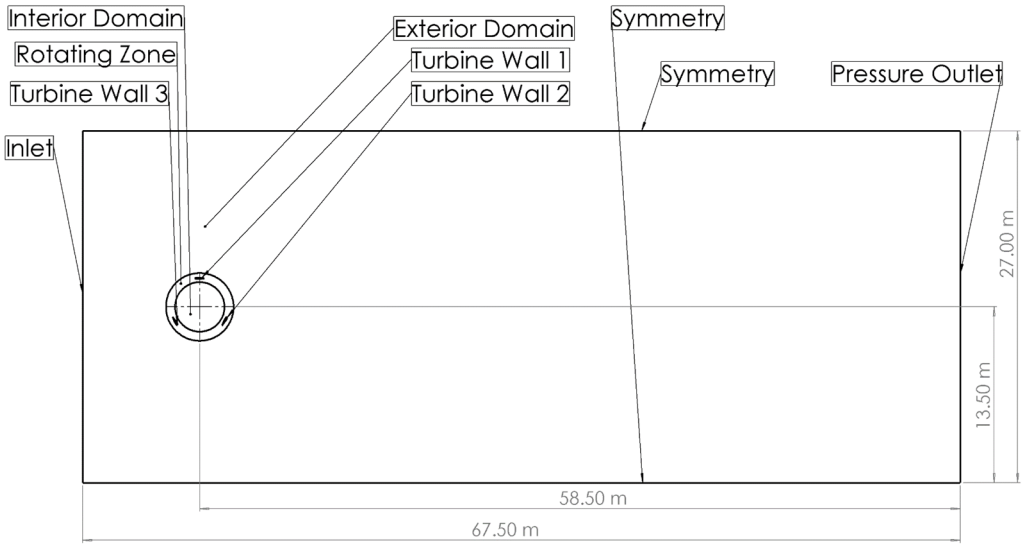

FIGURE 5. Computational domain.

Mesh and time-step independence study

A combination of three element sizes and four time-steps were studied to achieve independence as illustrated in Fig. 6. The gradient of the curve for all mesh sizes reduced as the time-step size reduced. The final time-step selected was 0.0005 seconds and mesh size of 900,000 elements.

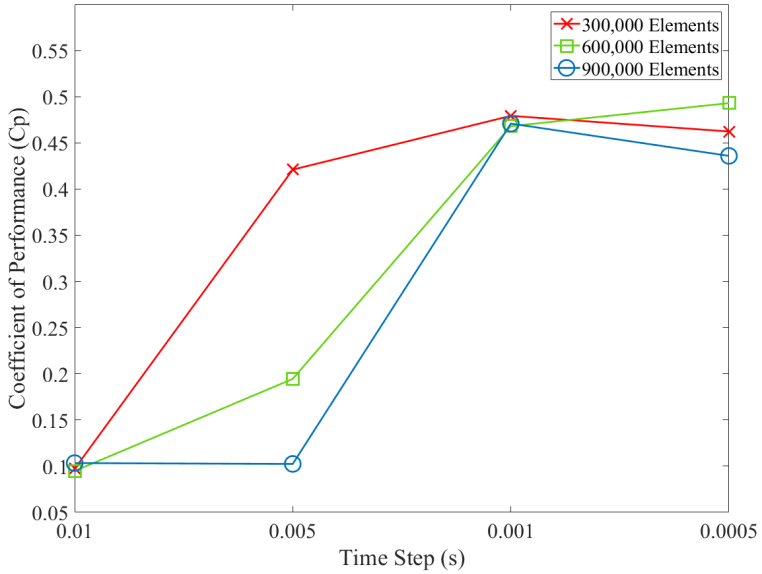

FIGURE 6. Independence study.

Numerical study result

A numerical study of a single wind turbine was done to estimate the length of the wake created, this is shown in Fig. 7. Another study consisting of two wind turbines was done to observe the effect of the wake from the first turbine on the second turbine. This was used to select 10 times the diameter of the wind turbine as the optimum distance between the turbines. As seen in the Fig. 8 there is enough distance between the two wind turbines to prevent the wake effect from the first turbine. The wake of the first turbine starts degrading before 10 times the diameter as seen in Fig. 7. The contour colour of the air approaching the second turbine is similar to the colour at the inlet, which shows the air has regained most of its initial energy.

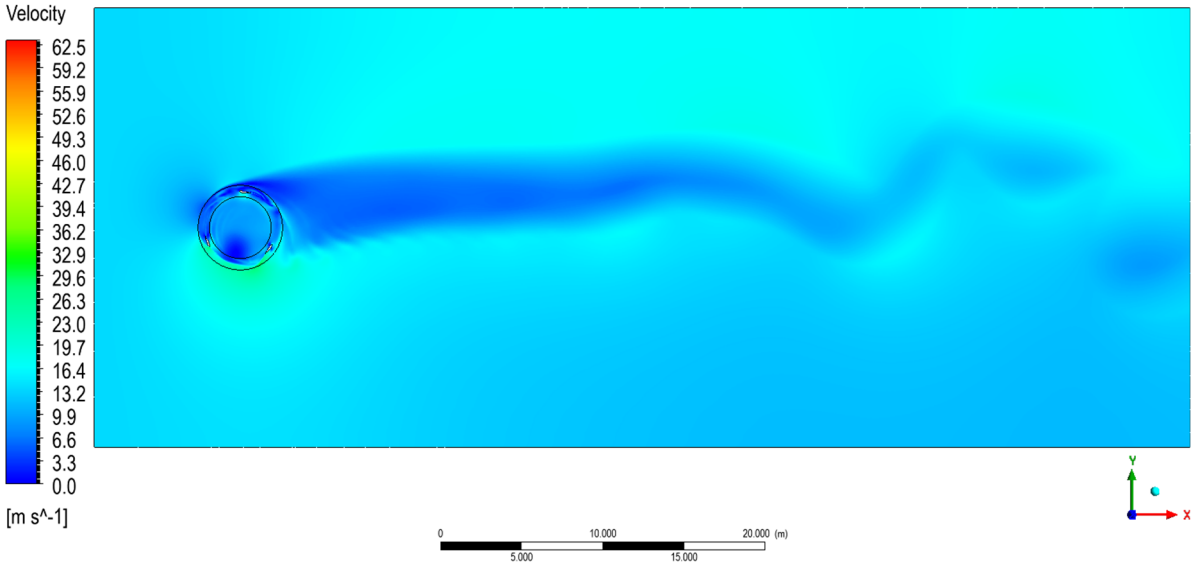

FIGURE 7. Single vertical axis wind turbine simulation.

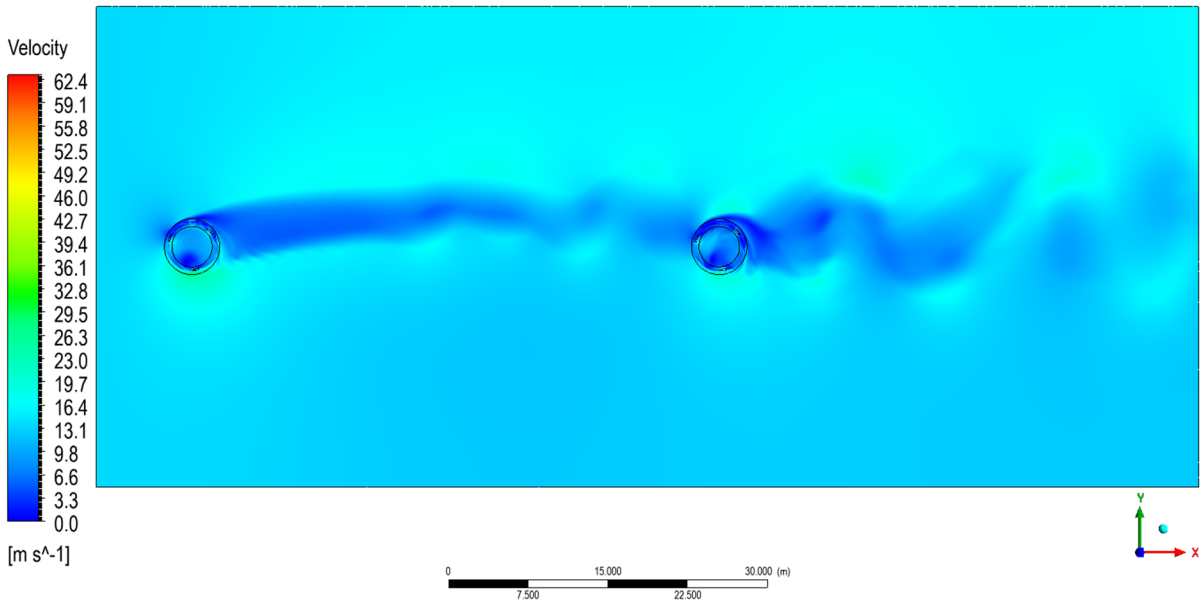

FIGURE 8. Two vertical axis wind turbines simulation.

RESULTS AND DISCUSSION

The MATLAB Simulink energy model used the weather data to generate daily energy generation, land use, amount of components and environmental economic information. All the governorates produced above the required 19,745 Kilo-watt hour energy, as the number of installable solar photovoltaic panels and wind turbines need to be in whole numbers. The estimated values of the amount of solar photovoltaic and vertical axis wind turbines were initially in fraction before approximation to whole numbers as shown in Fig. 10 and Fig. 11. The estimated energy production for all the cases was 19,745 Kilo-watt hour as shown in Fig. 9. The graph on Fig. 12 shows the Red Sea governorate generated the highest energy for the wind turbine only case at about 23,939 Kilo-watt hour. This is supported by the weather data, as the location selected in Red Sea has a high wind power density relative to other areas. The New Valley has the highest energy production in the solar photovoltaic case only at 21,255 Kilo-watt hour, as the area on the map has a high solar energy potential. As for all the hybrid cases as shown in Fig. 12, the Red Sea generated the highest amount of energy at 27,502 Kilo-watt hour due to high wind power density and solar energy potential.

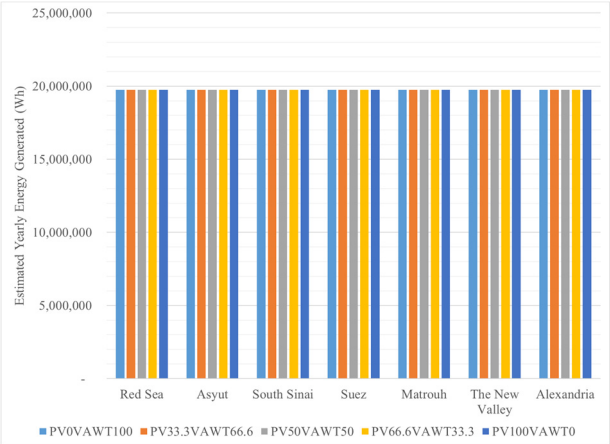

FIGURE 9. Estimated yearly energy generated.

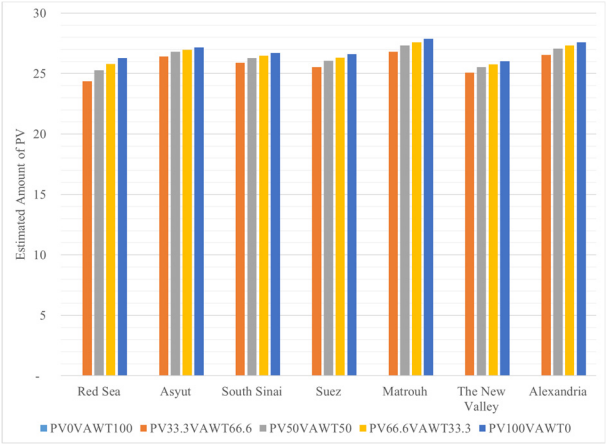

FIGURE 10. Estimated amount of solar photovoltaic panels needed.

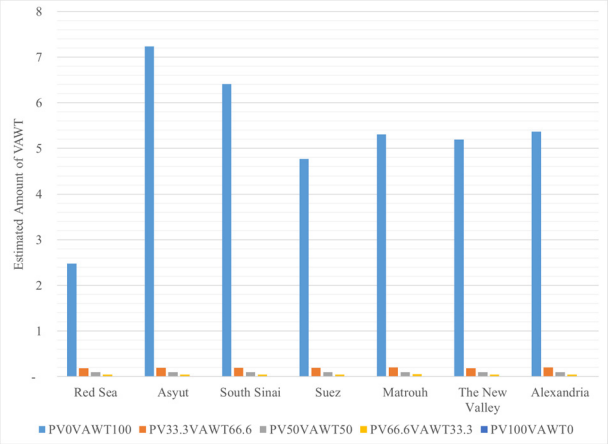

FIGURE 11. Estimated amount of vertical axis wind turbines needed.

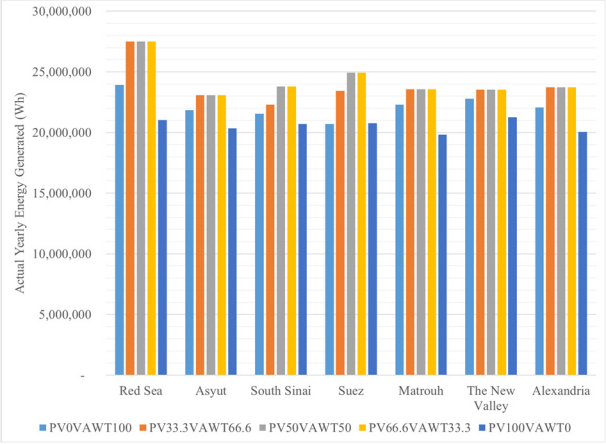

FIGURE 12. Actual yearly energy generated.

The total area of land required varies widely between the Wind turbine only cases and all the other cases as shown in Fig. 13. The wind turbine only cases need more than a single wind turbine, so there needs to be a distance to reduce the effect of the wakes from the turbines on each other. This reason makes any case which requires more than a single turbine consume a large amount of land compared to needing a single or no wind turbine. The cases which require solar photovoltaic panels only need the lowest land sizes. The hybrid cases require a bit more land than the solar photovoltaic cases. The wind turbine only case in Asyut needed the largest land of about 9,858 square meters. While all the solar photovoltaic cases for all the governorates used same area of 130 square meters.

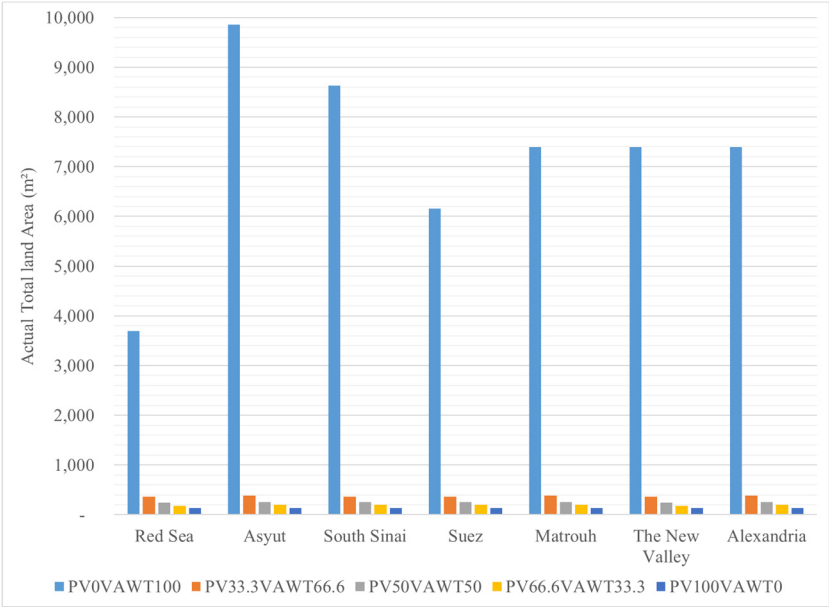

FIGURE 13. Actual total area of land required.

The number of solar photovoltaic panels needed varied a little between 26 to 28 as shown in Fig. 14. The little variation is due to low variation of solar irradiance between the locations selected, as all the areas had received a high amount of solar irradiance. The total amount of vertical axis wind turbines needed varied from 3 to 8 as shown in Fig. 15. This is due to the wide variation in wind speed across the country. For the wind turbine only case, the Red Sea needed the lowest amount of wind turbines due to high wind speed, while Asyut needed the highest amount of wind turbines due to having the lowest wind speed among the selected locations. All the hybrid cases used a single wind turbine to achieve the energy requirement. This shows the higher the wind speed in a region, the lower the amount of wind turbines required to generate a specific energy. Also, the higher the irradiation, the lower the number of solar photovoltaic panels needed to meet the energy requirement.

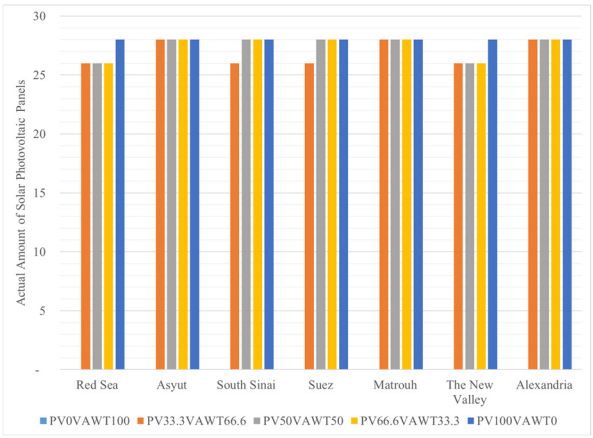

FIGURE 14. Actual amount of solar photovoltaic panels needed.

The solar photovoltaic cases were the only case with a realistic and feasible payback period ranging from 11 to 12 years as shown in Fig. 16. All the cases using vertical axis wind turbine were not feasible due to payback periods of 46 years and above, which exceeds the project lifetime of 20 years. The project lifetime carbon emission reduction for all cases ranged from 429 to 594 tonnes as shown in Fig. 18. The capital cost for all the solar photovoltaic on cases ranged from 3,832 to 4,006 dollars, while all the which include the vertical axis wind turbine ranged from 21,126 to 140,343 dollars as shown in Fig. 19. The solar photovoltaic case in the New Valley had the best levelised cost of electricity at 0.009 dollar per Kilo-watt hour in Fig. 17.

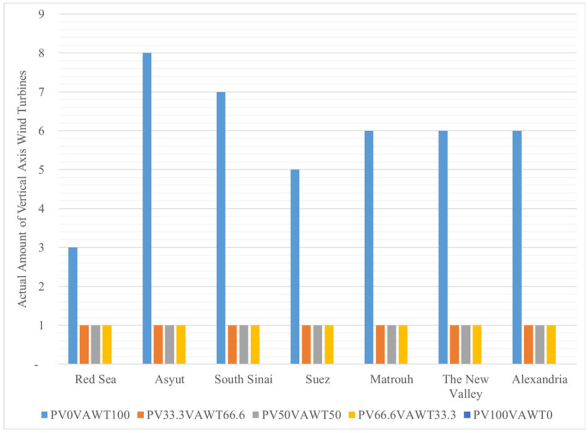

FIGURE 15. Actual amount of VAWT needed.

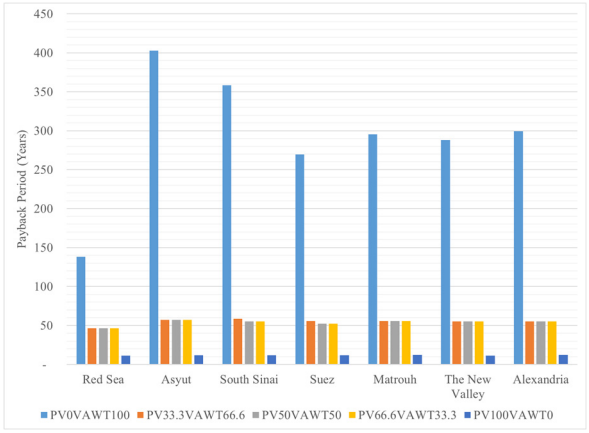

FIGURE 16. Payback period.

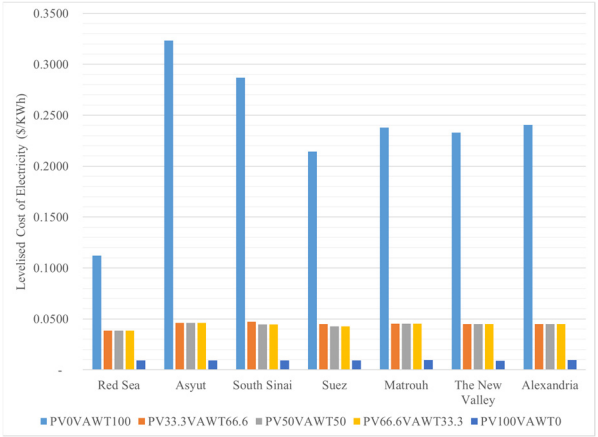

FIGURE 17. Levelised cost of electricity.

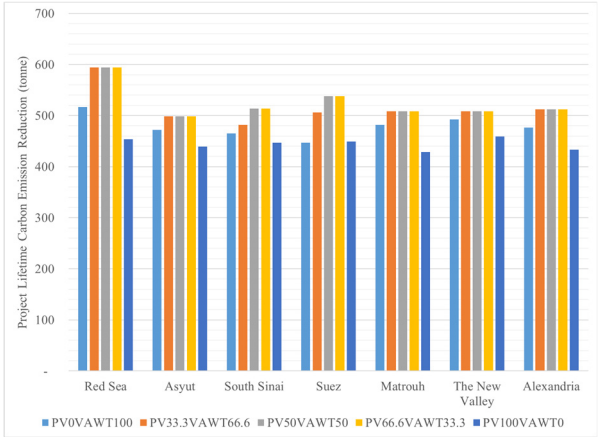

FIGURE 18. Project lifetime Carbon emission reduction.

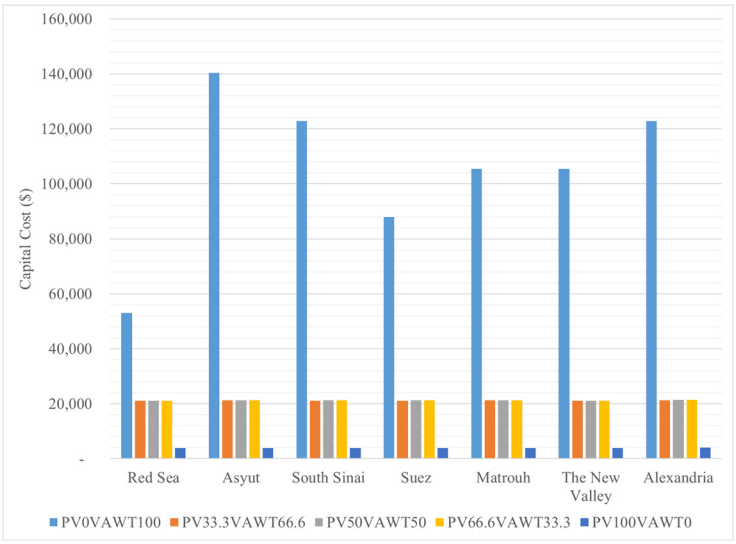

FIGURE 19. Capital Cost.

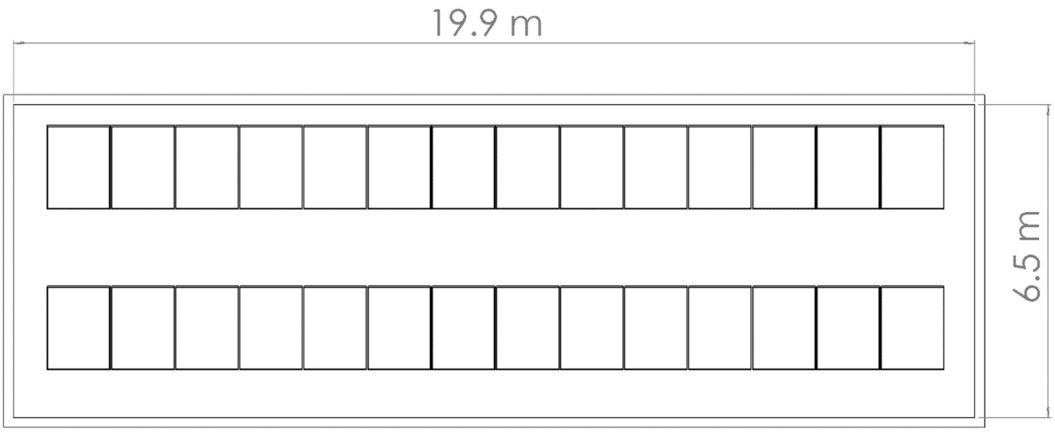

FIGURE 20. The New Valley solar photovoltaic only.

The New Valley had the minimum capital of 3,832 dollars and the minimum payback period of 11 years. This case generated about 21,255 Kilo-watt hour, which was the highest generation for photovoltaic only energy generation. As shown in Fig. 20, it used a total area of 130 square meter. This is the best performing case.

CONCLUSION

In conclusion, solar irradiation and wind speed data were obtained. The data was used for geospatial analysis to identify areas of high energy density. The same data was inputted into the MATLAB Simulink energy model to generate information about daily energy generation, total land used, amount of solar photovoltaic panels required, amount of vertical axis wind turbines required and environmental economic information. The solar photovoltaic only cases were substantially cheaper in capital cost and had feasible payback periods compared to the cases using vertical axis wind turbines. The best case was the solar photovoltaic only for the New Valley. It had a payback period of 11 years, capital cost of 3,832 dollar, a levelised cost of electricity of 0.009 dollar per Kilo-watt hour and used 28 solar photovoltaic panels occupying an area of 130 square meter.

ACKNOWLEDGEMENT

This paper is based upon work supported by Science, Technology & Innovation Funding Authority (STDF) under grant number (ID-46097).

REFERENCES

1. G. Wang, M. Sadiq, T. Bashir, V. Jain, S.A. Ali, and M.S. Shabbir, Energy Strateg. Rev. **42**, (2022).
2. L. Liu, Z. Wang, Y. Wang, J. Wang, R. Chang, G. He, W. Tang, Z. Gao, J. Li, C. Liu, L. Zhao, D. Qin, and S. Li, Renew. Sustain. Energy Rev. **132**, (2020).
3. J. Lian, Y. Zhang, C. Ma, Y. Yang, and E. Chaima, Energy Convers. Manag. **199**, (2019).
4. J. K. Lundquist, K. K. DuVivier, D. Kaffine, and J. M. Tomaszewski, Nat. Energy **4**, 26 (2019).
5. A. M. Ghaithan and A. Mohammed, Process Integr. Optim. Sustain. **6**, (2022).
6. R. Khezri, A. Mahmoudi, and M. Haque, IEEE Trans. Sustain. Energy **12**, 2184 (2021).
7. B. Ji, K. Zhong, Q. Xiong, P. Qiu, X. Zhang, and L. Wang, Energy **249**, (2022).
8. J. Bosch, I. Staffell, and A. D. Hawkes, Energy **189**, (2019).
9. B. Chang and K. Starcher, Renew. Energy **132**, 1348 (2019).
10. United States Energy Information Administration, *State Electricity Profiles* (2022).
11. M. Nasser, T.F. Megahed, S. Ookawara, and H. Hassan, Energy Convers. Manag. **267**, (2022).
12. N.N.S.R. Database, (n.d.).
13. J.R.C. European Commission, (n.d.).
14. NASA, (n.d.).
15. R. Lanzafame, S. Mauro, and M. Messina, in *Energy Procedia* (Elsevier Ltd, 2014), pp. 131–140.

Techno-Economic and Environmental Analysis of a Hybrid Energy System Using a Pumped Hydro Storage System for Powering a University Building

Simon Juma Bullen[1, b)] Mohamed Emam[1, 2,)] Hidetoshi Sekiguchi [3,)] Hamdy Hassan[1, 4, a)]

[1] *Energy Resource Engineering Department, Egypt-Japan University of Science and Technology (E-JUST), Alexandria, Egypt*
[2]*Mechanical Engineering Department, Benha University, Shoubra Faculty of Engineering, Shoubra Street, Cairo, Egypt*
[3]*Department of Chemical Engineering, Tokyo Institute of Technology, Tokyo, Japan*
[4]*Mechanical Power Engineering Department, Faculty of Engineering, Assiut University, Assiut, Egypt*

Corresponding author: [a)]hamdy.aboali@ejust.edu.eg
[b)] simon.manase@ejust.edu.eg

Abstract. This study aims to investigate the techno-economic viability of an on-grid and off-grid hybrid renewable energy system for powering a building at the Egypt-Japan University of Science and Technology. The results found indicate that an on-grid hybrid system of wind turbine capacity of 50KW with a Net Present Cost (NPC), Cost of Electricity (COE), payback period, and reduced carbon emissions of $184,384, 0.037$/kWh, 8.5 years, and 27347kg/year respectively is the optimum viable solution. This system sells 60,300kWh/year to the grid. The off-grid hybrid system consists of 66KW Solar (PV) capacity,6OKW wind turbine capacity, and 5000 meters cubic of water in the upper reservoir of the Pump Hydro Storage System (PHSS) which is sufficient to meet the electric load demand with a Net Present Cost, Cost of Electricity and negligible carbon emissions of $552,694 0.135$/kWh. Sensitivity analysis reveals that the on-grid system is more stable in meeting the future energy demand. This explains why a complete switch to off-grid renewable energy systems are expensive though economically and environmentally advantageous**.**

INTRODUCTION

Global energy consumption is rising due to increased industrialization, technological advancement, and population increase. Energy demand is expected to increase by 30% in 2030 [1] renewable energy sources, such as solar and wind, are a sustainable alternative to non-renewable sources like fossil fuels, offering environmental benefits like reduced greenhouse emissions. Egypt aims to meet 42% of its energy demand by 2035 through renewable sources, including solar, hydroelectricity, and wind energy, with 25%, 2%, and 14% [2]. However renewable energy is intermittent and therefore requires storage for sustainable and continuous operation, learning institutions such as universities should lead in the transition to renewable energy[3]

Ayooluwa et al.[4] they have designed a system using Homer Pro for Covenant University in Nigeria. Their results reveal that hybrid PV(Photovoltaic)-Diesel Generator-Grid-BESS (Battery Energy System Storage) met the university's electric load. The generator was only for backup since the wind energy was not feasible. Energy costs can be significantly reduced around the world as demonstrated by Yingming et al. [5], that solar PV power generation covered (33-46) % of the electricity cost after constructing four microgrids of 156kW solar capacity at SCU Jiangnan University campus. Examining the literature more closely reveals that the technical and economic feasibility studies of grid-connected or off-grid for supplying learning institutions in Egypt have not been explored. This study aims to explore the technical and economic feasibility of grid-connected and off-grid hybrid energy systems for Egypt Japan University of Science and Technology using Homer Pro software to investigate the use of solar PV, wind energy, and pumped hydro-storage for electricity supply.

Technologies and Materials for Renewable Energy, Environment and Sustainability
AIP Conf. Proc. 3321, 040013-1–040013-11; https://doi.org/10.1063/5.0290626
Published under an exclusive license by AIP Publishing. 978-0-7354-5231-2/$30.00

This study is organized as follows: Section 2 provides the methodology, technical, and component modeling; Section 3 presents the results, discussion, and sensitivity analysis of the best hybrid energy system; Section 4 includes the conclusion.

PROPOSED HYBRID ENERGY SYSTEM

The hybrid energy system to be simulated using Homer Pro software consists of solar PV, wind turbine, pumped hydro storage system, and the electric grid. Shows the methodology of the study Sensitivity analysis is performed on the most feasible hybrid energy system, the on-grid system hybrid energy system should contribute higher percentage of renewable energy supply, Fig. 1 reveals the study approach.

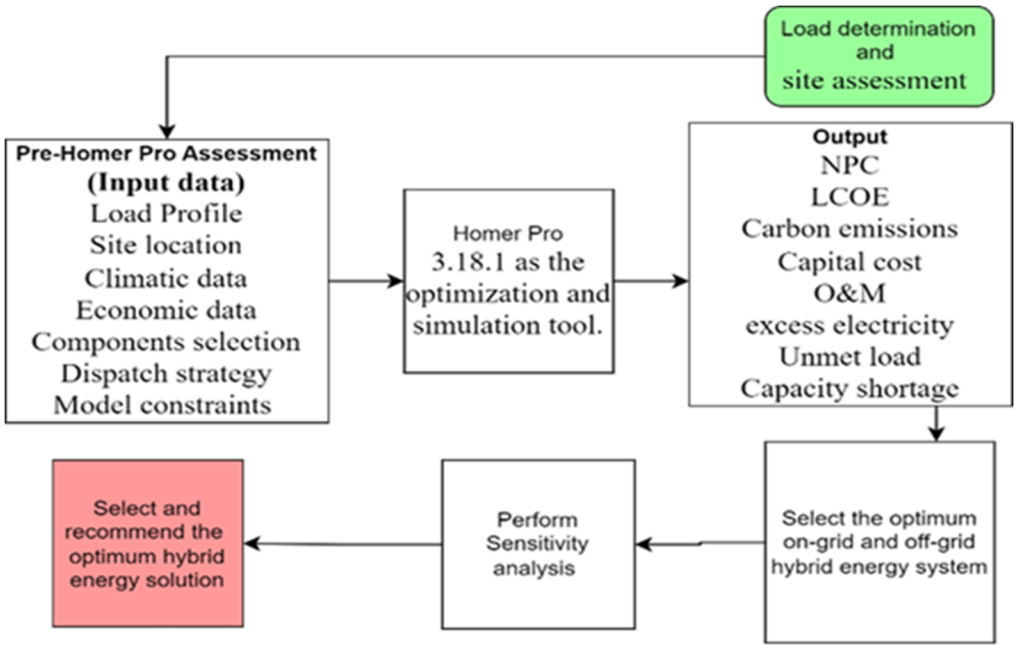

FIGURE 1. Methodology of study.

Location

The hybrid energy system in this study is proposed for supplying electricity to a building at Egypt- Japan University of Science and Technology (EJUST) [6], the location coordinates are (30°52.0' N, 29°34.9'E). Homer Pro uses metrological data from NASA indicating that this site has a good level of solar irradiation and wind speed, it receives annual solar irradiation of 5.41kWh/m2/day with the highest solar irradiation recorded in July at 8.03KWh/m2/day and the lowest in December at 2.64kWh/m2/day, the corresponding annual average temperatures are 20.59°C with the highest temperature recorded in August at 27.59°C as shown in Fig. 2.The wind speed at the site indicates an annual average wind speed of 5.38 m/s with the highest wind speed recorded in February at 6.35 m/s and the lowest in October at 5.38 m/s which is complementary with the solar resources making the site suitable for hybrid energy system as indicated in Fig. 3.

Load profile

The building's daily load energy demand is audited to be 847.26kWh/day with a peak energy demand of 75KW at 2:00 pm and a relatively constant energy demand of 26.6KW between 18:00 and 7:00 am as denoted in Fig. 4.

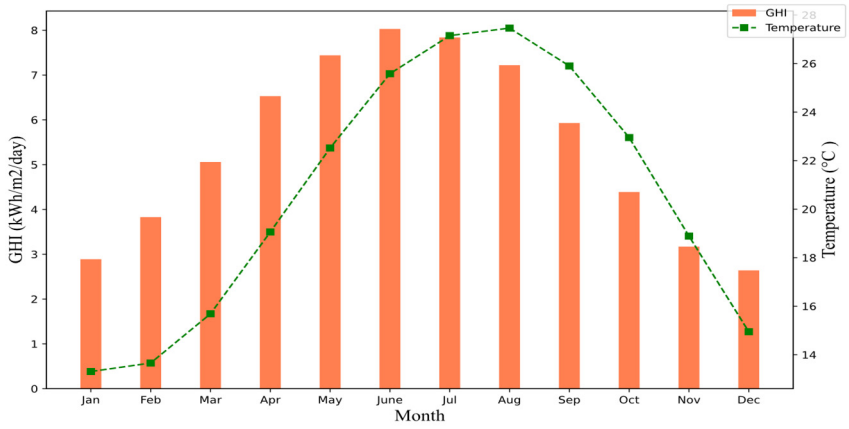

FIGURE 2. Average Monthly GHI and Temperature.

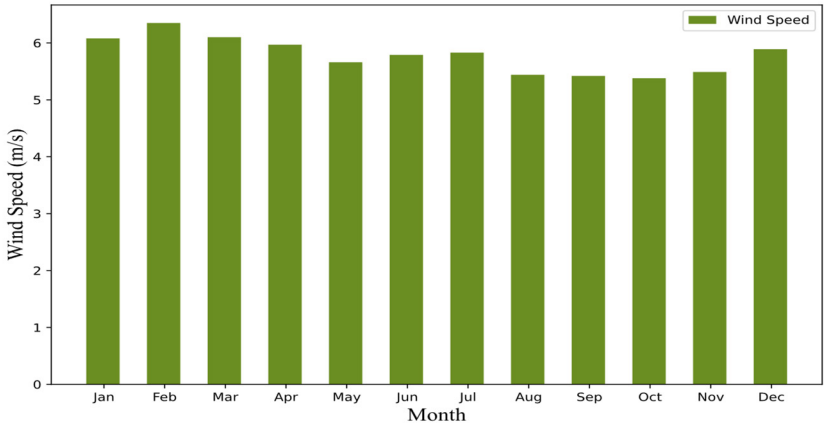

FIGURE 3. Average monthly wind speed.

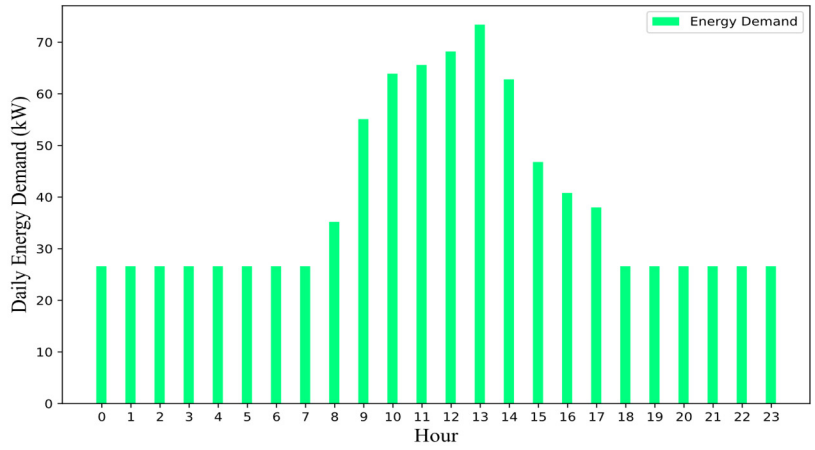

FIGURE 4. Daily energy demand.

Components modeling

The schematic of hybrid energy on-grid and off-grid system using PHSS as modeled in Homer Pro is shown in Fig. 5 with technical and economic details in Table 1 and model constraints in Table 2

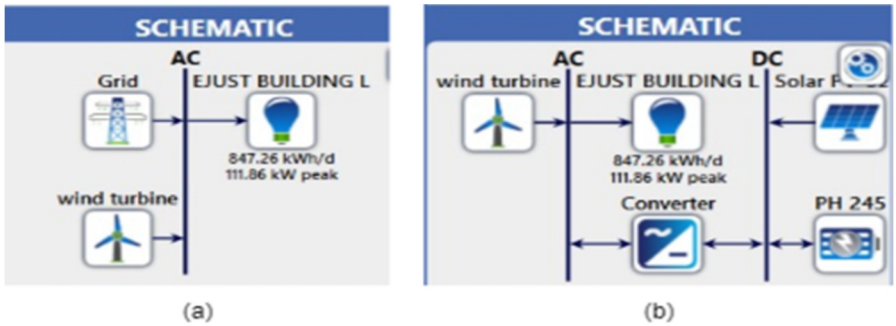

Figure 5. (a), On-grid hybrid energy system (b), Off-grid hybrid energy system.

TABLE 1. Technical and economic component specification.

Component	Solar PV	WT	PHSS	Converter
Type	Canadian Solar [7],[8]	Enair [9],[10]	PH 245kWh [11]	Generic system converter[10]
Size (KW)	0.325	10	-	-
Efficiency (%)	16.94	-	90	95
Cost($/kW)	1000	1250	22000	527
Replacement cost ($)	1000	1250	13000	527
O&M ($/year)	5	100	2000	-
Lifetime(years)	25	25	25	15

TABLE 2. Model parameters constraints.

Parameter	Value
Nominal discount rate [12]	9.25
Inflation rate[12]	3.4
Electricity grid buying price[13]	$0.053/kWh
Electricity grid selling price [Assumed]	$0.053/kWh
Capacity shortage[12]	0

Solar PV modeling

Solar PV power output using Homer Pro according to [14]can be estimated using the 'equation (1)'.

$$P_{output} = Y_{pv} f_{pv} \left(\frac{G_T}{G_{T,STC}}\right)[1 + \alpha_p (T_c - T_{c,STC})] \quad (1)$$

Where Y_{PV} (kW), is the module's rated capacity f_{PV} is the derating factor in (percentage), G_T (kW/m2) is the global solar irradiation. and $G_{T,STC}$ is the standard incident radiation at the standard test condition at (25°C). and αp (%/°C) is the temperature coefficient, the power Tc is PV cell temperature, $T_{c,STC}$ are the standard PV cell temperature in degrees Celsius respectively

Converter modeling

The converter serves as a link between DC and AC buses. Homer Pro estimates the converter's capacity using an 'equation (2)' that measures the energy transfer from DC to AC[1] . Homer Pro computes the converter size using equation (2) where Pout is the power output, Pin represents the inverter's power input and η_{in} is efficiency which is 95%.

$$P_{out} = P_{in} \times \eta_{in} \tag{2}$$

Economic modeling

The unit cost of energy generated is calculated using Net Present Cost (NPC) and Cost of Electricity (COE) economic factors, expressed in $/kWh, according to 'equation (3)' [15].

$$Min_{LCOE}(\frac{\$}{kwh}) = \frac{NPC_T \times CRF(v,t)}{\sum E_{gen(t)}} \tag{3}$$

MinLCOE is the minimum levelized energy cost and NPCT is the total net present cost. CRF is the capital recovery factor, v is the annual discount rate, t is the lifetime of the plant, Egent(t) energy is generated by integrated renewable energy. CRF converts total NPC to the annual capital cost as below in the 'equation (4)'.

$$CRF = \frac{v(1+v)v}{(1+v)v-1} \tag{4}$$

Likewise, the net present cost includes the present value of the initial investment cost (IIC) and the Operation and Management Cost (O&M) that are expected to be incurred periodically.

Wind turbine modeling

Wind turbine power output starts at cut-in speed until it reaches the cut-off speed with maximum power output at the rated speed, the equation (5) below is used to estimate the power output of wind turbine [16]

$$P_{WT} = \begin{cases} = 0 \rightarrow for, V < V_{cut-in,} and, V > V_{cut-out} \\ = P_{rates} \rightarrow for, V_{rated} < V \leq V_{cut-out} \\ = P_{rated} \times \frac{V^3 - V_{cut-in}^3}{V_{rated}^3 - V_{cut-in}^3} \rightarrow\rightarrow for, V_{cut-in} \leq V \leq V_{rated} \end{cases} \tag{5}$$

Where Pwt is the power output of the wind turbine, Vcut-in is the cut-in wind speed, Vcut-off is the cut-off wind speed, Vrated is the rated wind speed that gives the Prated power and V is the wind speed at the particular time.

Pumped hydro storage modeling

A pumped hydro storage system works on the concept that during excess energy, water is pumped from the lower reservoir to the upper reservoir known as charging. And during an energy shortage, water from the upper reservoir flows through a turbine to generate electricity. Equation (6) estimates that E is the energy stored in joules and should be divided by 3.6 x 106 to convert to kWh, Pwater is the density of water (1000kg/m3), Vres is the water volume of the upper reservoir in meters cubic, Hhead and ŋ are the head height in meters and the efficiency, the Homer pro generic PH245 has a head height of 100 meters and can generate 245kWh in 12 hours [1]

$$E(J) = 9.8 P_{water} \times V_{res} \times H_{head} \times \eta \tag{6}$$

Grid modeling

The on-grid system sells excess energy from a hybrid system to the grid [16], while purchasing energy during shortages, allowing for net energy calculation from the equation (7).

$$GEC_{(M)} = \sum_{p}^{r} \sum_{q}^{12} \begin{Bmatrix} E_{j.net}(G), _{p,q}\ geC_{G,p\rightarrow} 1\phi E_{j.net}(G)_{p,q} \geq 0 \\ E_{j.net}(G), _{p,q}\ geC_{S,p} \rightarrow 1\phi E_{j.net}(G)_{p,q} < 0 \end{Bmatrix} \quad (7)$$

$GEC_{(M)}$ represents the energy charges in (kWh) when the net generation is accounted for monthly Ej·net(G), p, q equals to the net energy purchased in (kWh) from the grid (G) in month q during the applied rate (r) of price (p), geCG,p, p, p is the power price for rate p in $/kWh, geCS,p indicates the selling price(S) for rate p in $/kWh.

RESULTS AND DISCUSSION

This study proposed a hybrid energy system consisting of solar PV, wind turbine, and PHSS to power a university building, the current grid connection was taken as the base case. Different feasible configurations are identified and compared based mainly on NPC, LCOE, and other technical parameters, the optimization results of the three systems are presented in Table 3.

Table 3. Optimization results of the on-grid and off-grid hybrid energy system.

Component	Case I: Grid	Case II: WT/Grid	Case III: PV/WT/PHSS
COE($/kWh)	0.053	0.037	0.135
NPC ($)	216,514	184,384	552,494
O&M($/year)	0	121,611	243,230
Capital Cost ($)	0	62,500	293,865
PHSS upper reservoir(m3)	-	-	5000
Solar PV (KW)	-	-	66
Wind turbine (KW)	-	50	60
Converter (KW)	-	-	81
Energy production (kWh/year)	309,249	266,011	441,060
Sold to Grid(kWh/year)	0	60,300	NA
Purchased from Grid (kWh/year)	309,249	103,571	NA
Net energy kWh/year	309,249	43271	NA
Excess energy (kWh/year)	0	0	112,704
Carbon Emissions (kg/year	195,445	27,347	0

Technical analysis

The technical performance of the hybrid energy system in this study is based on the net electricity that is, the difference between the amount of electricity purchased from the grid and the electricity sold to the grid and excess electricity Fig. 6. Indicates both Case I and Case II have zero excess electricity this is because the system is grid-connected. Case III has excess electricity of 112,704kWh/year because it's an off-grid standalone system, Case I and Case II have annual net electricity of 309,249kW and 43271kW. Overall, technical Case II presents a more suitable hybrid system since the grid acts as storage that doesn't require more storage extension costs. The load is projected to increase to consume the excess electricity produced by Case III.

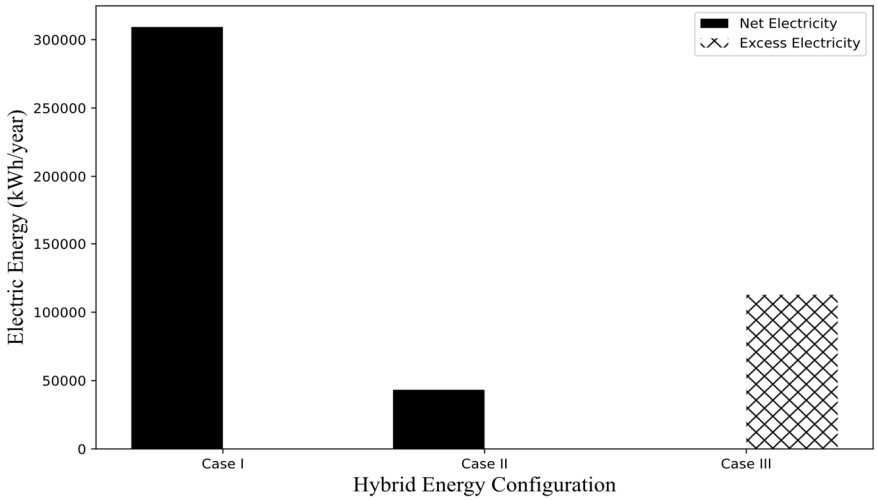

Figure 6. Net electricity and Excess electricity.

Annual electricity production and carbon emissions

Figure 7. Present the yearly electricity production of the three cases. It indicates that Case III has the highest renewable energy production of 441,060kW with 26.2 percent (115,719 kWh/year) from solar PV and 73.7 percent (325,341 kWh/year) from wind, indicating the site has more wind energy potential than solar PV. Case II renewable energy production from wind energy is 266,011kWh/year, representing 71.9 percent of the total electricity production, with the remaining 28.1 percent purchased from the grid. Case I is grid electricity of 309,249kWh/year hence contributing the highest carbon emissions of 195, 445kg/year. Fig. 8, introducing renewable in Case II reduces the carbon emissions by 12% to 27,347kg/year, and Case III is considered clean source of energy with negligible carbon emissions. Case II has both environmental advantages and renewable energy contributions as denoted in Fig. 8.

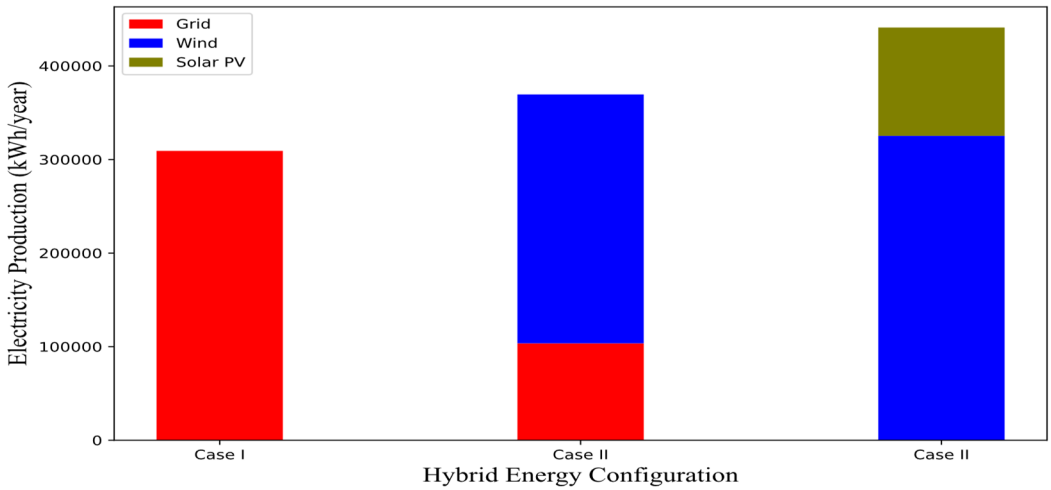

Figure 7. Total annual electricity production.

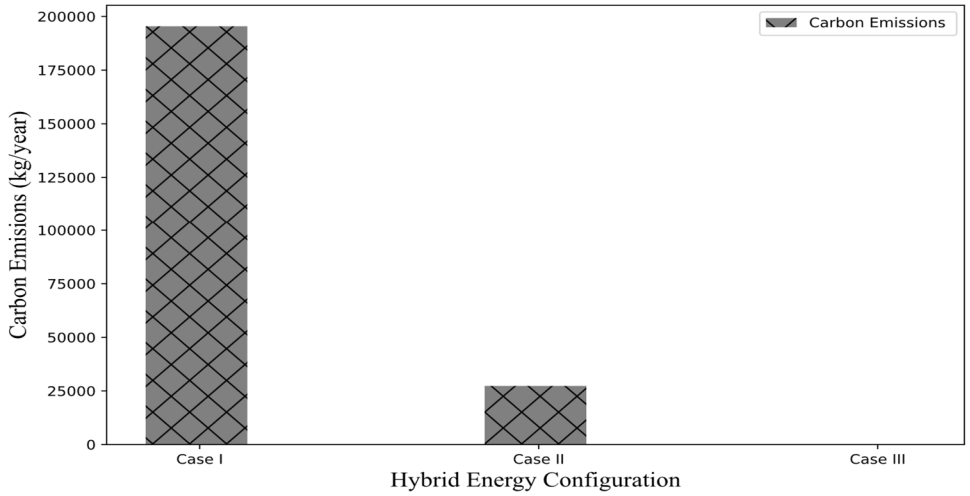

Figure 8. Total annual carbon emissions.

Economic analysis

Table 3, shows the comparison between Cases I and II; the off-grid Case III has the highest NPC and COE of ($552,494,0.135 $/kWh) respectively. It is expensive because of the addition of the PHSS and excess energy dumped into the load rather than sold to the grid. On the other hand, Case II has the lowest NPC and COE ($184,384, 0.037 $/kWh) and an 8.5-year payback period. Thus, Case II (wind turbine and grid) is an economically advantageous system, as shown in Fig. 9 and Fig. 10.

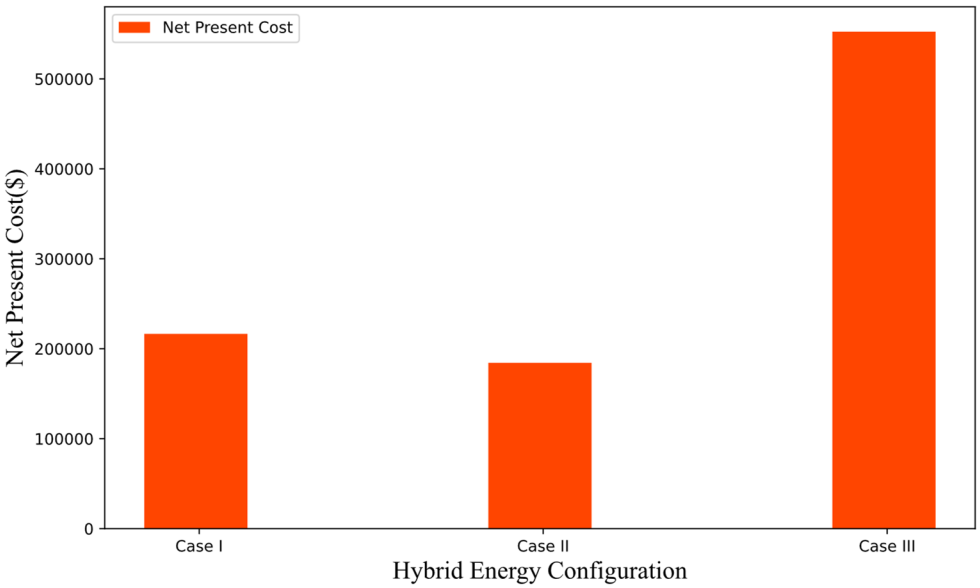

Figure 9. Hybrid system net present cost

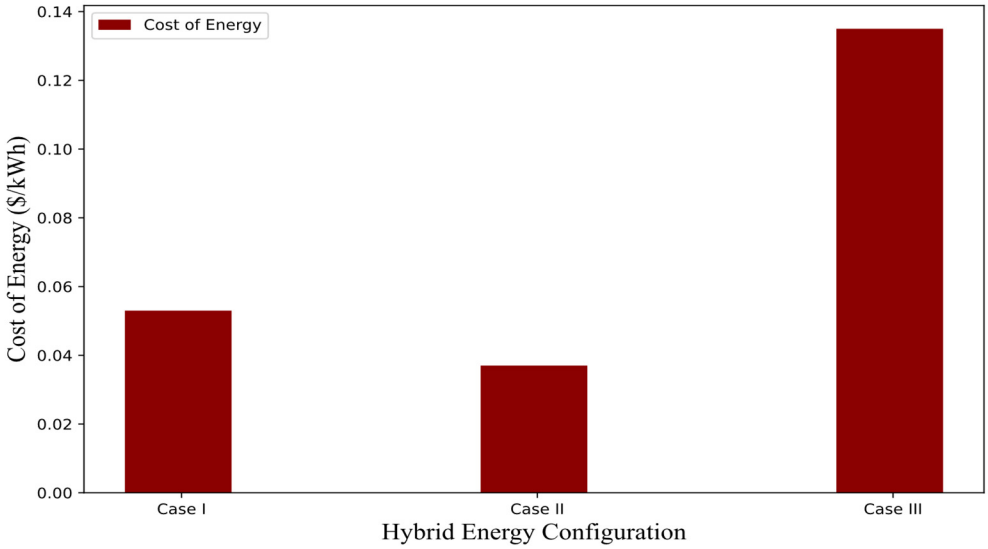

Figure 10. Hybrid system Cost of Energy

Dispatch strategy

Figure 11. Presents Case II's electricity dispatch. It is evident that the load's energy need is satisfied by erratic wind power, therefore the grid serves as an ideal storage to store electricity and send it to the load when as demanded.

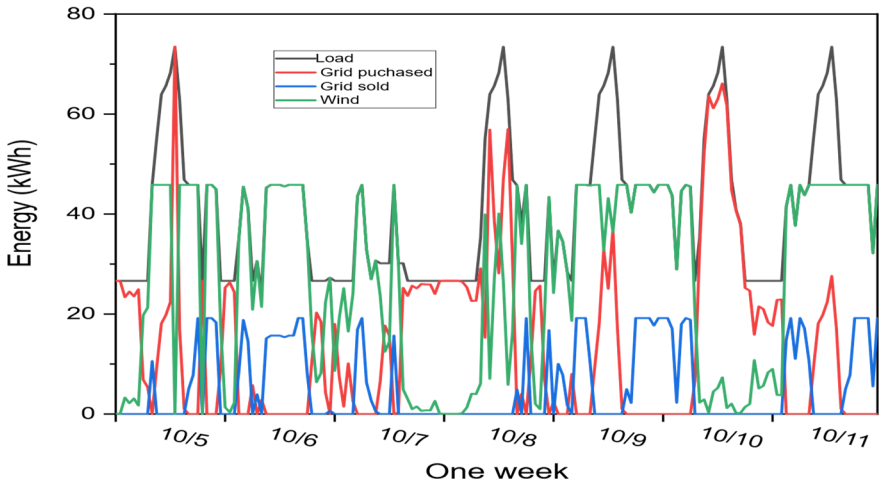

Figure 11. Electricity dispatch strategy.

Sensitivity analysis

Case II is selected as the better hybrid energy system and the following parameters are considered for sensitivity analysis. daily load increased from 847.26 kWh/day by 30% and 50%. and power price increased from $0.053 to $0.060, $0.070 then Nominal discount rate increased from 9.25% to 12%,15%.
The results demonstrate that regardless of the changes, 50kW wind turbine capacity is sufficient to meet and maintain the desired 50% renewable energy contribution up to 1271kWh/day load demand with higher grid price and NDR hence a shortened payback period. however, at a lower grid price, the grid only becomes the optimum solution Fig. 12. Shows that at the highest increase in NDR, grid price and electric load lead to an NPC and LCOE increase by 24.47% ($184,383 to $235,802) and 40.86% (0.037$/kWh to 0.056$/kWh) with a shortened payback period of 6.5 years, this explains why for renewable energy to penetrate it will require electricity from non-renewable to be more expensive. This explains why for renewable energy to penetrate, it will require electricity from non-renewable to be more expensive. Since Case II is selected as the better hybrid energy system for supplying the university building, sensitivity analysis is necessary to determine the impact of the increase in electric load demand, power price, and changes in the nominal discount.

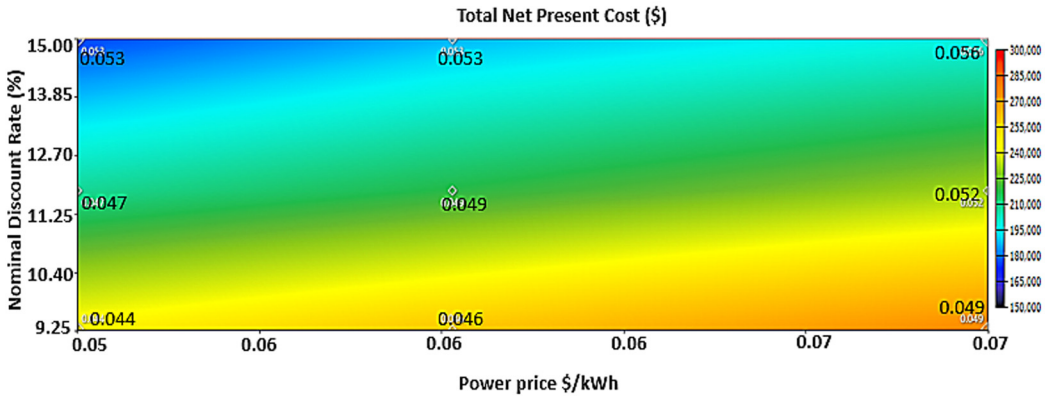

Figure 12. Sensitivity analysis, NDR versus Power Price, with NPC and superimposed COE investigating the response to increased energy demand.

CONCLUSION

The study achieved to determine the optimum on-grid and off-grid hybrid renewable energy system for EJUST to reduce energy purchasing costs and greenhouse gas emissions, after hybrid system simulations and comparison from the techno-economic point of view, the results show that Case II (wind and grid) has the lowest NPC, COE, ($184,384,0.037$/kWh) and archived carbon emissions reduction by 12% from 195,445 kg/year to 168,098 kg/year meanwhile the optimum off-grid hybrid energy system is Case(PV/WT/PHSS) has the NPC, COE ($552,494,0.135$/kWh) and negligible greenhouse emissions. sensitivity analysis reveals that Case II has more system stability especially if the electricity power price increases. this demonstrates that the best option for the energy transition at the university building is a grid-tied energy system as a complete switch to off-grid is costly though environmentally advantageous.

ACKNOWLEDGMENTS

The authors sincerely thank the Japan International Cooperation Agency (JICA) and the Egypt-Japan University of Science and Technology (EJUST) for offering financial support and research facilities through the TICAD7 scholarship.

REFERENCES

1. B.M. Abderahim, G. Leila, and L.B. Hadj, in *2022 IEEE International Conference on Electrical Sciences and Technologies in Maghreb, CISTEM 2022* (Institute of Electrical and Electronics Engineers Inc., 2022).
2. T. Khatib, A. Mohamed, and K. Sopian, Renewable and Sustainable Energy Reviews **22**, 454 (2013).
3. A.A. Ajiboye, S.I. Popoola, O.B. Adewuyi, A.A. Atayero, and B. Adebisi, Sustainable Energy Technologies and Assessments **52**, 102189 (2022).
4. Y. Zhu, F. Wang, and J. Yan, Energy Procedia **145**, 582 (2018).
5. A. Rashwan, A. Faragalla, E.M. Abo-Zahhad, A.Z. El-Dein, Y. Liu, Y. Chen, and E.H. Abdelhameed, Smart Grids and Sustainable Energy **9**, (2024).
6. [10] A.M. Abdelshafy, J. Jurasz, H. Hassan, and A.M. Mohamed, Energy **192**, 116615 (2020).
7. U.G. Onu, G.S. Silva, A.C. Zambroni de Souza, B.D. Bonatto, and V.B. Ferreira da Costa, Renew Energy **198**, 1021 (2022).
8. K.M. Kotb, M.R. Elkadeem, A. Khalil, S.M. Imam, M.A. Hamada, S.W. Sharshir, and A. Dán, Energy Convers Manag **235**, (2021).
9. N. Yimen, O. Hamandjoda, L. Meva'a, B. Ndzana, and J. Nganhou, Energies (Basel) **11**, 2644 (2018).
10. K.M. Kotb, M.R. Elkadeem, A. Khalil, S.M. Imam, M.A. Hamada, S.W. Sharshir, and A. Dán, Energy Convers Manag **235**, (2021).
11. M.R. Elkadeem, K.M. Kotb, M.A. Abido, H.M. Hasanien, E.G. Atiya, D. Almakhles, and M.F. Elmorshedy, Energy **289**, 129816 (2024).

Performance analysis of a novel solar chimney design for building ventilation

Prince Adolphus Juah[1, b)] Mohamed Emam[1], Sameh Nada[1], Shinichi Ookawara[2], Hamdy Hassan[1, a)]

[1]*Department of Energy Resources Engineering, Egypt Japan University of Science and Technology, Alexandria, Egypt*
[2]*Department of Chemical Science and Engineering, Tokyo Institute of Technology, Tokyo, Japan*

Corresponding Author: [a)]hamdy.aboali@ejust.edu.eg
[b)]prince.juah@ejust.edu.eg

Abstract. Solar chimneys utilize solar energy to induce air into a building for space ventilation. This application of solar energy has played a significant role in reducing building energy consumption. Previous researchers have studied solar chimneys under several configurations both numerically and experimentally. In this, paper a non-absorbent base solar chimney is investigated numerically using Computational Fluid Dynamic (CFD) Software. The Renormalization Group (RNG) k-epsilon turbulent model has been applied to predict the volumetric flow rate of this novel solar chimney. This novel configuration arranges multiple outlets with variable tilt angles along the chimney wall. The influencing factor is the solar chimney outlet tilt angle arrangement, considering the base and reverse case of the outlet tilt angle arrangement and the external wind blowing normal to the outlet. The findings from the study reveal that both arrangements of the outlet tilt angle for the base and reverse case obtained a maximum flow rate of 3.6 m³/s accordingly. The reverse case was reported to have the best overall performance due to the lesser occurrence of reverse flow. This application is essential as it reduces reliance on mechanical ventilation systems and compensates for some percentage of building energy consumption.

INTRODUCTION

With the consistent growth in the human population coupled with the fast depletion of conventional energy resources, it's most likely that the world will face a serious energy crisis if preventive measures are not employed. Therefore, to provide an ultimate solution to the already predicted energy crisis and the environmental challenges posed by climate change, energy resources engineers have shifted to identifying a way to utilize the available renewable energy resources as a means of preventing the presumptive occurrence of the energy crisis that many researchers have reported. Currently, urban regions are home to more than half of the world's population. By the middle of the 21st century, the world's urban population is predicted to have increased by 1.5 times due to population growth and fast urbanisation supplying more than 70% of overall energy consumption and greenhouse gas emissions[1]. Urban areas have also been acknowledged as essential for reducing energy hazards and combatting climate change [2]. Solar energy is regarded as the safest and most sustainable source of renewable energy to combat this energy shortage. Solar radiation reaching the earth's surface is abundant and environmentally friendly. One of the advantages of solar energy is its multiple applications. The applications of solar energy through passive solar ventilation, also called solar chimneys, are a unique and natural way to ventilate a building and provide heating during the cold climate [3]. Proper ventilation is essential for the comfort and healthy living of occupants inside the building[4]. Following the outbreak of COVID-19, to prevent the spread of the virus, inhabitants spent much of their time indoors; however, spending so much time in a place that isn't ventilated is likely to expose people to infection [5]. For instance, [6] theoretically and numerically analyzed the buoyancy ventilation of a vertical solar chimney in a multi-story building. Their research revealed that as the specific vent size is increased, the increasing trend in ventilation rate tends to decline. For low buildings, the air channel cavity gap had an impact on the volume flow rates, however, their study did not address the impact of varying the outlet configuration on the chimney performance. As the study's findings showed, the air change per hour rose at a given solar radiation when the vent inlet was positioned in the middle. At solar radiation of 700 w/m², the vent produced a minimum velocity of 2.227 m/s for the vent placed

Technologies and Materials for Renewable Energy, Environment and Sustainability
AIP Conf. Proc. 3321, 040014-1–040014-11; https://doi.org/10.1063/5.0289688
Published under an exclusive license by AIP Publishing. 978-0-7354-5231-2/$30.00

at the top while the velocity increased to 2.267 m/s for the middle inlet position. As discussed by [7], an increase in the outlet width of a solar chimney with a horizontal absorber surface beyond a certain limit reduces its flow rate and thermal efficiency. This is attributed to the reverse flow that occurred at the chimney outlet. However, an increase in the width of the same chimney inlet increased the flow rate and thermal efficiency until it maintained a constant value at an inlet width of 0.2m. The Investigation of a vertical rooftop solar chimney under varying inlet configurations was conducted numerically and experimentally by [8]. From the study, the inlet with the horizontal configuration under-predicted the air velocity, whereas the vertical configuration of the chimney produced the ultimate velocity. In another study by [9], the increase in the inclination of the angle of an incline solar chimney increases its flow rate for an angle from 0° to 90°. The ventilation rate in a rooftop solar chimney investigated by [10] increases as the solar radiation increases. However, the increase in the external wind speed had a negative impact on the ventilation rate, as the wind speed increased from 1.5 m/s to 6 m/s at a radiation of 900 w/m, the overall performance of the system was reduced by 25%. Both the geometric configuration and environmental condition of a solar chimney have been investigated extensively, however, there is limited or no report on a non-absorbent solar chimney's performance, also the investigation of wind blowing directly into the outlet of the chimney is yet to be studied. This present work endeavours to investigate the performance of a solar chimney that doesn't utilise an absorber. The impact of blowing wind into the outlet and the outlet tilt angle of the chimney are studied for the first time to the best of the author's knowledge.

MODEL DESCRIPTION

The installed chimney on top of building 9 at the Egypt-Japan University of Science and Technology (E-JUST) campus, located in Alexandria, Egypt, with a latitude of 32°N. It has a rectangular cross-section and consists of a 14 mm diameter laminated glass cover inclined along its walls to receive solar radiation from all directions and transmit it to the air in the channel. Unlike conventional solar chimneys, the chimney does not use an absorber plate. Instead, it is completely made of glass with a 25 mm diameter stainless steel pipe, which serves as the connecting point between the glass and the concrete wall for structural support. The top of the chimney is covered with an Aluminium cover which is used to enhance ventilation and control of the internal environment. Both the inlet and the outlet are located at the bottom and the sides of the chimney from the outside (along the wall) and within the building respectively (on each floor). It has a total of five inlets, with two inlets on both the first and second floors with a dimension of 0.72 m×0.72 m while the vertical distance from each inlet to the next floor is 2.292 m, thus the height of each floor in the building is 3.012 m. The ground floor has its inlet from the bottom, therefore, promoting natural ventilation as the warm air within the channel rises and exits at the outlets. The chimney features 120 outlets on all four sides, covered with glass at varying inclination angles. The chimney consists of angles ranging from 5° to 75°. Unlike glasses at 5°, the rest of the glass arrangement moving upward from 15° to 75° has an angle of 15° intervals. The outlet with the inclination angle, of 75° is located at the highest height, thus the outlet with the maximum opening. In contrast, the outlet with the inclination angle, of 5° is placed at the lowest level, therefore the outlet with the smallest opening. The chimney has a huge gap of 3.30 m and a total height of 7.3 m, thus having a gap-to-height ratio of 0.45 m. A 2-dimension drawing of the model of the chimney described above was drawn in ANSYS Design Modeler to assess the model's performance through simulation. All descriptions and dimensions mentioned before were considered except that the number of inlets and outlets was reduced and the 5° incline glasses were assumed to be at an angle of 90°. Fig. 1a presents the physically installed chimney while Fig. 1b is the model design in Solidworks.

(a)

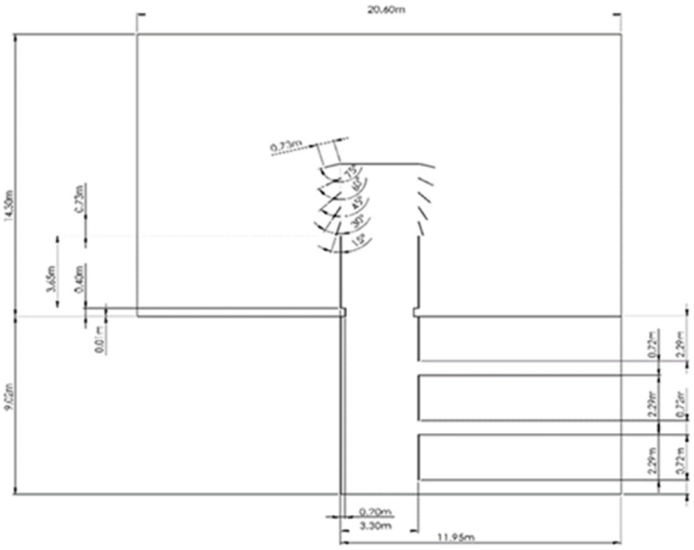

(b)

FIGURE 1. (a) Installed Solar chimney (b) model design in Solidworks

METHODOLOGY

This research focuses on analyzing the airflow rate of a non-absorbent-based solar chimney with an emphasis on the outlet configuration of the chimney. As a novel design, the major configuration of the chimney outlet is based on its inclination angle and the number of openings at a specified wind speed. To assess the real impact of wind on the chimney performance, the wind is assumed to be normal to the outlet of the chimney.

Governing Equation

The following assumptions were considered during the simulation of the solar chimney in ANSYS FLUENT.

i. 2-D and steady flow
ii. The air is considered incompressible
iii. All walls, unlike the chimney, are considered adiabatic
iv. The Boussenisq approximation is used to account for density variation.
v. Heat loss from the glass walls is neglected

vi. No slip boundary condition is applied to all solid zones.

The Navier –Stroke equations that govern an incompressible Steady two-dimensional flow were employed to solve the above model. The following equations, Continuity equation (1), Momentum equation (2) and Energy equation (3) were solved in ANSYS FLUENT SOFTWARE, Academic version 2020R2. To model the impact of the buoyancy within the chimney the Boussenisq approximation was used [11]. As shown in equation (4), the Boussenisq approximation is valid only for a small temperature change, thus it's temperature dependent.

Continuity equation:

$$\frac{\partial(u)}{\partial x}+\frac{\partial(v)}{\partial y}=0 \tag{1}$$

Momentum equations:

$$p(u\frac{\partial u}{\partial x}+v\frac{\partial u}{\partial y}=-\frac{\partial p}{\partial x}+\mu(\frac{\partial u}{\partial x}+\frac{\partial u}{\partial y})+S_X, \tag{2}$$

$$p(u\frac{\partial u}{\partial x}+v\frac{\partial u}{\partial y}=-\frac{\partial p}{\partial x}+\mu(\frac{\partial v}{\partial x}+\frac{\partial v}{\partial y})+S_Y,$$

Energy equation: The air thermal properties are assumed to be constant under a minimal increase in the system temperature, thus the heat transfer can be modelled from the energy equation [8].

$$pCp(u\frac{\partial T}{\partial x}+v\frac{\partial T}{\partial y})=-K(\frac{\partial^2 T}{\partial x^2}+\frac{\partial^2 T}{\partial y^2}) \tag{3}$$

Boussinesq approximation:

$$\rho-\rho_o=\rho_o\beta(T-T_o) \tag{4}$$

Where, p is the statics pressure, u and v are the velocity in the x and y directions respectively, and S is the source term in both the X and Y momentum, and are the density and the reference density, μ is the air viscosity. At the same time, T and K are the temperature and air thermal conductivity, respectively.

Boundary Condition

The boundary condition of CFD simulation plays a significant role in the accuracy of the simulation result. Therefore, to accurately predict the result of the model, the boundary condition must be correctly defined. In this study, atmospheric pressure was applied at the inlet of the building's three openings, one for each floor. To assess the impact of the blowing wind on the solar chimney performance, the wind was applied to the upper right of the computation domain in the direction normal to the channel outlet, right above the third floor. The domain's upper left and top sections were subjected to outlet pressure boundary conditions. To model the thermal boundary condition at the glass surfaces, the average solar irradiance of 500 W/m², for New Borg El Arab, was considered throughout the study. The absorptivity of the glass (α_g), and the aluminium cover (αac) are 0.5, and 0.96 respectively, while the transmissivity of the glass (τ_g) is 0.4. Volumetric heat generation rate (Q) has been used in previous studies to simulate a traditional solar chimney to enhance its performance [11]. In this study heat generation rate was applied to, the aluminium cover, and the glass surfaces, both the aluminium cover and the glass have a thickness (t) of 0.014 m. The heat generated by the glass and the aluminium cover is calculated from equations 5 to 7. The properties of the materials used are shown in Table 1.

Aluminium cover heat generation rate:

$$Q_{al}=\frac{G\times\alpha_a}{t} \tag{5}$$

Right glass heat generation rate:

$$Q_r=\frac{G\times\alpha_r}{t} \tag{6}$$

Left glass heat generation rate:

$$Q_l = \frac{G \times \alpha_l \times \tau_g}{t} \tag{7}$$

Q is the heat generation rate, α and τ are the glass absorptivity and transmissivity, respectively. While G is the solar radiation and t is the glass thickness.

Mesh and Computational Domain

The air channel was enclosed with a computational domain to allow the flow to adapt to the environment as suggested by [12]. Unlike the computational domain used in other studies, the computational domain as shown in Fig. 2. Coincides with the inlet of the attached building. The air channel and the extended computational domain used an unstructured triangular mesh. The mesh was refined on all walls within the air channel to capture the flow at the thermal boundary layers. As shown in Fig. 3. A Grid Independence Test (GIT) was conducted for four different mesh sizes. Increasing the mesh from 480000 to 530000 did not contribute to any significant difference in the volumetric flow rate. Thus, the case with 480000 was selected for this simulation to save the computational cost. A detail of the selected mesh used in this paper is shown in Table 2. Shown in Table 3 is the result obtained from the Grid Independence Test (GIT).

TABLE 1. Material Properties

Materials	**Density (kg/m³)**	**Thermal Conductivity [W/(m K)]**	**Heat Capacity [J/(kg K)]**
Air	1.225	0.0242	1006.43
Glass	2220	1.15	830
Aluminium	2719	202.4	871

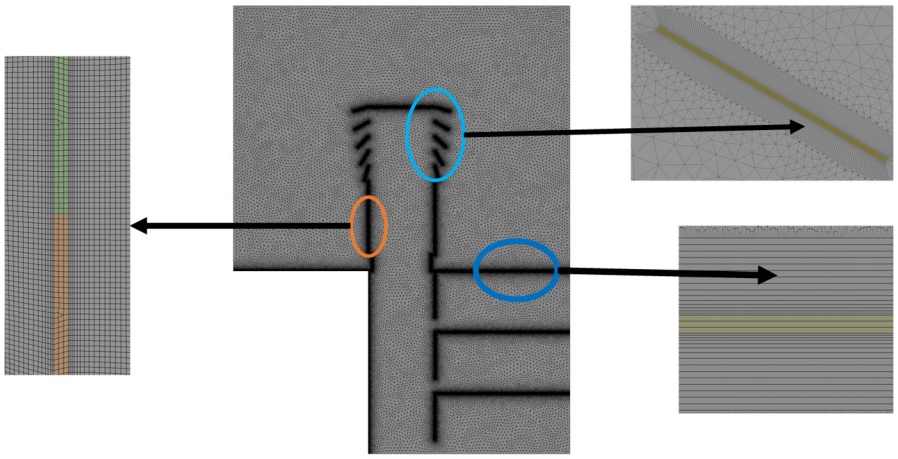

FIGURE 2. Mesh and Computational Domain

TABLE 2. Mesh Properties

Meshing Method	**Triangular**
Element Size	5mm
First layer thickness	1.5mm
Elements	483357
Nodes	427709

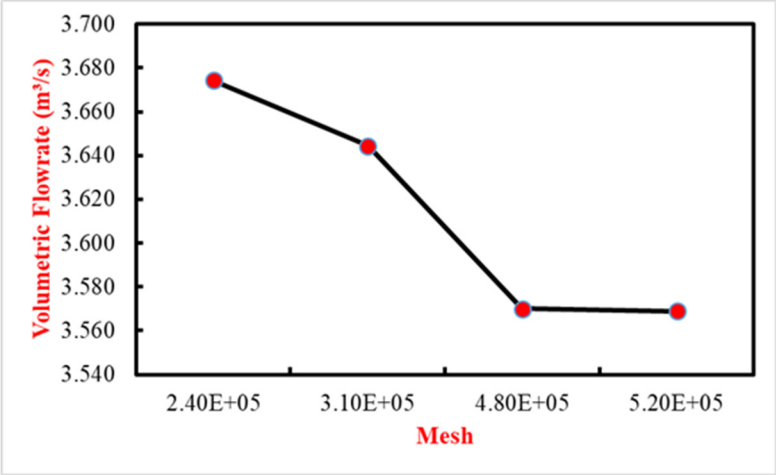

FIGURE 3. Grid Independence Test

TABLE 3. Grid Independence Test (GIT) Results

Resolution	Elements	Volumetric flow rate (m^3/s)
1	240000	3.674
2	310000	3.665
3	480000	3.570
4	520000	3.569

Numerical Scheme

Ansys fluent software, academic version 2020R2 was used to solve the model. The RNG, k-ε (k-epsilon) turbulent model was adopted in this study to predict the volumetric flow rate for this model. The selected turbulent model has previously been used in previous studies [13] to predict the flow rate of a solar chimney. Pressure-velocity coupling was employed to solve both the momentum and continuity equations. The PRESTO method for interpolating the pressure on the staggered mesh was adopted in the numerical setup. A Second-order Upwind scheme for the turbulent kinetic energy (k) and the rate of dissipation of turbulent kinetic energy (ε) and a second-order Upwind scheme for both the momentum and energy equations were employed. The residual was set to 10^{-5} for all cases except for the continuity equation which was set to 10^{-4}.

Model Validation

The model was validated against the experimental and numerical works of [14] and [13] respectively. In the reference study, the model had a height of 1.05 m and an air gap of 0.04 m. To validate the experiment, a uniform heat flux of 400 W/m² to 1000 W/m² was applied to predict the mass flow rate. Fig. 4. Indicates the mass flow rate results versus heat input obtained in this study against the reference cases. A good agreement is seen for all cases, with a deviation of 9.0% between the present numerical work and the experimental model.

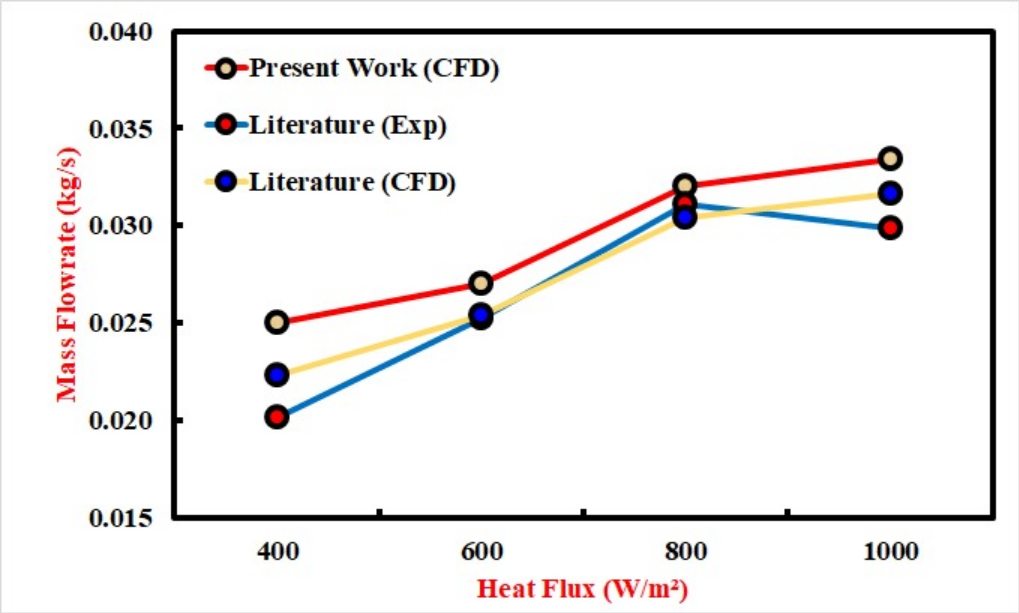

FIGURE 4. Variation of the mass flow rate heat flux, for the experimental [14] and the numerical model [13]

RESULT AND DISCUSSION

The chimney is investigated throughout the study with a fixed gap-to-height ratio, as the variation of the chimney height and gap is beyond the scope of this study. Constant solar radiation is considered to calculate the heat generated by the chimney glass and aluminium covers throughout this study. The volumetric flow rate and air velocity variation at the throat of the chimney and the attached building were examined at variable external wind velocity applied normal to the chimney outlet from the right, and the impact of the tilt angle and the number of openings of the chimney outlet.

Effect of External Wind Velocity

The base case configuration of the solar chimney is tested under the condition of variable external wind velocity at the outlets of the solar chimney. As shown in Fig. 5a. Increasing the wind external velocity initially from 0m/s to 0.5 m/s increases the volumetric flowrate at all inlets, however, a further increase in the blowing wind into the chimney from the outlet disrupts the buoyancy effect within the channel and reversed flow begins to occur as the wind speed approaches 2 m/s. The inlet with the best overall performance in the base case configuration is inlet 1, this is due to its distance away from the blowing wind at the outlet while the third inlet had the worst performance, with a strong reverse flow of -0.07 m^3/s for the wind velocity beyond 0.5 m/s. Fig. 5b. displays the velocity distribution within the channel, as the wind speed increases, a similar trend is observed for all cases of wind velocity. In all cases, a maximum velocity is reached as the air entering from all inlets converges closer to the left wall and then begins to decrease as the air moves away from the left wall. However, it's important to note that increasing the wind velocity up to 2 m/s causes a reduction in the velocity closer to the left wall by 13.5%. Another reason for the reduction in the velocity distribution could be due to the overpowering of the buoyancy effect by the strong wind blowing directly into the chimney from the outlet, thereby increasing the reverse flow at the inlets. Presented in Fig. 6 is the velocity contour for both the minimum and maximum external wind speeds of 0 m/s (Fig. 6a) and 2 m/s (Fig. 6b) for the result discussed in Fig. 5.

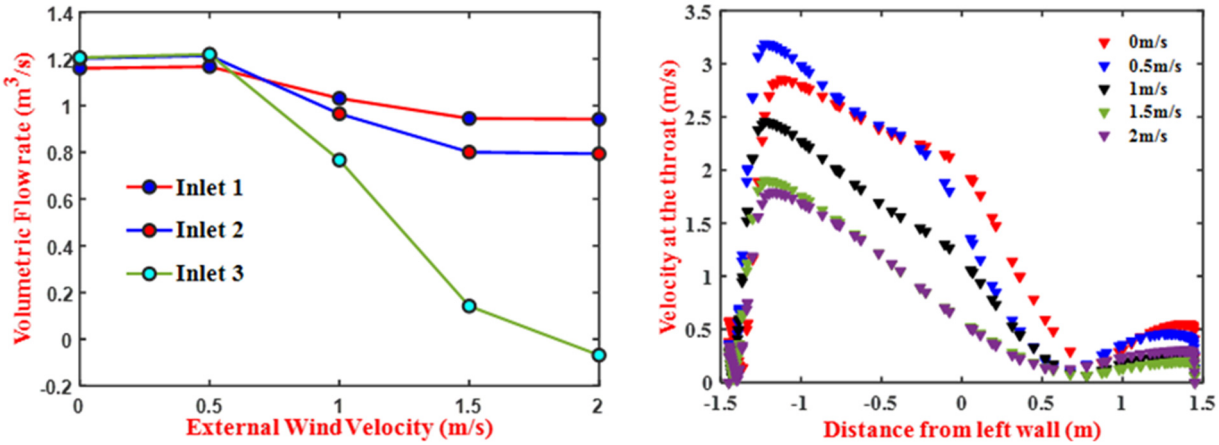

(a) (b)

FIGURE 5. Base Case (a) Volumetric Flowrate (b) Velocity Distribution

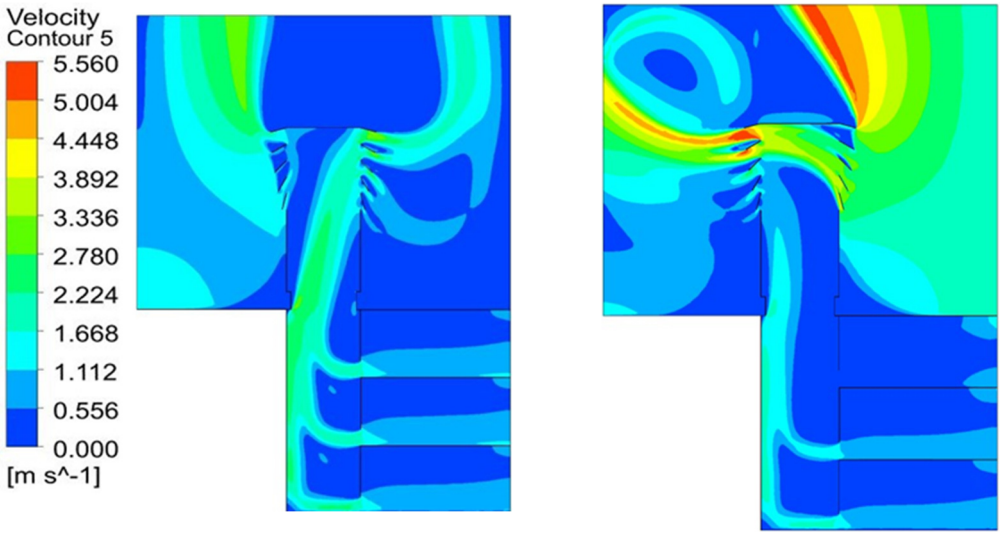

(a) (b)

FIGURE 6. Base Case velocity contours: (a) 0 m/s and (b) 2 m/s

In the reverse case configuration, the opening of the chimney outlets is changed with the maximum opening at the bottom while the lowest was placed at the top. Similar to the result presented in Fig. 5a. as the wind speed increases the flow rate increases and then reaches a point at which it begins to decline. Despite the reduction in the flow rate in the reverse case, there is no negative flow rate observed. This is due to the size of the opening at the top because the wind blowing towards the minimum opening at the top met resistance due to the tilt angle of the glass. The huge magnitude of the air begins to flow above the chimney instead of entering the channel at a higher external wind speed. The flow rate and velocity plots of the reverse case are presented in Fig. 7a and 7b respectively. The volumetric flow rate for both inlet 2 and inlet 3 reaches a maximum value at a lower wind speed and declines drastically at a higher wind speed. However, when the wind speed increased beyond 0.5 m/s, inlet 1 achieved the best performance. The maximum average velocity of 1.012 m/s, at the throat was achieved when the buoyancy effect within the chimney was stronger than the external wind speed of 0 m/s to 0.5 m/s, as shown in Fig. 7b. Illustrated in Fig. 8a and Fig. 8b, is the velocity contour for the minimum and maximum external wind velocity of 0 m/s and 2 m/s for the velocity plot shown in Fig. 7b.

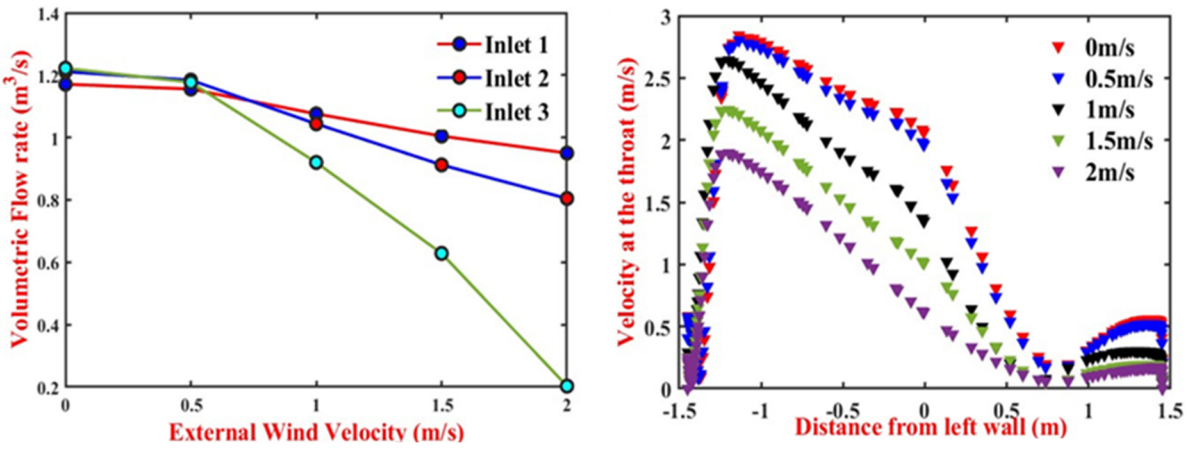

(a) (b)

FIGURE 7. Reverse Case (a)Volumetric Flowrate (b)Velocity Distribution

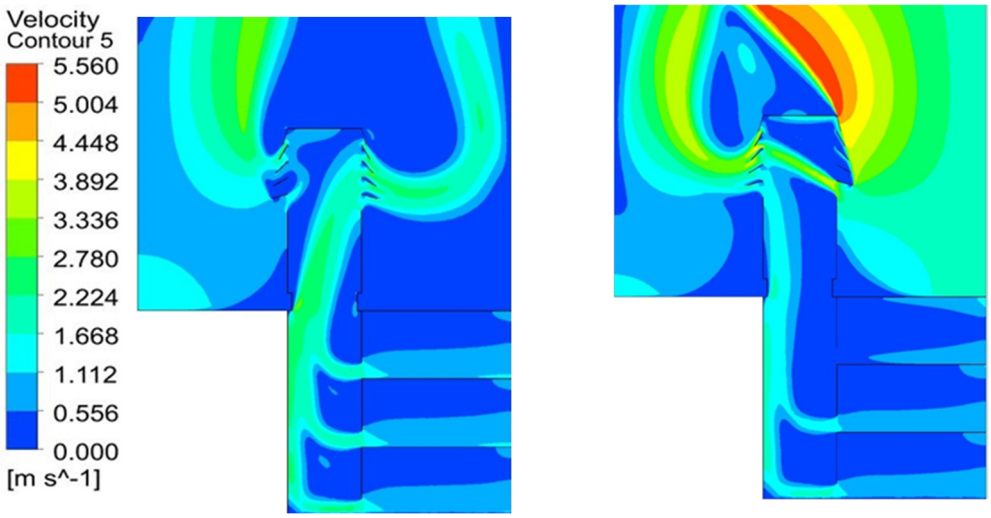

(a) (b)

FIGURE 8. Reverse Case velocity contours : (a) 0 m/s and (b) 2 m/s.

Comparison of Net Flow Rate

The net volumetric flow rate obtained from both the base case and the reverse case is presented in Fig. 9. In both cases, the volumetric flow rate increases as the wind speed increases from 0 m/s to 0.5 m/s. Also, the maximum flow rate achieved by the chimney in all cases is 3.6 m^3/s. This indicates that the overall effect enhances the flow rate even when the wind opposes the chimney exit velocity. It is observed that both the base and reverse cases had a similar trend. There is a reduction in both cases as the wind blowing into the chimney outlet is subjected to a further increase in the wind velocity above 0.5 m/s, which is caused by the occurrence of reverse flow. It is important to note that the decrease in the flow rate for the base case reduces drastically due to the large outlet openings located at the top which induces more wind into the chimney thereby pulling the hot air back into the building at a higher wind speed. The same decreasing trend is noticed in the reverse case, but this reduction of the flow rate is less compared to the base case, this behaviour is due to the placement of the largest opening of the outlet at a lower height along the chimney wall. This configuration, reduces the amount of wind entering the outlet due to the low tilt angle at the top which prevents a huge percentage of the external wind from directly blowing into the chimney. Despite this steady reduction in reverse case configuration, its overall performance is better than the base case.

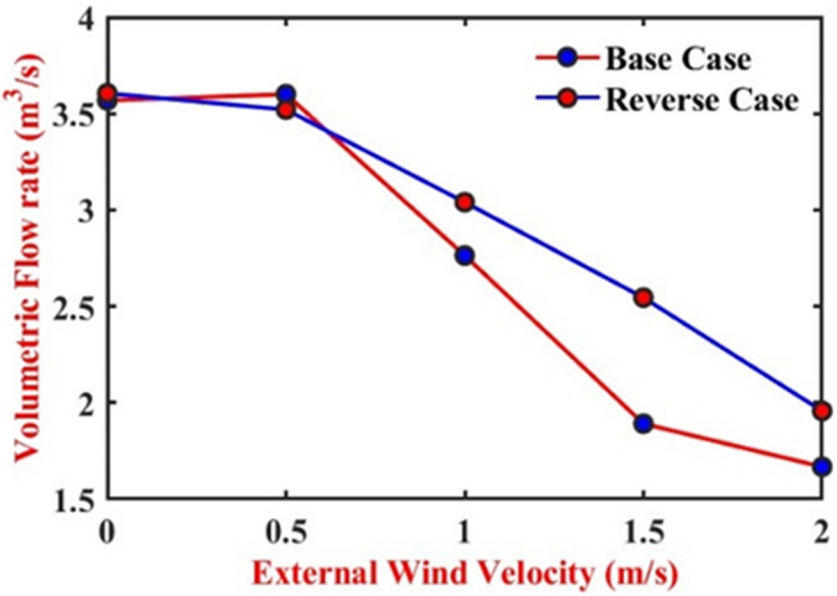

FIGURE 9. Net flow rate for both cases

CONCLUSION

The main objective of this work was to investigate the impact of the external wind and outlet tilt angle. The number of outlet openings on the ventilation performance and velocity distribution of a novel solar chimney design. The findings presented in this work show that the most influencing factor on the air velocity at the throat of the chimney and the chimney ventilation rate was the external wind velocity. The flow rate increases at a lower velocity and decreases at a higher velocity. The result presented for both the base and reverse case reveals that the reverse case had the best overall performance regardless of the flow reversal at higher wind speed. The number of openings and tilt angle also had a significant influence on the chimney performance. The optimal value of the wind under which there was no occurrence of reverse flow for all configurations was from 0 m/s to 0.5 m/s. beyond this external wind speed, a flow reversal begins to occur in all cases. The inlet that contributed the maximum ventilation rate throughout the study was the first inlet due to its distance away from the incoming wind while the third inlet had the worst performance.

ACKNOWLEDGEMENT

Thanks to the Egypt-Japan University of Science and Technology (E-JUST) and the Egypt Ministry of Higher Education (MoHE) through the TICAD 7 Scholarship for providing me with the facilities to undertake this research work.

REFERENCES

1. F. Johari, G. Peronato, P. Sadeghian, X. Zhao, and J. Widén, Renew. Sustain. Energy Rev. **128**, (2020).
2. Z. Liu, X. Zhang, Y. Sun, and Y. Zhou, Energy Build. **297**, 113436 (2023).
3. H. Zhang, Y. Tao, and L. Shi, Encyclopedia **1**, 409 (2021).
4. H.M. Maghrabie, M.A. Abdelkareem, K. Elsaid, E.T. Sayed, A. Radwan, H. Rezk, T. Wilberforce, A.G. Abo-Khalil, and A.G. Olabi, Sustain. Energy Technol. Assessments **52**, 102082 (2022).
5. J. He, Y. Cai, X. Huang, B. Hong, and F. Zhao, **03051**, (2022).
6. H. Zhang, Y. Tao, G. Zhang, J. Li, S. Setunge, and L. Shi, Energy **261**, 125200 (2022).
7. Y.Q. Nguyen and J.C. Wells, J. Build. Eng. **28**, 101050 (2020).
8. K.E. Amori and S.W. Mohammed, Energy Build. **47**, 450 (2012).
9. Z.D. Chen, P. Bandopadhayay, J. Halldorsson, C. Byrjalsen, P. Heiselberg, and Y. Li, Build. Environ. **38**, 893

(2003).
10. H.H. Al-Kayiem, S. K.v., and S.I.U.H. Gilani, Energy Build. **68**, 305 (2014).
11. J. Gong, K.X. Cheng, H. Liu, L.W. Chew, and P.S. Lee, Build. Environ. **224**, 109569 (2022).
12. J.. Nguyen, Y Q, Wells, (2019).
13. Y.Q. Nguyen, IOP Conf. Ser. Mater. Sci. Eng. **1109**, 012044 (2021).
14. S.A.M. Burek and A. Habeb, Energy Build. **39**, 128 (2007).

A Developed Trombe Wall as a Passive System for Residential Buildings: A Simulation Study

A. Abdelsamea[1,2, a)], H. Hassan[3,4], H. Shokry [1], T. Asawa[5] and H. Mahmoud[1,6]

[1] *Department of Environmental Engineering, Egypt-Japan University of Science and Technology, New Borg El-Arab City, Egypt.*
[2]*Department of Architecture Engineering, Faculty of Engineering, Assiut University, Assuit, Egypt.*
[3] *Department of Energy Resources, Egypt-Japan University of Science and Technology, New Borg El-Arab City, Egypt.*
[4]*Mechanical Power Engineering Department, Faculty of Engineering, Assiut University, Assiut, Egypt.*
[5]*Department of Architecture and Building Engineering, School of Environment and Society, Tokyo Institute of Technology,Yokohama, Japan.*
[6]*Department of Architecture Engineering, Engineering Faculty, Aswan University, Aswan, Egypt.*

[a)] Corresponding author: ahmed.abdelsamea@ejust.edu.eg

Abstract. The Trombe Wall (TW) is a sustainable passive design technique known for enhancing the thermal performance of interior spaces. Despite its effectiveness, its application remains limited, with most research focusing on single-zone implementations. This study aims to suggest a contemporary advance to the typical TW to be applied to multi-story residential buildings and investigate its impact on thermal performance. A two-stage simulation study was conducted on a proposed multi-story Trombe Wall (MSTW) system in a case study in a hot climate using DesignBuilder software. In the first stage, the thermal performance of the base case was compared with the proposed system (geometrical parameters were suggested as a start). Then, the proposed system geometrical parameters (depth and width) were optimized to achieve the optimum MSTW design. The results showed that the proposed MSTW design enhanced indoor thermal performance by up to 1.6 °C increase during the heating period and up to 0.7 °C decrease during the cooling period, while also improving PMV values by 0.5 and 0.4, respectively. In addition, the indoor temperature increases with width and decreases with depth. The optimum MSTW depth-width values were 10 cm–375 cm and 70 cm–175 cm during winter and summer, respectively.

Keywords: passive design techniques; trombe wall; thermal comfort; building simulation.

INTRODUCTION

Ensuring thermal efficiency in indoor spaces is of utmost importance, particularly in light of pressing global environmental challenges such as global warming and the energy crisis. In recent years, there has been a significant rise in energy consumption rates, which depend mainly on fossil fuels, which have detrimental effects on the environment. Buildings are responsible for a substantial share of the world's energy consumption, particularly for cooling, heating, and lighting. To meet the ever-increasing demand for energy, there is an immediate and pressing requirement to implement sustainable methods that are more environmentally friendly and energy-efficient at both urban and building levels [1]. The adoption of the concepts of passive design is a practical approach to tackling these problems. Passive design exploits natural capabilities, such as sunlight, wind, and thermal mass, to decrease the necessity for mechanical HVAC systems, thereby reducing energy consumption and CO2 emissions [2]. These strategies also concentrate on optimizing the building's design and components to improve thermal and energy performance. There are many passive design strategies, including green roofs and facades [3], solar chimneys [4], shading systems [5], cool roof materials [6], and Trombe walls.

The Trombe Wall (TW) is an effective and sustainable design strategy for enhancing buildings thermal performance [7]. It is a passive solar system that harnesses solar energy to regulate indoor temperatures. In its typical design, TW consists of a thick, south-facing concrete wall and a glazing layer spaced a few inches apart from the wall [8]. This arrangement forms an air gap between the wall and the glass, allowing the sun's rays to pass through and be absorbed by the wall throughout the day. There are also four vents: two in the concrete wall and two in the glazing

Technologies and Materials for Renewable Energy, Environment and Sustainability
AIP Conf. Proc. 3321, 040015-1–040015-13; https://doi.org/10.1063/5.0289837
Published under an exclusive license by AIP Publishing. 978-0-7354-5231-2/$30.00

layer. These vents help control working modes during the summer and winter [9]. Figure 1 shows Vents scenarios and air directions over different seasons.

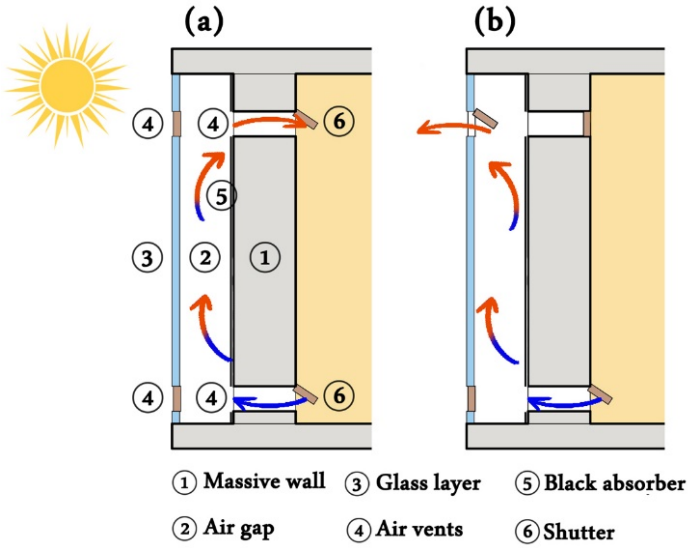

FIGURE 1. Vents opening scenarios during TW: (a) winter modes, (b) summer mode.

We can classify the factors affecting the Trombe Wall's performance into three groups. The first is related to environmental factors such as amounts of solar radiation, ambient temperature, and wind speed [10]. The second is related to TW component design and characteristics. Finally, other technologies are integrated with TW to enhance its performance and provide new functions. TABLE 1. shows a summary of TW environmental, design factors, and integration research.

Regarding environmental factors, Dragiûeviû examined the effects of different environmental factors, including solar radiation, wind velocity, and ambient temperature. The maximum efficiency was obtained at air velocity up to 2 m/s and solar radiation up to 600 W/m2 [11]. Oltarzewska and Krawczyk Conducted variations to the TW system across four locations under different weather conditions. The proposed system enables it to sustain thermal comfort for over 20% of the year [12]. Duan et al. studied the impact of solar radiation intensity on PCM Trombe wall performance in Mianyang (China). They were able to increase the temperature by 3.27 °C [13].

Various studies have examined the impact of enhancing the design of TW componants on its efficiency, particularly for heating applications. Abbas et al. studied the effect of air gap depth on the thermal performance of the Trombe wall system. The maximum indoor air temperature was achieved with an air gap width of 20 cm [14]. Another study was conducted to investigate the effect of different glazing ratios and kinds on TW thermal performance. The use of advanced glazing reduces the heating period by 48.8% and improves the comfort conditions by 23.9% [15]. Dabaieh and Elbably painted the massive wall gray and added two wool curtains and natural wool insulation. They improved design reduced heating demand by 94% and cooling demand by 73%, resulting in 53,631 kWh of annual savings [16]. Rabani tested a Trombe wall with three glazing sides and a narrow air gab. This design allows for the capture of solar radiation from three different orientations. He achieved a 6% increase in energy efficiency [17]. Bevilacqua et al. tested different hot and cold climate TW ventilation methods. Their heating and cooling loads decreased by 71.7% and 36.1% in warm climates and 18.2% and 42.4% in cold climates [7]. Abbassi and Dehmani studied different thicknesses for four massive wall materials. A reduction of 50% in heating loads was achieved with 34 and 32 cm of stone and concrete walls, respectively [18].

Concerning integrated technologies, several studies have aimed to enhance the performance of TW by integrating it with other techniques. Saadatian et al. identified nine different types of TW , which involve alterations in design and integrations with other technologies such as PCM, fins, blinds, photovoltaic cells, and evaporative cooling [9].

Utilizing PCM's latent heat energy in integration with TWs proved to be an efficient method to improve TW performance, where melting point temperature and thickness are the factors governing the efficiency of PCM. [19] utilized dual PCM layers and chieved up 0.93 °C reduction in summer temperature and up to 6.6 °C increase in winter

temperature. Li et al. determined that the optimal phase change temperature in Changsha, China, should be 7 °C lower than the maximum outdoor temperature in winter and 8 °C higher in summer [20].

Many studies have included fins. It is mostly attached to the concrete wall. Most of these studies focused on the fins' material, height, and spacing. Copper fins were found to be the most effective. It increased heat transfer through convection by 6% [21]. Wu et al. achieved the best thermal performance when the fin height was 0.75 m and the spacing was 0.06 m [22]. Also, Integrating Blinds can help regulate air movement and solar radiation [23]. They are usually placed in the middle of the air gab. The blind angle has a significant imact. [24] acheaved maximum thermal efficiency at a 45° blind angle.

Many studies have been conducted to integrate photovoltaic cells with the Trombe wall to add another value for electricity generation, with some placing the cells adjacent to the concrete wall [25], others integrating them with the glazing layer [26], and some placing them in the air gap [27]. Various types of photovoltaic cells were used, such as monocrystalline [28] and polycrystalline [29]. studies have reached thermal efficiency levels of 74.4% and energy efficiency of 13.9% [30].

TABLE 1. References for TW Environmental, design factors, and integration research.

Reference	Location	Method	Factors	Results	Heating/ Cooling	Study level	Factor Type
[11]	(Serbia)	N	solar radiation, wind velocity	2 m/s and 600 W/m2 obtained maximum efficiency.	H	Single room	Envirnmental factors
[12]	Five different locations	S	climatic conditions for 4 locations	20% of the year in thermally comfortable conditions.	H & C	Single room	
[13]	Mianyang (China)	N & E	PCM and solar radiation	Increase the temperature by 3.27 °C.	H	Single room	
[14]	Kirkuk (Iraq)	S	air gap width	maximum temperature at 20 cm air gap width.		Single room	Design parameters
[15]	Tabriz (Iran)	N - S	Glazing	reduces the heating period by 48.8% and improves the comfort conditions by 23.9%.	H & C	Single room	
[17]	Yazd (Iran)	N - E	width & 3 sides glazing	Improve efficiency by 6%.	H	Single room	
[18]	(Tunisia)	S	Wall thickness	reduction by 50% in heating loads.	H	Single room	
[7]	Granada & Copenhagen & Pisa	S	ventilation strategies	decreased heating and cooling loads by 71.7%, 36.1% in warm climates, and by 18.2%, 42.4% in cold climates.	H & C	Single room	
[16]	Sinai (Egypt)	S-E	Wall paint & insulation	respectively , 94% and 73% reduced heating and cooling.	H & C	Single room	
[22]	-	N - E	Fin height - spacing.	Fins optimum height was 0.75 m, spacing was 0.06 m.	H	Single room	Integrated technologies
[27]	Hefei (China)	N & E	PV in the air gap	13.23% electrical efficiency, 36% thermal efficiency.	H	Single room	
[19]	Tianjin (China)	N - E	double PCM layers	0.4-0.93 °C decrease in summer and 0.3-6.6 °C increase in winter.	C & H	Single room	
[20]	Changsha (China)	N - E	melting temperature of PCM	PCM phase change temp. should be 7°C lower and 8°C higher than outdoor temp. in winter and summer.	C & H	Single room	
[28]	Kirkuk (Iraq)	N & E	PV on glazing level	9.2% electrical efficiency, 62.9% thermal efficiency.	H	Single room	
[21]	Yazd (Iran)	N - E	Fin materials	Improve convection by 6%.	H	Single room	

[23]	Hong Kong	N - S	temp. & solar radiation	5.8% energy savings.	C	Single room
[31]	Hefei (China)	N - E	Blinds angle, channel width	A big blind angle can reduce cooling energy.	C	Single room
[32]	Hefei (China)	N & E	PV blind	11.1% electrical efficiency, 46.8% thermal efficiency.	H	Single room
[25]	Izmir (Turkey)	N & E	PV on glazing level	4.52% electrical efficiency, 27.2% thermal efficiency.	H	Single room

Note: Simulation (S); Numerical (N); Experimental (E).

Despite the valuable contributions of previous studies, the use of TWs has been primarily confined to single-zone or single-space applications. This paper aims to suggest a contemporary advance to the typical TW to be applied to multi-story residential buildings and investigate its impact on the thermal performance of indoor spaces. A two-stage simulation study was conducted on a proposed multi-story Trombe Wall (MSTW) system in a case study in a hot climate using DesignBuilder software. In the first stage, the thermal performance of the base case was compared with the proposed system (geometrical parameters were suggested as a start). Then, the proposed system geometrical parameters (depth and width) were optimized to achieve the optimum MSTW design.

METHODOLOGY

A simulation study was conducted on a multi-story residential building in New Borg El-Arab city, Egypt. The modeling was built using DesignBuilder software. Then the model was calibrated using actual indoor temperature-measured data. Following that, a two-stage simulation was performed. In the first stage, we compared the thermal performance of the base case (without MSTW) with that of the proposed MSTW, suggesting a depth and width of 10 and 375 cm, respectively. Then, the proposed system geometrical parameters (depth-width) were optimized to determine the effect of depth-width changes on the thermal performance and to achieve the optimum MSTW design. Figure 2 illustrates the study methodology.

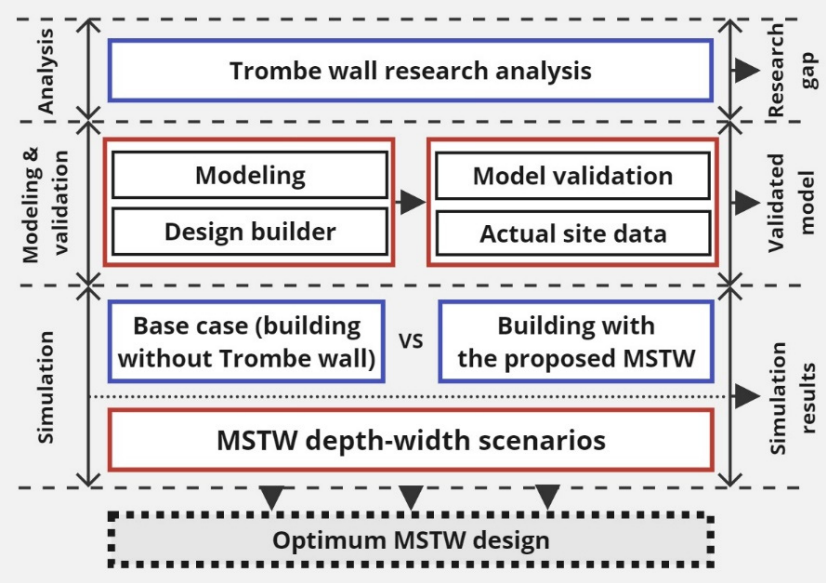

FIGURE 2. Research methodology.

Case Study Location and Description

As shown in Figure 3, the New Borg Elarab city is located in the governorate of Alexandria in northwest Egypt. By Köppen's classification, the city is located in Zone BWh, which describes its hot and dry desert climate. In January

and August, the temperatures reach their extremes. The chosen building is located in the Egyptian-Japanese University's residential compound. The compound includes 28 separate residential buildings with the same typical design, divided into two groups. As illustrated in Figure 4 , each building consists of five floors, with each floor containing four residential units. The building's exterior façade is presented in Figure 5.

(a) (b) (c)

FIGURE 3. (a) New Borg Elarab city location; (b) the Egyptian-Japanese University's residintial compound; (c) the selected residintal building.

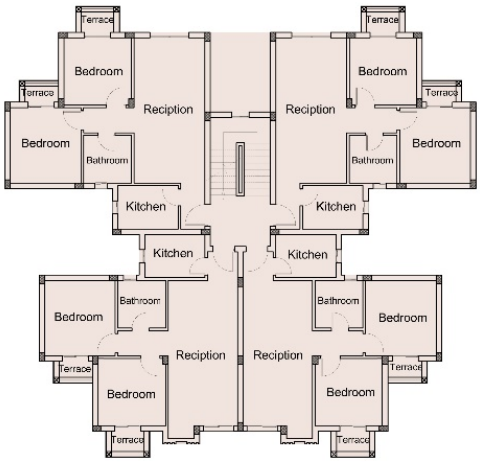

FIGURE 4. The typical floor plan.

FIGURE 5. The residential building façade.

Modeling and validation

The building design and features were accurately modeled. The building's location and orientation were determined. Construction materials, doors, windows, lighting, devices, timetables, and HVAC systems were all added according to the field survey. The building is constructed with a reinforced concrete structural system. The thickness of the exterior and interior walls is 25 cm and 12 cm, respectively, both made of red brick without thermal insulation. The walls have a 2 cm finishing layer of cement plaster and beige paint. Slabs are built of 12 cm reinforced concrete with a 10 cm finishing, while the windows are made of PVC and glass. Moreover, all rooms are considered to have only natural ventilation. In addition, the type of activity in each room was determined, as it affects body temperature and, consequently, the temperature of the room. Figure 6 presents the residential building model visualization in Design Builder.

The validation process seeks to ascertain the degree to which the outcomes generated by the simulation align with the actual conditions, as well as the degree to which the model accurately represents the performance of the building. The actual hourly temperature measurements in one of the ground floor bedrooms were compared with the simulation results for the same time period of 24 hours. The findings indicated that the average temperature variation was 1.43 °C, and the variation ranged between 0.77 and 1.63 °C. Therefore, it falls within the acceptable range [33].

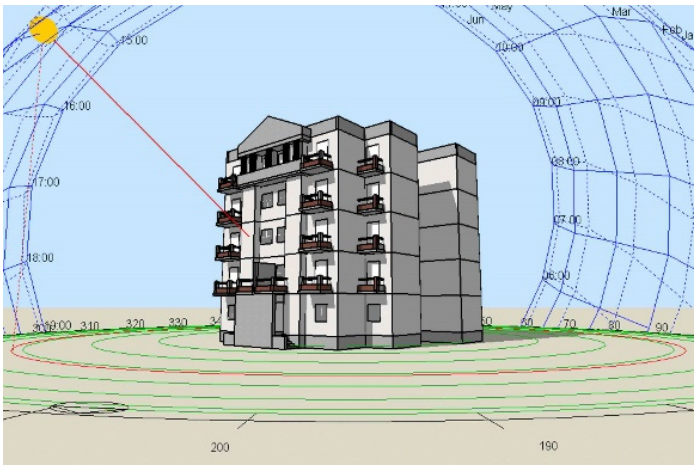

FIGURE 6. The residential building model**.**

MSTW Design and Simulation Scenarios

The proposed TW design has a multi-storey design integrated into the south-east façade, connected to the bedrooms, with a 375 cm width and 10 cm depth. The thickness of the concrete wall is 25 cm, with upper and lower vents on each floor equipped with shutters, and each vent is 0.25 m2. 6 mm of thermochromic glazing was utilized. This type of glass has the ability to respond to the level of solar radiation in both summer and winter operation modes [34]. In the winter mode, the vents in the massive wall are always open, whereas the vents in the glazing layer are closed. In the summer mode, the massive wall 's lower vents are opened and the upper vents are closed. The glazing layer's upper vent remains open. Also, the room window in the summer mode should remain open. We conducted the simulation for hourly temperatures and PMV values during a winter representative week (from February 3 to 10) and a summer representative week (from July 13 to 20). The predicted mean vote (PMV) assesses the user's thermal comfort on a scale of seven points, ranging from cold (-3) to hot (3), with zero being an optimal value, whereas recommended limits range from -0.50 to 0.5 [35]. Figure 7 shows the proposed MSTW summer and winter designs.

The proposed scenarios include five-width alternatives ranging from 175 to 375 cm, with 0.5-meter steps. In terms of depth, they provide five options ranging from 10 cm to 70 cm, with a step every 15 cm, for a total of 25 scenarios, as shown in Figure 8. We coded the names of the various spaces to display the depth (D) and the width (W) of the MSTW and the room's floor number (F), with their respective values following each variable. At the same time, the case without the Trombe wall is named (W), followed by the floor number.

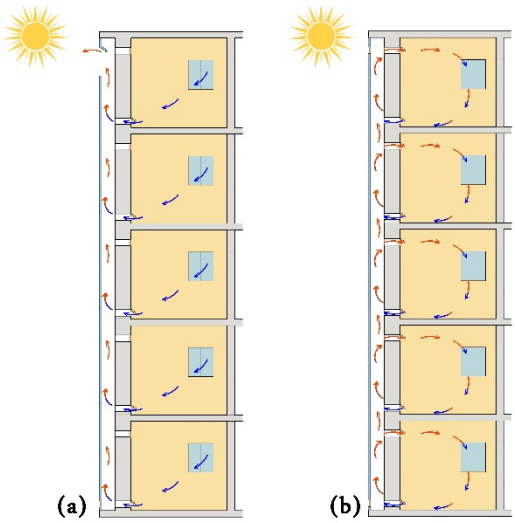

FIGURE 7. Proposed MSTW. (a) summer mode, and (b) winter mode.

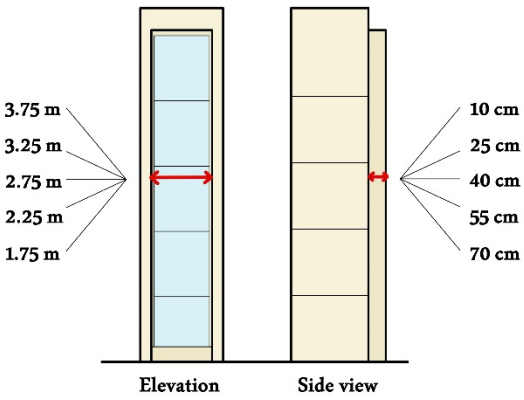

FIGURE 8. MSTW depth and width values.

RESULTS AND DISCUSSION

The indoor temperatures and PMV levels during a typical winter and summer weeks was evaluated. Regarding the winter mode, Figure 9 (a) shows the comparison of the base case (W3) after incorporating the suggested MSTW (D10W375F3). The implementation of the suggested system resulted in a significant rise in temperature levels throughout the day, with an increase up to 1.6 °C. The most pronounced temperature rise was observed between 4 p.m. and 12 a.m. The change can be ascribed to the operational concept of TW, which operates by absorbing and storing heat during the day and thereafter discharging it gradually throughout the night, thereby mitigating sharp temperature fluctuations. The temperature increase throughout the day ranges between 0.4 and 1.6 °C.

Figure 9 (b) illustrates the temperature comparison when the width of the MSTW was fixed at 375 cm, but the depth varied from 10 to 70 cm in increments of 15 cm. Based on the graph, it can be shown that all suggested depths result in a rise in temperature compared to the base case (w3). Nevertheless, it is worth mentioning that as the MSTW depth increases, the rate of temperature growth decreases. As a result, the MSTW with a depth of 10 cm has the highest rate of temperature increase and the best thermal performance during the winter period. Also, as shown in Figure 9 (c), all of the suggested widths had a temperature increase over the base case throughout the day, with the exception of 175 and 225 cm, which had temperatures less than or equal to the base case from 11 a.m. to 3 p.m. It is obvious that the broader the width, the higher the temperature, as the MSTW absorbs a greater amount of solar radiation. As a consequence, the 375 cm width had the maximum rate of temperature increase, making it the optimal width for winter mode.

Figure 9 (d) depicts a graph that compares the application of the optimal MSTW configuration in winter mode, with a width of 375 cm and a depth of 10 cm, to the base case over different floors. It is observed that the MSTW resulted in a significant enhancement of temperatures across all floors. In addition, Figure 9 (e) demonstrates the rise in PMV values seen throughout the day when implementing the MSTW. The increase in PMV values has reached 0.5. However, despite this enhancement, it is insufficient to bring the PMV values within the thermal comfort range.

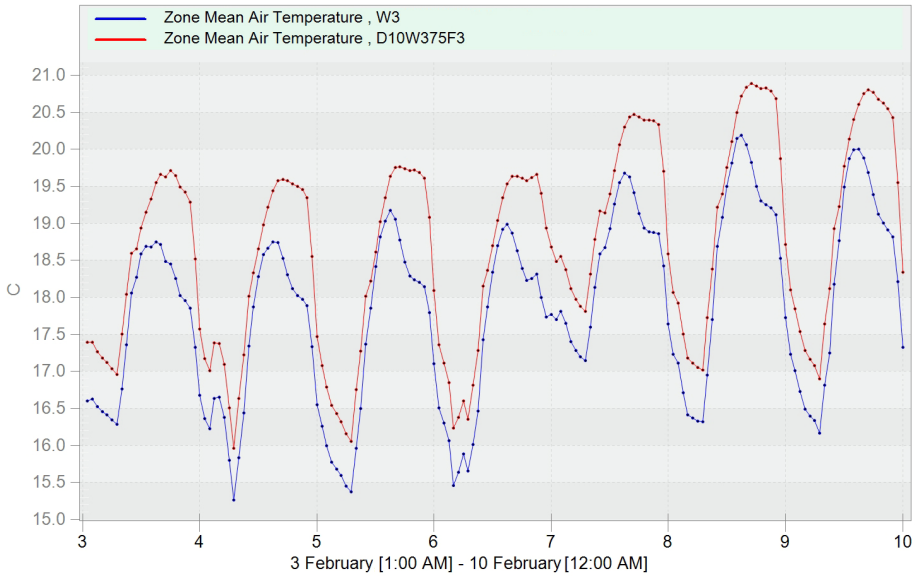

FIGURE 9 (a)

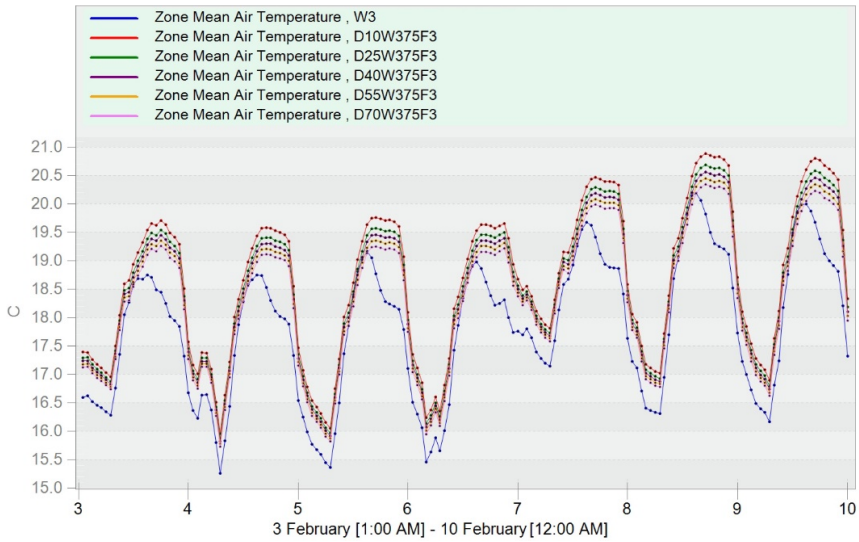

FIGURE 9 (b)

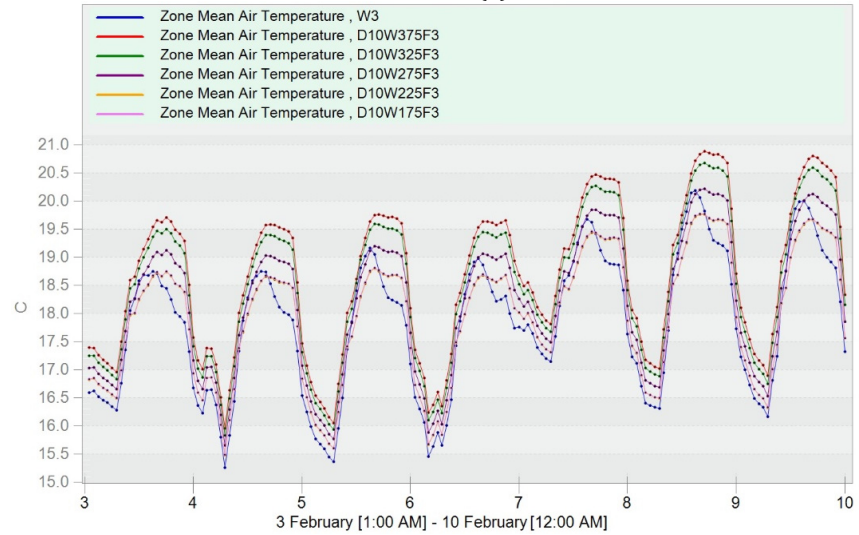

FIGURE 9 (c)

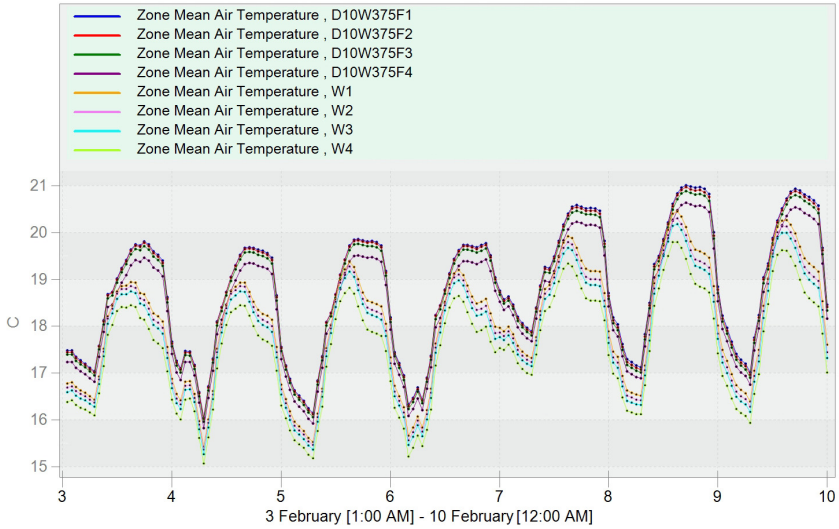

FIGURE 9 (d)

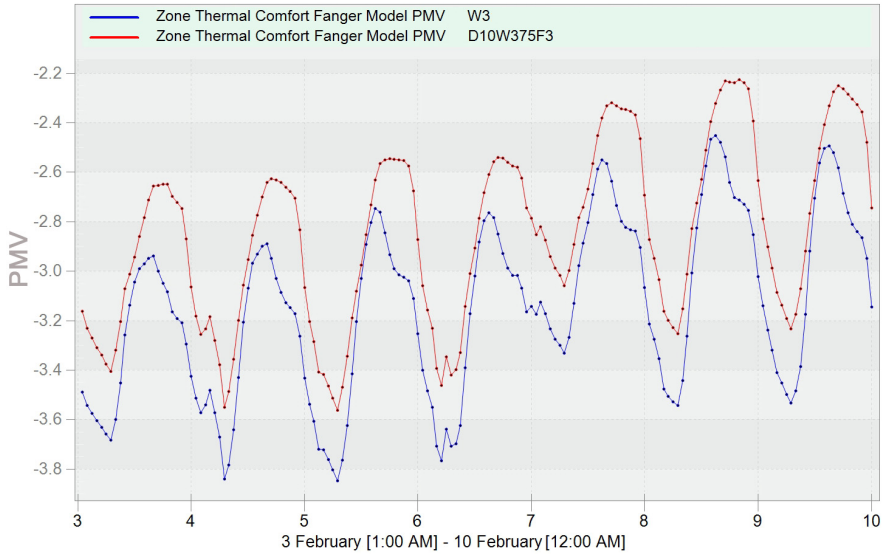

FIGURE 9 (e)

FIGURE 9. Simulation results for the base case scenario, the MSTW proposed system, and the system's various width and depth configurations for winter mode.

Regarding the summer mode, Figure 10 (a) shows the comparison of the base case (W3) after incorporating the suggested MSTW (D70W175F3). The lowest width (175) was chosen so that it receives the least amount of solar radiation. The implementation of the suggested system resulted in a significant reduction in indoor temperature throughout the day, with a decrease up to 0.7 °C. Figure 10 (b) illustrates the temperature comparison when the width of the MSTW was fixed at 175 cm, but the depth varied from 10 to 70 cm in increments of 15 cm. Based on the graph, it can be shown that all suggested depths result in a decrease in temperature compared to the base case (w3). Also, the MSTW with a depth of 70 cm has lower indoor temperature and the best thermal performance during the summer period. However, changing the depth had a tiny impact, though, since the largest decrease value between the largest and the smallest depths was 0.15 °C. As a result, the MSTW with a depth of 70 cm and a width of 175 cm has the highest rate of temperature decrease performance during the summer period.

Figure 10 (c), depicts a graph that compares the application of the optimal MSTW configuration in summer mode, with a width of 175 cm and a depth of 70 cm, to the base case over different floors. It is observed that the MSTW resulted in a significant enhancement of temperatures across all floors.

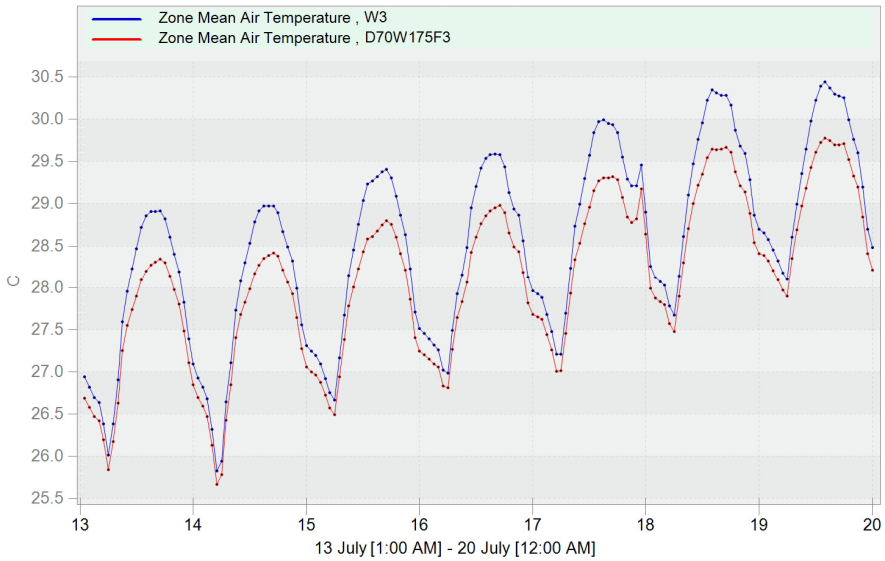

FIGURE 10 (a)

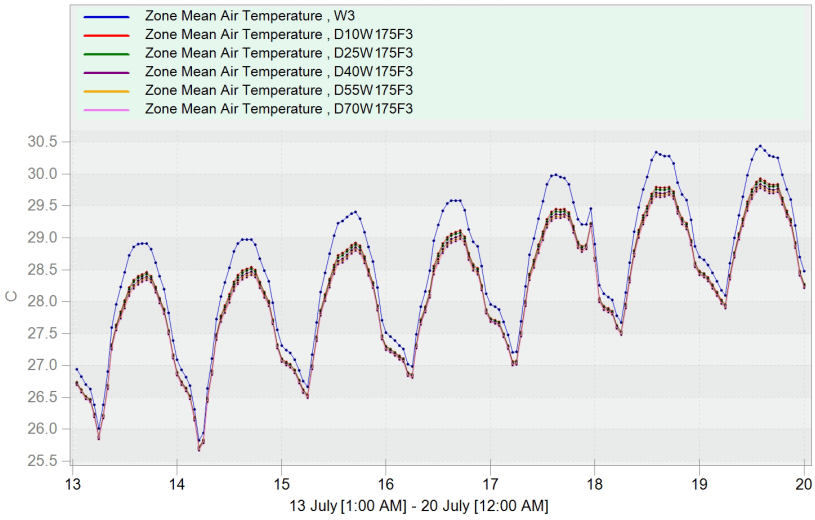

FIGURE 10 (b)

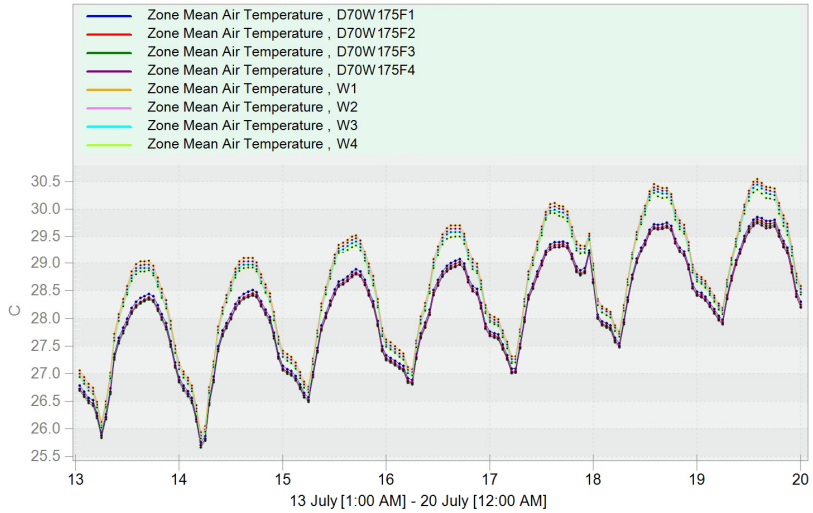

FIGURE 10 (c)

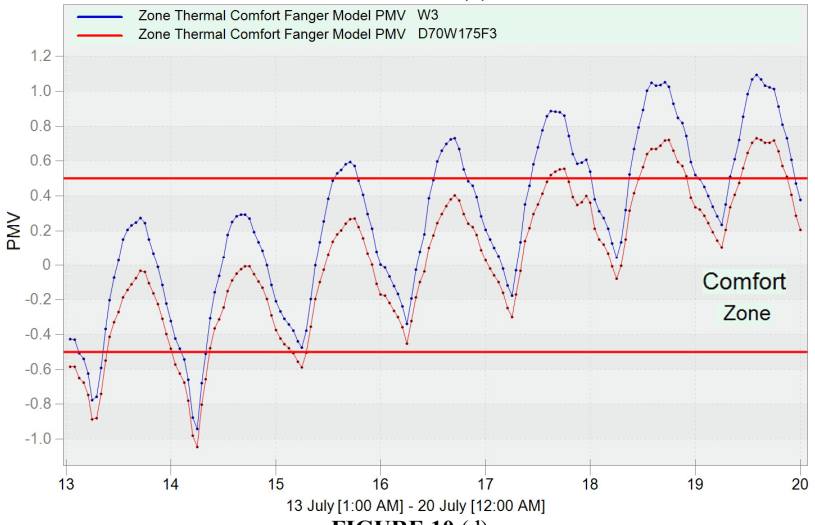

FIGURE 10 (d)

FIGURE 10. Simulation results for the base case scenario, the MSTW proposed system, and the system's various width and depth configurations for summer mode.

Concerning PMV values, Figure 10 (d) demonstrates a decrease in PMV values seen throughout the day when implementing the MSTW. The decrease in PMV values has reached 0.4. This decrease led to an increase in the number of hours of thermal comfort during the measurement period.

CONCLUSION

This study aims to suggest a contemporary advance to the typical TW to be applied to multi-story residential buildings and investigate its impact on thermal performance. A two-stage simulation study was conducted on a proposed multi-story Trombe Wall (MSTW) system in a case study in a hot climate using DesignBuilder software. In the first stage, the thermal performance of the base case was compared with the proposed system. Then, the proposed system geometrical parameters (depth and width) were optimized to achieve the optimum MSTW design. The results revealed that:

- The suggested MSTW system leads to a significant improvement in temperature and PMV levels throughout the day.
- The optimal MSTW depth and width are 70–175 cm during summer mode (cooling period) and 10-375 cm during winter mode (heating period).
- The proposed MSTW design enhanced indoor thermal performance by up to a 1.6 °C increase during the heating period and up to a 0.7 °C decrease during the cooling period.
- The proposed MSTW design improved PMV values by up to 0.5 and 0.4 during the heating and cooling periods, respectively.

Further studies are recommended to achieve more improvements to the proposed MSTW system using integration with other technologies or by optimizing its components.

ACKNOWLEDGMENTS

Ahmed Abd Elsamea reports that the Egypt Ministry of Higher Education Cultural Affairs and Missions Sector provided financial support (PhD funding grants).

REFERENCES

1. N. M. Waly, H. Hassan, R. Murata, D. J. Sailor, and H. Mahmoud, “Correlating the urban microclimate and energy demands in hot climate Contexts: A hybrid review,” *Energy and Buildings*, vol. 295, no. June, p. 113303, 2023, doi: 10.1016/j.enbuild.2023.113303.
2. D. K. Bhamare, M. K. Rathod, and J. Banerjee, “Passive cooling techniques for building and their applicability in different climatic zones—The state of art,” *Energy and Buildings*, vol. 198, pp. 467–490, 2019, doi: 10.1016/j.enbuild.2019.06.023.
3. M. E. Abdalazeem, H. Hassan, T. Asawa, and H. Mahmoud, “Enhancing energy efficiency in hot climate buildings through integrated photovoltaic panels and green roofs: An experimental study,” *Solar Energy*, vol. 270, no. February, p. 112419, 2024, doi: 10.1016/j.solener.2024.112419.
4. A. S. H. Abdallah, Y. Hiroshi, T. Goto, N. Enteria, M. M. Radwan, and M. A. Eid, “Parametric investigation of solar chimney with new cooling tower integrated in a single room for New Assiut city, Egypt climate,” *International Journal of Energy and Environmental Engineering*, vol. 5, no. 2–3, pp. 1–9, 2014, doi: 10.1007/s40095-014-0092-6.
5. R. M. Ahmad, Z. El-Sayed, D. Taha, H. Shokry, and H. Mahmoud, “An approach to select an energy-efficient shading device for the south-oriented façades in heritage buildings in Alexandria, Egypt,” *Energy Reports*, vol. 7, pp. 133–137, 2021, doi: 10.1016/j.egyr.2021.06.024.
6. Y. A. Basyouni and H. Mahmoud, “Affordable green materials for developed cool roof applications: A review,” *Renewable and Sustainable Energy Reviews*, vol. 202, no. June, p. 114722, 2024, doi: 10.1016/j.rser.2024.114722.
7. P. Bevilacqua, F. Benevento, R. Bruno, and N. Arcuri, “Are Trombe walls suitable passive systems for the reduction of the yearly building energy requirements?,” *Energy*, vol. 185, pp. 554–566, 2019, doi: 10.1016/j.energy.2019.07.003.
8. F. Stazi, A. Mastrucci, and C. Di Perna, “The behaviour of solar walls in residential buildings with different

insulation levels: An experimental and numerical study," *Energy and Buildings*, vol. 47, pp. 217–229, 2012, doi: 10.1016/j.enbuild.2011.11.039.
9. O. Saadatian, K. Sopian, C. H. Lim, N. Asim, and M. Y. Sulaiman, "Trombe walls: A review of opportunities and challenges in research and development," *Renewable and Sustainable Energy Reviews*, vol. 16, no. 8, pp. 6340–6351, 2012, doi: 10.1016/j.rser.2012.06.032.
10. K. Sergei, C. Shen, and Y. Jiang, "A review of the current work potential of a trombe wall," *Renewable and Sustainable Energy Reviews*, vol. 130, no. May, p. 109947, 2020, doi: 10.1016/j.rser.2020.109947.
11. S. Dragiûeviû, "Influence of constructive and operating parameters on a modified Trombe wall efficiency," vol. XI, no. 4, 2011, doi: 10.1016/S1644-9665(12)60080-6.
12. A. Oltarzewska and and D. A. Krawczyk, "Trombe Walls – Characteristic , Overview and Simple Case Study for Different Climate Conditions Trombe Walls – Characteristic , Overview and Simple Case Study for Different Climate Conditions," pp. 0–9, 2021, doi: 10.1088/1755-1315/943/1/012027.
13. S. Duan, L. Wang, Z. Zhao, and C. Zhang, "Experimental study on thermal performance of an integrated PCM Trombe wall," *Renewable Energy*, vol. 163, pp. 1932–1941, 2021, doi: 10.1016/j.renene.2020.10.081.
14. E. F. Abbas, A. Al-Abady, V. Raja, H. A. Z. AL-Bonsrulah, and M. Al-Bahrani, "Effect of air gap depth on Trombe wall system using computational fluid dynamics," *International Journal of Low-Carbon Technologies*, vol. 17, no. June, pp. 941–949, 2022, doi: 10.1093/ijlct/ctac063.
15. A. Pourghorban and H. Asoodeh, "The impacts of advanced glazing units on annual performance of the Trombe wall systems in cold climates," *Sustainable Energy Technologies and Assessments*, vol. 51, no. January, p. 101983, 2022, doi: 10.1016/j.seta.2022.101983.
16. M. Dabaieh and A. Elbably, "Ventilated Trombe wall as a passive solar heating and cooling retrofitting approach; a low-tech design for off-grid settlements in semi-arid climates," *Solar Energy*, vol. 122, pp. 820–833, 2015, doi: 10.1016/j.solener.2015.10.005.
17. M. Rabani, "Experimental comparison of energy and exergy analysis of a new designed and a Normal Trombe wall," *Energy*, vol. 260, no. March, p. 125050, 2022, doi: 10.1016/j.energy.2022.125050.
18. F. Abbassi and L. Dehmani, "Optimum Trombe wall thickness in the Mediterranean Tunisian context : An energetic and economic study," no. March, pp. 2930–2939, 2022, doi: 10.1002/ese3.1179.
19. X. Kong, J. Li, M. Fan, W. Li, and H. Li, "Study on the thermal performance of a new double layer PCM trombe wall with multiple phase change points," *Solar Energy Materials and Solar Cells*, vol. 240, no. June 2021, p. 111685, 2022, doi: 10.1016/j.solmat.2022.111685.
20. J. Li *et al.*, "Thermal comfort in a building with Trombe wall integrated with phase change materials in hot summer and cold winter region without air conditioning," *Energy and Built Environment*, no. April, 2022, doi: 10.1016/j.enbenv.2022.07.007.
21. M. Rabani and M. Rabani, "Heating performance enhancement of a new design trombe wall using rectangular thermal fin arrays: An experimental approach," *Journal of Energy Storage*, vol. 24, no. May, p. 100796, 2019, doi: 10.1016/j.est.2019.100796.
22. S. Y. Wu, H. Zheng, L. Xiao, and Y. Xiang, "Experimental investigation on the impact of fin structure factors on the finned-Trombe wall thermal performance," *Journal of Building Engineering*, vol. 70, no. March, p. 106402, 2023, doi: 10.1016/j.jobe.2023.106402.
23. X. Hong, M. K. H. Leung, and W. He, "Effective use of venetian blind in Trombe wall for solar space conditioning control," *Applied Energy*, vol. 250, no. May, pp. 452–460, 2019, doi: 10.1016/j.apenergy.2019.04.128.
24. S. Hei, H. Zhang, and W. Pan, "A Novel Combined Trombe Wall System for Village Houses in Cold Regions of China," *Journal of Thermal Science*, vol. 30, no. 6, pp. 2254–2266, 2021, doi: 10.1007/s11630-021-1509-1.
25. B. K. Koyunbaba, Z. Yilmaz, and K. Ulgen, "An approach for energy modeling of a building integrated photovoltaic (BIPV) Trombe wall system," *Energy and Buildings*, vol. 67, pp. 680–688, 2013, doi: 10.1016/j.enbuild.2011.06.031.
26. N. Islam, K. Irshad, M. H. Zahir, and S. Islam, "Numerical and experimental study on the performance of a Photovoltaic Trombe wall system with Venetian blinds," *Energy*, vol. 218, p. 119542, 2021, doi: 10.1016/j.energy.2020.119542.
27. W. Ke, J. Ji, C. Zhang, H. Xie, Y. Tang, and C. Wang, "Effects of the PCM layer position on the comprehensive performance of a built-middle PV-Trombe wall system for building application in the heating season," *Energy*, vol. 267, no. November 2022, p. 126562, 2023, doi: 10.1016/j.energy.2022.126562.
28. A. A. Abed, O. K. Ahmed, M. M. Weis, and K. I. Hamada, "Performance augmentation of a PV/Trombe wall using Al2O3/Water nano-fluid: An experimental investigation," *Renewable Energy*, vol. 157, pp. 515–529,

2020, doi: 10.1016/j.renene.2020.05.052.
29. K. Irshad, S. Algarni, N. Islam, and S. Rehman, “Case Studies in Thermal Engineering Parametric analysis and optimization of a novel photovoltaic trombe wall system with venetian blinds : Experimental and computational study,” *Case Studies in Thermal Engineering*, vol. 34, no. March, p. 101958, 2022, doi: 10.1016/j.csite.2022.101958.
30. A. A. Abdullah, F. Saleh, S. Algburi, and O. K. Ahmed, “Results in Engineering Impact of a reflective mirrors on photovoltaic / trombe wall performance : Experimental assessment,” *Results in Engineering*, vol. 16, no. August, p. 100706, 2022, doi: 10.1016/j.rineng.2022.100706.
31. Z. Hu, W. He, X. Hong, J. Ji, and Z. Shen, “Numerical analysis on the cooling performance of a ventilated Trombe wall combined with venetian blinds in an office building,” *Energy and Buildings*, vol. 126, pp. 14–27, 2016, doi: 10.1016/j.enbuild.2016.05.016.
32. Z. Hu *et al.*, “Design, construction and performance testing of a PV blind-integrated Trombe wall module,” *Applied Energy*, vol. 203, pp. 643–656, 2017, doi: 10.1016/j.apenergy.2017.06.078.
33. M. M. Rahman, M. G. Rasul, and M. M. K. Khan, “Energy conservation measures in an institutional building in sub-tropical climate in Australia,” *Applied Energy*, vol. 87, no. 10, pp. 2994–3004, 2010, doi: 10.1016/j.apenergy.2010.04.005.
34. M. Kamalisarvestani, R. Saidur, S. Mekhilef, and F. S. Javadi, “Performance, materials and coating technologies of thermochromic thin films on smart windows,” *Renewable and Sustainable Energy Reviews*, vol. 26, no. 2013, pp. 353–364, 2013, doi: 10.1016/j.rser.2013.05.038.
35. A. M. A. El-Samea, N. M. Hassan, and A. S. H. Abdallah, “The Effect of Courtyard Ratio on Energy Consumption and Thermal Comfort in a Primary Governmental School in New Assiut City, Egypt,” *Architecture and Urbanism: A Smart Outlook*, pp. 121–131, 2020, doi: 10.1007/978-3-030-52584-2_9.

Harvesting Power from Saturated Steam: Utilizing TEG Systems for Waste Heat Recovery

M.A. Mahmoud [1,2,a)], Sameh Nada[1,2], Shinsuke Mori [1,3], and Hamdy Hassan [1,4]

[1] *Department of Energy Resources Engineering, Egypt-Japan University of Science and Technology (E-JUST), Alexandria 21934, Egypt*
[2] *Department of Mechanical Engineering, Benha Faculty of Engineering, Benha University, Benha 13511, Egypt*
[3] *Department of Chemical Science and Engineering, Tokyo Institute of Technology, 2-12-1 Ookayama, Meguro-Ku, Tokyo 152-8550, Japan*
[4] *Mechanical Power Engineering Department, Faculty of Engineering, Assiut University, Assiut 71516, Egypt*

[a)] Corresponding author: mohammed.mahmoud@ejust.edu.eg

Abstract. Due to the substantial latent heat content in the saturated steam exiting steam turbines in steam power plants characterised by high mass flow rates and velocities, our mathematical model addresses a group of thermoelectric generators arranged inside a heat exchanger. The saturated steam inlet to the heat exchanger serves as the heat carrier, complemented by cooling water for efficient heat management. Calculations demonstrate that adjusting specific parameters can optimise the system's performance. Initially, calculations are based on a proposed steam mass flow rate of 20 kg/sec with inlet temperatures of 100°C and a water mass flow rate of 20 kg/sec with an inlet temperature of 10 °C. The key driver is the vapor amount with a quality of 0.97 in the hot source, providing significant latent energy depending on the convection heat transfer coefficient. The study investigates the variation of steam mass flow rate from 5 to 20 kg/sec across one heat exchanger and the distribution of steam mass flow rate across multiple heat exchangers. Results demonstrate that with water and steam mass flow rates at 20 kg/sec, the system generates 2094.141 watts using a 1254 thermoelectric generator, with an overall efficiency of 4.786%. Conversely, when the steam mass flow rate is 5 kg/sec and the water flow rate is 20 kg/sec across four heat exchangers, the system produces 2096.25 watts with an efficiency of 4.793%. This is attributed to heat transfer efficiency between hot and cold fluids in each heat exchanger, with each unit employing 313 TEGs. Additionally, variations in water inlet temperature significantly affect system performance in terms of power generation and efficiency.

INTRODUCTION

Approximately 70% of the energy utilized in industrial processes is lost as low-grade heat at a temperature below 100 °C 1. This represents a massive untapped resource that, if harnessed, could significantly contribute to sustainable development. Traditional energy sources like fossil fuels generate most of this waste heat, leading to resource depletion and contributing to environmental issues. We need a multi-faceted approach focusing on energy conservation and innovative energy conversion technologies to address these challenges. Thermoelectric generators (TEGs) offer a promising solution for converting waste heat into electricity 2. Unlike conventional methods such as the Organic Rankine Cycle, Kalina Cycle, or Uehara Cycle, TEGs rely on the Seebeck effect to convert heat directly into electricity 3. This method has several advantages: TEGs have no moving parts, do not require refrigerants, and do not emit carbon dioxide. Additionally, they operate silently and are simple in structure, making them suitable for various applications. However, the main limitation of TEGs is their relatively low conversion efficiency, typically around 5% 4 5. Despite this, TEGs remain appealing because they use waste heat, an effectively free resource 5. TEGs contribute significantly to overall energy efficiency. Their efficiency hinges on effective heat transfer between the hot and cold fluids. Two primary factors require careful consideration to optimize heat transfer in thermoelectric generator (TEG) systems: design strategies and operational parameters. Design strategies focus on selecting heat exchanger wall materials with high thermal conductivity, as this promotes efficient heat transfer. Optimizing internal channel dimensions, geometry, and configuration can significantly impact fluid dynamics and heat transfer rates. Techniques such as fins or microchannels can increase the effective surface area, enhancing heat exchange. On the other hand, operational parameters involve controlling the flow rate of working fluids to balance efficient heat transfer and reduced pumping power. The temperature differential between the hot and cold fluids is also crucial; a greater temperature differential can theoretically improve efficiency.

Technologies and Materials for Renewable Energy, Environment and Sustainability
AIP Conf. Proc. 3321, 040016-1–040016-14; https://doi.org/10.1063/5.0289629
Published under an exclusive license by AIP Publishing. 978-0-7354-5231-2/$30.00

However, practical constraints such as heat source availability and working fluids' properties must be considered. Various studies have examined these aspects to improve TEG system efficiency and more effectively harness waste heat. Numerous studies have explored various strategies to improve the performance of thermoelectric generator (TEG) systems, focusing on factors such as fluid inlet temperature, flow rate, thermal and electrical contact resistance, and heat exchanger design. Niu et al. 6 emphasized that higher hot fluid inlet temperatures and optimized flow rates can significantly boost system output power. Similarly, Sasaki et al. 7 demonstrated the scalability of TEG systems by constructing a water-based TEG with over 2,500 modules, achieving a peak output of around 900 W using spring water at temperatures between 82-96 °C. Ahiska et al. 8 found that increasing flow rates for both hot and cold fluids led to higher output power and increased temperature differentials across the TEG. Kumar et al. 9 showed that a counterflow configuration in fluid flow provides superior performance compared to a co-flow design. Thermal and electrical contact resistance are crucial for efficient TEG operation. Liu et al. 10 proposed using silicone grease to mitigate thermal resistance, while Chen et al. 11 added concave grooves on heat exchangers to reduce thermal resistance, enhancing TEG output. Electrical contact resistance, however, can hinder output power. Introducing an interface barrier between electrodes and thermoelectric materials, as suggested by W. Liu et al. 12 and R. He et al. 13, is one solution to this problem. Lesage et al. 14 explored vortex generator designs and found that the slotted flat plate type yielded the highest power output, despite its increased flow resistance. Rezania et al. 15 integrated microchannel heat exchangers into TEG systems, significantly improving net output power. Wang et al. 16 utilized specific material to enhance heat transfer efficiency within TEGs, leading to notable performance improvements. Yang et al. 17 optimized heat transfer efficiency using flat fins and a variable cross-section area header, achieving high output power and effective pressure drop management. Different cooling methods have also been explored. Lv et al. 18 demonstrated the effectiveness of heat pipe heat exchangers in enhancing TEG output, while Li et al. 19, 20 designed a five-layer TEG system for low-grade geothermal water recovery, showcasing its potential for on-site geothermal energy harnessing. Lee et al. 21 suggest a mesh arrangement within heat exchangers to enhance heat transfer. In a comprehensive study, Xiangrong Ma et al. 22 examined the effects of varying inlet saturation steam temperature and mass flow rate and turbulators and vapor gas concentration on TEG performance. The study revealed that high inlet temperature and specific vapor concentrations yielded optimal net efficiency. Research by Zhao et al. 23-25 focused on the role of condensation in optimizing TEG performance, particularly when using natural gas boiler exhaust. Their studies demonstrated that humidification and condensation increase output power and exergy efficiencies by utilizing sensible and latent heat from waste streams. Zhao et al. 26 introduced an innovative approach involving intermediate fluid TEGs to enhance power generation from automobile exhaust, achieving a 32.6% increase in maximum output power and reducing optimal TEG module area by 73.8%.

These studies demonstrate a wide range of approaches to enhancing TEG system performance, from optimizing fluid flow and thermal resistance to exploring innovative heat exchanger designs and operational configurations. This study examines a new approach to harnessing low-grade waste heat from the steam exits from turbines in small power plants. Our method focuses on the latent heat contained in steam as it exits the turbine and enters the condenser. Utilizing a specifically engineered heat exchanger, we capture the heat released during condensation and transfer it to TEG modules made from Bismuth Telluride (Bi2Te3). The heat is converted into electricity as the steam transitions from a quality of 0.97 to a fully saturated state at a saturated temperature of 100 °C and a pressure of 1 atm. This transition allows us to reclaim significant energy that would otherwise be lost. The proposed approach offers a practical solution for enhancing electricity generation in small power plants. This method improves overall energy efficiency and aligns with sustainable energy practices by capturing and converting waste heat into electricity. This innovative use of TEGs could pave the way for broader applications, helping to turn waste heat into a valuable resource and contributing to a more sustainable energy future.

MATHEMATICAL MODELLING

A mathematical model will be created to estimate the power generation potential from low-grade waste heat in wet steam that exits steam turbines. This model will be implemented and solved using MATLAB, considering critical factors such as heat transfer within the system and the properties of the thermoelectric generator (TEG) materials. The system used for this analysis features a specialized heat exchanger designed to facilitate the transfer of heat from the steam as it exits the turbine (the hot stream) to thermoelectric generator (TEG) modules made of Bismuth Telluride (Bi2Te3). These modules are strategically placed within the heat exchanger to maximize heat transfer. The efficiency of electricity generation depends on the characteristics of the TEG materials, specifically their Seebeck coefficient, electrical conductivity, and thermal conductivity.

Properties Of TEG Module Material

Power generation in thermoelectric generator modules is driven by a combination of phenomena, including the Seebeck effect, the Peltier effect, thermal conduction, and Joule heating, as previously mentioned. The Seebeck effect, which is the core mechanism, creates an electric current when there is a temperature gradient across an electrical conductor. TEG modules typically consist of a series of n-type and p-type semiconductor blocks arranged between electrical conductors. These are encapsulated by insulating layers and ceramic substrates on both sides, creating a structured design that supports the generation of electricity as shown in Figure 1. The modules operate based on the principle of temperature differentials commonly referred to as ΔT where a greater temperature difference between the hot and cold sides leads to a higher electrical power output. The following equations describe the heat transfer dynamics within a thermoelectric generator (TEG) module, where heat is supplied to the hot side (Qh) and removed from the cold side (Qc) of the TEG:

$$Q_h = n\,[\alpha_{pn} * I * T_h + K_{pn} * (T_h - T_c) - 0.5 * I^2 * R_{pn}] \quad (1)$$

$$Q_c = n\,[\alpha_{pn} * I * T_c + K_{pn} * (T_h - T_c) - 0.5 * I^2 * R_{pn}] \quad (2)$$

where αpn, Seebeck coefficient, Kpn thermal conductance, and Rpn internal resistance of the module. I denote the current generated by the module when the hot stream temperature is (Th) and the cold stream temperature is (Tc). Equations (3) through (6) define αpn, Kpn, Rpn, and the generated current I, considering the dimensions and properties of the TEG module:

$$\alpha_{pn} = \alpha_p - \alpha_n \quad (3)$$

$$k_{pn} = (k_p + k_n) * A_{leg}/L_{leg} \quad (4)$$

$$R_{pn} = (\rho_p + \rho_n) * L_{leg}/A_{leg} \quad (5)$$

$$I = (\alpha_{pn} * (T_h - T_c))/\, R_{pn} + R_{load} \quad (6)$$

Each property, including the Seebeck coefficients (αp and αn), thermal conductance (kp and kn), and electric resistances (ρp and ρn), of both positive and negative legs material, is temperature dependent. Their values can vary depending on the temperature limit, typically start from 300 K to 518 K 27, and can calculated using the following equations (7) to (12).

$$\alpha_{p,(t)} = [5.9213 * 10^{-13}\, T^3 - 3.2742 * 10^{-9}\, T^2 + 2.4223 * 10^{-6}\, T - 2.743842 * 10^{-4}] \quad (7)$$

$$\alpha_{n,(t)} = [1.2916 * 10^{-13}\, T^3 + 1.0744 * 10^{-9}\, T^2 - 9.2717 * 10^{-7}\, T + 8.9588 * 10^{-6}] \quad (8)$$

$$\sigma_{p,(t)} = [2.2488 * 10^{-14}\, T^3 - 1.2508 * 10^{-10}\, T^2 + 1.3881 * 10^{-7}\, T - 2.244 * 10^{-5}]^{-1} \quad (9)$$

$$\sigma_{n,(t)} = [-1.246 * 10^{-14}\, T^3 - 6.4290 * 10^{-11}\, T^2 + 9.1030 * 10^{-8}\, T - 1.0496 * 10^{-5}]^{-1} \quad (10)$$

$$K_{p,(t)} = [1.2516 * 10^{-7}\, T^3 - 1.2428 * 10^{-4}\, T^2 + 3.873788 * 10^{-2}\, T - 2.362707] \quad (11)$$

$$K_{n,(t)} = [-1.59265 * 10^{-8}\, T^3 + 2.9058 * 10^{-5}\, T^2 - 1.58323 * 10^{-2}\, T + 3.727526] \quad (12)$$

Performance of TEG

Thermoelectric generators (TEGs) convert waste heat into electricity through the Seebeck effect, which occurs when a temperature gradient between two ends of a conductive material creates a voltage difference. TEGs leverage this effect by arranging p-type and n-type semiconductor materials to form thermoelectric modules. The Seebeck coefficient is crucial to TEG performance as it determines the voltage a given temperature difference produces. However, internal resistance can reduce power output by impeding current flow. Thermal conductance also plays a key role in heat transfer; lower conductance allows for larger temperature gradients, leading to more efficient electricity generation. The electrical output power (Po) of a TEG module is influenced by the heat transfer from the hot source (Qh) to the hot side and from the cooling fluid (Qc) to the cold side. To understand these relationships, it is important to examine the structural dimensions of the module's p-type and n-type legs, as they greatly affect both electrical resistance and thermal conductance. Table 1 provides a detailed overview of these dimensions, essential for accurate calculations. This information is critical for evaluating the efficiency and power output of thermoelectric generators. Certain assumptions are used to simplify calculations: PN couples are connected in series and remain steady, contact thermal resistance and copper's impact are disregarded, all p-type and n-type materials have identical dimensions and heat conduction along the heat exchanger is negligible. The Thomson effect is also ignored. Accurate

calculation based on these assumptions is key to assessing a TEG's efficiency and power generation potential. The combination of structural factors, thermoelectric properties, and these simplifying assumptions sets the stage for accurate calculation of TEG power output and efficiency. Thus, the combination of structural factors, thermoelectric properties, and calculated assumptions lays the groundwork for calculating TEG power output (Po) and efficiency (ηteg), offering insights into how these generators can be optimized for better performance.

$$P_o = Q_h - Q_c = I^2 . R_{load} \quad (13)$$

$$\eta_{teg} = P_o / Q_h \quad (14)$$

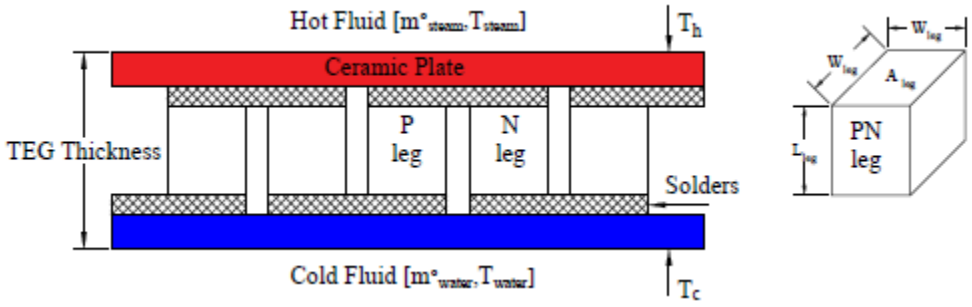

FIGURE 1. Thermocouples' layout structure

TABLE 1. Basic parameter TEG module **28**

Parameter	unit	Value
TEG model		SP184827145
PN thermocouples		127 thermocouples
Dimension of PN couple (length × width× height)	mm	1.4×1.4×1.6
Dimension of ceramic chip (length × width× height)	mm	40×40×0.8
TEG model dimension (width × length× thickness)	mm	40×40×3.9

PHYSICAL MODEL OF WHR SYSTEM

Thermal Resistance Model of the TEG Model

To maximize efficiency, the system employs aluminum plate-fin heat sinks on both the TEG module's hot and cold heat exchangers, as shown in Figure 2. a, featuring a thermal conductivity of 235 W/m·K The hot side heat sink ensures a sufficient heat supply and maintains a high temperature at the hot surface of the TEG module, which is essential for generating electricity. The cold side heat sink effectively dissipates heat, keeping a low temperature at the cold junction. This arrangement maximizes the temperature differential between the two sides, a critical factor for efficient TEG operation. Figure 2.b illustrates a thermal resistance model for waste heat recovery, outlining the system's key segments: the hot side (saturated steam), the cold side (cooling fluid), and the TEG module itself. The heat transfer process on both the hot and cold sides is influenced by three primary types of thermal resistance: Contact Thermal Resistance (Rc): This arises from imperfect contact between various interfaces within the system 29. Base Material Thermal Resistance (Rb): This reflects the inherent resistance to heat flow through the base material of the plate-fin heat sinks.

Convection Thermal Resistance (Rconv): This accounts for the resistance to heat transfer between the fluid and solid surfaces. The following table provides the geometrical dimensions of the aluminum plate-fin heat sinks used in this system 27 . These dimensions are crucial for ensuring the heat sinks' efficiency in maximizing the temperature difference across the TEG module. The design and positioning of the heat sinks, as shown in Table 2, play a significant role in optimizing heat transfer and TEG performance. The thermal resistances for the contact TEG surface and the base of the heat sink can be expressed by the equation stated below

$$R_c = R''_{t,c} / A_{base} \quad (15)$$

where R"t,c is the value of the Thermal resistance of representative solid/solid interfaces 29

The thermal resistance for the base Rb of the plate-fin heat sink can be written by the following equation

$$R_b = L_b / K_b A_{base} \quad (16)$$

where Kb is the thermal conductivity of the base material.

In accordance with Newton's law of cooling, heat transfer between fluid and solid surface gives rise to a convection thermal resistance (Rconv). This resistance (Rconv) can be quantified in relation to the convective heat transfer coefficient (h) and the effective heat transfer area (Aeff), as demonstrated in the equation below.

$$R_{conv} = 1/hA_{eff} \tag{17}$$

Plate fin heat sink's effective heat transfer area (Aeff) and fin efficiency (ηf) can be determined utilizing equations (18) through (20). Here, n denotes the number of fins, while Lfin, Wfin, tfin, and d represent the fin height, width, thickness, and fin-to-fin distance, respectively.

$$A_{eff} = (2n \times W_{fin} \times L_{fin}) \times \eta_f + (n-1) \times W_{fin} \times t_{fin} \tag{18}$$

$$\eta_f = (\tanh m.\ L_{fin})/\ m.\ L_{fin} \tag{19}$$

$$m = \sqrt{\frac{2h_{conv}}{K_{fin}.t_{fin}}} \tag{20}$$

Thermal resistance R_{teg} between two sides of the TEG module can be written by following the equation

$$R_{TEG} = (T_h - T_c)/\ (Q_h - Q_c) \tag{21}$$

Basic Equations for Heat Transfer in Cold and Hot Fluid

To estimate the convection heat transfer coefficient for both the hot and cold sides as shown in Figure 2.a. of a thermoelectric generator (TEG) system, specific methods are applied based on the unique conditions in each section (as outlined in Table 3, which provides a detailed overview of the system's operational parameters and flow characteristics). On the hot side, where steam quality decreases as it passes through the TEG module, the convection heat transfer coefficient must reflect the changing state of the steam. As steam condenses and its quality approaches zero as shown in Figure 3. The associated heat transfer characteristics require careful consideration to ensure accurate calculations. A widely used method for this is the general correlation for heat transfer during film condensation in pipes, as outlined by Shah 31

$$h_{conv,steam} = h_{conv,liq} \times [1 + \frac{3.8}{Z^{0.95}}] \tag{22}$$

$$h_{conv,liq} = 0.023 \times [(J_m.(1 - x_{inlet}).D_h)/\mu_{liq}]^{0.8} \times [\frac{{Pr_{liq}}^{0.4}.K_{liq}}{D_h}] \tag{23}$$

$$Z = [\frac{1-x}{x}]^{0.8}.P_r^{0.4} \tag{24}$$

$$J_m = \dot{m}_{steam}/D_h \tag{25}$$

where is Pr is reduced pressure, and J_m is the mass velocity [kg/m^2. sec].

TABLE 2. Gematrical dimensions of the Aluminium plate- fin heat sink 30

Parameter	Variable	Units	Value
Heat sink width	W	mm	41
Heat sink length	L	mm	40.5
Fin height	L_{fin}	mm	36
Fin width	W_{fin}	mm	41
Base height	L_b	mm	4
Fin thickness	t_{fin}	mm	1.3
Fin- to- fin distance	D	mm	0.9
Number of fins	N		19

For the cold side, the Dittus-Boelter equation is a commonly used method for calculating the convection heat transfer coefficient, especially in turbulent flow within pipes. This empirical equation relates the heat transfer coefficient to fluid properties and flow conditions. It is defined as:

$$Nu = 0.0230.023 \times Re^{0.8} \times Pr^{0.4} \tag{26}$$

$$h_{conv,water} = (Nu \times K_{water})/D_h \tag{27}$$

where Re is the Reynolds number, and Pr is the Prandtl number.

The previous formula accounts for factors such as flow velocity, fluid viscosity, and thermal conductivity, providing a reliable means to estimate the heat transfer coefficient on the cold and hot side. The convective heat transfer equation of hot fluid is given by

$$Q_h = h_{conv,steam} \times A_{teg} \times (T_{steam}\text{-}T_h) = (T_{steam}\text{-}T_h)/R_{th,total,hot} \quad (28)$$

The convective heat transfer equation of cold fluid is given by

$$Q_c = h_{conv,water} \times A_{teg} \times (T_c\text{-}T_{water}) = (T_c\text{-}T_{water})/R_{th,total,cold} \quad (29)$$

where R th, total is the total thermal resistance on each side

$$R_{th,total} = R_c + R_b + R_{conv} \quad (30)$$

The energy change when a cold fluid flows through a thermoelectric generator (TEG) module is a critical aspect of its operation. It is generally expressed in terms of heat transfer, which can then be related to the generated electrical energy. To calculate this energy change, you consider the heat removed from the cold side of the TEG module. This change in energy can be determined by examining the enthalpy difference between the fluid's inlet and outlet temperatures.

$$Q_c = \dot{m}_{water} \times Cp \times (T_{e,water} - T_{i,water}) \quad (31)$$

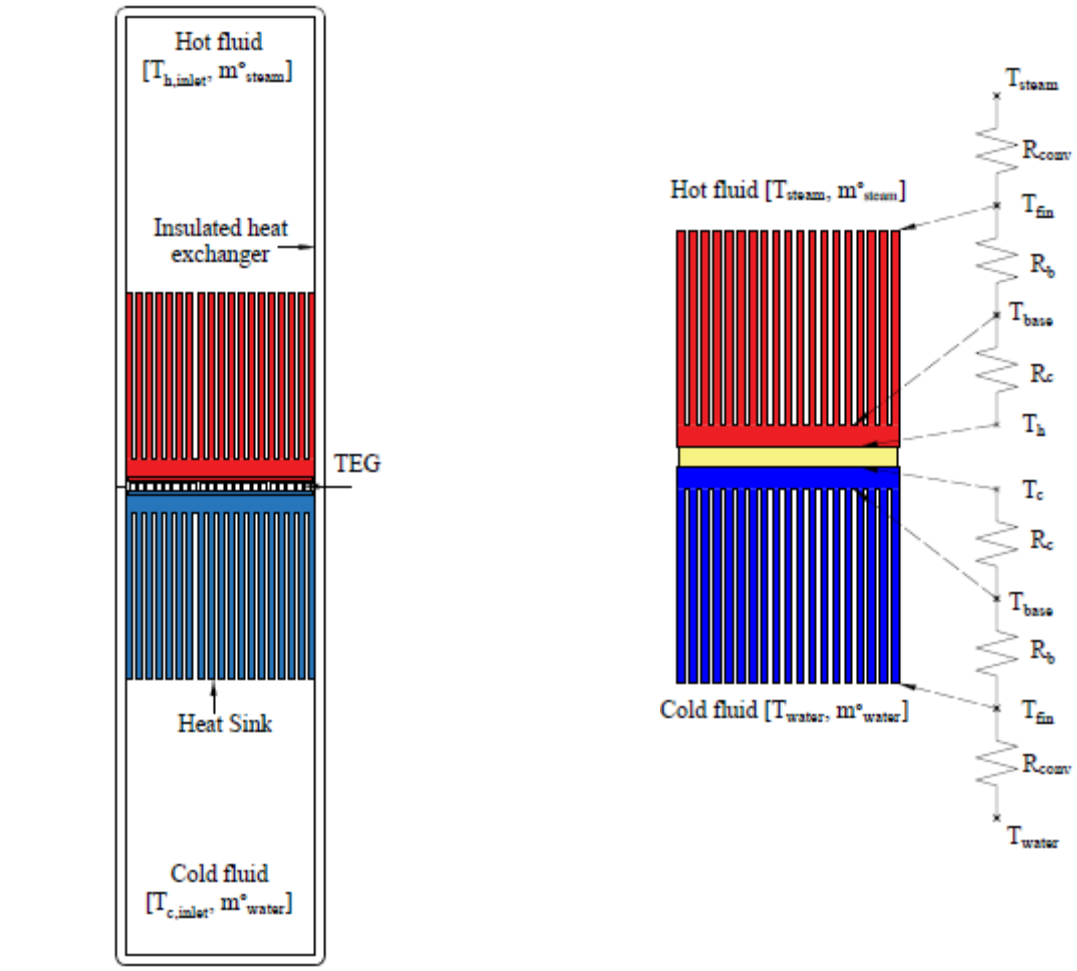

(a) Thermoelectric generator model with a heat sink (b) Thermal resistance model

FIGURE 2. TEG model

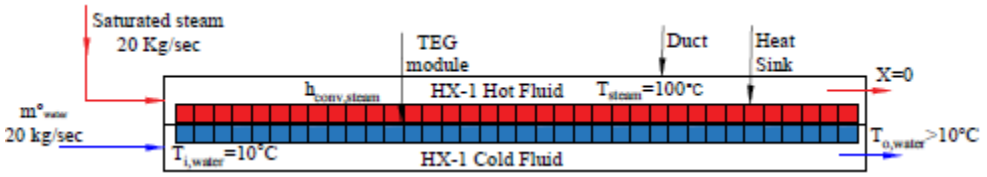

FIGURE 3. Heat transfer characteristics between hot and cold streams

An iterative approach computes the required values for Th, Tc, and I. This involves substituting Th, Tc, and I into the appropriate equations to derive the corresponding results. Specifically, Th, Tc, and I are input into equation (1), corresponding to equation (28), representing the heat transfer equation for the hot fluid. Similarly, by substituting Th , Tc, and I into equation (2), which aligns with equation (29), you can determine the heat transfer for the cold fluid. Power equation (13) is also used, as it addresses heat transfer on both the hot and cold sides. Using an iterative method with MATLAB, we can obtain precise values for Th, Tc, and I by integrating these equations. This iterative approach, which accommodates various initial conditions and diverse input data, leads to accurate estimates for temperature and current, providing a solid basis for analyzing heat transfer and electrical efficiency within the system.

TABLE 3. The system's operational parameters and flow characteristics

Parameter	Variable	Units	Value
Duct width	W_{duct}	mm	41
Duct height	H_{duct}	mm	100
Parameters of saturated steam			
Inlet temperature	T_{steam}	°C	100
Inlet pressure	P_{sat}	atm	1
Mass flow rate	$\dot{m}_{steam}$	kg/sec	20
Inlet quality	X	-	0.97
Parameters of the cooling fluid			
Inlet temperature	T_{water}	°C	10
Inlet pressure	P	atm	1
Mass flow rate	$\dot{m}_{water}$	kg/sec	20

RESULTS AND DISCUSSION

Impact of Variations in Steam Mass Flow Rate on the Performance of TEG Systems

Figure 4.a presents four curves representing the steam mass flow rates entering a thermoelectric generator (TEG) system: 5 kg/sec, 6.67 kg/sec, 10 kg/sec, and 20 kg/sec. As the steam contacts the heat sink in the TEG module, it condenses, releasing latent heat. The analysis reveals a clear relationship between the steam mass flow rate and the power output of the TEG system. The power output decreases as the steam condenses and releases latent heat. This is expected as the temperature gradient, which drives the TEG, diminishes during condensation. Interestingly, the power output decline differs among the curves. Notably, the curve corresponding to the 20 kg/sec steam mass flow rate shows a steeper drop in output compared to other curves, indicating a higher loss of latent heat and reduced efficiency as shown in Figure 4. c. This decrease is primarily due to a larger number of TEG units used with higher mass flow rates to maintain stable power generation. Maintaining consistent power output requires scaling the number of TEG units proportionate to the steam mass flow rate. For example, as shown in Figure 4.b, a steam mass flow rate of 5 kg/sec utilizes 313 TEG units to generate 524.1 watts of power. In contrast, a steam mass flow rate of 20 kg/sec requires a much higher number of TEG units, 1254, to generate 2094.12 watts. This observation underscores the direct correlation between steam flow rate and the number of TEG units needed to capture and convert waste heat into electrical energy. These findings demonstrate that while higher mass flow rates might theoretically suggest greater power output, the need for additional TEG modules to maintain efficiency presents a practical limitation. This leads to a more complex balance between increased energy generation and the resources required to achieve it.

Figure 4.c provides additional insights into the relationship between steam mass flow rate and thermoelectric generator (TEG) system efficiency. The Figure shows that the curves representing different steam mass flow rates intersect at various points, indicating that there may be an optimal range of steam quality where the TEG system achieves maximum efficiency for each flow rate. Initially, all four curves demonstrate a relatively high efficiency, approximately 4.79%, under the specific input conditions for each curve. However, as steam condenses and the system loses latent heat, the efficiency generally decreases, leading to points of intersection among the curves. These intersections represent critical thresholds where system behavior changes, suggesting that efficiency tends to drop as steam quality transitions from higher to lower levels. The intersection point between the curve for a steam mass flow rate of 5 kg/sec and that for 20 kg/sec occurs at a steam quality of about 0.86. At this point, the higher flow rate system

begins to experience a more pronounced drop in efficiency, while the lower flow rate system maintains relatively higher efficiency. This shift implies that beyond this intersection, a system with a lower steam mass flow rate of 5 kg/sec may operate more efficiently than one with a higher mass flow rate of 20 kg/sec. These findings are significant because they reveal that steam mass flow rates and steam quality levels can influence the efficiency of TEG systems. The results suggest that maintaining an optimal balance between these factors can lead to more sustainable and effective energy conversion, emphasizing the need to carefully examine steam quality to maximize TEG performance.

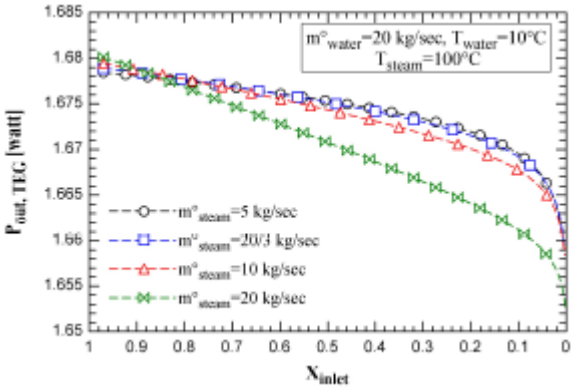

(a) Effect of change in steam mass flow rate on the TEG output power

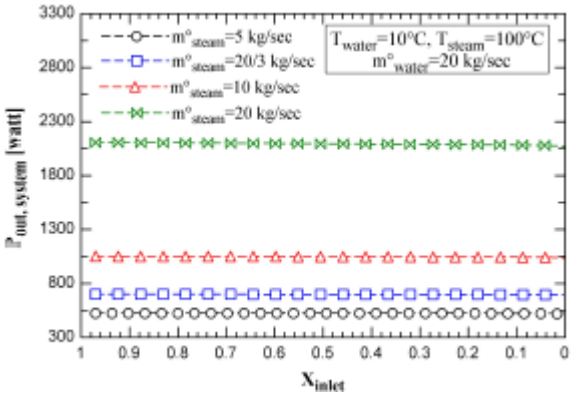

(b) Effect of change in steam mass flow rate on the system output power

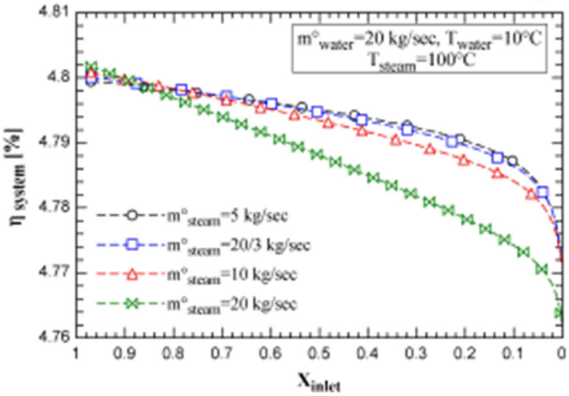

(c) Effect of change in steam mass flow rate on system efficiency

FIGURE 4. Effect of change in steam mass flow rate

Impact of Water and Steam Flow Rate Changes on TEG System Performance

When both water and steam mass flow rates vary, the system's power output decreases slightly compared to when the water mass flow rate is constant, as shown in Figure 5. a. This reduction in power generation may be due to the changing conditions affecting heat transfer efficiency. For example, when both the water and steam flow rates are 5 kg/sec, the system generates 520.66 W, as shown in

Figure 5.b, with an efficiency of 4.762%. Although the power output is slightly lower, the efficiency tends to increase as both water and steam mass flow rates increase, peaking at 4.786% when the steam flow rate is 20 kg/sec and the water flow rate is also 20 kg/sec. This efficiency is higher compared to the 4.762% observed when both steam and water flow rates are 5 kg/sec, likely due to improved heat distribution and optimized steam quality, as shown in Figure 5.c. Comparing the effects of varying water and steam mass flow rates, as opposed to constant water flow with varying steam flow, provides valuable insights into thermoelectric generator (TEG) system performance. When both water and steam mass flow rates are 10 kg/sec, the system generates 1044.132 W, as shown in Figure 5.b, with an overall efficiency of 4.776%. This setup, where both flow rates change, demonstrates a more stable efficiency trend, indicating that the system adapts well to varying conditions. Despite slightly lower power output compared to constant water flow scenarios, the efficiency remains relatively stable, suggesting better heat distribution and optimized steam quality, as shown in Figure 5.c. In contrast, when the water mass flow rate is constant at 20 kg/sec and the steam flow rate varies, the TEG system produces 1047.62 watts at a steam flow rate of 10 kg/sec, with an efficiency of 4.792%.

Although the power output is similar, the constant water flow case generally has a higher efficiency, albeit with notable fluctuations as the steam mass flow rate increases. This comparison indicates that while a constant water mass flow rate can achieve higher efficiency, the varying steam flow can lead to a significant drop in efficiency at higher steam mass flow rates. As the steam flow rate increases to 20 kg/sec, the power output rises to 2094.141 watts, but the overall efficiency decreases to 4.786%. This decline could be due to increased thermal resistance and greater TEG modules required to maintain power generation. On the other hand, when both water and steam mass flow rates vary, the system's efficiency profile remains more consistent across different flow rates. Although the power output is slightly lower, as shown in

Figure 5.a. This approach provides a balanced thermal condition, suggesting that such configurations can be advantageous for maintaining efficiency while still generating substantial power. Ultimately, these comparisons help identify the optimal setup for TEG systems, with a focus on achieving both high power output and consistent efficiency. The insights derived from this analysis can guide system design and operational decisions to optimize thermoelectric power generation.

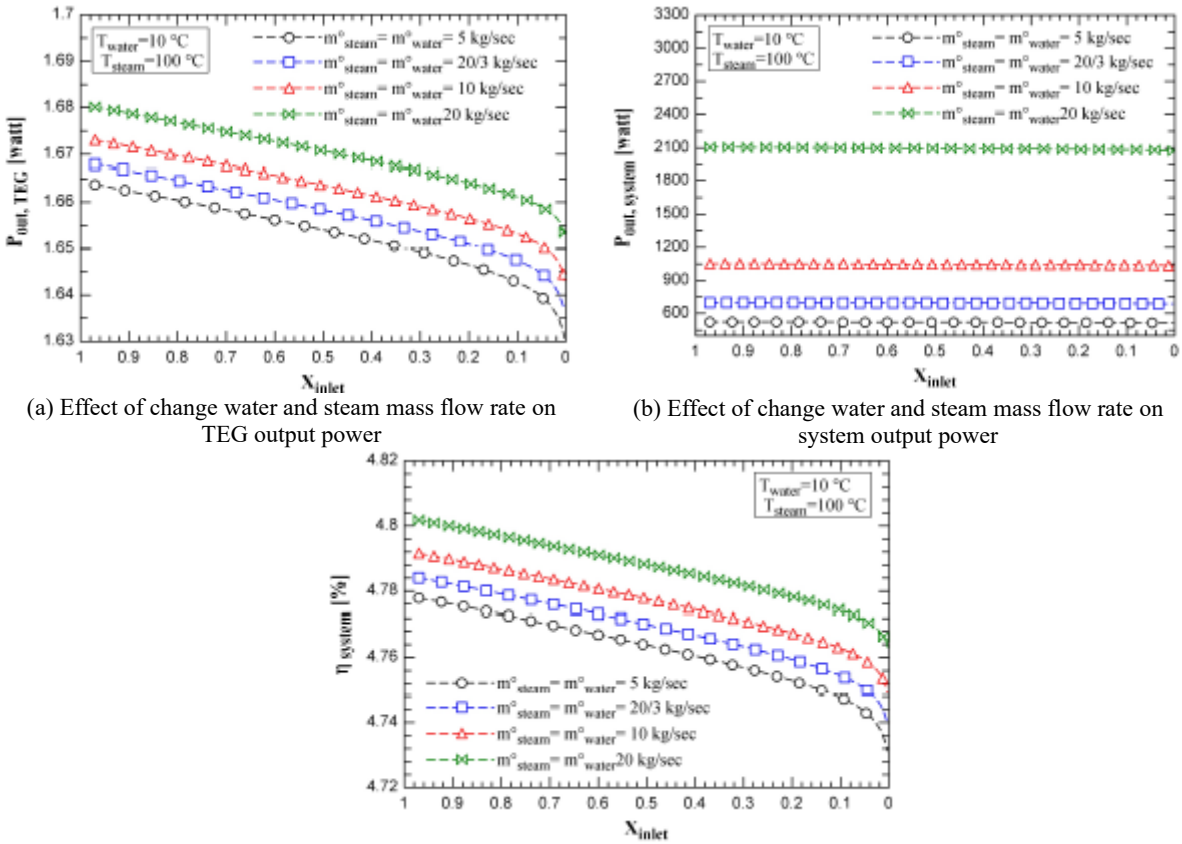

(a) Effect of change water and steam mass flow rate on TEG output power

(b) Effect of change water and steam mass flow rate on system output power

(c) Effect of change in water and steam mass flow rate on system efficiency

FIGURE 5. Effect of changing the water and steam mass flow rate

Impact of Variations in Steam Mass Flow Rate on the Performance of TEG Systems

Figures 6. a to 6 c illustrate using a different number of heat exchangers when distributing steam mass flow rates, while keeping the inlet conditions of both the cooling and hot fluids constant. In these Figures, each heat exchanger receives water as the cooling fluid with constant properties: a mass flow rate of 20 kg/sec and an inlet temperature of 10 °C. The hot fluid, saturated vapor with a consistent quality of x=0.97 and a temperature of 100 °C, enters each heat exchanger, while the steam flow rates vary. This setup offers a comparative perspective on distributing steam mass flow rates across different numbers of heat exchangers while keeping the inlet conditions consistent for both hot and cold fluids. Distributing the steam mass flow rate across multiple heat exchangers significantly impacts the overall power generation and efficiency of a thermoelectric generator (TEG) system. By analyzing the performance of configurations with different numbers of heat exchangers, it is possible to identify optimal power output and efficiency

setups. Comparing the effects of distributing steam mass flow among different numbers of heat exchangers, notable differences in power output and system efficiency emerge.

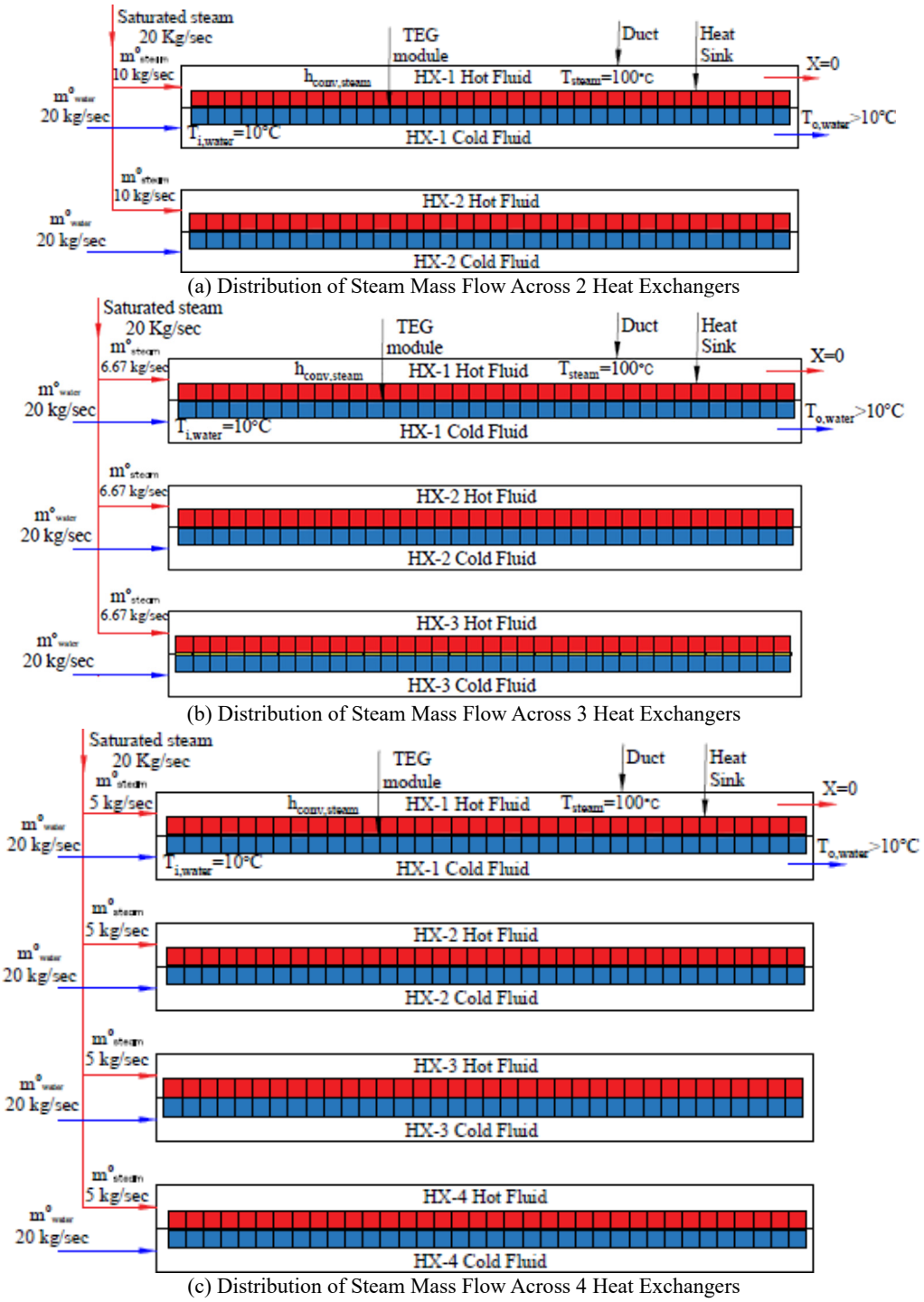

(a) Distribution of Steam Mass Flow Across 2 Heat Exchangers

(b) Distribution of Steam Mass Flow Across 3 Heat Exchangers

(c) Distribution of Steam Mass Flow Across 4 Heat Exchangers

FIGURE 6. Distribution of steam mass flow across different numbers of HX

When steam flow is divided among four heat exchangers, each generates 524.06 watts with 313 TEG modules, resulting in a total power output of 2096.25 watts as shown in Figure 6.b and an efficiency of 4.793% as shown in Figure 7.c. This configuration achieves consistent power generation thanks to the even distribution of steam. In contrast, with three heat exchangers, each generates 698.2 watts using 417 TEG modules, yielding a combined output

of 2094.5 watts and a slightly higher efficiency of 4.796%. Although the total power output is somewhat lower than in the four-heat-exchanger setup, the efficiency improvement suggests that distributing steam across three units enhances heat transfer and reduces thermal resistance. For two heat exchangers, each generates 1047.62 watts, contributing to a total power output of 2095.24 watts using 1252 TEG modules. The overall efficiency drops to 4.792%, potentially due to increased heat transfer resistance from concentrating steam flow in fewer heat exchangers. This highlights the importance of balance in distributing steam to maintain efficiency and power generation. In the final case, when the steam and water mass flow rates are 20 kg/sec with one heat exchanger, the system produces power outputs similar to those with multiple heat exchangers. However, concentrating the steam flow in a single unit can increase the burden on that heat exchanger, potentially leading to greater heat transfer resistance and a slight drop in efficiency. Another aspect to consider is that the system initially generates more power when using a single heat exchanger than other configurations. Still, this trend reverses at an intersection point of approximately x = 0.58 as shown in Figure 7.b, after which the power output from the single heat exchanger decreases more rapidly than those with multiple heat exchangers. This is likely due to the inefficiencies caused by concentrating the steam flow in one unit. These variations demonstrate that distributing steam mass flow across multiple heat exchangers can lead to more stable power output and efficiency. By optimizing the number of heat exchangers, the system can achieve a balance between power generation and thermal resistance, ensuring efficient operation. Configurations with three to four heat exchangers generally provide a good balance, while configurations with fewer heat exchangers might require additional considerations to maintain consistent performance.

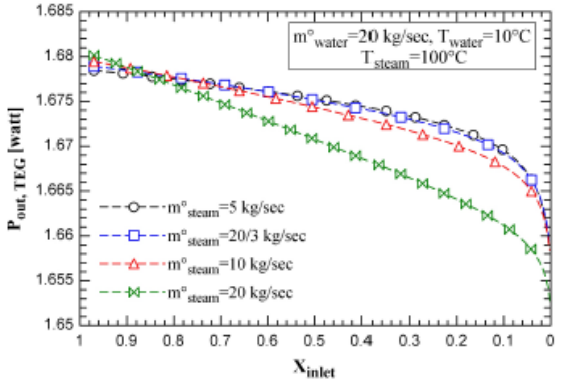

(a) Effect of change steam mass flow rate on TEG output power

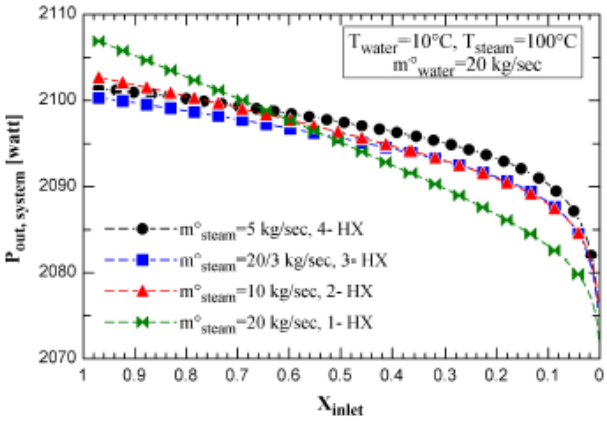

(b) Effect of distributed steam mass flow rate on system output power

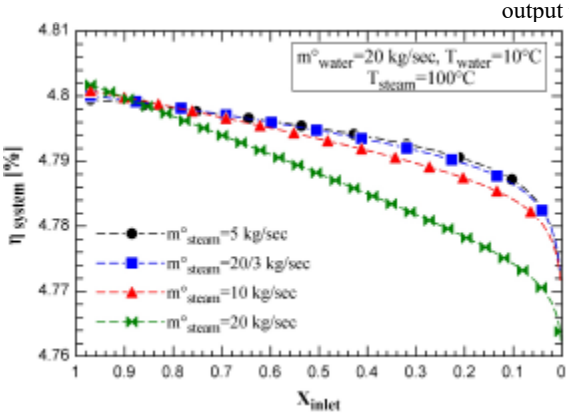

(c) Effect of change steam mass flow rate on system efficiency

FIGURE 7. Effect of distributing steam mass flow rate

Effect of Distributing Steam Flow Across Multiple Heat Exchangers on TEG System Performance

The inlet temperature of the cooling fluid plays a crucial role in shaping the performance of a thermoelectric generator (TEG) system. The variation in the inlet cooling fluid temperature, ranging from 7.5 °C to 15 °C, examines

the impact on performance and efficiency. This study utilizes this temperature range to demonstrate how cold fluid temperature alterations affect performance and efficiency while maintaining a constant mass flow rate of 20 kg/sec for both water and steam across a single heat exchanger. This analysis aims to uncover the intricate interplay between temperature differentials and power generation efficiency in TEG systems. As depicted in Figure 8.a., the impact of inlet water temperature on power generation per module becomes apparent. At an inlet water temperature of 7.5 °C, the initial TEG module produces 1.77413 watts, while the final module generates 1.74553 watts after the inclusion of 1221 TEGs. This consistent power generation suggests a potential stabilizing effect. Conversely, as the water temperature increases, the power output per TEG module decreases. For example, at 12.5 °C, TEG modules generate 1.588613 watts initially, reducing to 1.561895 watts after 1289 TEGs. This decline necessitates the use of additional TEG modules to extract energy from saturated steam, primarily due to the reduced temperature differential between the hot and cold sides, as depicted in equations (1, 2). Subsequently, Figure 8.b illustrates the variation in total power generation across different cases. At an inlet water temperature equal 7.5 °C, the system yields 2153.465 watts of total power using 1221 TEGs, whereas, at inlet water temperature equal 12.5 °C, it generates 2034.982 watts using 1289 TEGs. Notably, total power generation is higher at lower inlet water temperatures, indicating a direct correlation between cooling fluid temperature and power output. This correlation can be attributed to the Seebeck coefficient, a pivotal factor influencing power generation, which depends on the temperature difference between the two sides of the TEG. By lowering the cooling fluid temperature, a larger temperature differential is maintained, facilitating greater power extraction from the hot source while ensuring system stability. Finally, as highlighted in Figure 8.c, the system's efficiency diminishes with increasing inlet cooling fluid temperature, as per equation 14. This decline stems from the reduced amount of power extracted from each system, despite employing more TEGs. For instance, at a water temperature of 7.5 °C, the system achieves an efficiency of 4.922%, generating 2153.465 watts using 1221 TEGs. In contrast, with a water temperature of 15 °C, the system yields 1975.724 watts using 1326 TEGs, resulting in an efficiency of 4.515%. This discrepancy underscores the adverse impact of rising water temperature on the TEG system's efficiency.

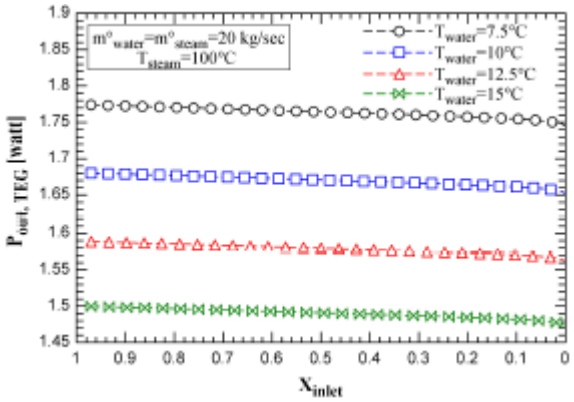

(a) Effect of change the inlet water temperature on TEG output power

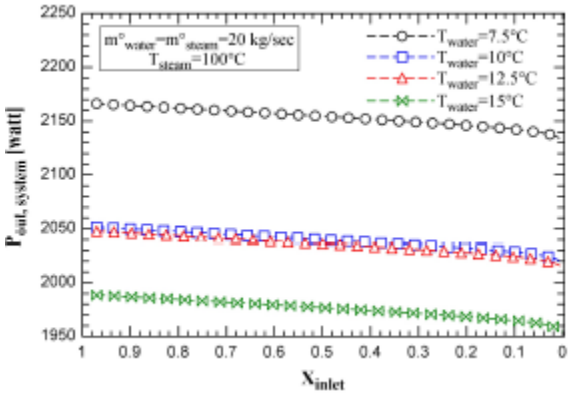

(b) Effect of change the inlet water temperature on system output power

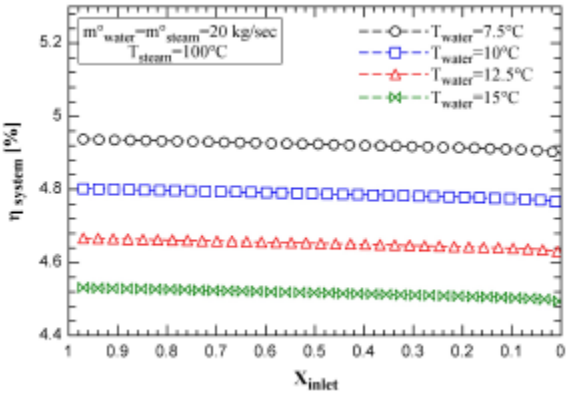

(c) Effect of change in inlet water temperature on system efficiency

FIGURE 8. Effect of change in inlet water temperature

CONCLUSIONS

A significant amount of water vapor exists in the exhaust-saturated steam from steam turbines. As this vapor condenses, it releases substantial latent heat until it becomes saturated. Drawing inspiration from this phenomenon, the paper examined the performance of a waste heat recovery system. The main conclusions are as follows: Distributing the steam mass flow rate across four heat exchangers increases the power generation performance due to higher heat transfer between hot and cold fluids in each heat exchanger. This suggests that optimizing the number of heat exchangers can significantly enhance system efficiency and power output. The water inlet temperature plays a critical role in increasing the amount of power generation. While the power generation is not directly affected by changes in water temperature, the system efficiency is notably impacted. Lower water temperatures increase power generation and overall system efficiency, highlighting the importance of controlling cooling fluid temperatures for optimal system performance. In conclusion, optimizing the distribution of steam mass flow rate and controlling water inlet temperatures are key factors for improving the performance of waste heat recovery systems. By carefully considering these variables, significant enhancements in power generation and overall system efficiency can be achieved, contributing to more sustainable energy practices and resource utilization.

REFERENCES

1. Luberti M, Gowans R, Finn P. An estimate of the ultralow waste heat available in the European Union. *Energy* 2022; 238:121967.
2. D.M. Rowe, Thermoelectrics Handbook, CRC Press, 2005
3. Rowe DM, Bhandari C. Modern thermoelectrics. Prentice Hall; 1983.
4. Rowe DM, Min G. Evaluation of thermoelectric modules for power generation. J Power Sources 1998;73(2):193–8.
5. Riffat SB, Ma X. Thermoelectrics: a review of present and potential applications. Appl Therm Eng 2003;23(8):913–35.
6. Niu X, Yu J, Wang S. Experimental study on low-temperature waste heat thermoelectric generator. J Power Sources 2009;188(2):621–6.
7. Sasaki K, Horikawa D, Goto K. Consideration of thermoelectric power generation by using hot spring thermal energy or industrial waste heat. J Electron Mater 2015; 44:391–8.
8. Ahiska R, Mamur H. Design and implementation of a new portable thermoelectric generator for low geothermal temperatures. IET Renew Power Gener 2013;7(6): 700–6.
9. Kumar S, Mandal SK, Singh PK, et al. Performance analysis of a thermoelectric generation system with different flow configure urations. J Electron Mater 2019;48: 4607–17.
10. Liu C, Chen P, Li KA. 500 W low-temperature thermoelectric generator: design and experimental study. Int J Hydrogen Energy 2014;39(28):15497–505.
11. Chen J, Li K, Liu C, et al. Enhanced efficiency of thermoelectric generator by optimizing mechanical and electrical structures. Energies 2017;10(9):1329.
12. W. Liu, H. Wang, L. Wang, X. Wang, G. Joshi, G. Chen, Z. Ren, Understanding of the contact of nanostructured thermoelectric n-type Bi2Te2.7Se0.3 legs for power generation applications, J. Mater. Chem. 1 (2013): 13093.
13. R. He, G. Schierning, K. Nielsch, Thermoelectric devices: a review of devices, architectures, and contact optimization, Adv. Mater. Technol. 3 (2018): 1700256.
14. Lesage FJ, Sempels ´E V, Lalande-Bertrand N. A study on heat transfer enhancement using flow channel inserts for thermoelectric power generation. Energy Convers Manag 2013; 75:532 41.
15. Rezania A, Rosendahl LA, Andreasen SJ. Experimental investigation of thermoelectric power generation versus coolant pumping power in a microchannel heat sink. Int Commun Heat Mass Tran 2012;39(8):1054–8.
16. Wang T, Luan W, Liu T, et al. Performance enhancement of thermoelectric waste heat recovery system by using metal foam inserts. Energy Convers Manag 2016; 124:13–9.
17. Yang W, Xie H, Sun L, et al. An experimental investigation on the performance of TEGs with a compact heat exchanger design towards low-grade thermal energy recovery. Appl Therm Eng 2021; 194:117119.
18. Lv S, He W, Jiang Q, et al. Study of different heat exchange technologies influence on the performance of thermoelectric generators. Energy Convers Manag 2018; 156:167–77.

19. Li K, Garrison G, Moore M, et al. An expandable thermoelectric power generator and the experimental studies on power output. Int J Heat Mass Tran 2020;160: 120205.
20. Li K, Garrison G, Zhu Y, et al. Thermoelectric power generator: field test at Bottle Rock geothermal power plant. J Power Sources 2021; 485:229266.
21. Lee W, Lee J. Development of a compact thermoelectric generator consisting of printed circuit heat exchangers. Energy Convers Manag 2018; 171:1302–10.
22. Xiangrong Ma, Shenhua Hu, Wuyuan Hu, Experimental investigation of thermoelectric system with condensation heat transfer process, Thermal Science and Engineering Progress, Volume 48, 2024, 102430, ISSN 2451-9049.
23. Yulong Zhao, Shixue Wang, Minghui Ge, Yanzhe Li, Zhaojun Liang, Analysis of thermoelectric generation characteristics of flue gas waste heat from natural gas boiler, Energy Conversion and Management, Volume 148, 2017, Pages 820-829, ISSN 0196-8904,
24. Yulong Zhao, Shixue Wang, Minghui Ge, Yanzhe Li, Yurong Yang, Energy and exergy analysis of thermoelectric generator system with humidified flue gas, Energy Conversion and Management, Volume 156, 2018, Pages 140-149, ISSN 0196-8904,
25. Yulong Zhao, Shixue Wang, Minghui Ge, Yanzhe Li, Zhaojun Liang, Yurong Yang, Performance analysis of a thermoelectric generator applied to wet flue gas waste heat recovery, Applied Energy, Volume 228, 2018, Pages 2080-2089, ISSN 0306-2619,
26. Yulong Zhao, Shixue Wang, Minghui Ge, Zhaojun Liang, Yifan Liang, Yanzhe Li, Performance investigation of an intermediate fluid thermoelectric generator for automobile exhaust waste heat recovery, Applied Energy, Volume 239, 2019, Pages 425-433, ISSN 0306-2619,
27. Chen, M., Rosendahl, L.A., Condra, T., 2011. A three-dimensional numerical model of thermoelectric generators in fluid power systems. Int. J. Heat Mass Transf. 54, 345–355,
28. Hesham Khalil, Hamdy Hassan, Enhancement of waste heat recovery from vertical chimney via thermoelectric generators by heat spreader, Process Safety and Environmental Protection, Volume 140, 2020, Pages 314-329, ISSN 0957-5820.
29. Peterson, G. P., and L. S. Fletcher, "Thermal Contact Resistance of Silicon Chip Bonding Materials," Proceedings of the International Symposium on Cooling Technology for for Electronic Equipment, Honolulu, 1987, pp. 438–448.
30. Toni Pujol, Ilya T'Jollyn, Eduard Massaguer, Albert Massaguer, Ivan R. Cózar, Michel De Paepe, Design optimization of plate-fin heat sink with forced convection for single-module thermoelectric generator, Appl Therm Eng , Volume 221, 2023, 119866, ISSN 1359-4311,
31. Shah, M. M., A general correlation for heat transfer during film condensation inside pipes, Int. J. Heat Mass Transfer, 22, 547, 197

Emission Characteristics of a Gas Turbine Swirl Combustors Firing NH_3/H_2 Fuel Mixture

Ehab Sabry Rashed[1 2, a)], Saleh Abo-Elfadl[3], Mohamed Emam[1 4], S Mori[5], and Hamdy Hassan[1 3]

[1]*Department of Energy Resources Engineering, Egypt-Japan University of Science and Technology, Alexandria, 21934, Egypt*
[2]*Department of Engineering Mathematics and Physics, Faculty of Engineering, Alexandria University, Alexandria 21544, Egypt*
[3]*Department of Mechanical Power Engineering, Faculty of Engineering, Assiut, University, Assiut, Egypt*
[4]*Mechanical Engineering Department, Benha University, Shoubra Faculty of Engineering, 108 Shoubra Street, Cairo, Egypt*
[5]*Department of Chemical Science and Engineering, Tokyo Institute of Technology 2-12-1 Ookayama, Meguro-Ku, Tokyo, 152-8550, Japan*

[a)] Corresponding author: ehab.rashed@ejust.edu.eg

Abstract. According to projections from the International Energy Agency (IEA), there is an anticipated decline in the proportion of fossil fuels in the global energy composition, dropping from the current 80% which has remained consistent for many years to below 75% by 2030. Ammonia and hydrogen, being carbon-free, emerge as promising solutions to address environmental challenges. This study presents a computational investigation into NH_3/H_2 combustion within a gas turbine swirl combustor. Through three-dimensional CFD simulations utilizing CONVERGE and the SAGE detailed chemical kinetics solver coupled with the recently developed CEU-NH3 mechanism, the influence of swirler type on combustion characteristics and emissions is explored. Irrespective of the vane count, the swirlers with a swirl angle of 45° resulted in the broader dispersion of OH radicals and elevated levels of exhaust NO_x emissions. These results offer significant guidance for designing gas turbine burners capable of utilizing carbon-neutral fuels, thereby helping alleviate environmental pollution from combustion activities.

INTRODUCTION

As outlined in the announcement pledge scenario (APS), the demand for all fossil fuels is projected to decrease by 2030 due to efforts to fulfill climate commitments, amplifying the urgency for carbon-free fuels like hydrogen [1]. Ammonia, serving as a hydrogen carrier, presents crucial advantages over hydrogen, including more cost-effective transport over long distances, greater volumetric energy density, and reduced risks of leakage and explosion [2]. However, the adoption of ammonia faces challenges due to its low flame speed, extended ignition delay, comparatively lower flame temperature, and inherent instability [3]. Hayakawa et al. [4] studied the premixed flame of NH_3/air utilizing a swirl combustor. Stable flames were achieved under varied inlet conditions, with significant influence from burner dimensions and swirl number on blow-off limits. High NO emissions were recorded under a lean inlet mixture, peaking at an equivalence ratio of 0.9 before decreasing sharply. Optimal emission performance was identified within an equivalence ratio range of ϕ = 1.15 to 1.2. Zhang et al. [5] utilized a swirl combustor to examine the blow-off characteristics of NH_3 and NH_3/CH_4 flames. The inclusion of CH_4 extended the poor lean flame stability limit of NH_3. Subsequent to their prior study, they delved deeper into understanding how the inclusion of CH_4 and H_2 influences the emission behavior of NH_3/air flames within the context of a gas turbine swirl combustor [6]. The H_2 demonstrates more potential in regulating flame properties and controlling emissions than NH_3/CH_4/air flames, particularly for ammonia concentrations of 30 vol%.

Kurata et al. [7] conducted experiments using a micro gas combustor using NH_3/air and NH_3/CH_4/air blends to assess stability and NO_x emissions. Despite the low laminar flame speed of NH_3/air flames, stable combustion was achieved under high swirling inlet flow conditions. However, elevated NO_x emissions and unburned NH_3 were observed. Valera-Medina et al. [8] investigated the stability and emissions of NH_3, NH_3/CH_4, and NH_3/H_2 in gas turbines using a custom swirl burner. They found that efficient and stable combustion could be maintained at high power levels within a narrow equivalence ratio range. Blending ammonia with hydrogen or methane yielded low NO_x

Technologies and Materials for Renewable Energy, Environment and Sustainability
AIP Conf. Proc. 3321, 040017-1–040017-9; https://doi.org/10.1063/5.0289662
Published under an exclusive license by AIP Publishing. 978-0-7354-5231-2/$30.00

emissions under fuel-rich conditions, contrasting with high NO_x emissions under fuel-lean conditions. Valera-Medina et al. [9] utilized a generic swirl burner to investigate the stability and emissions of NH_3/CH_4 flames. The study concluded that fully premixed NH_3/CH_4 blends were not the most effective strategy for stable and efficient combustion, suggesting a need for a more stratified injection approach in future research. Wang et al. [10] compared NH_3 and CH_4 non-premixed flames. Results showed that due to fuel nitrogen, NH_3/air flames had lower temperatures but significantly higher NO_x emissions.

While NH_3/H_2 is a carbon-free and potentially clean fuel mixture, yielding only N_2 and H_2O upon complete combustion, studies addressing the combustion of NH_3/H_2 blends are significantly limited compared to NH_3/CH_4 blends. Therefore, this study aims to bridge this gap by examining the impact of swirl number on NH_3/H_2 combustion in a gas turbine burner. This investigation utilizes the modeling of Reynolds-averaged Navier-Stokes (RANS) equations and a detailed chemical kinetic mechanism to explore combustion dynamics comprehensively.

MATHEMATICAL MODEL AND NUMERICAL PROCEDURE

The computational domain typically consists of two main sections: the 70 × 70 × 180 mm^3 combustion chamber and the swirler, as depicted in FIGURE 1. Three axial swirlers were meshed to simulate the swirl flow directly. One with a 30° vane angle and two with a vane angle of 45°, dimensions of the swirlers are summarized in TABLE 1. The intensity of the swirl motion, represented by the swirl number, S, is calculated to be 0.73 for the 45° swirlers (swirler 1 and swirler 3) and 0.42 for the 30° swirler based on the following equation:

$$S = \frac{2}{3}\tan\theta \, \frac{\left(1-\left(\frac{D_i}{D_o}\right)^3\right)}{\left(1-\left(\frac{D_i}{D_o}\right)^2\right)} \tag{1}$$

$\mathbf{D_o}$ and $\mathbf{D_i}$ represent the diameter of the swirler and the swirler hub, respectively, and $\boldsymbol{\theta}$ is the angle between the axial centerline and the swirl blade.

Besides the species transport equation, the solution of the physical model mathematically is based on solving the mass, momentum, and energy equations [11].

$$\frac{\partial \rho}{\partial t} + div\,(\rho U) = 0 \tag{2}$$

$$\frac{\partial \rho \mu_i}{\partial t} + div\,(\rho \mu_i U) = \frac{\partial p}{\partial x_i} + div\,(\mu\ grad\ \mu_i) + S \tag{3}$$

$$\frac{\partial \rho h}{\partial t} + \frac{\partial \rho \mu_i}{\partial x_i} = -p\ div\ U + div(\lambda\ grad\ T) + \phi + S_h \tag{4}$$

where $\boldsymbol{\rho}$ is density, **U** is velocity, $\boldsymbol{\mu}$ is the hydrodynamic viscosity, **p** is the static pressure, **S** is the source term, **h** is the fluid ratio, $\boldsymbol{\phi}$ is the dissipative function equation of state, $\mathbf{S_h}$ is the internal heat source, and $\boldsymbol{\lambda}$ is the thermal conductivity.

CONVERGE [12] was used to perform the three-dimensional CFD simulation. The overall computational domain is divided into nearly 500,000 cells. Fixed embedding was employed to refine the mesh by doubling its resolution around the centerline of the head section of the combustion chamber, extending from the swirlers to the middle of the combustion chamber. A modified density-based Pressure Implicit with Splitting of Operator (PISO) algorithm was adopted to consider pressure-velocity coupling [13]. The effect of molecular diffusion is considered in the current study. RANS turbulence model solves the mass, momentum, energy, and species transport equations. The performance of the standard k-ε turbulence model for the simulation of a wide range of flows, therefore, is used in the current simulations. Modeling turbulent combustion faces significant challenges, particularly in achieving precise calculations of the mean reaction rate and accurate representation of chemical processes. The SAGE detailed chemical kinetics

TABLE 1. Dimensions of the swirlers.

	$\mathbf{D_i}$ (mm)	$\mathbf{D_o}$ (mm)	$\boldsymbol{\theta}$	*vanes*
Swirler 1	13	35	45	12
Swirler 2	13	35	30	6
Swirler 3	13	35	45	6

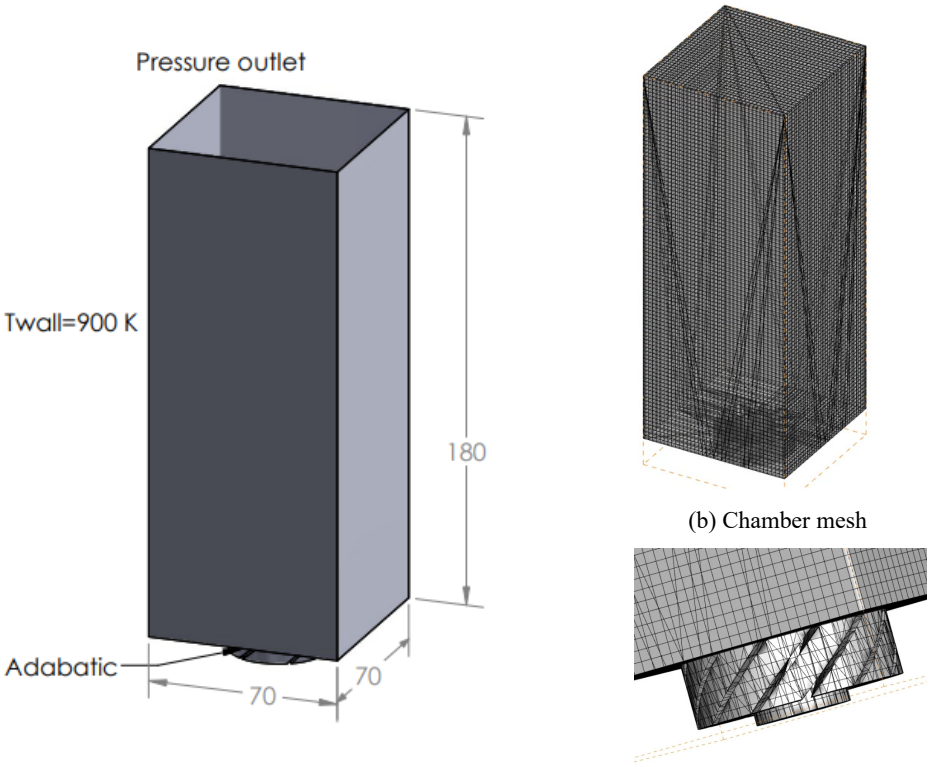

FIGURE 1. The swirl combustion chamber: a) schematic of the geometry, dimensions, and boundary conditions, b) section of the chamber mesh, and c) swirler mesh.

TABLE 2. The boundary conditions of the computational domain.

Inlet mixture temperature (K)	700	
Inlet mixture flow rate (kg/s)	0.00161222	
Combustion chamber wall	Constant temperature (K)	1000
	Velocity	No slip
Swirler and inlet pipe	Insulated	
	Velocity	No slip
Furnace outlet	Pressure (Pa)	1.01325×10^5

solver is adopted to model constant-volume combustion in the present model [14]. The numerical solution of ordinary differential equation systems is facilitated by employing the variable-coefficient ordinary differential equations (CVODE) with a dense solver integrated into SAGE [15].

In order to expedite the computational process, an adaptive zoning approach with a fixed zone size is applied, which groups computational cells based on similar equivalence ratios and temperatures. The NH_3/H_2 cases are simulated using the recently developed CEU-NH_3 mechanism [16], consisting of 91 species and 444 reactions. The total flow rate of the inlet mixture is kept at 0.0016 kg/s for every case, equivalent to 4.5 kW of thermal power. The stoichiometric inlet fuel mixture comprised 70 vol% NH_3 and 30° vol% H_2. Details of the boundary conditions are illustrated in TABLE 2.

RESULTS AND DISCUSSION

Validation of the chemical mechanism

The accuracy of the CEU-NH_3 mechanism was confirmed through validation against experimental data on ignition delay times, species profiles, and laminar flame speed. This validation process encompassed NH_3 blends with H_2, CH_4, CH_3OH, and C_2H_5OH mixtures at elevated temperatures [16]. To further enhance computational efficiency, dynamic mechanism reduction (DMR) is implemented, resulting in a reduction of nearly half the computational time for combustion without compromising the accuracy of the results. Additionally, in the present work, the CEU-NH_3 mechanism is validated against experimental and numerical work, as shown in **FIGURE 2**, and a good agreement is depicted. Therefore, the CEU-NH_3 mechanism is used in current investigations.

General aerodynamics characteristics

FIGURE 3 reflects the flow field distribution of the combustion chamber under different swirler types. It can be seen that the flow field contains an internal recirculation zone around the combustion chamber axis and an external recirculation zone in the lower corners of the combustion chamber in the vicinity of the burner. The size and shape of the internal recirculation zone are similar in swirler 1 and swirler 3, which is attributed to having the same swirl angle of 45° and swirl intensity of 0.73, proving that the swirl intensity does not depend on the number of vanes. In swirler 2, The internal recirculation zone is smaller due to less swirl intensity (0.42).

Thermal characteristics

FIGURE 4 displays the temperature distribution of the combustion chamber under different swirlers. In all simulated cases, a high-temperature region is discernible in the central area of the combustion chamber, reflecting the internal recirculation zone. Decreasing the swirl angle increases the length and width of the high-temperature region, indicating that the high-temperature region follows the shape of the internal recirculation zone. It can be noticed that the temperature in the outer recirculation zone diminishes compared to the internal recirculation zone for all simulated cases, indicating that the outer recirculation zone does not play a role in flame stabilization [5]. It is worth emphasizing that the temperature in the combustion chamber reaches around 2500 K, which is considered a high temperature and may lead to high NO_x emissions.

FIGURE 5 shows the impact of the swirler type on the maximum temperature distribution in the combustion chamber. The maximum temperature hits 2364 K in the swirler 3 case (swirler with six vanes and a 45° angle) and a minimum of 2321 K in the swirler 2 case. It can be concluded that the swirler with the 30° angle is favored in terms of temperature uniformity, which is favored to minimize the NO_x formation through the thermal route [18].

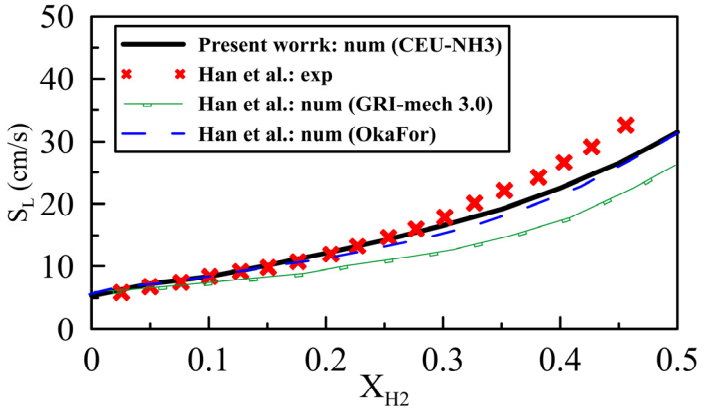

FIGURE 2. Validation of the predicted laminar burning velocity, S_L, of NH_3/H_2/air using CEU-NH_3 mechanism in the present work compared to the results of Han et al. [17]. The figure is original and generated based on the authors' simulation results.

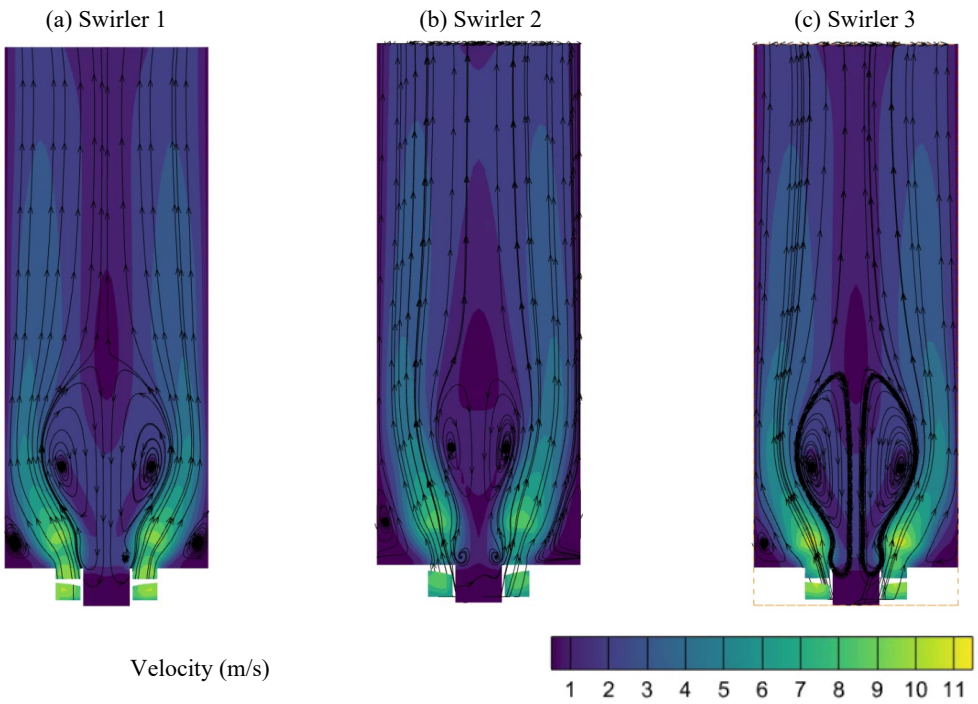

FIGURE 3. Flow field structure of combustion chamber using different swirler types.

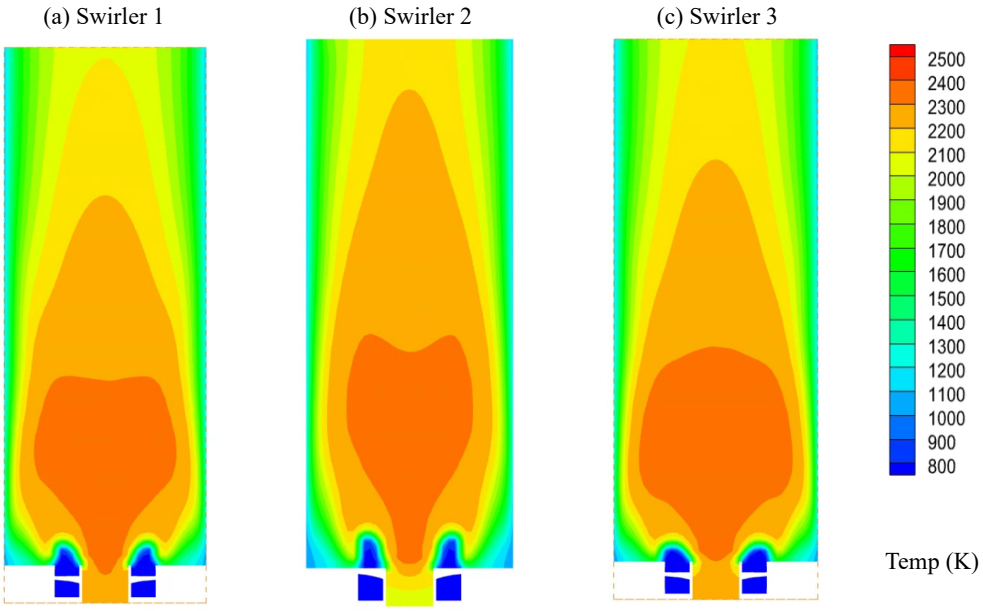

FIGURE 4. Temperature distribution of combustion chamber using different swirler types.

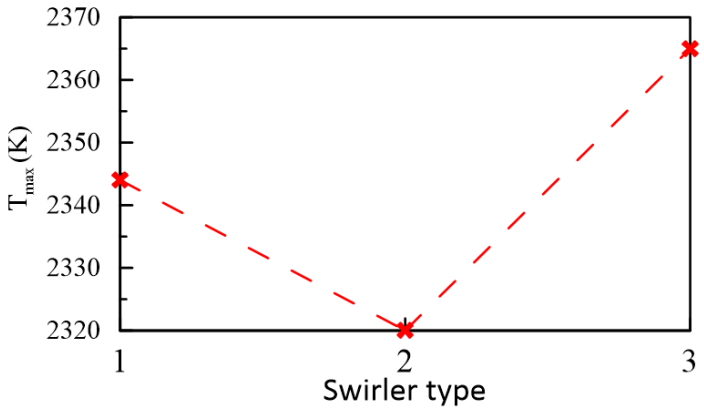

FIGURE 5. The maximum temperature within the combustion chamber for different swirler types.

NO emissions analysis

The formation of NOx can occur in two ways: thermal NOx and fuel NOx [19]. Thermal NOx was first described by Zeldovich [18] through the reaction of diatomic nitrogen in the air with the light radicals (H, O, and OH. Fuel NOx is formed through the conversion of nitrogen in the fuel to NOx, primarily through the HNO path (NH3→NH2→HNO→NO) [19]. According to the numerical simulations by Kumar and Meyer [20], the ammonia oxidation process in NH3/H2/air combustion is primarily governed by the concentration of light radicals. As the H2 mole fraction increases in NH3/H2/air combustion, the importance of nitrogen sub-mechanisms progressively diminishes; however, the relevance of the H2/O2 reaction intensifies. The most significant enhancement facilitated by adding H2 to the ignition and laminar burning velocity of NH3 arises from reactions such as O + H2 = OH + H and H + O2 = OH + O). Conversely, the reaction H2 + OH = H2O + H plays a notable inhibiting role [21]. FIGURE 6 shows the OH radical concentration for different swirler types. It can be seen that the distribution of the OH radical follows the shape of the recirculation zone. Furthermore, the swirlers with 45° angles give a broader OH distribution. In comparison, the 30° angle gives thinner and longer OH distribution due to the low resistance of the swirlers to the inlet jet with decreasing the swirling angle.

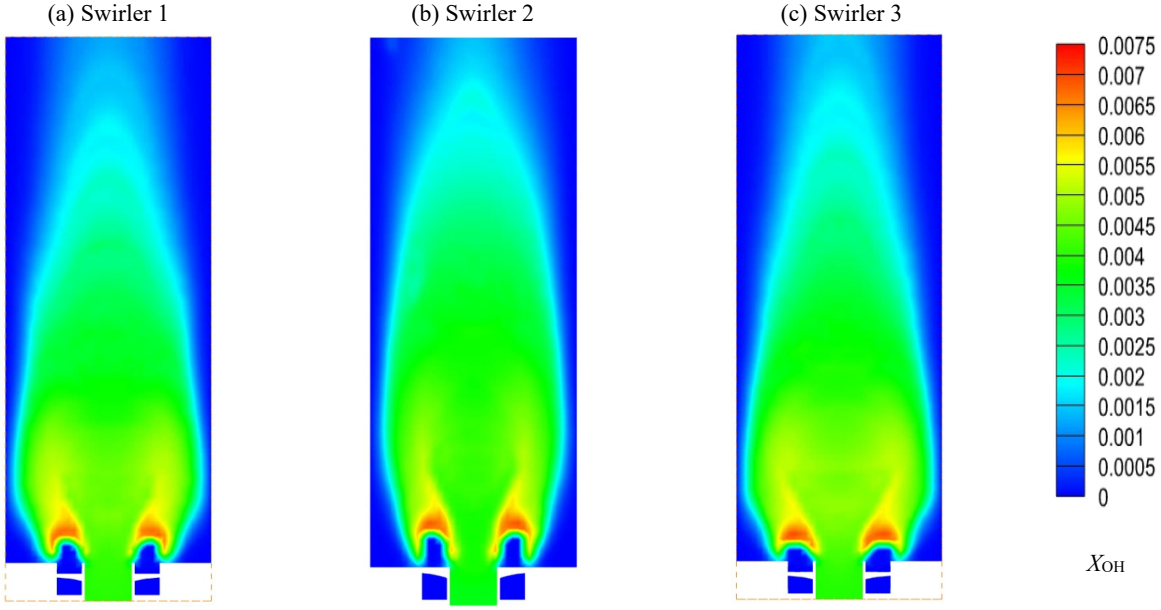

FIGURE 6. Distribution of OH mole fraction, X_{OH}, in combustion chamber using different swirler types.

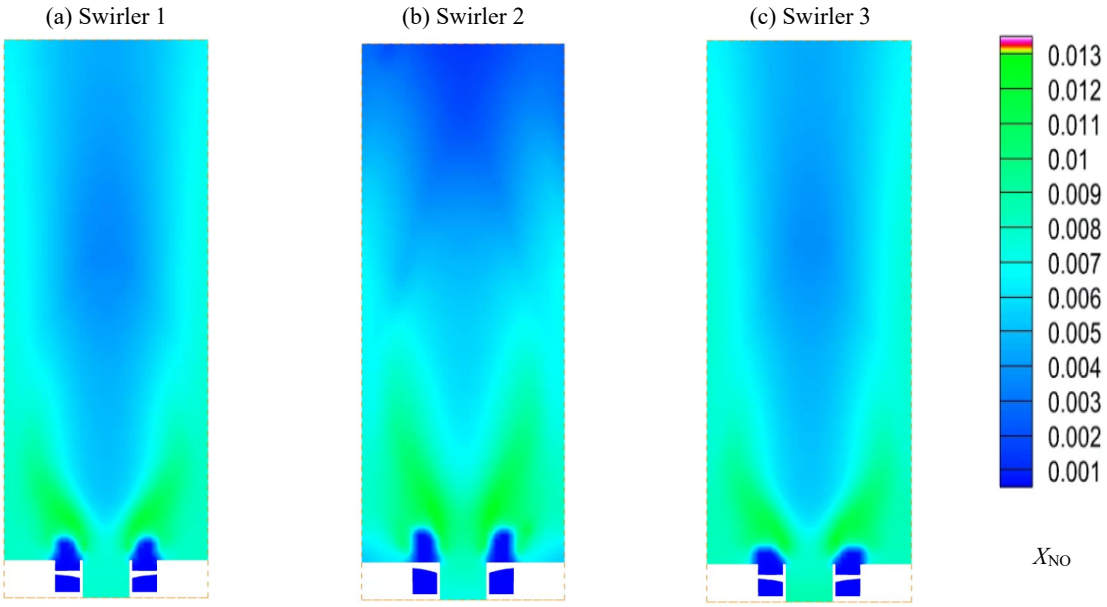

FIGURE 7. The distribution of NO mole fraction, X_{NO}, in the combustion chamber using different swirler types.

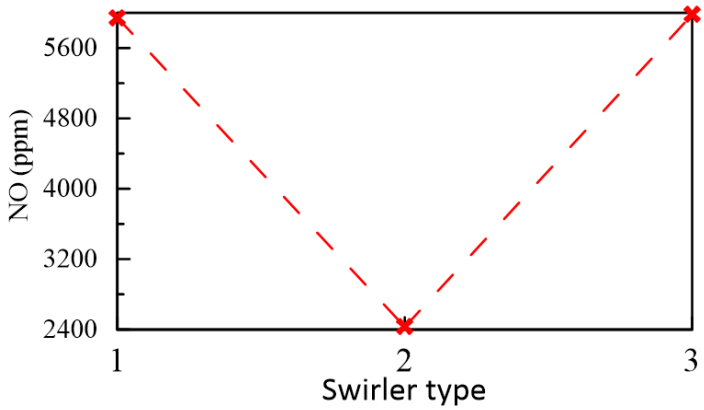

FIGURE 8. Exhaust NO_x emissions of the combustion chamber for different swirler types.

FIGURE 7 shows the NO distribution within the domain for different swirler types. As depicted, most of the NO is formed outside the internal recirculation zone due to the increased concentration of the light radicals (O, H, and OH) before being consumed in the high-temperature region through the NO dissociation reactions [22].

FIGURE 8 shows the exhaust NOx emissions in the combustion chamber exhaust gas for different swirler types. Notably, the data reveals that the highest levels of exhaust NO emissions were recorded with the 45° swirlers, while the exhaust NO emissions were nearly halved with the implementation of the 30° swirlers. This discrepancy can be attributed to the fact that maximum temperatures were notably higher in the 45° swirlers than in the 30° swirlers, as evidenced by the findings in FIGURE 5. The elevated temperatures in the 45° swirlers elevate the formation of thermal NOx, contributing to the higher NO emissions observed. The increased temperature in the 45° swirlers provides the necessary conditions for this reaction to occur more extensively, leading to higher levels of thermal NO_x production. In contrast, the lower temperatures associated with the 30° swirlers result in reduced thermal NO_x formation due to the less favorable conditions. Consequently, the exhaust NO emissions from the 30° swirlers are significantly lower compared to those from the 45° swirlers.

CONCLUSION

In this study, CONVERGE with the SAGE detailed chemical kinetics solver is used to model a combustion chamber with three types of axial swirlers. The methodology involved adaptive zoning and dynamic mechanism reduction, resulting in efficient simulations with reduced computational burden. The impact of different swirlers on NH_3/H_2 combustion characteristics and emissions. The results show that varying the swirl angle significantly influenced flow field distribution, temperature profiles, and species concentrations within the combustion chamber. Regardless of the number of vanes, increasing the swirl angle led to broader OH radical distribution and higher exhaust NO_x emissions. The study highlighted the role of light radicals like H, O, and OH in NH_3/H_2 combustion, with H_2 enhancing ignition and burning velocity. These findings provide valuable insights for developing a gas turbine burner that can operate with carbon-free fuels, mitigating environmental pollution from combustion processes.

ACKNOWLEDGMENT

The authors would like to acknowledge the Mission Department of the Ministry of Higher Education (MOHE) of Egypt for providing a scholarship to conduct this study, and the Science, Technology & Innovation Funding (STDF) department which is sponsoring the research work to conduct this study under project No. 46447. Convergent Science provided CONVERGE licenses and technical support for this work.

REFERENCES

1. "IEA (2023), Global Energy and Climate Model, IEA, Paris https://www.iea.org/reports/global-energy-and-climate-model, License: CC BY 4.0".
2. J. Tian *et al.*, "Enhancing combustion efficiency and reducing nitrogen oxide emissions from ammonia combustion: A comprehensive review," *Process Saf. Environ. Prot.*, vol. 183, pp. 514–543, Mar. 2024, doi: 10.1016/j.psep.2024.01.020.
[3. M. Aziz, F. B. Juangsa, A. R. Irhamna, A. R. Irsyad, H. Hariana, and A. Darmawan, "Ammonia utilization technology for thermal power generation: A review," *J. Energy Inst.*, vol. 111, p. 101365, Dec. 2023, doi: 10.1016/j.joei.2023.101365.
4. A. Hayakawa, Y. Arakawa, R. Mimoto, K. D. K. A. Somarathne, T. Kudo, and H. Kobayashi, "Experimental investigation of stabilization and emission characteristics of ammonia/air premixed flames in a swirl combustor," *Int. J. Hydrog. Energy*, vol. 42, no. 19, pp. 14010–14018, May 2017, doi: 10.1016/j.ijhydene.2017.01.046.
5. M. Zhang, X. Wei, J. Wang, Z. Huang, and H. Tan, "The blow-off and transient characteristics of co-firing ammonia/methane fuels in a swirl combustor," *Proc. Combust. Inst.*, vol. 38, no. 4, pp. 5181–5190, 2021, doi: 10.1016/j.proci.2020.08.056.
6. M. Zhang *et al.*, "The regulation effect of methane and hydrogen on the emission characteristics of ammonia/air combustion in a model combustor," *Int. J. Hydrog. Energy*, vol. 46, no. 40, pp. 21013–21025, Jun. 2021, doi: 10.1016/j.ijhydene.2021.03.210.
7. O. Kurata *et al.*, "Performances and emission characteristics of NH3–air and NH3CH4–air combustion gas-turbine power generations," *Proc. Combust. Inst.*, vol. 36, no. 3, pp. 3351–3359, 2017, doi: 10.1016/j.proci.2016.07.088.
8. A. Valera-Medina *et al.*, "Ammonia, Methane and Hydrogen for Gas Turbines," *Energy Procedia*, vol. 75, pp. 118–123, Aug. 2015, doi: 10.1016/j.egypro.2015.07.205.
9. A. Valera-Medina *et al.*, "Ammonia–methane combustion in tangential swirl burners for gas turbine power generation," *Appl. Energy*, vol. 185, pp. 1362–1371, Jan. 2017, doi: 10.1016/j.apenergy.2016.02.073.
10. Y. Wang, J. Liu, L. Wang, Z. Fu, and P. Weng, "Non-premixed combustion and NOX emission characteristics in a micro gas turbine swirl combustor fueled by methane and ammonia at various heat loads," *Heliyon*, vol. 9, no. 3, p. e14521, Mar. 2023, doi: 10.1016/j.heliyon.2023.e14521.
11. L. Zhang, X. Wei, Z. Zhang, and S. Li, "Modeling De-NOx by Injection Ammonia in High Temperature Zone of Cement Precalciner," *J. Therm. Sci.*, vol. 30, no. 2, pp. 636–643, Mar. 2021, doi: 10.1007/s11630-020-1324-0.
12. K. J. Richards, P. K. Senecal, and E. Pomraning, "CONVERGE (v3. 0), Convergent Science," *Inc Madison WI*, 2021.

13. R. I. Issa, “Solution of the implicitly discretised fluid flow equations by operator-splitting,” *J. Comput. Phys.*, vol. 62, no. 1, pp. 40–65, Jan. 1986, doi: 10.1016/0021-9991(86)90099-9.
14. P. K. Senecal *et al.*, “Multi-Dimensional Modeling of Direct-Injection Diesel Spray Liquid Length and Flam Lift-off Length using CFD an Parallel Detailed Chemistry”.
15. R. Serban and A. C. Hindmarsh, “CVODES: The Sensitivity-Enabled ODE Solver in SUNDIALS,” in *IDETC-CIE2005*, Volume 6: 5th International Conference on Multibody Systems, Nonlinear Dynamics, and Control, Parts A, B, and C, Sep. 2005, pp. 257–269. doi: 10.1115/DETC2005-85597.
16. X. Han, Z. Wang, Y. He, Y. Zhu, and K. Cen, “Experimental and kinetic modeling study of laminar burning velocities of NH3/syngas/air premixed flames,” *Combust. Flame*, vol. 213, pp. 1–13, Mar. 2020, doi: 10.1016/j.combustflame.2019.11.032.
17. X. Han, Z. Wang, M. Costa, Z. Sun, Y. He, and K. Cen, “Experimental and kinetic modeling study of laminar burning velocities of NH3/air, NH3/H2/air, NH3/CO/air and NH3/CH4/air premixed flames,” *Combust. Flame*, vol. 206, pp. 214–226, Aug. 2019, doi: 10.1016/j.combustflame.2019.05.003.
18. Y. A. Zeldovich, D. Frank-Kamenetskii, and P. Sadovnikov, *Oxidation of nitrogen in combustion*. Publishing House of the Acad of Sciences of USSR, 1947.
19. A. Stagni, A. Frassoldati, M. Pelucchi, and T. Faravelli, “Chemistry of nitrogen oxides (NOx) formation in flameless combustion,” in *Fundamentals of Low Emission Flameless Combustion and Its Applications*, Elsevier, 2022, pp. 421–451. doi: 10.1016/B978-0-323-85244-9.00011-3.
20. P. Kumar and T. R. Meyer, “Experimental and modeling study of chemical-kinetics mechanisms for H2–NH3–air mixtures in laminar premixed jet flames,” *Fuel*, vol. 108, pp. 166–176, Jun. 2013, doi: 10.1016/j.fuel.2012.06.103.
21. W. S. Chai, Y. Bao, P. Jin, G. Tang, and L. Zhou, “A review on ammonia, ammonia-hydrogen and ammonia-methane fuels,” *Renew. Sustain. Energy Rev.*, vol. 147, p. 111254, Sep. 2021, doi: 10.1016/j.rser.2021.111254.
22. F. Zhang, G. Chen, D. Wu, T. Li, Z. Zhang, and N. Wang, “Characterising premixed ammonia and hydrogen combustion for a novel Linear Joule Engine Generator,” *Int. J. Hydrog. Energy*, vol. 46, no. 44, pp. 23075–23090, Jun. 2021, doi: 10.1016/j.ijhydene.2021.04.110.

Apply Green Economy to Waste Management

Nassif J. Alkhattabi [1, a] ,Hayder Al-Guboori [2, b], Joumana A. Younis [3,c]

[1]*Governorate of Holy Karbala, Karbala, Iraq*
[2]*Department of Metallurgical Engineering, College of Materials Engineering, University of Babylon, Babylon, Iraq*
[3]*Faculty of Business Administration, Jinan University, Beirut, Lebanon, Dicen-IdF (EA7339), CNAM and, CORHIS (EA7400), Paul-Valéry Montpellier 3 University, Paris, France.*

[a] Corresponding author: alkhattabinassif@gmail.com
[b] mat.hayder.abadhassan@uobabylon.edu.iq
[c] joumana.younis@jinan.edu.lb

Abstract. In our present world we aim to manufacture products with the lowest costs and less danger to the environment and this falls under the name of green economy. Waste Management classification and identification of wastes according to their type to benefit from them as much as possible By operation or by any process . This research focuses on economic and environmental aspects and reach to optimization.

Keywords: Green Economy, waste management , stratigies, image processing

INTRODUCTION

In order to achieve our goal, we must arrange things in order to achieve better results. When we talk about waste, we do not necessarily talk about things that have been used before. Anything that has not been introduced into the industry, as in waste from extraction. Waste Management is a tool that enables the control of wastes and their organization for easy distribution during the process of recycling. Management waste has been known as a crucial need as it may reduce resources consumption , rigid regulations regarded to the environment and occupational health and safety , and growing customer preference for environmental-friendly products [1].Green economy is an effective tool in the use of natural resources to reduce the impact of air pollution and environmental impacts, taking into account the natural risks and the role of environmental management and natural capital in the prevention of physical disasters and must be comprehensive growth[2].A principle 3R (Reduce ,Reuse ,Recycle) can be used in solid waste management and it is considered interesting at present. There are several types of waste including solid, liquid, gaseous and also radioactive waste, but we will focus on solid waste . Also the waste classified into two types [10,11,12](a-hazardous , b- non-hazardous).We are looking for optimal implementation of these concepts or work on the ground to serve human beings by all available means and also to create new means if necessary.

SOLID WASTE AND MANAGEMENT

Solid waste is everything that is not liquid. It may produce from the cans, bottles ,Auto parts, old machines,[13,14] wood, metal from factories or mining ,Building materials. Municipal solid waste, commonly known as trash or garbage (US), refuse or rubbish (UK) is a waste type consisting of everyday items we consume and discard[3].
The benefit of waste management is to keep it clean and uncooperative and this can be achieved through the cooperation of individuals. Paper, glass containers and plastics can be separated from the waste sorting plant and sent to production plants such as glass, aluminium and paper or sent to recycling plants for organic fertilizer or various types of plastics, hazardous household wastes such as batteries and dyes are collected and sent to the site of hazardous household waste, but these are not hazardous industrial waste, Solid waste is an environmental problem in itself because it leads to pollution of the environment if it is not recycled and used instead of being thrown randomly.

Technologies and Materials for Renewable Energy, Environment and Sustainability
AIP Conf. Proc. 3321, 040018-1–040018-8; https://doi.org/10.1063/5.0289594
Published under an exclusive license by AIP Publishing. 978-0-7354-5231-2/$30.00

RECYCLING

Recycling means the use of materials as much as possible and the reduction of the demand for raw materials to preserve natural resources. This is followed by serial operations starting with the collection and sorting of materials and ending with their delivery to factories. Iron, aluminium, wood and plastics are an example of recyclable materials, Some are subject to magnetic sorting or aerial screening, and then are compressed and then re-manufactured[15,16] .
The costs of different waste management techniques are subject to many variables making it difficult to distinguish between them in purely economic terms , however ,when comparing landfill, incineration are recycling , recycling has considerable economic merit [4,17,18].

ECONOMY GREEN

The green economy has become a fundamental and inevitable demand for most countries of the world due to environmental degradation and understanding of the deterioration of climate change ,this type of economy is a new model of rapid economic growth models. As it is based primarily on the knowledge of environmental economics, which aims to address the mutual relationship between the human economies and the natural ecosystem[5,19,20,21].
The establishment of the green economy means the proper management of chemical resources and waste. The rapid increase in their use and the production of solid materials inevitably lead to environmental pollution.[21,22,23]
The deterioration in the environment due to the traditional economic system has contributed to the strength of the green economy. It also contributed to the fatigue caused by the simultaneous crises and market collapses that occurred during the first decade of the new millennium, including the collapse of the economy in 2008 in particular [6,25,32,33].

MOVING INTO A GREEN ECONOMY

There is two tracks to move into green economy : [7,24,34,35]
1-The first track: The launch of green projects, which includes the launch of new projects for social and economic development taking into account the environmental considerations in the first stage, from the project design and then in all stages of implementation and balance and evaluation, the first focuses on the focus on environmental goods and services, which in turn promotes carbon-free activities. This course also focuses on renewable energy production and distribution to create new areas for economic growth, the promotion of green curricula, innovative activities, research and development activities and transfer of technology at the regional level in order to create new opportunities and sources of income, promote the spirit of initiative, education, retraining and rehabilitation for the employment of young people in new sector 2-Redirecting current patterns of production and consumption or correcting them through environmental performance [25,26,36,37]These two tracks are complementary and interlinked and can be supported by a series of policies and government programs that encourage the private sector and civil society to participate and ensure the commitment of designated entities in the region to move to the green economy, this is by promoting sustainable transport in order to reduce carbon emissions, as well as converting construction and design projects into green projects and converting electricity production projects into green projects. This course shows that improving the efficiency of water management systems and its analysis and distribution to reduce water scarcity and Improving food security, developing rural areas and increasing income, this path suggests that the promotion of sustainable livelihoods and sustainable agriculture reduces land degradation and desertification[8,27,28,29].
The process of transformation is achieved by convolving functions that are often orthogonal, resulting in an invertible transform. This implies that the initial function in the initial domain can be retrieved without any loss of data [10,30.31].

WORK AND STATISTICS

Having identified the basic concepts of research, we must now turn to vital work and obtain data and conclusions embodying all concepts.
Information on the quantity of waste to be collected by specific areas in Zayouna and Salhiya in Baghdad for a month has been collected. The waste bags were distributed to the residential apartments in the two areas mentioned above and the population was instructed to place each item in its place, We got the following results:

Table 1. Quantity of waste for the Salheya apartments [9] .

No	Date	Organic Waste (kg)	Foliar waste (kg)	Metal, plastic and glass wastes (kg)
1	1/5/2015	287.730	1.43	96.749
2	2/5/2015	209.077	40.135	56.945
3	3/5/2015	222.378	34.863	52.436
4	4/5/2015	291.252	36.945	59.229
5	5/5/2015	269.21	27.554	54.622
6	6/5/2015	289.4	41.752	90.132
7	7/5/2015	302.829	28.45	61.43
8	8/5/2015	284.316	41.329	46.73
9	9/5/2015	249.858	32.517	99.15
10	10/5/2015	281.256	59.835	61.464
11	11/5/2015	247.653	41.255	74.635
12	12/5/2015	260.251	36.754	46.507
13	13/5/2015	241.095	19.534	37.428
14	14/5/2015	206.257	26.051	39.458
15	15/5/2015	253.556	23.079	47.006
16	16/5/2015	276.553	21.898	41.877
17	17/5/2015	281.892	61.066	40.212
18	18/5/2015	273.066	26.809	56.792
19	19/5/2015	273.413	27.107	47.075
20	20/5/2015	254.733	20.872	43.758
21	21/5/2015	272.095	28.614	67.568
22	22/5/2015	233.897	30.42	52.378
23	23/5/2015	235.987	26.98	47.842
24	24/5/2015	343.183	56.021	63.503
25	25/5/2015	256.541	39.379	44.78
26	26/5/2015	252.464	37.305	37.529
27	27/5/2015	297.765	34.03	50.987
28	28/5/2015	181.63	17.635	36.927
29	29/5/2015	186.856	26.604	48.962
30	30/5/2015	170.552	36.924	65.688
31	31/5/2015	259.325	58.204	59.210
	Total	8.244.81	1.041.351	1.728.909

Table 2. Quantity of waste for the Zayouna apartment [9].

No	Date	Organic Waste (kg)	Foliar waste (kg)	Metal, plastic and glass wastes (kg)
1	1/5/2015	127.4	30.61	38.55
2	2/5/2015	183.67	24.38	215.815
3	3/5/2015	185.108	27.08	71.505
4	4/5/2015	158.725	37.88	64.405
5	5/5/2015	165.4	40.94	44.43
6	6/5/2015	140.44	44.88	68.44
7	7/5/2015	266.94	49.68	66.695
8	8/5/2015	193.68	44.53	62.495
9	9/5/2015	203.68	32.895	34.499
10	10/5/2015	203.15	47.39	43.515
11	11/5/2015	199.91	55.88	92
12	12/5/2015	201.045	62.57	70.59
13	13/5/2015	190.84	48.285	56.99
14	14/5/2015	228.81	49.17	57.72
15	15/5/2015	220.36	57.655	51.55
16	16/5/2015	187.36	49.91	61.71
17	17/5/2015	251.23	45.609	55.81
18	18/5/2015	147.26	40.83	32.05
19	19/5/2015	155.51	39.59	41.59
20	20/5/2015	225.08	209.24	63.04
21	21/5/2015	239.12	50.42	59.37
22	22/5/2015	252.38	23.62	39.115
23	23/5/2015	194.99	38.17	42.41
24	24/5/2015	246.02	43.775	55.731
25	25/5/2015	180.56	142.975	76.142
26	26/5/2015	194.471	149.387	65.294
27	27/5/2015	189.83	41.971	64.388
28	28/5/2015	225.13	35.23	65.003
29	29/5/2015	182.07	52.937	72.996
30	30/5/2015	209.796	42.236	51.46
31	31/5/2015	187.68	56.726	60.965
	Total	6.092.645	1.716.451	1.946.273

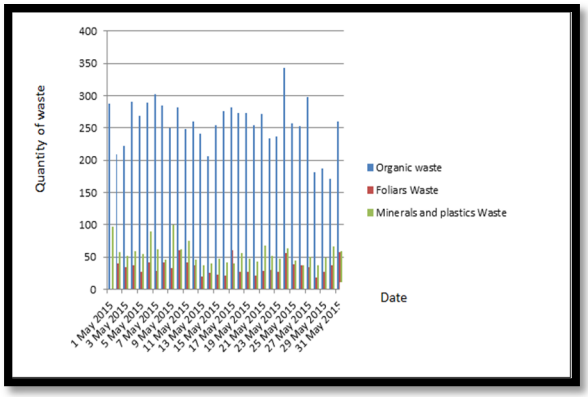

Figure 1. The analytical results of waste of Al-Salhya apartment.

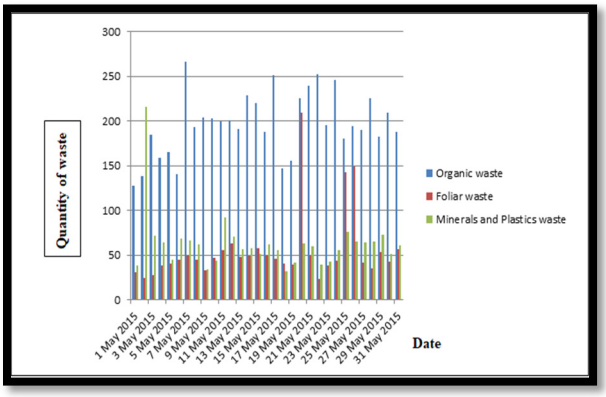

Figure 2. The analytical result of waste of Zayouna apartments.

In the two forms we note that organic waste is much higher than other types. When comparing the proportions between the current compound and the Zayouna apartment, we find that Zayouna rates are higher in the production of foliar waste, but the proportion of organic waste is slightly less than the waste of Salhya apartment.
It is illustrated in the following more forms:

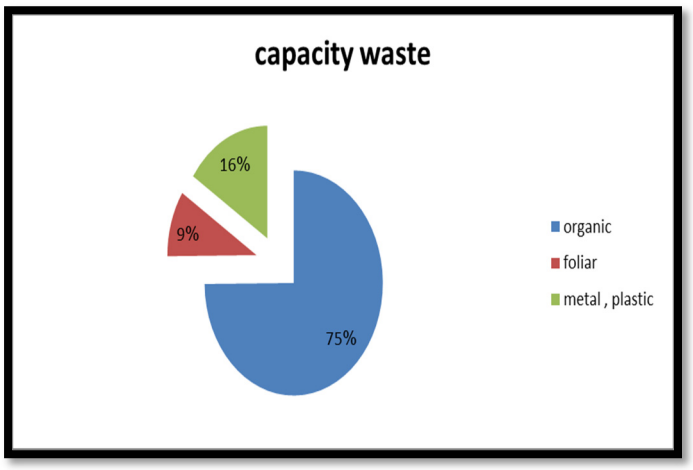

Figure 3. Alsalhya Waste.

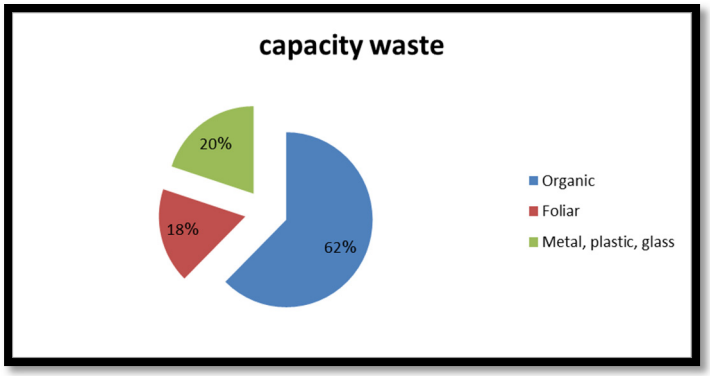

Figure 4. Zayouna Waste.

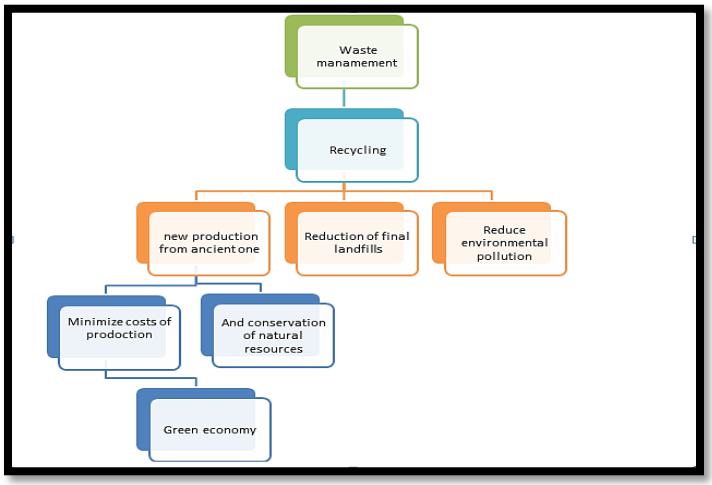

Figure 5. shows a summary of conclusions and the proposed process flowchart

We obtained these results through the commitment of the population to the instructions and also the commitment of workers and supervisors to work, as mentioned previously, these results are May-specific and may change as the seasons or months change.
The importance of sorting waste from each other is to preserve the cleanliness of some species to be recyclable, and also to keep the cleaners safe from the toxic substances that may be exposed to them during the sorting of waste in places sorted, and reduce the number of hands working also.

MATHEMATICAL CALCULATIONS GOALS

The study of waste management and the results it leads to whether it is positive or negative, whether on society or on the economy
A statement of how waste management is associated with the green economy and showing the means linking them
Increase citizens' awareness in the sorting and regulation of waste, including the preservation of the environment
Is Green Economy an Effective Role in Waste Management?

CONCLUSION

Through our study of waste sorting and management and the consequent results, we found that the awareness of the inhabitants of the designated land must be increased by complying with the laws and instructions of waste management by them because this leads to several positive things:
Reducing the environmental risks that may result from mixing different types of waste.
Reduce the areas allocated to the waste stream and thus we have reduced environmental risk-

The management of waste in the places put forward leads to the reduction of workers working on this work and thus preserve the safety of as many people as possible from the radiation or toxic substances contained in those wastes. Waste management leads to sorting out good types of waste and sending them to recycling plants.
To manage and maintain the concept of green economy the proposed system flowchart described in Fig 5. in which, we have reduced the cost of waste disposal and cost it to transfer to recycling plants, and we obtained new products also at a lower cost, and reduced the consumption of natural resources and thus we reached the green economy through the management of waste.

REFERENCES

1. JayalAD , Badurdeen F, Dillon Jr OW , Jawahir IS.," Sustaniable manufacturing: modeling and optimization challenges at the product , process and system levels ", (2010), CIRP Jounral of Manufacturing Science and Technology.
2. Kasztelan, Armand, "Green Growth, Green Economy and Sustainable Development: Terminological and Relational Discourse", 2017/05, Prague Economic Papers, 487-499 Vol 26 Doi 10.18267/j.pep.626
3. Allen, C., Clouth, S. (2012). "A Guidebook to the Green Economy. Issue 1: Green Economy, Green Growth, and Low -Carbon Development" – History, Definitions and a Guide to Recent Publications. UN Division for Sustainable Development.
4. Barbier, E. B. (2009)."Rethinking the Economic Recovery: A Global Green New Deal. Report prepared for the Economics and Trade Branch, Division of Technology", Industry and Economics, UNEP.
5. Barbier, E. B. (2011). "The Policy Challenges for Green Economy and Sustainable Economic Development:. Natural Resources Forum 35(3), 233–245. https://doi.org/10.1111/j.1477-8947.2011.01397.x.
6. Caprotti, F., Bailey, I. (2014)." Making Sense of the Green Economy. Geografiska Annaler: Series B, Human Geography", 96(3), 195–200. https://doi.org/10.1111/geob.12045
7. Diyar, S., Akparova, A., Toktabayev, A., Tyutunnikova, M. (2014). Green Economy - Innovation-Based Development of Kazakhstan.Procedia - Social and Behavioral Sciences, 140,695–699. https://doi.org/10.1016/j.sbspro.2014.04.497.
8. Endl, A., Sedlacko, M., " National Sustainable Development Strategies – What Future Role with Respect to Green Economy? UNCSD Side Event Policy Brief, European Sustainable Development Network (ESDN)" , Vienna.Global Green Growth Institute (GGGI) (2012).
9. "Green Growth Planning GGGI Country Programs. "[Retrieved 2015-10-05] Available at: http://www.gggi.org/project/mainGreen Economy Coalition (2010).
10. " Green, Fair and Productive: How the 2012 Rio Conference Can Move the World Towards Sustainability " . [Retrieved 2015-11-03] Available at: http://www.greeneconomycoalition.org/sites/default/files/documents/GEC_Rio2012_0510.pdf
11. Green Growth Leaders (2011). Shaping the Green Growth Economy. A Review of the Public Debate and the Prospects for Green Growth. Copenhagen
12. Volkery, A., Rouabhi, S. (2015). Green Economy and Sustainable Development. A Historical Account of the Discourse around Sustainable Development and Green Economy, KNOSSOS Policy Briefings: Green Economy, Discussion Paper, UNEP, IEEP, GLOBE-EU. [Retrieved 2015- 11-03] Available at: http://www.unep.org/research4policy/ policybriefs/tabid/78428/Default.aspx
13. WCED (UN) (1987). Our Common Future . Report of the World Commission on Environment and Development, New York: World Commission on Environment and Development. World Bank (2012). Inclusive Green Growth: The Pathway to Sustainable Development . Washington D.C.: The World Bank. [Retrieved 2015-11-03] Available at: http://siteresources. worldbank.org/EXTSDNET/Resources/Inclusive_Green_Growth_May_2012.pdf
14. Zervas, E. (2012). ""Green Growth versus Sustainable Development. Recent Advances in Energy, Environment and Economic Development ", ed. Eslamian S., Proceedings of the 3rd International Conference on Development, Energy, Environment, Economics (DEEE '12), Paris, France, December 2–4, 2012, 399–404.
15. B.J AlKhafaji, Image Improvement Using The Combination of Wavelet and Multiwavelet Transform 2010 - Ibn AL-Haitham Journal For Pure and Applied Science VO L.23 (3).
16. Portilla, J., Strela, V., Wainwright, M., Simoncelli, E.P., "Image Denoising using Gaussian Scale Mixtures in a Wavelet Domain", TR2002-831, Computer Science Dept, New York University. 2002.
17. Iptehaj Alhakam, Nassir H Salman(2022), "An Improved Probability Density Function (PDF) for Face Skin Detection", Iraqi Journal of Science, Vol. 63, No. 10, pp: 4460-4473, DOI: 10.24996/ijs.2022.63.10.31

18. B.J AlKhafaji, M Salih, S Shnain, Z Nabat ," segmenting video frame images using genetic algorithms",2020 Periodicals of Engineering and Natural Sciences 8 (2), 1106-1114
19. W. H. Abdulsalam, R. S. Alhamdani, and M. N. Abdullah, "Emotion recognition system based on hybrid techniques," International Journal of Machine Learning and Computing, vol. 9, 2019.
20. B.J AlKhafaji, MA Salih, SAH Shnain, OA Rashid, AA Rashid, MT Hussein,2021, "Applying the Artificial Neural Networks with Multiwavelet Transform on Phoneme recognition ",Journal of Physics: Conference Series 1804 (1), 012040.
21. RAHMA, A.M.S., RAHMA, M.A.S., and RAHMA, M.A.S. (2015)" Automated analysis for basketball free throw". In: Proceedings of the 7th International Conference on Intelligent Computing and Information Systems, Cairo, December 2015. Piscataway, New Jersey: Institute of Electrical and Electronics Engineers, pp. 447-453.
22. B.J AlKhafaji," Steganography techniques using tunes and Discrete Cosine Transform (DCT)"" Journal of Xi'an University of Architecture & Technology, S. (2020). Volume XII, Issue IV, - 5234- 5244
23. Abdulsalam WH, Alhamdani RS, Abdullah MN." Facial emotion recognition: A survey. International ", Journal of Advanced Research in Computer Engineering & Technology (IJARCET). 2018 Nov;7(11)
24. B.J AlKhafaji, M Salih, S Shnain, Z Nabat ,"improved technique for hiding data in a colored and a monochrome images" ,2020, Periodicals of Engineering and Natural Sciences 8 (2), 1000-1010
25. Ali RH, Abdulsalam WH. "The prediction of COVID 19 disease using feature selection techniques" .Journal of Physics: Conference Series 2021 May 1 (Vol. 1879, No. 2, p. 022083). IOP Publishing.
26. Baydaa Jaffer Al-Khafaji, Abdul Monem S Rahma, (2023). "Proposed new modification of AES algorithm for data security", Global Journal of Engineering and Technology Advances, Vol. 3, No. 12, pp 117–122
27. AlSaidi, Bushra Kh, Baydaa Jaffer Al-Khafaji, and Suad Abed Al Wahab. "Content Based Image Clustering Technique Using Statistical Features and Genetic Algorithm." Engineering, Technology & Applied Science Research 9.2 (2019).
28. Al-Khafaji, Baydaa Jaffer. "Proposed speech analyses method using the multiwavelet transform." Ibn AL-Haitham Journal For Pure and Applied Science 27.1 (2017): 394-401.
29. Baydaa J Al-Khafaji, Detect The Infected Medical Image Using Logic Gates." Ibn AL-Haitham Journal For Pure and Applied Science Vol. 27.2 (2014): p.260-267.
30. Baydaa Jaffer Al-Khafaji ,"Color image analyses using four deferent transformations (FFT-DCT-DWT-DMWT)".(2014) Computer Engineering and Intelligent Systems www.iiste.org ISSN 2222-1719 Vol.5, No.10, pp 16–24
31. Baydaa-Jaffer Al-Khafaj Abdul Monem S. Rahma, "Optimizing Symmetric vs. Asymmetric Image encryption mathematically", International Journal of Advances in Engineering and Management (IJAEM) Volume 4, Issue 9 Sep. 2022

Dye Sensitized Solar Cell Based on TiO_2-SnO_2 Mesoporous Film

Zahraa Faisal Ghazi [1, a)] Odai N. Salman [1, b)] and Mohammed O. Dawood [2, c)]

[1] *Applied Sciences Department, University of Technology- Iraq, Baghdad, Iraq.*
[2] *Department of Physics, College of Science, Mustansiriyah University, Baghdad, Iraq*

[a)] *Corresponding author: zahraafaisal82@gmail.com.*
[b)] *micro_ud@yahoo.com.*
[c)] *mohammedodda20117@uomustansiriyah.edu.iq.*

Abstract. In this study, SnO_2 paste was formulated using 0.14 g and 0.16 g of SnO_2 nanoparticles. The SnO_2 films were applied as scattering layers in Dye-Sensitized Solar Cells (DSSC) via screen printing and doctor blade techniques. XRD, FE-SEM, AFM, reflection, and FTIR were used to look at the paste's crystal structure, shape, and heat stability. The main goal of the study was to find out how the scattering layer affected the performance of the DSSC. The results showed a crystalline structure mostly made up of rutile SnO2 crystals arranged in a tetragonal pattern. The smallest crystallites were about 100 nanometers across. SEM pictures showed that the SnO2 surface looked like a sponge and had small holes in it, which made it easier for dye to stick to it and for electrons to move around. It was also seen that the average particle size got smaller as the dye concentration went up. At lower dye concentrations, SnO2 particles stayed smaller than 100 nanometers.

Keywords: *FE-SEM, AFM, scattering layer, doctor blade method, crystal structure analysis*.

INTRODUCTION

When tin dioxide and antimony oxide are mixed together, they work as a semiconductor in solar systems [1]. It is also used as a clear, electrically conductive layer in optical beams and liquid crystal screens [2]. It is also used in gas monitors, where oxidizable gases or vapors cause it to change its resistance [3]. Tin dioxide is also used as a cleaning powder for metals and glass, in addition to these uses. As a clear, white opacifying agent, it is used to make pottery glazes, frosted glass, and enamel. It is also used to fix cracked glass and speed up different chemical reactions [4]. Tin dioxide is the primary component of the mineral cassiterite, also known as tin stone, making it the main source for producing pure tin. Cassiterite, a common oxide mineral, has a metal-to-oxygen molar ratio of 1:2 and crystallizes in the tetragonal crystal system with the chemical formula SnO_2 [5]. It forms short to long, prismatic, needle-shaped, or bipyramidal crystals, as well as granular to massive aggregates, in colors ranging from brown-black, gray, yellow-brown, and green to red [6]. There are also colorless crystals, with translucent ones exhibiting weak dichroism in yellow and reddish-brown [7]. The theoretical tin content in the mineral is 78.8 percent, but this is often reduced due to the partial replacement of tin atoms by iron, titanium, niobium, tantalum, or zirconium atoms [8]. Cassiterite belongs to the rutile group, along with minerals such as argutite, paratellurite, plattnerite, pyrolusite, rutile, and tripuhyite [9]. Due to its high tin content, cassiterite (also known as tin stone) has been utilized since the 6th millennium BC. By the 1st century BC, it was being mined, making it one of the earliest ores used by humans [10]. Cassiterite is mainly found in hydrothermal veins and granitic pegmatites, but it can also be present as placer deposits in river sediments [11]. With a theoretical tin content of 78.8 percent, cassiterite is the world's only significant tin ore. However, the actual tin content is often lower because tin atoms are frequently partially replaced by iron, titanium, niobium, tantalum, or zirconium atoms [12, 13]. Cassiterite is smelted at approximately 1000 degrees Celsius [14]. The extracted tin is used as a non-toxic, rust-resistant coating for steel containers (tinplate) and for manufacturing various household items like plates and jugs, as well as decorative and play items like tin figures. Additionally, when alloyed with lead, tin serves as a low-melting soft solder [15]. Well-formed cassiterite crystals are crafted into gemstones for jewelry. However, their sensitivity to various acids and heat depends on their tin content. Due to its color and luster, cassiterite can be easily mistaken for colored diamonds, smoky quartz, scheelite, zircon, and other minerals [16, 17]. The dye is a crucial component of solar cells, as it absorbs light and generates electron-hole pairs [18]. These dyes are typically complex molecules with structures

Technologies and Materials for Renewable Energy, Environment and Sustainability
AIP Conf. Proc. 3321, 040019-1–040019-6; https://doi.org/10.1063/5.0289703
Published under an exclusive license by AIP Publishing. 978-0-7354-5231-2/$30.00

similar to chlorophyll. Numerous dyes have been tested in laboratories, including (5-amino-1,10-phenanthroline) bis-(2,2'-bipyridyl-4,4'-dicarboxylate acid)-ruthenium(II) (Ru1), (1,10-phenanthroline) bis-(2,2'-bipyridyl-4,4'-dicarboxylate acid)-ruthenium(II) (Ru2), (5-amino-1,10-phenanthroline) bis-(2,2'-bipyridine)-ruthenium(II) (Ru3), and cis-dithiocyanato-N,N-bis-(2,2'-bipyridyl-4,4'-dicarboxylate acid)-ruthenium(II) (N3) [19]. The ruthenium bipyridine complex, specifically cis-dithiocyanato bis(2,2'-bipyridyl-4',4'-dicarboxylate acid)-ruthenium(II) (N_3), with a band gap of 1.63 eV, has demonstrated the best performance [20]. This dye is effective in capturing much of the sunlight when applied as a monolayer on a porous TiO_2 surface. Besides strong light absorption in the visible/near-infrared range, which is essential for efficient solar spectrum utilization, the dye must meet several other requirements, making it a complex component despite its seemingly simple role as a light absorber [21]. A major breakthrough occurred in the early 1990s with the use of the trinuclear ruthenium complex $[Ru(bpy)2(CN)2]2Ru(bpy(COO)_2)_2$ $2-$ for sensitizing the TiO_2 layer, achieving efficiencies close to 8% at an intensity of 750 W/m² (AM 1.5). Since then, many dyes have been explored, with cis-Ru(2,2'-Bipyridyl-4,4'-Dicarboxylato acid)$2(NCS)_2$ standing out as exceptional [22].

In this study, dye-sensitized solar cells (DSSCs) incorporating SnO_2 were produced by mixing different quantities (0.14g and 0.16g) of SnO2 with the N719 dye to improve solar cell performance. The newly created solar cells were then analyzed using XRD, TGA, and FE-SEM techniques.

PREPARATION METHODS

SnO_2 paste was applied to FTO-coated glass substrates using the Doctor-Blade method. The paste was then annealed at 450 ºC for 30 minutes, followed by immersion in a dye solution for 24 hours to create the final paste. To find out how the amount of SnO_2 affected the paste, we looked at how it affected the N719 dye, which is a common dye from the Australian company Dyesol Ltd. Using the N719 color, four different samples were made, each with between 0.14g and 0.16g of SnO_2. The SnO_2 pastes on glass surfaces have been studied utilizing a Shimadzu XRD 6000 with a Cu K± line of 0.15419 nm to find out more about them. A Differential Scanning Calorimeter (DSC), Model PT-1000, which works from 0 ºC to 600 ºC, was used to measure the changes in the samples' physical properties. A 20 mg sample was cooked at a rate of 10 ºC/min so that it could be looked at. A FE-SEM (Zeiss) was also used to look at the physical properties of the SnO_2 pastes. SnO_2 was also studied in terms of its shape, and SnO_2 pastes were looked at with a FE-SEM (Zeiss).

RESULTS AND DISCUSSION

There were two samples made with different amounts of SnO_2: 0.14 and 0.16. Figure 1 shows that the XRD patterns of these materials have similar peak locations and intensity ranges. All of the peaks were found to be rutile SnO_2 (cassiterite phase, JCPDS file card #41-1445), and all of the samples showed planes (1 1 0), (1 0 1), (2 0 0), (2 1 1), and (3 0 1). The sample made at 200 °C, on the other hand, had more crystals and had extra surfaces (2 2 0), (0 0 2), (3 1 0), and (2 0 2) [23]. The crystallinity of the materials was evaluated using the full width at half maximum (FWHM) of the main reflections, specifically the (1 1 0), (1 0 1), (2 2 0), and (2 1 1) planes, calculated using the Scherrer equation and presented in Table 1. It is observed that with an increase in concentration from 0.14 to 0.16, the crystallite size increased from 80 to 100 nm. The lattice constants calculated from the XRD patterns are a = 4.738 Å and c = 3.187 Å, indicating a consistent trend with the variations in temperature [24-26].

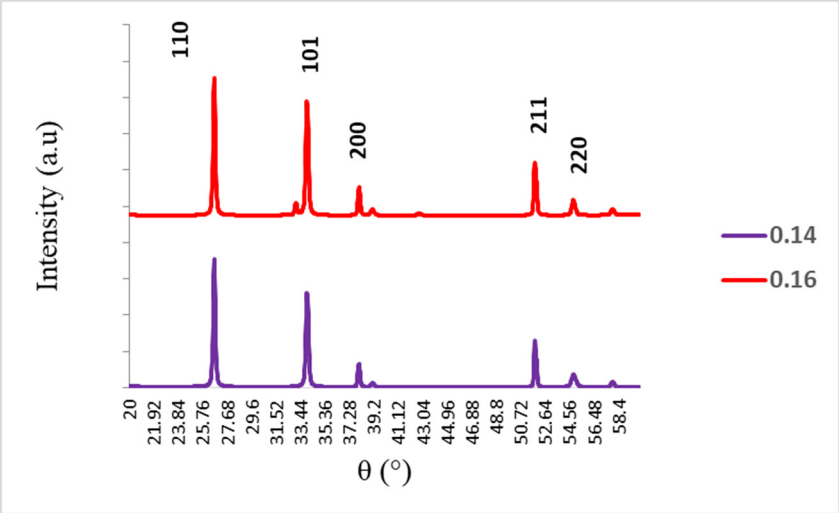

FIGURE 1. The XRD patterns of the manufactured samples at two different concentrations

Batch adsorption experiments

The values of d and (hkl) that have been utilized to match the XRD pattern seen in Figure 2 to drive the lattice parameters in a computer program based on Cohen's least squares method. These are the values for the transition temperature parameters Tc (displacement) [35–40], Tc (onset), excess oxygen ε(O2), lattice parameters a, b, c, and volume fraction Vph(1223). It's important to note that the current results have an experimental error of about 5%.

TABLE 1. FWHM and crystallite size for the prepared samples

Sample	**(1 1 0)**		**(1 0 1)**		**(2 1 1)**	
SnO_2 concentration	FWHM (°)	Crystallite size (nm)	FWHM (°)	SnO_2 concentration	FWHM (°)	Crystallite size (nm)
0.14	0.6	3.1	0.5	0.14	0.6	3.1
0.16	0.32	20.2	0.45	0.16	0.32	20.2

FE-SEM analysis was conducted to examine the morphologies and surface characteristics of the samples synthesized at different concentrations. In Figure 2(a), the sample with a concentration of 0.14 exhibited a uniform distribution of nanoparticles (NPs) ranging from approximately 100 to 200 nm in diameter, with minimal agglomeration and evident porosity within the nanostructure. Upon increasing the concentration to 0.16, as illustrated in Figure 2(b), a distribution of spheroidal particles was observed, with one group centered around 100-200 nm and another around 700-800 nm. Further analysis in Figure 2(c and d) revealed that the basic building blocks of the larger particles remained in the 100-200 nm range. The decrease in the spacing between particles (i.e., porosity) with increasing SnO_2 concentration is apparent. It's noteworthy that the distribution of small nanoparticles and large spheres is non-uniform, with small nanoparticles constituting approximately 70% of the composition, while the larger spheres represent about 30%. The hydrothermal method harnesses variations in water's fundamental properties in response to changes in temperature and pressure, affecting parameters such as density, ionic product, viscosity, thermal conductivity, dielectric constant, and heat capacity. Adjustment of solvent properties and experimental parameters can be used to manipulate the hydrothermal process. The theoretical framework of the hydrothermal process employs thermodynamic functions to elucidate nucleation processes that lead to particle formation, where stable nuclei form at the solid/liquid interface and subsequently grow into larger particles via Ostwald ripening [25-29].

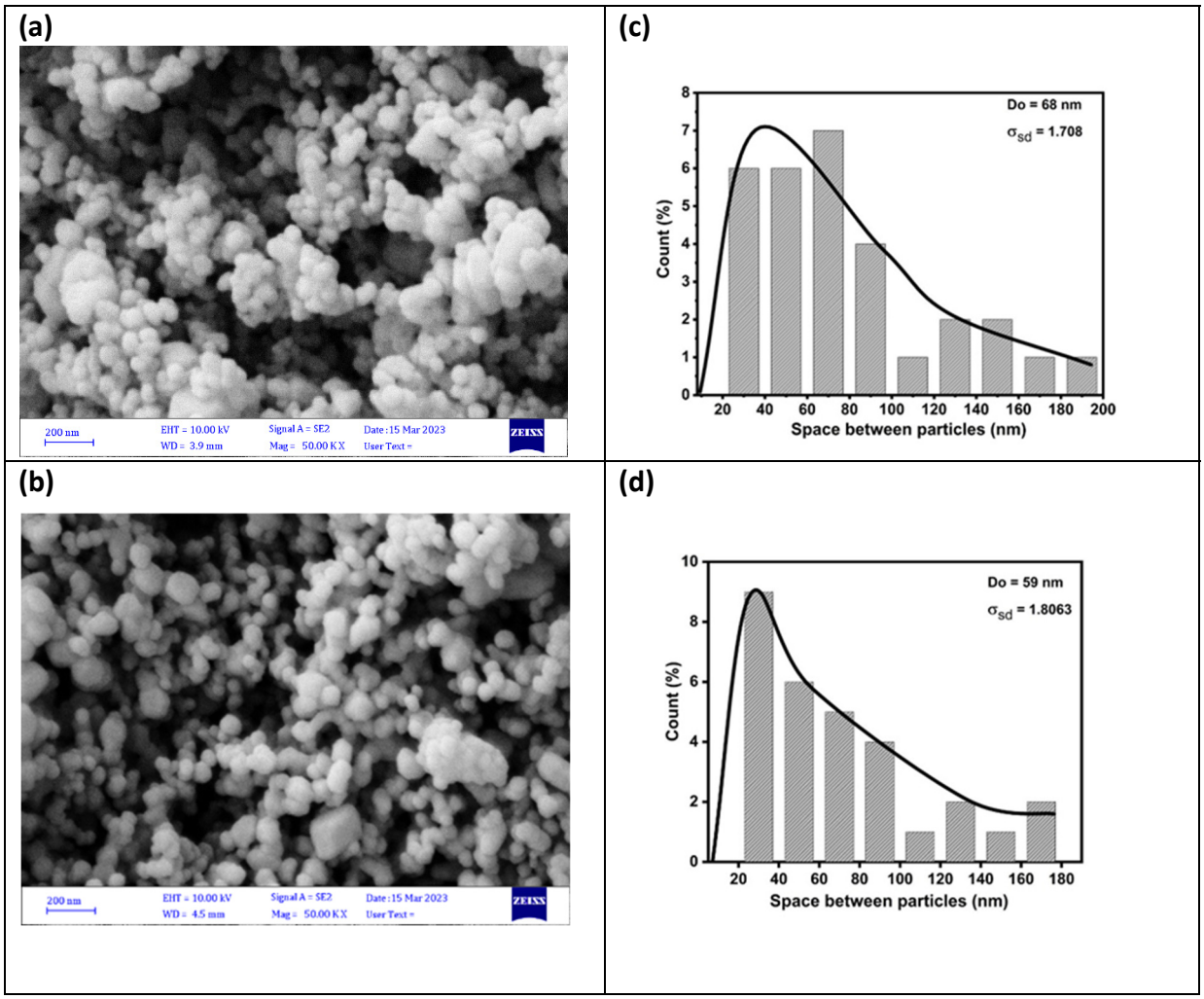

FIGURE 2. FESEM image of a nanocrystalline SnO_2 layer. The nanocrystalline particles, fused into a composite and accompanied by a sponge-like structure, are distinctly observable. The scale bar in the image represents a length of 100 nm

The TGA results for all samples (S3=0.14 g, S4=0.16 g) obtained under a nitrogen flow are illustrated in Figures 3. Three distinct stages can be identified. The initial stage, occurring between 100 and 150 °C, corresponds to the dehydration process, during which water, primarily adsorbed from the surroundings, is released from the larger pores of SnO2. Between 250 and 350 °C, the release of CO2 is observed, originating from the decarboxylation process of N719 [30-35]. This reaction involves converting the four carboxylate groups on the two bipyridine ligands into CO2 [36-40]. The final exothermic stage, observed in the interval of 350–400 °C, is attributed to the burning of organic residues [41-45].

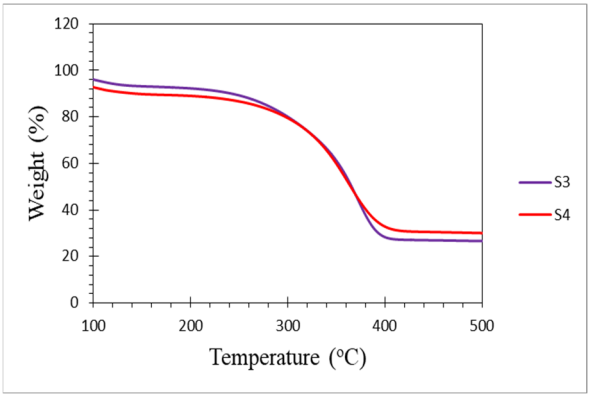

FIGURE 3. The TGA spectra of SnO2@N719 dye at four different concentrations

CONCLUSION

This study focused on the utilization of SnO_2 by incorporating varying amounts (0.14 g and 0.16 g) of SnO_2 and N719 dye. The SnO_2 paste used in the DSSCs exhibited a crystalline structure primarily composed of rutile SnO2 crystals arranged in a tetragonal configuration, with individual crystallites measuring approximately 100 nanometers in diameter. FE-SEM pictures showed that the SnO2 had a surface that looked like a sponge, with small holes that made it easier for dye to stick to it and for electrons to move around. It was seen that as the amount of color went up, the average particle size went down. The average grain size of the SnO2 paste was less than 100 nanometers when the color content was low. TGA tests showed that N719 broke down completely around 400 °C. The results of this study show that adding SnO2 and N719 color could improve the performance of DSSCs. The crystalline structure of the SnO2 paste, which is mostly made up of rutile SnO2 crystals, suggests that it could be used in solar cell uses. Small holes on the surface of SnO2 make it easier for dyes to stick to it and for electrons to move around inside the material, which improves the performance of the device. Also, the fact that the average particle size decreased as the dye concentration went up suggests a possible way to improve the SnO2 paste's qualities for better solar cell performance. As a result of the TGA analysis, we can see that the SnO2@N719 dye mixture is thermally stable. The dye completely breaks down at temperatures around 400°C, which is important for understanding how the material works. Overall, these results help us learn more about and make better SnO2-based DSSCs for use in green energy systems.

REFERENCES

1. J. Shen *et al.*, “Improvement of Photovoltaic Performance of Perovskite Solar Cells by Synergistic Modulation of SnO_2 and Perovskite via Interfacial Modification,” *ACS applied materials & interfaces*, May 2024, doi: https://doi.org/10.1021/acsami.4c03595.
2. A. S. Jasim and O. N. Salman, “Hydrothermally native defect induced transparent p-n TiO2 homojunction diode,” *Optical and quantum electronics*, vol. 55, no. 8, Jun. 2023, doi: https://doi.org/10.1007/s11082-023-04984-6.
3. N. Assoudi et al., “Comparative examination of the physical parameters of the sol gel produced compounds La0.5Ag0.1Ca0.4MnO3 and La0.6Ca0.3Ag0.1MnO3,” Optical and Quantum Electronics, vol. 54, no. 9, Jul. 2022, doi: https://doi.org/10.1007/s11082-022-03927-x.
4. Randa Taleb Hello, Odai Naem Salman, and Khaleel Ibrahim Hassoon, “Determination of band gap energy for fluorine tin oxide using reflection date,” *AIP conference proceedings*, Jan. 2024, doi: https://doi.org/10.1063/5.0185280.
5. A. T. Sami, O. N. Salman, and M. M. Ismail, “Ferroelectric Photodiode Based on $BaTiO_3$ Nanorods Film,” *Journal of physics. Conference series*, vol. 1795, no. 1, pp. 012047–012047, Mar. 2021, doi: https://doi.org/10.1088/1742-6596/1795/1/012047.
6. O. N. Salman, M. M. Ismail, and M. O. Dawood, “Porous BaTiO3 film for dye-sensitized solar cells,” *Optical and quantum electronics*, vol. 55, no. 5, Apr. 2023, doi: https://doi.org/10.1007/s11082-023-04741-9.
7. Selma, O. N. Salman, and N. A. Yousif, “INFLUENCE OF GROWTH TIME ON STRUCTURAL, OPTICAL AND ELECTRICAL PROPERTIES OF TiO_2 NANOROD ARRAYS DEPOSITED BY HYDROTHERMAL

METHOD," *Surface Review and Letters*, vol. 26, no. 03, pp. 1850155–1850155, Mar. 2019, doi: https://doi.org/10.1142/s0218625x1850155x.
8. L. Xiao *et al.*, "Electron Transfer Dynamics at Dye-Sensitized SnO2/TiO2 Core-Shell Electrodes in Aqueous/Nonaqueous Electrolyte Mixtures," Apr. 2024, doi: https://doi.org/10.26434/chemrxiv-2024-hn590.
9. Jasim, A.S., Salman, O.N. Hydrothermally native defect induced transparent p-n TiO_2 homojunction diode. *Opt Quant Electron* **55**, 702 (2023). https://doi.org/10.1007/s11082-023-04984-6
10. Odai N. Salman *et al* 2023 *ECS J. Solid State Sci. Technol.* **12** 065001 https://doi.org/10.1149/2162-8777/acdb99
11. Mohammed, M.A., Salman, O.N. & Bülbül, M.M. Preparation of Ag@SiO_2 core–shell nanoparticles for plasmonic dye-sensitized solar cell application using laser ablation in liquid technique. *Opt Quant Electron* **56**, 40 (2024). https://doi.org/10.1007/s11082-023-05609-8
12. Lokeswararao Dhavala, Sai Muthukumar V, Vijay Sai Kollipara, and Varma, "Superior dielectric and varistor properties of ZnO or SnO2 diffused calcium copper titanate ceramics," *Journal of applied physics*, vol. 133, no. 9, Mar. 2023, doi: https://doi.org/10.1063/5.0139359.
13. G. Yang, Z. Yan, and T. Xiao, "Preparation and characterization of SnO2/ZnO/TiO2 composite semiconductor with enhanced photocatalytic activity," *Applied Surface Science*, vol. 258, no. 22, pp. 8704–8712, Sep. 2012, doi: https://doi.org/10.1016/j.apsusc.2012.05.078.
14. G. Liu *et al.*, "Near-unity, full-spectrum, nanoscale solar absorbers and near-perfect blackbody emitters," vol. 190, pp. 20–29, Feb. 2019, doi: https://doi.org/10.1016/j.solmat.2018.10.011.
15. V. Y. Kumkale *et al.*, "Synthesis of Tin Oxide Nanoparticles using Microwave-Assisted Method for Dye-Sensitized Solar Cell Application," *ES energy & environment*, Jan. 2024, doi: https://doi.org/10.30919/esee1104.
16. Ismail, M.M., Salman, O.N. & Ali, T.H. Effect of TiO_2 nanorod thickness on optical properties of $Ba_{0.8}Sr_{0.2}TiO_3$ film via hydrothermal method. *J Solid State Electrochem* **25**, 2429–2441 (2021). https://doi.org/10.1007/s10008-021-05022-9
17. M. Rasheed, Suha Shihab, O. Alabdali, and H. H. Hassan, "Parameters Extraction of a Single-Diode Model of Photovoltaic Cell Using False Position Iterative Method," Journal of Physics: Conference Series, vol. 1879, no. 3, p. 032113, May 2021.
18. Salman, O.N., Ismail, M.M. & Dawood, M.O. Porous $BaTiO_3$ film for dye-sensitized solar cells. *Opt Quant Electron* **55**, 469 (2023). https://doi.org/10.1007/s11082-023-04741-9
19. Ismail, M.M., Salman, O.N. & Ali, T.H. Effect of TiO_2 nanorod thickness on optical properties of $Ba_{0.8}Sr_{0.2}TiO_3$ film via hydrothermal method. *J Solid State Electrochem* **25**, 2429–2441 (2021). https://doi.org/10.1007/s10008-021-05022-9
20. Reem A. Saleh , Odai N. Salman, and Mohammed O. Dawood. Structural and Optical Properties of P-type Cr-Doped TiO2 Nanorods Film. Journal of nanostructures vol. 11, issue 4, 678-683 (2021). https://doi.org/10.22052/JNS.2021.04.006
21. Hello, R.T., Salman, O.N., Hassoon, K.I. Determination of Band gap Energy for Fluorine Tin Oxide using Reflection Date. AIP Conf. Proc. 2922, 210010 (2024). https://doi.org/10.1063/5.0185280
22. Husam Nahedh *et al* 2024 *ECS J. Solid State Sci. Technol.* **13** 043009 https://doi.org/10.1149/2162-8777/ad3d08
23. Odai N. Salman *et al* 2021 *J. Phys.: Conf. Ser.* **2114** 012063 https://doi.org/10.1088/1742-6596/2114/1/012063
24. O N Salman *et al* 2019 *IOP Conf. Ser.: Mater. Sci. Eng.* **518** 032012 https://doi.org/10.1088/1757-899X/518/3/032012.
25. M. Rasheed, S. Shihab, O. Y. Mohammed, and A. Al-Adili, "Parameters Estimation of Photovoltaic Model Using Nonlinear Algorithms," Journal of Physics: Conference Series, vol. 1795, no. 1, p. 012058, Mar. 2021.
26. Salman, O.N., Agool, I.R. & Ismail, M.M. Preparation of the scattering layer based on TiO_2 nanotube and their dye sensitized solar cell applications. *Appl. Phys. A* **123**, 402 (2017). https://doi.org/10.1007/s00339-017-1012-4.

Simulation of Interaction Energy and Thermodynamics Properties of Developed Nano Drug Docking With Glucose for the Diabetes Treatment

Shaymaa A. Jaber [1,2,a)], Bahjat B. Kadhim [1,b)], Ali Taher Mohi[1,c)]

[1] *Department of Physics, College of Education, Mustansiriyah University, Baghdad, Iraq.*
[2]*Department of Physics, College of Science, Sumer University, Baghdad, Iraq.*

[a)] shimaa.aziz@uos.edu.iq
[b)]Corresponding author: sci.phy.bbk@uomustansiriyah.edu.iq
[c)] dr.alitaher@uomustansiriyah.edu.iq

Abstract: In this study Gaussian 16 software was used to investigate the electronic and thermodynamic properties of the nanomaterial coupling process. Especially nanocinnamon and $(MgO)_4$, deoxyhemoglobin and glucose analyzes were performed using density functional theory at the B3LYP level. he aim of this studTy was to evaluate the potential toxicity and therapeutic benefit of these nanomaterials in diabetes treatment. The results indicate that the nanoparticles with higher ionization energy and chemical hardness increase stability and reduce reactivity, conversely, those with higher ionization strength, and a lower chemical hardness will have a higher reactivity. The coupling reaction between deoxyhemoglobin, nanomaterial's and glucose changes depending on their thermodynamic and electronic properties. The Gibbs free energy for docking $(MgO)_4$ and nanocinnamon with deoxyhemoglobin is larger (1.601857148 eV) compared to that of glucose (0.561798306 eV), indicating that the interaction with deoxyhemoglobin is beneficial in vivo, more of the docking of deoxyhemoglobin with $(MgO)_4$ and nanocinnamon. The nanocinnamon and $(MgO)_4$ use represents a promising development in the advancement of treatment for advanced diabetes.

Keywords: nanomaterial, $(MgO)_4$, blood sugar, Density Functional Theory, thermodynamic properties, cinnamon.

INTRODUCTION

Despite the typical form of nanomaterial, these have unique properties and capabilities. The precision this has enabled is so critical to medical advancements. A better understanding of biology leads to better diagnoses, which in turn results in improved treatment outcomes. This is because of the immense size at the nanoscale. They are typically 0.1 to 100 nanometers in size and have a high surface area to volume ratio. They show increased responsiveness to chemical stimuli and have a high ability to bind to biological molecules. Quantum dots have a wide range of applications, such as biosensing and targeted drug administration. This is due to the quantum effects that their small size induces. These effects therefore change the optical and electromagnetic characteristics[1, 2]. Improved health assessments and treatment options allow for precise drug delivery using nanoparticles. This leads to an increase in treatment efficacy and a decrease in side effects. For example, metal-organic frameworks (MOF) have shown significant efficacy enhancements compared to traditional cancer treatments[3].

Building advanced diagnostic devices with nanomaterials can achieve early and more accurate disease diagnosis. Economical, Nanomaterials are generally less expensive and easier to apply compared with traditional alternatives[2]. This, in turn, is the result of nanotechnological achievements that lead to made-in-the-lab materials that are truly biocompatible with any biological medium. Despite the numerous opportunities, some limitations, such as potential toxicity and regulatory obstacles, still challenge the use of nanomaterials. It is only by combining innovation and safety that it can be moved forward in the development of nanomedicine [4].

Technologies and Materials for Renewable Energy, Environment and Sustainability
AIP Conf. Proc. 3321, 040020-1–040020-9; https://doi.org/10.1063/5.0289620
Published under an exclusive license by AIP Publishing. 978-0-7354-5231-2/$30.00

The molecular interactions possess considerable therapeutic promise. When hemoglobin interacts with nanomaterials and other medicinal chemicals, it enhances their reactivity and utility, potentially opening up novel approaches for treating diseases such as cancer and ischemic stroke [5].

Bio inspired glucose-sensitive nanomaterials that trigger controlled release of drugs are one type which has been proven to improve the treatment efficacy of diabetes. This innovation improves health outcomes by reducing the likelihood of adverse events and improving patient compliance. Nanotechnologies and risks The advantageous potential of nanotechnology in diabetes treatment should be balanced against the fact that it might cause toxic side effects, which is a risk [6].

The red blood cells contain a crucial protein called hemoglobin (HB), which is responsible for carrying oxygen throughout the body[7]. The heme molecule that gives blood its red color is present in each of the four globin peptides that make up this structure [8].

Given that the usual hemoglobin range is between 12.5 and 17.0 g/dL prior to blood donation, abnormal hemoglobin levels may be a sign of health issues. Research [9] has linked high hemoglobin levels within the normal range to poor metabolic profiles, a higher risk of type 2 diabetes, the buildup of fat in the liver, and higher death rates, particularly from cardiovascular diseases.

The aim of this study was to investigate the effects of nano-materials $(MgO)_4$ and cinnamon nanoparticles on hemoglobin, as well as their probable toxicities. It also seeks to resonate their effectiveness in controlling glucose levels, and measure the extent of development accomplished through nanomaterials towards restoring blood sugar. These two stages correspond to the docking of the nanomaterial (MgO)4 with naoncinnamon, followed by the docking of glucose with the nanomaterial (MgO)4 with naoncinnamon.. The challenge is to develop a therapeutic intervention that leads at a quicker pace on decreased blood glucose level. Caussian16 duplicates all of this.

THEORETICAL CONSIDERATIONS

The nature of the electronic properties can be keyed to how hemoglobin comes off a precious cargo site, docks with nanomaterials or not in pathogens and also their homage docking for therapies. They also leave a huge influence in the field of biosensors and bioelectrochemical systems as well as many other eventual fields. In this case, these properties belong to the total energy (E_T) of a system wherein it is defined as sum-coherent kinetic energies of electrons, -electron-nuclei interaction, attraction - energy and repelling - energy and exchange-bonding.

When a molecule is in its steady state, its energy gap (E_g) is the difference between the energies of its highest occupied (HOMO) and lowest unoccupied (LUMO) molecular orbital[10, 11]:

$$E_g = (\varepsilon_{LUMO} - \varepsilon_{HOMO}) \ldots\ldots \qquad \ldots\ldots\ldots\ldots (1)$$

The molecular electrostatic potential aids in identifying regions of different potentials, which contributes to understanding molecular interactions. Ionization energy (IP) [12] and electron affinity (EA) [13] represent the amount of energy required to remove or gain an electron:

$$IP = -\varepsilon_{HOMO} \qquad \ldots\ldots \qquad \ldots\ldots (2)$$

$$EA = -\varepsilon_{LUMO} \qquad \ldots \qquad \ldots\ldots (3)$$

The Fermi energy (E_F) [14] and work function (ϕ_m)[15] determine the energy level separating the conduction and valence bands, as well as the energy required to remove an electron from the material's surface:

$$E_F = -\frac{IP + EA}{2} \qquad \ldots\ldots\ldots \qquad \ldots\ldots (4)$$

$$\phi_m = LUMO - E_F \qquad \ldots\ldots\ldots\ldots \qquad \ldots (5)$$

The width of the valence and conduction bands influences the electronic properties of materials. Chemical potential(Ω) (Fermi energy) [16] measures the tendency of electrons to escape. while chemical hardness(η) and softness (ζ) [17]express the resistance of a system to charge transfer:

$$\eta = \frac{(IP - EA)}{2} \qquad \ldots\ldots\ldots \qquad \ldots\ldots (6)$$

$$\zeta = \frac{1}{2\eta} \qquad \ldots\ldots \qquad \ldots\ldots (7)$$

Electrophilicity (ω)[18] measures the energy released by the flow of electrons between a donor and an acceptor:

$$\omega = \frac{\chi^2}{2\eta} \qquad \ldots. \qquad \ldots (8)$$

Electronegativity (χ)[19] is a measure of how strongly an atom pulls electrons toward itself in a molecule. which is critical for understanding molecules' reactivity:

$$\chi = \frac{IP + EA}{2} \quad \ldots\ldots \quad \ldots (9)$$

Binding energy (E_B)[20]expresses the strength of bonds in solids, while interaction energy (E_{int}) [21] is critical to understanding molecular binding and porous material behavior:

$$E_B = [(N\,E_X + M\,E_Y) - E_{XY}]/(N + M) \quad \ldots\ldots\ldots \quad \ldots (10)$$

$$E_{int} = E_{Docking} - \left(E_{DHB} + E_{Drug}\right) \ldots\ldots \quad \ldots (11)$$

Where $E_{docking}$ refers to the total energy of the docking atoms of nanomaterials with glucose and Deoxy HB. The E_{drug} and E_{DHB} energies of atoms of nanomaterials $(MgO)_4$ and nano Cinnamon, and Deoxy HB. respectively. N and M are the number of atoms of nanomaterials and Deoxy HB present in the structure of the system, respectively.

The thermodynamic parameters, including enthalpy (ΔH), entropy (ΔS), and free Gibbs energy (ΔG) changes, are crucial for understanding the interactions between proteins like hemoglobin (HB) and nanomaterials. These parameters not only indicate the spontaneity and strength of binding processes, but they also have important implications for biological effects and health risks. Enthalpy and stability the enthalpy character of protein-nanomaterial interactions can influence protein stability [22]. Changes in entropy during binding can affect proteins' overall stability and functionality, potentially leading to biological alterations such as oxidative stress and DNA damage [23]. Free energy changes the changes in free energy that happen because of these interactions help us understand how binding happens on its own, which is important for checking the safety and effectiveness of nanomaterials in biomedical settings [24].

$$\Delta G = \Delta H - T\Delta S \quad \ldots \quad \ldots . (12)$$

T is its temperature in kelvin.

MATERIALS AND METHODOLOGY

Simulation of the interaction energy and thermodynamic properties of a herbal medicine developed by a nanomaterial represented by magnesium oxide for the purpose of docking with glucose, which causes diabetes, to increase the efficiency of treatment. The herbal material was able to be made with the nano cinnamon substance with the chemical structure (C_9H_8O), and its spatial structure [25], where it was used to implement the simulation requirements. The nano cinnamon substance was developed by docking it with the nano magnesium oxide substance, which has the spatial structure as shown in Figure 1b [26]. Increased concentration of glucose in the blood leads to diabetes, and the glucose has the chemical formula ($C_6H_{12}O_6$), beside Figure 1c shows the spatial structure of glucose [27]. The structure of oxidized and deoxidized hemoglobin was used to know the effect of nano cinnamon and nano magnesium oxide on hemoglobin by comparing the thermodynamic results with oxidized hemoglobin. The chemical formula of hemoglobin is($C_{42}H_{45}FeN_7O_5$), and Figure 1d shows the spatial structure of oxidized hemoglobin [28]. The simulation was performed using program 16 by choosing the density functional theory at the B3LYP level, and with the help of the basis set 6 – 311G(d,p). The simulation was implemented through the Gaussian 16 computing program for the purpose of calculating the electronic properties described in equations (1 – 9). The total energy of the materials under study is obtained through the simulation output data, through which the interaction energy of each material is calculated through equation (11). The thermodynamics properties were calculated through equation (12), which is represented by Gibbs's free energy, enthalpy and entropy.

RESULTS AND DISCUSSION

Before the docking process, it was used the basis set (6-311G(d,p)) to run B3LYP simulations to find the best structures of oxygen, O_2, deoxhemoglobin DHB, glucose, $(MgO)_4$ nanoparticles, and nano cinnamon. The electronic and thermodynamic properties, represented by Gibbs free energy, enthalpy, entropy, and docking energy, as shown in Figures (2a, 2b, 2c, 2d, and 2e) were studied respectevely.

Figure 3a illustrates the docking process between oxygen and DHB, which produces OHB, a representation of the human body in its natural, healthy state. It can be compared all the results with OHB as a point of reference. Therefore, to assess the impact of nanomaterials on the human body and to determine their potential toxicity, our findings align with the research[29] .

Nano cinnamon and $(MgO)_4$ nanoparticles are shown in Figures (3d), (3c), and (3b). It can be docked DHB with them to find out how they affect human body and if they are toxic by using what we know about Gibbs free energy and enthalpy. Figures 4a and 4b illustrate the process of docking nanomaterials with glucose to determine the effect of treatment on blood sugar. Figure 4c illustrates the process of docking nano cinnamon and $(MgO)_4$ nanoparticles with glucose to determine the effect of the treatment and its development in treating blood sugar.

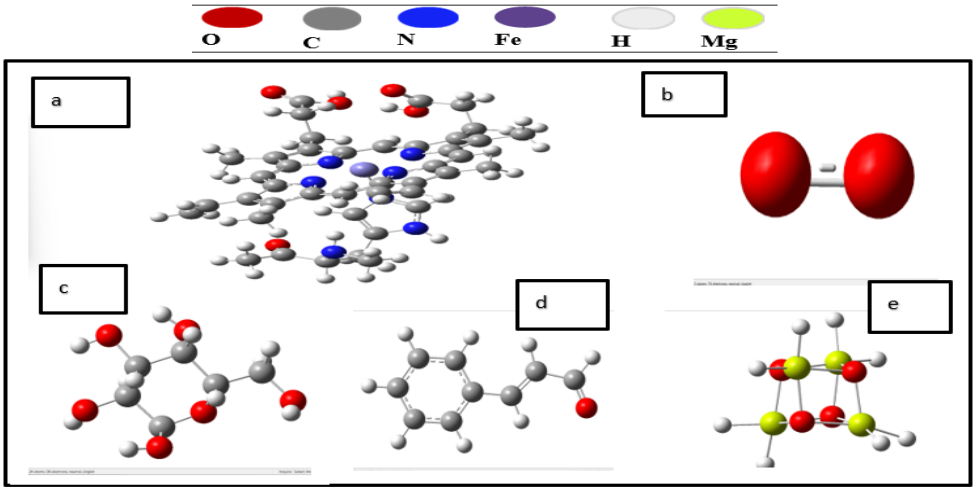

Figure 1: Structures of optimized molecular by B3LYP/6-311G(d,p). (a) Deoxyhemoglobin (DHB). (b) Oxegen. (c) glucose. (d) nano cinnamon. (e) $(MgO)_4$.

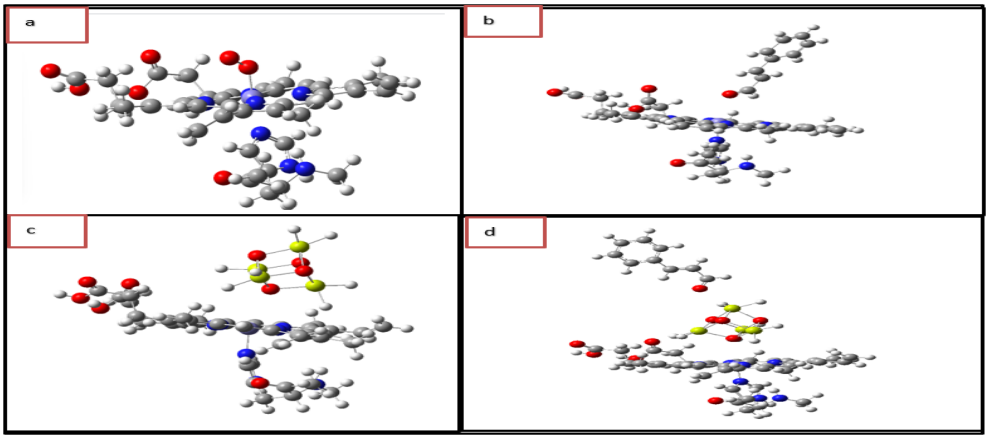

Figure 2: Structures of docking optimized molecular by B3LYP/6-311G(d,p) route. (a) oxyhemoglobin (OHB). (b) DHB with nano Cinnamon. (c) DHB with $(MgO)_4$. (d) Nano Cinnamon with $(MgO)_4$ with DHB.

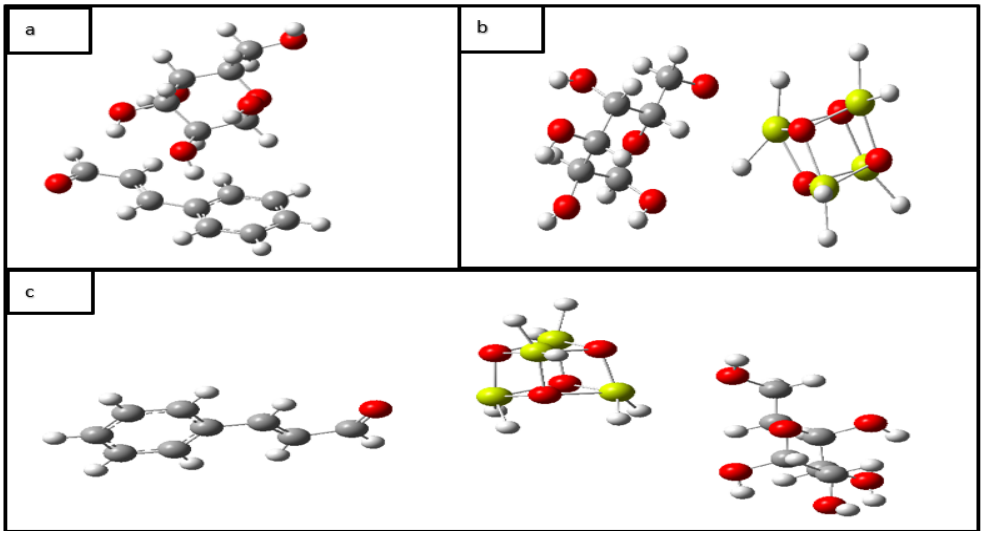

Figure 3: Structures of docking optimized molecular by B3LYP/6-311G(d,p) route. (a) glucose with Nano Cinnamon. (b) glucose with $(MgO)_4$. (c) Nano Cinnamon with $(MgO)_4$ with glucose.

Table 1 shows an analysis of the energy gaps as well as the highest HOMO and lowest LUMO energy levels, reflecting their reactivity and stability. First, it can be noticed that the oxygen (O_2) has a medium energy gap, which gives it a medium ability to transfer electrons between energy levels, indicating relative stability and medium reactivity with other molecules. The energy levels indicate that oxygen requires less energy to lose electrons but more energy to receive them.

It has a higher HOMO energy than oxygen and a larger energy gap for the DHB compound, reflecting greater stability and difficulty in transferring electrons, which makes it less reactive compared to oxygen. On the other hand, it was found that the $(MgO)_4$ nanoparticles compound has the lowest HOMO energy level and the smallest energy gap, indicating its high willingness to lose electrons and its ability to react easily and transfer charge efficiently. This quality makes it ideal for products that require quick and efficient charging. Nano cinnamon has a comparable HOMO energy level with oxygen, indicating moderate stability. However, it can harness this dramatic energy difference as a protective mechanism to lower the toxic side effects of medical therapies. On the other hand, glucose ($C_6H_{12}O_6$) has the greatest energy difference and lowest HOMO. This attribute renders glucose the most stable and least reactive chemical within this group. The metabolic potential of glucose is low, as indicated by the presence of only one positive LUMO level for these molecules, explaining why it serves a largely non-metabolic purpose in the human system.

The average energy gap for OHB is 2.144 eV, making it a stable molecule with moderate reactivity. That energy gap, the average, is the balance between stability and reactivity, which is why I believe OHB is the right candidate for in vivo use with high safety and minimum adverse effects. However, $(MgO)_4$ nanoparticles interacting with DHB has a small energy gap of 0.645 eV, which makes it very strong at transferring charges and interacting with molecules. The negligible difference in energy levels increases the capability of transferred charges, making it impeccable for improving the metabolic reactions in the human body and possibly accelerating the processes related to sugar in the blood. The DHB molecule completes this nanoparticles, forming nano cinnamon. The nano cinnamon energy gap is 2.241 eV, which is considered to be a medium level of stability and has a greater capacity to chemically interact and link with biomolecules. As a result of its intrinsic stability, this molecule can enhance the properties of drugs used in diabetes treatment without having any adverse side effects through interactions or otherwise.

The docking of nano cinnamon, $(MgO)_4$ nanoparticles and DHB absorbed light with an energy gap of 0.791 eV, creating a strong resonance and a large possibility of transferring electric charges. These properties enhance its effectiveness in promoting any chemical reaction in the human body, making it an ideal molecule for treating diabetes, as it aids in lowering blood glucose levels and enhancing the body's response to insulin. The $(MgO)_4$ nanoparticles with glucose complex exhibits an energy gap of 1.810 eV, indicating moderate stability and moderate reactivity. This docking can enhance the effectiveness of glucose in the human body by improving its absorption and regulation, which may contribute to better management of blood sugar levels, and this is consistent with the scientific study[30].

Nano cinnamon docked with glucose, on the other hand, has a big energy gap of 4.351 eV, which means it is very stable and hard to react with other materials. According to the scientific study [31], this complex can make glucose more stable and stop it from interacting too much with other molecules in the body. This could lower the drug's side effects and make it work better.

Nano cinnamon docked with $(MgO)_4$ nanoparticles and glucose has a small energy gap of 1.011 eV, which means it reacts quickly. This could increase the complex's effectiveness in accelerating charge transfer and stimulating biochemical reactions associated with regulating blood sugar levels, making it a strong candidate for diabetes treatment. Based on this data, nano cinnamon with $(MgO)_4$ nanoparticles and glucose appears to be the most suitable of the three options for treating diabetes, it has high ability to interact and facilitate the regulation of blood sugar levels.

Table 1: HOMO, LUMO and energy gap of the optimized structures before docking.

Energies, (eV)	**HOMO**	**LOMO**	**Energy gap**
O2	-6.926	-4.986	1.939
DHB	-4.780	-1.945	2.835
$(MgO)_4$	-7.065	-6.154	0.911
nano cinnamon	-6.716	-2.378	4.337
glucose	-7.177	0.146	7.324
OHB	-5.027	-2.882	2.144
$(MgO)_4$ with DHB	-5.326	-4.680	0.645
nano cinnamon with DHB	-4.697	-2.455	2.241
nano cinnamon with $(MgO)_4$ with DHB	-5.046	-4.255	0.791
$(MgO)_4$ with glucose	-7.342	-5.531	1.810

nano cinnamon with glucose	-7.077	-2.725	4.351
nano cinnamon with $(MgO)_4$ with glucose	-6.124	-5.112	1.011

Table 2 shows that glucose and $(MgO)_4$ nanoparticles docking with glucose both have high ionization energy (7.177 eV and 7.342 eV) respectively, indicating a strong resistance to losing electrons and thus greater stability. The docking of nano cinnamon with DHB and DHB have lower ionization energies (4.780 eV and 4.697 eV) respectively, which means they are more likely to lose electrons and react more. While the electron affinity of $(MgO)_4$ nanoparticles and $(MgO)_4$ docking with glucose is high (6.154 eV and 5.531 eV) respectively, making them more capable of accepting electrons and thus increasing their reactivity in certain contexts. Glucose shows a negative value for electron affinity (-0.146 eV), indicating its lower tendency to accept electrons and enhancing its less reactive stability.

Fermi Energy $(MgO)_4$ and $(MgO)_4$ docking with glucose, they have low Fermi energy (-6.609 eV and -6.437 eV) respectively, reflecting greater stability due to the high negative electron energy state. Glucose shows lower Fermi energy (-3.515 eV), indicating less stability compared to other materials with high negative energy. Work Function of $(MgO)_4$ and $(MgO)_4$ docking with glucose, they have low work functions (0.455 eV and 0.905 eV) respectively, which means they can release electrons more easily and are more reactive.

Glucose and nano cinnamon docking with glucose, they have high work functions (3.662 eV and 2.175 eV) respectively, which means they are less stable and react more slowly. The chemical potential of $(MgO)_4$ and $(MgO)_4$ docking with glucose is significantly lower. They have a lower chemical potential (-6.609 eV and -6.437 eV) respectively, indicating their tendency to interact more actively. Glucose has a higher chemical potential (-3.515 eV), which reflects greater stability and reduces its reactivity.

Chemical Hardness of Glucose has a higher value (3.662 eV), which reflects greater stability and reduces its reactivity. $(MgO)_4$ and the dockinf of $(MgO)_4$ with glucose, they exhibit low chemical hardness (0.455 eV and 0.905 eV), respectively, indicating their easier interaction. The electrophilic index for $(MgO)_4$ and $(MgO)_4$ docking with DHB is as follows, they have a high elecleophilic index (47.928 and 38.751), respectively, which enhances their ability to attract electrons and increase reactivity.

The docking of Glucose with nano cinnamon, they have a low elecleophilic index (1.687 and 5.521) respectively, which reflects higher stability and less reactivity. The chemical softness of the docking of $(MgO)_4$ nanoparticles with DHB and $(MgO)_4$ with glucose, they have high chemical softness values (1.097 and 0.552) respectively, which enhances their reactivity and ability to interact with other materials. Glucose and nano cinnamon with glucose exhibit low chemical ductility (0.136 and 0.229) respectively, which reduces their reactivity.

Table 2: Electronic properties.

Energies, (eV)	IP	EA	E_F	ω	Ω	η	χ	ζ
O2	6.926	4.986	-5.956	0.969	-5.956	0.969	18.290	0.515
DHB	4.780	1.945	-3.363	1.417	-3.363	1.417	3.989	0.352
$(MgO)_4$	7.065	6.154	-6.609	0.455	-6.609	0.455	47.928	1.097
nano cinnamon	6.716	2.378	-4.547	2.168	-4.547	2.168	4.767	0.230
glucose	7.177	-0.146	-3.515	3.662	-3.515	3.662	1.687	0.136
OHB	5.027	2.882	-3.954	1.072	-3.954	1.072	7.292	0.4662
$(MgO)_4$ with DHB	5.326	4.680	-5.003	0.322	-5.003	0.322	38.751	1.548
nano cinnamon with DHB	4.697	2.455	-3.576	1.120	-3.576	1.120	5.706	0.446
nano cinnamon with $(MgO)_4$ with DHB	5.046	4.255	-4.651	0.395	-4.651	0.395	27.336	1.263
$(MgO)_4$ with glucose	7.342	5.531	-6.437	0.905	-6.437	0.905	22.884	0.552
nano cinnamon with glucose	7.077	2.725	-4.901	2.175	-4.901	2.175	5.521	0.229
nano cinnamon with $(MgO)_4$ with glucose	6.123	5.112	-5.618	0.505	-5.618	0.505	31.206	0.988

Table 3 demonstrates that the substances with negative values of Gibbs free energy, like O_2, are more spontaneous

and stable. Substances with high values, such as DHB, are less stable and require energy to initiate the reaction. Enthalpy energy shows that the substances with high values, such as DHB and glucose, have a lot of chemical energy that can be released during the reaction, they are exothermic. Substances with low values, such as O_2 and $(MgO)_4$, require less energy to react, the reaction is endothermic. Entropy energy shows that the substances with high entropy, such as DHB, have a high degree of randomness, which increases their reactivity, while substances with low entropy, such as O_2, are more stable and less random.

Table 3: Thermodynamic proprieties.

Structure	Gibbs, eV	Enthalpy, eV	Entropy, eV
DHB	19.525	23.485	3.959
O_2	-0.414	0.190	0.605
glucose	4.361	5.738	1.376
$(MgO)_4$	0.271	1.448	1.176
Nano cinnamon	2.947	4.1487	1.201

In Table 4, it can be noticed that the Gibbs free energy (ΔG) of OHB indicates a non-spontaneous reaction. The docking processes of $(MgO)_4$ nanoparticles with DHB and nano cinnamon with DHB also exhibit non-spontaneous reactions. In contrast, the docking process of nano cinnamon with glucose shows a largely spontaneous reaction, indicating the remarkable stability of this compound. The Gibbs free energy also shows that the docking reactions of $(MgO)_4$ nanoparticles with nano cinnamon, DHB, and glucose is not natural.

As for the enthalpy, the table shows that the OHB and the docking process of nano cinnamon with glucose are endothermic processes, meaning that they consume energy from the surrounding environment. The exothermic nature of the remaining docking processes enhances their stability.

As for the entropy energy, negative values indicate that the system becomes more organized after the reaction, which enhances its stability. In the case of nano cinnamon docking with glucose, it was found that the entropy energy is positive and unusually high, indicating that the system becomes less organized after the interaction. Based on these results, it can be concluded that all of the studied materials do not negatively affect DHB, particularly the docking process between $(MgO)_4$ and nano cinnamon docking with DHB, which is an effective step in developing the treatment. Nanomaterials (nano cinnamon and $(MgO)_4$ and glucose were docked, and the results showed that the nano cinnamon was much better at treating blood sugar than $(MgO)_4$ nanoparticles, which is in line with research [32-34]. However, $(MgO)_4$ nanoparticles remains useful in treating blood sugar, but with less efficiency than nano cinnamon. When nano cinnamon docks with MgO_4 nanoparticles in the presence of glucose, it appears to function similarly to drugs like metformin and Forxiqa, thereby enhancing its effectiveness in managing blood sugar levels, as supported by studies and research[32, 35] .

High binding energy values demonstrate a strong binding strength within the compound, indicating greater stability. The $(MgO)_4$ and nano cinnamon docking with DHB complex shows a large negative value, indicating that the reaction is exothermic or has a substantial interaction strength. On the other hand, high interaction energy, as in OHB and $(MgO)_4$ docking with DHB, indicates excellent structural stability. The nano cinnamon-glucose complex has a negative value, indicating low stability and exothermic reaction.

Table 4: Thermodynamic and pharmacodynamics proprieties.

docking energies (eV)	ΔG	ΔH	ΔST	$E_{binding}$	E_{int}
$(MgO)_4$ with Nano Cinnamon with DHB	1.60	-0.213	-1.855	-213.679	9.291
$(MgO)_4$ with Nano Cinnamon with glucose	0.561	-0.118	-0.679	17.692	7.745

CONCLUSION

This study primarily focuses on the impacts of nanomaterials docking with DHB and glucose, aiming to fulfill the body's needs through these dockings. This differs from the current body's perspective, as nanosubstances have a tendency to overattack defenses compared to drug development stages. The present work evaluated their interaction energy and thermodynamic properties. Docking $(MgO)_4$ with DHB is reassuring as it can be reduced the energy gap, resulting in swift charge transfer and favorable metabolic processes. The docking energy difference between

nanocinnamon and DHB is moderate. This suggests a potential way to improve the effects of diabetes therapy and reduce side effects. Nanocinnamon, $(MgO)_4$, and glucose show another optimized configuration with the small gap lowered for globe encapsulation. These results suggest that nanocinnamon may aid in achieving normoglycemia by improving glucose homeostasis control. It can be demonstrated that the most efficient treatment for diabetes is nanocinnamon with $(MgO)_4$ and glucose, which has excellent sensing properties among one another in order to control blood sugar levels. Glucose and docking $(MgO)_4$ with glucose have a high ionization energy, resulting in stable species that are less reactive. Because of their low ionization energy, DHB is more likely to loosen and gain electrons when docked with nanocinnamon. After docking glucose with $(MgO)_4$ and nano cinnamon, these two systems have low Fermi energy and work function, which plays an important role in strengthening chemical activity. It is chemically harder than glucose, making it more stable and less reactive. It can be observated that the nanocinnamon and DHB share many common functional groups but also have a few differences, meaning they are very chemically flexible compared to glucose; this flexibility allows them to easily react with other species. Nanomaterials $(MgO)_4$, which can be show promised in treating conditions related to high blood sugar. This is because they have special properties at the nanoscale level that make it possible to deliver drugs precisely and improve the effectiveness

REFERENCES

1. O.O. Ogochukwu, M.B. Fabiyi, O.S. Aworunse, O.A. Oyewole, P.O. Isibor, Nanoparticle Properties and Characterization, Environmental Nanotoxicology: Combatting the Minute Contaminants, Springer2024, pp. 23-40.
2. A.P.S. Chouhan, A. Verma, V. Singh, The Significance of Nanomaterials in Medical Imaging and Diagnostics, Cutting-Edge Applications of Nanomaterials in Biomedical Sciences, IGI Global2024, pp. 301-325.
3. M. Nikandish, H. Wang, X. Bao, M. Nikandish, Enhancing Drug Delivery Precision: Development and Optimization of Nanoparticle-Based Formulations for Targeted Therapy in Preclinical Models, ESI Preprints 26 (2024) 232-232.
4. M. Salman, S. Babar, M. Mariam, Nanomedicine, Modeling and Simulation of Functional Nanomaterials for Forensic Investigation, IGI Global2023, pp. 108-130.
5. S. Kaviarasi, E. Yuba, A. Harada, U.M. Krishnan, Emerging paradigms in nanotechnology for imaging and treatment of cerebral ischemia, Journal of Controlled Release 300 (2019) 22-45.
6. C. Domingues, A. Santos, C. Alvarez-Lorenzo, A. Concheiro, I. Jarak, F. Veiga, I. Barbosa, M. Dourado, A. Figueiras, Where is nano today and where is it headed? A review of nanomedicine and the dilemma of nanotoxicology, ACS nano 16(7) (2022) 9994-10041.
7. S. Liang, F. Li, C. Wang, C. Du, Z. Wang, L. Wang, Hemoglobin-inorganic hybrid nanoflowers: Synthesis and applications for carbene N–H insertion reaction, Biocatalysis and Biotransformation (2023) 1-8.
8. H.F. Ananda, Overview of Hemoglobin in Rejected Donors at PMI in 2020-2021 and Influencing Factors, Jaringan Laboratorium Medis 5(1) (2023) 34-38.
9. J. Tapio, H. Vähänikkilä, Y.A. Kesäniemi, O. Ukkola, P. Koivunen, Higher hemoglobin levels are an independent risk factor for adverse metabolism and higher mortality in a 20-year follow-up, Scientific Reports 11(1) (2021) 19936.
10. V.H. Rezvan, Molecular structure, HOMO–LUMO, and First Order Hyperpolarizability studies of some quinoxaline 1, 4-dioxide derivatives: hybrid computational (HF and DFT) analysis, (2023).
11. P. Kimber, F. Plasser, Energy component analysis for electronically excited states of molecules: why the lowest excited state is not always the HOMO/LUMO transition, Journal of Chemical Theory and Computation 19(8) (2023) 2340-2352.
12. V.U. Nazarov, Breakdown of the ionization potential theorem of density functional theory in mesoscopic systems, The Journal of Chemical Physics 155(19) (2021).
13. S. Yan, R. Zhang, C. Ning, Precision Measurement of the Electron Affinity of Chlorine via High-Resolution Photoelectron Spectroscopy, The Journal of Physical Chemistry Letters 15 (2024) 7735-7739.
14. R. Abinaya, E. Vinoth, S. Harish, S. Ponnusamy, J. Archana, M. Shimomura, M. Navaneethan, Modulating Fermi energy in few-layer MoS 2 via metal passivation with enhanced detectivity for near IR photodetector, Journal of Materials Chemistry C 12(14) (2024) 5247-5256.
15. B.B. Sharma, N.K. Sharma, A. Banshwar, H. Malik, F.P.G. Marquez, Novel approach to design matched digital filter with Abelian group and fuzzy particle swarm optimization vector quantization, Information Sciences 624 (2023) 686-708.
16. N. Chagnet, K. Schalm, Hydrodynamics of a relativistic charged fluid in the presence of a periodically modulated chemical potential, SciPost Physics 16(1) (2024) 028.

17. M.J. Sani, Spin-orbit coupling effect on the electrophilicity index, chemical potential, hardness and softness of neutral gold clusters: A relativistic ab-initio study, HighTech and Innovation Journal 2(1) (2021) 38-50.
18. F.M. Bickelhaupt, I. Fernández, What defines electrophilicity in carbonyl compounds, Chemical Science 15(11) (2024) 3980-3987.
19. H. Zarrok, S. Daoui, N. Benzbiria, A. Barrahi, F. Benhiba, M. Galai, M.E. Touhami, I. Warad, K. Karrouchi, N. Benchat, Study of the inhibition of carbon steel corrosion by two pyridazin derivatives in 1 M HCl: Experimental study and theoretical approach☆, Chemical Data Collections 51 (2024) 101140.
20. J. Hofierka, J. Klimeš, Binding energies of molecular solids from fragment and periodic approaches, Electronic Structure 3(3) (2021) 034010.
21. M. Loipersberger, F.D. Malone, A.R. Welden, R.M. Parrish, T. Fox, M. Degroote, E. Kyoseva, N. Moll, R. Santagati, M. Streif, Interaction Energies on Noisy Intermediate-Scale Quantum Computers, arXiv preprint arXiv:2207.00218 (2022).
22. G. Skvarnavičius, Thermodynamic parameters in protein-ligand model systems: determination of binding volume and enthalpy, Vilniaus universitetas, 2022.
23. H. Kaur, A. Thakur, R.C. Thakur, A. Kumar, Interaction of Nanoparticles With Proteins, Sustainability, Safety, and Applications of Nanomaterials-Based Corrosion Inhibitors, IGI Global2024, pp. 246-276.
24. S.G. Sanad, M. Shebl, Association thermodynamic parameters for nano Cu (NO 3) 2· 2.5 H 2 O with ligands at different temperatures, RSC advances 12(45) (2022) 28902-28909.
25. H. Mollazadeh, H. Hosseinzadeh, Cinnamon effects on metabolic syndrome: a review based on its mechanisms, Iranian journal of basic medical sciences 19(12) (2016) 1258.
26. M.C. Wobbe, A. Kerridge, M.A. Zwijnenburg, Optical excitation of MgO nanoparticles; a computational perspective, Physical Chemistry Chemical Physics 16(40) (2014) 22052-22061.
27. R.C. Pettersen, The chemical composition of wood, The chemistry of solid wood 207 (1984) 57-126.
28. J.F. Storz, Hemoglobin: insights into protein structure, function, and evolution, Oxford University Press2018.
29. M.A. Abdulsattar, N.M. Almaroof, H.R. Jabbar, Interaction thermodynamics of human hemoglobin with environmental and toxic gases: A density functional theory study, Journal of Physics: Conference Series, IOP Publishing, 2021, p. 012132.
30. M. Fazlali, F. Kharazmi, M. Kamran, K. Malekzadeh, A. Talebi, F. Khosravi, N. Soltani, Effect of oral magnesium sulfate administration on lectin-like oxidized low-density lipoprotein receptor-1 gene expression to prevent atherosclerosis in diabetic rat vessels, Journal of diabetes investigation 10(3) (2019) 650-658.
31. S.L. Miller, B.P. Wiebenga-Sanford, C.D. Rithner, N.E. Levinger, Nanoconfinement raises the energy barrier to hydrogen atom exchange between water and glucose, The Journal of Physical Chemistry B 125(13) (2021) 3364-3373.
32. M.A. Elobeid, Amelioration of Streptozotocin Induced Diabetes in Rats by Eco-friendly Composite Nano-Cinnamon Extract, Pakistan Journal of Zoology 48(3) (2016).
33. H. Zelicha, J. Yang, S.M. Henning, J. Huang, R.-P. Lee, G. Thames, E.H. Livingston, D. Heber, Z. Li, Effect of cinnamon spice on continuously monitored glycemic response in adults with prediabetes: a 4-week randomized controlled crossover trial, The American Journal of Clinical Nutrition 119(3) (2024) 649-657.
34. H. Bakhach, M. Nuffer, S. Tall Bull, W. Nuffer, A Systematic Review Evaluating Cinnamon's Effects on Glucose Utilizing a Ranking System to Assess Bias and Study Quality, Journal of Medicinal Food (2024).
35. A. Shaukat, H. Anwar, A. Mahmood, G. Hussain, A. Rasul, M.U. Ijaz, M.N. Faisal, M. Ibrahim, A. Ali, Synthesis cum characterization of MgO and MnO nanoparticles and their assessment as antidiabetic and antioxidative agents in diabetic rat model, Physica B: Condensed Matter 602 (2021) 412570.

The effectuation of changing the weight fraction of some agricultural waste powders on some mechanical and thermal properties of unsaturated polyester composites

Abdulraheem Dheyaa Ibrahim [1,a)], Suad H.Aleabi [1,b)]

[1)]*Department of Physics, College of Education for Pure Science (Ibn-AL-Haitham), Baghdad University, Baghdad, Iraq*

[a)] Corresponding author Abd.Ali2204p@ihcoedu.uobaghdad.edu.iq
[b)] soaad.h.l@ihcoedu.uobaghdad.edu.iq

Abstract In this research, two types of natural composite materials were prepared. One of them was a single composite material that included unsaturated polyester as a base material with the addition of sawdust powder. As for the hybrid composite material, it included adding both walnut shells and sunflower seeds to the single composite material. Both types of single and hybrid composite materials were prepared in weight ratios (5,10,15)% and the particle size (75) µm , The study included conducting some mechanical and thermal properties, including a wear rate under the influence of increased applied load, hardness, impact, and thermal conductivity for both the single and hybrid composite material The obtained results explain a decrease in the wear rate with an increase in the weight fraction for both the composite, single, and hybrid materials, as well as an increase in the wear rate value with an increase in the applied load. As for the hardness test, the results showed an increase in the hardness value with an increase in the weight fraction for both the single and hybrid composite materials. Likewise, for the impact test, there is an increase in the impact value with an increase Weight fraction, as for thermal conductivity, the results showed a decrease in the value of the thermal conductivity coefficient for all the samples.

INTRODUCTION

Polymer composites are widely used for various applications. However, they do not easily biodegrade, leading to the generation of solid waste and environmental pollution. To address this issue, researchers are now concentrating on creating biodegradable composites using natural fibers or fabrics, known as green composites. Sure, here is the revised text:

"Several green composites have already been developed using materials such as sisal, banana, bamboo, Alfa, and coir. Their properties have been studied, and it has been found that natural fiber composites are biodegradable, renewable, lightweight, low-cost, and have high specific strength and modulus. They also lead to reduced tool wear and involve a safe manufacturing process. Natural fiber composites find applications in construction, packaging, furniture, and automotive fields. In the automotive industry, natural fiber composites are used in the interiors of automobiles, including door panels, trunk liners, seal backs, packages, engine and transmission covers."[1,2].

It has been used since ancient times in many agricultural parasites (residues). For many purposes to verify human requirements, which are provided by sources with (agricultural waste). High value according to its use, and sometimes even a high price for agricultural products because of their fundamental importance in medical fields. One of the uses of agricultural waste is as a raw material in various industries. The wooden one. I want to stop the unwanted increase in economic wealth through change Studies on the composition, properties and availability of these materials through collection and manufacturing, which are considered. An important alternative to natural wood to reduce its import. This field requires knowledge of what agricultural waste (residues) is, as it can be defined as everything that is produced.

Incidentally or secondarily during the production of various agricultural crops, whether through operations Harvesting and gathering or preparing for marketing these crops. These resources are of economic value High, especially in some

Technologies and Materials for Renewable Energy, Environment and Sustainability
AIP Conf. Proc. 3321, 050001-1–050001-10; https://doi.org/10.1063/5.0289905
Published under an exclusive license by AIP Publishing. 978-0-7354-5231-2/$30.00

countries that suffer from a severe shortage of forests, this puts them in urgent need. To cover the deficiency in wood resources by developing and manufacturing various alternatives, the most important of which is the use of agricultural crop waste, which varies and differs from one country to another depending on the country's production of each. An agricultural crop and the amount of waste produced from it. These materials are composed mainly of cellulose (-OH) and contains a large number of hydroxyl groups (Lignin) and lignin (Cellulose)Aromatics and Aliphatic [3]. This kind of garbage is distinguished by its high amounts of fibre and low crude protein content (2–5%). Some of them have a percentage of silica. This, in turn, can exchange the action chemically with some different polymeric materials, and there is a large diversity. The sources of agricultural waste are split into two major groups:

1. Natural organic waste is produced by the sustainable natural regeneration of crops such as grasses, twigs, and tree leaves. In addition to harvesting crops' grains, stems, and dry leaves. Resulting from the harvest of grains in general, the most important of which are plant by-products (wheat, barley, rice, and several types of corn, among others).
2. Industrial organic waste: It results from various manufacturing processes represented in the manufacture of tobacco. And cotton, sugar cane, papyrus, wood carpentry.

Many studies have been conducted recently on natural fillers, such as coconut shell, pomegranate core, pineapple leaf, ginger, palm kernel, etc., to replace conventional fillers. By using the natural fillers as a reinforcement material in polymer matrix composites, the cost and productivity of the materials can be increased in addition to the mechanical properties being improved. [4].

In order to adjust the topological qualities of some agricultural waste—wear resistance and hardness—Rola et al. (2018) investigated the topological behaviour of the trash after it was converted to plastic flooring under both dry and wet operation circumstances [5]. The researchers studied (Bheel, N.; Memon, et.al., 2020) Experimental verification of physical and mechanical properties for concrete reinforced with sisal fibres, the study showed good tensile strength as sisal fibres were added At different weight percentages of cement, The physical properties that have been measured include workability, water absorption, and density. The mechanical properties that have been examined are compressive strength, tensile strength, and constant modulus of elasticity. A comparison has been made between the calculated elasticity values of concrete with sisal fibres and the expected values in some common designs. The research indicated that sisal fibres have the potential to improve the split tensile strength and Young's modulus of concrete, but they do not enhance its workability, water absorption, or compressive strength.[6]. Raya et al. (2020) investigated the impact of wood minutes reed on a few physical properties of (EP+W) composites. By using the casting procedure, it is prepared. The most findings were obtained from the investigation of some mechanical qualities, such as tensile strength, curvature, and creep. Boost flexibility and bending resistance wood shavings for epoxy reinforcement [7].

The purpose of this research is to attempt to reap the benefits of recycling cellulosic agricultural waste by manufacturing composite materials such as plastic wood that is beneficial to the environment, as there are many attempts to reduce the impact of these wastes on the environment and protect the environment from them.

EXPERIMENTAL MATERIALS AND METHODS

In this study, polyester was used Saudi saturator created by the Industrial Resins Company Ltd. as a base material in the prepared composite materials, which is It is a viscous liquid that has good characteristics as it is prepared A low molecular weight polymer known as an oligomer Accordingly, this substance can be transformed into an oligomer .The solid state when it is solidified by adding the solidifying material (Methyl ethyl ketone peroxide) type (Hardener) It is a liquid substance with a light consistency and a transparent color (MEKP).It is added to the resin at a weight rate of (2%), noting that These solidification reactions occur at room temperature. As for the reinforcement materials used in the research, they are powders from agricultural waste, represented by sawdust wood, in addition to powder from walnut shells, sun flower seed whose particle sizes were measured using a sieving analysis, where the particle size was 75μm. Composites were prepared from polyester and agricultural waste powders by (Hand lay – up molding technique).

Experimental Test

Wear rate

Wear is defined as the procedure of erosion of surface a solid as a resultant of its impact on surface of another solid body [8]. The test is carried out using a sliding wear device consisting of an iron disc rotating at a constant speed (500) rpm and the hardness of the iron disc is (269) HB and the wear rate can be calculated by the Equation below:

War rate= (ΔW)/(SD) …… ……. (1)

Where (ΔW): the difference in mass in units (gm) after and before test by effect load equal (5N) and time (5min), SD: sliding distance in units (cm) . It is calculated from the relationship:

SD = 2πrnt …… …. (2)

r: radius (from center of sample) in (cm), n: the disc revolution per minute, t: time of test equal (5min).

I.S= U/A (J/m2) …… ……..(3).

Impact Test

Testing machines at Amityville, New York produced Charpy impact experiment equipment, which was used for performance impact testing on the prepared samples. The instrument's two primary parts are the pendulum and the energy normal gauge. A standard test part is cracked in a single stroke of the hammer swinging in the Charpy impact test. The hammer must be raised to its highest position and fixed firmly before the samples are inserted to maximize the instrument's performance. Potential energy is transformed into kinetic energy by swing motion, however the quantity of this energy is lost in fractured samples. Consequently, the amount of broken energy will be shown on an indicator scale, and the relation (3) will be used to calculate the sample impact strength. [9].

Hardness Test

The definition of hardness is a material's resistance to abrasion or penetration. The hardness of plastic materials can be measured using a variety of general standards. The Shore D's hardness is the most prevalent of these. Force causes the penetration to happen slowly on the sample's surface, which causes a local creep. Following the influence force's disappearance, a somewhat gradual retrieval takes place, changing the dimensions [10]. Every sample's hardness was assessed in compliance with the Shore (D) device's standard specification (TH 210).

Thermal Conductivity

The well-known phenomena known as thermal conductivity occurs when there is a temperature differential between two surfaces, causing heat to move from the high-temperature side to the low-temperature surface. Based on this, the rate at which heat moves across a unit area in a unit of time when there is a one-degree Celsius thermal gradient between two surfaces is defined as thermal conductivity. Depending on the material (solid, liquid, or gas), thermal conductivity determines whether a material is a heat conductor or a dielectric [11]. While thermal conductivity in composite materials is used where the composite material appears to have a high conductivity, such as in fibre orientation (by the thickness) or a weak conductivity in the longitudinal direction of the fibre, thermal conductivity in metallic materials is dependent on the passage of free electrons. In general, resins with fibre reinforcement have higher thermal conductivities than base materials. This increase is expected due to the fibber's overall capacity for heat conductivity, Using Lee's disk (Griffin and George, England), the coefficient of thermal conductivity was calculated using the following relationships [12].

$$k[T_B - T_A/d_s] = e[T_A + 2/r(d_A + 1/4d_s)T_A + 1/2rd_sT_B]\ldots\ldots\ldots\ldots \quad \ldots. (4)$$

$$IV = \pi r^2 e(T_A + T_B) + 2\pi re[d_AT_A + d_s(T_A + T_B/2) + d_BT_B + d_cT_c]\ldots\ldots\ldots\ldots \quad \ldots\ldots. (5)$$

When [e] is the unit of heat energy transient (w/m2^{o}C) in disc material space, it is represented as follows: unit per second. I, a current flowing through a coil of convector. Heat for discs A, B, and C (TA, TB, TC,) (^{o}C) and (ds), the sample thickness (mm)

RESULTS AND DISCUSSION

Wear Rate

The wear test is one of the most important surface mechanical tests in tribology that can be used. It is used to study the behavior of composite materials under the influence of frictional forces to measure surface resistance. The joints are vertical under a relative sliding motion. In addition, friction and wear processes lead to large economic losses in engineering materials. Although wear and tear does not occur suddenly, it is distinguished with a gradual decrease in efficiency or failure to obtain the required performance, as it was found that the adhesion strength surface the interface between the components of the wood-plastic composite has a clear impact on the resistance of these materials to wear.[13, 14].From the figures (1,2,3) that illustrate the relationship between the wear rate and the change in the weight fraction of unsaturated polyester resin before and after reinforcement with sawdust powder as a single composite material (UP+ sawdust powder) and for different loads that included (5, 10, 15) N, where the results obtained show that there is a decrease in the wear rate for all percentages of the single composite material and for all the loads used, where the lowest percentage of wear rate for the sample with a weight fraction of 15% was (1.0542) gm/cm^3 at the load of 5 N, (1.0531) at the load of 10 N, and (3.4864) at the load of 15 N , As for the hybrid composite material (UP+ sawdust powder + walnut shell +sun flower seed) from figures (4,5,6) , it is also noted that there was a decrease in the wear rate with an increase in the weight fraction, as the lowest value of the wear rate for the (15%) ratio was (1.01518) gm/cm^3 at the load of 5 N, (1.2121) gm/cm^3 at the load of 10 N, and (1.2393) gm/cm^3 at the load of 15 N compared with the pure material (UP) where value of the wear rate for pure material was 5N(1.2355) gm/cm^3 and (2.1867) gm/cm^3 when the load was 10 N and (5.0130) gm/cm^3 when the load was 15 N. The reason for the decrease in wear rate can be attributed to the strong linking between the two phases at the interface and to the distribution of(sawdust wood, walnut shell, sun flower seed) within the matrix material, which lead to protect them from corrosion and damage, this occurs as a result of the sliding movement between the surfaces, and the separating force between the protrusions was less than the bonding strength of the polymeric substrate atoms and the reinforcement material[14].

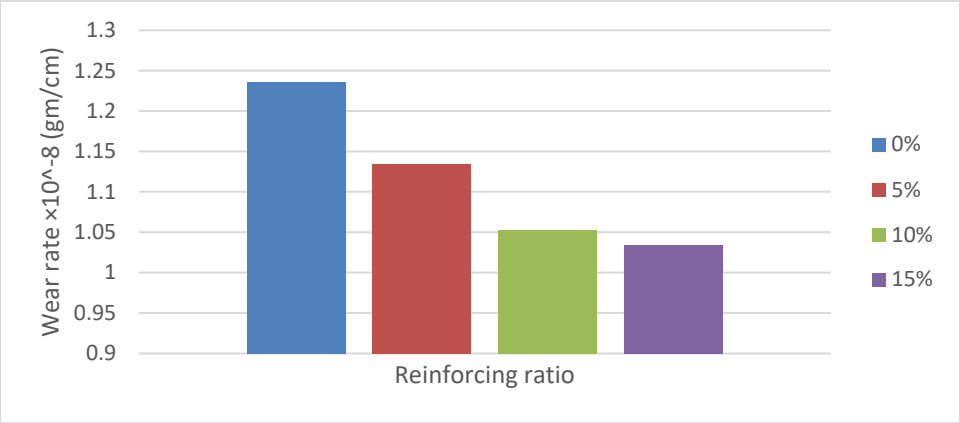

Figure1. shows the relationship between the wear rate and the weight fraction of single composite material (UP+ sawdust) at load (5)N.

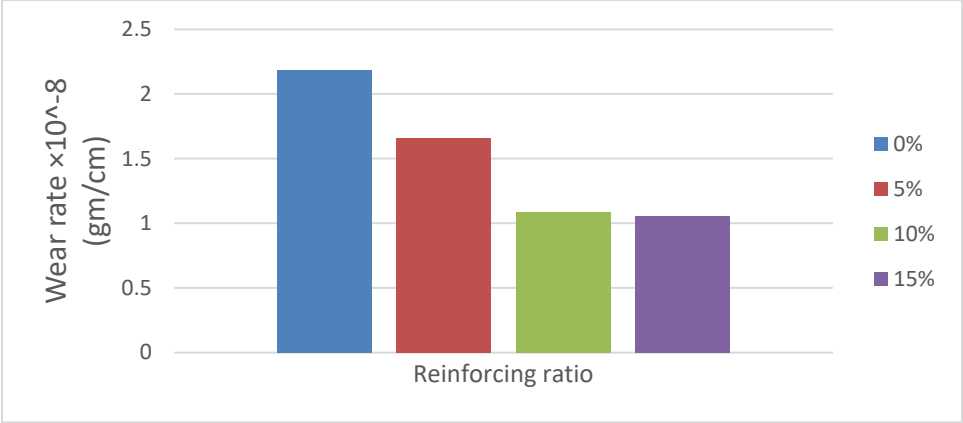

Figure 2. shows the relationship between the wear rate and the weight fraction of single composite material UP+ sawdust) at load (10)N.

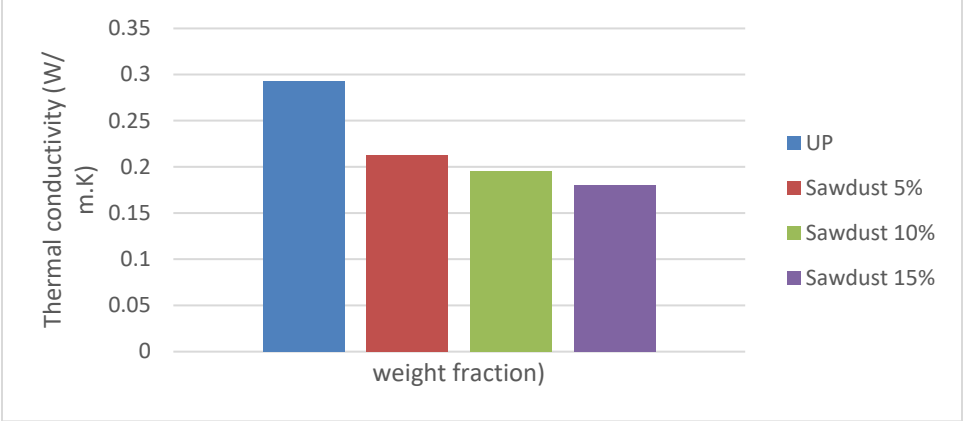

Figure 3. shows the relationship between the wear rate and the weight fraction of single composite material UP+ sawdust) at load(15)N

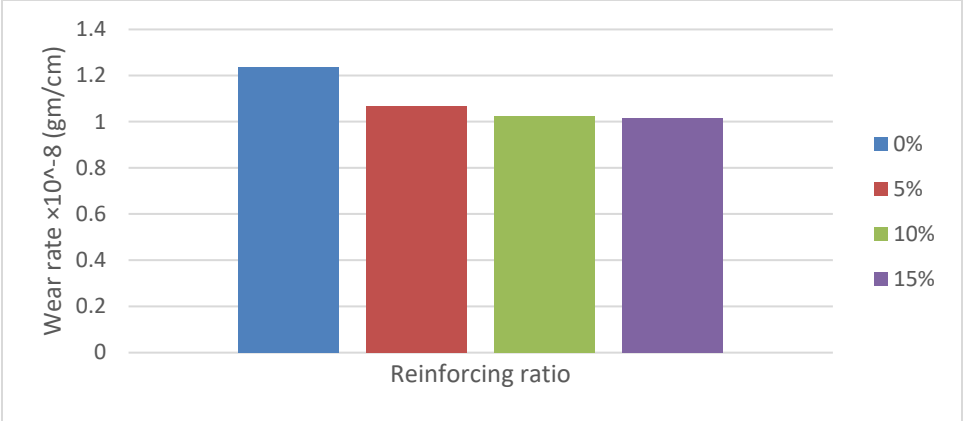

Figure 4. shows the relationship between the wear rate and the weight fraction of the Hybrid composite material (UP+ sawdust + walnut shell+ sun flower seed) at load (5)N.

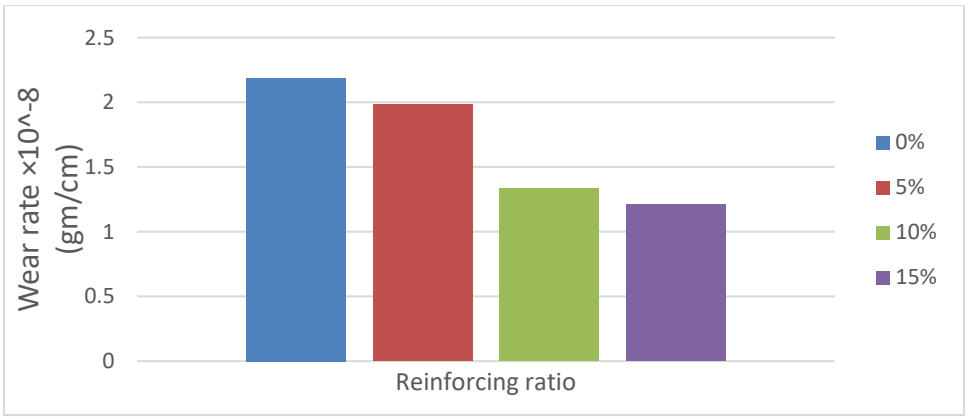

Figure 5. shows the relationship between the wear rate and the weight fraction of the Hybrid composite material (UP+ sawdust + walnut shell+ sun flower seed) at load (10)N.

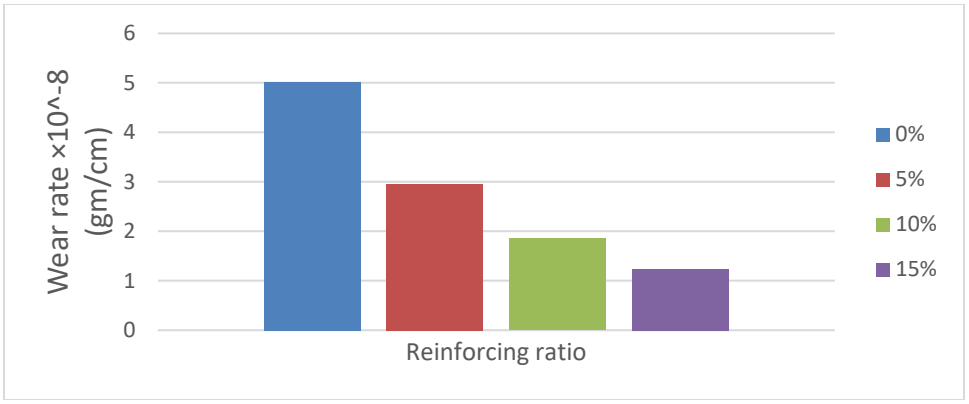

Figure 6. shows the relationship between the wear rate and the weight fraction of the Hybrid composite material (UP+ sawdust + walnut shell+ sun flower seed) at load (15)N.

The change in the wear rate was studied with the change in the loads used. Three loads (5, 10, 15) N, were used for all samples of the single and hybrid composite material. From observing Figures (7,8), which represent the relationship between the wear rate and loads for the single and hybrid composite material, it is noted that the two figures show an increase in the wear rate with an increase in the applied load for the single and hybrid material and for all proportions studied ,the reason for the increase in the wear rate of all samples with the increase in the applied load is due to the proportionality of the force of the loads (N) directly proportional to the compressive force (F) friction.[15]

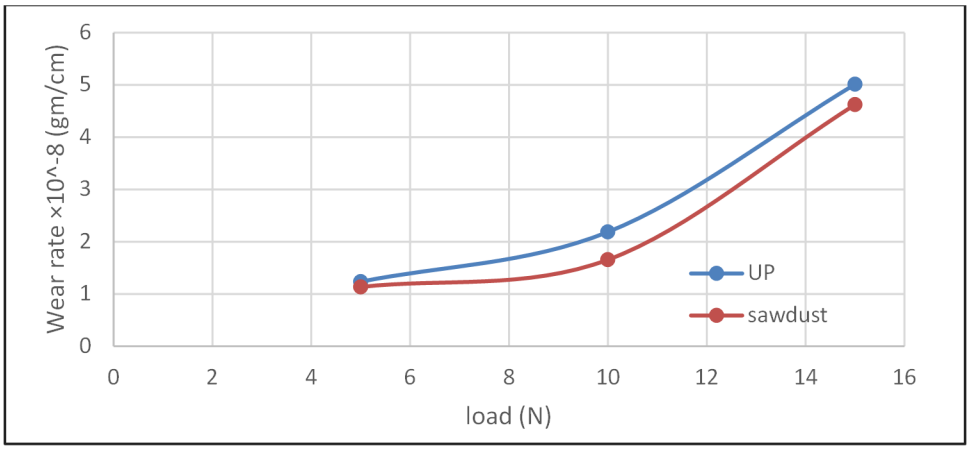

Figure 7. shows the relationship between wear rate and load change for a single composite material (UP+ sawdust powder) for all ratios.

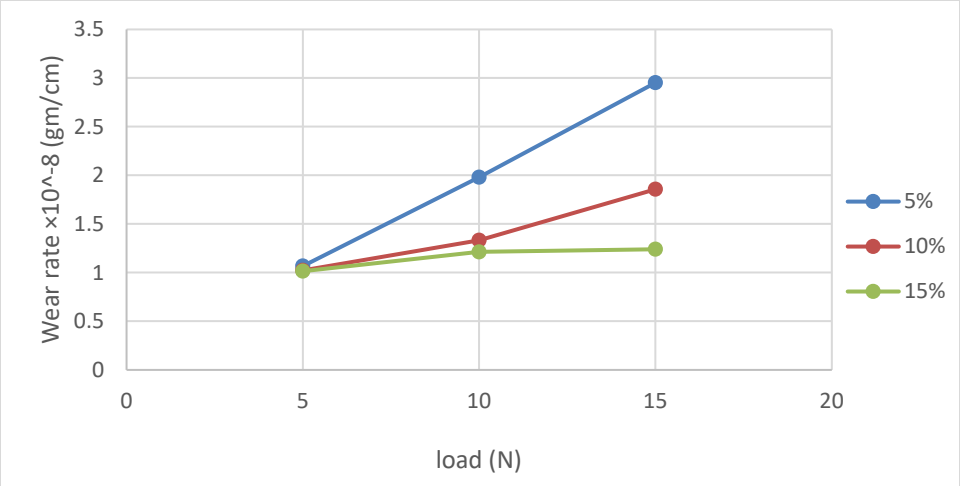

Figure 8. shows the relationship between wear rate and load change for a Hybrid composite material and for all ratios used.

Impact strength

The impact test's fundamental principle is the test sample's absorption of the hammer's initial kinetic energy prior to fracture; the quantity of energy absorbed is determined by the composite material's internal components. It also relies on how resilient the sample is to outside pressures placed on it. From the figures (7 , 8), which Explain the relationship between the (impact strength) and the weight fraction for both the single and hybrid composite material for all weight fractions, it is noted that an increase in the value of the impact strength with the increase in the weight fraction, where 15% had the highest value of the impact strength for the single composite material amounting to (0.4) KJ/m^2 As for the hybrid composite material, the highest impact toughness value was reached at 15%, reaching (0.6) KJ/m^2 compared to the pure material that has an impact toughness of (0.25) KJ/m^2. This is due to the increased impact strength of the single and hybrid composite materials due to the small size of sawdust and walnut shell and sun flower seed powders which enables it to spread well within the matrix material and thus has the ability to resist impact and thus increase the durability of the impact.[16]

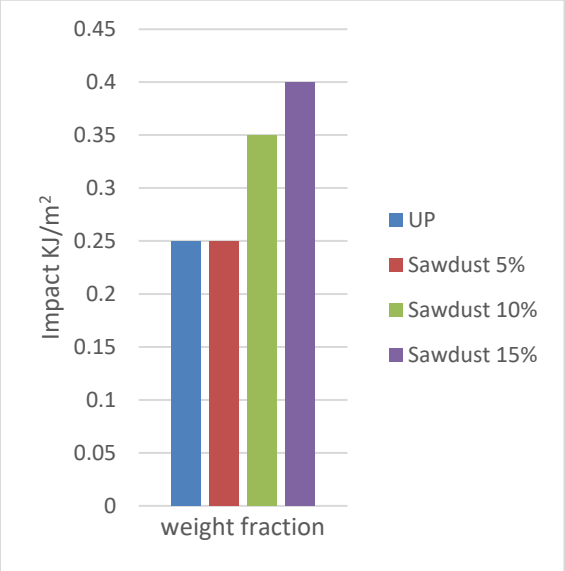

Figure 9. shows the relationship between impact toughness and weight fraction of a single composite material (UP+ sawdust powder).

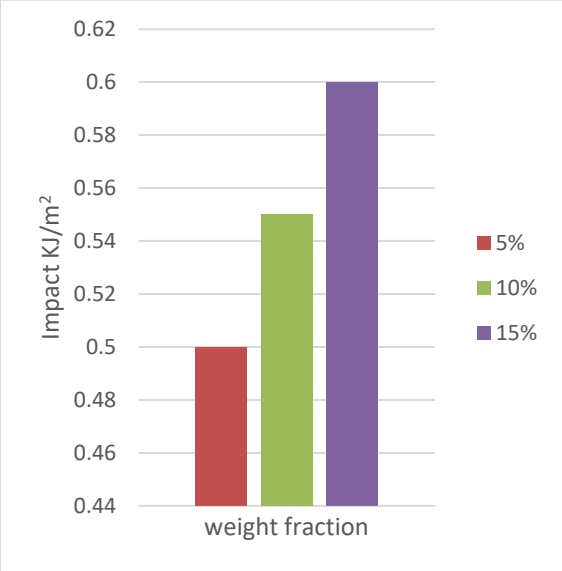

Figure 10. shows the relationship between impact toughness and weight fraction of a Hybrid composite material (UP+ sawdust+ walnut shell+ sun flower seed)

Hardness

The property of hardness is the resistance of the surface of the material to permanent deformation caused by notching, cutting, wear, scratching, penetration, and workability. The kind of bonding force that exists between molecules or atoms, as well as surface type, high temperature, and heat treatment, all affect how hard a material is[17].
The figure (9,10) shows the relationship between the hardness value and the weight fraction of the single composite material and the hybrid material, respectively. It is noted from the figure an increase in the hardness value of the single composite material and the hybrid material with an increase in the weight fraction, as the highest value of hardness for the single composite material at 10% reached (83), while for the hybrid composite material the highest hardness value at 15% reached (84.8) compared to pure polyester, which reached (72) When the powders of the reinforced materials are distributed throughout the base material during the manufacturing process, the voids that were previously present are filled, increasing the strength of the bond between the reinforced materials and the base material and, as a result, the hardness value of the single and hybrid composite materials[19].

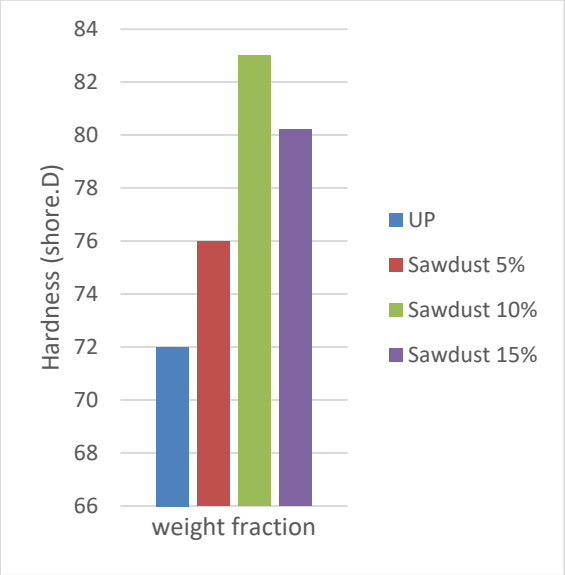

Figure 11. shows the relationship between the hardness value and the weight fraction of the single composite material(UP+ sawdust powder).

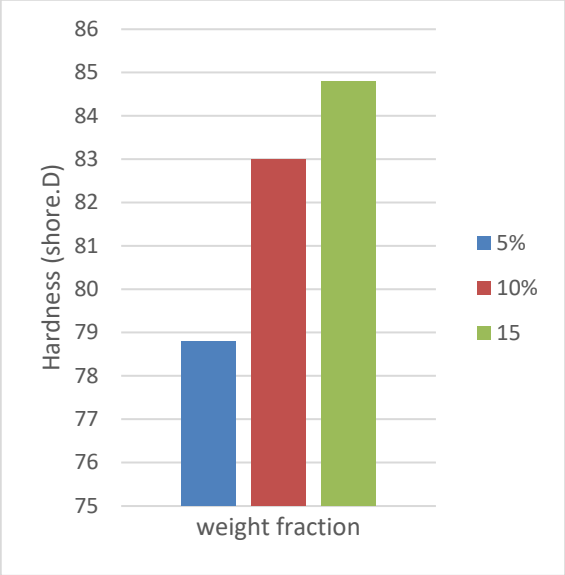

Figure 12. shows the relationship between the hardness value and the weight fraction of the Hybrid composite material (UP+ sawdust+ walnut shell+ sun flower seed).

Thermal conductivity

Thermal conductivity is one of the transfer phenomena in solid materials, heat, as we know it .A type of energy like other types of energy such as electrical energy and sound energy and others, and if heat is available, this is equal to the amount of work expended in generating it. Heat is transferred from (Conduction) The hot position to the cold position by some or all of the following methods: Conduction here in this study, radiation, convection, and convection will be highlighted On heat transfer by conduction, because heat transfer by convection only occurs in liquids and gases.
From the figure (11,12), which shows the relationship between the thermal conductivity coefficient and the weight fraction for both the single and hybrid composite material, where it is noted that there is a decrease in the value of the thermal conductivity coefficient for both the single and hybrid composite material, respectively, as the lowest value of the thermal conductivity coefficient for the single material at the ratio reached 15%. (0. 1951) W/ mk, while the lowest value of the thermal conductivity coefficient for the hybrid composite material reached (0.1561) W/ mk when the ratio was also 15% Compared to the value of the thermal conductivity coefficient of the resin, which is (0.2928)W/ mk, The reason for the decrease in the thermal conductivity coefficient is that the structural vibrations of the resin begin to decrease when adding powders of natural reinforced materials, which work to impede the structural vibrations responsible for the thermal transfer of the resin, which consequently leads to a decrease in the thermal conductivity

coefficient, as the percentage of thermal insulation increases as a result of hindering the internal structural vibration by reinforcing powders[12, 19].

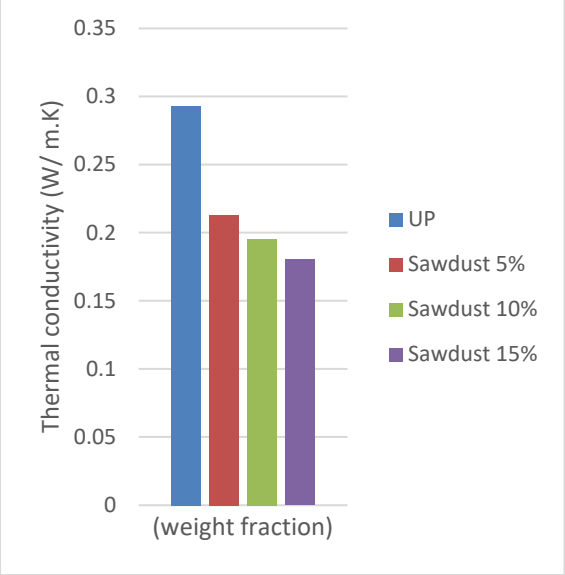

Figure 13. shows the relationship between thermal conductivity and the weight fraction of the single composite material(UP+ sawdust powder).

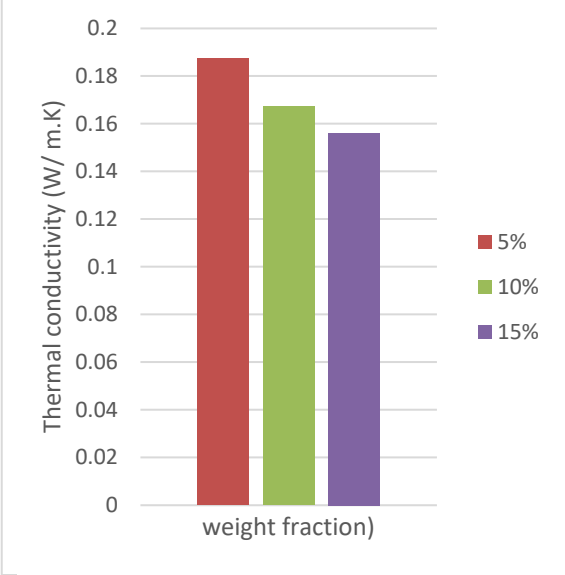

Figure 14. shows the relationship between the thermal conductivity and the weight fraction of the Hybrid composite material (UP+ sawdust+ walnut shell+ sun flower seed).

1

CONCLUSION

From the results obtained in the research, the following is revealed

- Regarding the mechanical properties in the wear rate test, and from observing the results, it was shown that there was a decrease in the value of the wear rate of the material after reinforcement, whether in the case of reinforcement with sawdust for the single composite material or in the case of the hybrid composite material when adding both walnut shell powder and sunflower seeds, which indicates an increase in resistance. Wear and tear of the material when reinforced

As for the change in the wear rate by increasing the applied loads, an increase in the value of the wear rate was observed by increasing the load applied to the material, for all weight ratios and for the single and hybrid composite material.

To test the hardness and impact strength, the increase resulting from the increase in weight percentages added to both the single and hybrid composite material can be observed compared to the pure unsaturated polyester material.

- As for the thermal properties represented by calculating the thermal conductivity coefficient, it was shown that there was a decrease in the value of thermal conductivity after adding the reinforced materials to the single and hybrid composites. The reason for this can be attributed to the insulating nature of the added materials, which are all of sawdust, walnut shell powders, and sunflower seeds.

REFERENCES

1. B.F. Yousif, A. Shalwan, C.W. Chin, K.C. Ming, Flexural properties of treated and untreated kenaf/ poxy composites,Mater. Design 40, 2012, 378−385.
2. M. Rokbi, H. Osmani, A. Imad, N. Benseddiq,Effect of Chemical treatment on Flexure Properties of Natural Fiber-reinforced Polyester Composite, Procedia Engineering 10 , 2011, 2092−2097
3. Mohammed Mundher Hussein, " Preparation of Polymeric Composites Reinforced Cellulose Materials and Studying some of their Physical Properties", Master's thesis, Diyala University,College of science, 2018.

4. Orhan S. Abdullah, " Experimental Study to the Effect of Natural Particles Added toUnsaturated Polyester Resin of a Polymer Matrix Composite", Al-Khwarizmi Engineering Journal,Vol. 13, 2017, No. 1, P.P. 42- 49 .
5. Rola Abdel-Khader Abbas,Ziad Tariq Khudair, Mohamed MuntherHussein, characterization of the topological behavior of some agricultural waste after conversion to plastic flooring in dry and wet operating conditions, Journal of Engineering and Sustainable Development, 2018,22,2, 2520-0917.
6. Bheel, N.; Memon, F.A.; Meghwar, S.L, "Study of Fresh and Hardened Properties of Concrete Using Cement with Modified Blend of Millet Husk Ash as Secondary Cementitious Material, 2020, Silicon", 1–12.
7. Abed, R. A.; Al-sarrafand, A.; Almaamori, M. Influence of wood minutes (reed) on some physical and mechanical characteristics for (EP+ W) composites. Materials Science and Engineering 2020,928, ,7, ,072128. doi:10.1088/1757-899X/928/7/072128
8. Mohammed M. Yahyaa, Suad H. Aleabi, " Comparison between some mechanical and thermal conductivity of epoxy Nano and micro-composites", AIP Conf. Proc. 2769, 020059-1–020059-8; https://doi.org/10.1063/5.0129376 , 2023.
9. Mohammed M. Yahyaa , Suad H. Aleabi " Enhancing Some Mechanical Properties (Compression, Impact, Hardness, Young modulus) and Thermal Conductivity, Diffusion Coefficient of Micro Epoxy Composites" , Ibn Al-Haitham Journal for Pure and Applied Sciences, 2022.
10. Zinah Abdulateef Abbas, and Suad H. Aleabi, " Studying some of mechanical properties (tensile, impact, hardness) and thermal conductivity of polymer blend reinforce by magnesium oxide" , AIP Conference Proceedings 2123, 020036, 2019, https://doi.org/10.1063/1.5116963
11. Suad. H. Aleabi, " The effect of using Al2O3 additives on some mechanical properties of unsaturated polyester", College of Education for Pure Sciences Ibn Al-Haitham, 27.2014.
12. Suad H. Aleabi, Anaam W. Watan, Ebtisam M.-T. Salman, Kareem A. Jasim, Auday H. Shaban, and Tagreed M. AlSaadi " The study effect of weight fraction on thermal and electrical conductivity for unsaturated polyester composite alone and hybrid", AIP Conference Proceedings 1968 020019 ,2018.
13. T. Berhanu, P. Kumara and I. Singha "Sliding Wear Properties of Jute Fabric Reinforced Polypropylene Composites" Procedia Engineering 97,402– 411, 2014.
14. P.K Bajpai, I. Singh and J. Madaan, "Frictional and adhesive wear performance of natural fibre reinforced polypropylene composites" Proc IMechE Part J:J Engineering Tribology 227(4) 385–392. 2012.
15. Suad H. Aleabi, " Study of the effect of wear on Unsaturated polyester resin reinforced with rice husk ", , Ibn Al-Haitham Journal for Pure and Applied sciences , 2012.
16. Shatha H Mahdi et al, "Preparation of unsaturated polyester/Nano ceramic composite and study electric, thermal and mechanical properties", Iraqi Journal of Physics, 15, 188-201, 2017.
17. Suad H. Aleabi,Mahmood Radhi Jobayr, et.al " Properties Evaluation of a Composite of Unsaturated Polyester Resin Reinforced with Mullet ", Solid State Technology ISSN: 0038-111X Vol. 63, No. 1, 2020.
18. Shatha H. Mahdi, Suad H. Aleabi, Rawnaq Qays Ghadhban and Ebtisam M-T. Salman, " Effect of Pyrex Waste on the Electrical and Mechanical Properties of an Epoxy Resin", Journal of Xi'an University of Architecture & Technology, Volume XII, Issue V, 2020.
19. Iman Nasr Fadhil , Abdulhameed Raheem Al-Sarraf, " Preparation and characterization of plastic wood from cellulosic residues", Ibn Al-Haitham Journal for Pure and Applied Sciences, IHJPAS. 36 (4) 2023.

Batch adsorption experiment based mullite/zinc ferrite for heavy metals removal from wastewater

Wasan Ziedan [a] Mukhlis M. Ismail [b] and Wafaa A. Hussain [c]

Applied Sciences Department, University of Technology- Iraq, Baghdad, Iraq.

[a] *Corresponding author: wasanalmushhadany@gmail.com.*
[b] *mmismail009@gmail.com.*
[c] *wafaloay@yahoo.com.*

Abstract. Adsorption has grown in popularity and affordable method for removing pollutants from wastewater in recent years. This study investigates use of batch experiments for removal of Pb(II) from wastewater using Mullite/$ZnFe_2O_4$ composite. Various conditions: solution pH (3, 5, 7, 9), initial Pb (II) concentrations (100, 150, 200, 250) ppm, adsorbent dosages (0, 3, 5, 7, 10) %, and contact times (10, 30, 50, 70, 90 min and 4, 8, 24 hour), were studied. X-ray diffraction (XRD) confirmed the transform of kaolin to Mullite and trace amount of Cristobollite phase after heat treatment and this agreement with the result of Fourier-transform infrared (FTIR) spectra that the hydroxyl peaks were disappeared, indicating the dehydroxylation of kaolin occurred and produce mullite phase. XRD of Zinc Ferrite shows a single phase with a spinel crystal structure and this agreement with FTIR results. The batch investigation of Mullite/$ZnFe_2O_4$ composite revealed that the optimum removal efficiency of Pb(II) at (MZ_{10} composite sample, pH 3, contact time 24 hour, Pb concentration 250 ppm) and the removal efficiency was increased to 100% when an external magnet was applied to the sample using MZ_{10}, pH 9, contact time 8 hours, and lead concentration 250 ppm. Energy Dispersive Spectrum (EDS) results confirm the presence of zinc, iron, oxygen, aluminium, silicon and carbon, which is attributed to the elemental composition found in MZ_{10}, in addition to Pb(II) element after adsorption process. It was found from Brunauer-Emmett-Teller (BET) and Barrett-Joyner-Halenda (BJH) result that the specific surface area was increased with increases the percentage of ferrite, and all show a typical pattern of mesoporous materials.

Keywords: *Batch experiment, heavy metals, sol-gel method, Zinc ferrite, kaolin.*

INTRODUCTION

There are many advantages that metals offer in daily life. In certain instances, they are vital for preserving the body's metabolism in humans or animals, or they are necessary as microelements for plants to grow. But if metal concentrations rise above a certain point; even in trace amounts; they can contaminate the environment and have a disastrous impact on living things [1, 2]. One global environmental issue is the release of industrial wastewater that contaminates water with harmful heavy metals [3, 4]. One significant contaminant that has been added to natural waters is lead. Even at relatively low concentrations, aquatic flora and fauna are at risk from lead present in wastewater. Wastewater from process industries producing paints, oils, batteries, electronic wood, burning fossil fuels, sewage wastewater, etc. are the main sources of lead contamination [5]. Various techniques have been developed to treat wastewater that contains ions of heavy metals, such as chemical precipitation, flocculation, reverse osmosis, electrodialysis, membrane filtration, and adsorption. Adsorption is the most sophisticated and effective technique in terms of cost-effectiveness and environmental friendliness [6, 7]. The field of contaminated water treatment, which involves removing contaminants from water, is largely concerned with nanotechnology, where the surface area of nanoparticles is large and numerous effective sites make it suitable for eliminating impurities. The higher surface area of nanomagnetic spinel ferrites enhances their ability for water treatment [8]. Magnetic and biosorbents have become popular as economical and ecologically friendly substitutes because of their special qualities and affordability [9]. Recently, it was discovered that spinel ferrites are a new class of adsorbents that work best for treating water [10]. Several researches undertaken in underdeveloped countries have also investigated the use of clay for the purpose of eliminating harmful contaminants from polluted water sources. Materials such as kaolinite, montmorillonite, illite, and bentonite are often used because to their large specific area, widespread availability, stability, and structural properties. The environment is full of these minerals, safe, and essential to the process of removing contaminants found in wastewater through ion exchange and adsorption, or both. For this reason, their main use is as depolluting

Technologies and Materials for Renewable Energy, Environment and Sustainability
AIP Conf. Proc. 3321, 050002-1–050002-10; https://doi.org/10.1063/5.0289698
Published under an exclusive license by AIP Publishing. 978-0-7354-5231-2/$30.00

agents [11, 12]. Through an analysis of the performance of fired zinc ferrite/kaolin powder and its potential as an effective adsorbent for removing lead and aiding in effective water treatment, the objective of this study is to conduct a thorough investigation of the effects of various factors, including pH, metal ion concentration, contact time, and adsorbent dose.

Normal Distribution

In probability and statistics, the normal distribution bell curve is one of the most important continuous probability distributions. The normal distribution is defined as the probability density function f(x) for the continuous random variable x , in the system. A normal distribution is a very important statistical data distribution pattern occurring in many natural phenomena, such as height, blood pressure, lengths of objects produced by machines, etc [24, 25].

MATERIALS AND METHODS

Synthesis of Zinc Ferrite

Zinc ferrite nanoparticles were manufactured using the sol-gel auto combustion process. Traditionally, deionized water was used to dissolve ferric nitrate ($Fe(NO_3)_3.9H_2O$), zinc nitrate ($Zn(NO_3)_2.6H_2O$), and citric acid ($C_6H_8O_7$), and Ammonium hydroxide (99)% pure, analytical grade, from (CDH)/India. The molar ratio of zinc nitrate, ferric nitrates to citric acid ratio to prepare Zinc ferrite was 1:2:3, while pH adjusted to 7 using Ammonium hydroxide (NH_4OH). Magnetic stirring and heating were used to form a gel, which led to the formation of a loose structure (ash) to obtain zinc ferrite nanoparticles.

Batch adsorption experiments

The heavy metals were removed via a batch adsorption experiment utilizing structure containing adsorbent materials in polluted solution. Adsorbent material in the form of a crushed sample that was previously made from kaolin of (75) μm particle size and charcoal of (25) μm at 8:2 ratio which loaded with (0, 3, 5, 7, 10) of ZnFe2O4 nano particle using slip casting method, samples were dried at 100 oC and fired at (1050) oC. In a glass beaker, 1 gm of adsorbent composite powder was placed in (100) ml of deionized water containing Pb(CH3COO)2.3H2O. The mixtures were stirred for two hours while the following conditions were applied. After that, 0.45 μm-diameter filter paper was used as filter, to investigate the impact of pH value, ions concentration, and adsorbent dose and contact time to calculate the effect of the most important adsorption factor. All tests were conducted at room temperature. The batch experiment is shown in Figure 1. Using solutions with concentration 250 ppm of (Pd+2) in 100 ml of deionized water to investigate the pH effects on Pb2+ adsorption. The pH was subsequently changed to (3, 5, 7, and 9) utilizing HCl or NaOH to get the desired pH for composite sample (MZ10) at room temperature. Using solutions with concentrations of (100, 150, 200, and 250) ppm, each solution containing sample (MZ10), the impact of initial concentrations of Pb2+ was investigated. Using NaOH, the PH of each solution was brought to 9. Using composite samples MZ0, MZ3, MZ5, MZ7, and MZ10 in a 250 ppm Pb2+ solution, examine the effects of the adsorbent dosage. NaOH was used to raise each solution pH to 9. Using solutions with 250 ppm concentration of Pb2+, containing composite sample (MZ10). The solution pH was brought to 9 by using NaOH. After 10, 30, 50, 70, 90 minutes and 4, 8, 24 hours, the precipitate solution was obtained. The removal efficiency (η) was determined utilizing the following equation [13]

$$\eta = \frac{C_o - C_e}{C_o} \times 100\% \quad (1)$$

where C_o, C_e initial ion concentration before and after treatment (ppm) respectively.

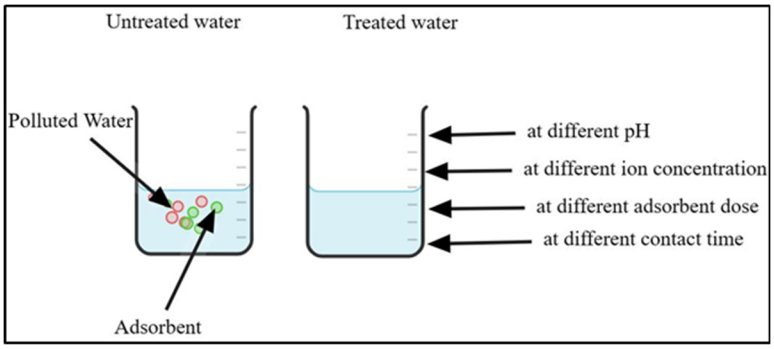

FIGURE 1. Batch experiment for Mullite/ZnFe2O4 composite powder.

Characterization

X-ray diffraction (XRD) to ascertain the crystal structure, using (XRD–6000) Shimadzu - Japan) with Cu, and a wavelength of 0.15406 nm. Fourier-transform infrared (FT-IR) spectroscopy for chemical composition analysis, model (Shimadzu- Japan) is a tool for analysis that molecular vibrations in the 400–4000cm–1 range. The collected water from batch adsorption method was identified using an atomic absorption spectrophotometer (AAS) of the AA-7000-SHIMADZU type. Thermo Scientific Company Axia Chemi-SEM uses energy dispersive Energy Dispersive Spectrum (EDS), a technique that is vital to determining the purity since it can analyze a material's elemental composition. Sample MZ10 underwent elemental analysis at pH 3 and pH 9 both prior to and following adsorption. The Brunauer-Emmett-Teller (BET) and Barrett-Joyner-Halenda (BJH) methods are two distinct approaches used in the analysis of porous materials; BET was examined for samples (MZ0, MZ3, and MZ10) samples. All the samples were outgassed at 77 °C and 88 Kpa.

RESULTS AND DISCUSSION

The XRD of ZnFe2O4 nanoparticles, Kaolin and Mullite are displayed in Fig 2. The outcome of Zinc Ferrite nano powder demonstrates that the sample has a spinel crystal structure and was formed in a single phase and all peaks match using the JCPDS (22-1012) [15]. The zinc ferrite peaks appeared at 29.86, 35.09, 42.7, 53.04, 56.46, 62.2, 70.5, 73.56 and 74.48o related to the miller indices (220), (311), (400), (422), (511), (440), (620), (533) and (622), respectively. The peak at 35.09 was the highest intensity and the preferred orientation. The crystallite size by using scherrer equation for ZnFe2O4 was found to be 17.1nm. X-ray diffraction (XRD) pattern of Kaolin both before and after heat treatment at 1050 ^{o}C are also displayed in Fig. 2. The XRD analysis revealed that the phases of kaolin powder were kaolinite, quartz and a trace amount of illite phase. Upon heat treatment, the pattern shows that kaolinite peaks are not observed which transformed to Mullite phase and trace amount of cristobalite phase, as shown in the equation below, which represent the phase change of kaolin upon heat treatment [16]:

$$3(2Al2O3.3SiO2) \xrightarrow{1050\ ^{o}C} 2(3Al2O3.2SiO2) + 5SiO2 \quad (2)$$

FTIR spectra of as-prepared Zn-Fe2O4 powder, Kaolin and Mullite are shown in Fig 3. There are several peaks appeared, 422, 543, 1132.21, 1384, 1581, 3325 and 3695 cm-1 that related to Zinc Ferrite pattern. Strong peaks that show up at 543 cm−1 and 422 cm−1 correspond to tetrahedral and octahedral sites of ZnFe2O4, respectively; these were attributed to Fe–O and Zn–O vibrations [17]. This result indicates to single phase spinal structure formation [18-21]. Moreover, the bending mode of OH at 3325 and 3695 cm-1 suggested the presence of hydroxyl group on the surface of ZnFe2O4 nanoparticles. The asymmetric and symmetric bending vibration of C=O are responsible for the absorption peaks at 1581 cm^{-1} and 1384 cm^{-1}, respectively [22-26]. The band located at 1132.21 cm^{-1} could be allocated to the vibrations of the –OH groups coordinated to Fe(III) cations [27-30]. FTIR spectra of kaolin both before and after heat treatment are also shown in Fig. 3. Before heat treatment the band at about 451.24 and 520.04 cm-1 that related to kaolin represents Si-O and Al-O-Si deformation, respectively [31-35]. These spectral features related to mixed vibrations of the Si-O network at 748.83 cm-1 for kaolin represents the bending vibration of the Si-O bond in the kaolinite structure, at 972.59, 909.03, 642.91 and 991.96 cm-1 are show vibration Al-OH which is a typical uptake of kaolinite minerals. The bands at 1115.45 and 1024.69 cm-1 for kaolin represent the stretching vibrations of the Si-O bond and the Al-OH in the kaolinite structure, respectively [36]. Kaolin has OH bending (deformation) of water at

bands 1638.33cm-1. The absorption bands of kaolinite are located between 3620.62, 3651.05, and 3691.74 cm-1 corresponding to stretching frequencies of -OH groups, -OH stretching vibration mode, due to the existence of H2O in kaolin structure (Al2Si2O5(OH)4). After calcination, it can clearly be seen that the hydroxyl peaks in the region 3620.62, 3651.05 and 3691.74 cm-1 disappeared, indicating the dehydroxylation of kaolin occurred. The heat treatment to produce mullite are connected to the appearance of specific band within the spectra, there is an intense broad band at 1032.26 cm-1 were assigned to (SiO2), and the bands of about 410 cm-1 and 538 cm-1 were belong to the bending vibration of Al-O-Si and Si-O-Si, respectively.

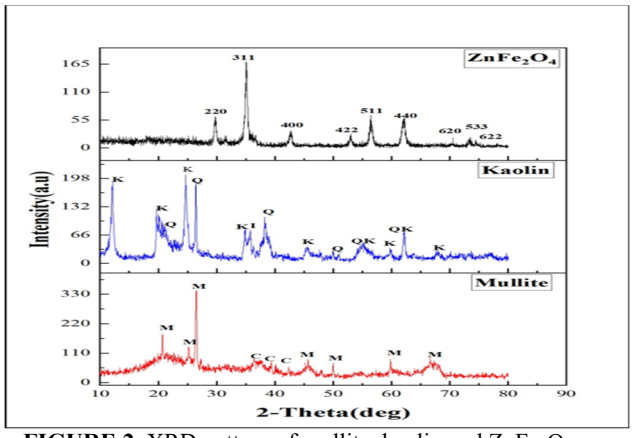

FIGURE 2. XRD pattern of mullite, kaolin and $ZnFe_2O_4$

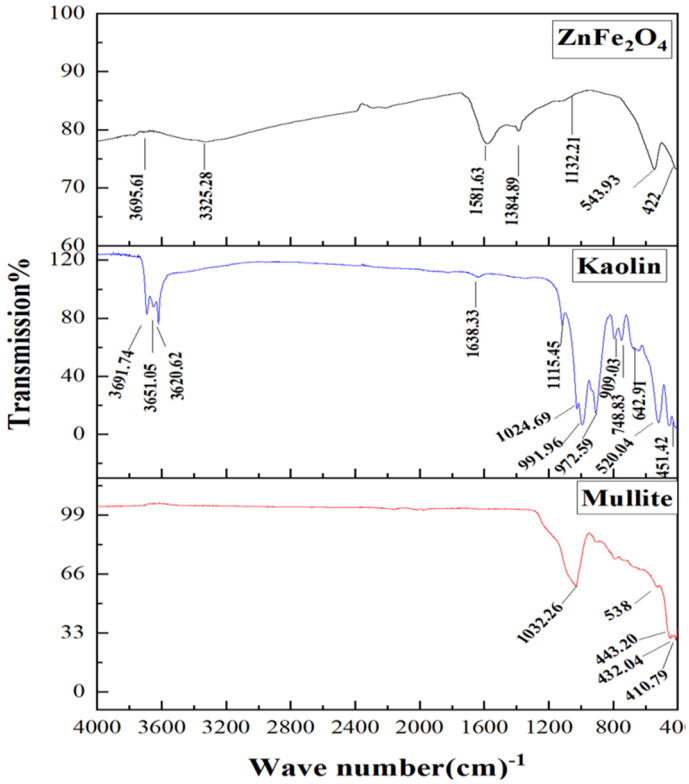

FIGURE 3. FTIR spectra of mullite, kaolin, and $ZnFe_2O_4$

The changing the pH solution (3, 5, 7, and 9) with 250 ppm of lead solution mixed with Mullite/ZnFe2O4 composite with 10% adsorbent dosage (MZ10) to examine their removal efficiency percentage. These findings are illustrated in Fig 4. When pH values increased the lead removal efficiencies decreased. The greatest lead removal efficiency was observed at pH 3, where 88.563% of the lead was removed. The rationale behind this is that at low pH levels, a greater proportion of the functional group would be in the dissociated state, attracting negative charges to the

metal ions. This suggests that the surface became negatively charged at low pH levels, which in turn promoted the attraction of positively charged (Pb2+) to the negatively charged surface [26]. The highest and lowest efficiency at pH 3 and pH 9 respectively, which obtained was relied upon for application in subsequent tests.

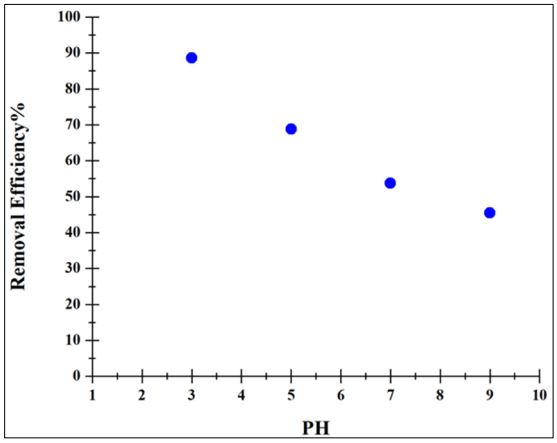

FIGURE 4. Removal efficiency of MZ10 sample with different pH

The pb ion concentrations 100, 150, 200, and 250 ppm containing MZ10 sample at pH3 and pH9 significantly affected the adsorbent's capacity as illustrated in Fig 5. Greater concentrations of metal ions generally speed up the adsorption process to a point, so maximum percentage was achieved at high concentration (250 ppm). As a result, it appears that removal efficiency increasing at high concentration of lead ion at pH 3 from 12.22, 43.22 % to 45.53, 88.56 % respectively. Elevated levels of metal ions can accelerate the adsorption process through several factors: enhancing competitive dispersion at available adsorbent surface sites which leads to the closure of pores on the adsorbent surface, enhancing mass transfer through the boundary layer of the adsorbent and facilitating the distribution of metal ions to the outer surface. It can also lead to an increased chance of collisions between metal ions and adsorption sites on the adsorbent surface [27].

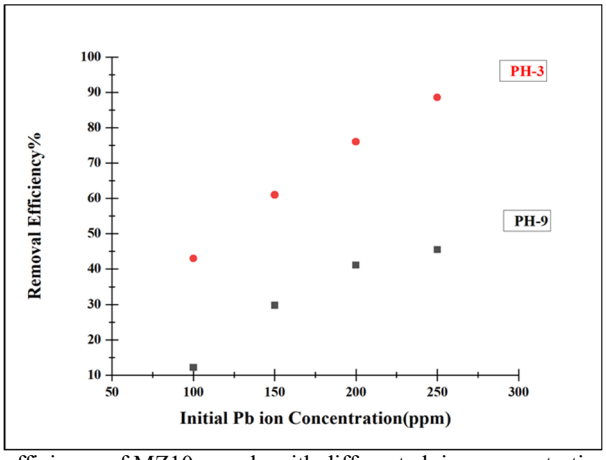

FIGURE 5. Removal efficiency of MZ10 sample with different pb ion concentration at pH 3 and pH 9

The amount of adsorbent zinc ferrite affects the percentage of (250) ppm Pb(II) removal as illustrated in Figure 6. ZnFe2O4 was added in a dose of (0, 3, 5, 7, 10) %, and the solution pH was brought to 3 and 9. According to the experimental results it was found that the percentage of removal efficiency was 45.37 and 25 % respectively. The value of removal efficiency is due to mullite which is regard a heat-resistant ceramic material that has adsorption properties [28]. When increasing ZnFe2O4 it was found to increase the removal efficiency percentage value and reaches its greatest removal at a given adsorbent concentration. It is evident that 10% of ZnFe2O4 achieved the maximum removal of 88.56 and 45.53% for pH 3 and pH 9.

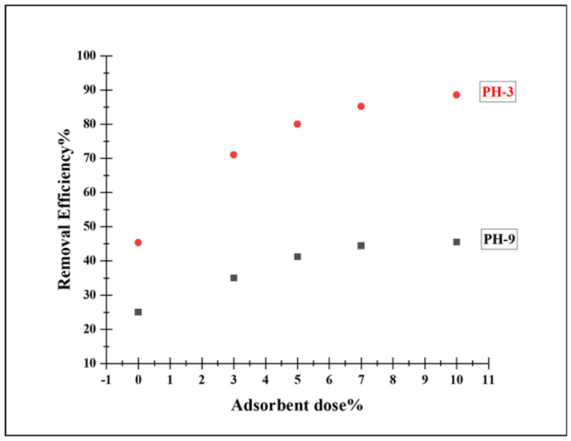

FIGURE 6. Removal efficiency of mullite/$ZnFe_2O_4$ with different adsorbent dose at pH 3 and pH 9

The effect of contact time on removal efficiency of Pb^{2+} at pH 3 and pH 9 with a concentration of 250 ppm using MZ10 is shown in Figure 7. The precipitate solution was obtained after 10, 30, 50, 70, and 90 minutes, as well as after 4, 8, and 24 hours, and the results were compared with and without using a magnetic bar on the solution. The results showed that the removal efficiency of both cases increases with increasing contact time. The highest efficiency in removing lead (II) is 100% at 30 min. at pH 3, while at pH 9 is 96.5 % at 24 hours without using the magnetic bar as shown in Figure (8-A). Using the magnetic bar during adsorption process, made the removal efficiency reaches to the maximum efficiency 100% in shorter time 10 min. at pH 3 and 8 hours at pH 9 as shown in Figure (8-B). The magnetic bar separates the adsorbed material from the solution.

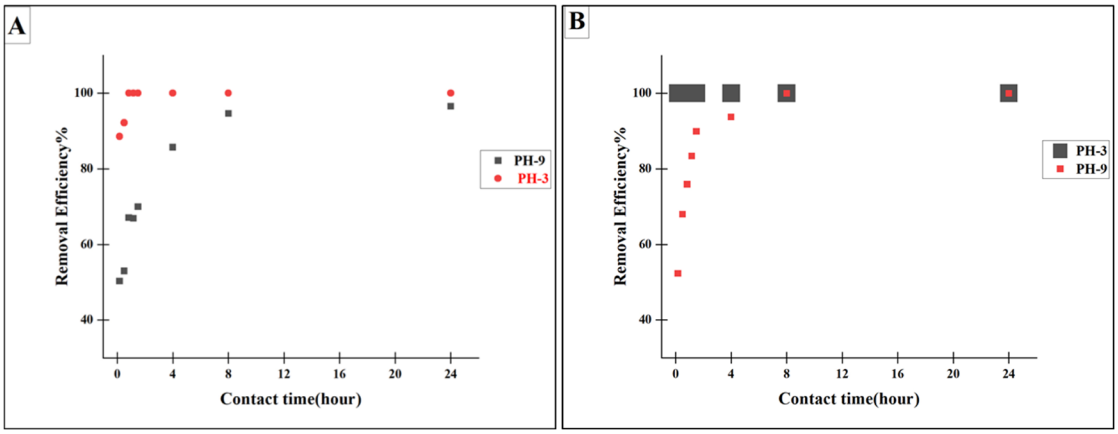

FIGURE 7. Removal efficiency of MZ10 sample with different contact time at pH3 and 9, A) without magnetic bar, B) with magnetic bar

EDS test was performed to study the elements of sample MZ10 as shown in Figure 8 before and after the adsorption process at pH3 and pH9. The resulting graph and the table attached to Figure 8 (A) confirm the presence of zinc, iron, oxygen, aluminum, silicon and carbon, and are attributed to the composition of elements found in MZ10. The presence of carbon is often derived from citric acid, which acts as a chelating agent and fuel in the synthesis process. The presence of the mullite phase was also observed, especially the presence of aluminum (Al) and silicon (Si) elements. The high percentage of Al and Si is due the high content (90%) of mullite in the sample. This analysis helps confirm the purity and chemistry of the mullite phase. At PH3 after adsorption process, the pattern and the table attached to Figure 8 (B) confirms the presence of Cl and Pb in addition to the same elements present before. Presence of Cl refers to HCl used to adjust the pH 3 and presence of Na refers to NaOH to adjust the pH 9 as in the table accompanying the Figure 8 (C). The percentage of Pb at pH 3 is 1.5, while at PH 9 the percentage decreased to 0.2 as illustrated in the Table of Figure 8 (B) and (C) respectively. These results confirm the results obtained from removal efficiency at different pH.

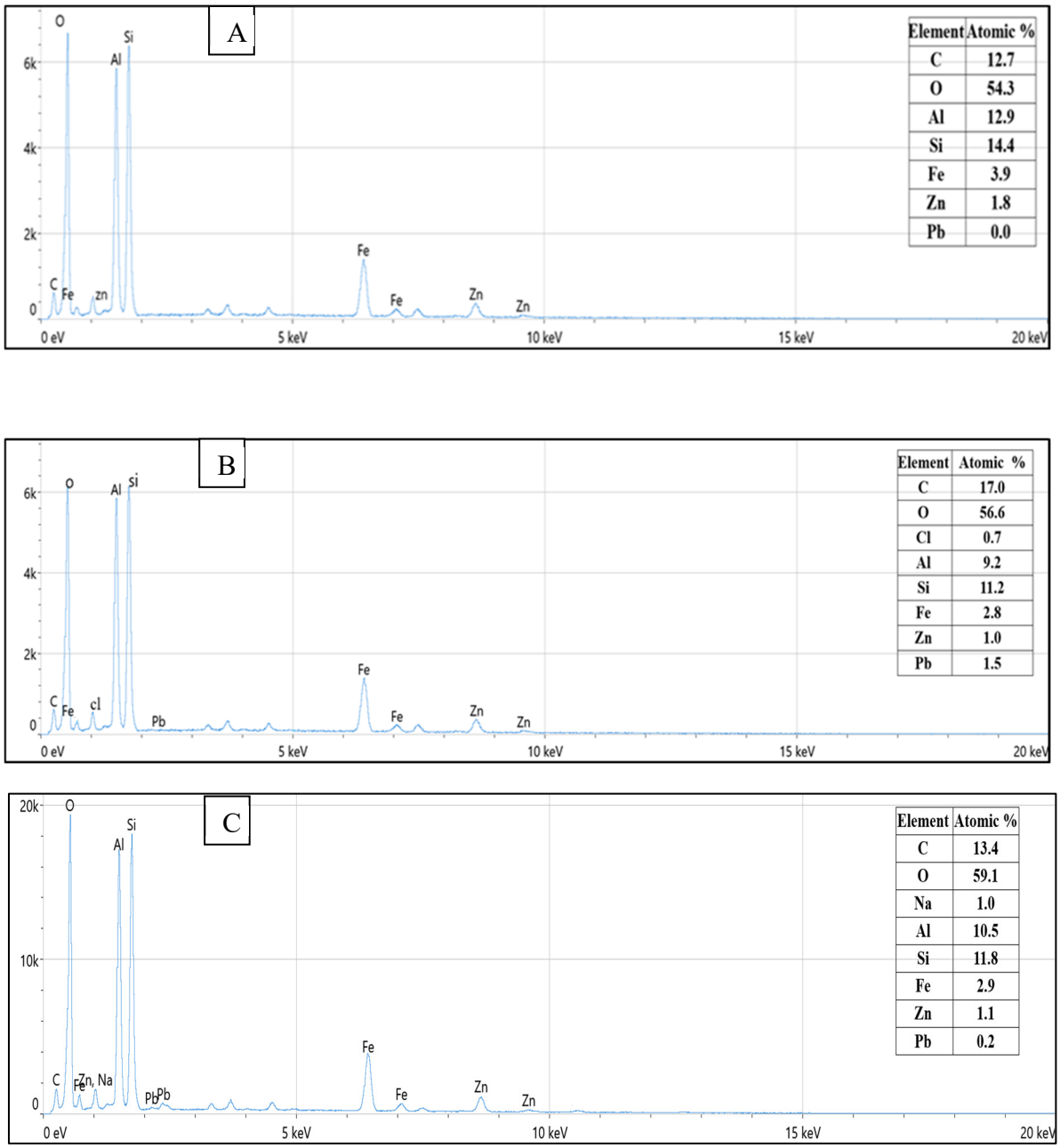

FIGURE 8. EDS elemental analysis of MZ10 (A) before adsorption, (B, C) after adsorption process at pH3 and pH9, respectively

The physical adsorption-desorption isotherms of an inert gas such as nitrogen for the prepared samples are shown in Figure 9. The adsorption isotherms produced were used to determine the specific surface area, total pore volume, average pore volume, and pore size distribution. The BET analysis was examined for the reference samples MZ0 (without adding ferrite) and for samples MZ3 and MZ10 with ferrite added at (3 and 10) %, respectively, the results are summarized in Table 1. All samples were outgassed at 77 K and a vapor pressure of 88 kPa. The size of visible pores in materials is determined by the quantity of nitrogen gas that is absorbed by the robust pores. The isotherm curve of the samples starts from zero and increases slowly with the increase of P/P0 in exponential curve, and the adsorption capacity of the material increases until the relative pressure reaches unity. It was found that the specific surface area of BET is (3.9966) m2.g-1 for mullite sample. Since the surface area is small, the particle size was large, especially when using kaolin with a particle size of 75 µm. It was found an increase in surface area values when the ferrite nano powder was added and when its percentage increased from 3 to 10%. A higher BET value indicates a

larger surface area, which can help predict the adsorption performance which may increase the number of active sites available for adsorption processes. From the BJH test, the pore size distribution of the samples is not uniform and most of the pores are located in the size less than 50 nm, which all show a typical pattern within mesoporous materials, which has the characteristic of hysteresis loop with capillary condensation.

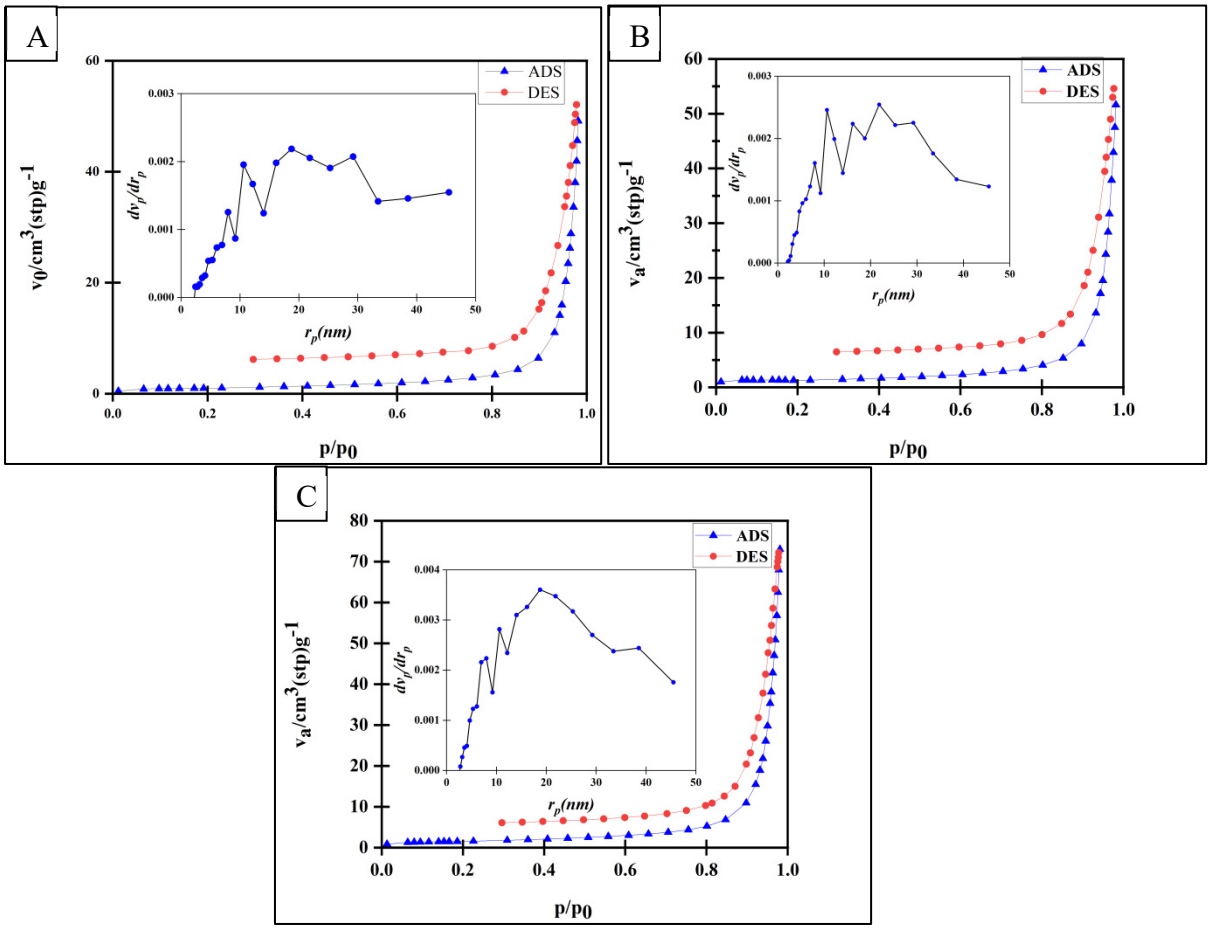

FIGURE 9. N2 adsorption-desorption isotherm for (A) MZ0, (B) MZ3 and (C) MZ10

The standard normal distribution

TABLE 1. The Brunauer–Emmer-Teller (BET) results

Code	S_{BET} (m^2/g)	Pore Volume (cm^3/g)	Pore diameter (nm)
MZ_0	3.9966	0.076029	76.093
MZ_3	5.6743	0.079851	56.29
MZ_{10}	5.8298	0.1129	77.49

CONCLUSION

The sol-gel process was used to effectively produce zinc ferrite nanoparticles. A composite of prepared ferrite was combined with mullite which was used to remove heavy metals from wastewater. The characterization results indicated that the formulation was fruitful. Various conditions: solution pH (3, 5, 7, 9), initial Pb(II) concentrations (100, 150, 200, 250) ppm, adsorbent doses (0, 3, 5, 7, 10) %, contact times (10, 30, 50, 70, 90 minutes and 4, 8, 24 hours), all had an effect on the removal efficiency values of Pb(II) from wastewater. The best lead removal value achieved when an external magnet was applied and made the contact time shorter. The EDS result, confirms the presence of zinc, iron, oxygen, aluminum, silicon and carbon, which is attributed to the composition of elements found in MZ10 in addition to the percentage of Pb after adsorption process. From BET and BJH results it was found that the

specific surface area value was increase with increasing Zinc ferrite percentage which can help predict the adsorption performance that may increase the number of active sites available for adsorption processes.

REFERENCES

1. Aragaw, T. A., & Angerasa, F. T. (2020). Synthesis and characterization of Ethiopian kaolin for the removal of basic yellow (BY 28) dye from aqueous solution as a potential adsorbent. Heliyon, 6(9), 04975.
2. Hussain, W. A., Ismail, M. M., and Hashim, F. S. (2022). Bio-Application of poly (Vinyl Alcohol)/Biphasic calcium phosphate scaffold as bone tissue replacement. Current Materials Science, 15(3), 271–279.
3. Mousavi, H. Z., & Seyedi, S. (2010). KINETIC AND EQUILIBRIUM STUDIES ON THE REMOVAL OF PB (II) FROM AQUEOUS SOLUTION USING NETTLE ASH. Journal of the Chilean Chemical Society, 55(3), 307–311.
4. Hashim, F., Ismail, M. M., and Hussain, W. (2021). Tri-calcium phosphate (Nanoparticles/Nanofibers)/PVA for bone tissue engineering. Acta Physica Polonica A, 140(4), 337–343.
5. Mouni, L., Belkhiri, L., Tafer, M., Zouggaghe, F., & Kadmi, Y. (2014). Studies on the removal of Pb(II) from wastewater by activated carbon developed from Apricot stone activated with sulphuric acid. Moroccan Journal of Chemistry, 2(5), 452-456.
6. M. Rasheed, Suha Shihab, O. Alabdali, and H. H. Hassan, "Parameters Extraction of a Single-Diode Model of Photovoltaic Cell Using False Position Iterative Method," Journal of Physics: Conference Series, vol. 1879, no. 3, p. 032113, May 2021.
7. Hussain, W. A., Ismail, M. M., and Taher, S. (2022).Incorporation of treated woven carbon fiber to methacrylate resin for Heat-Cured acrylic denture composite. Journal of Biomimetic, Biomaterials and Biomedical Engineering, 56, 153–164.
8. Taher, S.Y., Hussain, W.A. (2021). The effect of acidic treatment of carbon fiber on denture mechanical properties. Journal of Physics: Conference, 1879(3), 032082.
9. Ziedan, W., Hussain, W.A. & Ismail, M.M. (2024). Porous Adsorbent Based on Kaolin and Nanomagnetic Cobalt Ferrite for Effective Removal of Pb(II) from Wastewater. Journal of Superconductivity and Novel Magnetism, 37, 587-596.
10. Manzoor, K., Ahmad, M., Ahmad, S., & Ikram, S. (2019). Removal of Pb(ii) and Cd(ii) from wastewater using arginine cross-linked chitosan–carboxymethyl cellulose beads as green adsorbent. RSC Advances, 9(14), 7890–7902.
11. Asim, F. A., Al-Mosaweb, E. H., & Hussain, W. A. (2022). Studying the Physical and Biological Characteristics of Denture Base Resin PMMA Reinforced With ZrO2 and TiO2 Nanoparticles. Karbala International Journal of Modern Science, 8(3), 503–513.
12. Wafaa A, Enas M, Mukhlis M, Luay H. (2020). Preparation of Household Water Filter. Journal of Applied Science and Engineering, Vol.23, No. 1, pp. 61_68.
13. Osman, A. I., El-Monaem, E. M. A., Elgarahy, A. M., Aniagor, C. O., Hosny, M., Farghali, M., Rashad, E., Ejimofor, M., López-Maldonado, E. A., Ihara, I., Yap, P., Rooney, D., & Eltaweil, A. S. (2023). Methods to prepare biosorbents and magnetic sorbents for water treatment: a review. Environmental Chemistry Letters, 21(4), 2337–2398.
14. Bakr, A., Moustafa, Y. M., Motawea, E. A., Yehia, M., & Khalil, M. M. (2015). Removal of ferrous ions from their aqueous solutions onto NiFe2O4–alginate composite beads. Journal of Environmental Chemical Engineering, 3(3), 1486–1496.
15. Mustapha, S., Ndamitso, M. M., Abdulkareem, A. S., Tijani, J. O., Mohammed, A. K., & Shuaib, D. T. (2019). Potential of using kaolin as a natural adsorbent for the removal of pollutants from tannery wastewater. Heliyon, 5(11), 02923.
16. M. Rasheed, S. Shihab, O. Y. Mohammed, and A. Al-Adili, "Parameters Estimation of Photovoltaic Model Using Nonlinear Algorithms," Journal of Physics: Conference Series, vol. 1795, no. 1, p. 012058, Mar. 2021.
17. Sajjia, M., Oubaha, M., Hasanuzzaman, M., and Olabi, A.," Developments of cobalt ferrite nanoparticles prepared by the sol–gel process", Ceramics International, 40(1), 1147–1154, 2014.
18. Cheng, Y., Xing, J., Bu, C., Zhang, J., Piao, G., Huang, Y., Xie, H., & Wang, X. (2019). Dehydroxylation and structural distortion of kaolinite as a High-Temperature sorbent in the furnace. Minerals, 9(10), 587.
19. S Husain, M Yusup, N H Haryanti, Suryajaya, M Saukani, Rodiansono, S Arjo, A Riyanto. (2021). Characteristics of zinc ferrite nanoparticles (ZnFe2O4) from natural iron ore. Earth and Environmental Science. 758: 012001.

20. Samoilă, P., Cojocaru, C., Crețescu, I., Stan, C. I., Nica, V., Săcărescu, L., & Harabagiu, V. (2015). Nanosized Spinel Ferrites Synthesized by Sol-Gel Autocombustion for Optimized Removal of Azo Dye from Aqueous Solution. Journal of Nanomaterials, 1–13.
21. Rameshbabu, R., Ramesh, R., Kanagesan, S., Karthigeyan, A., & Ponnusamy, S. (2013). Synthesis and study of structural, morphological and magnetic properties of ZNFE2O4 nanoparticles. Journal of Superconductivity and Novel Magnetism, 27(6), 1499–1502.
22. P. S. KUMARa, K. THYAGARAJANb, A. G. KUMARc. (2018). INVESTIGATIONS ON PHYSICAL PROPERTIES OF Zn FERRITE NANOPARTICLES USING SOL-GEL AUTO COMBUSTION TECHNIQUE. Digest Journal of Nanomaterials and Biostructures Vol.13, No.4, 1117-1122.
23. Bahtiar, S., Taufiq, A., Sunaryono, S., Hidayat, A., Hidayat, N., Diantoro, M., Mufti, N., & Mujamilah. (2017). Synthesis, Investigation on Structural and Magnetic Behaviors of Spinel M-Ferrite [M = Fe; Zn; Mn] Nanoparticles from Iron Sand. IOP Conference Series: Materials Science and Engineering, 202, 012052.
24. Stoia, M., Muntean, C., & Barvinschi, P. (2013). SYNTHESIS OF NANOCRYSTALLINE ZNFE2O4 AND ITS USE FOR THE REMOVAL OF CONGO RED FROM AQUEOUS SOLUTIONS. Environmental Engineering and Management Journal, 12(5), 959–967.
25. Dewi, R., Agusnar, H., Alfian, Z., & Tamrin. (2018). Characterization of technical kaolin using XRF, SEM, XRD, FTIR and its potentials as industrial raw materials. Journal of Physics: Conference Series, 1116, 042010.
26. Ekosse, G. (2005). Fourier transform infrared spectrophotometry and X-ray powder diffractometry as complementary techniques in characterizing clay size fraction of kaolin. Journal of Applied Sciences and Environmental Management, 9(2), 43 – 48.
27. Varpe, A. S., & Deshpande, M. (2020). Study of structural, optical, and dielectric properties of sol–gel derived ZnFe2O4–Al2O3 composite nanoparticles. Journal of Sol-Gel Science and Technology, 96(3), 718–727.
28. Mondal, M. K. (2010). Removal of Pb(II) from aqueous solution by adsorption using activated tea waste. Korean Journal of Chemical Engineering, 27(1), 144–151.
29. N. Assoudi et al., "Comparative examination of the physical parameters of the sol gel produced compounds La0.5Ag0.1Ca0.4MnO3 and La0.6Ca0.3Ag0.1MnO3," Optical and Quantum Electronics, vol. 54, no. 9, Jul. 2022.
30. Al-Senani, G. M., & Al-Fawzan, F. F. (2018). Adsorption study of heavy metal ions from aqueous solution by nanoparticle of wild herbs. The Egyptian Journal of Aquatic Research, 44(3), 187–194.
31. Yaoyao Zhang, Zhengwen Wei, Mengyao Li, Xishe Wu, and Wei Wang (2020). Preparation and Modification of Mullite Whiskers/Cordierite Porous Ceramics for Cu2+ Adsorption and Removing. American Chemical Society, 5, 25, 15691–15701.
32. Ziedan, W., Hussain, W.A. & Ismail, M.M. (2024). Physical and Structural Properties of Porous Kaolin/Co-Ferrite for Water Treatment. Journal of Applied Sciences and Nanotechnology, 4, 1.
33. Kalunge, S., Humbe, A. V., Khedkar, M. V., More, S. D., Keche, A. P., & Pandit, A. A. (2020). Investigation on Synthesis, Structural and Electrical properties of Zinc Ferrite on Gamma Irradiation. Journal of Physics: Conference Series, 1644(1), 012017.
34. Shinoda, Y., Suzuki, Y., & Yoshida, K. (2013). TEM analysis of nanocrystalline SiC ceramics sintered by SPS using Al2O3–TiO2 additive. Journal of Asian Ceramic Societies, 1(3), 267–273.
35. Cychosz, K. A., & Thommes, M. (2018). Progress in the physisorption characterization of nanoporous gas storage materials. Engineering, 4(4), 559–566.
36. Lawtae, P., & Tangsathitkulchai, C. (2021). The Use of High Surface Area Mesoporous-Activated Carbon from Longan Seed Biomass for Increasing Capacity and Kinetics of Methylene Blue Adsorption from Aqueous Solution. Molecules, 26(21), 6521.

The Impact of Emotional Stress on the Food Behavior of Lebanese Population

Reem Elkawam[1] , Rola Elcheikh[1,], Ali Amhaz[2,], Maha Krayem[3], Samer Sakr[3] and Imtithal Sheet[2,3 a)]

[1]*Department of Nutrition and Food Sciences, School of Arts and Sciences, Lebanese International University, Beirut, Lebanon*
[2]*Department of Biomedical Sciences, School of Arts and Sciences, Lebanese International University, Beirut, Lebanon*
[3]*Department of Biological and Chemical Sciences, School of Arts and Sciences, Lebanese International University, Beirut, Lebanon*

[a)] *Corresponding author: imtithal.sheet@liu.edu.lb*

Abstract. In 2019, lockdowns and quarantines were implemented worldwide to contain the spread of the SARS-CoV-2 virus, this led to a switch to remote work and online education, which changed the dietary habits and lifestyle choices. The pandemic's social isolation had a negative impact on mental health, as well as increase in anxiety, insomnia, and depression. Lebanon has been grappling with financial challenges for the past thirty years, which have had a significant impact on its healthcare system. The economic crisis, which came to peak in August 2019, was further exacerbated by the pandemic. Both crises have influenced eating habits and lifestyle behaviors in Lebanon, forcing the population to adapt to cope with emotional stress and adopt new dietary habits. The current study investigates the possible correlation between emotional stress caused by both economic crisis and COVID-19 pandemic and the eating behavior among Lebanese population. A cross-sectional study was conducted between March and August 2022. The questionnaire included 28 questions, divided into 5 main parts. The results were analyzed via statistical analysis and were computed using the IBM – Spss 25 ® software. Our findings demonstrated that challenges and public health consequences caused by the economic crisis and the COVID-19 pandemic in Lebanon resulted in a slight decrease in some magnesium sources among married couples, part time and retired employees. Additionally, the inflation of food costs was positively correlated with the consumption of unhealthy snacks (chips, crackers, chocolate) and high fat diet especially among unemployed participants ($p<0.001$). As a conclusion, the long-term economic crisis and the pandemics reform emotional health status among the Lebanese population. The main findings of the current study could be used by the responsible authorities to raise awareness and propose tangible recommendations to relieve these issues

INTRODUCTION

Stress is commonly recognized as a trigger that elicits a physiological and psychological response in the body. Over the past years, the understanding of stress biology has evolved significantly [1]. Stress is now regarded as a continuous, adaptive mechanism that enables individuals to assess, cope with, and anticipate continually changing environments, rather than being a momentary reaction to transient threats [2]. However, the capacity of this stress system is finite and once it becomes overloaded, it ultimately leads to adverse health outcomes, particularly related to health diet and mental illness [3].

One key aspect of maintaining a healthy diet during stressful times is ensuring an adequate intake of magnesium. As the second most abundant intracellular cation, magnesium is a crucial nutrient with a well-known impact on human health and well-being [4]. It plays a vital role in nearly all major metabolic and biochemical processes, serving as a cofactor in hundreds of enzymatic reactions [5]. Some of its functions include protein and nucleic acid synthesis, regulation of metabolic pathways, neuronal transmission, neuromuscular function, and regulation of cardiac rhythm [6]. Previous studies showed that magnesium deficiency affects a significant portion of the general population, leading to an increased risk of both physical and mental health issues over time [7]. Notably, symptoms of stress, such as fatigue, irritability, and mild anxiety, closely resemble those of magnesium deficiency [8-10].

The relationship between magnesium status and stress has been intensively investigated, where multiple studies show the direct correlation between stress and magnesium deficiency, with magnesium deficiency and stress exacerbating each other's negative consequences. This concept of a bidirectional relationship between magnesium and stress was first proposed in the early 1990s and has since been referred to as the "vicious circle" [9]. According to this vicious cycle, stress can increase magnesium loss, resulting in a deficit that, in turn, heightens the body's vulnerability

Technologies and Materials for Renewable Energy, Environment and Sustainability
AIP Conf. Proc. 3321, 060001-1–060001-15; https://doi.org/10.1063/5.0289820
Published under an exclusive license by AIP Publishing. 978-0-7354-5231-2/$30.00

to stress [5]. Magnesium is naturally found in various food categories, including nuts, legumes, whole cereals, and fruits [11, 12]. However, due to the economic crisis in Lebanon and the COVID-19 pandemic, the prices of magnesium-rich food items, have significantly increased over the past two years.

Amidst the severe economic crisis in Lebanon, the Lebanese population had to adapt their dietary habits due to reduced incomes and higher unemployment rates. This has led to the replacement of expensive food items with more affordable alternatives or even a decrease in their consumption [13]. While these substitutions may help to manage hunger and prices fluctuations, they could pose challenges by potentially obscuring the importance of balancing nutritious and cost-effective food choices, particularly if done without a thorough understanding of their nutritional impact [14].

Additionally, the emergence of the economic crisis led to political changes and pushed the country into an economic catastrophe, causing a massive devaluation of the national currency, the Lira [15]. The economic crisis was further exacerbated by government restrictions and lockdowns implemented to combat the virus [16]. As the unemployment rate soared during this critical period, the number of individuals experiencing low income also increased. The surge in food prices, coupled with rising unemployment rates and salary reductions, likely worsened nutrition habits and quality of life for low-income families. Consequently, individuals resorted to consuming particular types of food, often starchy and deficient in essential nutrients like magnesium, which they needed the most during their emotional stress. [17]. This study aims to investigate the potential correlation between emotional stress caused by the COVID-19 pandemic and the economic crisis, and how it has impacted Lebanese people's dietary habits and magnesium intake.

METHODOLOGY

STUDY DESIGN

A cross-sectional questionnaire-based survey was administered among random samples of Lebanese citizens. Questions were selected based on previous studies aimed at assessing impact of emotional stress on the food behavior of the Lebanese population. The study involved 501 participants from different regions including Beirut, Bekaa, Mount Lebanon, North and South, offering a comprehensive snapshot of the sample population.

SAMPLE SIZE

A total of 501 Lebanese citizens above 18 years participated in this survey through social media platforms using an electronic link Google form between March 23 and August 22, 2022.

QUESTIONNAIRE STRUCTURE

The questionnaire included 28 questions, divided into 5 main parts. The first part studied the socio-demographic data of the participants including: gender, age, educational status, marital status, and employment status. The second part included questions pertinent to anthropometric data such as weight. The third part included two questions related to the impact of emotional stress on the dietary supplement intake. The fourth part of the questionnaire included questions related to the impact of emotional stress on the dietary behavior. The last part assessed stress relieving activities by the participant such as physical activity, meditation, and drawing.

QUESTIONNAIRE VALIDATION

The survey was designed by the research team and available in Arabic and English languages. The participants were informed about the study's objectives and ensured of the confidentiality and privacy of their survey responses and personal information, with an assurance that the information gathered through the survey would be used for research purposes only. A pilot study with 15 participants was conducted to assess the questionnaire's reliability, with Cronbach's alpha coefficient indicating acceptable reliability at 0.687. Minor modifications were made to the questionnaire for further reliability assessment.

STATISTICAL ANALYSIS

The data was analysed using SPSS software version 25, with Spearman correlation calculated for association between variables. Chi-Square test of independence and Fischer exact test were performed to assess associations between categorical variables. Pearson correlation was used to validate responses to the total score. Significant results were considered for ($p<0.05$).

RESULTS

SOCIO-DEMOGRAPHIC CHARACTERISTICS OF PARTICIPANTS

The provided information outlines the demographic distribution of participants in a survey, shedding light on various factors such as age, gender, marital status, region of residence, employment status, and education level. The majority of respondents were distributed across different age brackets, with 36.7% falling between 18 to 25 years, 44.3% between 26 to 45 years, 16.4% between 46 to 65 years, and 2.6% being older than 65. Gender-wise, the survey included 68.9% females and 31.1% males. Geographically, the distribution covered various regions, with 27.3% residing in Beirut, 6.6% in Bekaa, 8.8% in Mount Lebanon, 5.0% in the North, and 52.3% in the South.

Employment status reflected a diverse range, with 42.7% being full-time employees, 21.4% part-time employees, 1.6% retired, and 34.3% unemployed. Education levels varied, showcasing a well-educated sample, including 4.2% with a high school degree or below, 58.1% with a bachelor's degree, 23.8% holding a master's degree, and 4.0% possessing a PhD or MD. This demographic breakdown lays the foundation for a comprehensive understanding of the survey's participant profile, setting the stage for further analysis and interpretation of the gathered data.

THE CONSUMPTION OF CERTAIN FOOD ITEMS BEFORE THE ECONOMIC CRISIS

The provided information is a detailed summary of the consumption patterns of various food items among different age groups, genders, marital statuses, regions of residence, employment statuses, and education levels. It highlights the frequency of intake for nuts, dark chocolate, avocados, bananas, whole grains, broccoli, kidney beans, and spinach.

When it comes to nuts, 66.8% of participants of age groups (18-25) consumed nuts once per month, while 33.2% rarely or never consumed them. Among those aged 26-45(32.9%) and 46-65 (76.8%) consumed nuts twice per week. However, 91.7% of those above the age of 65 consumed nuts daily. When it comes to comparing the consumption of nuts in Females and males it was noticed that 50.6% of the females consumed nuts once per month, however, males were likely to consume nuts more than two times per week. Finally, married individuals with a percentage of 35.7% consumed nuts once per month, where 32.8% of non-married individuals consumed nuts more than two times per week.

As reported in table 2, consumption of dark chocolate varied with age, gender, and marital status. 59.8% of younger participants (18-25 age group) consumed dark chocolate rarely or never while 91.7% of older participants (above 65 years) consumed it more frequently. Males tended to consume dark chocolate more frequently than females. It was also reported that unmarried individuals showed less consumption of dark chocolate compared to married participants. Regarding the consumption of avocados, it increased with age. In the 18-25 age group, 51.1% consumed avocados rarely, while 36.4% of those above 65 consumed them daily. Females consumed avocados more frequently than males. Married participants consumed avocados more frequently compared to unmarried individuals. Moreover, the consumption of bananas increased with age. However, females and unmarried participants consumed bananas more frequently than males and married individuals.

On the other hand, consumption of whole grains increased with age, with older individuals consuming them daily (91.7% above 65 years). Males and married individuals tended to consume whole grains more frequently. Moreover, consumption of broccoli increased with age, with older individuals consuming it daily (75% above 65 years). Both genders consumed broccoli rarely or never, with males consuming it more frequently than females. Moreover, consumption of kidney beans increased with age, with older individuals consuming them daily (91.7% above 65 years). Males consumed kidney beans more frequently than females, and married participants consumed them more often than unmarried individuals.

For Consumption of spinach, it decreased with age, with younger individuals rarely or never consuming it (77.2% in the 18-25 age group). Males and unmarried participants consumed spinach less frequently than females and married individuals.

THE CHANGE OF CONSUMPTION OF VARIOUS FOOD ITEMS DURING THE ECONOMIC CRISIS

The context of economic challenges compounded by the ongoing pandemic has cast a discernible impact on the dietary habits of the Lebanese population. Table 3 delves into the intricate details of these shifts, focusing specifically on alterations in the consumption of magnesium-rich foods. Remarkably, there is a discernible trend of decreased magnesium-rich food intake across different age groups, starting with respondents aged 18-25 and intensifying in older age brackets ($P<0.001$). Both genders experienced significant reductions, with 33% of females and 33.3% of males curtailing their magnesium-rich food consumption. Marital status emerged as a factor, with married couples showing a slight decline (37.6%), while unmarried individuals exhibited a more pronounced decrease (34.1%) in consumption ($P=0.017$). Geographical nuances in dietary patterns became evident, as Beirut and Mount Lebanon exhibited slight decreases (40.9%), contrasting with the North (40%), Bekaa (35.1%), and South regions, where significant declines in magnesium-rich food consumption were reported.

Employment status played a role, with full-time employees showing a modest reduction in intake (38.3%), while retired individuals (40.2%) and unemployed participants (32.6%) reported a noteworthy decrease in consumption ($P=0.001$). Educational levels also contributed to the shifting dietary landscape, as participants across various education levels—ranging from secondary education (29.6%) to bachelor's degree (33.3%), master's degree (32.8%), and PHD/MD (45%)—indicated significant decreases in magnesium-rich food consumption ($P<0.01$). This comprehensive analysis of dietary changes amidst economic and pandemic-related challenges provides valuable insights into the intricate dynamics shaping the nutritional behaviors of the Lebanese population across diverse demographic categories.

THE CORRELATION BETWEEN INTAKE OF SUPPLEMENTS AND THE SOCIODEMOGRAPHIC GROUPS

The study investigates the correlation between sociodemographic factors and the consumption of magnesium supplements during stressful periods. Magnesium, an essential mineral, plays a crucial role in various physiological functions, including stress management. Given the current economic crisis and the challenges posed by the ongoing pandemic, understanding how different sociodemographic groups cope with stress through magnesium supplementation is crucial.

Among various age groups, 40.8% of individuals aged 18-25 and 30.6% from the 26-45 age group reported taking magnesium supplements when physically tired. On the other hand, 35.4% of those aged 46-65 and 38.5% of those over 65 took the supplements when emotionally stressed.

In terms of gender, there was a noticeable pattern in magnesium supplement intake based on specific circumstances. Approximately 38.3% of females tended to take magnesium supplements when experiencing physical fatigue, while 33.0% of males opted for these supplements during times of emotional stress. Employment status emerged as a significant factor influencing supplement choices. Notably, 38.8% of full-time employees and 40.2% of part-time employees reported taking supplements without a specific reason. Among retired individuals, a substantial 75.0% turned to supplements during periods of emotional stress, in contrast to 32.6% of unemployed individuals ($P=0.001$). Additionally, educational background played a role in supplement preferences, as evidenced by 38.8% of full-time employees and 42.1% of part-time employees taking supplements without a specific reason ($P<0.001$). Participants with a senior high school diploma or below (41.6%) and those with a Master's degree (31.9%) also exhibited a propensity for taking supplements when physically tired ($P<0.001$).

THE IMPACT OF THE CONSUMPTION FREQUENCY OF THE FOOD ITEMS UNDER STRESS IN CORRELATION WITH THE WEIGHT STATUS

Diet plays a pivotal role in overall health, and stress accompanied by the pandemic and economic crisis can significantly impact eating behaviors, potentially leading to both healthy and unhealthy dietary patterns which may lead to weight gain. Therefore, the current study aims to investigate the impact of emotional stress on the eating behavior among the Lebanese population.

By exploring these factors, the research seeks to provide insights into how stress manifests in dietary behaviors within this specific demographic. The findings may contribute to a broader understanding of the complex interplay between stress, age, and dietary choices, offering valuable implications for health interventions and tailored strategies to promote well-being in the face of challenging circumstances.

Among participants aged 26-45, though not statistically significant (p>0.05), certain patterns emerged. Approximately 51.8% of this age group opted for unhealthy food consumption, while 38.8% consumed four meals per day, and 41.4% reported weight gain. Gender variations were evident, with 39.7% of females choosing unhealthy food, contrasting with 76.3% of males who leaned towards such choices when stressed. Additionally, 48.9% of females consumed four meals per day, and 45.2% reported weight gain, although these associations did not reach significance (p>0.05). Among full-time employees, 43.0% consumed unhealthy food under stress, and 43.8% consumed four meals per day. Notably, 51.9% of full-time employees reported weight gain, showing statistical significance (p=0.015). Additionally, it was noticed that individuals living in 63.0% of the individuals living in the South consumed unhealthy food and therefore, 37.8% of these same individuals reported weight gain as a result. Part –time employees consumed high fat foods under stress 51, 4% with 40.2% reporting weight gain. When taking into consideration anxiety levels, participants with senior high school education or below 33.8% tended to opt for healthy food during stress, while 54.0% of those with a bachelor's degree and 83.2% of those with a master's degree chose unhealthy options under stress. However, the association between education level and weight gain did not achieve statistical significance (p=0.281).

THE ASSOCIATION BETWEEN SOCIO-DEMOGRAPHIC CHARACTERISTICS WITH THE WAYS TO RELIEVE STRESS

The study expands its focus to explore a range of stress-relieving behaviors adopted by individuals during periods of crisis. Against the backdrop of prevailing economic challenges and the enduring impact of the global pandemic, understanding how individuals cope with stress has gained paramount importance.

TABLE I. Sociodemographic characteristics of the Lebanese Population (n=501)

		n(%)
Age	**18-25**	184(36.7%)
	26-45	222(44.3%)
	46-65	82(16.4%)
	65+	13(2.6%)
Gender	**Female**	345(68.9%)
	Male	156(31.1%)
Marital Status	**married**	237(47.3%)
	Not married	264(52.7%)
Region	**Beirut**	137(27.3%)
	Bekaa	33(6.6%)
	Mount Lebanon	44(8.8%)
	North	25(5%)
	South	262(52.3%)
Employment Status	**Full time job**	214(42.7%)
	Part time job	107(21.4%)
	Retired	8(1.6%)
	Unemployed	172(34.3%)
Education Level	**Bacc II or below**	71(14.2%)
	Bachelor degree	291(58.1%)
	Master's degree	119(23.8%)
	PHD/MD	20(4.0%)

TABLE 2. The Intake of the Following items in the Absence of crisis in correlation with the Socio-demographic

		Nuts consumption (p<0.001)					Dark Chocolate consumption (p<0.001)					Avocado consumption (p<0.001)				
		Rarely /Never	Once per month	two times / week	More than 2 times	Daily	Rarely /Never	Once per month	two times per week	More than 2 times	Daily	Rarely /Never	Once per month	two times/week	More than 2 times	Daily
Age	**18-25**	61 (33.2 %)	123 (66.8 %)	0	0	0	110 (59.8 %)	74 (40.2 %)	0	0	0	94 (51.1 %)	58 (31.5 %)	31 (16.8%)	0 (0.0%)	1 (0.5%)
	26-45	0	85 (38.3 %)	64 (28.8 %)	73 (32.9 %)	0	0	92 (41.4 %)	60 (27.0 %)	70 (31.5 %)	0	40 (18.0 %)	46 (20.7 %)	68 (30.6%)	68 (30.6 %)	0
	46-65	0	0	0	63 (76.8 %)	19 (23.2 %)	0	0	0	58 (70.7 %)	24 (29.3 %)	2 (2.4%)	1 (1.2%)	3 (3.7%)	69 (84.1 %)	7 (8.5%)
	65+	1 (8.3%)	0	0	0	11 (91.7 %	1 (8.3%)	0	0	0	11 (91.7 %)	1 (9.1%)	1 (9.1%)	2 (18.2%)	3 (27.3 %)	4 (36.4 %)
Gender	**Female**	44 (12.8 %)	174 (50.6) %	35 (10.2 %)	67 (19.5 %)	24 (7.0%)	89 (25.9 %)	136 (39.5 %)	31 (9.0%)	64 (18.6 %)	24 (7.0%)	115 (33.4 %)	77 (22.4 %)	66 (19.2%)	76 (22.1 %)	10 (2.9%)
	Male	18 (11.5 %)	34 (21.8 %)	29 (18.6 %)	69 (44.2 %)	6 (3.8%)	22 (14.1 %)	30 (19.2 %)	29 (18.6 %)	64 (41.0 %)	11 (7.1%)	22 (14.2 %)	29 (18.7 %)	38 (24.5%)	64 (41.3 %)	2 (1.3%)
Marital status	**Married**	53 (22.3 %)	85 (35.7 %)	42 (17.6 %)	50 (21.0 %)	8 (3.4%)	53 (22.3 %)	92 (38.7 %)	35 (14.7 %)	50 (21.0 %)	8 (3.4%)	92 (38.8 %)	42 (17.7 %)	48 (20.3%)	52 (21.9 %)	3 (1.3%)
	Not married	9 (3.4%)	123 (46.9) %	22 (8.4%)	86 (32.8 %)	22 (8.4%)	58 22.1%	74 28.2%	25 9.5%	78 29.8 %	27 10.3 %	45 17.2 %	64 24.4 %	56 21.4%	88 33.6 %	9 3.4%
Region	**Beirut**	62 (45.3 %)	75 (54.7) %	0	0	0	111 (81.0 %	26 (19.0 %)	0	0	0	88 (64.2 %)	37 (27.0 %)	11 (8.0%)	0	1 (0.7%)
	Bekaa	0	33 (100.0)%	0	0	0	0	33 (100.0 %)	0	0	0	4 (12.1 %)	14 (42.4 %)	15 (45.5%)	0	0
	Mount Lebanon	0	44 (100.0)%	0	0	0	0	44 (100.0 %)	0	0	0	30 (68.2 %)	8 (18.2 %)	6 (13.6%)	0	0
	North	0	25 (100.0)%	0	0	0	0	25 (100.0 %	0	0	0	10 (40.0 %)	15 (60.0 %)	0	0	0
	South	0	31 (11.9) %	64 (24.5 %)	136 (52.1 %)	30 (11.5 %)	0	38 (14.6 %)	60 (23.0 %)	128 (49.0 %)	35 (13.4 %)	5 (1.9%	32 (12.3 %)	72 (27.7%)	140 (53.8 %)	11 (4.2%)
Employ-ment status	**Full time job**	61 (28.5 %)	153 (71.5 %)	0	0	0	110 (51.4 %)	104 (48.6 %)	0	0	0	122 (57.0 %)	59 (27.6 %)	32 (15.0%)	0	1 (0.5%)
	Part time job	0	55 (51.4 %	52 (48.6 %)	0	0	0	62 (57.9 %)	45 (42.1 %)	0	0	11 (10.3 %)	41 (38.3 %)	55 (51.4%)	0	0
	Retired	0	0	8 (100.0 %)	0	0	0	0	8 (100.0 %)	0	0	0	0 (0.0%)	8 (100.0%)	0	0
	Unemployed	1 (0.6%)	0	4 (2.3%)	136 (79.5 %)	30 (17.5 %)	1 0.6%	0	7 4.1%	128 74.9 %	35 20.5 %	4 2.4%	6 3.5%	9 5.3%	140 82.4 %	11 6.5%)
Educational level	**Bacc II or below**	61 (85.9 %)	10 (14.1 %)	0	0	0	71 (100.0 %)	0	0	0	0	63 (88.7 %)	8 (11.3 %)	0	0	0
	Bachelor degree	0	198 (68.0 %)	64 (21.9 %)	29 (9.6%)	0	39 (13.4 %)	166 (57.0 %)	60 (20.6 %)	26 (8.0%)	0	71 (24.4 %)	92 (31.6 %)	98 (33.6%)	29 (9.9%)	1 (3.0%)
	Master's degree	0	0	0	107 (89.1 %)	12 (10.1 %)	0	0	0	102 (85.7 %)	17 (14.2 %)	2 (1.6%)	5 (4.2%)	2 (1.6%)	104 (87.4 %)	6 (5.0%)
	PHD/ MD	1 (5.3%)	0	0	0	18 (94.7 %)	1 (5.3%)	0	0	0	18 (94.7 %)	1 (5.6%)	1 (5.6%)	4 (22.2%)	7 (38.9 %)	5 (27.8 %)

		Banana consumption (p<0.001)					Legumes consumption (p<0.001)					Whole grains consumption (p<0.001)				
		Rarely /Never	Once per month	two times / week	More than 2 times	Daily	Rarely /Never	Once per month	two times /week	More than 2 tim	Daily	Rarely /Never	Once per month	two times / week	More than 2 time	Daily
Age	18-25	41 (22.3 %)	97 (52.7 %)	46 (25. 0%)	0	0	34 (18. 5%)	145 (78. 8%)	5 (2.7%)	0	0	45 (24.5 %)	139 (75. 5%)	0	0	0
	26-45	0	0	163 (73. 4%)	59 (26.6%)	0	0	0	206 (92.8 %)	16 (7.2 %)	0	0	25 (11. 3%)	179 (80.6 %)	18 (8.1 %)	0
	46-65	0	0	0	11 (13.4%)	71 (86. 6%)	0	0	0	37 (45. 1%)	45 (54. 9%)	0	0	0	31 (37. 8%)	51 (61.2 %)
	65+	1 (8.3 %)	0	0	0	11 (91. 7%)	1 (8.3 %)	0	0	0	11 (91. 7)	1 (8.3 %)	0	0	0	11 (91.7 %)
Gender	Female	34 (9.9 %)	68 (19.8 %)	165 (48. 07%	23 (6.7%)	54 (15. 7%)	34 (9.9 5)	96 (27. 9%)	150 (43.6 %)	27 (97. 8%)	37 (10. 8%)	34 (9.9 %)	124 (3%	122 (35.5 %)	21 (6.1 %)	43 (12.5)
	Male	8 (5.1 %)	29 (18.5 %)	44 (28. 2%)	46 (30.1%)	28 (17. 9%)	1 (0.6 %)	49 (31. 4%)	61 (39.1 %)	26 16. 6%	19 12.1 %)	12 (7.8 %)	40 (25. 6%)	57 (36.5 %)	28 (17. 9%)	19 (12.1 %)
Marital status	Married	42 (17.6 %)	11 (4.6 %)	127 (53. 6%)	11 (4.6%)	47 (19. 7%)	35 (14. 7%)	(18) (7.5 %)	127 (53.3)	37 (15. 5%)	21 (8.8 %)	46(1 9.3%)	32 (13. 4%)	102 (42.8 %)	31 (13. 0%)	27 (11.3 %)
	Not married	0	86 (32.8 %)	82 (31. 2%)	59 (22.5%)	35 (13. 3%)	0	127 (48. 4%)	84 (32.0 %)	16 6.1 %	35 (13. 3%)	0	132 (50. 3%)	77 (29.3 %)	18 (6.8 %)	35 (13.3 %)
Region	Beirut	0	0	92 (97	11 (8.0%)	34 (24.	0	0	92 (67.1	37 (27.	8 (5,5	0	132 50.	77 (29.3	18 (6.8	35 (13.3
	Bekaa	9 (27.2	0	11 (33.	0	13 (39.	9 (27.	0	11 (33.3	0	13 (39.	9 (27.2	0	11 (33.3	0	13 (39.3
	Mount Leba	0	0	44 (100 %)	0	0	0	10 22.7 %	34 (77.3 %)	0	0	0	40 (90. 9%)	25 (100 %)	0	0
	North	11 (44.0	13 (52	1 (4.0	0	0	4 (16.	20 (80	1 (4.0)	0	0	15 (60.0	9 (36.	1 (4.0	0	0
	South	1 (0.4	84 (32.1	82 (31.	50 (22.6%)	35 (13.	1 (0.3	125 (47.	84 (32.1	16 6.1	35.1 5.5	1 (0.3	130 (49.	77 (29.5	18 (6.8	35 (13.3)
Employment status	Full time	41 (19.2	97 (45.3	76 (35.	0	0	34 (15.	145 (67.	35 (16.3	0	0	45 (21.0	164 (76.	5 (2.3	0	0
	Part time	0	0	107 (100	0	0	0	0	107(100%	0	0	0	0	107 (100	0	0
	Retired	0	0	8 (100	0	0	0	0	8 (100	0	0	0	0	8 100%	0	0
	Unemployed	1 (0.5 %)	0	18 (10. 5%)	70 (40.9%)	82 (47. 9%)	1 (0.5 %)	0	61 (35.6 %)	53 (30. 9%)	56 (32. 7%)	1 (0.5 %)	0	59 (34.9 %)49	49 (28. 6%)	62 (36.2 %)
Educational ,level	Bacc II or below	41 (57.7 %)	30 (42.2 %)	0	0	0	34 (47. 8%)	37 (52. 1%)	0	0	0	45 (63.3 %)	26 (36. 6%)	0	0	0
	Bachelor degree	0	67 23.0 %	209 78.1 0%	15 (5.1%)	0	0	108 37.1 5	183 (62.8 %)	0	0	0	138 47. 4%	153 52.5 %	0	0
	Master's degr	0	0	0	55 (46.2%)	64 (53. 7%)	0	0	28 (23.5 %)	53 (44. 5%)	38 (31. 9%)	0	0	26 (21.8 %)	49 (41. 01%	44 (36.9 %)
	PHD /MD	1 (5.3 %)	0	0	0	18 (94. 7%)	1 (5.3 %)	0	0	0	18 (94. 7%)	1 (5.3 %)	0	0	0	18 (94.7 %)

		Broccoli consumption (p<0.001)					Kidney Beans consumption (p<0.001)					Spinach consumption (p<0.001)				
		Rarely /Never	Once per month	two times per wee	More than 2 times/ week	Daily	Rarely /Never	Once per month	two times per week	More than 2 tim	Daily	Rarely /Never	Once per month	two times per week	More than 2 time	Daily
Age	18-25	182 (100	0	0	0	0	98 (53.	86 (46.	0	0	0	142 (77.2	42 (22.	0	0	0
	26-45	8 (3.6 %)	96 (43.2 %)	89 (49. 4%)	39 (13.1%)	0	0	31 (14. 0%)	121 (54.5 %)	70 (31. 5%)	0	0	54 (24. 3%)	110 (49.5)%	58 (26. 1%)	0
	46-65	0	0	0	82 (100%)	0	0	0	0	77 (93. 9%)	5 (6.1 %)	0	0	0	82 (100 .0%)	0
	65+	1 (8.3 %)	0	0	2 (16.7%)	9 (75. 0%)	1 (8.3 %)	0	0	0	11 (91. 7%)	1 (8.3 %)	0	0	1 (8.3 %)	11 (91.7 %)
Gender	Female	141 (40.9 %)	91 (26.4 %)	48 (13. 9%)	59 (17.1%)	4 (2.5 %)	77 (22. 3%)	87 (25. 2%)	92 (26.7 %)	78 (22. 6%)	10 (2.6 %)	102 (29.6 %)	85 (24. 7%)	81 (23.5 %)	71 (20. 6%)	5 (1.5%)
	Male	52 (53.3 %)	5 (3.2 %)	41 (26. 2%)	54 (34.6%)	6 (2.5 %)	22 (1.1 %)	30 (19. 2%)	29 (18.5 %)	69 (44. 2%)	10 (3.8 %)	41 (26.0 .%)	11 (7.0 %)	29 (18.5 %)	28 (17. 9%)	5 3.2%)
Marital status	Married	61 (25.6	96 (40.3	23 (9.6	52 (21.8%)	6 (2.5	53 (22.	31 (13.	96 (40.3	50 (21.	8 (3.3	53 (22.2	54 (2.2	83 (30.6	51 (21.	7 (2.9%
	Not mar	132 (50.3	0	66 (25.	61 (23.2%)	1.1 %	46 (17.	86 (32.	25 (9.5%	97 (37.	35 (13.	90 (34.3	42 (16.	37 (14.1	90 (634	7 (2.9)
Region	Beirut	8 (5.8	84 (61.3	0	41 (29.9%)	4 (2.9	0	31 (22.	61 (44.5	39 (28.	6 (4.3	0	54 (39.	38 (27.7	40 29.2	5 (3.6%
	Bekaa	9 (27.2	11 (33.3	0	11 (33.3%)	2 (6.0	9 (27.	0	11 (33.3	11 (33.	2 (6.0	9 (27.2	0	11 (33.3	11 (33.	2 (6.0%
	Mount	23 (52.3	21 (47.7	0	0	0	0	44 (100	0	0	0	0	44 (10	0	0	0
	North	24 (96.0	0	1 (4.0	0	0	21 (96.	0	1 (4.0)	0	0	21 (96.0	0	1 (4.0	0	0
	South	131 (50.1	0	66 (25.	61 (32.3%)	3 (1.1	45 (70.	86 (32.	25 (9.5%	97 (37.	8 3.0	89 (34.2	42 (16.	37 (14.1	90 (34.	3 (1.1)
Employ-ment status	Full time job	192 (89.7 %)	22 (10.2 %)	0	0	0	98 (45. 7%)	116 (54. 2%)	0	0	0	142 (66.3 %)	72 (33. 6%)	0	0	0
	Part time job	0	74 (69.1 %)	33 (30. 8%)	0	0	0	1 (0.9 %)	106 (99.0 %)	0	0	0	24 22. 4%	83 (77%)	0	0
	Retired	0	0	8 (100	0	0	0	0	8 (100	0	0	0	0	8 100%	0	0
	Unemployed	1 (0.5 %)	0	48 (28. 0%)	113 (66.0%)	9 (5.2 %)	1 (0.5 %)	0	7 (4.0%)	147 (85. 9%)	16 (9.3 %)	1 (0.5 %)	0	19 (11.1 %)	141 (81. 2%)	10 (5.8%)
Educational level	Bacc II or belo	71 (100. 0%)	0	0	0	0	71 (10 0%)	0	0	0	0	71 (100 %)	0	0	0	0
	Bachelor degree	121 (41.5 %)	96 (32.9 %)	74 (25. 4%)	0	0	57 (9.2 %)	174 (42 %)	121 (41.5 %)	26 (8.9 %)	0	71 (24.3 %)	96 (30. 9%)	110 (37.8 %)	14 (2.8 %)	0
	Master's degr	0	0	15 (12. 6%)	104 (87.3%)	0	0	0	0	119 (10 0%)	0	0	0	0	119 (100 %)	0
	PHD /MD	1 (5.2 %)	0	0	9 (47.3%)	9 (47. 3%)	1 (5.2 %)	0	0	2 (10. 5%)	16 (84. 2%)	1 (5.2 %)	0	0	8 (40. 1%)	10 (52.6 %)

While dietary habits have been examined, this study ventures into the broader landscape of stress management, investigating various alternative methods employed by participants across diverse sociodemographic groups. The majority of participants, representing diverse sociodemographic characteristics, expressed involvement in alternative methods to alleviate stress. Notably, those aged between 26 and 45 years old had the highest percentage, with 80.6% engaging in other Limit stress-relieving activities compared to their counterparts in different age groups.

A significant gender-based discrepancy emerged, revealing that 78.8% of females and 76.5% of males reported no other stress-relief methods, highlighting a notable association (p=0.001). Both unmarried individuals (80.6%) and married individuals (70.2%) indicated participation in other stress-relieving activities. Notably, part-time employees stood out, with a considerable 98.1% being more likely to employ alternative stress-relieving methods. Moreover, education level played a role, with 85.2% of those with a bachelor's degree, 80.7% with a master's degree, and 80% with a PhD actively participating in other stress-relieving behaviors.

By exploring this multifaceted aspect of stress management, the study aims to contribute to a more comprehensive understanding of individuals' coping mechanisms during challenging times.

***TABLE* 3.** The change of the consumption of the above food items in times of crisis.

		Change in the consumption of food items						
		Slightly decreased	**Significantly decreased**	**Significantly increased**	**Unchanged**	**Stopped**	**I cannot determine**	**p Value**
Age	**18-25**	69 (37.5%)	55 (29.9%)	20 (10.9%)	32 (17.4%)	1 (0.5%)	7 (3.8%)	p<0.001
	26-45	84 (37.8%)	77 (34.7%)	14 (6.3%)	32 (14.4%)	3 (1.4%)	12 (5.4%)	
	46-65	17 (20.7%)	29 (35.4%)	5 (6.1%)	21 (25.6%)	5 (6.1%)	5 (6.1%)	
	65+	1 (7.7%)	5 (38.5%)	0	1 (7.7%)	2 (15.4%)	4 (30.8%)	
Gender	**Female**	116 (33.6%)	114 (33.0%)	35 (10.1%)	53 (15.4%)	8 (2.3%)	19 (5.5%)	p=0.114
	Male	55 (35.3%)	52 (33.3%)	4 (2.6%)	33 (21.2%)	3 (1.9%)	9 (5.8%)	
Marital status	**married**	89 (37.6%)	76 (32.1%)	22 (9.3%)	31 (13.1%)	9 (3.8%)	10 (4.2%)	p=0.017
	Not married	82 (31.1%)	90 (34.1%)	17 (6.4%)	55 (20.8%)	2 (0.8%)	18 (6.8%)	
Region	**Beirut**	56 (40.9%)	41 (29.9%)	16 (11.7%)	19 (13.9%)	1 (0.7%)	4 (2.9%)	p=0.069
	Bekaa	8 (24.2%)	10 (30.3%)	1 (3.0%)	11 (33.3%)	0	3 (9.1%)	
	Mount Lebanon	18 (40.9%)	13 (29.5%)	8 (18.2%)	4 (9.1%)	0	1 (2.3%)	
	North	10 (40.0%)	10 (40.0%)	1 (4.0%)	1 (4.0%)	2 (8.0%)	1 (4.0%)	
	South	79 (30.2%)	92 (35.1%)	13 (5.0%)	51 (19.5%)	8 (3.1%)	19 (7.3%)	
Employment status	**Full time job**	82 (38.3%)	64 (29.9%)	25 (11.7%)	34 (15.9%)	1 (0.5%)	8 (3.7%)	p< 0.001
	Part time job	42 (39.3%)	43 (40.2%)	5 (4.7%)	11 (10.3%)	3 (2.8%)	3 (2.8%)	
	Retired	0	3 (37.5%)	1 (12.5%)	3 (37.5%)	0	1 (12.5%)	
	Unemployed	47 (27.3%)	56 (32.6%)	8 (4.7%)	38 (22.1%)	7 (4.1%)	16 (9.3%)	
Educational level	**Bacc II or below**	34 (47.9%)	21 (29.6%)	8 (11.3%)	5 (7.0%)	1 (1.4%)	2 (2.8%)	p<0.001
	Bachelor degree	103 (35.4%)	97 (33.3%)	25 (8.6%)	51 (17.5%)	3 (1.0%)	12 (14.1%)	
	Master's degree	32 (26.9%)	39 (32.8%)	6 (5.0%)	28 (23.5%)	4 (3.4%)	10 (8.4%)	
	PHD/MD	2 (10.0%)	9 (45.0%)	0	2 (10.0%)	3 (15.0%)	4 (20.0%)	

***TABLE* 4.** The correlation between supplements intake and sociodemographic groups.

		When are Mag. supplements taken				
		Other	when emotionally stressed	when physically tired	without any specific reason	p value
Age	**18-25**	7 (3.8%)	32 (17.4%)	75 (40.8%)	70 (38.0%)	p<0.001
	26-45	21 (9.5%)	64 (28.8%)	68 (30.6%)	69 (31.1%)	
	46-65	26 (31.7%)	29 (35.4%)	22 (26.8%)	5 (6.1%)	
	65+	5 (38.5%)	5 (38.5%)	0	3 (23.1%)	
Gender	**Female**	33 (9.6%)	74 (21.4%)	132 (38.3%)	106 (30.7%)	p<0.001
	Male	26 (16.7%)	56 (35.9%)	33 (21.2%)	41 (26.3%)	
Marital status	**married**	25 (10.5%)	43 (18.1%)	83 (35.0%)	86 (36.3%)	p<0.001
	Not married	34 (12.9%)	87 (33.0%)	82 (31.1%)	61 (23.1%)	
Region	**Beirut**	4 (2.9%)	19 (13.9%)	57 (41.6%)	57 (41.6%)	p<0.001
	Bekaa	3 (9.1%)	11 (33.3%)	11 (33.3%)	8 (24.2%)	
	Mount Lebanon	1 (2.3%)	4 (9.1%)	21 (47.7%)	18 (40.9%)	
	North	1 (4.0%)	1 (4.0%)	11 (44.0%)	12 (48.0%)	
	South	50 (19.1%)	95 (36.3%)	65 (24.8%)	52 (19.8%)	
Employment status	**Full time job**	8 (3.7%)	34 (15.9%)	89 (41.6%)	83 (38.8%)	p<0.001
	Part time job	3 (2.8%)	27 (25.2%)	32 (29.9%)	45 (42.1%)	
	Retired	1 (12.5%)	6 (75.0%)	1 (12.5%)	0	
	Unemployed	47 (27.3%)	63 (36.6%)	43 (25.0%)	19 (11.0%)	
Educational level	**Bacc II or below**	2 (2.8%)	5 (7.0%)	29 (40.8%)	35 (49.3%)	p<0.001
	Bachelor degree	13 (4.5%)	77 (26.5%)	97 (33.3%)	104 (35.7%)	
	Master's degree	38 (31.9%)	39 (32.8%)	38 (31.9%)	4 (3.4%)	
	PHD/MD	6 (30.0%)	9 (45.0%)	1 (5.0%)	4 (20.0%)	

***TABLE* 5.** The impact of crisis on the time of food consumed and meal frequency on weight change in correlation with sociodemographic characteristics.

		Food preference					Number of meals						Weight change			
		Both healthy & unhealthy	Healthy	High fat foods	Unhealthy	P Value	1	2	3	4	5	P Value	no weight change	Weight gain	Weight loss	p Value
Age	18-25	14 (7.6%)	25 (13.0 %)	60 (32.6 %)	85 (46.2%)	p=0.930	10 (6.2%)	61 (37.9 %)	7 (4.3%)	70 (43.5 %)	13 (18.1 %)	p=0.08	18 (9.8%)	97 (52.7 %)	69 (37.5 %)	p=0.098
	26-45	52 (23.4 %)	0	55 (24.8 %)	115 (51.8%)		3 (100.0 %)	0	0	0			51 (23.0 %)	92 (41.4 %)	79 (35.6 %)	
	46-65	6 (7.3%)	10 (12.2 %)	0	66 (80.5%)		0	0	0	0	0		11 (13.4 %)	35 (42.7 %)	36 (43.9 %)	
	65+	0	1 (7.7%)	0	12 (92.3%)		3 (100.0 %)	0	0	0	0		3 (23.1 %)	5 (38.5 %)	5 (38.5 %)	
Gender	Female	68 (19.7 %)	25 (7.2%)	99 (28.7 %)	153 (44.3%)	p<0.001	18 (14.9 %)	39 (32.2 %)	7 (5.8%)	45 (37.2 %)	12 (9.9%)	p=0.011	56 (16.2 %)	156 (45.2 %)	133 (38.6 %)	p=0.846
	Male	4 (2.6%)	11 (7.1%)	16 (10.3 %)	153 (44.3%)		3 (5.9%)	22 (43.1 %)	0	25 (49.0 %)	1 (2.0%)		27 (17.3 %)	73 (46.8 %)	56 (35.9 %)	
Marital Status	Married	45 (19.0 %)	25 (10.5 %)	68 (28.7 %)	99 (41.8%)	p<0.001	18 (30.0 %)	42 (70.0 %)	0	0	0	P<0.001	45 (19.0 %)	103 (43.3 %)	90 (37.8 %)	p=0.317
	Not mar	27 (10.3 %)	10 (3.8%)	46 (17.5 %)	165 (62.7%)		8 (7.8%)	52 (51.0 %)	5 (4.9%)	37 (36.3 %)	0		38 (14.4 %)	102 (43.0 %)	90 (38.0 %)	
Region	Beirut	14 (10.2 %)	26 (19.0 %)	60 (43.8 %)	37 (27.0%)	p<0.001	11 (8.0%)	61 (44.5 %)	7 (5.1%)	58 (42.3 %)	0		10 (7.3%)	70 (51.1 %)	57 (41.6 %)	P=0.930
	Bekaa	0	9 (27.3 %)	0	22 (66.7%)		1 (11.1 %)	8 (88.9 %)	0	0	0	P<0.001	5 (15.2 %)	15 (45.5 %)	13 (39.4 %)	
	Mount Lebanon	12 (57.1 %)	9 (42.9 %)	0	0		0 0.0%	1 (5.0%)	2 (10.0 %)	14 (70.0 %)	3 (15.0 %)		1 (4.8%)	10 (47.6 %)	10 (47.6 %)	
	North	2 (8.0%)	6 (24.0 %)	16 (64.0 %)	1 (4.0%)		0	0	0	0	0		1 (4.0%)	16 (64.0 %)	8 (32.0 %)	
	South	27 (10.3 %)	11 (4.2%)	44 (16.8 %)	165 (63.0%)		9 (8.7%)	52 (50.5 %)	5 (4.9%)	37 (35.9 %	0 (0.0%)		38 (14.5 %)	125 (47.7 %)	99 (37.8 %)	
Employment status	Full time job	38 (17.8 %)	24 (11.2 %)	60 (28.0 %)	92 (43.0%)	p=0.64	9 (5.6%)	61 (38.1 %)	7 (4.4%)	70 (43.8 %)	13 (8.1%)		26 (12.1 %)	111 (51.9 %)	77 (36.0 %)	
	Part time job	7 (6.5%)	0	55 (51.4 %)	45 (42.1%)		0	0	0	0	0	P=0.008	25 (23.4 %)	43 (40.2 %)	39 (36.4 %)	p=0.008
	Retired	0	0	0	8 (100.0 %)		0	0	0	0	0		4 (50.0 %)	1 (12.5 %)	3 (37.5 %)	
	Unemployed	27 (15.7 %)	11 (6.4%)	0	111 (64.5%)		1 (100.0 %)	0	0	0	0		28 (16.3 %)	74 (43.0 %)	70 (40.7 %)	
Educational level	Bacc II or below	14 (19.7 %)	24 (33.8 %)	33 (46.5 %)	0	p=0.66	1 3.4%	9 (31.0 %)	2 (6.9%)	14 (48.3 %)	3 (10.3 %)	P=0.013	2 (2.8%)	42 (59.2 %)	27 38.0 %	p=0.281
	Bachelor degree	52 (17.9 %)	0	83 (28.5 %)	156 (53.6%)		8 6.1%	52 (39.7 %)	5 (3.8%)	56 (42.7 %)	10 (7.6%)		61 (21.0 %)	126 (43.3 %)	104 (35.7 %)	
	Master's degree	6 (5.0%)	10 (8.4%)	0	99 (83.2%)		0	0	0	0	0		17 (14.3 %)	52 (43.7 %)	50 (42.0 %)	
	PHD/MD	0	1 (5.0%)	0	0		1 (100.0 %)	0	0	0	0		3 (15.0 %)	9 (45.0 %)	8 (40.0 %)	

***TABLE* 6.** Other ways to relieve in correlation with socio demographic characteristics.

		Other ways to relieve stress		
		NO	Yes	p value
Age	**18-25**	46 (25.0%)	138 (75.0%)	**p<0.001**
	26-45	43 (19.4%)	179 (80.6%)	
	46-65	19 (23.2%)	63 (76.8%)	
	65+	6 (46.2%)	7 (53.8%)	
Gender	**Female**	81 (23.5%)	264 (76.5%)	**p=0.001**
	Male	33 (21.2%)	123 (78.8%)	
Marital status	**Married**	65 (27.4%)	172 (72.6%)	**p<0.001**
	Not married	49 (18.6%)	215 (81.4%)	
Region	**Beirut**	47 (34.3%)	90 (65.7%)	**p<0.001**
	Bekaa	0	33 (100.0%)	
	Mount Lebanon	0	44 (100.0%)	
	North	0	25 (100.0%)	
	South	67 (25.6%)	195 (74.4%)	
Employment status	**Full time job**	46 (21.5%)	168 (78.5%)	**p<0.001**
	Part time job	4 (3.7%)	103 (96.3%)	
	Retired	7 (87.5%)	1 (12.5%)	
	Unemployed	57 (33.1%)	115 (66.9%)	
Education level	**Bacc II or below**	46 (64.8%)	25 (35.2%)	**p<0.001**
	Bachelor degree	38 (13.1%)	253 (86.9%)	
	Master's degree	22 (18.5%)	97 (81.5%)	
	PHD/MD	8 (40.0%)	12 (60.0%)	

DISCUSSION

The COVID-19 pandemic has had a profound global impact, leading to unpredictable and abrupt changes in people's lives, particularly due to its severe impact on the world economy [18]. Lifestyle habits, such as sleep, physical activity, and dietary choices, have undergone drastic changes in response to the pandemic [19]. Moreover, Lebanon has been facing one of its worst economic crises in history, which was further exacerbated during the lockdown, significantly impacting the emotional health of its people [20]. While magnesium is commonly known as a calming supplement [21], it is also found in certain food items that offer health benefits. However, the economic crisis caused many magnesium-rich foods to become costly, resulting in a drastic decrease in their consumption and an increased susceptibility to deficiency.

There is a limited data on consumption and purchasing habits before times of crisis. Previous studies showed that the Lebanese population found it easier to obtain goods from supermarkets prior the economic crisis. The pandemic's economic fallout is proving to be more severe than the financial crisis of 2008-2009, with public health measures to control the virus spreading having a huge impact on economies and businesses globally [22].

During times of crisis, dietary intake is significantly affected. A study in Spain demonstrated that households limited their daily consumption of certain food items during the economic crisis, leading to more perilous consumption habits for Spanish residents [23]. Similar outcomes were found in the current study, which examined the consumption of magnesium-rich foods both before and during the crisis in Lebanon. Living in risky conditions could alter individuals' food patterns and purchasing habits [24]. People begin to adopt saving techniques, such as buying less, opting for cheaper brands, and preparing simpler dishes [25]. Consequently, individuals tend to focus on specific dietary sources rather than a varied diet. These results are in line with those reported in Spain [26]. Regarding the age group of 18-25, the consumption of certain magnesium foods slightly decreased during the crisis, possibly due to the presence of university students in this group, who may have more knowledge about the impact of an adequate magnesium diet on mental health [26]. On the other hand, those aged between 46-55 showed a significant decrease in the intake of certain food items rich in magnesium. This may be because they lack awareness of magnesium's impact on emotional health and virus symptoms, or they rely more on supplements than dietary sources. Usually, married individuals are considered to have a broader knowledge of household meal constituents. However, during times of crisis, the consumption and purchase of certain food items become doubtful. It's worth noting that a high magnesium diet not only influences emotional status but is also considered heart-friendly [26].

Conflicting results were found in China regarding legume consumption during the pandemic, with an increase in the population's intake reported [27]. Comparing the consumption of magnesium sources, full-time employees showed a slight decrease, while part-time employees or the unemployed significantly reduced their intake, possibly due to differences in income levels [27]. Surprisingly, individuals with lower education levels, such as senior high or undergrad students, demonstrated only a slight decrease in magnesium intake. This might be because the younger generation, not financially independent, relies on consuming these foods at their parents' households. Conversely, those with MS or PHD degrees significantly decreased their magnesium intake, likely influenced by remote work and financial instability during the crisis.

Additionally, magnesium can be obtained from dietary supplements, and during times of crisis, individuals are more prone to anxiety and depression, leading to an increased intake of magnesium supplements [28]. Magnesium deficiency may be linked to heightened stress and anxiety symptoms [28]. According to the current study, it was noteworthy that individuals in the higher age group (46-55) showed a 35.4% increase in supplement intake when emotionally stressed. This could be attributed to their health concerns and the added pressure of coping with the financial crisis. Surprisingly, women (38.3%) took supplements mainly when physically tired, possibly due to their increased responsibilities for household chores and remote work during the pandemic and economic crisis.

Married couples (35%) consumed supplements when physically tired, likely because their responsibilities multiplied, taking care of work and their children's online schooling simultaneously. On the other hand, unmarried individuals (33.0%) took supplements when emotionally stressed, possibly due to delayed plans and dreams caused by the crisis. Regarding employment status, 41.9% of full-time employees took supplements when physically tired, while 29.9% of part-time employees took them when emotionally tired. This could be because full-time employees work longer hours, while part-time employees have more flexibility and time to rest. On the other hand, Individuals with higher education levels, such as master’s degree holders (32.8%) and Ph.D./MD holders (45%), took supplements when emotionally stressed. This might be due to the shift to remote work and the challenges of finding suitable jobs after the lockdown and crisis. Moreover, psychological and financial stress negatively influenced the consumption of unhealthy food items [29]. The study's findings may have been influenced by the fact that it took place more than two years after the start of the financial crisis and lockdown, impacting respondents' responses. Stress during the crisis may lead to anxiety and depression [29], which could influence food choices.

Emotional stress can disrupt eating behavior, leading to increased meal consumption during the day, potentially unhealthy in terms of high salt, sugar, or fat content, resulting in higher caloric intake [30]. Surprisingly, the study found that those aged between 46-55 67.1% were the most likely to consume unhealthy snacks, possibly influenced by remote work during the pandemic and economic crisis. Hormonal factors could play a role in women's high-fat food consumption during stress, leading to weight gain. Married individuals may have better knowledge about healthy food choices due to family responsibilities, while unmarried individuals may lack such influence and resort to consuming unhealthy snacks.

Regional differences also surfaced, with individuals in the Bekaa and Mount Lebanon consuming healthier food during stress, possibly due to self-cultivated crops. The south region, on the other hand, was more likely to consume unhealthy snacks, possibly influenced by easier delivery options and the use of US dollars, making food feel less expensive and another explanation for this could be due that fact that the majority of the population reside in the South. Full-time employees may consume unhealthy snacks due to longer work hours, while those with Master's or Ph.D. degrees might consume such snacks due to job market challenges and emotional stress. Similarly, those aged between 26-45 may have gained weight due to economic crisis-related stress.

During crises, individuals may seek other ways to relieve stress, with 75% of those aged between 18-25 engaging in other activities, possibly sports. Men and women also reported engaging in various activities to relieve stress, with more than 80% of unmarried individuals doing the same, possibly due to fewer responsibilities. However, contrary to expectations, part-time employees (91.8%) engaged in other ways to relieve stress more than full-time employees (70%), possibly due to more leisure time for part-timers. The academic life of students and professors was greatly impacted by the shift to online learning, resulting in severe perceived stress for university students. Rather than resorting to emotional eating, students with a Bachelor's Degree (85.2%) and Master's/PhD holders (80%) reported using other stress-relieving strategies, possibly due to their training on stress management during crises.

To address the findings, policymakers should consider the impact of inadequate magnesium intake on emotional health during crises and raise awareness about mental health and its relation to crises. It is crucial for individuals to gain a broader understanding of their mental health.

CONCLUSION

In conclusion, the findings of the current study present a mixed picture of the impact of crises on one's emotional health. The data revealed that the population's magnesium intake experienced slight decreases in some groups and significant decreases in others during times of crisis. This suggests that economic downturns and pandemic-related challenges had varying effects on people's dietary habits.

However, a concerning trend emerged from the study - the majority of the population especially from the south region shifted towards consuming unhealthy foods during times of perceived stress. This suggests that stressors brought about by the crises may have influenced individuals to resort to less healthy food choices as a coping mechanism. While the study provides valuable insights into the dietary behavior of individuals during challenging times, it also highlights the importance of addressing the negative consequences on emotional health. The decrease in magnesium intake and the preference for unhealthy foods during stress call for measures to raise awareness about proper nutrition and its impact on emotional well-being during crises.

In light of these findings, policymakers and healthcare professionals should consider targeted interventions to promote healthier dietary habits, especially during times of economic hardship and uncertainty. It is essential to recognize that individual responses to crises can vary significantly, and supporting mental health and nutrition during such times requires a multifaceted approach. Overall, the current study contributes valuable insights to the understanding of how crises impact dietary habits and emotional health. By acknowledging the nuances of these effects, we can work towards developing comprehensive strategies to promote healthier behaviors and support individuals in navigating challenging times more effectively.

ETHICAL APPROVAL AND CONSENT TO PARTICIPATE

The Lebanese International University Institutional Review Board (IRB) approved the study on March 24,2022 with informed consent was obtained from all participants. The study included a questionnaire with a consent form, ensuring confidentiality and anonymity, and stating that participation is voluntary.

Approval reference (LIUIRB-220301-IS-122).

ACKNOWLEDGMENT

The authors express their gratitude to Lebanese International University for their cooperation and to the voluntary participants who participated in the investigation.

REFERENCES

1. M. Al Alawi, S.W. Majoni and H. Falhammar. Int. J. Endocrinol. 9041694 (2018)
2. J.J. DiNicolantonio, J.H. O'Keefe, W. Wilson. Open Heart. 5:e000668. (2018)
3. American Psychological Association Stress Effects on the Body. [(accessed on 30 June 2021)]; Available online: https://www.apa.org/helpcenter/stress
4. American Psychological Association Understanding Chronic Stress. [(accessed on 30 June 2021); Available online: https://www.apa.org/helpcenter/understanding-chronic-stress.aspx

5. G.K. Schwalfenberg and S.J. Genuis. Scientifica, 4179326 (2017):
6. Institute of Medicine (IOM). Food and Nutrition Board. Dietary Reference Intakes: Calcium, Phosphorus, Magnesium, Vitamin D and Fluorideexternal link disclaimer. Washington, DC: National Academy Press, 1997.
7. R.K. Rude. Magnesium. In: Ross AC, Caballero B, Cousins RJ, Tucker KL, Ziegler TR, eds. Modern Nutrition in Health and Disease 2012. 11th ed. Baltimore, Mass: Lippincott Williams & Wilkins:159-75.
8. B.M. Spruijt, R. Van den Bos, and F.T. Pijlman, Appl. Anim. Behav. Sci; **72**(2), 145-171 (2001).
9. G. Pickering, A. Mazur, M. Trousselard, P. Bienkowski, N. Yaltsewa, M. Amessou, L. Noah, and E. Pouteau, Nutr, **12**(12), 3672.(2020)
10. S. Lu, F. Wei and G. Li. Cell Stress **5**(6), 76–85 (2021)
11. L. Galland, Magnes Trace Elem, **10**, 287–301 (1991)
12. M.S. Seelig, J. Am. Coll. Nutr. **13**, 429–446 (1994)
13. S. Kharroubi, F. Naja, M. Diab-El-Harake and L. Jomaa. *Nutrients* **13**(9), 2976 (2021).
14. M. Brown. The transmission of banking crisis to households: lessons from the 2008-2011 crises in the Eca region 2013World Bank Policy Research Working Paper 6528.
15. S. Abou Naoum. The olitical economy of currency depreciation in Lebanon 1989-2022 (Doctoral dissertation, Notre Dame University-Louaize). Epub 2022.
16. A. Bisat, M. Cassard and I. Diwan. Lebanon's economic crisis: A tragedy in the making. Middle East Institute. Retrieved September 1, 2021, from(March 29,2021).
17. N. Mucci, G. Giorgi, M. Roncaioli, J. Fiz Pere and G. Arcangeli, Neuropsychiatr Dis Treat, **12**, 983–993 (2016)
18. A. Sidor and P. Rzymski, Nutr, **12**(6), 1657 (2020)
19. S. Xiang, S. Rasool, Y. Hang, K. Javid, T. Javed, and A.E. Artene, Front. Psychol. **1178** (2021).
20. M. Prete, A. Luzzetti, L.S. Augustin, G. Porciello, C. Montagnese, I. Calabrese I and A. Crispo. Nutr **13**(6) 1923 (2021)
21. X. Lu and Z. Lin. COVID-19, Front. Psychol. **5285** (2021)
22. D. Hadar-Shoval, M. Alon-Tirosh, K. Asraf, L. Tannous-Haddad and O. Tzischinsky, Am. J. Men's Health **16**(2), 15579883221082427 (2022).
23. M. Alon-Tirosh, D. Hadar-Shoval, K. Asraf , L. Tannous-Haddad and O. Tzischinsky. Int J Environ Res Public Health **18**(18), 9695 (2021)
24. ILO. COVID-19 and the World of Work: Impact and Policy Responses. Available online: https://www.ilo.org/wcmsp5/groups/public/---dgreports/---dcomm/documents/briefingnote/wcms_738753.pdf (accessed on 11 May 2023).
25. C. Díaz-Méndez, and G. Ramos-Truchero, Int. J. Gastron. Food Sci. **31**, 100655 (2023)
26. M. Gracia-Arnaiz, Appetite. **171**, 105906 (2021)
27. X. Han, Y. Guo, P. Xue , X. Wang, and W. Zhu, Nutr. **14**(13), 2704 (2022)
28. R.F.Rodgers, C. Lombardo, S. Cerolini , D.L. Franko, M. Omori, J. Linardon, S. Guillaume, L.E. Fischer, and M.F. Tyszkiewicz, *Appetite* **160**, 105110 (2021)
29. S.B. Sartori, N. Whittle, A. Hetzenauer, and N. Singewald, Neuropharmacol**, 62**(1), 304–312 (2012)
30. M.A. Beydoun. J Nutr. **144**(8), 1139-1141 (2012).

Spatial equity in planning youth and sports forums in the city of Baghdad

Tahini Salman Fankal [a], Moheb Kamel AL-Rawe

Urban and Regional Planning Center for Postgraduate Studies, University of Baghdad, Baghdad, Iraq

[a] Corresponding Author: Tahany.Salman2100m@iurp.uobaghdad.edu.iq

Abstract: equity in the distribution of youth and sports forums leads to improved spatial distribution and facilitates self-improvement and healthy development of the city. Youth and sports forums have typical general social characteristics. The research dealt with the concept of spatial equity, and spatial equity was classified into vertical spatial equity and horizontal spatial equity, as well as the distribution of youth and sports forums to spatial units (municipalities) in the city of Baghdad. The field study was relied upon to obtain data and information, and to measure justice in the distribution of youth and sports forums, it was used The Location entropy of each spatial unit in the study area. The spatial units were divided into five levels based on the site entropy values for each municipality and the levels were represented on a map of the city of Baghdad based on the geographic information systems program (ARCGIS 10.8), so that the research found an imbalance in the distribution of youth forums. And sports in the city of Baghdad and the inefficiency in the equitable distribution among the administrative units of the study area, which required the use of correct planning standards in signing these services.

Keywords: (spatial equity, youth and sports forums, planning standards, Location entropy, Municipal units)

INTRODUCTION

Good planning of youth and sports facilities leads to improved planning of urban space and facilitates self-improvement and healthy development, as it is an important part of urban space, as urban space is the physical carrier of social and economic development and human activities, and an important factor in allocating resources and various interests, and youth and sports forums have social characteristics. General model.

Equity and justice are the core values of urban planning, so research on the spatial equity of public service facilities has become an important topic in the field of urban planning. Since accessibility was first proposed, it has become an important indicator for evaluating the equity and justice performance of facilities. There is a relationship between accessibility and the economic and social status or social needs of the population. Due to the significant trend in the pattern of social spatial differentiation, issues related to the optimal allocation of facilities within the scope of social equity have attracted great attention from governments at all levels.

Although research on the spatial equity of urban public facilities has already included “space matching” between facilities and residents, research in this area on facilities for youth and sports forums is rare, and research methods are usually of a qualitative nature. In other words, planning Facilities for Youth and Sports Forums Traditional sports is a per capita indicator in an attempt to ensure that the spatial allocation of public facilities reaches the goal of social equity, but it lacks an effective way to evaluate the “spatial matching” of facilities and residents, and neglects the social factors that influence the achievement of equity in the distribution of youth and sports forums.

The research started from the problem of the extent to which justice has been achieved in the distribution of youth and sports forums in the city of Baghdad. The research aims to reveal the reality of the spatial distribution of youth and sports forums in a fair manner, achieve the most appropriate planning and spatial indicators and standards, and achieve spatial equity in their distribution. The research assumed the absence of justice in the distribution Youth and sports forums in the city of Baghdad and their failure to comply with approved planning standards and indicators.

Technologies and Materials for Renewable Energy, Environment and Sustainability
AIP Conf. Proc. 3321, 060002-1–060002-7; https://doi.org/10.1063/5.0290402
Published under an exclusive license by AIP Publishing. 978-0-7354-5231-2/$30.00

Spatial equity

Equity means: “justice” in distributing the costs and benefits of a policy or program, and the concept of spatial justice in distributing facilities can be classified into two categories: vertical spatial justice and horizontal spatial justice (Soja, 2010.).

- Horizontal spatial justice: It means equal distribution of facilities among residents regardless of their location or social and economic status. This approach aims to increase equality in terms of residents’ access to facilities.
- Vertical spatial justice: refers to the fair distribution of facilities over a specific area, in relation to the needs or demand of the user population, and the focus of this approach is to reduce inequality in the distribution of facilities by ensuring unequal treatment with inequality (Dadashpoor& Faramarz,2017)

A needs-based approach to justice suggests that most socially disadvantaged populations should receive more services, because these groups have certain circumstances that make them more in need than any other population group. Therefore, the redistribution policy must be in a compensatory manner (Boone, 2009).

According to the demand-based approach, there must be more services where there is a potential consumer, and with the increase in potential users, competition between users to access the service also increases. The concept of “equality” is one of the principles of horizontal spatial justice, while the approaches based on “Need” and “demand” with the idea of vertical spatial justice (Kelobonye,2019).

To implement the need and “demand” based approach, it is necessary to identify the need and demand of the population, low income, poverty, minorities, etc., who are collectively termed as socially disadvantaged, and the demand can be measured by identifying the actual users of the facility (Jian, Yi.2021).

Since the spatial accessibility scale deals with the characteristics of the social, economic, demographic and cultural constraints of the user population ('acceptability', 'affordability', 'awareness' of the facility), through this scale, the 'need' and 'need'-based approach Demand” can be used to measure spatial justice (Ashik, & Meher ,2020).

Accessibility can be used as a measure to evaluate the level of fairness in the spatial arrangement of urban facilities, as the accessibility of urban facilities can be estimated over distance. The accessibility gap can be used as a technique to measure inequality across space, to assess the horizontal spatial equity of urban amenities, and it is essential that all urban residents have as much equal access as possible to urban amenities(Dadashpoor& Faramarz,2017 a) .

Spatial justice refers to distributing resources and opportunities fairly in various regions with the aim of achieving balance and improving the quality of life. Spatial justice is considered part of social justice as it seeks to achieve balance in the spatial distribution of services, job opportunities, and infrastructure. This requires consideration of varying needs and circumstances in different regions with the aim of improving life for all without discrimination.

Youth and Sports Forums:

Youth and sports forums have had many different definitions from different points of view. Youth and sports forums have been known as one of the optional cultural, educational and social institutions that help form the balanced personality of young people, through their practice of sporting and cultural social events and activities. They are professional institutions that work to develop the energies of... And capabilities for young people and giving them positive behavior and rejecting negative behavior in society (Al-Kaabi, & Jamal ,2017) .

Forums are defined as a body established by local councils, the state, or individuals in villages and cities, and which are equipped with buildings and capabilities with the aim of investing young people’s leisure time in practicing cultural, social, recreational and sporting activities, and developing young people in different age stages, and this process is under the supervision of specialized leadership and management (Hamarsheh, 2006) .

They are community institutions established by the government to support educational institutions (schools and universities) to enhance the cultural and social upbringing of the youth group, as they are the most important group in society because they possess capabilities and energies that can be invested in bringing about change and development in their communities (Ali, 2022) .Social institutions work to satisfy the needs of young people in various cultural, social and sporting aspects, by providing literary, scientific, entertainment, sports and musical activities, and they allow young people to form friendships and establish social relationships. These institutions have a role in the socialization process, through discovering young people, identifying their inclinations, developing them, and giving them various skills. Developing their sense of belonging.

METHODOLOGY

Research method

Location entropy was used in the spatial analysis of the distribution of youth and sports forums in the city of Baghdad, where location entropy was first proposed by P Haggett and applied in spatial signature. Entropy is used to measure the state of the spatial distribution of facilities or resources in an area (Aiginger, 20040), as well as to understand the variation in the spatial distribution of facilities in different spatial units, indicate the extent of imbalance in the distribution of these facilities, and measure the extent of concentration and dispersion in the studied area (Chen F& X, Zhang, 2015]. Entropy is also used. To measure spatial justice in the distribution of youth and sports facilities, the higher the location entropy value, the larger the per capita share of these facilities, and the lower the location entropy value, the lower the per capita share of youth and sports facilities. To measure Location entropy, we use the formula (1):

$$LQj = (Tj / Pj)(T / P) \quad (1)$$

LQJ refers to the Location entropy of the spatial unit (municipality), TJ refers to the total area of youth and sports forums in the spatial unit, PJ is the total population of youth in the spatial unit, T is the area of forums within the study area, and p is the total population of youth in the study area (Iraqi Ministry of Youth and Sports, 2024)

Study area: Baghdad city

The area of the city of Baghdad is (980) km2, and it is administratively divided into two sides, Al-Karkh and Al-Rusafa, and each side is divided into municipalities. The number of municipalities is 14, Fig 1. (Baghdad Municipality, 2023). The estimated population for the year 2023 is (10,971,020) million people. It is considered the largest city in Iraq is the second largest capital in the Arab world in terms of population size (Ministry of Planning ,2022) . The population of the city of Baghdad has increased significantly and significantly over the past few decades, and this increase was reflected in the increasing population overcrowding in its areas, especially the city center, which led to a significant shortage in the services provided to the population. Services have become disproportionate to the size of the current population.##

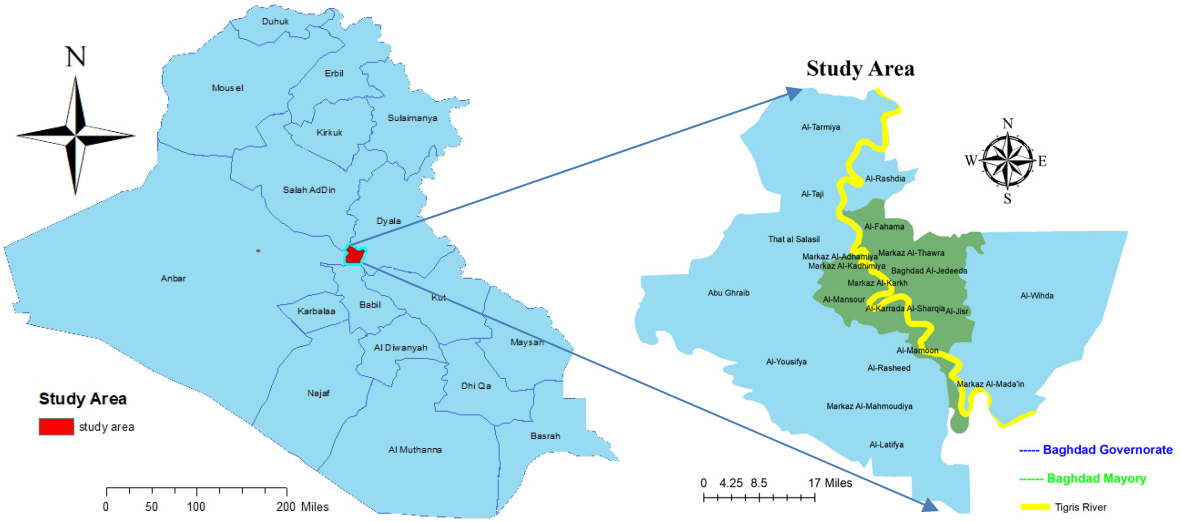

Figure 1. The location of the city of Baghdad

Reference: The researcher

In order to achieve the correct scientific application of the location entropy model, it was necessary to know the population numbers for each municipal unit as well as the area of the municipality, and the current spatial distribution of youth forums and the area of each forum. Table .1, shows the number of population in each municipality and its area, while Table. 2 shows the distribution Forums on municipalities in the city of Baghdad. Through Fig .2, the spatial

distribution of forums in the city of Baghdad can be identified. The number of young people according to the standard is 21.14% is placed in the table.

Table 1. Area and population in the city of Baghdad

Sequence	Municipalities	Area m2	The ratio%	population	The ratio%	The number of young people
1.	Adhamiya	27158468	3.05	1366502	12.46	288878
2.	aldawruh	85682317	9.62	1811042	16.51	382854
3.	Karrada	68140575	7.65	376148	3.43	79517
4.	Al-Karkh	23735201	2.67	133875	1.22	28301
5.	Al-Mansour	126104775	14.16	513360	4.68	108524
6.	Al-Rashid	130598650	14.67	18409	0.17	3891
7.	Rusafa	23914538	2.69	2056265	18.74	434694
8.	Al-Sadr First	30980688	3.48	805007	7.34	170178
9.	Al-Sadr Second	21015060	2.36	572130	5.21	120948
10.	alshaeb	98623326	11.08	972802	8.87	205950
11.	Al-Shuala	89201033	10.02	307708	2.80	65049
12.	Al-Kadhimiya	56037086	6.29	496984	4.53	105062
13.	baghdad aljadida	63840469	7.17	1430776	13.04	302466
14.	Al-Ghadir	45325098	5.09	110012	1.00	23256
total		890357284	100.00	10971020	100.00	2319273

Reference: The researcher's work based on the Ministry of Planning, Population Estimates of the Central Bureau of Statistics, Directorate of Population Census and Manpower,(2022), and the Municipality of Baghdad, Basic Design Department, Geographic Information Systems Division, Municipalities of the Municipality of Baghdad,(2023)

Table 2. Distribution of forums and their area according to each municipality

Municipalities	Number of forums	The ratio%	Area /m2	The ratio%
Adhamiya	3	10.34	49584	10.94
aldawruh	1	3.45	19358	4.27
Karrada	2	6.90	67404	14.87
Al-Karkh	1	3.45	4725	1.04
Al-Mansour	3	10.34	108302	23.89
Al-Rashid	2	6.90	50693	11.18
Rusafa	0	0	0	0
Al-Sadr First	1	3.45	10062	2.22
Al-Sadr Second	7	24.14	50504	11.14
alshaeb	3	10.34	34181	7.54
Al-Shuala	2	6.90	51444	11.35
Al-Kadhimiya	1	3.45	2067	0.46
baghdad aljadida	1	3.45	1250	0.28
Al-Ghadir	2	6.90	3679	0.81
total	29	100.00	453253	100.00

Reference: The researcher, relying on the Iraqi Ministry of Youth and Sports, Central Coordination and Follow-up Department, Central Follow-up Department, (2024).

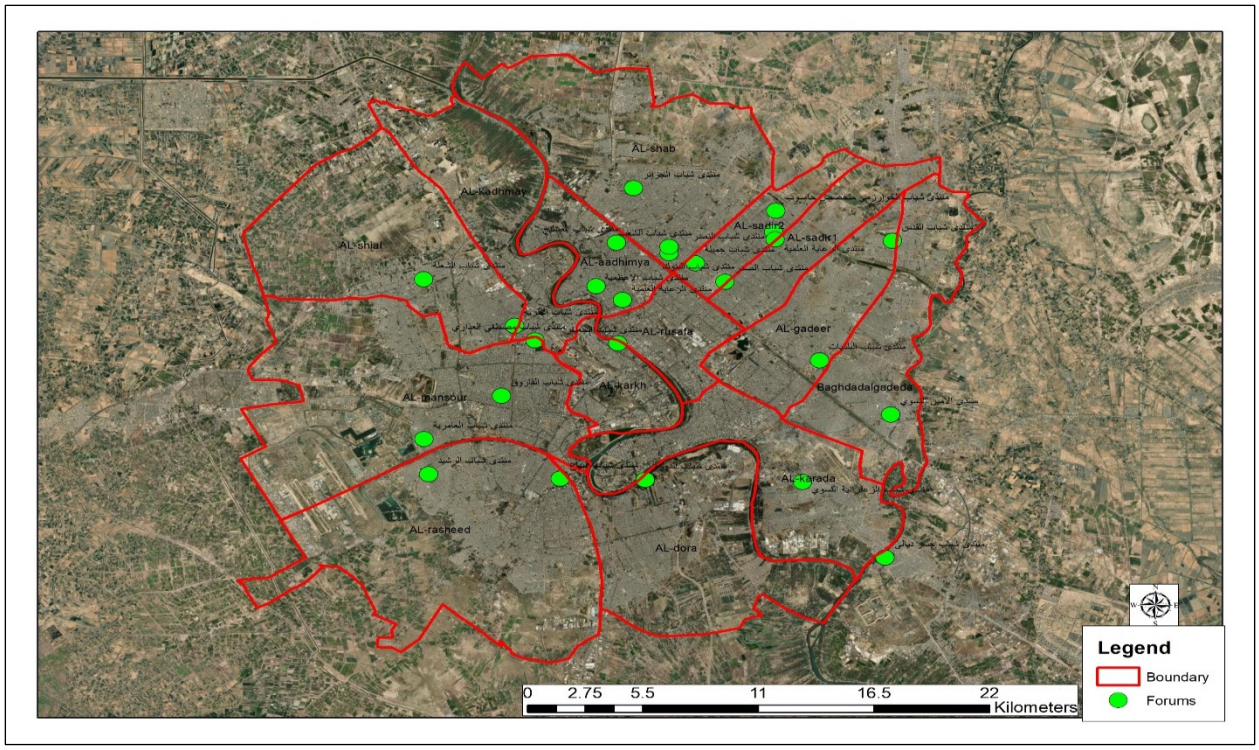

Figure 2. Distribution of youth and sports forums in the city of Baghdad
Reference: The researcher's work based on the data in Table (2)

RESULTS AND DISCUSSION

Location entropy analysis:

As shown in Table. 3. Fig. 3., the spatial units in the city of Baghdad were divided into five levels based on the location entropy. Through Table. 4, it was shown that the number of municipalities with very low location entropy was (4) municipalities, representing a percentage (28.57%) of the total number of spatial units, which are the municipalities of (Al-Dora, Al-Rusafa, Al-Kadhimiya, and Baghdad aljadida). Their location entropy value was less than (0.01), and the area of these municipalities reached (229,474,410) (25.77%) of the area of the city of Baghdad, which is (28.57%). 890357284), as it becomes clear to us that the number of municipalities with low entropy with a value ranging between (0.01-0.04) was (5) municipalities with a ratio of (35.71), which are the municipalities of (Al-Adhamiya, Al-Karkh, Al-Sadr Al-Thani, Al-Shaab, Al-Ghadir) and their area reached 22582278) and a ratio of (25.36 %) (of the city's area. As for the municipalities with an average location entropy value (0.04-0.09), it is the municipality of Al-Sadr, second only, with a percentage of (7.14). The area of this municipality reached 21,015,060 and represented 2.36% of the area of the study area. As for the number of municipalities with high location entropy (0.09-0.20). They are the municipalities of Karrada, Mansour, and Al-Shuala (at a rate of 21.42%), with an area of 283,446,383, and with a rate of (31.83%) of the area of the study area. Al-Rashid municipality dominates the site entropy to record a very high level (greater than 1.00), as its percentage reached 7.14), with an area of 130,598,650, and at a rate of (14.66%) of the area of the study area. From the above, we note that there is an imbalance in the distribution of youth and sports forums among the municipalities of the city of Baghdad. There is a very large disparity in the number of forums and their area relative to the population of the municipalities between one municipality and another. This indicates inefficiency and unfair distribution in the distribution of facilities for youth and sports forums in the city of Baghdad.

Table 3. number and proportions of spatial units according to the entropy of the location

Level	Location entropy	Number of units	Proportion%	Unit area/m	Proportion%
Extremely low	**0.01 <**	**4**	**28.57**	**229474410**	**25.77**
Low	**0.01-0.04**	**5**	**35.71**	**225822781**	**25.36**

Medium	**0.04-0.09**	**1**	**7.14**	**21015060**	**2.36**
High	**0.09- 0.20**	**3**	**21.43**	**283446383**	**31.84**
Extremely high	**1.00 >**	**1**	**7.14**	**130598650**	**14.67**

Reference: researcher's work based on the site entropy formula

Table 4. Spatial entropy distribution of municipalities

Level	Municipalities
Extremely low	AL- dawruh Rusafa Al- Kadhimiya Baghdad aljadida
Low	Adhamiya Al-Karkh Al-Sadr First Al- shaeb Al- Ghadir
Medium	Al-Sadr Second
High	Al-Shuala Karrada Al-Mansour
Extremely high	Al-Rashid

Reference: The researcher's work based on Table (3).

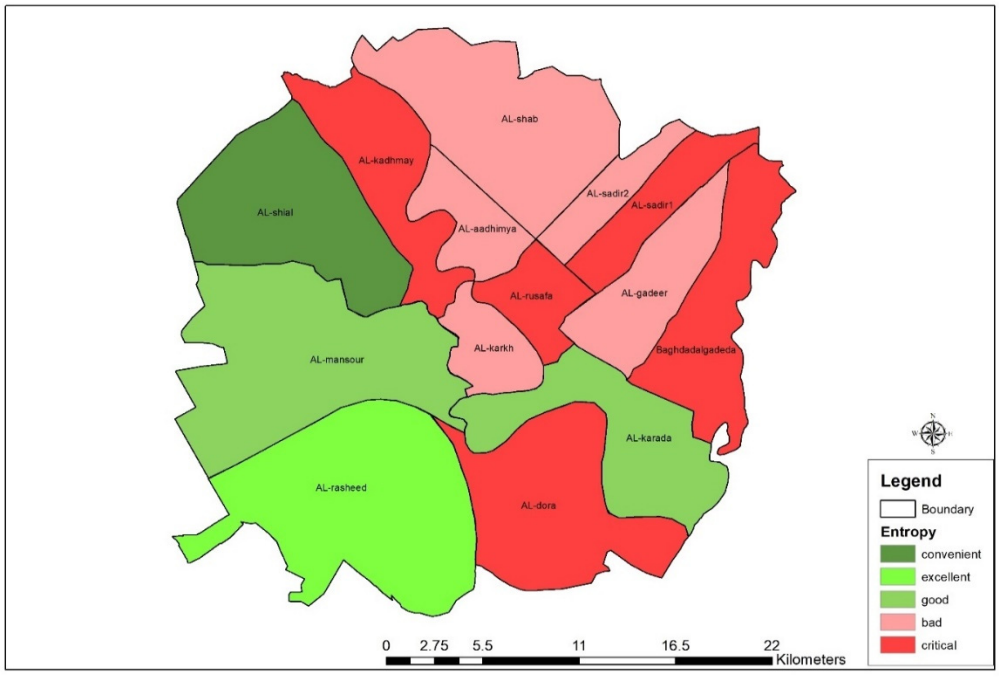

Figure 3. Division of municipalities according to spatial entropy levels

CONCLUSIONS

There is an imbalance in the distribution of youth and sports forums between spatial units in the city of Baghdad, and this confirms the unfairness of the distribution. Youth and sports forum facilities are concentrated in some municipalities, and some municipalities do not have this service. The number of youth and sports forums and the population size are not disproportionate in most municipalities in the city of Baghdad. It turned out that the area of

some forums, youth and sports is very small and is not suitable for forum activities to be held in order to achieve the desired goals.

REFERENCES

1. Ashik, F. R., Mim, S. A., & Neema, M. N. (2020). Towards vertical spatial equity of urban facilities: An integration of spatial and aspatial accessibility. *Journal of Urban Management*, *9*(1), 77-92. https://doi.org/10.1016/j.jum.2019.11.004
2. Al-Kaabi, I. M. J& Abdul-Mardi, J. 2017, Contributions of youth centers to implementing social welfare policies), Master's thesis, Qatar University.
3. Ali, Z. A., 2022 Professional intervention activities for social service using a resource-sharing strategy to improve services provided in youth centers), Journal of Research in Developmental Social Service, Volume 3, Part 1, Beni Suef University. https://dx.doi.org/10.21608/baat.2022.149728.1004
4. Aiginger, K., & Pfaffermayr, M. (2004). The single market and geographic concentration in Europe. Review of international economics, 12(1), 1-11. https://doi.org/10.1111/j.1467-9396.2004.00427.x
5. Boone, C. G., Buckley, G. L., Grove, J. M., & Sister, C. (2009). Parks and people: An environmental justice inquiry in Baltimore, Maryland. Annals of the association of American geographers, 99(4), 767-787. https://doi.org/10.1080/00045600903102949
6. Baghdad Municipality, (2023) Basic Design Department, Geographic Information Systems Division, Municipalities of Baghdad Municipality.
7. Chen, Y., Lin, N., Wu, Y., Ding, L., Pang, J., & Lv, T. (2021). Spatial equity in the layout of urban public sports facilities in Hangzhou. PloS one, 16(9), 0256174. https://doi.org/10.1371/journal.pone.0256174
8. Chen, F., Ji, X. F., Ji, X., & Zhang, H. D. (2015). The measurement method and spatial differentiation of urban transport equity. Economic Geography, 35(04), 70-5.
9. Dadashpoor, H., & Rostami, F. (2017). Measuring spatial proportionality between service availability, accessibility and mobility: Empirical evidence using spatial equity approach in Iran. Journal of Transport Geography, 65, 44-55. https://doi.org/10.1016/j.jtrangeo.2017.10.002
10. Hamarsheh, M. S., 2006, Contributions of the Deanships of Student Affairs in Providing Recreational Activities for Palestinian University Students as Seen by Students and Staff) , Master's Thesis, Al-Quds University.
11. Iraqi Ministry of Youth and Sports, 2024 Central Coordination and Follow-up Department, Central Follow-up Department, unpublished data.
12. Jian, Y. (2021). Towards a just city: spatial justice planning of public open space in private developments.
13. Kelobonye, K., McCarney, G., Xia, J. C., Swapan, M. S. H., Mao, F., & Zhou, H. (2019). Relative accessibility analysis for key land uses: A spatial equity perspective. Journal of Transport Geography, 75, 82-93. https://doi.org/10.1016/j.jtrangeo.2019.01.015
14. Iraqi Ministry of Planning, (2022) Population Estimates of the Central Bureau of Statistics, Directorate of Population Statistics and Manpower.
15. Soja, E. W. (2013). Seeking spatial justice (Vol. 16). U of Minnesota Press.

Knowledge, Attitude, Practice and Prevalence of Food Allergy Among Young Lebanese Population

Ghinwa Nemer[1b], Samer Sakr[2a], Imtithal Sheet[3c], Lamis Karaki[2d], Nivine Bachir[1e], Suzana Salhab[4f], and Ali Al Khatib[1g]

[1]*Department of Nutrition and Food Sciences, School of Arts and Sciences, Lebanese International University, Beirut Lebanon.*
[2]*Department of Biological and Chemical Sciences, School of Arts and Sciences, Lebanese International University, Beirut Lebanon.*
[3]*Department of Biomedical Sciences, School of Arts and Sciences, Lebanese International University, Beirut Lebanon.*
[4]*Department of Biological Science, Faculty of Science, Beirut Arab University, Beirut, Lebanon*

[a] *Corresponding Author:* samer.sakr@liu.edu.lb
[b] 11730228@students.liu.ed.lb
[c] imtithal.sheet@liu.edu.lb
[d] lamis.karaki@liu.edu.lb
[e] nivine.bachir@liu.edu.lb
[f] suzana.salhab994@gmail.com
[g] ali.alkhatib@liu.edu.lb

Abstract. Food allergy is considered a major public health concern, with prevalence rates on the rise globally. This study aimed to assess the knowledge, attitudes, and practices related to food allergies among a sample of young Lebanese adults. A cross-sectional survey was conducted, gathering data on demographics, food allergy prevalence, knowledge, attitudes, and practices. Food allergy prevalence was estimated to be 23.7% in adults, and 6.3% in children. Spices and Strawberry were reported as top food allergens (5.3%), where hives itching and redness were the most commonly reported symptoms (19.7%). The majority of respondents demonstrated adequate knowledge, a positive attitude, and good practices regarding food allergies. Improved knowledge and practices regarding food allergies can lead to better management, informed dietary choices, and a safer environment for individuals with allergies in Lebanon. This might enhance their quality of life and safety by reducing the potential risk of accidental exposure and adverse reactions.

INTRODUCTION

Food allergy (FA), a multifaceted immunology-mediated disorder, influences individuals of all age groups worldwide. Several prevalence studies revealed that it affected approximately 8% of children and 5% of adults [1, 2]. This condition arises when the immune system reacts adversely to specific proteins in food, triggering a range of symptoms from mild to severe. It's worth mentioning that food allergies are often confused with food intolerance, which is a more common occurrence that doesn't involve the immune system, though it can still cause discomfort [3].

The most prevalent food allergens that trigger immunological reactions include peanuts, milk, eggs, fish, shellfish, wheat, and soy [4]. FA can lead to a spectrum of symptoms, ranging from mild skin reactions to severe and potentially life-threatening anaphylactic reactions [5]. These symptoms include nausea, vomiting, abdominal pain, atopic dermatitis, asthma, and anaphylactic shocks. Typically, these manifestations occur within minutes to 1-2 hours after consuming the allergenic food [6]. Treatment options for food allergies remain a subject of controversy, with no FDA-approved therapy available to date [4]. Existing approved strategies emphasize the importance of avoiding the food allergen as the primary means of managing food allergies. However, this approach can be challenging, as many common food allergens are widespread in the diet leading to accidental ingestion of trace amount of allergenic proteins. Hence, in emergency situations, the use of medications like epinephrine is recommended to alleviate symptoms [7, 8]. A crucial aspect of managing food allergies is enhancing awareness among patients and their support networks. This includes educating them about cross-contamination risks, the importance of monitoring food labels, and the prompt recognition and treatment of allergic reactions. This proactive approach is fundamental to effectively managing food allergies. Worldwide many countries have implemented allergen labelling legislation and guidelines to protect food-allergic

Technologies and Materials for Renewable Energy, Environment and Sustainability
AIP Conf. Proc. 3321, 060003-1–060003-9; https://doi.org/10.1063/5.0289718
Published under an exclusive license by AIP Publishing. 978-0-7354-5231-2/$30.00

consumers from inadvertent exposure [8, 9]. According to the Lebanese Ministry, in Lebanon, food producers must list all ingredients on pre-packaged food labels. However, there is currently no governmental mandate requiring precautionary allergy labelling.

FA is a serious public health condition that is impacting the health of millions of people. The global prevalence of FA varied from 1% to 10%, with an approximate average of 2.5%, as stated by the World Allergy Organization [10, 11]. While there is limited data on food allergy rates in the Middle East region, previous studies from Saudi Arabia and the UAE suggested rates of approximately 19.7% and 8% [12, 13]; respectively. In Lebanon, research indicated that around 3.2% of adults and 4.1% of infants have food allergies [14], with recent reports showing 6% prevalence among children [15]. Moreover, the level of knowledge, beliefs, and practices regarding food allergies among people have not been widely studied in the Middle East region [16], and particularly among those with and without direct experience of food allergies in Lebanon. It is worth mentioning that the level of knowledge and practices can greatly contribute to a better management, increased awareness, and policy development in order to empower consumers, healthcare professionals, and policymaker to address this on-growing health concern effectively. The main aim of this study is to investigate how food allergies influence dietary and lifestyle choices among individuals in Lebanon. Furthermore, to evaluate the knowledge, attitudes, and behaviours of the participants related to food allergies. This research will provide up-to-date insights and a guide of implementation of effective interventions to promote the wellbeing of young Lebanese adults.

MATERIALS AND METHODS

Study design, sampling and sample size

A cross-sectional study was conducted between the 16th and the 22th of July 2022 to assess the prevalence, knowledge, attitudes and practice regarding food allergies among young Lebanese adults. The sample size was 304 (n=304); individuals who agreed to participate in the study met the inclusion criteria. Data collection was carried out using an online platform, Google Form, with participants recruited through various social media platforms such as Facebook, WhatsApp, and Instagram. The questionnaire was translated into Arabic language along with an English version using questions from validated surveys employed in previous studies [17]. The questionnaire is divided into four sections. The respondents' characteristics were documented in the first section. In the second section, each participant was asked to mention if he/she or a family member has FA, and to specify the allergen and symptoms experienced. Notably, this information is self-reported and not cross-checked with medical records. The third section included nine questions that assessed the knowledge towards food allergies. The fourth and the final section of the questionnaire included eleven questions that were tailored to assess the attitudes and practices of the participants towards food related allergies. Participants were informed about the aim of the study and were notified that their participation in this study is confidential and their responses will solely be used for the purpose of the study.

Scoring criteria

Nine questions regarding knowledge were asked, and evaluations were conducted using a mean cut-off point of (34). Participants were classified into groups based on their knowledge levels: those with scores below (67) were categorized as having inadequate knowledge, while those scoring above (2) were classified as having adequate knowledge. Additionally, questions regarding attitudes and practices were evaluated using a mean cut-off of (54), with participants considered to have a positive attitude and practice if their score surpassed (5), in the survey analysis, each correct answer was assigned 1 point.

Ethical approval

Approval for the study was granted by the LIU Institutional Review Board. Prior to their participation, all subjects provided informed consent, and measures were taken to guarantee the confidentiality and privacy of their information.

Statistical analysis

The Statistical Package for Social Sciences (SPSS) version 22 and Microsoft Office Excel 2016 were used, respectively, for data collection and analysis. Categorical variable frequencies with percentages and continuous variable means were reported using descriptive statistical approaches. For inferential analysis,

significant differences between variables were analysed Chi-square test examined relationships between knowledge and percentage of correctly answered questions, and Spearman correlation was calculated in order to compute the association between several different variables. Moreover, ANOVA t-test was used to compare means. Results were considered significant for p values < 0.05. The reliability of the survey instruments was determined using Cronbach's alpha. For the 'Prevalence/Knowledge/Attitudes and Practices' construct with 22 items, Cronbach's alpha was 0.667, indicating moderate reliability. In contrast, the 'Prevalence' construct with 2 items had a Cronbach's alpha of 0.769, suggesting acceptable reliability. These results indicate that the items being measured are consistently reliable.

RESULTS

The research involved 304 individuals, predominantly female (79.3%). Most participants fell within the 18 to 25 age (62.8%), with 75% having attained a bachelor's degree and 80% possessing a health-related educational background. Additionally, over half of the participants (68.4%) resided in urban areas. Table 1 showed the socio-demographic characteristics. Regarding allergy history, 23.7% adults and 6.3% children suffer or presently are suffering from a food allergy. Among the listed food allergens, spices and strawberries were the most prevalent, each representing 5.3%, while milk and eggs accounted for 3.5% each.

TABLE 1. Socio-demographic characteristics of participants (n=304).

Characteristics		Frequency N	Percent %
Age	From 18 to 25 years	191	62.8
	From 26 to 40 years	98	32.2
	From 41 to 64 years	14	4.6
	More than 65 years	1	3
Gender	Female	241	79.3
	Male	63	20.7
Educational level	Bachelor’s degree (BS)	228	75
	Master’s degree	61	20.1
	PHD	1	3
	MD	14	4.6
	Health related majors	243	80
	Non health related majors	24	7.9

Field of study	Other	37	12.2
Marital status	Not married	238	78.3
	Married without children	19	6.3
	Married with children	47	15.5
Economic status	≥750000	72	23.7
	750000 ≤ income ≤ 2000000	108	35.5
	2000000 ≤ income ≤ 5000000	68	22.4
	≥ 5000000	56	18.4
Employment status	Unemployed	137	45.1
	Employed Part time	63	20.7
	Employed Full time	104	34.2
Living Area	Mostly in the city	208	68.4
	Mostly in the village	77	25.3
	Work in a city and live in a village	19	6.3

The predominant allergic symptoms were skin-related, with 19.7% experiencing symptoms like hives, itching, and redness, followed by angioedema at 3%, as indicated in Table 2.

TABLE 2. Prevalence of food allergy (n=72).

Questions		Count N	Percent %
1. Did you suffer or presently are you suffering from a food allergy?	Yes	72	23.7
	No	207	68.1
	I do not know	25	8.2
	No	188	61.8

2. Does anyone in your family suffer from a food allergy?	Yes “adult”	72	23.7
	Yes “children”	19	6.3
	Both adult and children	9	3
	I don’t know	16	5.3
3. What are the food allergen that are you sensitive to?	Eggs	12	3.9
	Strawberry	16	5.3
	Fish	10	3.3
	Milk and derivatives	12	3.9
	Nuts	6	2
	Peach	5	1.6
	Spices	16	5.3
	Wheat and its products	3	1
	I do not know	28	9.2
4. What are your food allergy symptoms?	Angioedema	1	3
	Cough	7	2.3
	Facial swelling	4	1.3
	Hives itching and redness	60	19.7
	Shortness of breath	6	2
	Other	28	9.2

The knowledge score of the participants was 34.07 ± 15.61. Almost all participants (90.5%) understood food allergy as an abnormal immune response to harmless food or ingredients, while only 19.1% recognized it as an inherited disease. More than half of the respondents (60%) believed that major allergen names should be legally reported on labels. Furthermore, one third of the participants answered correctly that allergy symptoms could be healed without medical treatment and only 46.1% differentiate between lactose intolerance and the allergy of milk. Responses related to knowledge were depicted in Table 3.

TABLE 3. Right responses to knowledge statements about FA (T: True, F: False, Y: Yes, N: No).

Questions	Frequency N	Percent %
Food allergy is an abnormal response of the immune system to an ordinarily harmless food or ingredient in a food (T)	275	90.5
Allergy is an inherited disease (F)	58	19.1

Allergy symptoms could be healed without medical treatment (F)	105	34.5
Lactose intolerance and the allergy of milk are the same disease (F)	140	46.1
Epinephrine injection in the muscle should only be given by pharmacist, nurse or doctor (T)	164	53.9
The names of major allergens were required legally to be reported on labels (Y)	184	60.5
Did the advisory labels are required by law (Y)	143	47

With respect to attitude, as shown in table 4, score of the participants was 54.35 ± 17.08. The majority of participants understood that individuals with food allergies could not ingest even small amounts of the food that caused allergy (69.7%). They were also aware that cooking, heating (75.7%), or diluting the allergen in cold water (34.9%) would not reduce food allergies. When purchasing food, 44.4% always checked the ingredients on the package, and 41.4% sometimes checked, while 14.1% do not check all food labels.

TABLE 4. Attitudes and practices of participants towards FA.

Questions		Count N	Percent %
Person with a food allergy can consume a small amount of that food.	True	49	16.1
	False	212	69.7
	I don't know	43	14.1
Can we prevent food allergy by cooking or heating the food?	Yes	21	6.9
	No	230	75.7
	I don't know	53	17.4
If you can suffer from an allergic reaction, do you consume cold water to dilute or relieve the allergen?	Yes	77	25.3
	No	106	34.9
	I don't know	121	39.8
When purchasing, do you check the product ingredients?	Yes	135	44.4
	No	43	14.1
	Sometimes	126	41.4

Our findings revealed that there were no notable correlations between the mean levels of knowledge, attitude, and practice and sociodemographic factors. Additionally, no significant associations were observed between sociodemographic variables and both prevalence and attitude scores. However, there were significant

associations between knowledge scores and certain demographics. Specifically, age group (p-value = 0.001) and educational level (p-value = 0.016) showed significant relationships with knowledge scores. Additionally, marital status (p-value = 0.007) and employment status (p-value = 0.020) exhibited significant associations with knowledge scores as well (Table 5). The t-test aimed to ascertain any significant differences between genders (male and female) concerning attitudes, knowledge, and prevalence responses regarding food allergies. The findings showed that there was no significant association in attitude, knowledge, and prevalence between males and females (p-values = 0.101, 0.460, 0.690; respectively).

TABLE 5. Socio-demographic factors and their association with attitudes, knowledge and prevalence.

Variable	Association with attitude (p-value)	Association with knowledge (p-value)	Association with prevalence (p-value)
Age Group	0.215	**0.001**	0.146
Educational level	0.396	**0.016**	0.085
Marital status	0.526	**0.007**	0.488
Field of study	0.164	0.067	0.127
Employment status	0.181	**0.020**	0.894
Living Area	0.856	0.737	0.498

DISCUSSION

The study focused on determining the prevalence of food allergies (FA) and understanding the knowledge and practices related to this condition among young Lebanese individuals. Moreover, the participation rate of females in the present study was considerably higher than males, approximately more than 3.83 times. This could be attributed to female participation in food-related research, likely because women often bear more responsibility for household shopping and meal preparation [18]. Results showed that 23.7% of young adult participants reported having food allergies, which is a rate lower than that revealed in previous studies performed in Lebanon [14]. Furthermore, the prevalence of FA among children accounted to 6.3%, which was in line with a previous study conducted among school children in Lebanon [19], on the other hand contradicted with the results of another study conducted on school children in Kuwait [20]. According to Irani & Maalouly (2015), the highest self-mentioned food allergens were eggs (19%), followed by strawberry (16%), peach, and milk (14%) [14]. Additionally, Elrahi et al. (2023) found that fruits (29.6%), spices (21.4%), and vegetables (12.9%) were the most commonly self-reported food allergens (18). Interestingly, these results contradicted with ours, in which spices (5.3%) and strawberries (5.3%) were the top allergen, followed by milk and its derivatives (3.9%), and eggs (3.9%) [17]. However, assessing the prevalence and incidence of food allergies can be challenging due to various factors influencing their evaluation. These factors include differences in allergy definitions, study populations, methodologies, geographic variations, age demographics, and dietary exposures [1]. Concerning the symptoms of food allergy, hives, itching, and redness were the most commonly reported. Our findings were different than those reported in previous studies conducted in Mauritius and Lebanon, where cutaneous and gastrointestinal symptoms were identified as the most commonly revealed food allergy symptoms [18, 19].

The knowledge score of the participants (34.07%) was considered high. There was a statistically significant relationship between age group and educational level with knowledge scores. Our findings showed that females exhibited greater knowledge of food allergies and allergens compared to males; this was in line with previous findings from similar studies conducted at Saudi Arabia [16]. Furthermore, the majority of the participants showed awareness that FA involves an abnormal immune system response. However, regarding the hereditary aspect of allergies, a significant gap in knowledge was observed with less than one fourth of respondents correctly identifying this. This emphasized the need for additional educational programs and

campaigns to be implemented on food allergy awareness, preventive measures, and treatment guidelines. Additionally, less than half of the participants were aware that allergy symptoms could not be alleviated without medical intervention. Around 53.9% of the participants reported that pharmacist, nurse or doctor should only give epinephrine injection in the muscle which is much lower compared to other finding [16]. Furthermore only 46.1% of the participants differentiate between lactose intolerance and the allergy of milk, this was in line with findings from previous studies, where 80% of the participants considered lactose intolerance as a form of food allergy [21].

In our study, more than half of the respondents recognized that individuals with food allergies cannot safely consume even small amounts of the allergenic food. Moreover, the misconception that cooking methods, such as frying, can eliminate food allergens was not prevalent among the participants. Our findings were consistent with those of previous studies conducted in Lebanon [16, 17]. Additionally, almost 40% of the participants reported always or sometimes checking product ingredients when making purchases, which contradicted with the results of a previous study performed in Lebanon [22].

where only 4.4% of the respondents checked product ingredients before purchasing them.

CONCLUSION

In conclusion, our study sheds light on the knowledge, attitudes, and practices regarding food allergies among Lebanese adults. Even though adequate knowledge was noticed among the participants, notable gaps in some aspects were observed. Ongoing education is crucial for improving knowledge and practices of individuals with food allergies in Lebanon. This can be achieved by offering the individuals having FA the tools and resources they need to effectively manage their conditions and minimize the impact of allergens on their daily lives. By addressing these gaps, the overall management and wellbeing of individuals with FA in Lebanon might be enhanced. Indeed, in Lebanon, it is necessary to improve the KAP towards food allergies by implementing effective awareness providing a safer environment for individuals of all age groups

ACKNOWLEDGMENT

The authors express their gratitude to Lebanese International University for their cooperation in addition to those who participated in the investigation.

HUMAN AND ANIMAL RIGHTS

This study was based on research that did not include the use of animals. Participants provided informed consent before participating in the study, and all human procedures followed modern standards.

REFERENCES

1. Sicherer S H and Sampson H A. Food allergy: epidemiology, pathogenesis, diagnosis, and treatment. *J Allergy Clin Immunol*. 2014;**133**(2): 291.e5–307.e5. doi:10.1016/j.jaci.2013.11.020.
2. Ben-Shoshan M, Harrington DW, Soller L, Fragapane J, Joseph L, St Pierre Y, Godefroy SB, Elliott SJ and Clarke AE. A population-based study on peanut, tree nut, fish, shellfish, and sesame allergy prevalence in Canada. *J Allergy Clin Immunol*. 2010;**125**(6):1327–13351.
3. Ortolani C and Pastorello EA. Food allergies and food intolerances. *Best Pract Res Clin Gastroenterol*. 2006;**20**(3):467-83. doi: 10.1016/j.bpg.2005.11.010.
4. Iweala OI, Choudhary SK, and Commins SP. Food allergy. *Curr Gastroenterol Rep*. 2018;**20**(5):17.
5. Yu W, Freeland DMH and Nadeau KC. Food allergy: immune mechanisms, diagnosis and immunotherapy. *Nat Rev Immunol*. 2016;**16**(12):751–65. doi: 10.1038/nri.2016.111.
6. Gupta RS, Warren CM, Smith BM, Jiang J, Blumenstock JA, Davis MM, Schleimer RP and Nadeau KC. Prevalence and severity of food allergies among US adults. *JAMA Netw Open*. 2019 Jan 4;**2**(1) doi:10.1001/jamanetworkopen.2018.5630.
7. Chung SY, Reed S and Zhang D. Peanut allergens attached with p-aminobenzamidine are more resistant to digestion than native allergens. *Food Nutr Sci*. 2016;**7**(14):1352–63. doi: 10.4236/fns.2016.714123.

8. Licari A, Manti S, Marseglia A, Brambilla I, Votto M, Castagnoli R, Leonardi S and Luigi Marseglia G. Food allergies: current and future treatments. *Medicina*. 2019;**55**(5):120.
9. Chafei H. *Food allergen labeling: A case of Lebanon*. Thesis submitted in partial fulfillment of the requirements for the degree of Master of Science to the Department of Nutrition and Food Sciences of the Faculty of Agricultural and Food Sciences at the American University of Beirut, Beirut, Lebanon. April 2021.
10. Loh W and Tang MLK. The epidemiology of food allergy in the global context. *Int J Environ Res Public Health*. 2018 Sep 18;**15**(9):2043. doi: 10.3390/ijerph15092043.
11. Lloyd M, Dunn Galvin A and Tang MLK. Measuring the impact of food immunotherapy on health-related quality of life in clinical trials. *Front Allergy*. 2022 Jul 12;**3**: 941020. doi: 10.3389/falgy.2022.941020.
12. Althumiri NA, Basyouni MH, AlMousa N, AlJuwaysim MF, BinDhim NF and Alqahtani SA. Prevalence of self-reported food allergies and their association with other health conditions among adults in Saudi Arabia. *Int J Environ Res Public Health*. 2021 Jan 5;**18**(1):347. doi: 10.3390/ijerph18010347
13. Al-Hammadi S, Al-Maskari F and Bernsen R. Prevalence of food allergy among children in Al-Ain city, United Arab Emirates. *Int Arch Allergy Immunol*. 2010;**151**(4):336-42. doi: 10.1159/000250442. Epub 2009 Oct 22.
14. Irani C and Maalouly G. Prevalence of self-reported food allergy in Lebanon: a Middle-Eastern taste. *Int Scholarly Res Notices*. 2015; **2015**:1–5. doi: 10.1155/2015/639796.
15. Sakakini J, Irani C, Bikai R, Sahyoun G, Hallit S, Salameh P and Dano D. Prevalence of food allergy among schoolchildren in Lebanon. *Int Arch Allergy Immunol*. 2022;**183**(6):611-616. doi: 10.1159/000521147.
16. Dimassi H, Haidar S, Issa S and Hassan HF. Food allergies and allergens: characterization and perceptions among diagnosed food allergic individuals in Lebanon. *World Allergy Organ J*. 2020 Nov 9;**13**(11):100481. doi: 10.1016/j.waojou.2020.100481
17. Elrahi B, Mehanna Z, Haidar S, Serhan M and Hassan HF. Food allergies and allergens in Lebanon: characterization and perceptions toward labeling. *World Allergy Organ J*. 2023 Jan 20;**16**(2):100743. doi: 10.1016/j.waojou.2023.100743.
18. Soogali NB and Soon JM. Food allergies and perceptions towards food allergen labelling in Mauritius. *Food Control*. 2018; **93**:144–149.
19. Sakakini J, Irani C, Bikai R, Sahyoun G, Hallit S, Salameh P and Dano D. Prevalence of food allergy among schoolchildren in Lebanon. *Int Arch Allergy Immunol*. 2022;**183**(6):611-616. doi: 10.1159/000521147.
20. Ziyab AH. Prevalence of food allergy among schoolchildren in Kuwait and its association with the coexistence and severity of asthma, rhinitis, and eczema: a cross-sectional study. *World Allergy Organ J*. 2019 Mar 30;**12**(4):100024. doi: 10.1016/j.waojou.2019.100024.
21. Gohal G. Food allergy knowledge and attitudes among school teachers in Jazan, Saudi Arabia. Open Allergy J. 2018;9(1):1–7. doi: 10.2174/1874838401809010001.
22. Khanafer M, El Harake MD, Toufeili I and Kharroubi SA. Knowledge, attitudes and practices of the Lebanese community toward food adulteration. *Foods*. 2022 Oct 12;**11**(20):3178. doi: 10.3390/foods11203178.

Circular economy and sustainable development goals approaches for environment improvement in Uzbekistan

Ergash Egamberdievich Kobilov[1], Kh.F. Batirov[1], F.S. Mardonava[1], Anzhelika Karaeva[2], Alberto Pietro Damiano Baltrocchi[2], Marco Carnevale Miino[2], Ramona Giurea[3,4], Marco Ragazzi[5], Vincenzo Torretta[2], Elena Cristina Rada[2,a)]

[1]*Department of Ecology and Life Safety, Samarkand State University, Samarkand, Uzbekistan*
[2]*Department of Theoretical and Applied Science, Insubria University, Varese, Italy*
[3]*Department of Industrial Engineering and Management, Lucian Blaga University of Sibiu, Sibiu, Romania*
[4]*Department of Communications, IT and Cyber Security Nicolae Balcescu Land Forces Academy, Sibiu, Romania*
[5]*Department of Civil Environmental and Mechanical Engineering, University of Trento, Trento, Italy*

corresponding author: [a)]*elena.rada@uninsubria.it*

Abstract. The article examines some criticalities of environmental pollution in Uzbekistan, which in the current situation will inevitably lead to sad consequences and threats to the population of the Republic and in general in the field of environmental management. This scenario requires already today urgent solutions from the perspective of modern requirements. Considerations on subjects potentially linked to circular economy are reported: sectors concern first waste management but also wastewater, water and air pollution for their direct and indirect connection with circular economy activities.

INTRODUCTION

Since the present millenium, the World's scientists and the United Nations worked togheter in order develop documents that could help the improvements of the human life in all its issues. The vision is aimed to put in the first place the environment sustainability and the citizen from all the World, thanks also to global partnerships. MDGs (Millenium Development Goals) known also as United Nations Millennium Declaration was presented in 2000 and gave the targets to be achieved until 2015 through 8 goals [1]. The official MDG Gap Task Force Report from 2015 showed that the obtained progress still have some gaps [2,3]. A new Agenda for 2030, known as Sustainable Development Goals or Agenda 2030 with 17 goals, was issued in order to have better results in prosperity and planet sustainability for future generations, and also to arrive to improvements in education, health, equitable growth and sustainable production and consumption all thanks to a strong collaboration at global level [4-10]. This new Agenda together with new Circular Economy Action Plan, issued in 2020, updating all the other Circular Economy (CE) concepts, and FIT for 55 Packages are useful for arriving to a green World and an EU climate-neutral by 2050, indicating as prority to focus on waste with more attention to Municipal Solid Waste (MSW), drinking water (DW), wastewater (WW) sectors and specifically to their management and treatment in view of resource and energy recovery [11-19].

Countries worked to implement them not only at EU level but in all the World [20-28]. A research on the Scopus® database regarding CE and MSW, WW, DW showed that scientists published since 2007 reserch on WW, since 2009 research on MSW (less than one third of papers compared with the ones from WW) and only since 2011 research on DW (that represents only 5% compared to the articles on WW).

Central Asia is made up of Kazakhstan, Kyrgyzstan, Turkmenistan, Tajikistan, and Uzbekistan. In recent years also in these countries the Circular Economy and Sustainable Developments Goals have become important and it is necessary to have them implemented.

Taking into account the aspects reported above, in order to decrease environmental pollution and to implement SDGs, the present paper presents and discusses proactively a state of the art of Uzbekistan. In this frame, it must be pointed out that Circular Economy is not yet implemented in Uzbekistan as officially declared by the Environmental

Technologies and Materials for Renewable Energy, Environment and Sustainability
AIP Conf. Proc. 3321, 060004-1–060004-7; https://doi.org/10.1063/5.0290581
Published under an exclusive license by AIP Publishing. 978-0-7354-5231-2/$30.00

Ministry late in 2023 [29]. That makes strategic the contribution of the present article to the implementation of CE in this context.

MATERIALS AND METHODS

The starting point of the research was the Scopus® database and the national Reports regarding the environment quality in Uzbekistan and national norms and/or legislation for MSW, WW and DW [42-45]. Topics potentially linked to circular economy were considered. Sectors of interest were first waste management but also wastewater, water and air pollution for their direct and indirect connection with circular economy. The following point of the work was oriented to discuss criticalities emerged in the first point and perspectives of improvement.

Being clear that environmental pollution, from a large perspective, is one of the main problems in Uzbekistan, and is and was caused by many sources (e.g., transboundary waters, underground nuclear explosions, domestic and industrial wastes, transport, etc with effects on human health [46-49]) the core of the present work is CE.

RESULTS AND DISCUSSION

Some scientists published papers concerning CE and SGDs in these countries pointing out that there are many barriers but also some prospective [30-36]. Regarding the Uzbekistan country the papers covered by the Scopus® database are few and with a variable subject (e.g., MSW dinamics in a landfilling, sorting useful materials from MSW, the use of the laser biotechnology for reclamation of contaminated soil, wastewater treatment, air pollution [37-41]). An overall vision is presented in Table 1, regarding, as an example, subjects like:

1. Microplastics in river.
2. Cement factories and co-combustion.
3. Food waste management in restaurants.
4. Dust storm.

Table 1. Details on Scopus® database and keywords of interest

Keywords	Number of articles (early June 2024)
Uzbekistan and environment	259
Uzbekistan and waste	49
Uzbekistan and air pollution	49
Uzbekistan and wastewater	12
Uzbekistan and sewage sludge	0
Uzbekistan and circular economy	0

Waste

According to [50, 51], up to 7 million tons of MSW is generated on the territory of Uzbekistan. Every year, on average, each citizen produces about 165 kg of municipal solid waste annually. This per-capita generation value is in contrast with what can be read in the National Report [29] where a value more than 4 times higher is reported. This discrepancy cannot be explained by the rate of collection of waste in the territory as the service of collection covers around 85% of the users [29].

The Presidential decree of 4.01.2024 identified the following shortcomings and problems in this area [52]:

1. the condition of the existing landfills does not meet environmental and sanitary requirements;
2. other facilities for waste management are lacking;
3. Over the past four years, the tariffs for waste management services have not been revised. This had a negative impact on the economic condition of sanitary cleaning enterprises;
4. as a result of the human factor in making payments for sanitation services, problems of incomplete implementation of a centralized electronic payment system and lack of integration with interdepartmental systems, accounts receivable for services rendered increased;
5. Contracts for the provision of waste collection and disposal services to legal entities have not been concluded, and the responsibility of legal entities on this issue has not been determined.

About one third of waste is sent for recycling, with and increasing trend as pointed out in Table 2. No information is available on the residues from recycling treatments: the focus on that is compulsory (e.g., to avoid anomalies as the uncontrolled discharge of plastic in the rivers). The rest is sent to landfills or disposed of, for example, by incineration, both supposed to be highly impacting [51]. Focus on food waste [52] could open to new perspectives of material recovery: compost production from source separated waste could contrast the chemicalization of agricultural production. Criticalities of food waste management are not fully clear as in the National Report we can read [29]: "Organic food waste is the least hazardous waste, as it does not damage the environment and decomposes relatively quickly (in about 2 weeks)". This is not correct as decomposition of food waste in landfills is responsible for greenhouse gas emissions and its composition needs more time. Supposing that high percentage of food waste will remain for many years in the unsorted MSW, the potentialities of biodrying should be explored in order to decrease, by co-combustion, the consumption of coal in cement factories and thermail power plants.

The disposal of toxic waste is also one of the challenges in the field of waste management: according to data for 2022, only 7.9% of highly toxic waste was sent for disposal, while in 2018 this figure was only 0.1%, which indicates the positive results of the programs implemented by the government (but a long way is still to do). Table 2 shows the main indicators of Uzbekistan in the field of waste management.

Power generated by the solar PV panel is dependent on the ambient temperature, solar irradiation, size of the solar panel and conversion efficiency of the PV module. The solar PV power generation is calculated on an hourly interval, as the weather conditions obtained were hourly [5].

Table 2. The main indicators of Uzbekistan in the field of waste management in the period from 2018 to 2022 [51]

Indicator	2018	2019	2020	2021	2022
Formation of highly toxic industrial waste per capita, tons	13.7	13.1	10.6	8.5	0.8
The share of neutralized waste of high hazardous class, %	0.12	0.2	0.2	0.29	7.6
The total volume of recycled waste, thousand tons, thousand tons	1370.1	1399.9	1025.9	1698.2	2200.0

In 2022 in Uzbekistan a lot of MSW was sent to 197 landfills, but most of them do not meet environmental and sanitary requirements [53]. The interest of foreign investor is opening to new approaches [54]. A plan for the construction of a MSW incineration was proposed in May 2024, thanks to a collaboration with China [55]. To this concern, attention to regulation for management and control should be made taking to account the expertise of a wider area in the World.

Overall, the country's solid waste management systems are poorly equipped to meet current demand. Only rudimentary waste management systems operate outside of Tashkent, collected waste is simply thrown into open landfills outside the settlement. Currently, the Government of Uzbekistan is developing and implementing programs to improve MSW management system and introduce selective waste collection, taking into account that the amount of waste is increasing because of population growth and economic development.

The recent Decree of the President of the Republic of Uzbekistan on Measures to Transform the Sphere of Ecology and Environmental Protection and the Organisation of the Activities of the Authorised State Body, 31 May 2023, No. UP-81 [56] seems to open to a more organised system of source separation and recycling of waste, to be integrated with energy recovery; indeed it is planned to:

- Introduce CE practices minimising landfilling;
- Gradually achieve full recycling and incineration of waste in landfills.

The first point shows that the vision for landfilling (minimisation) is in line with the one of the European Union (EU) where a target of maximum 10% of MSW generated must be complied with in the future.The second point focuses on the interest of material and energy recovery from sites to be remediated. In the EU the benefits of this strategy find obstacles from the economic sustainability of the interventions. However the different economic context of Uzbekistan could give different results is feasibility studies were made.

Despite the ongoing environmental control, there is still waste dumping by the population, including the formation of illegal dumps in settlements, on the lanes of highways, along the edges of fields, and on the banks of water bodies [29]. It is clear that a sensibility/awareness to environmental issues must be created. To this concern, Article 4 of the Law of the Republic of Uzbekistan on Nature Protection prescribes compulsory nature education in all types of educational institutions. Cabinet of Ministers Decision No. 434 of 27 May 2019 approved the Concept for the Development of Environmental Education in the Republic of Uzbekistan. The aim of the Concept is "to form and

develop environmental knowledge, awareness, and culture among the younger generation, to organize the environmental teaching and educational process effectively, and to further improve science in the field of ecology, using advanced and innovative technologies" [29].

Delays and potentialities of CE can be seen by looking at the data from sectors different from MSW [29]:

- In a frame where about 115 million tons of industrial waste are generated annually, only an insignificant part of them is used as secondary raw materials.
- Only 2% of construction waste was recycled in 2021-2022.
- Infected medical waste is destroyed by autoclaving at the sites where it is generated but cases when medical waste is thrown away together with household waste are not exceptional and no CE activity is reported after treatment.

Water and wastewater

According to [57], Uzbekistan may face a large shortage of fresh water by 2040. In the whole country, the area of irrigated land is about 4.3 million hectares, which is about 14% of agricultural land. One of the causes of land degradation and desertification is the excessive use of water resources. Irrational irrigation practices and outdated water supply infrastructure requiring large-scale reconstruction have led to rapid desertification and drying up of the Aral Sea. Climate change will further exacerbate water scarcity in Uzbekistan, may increase the duration and frequency of droughts, as it was in 2000, 2008, 2011, 2014 and 2018, and cause serious problems with meeting the needs of the economy in water. Over the past 15 years, water availability per capita has decreased from 3,048 m3 to 1,400 m3. This use of water, far to be optimized, dilutes the pollutants making more complex its treatment and re-valorisation.

Zooming on the facilities, in Uzbekistan there are 5 large WW treatment plants. Limits for dozens of pollutants are reported in terms of primarily maximum permissible concentrations (MAC) and maximum permissible emissions (MPC) [58,59] thus the problem of the sector seems to be the lack of plants, the management of the existing ones and their age (two of them were constructed early in the '60s). The main problem that the WWTPs in Uzbekistan have is that they were built in a different hystorical context and now most of them is not operating due to equipment depreciation or even if they operate, the quality of treatment is extremely low. Currently the Uzbekistan state is implementing many projects for improving wastewater system in the whole country.

According to the National Report [29], "dewatered sludge from municipal wastewater treatment plants is successfully used as organic fertilizer in farms near cities". That could hidden a problem as one of the biggest problems emerged in the European Union is the contamination of sludge (e.g. heavy metals) that makes them not compatible with agriculture.

Air Pollution

Pollution from stationary sources is largely caused by the main industries: energy, oil and gas industry, metallurgy, chemical industry, construction industry and utilities. Pollution from mobile sources is mainly caused by an increase in the number of vehicles. Air pollution is aggravated by the unfavorable climatic conditions of Uzbekistan (arid and drought-prone climate). Dust of natural origin can explain the fact that the regulation limit of PM10 for air quality is higher than the one in force in the European Union. Emissions from mobile sources significantly exceed emissions from stationary sources, which is due to the large number of cars and relatively low fuel requirements. A ban on the use of fuel below the Euro-4 standard was introduced only in 2020. Most of the cars produced and in use comply with the Euro-2 standard [60-66]. Recently, air pollution in the cities of Uzbekistan, and especially the city of Tashkent worsened [67]. This pollution is mainly made by the 11.9 thousand factories located within citied. The modernization of these in order to reduce the environmental pollution is expensive and not profitable for most entrepreneurs since their main goal is to maximize profits and without a legislative requests and fines will not be considered. Today, there are about 4 million cars in the country, of which 100,000 are defective, which leads to an increase in emissions of pollutants. There is an increase in the number of personal vehicles, which leads to an increase in the number of emissions from motor vehicles. Since 2020, Uzbekistan has prohibited the commissioning of new capacities for the production of motor fuels of an ecological class below Euro-4. From the point of view of CE what can expect from the substitution of old vehicles by modern ones as a consequence of the introduction of more stringent limits on the emissions is:

- An increase of waste from end of life vehicles. This waste could be an opportunity for developing new strategies of recycling

- The introduction of modern vehicles that could be in part designed with a strategy of material recycling.

Discussion

To combat environmental pollution, it is necessary to take measures to reduce emissions of harmful substances, increase the efficiency of resource use and develop environmentally friendly technologies. But not everything depends on the state; citizens must also understand the level of responsibility for the environment in general, save water, sort waste, etc.

Ensuring environmentally safe sustainable development in market conditions should include:

- environmentally safe placement of productive forces;
- environmentally friendly development of industry and agriculture;
- sustainable use of renewable natural resources;
- rational use of non-renewable natural resources;
- waste disposal, expanded reproduction of secondary resources;
- Emergency prevention.

Thus, only through joint efforts Uzbekistan can avoid going beyond the point of no return, since it have already learned from the bitter experience of the disappearance of the Aral Sea and can no longer make mistakes.

In this frame, some considerations can be made as integration of the vision and strategies that presently the Ministry of the Environment wrote in the recent National Report on the environment [29]:

- Residual MSW has a composition suitable for a treatment of biodrying followed by post treatments aimed to material recovery [68, 69]. A feasibility study to analyse its potentiality for producing solid recovered fuel to be used in cement factory could be useful to check if this strategy can help to decrease the pressure on the landfills and open to a new strategy for energy and material recovery (in coherence with circular economy).
- Sewage sludge should be subject to adequate (enhanced) characteristion in order to exclude the ones not compatible with agriculture [70, 71].
- Hospital waste management in Uzbekistan is in a transient pilot period. For that reason it could be useful to check the viability of an additional process not cited by the National Report, based on sterilisation and material recovery, presently under validation by a multy-year research based in Italy but having an international network as support [72].
- Being Circular Economy not yet introduced in the national strategies, its development could be helped by the cooperation of universities taking into account also the recent agreement signed between Uzbekistan and Italy [73].
- The recent agreement between Italy and Uzbekistan (2023) [73] takes into account also the need of improving the environmental consciousness of the population. In this frame the role of primary school is not taken into account. What should be explored as additional strategy is the potentiality of involving primary school pupils in international bilateral collaboration.

CONCLUSIONS AND DEVELOPMENTS

Uzbekistan is facing a transition in the management of waste. Criteria for that can be found in ministerial documents but a common need is the development of an adequate campaign of characterizations of the waste streams, present and expected. Only through a careful characterization of them it will be possible to set a modern approach for their management. Contacts with contexts where Circular Economy is already visible in the society can help in accelerating this transition that can develop in parallel with the involvement of all the levels of the education as a correct management of the environment cannot be based only on technical aspects. In this frame the contacts with Italian bodies can be an additional opportunity for improving the management of the environment.

REFERENCES

[1] https://www.who.int/news-room/fact-sheets/detail/millennium-development-goals-(mdgs)#:~:text=The%20United%20Nations%20Millennium%20Declaration,degradation%2C%20and%20discri

mination%20against%20women.
[2] https://www.un.org/millenniumgoals/pdf/MDG_Gap_2015_E_web.pdf
[3] Georgeson L and Maslin M 2018 *Geo: Geograph Environ.* **5**(1), e00049.
[4] https://sdgs.un.org/goals
[5] Kanie N, Abe N, Iguchi M, Yang J, Kabiri N, Kitamura Y, Mangagi S, Miyazawa I, Olsen S, Tasaki T, Yamamoto T, Yoshida T, Hayakawa Y 2014 *Sustain.* **6**(4), 1761–1775.
[6] Ciglazier W 2015 *Sci.* **349**(6252), 1048-1050.
[7] Wagner DA 2015 *Int. Rev. Educ.* **61**(3), 372-341.
[8] Buse Hawkes S 2015 *Global. Health* **11**(1), 13.
[9] Georgeson L Maslin M 2018 *Geo: Geograph. Environ.* **5**(1), e00049.
[10] Hickmann T, Biermann F, Spinazzola M, Ballard C, Borger M, Forestier O, Kalfagianni A, Kim R, Montesano FS, Peek T, Senit CA, Van Driel M, Vijge MJ, Yunita A 2023 *Sustain. Develop.* **31**(3), 1214–1225.
[11] https://environment.ec.europa.eu/strategy/circular-economy-action-plan_en
[12] Rada EC 2023 *Environ. Climate Technol.* **27**(1), 989-998.
[13] https://www.consilium.europa.eu/en/policies/green-deal/fit-for-55/
[14] Raman R, Lathabhai H, Pattnaik D, Kumar C, Nedungadi P, 2024 *Discov. Sustain.* **5**(1), 7.
[15] Arun M, Barik D, Chandran SSR 2024 *Chem. Eng. J. Adv.* **18,** 100589.
[16] Skare M, Gavurova B, Kovac V 2024 *Resour. Policy* **92,** 104962.
[17] Collivignarelli MC, Abbà A, Miino MC, Caccamo FM, Torretta V, Rada EC, Sorlini S 2021 *Int. J. Environ. Res. Public. Health* **18**(1),77, 1-24.
[18] Kiselev A, Glushankova I, Rudakova L, Baynkin A, Magaril E, Rada EC 2020 *Int. J. Energ. Product. Manage*. **5**(3), 234-244.
[19] Kiselev AV, Magaril ER, Rada EC 2020 *WIT Transact. Ecol. Environ.* **237,** 109-120.
[20] Paes MX, Puppim de Oliveira JA, Mancini SD, Rieradevall J 2024 *Habitat Int.* **143**, 102990.
[21] Delgado A, Rodriguez DJ, Amadei CA, Makino M 2024 *Utilit. Policy* **87,** 101604.
[22] Maalouf A and Agamuthu P 2023 *Waste Manage. Res.* **41**(9), 1420–1434,.
[23] Adeleke O, Akinlabi S, Jen TC, Dunmade I 2021 *Transact. Royal Soc. of South Africa* **76**(1), 53–66.
[24] Smol M 2023 *Adv. Sci. Technol. Innov*. 199–211.
[25] Koseoglu-Imer DY, Oral HV, Coutinho Calheiros CS, Kreminski P, Guclu S, Pereira SA, Surmacz-Gorska J, Plaza E, Samaras P, Binder PM, van Hullebusch ED, Devolli A 2023 *J. Environ. Manage.* **345,** 118627.
[26] Chioatto E and Sospiro P 2023 *Environ. Develop. Sustain.* **25**(1), 249–276.
[27] Pao HT and Chen CC 2022 *Waste Manage. Res*. **40**(7), 969–979.
[28] Jąderko K 2018 *Proc. Int. Multidiscip. Sci. GeoConf. Surv. Geol Mining Ecol. Manage.* **18(**4.2), 17–24.
[29] Ministry of Ecology, Environmental Protection and Climate Change of the Republic of Uzbekistan. (2023). National state of the environment report: Uzbekistan. International Institute for Sustainable Development.
[30] Filipovic S, Orlov A, Panić AA 2024 *Energ. Sustain. Soc.* **14**(1), 25.
[31] Litvinova TN, Karrieva YK, Alisheva PK, Sanovic M.A 2023 *Environ. Footpr. Eco-Design. Prod. Process.* **Part F1766**, 399–407.
[32] Radelyuk I, Jia X, Yelubay M, Assanov D 2020 *Sustain. Water Resour. Manage*. **10**(2), 79.
[33] Bjelić D, Markić DN, Prokić D, Malinović BN, Panić AA 2024 *Energ. Sustain. Soc.* **14**(1), 3.
[34] Wang W, Liu T, Luo G 2022 *Arid Zone Res.* **39**(6), 1801–1809.
[35] Wang X, Chen Y, Fang G, Li Z, Liu Y 2022 *J. Clean. Prod.* **378,** 134574.
[36] Serafimova E and Petkova V 2021 *J. Chem. Technol. Metallurg.* **56**(2), 348–352.
[37] Doanh T, Hareb H, Hans S, Boutin C, Anarbaev M, Wu W 2012. *Geotech. Special Publ.* ***179,*** 253–260.
[38] Abduganiev N, Tursunov O, Kodirov D, Sabirov E, Kilichov O 2020 *Proc. IOP Conf. Series: Earth and Environ. Sci.* **614**(1), 012005.
[39] Khankelov TK 2021 *Acad. J. Manufact. Eng,* ***19***(4), 97–102.
[40] Tursunov O, Dobrowolski JW, Khujaev O, Abduganiev N, Nazarova OJ, Yuldosheva DJ 2021 *Proc. IOP Conference Series: Earth and Environ. Sci.* **939**(1), 012083.
[41] Khankelov T, Mukhitdinov A, Ibrokhimov S, Aslonov N, Mirkholikov S 2022 *AIP Conf. Proc.* **2432**, 030028.
[42] https://www.iisd.org/system/files/2024-02/uzbekistan-state-of-the-environment-en.pdf. International Institute for Sustainable Development, 2023. National report on the state of the environment: Uzbekistan.

[43] Kobilov EE, Batirov KhF, Ozdamirova EM 2023 *Proc. BIO Web of Conf.* **63**, 03002.
[44] Nosirov MG and Kobilov E 2024 *Proc. Int Conf on Circular. Sustain. and Resil. in Water,* Italy.
[45] https://www.norma.uz/uz/qonunchilikda_yangi/aholi_alohida_chiqindi_yigish_uchun_mahsus_paketlar_bilan_taminlanadi. Decision "On measures to improve waste management and reduce their negative impact on the environmental situation".
[46] Nurmatova A, Dzholdosheva T, Esenamanova N, Toktosunova C, Niyazbekova S, Rozhkov V 2024 *Proc. BIO Web of Conf.* **93**, 04017.
[47] Khasanov S, Akhmedova G, Tukhtaev U, Safarov A, Proshad R 2023 *Environ. Monit. Assess.* **195**(12), 1412.
[48] Yuldasheva S and Norboev Z 2023 *Proc. BIO Web of Conf.* **65**, 07005.
[49] Baltrocchi APD, Maggi L, Dal Lago B, Torretta V, Szabó M, Nasirov M, Kabilov E, Rada EC 2024 *Sustain.* **16**(1), 324.
[50] https://ns1.stat.uz/goal/15 SDG 12: Responsible consumption and production. Statistic agency under the president development of the republic of Uzbekistan. (In Russian)
[51] https://nsdg.stat.uz/publications/27_Sustainable Development Goals in the Republic of Uzbekistan 2023. (In Russian)
[52] Kobilov EE, Batirov KhF, Aslakhanova SA 2023 *Proc. SHS Web of Conf.* **172**, 02007.
[53] https://lex.uz/ru/docs/6733912_Decree of the President of the Republic of Uzbekistan, dated 04.01.2024 No. UP-5 "On measures to improve the waste management system and reduce their negative impact on the environmental situation". (In Russian)
[54] https://www.roedl.com/insights/life-sciences-law/uzbekistan-waste-management-reform-disposal-foreign-investors-investment
[55] https://daryo.uz/en/2024/05/06/uzbekistan-plans-to-build-first-waste-incineration-plant-in-partnership-with-china).
[56] Decree of the President of the Republic of Uzbekistan on Measures to Transform the Sphere of Ecology and Environmental Protection and the Organisation of the Activities of the Authorised State Body, 31 May 2023, No. UP-81
[57] https://www.suez.com/en/africa/news/water-conservation-and-efficient-usage-in-uzbekistan-has-become-a-top-priority-at-the-presidential-level. Water conservation and efficiency in Uzbekistan: an inspiring example for the African continent. Suez.
[58] https://www.isdb.org/sectors/case-studies/tashkent-sewerage-project-uzbekistan
[59] https://www.ebrd.com/work-with-us/projects/psd/horezm-wastewater-project.html
[60] Torretta V, Rada EC, Panaitescu V, Apostol T 2012 *UPB Sci. Bull. Series D: Mech. Eng*. **74**(4), 241-248.
[61] Ionescu G, Apostol T, Rada EC, Ragazzi M, Torretta V, 2013 *UPB Sci. Bull. Series D: Mech. Eng,* **75**(2), 175-186
[62] Istrate IA, Oprea T, Rada EC, Torretta V 2014 *WIT Transact. Ecol. Environ.* 191, 1381-1389.
[63] Dimitrovski D, Manev N, Dzinlev V 2023 *Environ. Eng. Manage. J.* **22**(12), 2045–2055.
[64] Čekerevac Z, Dvořák Z, Prigoda L 2022 *Commun. Sci. Lett. of the Univ of Žilina* **24**(1), B49–B58.
[65] Zhang G, Wu L, Chen J 2021 *Int. J. Environ. Res. Public Health* **18**(4), 1–18, 1594.
[66] https://www.iqair.com/world-air-quality-ranking
[67] Shukhrat U, Kobilov EE, Batirov HF, Tukhtaev MK, Agzamov VB 2023 *Proc. BIO Web of Conf.* **76,** 01014.
[68] Rada E.C, Ragazzi M, Badea A 2012 *UPB Sci. Bul. Series D: Mech Eng.* **74**(3), 209-216.
[69] Velis CA, Longhurst PJ, Drew GH, Smith R, Pollard SJT 2009 *Bioresour. Technol.* **100**(11), 2747-2761.
[70] Sugurbekova G, Nagyzbekkyzy E, Sarsenova A, Danlybayeva G, Anuarbekova S, Kudaibergenova R, Frochot C, Acherar S, Zhatkanbayev Y, Moldagulova N 2023 *Sustain.* **15**(7), 6112.
[71] Buta M, Hubeny J, Zieliński W, Harnisz M, Korzeniewska E 2021 *Ecotoxicol. Environ. Saf.* **214,** 112070
[72] Castellucci A, Ragazzi M, Berghi F, Guirreri D, Rama I 2022 *WIT Transact. Ecol. Environ.* **257,** 97-106.
[73] Bilateral Agreement Italy – Uzbekistan, 8th June 2023: https://www.governo.it/it/articolo/dichiarazione-congiunta-relazioni-di-partenariato-strategico-tra-italia-e-uzbekistan/22843